

# Dynamic Stall Suppression Using Combustion-Powered Actuation (COMPACT)

*Claude G. Matalanis, Patrick O. Bowles, Solkeun Jee, Byung-Young Min,  
Andrzej E. Kuczek, Paul F. Croteau, and Brian E. Wake  
United Technologies Research Center, East Hartford, Connecticut*

*Thomas Crittenden and Ari Glezer  
Georgia Institute of Technology, Atlanta, Georgia*

*Peter F. Lorber  
Sikorsky Aircraft Corporation, Stratford, Connecticut*



## NASA STI Program ... in Profile

Since its founding, NASA has been dedicated to the advancement of aeronautics and space science. The NASA scientific and technical information (STI) program plays a key part in helping NASA maintain this important role.

The NASA STI Program operates under the auspices of the Agency Chief Information Officer. It collects, organizes, provides for archiving, and disseminates NASA's STI. The NASA STI Program provides access to the NTRS Registered and its public interface, the NASA Technical Reports Server, thus providing one of the largest collections of aeronautical and space science STI in the world. Results are published in both non-NASA channels and by NASA in the NASA STI Report Series, which includes the following report types:

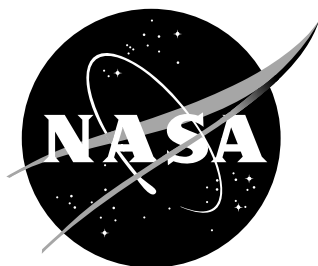
- **TECHNICAL PUBLICATION.**  
Reports of completed research or a major significant phase of research that present the results of NASA programs and include extensive data or theoretical analysis. Includes compilations of significant scientific and technical data and information deemed to be of continuing reference value. NASA counterpart of peer-reviewed formal professional papers, but having less stringent limitations on manuscript length and extent of graphic presentations.
- **TECHNICAL MEMORANDUM.**  
Scientific and technical findings that are preliminary or of specialized interest, e.g., quick release reports, working papers, and bibliographies that contain minimal annotation. Does not contain extensive analysis.
- **CONTRACTOR REPORT.**  
Scientific and technical findings by NASA-sponsored contractors and grantees.

- **CONFERENCE PUBLICATION.**  
Collected papers from scientific and technical conferences, symposia, seminars, or other meetings sponsored or co-sponsored by NASA.
- **SPECIAL PUBLICATION.**  
Scientific, technical, or historical information from NASA programs, projects, and missions, often concerned with subjects having substantial public interest.
- **TECHNICAL TRANSLATION.**  
English- language translations of foreign scientific and technical material pertinent to NASA's mission.

Specialized services also include organizing and publishing research results, distributing specialized research announcements and feeds, providing information desk and personal search support, and enabling data exchange services.

For more information about the NASA STI Program, see the following:

- Access the NASA STI program home page at [\*\*http://www.sti.nasa.gov\*\*](http://www.sti.nasa.gov)
- E-mail your question to [\*\*help@sti.nasa.gov\*\*](mailto:help@sti.nasa.gov)
- Phone the NASA STI Help Desk at 757-864-9658
- Write to:  
NASA STI Information Desk  
Mail Stop 148  
NASA Langley Research Center  
Hampton, VA 23681-2199



# Dynamic Stall Suppression Using Combustion-Powered Actuation (COMPACT)

*Claude G. Matalanis, Patrick O. Bowles, Solkeun Jee, Byung-Young Min,  
Andrzej E. Kuczek, Paul F. Croteau, and Brian E. Wake  
United Technologies Research Center, East Hartford, Connecticut*

*Thomas Crittenden and Ari Glezer  
Georgia Institute of Technology, Atlanta, Georgia*

*Peter F. Lorber  
Sikorsky Aircraft Corporation, Stratford, Connecticut*

National Aeronautics and  
Space Administration

Langley Research Center  
Hampton, Virginia 23681-2199

The use of trademarks or names of manufacturers in this report is for accurate reporting and does not constitute an official endorsement, either expressed or implied, of such products or manufacturers by the National Aeronautics and Space Administration.

Available from

NASA STI Program  
Mail Stop 148  
NASA Langley Research Center  
Hampton, VA 23681-2199

National Technical Information Service  
5285 Port Royal Road  
Springfield, VA 22161  
703-605-6000

This report is available in electronic form at <http://www.sti.nasa.gov> and <http://ntrs.nasa.gov>

## I. Table of Contents

I.	Table of Contents.....	5
II.	Acknowledgments.....	9
III.	Executive Summary.....	10
IV.	Nomenclature.....	11
V.	Introduction and Background.....	14
VI.	Aerodynamic Design.....	17
1.	Summary.....	17
2.	Computational Method.....	17
A.	Geometry and Mesh.....	17
B.	CFD Solver and Flow Conditions.....	18
3.	Computational Results.....	19
A.	Preliminary Validation.....	19
B.	Two Dimensional Results.....	20
C.	Three-Dimensional Results.....	21
4.	Conclusions.....	23
VII.	Low Speed Test Article Design and Fabrication.....	40
1.	Actuator Chamber Design.....	40
2.	Pitching Airfoil Design and Fabrication.....	44
3.	Actuator Support Systems.....	48
VIII.	Low-Speed Wind Tunnel Tests.....	53
1.	Static Airfoil Results.....	53
2.	Dynamically Pitching Airfoil Results.....	59
IX.	Final Actuator Design Enhancements.....	71
1.	Actuator Design Changes Between Low- and High-Speed Models.....	71
X.	High-Speed Test Article Design and Fabrication.....	75
1.	VR-12 Airfoil: Fabrication and Assembly.....	79
2.	VR-12 Airfoil: Pre-Test Assembly and Instrumentation.....	82
3.	Actuator Design for Installation.....	83
A.	Initial Single-Row Actuator Design.....	83
B.	Modified Single-Row Actuator Design.....	86
C.	Dual-Row Actuator Design.....	89

D.	Actuator Control Systems.....	91
4.	Model Installation in the NASA Glenn IRT .....	93
5.	Pressure Sensors.....	101
6.	Control and Data Acquisition Systems .....	105
7.	Pressure Sensors.....	107
A.	Kulite Pressure Transducers .....	109
B.	Electronic Pressure Scanners.....	109
8.	Unsteady Data Processing.....	113
A.	Bad Tap Corrections.....	114
B.	Load Coefficients and Integration .....	115
C.	Tufts.....	118
9.	Particle-Image Velocimetry .....	119
10.	NASA Glenn Icing Research Tunnel .....	124
XI.	High-Speed Wind Tunnel Test Results.....	127
1.	High-Speed Model Configurations .....	127
2.	Baseline Model High Speed Wind Tunnel Test Results.....	131
A.	Steady Baseline Results.....	131
B.	Unsteady Baseline Results.....	136
C.	Comparison of Test Entries 1 and 2 .....	149
D.	Comparison of Baseline and Taped Slot Leading edges .....	159
3.	High-Speed Wind Tunnel Test Steady COMPACT Results.....	170
A.	Entry 1 .....	170
B.	Entry 2 .....	178
4.	High-Speed Wind Tunnel Unsteady COMPACT Results .....	199
A.	Single-Row COMPACT Results.....	199
B.	Dual-Row COMPACT Results .....	244
5.	Particle-Image Velocimetry Measurements.....	290
A.	Images and Seed Particles .....	291
B.	Steady Results.....	296
C.	Unsteady Results .....	303
6.	COMPACT Chamber Pressure Measurements.....	308
7.	Comments on Three-Dimensional Effects .....	308
8.	Post-Test Actuator Examination .....	311

9.	High-Speed Test Concluding Remarks .....	313
XII.	Post-Test CFD and Comparisons with Experiments .....	315
1.	Modified computational methods.....	315
2.	Post-test CFD results .....	316
A.	Steady airfoils .....	316
B.	Pitching airfoils.....	317
C.	Summary .....	319
XIII.	System-Level Modeling .....	333
1.	System-Level Modeling Approach .....	333
A.	Trim Solver.....	333
B.	Rotor Model.....	333
C.	Dynamic Stall Table .....	334
D.	Dynamic Stall Hysteresis Loop Scaling .....	335
2.	Performance Analysis Results.....	336
A.	Thrust Sweep .....	336
B.	Power and Thrust Benefit .....	341
C.	Speed Envelope Benefit.....	342
D.	Summary.....	343
XIV.	Comparisons with Other Flow Control Techniques.....	345
XV.	Conclusions.....	356
XVI.	New Technology .....	358
1.	Discoveries .....	358
2.	Software .....	358
XVII.	References .....	359
	Appendix 1. Structural Analysis.....	366
1.	Main Airfoil and Supporting Hardware .....	366
A.	Overview .....	366
B.	Actuators and Leading edge Components .....	380
2.	References .....	383
	Appendix 2. Low-Speed Wind Tunnel Test – Load Measurements.....	385
	Appendix 3. High Speed Test Baseline Data.....	400
	Appendix 4. High-Speed Wind Tunnel Tests – Unsteady Results .....	420
1.	Test Entry I – Test Results .....	420

A.    Unsteady Results .....	420
2.    Test Entry II – Test Results.....	443
A.    Unsteady Actuated Results .....	443
Appendix 5. High-Speed Wind Tunnel Test – PIV Results .....	554
1.    Steady Baseline Results .....	554
A.    Mach 0.2 .....	554
B.    Mach 0.3 .....	555
C.    Mach 0.4 .....	556
2.    Steady Results .....	557
A.    Mach 0.2 .....	557
B.    Mach 0.3 .....	571
C.    Mach 0.4 .....	586
3.    Unsteady Results .....	599
A.    Mach 0.3 .....	599
B.    Mach 0.4 .....	603
Appendix 6. Error in PIV Results due to Particle Size .....	607
Appendix 7. Weighting Factor Adjustments for Improved Drag Coefficient Measurements...	613

## **II. Acknowledgments**

The authors of this work graciously acknowledge the assistance received from colleagues at United Technologies Research Center, Georgia Institute of Technology, and Sikorsky Aircraft. Thanks are extended to Archer Jennings (UTRC), John Cannata (UTRC), Ulf Jonsson (UTRC), Gary Zadrozny (UTRC), Brian Gillis (UTRC), Naomi Cohen (UTRC), Paul Van Slooten (UTRC), Svyatoslav Yorish (GT), George Woo (GT), Yuehan Tan (GT), Benjamin Isabella (SA), Bruce Bailey (Eagle Aviation Technologies), and Callum Gray (Lavision).

The authors also acknowledge the NASA Rotary Wing Project for supporting this work. Norman Schaeffler (NASA-Langley) served as technical monitor and Susan Gorton (NASA-Langley) headed the Rotary Wing Project during the period in which this work was performed. Furthermore, the authors' would like to thank Norman Schaeffler for his technical guidance and assistance throughout the project, which were critical to its success.

<p>The use of trademarks or names of manufacturers in this report is for accurate reporting and does not constitute an official endorsement, either expressed or implied, of such products or manufacturers by the National Aeronautics and Space Administration.</p>
---



### **III. Executive Summary**

Retreating blade stall is a well-known phenomenon that limits rotorcraft speed, maneuverability, and efficiency. Airfoil dynamic stall is a simpler problem, which demonstrates many of the same flow phenomena. Combustion Powered Actuation (COMPACT) is an active flow control technology, which at the outset of this work, had been shown to mitigate static and dynamic stall at low Mach numbers. The attributes of this technology suggested strong potential for success at higher Mach numbers, but such experiments had never been conducted. The work detailed in this report documents a 3-year effort focused on assessing the effectiveness of COMPACT for dynamic stall suppression at freestream conditions up to Mach 0.5.

The work done has focused on implementing COMPACT on a high-lift rotorcraft airfoil: the VR-12. This selection was made in order to ensure that any measured benefits are over and above the capabilities of state-of-the-art high-lift rotorcraft airfoils.

The detailed Computational Fluid Dynamics (CFD) simulations, wind-tunnel experiments, and system-level modeling conducted have shown the following:

- COMPACT, in its current state of development, is capable of reducing the adverse effects of deep dynamic stall at Mach numbers up to 0.4;
- The two-dimensional (2D) CFD results trend well compared to the experiments; differences can be attributed to a number of configuration differences between CFD and experiments;
- Implementation of the CFD results into a system-level model suggest that significant rotor-level benefits are possible.

This report details the simulation and experiments performed. Conclusions and recommendations for future work are provided.

Because of the large amounts of data collected in both low-speed and high-speed tests, only key figures are provided in the body of this work along with their corresponding discussion and analysis. For completeness in documentation, however, all figures, including those left out of the main body, are provided in the appendices.

## IV. Nomenclature

The parameters and their symbols used throughout this document are provided as follows, along with a brief definition:

$a$	=	freestream speed of sound
$C_L, C_l$	=	lift coefficient
$C_D, C_d$	=	drag coefficient
$C_{D-inplane}$	=	drag coefficient (force tangential to rotor shaft plane producing torque)
$C_M, C_m$	=	moment coefficient
$C_T$	=	thrust coefficient
$C_Q$	=	torque coefficient
$C_\mu$	=	pulse jet momentum coefficient, $= \rho_{jet} U_{jet}^2 h / (\rho_\infty U_\infty^2 c)$
$c$	=	airfoil chord-length
$D$	=	drag
$De$	=	equivalent drag, $= (Q\Omega)/U_\infty + D$
$E_\alpha$	=	damping coefficient
$f_{act}$	=	actuation frequency, pulses/second
$f_{pitch}$	=	airfoil pitching frequency, cycles/second
$f_{pulse}$	=	pulse frequency, $= 1/T_{pulse}$ , cycles/second
$F^+$	=	nondimensional pulse frequency, $= f_{act} c / U_\infty$
$h$	=	slot throat height
$k$	=	reduced frequency, $= \omega c / (2U_\infty)$
$L$	=	Lift or spanwise length
$M, Ma$	=	Mach number
$M'$	=	Mach number in reference frame, which moves with freestream
$P$	=	power or pressure
$P_r$	=	pressure ratio, $P_{act,b} / P_{act,out}$
$P_{act,out}$	=	pressure just outside of actuator orifice on airfoil upper surface
$P_{act,b}$	=	pressure in actuator chamber just inside of where BC is applied
$P_\infty$	=	freestream pressure
$Q$	=	Volumetric flow rate or torque
$R$	=	rotor radius

$r$	=	radial location of blade section
$Re_c$	=	chord-based Reynolds number, $= U_\infty c / \nu$
$W$	=	Actuator width
$w$	=	Downwash velocity
$sr$	=	slot span to overall span ratio, $= L_{slot} / L_{span}$
$St_{act}$	=	actuation Strouhal number, $= f_{act} c / U_\infty$
$T$	=	thrust
$T_{conv}$	=	chordwise time-of-flight, $= c / U_\infty$
$T_{cycle}$	=	period of pitch cycle
$T_{pulse}$	=	pulse width
$t$	=	time
$U_{jet}$	=	pulse jet velocity
$U_\infty$	=	freestream velocity
$\Phi$	=	Mixture ratio
$\Gamma$	=	Circulation
$x$	=	streamwise coordinate, origin at airfoil leading edge
$z$	=	spanwise coordinate, origin at airfoil midspan
$\alpha$	=	airfoil angle-of-attack
$\alpha_0$	=	mean airfoil angle-of-attack
$\alpha_1$	=	amplitude of airfoil angle-of-attack
$\beta$	=	spanwise skew angle
$\varphi$	=	pitch cycle fractional phase, $= f_{pitch} t$
$\mu$	=	advance ratio
$\sigma$	=	rotor solidity
$\theta_o$	=	collective pitch input
$\theta_{1c}$	=	cyclic pitch input (cosine component)
$\theta_{1s}$	=	cyclic pitch input (sine component)
$\theta_{slot}$	=	slot angle defined with the center slot line and the airfoil surface line at the outlet
$\nu$	=	kinematic viscosity
$\psi$	=	rotor blade azimuthal position, advancing side at $90^\circ$ , retreating side at $270^\circ$
$\Omega$	=	rotor angular velocity
$\omega$	=	airfoil pitching frequency, $= 2\pi f$ , radians/second

### ***Acronyms and Abbreviations***

COMPACT = Combustion Powered Actuation

LE = Leading edge

CFD = Computational Fluid Dynamics

CSD = Computational Structural Dynamics

SA = Spalart-Allmaras turbulence model

IRT = Icing Research Tunnel

## V. Introduction and Background

Problems associated with dynamic stall continue to limit rotorcraft speed and efficiency. Retreating-blade stall (RBS) typically occurs between the blade midspan and tip near the  $\psi = 270^\circ$  position. Although it commonly occurs on rotorcraft operating near the edge of their flight envelope, performance at these conditions plays an important role in rotor design as demand increases for faster and more agile rotorcraft with higher lift capacity. Furthermore, rotor blades are designed so that the extreme conditions at which stall occurs size key parameters such as blade chord.

The adverse effects of RBS can be mitigated through alleviation of dynamic stall at Mach numbers from 0.2 to 0.5. Previous work involving leading-edge slats, miniature trailing edge effectors, vortex generators, and plasma actuation have shown some success, but each technique has its weaknesses or challenges [1][2][3][4][5][6] [7]. Slats are very effective aerodynamically; however, overcoming advancing-side drag penalty has proven to be extremely difficult in terms of mechanical design. Miniature trailing edge effectors have a strong ability to change the effective camber of an airfoil and can have positive impact on dynamic stall characteristics; however, they can also create significant drag penalties. Vortex generators applied or actively deployed at the leading edge of an airfoil have shown the ability to affect both peak lift coefficient and peak negative moment, but can cause adverse effects at higher Mach numbers. Plasma actuation has shown significant promise across a range of speeds, and is the subject of several current research efforts (see [6] and [7]).

Steady and oscillatory blowing to alleviate dynamic stall have been the topic of many previous flow control studies. Many have focused on flow control at fairly low Mach numbers (at or below 0.1). Yu et al. [8] and Weaver et al. [9] used very strong steady blowing ( $C_\mu > 0.06$ ) and showed significant ability to suppress or completely eliminate dynamic stall (for consistency, the  $C_\mu$  values cited here are adjusted to the  $C_\mu$  equation defined in this paper). Singh et al. [10] and Müller-Vahl et al. [11] used steady blowing with somewhat smaller momentum coefficients (0.005-0.01), but also showed the ability to suppress dynamic stall. Note that in the work of Singh et al. [10], experiments were performed at Mach 0.13 on an RAE 9645 airfoil, and the best results were achieved with the upper surface slot located at  $x/c = 0.12$ . These results are encouraging, but the main challenge with steady blowing is that such high, sustained momentum coefficients can require large mass flows which can be difficult to achieve in practice, particularly at high Mach numbers in the rotating frame.

The work of Greenblatt and Wygnanski [12] Traub et al. (2004) [13], and Traub et al. (2005) [14] explored the effectiveness of zero-net-mass-flux jets, commonly referred to as synthetic jets, for controlling dynamic stall at low Mach number ( $<0.1$ ). These experimental studies were conducted on a symmetric NACA 0015 airfoil and concluded that unsteady blowing could be very effective in suppressing the adverse effects of dynamic stall, particularly when the actuation frequency is at or near  $F^+$  values on the order of 1.0. It was also shown that the benefits of unsteady blowing could be realized at significantly lower momentum coefficients when compared to steady blowing. The numerical investigation of Raju et al. [15] used the natural frequencies present in the uncontrolled flow about a NACA 4418 airfoil to set the ideal actuation frequencies. Here, it was found that frequencies near the laminar separation bubble shedding frequency produced the best results. A detailed numerical study performed by Visbal [16] using

implicit large eddy simulation supported this conclusion and showed  $F^+$  value of 50 to have the best performance.

Some investigations using steady or unsteady blowing have included results at significantly higher Mach numbers, more relevant to rotorcraft applications. The work of Nagib et al. [17] showed both experimentally and computationally that with adequately high  $C_\mu$  and  $F^+$ , increases in maximum lift coefficient and reductions in lift hysteresis can be achieved with a VR-7 airfoil operating at Mach numbers up to 0.4. The works of Wake and Lurie [18], Lorber et al. [19], and Florea and Wake [20] showed computationally and experimentally that a well-designed synthetic jet actuator on a high-lift airfoil (SC2110) can provide stall suppression benefit at Mach 0.2 and 0.3, however, steady blowing at the highest level possible still provided the best results when compared to the highest actuator output levels. With the actuators used in P.F. Lorber, D. McCormick et al. [19], providing high peak or RMS momentum coefficients at high Mach numbers proved to be a significant challenge. Using CFD, Lefebvre et al. [21] showed massive increases in cycle-averaged lift coefficient for an SC-1095 airfoil in deep dynamic stall at Mach 0.3. This was done with a unique coflow jet flow control design whereby flow is ingested downstream along the upper surface of the airfoil and expelled tangentially closer to the leading edge.  $C_\mu$  levels were varied up to very strong levels of 0.12. Similar results at up to Mach 0.4 were shown later by the same research group [22]. A series of computational and experimental studies were conducted by the German Aerospace Center (DLR) on an OA209 airfoil at Mach numbers up to 0.5 [23][24][25] [26]. The configuration investigated featured circular portholes 0.01c in diameter oriented normal to the airfoil chordline at  $x/c = 0.10$ . Computational results (URANS) presented by Gardner et al. [23] suggest that at a freestream Mach number of 0.31, constant flow and pulsing can produce significant increases in static lift at angles higher than the static stall angle. In the dynamic stall experiments of Gardner et al. [24], steady blowing at substantial momentum coefficients ( $C_\mu \geq 0.06$ ) resulted in simultaneous and significant increases in cycle-averaged lift coefficient and decreases in peak negative moment at Mach 0.3. At Mach 0.4 and 0.5, strong reductions in peak negative moment were noted. In Gardner et al. [25], experimental results at Mach 0.3 were collected for pulsing jets of the same geometry and compared to steady blowing results. It was shown that pulsing jets could achieve results similar to steady blowing while requiring less overall mass flow. Finally, Gardner et al. [26] showed experimentally that for deep dynamic stall at Mach 0.5, strong momentum coefficients of up to 0.034 could produce significant decreases in peak negative moment.

Combustion-powered actuation (COMPACT) provides a potential means for mitigating dynamic stall across a broad range of Mach numbers. COMPACT actuation can provide high-velocity, high-impulse jets for flow control from a small on-blade package. Overall mass flow is very small while very high peak momentum coefficients can be achieved. This technology has been the subject of several research efforts since the late 1990s. Characterization of the basic actuator was previously reported in [27], and non-premixed actuator operation was reported in [28]. Reattachment of separated flows with COMPACT has been demonstrated in a number of different airfoil configurations [29][30][31][32][33] [34]. The studies performed thus far have been primarily using relatively low Mach numbers ( $<0.2$ ). The performance of COMPACT technology Mach numbers  $> 0.2$ , however, was regarded as uncertain at the outset of the current effort.

This report fully documents a multi-year collaborative effort between NASA, UTRC, Georgia Institute of Technology, and Sikorsky. The main objective of this work can be concisely stated

as follows: to assess the effectiveness of COMPACT for dynamic stall suppression at up to Mach 0.5. Particular focus was put on applying COMPACT to an airfoil already regarded as a state-of-the-art high-lift airfoil for rotorcraft. For this reason, the VR-12 was selected. As a strong corollary to the main objective, another focus of this work was on determining the mechanism(s) by which dynamic stall suppression is or is not achieved in order to help advance the state-of-the-art in this area.

## VI. Aerodynamic Design

### 1. Summary

Computational fluid dynamics (CFD) was conducted to determine the best configuration of COMPACT. Major geometry parameters for the actuator slot were investigated at high-speed conditions relevant to rotor dynamic stall. Optimal chordwise location, slot angle, and slot thickness were determined through 2D computations. It was discovered that the gap between slots in the span significantly reduced COMPACT effectiveness compared to the promising results shown in the 2D computations. Unique designs were developed to overcome these problems. The final 3D slot design, called the “vanishing gap,” produced the most 2D-like behavior. The vanishing gap concept was carried forward to high-speed experiments. Most technical contents in this section were presented as part of the American Helicopter Society 71<sup>st</sup> Annual Forum in 2015 [35].

### 2. Computational Method

#### A. Geometry and Mesh

Following the previous study [36], the baseline airfoil is a VR-12 with a 5% tab (see Figure 1). The chord length of the airfoil is  $c=15$  inches and is used for the reference length scale. COMPACT slots used in the parallel experimental study were implemented on the upper surface near the leading edge. Three key parameters, slot angle  $\theta_{\text{slot}}$ , chordwise slot position  $x_{\text{slot}}$ , and slot height  $h_{\text{slot}}$ , were investigated in this study. The slot angle is defined as the angle between the path of the jet along the center of chamber and the clean airfoil surface shape at the location where the jet line would intersect the clean airfoil. The practical limit for making slots tangential to the airfoil surface is approximately  $22^\circ$ . With two higher angles,  $56^\circ$  and  $90^\circ$ , the impact of the slot angle to the dynamic stall suppression was studied. Two chordwise locations were selected to investigate slot location impact,  $x_{\text{slot}}/c = 0.1$  and  $0.15$ . To assess potential benefits of a thicker slot, which also provides higher net jet momentum, two thicknesses  $h_{\text{slot}}/c=0.08\%$  (nominal) and  $0.16\%$  were simulated.

Structured computational meshes were constructed as shown in Figure 2 for 2D meshes. First, the following O-type grids were tested for the clean airfoil:  $201(\text{airfoil}) \times 73(\text{wall normal})$ ,  $401 \times 145$ , and  $801 \times 289$ . The medium  $401 \times 145$  grid provides very similar results to the fine grid (see Figure 3). The first wall normal grid point is located  $8 \times 10^{-6}c$  away from the wall, guaranteeing  $\Delta y_{\text{avg}}^+ < 1$  in the wall unit for the range of the angle-of-attack,  $\alpha=0-20^\circ$ . The far field boundary is located  $50c$  away from the airfoil. Based on the clean-airfoil medium grid, the actuator slot was introduced into the grid by clustering the grid in the streamwise direction near the slot (Figure 2) and keeping the rest of the grid the same as the clean-airfoil grid. This approach helps to numerically investigate how the modified airfoil behaves compared to the clean airfoil. The authors noticed that numerical results were altered by grid coarsening away from the slot through the slot addition. Clean and modified airfoils provide similar unsteady load traces for the current pitching simulation as shown in Figure 4. These results are consistent with the previous computations of [2] for the  $M=0.3$  case. Such small differences provide a suitable environment for assessing the flow control performance of COMPACT against the clean airfoil results. It is also physically expected for the small-scale flow control device. The slot of



$h_{\text{slot}}/c=0.08\%$  (Figure 2.c,d,f) and for  $h_{\text{slot}}/c=0.16\%$  (Figure 2.e) has 113(flow direction) $\times$ 97 and 145 $\times$ 145 grid points, respectively. The minimal wall normal size inside the slot is about  $2\times 10^{-6}c$ , and the boundary layer has about 20 grid points at the choked location when the actuation is on. Modified-airfoil 2D meshes have about 0.1-0.13M grid points, depending on the slot geometry.

Based on the nominal slot design used in the parallel experimental study, 3D geometry is also considered in the current study. In the experimental study, each slot spans 0.5 inch (0.033c), and slots are separated by 3/16-inch (0.013c) divider plates in along the span. Initial 3D simulations modeled the half slot and the half gap as shown in Figure 5a. With the given span ratio of slot with respect to the domain span,  $S_r=8/11$ , the skew angle  $\beta$  was varied in the 3D computations. The half slot and the half gap contain 25 and 9 grid points in the span, respectively, with the minimum spanwise grid size of  $1\times 10^{-5}c$  at the edge between the slot and the gap. The spanwise resolution was checked with a twice-refined grid in the span direction. The current 3D mesh for the half slot-gap geometry of  $h_{\text{slot}}/c=0.08\%$  has about 3.4M grid points. The symmetry boundary condition is applied to the two span planes.

Based on the promising results with non-zero  $\beta$ , a vanishing-gap slot was designed to eliminate the discrete actuator orifices (see Figure 5b). The bottom of the slot remains the same for the connection to the COMPACT plenum,  $L_{\text{slot,bottom}}=0.033c$ , but expands downstream of the throat to the airfoil surface. The slot on the airfoil surface has 49 grid points in the full span. The current 3D mesh for the vanishing-gap slot of  $h_{\text{slot}}/c=0.08\%$  and  $h_{\text{slot}}/c=0.16\%$  has 5.2M and 6.8M grid points, respectively. The spanwise domain size for vanishing-gap slots is  $L_{\text{span}}=0.046c$ . A larger spanwise domain (16M grid points) of  $L_{\text{span}}=0.14c$ , with three vanishing-gap slots in the span, was also tested and gave similar results obtained for the current grid with  $L_{\text{span}}=0.046c$ . However, it should be noted that detailed 3D features related to the dynamic stall vortex and its interaction with the pulsed jet remain to be seen with a larger domain in the spanwise direction,  $L_{\text{span}}=O(1c)$ . This simulation would require  $O(100M)$  grid points in the current CFD framework. The tunnel walls in the NASA Glenn Icing Research Tunnel (IRT) are not modeled in the current computations, assuming the tunnel height-to-chord ratio of 7.2 is large.

## B. CFD Solver and Flow Conditions

CFL3D was used for this study with the full Navier-Stokes solver option and the Spalart-Allmaras (SA) turbulence model [37]. The far-field boundary was located about 50c away from the airfoil, and the SA boundary condition  $\tilde{v}_{\infty} = 4\nu_{\text{molecular}}$  was used for these fully-turbulent flow computations. The upwind biased third-order Roe scheme is used for Euler fluxes. In the current 2D computations, 4000 time steps per pitch cycle and 30 subiteration per time step were used. A finer time step was required for convergence in 3D, so 3D results reported here are from computations with 8000 time steps per pitch cycle. Cycle-to-cycle convergence was achieved after the first three pitch cycles.

The pitching motion was prescribed as  $\alpha = \alpha_0 + \alpha_1 \sin(2U_{\infty}kt/c)$ , where the reduced frequency  $k$  is defined as  $\pi f_{\text{pitch}}c/U_{\infty}$  and selected to be representative of rotor conditions on the retreating side in the range of Mach number  $M = 0.3-0.5$ . The range of the Reynolds numbers is  $Re_c = 2.6-4.3\times 10^6$ . The reference velocity is the freestream velocity  $U_{\infty}$ , and the reference time is the convective time scale  $t_c=c/U_{\infty}$ .

COMPACT pulses are modeled with the actuation frequency  $f_{\text{act}} = 200$  Hz, the amplitude in terms of time-dependent pressure ratio  $P_r(t)$  with  $P_{r,\text{max}} = 2$ , and the pulse duration  $T_{\text{pulse}} = 1.25$  msec, as found in benchtop test of the actuators [36]. Half-cycle pulsing is applied, beginning at

the middle of the upstroke and ending at the middle of the downstroke. Based on the high peak pressure ratio achieved, it is assumed that at or near the peak pressure, the flow at the orifice is choked. The nondimensional actuation frequency is  $F^+ = 0.74$  and  $0.56$ , for Mach  $0.3$  and  $0.4$ , respectively.

Pulsing was implemented in CFL3D as follows: the pressure ratio  $P_r(t)$  is used in combination with stagnation relations in order to calculate the flow speed to be directly specified at the lower boundary of the slot (also referred to as the actuator surface).

$$U_{act,b} = a_\infty \sqrt{\frac{2}{\gamma - 1} \left( \left( \frac{P_r P_\infty}{P_{act,b}} \right)^{\frac{(\gamma-1)}{\gamma}} - 1 \right)} \quad (1)$$

The pressure  $P_{act}$  and density  $\rho_{act}$  are extrapolated from the interior solution, allowing  $T_{act} = T_\infty$ . The same extrapolation of the CFL3D boundary condition type (bctype) 2028 is used here. In contrast to bctype 2028 where only periodic velocity components can be specified, the current boundary condition allows a user to specify any time-dependent velocity. The direction of the flow is set normal to the actuator surface. Given the high pressure ratios associated with the COMPACT pulse, the slot is choked for most of the pulse duration. Note that the pressure ratio  $(P_r P_\infty)/P_{act}$  inside the parenthesis of Eq. 1 is usually larger than  $P_r$  as  $P_{act}$  is close to the external low pressure on the suction side near the actuator. This leads to passive blowing between pulses in the computations reported here. A separate CFD study of higher passive blowing velocities had no significant difference in the flow control effectiveness of COMPACT. At the actuator surface,  $\tilde{v}_{act} = 4v_{molecular}$  for the SA model.

### 3. Computational Results

#### A. Preliminary Validation

Steady, clean VR-12 airfoil results were compared with preliminary experimental data obtained from the Entry 1 of the high-speed wind tunnel test. A detailed description of the experimental configuration and results are provided in Section 10. Import items as they pertain to this discussion, are highlighted as follows. First, the geometry of the experimental clean airfoil was designed to be identical to the CFD geometry, including the airfoil shape and tab length. However, to facilitate (1) actuator installation and removal, (2) a permanent installation of pressure sensors, and (3) a spar of adequate structural integrity at high-Mach, small discrepancies in the geometry were introduced. Second, although the ratio of tunnel height to airfoil chord, which was  $7.2$ , was large, the experiment was not truly two-dimensional. The airfoil span was approximately  $68.5$  inches, nearly spanning the tunnel height, but with small gaps on the spanwise ends that introduced three-dimensionality. The effect upon the midspan pressure distribution could not be accounted for at present. Finally, the airfoil was equipped with an array of high-frequency pressure sensors at several spanwise stations. The chordwise distribution of these sensors was designed using a segmented Gaussian quadrature strategy to allow for accurate lift and moment measurements with a relatively small number of sensors at each spanwise station. However, these distributions would not allow for accurate absolute measurements of pressure drag.

CFD pressure profiles match reasonably well with the experimental data as shown in Figure 6. For small angles of attack before stall,  $\alpha \leq 16^\circ$ , the suction pressure peak is measured lower than

the CFD prediction. Further comparison with Sikorsky-UTRC proprietary data (not shown here) validated the suction pressure peak predicted in the current computations. For angles beyond stall,  $\alpha \geq 18^\circ$ , CFD provides flattened profiles on the suction side, which was similarly observed in the experiment. The aerodynamic forces at steady conditions for  $M=0.3-0.5$  are shown in Figure 7. Available experimental data are also plotted against the CFD results. The peak  $C_L$  and  $C_M$  in CFD agree well with the experimental data. The current pressure sensor distribution in the experiment is designed to capture only lift and moment accurately, so no experimental drag is included for the comparison. The drag predicted in the current CFD is reasonably matched with the Sikorsky-UTRC proprietary data. It should be noted that the experiment indicates the stall angle around  $\alpha_{\text{stall}}=16.25^\circ$  at  $M=0.3$ , whereas the stall angle is  $17.5^\circ$  in CFD. The delayed stall in CFD could be related to the well-known RANS limit for turbulent flow separation. For higher Mach numbers, the stall occurs due to shock, so the stall angle is similar to the experimentally measured angle. Overcoming the RANS limit with higher-fidelity computational approaches is currently beyond the project scope. The following numerical investigation on the slot geometry parameters includes various flow conditions from light to deep dynamic stall. Therefore, the slight discrepancy between the current CFD and the experiment on the stall angle minimally impacts the current study.

## **B. Two Dimensional Results**

Before the parametric study, it is important to understand how COMPACT mitigates dynamic stall. As shown in Figure 8, the actuation helps the boundary layer remain close to the airfoil surface that would otherwise separate near the leading edge without actuation. The actuation stabilizes the boundary layer, which reduces the strength of the stall vortex. The spanwise vorticity field in Figure 8 shows that the external flow massively separates when the airfoil pitches down (from  $\varphi=2/8$  to  $3/8$ ) in the no-actuation case, whereas the separation is delayed to about one third chord with actuation. The COMPACT pulse generates an impulsive jet tangential to the airfoil surface as shown in the close-up view of Figure 9. This jet periodically injects momentum into the boundary layer, which encounters a severe pressure gradient. The momentum injection into the boundary layer helps to mitigate flow separation. The close-up view indicates that the jet coming from the slot of  $\theta_{\text{slot}}=22^\circ$  is almost tangential to the airfoil surface, and is thereby able to penetrate the boundary layer up to  $x/c=0.2$  at the middle of pulse ( $\varphi=52/200$  and  $61/200$ ) duration. The pulse ends after  $\Delta\varphi=1/200$ . Vortices generated from the pulse convect downstream, interacting with the boundary layer, which pulls the shear layer toward the airfoil surface.

To examine the sensitivity of slot geometry on the COMPACT actuators ability to suppress dynamic stall, the three geometry parameters  $\theta_{\text{slot}}$ ,  $x_{\text{slot}}$ , and  $h_{\text{slot}}$ , were examined with 2D simulations. Three angles,  $\theta_{\text{slot}} = 22^\circ$ ,  $56^\circ$ , and  $90^\circ$ , were simulated at  $x_{\text{slot}}/c=0.1$  for Mach 0.3-0.5 (see Figure 10). At Mach 0.3 and 0.4, it is shown that the  $22^\circ$  slot can significantly enhance lift during the downstroke, while the higher slot angles result in degraded lift performance with respect to the clean airfoil. Additionally, the tangential slot eliminated the abrupt nose-down moment at  $Ma=0.3$ . Less control authority with a higher slot angle is related to the shorter time of flow interaction with the neighboring boundary layer. The tangential jet, as shown in Figure 9, is able to augment the boundary layer up to  $x/c=0.2$ . In contrast, a higher slot angle generates a larger wall normal velocity component for the jet, which passes through the thin boundary layer without providing significant momentum into the boundary layer in the direction of flow. Current simulations indicate that too large slot angles like  $\theta_{\text{slot}} = 90^\circ$  degrade the aerodynamic

performance of the baseline airfoil. It is expected that the high-impulsive wall-normal jet undesirably induces flow separation.

It was proposed early on in this work that flow-control effectiveness at higher Mach numbers could be increased by placing the slot further aft on the upper surface. To investigate this, the same three slot angles were run with the slot placed at  $x_{slot}/c = 0.15$  (see Figure 11). Results are fairly similar to the  $x_{slot}/c = 0.1$  results; and no significant difference was shown. Current results suggest that at Mach 0.4, the higher jet angles can reduce the peak negative moment substantially, but this reduction comes at a large reduction in lift. At Mach 0.5, none of the angles attempted produce significant enhancement in lift. Compared to the case of  $x_{slot}/c = 0.1$ , an increase in cycle-averaged lift of 1% was shown for Mach 0.3; however, the same quantity was degraded 3% for Mach 0.4. Average quantities for all angle and slot location variations at each Mach number are shown in Table 1 through Table 3. The control performance metrics, change in cycle-averaged lift  $\Delta C_{L,avg}$  and drag  $\Delta C_{D,avg}$ , and peak moment difference  $\Delta C_{M,peak}$ , were calculated relative to the clean airfoil. Overall, it appears that the  $x/c = 0.1$  location with a tangential slot performs best.

Benchtop experiments at Georgia Tech indicated that peak and net jet momentum could be increased by increasing the slot chordwise height. The initial slot height was set at  $h_{slot}/c = 0.08\%$ , and benchtop tests showed that doubling this height to  $h_{slot}/c = 0.16\%$  would increase both the peak and net momentum flux of the actuation pulse. To assess the potential for affecting dynamic stall, additional 2D CFD simulations were performed. Lift and moment results for the initial- and double-height slots are shown in Figure 12. It is clear from these results that the double-height slot performs better than the nominal height used in this study. Integral quantities are shown in Table 4 and indicate a 4% enhancement in cycle-averaged lift for Mach 0.3 and a 2% enhancement for Mach 0.4, when compared to the nominal height slot. For the double-height slot, it was found that the corner immediately aft of the slot gave rise to a more pronounced separation bubble during the pulsation; thus, additional modification was made wherein this corner was rounded to prevent this. Only a slight improvement is shown for Mach 0.5.

The spanwise vorticity field shown in Figure 13 indicates that the slot of  $h_{slot}/c = 0.16\%$  generates a strong jet, which penetrates the nearby boundary layer further downstream, compared to the  $h_{slot}/c = 0.08\%$ . Vortices generated from the double-height slot convect downstream up to  $x/c = 0.4$  at  $\varphi = 55/200$ . The boundary layer is less prone to separation before the next pulse ( $\varphi = 59/200$ ) for  $h_{slot}/c = 0.16\%$ , whereas it is clearly separating for  $h_{slot}/c = 0.08\%$ .

Through the 2D parametric study, it was discovered that the optimal 2D slot geometry is  $\theta_{slot} = 22^\circ$ ,  $x_{slot}/c = 0.1$ , and  $h_{slot}/c = 0.16\%$  as shown in Figure 2e. This final 2D geometry was investigated for various pitching conditions at Mach 0.4, which include mild and deep dynamic stall. The performance of the actuator is promising, providing over 10% enhancement in  $\Delta C_{L,avg}$  for the deep dynamic stall ( $\alpha_0 + \alpha_1 > 24^\circ$ ), about 10% reduction in  $\Delta C_{D,avg}$  and about 25% reduction in  $\Delta C_{M,peak}$  for the moderate dynamic stall cases, ( $16^\circ \leq \alpha_0 + \alpha_1 \leq 24^\circ$ ), as shown in Figure 14. Here all trajectories were simulated with  $k = 0.07$ .

### C. Three-Dimensional Results

Three-dimensional simulations were performed to examine the initial settings and provide a better geometry for improved actuator performance. For the initial actuator configuration, the slot-to-span ratio was  $L_{slot}/L_{span} = 8/11$  and the spanwise angle in the side slot wall was  $\beta = 0^\circ$

(see Figure 5a). The initial 3D geometry yielded significantly worse performance compared to its 2D counterpart (see Figure 15). To understand the large reduction, a detailed examination of the flow field was conducted. Figure 16a shows Mach number contours for the baseline geometry looking down on the airfoil from above, centered on the slot, with the flow going from left to right. Each snapshot was taken during a pulse, and the slot can be seen clearly by the regions of high Mach number flow that extends downstream. The high-velocity jet created by the COMPACT pulse tends to be reduced by the flow from the gap. The uncontrolled flow occurring in the gap tends to move towards the slot side as it proceeds downstream. This degradation in spanwise uniformity yields the reduced flow-control effectiveness when the gap is introduced.

These results of the initial 3D slot geometry showed that more aggressive means of returning to 2D performance were required. To counteract the flow development shown in Figure 16a, the gap side of the chamber was angled such that the actuation jet tends to flow into the gap region. This is illustrated in Figure 5a for  $\beta = 20^\circ$ . Unsteady load traces at Mach 0.3 for several skew angles are shown in Figure 15. A modest increase in skew angle has a small but positive effect; however, larger increases in skew angle ( $30^\circ$  and  $40^\circ$ ) helped to achieve more 2D-like performance. Mach number contours for  $\beta = 30^\circ$  are shown in Figure 16b. It is clear from these contours that the skew angle can counteract the separated flow region from the gap side and mitigate separation. This change in the flow field produces the more favorable lift hysteresis closure.

Even at the highest skew angles, cycle-averaged lift enhancement still falls short of the 2D predictions. A unique 3D slot was designed in order to further close this gap. The new design consists of a combination of skew angle and an increase in slot-to-span ratio at the airfoil surface. The dividers between actuators would be tapered away in the flow direction, at least up to the slot throat. Beyond this point, the gap has essentially ‘vanished’ (Figure 5b). Mach 0.3 results for this geometry are shown in Figure 17. These results suggest that this geometry produces the most 2D-like behavior. Simulations of two slot heights  $h_{slot}/c=0.08\%$  and  $0.16\%$  confirmed the more impactful aerodynamic performance of the vanishing-gap design.

The vanishing-gap design allows the jet to cover the entire span when it ejects from the slot as shown in Figure 18, which shows Mach number contours for three conditions: (a) no actuation, (b)  $h_{slot}/c=0.08\%$  and (c)  $h_{slot}/c=0.16\%$ , as viewed from above the airfoil. Compared to the no-actuation case, the low Mach flow separation region remains downstream of the actuator. The thicker slot pushed the separation further downstream, which is consistent with the 2D simulation. As expected, the jet is not uniform in the span due to the angle in the slot. This non-uniformity is highlighted by a streak at the midpoint of two actuators where the two jets collide. This jet interaction extends downstream to  $x/c=0.2$ . Figure 19 shows Mach and streamwise vorticity contours at selected chordwise locations when the COMPACT jet ejects from the slot. Two jets collide immediately at the slot outlet, the combined flow penetrates the boundary layer upward, as shown in the ‘pinched’ high Mach region in Figure 19a. This produces the pair of counter-rotating vortices in Figure 19b.

Table 5 provides the average quantities for all 3D simulations discussed in this section. The vanishing gap geometry proved to be the most effective. The thicker slot  $h_{slot}/c=0.16\%$  with vanishing-gap geometry provides nearly an 8% increase in lift and a 55% reduction in drag, which is very close to the 2D results, about 9% increase in the lift and 53% reduction in the drag

(Table 4) for the same flow condition at Mach 0.3. The final 3D slot design was carried forward to the high-speed wind tunnel experiments.

#### 4. Conclusions

Extensive 2D and 3D CFD simulations were conducted to determine the best 3D slot geometry. High-speed flow conditions relevant to rotor dynamic stall, i.e.,  $M=0.3-0.5$  and  $k=0.05-0.1$ , were considered in this study.

In 2D computations, the slot chordwise location, the slot angle, and the slot thickness were determined. The current results confirmed that the tangential slot performs best as suggested by in Ref. [36]. Compared to the downstream location  $x_{slot}/c=0.15$ , the nominal slot location  $x_{slot}/c=0.1$  provides slightly better improvement in cycle-averaged lift and drag, and moment peak reduction, so the location remained the same. As expected from the increased jet momentum observed in the benchtop experiment, the thicker slot of  $h_{slot}/c=0.16\%$ , further suppressed dynamic stall. The cycle-averaged lift enhancement of 5.6% by the initial height  $h_{slot}/c=0.08\%$  for Mach 0.3 condition increased to 9.4% with the thicker slot. The final 2D slot geometry,  $\theta_{slot}=22^\circ$ ,  $x_{slot}/c=0.1$ , and  $h_{slot}/c=0.16\%$ , shows promising COMPACT performance for light-to-deep dynamic stall conditions at Mach 0.4.

3D simulations were performed to examine the 2D simulation initial settings and provide a better geometry for improved actuator performance. For the initial actuator configuration, the slot-to-span ratio was  $L_{slot}/L_{span}=8/11$  and the spanwise angle in the side slot wall was  $\beta = 0$ . The initial 3D geometry yielded significantly worse performance compared to its 2D counterpart. Current results indicate that the effectiveness of the high-velocity jet created by the COMPACT pulse tends to be diminished by the uncontrolled flow through the gaps between the discrete actuator slots. It was determined that the gap and lack of spanwise jet component from the slot toward the gap reduced the COMPACT effectiveness. A skew angle of  $\beta=30-40^\circ$  counteracted the separated flow region stemming from the gap and helped bridge the difference between the 2D and 3D results. However, even at the highest skew angles, the cycle-averaged lift still fell short of the 2D predictions. To further reduce this difference, the unique vanishing-gap slot was designed. This final design produced the most 2D-like behavior. The vanishing-gap concept was carried forward to the high-speed test article design.

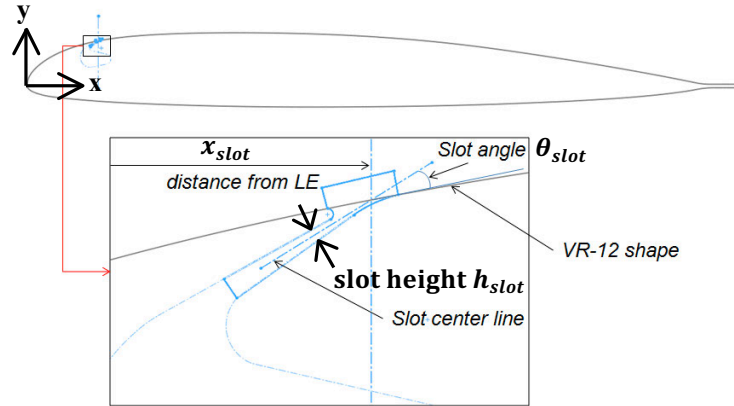


Figure 1. VR12 airfoil modified with a 5% tap and actuator slot.

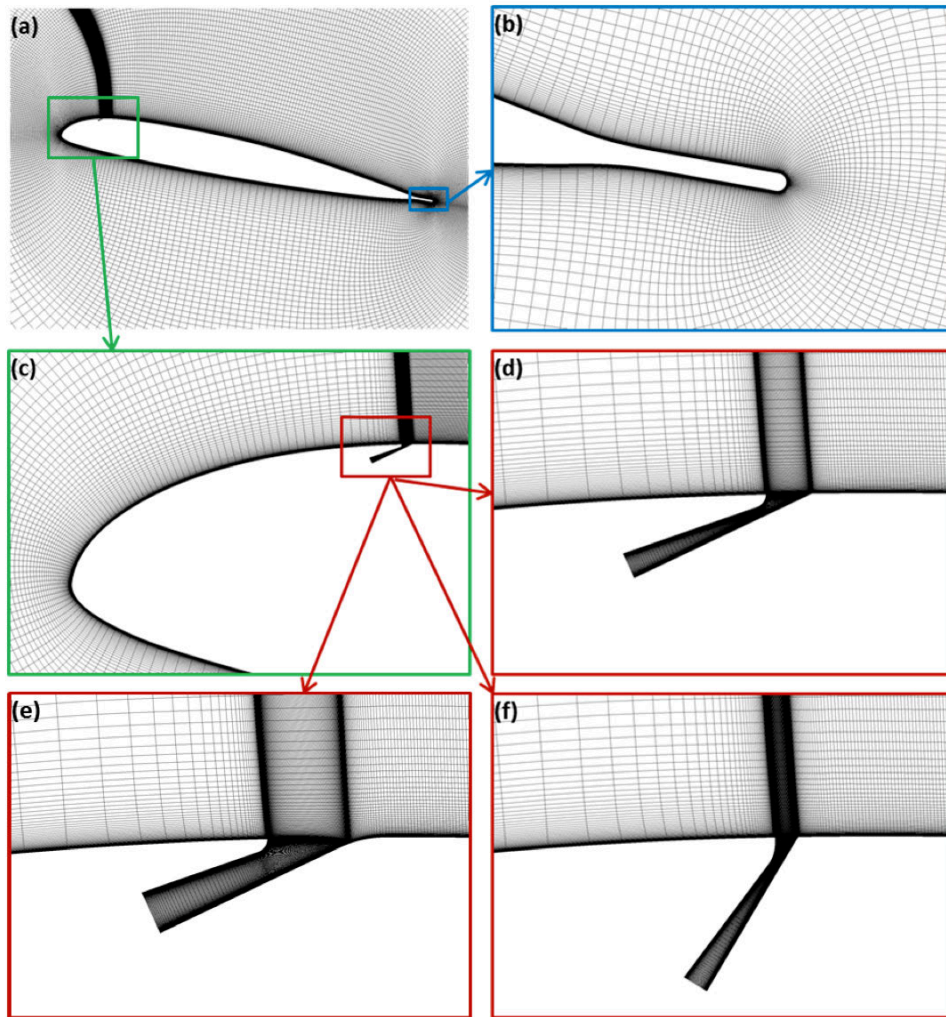
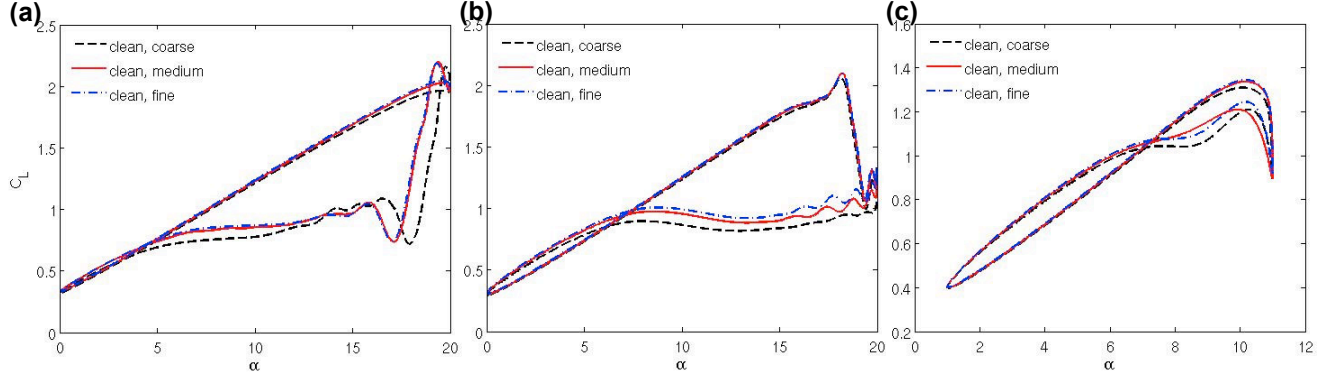
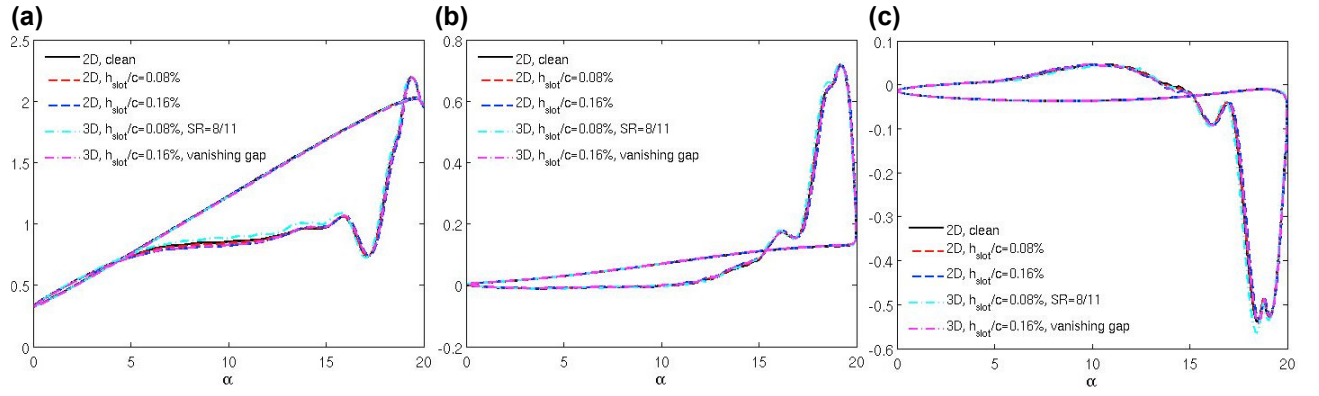


Figure 2. Computational 2D mesh for the modified VR12 airfoil (a-c) with three selected slot geometry (d)  $\theta_{slot} = 22^\circ$  and  $h_{slot} = 0.08\%c$ ; (e)  $\theta_{slot} = 22^\circ$  and  $h_{slot} = 0.16\%c$ ; (f)  $\theta_{slot} = 56^\circ$  and  $h_{slot} = 0.08\%c$ .



**Figure 3. Unsteady lift predicted by three different levels of grid resolutions for the clean VR12 airfoil. (a)  $Ma=0.3$  and  $k=0.1$ , (b)  $Ma=0.4$  and  $k=0.07$ , (c)  $Ma=0.5$  and  $k=0.05$ .**



**Figure 4. Unsteady lift (a), drag (b) and moment (c) traces for selected modified airfoils in 2D and 3D simulations for flow condition of  $Ma=0.3$  and  $k=0.1$ .**

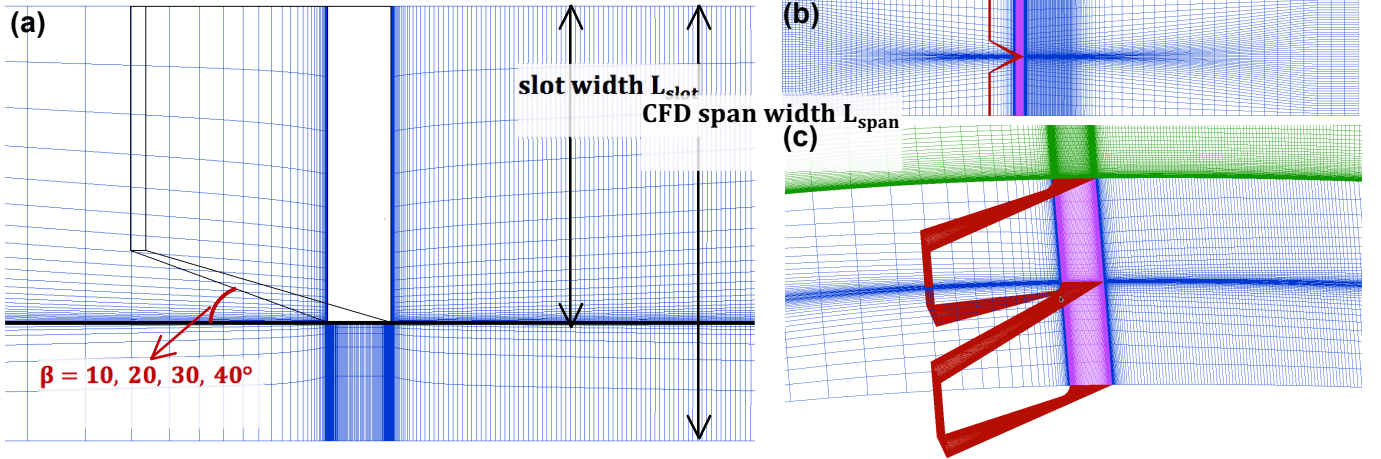


**Figure 5. Surface mesh for 3D computations. (a) Top-view of airfoil surface with outline of the slot geometry ( $\beta = 20^\circ$  shown here); (b) Top-view and (c) 3D-view mesh on selected surfaces for a vanishing-gap configuration for the slot.**



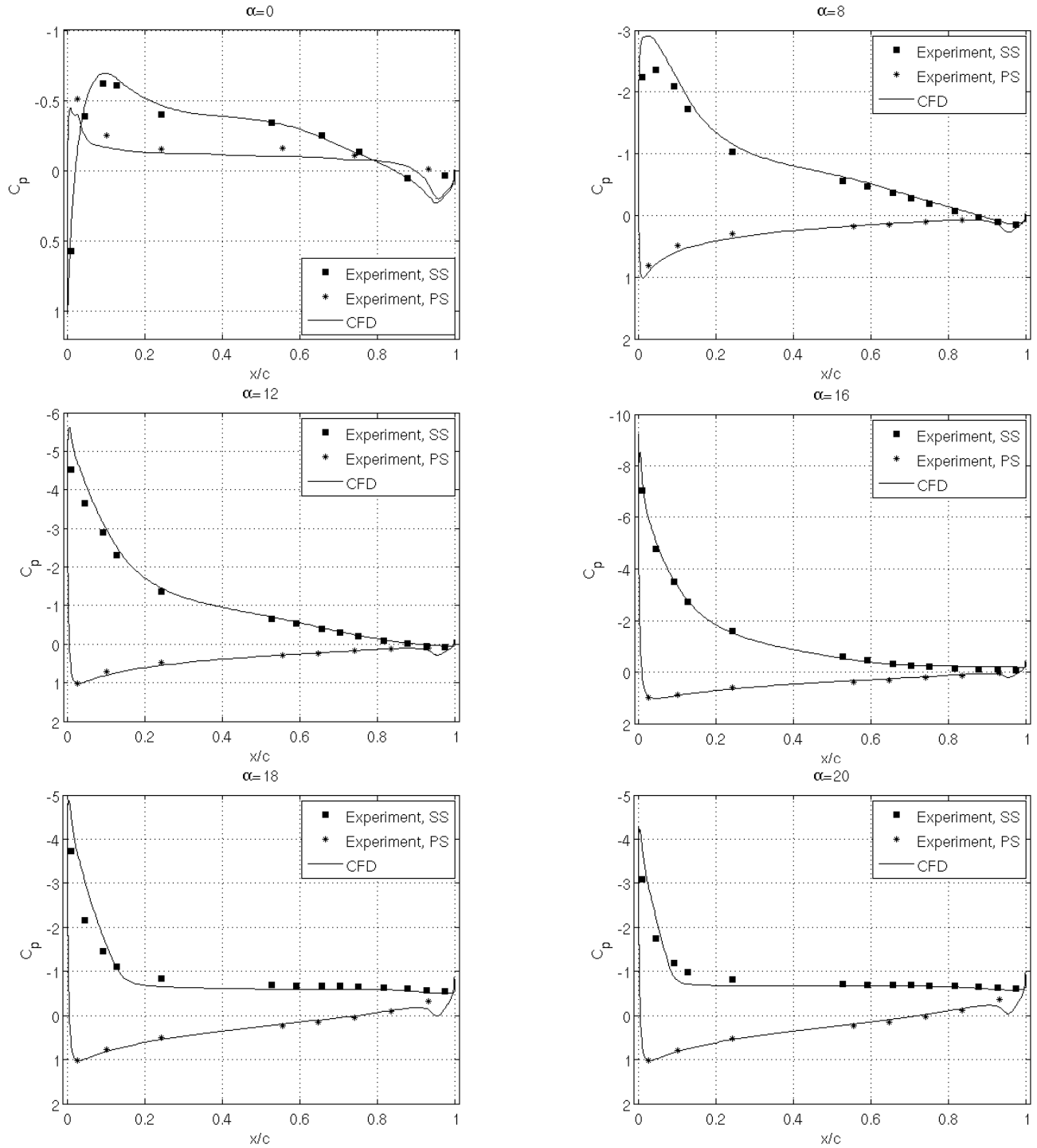


**Figure 6. Pressure coefficient profiles at steady conditions for the clean VR12 airfoil compared with the experimental data for  $Ma=0.3$ .**

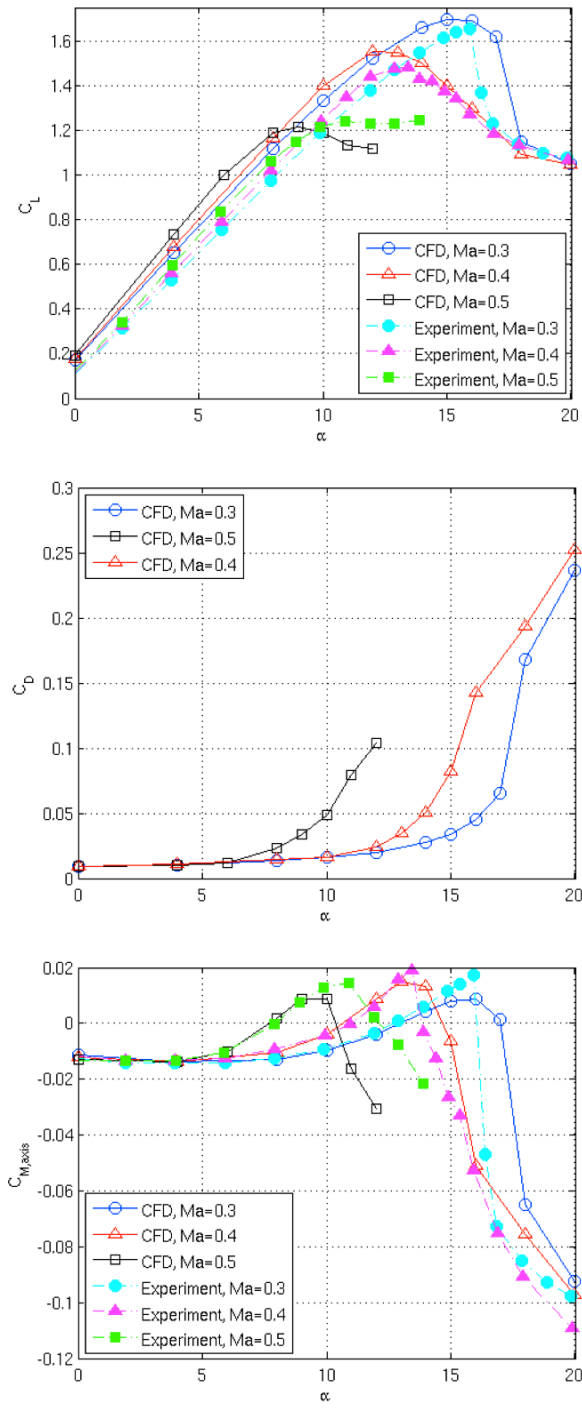


**Figure 7. Lift, drag, and moment coefficients for the clean VR12 airfoil at steady conditions of  $Ma=0.3-0.5$ . Lift and moment are compared with experimental data.**

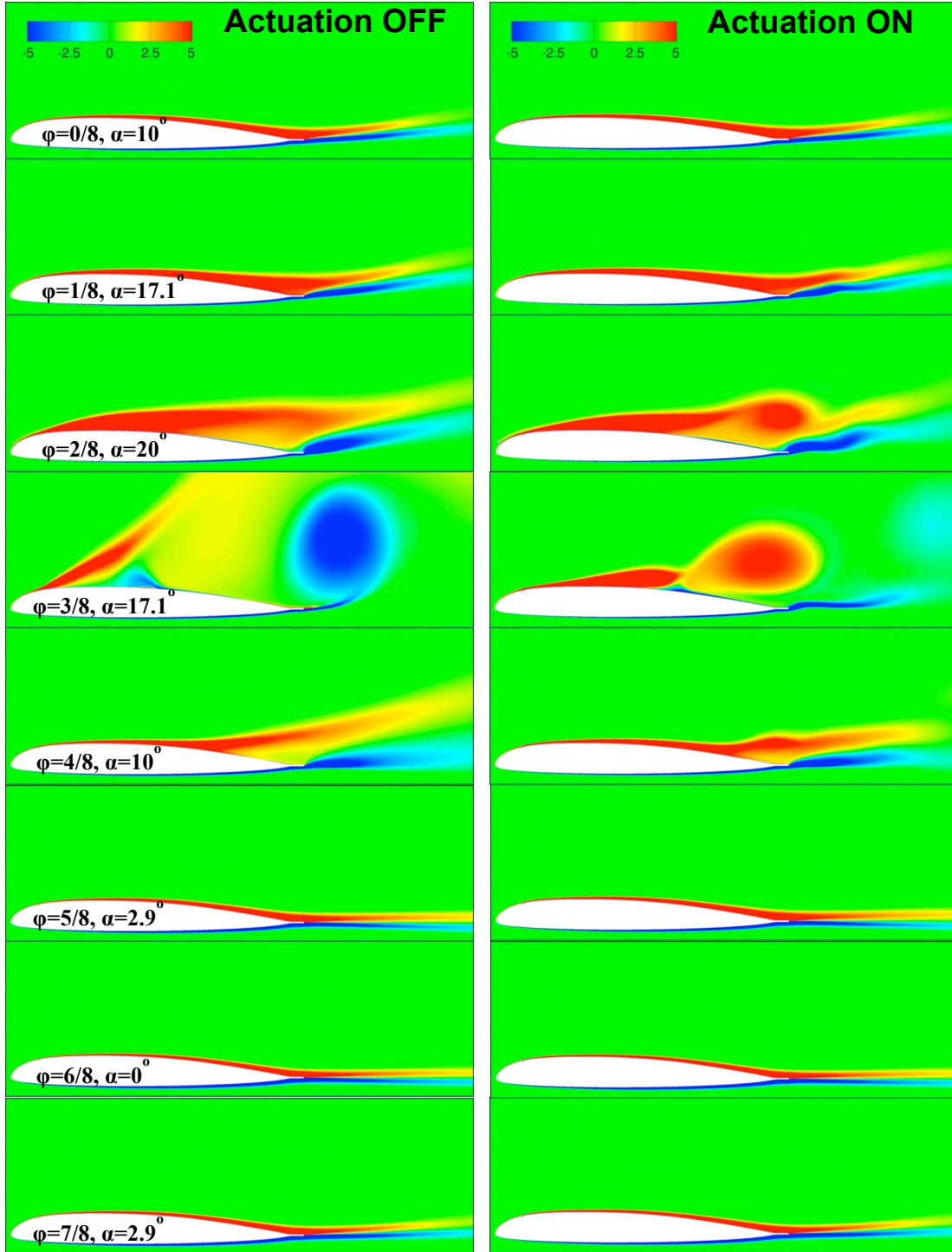


Figure 8. Spanwise vorticity field with actuation off (left) and on (right) for  $Ma=0.3$ ,  $k=0.1$ , slot at  $x_{slot}/c=0.1$  with  $\theta_{slot}=22^\circ$ ,  $h_{slot}/c=0.08\%$ , illustrating the effect of actuation. Actuation is on for the first half cycle ( $\varphi=0-4/8$ ).

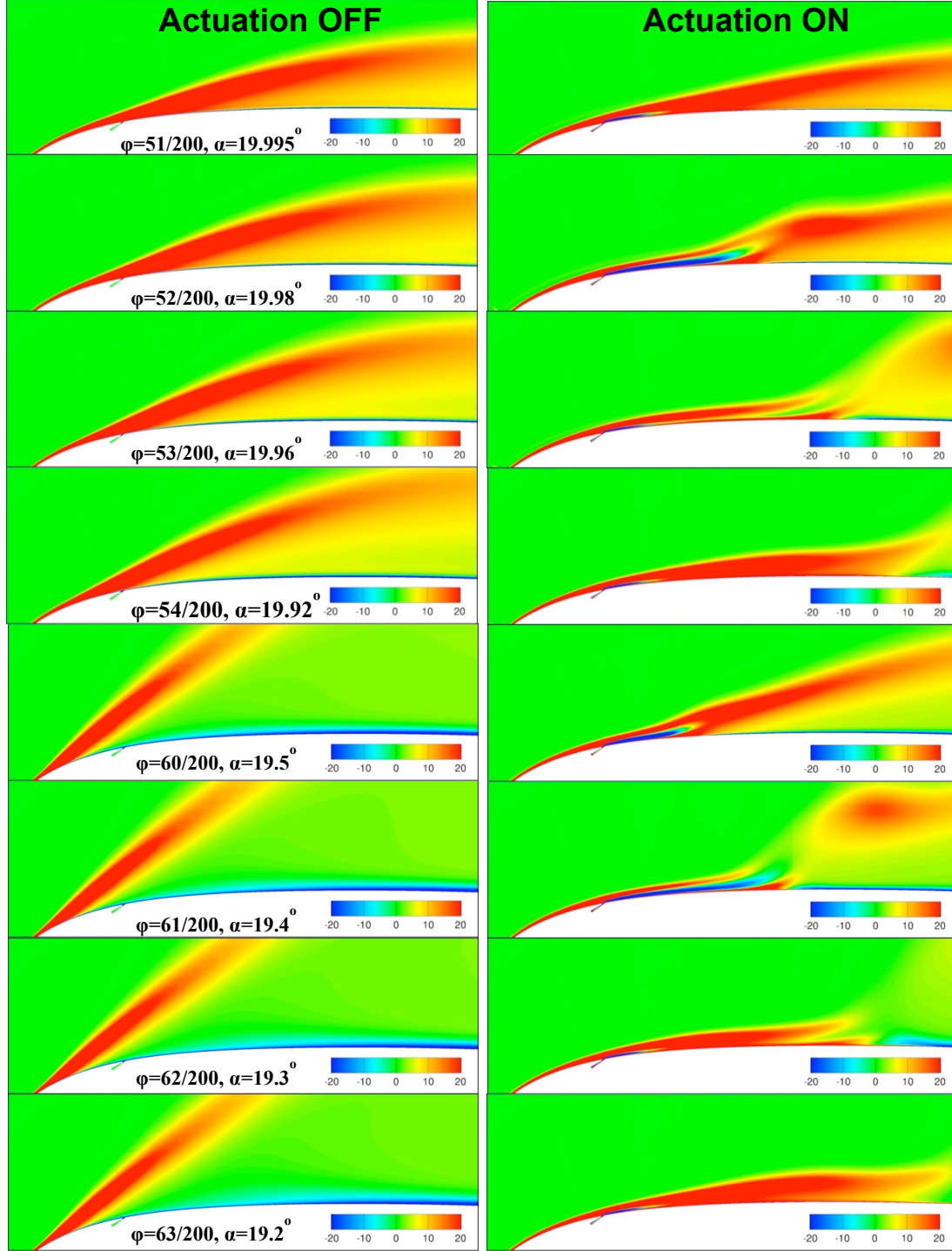
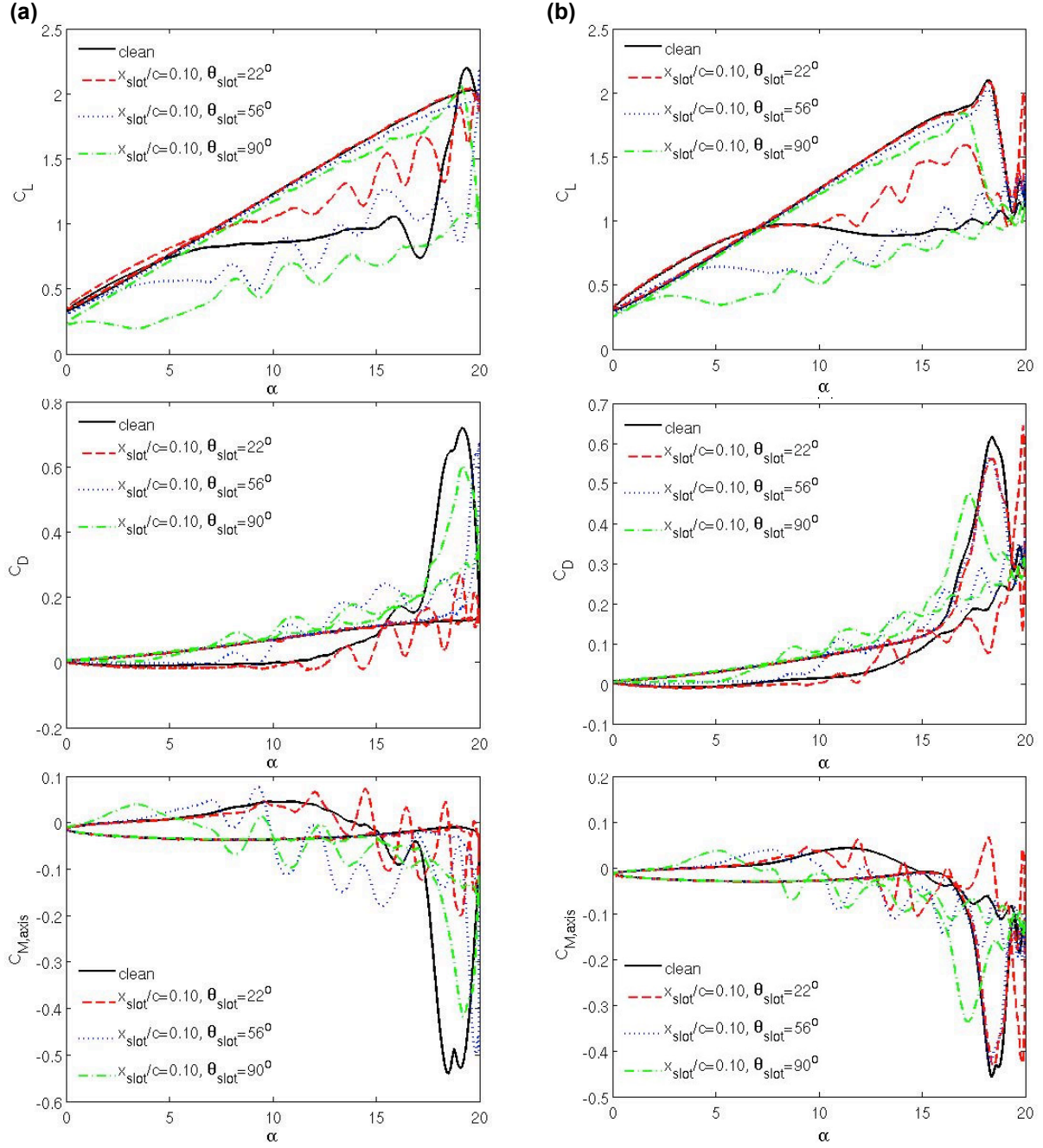
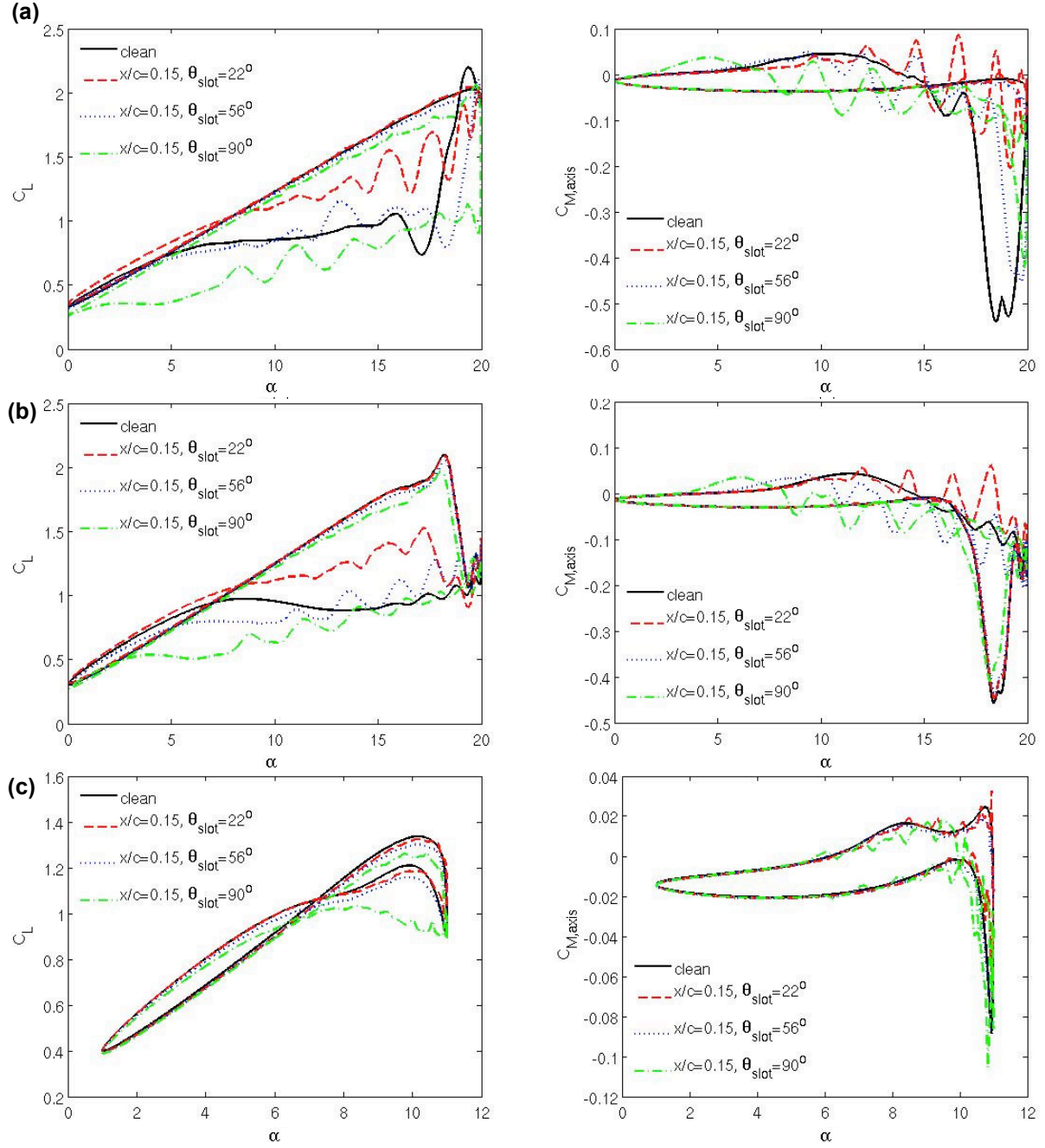


Figure 9. Spanwise vorticity field with actuation off (left) and on (right) for  $Ma=0.3$ ,  $k=0.1$ , slot at  $x_{slot}/c=0.1$  with  $\theta_{slot}=22^\circ$ ,  $h_{slot}/c=0.08\%$ , illustrating the effect of actuation, focusing on two pulsation phases, one around at  $\phi = 52/200$  and another at  $61/200$ , in the  $x$  range of  $x=0-0.4c$ .



**Figure 10. Unsteady lift, drag, and moment traces with COMPACT at  $x_{slot} = 0.1c$  with variations in the slot angle  $\theta_{slot}$ . (a)  $Ma=0.3$  with  $k=0.1$  and (b)  $Ma=0.4$  with  $k=0.07$ . The angle of attack,  $\alpha$ , is in degrees.**



**Figure 11. Unsteady lift and moment traces with COMPACT at  $x_{slot} = 0.15c$  with variations in the slot angle  $\theta_{slot}$ . (a)  $Ma=0.3$  with  $k=0.1$ , (b)  $Ma=0.4$  with  $k=0.07$ , and (c)  $Ma=0.5$  and  $k=0.05$ . The angle of attack,  $\alpha$ , is in degrees.**



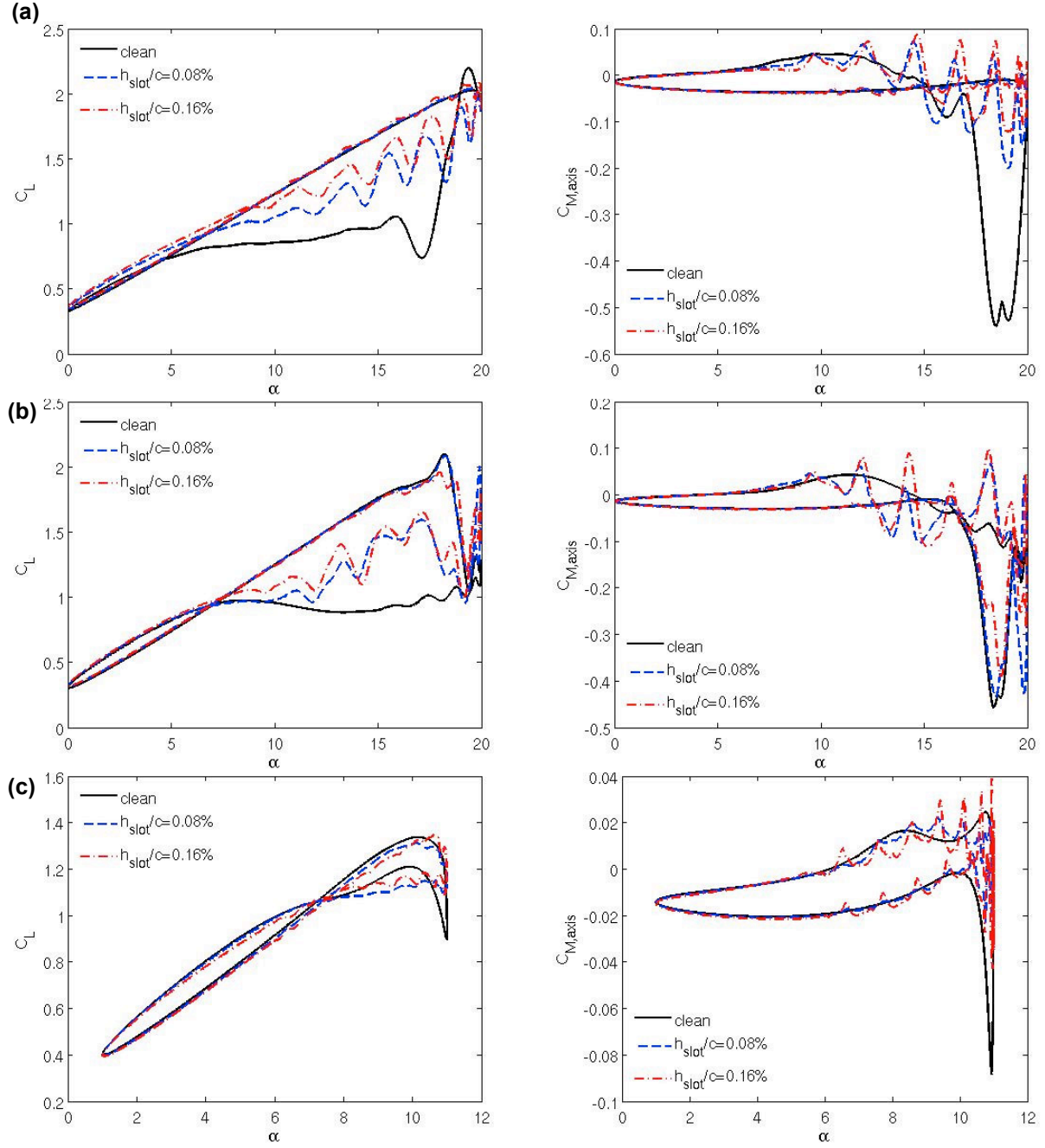


**Figure 12. Unsteady lift and moment traces with COMPACT at  $x_{slot} = 0.1c$  with variations in the slot thickness  $h_{slot}$ . (a)  $Ma=0.3$  with  $k=0.1$ , (b)  $Ma=0.4$  with  $k=0.07$ , and (c)  $Ma=0.5$  and  $k=0.05$ . The angle of attack,  $\alpha$ , is in degrees.**

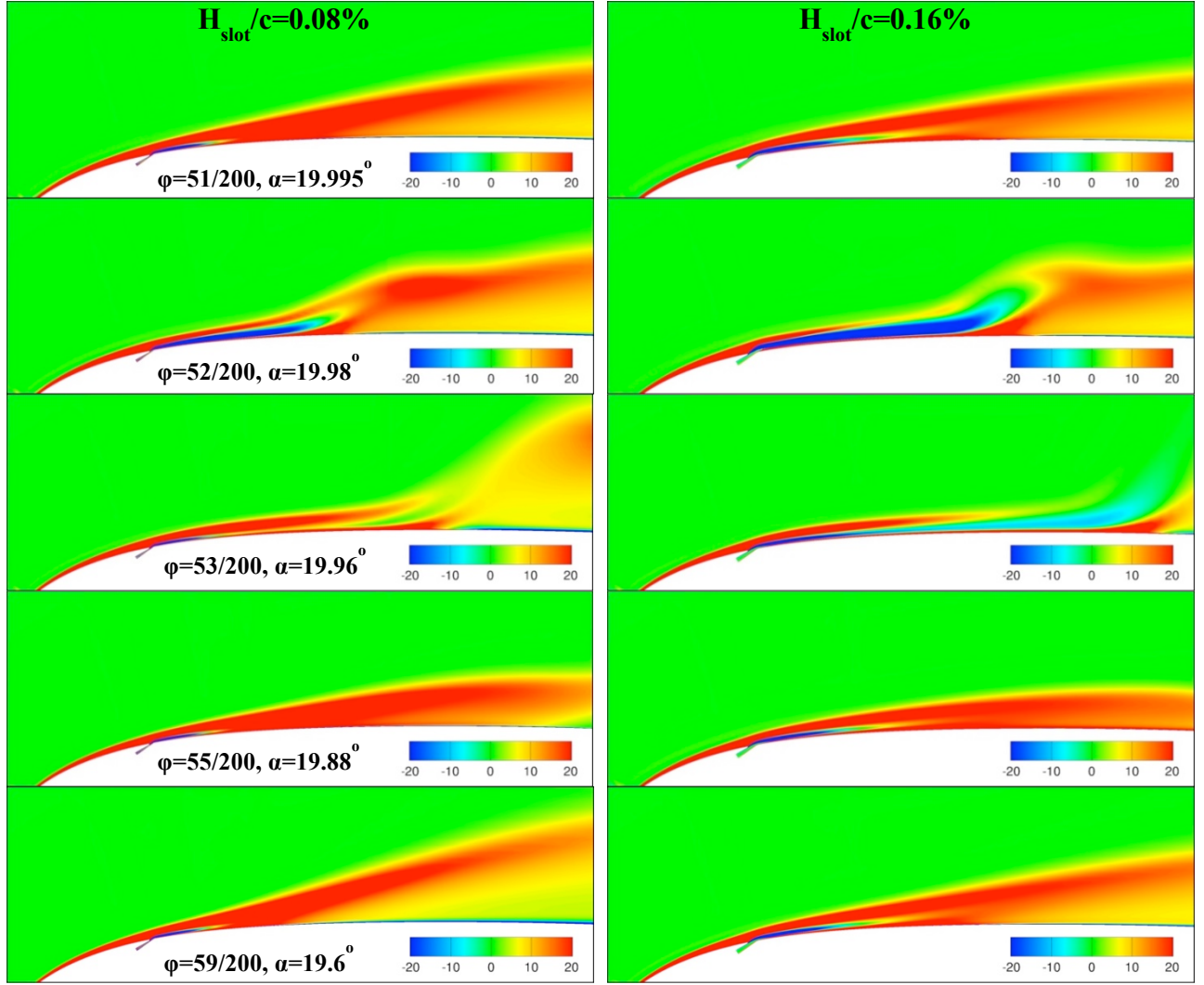
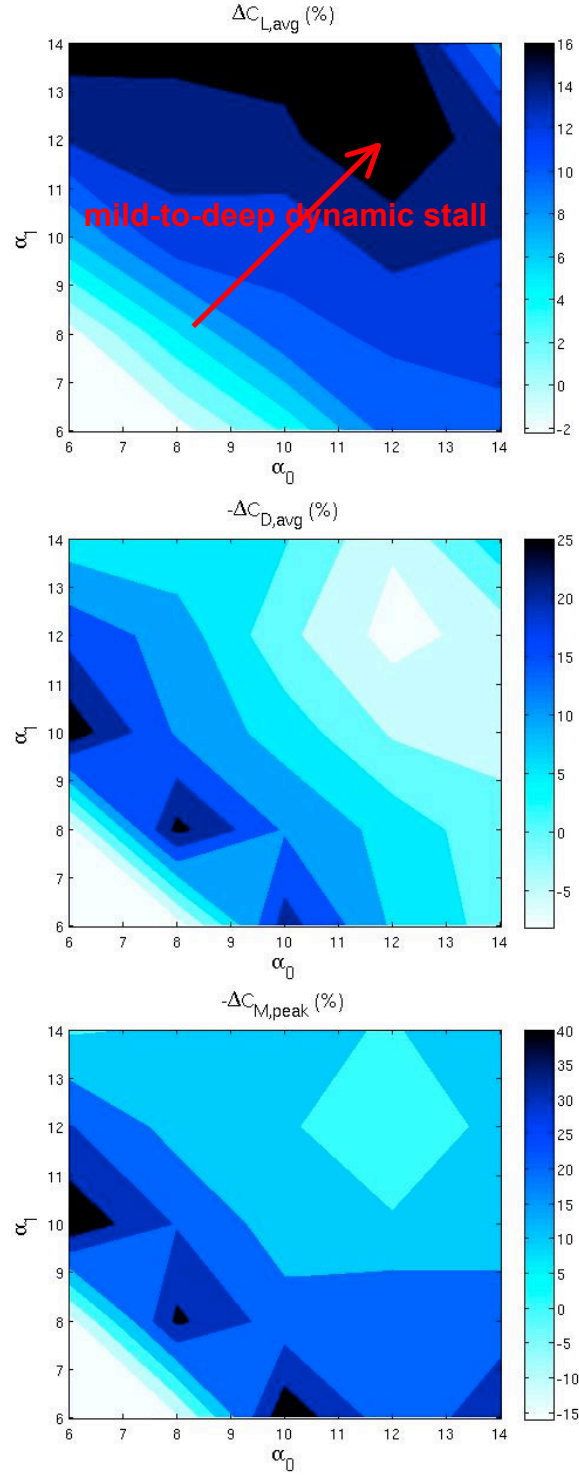
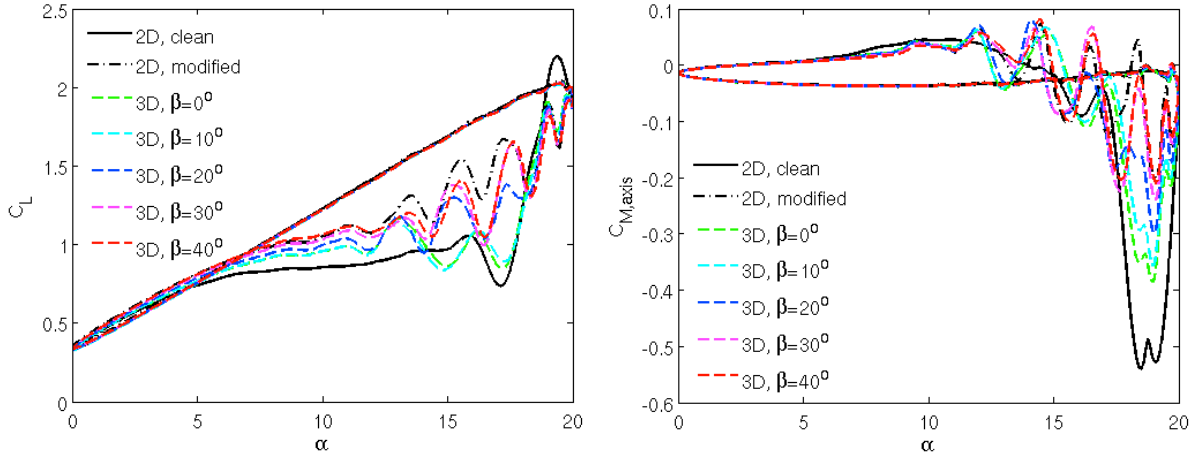


Figure 13. Spanwise vorticity field for  $Ma=0.3$ ,  $k=0.1$ , slot at  $x_{\text{slot}}/c=0.1$  with  $\theta_{\text{slot}}=22^\circ$ ,  $h_{\text{slot}}/c=0.08\%$  (left) and  $h_{\text{slot}}/c=0.16\%$  (right), illustrating the effect of slot thickness, focusing on the  $x$  range of  $(0, 0.4)$  and around maximum angle-of-attack.





**Figure 14. Cycle-averaged lift  $\Delta C_{L,avg}$  and drag  $\Delta C_{D,avg}$ , and peak moment  $\Delta C_{M,peak}$  with COMPACT at  $x_{slot}=0.1c$  with  $h_{slot}/c=0.16\%$  for various pitching conditions at  $Ma=0.4$  and  $k=0.07$ .**



**Figure 15.** Unsteady lift and moment traces subject to variations of the skew angle  $\beta$  for the pitching cycle of  $k = 0.1$ ,  $\alpha_0 = 10^\circ$ , and  $\alpha_1 = 10^\circ$  at  $Ma=0.3$  with slots located at  $x_{slot} = 0.1c$ .

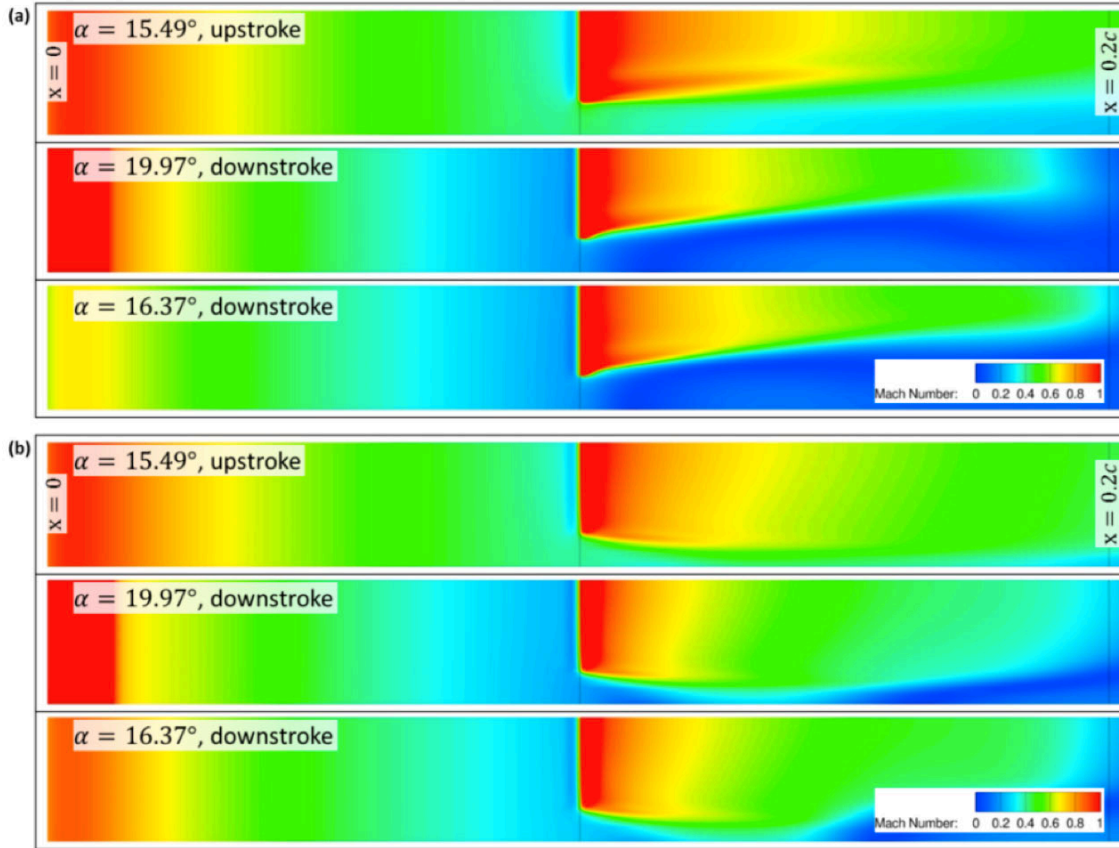


**Figure 16.** Contours of the Mach number at the constant distance away from the airfoil surface  $d_{wall} = 0.07\%c$  for the 3D simulation with the tangential slot of  $h_{slot}/c = 0.08\%$  and  $L_{slot}/L_{span} = 8/11$  at  $x_{slot} = 0.1c$ . (a)  $\beta = 0^\circ$  and (b)  $\beta = 30^\circ$ . The pitching motion of  $k = 0.1$ ,  $\alpha_0 = 10^\circ$  and  $\alpha_1 = 10^\circ$  at  $Ma=0.3$ .

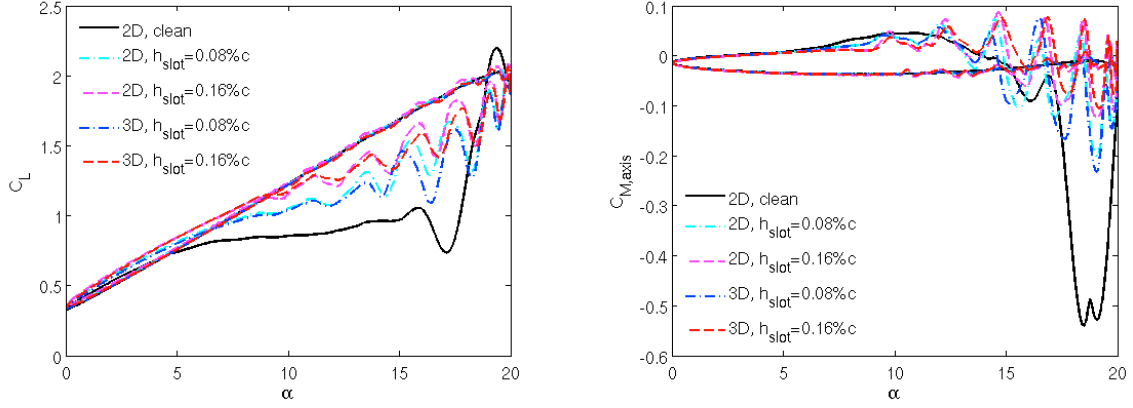


Figure 17. Effect of slot thickness  $h_{slot}$  on the unsteady lift and moment traces for the pitching cycle for  $Ma=0.3$  with slots located at  $x_{slot} = 0.1c$ . The vanishing gap geometry is used for the 3D simulation.

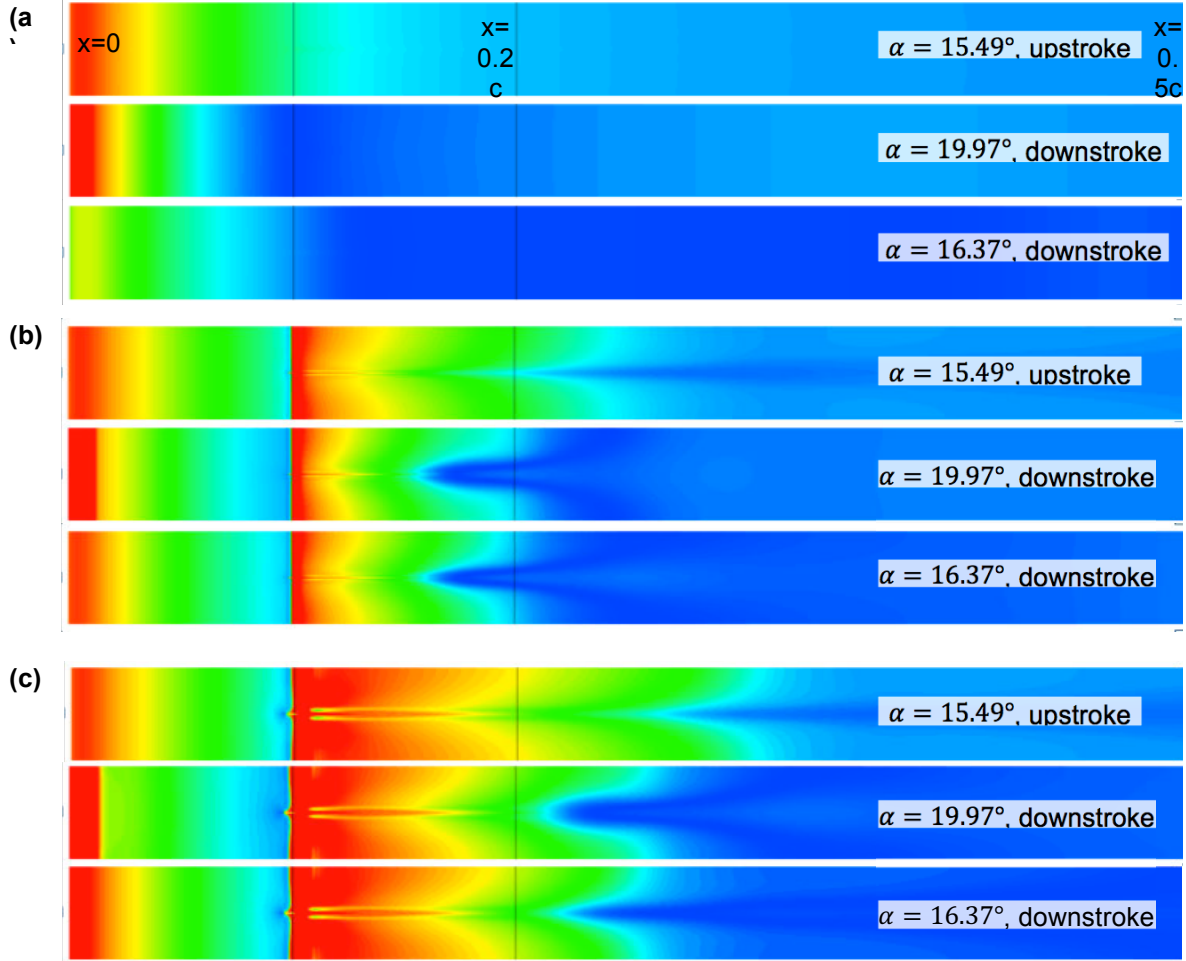


Figure 18. Contours of the Mach number at the constant distance away from the airfoil surface  $d_{wall} = 0.07\%c$  for the vanishing-gap slots at  $x_{slot}=0.1c$ . (a) No actuation; (b) actuation with  $h_{slot}=0.08\%c$ ; and (c)  $h_{slot}=0.16\%c$ . The pitching motion of  $k = 0.1, \alpha_0 = 10^\circ$  and  $\alpha_1 = 10^\circ$  at  $Ma=0.3$ . See Figure 16 for the contour level.

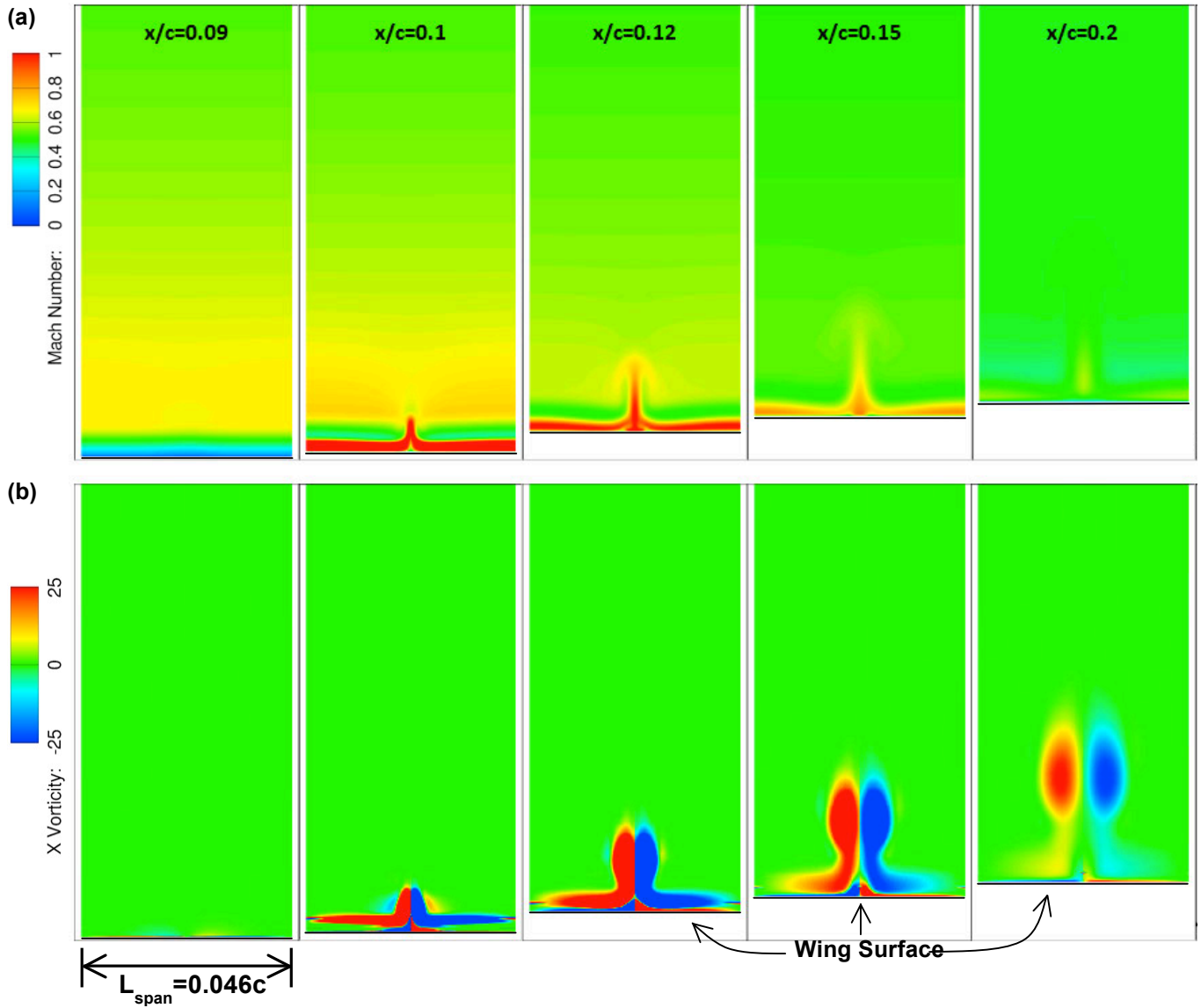


Figure 19. Contours of the Mach number (a) and the streamwise vorticity (b) at  $\alpha = 19.97^\circ$  downstroke on the selected x locations on the suction side of the VR 12 airfoil for the 3D simulation with the vanishing-gap slot of  $h_{\text{slot}}/c = 0.16\%$  and  $\theta_{\text{slot}} = 22^\circ$  at  $x_{\text{slot}}/c = 0.1$ . The pitching motion of  $k = 0.1$ ,  $\alpha_0 = 10^\circ$  and  $\alpha_1 = 10^\circ$  at  $\text{Ma} = 0.3$ .

**Table 1. 2D CFD results from slot angle and chordwise location variations at Mach 0.3.**

Slot Location (x/c)	Slot Angle (°)	Slot Height (c)	$C_{L,avg}$	$C_{D,avg}$	$C_{M,peak}$	$\Delta C_{L,avg}$ (%)	$\Delta C_{D,avg}$ (%)	$\Delta C_{M,peak}$ (%)
clean airfoil			1.09	0.10	-0.54	-	-	-
0.1	22	0.08%	1.15	0.06	-0.20	5.6	-45	-63
0.1	56	0.08%	1.00	0.12	-0.50	-8.1	17	-7.5
0.1	90	0.08%	0.82	0.14	-0.42	-25	32	-22
0.15	22	0.08%	1.16	0.05	-0.20	6.6	-49	-62
0.15	56	0.08%	1.05	0.10	-0.45	-3.9	-3.8	-16
0.15	90	0.08%	0.89	0.12	-0.42	-18	17	-22

**Table 2. 2D CFD results from slot angle and chordwise location variations at Mach 0.4.**

Slot Location (x/c)	Slot Angle (°)	Slot Height (c)	$C_{L,avg}$	$C_{D,avg}$	$C_{M,peak}$	$\Delta C_{L,avg}$ (%)	$\Delta C_{D,avg}$ (%)	$\Delta C_{M,peak}$ (%)
clean airfoil			0.96	0.11	-0.46	-	-	-
0.1	22	0.08%	1.06	0.12	-0.43	10.8	3.2	-5.1
0.1	56	0.08%	0.91	0.12	-0.42	-4.6	11.0	-7.1
0.1	90	0.08%	0.80	0.13	-0.34	-16.7	13.2	-26.4
0.15	22	0.08%	1.03	0.10	-0.45	7.8	-10.6	-2.6
0.15	56	0.08%	0.96	0.12	-0.44	-9.9	8.8	15.7
0.15	90	0.08%	0.88	0.12	-0.41	-17.3	11.6	8.1

**Table 3. 2D CFD results from slot angle and chordwise location variations at Mach 0.5.**

Slot Location (x/c)	Slot Angle (°)	Slot Height (c)	$C_{L,avg}$	$C_{D,avg}$	$C_{M,peak}$	$\Delta C_{L,avg}$ (%)	$\Delta C_{D,avg}$ (%)	$\Delta C_{M,peak}$ (%)
clean airfoil			0.88	0.028	-0.088	-	-	-
0.1	22	0.08%	0.87	0.024	-0.033	-0.10	-14	-62
0.1	56	0.08%	0.83	0.033	-0.10	-5.1	18	18
0.1	90	0.08%	0.75	0.047	-0.15	-14	69	71
0.15	22	0.08%	0.88	0.026	-0.069	0.0	-5.7	-22
0.15	56	0.08%	0.86	0.028	-0.086	-2.1	1.4	-7.7
0.15	90	0.08%	0.82	0.033	-0.11	-6.4	19	13

**Table 4. 2D CFD results from slot height variations across the Mach numbers**

Mach	Slot Location (x/c)	Slot Angle (°)	Slot Height (c)	$C_{L,avg}$	$C_{D,avg}$	$C_{M,peak}$	$\Delta C_{L,avg}$ (%)	$\Delta C_{D,avg}$ (%)	$\Delta C_{M,peak}$ (%)	Downstream Corner
0.3	0.1	22	0.08%	1.15	0.057	-0.20	5.6	-45	-63	Sharp
0.3	0.1	22	0.16%	1.19	0.048	-0.12	9.4	-53	-78	Rounded
0.4	0.1	22	0.08%	1.06	0.12	-0.43	11	3.2	-5.1	Sharp
0.4	0.1	22	0.16%	1.08	0.10	-0.39	13	-7.8	-15	Rounded
0.5	0.1	22	0.08%	0.87	0.024	-0.033	-0.10	-14	-62	Sharp
0.5	0.1	22	0.16%	0.88	0.026	-0.043	0.26	-7.5	-51	Rounded

**Table 5. 3D CFD results for skew angle variations and vanishing-gap slots for Mach=0.3**

Height (c)	Slot-to-Span Ratio	Skew angle (°)	$C_{L,avg}$	$C_{D,avg}$	$C_{M,peak}$	$\Delta C_{L,avg}$ (%)	$\Delta C_{D,avg}$ (%)	$\Delta C_{M,peak}$ (%)
0.08%	8/11	0.0	1.09	0.080	-0.38	-0.20	-22	-29
0.08%	8/11	10.0	1.09	0.076	-0.36	-0.37	-26	-34
0.08%	8/11	20.0	1.11	0.070	-0.30	1.8	-32	-45
0.08%	8/11	30.0	1.12	0.063	-0.24	3.1	-39	-56
0.08%	8/11	40.0	1.13	0.060	-0.21	3.5	-41	-61
0.08%	Vanishing-Gap	25.4	1.13	0.060	-0.23	3.7	-41	-57
0.16%	Vanishing-Gap	25.4	1.18	0.047	-0.11	7.7	-55	-80

## VII. Low Speed Test Article Design and Fabrication

### 1. Actuator Chamber Design

Two new configurations of COMPACT actuators were designed and fabricated with specific attention to the integration needs of the VR-12 wind tunnel model. In particular, it is expected that the air and fuel supplies within the model will be located downstream of the actuator location (in immediate proximity to the actuator orifice located at  $x/c = 0.1$ ) with connecting plumbing routing the flows forward within the model to the actuator arrays. In order to subsequently create blowing nearly tangential to the airfoil surface, the flow within the actuator must undergo a strong turn back to the direction from which it will initially enter the actuator. To accomplish this smoothly, the two 2-D actuator designs shown in Figure 20 were fabricated in aluminum using wire EDM.

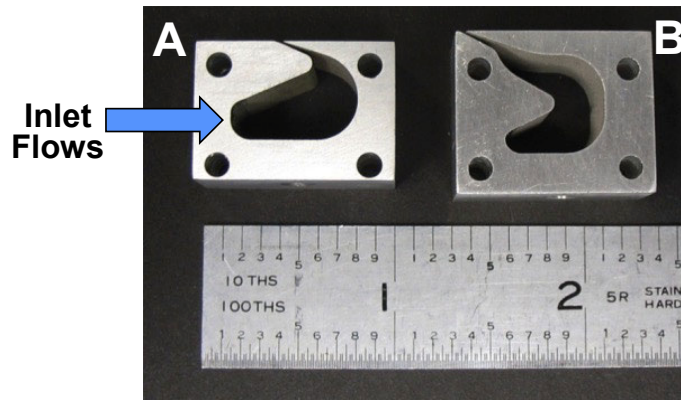


**Figure 20. Bench-top COMPACT actuators designed for VR-12 integration.**

Both actuators were 0.5" thick and had overall chamber volumes ( $V$ ) of approximately 1.5 cc. The 2-D slot orifice (created during the same cutting process as the chamber volume) was angled at 160 degrees from the flow inlet direction and has a minimum orifice thickness of about 0.0135". (This is ultimately 0.0009 $c$  of the VR-12 models and is slightly smaller than the 0.001 $c$  initially prescribed due to better than expected machining tolerances in the EDM process.) Actuator A (left) accomplished this with a turn basically at the orifice itself as it exits from the chamber. Actuator B (right) instead was shaped to change the direction of the bulk flow as it moves through the chamber before reaching the orifice. It is noteworthy that in both these designs, the orifice shape transitions smoothly from the chamber volume, which is different from earlier airfoil-integrated COMPACT designs that typically involved sharp transitions from the chamber volume to a fixed width orifice exiting normal to the surface of the model. It was anticipated that this feature would ultimately produce lower losses in the orifice and improved actuator jet strength (although this could not be confirmed directly from the bench-top measurement of chamber pressures, which might actually reflect reduced pressure levels in response to lower pressure drop at the actuator orifice).

Dynamic pressure measurements were acquired for both designs for a range of operating conditions. Sample dynamic chamber pressures are shown in Figure 21 for a range of firing frequencies ( $f_{act}$ ) at a fixed mixture flow rate ( $Q$ ) of 7 sL/min and a mixture ratio ( $\Phi$ ) of 0.5 with

air/H<sub>2</sub> mixture. For each actuator, the frequency performance was typical for COMPACT operation with increasing frequencies producing lower peak pressures and somewhat longer pressure pulse durations. This is due to scavenging inefficiencies yielding an effectively lower mixture ratio within the chamber at higher frequencies as it is unable to completely flush out products from previous combustion bursts. This effect is negligible at lower frequencies (both actuators show little change between 10 and 20 Hz) but more pronounced as the actuator approaches its ideal firing frequency (defined as the frequency at which the actuator is ignited once for each time the chamber receives a volume of gas sufficient to completely refill it, such that  $f_{ideal} \equiv Q/V$ ). For 1.5cc actuators with a flow rate of 7 sL/min,  $f_{ideal} = 77.8$  Hz. There were significant differences in the comparative performance of the two actuators. For Design A, higher peak pressure (3.15 atm) was achieved at the low baseline frequency of 10 Hz than for Design B (2.41 atm). This likely is the result of the more condensed chamber shape allowing more uniform and spherical flame propagation and thus higher chemical energy release rates. Somewhat lower heat transfer loss to the walls might also be expected due to the less convoluted chamber shape. However, the improved performance for Design A did not persist into the higher frequencies. For Design A, there was a significant peak pressure drop above 20 Hz up to a maximum stable operating frequency of 60 Hz. Design B showed much slower decrease in peak pressure with frequency and exceeded Design A's pressures at 60 Hz operation (1.78 atm vs. 1.61 atm). Design B continued to operate with stable ignition pulses up to 110 Hz, thus operating beyond the ideal firing frequency for these conditions. It was conjectured that the improved frequency performance of Design B was associated with improved mixing of the air and fuel streams in the lower section of the chamber where the inlets are co-located. Similar trends were observed for increased flow rates to the chamber; with pressures for  $Q=14$  sL/min ( $f_{ideal} = 155.6$  Hz) shown in Figure 22. As is typical for COMPACT, increased flow rates yielded somewhat higher flame propagation speeds with subsequently higher peak pressure and faster burn times at similar frequencies. Here, the low frequency baseline (10 Hz) peak pressures were 3.80 and 3.20 atm for Designs A and B, respectively. Design A operated to frequencies of 110 Hz (120 Hz is also shown but produces intermittent combustion bursts) and Design B operated to 160 Hz, with B yielding higher peak pressures above 90 Hz.



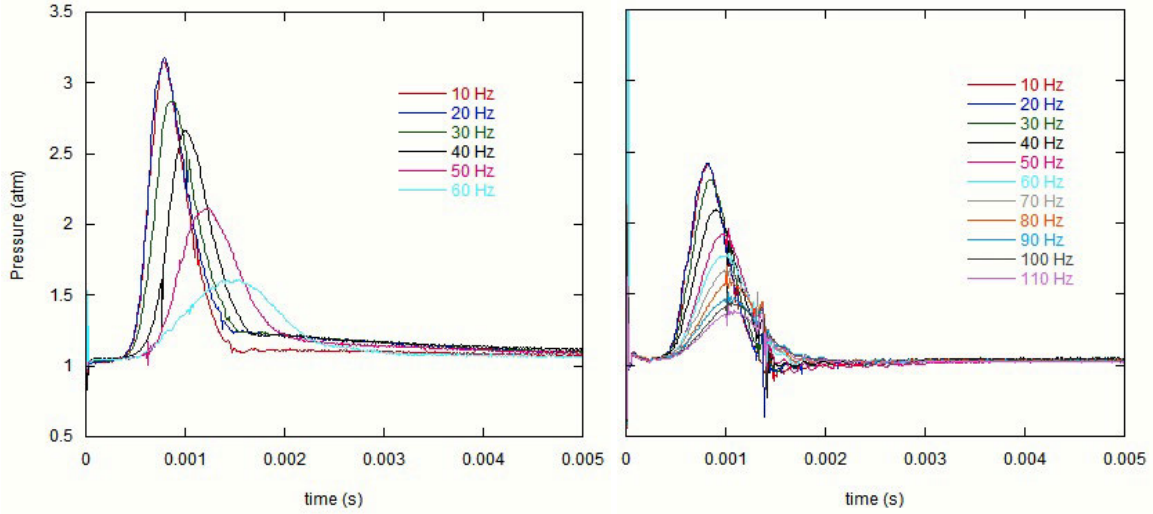


**Figure 21. Dynamic pressure measurements varying frequency for  $Q = 7$  sL/min and  $\Phi = 0.5$  for actuator A (left) and B (right).**

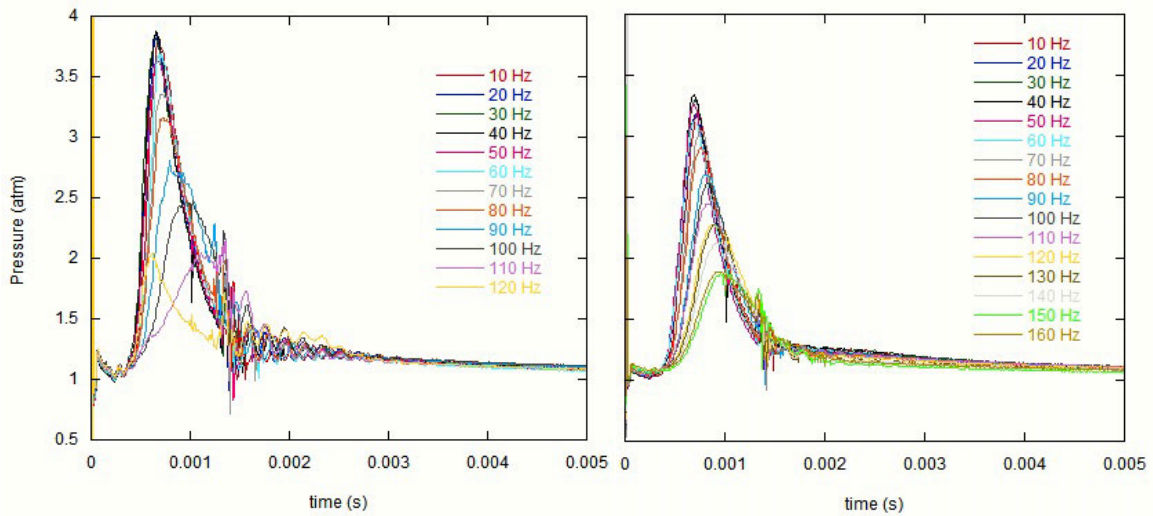


**Figure 22. Dynamic pressure measurements varying frequency for  $Q = 14$  sL/min and  $\Phi = 0.5$  for actuator A (left) and B (right).**

In the following quarter, another design concept was tested. This variant (labeled C in Figure 23 with previous Designs A and B shown for comparison) may be thought of as the inverse of Design A, such that the inlet flows are turned promptly near the entrance of the chamber rather than near the exhaust orifice. It was hoped that this configuration would combine some of the beneficial features of the earlier designs, including better initial air/fuel mixing and a less convoluted chamber shape. Sample dynamic chamber pressures are shown in Figure 24 for all three configurations over a range of firing frequencies  $Q = 7$  sL/min and  $\Phi = 0.5$  with air/H<sub>2</sub> mixture (results for Designs A and B are the same as those shown in Figure 21 above). In terms of low-frequency performance, Design C was similar to Design B and did not match the high pressure peaks achieved with Design A. A notable change in the performance of Design C, however, was that it had even better high frequency performance than Design B. At 60 Hz, for

example, Design C maintained a peak pressure level of 2.20 atm, well exceeding the levels for both Designs A and B (1.61 atm and 1.78 atm, respectively), and this improved performance held to a maximum stable operating frequency of 110 Hz for the given flow conditions.

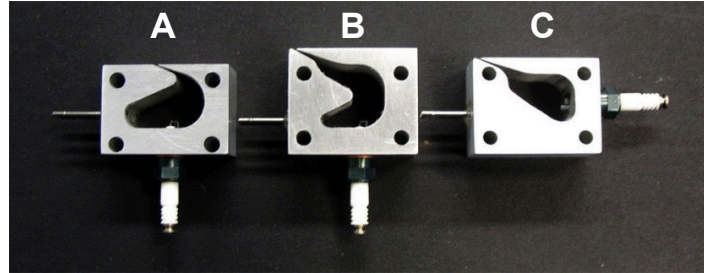


**Figure 23.** All test actuator designs shown with spark plugs and gas feedlines.

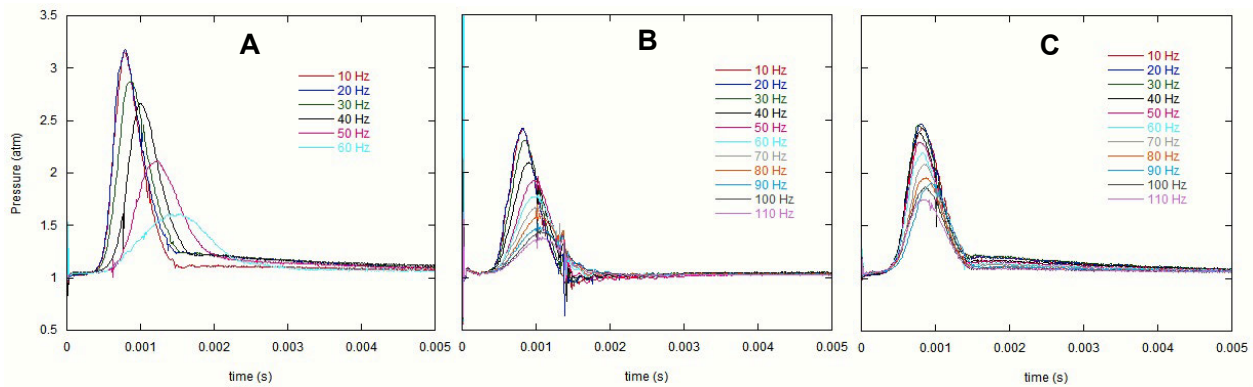


**Figure 24.** Dynamic pressure measurements varying frequency for  $Q = 7$  sL/min and  $\Phi = 0.5$  for actuator A (left), B (middle), and C (right).

The achieved peak pressures for each Design for two different flow rates (7 sL/min in red and 14 sL/min in blue) and a range of frequencies are shown in Figure 25. Design A consistently produced the highest pressure peaks at low frequencies, but showed a rapid drop in peak pressure at elevated frequencies and the lowest maximum stable operating frequency. Designs B and C have similar peak pressures at low frequencies, but showed a much slower decay in peak frequency than Design A, with Design C showing markedly better high frequency performance than even Design B. For Design C, the maximum stable operating frequency for 7 sL/min was 110 Hz, and for 14 sL/min it was 200 Hz. The ideal firing frequencies are shown for each flow rate as a dashed vertical line and Design C operates beyond this level for both cases. Extended testing with Design C at even higher flow rates (not presented here) showed operation at frequencies up to 290 Hz, which is a notably high operating frequency for the comparatively large volume ( $\sim 1.5$  cc) of these test chambers. Several variants of Design C with modified inlet configurations were also tested but with no arrangements found that produced significantly improved performance over the results presented above. Design C's superior high frequency performance made it the preferred actuator design for testing in both the low-speed and high-speed wind tunnel models.

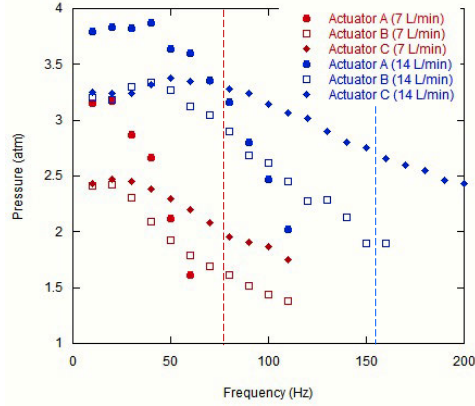


**Figure 25.** Peak dynamic pressures achieved varying frequency for  $Q = 7$  and  $14$  sL/min and  $\Phi = 0.5$  for actuator A, B, and C. Dashed line represents  $f_{ideal}$  for the two different flowrates (77.8 Hz and 155.6 Hz).

## 2. Pitching Airfoil Design and Fabrication

In parallel with the COMPACT actuator design and testing, work proceeded on the design of the low-speed VR-12 model to be tested in the Georgia Tech School of Mechanical Engineering Wind Tunnel. For reference, a scale drawing of the 15" chord VR-12 with the actuator A design incorporated with slot orifice at  $x/c=0.1$  is presented in Figure 26. As shown, a 1.5 cc COMPACT actuator requires a comparatively small volume within the model, leaving a large amount of available space for plumbing, electronics, etc., particularly within the context of the low-speed model where less model space must be dedicated to physical supporting structures. A schematic of the final actuator assembly near the leading edge of the airfoil is shown in Figure 27 with two 5-actuator arrays on either side of a center element with static pressure taps covering the full surface of the airfoil. This gave an approximately 8" active span in the model, which could then be bounded by fences or left unbounded to study 3-D interactions between actuated and unactuated regions as in previous work at Georgia Tech. Each of the individual elements was fabricated from aluminum via 2-D wire EDM processes, creating the external VR-12 shape and internal shape of the actuator cavity within the model. Individual actuator elements are shown at right in Figure 27 with the modular design allowing actuator slots with orientations both nominally tangential to the airfoil surface (actually  $20^\circ$ ) and normal to the airfoil chord (approximately  $80^\circ$  to the airfoil surface) to be tested interchangeably. Each 0.5" width actuator was stacked spanwise and surrounded by a 0.1875" dividing plate, which both separated the actuators from each other and provided the structural material to attach the actuators and leading edge to the larger rear section of the airfoil. (It is noted that a design update later in the low-speed testing changed these to individual 0.09375" walls for each actuator rather than the shared wall design shown in Figure 27.) Alignment pins oriented in both the spanwise and streamwise directions maintained the outer VR-12 shape during assembly.



**Figure 26. Scale representation of 15" VR-12 with integrated COMPACT actuator (Design A) at prototype scale.**

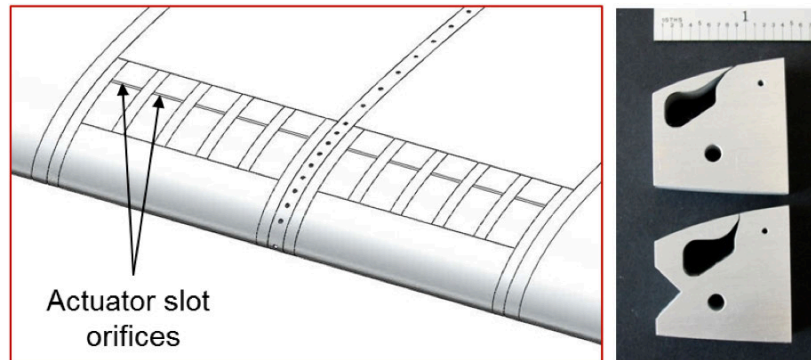


**Figure 27. Schematic of modular COMPACT actuator array in low-speed VR-12 model with fabricated normal and tangential slot actuators shown.**

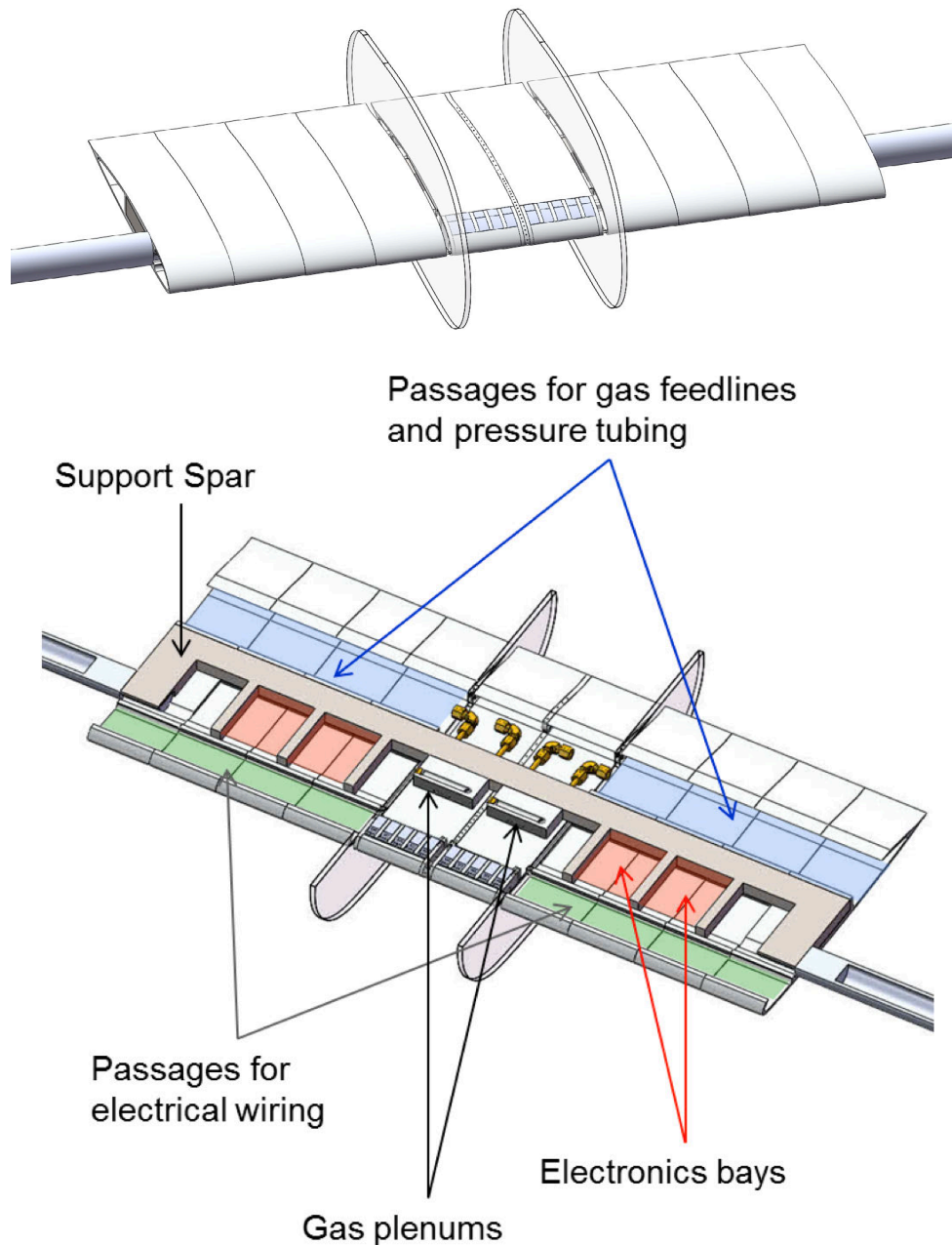


**Figure 28. Assembly drawings of low-speed VR-12 model showing top view (above) and cutaway view of internal structures (below).**

Assembly drawings of the entire ~36" span model with all components are shown in Figure 28. All support elements for interfacing to the Georgia Tech School of Mechanical Engineering Wind Tunnel pitch/plunge mechanism are included here and cutaway view in the lower image shows the internal areas intended for electronic components, wiring, and plumbing. In designing this, particular attention was paid to the overall stiffness of the model support in order to try to circumvent any problems with vibrations occurring at the same frequency levels as the pitching motion, thus contaminating the signals from the load sensors (a challenge faced with some prior wind tunnel models). The final design included a solid steel support spar, which interfaces with



the support rods at either side at the center of rotation at  $x/c = 0.25$  (and at the midpoint of the airfoil thickness at that streamwise location). The main structure of the support spar runs the full internal span of the model further downstream near  $x/c = 0.5$  with mechanical support “ribs” running forward at discrete locations. This offset (also seen in Figure 29 below) allows for sections forward of the spar to house support infrastructure (plumbing and electronics) for easier access to the actuators near the leading edge (with slots at  $x/c = 0.1$ ). FE analysis of the spar under the loading expected from the combined effects of the model weight and lift and drag forces generated at a freestream velocity of 40 m/s over a range of angles of attack indicated negligible deflection across the span of the model. The model in an intermediate state of assembly is shown in Figure 29, highlighting the internal structure of the spar and the VR-12 internal and external airfoil shapes produced through the wire EDM process. Note that Figure 29 shows a “clean” airfoil configuration with dummy sections in the region between fences for baseline measurements.

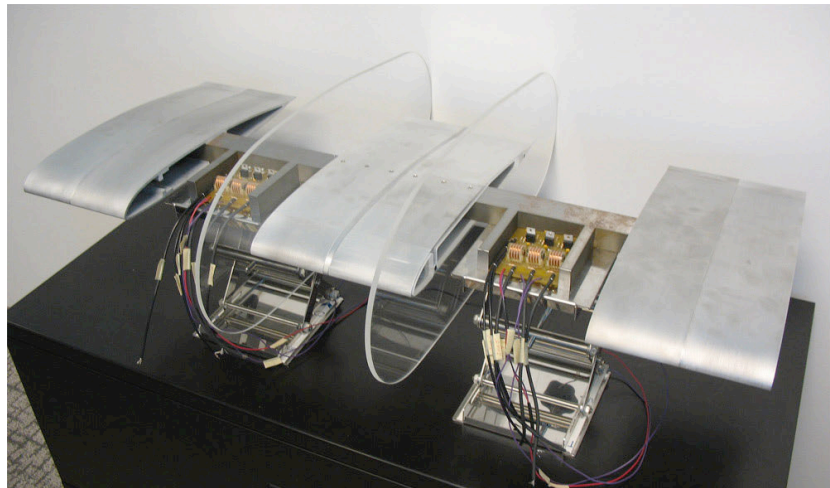


**Figure 29. Partially assembled low-speed wind tunnel model.**

The fully assembled model with actuators in place is shown mounted in the Georgia Tech School of Mechanical Engineering Wind Tunnel in Figure 30. In this case (and for most of the results presented herein), the fences have been moved to the far edge of the model focusing on preventing flow around the edges of the model while allowing the limited actuated span in the center of the model to fully interact with the larger unactuated regions on either side. This was done to more closely approximate both the expected conditions in the high-speed wind tunnel experiments and actual rotorblade implementations.

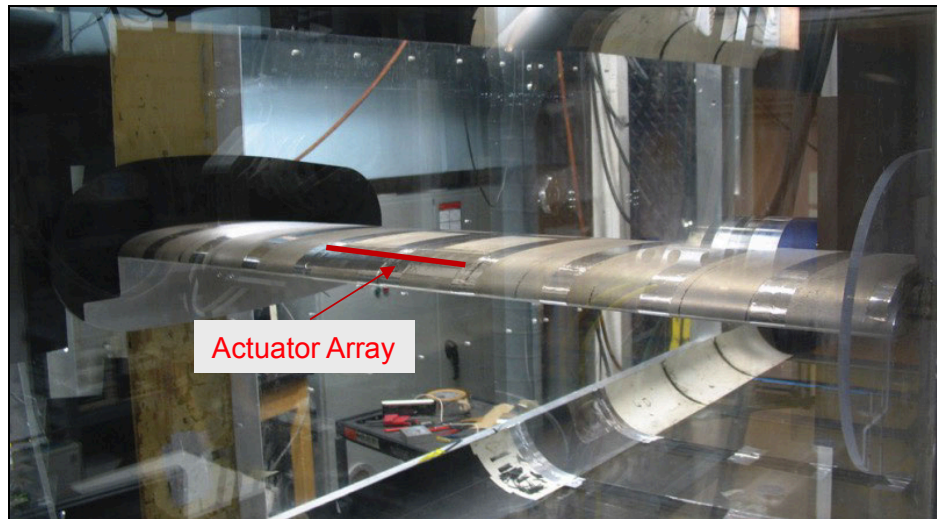


**Figure 30. Fully assembled low-speed VR-12 model mounted in the GT wind tunnel with actuated span highlighted in red.**

### **3. Actuator Support Systems**

In addition to the actuator and overall model design efforts, the first year of the program included several development efforts related to the support elements for the actuators with an eye towards integration requirements for both the low and high-speed VR-12 models. Specific efforts were made to reduce the volume dedicated to the spark ignition system for firing the COMPACT actuators. Bench testing of the actuators often involves the use automotive ignition system components, which are readily available but much too bulky for integration into wind tunnel models of this scale. The smallest available spark ignition system from commercially available plans and off-the-shelf components is shown in Figure 31. This is a capacitive discharge ignition (CDI) system, which takes a supply voltage of approximately 5V, uses elements on the circuit board to charge a capacitor to 250V, and then subsequently dumps the capacitor energy into an ignition coil (at left in Figure 31) to create the high-voltage spark. As shown, the whole package is approximately 2.25" by 1.375" by 0.75", with a total weight of 26.1 g (10.3 g for the coil and 15.8 g for the circuit board). It is noted that not every actuator requires a separate ignition circuit, as suitable wiring of the spark gaps can allow a single ignition system to ignite 2 to 4 actuators, depending upon the size of the spark gaps and their relative location to other grounded surfaces (and provided that they are to be fired simultaneously).

While reducing the size of the ignition coil beyond that shown was deemed unlikely to be possible within the scope of the current program, several efforts were undertaken to minimize the space dedicated to the ignition circuitry. The electronics laboratory at the Georgia Tech School of Mechanical Engineering demonstrated several prototype replacement circuits for the board shown with a 24V supply to eliminate the large transformer on the circuit board (wrapped in yellow in Figure 31) and several of the other smaller elements. 3-channel spark systems developed for use in the low-speed VR-12 model are shown at left in Figure 32 (these may also be seen integrated in the insets between of the spar in the lower image of Figure 29). The drive circuitry for this system is of an original Georgia Tech design and, as anticipated, eliminated several of the larger components prominent in commercially available ignition circuits. For the purposes of the low-speed airfoil integration, the circuit boards were sized specifically to fit into the bays in the spar; but as can be seen from the layout, the actual circuit size can be reduced

greatly by packing the elements more closely. Another prototype ignition circuit created by prioritizing miniaturization is shown at right in Figure 32. This was successfully demonstrated but produced significantly lower power sparks than the other systems. Another possibility that was successfully demonstrated was keeping the coils at a distance from the primary ignition electronics. In this case, the comparatively low-voltage pulse from the ignition circuit is routed to the coil, which is located in close proximity to the actuator. This minimizes the length of high-voltage wiring, which must be included (and the related EMI and RFI noise produced) while also only requiring the coils themselves to be located within the limited model space. This was the approach that was ultimately utilized for the high-speed VR-12 model.

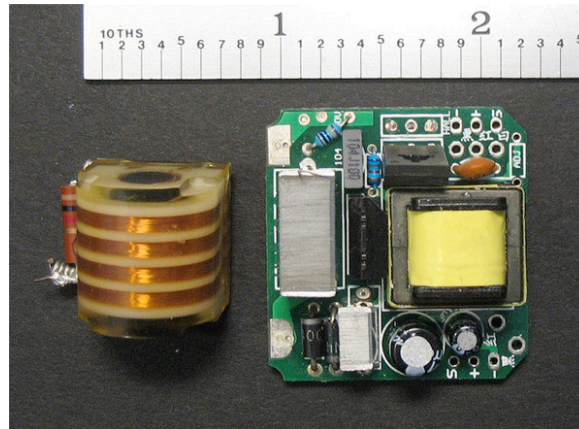


**Figure 31. Commercially available miniature CDI ignition system components.**

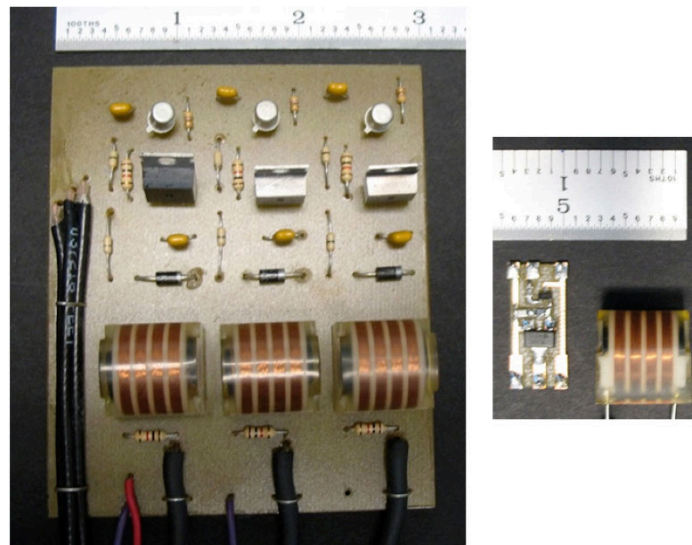


**Figure 32. 3-channel CDI ignition system for low-speed VR-12 model (left) and fully miniaturized prototype ignition circuit (right).**

In addition to the spark systems, possible changes to the approach for feeding gas to the actuators were considered. For the retreating blade stall problem, it is expected that the actuation will involve a burst of repetitive actuator firing during critical phases in the pitch cycle without the need for continuing actuation over the remainder of the cycle. When burst-mode firing has been implemented in the past with COMPACT, the flow of fuel and air has been allowed to remain



continuously on over the entire airfoil cycle, with air and fuel simply overflowing the chamber and providing a relatively low-velocity, steady bleed from the orifice between bursts. However, there may be benefits to changing this approach and trying to modulate the air and fuel flow to the actuator to match the burst window. Specifically, the net flow of air and fuel can be reduced proportionally to only the time window over which the actuator is actually firing. For the expected comparatively small duty cycles of the burst in this application, this can be a large percentage reduction in flow rates with potentially smaller plumbing lines having significant appeal in the limited internal space available within the high-speed VR-12 model. In addition, this approach might enable higher actuation frequencies (and the requisite peak gas flow rates during actuation) to be used without introducing increasingly large and potentially undesirable steady bleed levels between bursts.

A conceptual schematic of this approach is shown in Figure 33 with the valves controlling the gas flows located some distance (for the wind tunnel model, presumably outside of the model itself) from the actuator. Two key challenges for implementation were considered here. First, it was expected that the gas bursts produced by the valves would be damped to a degree by any elements producing pressure drops within the system such as the significant lengths of plumbing, fittings for changing the tube sizes or flow direction, gas distribution plenums, etc. Too much pressure drop in the system would create a large capacitor effect in the line and reduce the oscillation in the gas flow to a level where it effectively disappears. Second, the valve opening must be timed such that the gas burst reaches the actuator when the actuation burst is desired. Some phase lag between the two was expected simply from the pressure wave propagation time and might be exacerbated by the pressure drop elements described above.

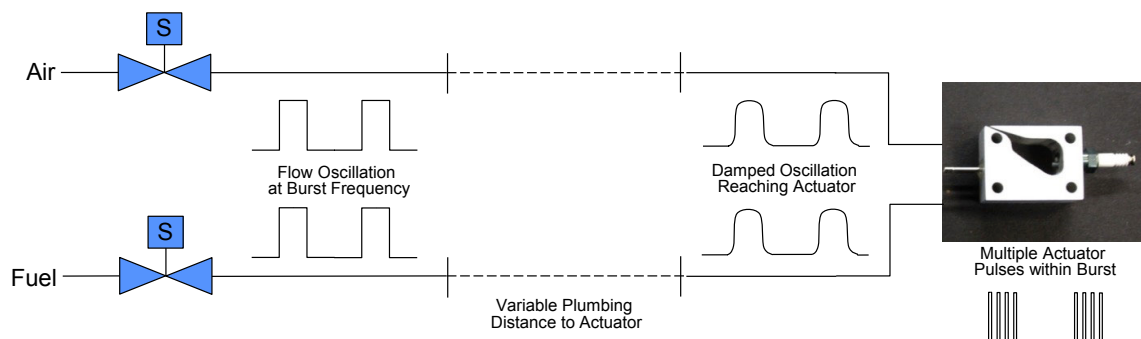


**Figure 33. Conceptual schematic of system for modulating actuator gas flows for burst mode operation.**

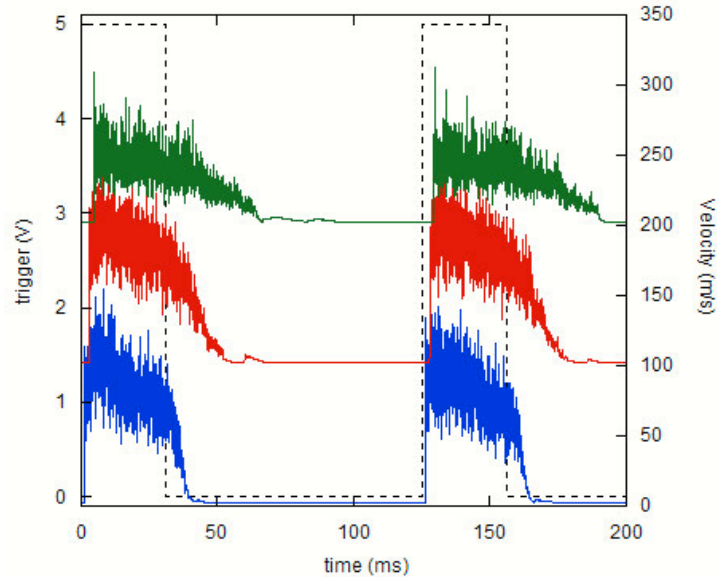


**Figure 34. Sample hot-wire data for jets emanating from valved flows with a downstream length of tubing (1", 24", and 48") between the valve and a reducing adapter leading to the jet. The data are offset in 100 m/s increments for visibility, and the valve trigger signal is shown as a dashed line.**

For proof-of-concept demonstrations of this approach, a fast-switching solenoid valve was tested (Festo model number MHJ-10-S-2,5-QS-4-MF) in several configurations with varying plumbing elements downstream of the valve location. The tests typically involved hot-wire measurements taken of the free jet emanating from end of the plumbing elements into the nominally quiescent atmosphere. A sample of these results is presented in Figure 34, where the valve was operated at 8 Hz (matching the expected pitching frequency for the high-speed wind tunnel tests) with a duty cycle of 25% and a time-averaged flow rate of nominally 3 sL/min. For these results, the lengths of tubing tested included 1", 24", and 48", with the line terminating in a reducing adapter, which reduced the internal diameter of the line from 0.105" to 0.042" (matching a common tubing size used for the inlets to the actuators). For all three of the tubing lengths tested, there was a very sharp rise in the velocity, as measured by a hot-wire (note that the results are offset in 100 m/s increments to allow the three signals to be seen clearly), shortly after the trigger signal (shown as a dashed line) initiated the valve opening. There is a slight delay between the trigger signal and the velocity increase that was associated with both the opening time of the valve and the wave propagation speed to reach the end of the tubing. The time lag between the varying configurations matched closely with the sonic propagation speed over the length of tubing and suggested that matching the timing of the valve opening to the desired start of the actuation burst could be fairly easily accomplished. The time lag between the closing of the valve and the end of the jet was significantly longer, however. This was a result of the plumbing's "capacitance" and did indeed increase with the length of tubing involved. There was also an appreciable reduction in velocity measured (particularly for the 48" length) as might be expected with the same time-averaged flow rate being spread out over a longer pulse duration. Even for the longest case, though, there was still an appreciable dead period between pulses, indicating the flow can be modulated to the actuator to a large extent. Some preliminary testing was performed with COMPACT actuators with the valves modulating the inlet flows and firing over short bursts was demonstrated but with some unevenness in the pressure levels between bursts and an

increased tendency to go to a steady flame (albeit one that was extinguished each time by the modulated inlet flow). For the purposes of the current program, it was decided that using a continuous gas feed would be preferable, although the valve-modulated feed concept might be revisited in future work.

## VIII. Low-Speed Wind Tunnel Tests

### 1. Static Airfoil Results

The low-speed wind tunnel testing began with holding the airfoil at static angles of attack to become familiar with the VR-12 design, which had not previously been tested in the Georgia Tech wind tunnel. As noted in Section 6, the low-speed airfoil model included actuator banks around the model centerline, comprising an active section of roughly 21% of the 36" model span. Interchangeable actuator modules allowed for actuators with both nominally normal (normal to the chord line;  $\sim 80^\circ$  to the local airfoil surface) and tangential ( $20^\circ$  to the local airfoil surface) actuation jets to be compared, with both actuator orifices located at  $x/c = 0.1$ . Primary diagnostics for this initial testing included static pressure measurements along the model centerline and PIV measurements aligned with the center of the actuator adjacent to the model centerline. The wind tunnel facility allowed for freestream velocities of 20 to 40 m/s ( $432,000 < Re < 875,000$ ) to be tested. For the majority of this testing, fences were only located at the far ends of the model span and the actuated and unactuated regions were allowed to fully interact with one another (as was expected to be the case for both the high-speed wind tunnel testing and practical implementations of COMPACT actuators on rotorblades). At the comparatively low freestream velocities examined, significant variation was initially observed in the angles at which separation occurred, with steady angles of attack ( $\alpha$ ) between  $15$  and  $18^\circ$  at times producing full attachment and at other times yielding full separation (and with occasional transitions between the two states with no apparent change in the tunnel operating conditions). To aid with repeatability, a small ( $\sim 0.001c$  diameter) trip wire was included over the actuated span, upstream of the actuators (at roughly  $x/c = 0.043$ ), which successfully regularized the flow for most measurements (it is noted that the COMPACT actuation produced flow reattachment even in the absence of the trip).

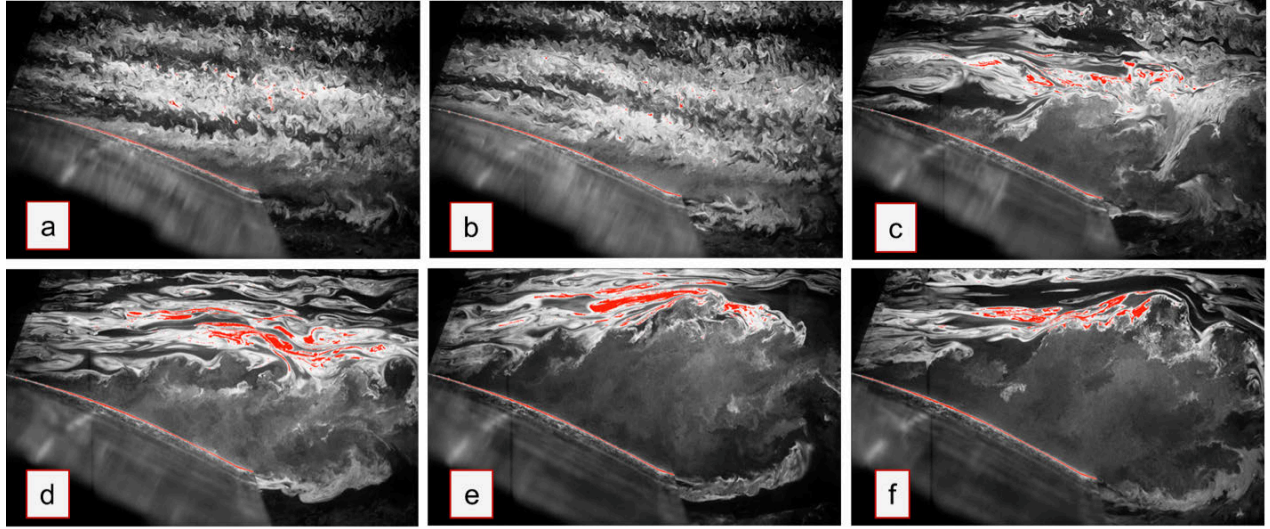


**Figure 35. Smoke flow visualization images for static low-speed model at  $Re=432,000$  for  $\alpha = 14$  (a), 15 (b), 16 (c), 17 (d), 18 (e), and 19 (f) degrees.**

Smoke flow visualization images (taken as part of the PIV data acquisition process) are presented in Figure 35 for the baseline flow at  $14^\circ \leq \alpha \leq 19^\circ$  for  $Re = 432,000$  showing the flow from approximately  $x = 0.4c$  to beyond the airfoil trailing edge. The degree of flow separation can readily be observed in these images with negligible separation at  $\alpha = 14^\circ$  and  $15^\circ$  (Figure 35a and b, respectively), beyond which the shear layer increasingly lifted off the surface of the airfoil at  $\alpha = 16^\circ$  and  $17^\circ$  (Figure 35c and d, respectively). Effectively full separation is observed at  $\alpha = 18^\circ$  (Figure 35e). Similar results were observed for the other values of  $Re$  tested such that effectively full separation is observed at  $\alpha = 18^\circ$  for all cases. This became the primary angle-of-attack used for actuation testing although similar actuation dynamics were observed in limited testing at angles as high as  $24^\circ$ .



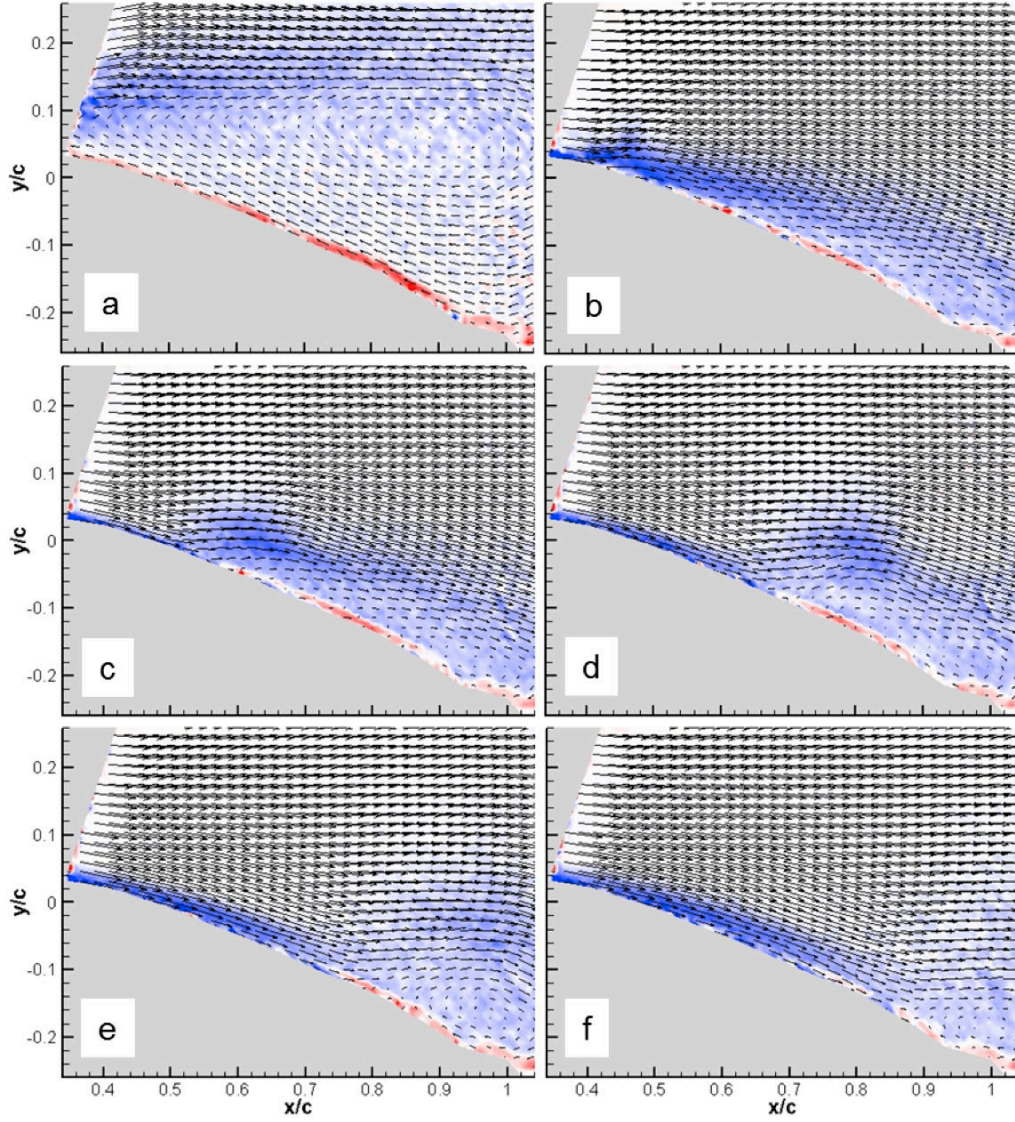


**Figure 36. Sample phase-locked PIV velocity vectors and vorticity contours for  $\alpha = 18^\circ$  and  $Re = 650,000$  with tangential slot orientation showing unforced baseline (a) and actuated cases for  $F^+ = 0.72$  and  $t/T_{pulse} = 0.0$  (b), 0.1 (c), 0.2 (d), 0.3 (e), and 0.4 (f).**

A sample of the processed phase-locked PIV data obtained for the static airfoil is shown in Figure 36 for  $\alpha = 18^\circ$  and  $Re = 650,000$  for the tangential actuator slot orientation. The unforced baseline (Figure 36a) is shown for reference, with large-scale separation of the flow and reversed flow near the surface of the airfoil as is evidenced by the counter-clockwise (CCW) vorticity concentration. Five phases during the repetition cycle for  $F^+ = 0.72$  are shown in Figure 36b through f for  $t/T_{act} = 0.0, 0.1, 0.2, 0.3$ , and  $0.4$ , respectively, representing the early part of the actuation cycle. The onset of the actuation ( $t/T_{act} = 0$ , Figure 36b) is demonstrated by the vorticity concentration near  $x/c = 0.45$  that protrudes over the nominal boundary layer. It is noteworthy here that while the boundary layer along the surface of the airfoil is relatively thick, there is virtually no evidence of reversed flow up to  $x/c \approx 0.9$  (demonstrating the lingering attachment from the previous actuation pulse). Following the momentary actuation pulse ( $T_{pulse} \ll T_{conv}$ ), the vortex that is formed by the actuation begins to grow and migrates

downstream along the surface (seen near  $x/c = 0.6$ ,  $0.8$ , and  $1.0$  for Figure 36c, d, and e, respectively) until it progresses beyond the trailing edge and outside the data window in Figure 36f. A remarkable feature of this advection is that the boundary layer upstream of the vortex is considerably thinner than the boundary layer downstream of the vortex, indicating that the vortex induces an upstream favorable pressure gradient, and in the wake behind this structure, flow attachment to the airfoil is nearly complete. Following the shedding of the vortex, the boundary layer begins to thicken and returns to its original state prior to the next actuation pulse. The actuator dynamics (with a severing of the existing shear layer and creation of a large vortical structure, which creates reattachment in its wake) are similar to those observed in previous COMPACT flow control demonstrations, e.g.; [30], [31], [32] even though those studies focused on normal actuator jet orientations.

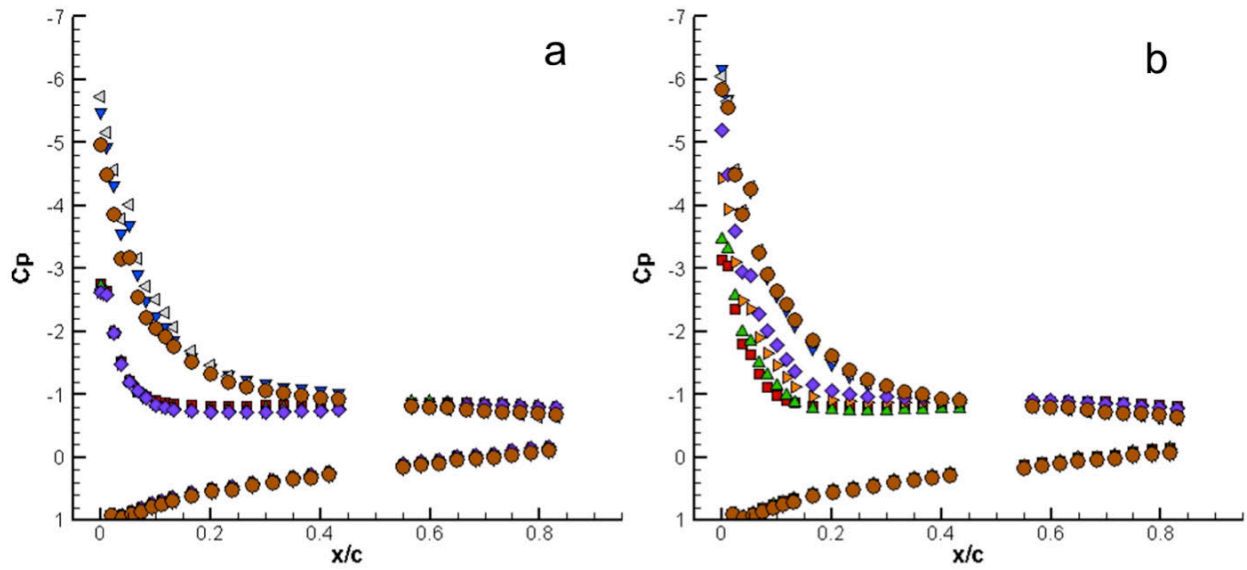


**Figure 37. Pressure coefficients for static airfoil at  $\alpha=18^\circ$  and  $Re=650,000$  for normal (a) and tangential (b) actuation jets including the baseline, unforced case ( $\blacksquare$ ), steady blowing at low ( $\blacktriangle$ ), medium ( $\blacktriangleright$ ), and high ( $\blacklozenge$ ) flow rates, and continuous COMPACT firing at  $F^+=0.72$  ( $\blacktriangledown$ ),  $1.07$  ( $\blacktriangleleft$ ), and  $1.43$  ( $\bullet$ ).**

The time-averaged actuation effect may be seen in the pressure coefficients from the large array of static pressure taps along the model centerline between the two actuator banks. These pressure taps provide wide coverage over the airfoil only missing a region around  $x/c = 0.5$  (where the spar prevented any taps from being placed) and after  $x/c \sim 0.85$  (where the airfoil thickness was insufficient to allow any taps to be included). Figure 37 shows a large array of data for the same conditions as the PIV of Figure 36 ( $\alpha = 18^\circ$  and  $Re = 650,000$ ) except in this case including both normal (Figure 37a) and tangential (Figure 37b) actuator slot configurations. Seven different data sets are presented here: the unforced baseline, COMPACT actuation at three different frequencies ( $F^+ = 0.72$ ,  $1.07$ , and  $1.43$ ), and steady bleed for three different flow rates corresponding to those utilized for the three COMPACT actuation cases ( $Q = 7$ ,  $10.5$ , and  $14$  sL/min/actuator). The fully actuated and steady bleed data are both presented to separate the

effects that might be associated with the blowing and mass introduced the actuator from the dynamic effects of the unsteady, high-speed actuation burst. The baseline pressure profile on the upper surface shows a small suction peak near the leading edge which disappears around  $x/c = 0.15$  with pressure levels essentially invariant after that. For both normal and tangential slot orientations, all three actuation cases produce significantly higher negative pressure peaks on the suction side of the airfoil compared to the baseline with continuously reducing pressure levels out to the pressure port nearest the trailing edge (as expected for an attached flow state). The pressure profiles for the three different actuation frequencies are very similar to one another, suggesting that the majority of the reattachment effect can be achieved without excessively high actuation frequencies (this will be discussed further in conjunction with Figure 39 below). For the normal blowing orientation, the three different levels of steady bleed have no apparent effect on the flow with pressure levels essentially identical to the baseline. However, for the tangential blowing orientation, there is a progressive increase in the size of the leading edge suction peak with the three different levels of steady bleed. This suggests that the steady blowing by itself may produce a Coanda-like attachment effect when it is oriented tangential to the surface (such an impact would not be expected for the normal blowing). This is significantly smaller though than the full actuation effect on the pressure levels, and it is anticipated that prohibitively high steady bleed flow rates would be necessary to replicate the attachment achieved with the transitory actuation effect by the COMPACT actuation.

Even larger differences between the normal and tangential slot orientations were observed at higher freestream velocities. Figure 38 presents similar data sets to Figure 37 but for  $Re = 875,000$  and with dimensionless actuation frequencies of  $F^+ = 0.53, 0.080, \text{ and } 1.06$  (the dimensional frequencies were held constant for the two different freestream velocities). Under these conditions, the tangential slot orientation (Figure 38b) continued to show strong reattachment of the flow for all of the tested actuation cases (and similar levels of attachment for each of the three frequencies) as well as some smaller measure of attachment due to the steady blowing alone (although this is notably less than the steady blowing effects at  $Re = 650,000$ ). However, only a greatly reduced effect is seen in any of the actuated results for the normal slot orientation (Figure 38a). This result (coupled with similar comparisons between normal and tangential slots that were performed as part of the CFD analysis of Section 5), led to the tangential slot orientation being the preferred approach both for bulk of the low-speed wind tunnel testing and the entirety of the high-speed wind tunnel testing.



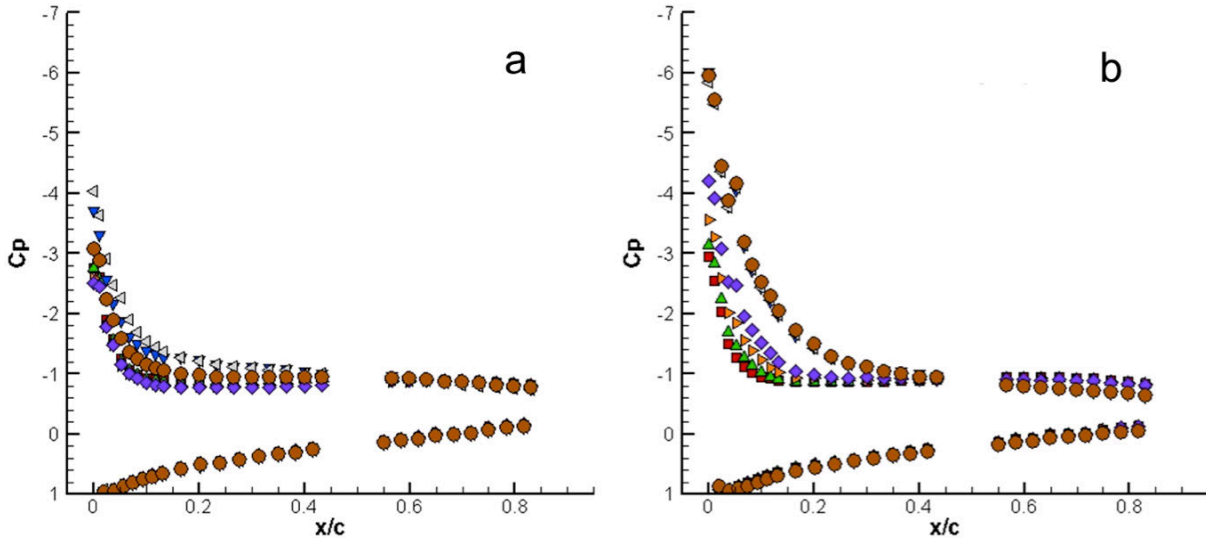


**Figure 38. Pressure coefficients for static airfoil at  $\alpha=18^\circ$  and  $Re=875,000$  for normal (a) and tangential (b) actuation jets including the baseline, unforced case ( $\blacksquare$ ), steady blowing at  $Q = 7$  ( $\blacktriangle$ ),  $10.5$  ( $\blacktriangleright$ ), and  $14$  ( $\blacklozenge$ ) sL/min/actuator, and continuous COMPACT firing at  $F^+ = 0.53$  ( $\blacktriangledown$ ),  $0.80$  ( $\blacktriangleleft$ ), and  $1.06$  ( $\bullet$ ).**

Further examinations of the effect of frequency on the reattachment were also performed, since as noted for the figures above, all of the initially tested actuation frequencies yielded similar results. This testing focused on using lower actuation frequencies given that effective operation at reduced frequencies inherently requires lower air and fuel flow rates, induces less heating of the actuator (with less possibility for failure of actuator components), and may enable actuator designs with fixed upper frequency limits to be of use at higher freestream velocities than were initially anticipated. Figure 39 presents data sets for  $\alpha = 18^\circ$  with tangential actuation slots for both  $Re = 650,000$  and  $875,000$ . Plots for both  $Re$  values include the baseline, unactuated case and steady blowing with at  $Q = 7$  sL/min/actuator (held constant in these cases while the actuation frequency was varied). For  $Re = 650,000$  (Figure 39a),  $F^+$  values of 0.14, 0.29, 0.50 and 0.72 are shown, and for  $Re = 875,000$  (Figure 39b),  $F^+$  values of 0.27, 0.37, and 0.53 are shown. (Note that the highest  $F^+$  value in each plot corresponds to the lowest values presented in the matching  $Re$  figures above.) Even as low as  $F^+ = 0.14$  at  $Re = 650,000$ , there is a significant degree of reattachment induced above the slight amount produced by the low, steady bleed. The pressure profiles for the remaining frequencies are largely invariant. Likewise for  $Re = 875,000$ , there is only a slight reduction in the degree of reattachment indicated for  $F^+ = 0.27$  with virtually identical levels for  $F^+ = 0.37$  and  $0.53$ . These results suggest that (at least for the low-speed testing)  $F^+$  values of  $\sim 0.3$  are sufficient to effectively achieve the full attachment effect. This is indicative of the fact that it actually takes several convective time scales ( $T_{conv}$ ) for the attachment effect from a single pulse to dissipate (as may be noted from the PIV of Figure 36, where the flow has not returned to the unforced state at the beginning of the next actuation burst despite the actuation period being less than the convective time scale).

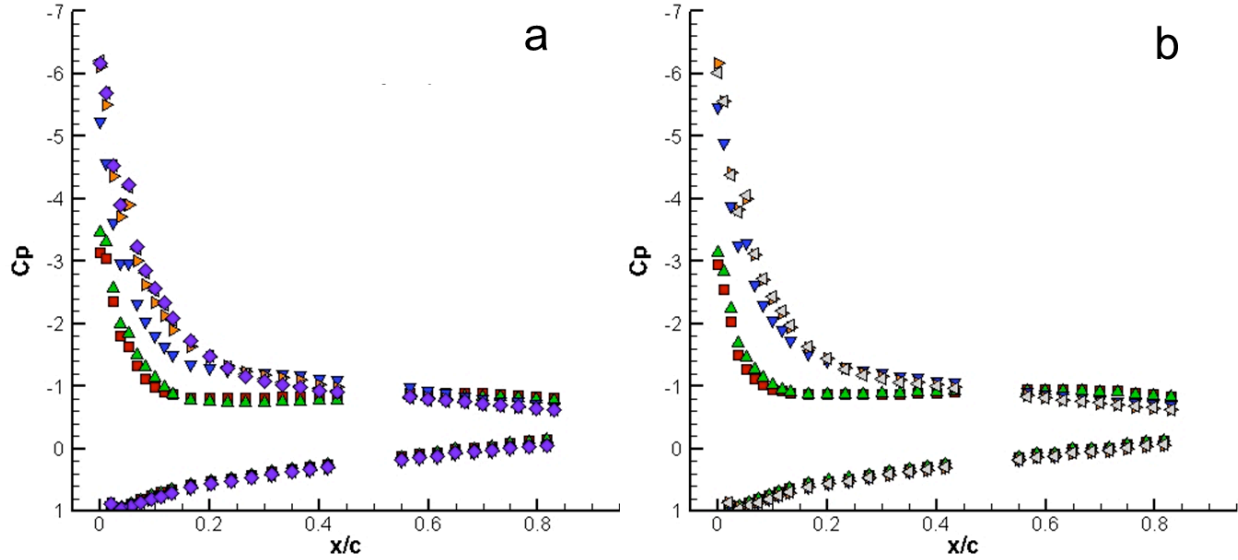


**Figure 39. Pressure coefficients for static airfoil at  $\alpha=18^\circ$  for tangential actuation jets at  $Re=650,000$  (a) and  $875,000$  (b). Both plots show the baseline, unforced case (■) and steady blowing (▲) at  $Q = 7$  sL/min/actuator. For (a),  $F^+$  values of 0.14 (▼), 0.29 (►), 0.50 (◄), and 0.72 (◆) are shown. For (b),  $F^+$  values of 0.27 (▼), 0.37 (►), and 0.53 (◄) are shown.**

## 2. Dynamically Pitching Airfoil Results

For the dynamically pitching testing of the low-speed VR-12 model, only the tangential slot orientation was tested given the static test results described above. The centerline static pressure tap segment was replaced by a filler piece with no pressure taps and data acquisition began to include direct measurements of aerodynamic forces through load sensors built into the dynamic pitching mechanism. It is noted that the load sensor measurements inherently measure the full span of the model, while the actuated region only covers 21% of that span. Thus, significantly greater local aerodynamic changes in the actuated region may be expected compared to the effective spanwise-averaged values presented herein.

As a first check of the characteristics of the VR-12 airfoil under low-speed conditions, a baseline measurement of  $C_l$  was taken over a pitching range of  $0^\circ \leq \alpha \leq 20^\circ$  at a freestream velocity of  $M = 0.06$  and at a reduced pitching frequency of  $k = 0.03$  (the maximum that the pitching mechanism could attain for these operating conditions). These results were then compared to both the baseline CFD performed during this program and an available result from the literature [38] with the three different plots shown together in Figure 40. Despite significant differences in the velocities (with both other plots for  $M = 0.4$ ) and reduced pitching frequencies (the results from [38], for  $k = 0.1$  and those from the CFD for  $k = 0.07$ ), the lift curves match reasonably well for all three, with loss of lift on the upstroke near  $16^\circ$ - $18^\circ$  and the hysteresis between the upstroke and downstroke curves closing in the  $5^\circ$ - $7^\circ$  range. This provided a confirmation that the aerodynamic characteristics and actuation approaches for the low-speed testing should be similar to those that might be employed for the high-speed wind tunnel testing and some direct comparison between the two would be feasible.

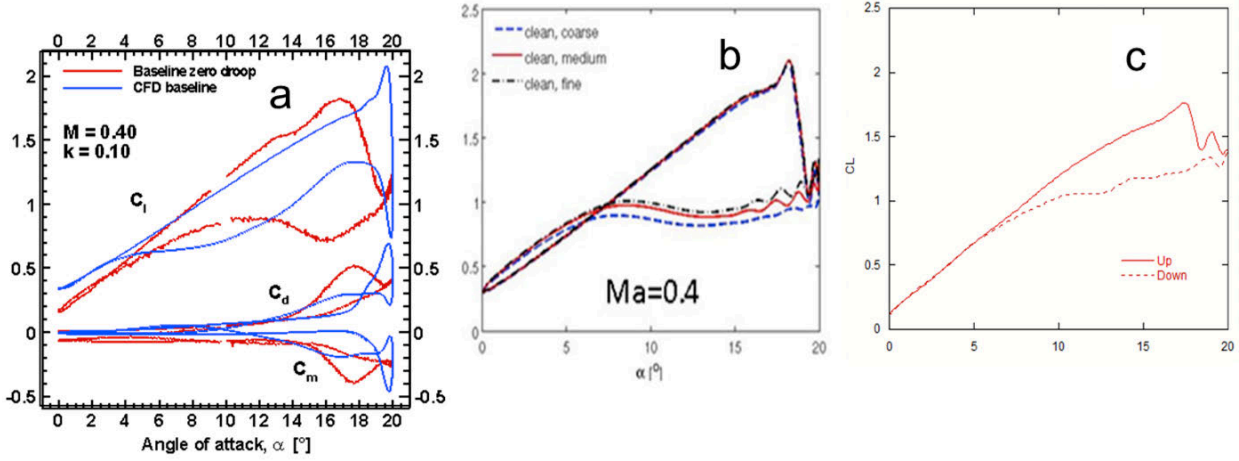


**Figure 40. Comparison of baseline  $C_l$  values for the VR-12 airfoil for  $0^\circ \leq \alpha \leq 20^\circ$  for [38] (a,  $M = 0.4$ ,  $k = 0.1$ ), current CFD (b,  $M = 0.4$ ,  $k = 0.07$ ), and low-speed experiments (c,  $M = 0.4$ ,  $k = 0.1$ ). Figure a is offset to keep zero levels matched.**

The test results, which follow, are limited to a pitching range of  $10^\circ \leq \alpha \leq 20^\circ$ . This was done to enable the pitching mechanism to attain reduced pitching frequencies more closely matched to those expected for the high-speed testing, while focusing investigations on the portions of the cycle during which large-scale separation was expected and, thus, actuator operation would be beneficial. Baseline profiles for  $C_l$  and  $C_m$  over this pitching range for  $M = 0.06$  and  $k = 0.06$  are presented in Figure 41. The large loss in lift here corresponding to full separation occurs between  $17^\circ$  and  $18^\circ$  on the upstroke and there is hysteresis between the upstroke and downstroke lift over the entire pitching cycle. Although not a focus of the research under this program, the  $C_m$  profile is noteworthy for the regions of negative damping at approximately  $13.5^\circ \leq \alpha \leq 17.5^\circ$  and  $19.5^\circ \leq \alpha \leq 20.0^\circ$ . Flow control actuation can have beneficial effects on the pitch stability of the cycle by eliminating these regions (e.g., [39]) and some discussion of the results in terms of changes to the aerodynamic damping coefficient,  $E_m$ , is presented herein (particularly in Figure 45 below).

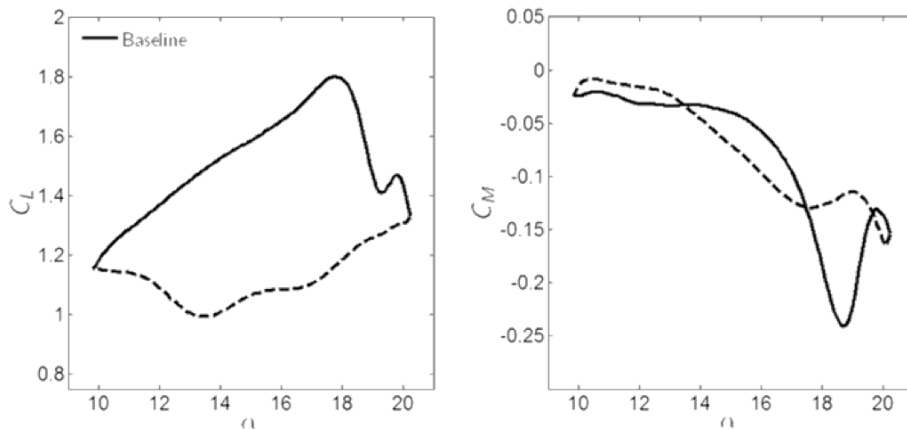


**Figure 41. Baseline profiles for  $C_l$  and  $C_m$  for  $10^\circ \leq \alpha \leq 20^\circ$  at  $M = 0.06$  and  $k = 0.06$ .**

The flow for the baseline pitching conditions was investigated with phase-locked PIV measurements as shown in Figure 42 for three upstroke angles ( $10.0^\circ$ ,  $15.0^\circ$ , and  $17.9^\circ$ ) and three downstroke angles ( $14.0^\circ$ ,  $12.1^\circ$ , and  $10.2^\circ$ ) over the pitching cycle. At  $\alpha = 10.0^\circ$  on the upstroke (Figure 42a), the flow is effectively fully attached with some separation of the shear layer from the airfoil surface only beginning to appear at the trailing edge by  $\alpha = 15^\circ$  (Figure 42b). Large scale separation and reversed flow near the airfoil surface are subsequently observed by  $\alpha = 17.9^\circ$  (Figure 42c) on the upstroke and the separated condition is maintained over the remainder of the upstroke and the majority of the downstroke to at least  $\alpha = 14.0^\circ$  (Figure 42d). Natural reattachment of the flow on the downstroke has occurred to a large extent by  $\alpha = 12.1^\circ$  (Figure 42e) with full attachment near the beginning of the next pitch cycle (Figure 42f).

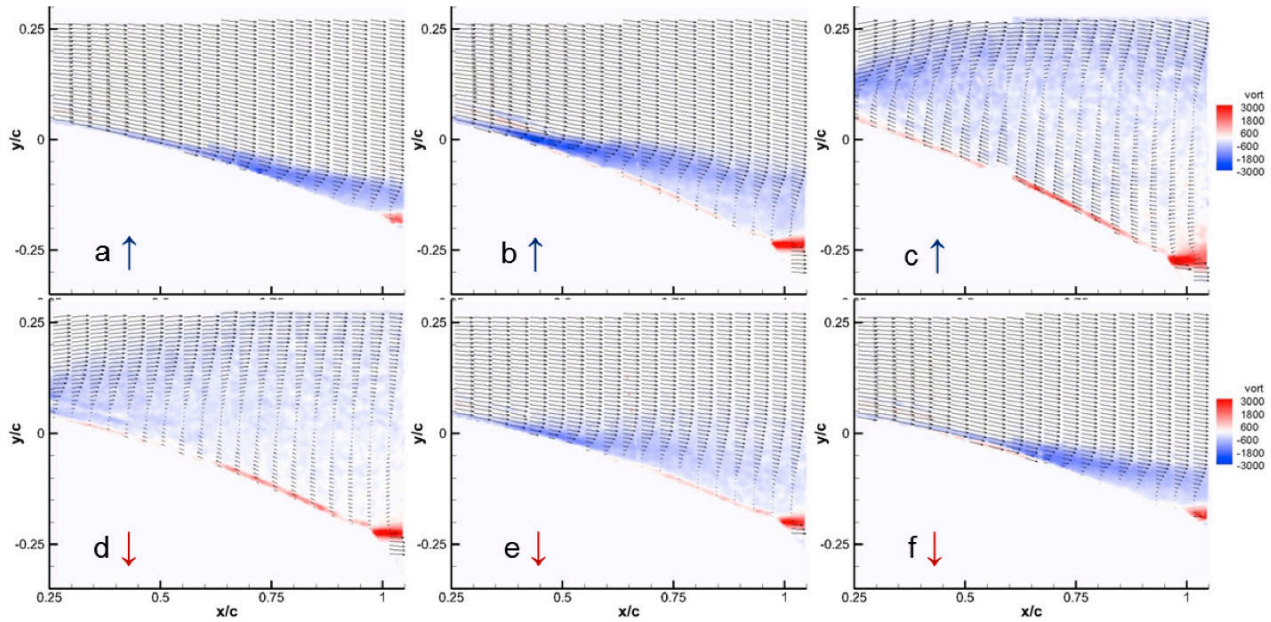


**Figure 42. PIV velocity vectors and vorticity contours of unactuated flow for  $10 \leq \alpha \leq 20^\circ$  at  $M = 0.06$  and  $k = 0.06$  at upstroke angles of  $\alpha = 10.0$  (a),  $15.0$  (b), and  $17.9$  (c) and downstroke angles of  $\alpha = 14.0^\circ$  (d),  $12.1^\circ$  (e), and  $10.2^\circ$  (f).**

For the dynamically pitching airfoil, COMPACT firing is not necessary over the large range of the cycle for which the flow is already attached, so bursts of actuation at specific points in the pitch cycle become of key interest. The discrete, on-demand pulses of COMPACT allow actuator firing at whatever times in the cycle are desired (provided the time between pulses does not exceed the maximum actuator operating frequency). This allows an effectively infinite variety of actuation patterns and timing to be implemented, focusing on points in the cycle where the flow is most receptive to actuation. An initial test of the actuator timing is presented in Figure 43, with  $C_L$  profiles of a pulse trains starting at  $\alpha = 15.5^\circ$  on the upstroke and increasing numbers of pulses at one degree increments up to  $\alpha = 15.5^\circ$  on the downstroke (in Figure 43, actuation points are denoted by red dots on the plots with the baseline  $C_L$  profile in gray). The maximum airfoil angle-of-attack is actually slightly less than  $20^\circ$  so only a pulse at  $19.5^\circ$  upstroke is used with no downstroke pulse at the same angle. (It is noted that while the spacing is equal in  $\alpha$  here, due to the sinusoidal motion of the airfoil, the time interval between actuation

pulses varies and there is no fixed actuation frequency.) In Figure 43a, the single pulse at  $15.5^\circ$  upstroke is shown and by itself provides a significant delay in the loss of lift compared to the baseline case. Further delays in stall on the upstroke are achieved for the additions of pulses at  $16.5^\circ$ ,  $17.5^\circ$ , and  $18.5^\circ$  (Figure 43b, c, and d, respectively) although with diminishing returns for the pulse at  $18.5^\circ$ . While there is an increase in lift during the upstroke for all of these cases, it is noteworthy that they all have reduced lift compared to the baseline near the beginning of the downstroke (roughly  $17.5^\circ \leq \alpha \leq 19.5^\circ$ ). No combination of actuation patterns tested in the present research was able to maintain flow attachment through the upstroke/downstroke transition (e.g., the actuation pulse at  $19.5^\circ$  upstroke - Figure 43e - is unable to prevent the separation and occurs while  $C_L$  is falling) and a downward spike in lift as the separation occurs is unavoidable and appears somewhat larger when the separation occurs at higher angles of attack. Averaging the lift over the cycle thus yields less impressive results for these upstroke actuation pulses than the delay in stall by itself would suggest. The downstroke actuation pulses begin with  $18.5^\circ$  (Figure 43f), which shows a sharp momentary lift recovery after the actuation pulse. Much more long lasting lift recovery over the remainder of the downstroke is observed when further pulses are added at  $17.5^\circ$ ,  $16.5^\circ$ , and  $15.5^\circ$  (Figure 43g, h, and i, respectively) with significant closure of the upstroke/downstroke hysteresis.

A related test approach for the actuator timing is shown in Figure 44. In this case, the final 9-pulse actuation pattern of Figure 43i is the starting point (shown again in Figure 44a) and pulses are incrementally removed from the beginning of the pulse train in the upstroke. With the removal of the pulse at  $15.5^\circ$  (Figure 44b), there is an immediate reduction in the peak  $C_L$  over the upstroke suggesting that a first pulse at  $16.5^\circ$  is insufficiently early to fully hold the attachment beyond the baseline condition. With the pulse at  $16.5^\circ$  also removed (Figure 44c), a sharp drop in lift is observed, although a momentary recovery is created by the following actuation pulses at  $17.5^\circ$  and  $18.5^\circ$ . Removal of further upstroke actuation pulses (Figure 44d through f) yields a reduction in  $C_L$  similar to the baseline but with the loss of lift happening at a slightly lower angle-of-attack likely due to lingering effects from the downstroke actuation pulses. However, removing the upstroke actuation pulses eliminates the negative spike in  $C_L$  at the beginning of the downstroke while yielding an even higher lift recovery over the bulk of the downstroke (comparing Figure 44a and f). Sequentially removing the downstroke pulses (Figure 44g through i) yields reducing amounts of lift recovery on the downstroke and suggest that a pulse comparatively early in the downstroke cycle (such as the one at  $18.5^\circ$ ) is advisable.



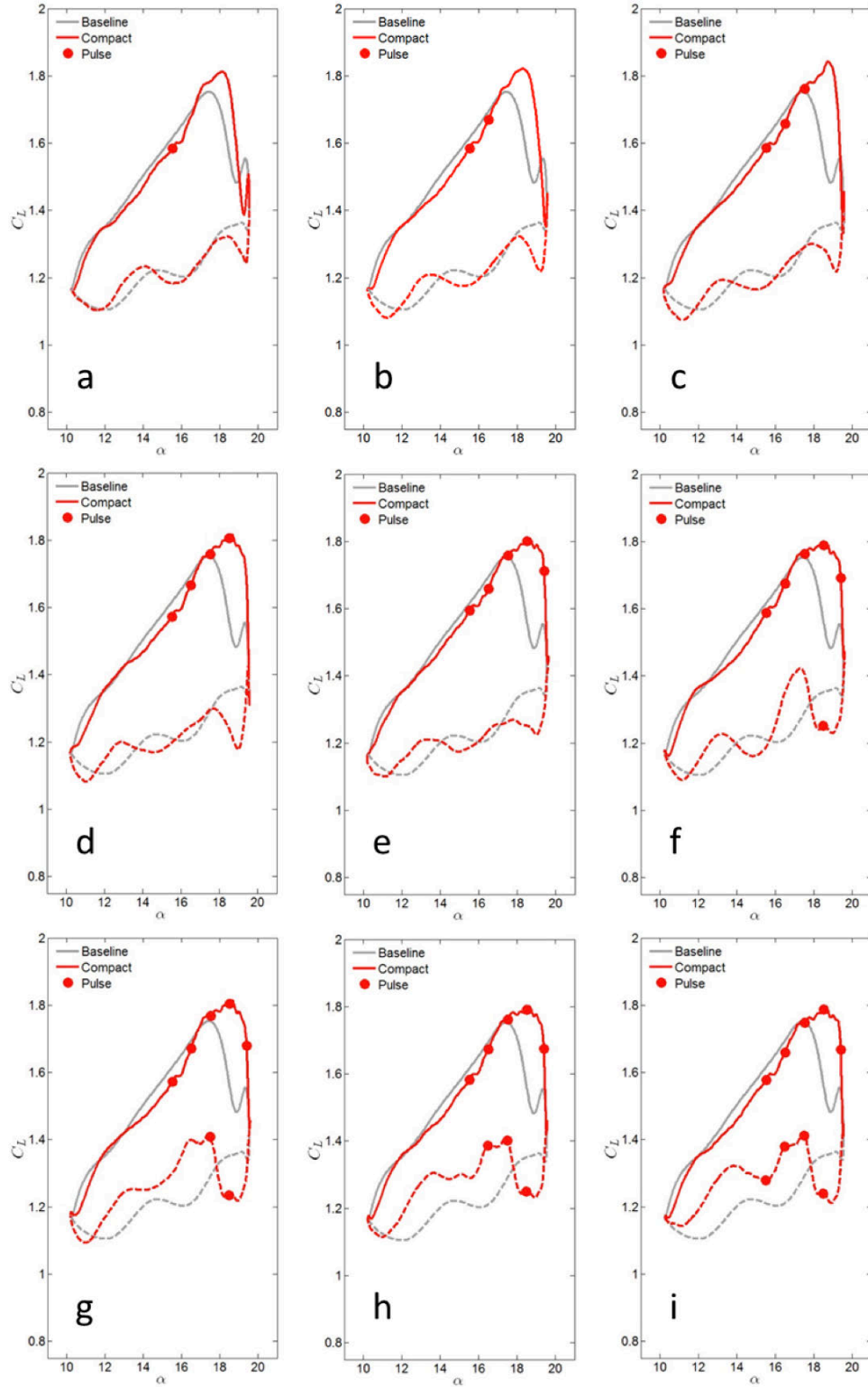


**Figure 43.** Lift coefficients over pitching cycle for  $10^\circ \leq \alpha \leq 20^\circ$  at  $M = 0.06$  and  $k = 0.06$  with initial actuation pulse at  $\alpha = 15.5^\circ$  upstroke (a) and sequentially added pulses at  $1^\circ$  increments -  $16.5^\circ$ ,  $17.5^\circ$ ,  $18.5^\circ$ , and  $19.5^\circ$  upstroke and  $18.5^\circ$ ,  $17.5^\circ$ ,  $16.5^\circ$ , and  $15.5^\circ$  downstroke (b through i).

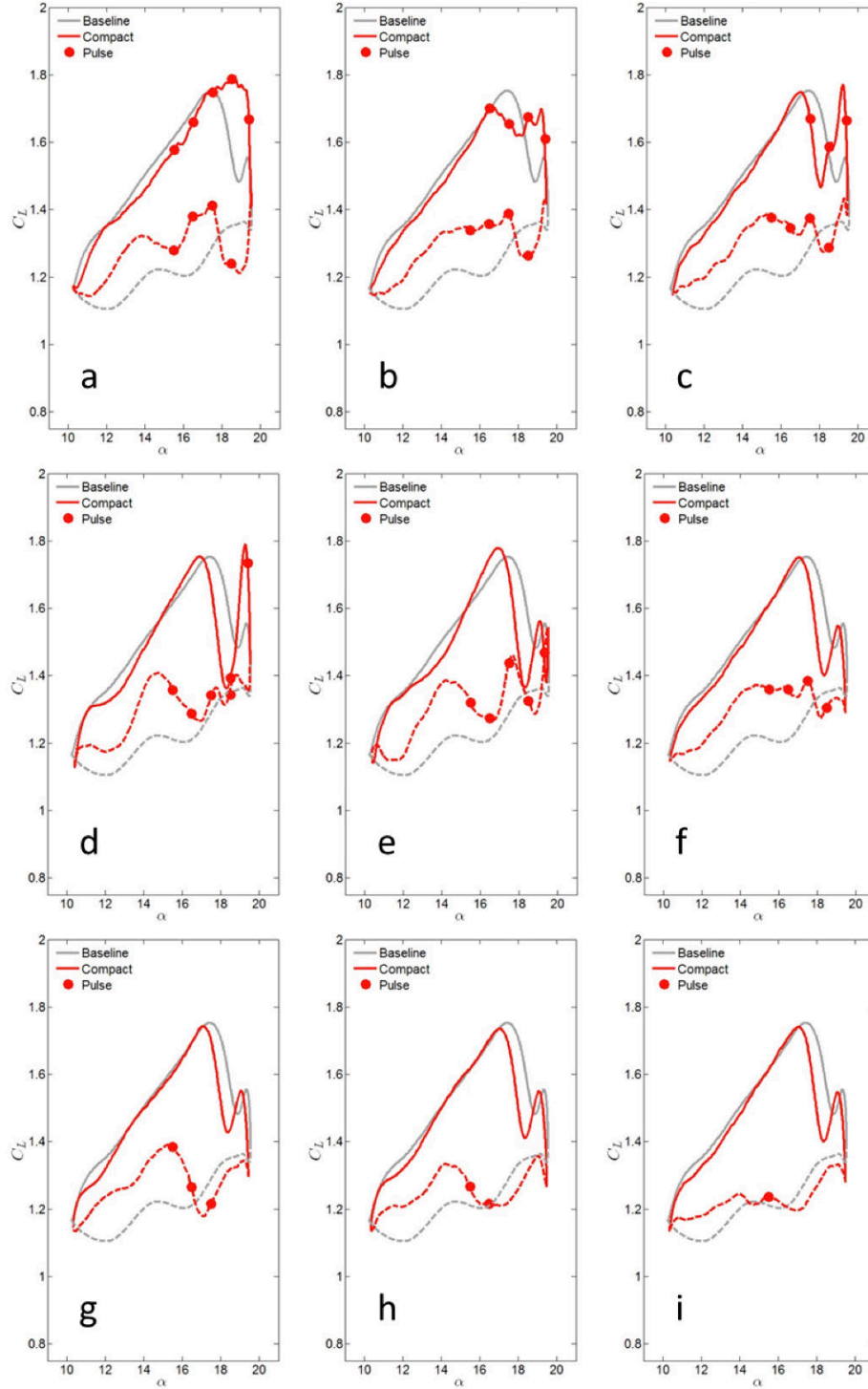


**Figure 44.** Lift coefficients over pitching cycle for  $10^\circ \leq \alpha \leq 20^\circ$  at  $M = 0.06$  and  $k = 0.06$  with 9 initial actuation pulses starting at  $\alpha = 15.5^\circ$  upstroke and following at  $1^\circ$  increments,  $16.5^\circ$ ,  $17.5^\circ$ ,  $18.5^\circ$ , and  $19.5^\circ$  upstroke and  $18.5^\circ$ ,  $17.5^\circ$ ,  $16.5^\circ$ , and  $15.5^\circ$  downstroke (a) with sequentially decreasing numbers of actuation pulses removing them in order (b through i).

As shown above, critical points in the pitching cycle can provide the maximum actuator effect while minimizing undesirable aerodynamic changes and the total actuator power applied. With this in mind, a wide variety of actuation patterns and timing were investigated. Figure 45 presents results for 27 different actuation patterns, showing the change in cycle-averaged lift  $\langle \Delta C_L \rangle$  for each case versus the change in damping coefficient  $\Delta E_w$ . All of the actuation patterns produced some improvement in lift with improvements of greater than 5-7% observed for about half of these. (It is again noted that these values reflect measurements of the entire span of the airfoil with only 21% of it actuated.) However, some actuation patterns actually reduced the damping coefficient and improved lift did not necessarily correlate directly with improved damping. Two actuation patterns are highlighted in Figure 45 both for their strong combination of improved lift and pitch stability and their relative similarity to each other. The inset on Figure 45 shows the  $C_L$  and  $C_M$  plots for both cases and the baseline with actuation pattern 1 featuring only downstroke pulses (18.0°, 16.0°, and 14.0°) and pattern 2 including the same downstroke pulses and a single upstroke pulse (14.5°). Both patterns attain a large increase in lift as part of the earlier reattachment caused by the downstroke actuation. Pattern 2 restores some additional lift from the single upstroke pulse, which holds the upstroke separation to the same angle as the baseline with only a small comparative reduction in lift at the start of the downstroke. In both cases, the regions of negative damping in the  $C_M$  profiles are nearly eliminated, resulting in the improvements in the damping coefficient. (A comprehensive set of results with  $C_L$  and  $C_M$  plots for all 27 actuation patterns presented in Figure 45 is provided in the appendices at the end of the report.)



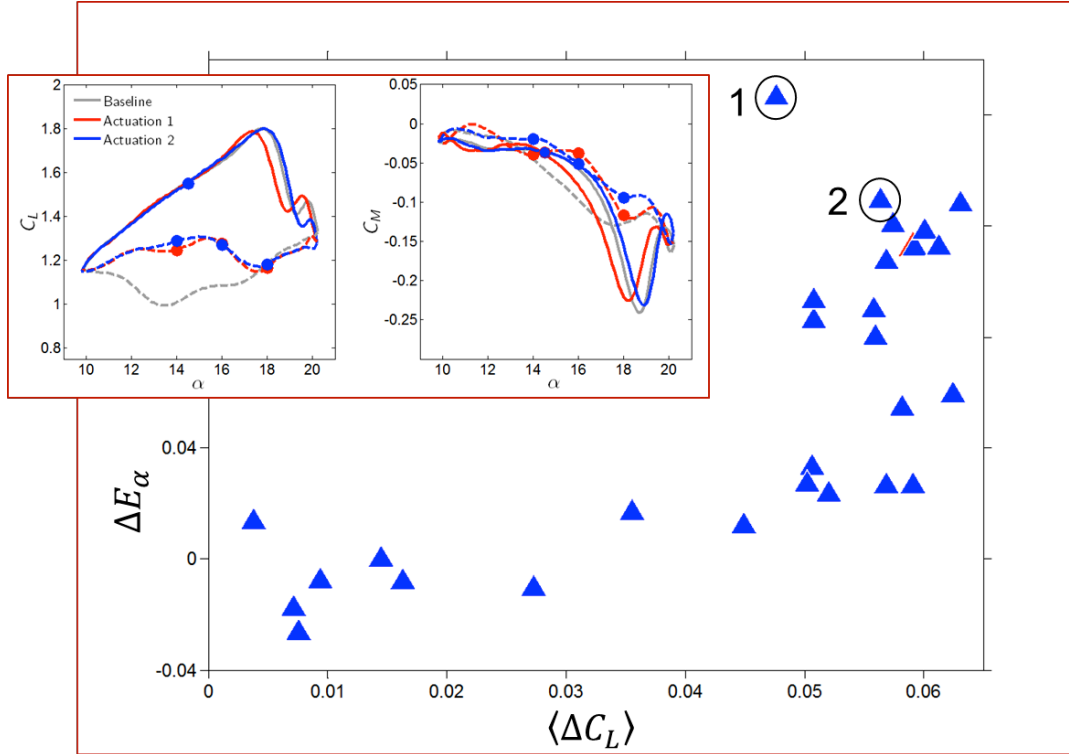


**Figure 45. Change in cycle averaged lift coefficient versus damping coefficient for 27 different actuation patterns which were tested for  $10^\circ \leq \alpha \leq 20^\circ$  at  $M = 0.06$  and  $k = 0.06$ . Inset shows  $C_L$  and  $C_M$  profiles for unforced case and two actuation patterns noted on larger plot.**

Phase-locked PIV measurements for several angles over the pitch cycle were used to examine the flow structures over the airfoil suction surface produced by the actuation programs described above. The measurement domain here was roughly  $0.25 < x/c < 1.05$  and  $-0.35 < y/c < 0.35$  where the referenced zero point is the tip of the leading edge at  $\alpha = 0^\circ$ . Two angles of interest during the upstroke ( $\alpha = 15.0^\circ$  and  $17.0^\circ$ ) are presented in Figure 46. The baseline data are generally similar to those presented in Figure 42 (for slightly different  $\alpha$  however) with initial separation observed moving upstream from the trailing edge at  $\alpha = 15.0^\circ$  (Figure 46a) and large separation over the entire measurement window at  $\alpha = 17.0^\circ$  (Figure 46d). Data for actuation program 1 (Figure 46b and e), which includes no upstroke actuation pulses, are very similar to the equivalent baseline data with slightly greater separation observed at each angle (as would be expected from the comparative  $C_L$  profiles shown in the inset of Figure 45). For actuation program 2, the single upstroke actuation pulse takes place at  $\alpha = 14.5^\circ$  and the resulting vortical structure is located near the trailing edge at  $\alpha = 15.0^\circ$  (Figure 46c). (Although not presented in detail here, it is noted that the flow structures for the dynamically pitching airfoil remain typical of those seen with COMPACT actuation as described in the discussion of the static airfoil PIV presented in Figure 36). By  $\alpha = 17.0^\circ$  (Figure 46f), the strengthening of the attachment created by the single actuating pulse is dissipating and large-scale separation is again appearing.

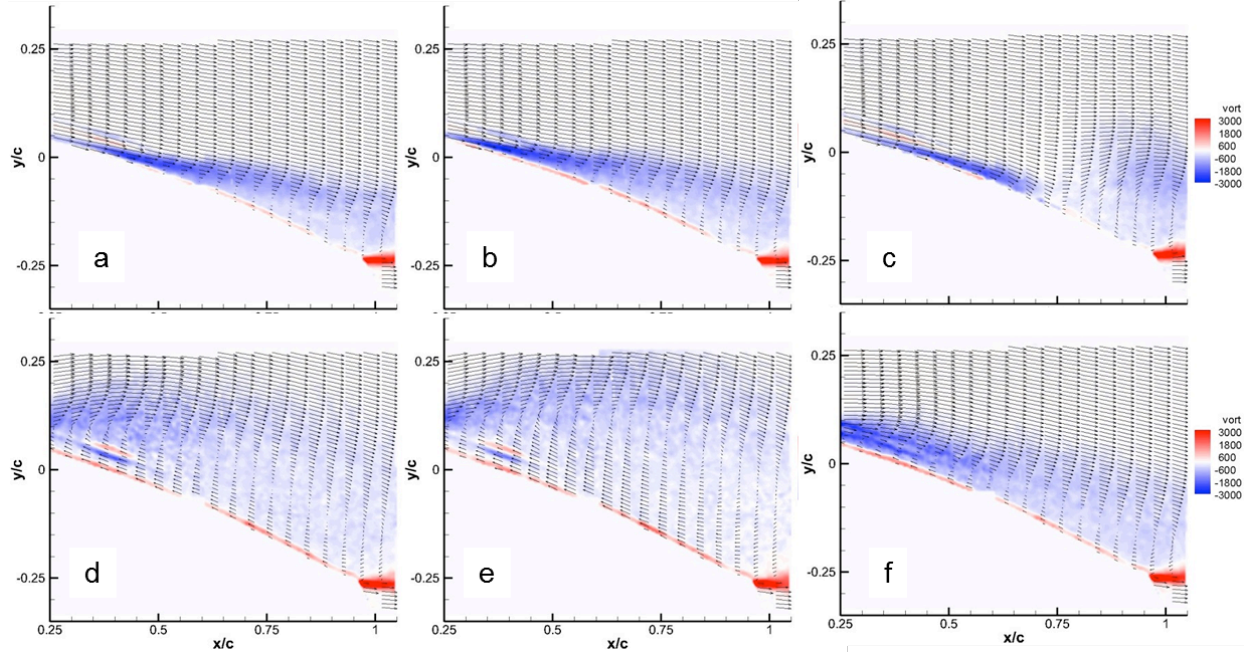


**Figure 46. Phase-locked PIV velocity vectors and vorticity contours for  $10^\circ \leq \alpha \leq 20^\circ$  at  $M = 0.06$  and  $k = 0.06$  at upstroke angles of  $\alpha = 15.0^\circ$  for baseline (a), actuation pattern 1 (b), and actuation pattern 2 (c) and  $\alpha = 17.0^\circ$  for baseline (d), actuation pattern 1 (e), and actuation pattern 2 (f).**

PIV for several angles on the downstroke are presented in Figure 47. With the downstroke firing patterns (at  $\alpha = 18.0^\circ$ ,  $16.0^\circ$ , and  $14.0^\circ$ ) identical between the two actuation cases, only actuation pattern 1 is presented in Figure 47, with nearly identical results observed for pattern 2. The baseline flow field (shown in Figure 47a, c, and e for  $\alpha = 17.9^\circ$ ,  $17.0^\circ$ , and  $15.0^\circ$ , respectively) shows very similar large-scale separation for all three angles presented with only slight indication of a reduction in the separation at  $\alpha = 15.0^\circ$ . For the actuated flow, the first actuation pulse ( $\alpha = 17.9^\circ$ ) has fired only briefly before the data for  $\alpha = 17.9^\circ$  (Figure 47b) and manifests as a disruption in the shear layer near  $x/c = 0.35$ . By  $\alpha = 17.0^\circ$  (Figure 47d), the structure from the first pulse has moved out of the field of view with a significant degree of attachment in its wake but a still large velocity deficit and some reversed flow near the trailing edge. At  $\alpha = 15.0^\circ$  (Figure 47f), the second actuation pulse has already come and gone and a much stronger attachment over the entire surface of the airfoil is observed.

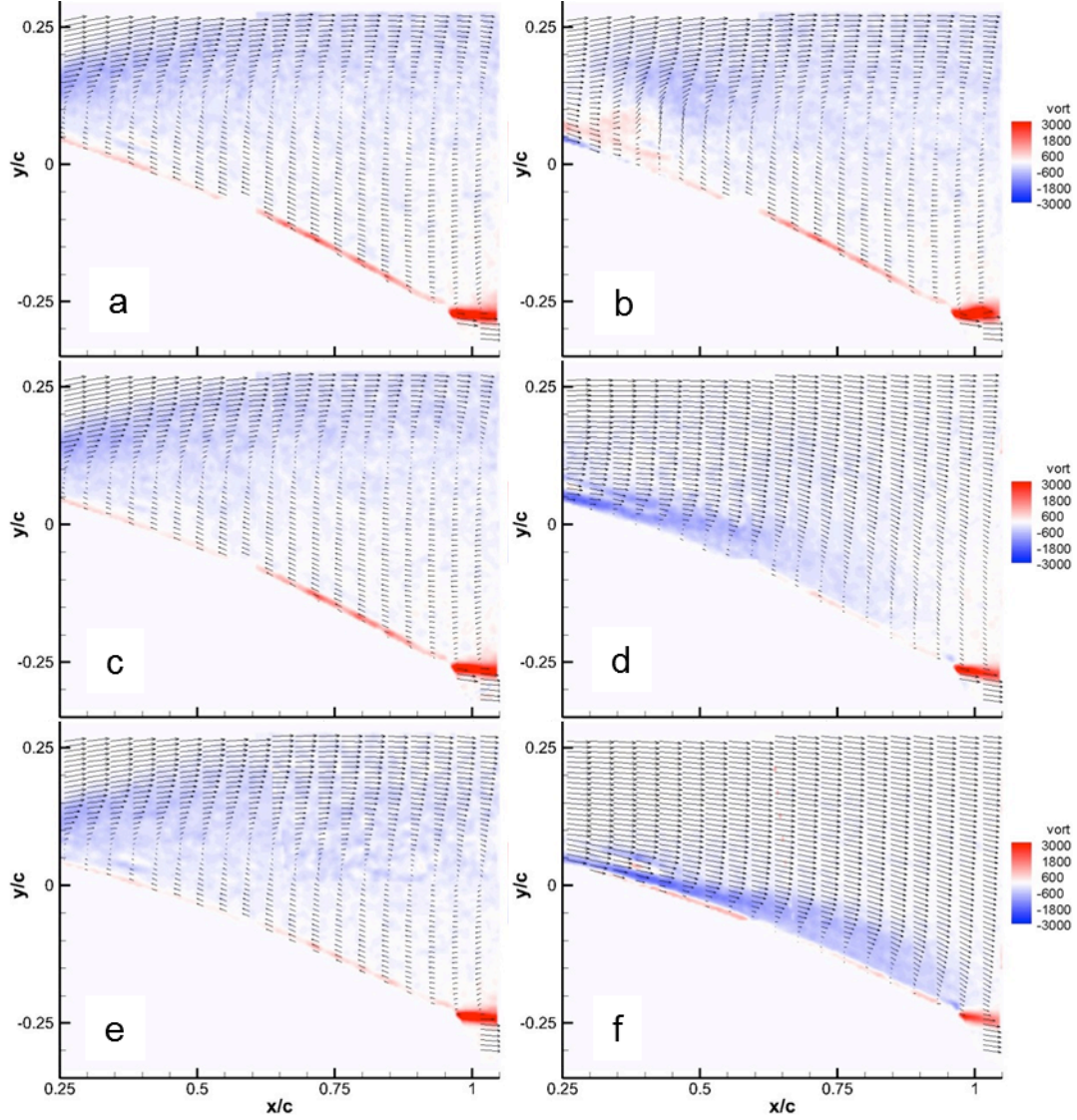


**Figure 47. Phase-locked PIV velocity vectors and vorticity contours for  $10^\circ \leq \alpha \leq 20^\circ$  at  $M = 0.06$  and  $k = 0.06$  at downstroke angles of  $\alpha = 17.9^\circ$  for baseline (a) and actuation pattern 1 (b),  $\alpha = 17.0^\circ$  for baseline (c) and actuation pattern 1 (d), and  $\alpha = 15.0^\circ$  for baseline (e) and actuation pattern 1 (f).**

PIV measurements with greater time resolution were used to map the velocity field in the near wake of the model for the baseline flow and for the two actuation patterns highlighted in Figure 45 above. The measurement domain was  $-0.1943 < x/c < 0.2365$  and  $-0.2820 < y/c < 0.7397$  where  $x$  and  $y$  here are measured relative to the position of the trailing edge when the airfoil is at  $\alpha = 10^\circ$ . The PIV images are acquired at 30 equally-spaced time increments, phase-locked to the airfoil's pitch cycle, and capture the full cross stream width of the near wake during the entire pitch cycle. These data are used to compute the vorticity flux across the wake at  $x/c = 0.0708$  during the pitch cycle shown in Figure 48a-c in color raster strips of the cross stream variation of the flux at each time (or  $\alpha$ ) increment during the pitch cycle in the absence of actuation and for

actuation programs 1 and 2, respectively. While the clockwise (CW) vorticity on the suction surface of the airfoil is taken to be negative, it is noted that its flux can change sign with the sense of the streamwise velocity in the near wake. In the absence of actuation (Figure 14a), the base flow over the airfoil begins to separate at  $\alpha \sim 15^\circ$  ( $t/T_{cycle} = 0.25$ ), where the precursor is the clear increase in the cross stream width of the wake evident from the spacing between the flux of the CW and CCW vorticity concentrations from the suction and pressure surfaces, respectively. The separation is marked by lower magnitude of the local flux due to diffusion of the CW vorticity across the wake and the center of the wake is marked by low concentrations of vorticity that are associated with the loss of lift during stall. It is remarkable that the CCW vorticity remains concentrated in a narrow layer and exhibits little or no mixing within the wake. As the angle-of-attack begins to decrease at the beginning of the downstroke ( $\alpha \sim 20^\circ$ ,  $t/T_{cycle} = 0.5$ ), the cross stream width of the wake begins to decrease and the CW and CCW vorticity layers converge. It is noted that the cross stream distribution of the flux at the end of the downstroke is not identical to the corresponding distribution at the beginning of the upstroke since the resolution of the present data is insufficient to capture the changes in the flux at as the airfoil switches the direction of its angular velocity. Figure 14b demonstrates the effect of actuation program 1 (downstroke pulses at  $\alpha = 18^\circ$ ,  $16^\circ$ , and  $14^\circ$ , corresponding to  $t/T_{cycle} = 0.65$ ,  $0.72$ , and  $0.78$ , respectively) on the concentration of vorticity flux. As expected, the cross stream width of the wake is similar to the baseline for the upstroke, while the downstroke actuation pulses each disrupt the wake in the immediate time interval after they are fired (leaving its position above the suction surface briefly indeterminate) and lead to accelerated attachment of the flow. Actuation program 2 (Figure 48c) utilizes the same actuation pattern during downstroke, but also includes a single actuation pulse during upstroke ( $\alpha = 14.5^\circ$ ;  $t/T_{cycle} = 0.24$ ). The single upstroke pulse leads to a momentary closing of the wake prior to a fully separated state similar to the baseline developing. As expected from the  $C_L$  plot in the inset of Figure 45, the downstroke wake for the two actuation cases is very similar with perhaps a slightly narrower wake for actuation pattern 2 wake when the actuation pulse at  $\alpha = 14^\circ$  takes place (reflected in the slightly higher lift at that point).

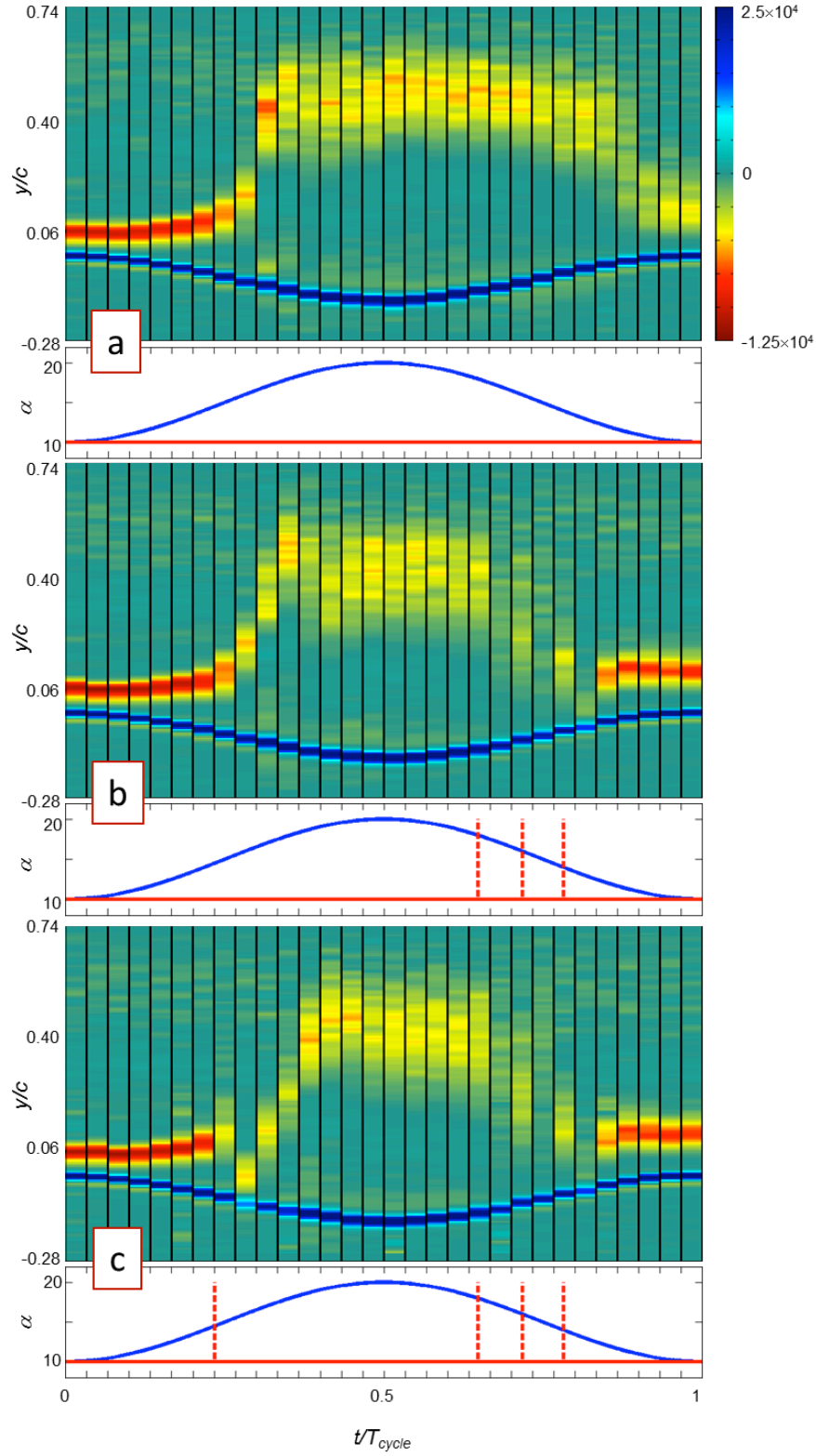


**Figure 48.** Color raster plots of the vorticity flux in the near wake of the airfoil for 30 equal time increments over the pitching cycle ( $10^\circ \leq \alpha \leq 20^\circ$  at  $M = 0.06$  and  $k = 0.06$ ) for baseline (a), actuation program 1 (b), and actuation program 2 (c).



## IX. Final Actuator Design Enhancements

### 1. Actuator Design Changes Between Low- and High-Speed Models

Further development and testing of COMPACT designs was pursued following the fabrication of the low-speed VR12 model to optimize actuator performance for the high-speed wind tunnel experiments. The actuator internal shape and fuel/oxidizer inlet orientation remained constant in the “C” configuration described in Section 6. The enhanced development effort focused on several parameters including the slot orifice height ( $h$ ) and the width of a single chamber ( $W$ ), noted on the physical actuators in Figure 49.

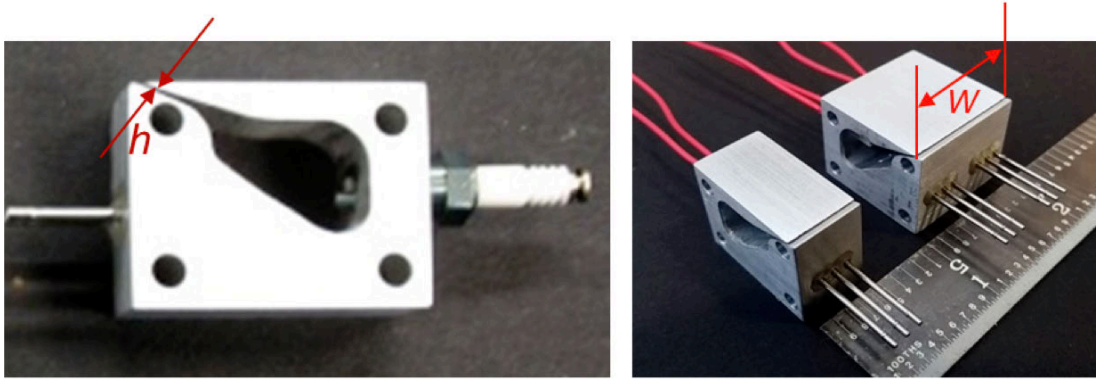


**Figure 49. Further tested actuator design variants highlighting orifice slot height ( $h$ ) and overall chamber width ( $W$ ).**

The slot orifice height can be altered with relative ease in the EDM cutting process that produces both the combustion chamber and the orifice. Initially, actuators with  $h = 0.012''$  (the minimum attainable by the available wire EDM procedure) were fabricated and tested. To test the sensitivity of the actuator pressure curve to larger orifices,  $h = 0.024''$  prototypes were fabricated and tested under similar gas flow rates and mixture ratios. A comparison of the variation of peak pressures attained over a range of actuation frequencies is shown in Figure 50a for four air/ $H_2$  flow rates (6/1, 6/1.5, 12/2, and 12/3 sL/min). As expected, the smaller orifice size leads to higher peak pressures for all comparable cases, and slightly higher operating frequency ranges for each flow rate. Using the measured peak pressures, the peak jet momentum fluxes are calculated at the throat of the slot orifice and shown in Figure 50b. The calculation is based on a number of assumptions (including uniform flow across the orifice, isentropic expansion of the gas, selected values for the instantaneous temperature and species composition of the flow at peak pressure, etc.), and should be taken as only a rough estimate of the actual values, which might be attained. It is noteworthy, however, that the peak momentum fluxes for  $h = 0.024''$  are from 47 to 95% larger than for  $h = 0.012''$  and may thus be expected to yield significant increases in peak momentum flux even taking the underlying assumptions into consideration. Given the importance of jet momentum ratio ( $C_j$ ) in flow control applications, it was deemed likely that the larger orifice size would be preferable for the high-speed wind tunnel experiments (even with a small reduction in frequency range). An  $h = 0.036''$  slot was also tested but with very poor results. At this size, the combustor operation nearly always failed with a standing flame created in the chamber as the pressure after ignition was insufficient to shut off the inlet

flow during the combustion process. An alternate inlet design produced successful combustion bursts at this orifice size but with very low peak pressures, frequency range, and peak momentum flux.

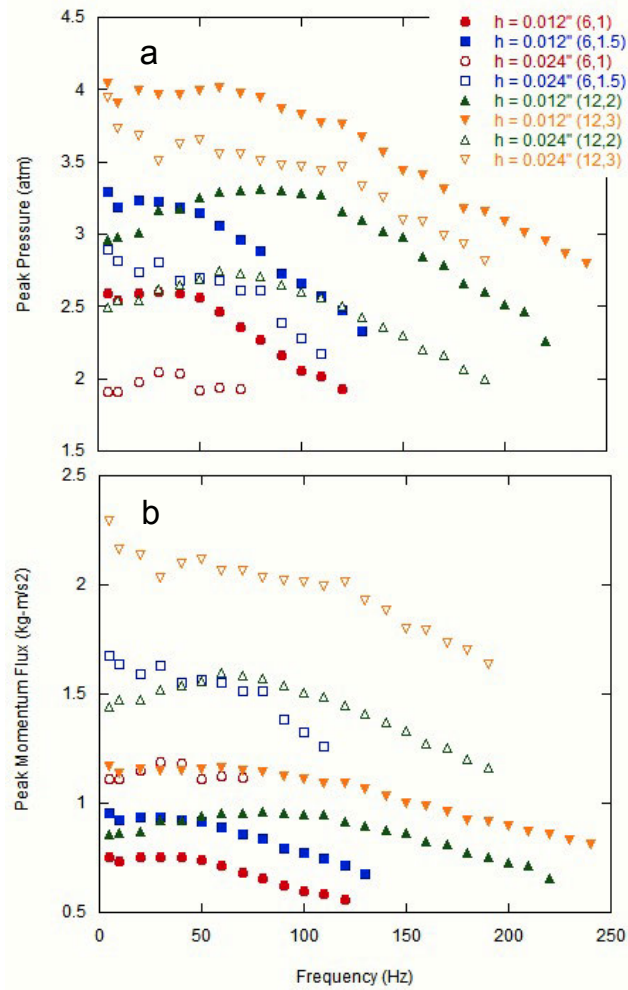


**Figure 50. Measured peak chamber pressures (a) and calculated peak jet momentum fluxes (b) for  $h = 0.012''$  (closed symbols) and  $0.024''$  (open) flow rates and firing frequency. Flow rates of air and H<sub>2</sub> denoted in parentheses.**

Investigation of the effect of the chamber width ( $W$ ) was considered specifically in response to the CFD results that indicated significant impact of the spanwise spacing between adjacent actuation slots on flow control effectiveness (see Section 5). In terms of implementation, completing eliminating the spanwise spacing would require eliminating the separating partitions between adjacent individual actuators to form a larger continuous combustion chamber, which could then be ignited from multiple spark ignition sites. The flow patterns and combustion propagation within the larger chamber, however, may not mimic an array of individual chambers with vanishingly thin partitions dividing them. A sample COMPACT actuator (using the original  $h = 0.012''$  orifice height) was built with the same cross-section but with double the width  $W$  (1" instead of 0.5"). Two spark igniters and sets of flow inlets were added to the chamber, repeating the same spacing and relative locations as for the original chamber design. Several sample pressure time traces for  $W = 1''$  and 0.5" at a repetition frequency of 5 Hz for

air/H<sub>2</sub> mixtures are shown in Figure 51a (12/2 sL/min) and Figure 51b (12/3 sL/min). Note that the comparable pressure curve for the original chamber size ( $W = 0.5''$ ) was actually taken for half the flow rates corresponding to the scaling of the total volume. For  $W = 1''$ , the pressure traces are shown for actuation of each spark igniter individually and actuation of both simultaneously. As expected due to the changes in flame propagation and chemical energy release rates, individual spark ignition produces a comparatively longer pressure pulse with a much reduced pressure peak compared to firing both igniters. There is some difference in the performance of the two individual spark igniters, which likely reflects differences in the bulk flow patterns on the two sides of the chamber. The  $W = 0.5''$  equivalent outperforms all of the pressure measurements for  $W = 1.0''$  in terms of peak pressure, although the difference is notably smaller for the case with higher hydrogen flow rate and mixture ratio.

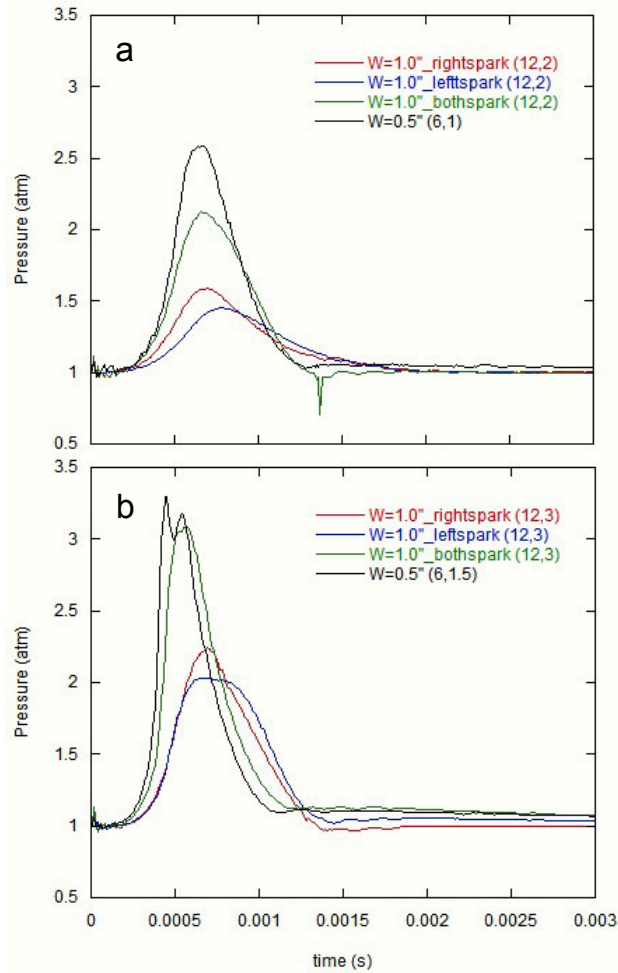


**Figure 51. Dynamic chamber pressures for  $W=1.0''$  chamber at  $f=5\text{Hz}$  for 12 sL/min air and 2 sL/min H<sub>2</sub> (a) and 12 sL/min air and 3 sL/min H<sub>2</sub> (b) varying spark ignition location.  $W=0.5''$  pressures at one half of the flow rates shown for comparison.**

Peak pressures over a range of actuation frequencies are shown in Figure 52 (comparing only  $W = 0.5''$  and actuation of both igniters for  $W = 1''$ ) with the same flow rates as Figure 51 shown in Figure 52a and double those flow rates shown in Figure 52b. The reduced peak pressures noted at repetition rate of 5 Hz at the original flow rates are significantly less of an issue at increased frequencies, with peak pressures nearly matching those of the narrower chamber for frequencies



of 50 Hz and above. The discrepancy is even further reduced for the increased flow rates of Figure 52b where the reduction in peak pressure is minor even at the lowest actuation frequencies. This likely reflects the extent to which increased bulk flow velocities within the chamber and increased flame propagation speeds can make the combustion process between the narrower and wider chambers more similar. However, it is noted that in all cases the frequency range is lower for the chamber with  $W = 1''$ , even though the pressure curves roughly match. This may indicate greater susceptibility to small flame pockets, which might be recirculating when the refill flow begins or simply greater heat build-up within the chamber in the absence of the additional thermal ballast provided by the narrower walls. In application to the wind tunnel model, this presents a significantly greater failure risk as a single, wider actuator misfiring and transitioning to constant flame would affect a much greater span of the airfoil. Given the promising CFD results for converting the actuator orifices into a pseudo-continuous slot, this was deemed to be the preferred approach to minimize the gap between actuator orifices and was implemented in the high-speed model actuators.

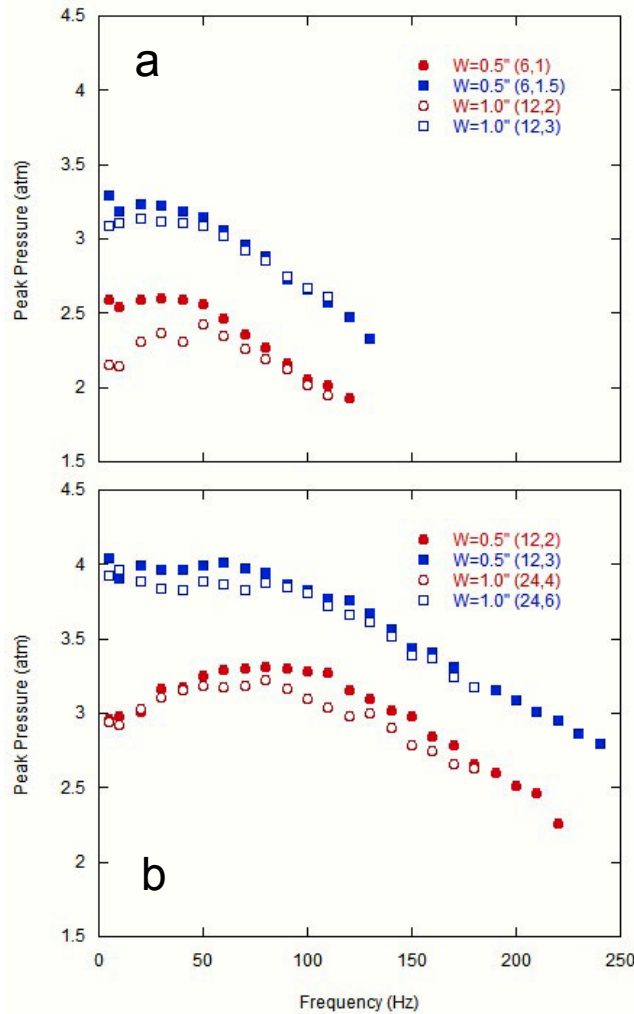


**Figure 52. Measured peak chamber pressures for  $W = 0.5''$  (closed symbols) and  $W = 1.0''$  (open symbols) for low (a) and high (b) flow rates.**

## **X. High-Speed Test Article Design and Fabrication**

An overall CAD-rendering of the experimental apparatus is shown in Figure 53. The airfoil consists of a spar (the main load bearing element), trailing edge (TE) skins, and a combination of leading edge (LE) actuators and sheaths. The LE and TE components are fastened directly to the spar. The airfoil is mounted vertically in the test section of the wind tunnel and spans from the floor to the ceiling. It is supported from above and below by identical spherical roller bearings. The upper spherical roller bearing is housed in a support, which is fastened directly to a top-plate, which itself is fastened to the ceiling structure of the wind tunnel in the same fashion as all of the other tunnel ceiling elements. The lower spherical roller bearing mounts to the lower support, which is fastened to the lower half of the tunnel balance, which is placed directly beneath the test section floor.

The actuation system and lower portion of the apparatus are shown in greater detail in Figure 54. Airfoil pitching is achieved via push-pull actuation of the hydraulic cylinders. One cylinder assembly is instrumented with a linear potentiometer to provide displacement feedback to the servo-valve controller. The cylinders are supported on the back side by a cylinder pivot bracket, which is fastened to the base plate. The base plate is fastened to the lower half of the tunnel balance beneath the wind tunnel test section. This portion of the apparatus was adapted from that used by Lorber, et al. [40].

Details of the upper mounting area are provided in Figure 55. No pitch moment is reacted in the upper area. A slip fit exists between the upper pivot post and bearing ID in order to allow the airfoil to move in the spanwise direction as it bends under aerodynamic load. This was implemented in order to avoid over-constraining of the structure. The upper spherical roller bearing is contained within the upper bearing housing, and upper bearing housing is fastened directly to the upper mount plate. The upper mount plate integrates with the ceiling structure of the wind tunnel test section ceiling in the same manner as all other ceiling elements of the wind tunnel. A large glass window is bonded in a recess of the upper mount plate in order to allow adequate optical access for the PIV camera.

Tubing to provide air and fuel to the actuators was routed through both the lower and upper pivot posts of the model as shown in Figure 56 and Figure 57. Although not shown in the CAD, green tubing was used for air, and yellow for hydrogen. Instrumentation cables were routed through the lower pivot post only coming from the region behind the spar. Electronic wiring for the ignition system was routed with the tubing.

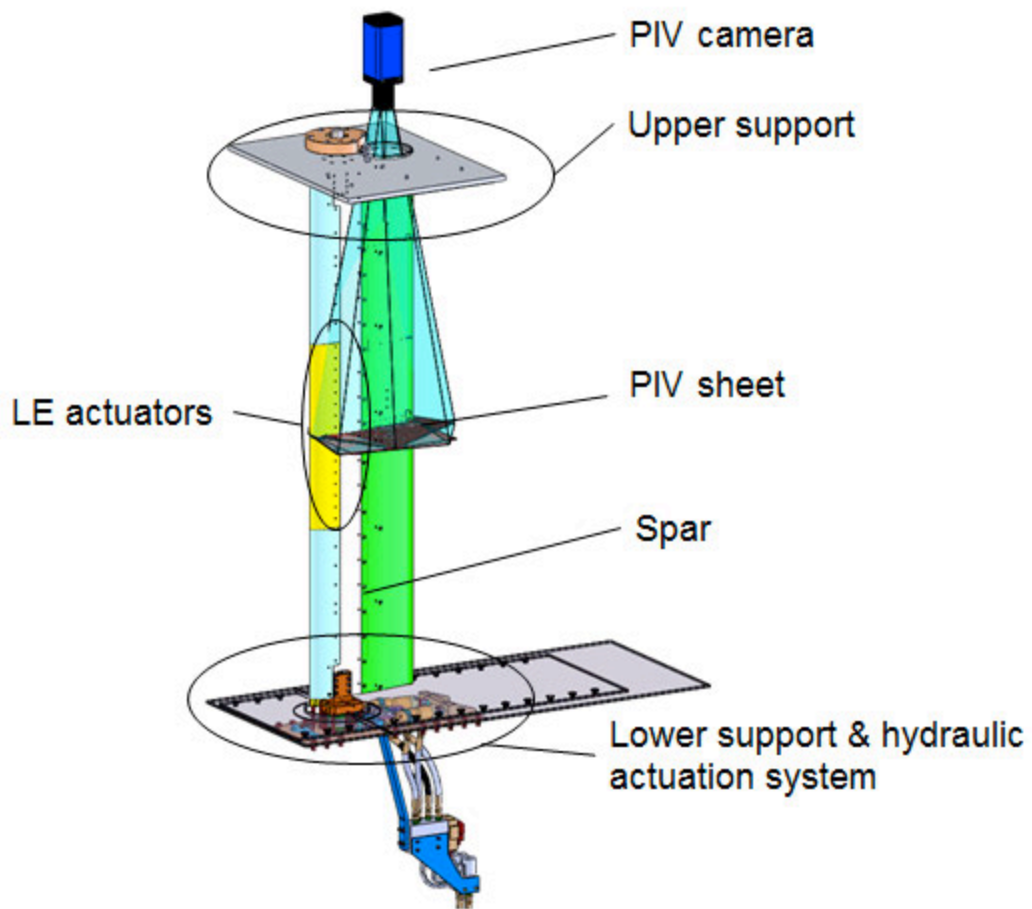


**Figure 53. Overall CAD-rendering of the experimental apparatus.**

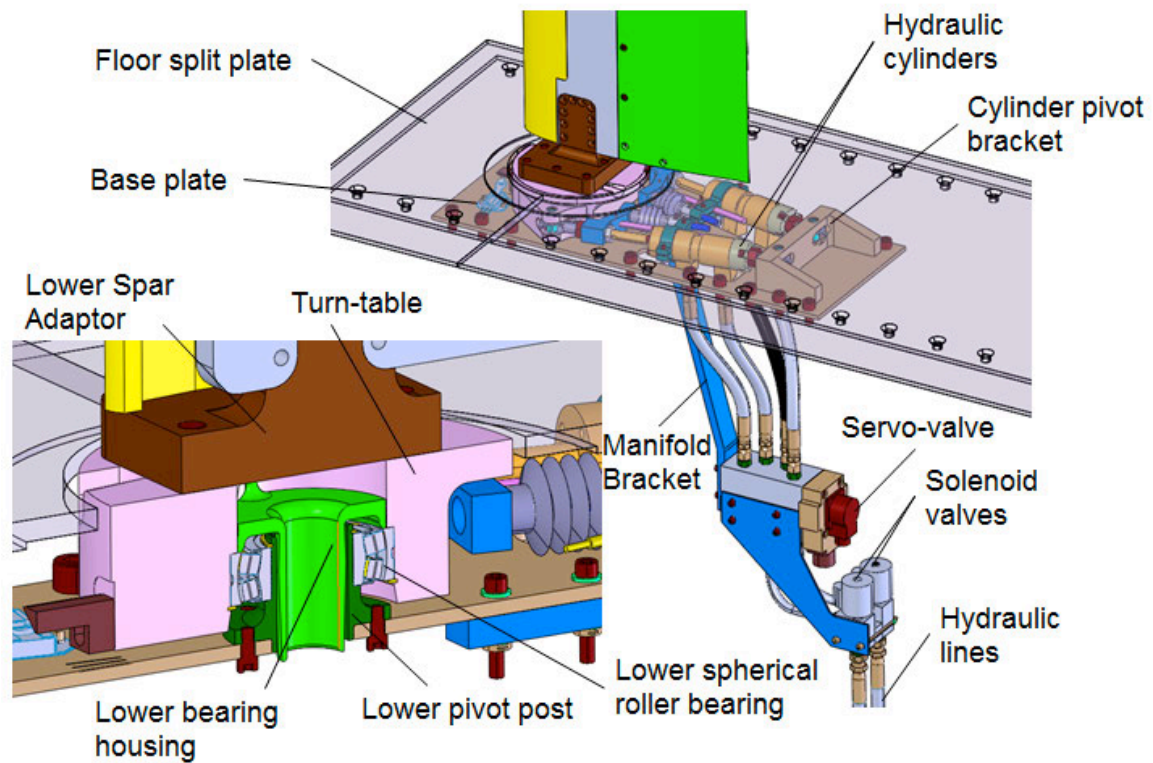


**Figure 54. Pitching airfoil actuation system.**

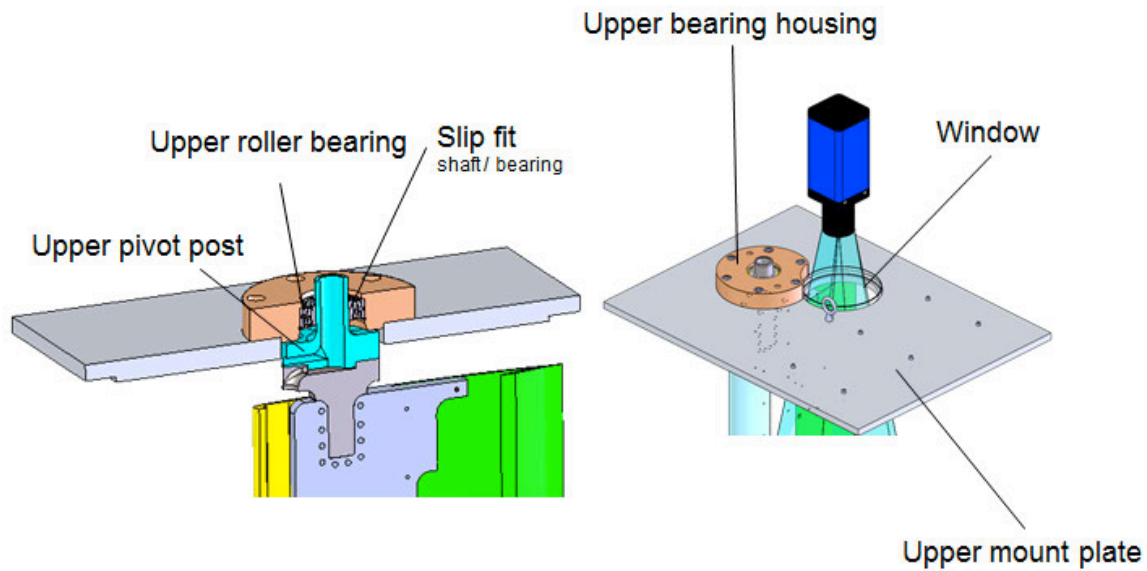


**Figure 55. Pitching airfoil upper mounting area.**

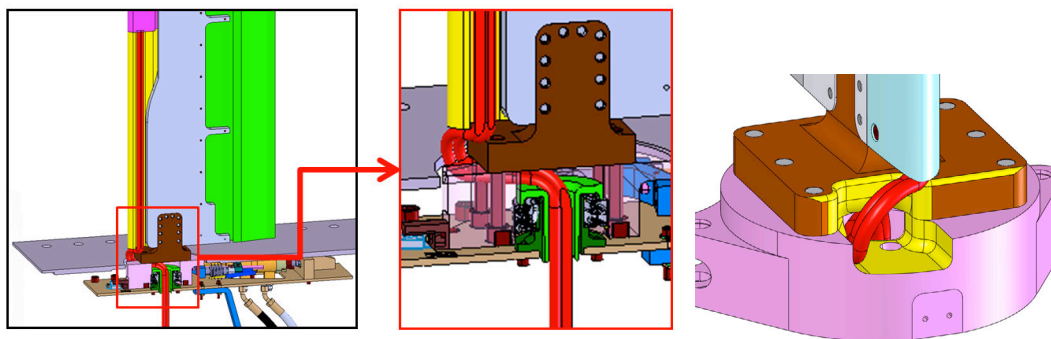


**Figure 56. CAD rendering to illustrate the tubing path through the lower area. Instrumentation cables will also be routed along this path and a similar path that connects the TE area of the airfoil.**

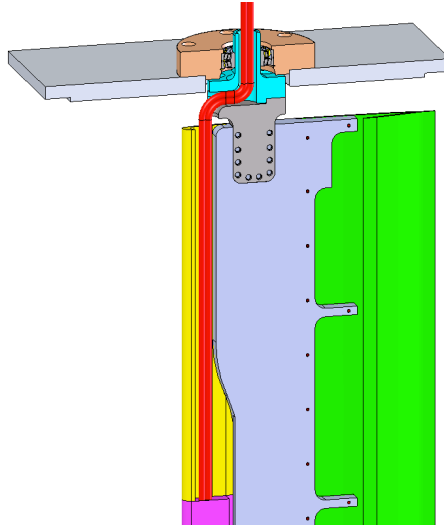


**Figure 57. Cut-away view CAD rendering to illustrate the tubing path through the upper area.**

### **1. VR-12 Airfoil: Fabrication and Assembly**

The fabrication of the VR-12 airfoil was completed as follows. The spar was machined from 17-4PH stainless steel using traditional CNC machining. The TE skins were fabricated using Newport NB321 7781 fiberglass composite. For the TE skins, tooling of the inner-most-layer (IML) was fabricated using CNC machining. To insure the geometry and finish after cure, the outer-most-layer (OML) of the composite lay-up was finished with CNC machining. Four composite sheets were fabricated in total, two for the upper surface and two from the lower surface, each approximately three-feet in span and extending from the TE of the OML portion of the spar to the true TE. The OML of each sheet was coated with a flat black enamel paint. Fabrication of the spar and composite sheets was performed by Eagle Aviation Technologies, LLC.

Each lower/upper pair of composite sheets was to be permanently bonded to form an upper panel and a lower panel, each of which would then be fastened to the spar. Prior to bonding, and in accordance with the design, all instrumentation was housed in the upper panel while the lower panel was totally uninstrumented. The upper panel contained two ESP modules, and numerous Kulite transducers (exact locations will be provided in a later section). All instrumentation work was conducted at UTRC. Cables and tubes were routed with extreme care in order to (1) insure that no sensors would come loose under vibratory loads, and (2) insure that the upper and lower sheets can come together for bonding without interference, thus maintaining the proper airfoil OML. To support the first objective, Kulite sensors were bonded using a slit brass ring bonded to the IML for support. The inside of the hole in the panel and the ring could then be coated with RTV and the sensor positioned from the outside in. The sensor face would flush-mounted with the OML of the airfoil. A schematic of this is shown in Figure 58.

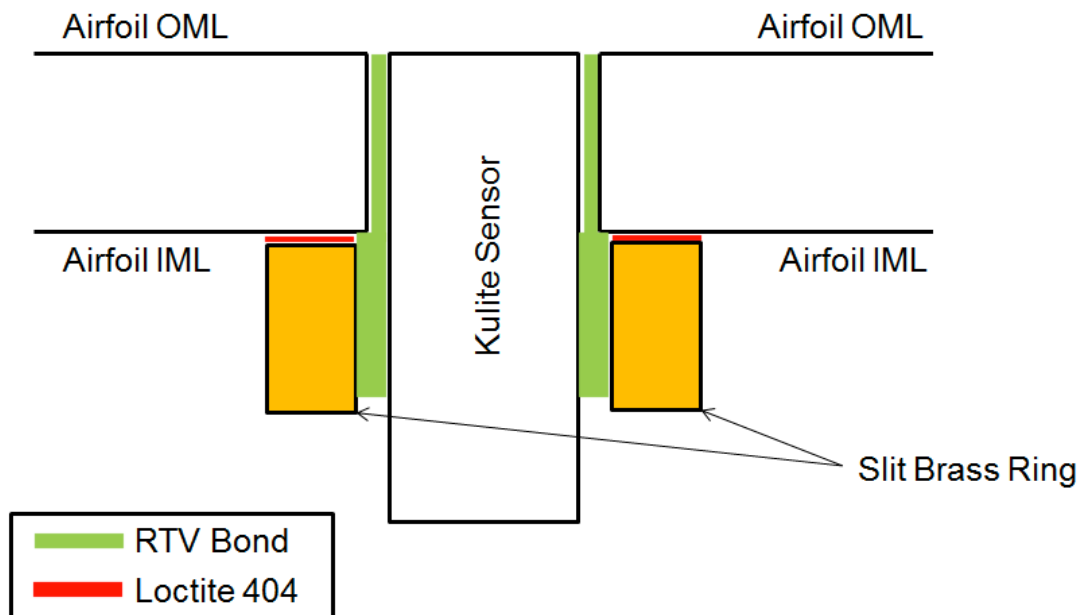


**Figure 58. Schematic representation of Kulite sensor mounting strategy.**

The ESP modules were mounted to aluminum brackets that were bonded to the IML of the airfoil in accordance with the design. The largest confluence of tubing and wires occurred near the midspan location at the inboard edge of the upper panel, as shown in Figure 59c.

Once all instrumentation had been bonded and its operability confirmed, final assembly of the panels was performed at UTRC, as outlined by the photographs in Figure 60. The IML near the TE was prepared for bonding using a 120-grit extra-clog-resistant sanding sheet (McMaster-Carr PN 4677A17) and thoroughly cleaned with alcohol after sanding. With all the instrumentation, cables, and tubes carefully placed (a-c), the upper composite sheets were fastened to the spar and assembly placed on the workbench with the upper surface down. The adhesive selected was Loctite EA9359.3 (formerly known as Hysol EA9359.3), a two-part aerospace-grade epoxy. This selection was made based on previous experience and risk-reduction testing done with the Newport composite, which demonstrated bond strength greater than the interlaminar strength of the composite itself. The mixed epoxy was applied to the TE IML of the upper surface, as shown in Figure 60d, then the lower surface was carefully placed on top and fastened to the spar while insuring that no cables or tubes had caused interference. This was done at approximately the same time for both the upper and lower panel. Once both panels were completely fastened to the spar, a pair of long aluminum brackets were used to clamp the lower and upper panels together at the TE as shown in Figure 60e,f. Risk-reduction tests had shown that a 24-hour room-temperature clamp-time was sufficient to achieve the desired bond strength. Figure 60g shows a photograph of the fully bonded lower panel.



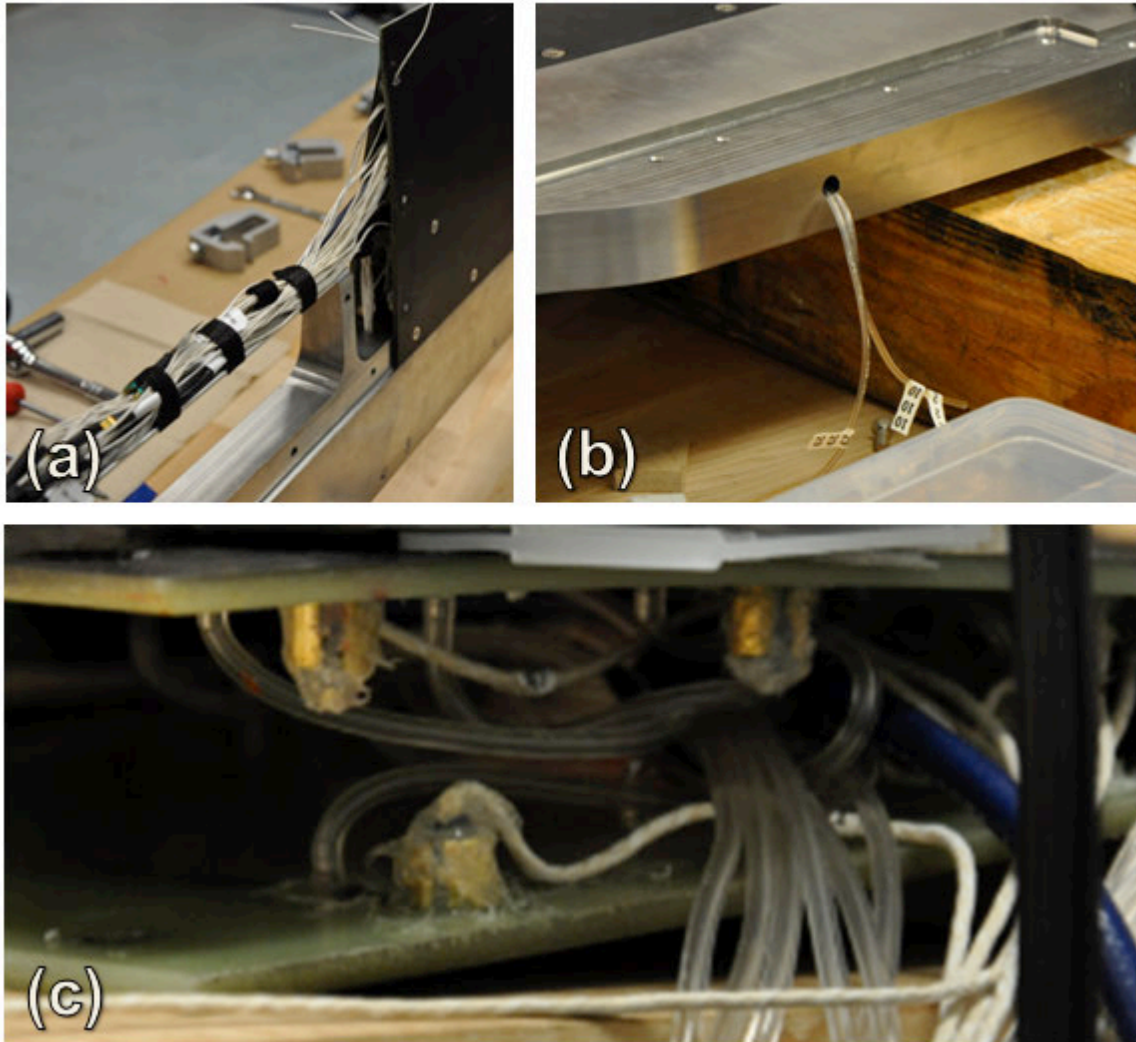


**Figure 59. Instrumentation of the test article on the upper composite panel.**



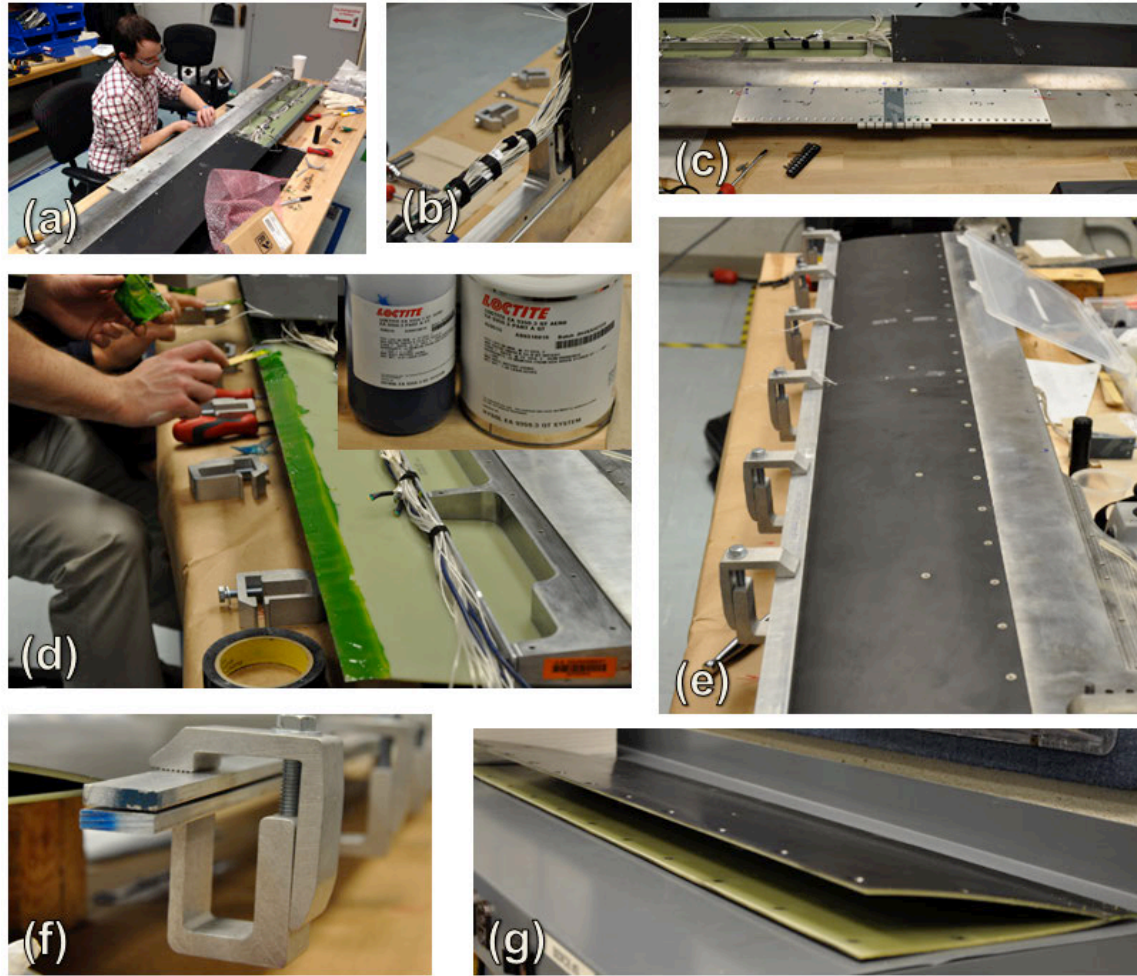


**Figure 60. Overview of airfoil final assembly procedure.**

## **2. VR-12 Airfoil: Pre-Test Assembly and Instrumentation**

The full-test article (including the actuation hardware) consisted of numerous parts fabricated by several vendors, thus several fit-checks were conducted as parts were completed. To insure successful integration of the airfoil, pitching mechanism, and instrumentation in the IRT, a tower assembly was constructed at UTRC using aluminum t-slotted framing with the objective of creating a surrogate for the IRT test section, particularly the ceiling and floor. The photographs of Figure 61 show several stages of assembly of the airfoil on the tower. The pitching mechanism was mounted approximately 2-3 feet above the laboratory floor as shown in (a). Prior to installing the spar onto the pitching mechanism turntable, all cables and tubes required for the wind tunnel test were routed through the lower pivot post bearing ID (with plastic sheath in place). Then the lower spar adaptor could be fastened (from underneath the turn-table) and kept in this configuration until final assembly at the IRT, significantly reducing setup time at the IRT.

With the spar mounted to the tower assembly, as shown in Figure 61b and c, numerous fit-checks were conducted, including that of the actuators, actuator plenums, hydrogen/air tubing, LE sheaths, and LE pressure module. A close-up view of the final actuator and LE pressure module fit-check is shown in Figure 61d.

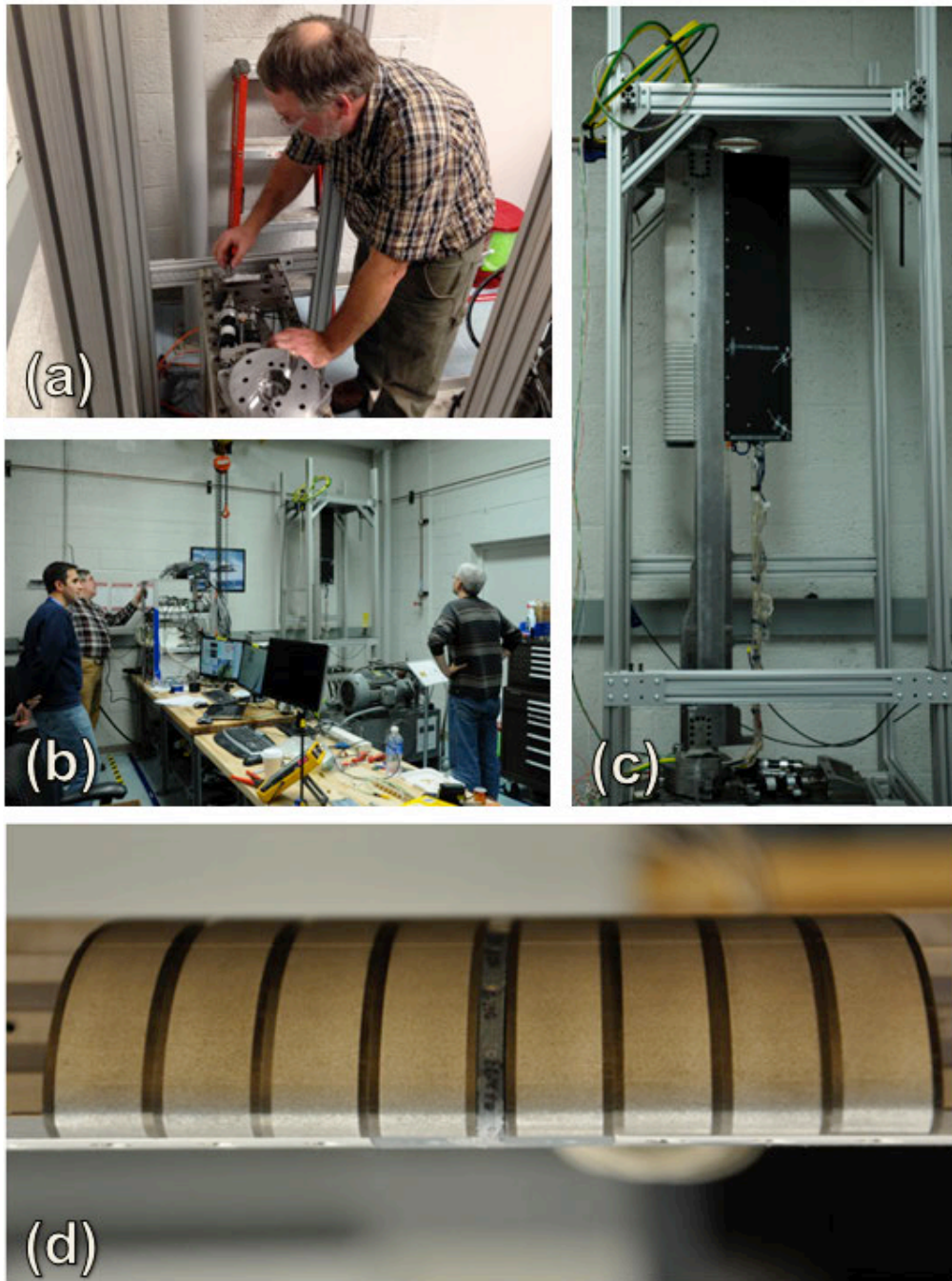


**Figure 61. Pre-test assembly of the test article in the UTRC Model Preparation Laboratory.**

### **3. Actuator Design for Installation**

#### **A. Initial Single-Row Actuator Design**

The VR-12 model for the IRT test was integrated with two arrays of COMPACT actuators located near the leading edge (LE), occupying roughly the middle 22.5 inches of the model (31%

of its total span). A CAD rendering of the spar and LE elements with the actuated span of the airfoil delineated is shown in Figure 62. The remainder of the model leading edge was inactive and consisted of aluminum cover plates providing room for electrical and gas connections underneath (shown in Figure 63 with the cover plates rendered transparent). Each cover plate was slightly less than 12" in length and the innermost cover also included a recess for holding the PC board on which the spark ignition coils for the actuators were mounted. The cover plates attached directly to the spar with flathead 10-32 screws from the upper and lower model surfaces. Figure 64 shows a rendering of an individual actuator module, which consisted of a nominally 0.50" wide combustor with a slot orifice exhausting to the surface of the airfoil and two 0.0625" width side walls that defined the span-wise ends of each combustor and were attached via miniature 1-72 screws. The sidewalls for each actuator contained a cutout section mimicking the orifice shape of the actuator to a limited depth in the side wall. While this did not match the tapered "vanishing gap" envisioned in the CFD (see Section 5b), it did create an effectively continuous slot on the upper surface of the airfoil while holding to a fully 2-D fabrication approach as constrained by the EDM process. Tests performed following the assembly of the actuator banks indicated sufficient jet expansion from the actuator span into the undercuts in the sidewalls to create a largely uniform jet at the model surface.

The 18 individual actuator modules were positioned adjacent to each other to form the actuator arrays on either side of the model centerline. While the individual actuators formed the shape of the upper surface and nose of the airfoil, two large cover plates formed the lower surface of the airfoil underneath most of each actuator array (shown in Figure 65). The white element shown in between the two large cover plates (in green) in Figure 65 is a centerline pressure module, which housed dynamic pressure transducers and formed the lower surface of the airfoil beneath the two actuators nearest to the model centerline. Internal to the model and underneath each of the actuator arrays was a gas plenum, which served to both distribute air and fuel to each individual actuator and as the mounting structure by which the actuators were attached to the spar. Each gas plenum (shown in cutaway views from the side and front in Figure 66) was mounted into the spar via 8 4-40 internal screws and interfaced with the key in the spar to hold it in place and provide further structural strength. Both internal and external 4-40 screws from the model upper surface connected each actuator to the gas plenum. Finally, the lower cover plates (and centerline pressure module) attached to both the individual actuators and the gas plenums with external 4-40 screws from the lower model surface (as may be seen in Figure 65).

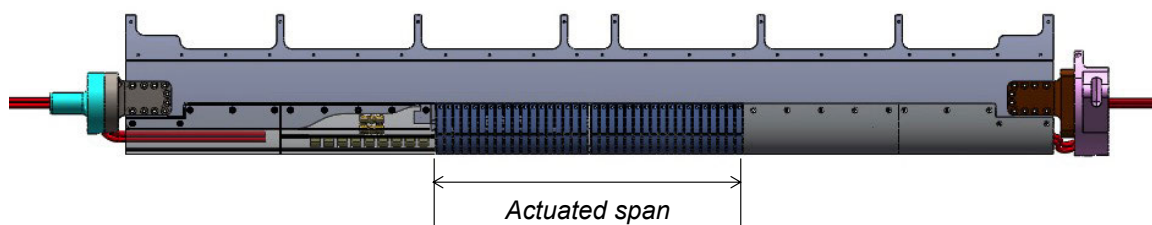


**Figure 62. Spar and leading edge of the airfoil.**



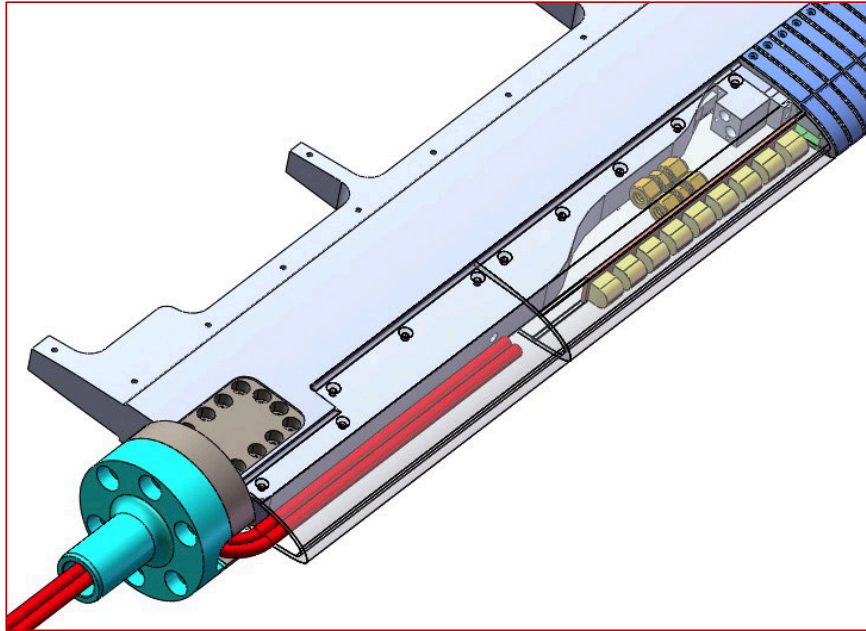


**Figure 63. Upper portion of the spar leading edge.**

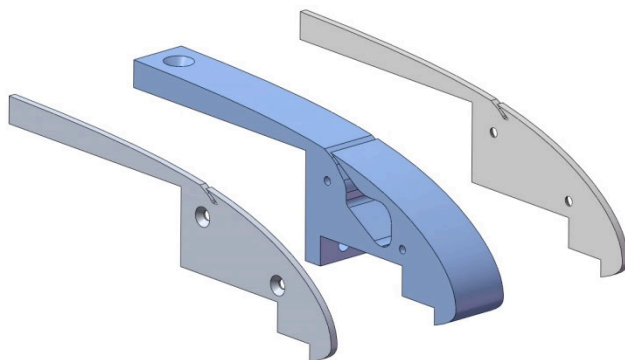


**Figure 64. CAD rendering of an individual actuator with sideplates.**

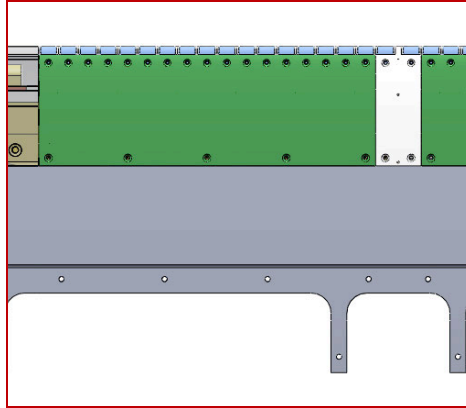


**Figure 65. CAD rendering of lower surface coverplate along one half of the actuated region.**

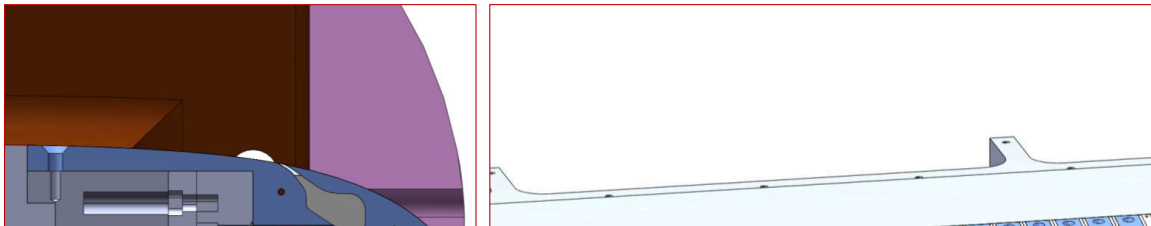


**Figure 66. Cut-away CAD renderings of the fuel and air plenums within the airfoil LE.**

### ***B. Modified Single-Row Actuator Design***

The actuator configuration described in the previous section represents the initial actuator mounting structure, which was used for the January 2015 wind tunnel entry. Several modifications to the COMPACT actuator arrays were performed in preparation for the second wind tunnel entry in May 2015. A critical challenge in the first entry involved maintaining even gas flow to all 36 actuators. Changes in both mixture ratio and mixture flow rates significantly impact COMPACT actuator performance and frequency range. Uneven flow through the gas plenums feeding the actuator arrays created varying conditions from actuator to actuator, thus effectively limiting the aggregate performance of the entire array. Attempts to control the flow with small set screws installed in the plenums on the hydrogen feeds to each actuator were able to overcome this to an extent in bench testing, but variations in pressure in the tunnel at different velocities (and at different spanwise locations on the model) are believed to have caused further unevenness in the flows, which could not be adjusted during wind tunnel operation.

Two concepts were considered to mitigate this problem for the second entry. The first would use choked orifices on the individual actuator feeds to maintain even flow rates to all actuators regardless of any downstream pressure variations they might experience (given equal upstream gas pressure at all of the choked orifices). The second concept would provide individual feedlines, metering valves, and flow meters to every single actuator thus allowing maximum flexibility to adjust the flow to each actuator as needed and providing confirmation of flow levels with the flow meters. After bench tests with choked orifices, a combination of these two approaches was deemed advisable with the air feeds to each actuator set via choked orifices and the hydrogen feed to each actuator provided through a variable area flow meter with an integrated needle valve. This combination allowed individual verification and control of the

mixture ratio while also keeping the amount of instrumentation to a manageable level. (Using individual flow meters and controls for both hydrogen AND air feeds to each actuator would have required 108 flow meters versus 36 for just the hydrogen feeds.) The choked orifices for the air and flow meters for the hydrogen were all located outside of the model with three nominally 1/16" diameter feedlines being routed into the model and to each actuator. This approach involved a larger overall tubing bundle dedicated for gas feed and larger pressure drops compared to the previous arrangement, but these trade-offs were acceptable with the available space inside the model and gas supply pressures. Scanivalve connectors within the model were used to connect the tubes from outside to those going to the actuators, with the actuators mounted to a newly fabricated hollow internal structure designed to serve the same mechanical purpose as the previous gas plenums (as shown in Figure 67 and in Figure 68). The new internal mounting structures allowed the gas lines to each actuator to be run in the downstream space behind them (as can be seen in Figure 68), with individual feed lines marked and tracked using a base 3 color coding system. The actuators themselves were modified to include bulged tubulations to attach the gas feed lines directly to each of them.

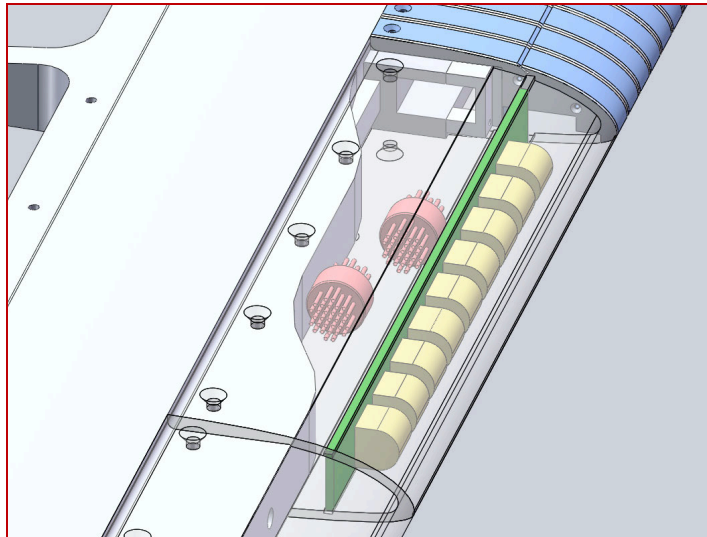


**Figure 67. Tubing connectors (red) and end view of new actuator mounting structure (shown with cover piece rendered transparent).**

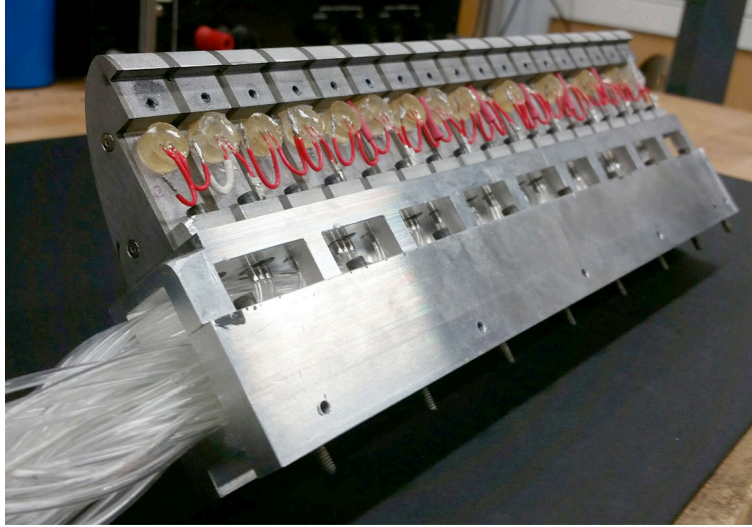


**Figure 68. Modified single-row actuator bank with new mounting structure, bulged tubulations on each actuator, and urethane tubing installed.**

In addition to modifications to the gas feed, some testing and modification of the actuators themselves was performed specifically related to assisting with ignition under low pressure conditions. Table 6 below shows the wind tunnel static pressures and peak dynamic pressures (over the range of angles of attack) during the initial high-speed wind tunnel entry as measured by the integrated pressure sensors closest to the actuator orifice for each of the primary Mach numbers tested. The surface pressures induced by the flow over the model should be equivalent to the internal actuator pressure since it is in direct fluid communication with the airfoil surface with minimal pressure drop through the actuator orifice. As seen in Table 6, this means that the internal combustion process for the actuator has to be initiated under significant vacuum conditions, with values as low as 0.30 atmospheres measured for  $M = 0.5$ . Although combustion can be achieved under these low-pressure conditions, ignition is somewhat more difficult with greater ignition energy required and larger spark gaps necessary to handle increases in quenching distance. During the first IRT entry, some actuator difficulties observed were likely due to ignition failures at the highest Mach numbers and subsequently lowest pressures. This may account for some observed tendency for actuator operation to be more reliable post-stall where higher surface pressures were being felt by the actuators (although it is difficult to separate any ignition difficulties from actuator flow unevenness induced by the pressures as described above). To mitigate this, bench testing in a vacuum chamber was performed, looking at variations in spark gap size and other characteristics. The only physical change to the actuators resulting from this testing was an increase in spark gap size to 1.2mm (from approximately 1 mm previously). This size was found to be the maximum to insure reliable arcing across both spark gaps on a given channel (with each ignition channel firing two actuators in series in the test set-up), although even larger gaps would likely be desirable in future experiments at low pressures. Easier ignition was also discovered for higher mixture ratios at low pressures and this influenced the mixture ratios used in the May 2015 test entry.

**Table 6. Freestream static pressures and peak surface pressures near actuator orifice for tested Mach numbers during January 2015 testing.**

<i>Mach number</i>	<i>Freestream Static Pressure (atm)</i>	<i>Peak Surface Pressure (atm)</i>
0.2	0.96	0.87
0.3	0.93	0.72
0.4	0.89	0.50
0.5	0.84	0.30

### **C. Dual-Row Actuator Design**

The window between IRT test entries also allowed for the final design and fabrication of additional actuator arrays featuring a second streamwise row of actuators. In this configuration, another set of combustion chambers are created and positioned such that the second slot orifice is located at  $x/c = 0.175$ , while maintaining the first actuator position with the slot orifice at  $x/c = 0.10$  (a cutaway view of the dual-row, leading edge assembly is shown at the top of Figure 69). In similar fashion to the revised single-row actuators, bulged tubulations are added to each actuator for gas connections and the gas feed lines are run in the open space underneath the actuators. Due to infrastructure limitations on the total number of actuators that could be supported, the spanwise extent of each actuator array was reduced to 5" with a reduction from 36 to 32 total actuators (to keep the number of actuators on each row even) and blank cover plates used to fill in the remainder of the previously actuated space (as seen in the bottom image of Figure 69). The EDM fabrication of these chambers was completed just prior to the beginning of the May test entry, so final assembly and testing of these actuators was actually performed on-site at the IRT while testing of the single-row actuators was on-going (the fully assembled model with the dual-row arrays installed is shown in Figure 70). Testing of the dual-row configuration at the end of the test window involved a number of actuation programs, including firing only the front (closer to the leading edge) row, firing only the second row, firing both rows simultaneously, and firing both rows with a time delay between the ignitions. The time delay was intended either to create a higher aggregate actuation rate (by running the actuators 180° out of phase) or to expose a pocket of fluid traveling over the airfoil to two actuation bursts rather than one (by introducing a small time delay roughly comparable to the convective time between the actuator slot locations).



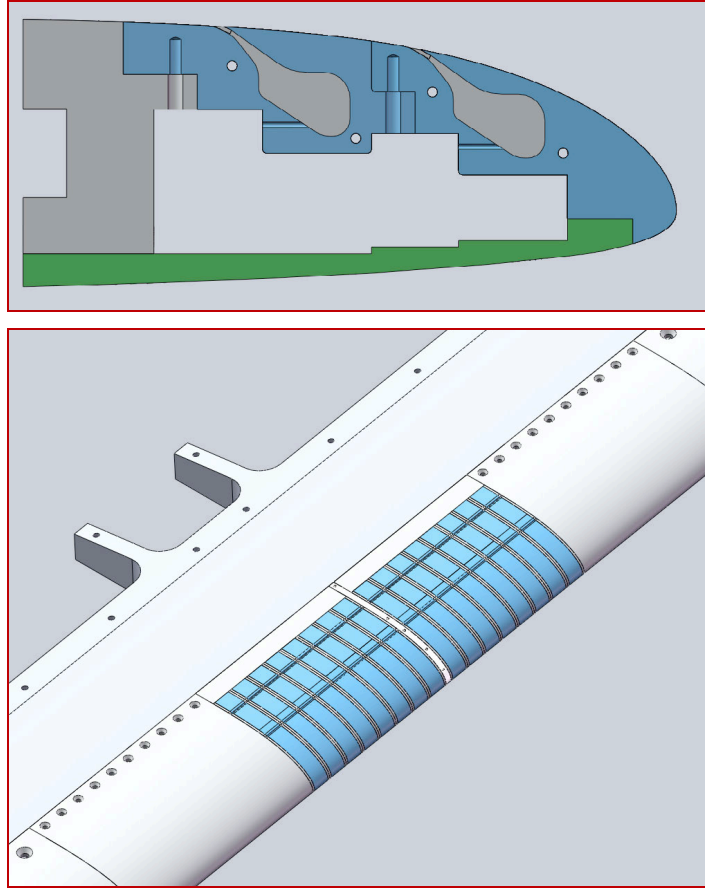


**Figure 69. Dual-row actuator arrays in side cutaway view (above) and top assembly view (below).**



**Figure 70. Installed dual-row actuator assembly.**

#### ***D. Actuator Control Systems***

Control of the COMPACT actuator arrays included two primary elements: the gas feeds and the spark ignition systems. Full details of the gas feed system and its operating procedures were provided under in the gas feed systems document prepared prior to testing, but a diagram of the system is shown below in Figure 71 including a shop air supply, a hydrogen cylinder, a nitrogen cylinder (for purging the lines), and a variety of components for controlling and measuring the flow rates. Air and fuel flow rates to each actuator array were monitored using thermal mass gas flow meters with the flow levels calibrated prior to tunnel operation via metering valves and adjustments to the regulated supply pressure levels. On/off control of the gas flow took place via solenoid valves operated from the control room with flow rates and line pressures monitored and displayed both locally at the gas control panels and remotely in the control room. In accordance with the changes described above between the two wind tunnel entries, gas plenums outside the model were added downstream of the gas control panels for the second test. The air plenums included directly mounted choked orifices, which subsequently fed to each of the actuators. The hydrogen plenums were fed by individual variable-area-flowmeters in order to control the hydrogen flow to each actuator. A sample bank of 6 of these flowmeters is shown in Figure 72.

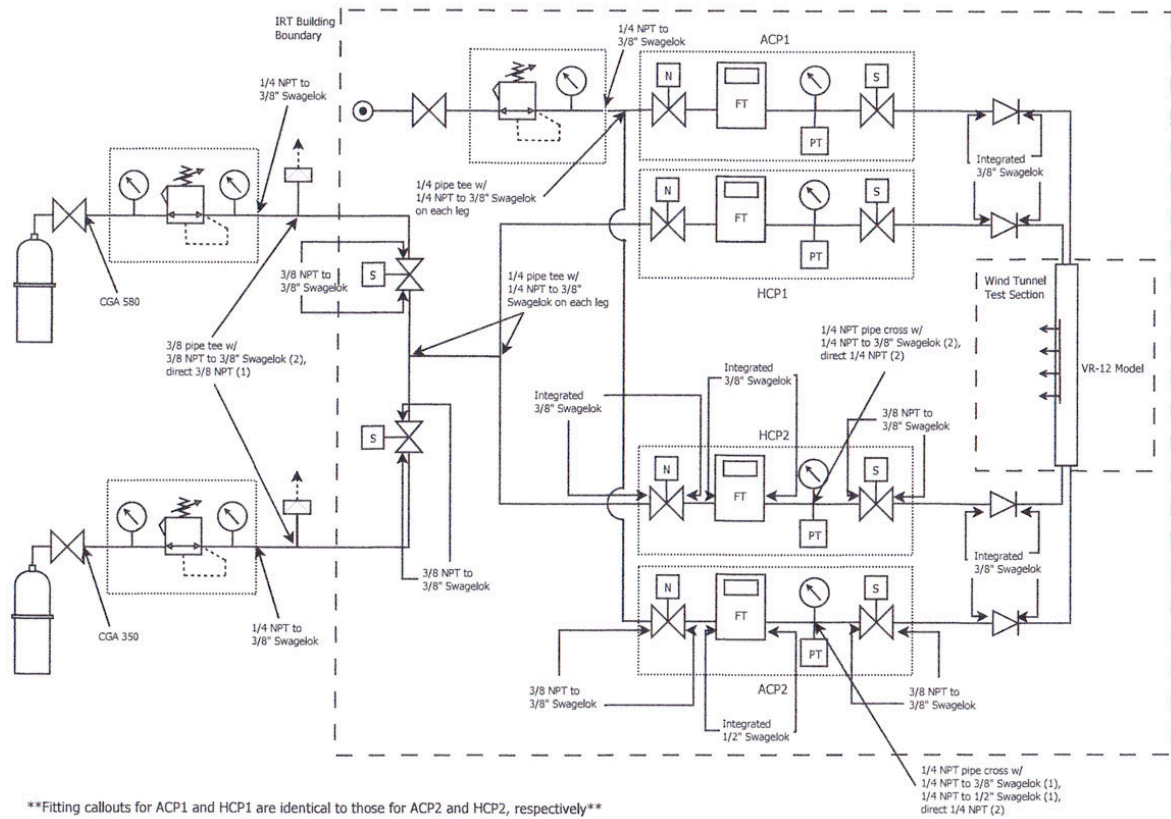


**Figure 71. Gas feed systems diagram.**

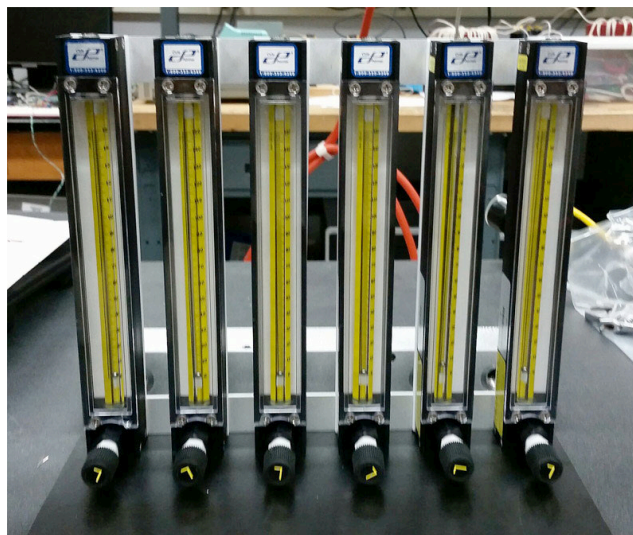


**Figure 72. Sample variable area flowmeter bank used for setting hydrogen flows in second test entry.**

Each individual actuation pulse was initiated by firing the spark ignition systems. These were triggered using 5V TTL signals generated from a computer in the control room with National Instruments boards and LabVIEW control VIs and sent to spark ignition boxes containing the ignition circuitry located near the model. The LabVIEW VIs allowed a variety of actuation patterns to be tested with pulses generated locked to the pitching cycle of the airfoil as indicated by the linear potentiometer on the pitching mechanism.

#### **4. Model Installation in the NASA Glenn IRT**

Installation of the clean LE model at the NASA Glenn IRT consumed most of the first day of this test entry. With the ceiling of the wind tunnel test section removed, installation began with the pitching airfoil mechanism, as shown in Figure 73. Using a lanyard routed between the hydraulic cylinders and the base plate, the entire mechanism, cable and tubes routed through the lower bearing ID, and 4 SCXI-1314 modules connected to these cables were lifted via hoist from the shop floor through the top of the test section. Hydraulic hoses were connected to the isolation valves at this time and also passed through the bottom of the test-section. The mechanism was then lowered slowly into place in the test section, as shown in Figure 73d. Before fastening the base plate to the lower half of the tunnel balance, the cables, tubes, and SCXI-1314 modules were passed from the inside of the test-section through the balance structure making them accessible to the data acquisition system below the test-section. Finally, a two-channel Dataforth module for amplifying thermocouple signals was fastened to the bottom of the baseplate and connected to thermocouples on the hydraulic manifold and inside the LE pressure module. With all tubes, cables, and hoses in place, the base-plate was fastened to the lower half of the tunnel balance.

With the pitching airfoil mechanism (up to the lower spar adaptor) in place, the ceiling structure of the tunnel was replaced without the ceiling window. The spar was then hoisted, lowered into the tunnel test section, and fastened to the lower spar adaptor, as shown in Figure 74b. Once fastened, the hoist was disengaged from the spar while physically supported by the present staff. With the spar aligned approximately vertically, the upper mount, which replaced one section of tunnel ceiling, was positioned on the tunnel ceiling frame and clamped down in a similar fashion to other ceiling pieces with the spar resting against the ID of the hole in the upper mount plate, as shown in Figure 74a. Finally, the upper bearing housing was placed from above the tunnel ceiling onto the spar and fastened to the upper mount plate.

With the spar securely fastened to the wind tunnel structure, assembly of the LE and TE elements began. Cables and tubes were connected to the TE panels and LE pressure module. Instrumentation cables were run along a thin bracket fastened across the TE of the spar on the lower half of the model, as shown in Figure 75. The first installation tested was the clean LE, however, air and hydrogen lines, which were already routed through the upper and lower bearings, were tucked inside the clean LE sheaths, as shown in Figure 75a.

Conversion from the clean LE to the actuated LE involved (1) removal of the clean LE sheaths, (2) installing and fastening the actuator LE banks, (3) completing the connectors and wiring for the actuation coils, and (4) interfacing hydrogen and air tubes to the top and bottom actuator plenums. A close-up view of the upper portion, midspan, and lower portion of the fully-assembled model with actuators is provided in Figure 76.

A photograph of the full VR-12 airfoil with actuators installed in the IRT test section is shown in Figure 77. A photograph of the NASA-COMPACT team alongside the fully assembled model is provided in Figure 78.

Finally, through the course of testing, some maintenance was required in order to maximize the amount of fully-operational instrumentation for each day of runs. Some of the MEMS-based pressure sensors became inoperable on certain days and needed to be rewired or replaced. Figure 79a shows the manner in which most repairs were done, with the lower TE panel removed and the upper TE panel on its side next to the model in order to minimize the amount of reconnection required. Such repairs were often done simultaneously with repairs to the LE, often done with the model configured as shown in Figure 79b, with the lower coverplate removed allowing access to actuator wires and terminals. Throughout these tests, the team's dedication, skill, persistence, and optimism was unrelenting, as captured in Figure 79c and d.



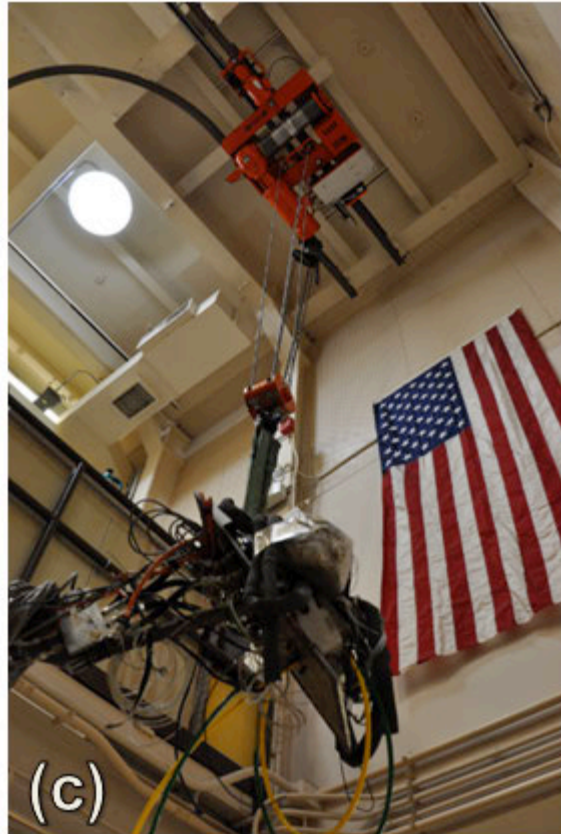
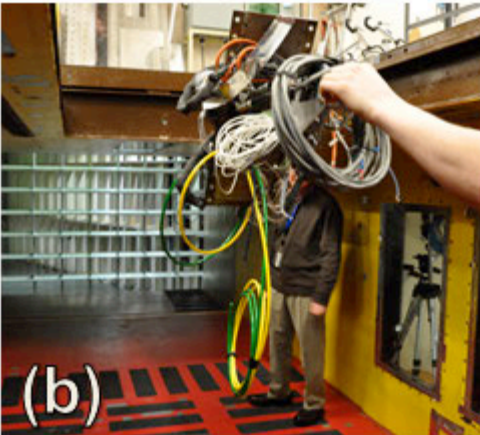
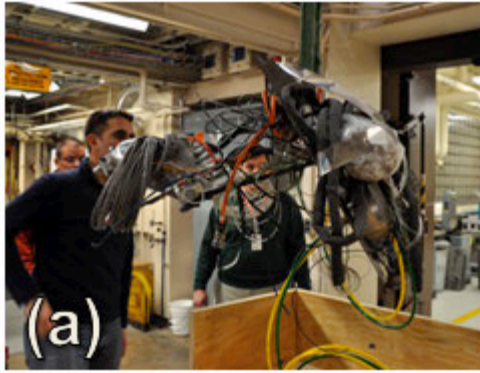


**Figure 73. Installation of the pitching airfoil mechanism.**

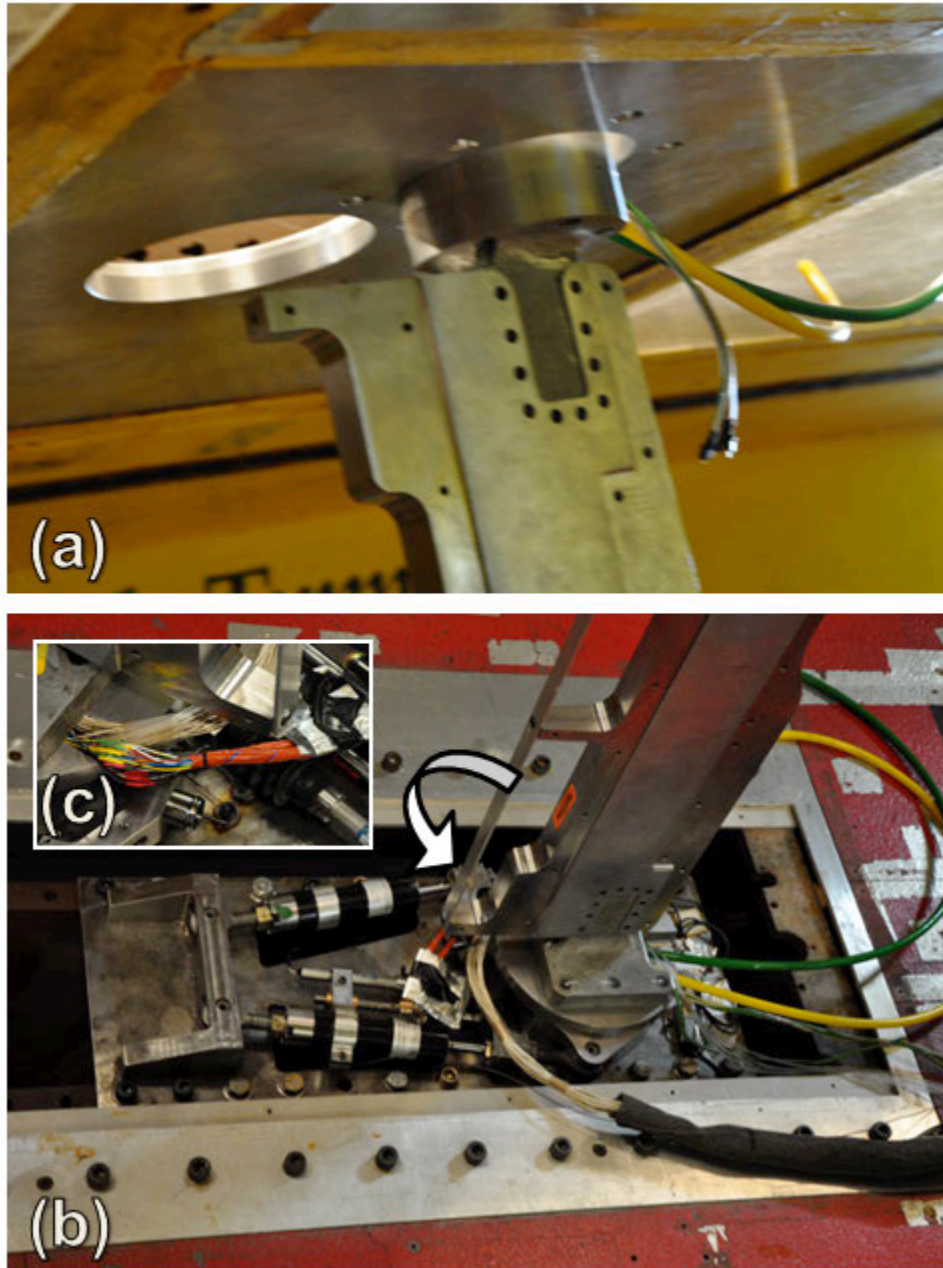


**Figure 74. Installation of the spar.**



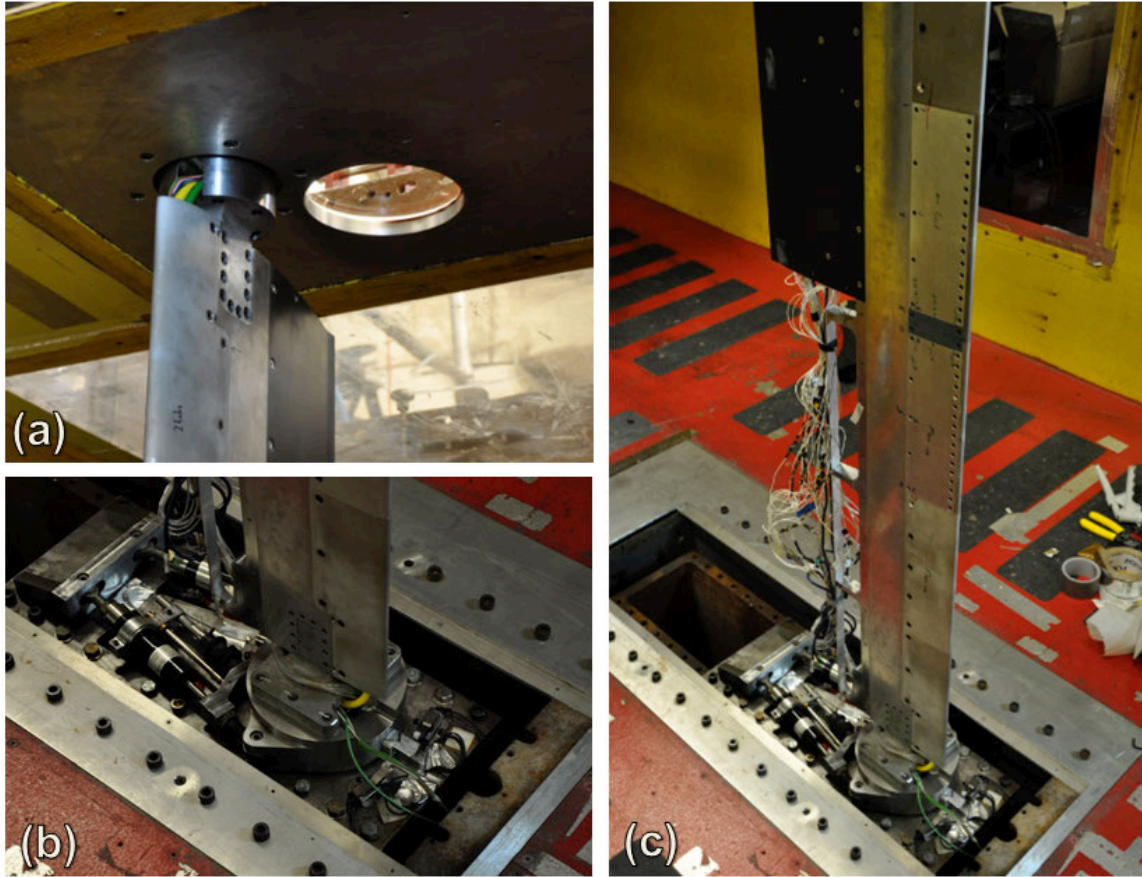


**Figure 75. Installation of the leading and trailing edge.**



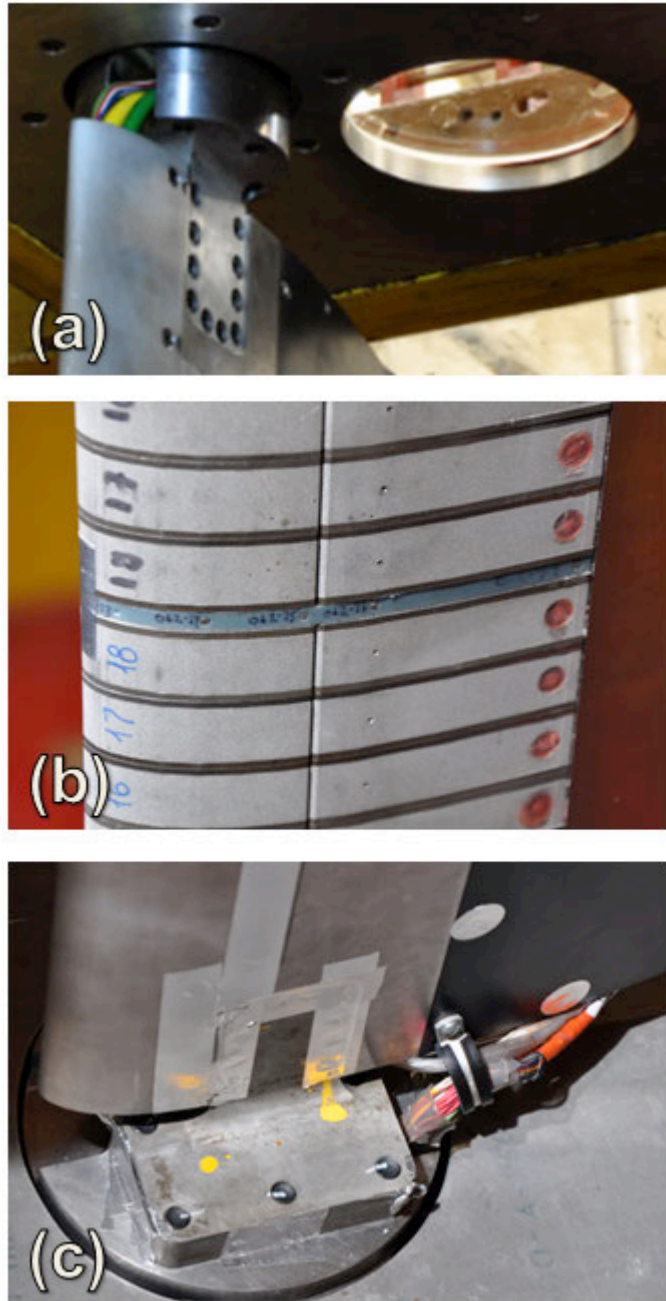


**Figure 76.** As-tested state of the (a) upper portion, (b) midspan, and (c) lower portion of the model.



**Figure 77. Full installation of VR-12 airfoil with actuator banks installed.**



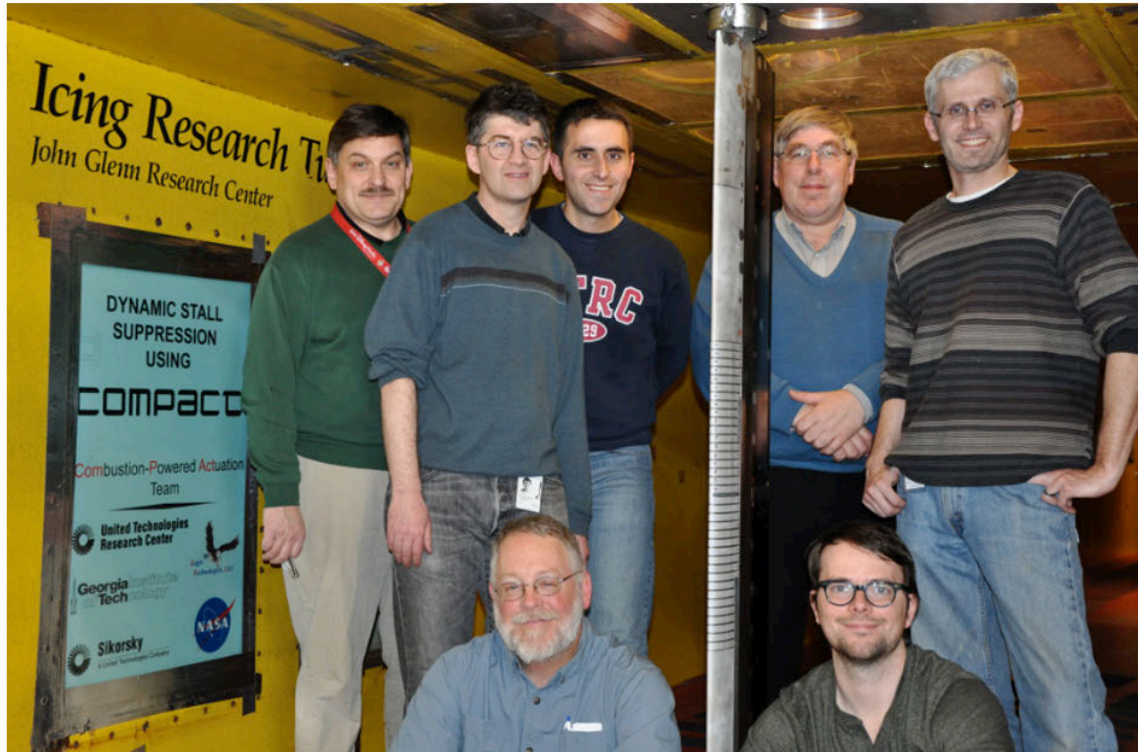


**Figure 78. NASA-COMPACT team. Back row (left-to-right): Norm Schaeffler (NASA), Slava Yorish (GT), Claude Matalanis (UTRC), Peter Lorber (SAC), Tom Crittenden (GT). Front row (left-to-right): Archer Jennings and Patrick Bowles (UTRC).**

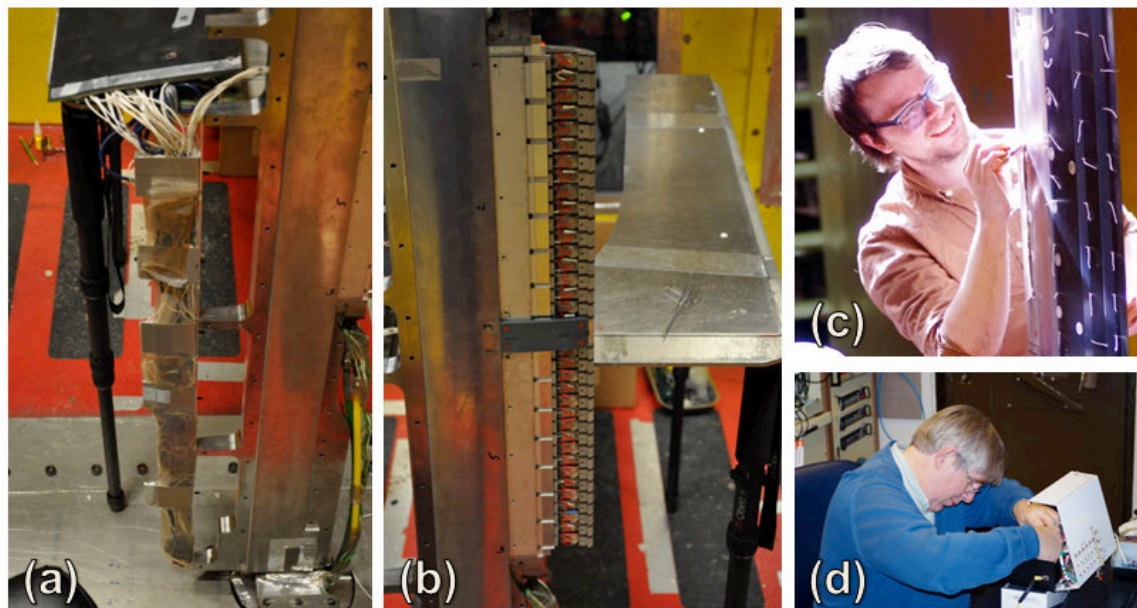


**Figure 79. Regular maintenance, repair, and clean-up procedures conducted between runs.**

## 5. Pressure Sensors

Four different sensors were used to measure pressure on the airfoil surface, each of which is described in Table 7.

**Table 7. Description of different sensors used to measure airfoil surface pressure.**

Manufacturer	Part no(s).	Size and Shape	Application
Kulite	XCS-062	0.066”D, 0.375”H	LE pressure module
Kulite	XCS-152	0.148”D, 0.375”H	Composite panels
Meggitt Endevco / UTRC	40931	0.5”D, 0.03”H	TE of composite panels
Measurement Specialties	16HD-0601020306	Miniature pressure scanner	Composite panels and clean LE

The first two and last required relatively little development work in order to achieve accurate pressure measurements. The third however, required significant development in order to successfully assemble a functional set of pressure sensors. The development effort is described as follows.

The Meggitt Endevco 40931 Sensor, which is 0.5 inch diameter and 0.03” high, was selected based on the potential for achieving a thin “pancake” sensor that can fit in the trailing edge of the airfoil. A schematic and photograph (acquired under a low-power microscope) of the bare sensor are shown in Figure 80.

The fully assembled pancake sensor consisted of one sensor, a circular PCB, and a PCB coverplate. The PCB was designed at UTRC and fabricated from Isola 370HR by Advanced Circuits, Inc. The completed PCB thickness was approximately 0.013”. A CAD rendering of the coverplate is shown in Figure 81. The coverplate was manufactured from 0.015” thick FR4 using traditional CNC machining with a 0.010” diameter end mill and a very low feed rate. It featured cutouts to allow the sensing face to be flush-mounted with the coverplate and airfoil surface, and to allow access for a four-wire cable to be soldered to the sensor.

The final assembly of the pancake sensor was performed as follows:

1. The PCB and coverplate were visually aligned and bonded using Devcon 5-minute epoxy with care taken to prevent epoxy from entering the sensor region of the PCB.
2. Conductive epoxy (EG58 - ElectroDag 5810 Conductive Silver Epoxy) was applied sparingly under a low-power soldering microscope to each solder pad using a height gage and dental pick (see Figure 82).
3. The sensor was placed onto the solder pads and very lightly (one-finger-touch) pressed.
4. The sensor was left to cure at room temperature for 24 hours.
5. Four-wire leads were soldered to the terminals

Photographs of a completed pancake sensor are shown in Figure 83.

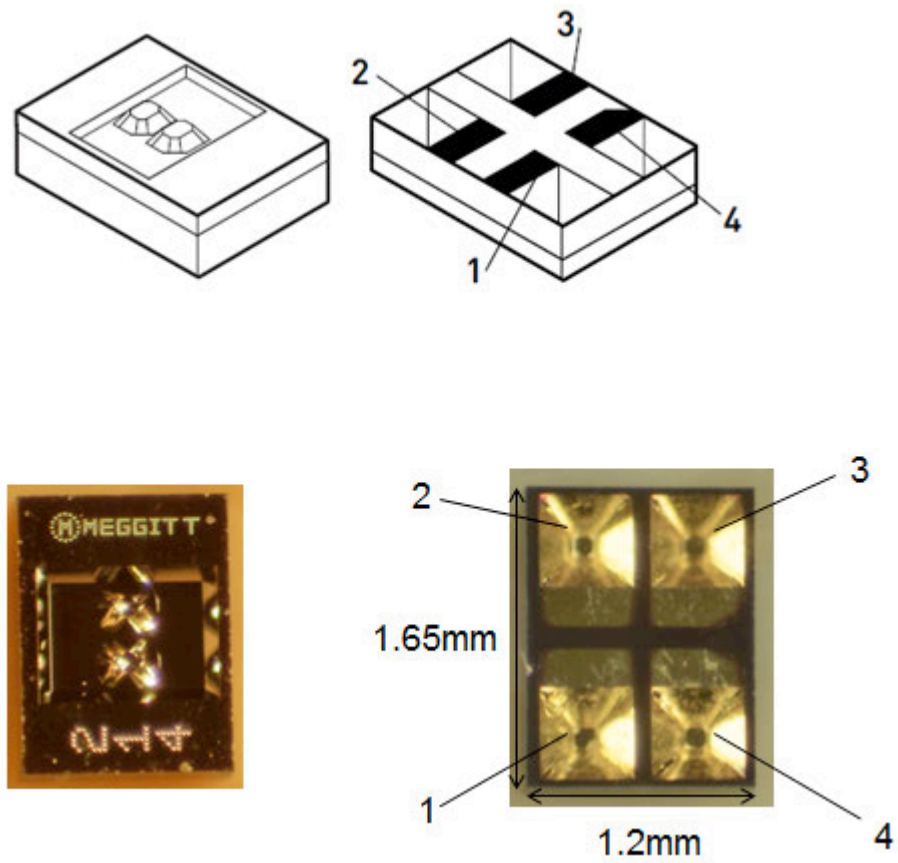


**Figure 80. Meggitt Endevco sensor schematic and photograph (prior to sensor assembly).**

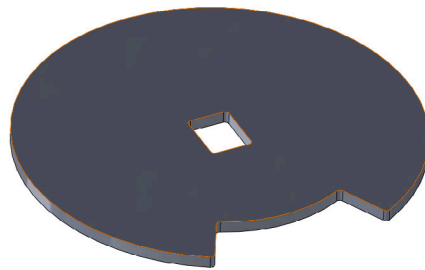


**Figure 81. Coverplate for pancake sensors.**



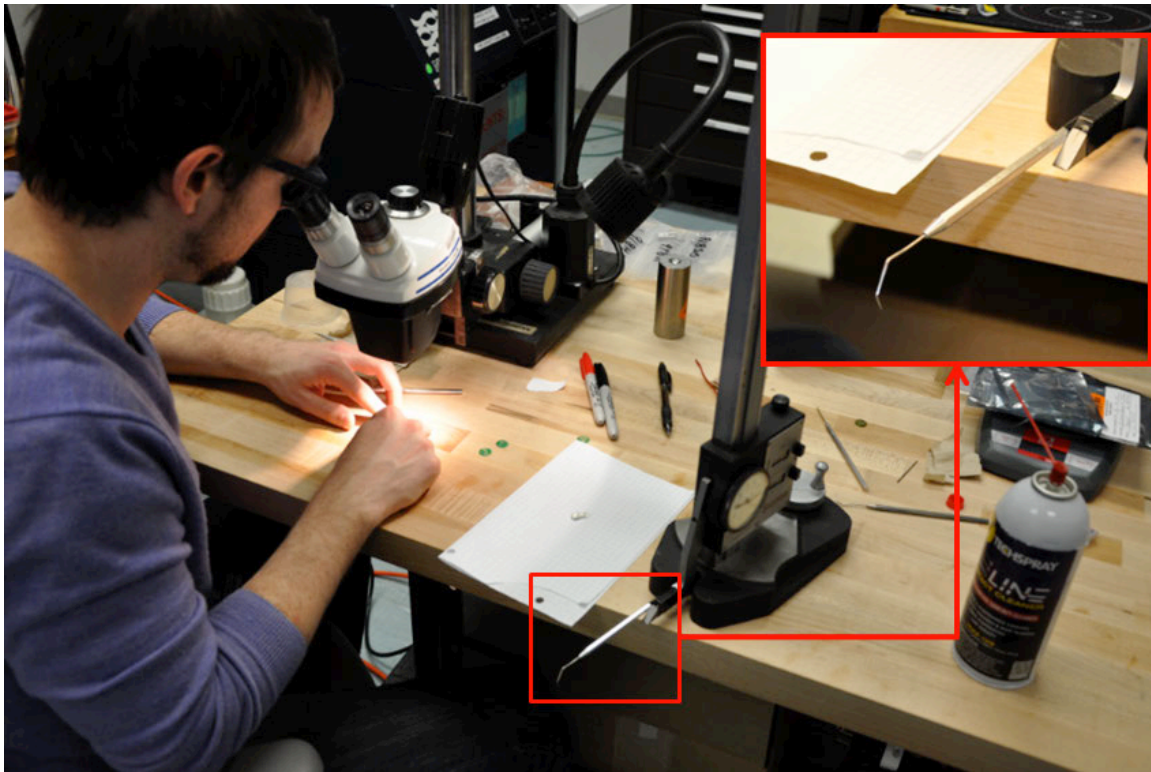


**Figure 82. Pancake sensor final assembly process.**

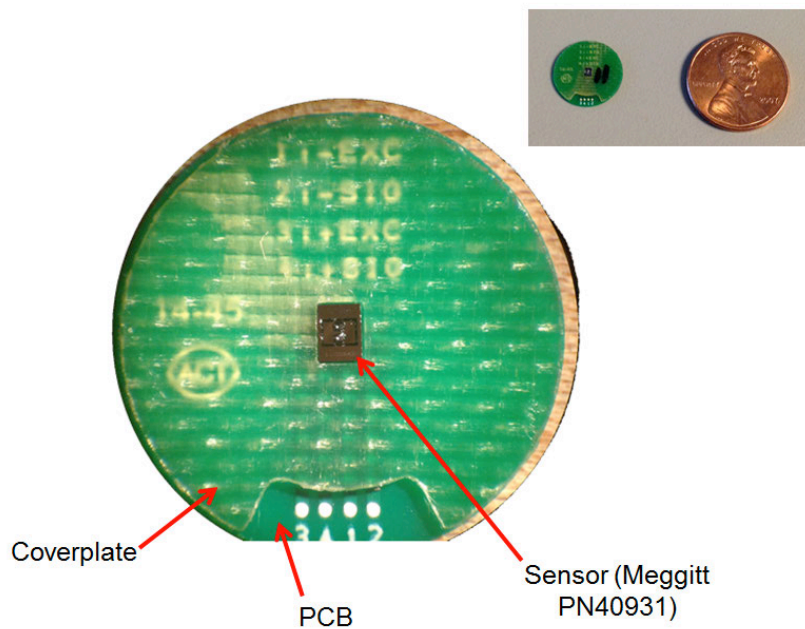


**Figure 83. Magnified and unmagnified photographs of a completed pancake sensor.**

The VR-12 model was instrumented with twenty-four high frequency response, piezo-resistive, Wheatstone bridge based pressure transducers manufactured by Kulite. Four MEMS pressure transducers manufactured by Meggitt Endevco were installed in the trailing edge of the VR-12.

An additional 30 pressure ports were connected via Tygon tubing to two Pressure Systems' scanning pressure transducers (referred to as ESPs). Each Pressure Systems module also contained a resistance temperature detector (RTD). Figure 84 indicates the chordwise and spanwise location of each category of probe. Note that all sensors aft of the spar are mounted to the upper composite panel. Most LE sensors are mounted to the LE pressure module at the midspan. Two additional pressure measurements on the LE are made 2 feet from the midspan using the ESPs.

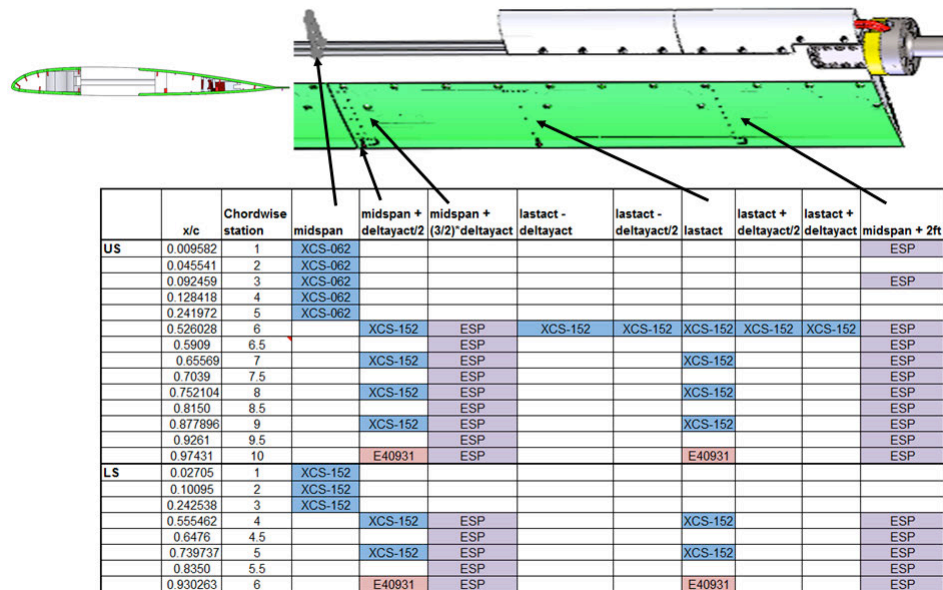


**Figure 84. Location and model of onboard surface pressure instrumentation in VR-12 wing.**

Figure 85 shows the tap layout and sensor names for each station. An SLA insert, also shown in Figure 85, was manufactured and used to mount the eight pressure transducers required in the leading edge. These eight probes were used for both STA1 and STA2 sectional load integration. A five-probe array along the span of the wing is centered at STA 3 and is not indicated. This array was implemented to provide some implication of the spanwise extent of the actuated flow into the non-actuated region of the wing.



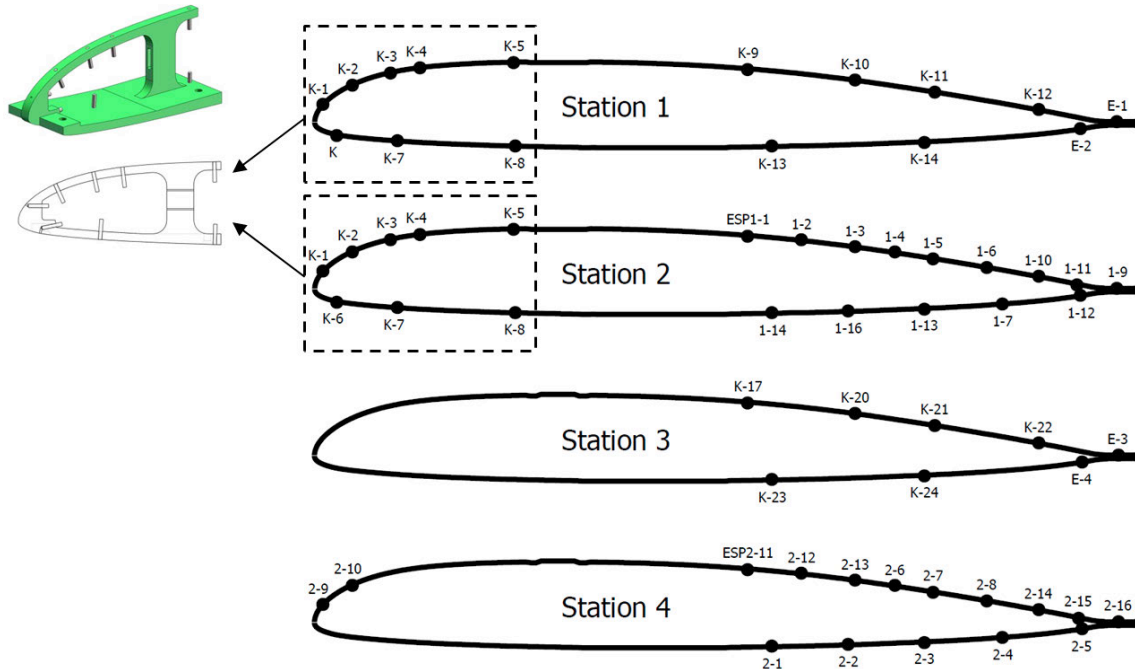


**Figure 85. Location and names of installed probes for each wing station.**

## 6. Control and Data Acquisition Systems

A single data system was used to command the wing pitching motion, to acquire data, and to process and display the results. Two primary hardware components were used, a National Instruments (NI) USB-6259 BNC unit and a USB-6259 Mass Termination (MT) Multifunction Data Acquisition (DAQ) unit, both controlled by a single PC using NI LabVIEW software, as outlined in Figure 86.

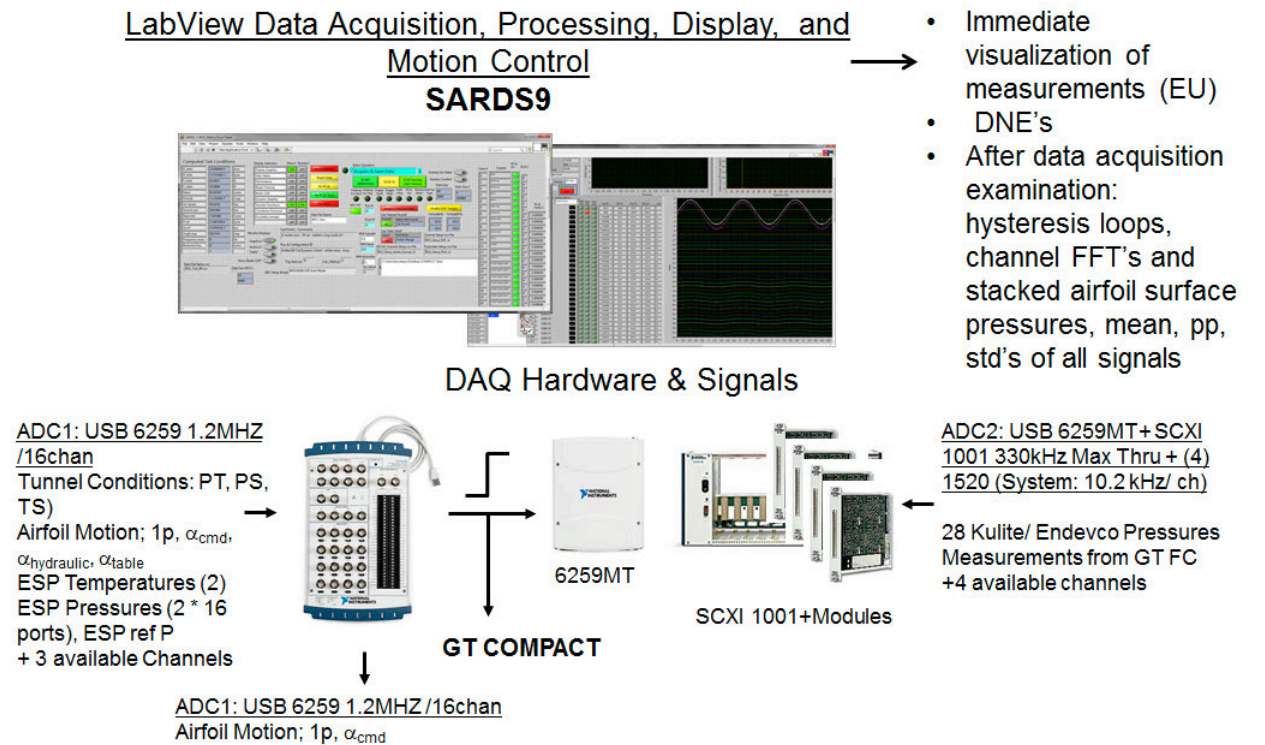


**Figure 86. Data acquisition hardware and software for VR-12 COMPACT model wing IRT test.**

The USB-6259 BNC sampled the following analog channels:

1. test section pressures and temperatures
2. electronic pressure scanner pressure and temperature (described in the following section)
3. the position of the model wing relative to the IRT yaw table, as measured by the linear potentiometer on one of the hydraulic actuators(  $\alpha_{hydraulic}$  )
4. the IRT yaw table position (  $\alpha_{table}$  )
5. the hydraulic angle command and one-per-rev timing signals
6. hydraulic fluid and leading edge Kulite temperatures

Additionally, the USB-6259 BNC provided control of the wing time-dependent motion through an analog command output to a Moog G122-824 PI servo amplifier, which provides position feedback control for the Moog G761-3005 16.5gpm hydraulic servo valve mounted underneath the two actuators. Once-per-rev and sample clock timing signals from the USB-6259 BNC are passed to the ESP controller (described below) and the USB-6259 MT. An additional one-per-rev output trigger can be phase shifted with respect to the time-dependent angle-of-attack at a user-specified upward or downward stroke angle, and is provided to set the start phase of the COMPACT pulse schedule. The USB-6259 BNC sampled at 2048 per pitch cycle, or 128 per cycle per ESP port (see below).

The USB-6259 MT connects to an NI SCXI 1001 chassis housing four eight-channel SCXI-1520 signal conditioning modules that provide regulated power to each of the 28 bridge based pressure sensors onboard the VR-12 model. Each differential output from the sensors can be programmed with individual amplifier gains and low-pass filter cutoff frequencies. The maximum aggregate

sampling rate of the SCXI chassis is 333 kHz, or  $\sim 10$  kHz / channel for 32 channels. Trigger and clock signals are provided from the USB-6259 BNC to the USB-6259 MT to synchronize data acquisition. In the first test entry the USB-6259 MT sampled at 512 per pitch cycle, and in the second test entry at 1024 per pitch cycle.

LabVIEW software was used to set, record, and monitor all acquired data signals. All individual signals were displayed immediately following acquisition. Figure 87 shows the installation in the IRT Control Room.



**Figure 87. Data acquisition and control hardware installed in IRT Control Room**

The hydraulic supply pressure was monitored via two electronic pressure gauges installed up and downstream of the proportional valve. A single thermocouple placed in the oil tank indicated oil temperature. Each system diagnostic has readouts on the motor/pump control panel that reside in the IRT control room. The limits on the pressure and temperature were 2900 psi and 130°F, respectively. Limit switches were used to detect motion beyond the angle limits. Two stop valves were installed in the pressure and return lines at the model to insure immediate cessation of motion if a fault was detected or the stop button was pushed.

## 7. Pressure Sensors

The VR-12 model was instrumented with fifty-eight pressure sensing ports arranged in 5 arrays, as identified in Table 8. They consisted of:

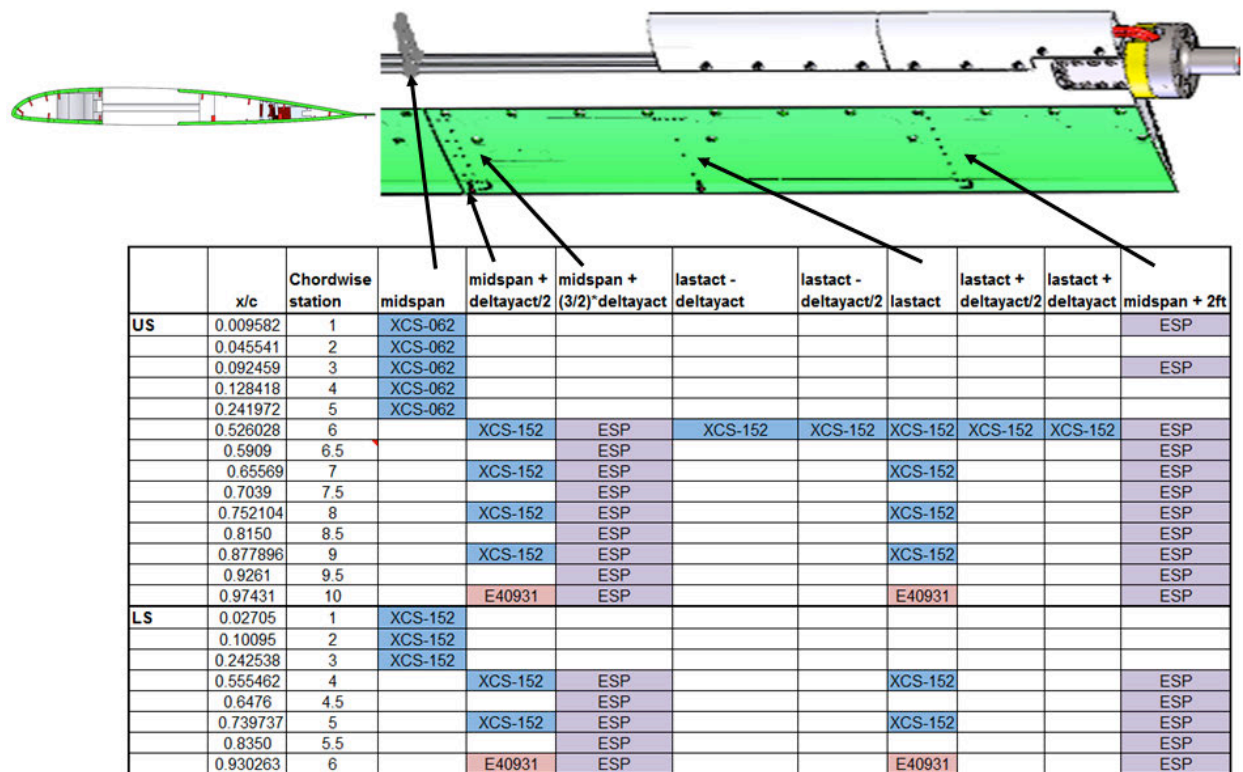
1. Twenty-four high frequency response, piezo-resistive, Wheatstone bridge based pressure transducers manufactured by Kulite.
2. Four MEMS pressure transducers manufactured by Meggitt Endevco and integrated by UTRC into low profile “pancakes” for use at the trailing edge.
3. Thirty surface pressure ports connected via short lengths of Tygon tubing to two Pressure Systems electronic scanning pressure (ESP) modules. The ESP modules were mounted inside the model, and each contained an array of 16 pressure transducers, signal conditioning, addressable switching, and a resistance temperature detector (RTD).

**Table 8. Pressure sensor stations.**

Station	Location	Number	Type
Sta 1 Chordwise	$z/c = a$	18	14 Kulite + 2 Pancake
Sta 2 Chordwise	$z/c = b$	22	8 Kulite + 14 ESP
Sta 3 Chordwise	$z/c = c$	8	6 Kulite + 2 Pancake
Sta 4 Chordwise	$z/c = d$	16	16 ESP
Spanwise	$x/c = 0.526$	4	4 Kulite

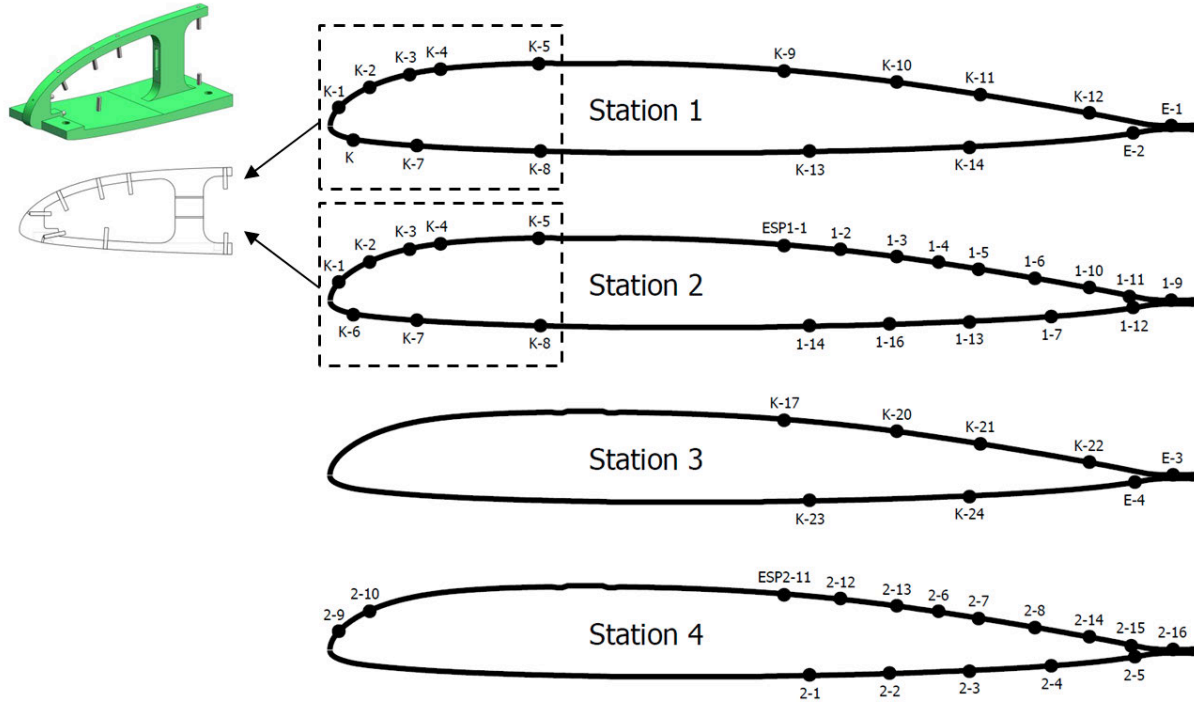
Figure 84 indicates the chordwise and spanwise location of each category of probe. Note that all sensors aft of the spar are mounted to the upper composite panel. Most LE sensors are mounted to the LE pressure module at the midspan. Two additional pressure measurements on the LE are made 2 feet from the midspan using the ESPs.

Figure 85 shows the tap layout and sensor names for each station. The green SLA insert was manufactured and used to mount the eight Kulite pressure transducers required in the leading edge. These eight probes were used for both STA1 and STA2 sectional load integration. A five-probe array along the span of the wing is centered at STA 3 and is not indicated. This array was implemented to provide some implication of the spanwise extent of the actuated flow into the non-actuated region of the wing.



**Figure 88. Location of onboard surface pressure instrumentation in VR-12 wing.**





**Figure 89. Location and names of installed probes for each wing station.**

#### **A. Kulite Pressure Transducers**

Two types of transducers were installed in this model:

1. XCS-062, which is 0.066 inch diameter, 0.375 inch high, and used in the leading edge
2. XCS-152, which is 0.148 inch diameter, 0.375 inch high, and used in the aft panels

All of the Kulites were 15 psi absolute sensors. The manufacturer provided individual sensitivity calibration sheets, which were verified after installation by placing a tube or vacuum bag over the port(s) and applying suction from a calibrated Druck 609 reference source.

While the Kulites were specified to have a thermal sensitivity of less than 1% full scale zero shift and less than 1% sensitivity shift per 100°F temperature change, an additional correction to account for thermal shift was added in the data processing, based on heating the installed LE pressure module and determining a linear fit to the zero shift:

$$P(T, V) = m \times (V - Z(T)),$$

$$Z(T) = Z_0(T_{ref}) + (T - T_{ref}) \times Z_1,$$

where  $m$  is the slope in psi/V,  $Z$  is the voltage at  $P=0$ , and  $T_{ref} = 0^\circ\text{F}$

Since the Kulites were installed with their sensing diaphragms flush with the surface, their inherent frequency response was quite high, greater than 100 kHz. This was confirmed for several typical installations using the acoustic calibrator described below in the ESP section.

#### **B. Electronic Pressure Scanners**

The two 16 port Measurement Specialties 16HD-0601020306 ESP modules were controlled using a Sikorsky custom-designed interface box. The box powered the modules, set their port

addresses, and signal conditioned the output pressure and temperature signals. In order to synchronize the model motion, the switching of the ESP addresses, and the data acquisition, the USB 62589 BNC provided the interface box with a clock pulse so that the port addresses were stepped at the same rate as the pressure and temperature data were sampled. The interface box sent a check-sum signal back to the USB 6259 to confirm that all address pulses were received and acted upon. The interface box could also be controlled by toggle switches for debugging. Tuned active filters in the pressure input lines were used to minimize ringing in the stepped pressure signals. The maximum ESP address step rate was 22 kHz, resulting in a maximum sample rate per port of 1/16 of that or 1300 Hz, which was 152 samples/cycle at the maximum wing pitching frequency of 8.5 Hz.

A full thermal and pressure calibration of all sensors in the ESP modules was performed, and thermal correction terms were included in the data reduction process:

$$\begin{aligned}
 P(T, V) &= m(T) \times (V - Z(T)), \\
 m(T) &= m_0(T_{ref}) + (T - T_{ref}) \times m_1 + (T - T_{ref})^2 \times m_2, \\
 Z(T) &= Z_0(T_{ref}) + (T - T_{ref}) \times Z_1 + (T - T_{ref})^2 \times Z_2, \\
 \text{where } m &\text{ is the slope in psi/V, } Z \text{ is the voltage at } P=0, \text{ and } T_{ref} = 0^\circ\text{F}
 \end{aligned}$$

The ESP modules were operated in differential mode, with the reference pressure being connected to wind tunnel total pressure. The reference pressure line was also used to perform calibration and functionality checks during the test entries.

The frequency response of the ESP pneumatic system was measured using the apparatus shown in Figure 90, modelled on the approach developed in Ref. [41]. The USB 6259 generated either white noise or a sinusoidal tone as an analog output, which was amplified and passed to an 8 Ohm, 60W acoustic driver (the large grey unit). The driver was screwed in to a small cavity inside the silver cylinder. For initial checks, a Tygon tube of appropriate length (4 inches) was connected between the top of the cavity and the ESP module, and a reference Kulite XCS-062 pressure transducer with a frequency response greater than 100 kHz was flush-mounted with the side of the cavity. Digital records 20 seconds long were recorded at 5 kHz, and the transfer function between the reference transducer and the ESP output was computed. The plots on the right-hand side of Figure 90 show typical amplitude and phase responses. The black lines are the white noise and the red circles are the tones. This nominal system is therefore able to resolve pressures up to at least 300 Hz, 2/3 of the resonance frequency, which is 35 times the maximum model oscillation frequency of 8.5 Hz. This is sufficient to define the unsteady loads and capture the signature of the dynamic stall vortex. The higher frequency response of the Kulites is required to resolve the COMPACT pulses.

For final checks on each port as installed in the model, the silver cylinder was placed directly on the airfoil using an O-ring seal, as in Figure 90. Figure 91 compares the measured frequency domain response of a typical ESP tap (ESP2-16) to the Bergh-Tijdeman (BT) multiple tube and volume theoretical response, originally described in Ref. [41]. Figure 91(a) shows the raw, single-sided amplitude response of the ESP (blue) and reference Kulite (red) to a white noise input. The two responses match up to 120 Hz. The response differs at higher frequencies. Figure 91(b) shows the coherence for both the white noise (black) and tonal inputs (circles). A coherence of unity suggests that there is a near linear input/output power transfer. The poor coherence observed at low frequency is a function of the low power produced by the acoustic

driver at low frequency. Figure 91(c) shows the amplitude transfer functions between the ESP and the reference Kulite for both white noise (black line) and tonal (red circles) inputs. Transfer functions for these two inputs are in good agreement.

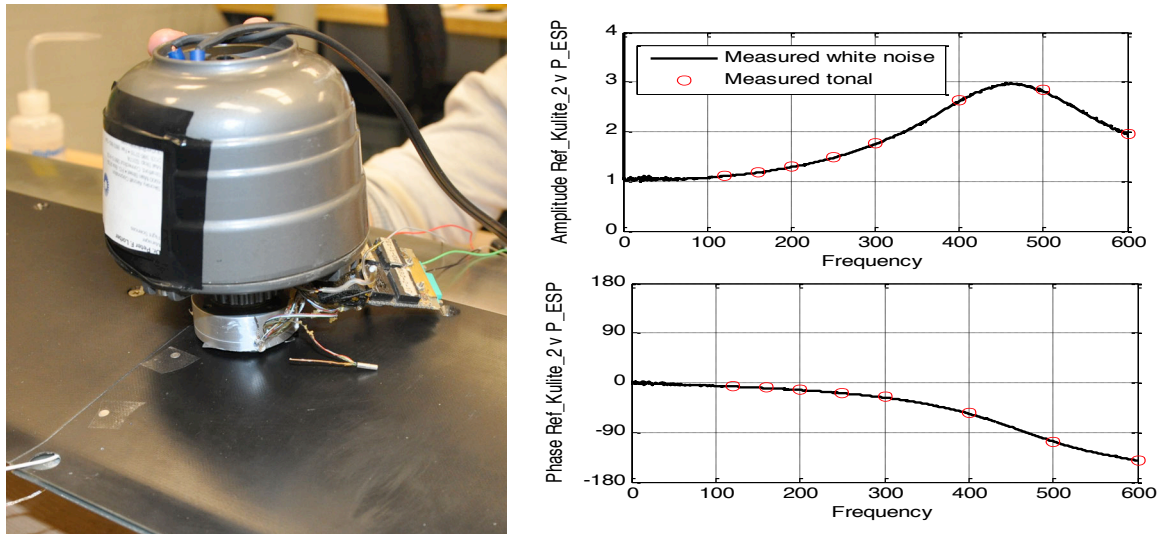


**Figure 90. ESP Frequency Response measurement hardware and typical results.**

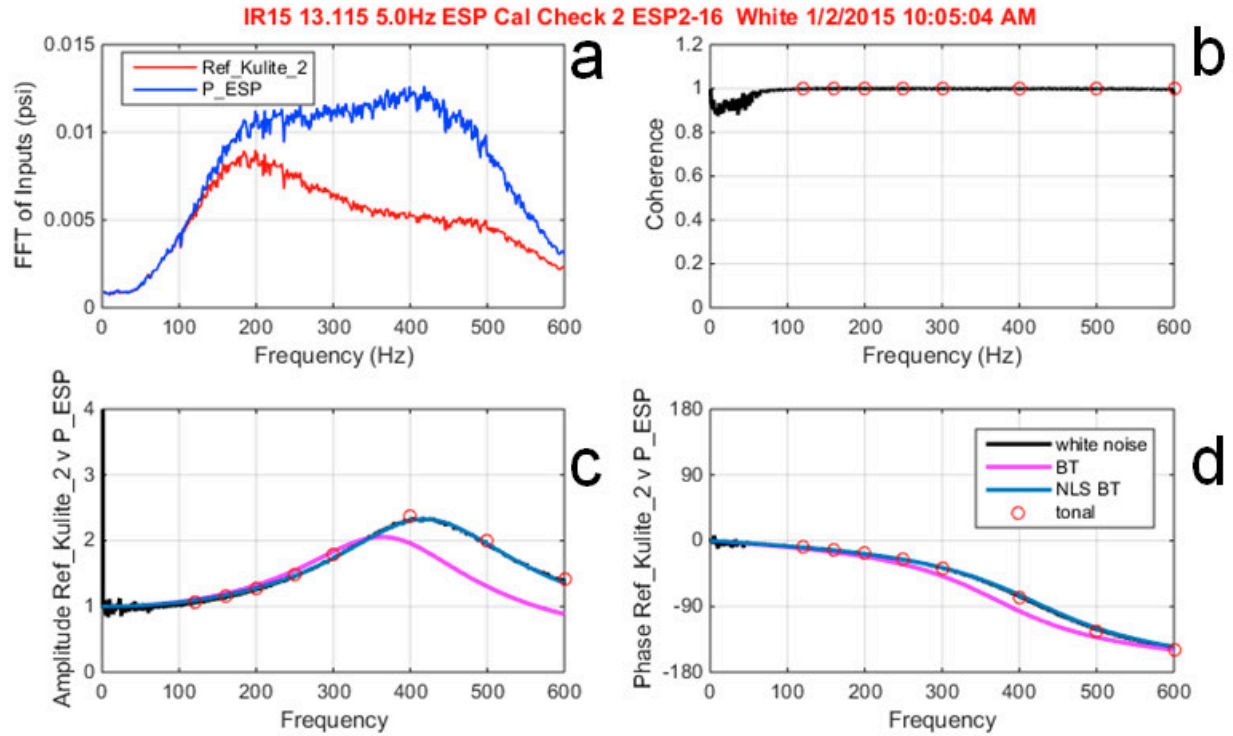


**Figure 91. Example of measured transfer function and B-T corrections using both measured tube geometry and non-linear least squares fit to the measured amplitude.**

Figure 91(c) and (d) also contain two theoretical BT transfer functions. The BT transfer function represents the pneumatics of the tap system as a series of tubes and volumes (in this case, two



tube elements and one volume element) and, through solution of a one dimensional Navier Stokes equation, relates the pressure fluctuations witnessed at the airfoil surface port to those measured at the transducer. The magenta curve uses the measured tubing lengths and inner diameters and the ESP volume. The match to the data is quite good up to 300 Hz, but the theory underpredicts the peak at 410 Hz. For straight tubes, the BT method can capture the transfer function of sensing systems very accurately. However, the model does not account for installation effects such as turns, kinks, and burrs. These effects can be included in the frequency compensation by deriving the best-fit BT geometry: effective tube lengths and diameters are determined from a non-linear least squares (NLS) fit of the measured white noise complex response. The NLS BT amplitude and phase response is shown as the blue line in Figure 91(c) and (d), respectively.

Table 9 compares the measured sensing system geometry to that derived through the regression analysis (L3 and D3 correspond to the ESP volume element). During data analysis, the NLS transfer function was applied in the frequency domain to correct the measured ESP pressures.

**Table 9. Comparison of measured and NLS fit tubing geometry for ESP2-16. Dimensions are in inches.**

	<b><i>L1</i></b>	<b><i>L2</i></b>	<b><i>L3</i></b>	<b><i>D1</i></b>	<b><i>D2</i></b>	<b><i>D3</i></b>
<b>Measured</b>	2.000	3.250	0.000	0.031	0.031	0.010
<b>NLS Fit</b>	2.000	3.330	0.000	0.024	0.036	0.010

Aside from occasional problems that arose from installation, the tube length connecting the surface tap to the pressure sensing volume has the most impact on the frequency response of the system. To reduce the required compensation and increase the inherent response capability, short tubes lengths were used when possible. Tube geometry was kept to 4 inches or less, producing resonance frequencies of 400 Hz or higher.

The exceptions to the 4-inch rule were the two leading edge surface taps at Station 4 (ESP2-9 and ESP2-10), which required at least 10 inch tubes. The frequency response and BT analysis for the white noise input for ESP2-9 are shown in Figure 92. The measured resonance frequency is 170 Hz, less than half that for the 4 inch tubes. The NLS regression fit improved the accuracy of the unsteady measurement, but for this tap was unable match the amplitude and phase response at frequencies exceeding 120 Hz.

The impact of the pneumatic system response on the unsteady pressure is small at the frequencies of interest for aerodynamic loads, even with the 10-inch tubes. Figure 93 compares the baseline raw and corrected time response of the surface pressure measured by ESP2-9 (STA4) at  $x/c=0.0096$ . The correction modifies the minimum measured pressures by no more than 0.3%. Several time-histories were examined, including high-frequency actuated cases; the overall effect of the BT correction was very small, but it was nonetheless included in the final data processing.

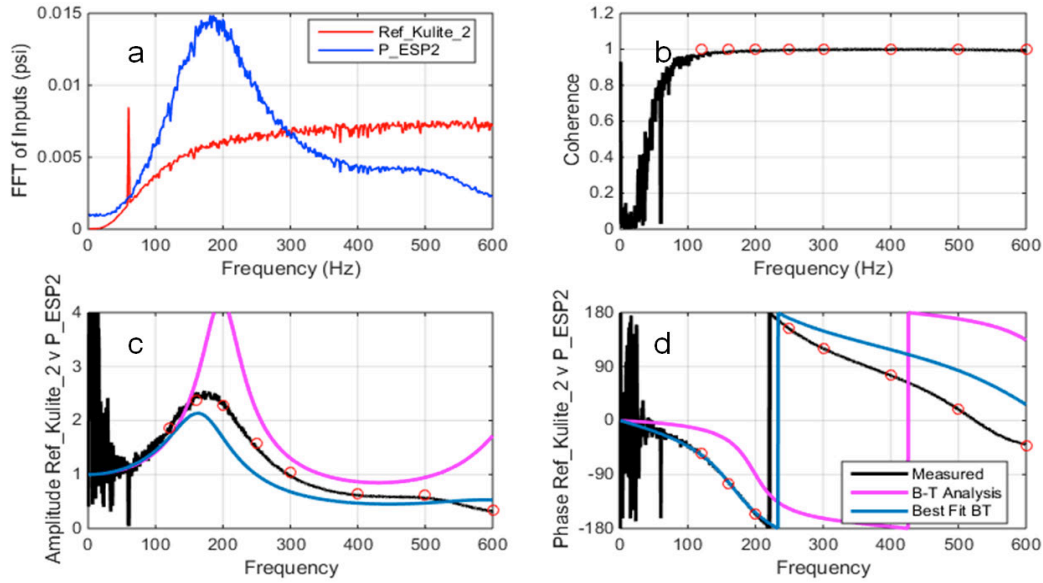


**Figure 92. ESP2-9 (STA4 LE) frequency response and BT compensation analysis.**

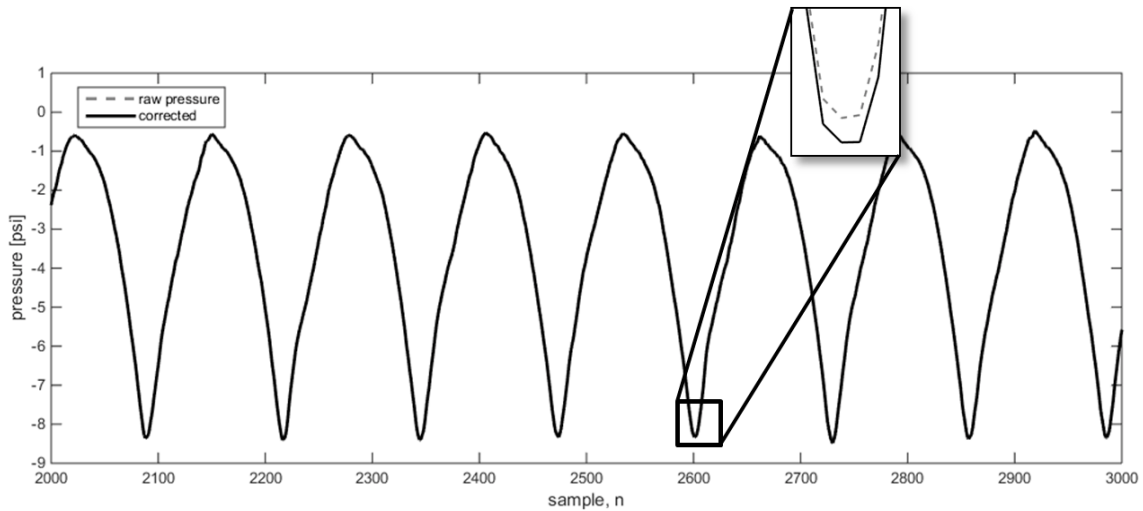


**Figure 93. Comparison of measured and corrected pressures for ESP2-9 (STA4 leading edge) at  $M=0.3$ ,  $f=8.4\text{Hz}$  for the clean VR-12.**

## 8. Unsteady Data Processing

The acquired data sets consist of sixty-four consecutive pitch cycles of data at each test point to ensure adequate ensemble averages. For steady pitch conditions, a 12.8 sec record is acquired using a virtual 5 Hz cycle. The samples are acquired at constant phase within each cycle, typically 128/cycle for each ESP pressure port and 1024/cycle for each of the Kulite and Endevco sensors. All signals are converted to engineering units and the entire time series is saved by the LabVIEW system.

MATLAB post-processing scripts compute the ensemble average over a pitch cycle and the rms variation about that average. The ensemble averages are phase-shifted to correct for lag in the hydraulic system between the command and the response so that the first displayed sample corresponds to the minimum of the 1p measured angle-of-attack. If necessary, a phase adjustment is added to re-synchronize the two ADC systems based on the one-p signal recorded on each system. This adjustment was necessitated by EMI from the COMPACT spark signal occasionally causing a false start trigger on the second ADC system.

Peak and cycle average quantities are then computed from the ensemble-averaged loads and surface pressures. The code is also capable of reprocessing the raw pressure data as well as comparing individual runs.

#### **A. Bad Tap Corrections**

Problems with various individual pressure sensors were encountered during the wind tunnel test. These problems were troubleshot when time was available but any errors carried into wind-on testing were tracked; corrections to these taps were included in the final data post processing. STA1 and STA2, due to their close proximity, were swapped with their chordwise counterpart or interpolated using measurements forward and aft in the same array. Non-functioning taps at the outboard stations were interpolated. ESP-12 at the trailing edge had a pinched hypo tube and never functioned. Only one difficulty arose with a Kulite sensor in the leading edge module during the test. The Station 1 pancake sensors worked well during the first entry, but all of the pancake sensors were generally non-functional during the second entry. Table 10 lists the run numbers where the ‘bad tap list’ was updated as well as the error producing taps. A fatigue failure in the power/signal cable to ESP1 disabled its 16 taps for Run 16, part of Run 35, and all of Run 36.

**Table 10. Tap correction list**

<b>Run</b>	<b>#Bad</b>	<b>Bad Tap List</b>
<b>Run 2-4</b>	6	E4, ESP1-12,ESP1-15,ESP2-9,ESP2-10, Kulite 14
<b>Run 5-10</b>	2	ESP1-12,E4,
<b>Run 11-17</b>	3	ESP1-12,E3,E4
<b>Run 18-24</b>	4	ESP1-12,E1,E3,E4
<b>Run 25-29</b>	3	ESP1-12,E3,E4 (E1 swapped with E3)
<b>Run 30-37</b>	3	ESP1-12,E3,E4
<b>Run 38-49</b>	5	ESP1-12,E3,E4,ESP2-9,ESP2-10 (disconnected)
<b>Run 50-51</b>	4	ESP1-12,E1,E3,E4
<b>Run 52</b>	5	ESP1-12,E1,E2,E3,E4
<b>Run 53-59</b>	7	ESP1-12,E1,E2,E3,E4, ESP1-6,Kulite5
<b>Run 60-61</b>	9	ESP1-12,E1,E2,E3,E4, ESP1-6,Kulite20,ESP2-10, ESP2-5
<b>Run 62-64</b>	7	ESP1-12,E1,E2,E3,E4, ESP1-6,ESP2-10
<b>Run 65.1-12</b>	6	ESP1-12,E1,E2,E3,E4, ESP2-10
<b>Run 65.13-75</b>	7	ESP1-12,E1,E2,E3,E4, ESP2-10,Kulite5
<b>Run 76-89</b>	7	ESP1-12,E1,E2,E3,E4, ESP2-10, ESP2-5
<b>Run 90</b>	10	ESP1-12,E1,E2,E3,E4, ESP2-10, ESP2-5,ESP1-6,ESP1-10,ESP1-11

Run	#Bad	Bad Tap List
Run 91	8	ESP1-12,E1,E2,E3,E4, ESP2-10, ESP2-5,ESP1-10

### ***B. Load Coefficients and Integration***

Only STA1 and STA2 are used for integration to determine the airfoil loads  $C_l$ ,  $C_{d,p}$ , and  $C_{m,c/4}$ . STA3 and STA4 were not outfitted with sufficient leading edge sensors. As determined from the wind tunnel test, three-dimensional effects limited the applicability of using the midspan pressure sensor array as part of STA3 and STA4 load tabulation. Two ESP taps at STA4 were passed through the wing spar and can be quantitatively compared to the sensors at the midspan's leading edge.

### ***Segmented Gaussian Quadrature***

A segmented Gaussian quadrature (SGQ) load integration routine (Ref. [42]) was developed to minimize sensor count while maintaining accurate load computation. Trapezoidal integration requires thirty or more sensors distributed over the airfoil's upper and lower surface to capture steady or unsteady sectional loads. The scheme employed during the current test program used only 16 measurement locations. Steady and unsteady two-dimensional CFD pressure distributions were extracted and used to develop the layout. The primary tap distribution was determined through minimizing the integration error of  $C_l$  and  $C_{m,c/4}$ ; the pressure drag,  $C_{d,p}$ , although important, was not the primary metric of the test and was therefore allowed to produce larger relative error. Figure 94 shows the final Station 1 pressure tap layout and a comparison of the CFD, SGQ, and trapezoidal integrated loads as well as the error between the SGQ and CFD. Note, the schematic of the VR-12 depicting internal spar and leading edge sheath are not the final configuration used during the test.

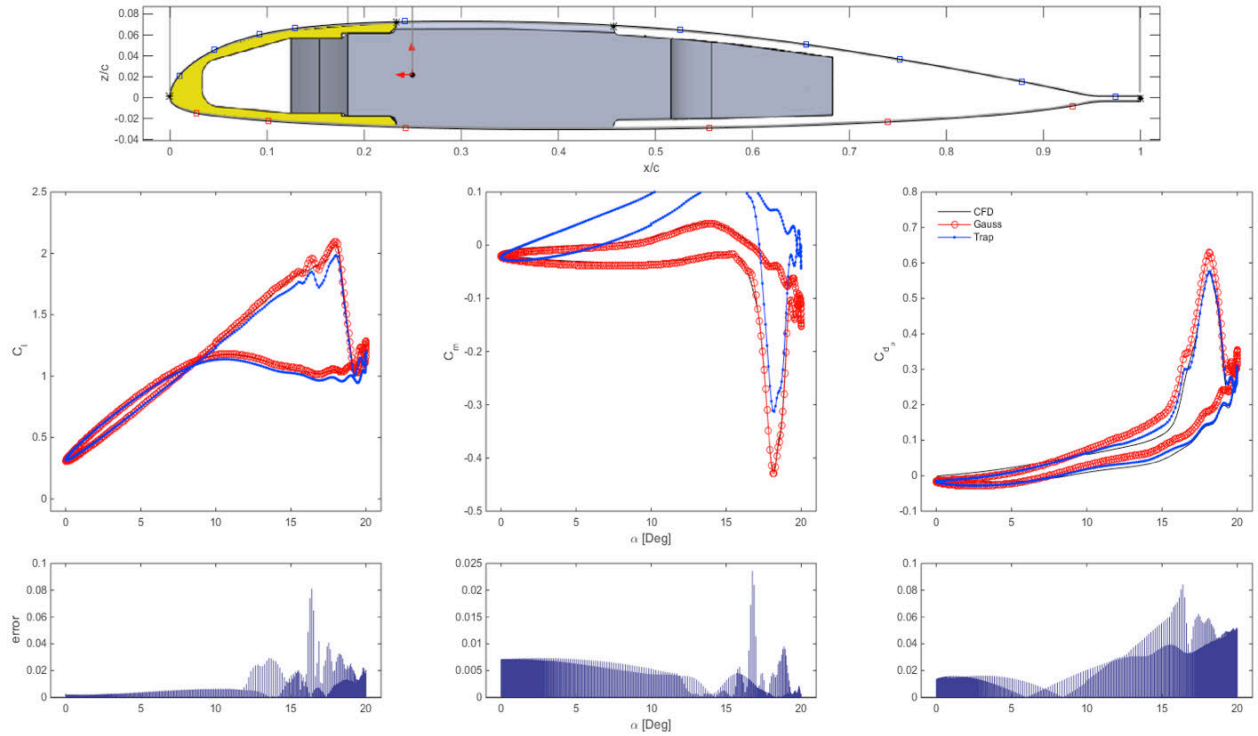


**Figure 94. VR-12 airfoil and final pressure sensor layout for Station 1 (top). Comparison of CFD, segmented Gauss quadrature, and trapezoidal integrated sectional loads (middle row). Error between segmented Gauss quadrature and CFD (bottom row).**

The individual integration weights, a combination of the Gaussian quadrature weights, the axial location of the pressure taps, and the non-pressure integrand terms are shown in Table 11 and Table 12 for stations 1 and 2, respectively. The body-axis integral quantities  $C_n$ ,  $C_{c,p}$ , and  $C_{m,le}$  are then a simple dot product of the tap  $C_p$  and the integration coefficients. The normal and chord force are then rotated to wind-axis, and the moment is translated to the quarter chord to produce  $C_l$ ,  $C_{d,p}$ , and  $C_{m,c/4}$ .

**Table 11. Center Span Station 1 Kulite integration coefficients**

Sensor Name	x/c	Surface	$C_n$	$C_{c,p}$	$C_{m,le}$
Kulite 1	0.0096	1	-0.0240	-0.0267	0.0002
Kulite 2	0.0455	1	-0.0450	-0.0205	0.0020
Kulite 3	0.0925	1	-0.0450	-0.0097	0.0042
Kulite 4	0.1284	1	-0.0240	-0.0029	0.0031
Kulite 5	0.2420	1	-0.2460	-0.0046	0.0595
Kulite 9	0.5260	1	-0.2460	0.0195	0.1294
Kulite 10	0.6557	1	-0.0644	0.0087	0.0422
Kulite 11	0.7521	1	-0.1206	0.0191	0.0907
Kulite 12	0.8779	1	-0.1206	0.0223	0.1059
E 1	0.9743	1	-0.0644	0.0000	0.0627
Kulite 6	0.0271	2	0.0640	-0.0125	-0.0017

<b>Kulite 7</b>	0.1010	2	0.0640	-0.0045	-0.0065
<b>Kulite 8</b>	0.2425	2	0.2710	-0.0071	-0.0657
<b>Kulite 13</b>	0.5555	2	0.2710	0.0048	-0.1505
<b>Kulite 14</b>	0.7397	2	0.1650	0.0071	-0.1221
<b>E 2</b>	0.9303	2	0.1650	0.0269	-0.1535

**Table 12. Center Span Station 2 ESP integration coefficients**

<b>Sensor Name</b>	<b>x/c</b>	<b>Surface</b>	<b><math>C_n</math></b>	<b><math>C_{c,p}</math></b>	<b><math>C_{m,le}</math></b>
<b>Kulite 1</b>	0.0096	1	-0.0240	-0.0267	0.0002
<b>Kulite 2</b>	0.0455	1	-0.0450	-0.0205	0.0020
<b>Kulite 3</b>	0.0925	1	-0.0450	-0.0097	0.0042
<b>Kulite 4</b>	0.1284	1	-0.0240	-0.0029	0.0031
<b>Kulite 5</b>	0.2420	1	-0.2460	-0.0046	0.0595
<b>ESP1-1</b>	0.5260	1	-0.2460	0.0195	0.1294
<b>ESP1-2</b>	0.5909	1	0.0000	0.0000	0.0000
<b>ESP1-3</b>	0.6557	1	-0.0644	0.0087	0.0422
<b>ESP1-4</b>	0.7039	1	0.0000	0.0000	0.0000
<b>ESP1-5</b>	0.7502	1	-0.1206	0.0191	0.0907
<b>ESP1-6</b>	0.8150	1	0.0000	0.0000	0.0000
<b>ESP1-10</b>	0.8779	1	-0.1206	0.0223	0.1059
<b>ESP1-11</b>	0.9261	1	0.0000	0.0000	0.0000
<b>ESP1-9</b>	0.9743	1	-0.0644	0.0000	0.0627
<b>Kulite 6</b>	0.0271	2	0.0640	-0.0125	-0.0017
<b>Kulite 7</b>	0.1010	2	0.0640	-0.0045	-0.0065
<b>Kulite 8</b>	0.2425	2	0.2710	-0.0071	-0.0657
<b>ESP1-14</b>	0.5555	2	0.2710	0.0048	-0.1505
<b>ESP1-16</b>	0.6476	2	0.0000	0.0000	0.0000
<b>ESP1-13</b>	0.7397	2	0.1650	0.0071	-0.1221
<b>ESP1-7</b>	0.8350	2	0.0000	0.0000	0.0000
<b>ESP1-12</b>	0.9303	2	0.1650	0.0269	-0.1535

### ***C. Tufts***

Tuft visualization was used extensively to qualitatively characterize the flow behavior, particularly for static configurations. Various arrays of white yarn tufts were placed all along the chord and span of the airfoil for a variety of test conditions white photographs and video were acquired. Sample photos of the tufts at two points during a steady angle-of-attack sweep are shown in Figure 95.



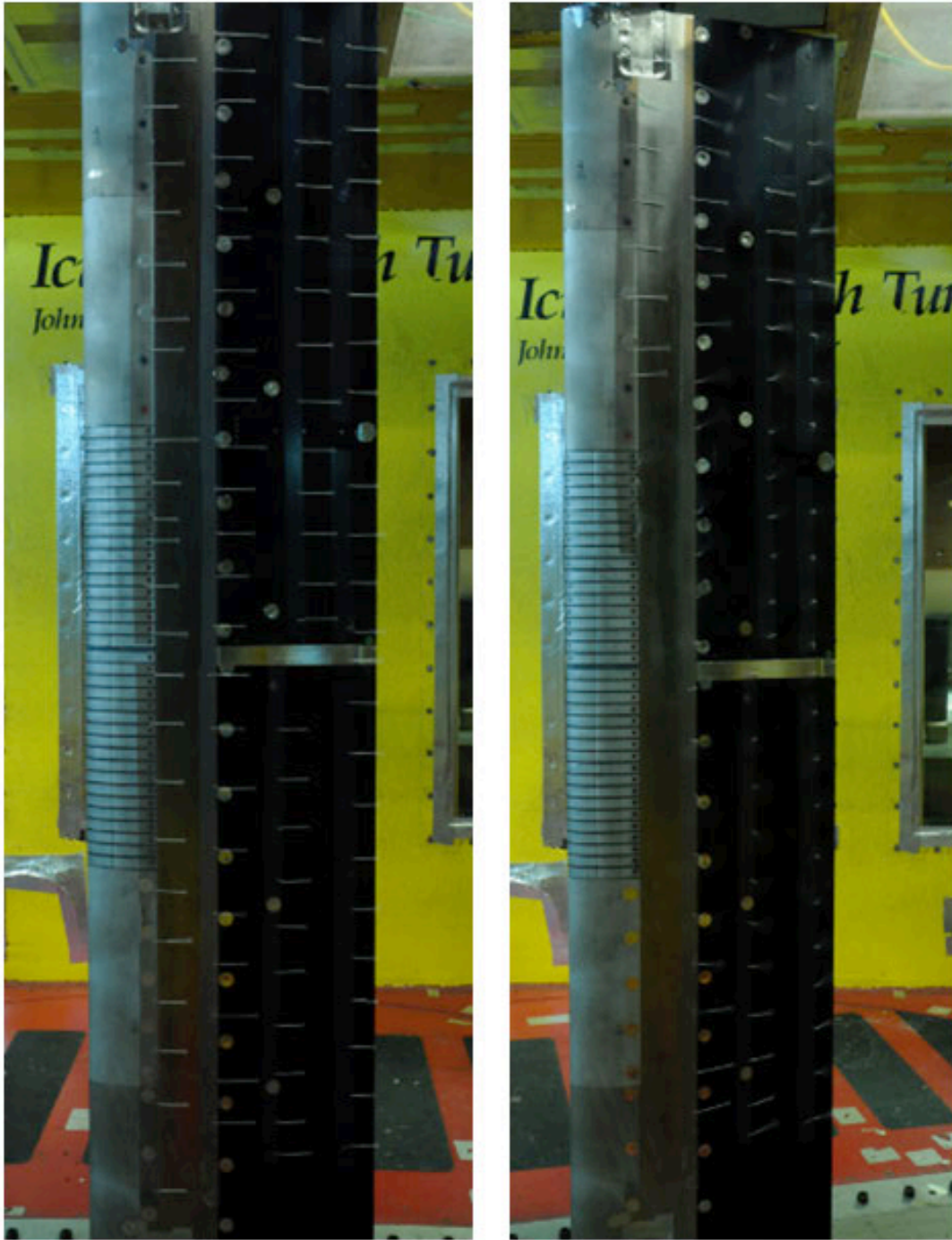


**Figure 95. Tuft visualization of attached (left) and stalled (right) flow.**

### **9. Particle-Image Velocimetry**

Particle-Image Velocimetry (PIV) is a non-invasive optical flow measurement technique used extensively by researchers in experimental fluid mechanics. The technique is simple in principle, but requires the use of (1) seed particles introduced into the flow, which will faithfully follow the flow, (2) a high-power pulsed laser and sheet-forming optics in order to illuminate

seed particles in the plane or region of interest, and (3) a high-speed camera capable of collecting image-pairs with a precise spacing in time.

A CAD-rendering of the experimental apparatus is shown in Figure 96. The region of interest is the plane perpendicular to the vertical direction near the midspan of the airfoil along the upper surface. The PIV camera will be mounted outside of the tunnel on the ceiling looking down.

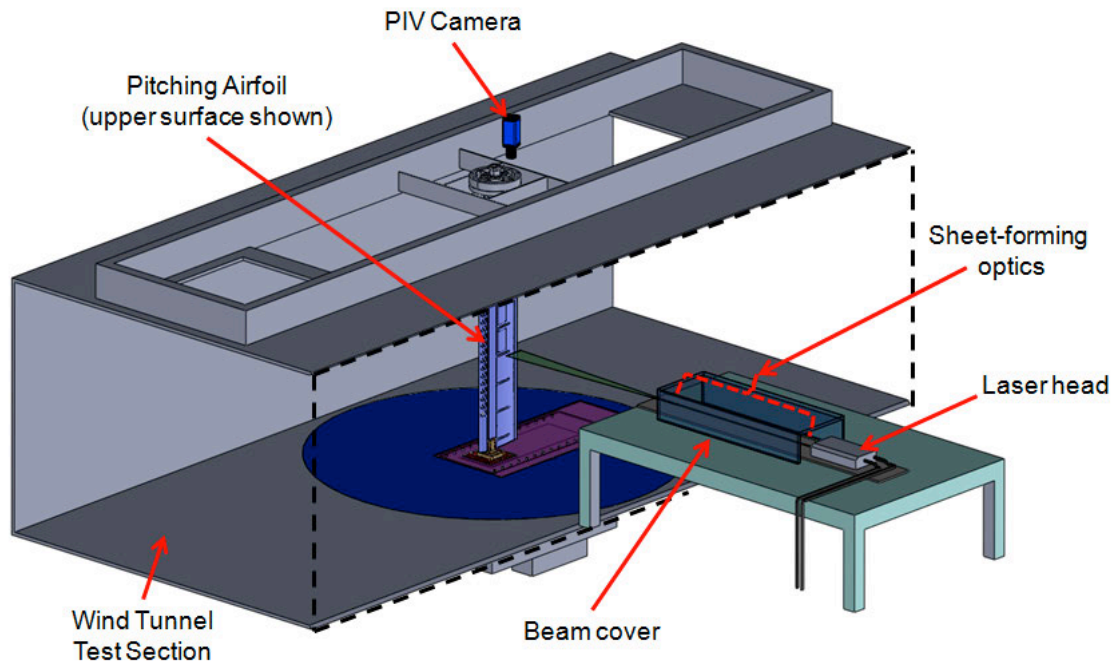


**Figure 96. CAD-rendering of the PIV experimental apparatus configured in the main control room.**

The laser head was placed on a table in the control room of the tunnel with the beam pointed towards the test section. Under the beam cover, sheet-forming optics consisting of mounted cylindrical lenses were used to expand the beam in the streamwise direction and focus the resultant sheet in the vertical direction in order to achieve a thin sheet in the region of interest. The laser sheet entered the tunnel through a small transparent window beneath the beam cover.

Details on the PIV laser are provided in Table 13 below.

**Table 13. PIV Laser specifications.**

<b>Manufacturer</b>	Quantel
<b>Model</b>	EverGreen
<b>Type</b>	Pulsed Nd:YAG, dual-head
<b>Class</b>	IV
<b>Wavelength</b>	532 nm
<b>Energy output</b>	200 mJ/head/pulse
<b>Beam shape</b>	Circular
<b>Beam diameter</b>	6.35 mm in near-field
<b>Divergence</b>	< 4 mrad
<b>Pulse width</b>	< 10 ns
<b>Repetition rate</b>	0-15Hz

To seed the flow, water droplets were generated by lowering the static temperature in the wind tunnel sufficiently close to the dew point, which created a typical condensation cloud. It had been shown in pre-tests conducted in 2014 that such particles would be adequate to obtain good PIV vectors, however, the droplets tend to be heavier than desired; therefore, their ability to faithfully follow the flow is limited in regions of high acceleration. However, the uncertainty due to the size of these particles is analyzed and discussed in Appendix 6 and shown to be small such that the PIV results do provide quantitative flow measurements and reveal details on the physical flow mechanisms associated with COMPACT and dynamic stall.

PIV data was collected for both static and pitching airfoil tests. For static airfoil tests, image-pairs were collected phase-locked with the COMPACT pulse train at all desired actuation frequencies. The signal used to initiate each COMPACT pulse provided to the PIV synchronizer. An image-pair would be collected at a user-defined delay time, typically measured in milliseconds. For pitching airfoil tests, the COMPACT pulse train was initiated via signal from the pitch-control computer in the usual fashion, and a second signal was provided to the PIV synchronizer at a user defined amount of phase delay,  $\omega t$ , from the pulse initiation signal.

Photographs of the PIV configuration in the control room and above the wind tunnel test section are provided in Figure 97 and Figure 98. A photograph of the laser sheet illuminated with a steam gun is shown in Figure 99.

All PIV measurements were executed with the direct assistance of Callum Gray of Lavision, Inc. The PIV equipment used in these tests was rented from Lavision.

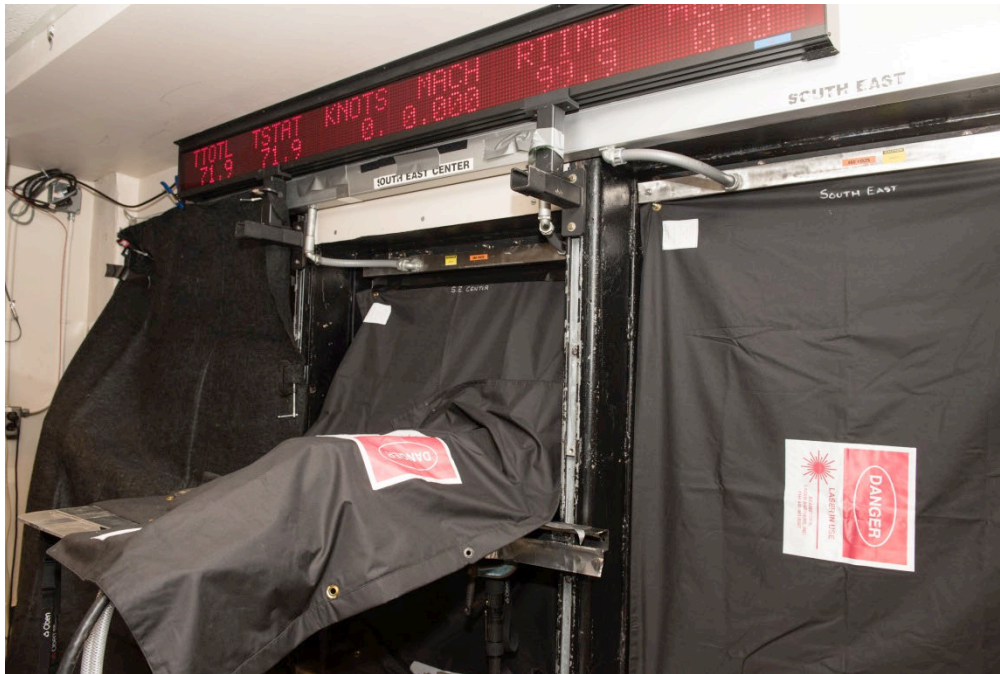


**Figure 97. PIV laser firing into the wind tunnel test section.**

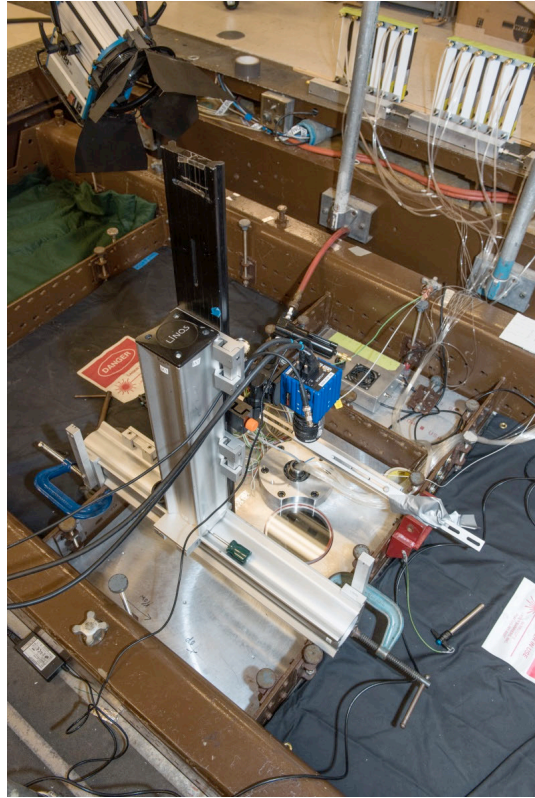


**Figure 98. PIV camera mounted above the test section looking into the tunnel at the region of interest.**



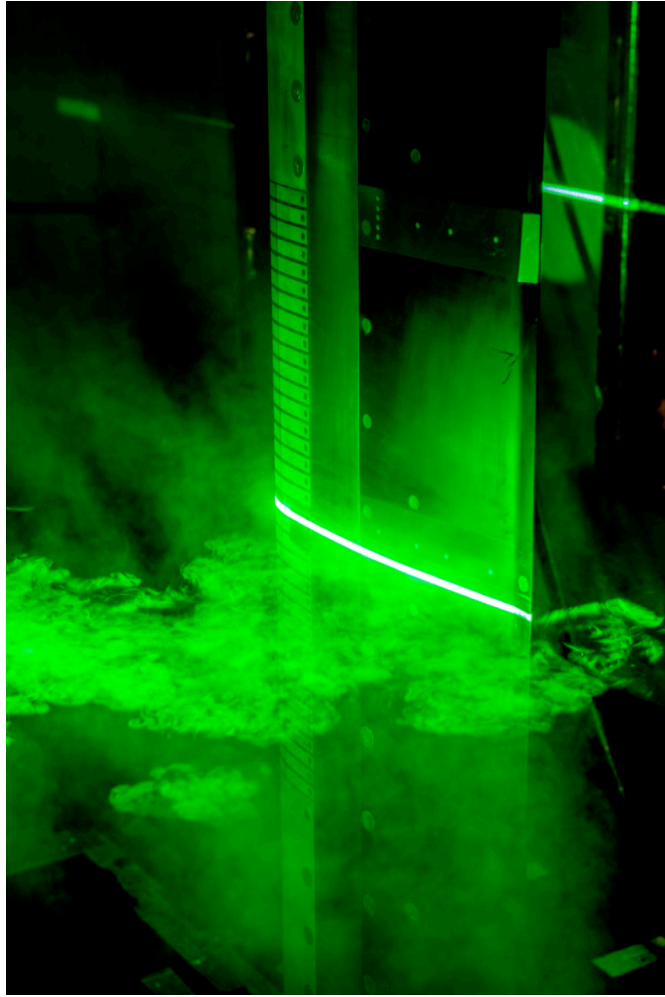


**Figure 99. PIV laser sheet illuminated via steam gun along the upper surface of the airfoil.**

## **10. NASA Glenn Icing Research Tunnel**

The following text draws heavily from [43], which provides a detailed description of the NASA Glenn Icing Research Tunnel (IRT). The IRT is a closed-loop atmospheric tunnel with a test section, which is 6 ft high, 9 ft wide, and 20 ft long. The Glenn IRT service building is a two-story structure that is connected to a balance chamber enclosing the test section by an airlock chamber and a model access door. The shop area on the first floor is available for model buildup. It has a 10.5-ft-wide by 10.67-ft-high model delivery access door located on the east side of the building. Figure 100 provides an overall schematic of the facility. Figure 101 provides breakdown various tunnel sections, and Figure 102 provides the volume of each section.

The maximum airspeed achievable in an empty IRT test section is 339 knots (390 mph). The tunnel circuit operates at or below atmospheric pressure, and the test section total-temperature range for chilled air is controlled between  $-20^{\circ}$  and  $+33^{\circ}\text{F}$ .



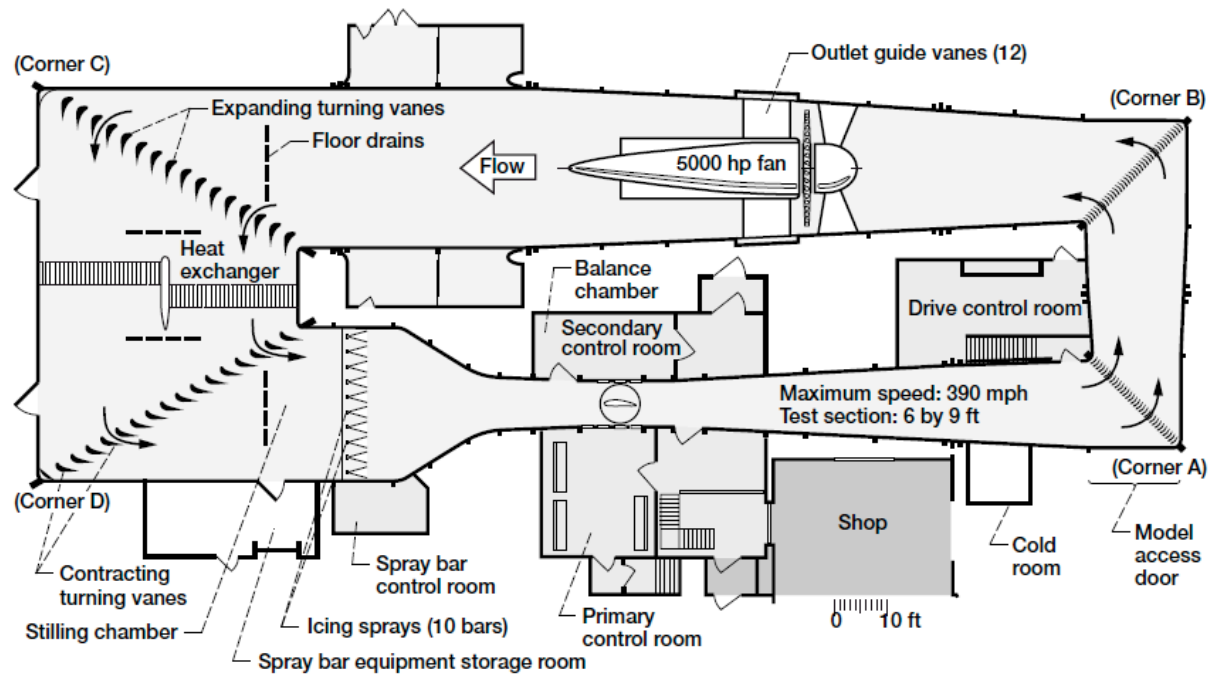


Figure 100. Figure 1 from [43], a schematic of the IRT layout.

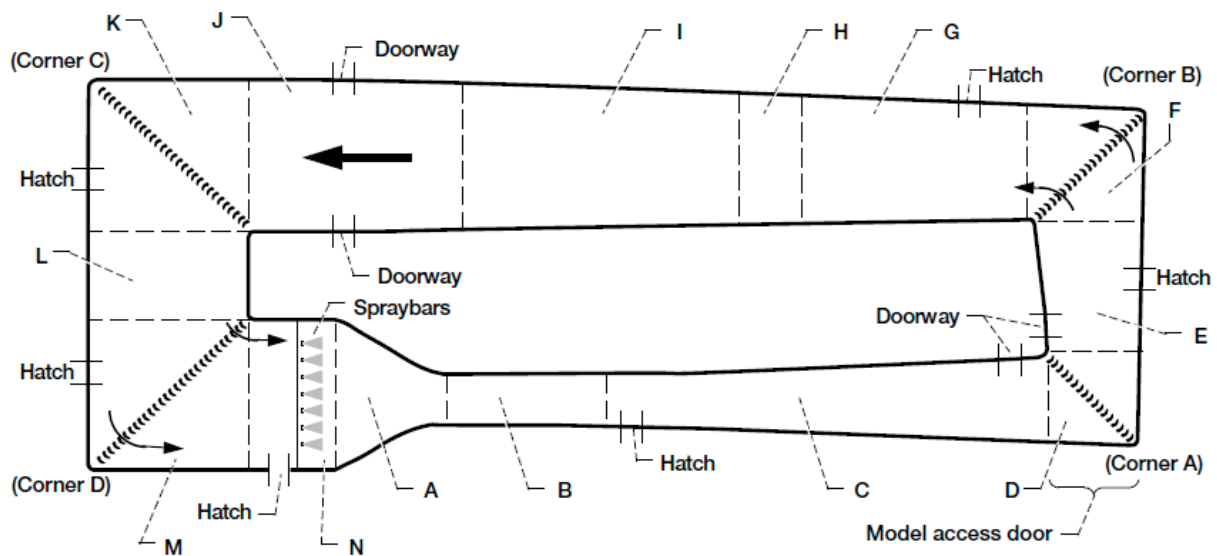


Figure 101. Figure 3 from [43], a schematic of the distinct volume sections of the IRT.

TABLE I.—ICING RESEARCH TUNNEL CIRCUIT DETAILS

Tunnel volume section <sup>a</sup>	Description	Volume, ft <sup>3</sup>
A	Front leg convergence	7 584
B	Test section	1 080
C	Front leg diffuser	11 387
D	Corner A: hollow turning vanes steam heated	4 197
E	Cross leg diffuser	6 907
F	Corner B: hollow turning vanes, steam heated	6 400
G	Back leg fan inlet diffuser and guide vanes	21 671
H	Fan housing	6 605
I	Back leg fan outlet diffuser and guide vanes	25 282
J	Back leg vent tower	32 444
K	Corner C: hollow turning vanes, unheated	39 612
L	Cross leg heat exchanger duct	19 147
M	Corner D: hollow turning vanes, unheated	39 612
N	Front leg spray bar duct	12 344
Total		234 272

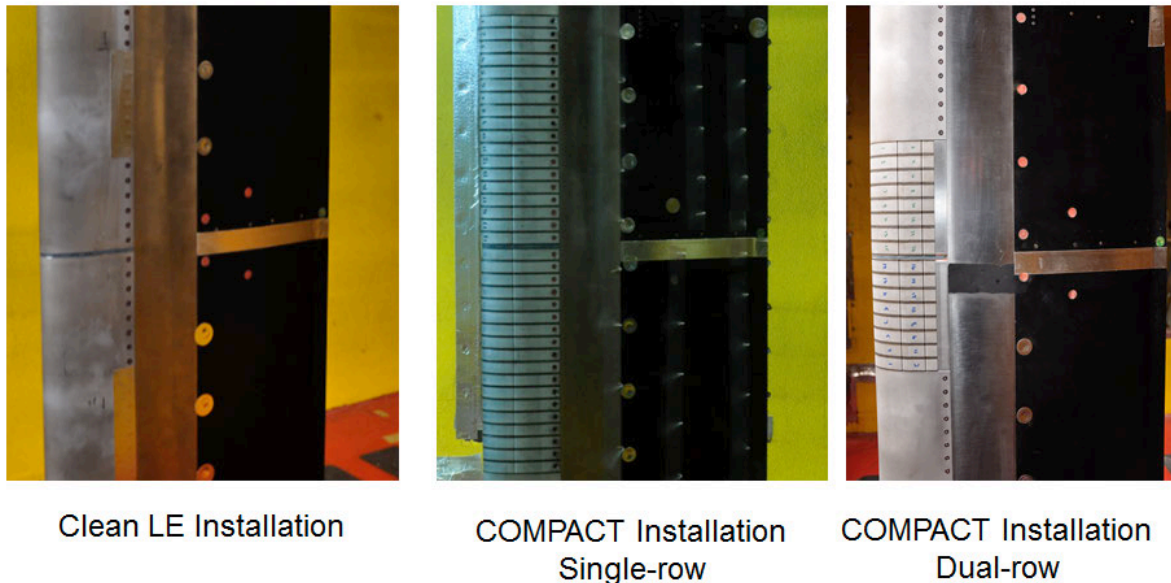
<sup>a</sup>Sections correspond to those labeled in figure 3.

Figure 102. Table 1 from [43], the volumes of each distinct section provided in Figure 101.

## XI. High-Speed Wind Tunnel Test Results

### 1. High-Speed Model Configurations

The three model configurations, baseline VR-12, single row COMPACT, and dual-row COMPACT, which were tested over the course of the two wind tunnel test entries are shown in Figure 103. The baseline has a smooth sheet metal leading edge. The single- and dual-row installations had identical internal combustion chambers. The single row maintained the leading edge contour, while the dual row required a slight modification to the VR-12 upper surface. This design change stemmed from the original slot design studied in CFD. The CFD geometry consisted of a smooth transition from the combustion chamber's exit slot to the VR-12 upper surface. The single-row geometry was manufactured with a small cusp at the interface of the slot and VR-12 surface. It is not believed that the small surface differences impact the measured results.



**Figure 103. Baseline and COMPACT test configurations. For wind-on cases, flow is left to right.**

Table 14 compares important configuration parameters associated with the configurations. Thirty-six actuators were used for the single-row configuration. The single-row actuators covered 33.1% of the wing span (22.7in. /68.5 in.). This included eighteen actuator units on both sides of the VR-12's midspan for a total of 36 unique actuators. The dual-row configuration used a total of eight COMPACT inserts on each side of the midspan, for a total of 32 slots covering 14.9% of the model's span (10.2 in./68.5 in.). Both single-row and dual-row actuators were separated with the 'vanishing-gap' actuator endplates. Fasteners were covered by clay/wax or 0.005 inch aluminum foil tape. 0.005 inch by 1 inch aluminum foil tape was used to bridge the trailing edge composite panels. Every attempt was made to smooth the small number of discontinuities present on the surface of the model.

**Table 14. Comparison of Baseline and COMPACT properties.**

Configuration	Effective Aspect Ratio	Slots	Actuated Span [%]	$x_{slot}/c$	Slot Exit Geometry
Baseline VR-12	4.6	NA		NA	NA
Single-Row COMPACT	1.5	36	33.1	0.10	Cusp
Dual-Row COMPACT	0.7	32	14.9	0.10 (Front) & 0.175 (Back)	Fillets

Table 15 specifies the operating conditions associated with the test. Test section freestream pressures and temperatures are approximate and varied between Entry 1 and Entry 2 due to atmospheric conditions and small, run-to-run variations. Similarly, actuator frequency varied as tunnel conditions shifted to maintain constant  $F^+$ . Humidity, although not called-out in Table 15, was much higher for Entry 2 (May 2015) as compared to Entry 1 (January 2015).  $C_p$  is calculated assuming a choked throat in the COMPACT slot and is based on the time-dependent measured internal pressure of the combustion chambers at Mach 0.3 (discussed later in this section, see Figure 311). Two outcomes should be noted with regard to  $C_p$  across the conditions associated with COMPACT operation:

1. Average and RMS  $C_p$  decreases with increasing freestream Mach number for fixed  $F^+$
2. Average and RMS  $C_p$  increases with increasing  $F^+$  at a fixed Mach number

**Table 15. Typical COMPACT Operating Conditions.**

	$M=0.1$	$0.2$	$0.3$	$0.4$	$0.5$
Freestream Pressure (psi)	14.4	14.13	13.67	13.03	12.29
Freestream Temperature	51.4°F	40.9°F	24.5°F	3.1°F	-21.7°F
Steady bleed $C_p$	0.0026	0.00067	0.00031	0.00018	0.00012
Peak $C_p$	0.18	0.044	0.019	0.011	0.0070
Hz at $F^+=0.2$	17.72	35.1	51.78	67.48	82.06
Avg $C_p$ , $F^+=0.2$	0.00054	0.00027	0.00018	0.00013	0.00010
RMS $C_p$ , $F^+=0.2$	0.00597	0.00209	0.00113	0.00073	0.00051
Hz at $F^+=0.4$	35.44	70.2	103.56	134.96	164.12
Avg $C_p$ , $F^+=0.4$	0.00108	0.00054	0.00035	0.00026	0.00020
RMS $C_p$ , $F^+=0.4$	0.0084	0.0030	0.0016	0.0010	0.00073
Hz at $F^+=0.6$	53.16	105.3	155.34	202.44	246.18
Avg $C_p$ , $F^+=0.6$	0.00163	0.00081	0.00053	0.00039	0.00030
RMS $C_p$ , $F^+=0.6$	0.01033	0.00364	0.00196	0.00126	0.00089
Hz at $F^+=0.8$	70.88	140.4	207.12	269.92	328.24
Avg $C_p$ , $F^+=0.8$	0.00217	0.00107	0.00070	0.00052	0.00040
RMS $C_p$ , $F^+=0.8$	0.01193	0.00420	0.00227	0.00146	0.00103
Hz at $F^+=1.0$	88.6	175.5	258.9	337.4	410.3
Avg $C_p$ , $F^+=1.0$	0.0027	0.00134	0.00088	0.00065	0.00050
RMS $C_p$ , $F^+=1.0$	0.01334	0.00469	0.00253	0.00163	0.00115

Figure 104 shows a single leading edge COMPACT module. In the collage of photos shown in Figure 105, Figure 105a shows a photograph of the actuators prior to assembly as used in the single-row installation. Figure 105b shows the lower actuator array hydrogen rotameter control bank. A similar bank was positioned on the test section ceiling. The eighteen mass flow controllers per side (floor/ceiling) set each actuator chamber's hydrogen supply through manual

adjustment. This allowed for unique control in the advent of undesired actuator characteristics; e.g., hydrogen rich mixtures could potentially result in a constant flame within the combustion chamber. The hydrogen output from the rotameters was delivered to the combustion chambers via long 6 ft lengths of Tygon tube. Two air lines were similarly supplied to each actuator chamber but were connected to a large manifold. Figure 105c shows the tube connection process during the upper COMPACT array installation. Figure 105d shows a picture of the lower VR-12 wing guide rail installed to pass the pneumatic tubing through the IRT test section's torque tube.

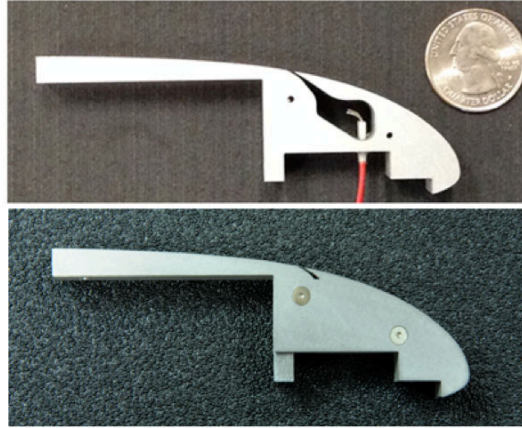


**Figure 104. Single-row COMPACT module without sidewalls (top) and with vanishing gap sidewalls (bottom).**



**Figure 105. Entry 2 COMPACT installation. (a) Final tubulation and spark connections. (b) Lower actuator array individual H<sub>2</sub> flow controllers. (c) Upper actuator array tubing. (d) Guide for passing air and hydrogen tubes through floor.**

Hydrogen gas flow was adjusted to each actuator to produce uniform spanwise actuation. Uniform operation was quasi-quantitatively established through inspection of live-feed infra-red (IR) camera imagery of the VR-12 actuated span. An example IR image is shown in Figure 106 after several seconds of actuation in quiescent conditions. The heat generated by the actuators is predominantly uniform across the span of the thirty-six COMPACT elements shown. The IR

video feed to the IRT control room allowed constant monitoring of the surface heat distribution during actuation.

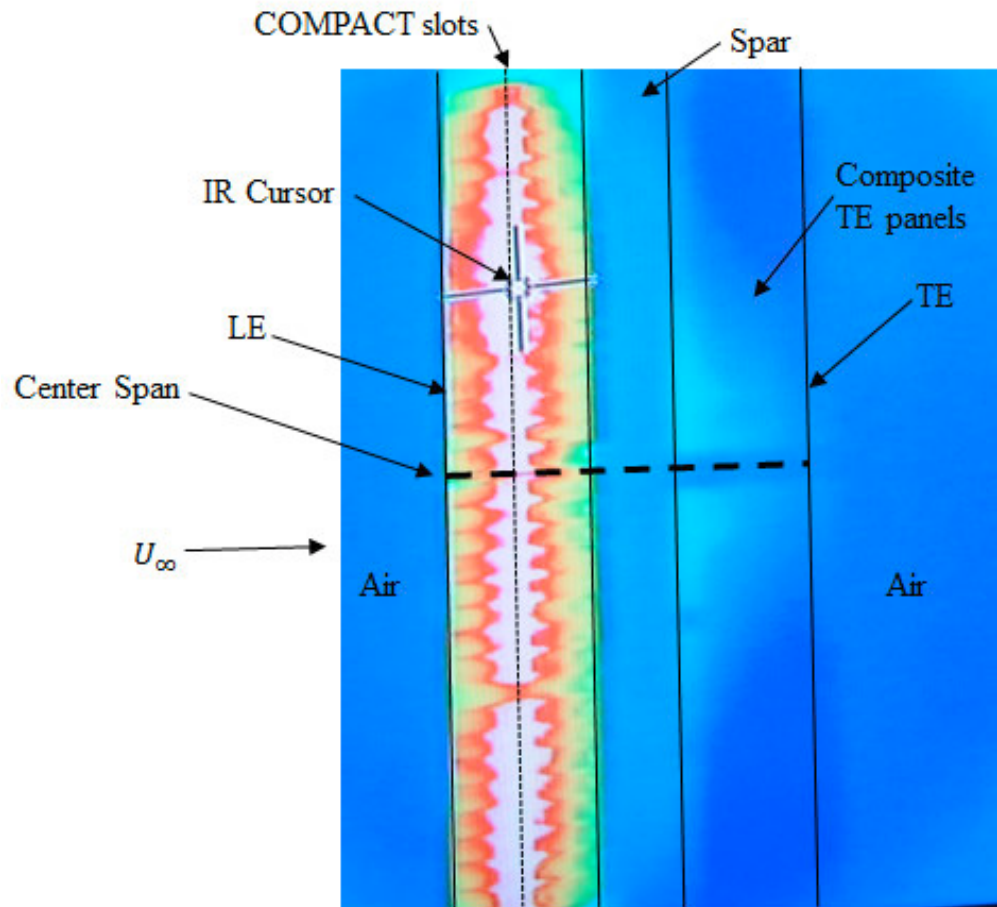


**Figure 106.** Example surface temperature distribution of single-row COMPACT installation. White indicates the hottest surfaces. The temperature distribution suggests that each individual actuator, excluding a single actuator on the lower bank, is heating uniformly.



## 2. Baseline Model High Speed Wind Tunnel Test Results

### A. Steady Baseline Results

Baseline smooth leading edge force and moment coefficient results at Mach numbers of 0.1 to 0.5 from Test Entry 1 are shown in Figure 107, as measured at the centerline ESP instrumentation array, Station 2. Table 16 identifies the acquired data sets used. The Mach 0.3 data were extended past the stall angle of  $\alpha=16.5^\circ$  to  $\alpha=30^\circ$ ; the other Mach number incidence sweeps extend to  $\alpha=20^\circ$  or less. As expected, the lift curve slope prior to stall increased as Mach number increased, and the stall angle is reduced. Compressibility also increases the positive (nose-up) pitching moment at higher angles prior to stall, as the pressure distribution becomes more weighted to the leading edge.

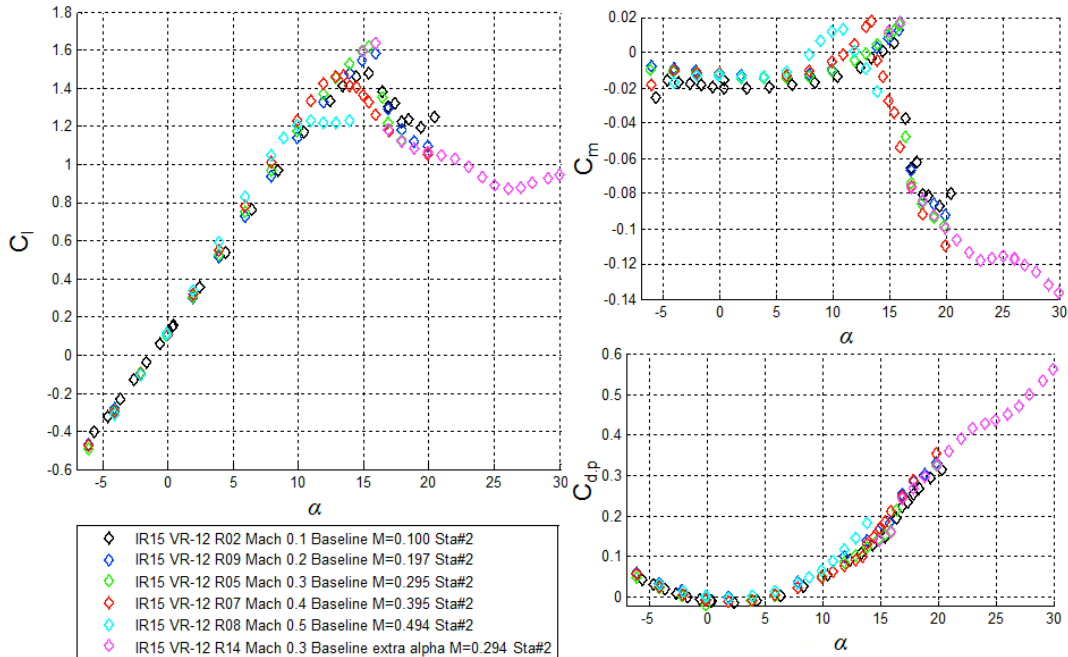


Figure 107. Lift, drag, and moment coefficients for steady baseline airfoil,  $M = 0.1$  to  $0.5$ , Station 2.

Table 16. Steady Baseline Data Sets, Entry 1.

Data Set	Name
1	R02 Mach 0.1 Baseline
2	R09 Mach 0.2 Baseline
3	R05 Mach 0.3 Baseline
4	R07 Mach 0.4 Baseline
5	R08 Mach 0.5 Baseline
6	R14 Mach 0.3 Baseline extra alpha
7	R15 Mach 0.5 Baseline extra alpha

### Pressure Distributions

Figure 109 shows pressure coefficient distributions at Mach 0.3 at angles of attack of  $-6^\circ$  to  $+20^\circ$ . The black curves are for Station 2, the most densely populated central measurement station. The distributions look quite conventional, with peak leading edge suction  $C_p$  of  $-7$  at  $\alpha=16^\circ$ , followed by a sharpening of the distribution near  $x/c=0.1$ , and then a reduction in the peak  $C_p$  as incidence increases.

While Station 2 will be used unless otherwise noted for discussing subsequent results, Figure 109 also shows pressure coefficients at the three other stations. The chordwise locations of the pressure taps and spanwise locations of all four stations are shown in Figure 108. The same set of leading edge Kulites is used for both of the central stations, while there are no leading edge taps at Station 3, and only 2 at Station 4.

The largest pressure distribution differences from Station 2 in Figure 109 are at Station 4 (the red symbols), which is closest to the upper wall. There is a 2 inch gap between the end of the airfoil and the wall, making the planform somewhat three dimensional, and likely reducing the local effective angle-of-attack. Prior to stall, Station 4 shows slightly lower leading-edge suction: At  $\alpha=15.5^\circ$  the central station suction reaches  $C_p^* = -6.8$ , close to the sonic value of  $C_p^* = -6.95$ , while Station 4 only reaches  $C_p = -6.1$ . After stall, at  $\alpha=19^\circ$ , the upper station has stronger leading-edge suction, and the trailing edge pressures are not as flat, implying that the flow near the wall may not be as deeply separated. The effective angle-of-attack reduction from 3D end effects is again the most likely explanation.

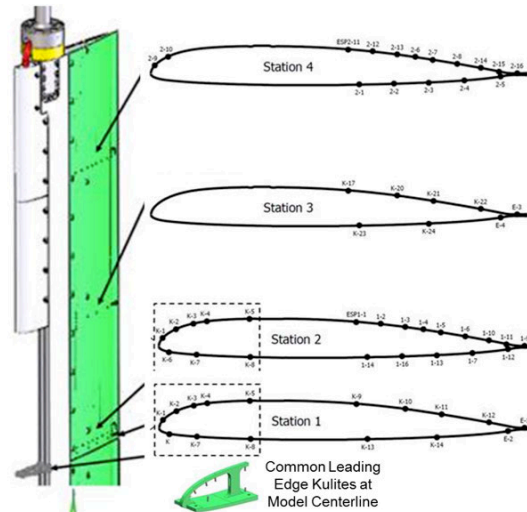


**Figure 108. Pressure sensor location key. CAD model of VR-12 without COMPACT arrays.**

Figure 110 compares the Station 2 pressures at the five Mach numbers for  $\alpha$  between  $8^\circ$  and  $20^\circ$ . The primary change is the expected early separation at  $M=0.5$ . Mach 0.2 and 0.3 are quite similar, with  $M=0.4$  showing a slightly earlier leading-edge separation, while  $M=0.1$  retains more suction at the highest angles. Appendix 3 shows the steady pressure distributions at the four remaining Mach numbers.

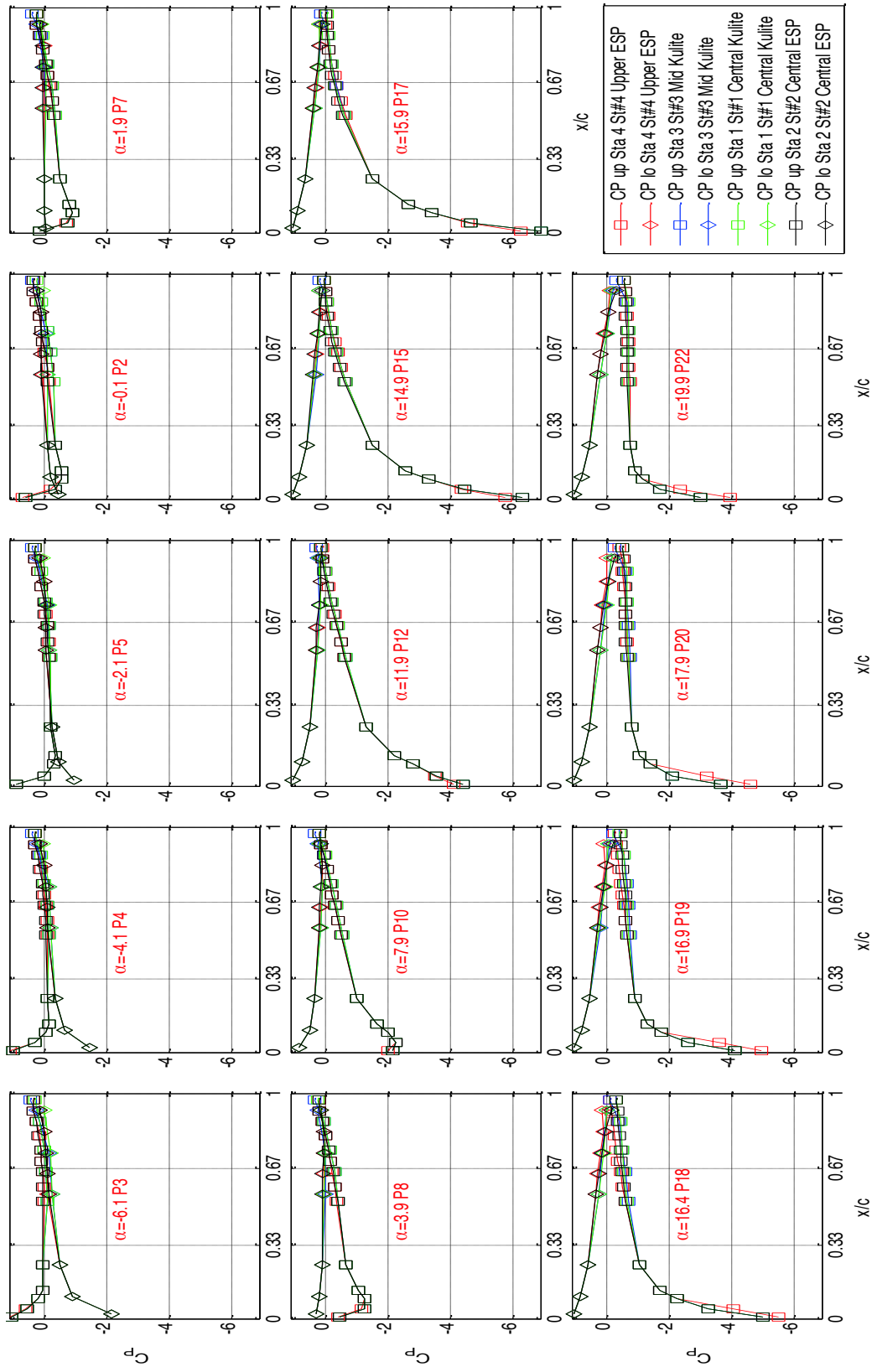


Figure 109. Pressure distributions for steady baseline airfoil at Mach 0.3, at all four stations.

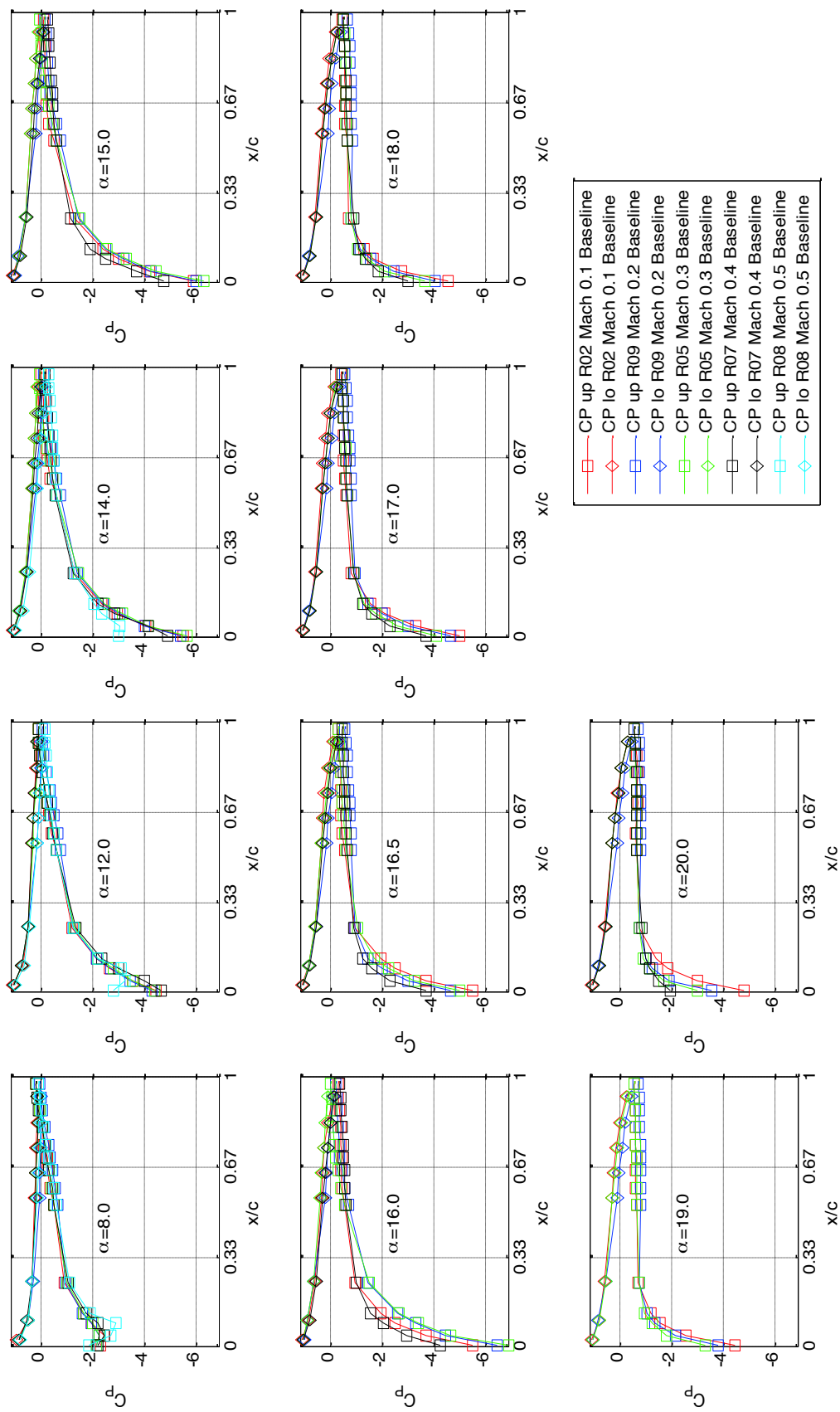
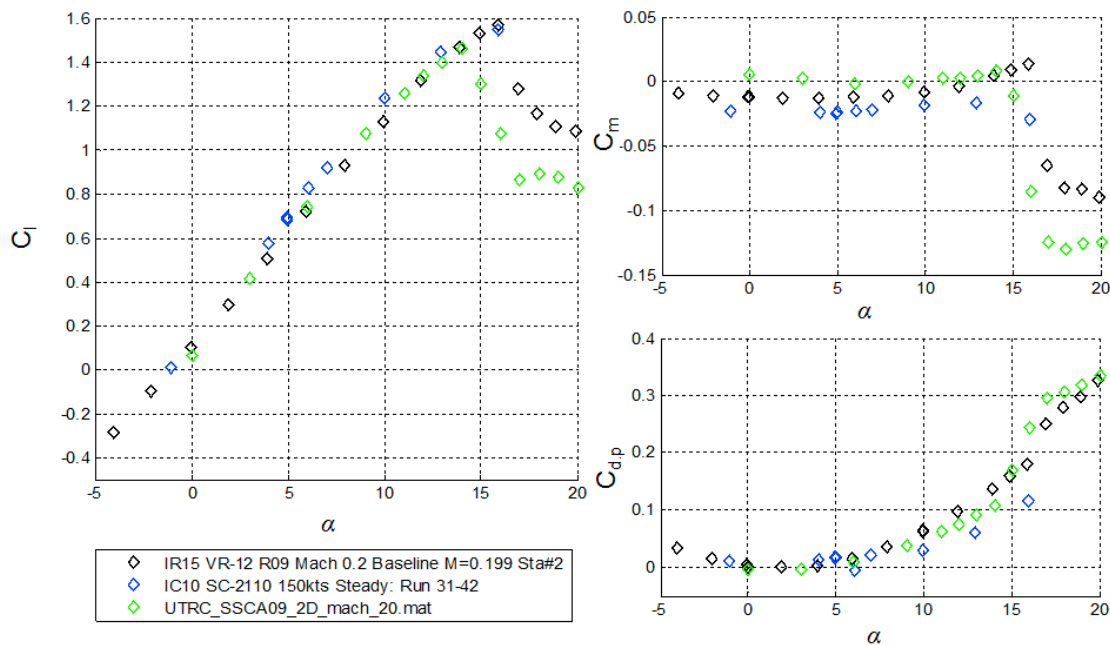


Figure 110. Pressure coefficients for steady baseline airfoil,  $M = 0.1$  to  $0.5$ , Station 2.

### Comparison with Steady Results from Other Airfoil Tests

The current baseline results can be compared with previously published results for other helicopter airfoils tested as high aspect ratio tunnel spanning blade sections. Figure 111 shows Mach 0.2 force and moment coefficients for the current test of a VR-12, for an SSC-A09 tested at UTRC in 1987 (Ref. [44] and [45]), and for an SC-2110 tested at the IRT in 2010 (Ref. [40]). The UTRC model had a chord of 17.3 in. and an aspect ratio of 5.5. This geometry compares favorably with the two IRT models, which had chords of 15 in. and aspect ratios of 4.8. Both tests were performed in unpressurized tunnels, so the Reynolds numbers at each Mach number are similar. The zero lift angles and lift curve slopes agree nicely, and the SC-2110 and VR-12 have similar values of stall angle and  $C_{l,max}$ , while the SSC-A09 stalls  $2^\circ$  earlier. This is to be expected, since the VR-12 and SC-2110 are inboard blade airfoils designed using similar methods to achieve high lift at moderate Mach number, while the SSC-A09 is a blade tip airfoil optimized to delay drag divergence at higher Mach number.



**Figure 111. Lift, drag, and moment coefficients for three steady airfoils,  $M = 0.2$ .**

Figure 112 compares the three airfoils at Mach 0.4. In this case the SC2110 stalls earlier than the VR-12. This difference seems larger than would be expected from analysis or from the results of prior tests of these same two airfoils in a different wind tunnel (not shown here). It was noted in Ref. [40] that the SC-2110 model tested in the IRT in 2010 showed larger than expected oscillations at high lift and Mach 0.4, which may have contributed to its reduced time average  $C_{l,max}$ . It is not apparent why those oscillations were not observed for the current test of the VR-12, which had the same chord, aspect ratio, and installation. Perhaps the different structural steel spar changed the natural torsional frequency of the model, or there may be an actual difference in the stall characteristics. In any case, the data for the current test of the VR-12 looks quite reasonable.

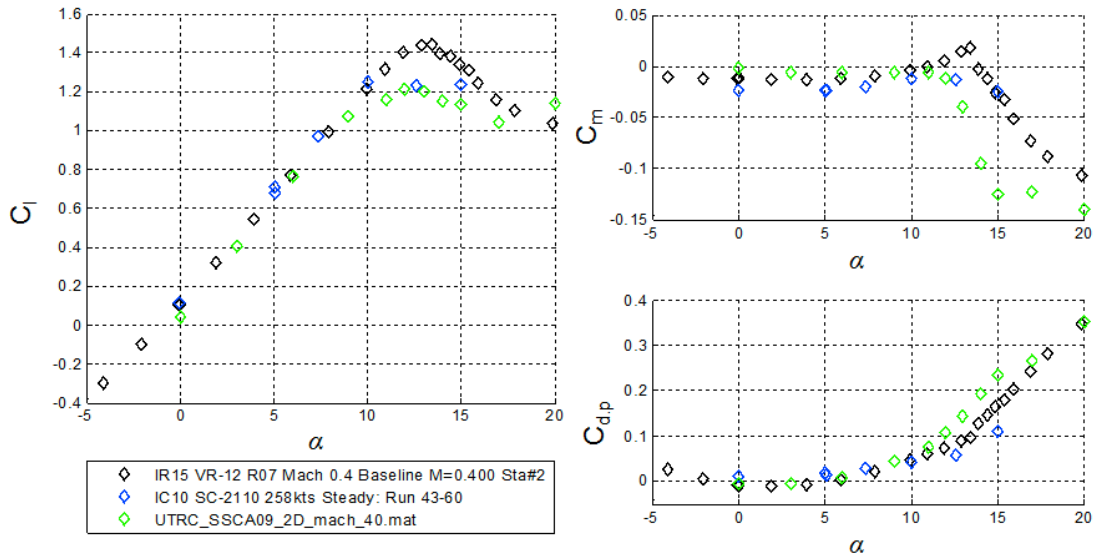


Figure 112. Lift, drag, and moment coefficients for three steady airfoils,  $M = 0.4$ .

### B. Unsteady Baseline Results

Table 17 lists the unsteady baseline data points acquired in Entry 1.

Table 17. Unsteady Baseline Data Entry 1 ( $\alpha = \alpha_0 - \alpha_1 \cos \omega t$ ;  $k = \omega c / 2U$ )

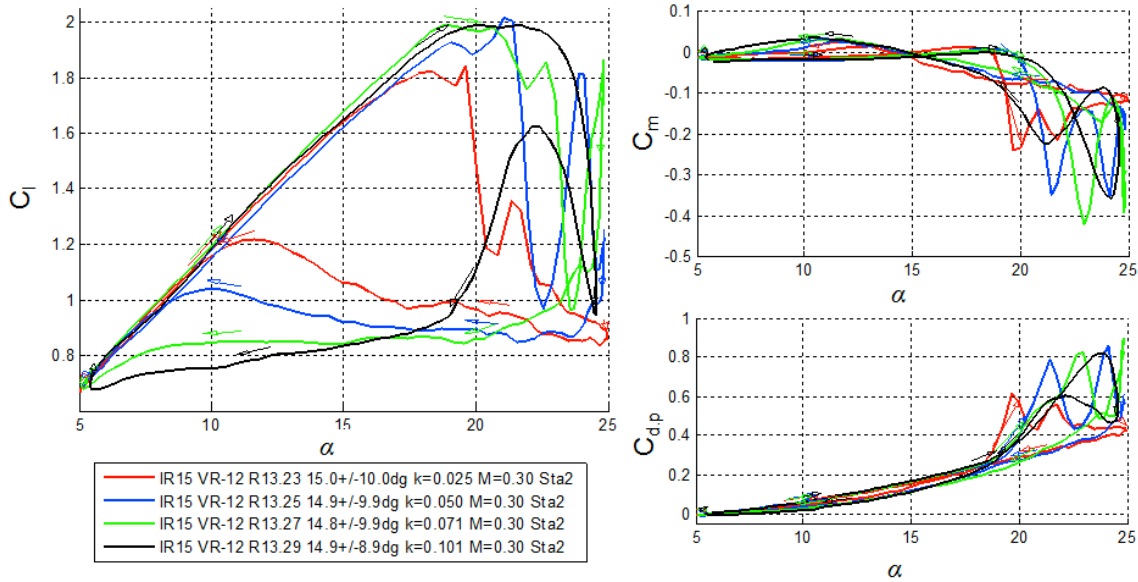
Run	Mach	$k$	$\alpha_0 [^\circ]$	$\alpha_1 [^\circ]$	Points	Notes
3	0.3	0.025	10	2,4,6	3-5	Initial Check
6	0.3	0.025, 0.05, 0.07, 0.10	8,10,15	5,8,10	2-32	Angle Trips
10	0.2	0.025, 0.050	20	6	1-3	Angle Trips
12	0.4	0.025, 0.05, 0.07	8	5,8,10	2-13	
12	0.4	0.025, 0.05, 0.07	10	5,8	15-22	
12	0.4	0.025, 0.05, 0.07	12	5,8	24-29	
13	0.3	0.05, 0.07, 0.10	8	8,10	5-10	
13	0.3	0.025, 0.05, 0.07, 0.10	10	8,10	12-19	
13	0.3	0.025, 0.05, 0.07, 0.10	15	8,10	22-29	
15	0.5	0.025, 0.05	4	5,8	5-7	
15	0.5	0.025, 0.05	6	5,8	8-12	
15	0.5	0.025, 0.05	8	5,8	13-17	
16	0.2	0.05, 0.07	10	8,10	4-8	ESP1 Fault
16	0.2	0.05, 0.07	15	8,10	11-14	ESP1 Fault

### Example of Unsteady Results at Mach 0.3

Figure 113 shows an example of the ensemble averaged lift, drag and moment coefficients at Station 2 for the baseline airfoil at Mach 0.3 and reduced frequencies  $k=0.025, 0.05, 0.07$ , and



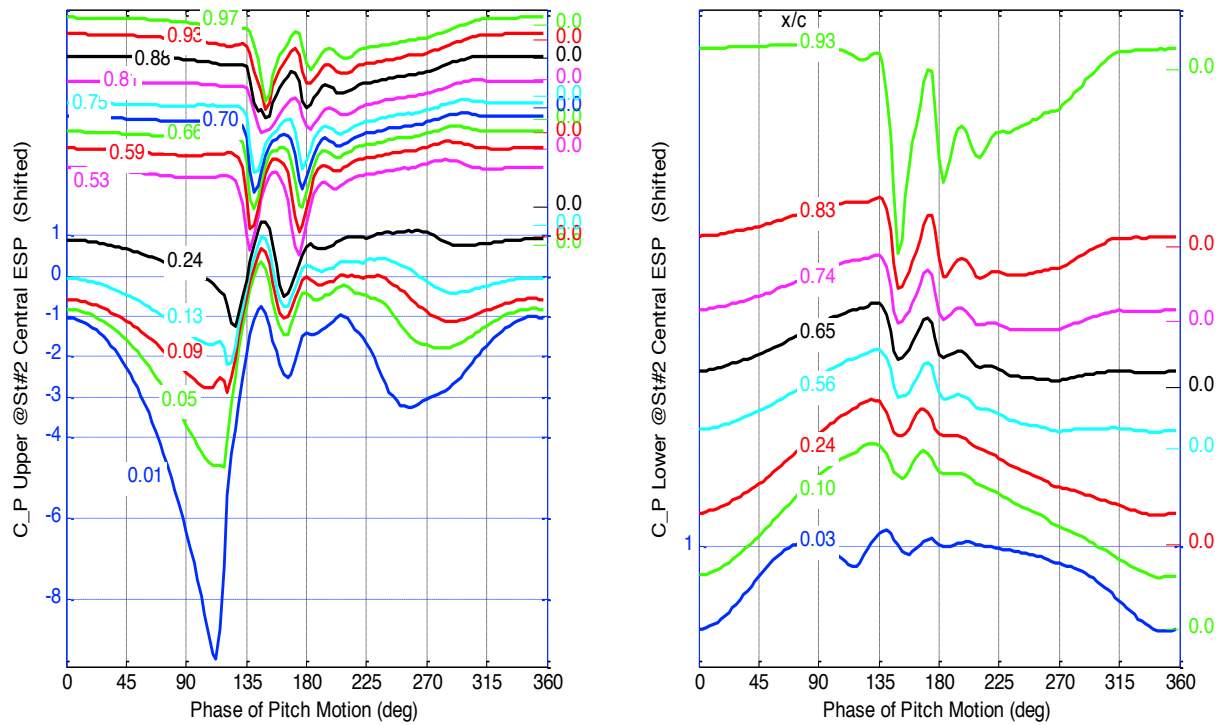
0.10, for  $\alpha=15^\circ-10^\circ\cos\omega t$ . The expected characteristics of dynamic stall (Refs. [46], [45]) are present: lift continues to increase well beyond the steady stall angle of  $16^\circ$ , and the extension in stall angle and  $C_{l,max}$  is increased with increasing  $k$ , as is the peak negative pitching moment and maximum drag. The post-stall  $C_L$  level is relatively unchanged by  $k$ , but the reattachment is delayed at higher  $k$ .



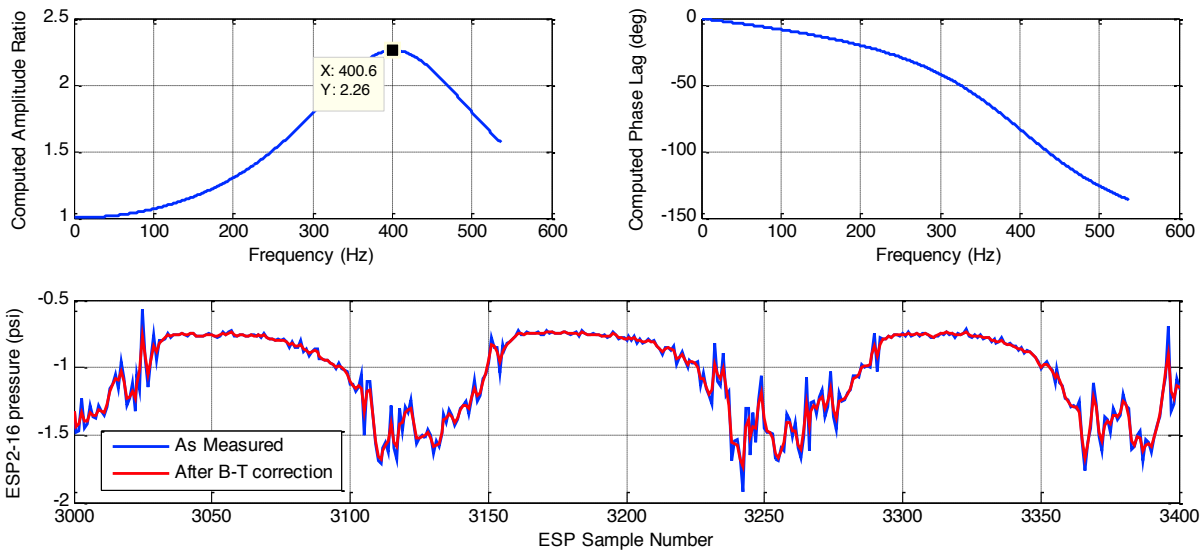
**Figure 113. Lift, drag, and moment coefficients for baseline airfoil at  $M = 0.3$ ,  $\alpha=15^\circ\pm10^\circ$ ,  $k=0.025, 0.050, 0.070$ , and  $0.100$ .**

Figure 114 shows Station 2 pressure coefficients vs. the phase of the pitch motion for  $k=0.07$ . The upper surface is on the left and the lower surface is on the right. The  $C_p$  scale on the left is for the lowest curve, the leading edge tap. The zeros along the right show the vertical offset of each successive curve. The classic features of dynamic stall can be seen: a sharp suction peak at  $\psi=40^\circ$  followed by a sharp loss of suction initiating near  $x/c=0.09$ , and the aft motion of the negative  $C_p$  valley from the primary dynamic stall vortex, which reaches the trailing edge at  $\psi=90^\circ$ . The first vortex is followed by a second, slightly weaker one. Reattachment begins near the leading edge near  $\psi=270^\circ$ . Figure 116 shows  $C_p$  vs  $x/c$  at 12 phase angles. There is a smooth increase in differential pressure, a distortion near  $x/c=0.10$  at  $\alpha=21^\circ$ , a massive separation at  $\alpha=23^\circ$ , and then reattachment at  $\alpha=20^\circ$  on the downstroke.

An example of the effect of the Bergh-Tijdeman (BT) correction (described in the previous section) on the measured ESP pressures at this test condition is shown in Figure 115. For this particular sensor located near the trailing edge at station 4, the tubing length is somewhat longer than average, so that the maximum amplitude ratio shown in the upper left plot of  $\sim 2.25$  at 400 Hz is greater than for the typical port. The lower plot shows the un-averaged pressure data over approximately three cycles of motion (there are 128 samples per cycle). The correction has a small effect on the lower frequency content but does reduce the magnitude of the high frequency content from that seen in the un-averaged signal.



**Figure 114. Pressure coefficients vs. phase for baseline at  $M = 0.3$ ,  $\alpha = 15^\circ \pm 10^\circ$ ,  $k = 0.070$ .**



**Figure 115. Example of Effect of B-T correction on an ESP port with a longer than average tube.**

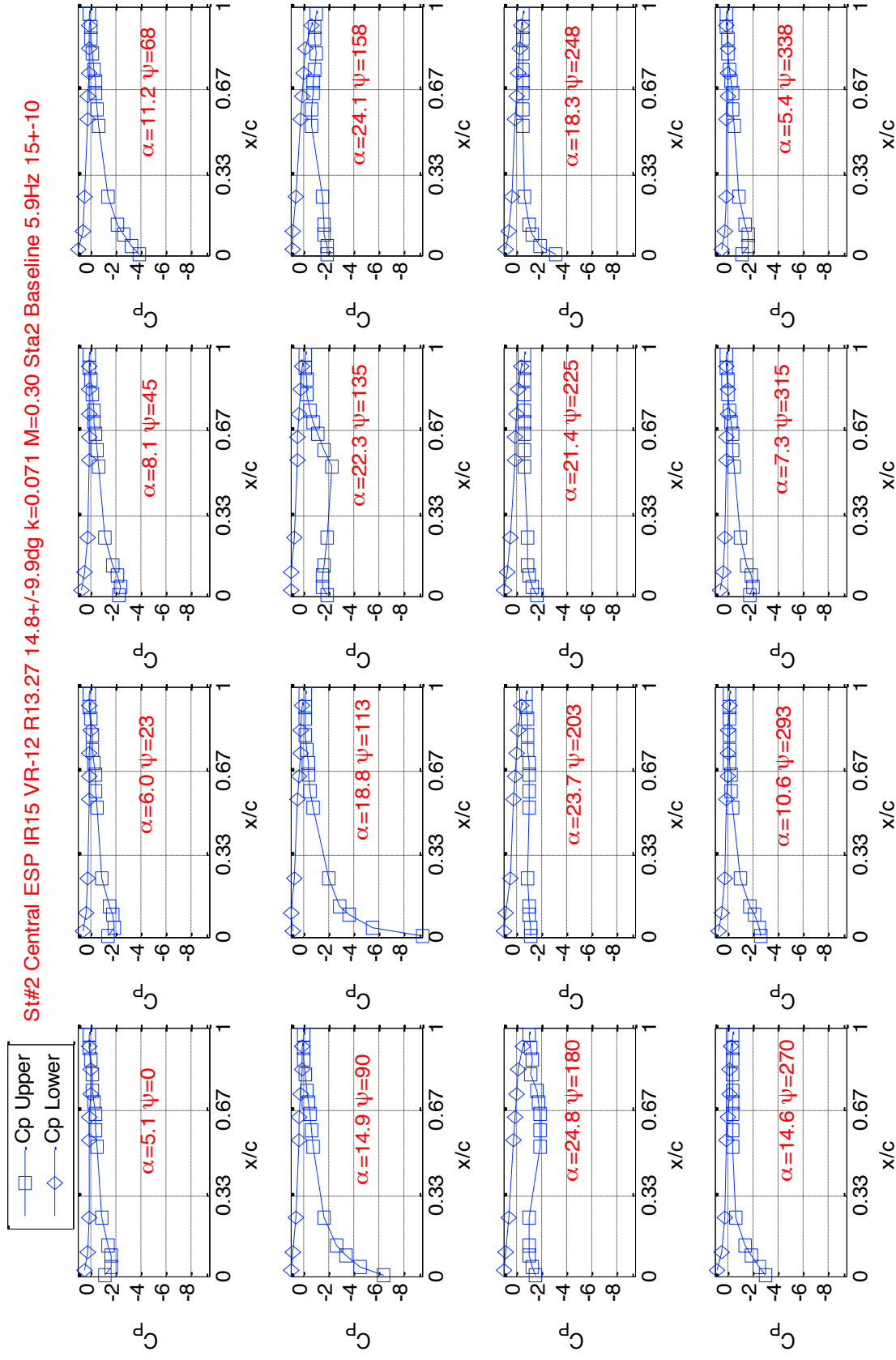


Figure 116. Pressure coefficients vs.  $x/c$  for baseline at  $M = 0.3$ ,  $\alpha = 15^\circ \pm 10^\circ$ ,  $k = 0.070$ .

### ***Unsteady Baseline Data Set***

The complete set of baseline unsteady results is shown in Appendix 3. This section discusses some of the key characteristics.

#### ***M=0.2***

Figure 117 shows the baseline lift coefficient traces with respect to angle-of-attack for a Mach of 0.2 at two reduced frequencies and five angular motions. The left-most cases at  $\alpha = 8^\circ \pm 8^\circ$  was unstalled. Increasing the peak  $\alpha$  beyond  $16.5^\circ$  (the steady stall angle for  $M = 0.2$ ), generated substantially larger lift and moment hysteresis for both  $k=0.07$  and  $0.10$ . For  $k=0.07$ , the pitching moment breaks at roughly  $20^\circ$ . Subsequently, the stall vortex sheds on the upstroke near maximum angle causing the large nose-down moment measured for  $\alpha = 15^\circ \pm 10^\circ$ . For  $k=0.1$ , the VR-12's pitching moment (Appendix 3) breaks much later in the airfoil's forced motion, near  $\alpha = 23^\circ$ . As a result, the dynamic stall vortex's influence is still experienced by the airfoil over the first few degrees of the downstroke. This leads to the lift recovery witnessed from the airfoil's peak angle down to  $20^\circ$  for the  $\alpha = 15^\circ \pm 8^\circ$  and  $\alpha = 15^\circ \pm 10^\circ$  trajectories.

#### ***M=0.3***

Figure 118 plots the lift at  $M = 0.3$  for the lowest reduced frequency tested,  $k=0.025$ . For this frequency, four motions were studied. Each pitching motion resulted in significant separation, lift hysteresis, and large, nose-down pitching moments. For  $\alpha = 10^\circ \pm 8^\circ$ , the peak unsteady angle exceeds the steady stall angle-of-attack by only  $2^\circ$ , causing the light dynamic stall behavior shown. Further increases in mean angle or amplitude resulted in a stronger adverse pitching moment, increased lift deficit, and the production of a third sub-loop in the pitching moment trace. The maximum lift also increased, displaying a rapid increase in  $C_l$  before degrading as the stall vortex convects into the airfoil's wake. Additional shedding led to secondary lift, drag, and moment peaks seen past lift stall for  $\alpha = 15^\circ \pm 8^\circ$  and  $\alpha = 15^\circ \pm 10^\circ$ .

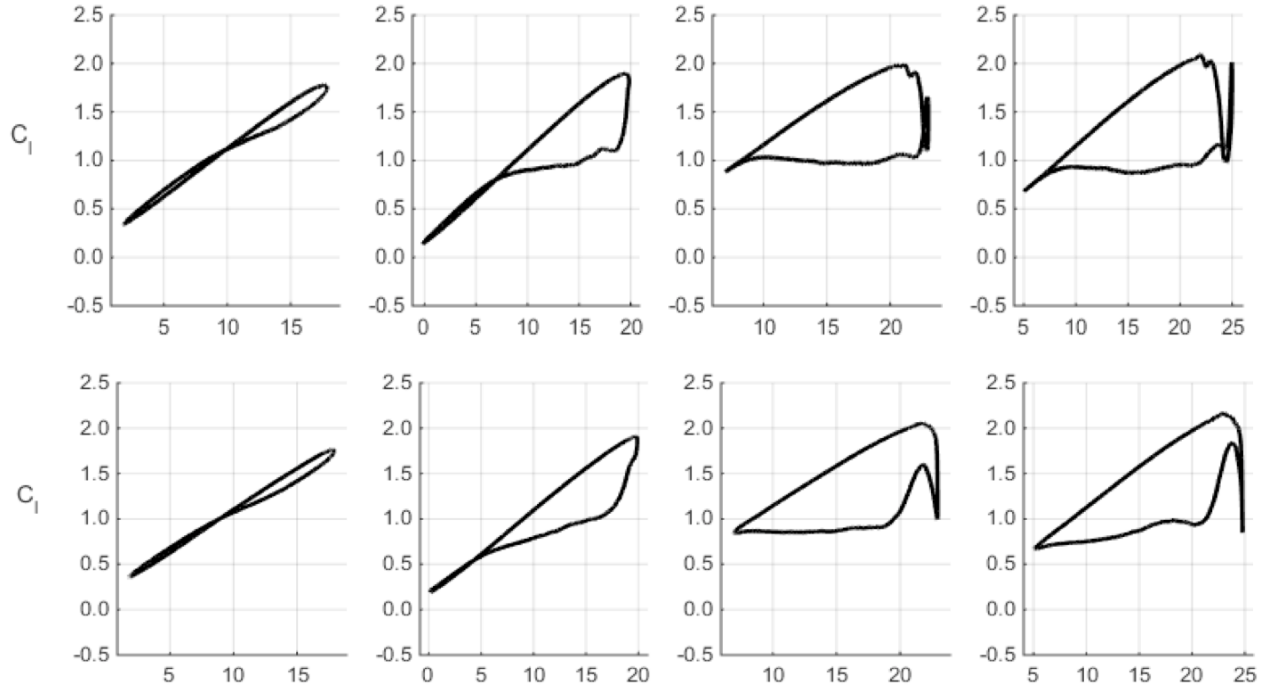


**Figure 117. Mach 0.2 baseline unsteady lift for  $k=0.07$  (top) and  $0.10$  (bottom). From left to right:  $\alpha = 10^\circ \pm 8^\circ$ ,  $\alpha = 10^\circ \pm 10^\circ$ ,  $\alpha = 15^\circ \pm 8^\circ$ ,  $\alpha = 15^\circ \pm 10^\circ$ .**

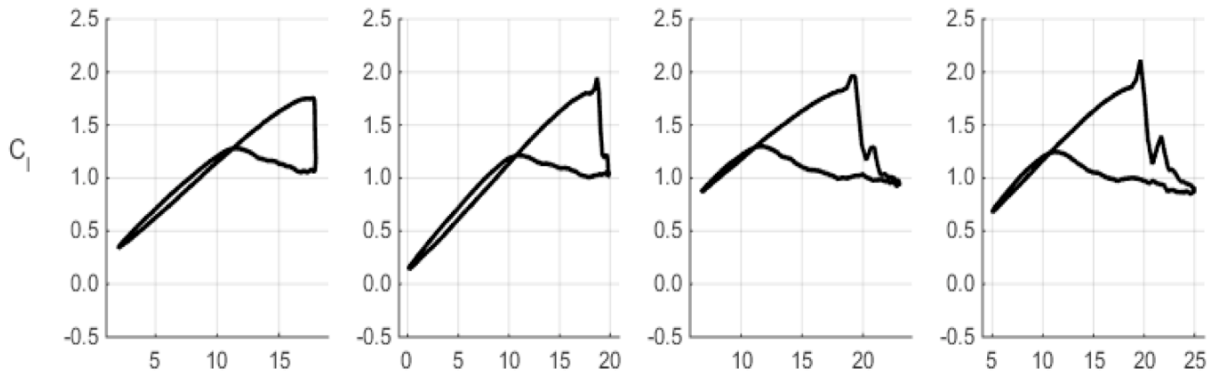


**Figure 118. Mach 0.3 baseline unsteady lift for  $k=0.07$ . From left to right:  $\alpha = 10^\circ \pm 8^\circ$ ,  $\alpha = 10^\circ \pm 10^\circ$ ,  $\alpha = 15^\circ \pm 8^\circ$ ,  $\alpha = 15^\circ \pm 10^\circ$ .**

The baseline  $M=0.3$  airfoil dataset also includes  $k=0.05$ ,  $0.07$ , and  $0.10$ . Figure 119 shows the lift at  $k=0.10$ . Overall, increasing the reduced frequency from  $0.025$  to  $0.05$  and then to  $0.07$  for each angle range delayed pitching moment and lift stall on the upstroke and delayed reattachment on the downstroke. Increasing from  $k=0.07$  to  $0.1$  significantly reduced the severity of the measured stall traits; i.e., the stall attributes shifted from light to no stall or deep to light stall. The long period of stall past  $18^\circ$  found for  $k=0.07$  is replaced by further increases in lift for  $\alpha=15^\circ \pm 8^\circ$  and  $\alpha=15^\circ \pm 10^\circ$ . As was seen in the  $M=0.2$ ,  $k=0.10$ ,  $\alpha_0 = 15^\circ$  results, the stall vortex's presence has a significant impact on the downstroke of the airfoil's motion, causing the lift and moment fluctuations recorded for  $\alpha = 15^\circ \pm 8^\circ$  and  $\alpha = 15^\circ \pm 10^\circ$ . The full set of loads are in Appendix 3.

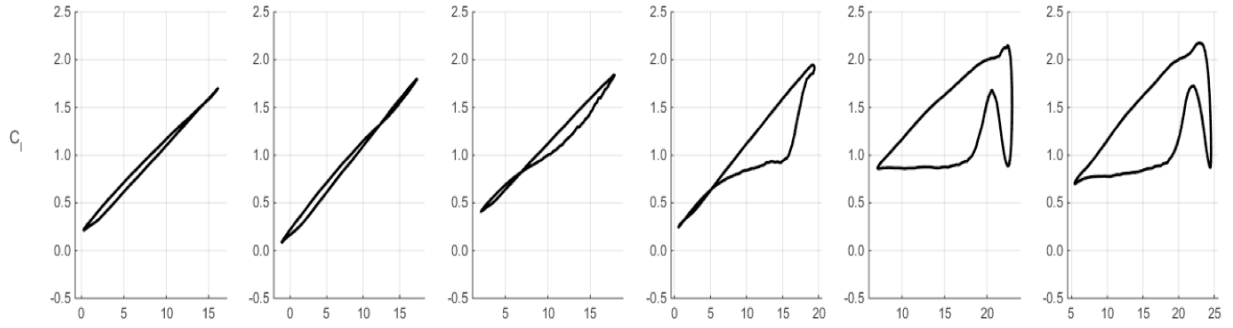


**Figure 119. Mach 0.3 baseline unsteady lift for  $k=0.10$ . From left to right:  $\alpha=8^\circ \pm 8^\circ$ ,  $\alpha=8^\circ \pm 10^\circ$ ,  $\alpha=10^\circ \pm 8^\circ$ ,  $\alpha=10^\circ \pm 10^\circ$ ,  $\alpha=15^\circ \pm 8^\circ$ ,  $\alpha=15^\circ \pm 10^\circ$ .**

#### ***M=0.4***

The Mach 0.4 test cases include  $k=0.025$ , 0.05, and 0.07. Eight unique pitching motions were investigated for  $k=0.025$  (Figure 120) and 0.05, while six cases were studied at  $k=0.07$  (Figure 121). A reduced frequency of 0.1 at  $M=0.4$  could not be attained as it exceeded the oscillation rig max attainable frequency of 9 Hz. Generally, the large lift coefficients, peak drag, and peak negative moment measured at  $M=0.2$  and 0.3 are decreased due to the onset of more significant compressibility effects limiting the growth of the leading-edge suction peak, strength of the dynamic stall vortex and its impact on the midspan loads as it convects over the upper airfoil surface.



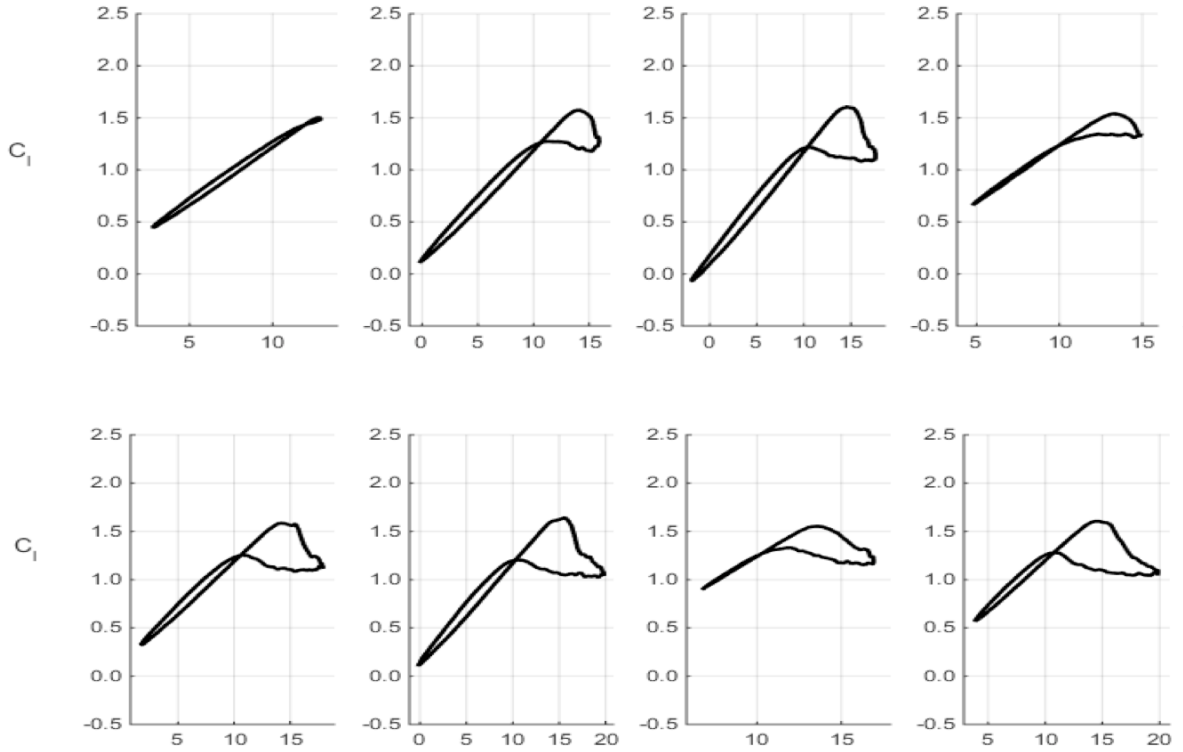


**Figure 120. Mach 0.4 baseline unsteady lift for  $k=0.025$ . From left to right: (top)  $\alpha=8^\circ \pm 5^\circ$ ,  $\alpha=8^\circ \pm 8^\circ$ ,  $\alpha=10^\circ \pm 10^\circ$ ,  $\alpha=10^\circ \pm 5^\circ$ , (bottom)  $\alpha=10^\circ \pm 8^\circ$ ,  $\alpha=10^\circ \pm 10^\circ$ ,  $\alpha=12^\circ \pm 5^\circ$ ,  $\alpha=12^\circ \pm 8^\circ$ .**

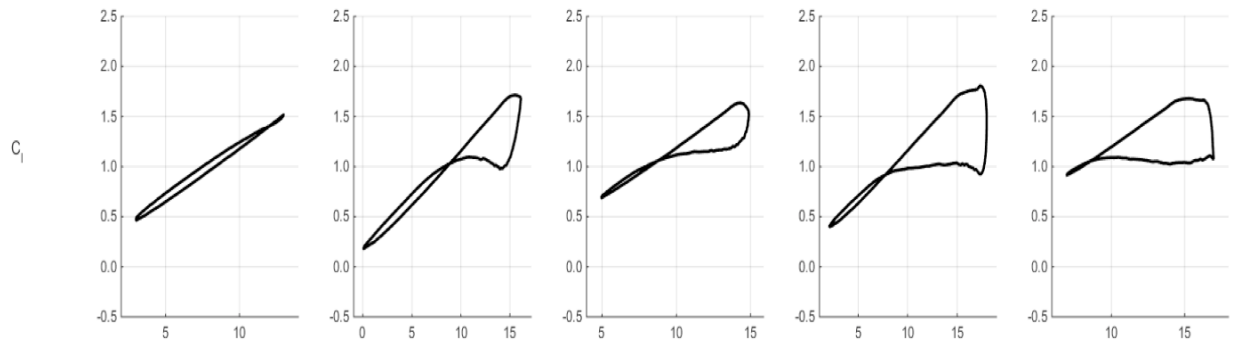


**Figure 121. Mach 0.4 baseline unsteady lift for  $k=0.07$ . From left to right:  $\alpha=8^\circ \pm 5^\circ$ ,  $\alpha=8^\circ \pm 8^\circ$ ,  $\alpha=10^\circ \pm 5^\circ$ ,  $\alpha=10^\circ \pm 8^\circ$ ,  $\alpha=12^\circ \pm 5^\circ$ .**

#### **$M=0.5$**

Reduced frequencies of  $k=0.025$  and  $0.05$  were tested at Mach  $0.5$ . Figure 122 shows  $k=0.05$ . Here, shock induced flow separation on the VR-12's upper surface further curtails the development of the leading-edge suction peak, weakening all subsequent vortex interactions. Increasing reduced frequency caused the usual separation and reattachment delays with respect to angle-of-attack as well as slightly augmented load peaks.

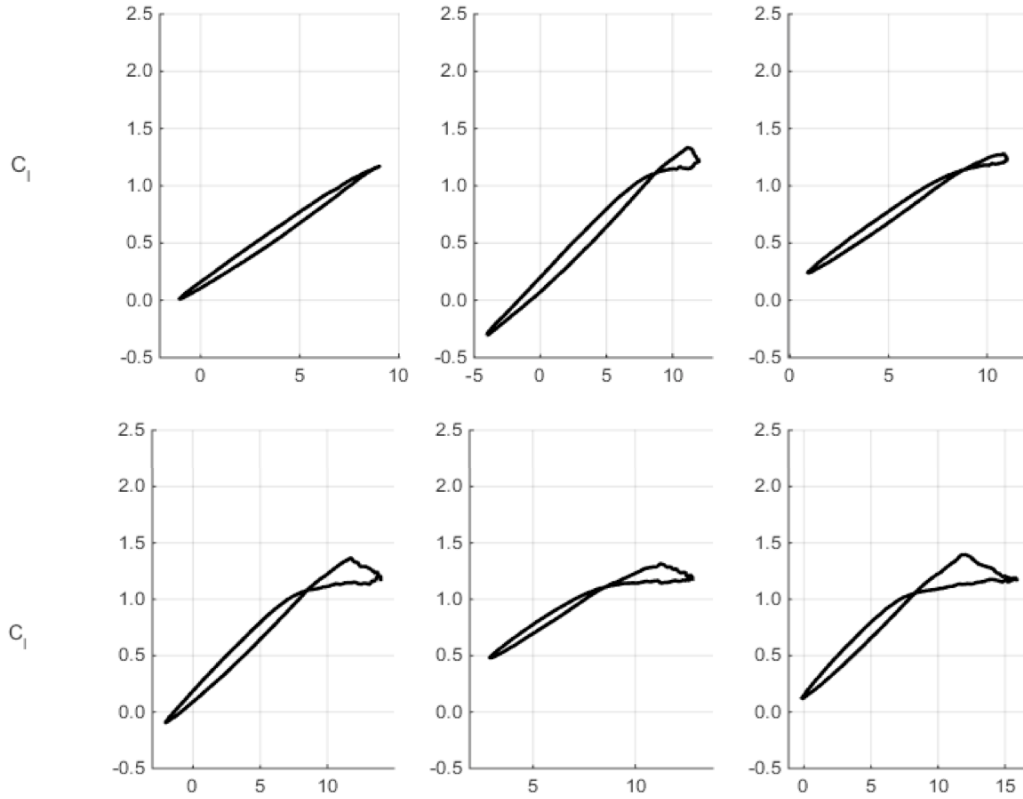


**Figure 122. Mach 0.5 baseline unsteady lift for  $k=0.05$ . From left to right: (top)  $\alpha=4^\circ \pm 5^\circ$ ,  $\alpha=4^\circ \pm 8^\circ$ ,  $\alpha=6^\circ \pm 5^\circ$ , (bottom)  $\alpha=6^\circ \pm 8^\circ$ ,  $\alpha=8^\circ \pm 5^\circ$ , and  $\alpha=8^\circ \pm 8^\circ$ .**

### ***Effect of Increasing Mach number***

One prescribed motion,  $k = 0.05$ ,  $\alpha = 8^\circ \pm 8^\circ$  was tested across the primary Mach number test points of 0.3, 0.4 and 0.5. The pitching profile provides a good case study to illustrate the effects of compressibility on the aerodynamic load traces. The resultant midspan loads for the clean model are shown in Figure 123 versus angle-of-attack. Roughly the same peak lift was recorded between  $M=0.3$  and 0.4, but the latter case exhibited strong dynamic stall traits not experienced at  $M=0.3$ . At Mach 0.5, the peak lift and adverse pitching moment decreased as moment and lift stall both occurred at reduced phase.

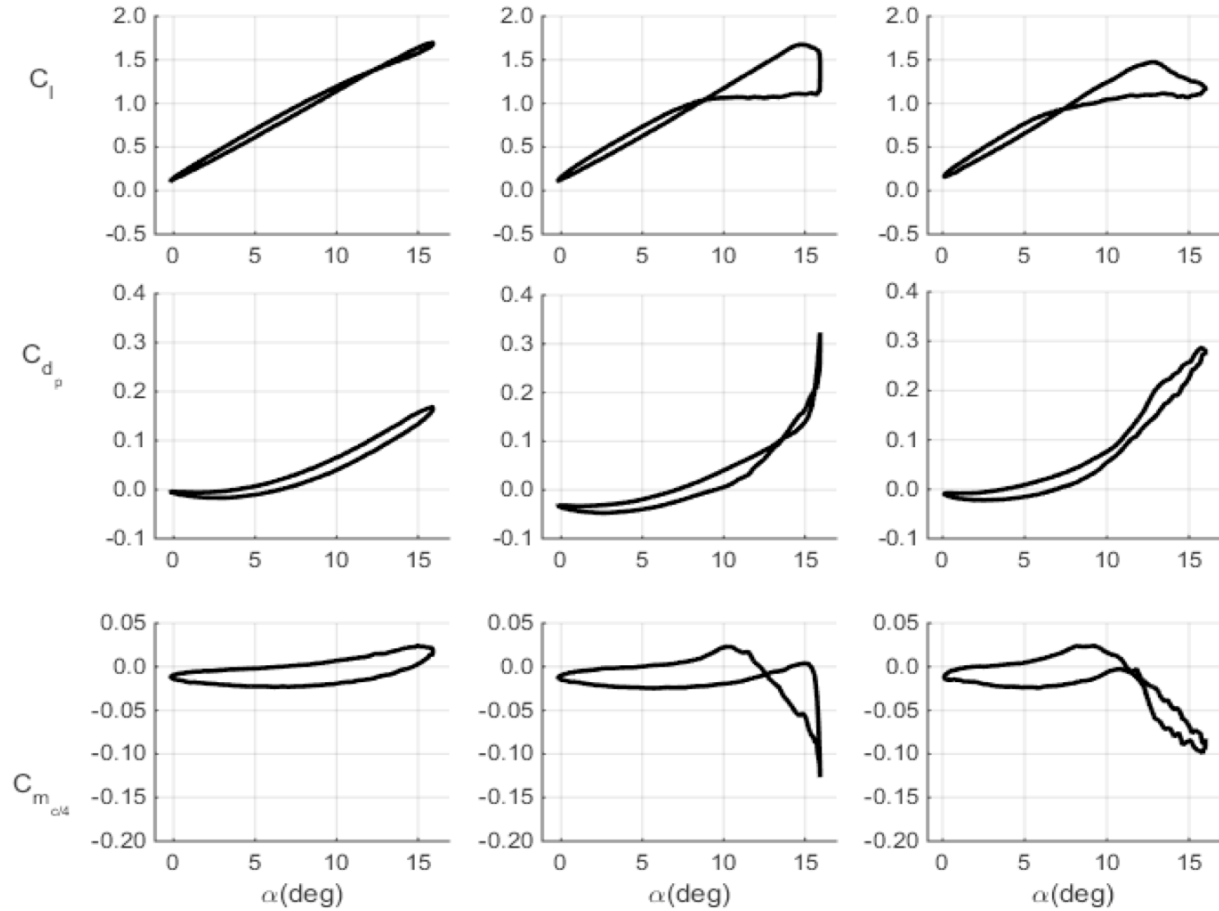


**Figure 123. Effect of increasing Mach number and compressibility on measured unsteady loads,  $k = 0.05$ ,  $\alpha = 8^\circ \pm 8^\circ$ . Left to right,  $M = 0.3, 0.4$ , and  $0.5$ .**

This is better understood through examination of the incurred loads as a function of the forced pitch motion's phase angle, as shown in Figure 124. The corresponding stacked upper surface pressures for the three cases are shown in Figure 125. Increased compressibility reduced loading as the leading-edge suction peak was reduced from -7.3 at Mach 0.3, to -6.0 at Mach 0.4, and ultimately down to -3.1, 0.4, at Mach 0.5. All three cases have local supersonic flow, since  $C_p^*$  is -6.95, -3.66, and -2.13, respectively. Mach 0.5 has the most obvious transition from supersonic to subsonic pressure levels corresponding to a strong shock.

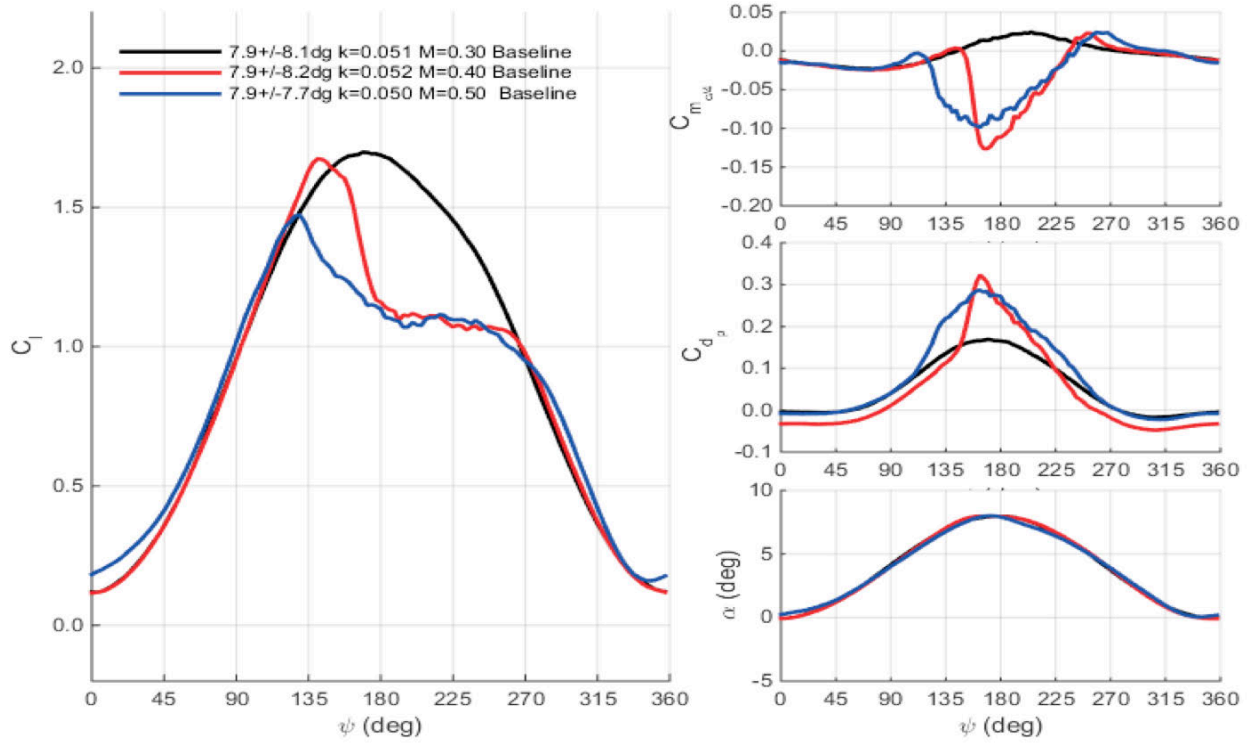


Figure 124. Effect of increasing Mach number on measured unsteady loads,  $k = 0.05, \alpha = 8^\circ \pm 8^\circ$ .

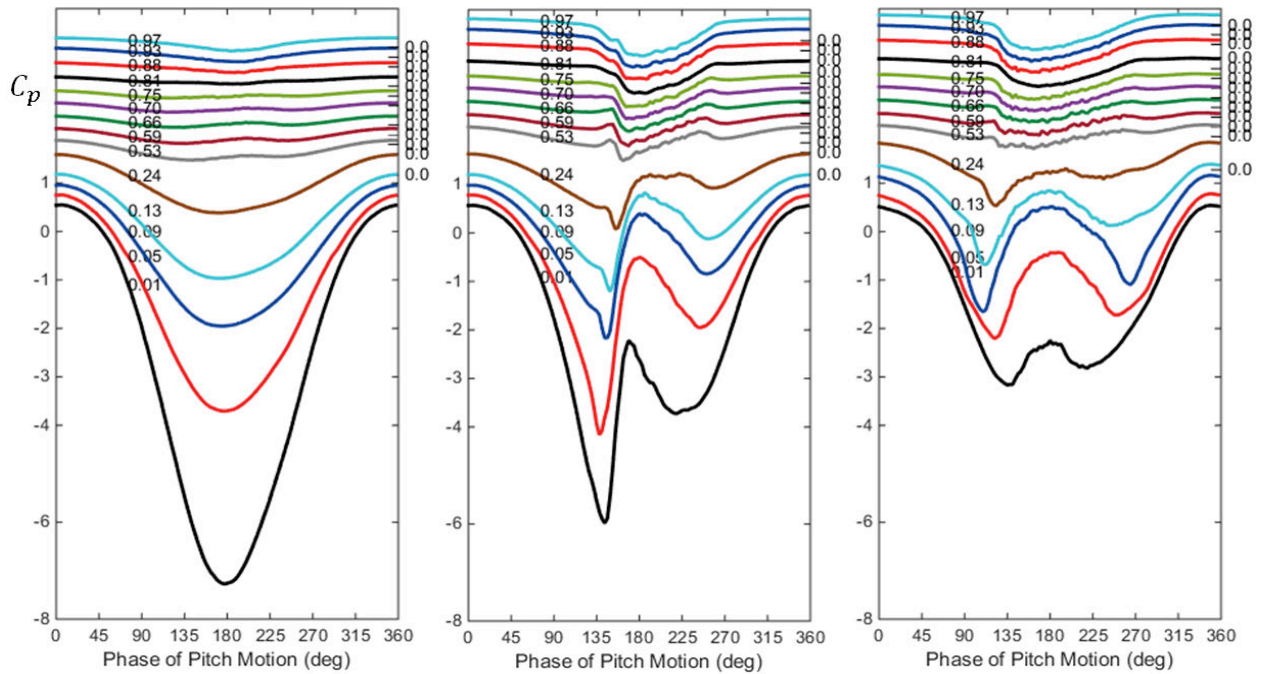
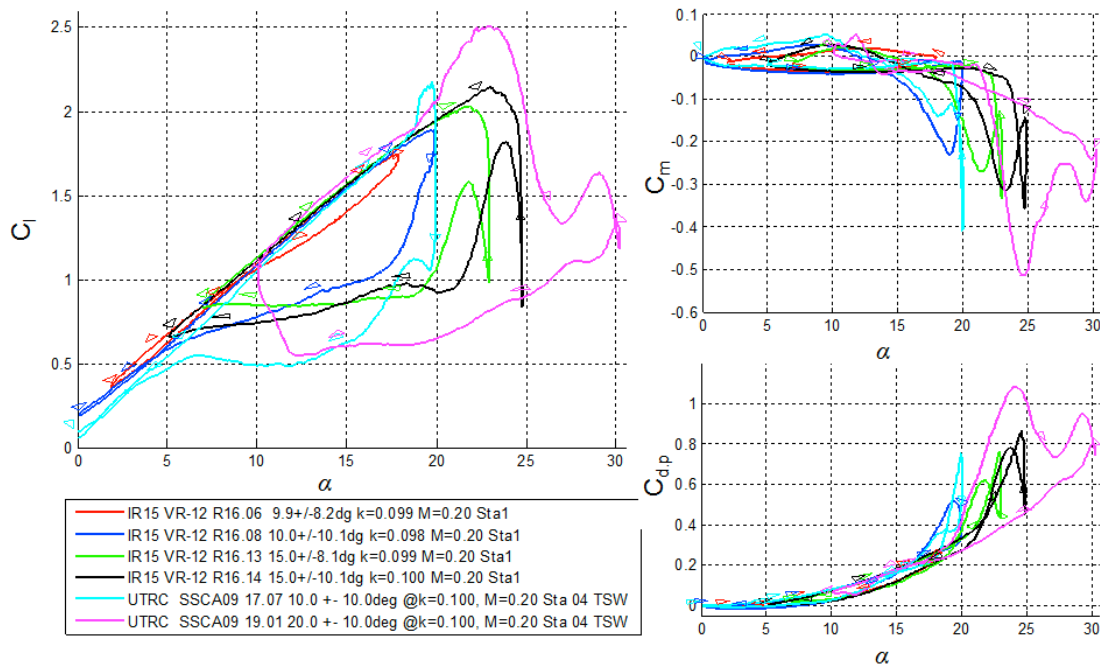


Figure 125. Comparison of phase averaged pressure coefficient for Mach sweep,  $k=0.05, \alpha = 8^\circ \pm 8^\circ$ . Left to right,  $M=0.3, 0.4$ , and  $0.5$ .

### Comparison with Unsteady Results for Other Tests

The first comparison is to the 1986 UTRC tests of an SSC-A09 airfoil, Refs. [45] and [44]. The SSC-A09, while from the same generation of helicopter airfoils as the VR-12, is a tip airfoil, optimized for low drag divergence, while the VR-12 was optimized for high lift coefficient at lower Mach numbers. Both tests employed tunnel spanning wings at similar aspect ratio, airfoil, Reynolds number, Mach number, and pitching motion.

Figure 126 compares VR-12 and SSC-A09 lift and moment coefficients at Mach 0.2 and  $k=0.10$ . Both tests show similar lift curve slopes and flat pitching moments in attached flow, but the SSC-A09 has higher overshoots in lift, moment, and drag, and has lower post-stall  $C_{L,max}$ .



**Figure 126. Comparison of unsteady force and moment coefficients at  $M=0.2$  and  $k=0.10$  for the current test and the 1986 SSC-A09.**

Figure 127 shows comparisons for Mach 0.3 and  $k=0.05$ . Stall of the VR-12 is delayed to  $\alpha=19^\circ$   $2.5^\circ$  higher than the SSC-A09, reflecting the airfoil design objectives. However, the VR-12 does have a higher peak pitching moment and drag.

The second comparison is to the lower Reynolds number. VR-12 baseline results from Ref [38]. Figure 128 shows loads coefficients at Mach 0.3 and  $k=0.10$ . The 2003 results have a similar lift slope, but a deeper stall with a later reattachment on the downstroke. There is also an offset to the pitching moment, which may be caused by a difference in the trailing edge tab configuration.

The 2010 SC-2110 test in the IRT, Ref. [40], did not provide a dynamic stall condition comparable to the current results because the unsteady amplitude and frequency was restricted during the earlier test.

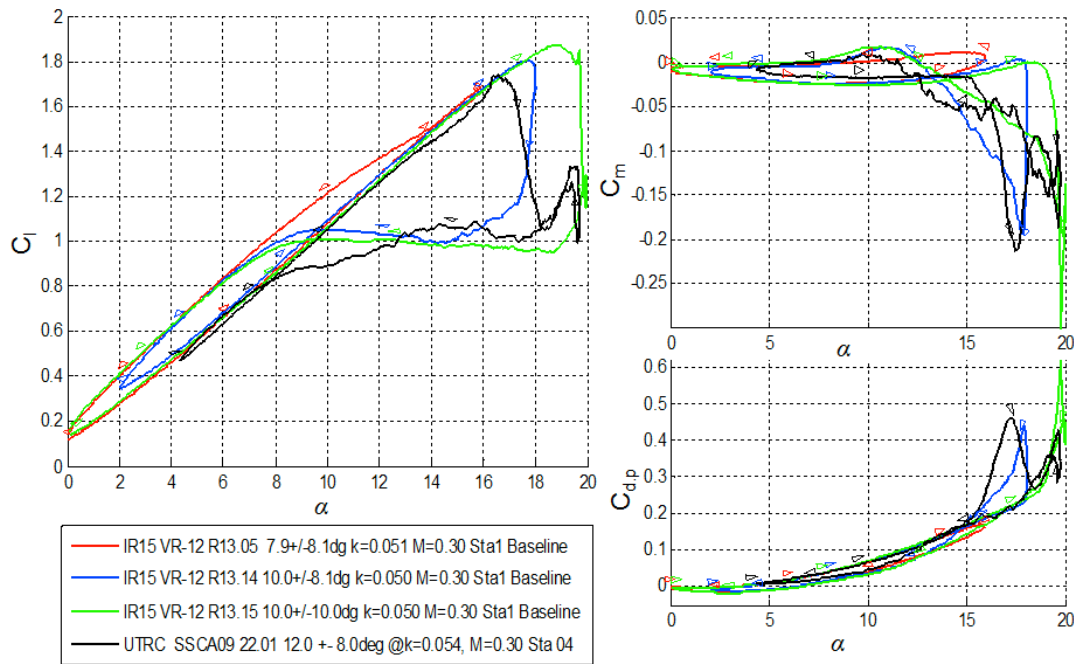


Figure 127. Comparison of unsteady force and moment coefficients for  $M = 0.3$  and  $k=0.05$  for the current test and the 1986 SSC-A09.

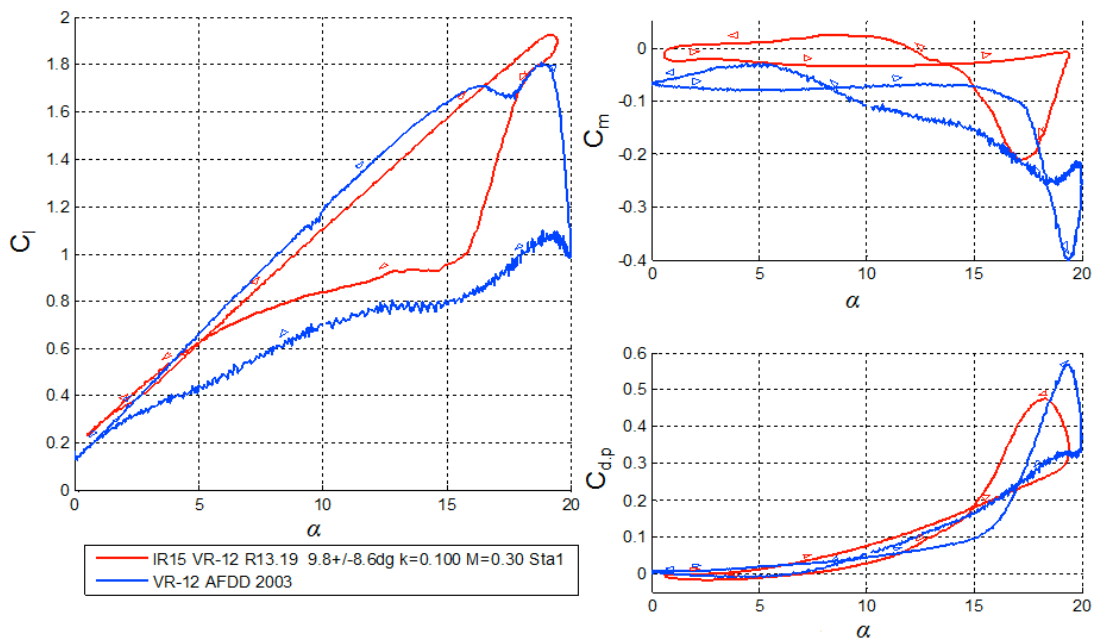


Figure 128. Comparison of unsteady force and moment coefficients for  $M = 0.3$  and  $k=0.10$  for the current test and the 2003 VR-12 at lower Re, Ref, [38].



### C. Comparison of Test Entries 1 and 2

The baseline smooth leading edge was reinstalled for the first test day of Entry 2. Steady angle-of-attack sweeps at Mach 0.2, 0.3, and 0.4, plus twenty-one unsteady pitch conditions were acquired. Some additional corrections were required for these early data because of issues with the pneumatic line connecting the onboard model ESPs to the wind tunnel reference pressures. The Mach 0.2 results (Run 51) in particular have higher than normal uncertainty.

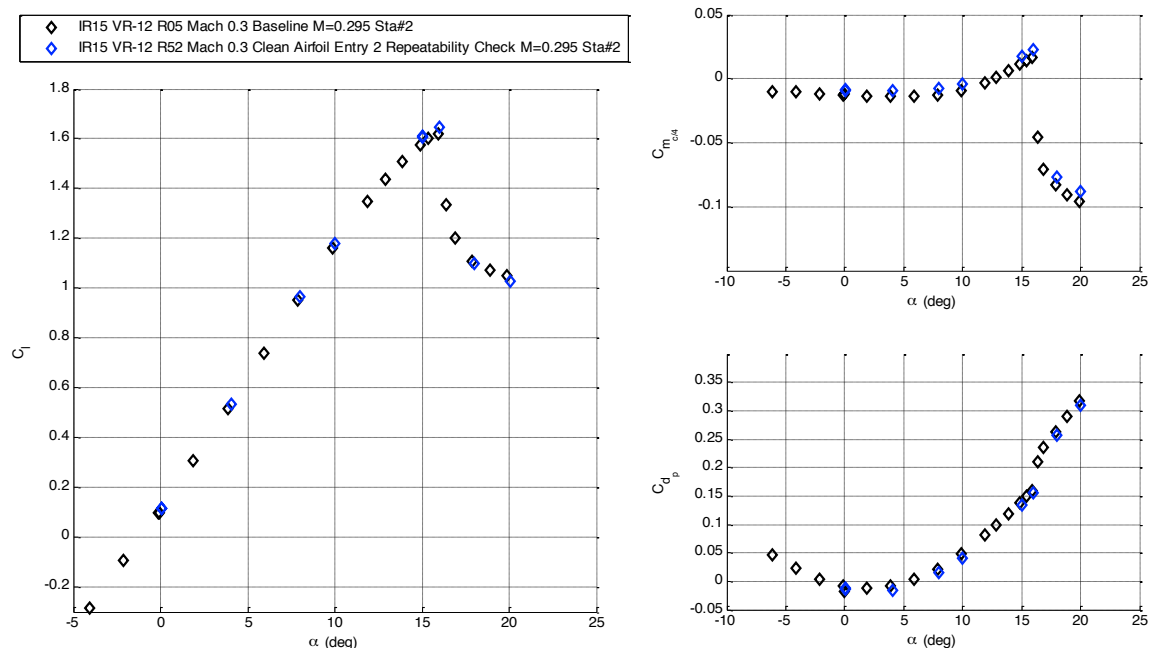
#### Steady Baseline Entry 1 v 2

Table 18 lists the steady baseline data sets for Entry 2.

**Table 18. Steady Baseline Data Sets, Entry 2.**

Data Set	Name
48	R50 Mach 0.2 Baseline Entry 2 1st Run Questionable
49	R51 Mach 0.2 Baseline Entry 2
57	R52 Mach 0.3 Baseline Entry 2
78-79	R53-54 Mach 0.4 Baseline Entry 2

Figure 129 compares the lift, pitching moment, and drag coefficients at Mach 0.3 measured in Entry 1 and in Entry 2, at the central spanwise Station 2. The agreement in terms of lift slope, stall angle, and post-stall characteristics is quite good. This indicates that the basic parameters of the Entry 2 setup were consistent with Entry 1: angle-of-attack, airfoil installation, surface finish, and normalization using wind tunnel parameters. Figure 130 shows that the pressure distributions also agree.



**Figure 129. Lift, drag, and moment coefficients comparison for baseline airfoil at M = 0.3: Entry 1 Run 5 vs. Entry 2 Run 52, Station 2.**

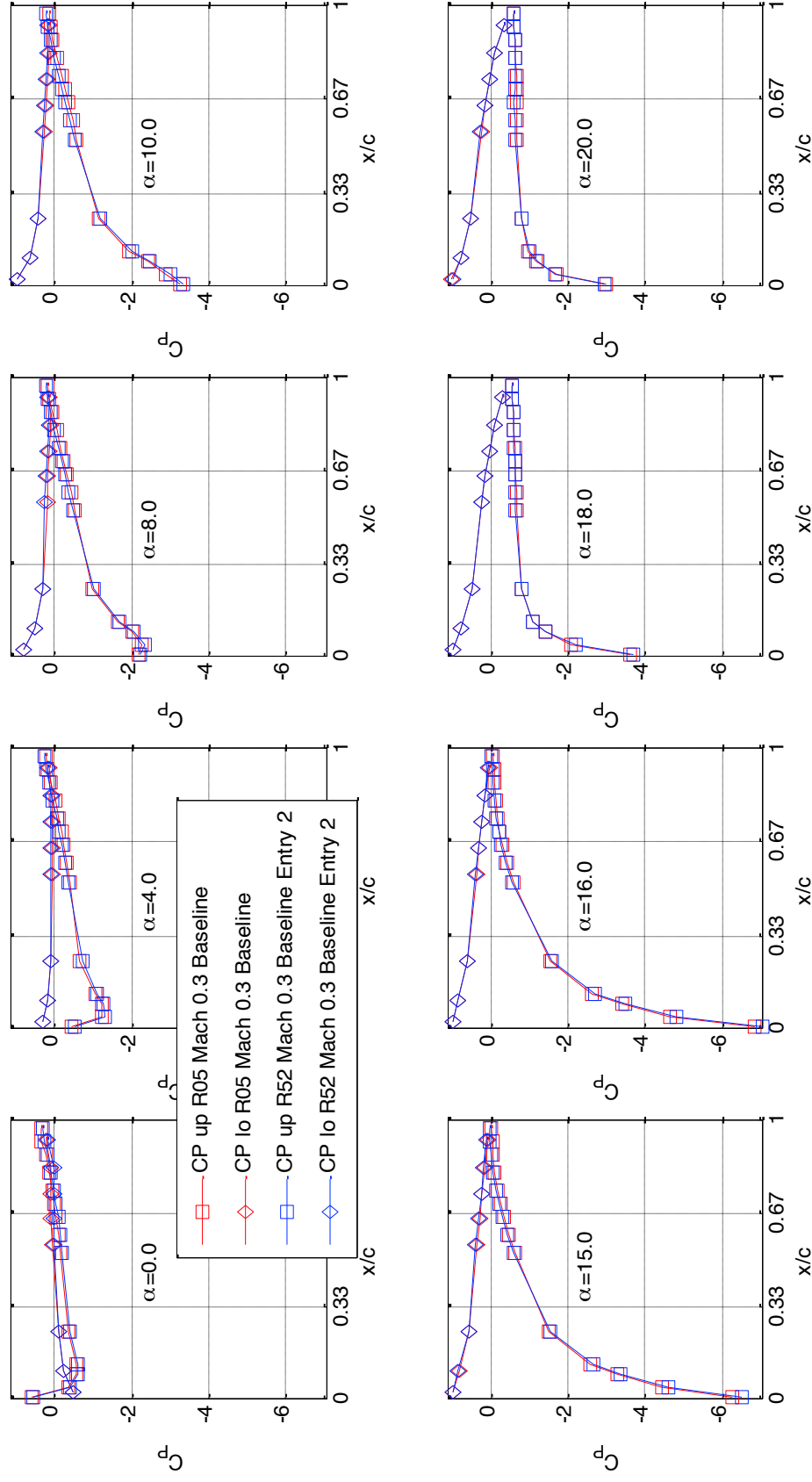
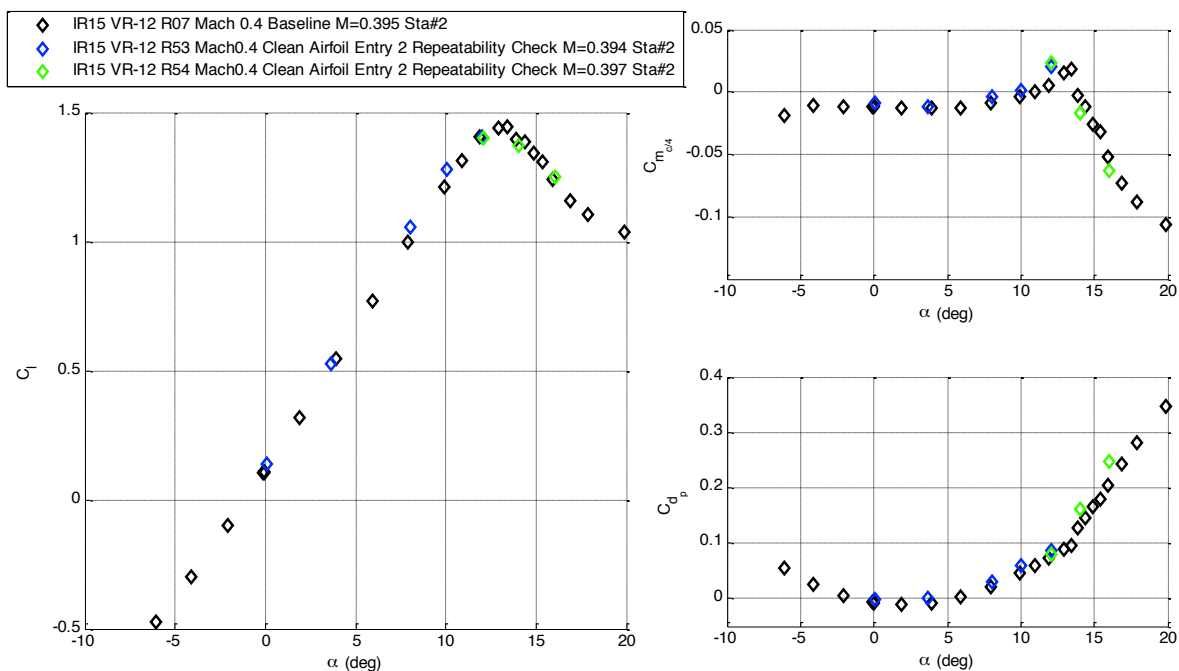


Figure 130. Pressure coefficient comparison for  $M = 0.3$  baseline: Entry 1 vs. 2, Station 2.

Figure 131 shows the steady baseline load coefficient comparison at Mach 0.4. While the final comparison was acceptable, there was an additional complication. Because Entry 2 was in May, the ambient outside temperature and humidity were much higher than during Entry 1 in January. At higher Mach number, the reduced static temperature in the test section caused condensation, which in addition to obscuring the view, could cause problems by either electrically shorting a Kulite or blocking the sense tube to an ESP port. In this case, Kulite 5, located at the aft end of the leading edge, seemed to suffer from a level shift at Mach 0.4 that was not present at lower Mach number. Figure 132 illustrates this effect using pressure distributions. The upper row is from Entry 1 and the middle row shows the measurements from Entry 2, highlighting Kulite 5's upper lump at  $x/c \sim 0.30$ . Because there is a large uninstrumented region aft caused by the exposed spar, this location has a large impact on the integrated lift. The normal method to correct faulty sensors is linear interpolation, which in this case caused an unrealistic shift, so a cubic fit was used instead, as shown in the lower row. Overall, this interpolation did quite well; any error introduced tended to over predict the suction at the Kulite 5 tap location. For direct comparison of baseline and actuated cases throughout this report, all attempts were made to post-process cases in an identical fashion to remove quadrature errors from the result and loads.

The most problematic steady baseline results from Entry 2 were at Mach 0.2. These runs were the first of Entry 2, and the wind tunnel pressure lines were not properly connected to ESP reference ports within the model, so that the static and dynamic pressures and Mach number used in data processing had to be computed from the static and total temperature measurements. There was also an issue with pinched internal reference lines for several of these early runs. With these corrections to the reference pressure, the Figure 133 results show acceptable agreement.



**Figure 131. Lift, drag, and moment coefficients comparison for  $M = 0.4$  baseline: Entry 1 Run 7 vs. Entry 2 Runs 53-54, Station 2.**

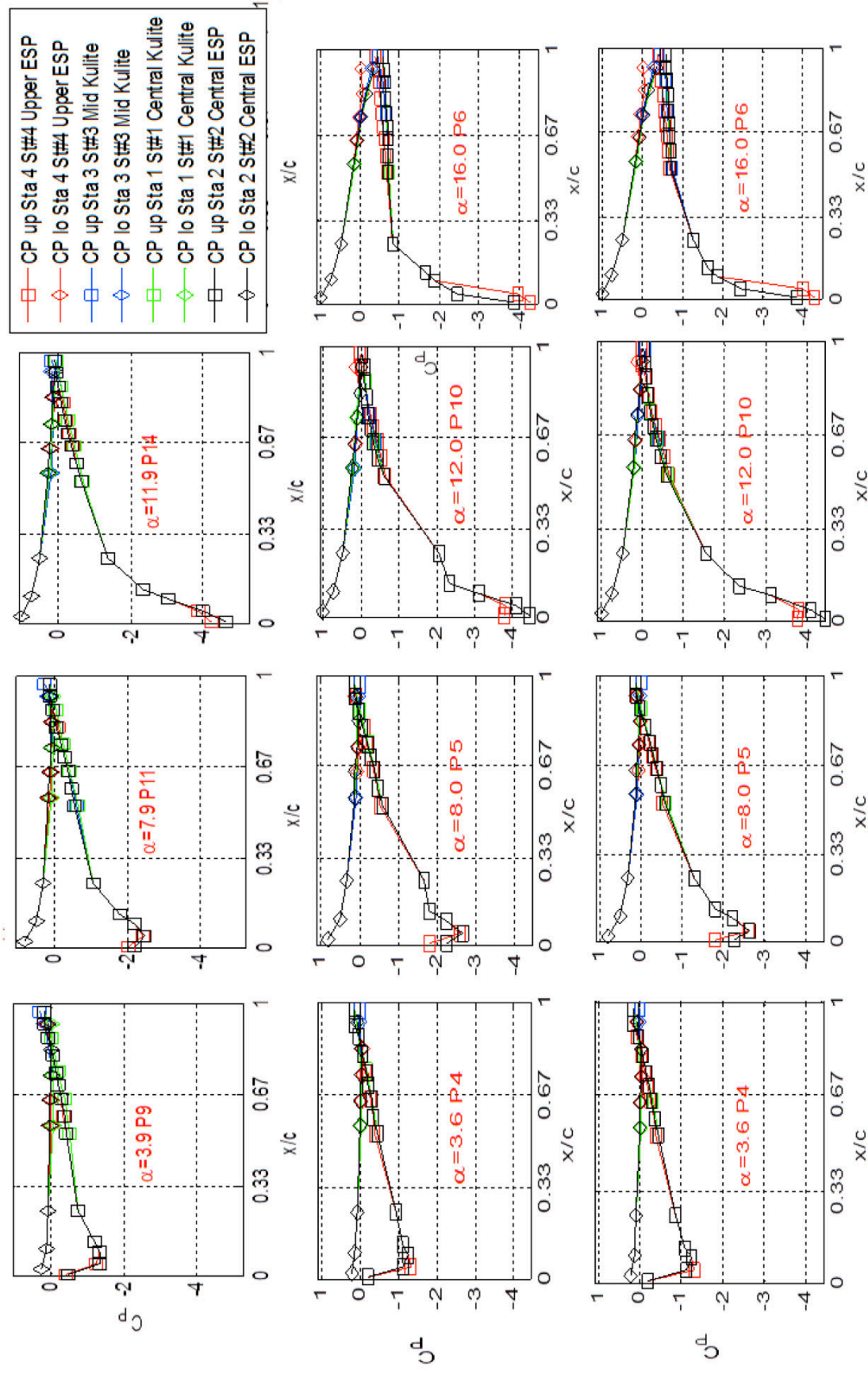
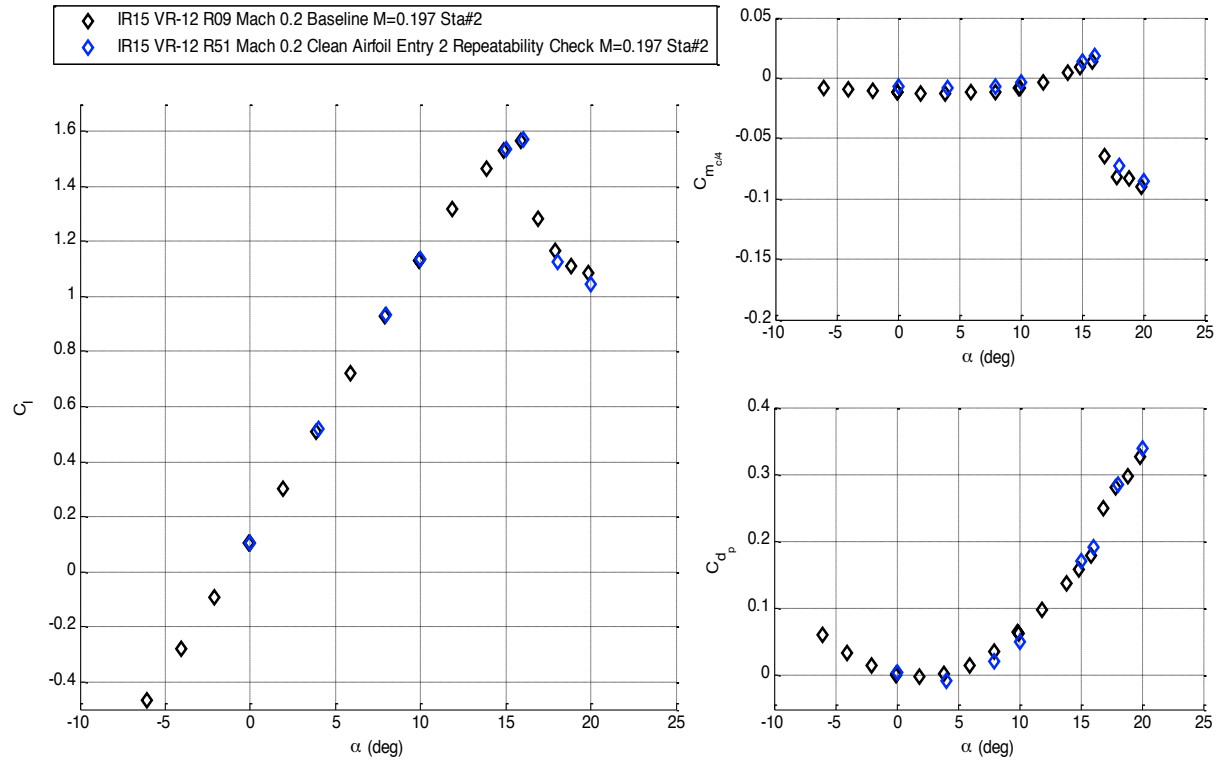


Figure 132. Interpolation effect on  $M = 0.4$  baseline Kulite pressure distributions: Top Row: Entry 1 Run 7, Middle Row: Entry 2 Run 53 without interpolation, Bottom Row: R53 with cubic interpolation



**Figure 133. Lift, drag, and moment coefficient comparison for baseline airfoil at  $M = 0.2$ : Entry 1 Run 9 vs. Entry 2 Run 51, Station 2.**

### *Unsteady Baseline Entry 1 v 2*

Unsteady baseline comparisons between Test Entries 1 and 2 were made at Mach 0.2, 0.3, and 0.4; the Entry 2 baseline data sets are shown in Table 19. Recall the definitions:  $\alpha = \alpha_0 - \alpha_1 \cos(\omega t)$  and  $k = \omega c / 2U$ .

**Table 19. Unsteady Baseline Data Entry 2**

Run	Mach	k	$\alpha_0$ [°]	$\alpha_1$ [°]	Points	Notes
50	0.2	0.05, 0.07	8, 10	8, 10	7-10	Initial Check
51	0.2	0.05, 0.07	10	8, 10	7-10	
51	0.2	0.05, 0.07	15	8, 10	12-15	
52	0.3	0.025, 0.05, 0.07, 0.10	10	8, 10	7-12	
52	0.3	0.025, 0.05, 0.07	15	8	14-16	
53	0.4	0.025, 0.05, 0.07	10	8	7-9	Condensation
54	0.4	0.05, 0.07	12	8	3-4	

Figure 134 shows comparisons for Mach 0.3,  $\alpha = 10^\circ \pm 8^\circ$  and  $10^\circ$ , and at the low frequency of  $k = 0.025$ . The qualitative features of the load loops match quite well; the red and green loops are at  $\alpha = 10^\circ \pm 10^\circ$  and the black and blue loops are at  $\alpha = 10^\circ \pm 8^\circ$ . There are some quantitative differences in the details. Figure 135 shows comparisons at the moderate frequency of  $k = 0.050$ . The Entry 1  $\alpha = 10^\circ \pm 10^\circ$  loop went to slightly higher angle than the Entry 2 loop, producing a stronger dynamic stall vortex and a higher peak  $C_L$ . Figure 136 shows the highest frequency case,

$k=0.10$ . The  $\alpha=10^\circ\pm 8^\circ$  comparison has the largest differences seen at any Mach number: the Entry 2 lift loop stalls at the same angle as the Entry 1 loop, but loses more lift and does not seem to reattach as rapidly.



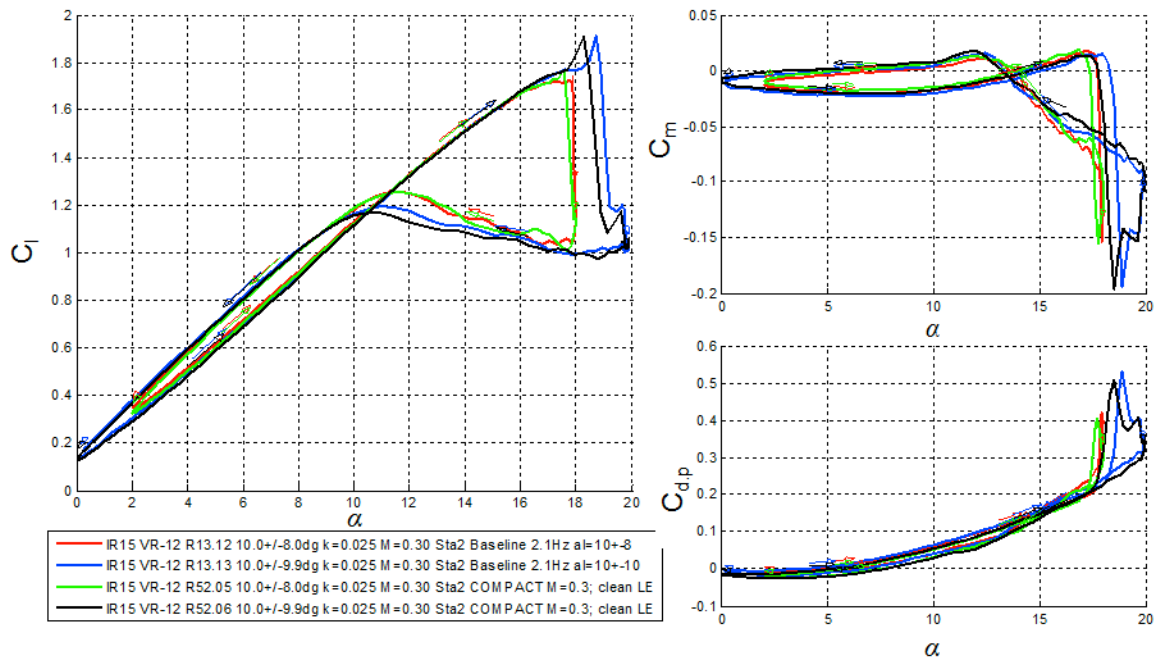


Figure 134. Lift, drag, and moment coefficients comparison for baseline airfoil at  $M = 0.3$ ,  $\alpha = 10^\circ \pm 8^\circ$  and  $\pm 10^\circ$ ,  $k = 0.025$ : Entry 1 Run 13 vs. Entry 2 Run 52, Station 2.

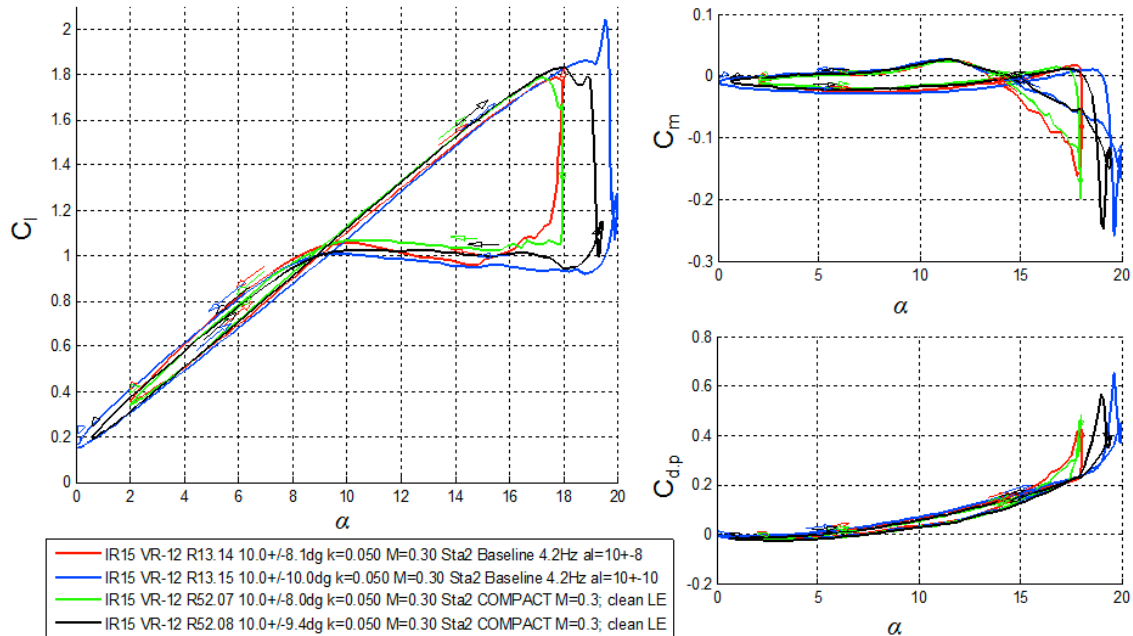
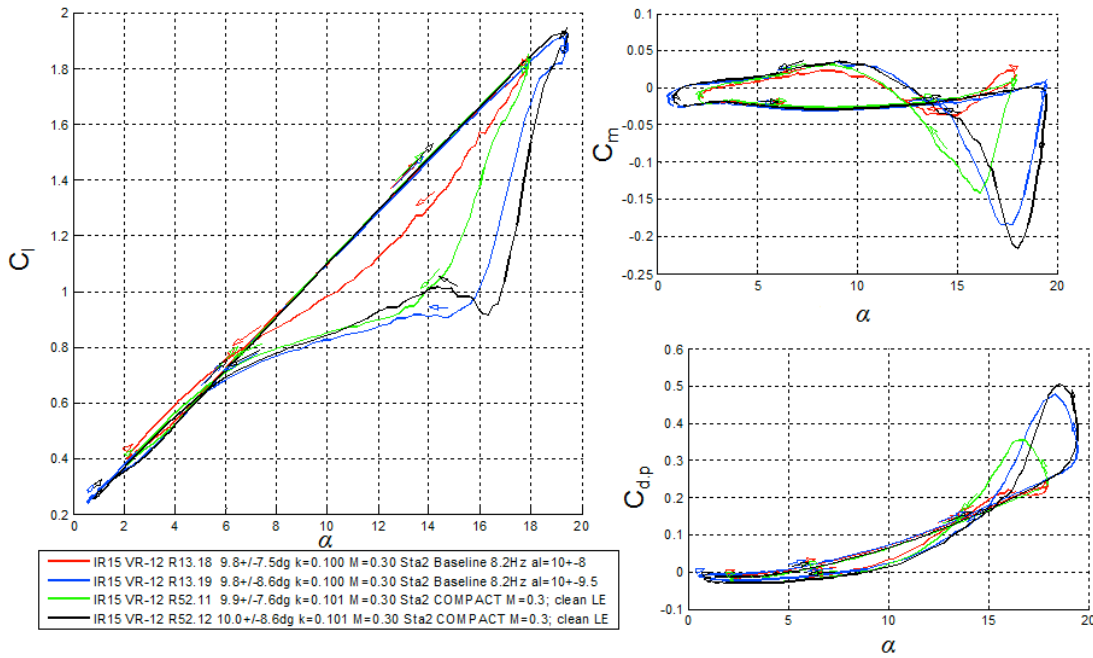


Figure 135. Lift, drag, and moment coefficients comparison for baseline airfoil at  $M = 0.3$ ,  $\alpha = 10^\circ \pm 8^\circ$  and  $\pm 10^\circ$ ,  $k = 0.050$ : Entry 1 Run 13 vs. Entry 2 Run 52, Station 2.



**Figure 136. Lift, drag, and moment coefficients comparison for baseline airfoil at  $M = 0.3$ ,  $\alpha = 10^\circ \pm 8^\circ$  and  $\pm 10^\circ$ ,  $k = 0.100$ : Entry 1 Run 13 vs. Entry 2 Run 52, Station 2.**

The upper surface pressure coefficients at  $k = 0.10$  in Figure 137 show that the same peak suction level for the two entries, but the loss of suction is more rapid in the second entry, and the convecting stall vortex stronger. The stronger stall vortex is responsible for the larger negative pitching moment coefficient seen in Figure 136. The cause of this difference is not understood, but is likely connected with the Entry 1 motion being just weak enough to not form a strong DSV. It is interesting that the  $\alpha = 10^\circ \pm 10^\circ$  loops agree much better, perhaps since both motions reach high enough angle to generate a strong vortex.

Figure 138 compares pairs of lift coefficients at Mach 0.4, for  $\alpha = 10^\circ \pm 8^\circ$  and for  $k = 0.025, 0.050$ , and  $0.070$ . The lower frequency pairs agree reasonably well, but as was true for Mach 0.3  $k = 0.10$ , the  $k = 0.07$  loops show more differences. The magenta Entry 2 loop has a sharper peak to a higher  $C_{l,max}$ , while the green Entry 1 loop is smoother up until it stalls abruptly at peak angle. The upper surface pressure distributions in Figure 139 show that Entry 2 stalls at the same phase angle, but has a lower suction peak and a stronger stall vortex.

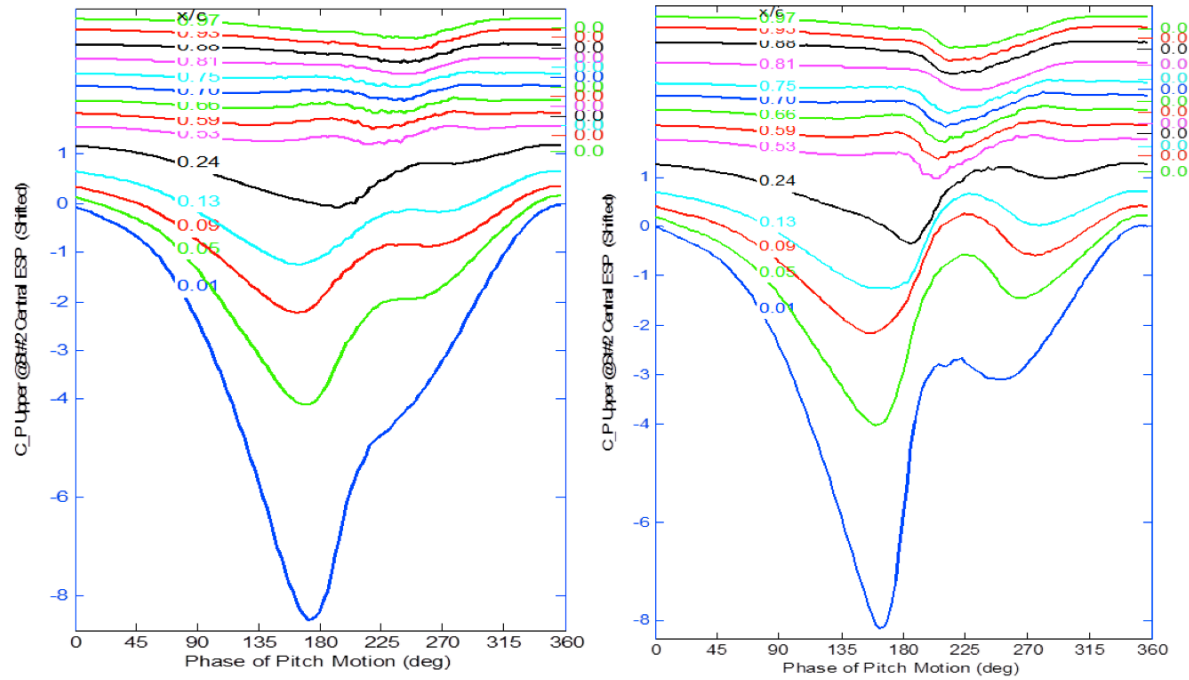


**Figure 137. Upper surface pressure coefficients comparison for baseline airfoil at  $M = 0.3$ ,  $\alpha = 10^\circ \pm 8^\circ$ ,  $k = 0.10$ : Entry 1 Run 13 vs. Entry 2 Run 52, Station 2.**

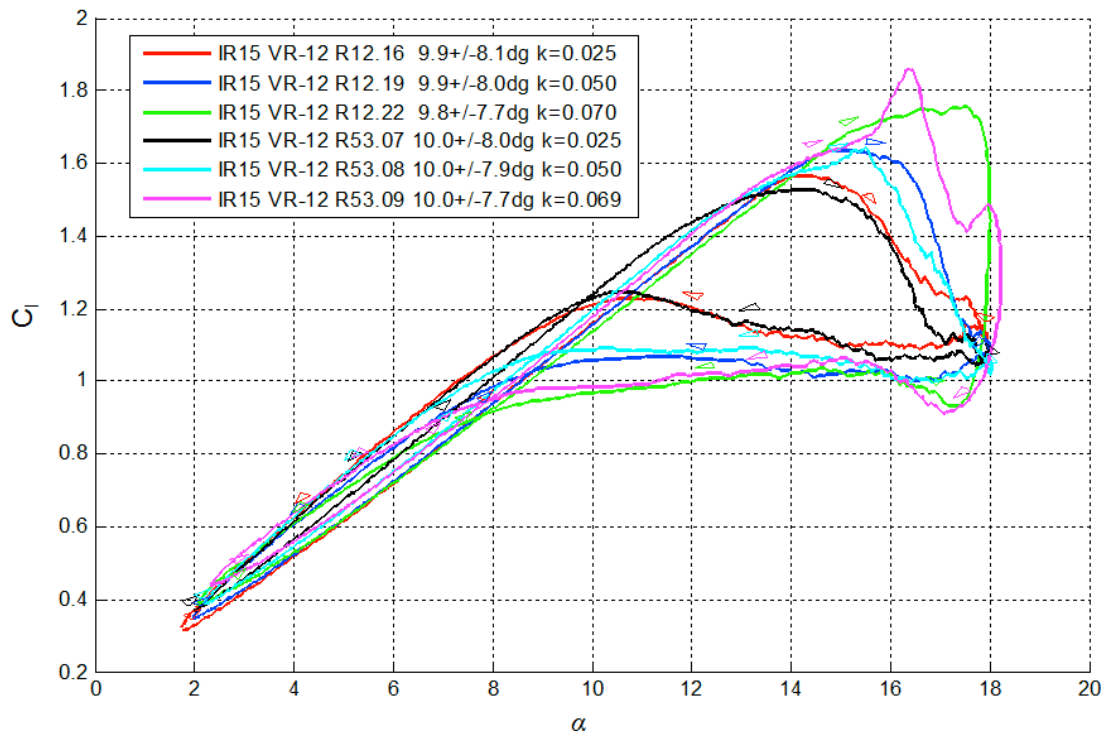


**Figure 138. Lift coefficients for baseline airfoil at  $Mach = 0.4$ ,  $\alpha = 10^\circ \pm 8^\circ$ ,  $k = 0.025, 0.05$ , and  $0.07$ : Entry 1 Run 12 vs. Entry 2 Run 53, Station 1.**

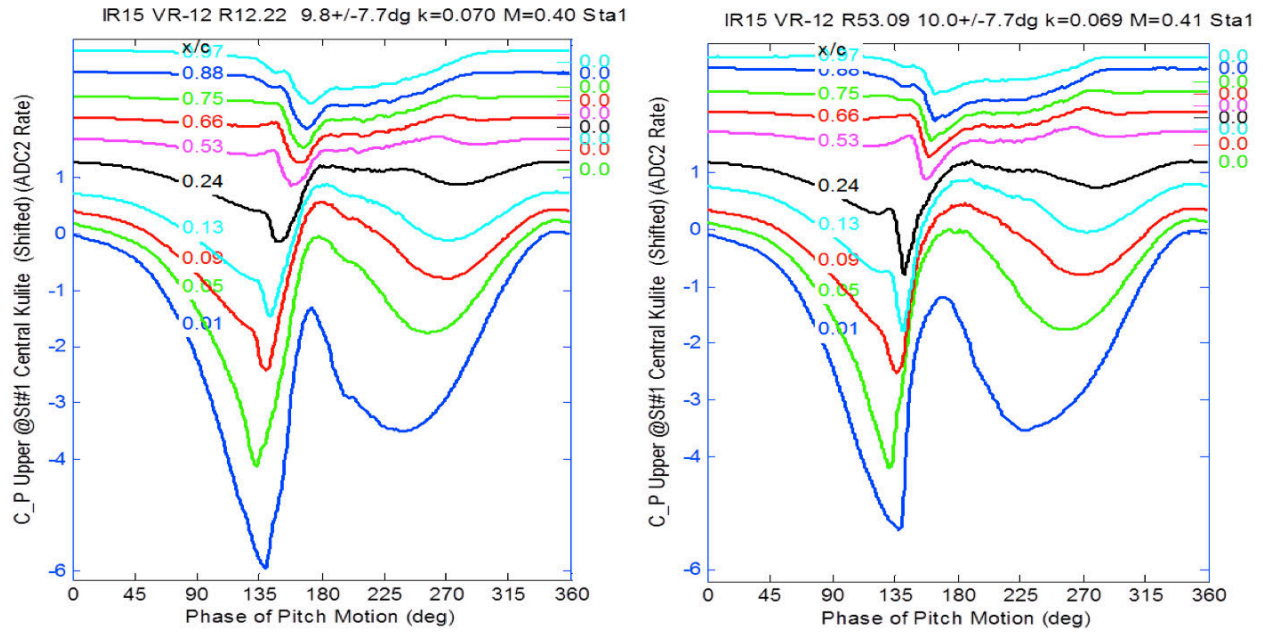


**Figure 139. Upper surface pressure coefficients for baseline airfoil at Mach=0.4,  $\alpha=10^\circ\pm8^\circ$ ,  $k=0.07$ : Entry 1 Run 12.22 vs. Entry 2 Run 53.09, Station 1.**

The final comparison of the unsteady baseline airfoil results to be presented is at Mach 0.2. Figure 140 compares two pairs of lift loops at  $k=0.070$  and high mean angle-of-attack:  $\alpha=15^\circ\pm8^\circ$  and  $\alpha=15^\circ\pm10^\circ$ . The agreement is generally quite good for  $C_{l,max}$ , the initial stall angle, the secondary lift oscillation, and the  $C_l$  value during the downstroke.

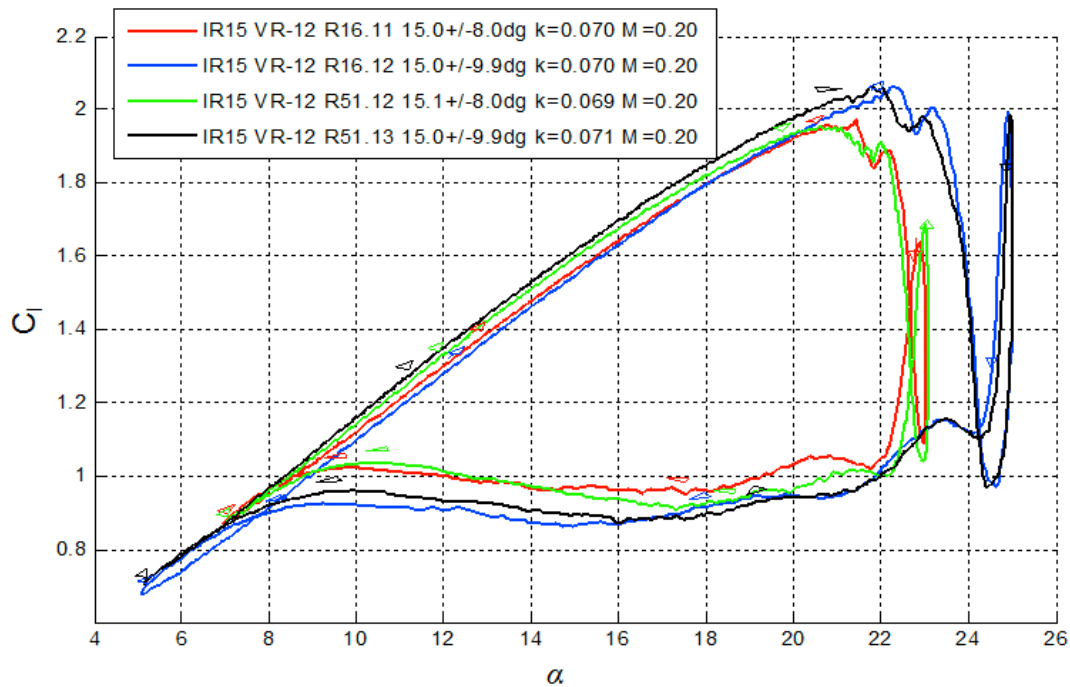


**Figure 140. Lift, drag, and moment coefficients for baseline airfoil at  $M = 0.2$ ,  $\alpha=15^\circ \pm 8^\circ$  and  $\pm 10^\circ$ ,  $k=0.070$ : Entry 1 Run 16 vs. Entry 2 Run 51, Station 1.**

#### ***D. Comparison of Baseline and Taped Slot Leading edges***

Despite a strong effort to mask the installation hardware of the discrete COMPACT arrays, including covering bolt locations with clay/wax, taping seams, sealing small gaps, and smoothing steps and discontinuities on the wing surface, differences between the clean leading edge VR-12 and the slot taped COMPACT configuration were detected. The tape configuration used 0.005 in thick aluminum tape to cover both COMPACT slot arrays. This subset of data is more limited compared to the other acquired data groups; the ramifications of the installed actuators proved to be fairly well defined across the Mach numbers of interest. Although reserved for the discussion of the actuator performance, it is worth noting that the difference between the taped slot and the open-slot-no-bleed configuration is small.

#### ***Steady State Conditions***

Table 20 lists the steady taped data sets acquired at Mach 0.2, 0.3, and 0.4. Test entry time-constraints prevented taped slot runs at Mach 0.5. Figure 141 compares the force and moment coefficients at Mach 0.3. There are few differences in the lift and moment below stall, but the taped slot leading edge has higher drag. The taped slot stalls at  $\alpha=16^\circ$  instead of  $16.5^\circ$ , and drops quickly to a lower post stall lift coefficient.

**Table 20. Steady Taped Slot Data Sets, Entry 1**

Data Set	Name
45	R44 Mach 0.2 Slot Taped
46	R45 Mach 0.3 Slot Taped
47	R46 Mach 0.4 Slot Taped

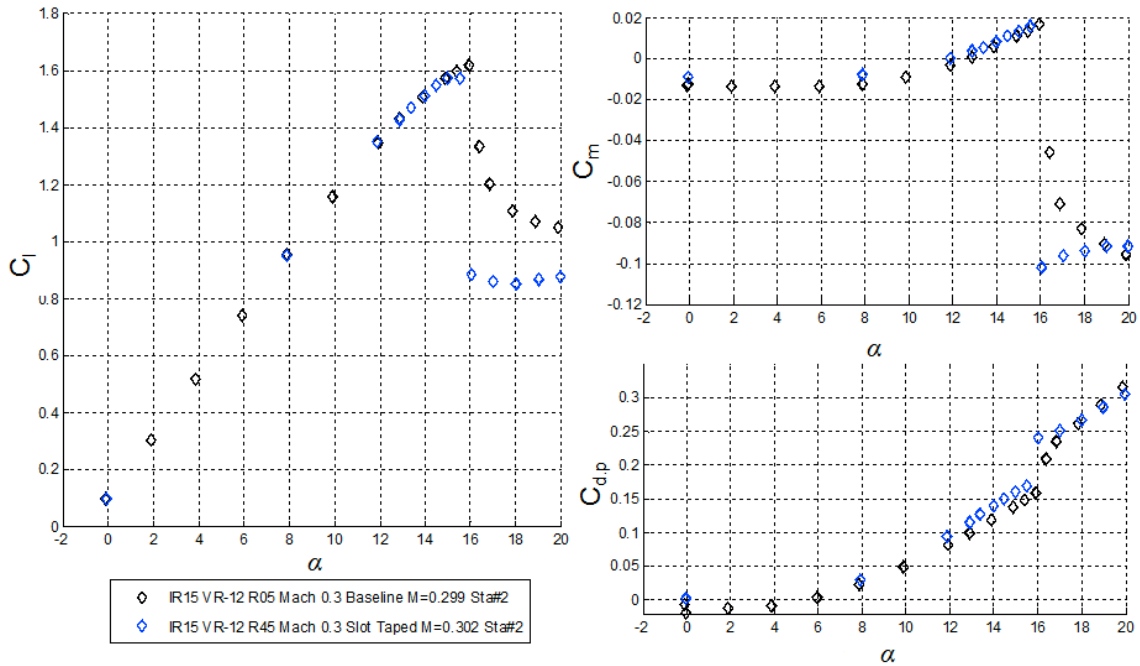


**Figure 141. Comparison of steady baseline and taped slot force and moment coefficients,  $M=0.3$ .**

Figure 143 compares the surface pressure distributions at Mach 0.3. The earlier stall with the taped slot is apparent. Figure 142 shows the  $C_l$  comparisons at Mach 0.2 and 0.4. At  $M=0.2$ , the stall angle appears unchanged, but the post-stall lift is lower. At  $M=0.4$ ,  $C_{l,max}$  is actually slightly higher, but again the post stall  $C_l$  is lower. Appendix 3 contains the remaining  $C_p$  comparisons.



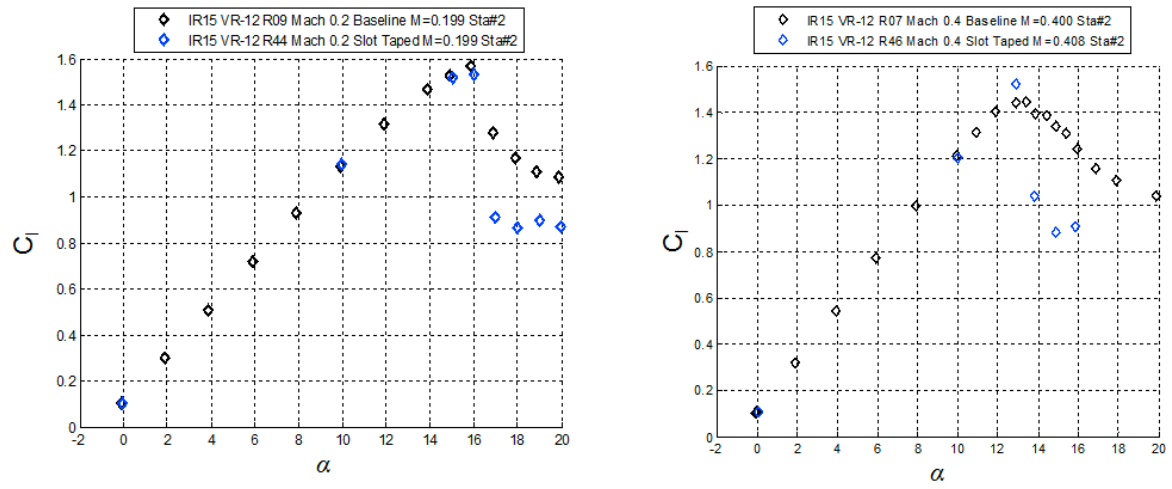


**Figure 142. Comparison of steady baseline and taped slot lift coefficients,  $M = 0.2$  and  $0.4$ .**

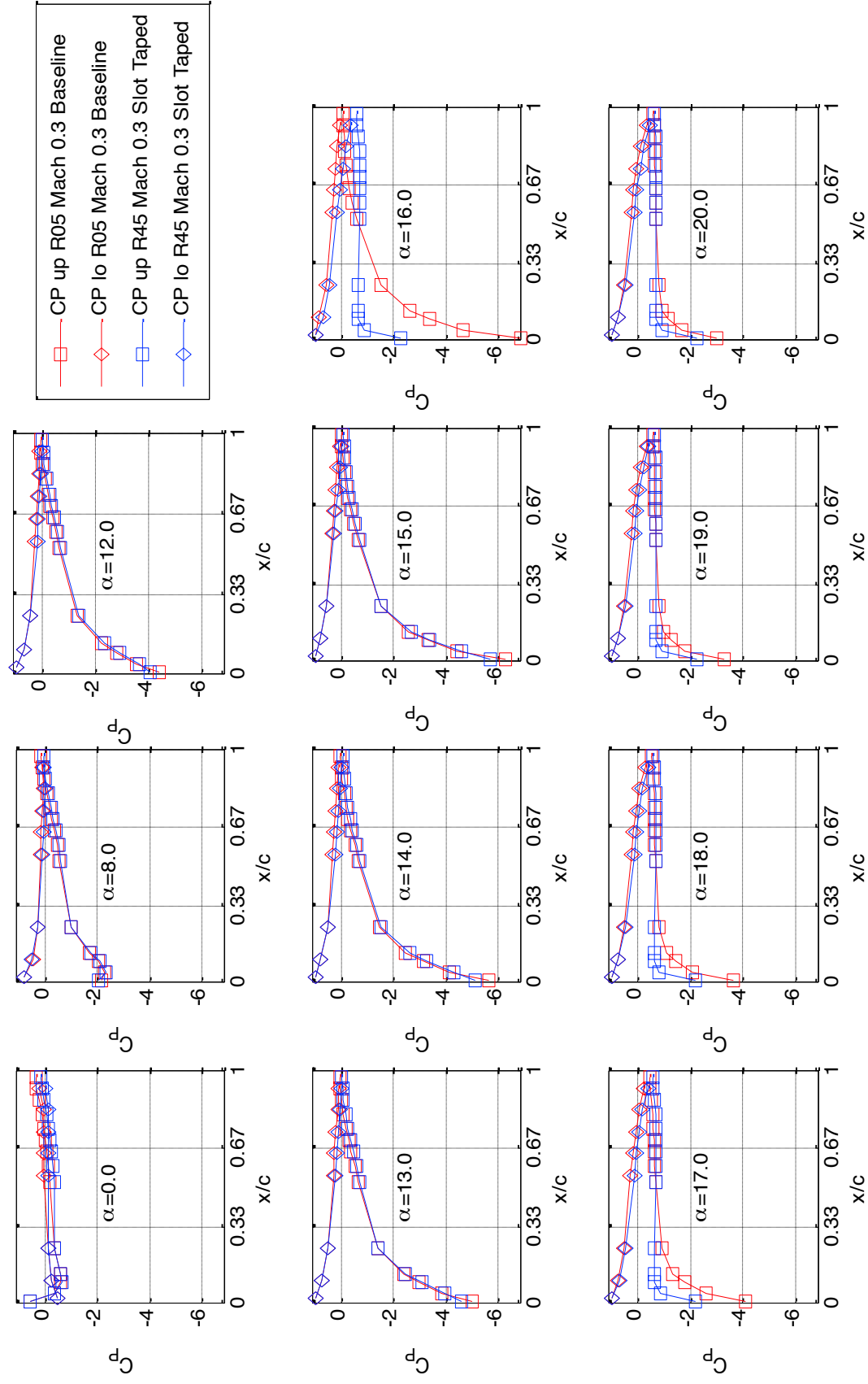


Figure 143. Comparison of steady baseline and taped slot pressure coefficients,  $M = 0.3$ .

### *Unsteady Motions*

Table 21 lists the taped slot unsteady data points.

**Table 21. Unsteady Taped Slots Entry 1**

Run	Mach	$k$	$\alpha_0[^\circ]$	$\alpha_1[^\circ]$	Points
44	0.2	0.05,0.07	10,15	8,10	4-12
45	0.3	0.025	10	10	5
45	0.3	0.10	10	8	6
45	0.3	0.07	15	10	14
46	0.4	0.05	10	10	3
46	0.4	0.07	10	5	4

Figure 144 and Figure 145 show the  $M = 0.2$  results for the clean and the taped-slot installations. Four prescribed angle-of-attack motions are shown in each figure. The calculated resultant motions are described in the figures' legends. The data shows differences between the aerodynamic loads occur predominantly on the downstroke. The upstroke differences are negligible, although subtle variations are present for the  $\alpha = 15^\circ \pm 10^\circ$  case in Figure 145 as the incidence nears  $25^\circ$ . As the downstroke commences, the differences between the measured loads grow more visible. In all test cases at  $M = 0.2$ , the taped geometry produced a larger lag in reattachment, decreasing the average lift. Peak lift, drag, and nose-down moment remain nearly identical for similar prescribed angle-of-attack oscillations.

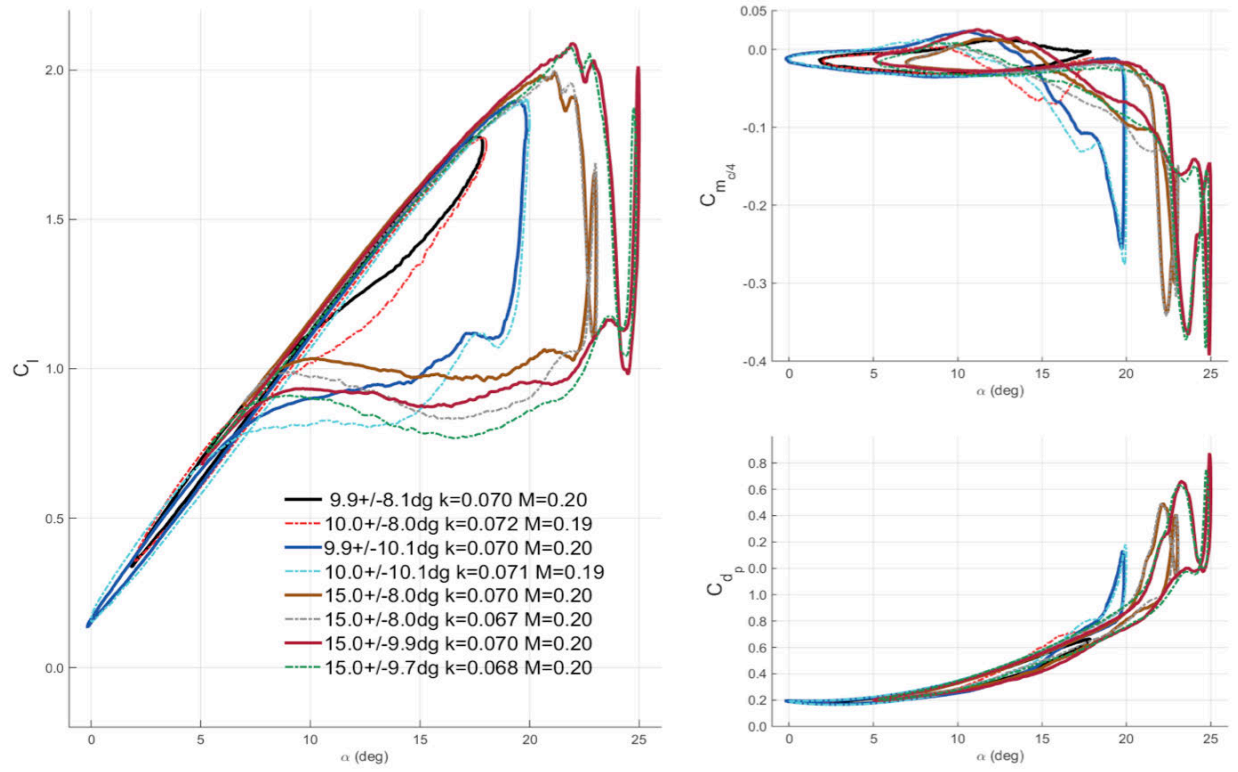


Figure 144. Comparison of unsteady load loops,  $M = 0.2$ ,  $k = 0.07$ . Solid lines are baseline, dashed lines are taped.

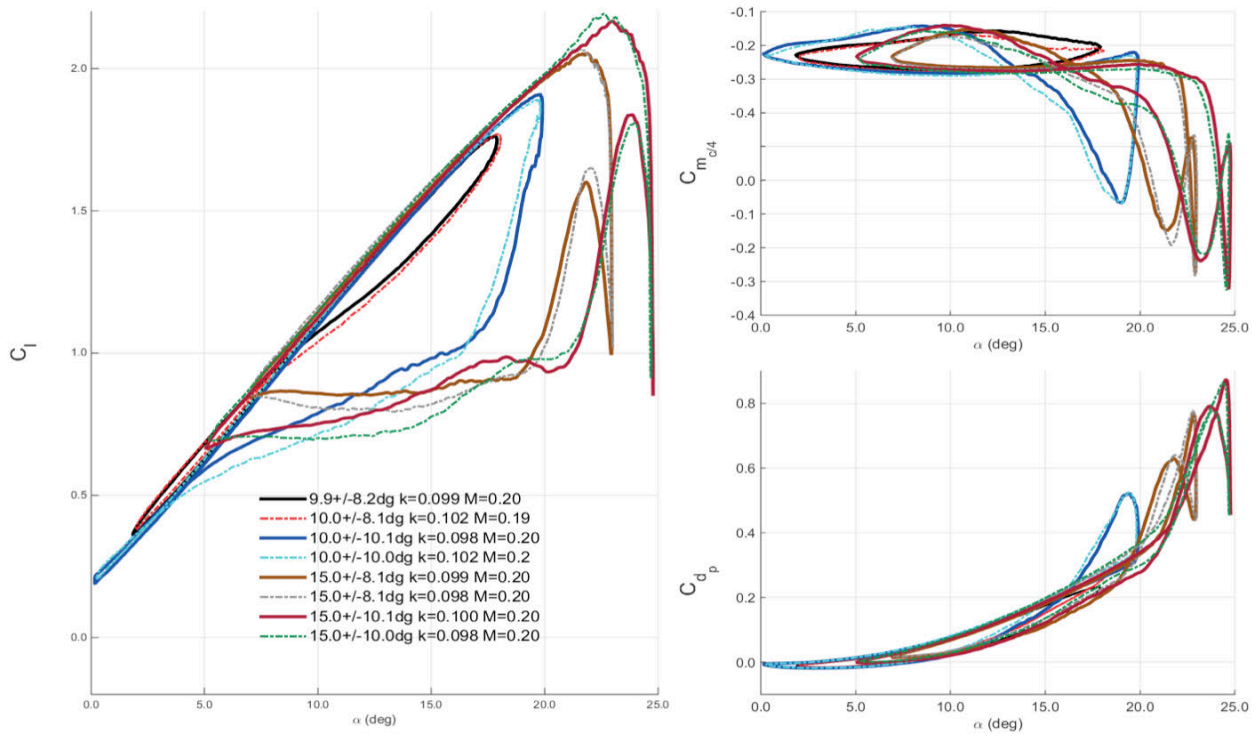
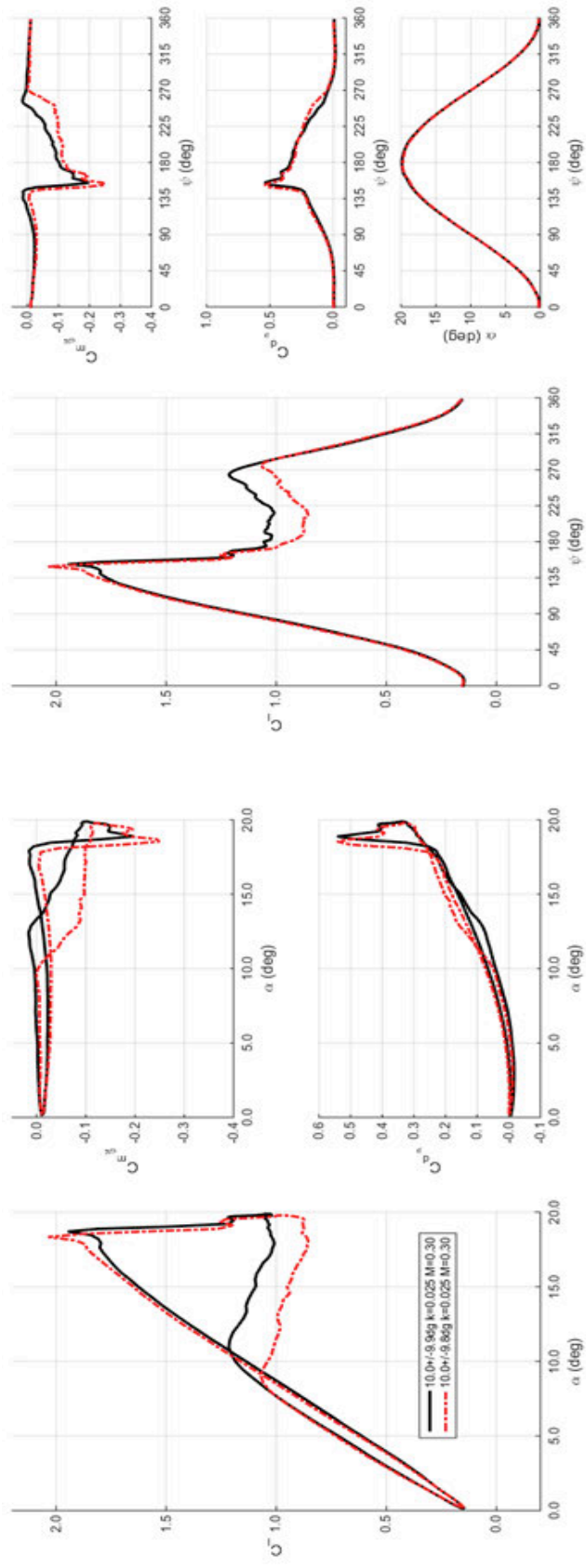


Figure 145. Comparison of unsteady load loops,  $M = 0.2$ ,  $k = 0.10$ . Solid lines are baseline, dashed lines are taped.

Figure 146 and Figure 147 show the unsteady aerodynamic load traces for two motion histories at Mach 0.3. Unlike the measured responses at  $M = 0.2$ , the Mach 0.3 and 0.4 cases produced distinct differences between the clean and taped airfoil configuration on the upstroke, particularly near moment stall and maximum lift. The loads show that the tape had a positive impact on the airloads on the upstroke, but, similar to  $M = 0.2$ , caused a delay in reattachment and prolonged the duration of separated flow through the downstroke.



**Figure 146.** Comparison of unsteady loads plotted as function of angle-of-attack and phase,  $M = 0.3$ ,  $k = 0.025$ ,  $\alpha = 10^\circ \pm 10^\circ$ . Solid lines are baseline, dashed lines are taped.



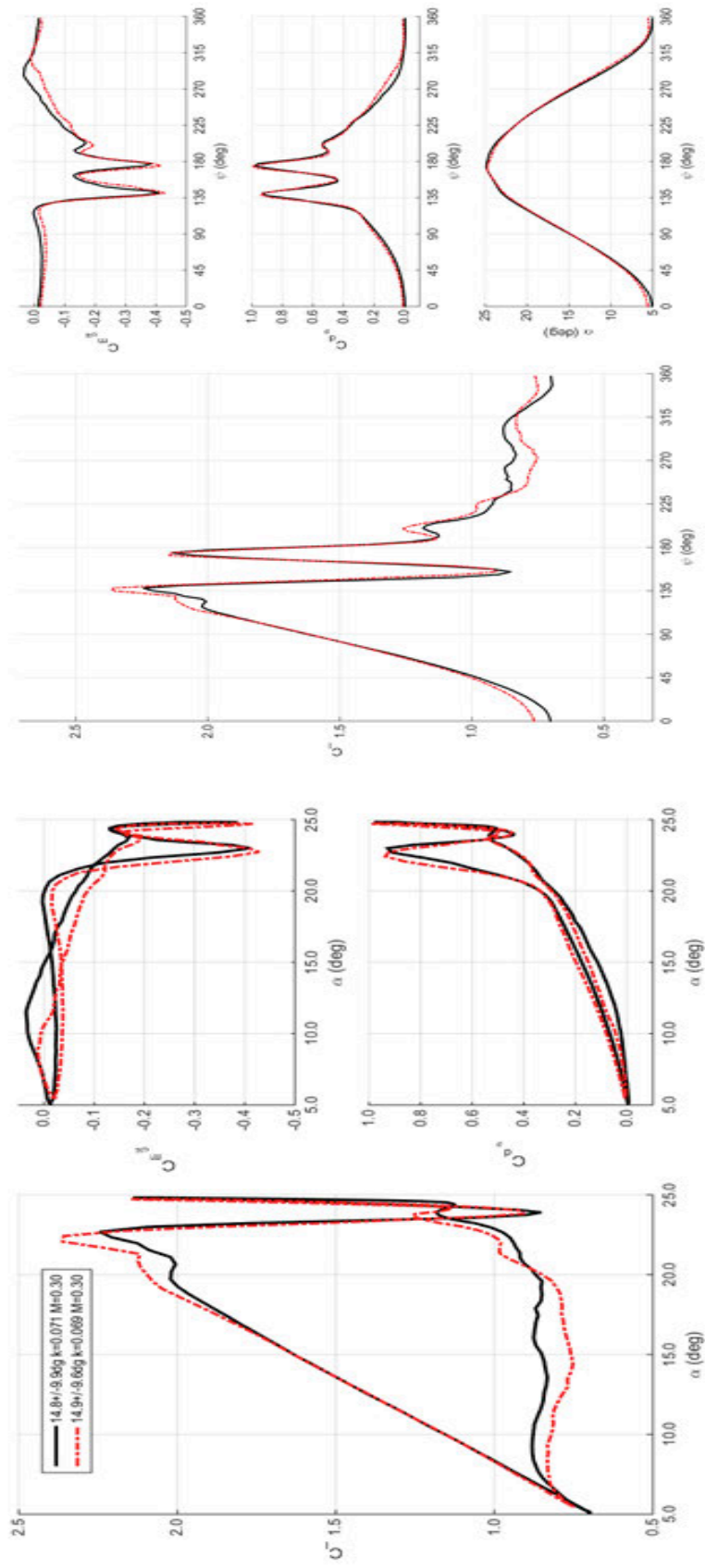
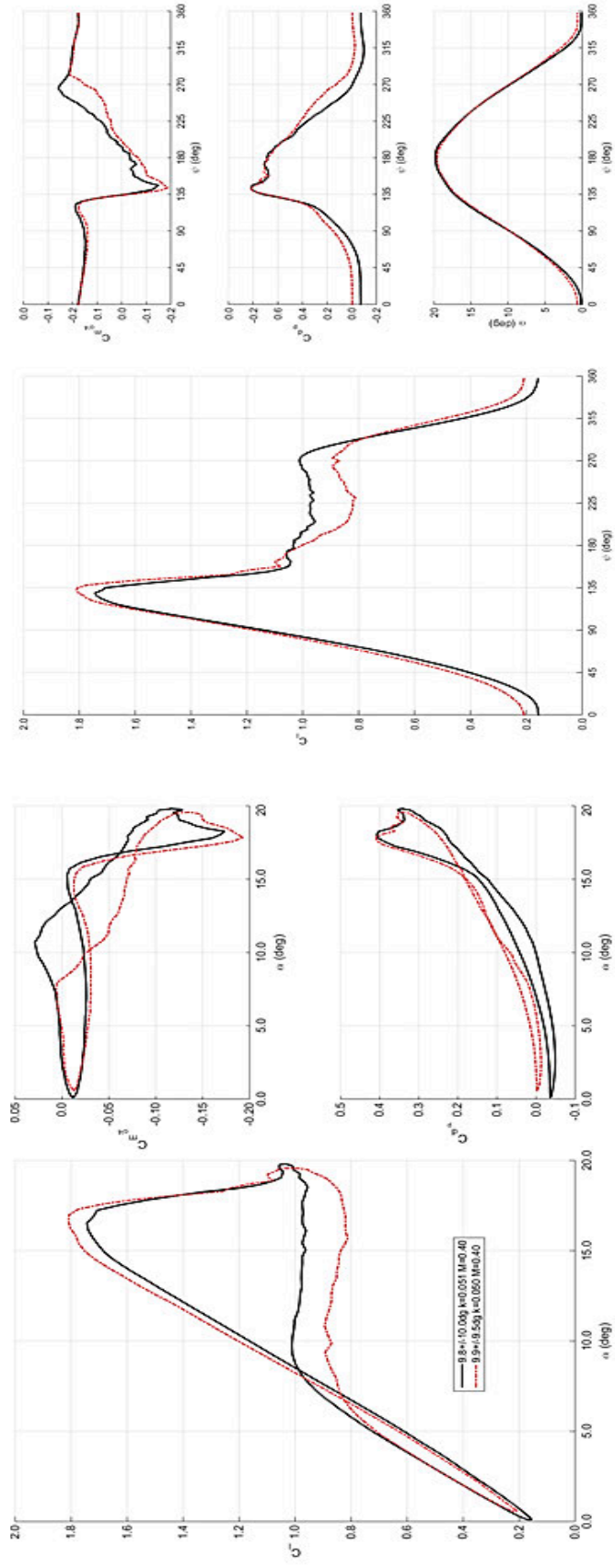
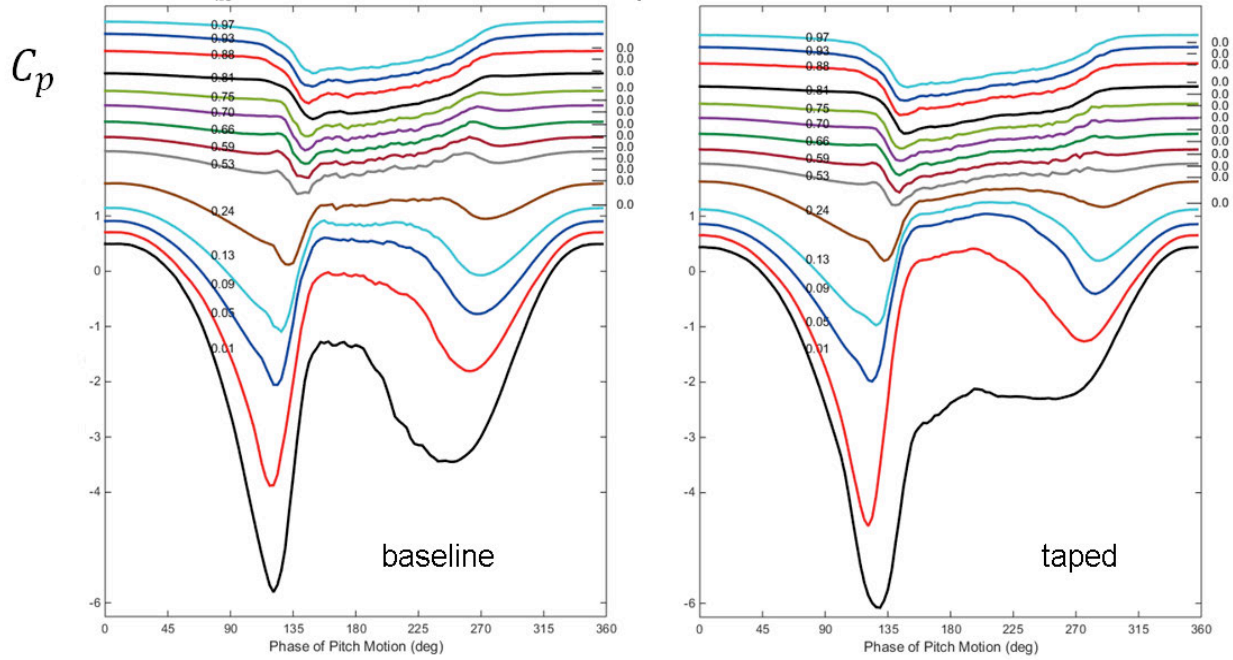


Figure 147. Comparison of unsteady loads plotted as function of angle-of-attack and phase,  $M = 0.3$ ,  $k = 0.07$ ,  $\alpha = 15^\circ \pm 10^\circ$ . Solid lines are baseline, dashed lines are taped.



**Figure 148.** Comparison of unsteady loads plotted as function of angle-of-attack and phase,  $M = 0.4$ ,  $k \approx 0.05$ ,  $\alpha = 10^\circ \pm 10^\circ$ . Solid lines are baseline, dashed lines are taped.

The loads develop in a similar fashion at Mach 0.4, as shown in Figure 148. The root cause of the increased upstroke airloads stems from an increase in leading-edge suction, as measured by the near leading edge pressure transducers. Figure 149 compares the  $M = 0.4$  suction-side  $C_p$  for  $k = 0.05$ ,  $\alpha = 10^\circ \pm 9.5^\circ$ . The forward transducer at  $x/c=0.01$  reached a peak suction of -6.08 for the taped slot, whereas it measured a suction peak of -5.81 for the baseline VR-12. The characteristics observed with the tape resemble that of a correctly sized trip.



**Figure 149. Upper surface pressure coefficient for  $M=0.4$ ,  $k = 0.05$ ,  $\alpha = 10^\circ \pm 10^\circ$ . Baseline left, taped slot right.**

### 3. High-Speed Wind Tunnel Test Steady COMPACT Results

#### A. Entry 1

The clean baseline leading edge was replaced with the COMPACT single-row actuated leading edge on the second and third days of Entry 1. Table 22 lists the steady actuated data sets.

**Table 22. Entry 1 Steady Data Sets**

Data Set	Name
8	R18 Mach 0.2 Bleed-off
9	R18 Mach 0.2 Bleed-on
10	R19 Mach 0.3 Bleed-off Alternating
11	R19 Mach 0.3 Bleed-on
12	R19 Mach 0.3 Bleed-off Sweep Up
13	R21 Mach 0.4 Bleed-off
14	R21 Mach 0.4 Bleed-on
15	R23 Mach 0.5 Bleed-off
16	R23 Mach 0.5 Bleed-on
17	R33 Mach 0.2 COMPACT Off Before
18	R33 Mach 0.2 COMPACT Off After
19	R33 Mach 0.2 COMPACT On $F^+=0.1$
20	R33 Mach 0.2 COMPACT On $F^+=0.2$
21	R33 Mach 0.2 COMPACT On $F^+=0.4$
22	R34 Mach 0.3 COMPACT Off Before
23	R34 Mach 0.3 COMPACT Off After
24	R34 Mach 0.3 COMPACT On $F^+=0.1$
25	R34 Mach 0.3 COMPACT On $F^+=0.2$
26	R34 Mach 0.3 COMPACT On $F^+=0.3$
27	R34 Mach 0.3 COMPACT On $F^+=0.4$
28	R35 Mach 0.4 COMPACT Off Before
29	R35 Mach 0.4 COMPACT Off After
30	R35 Mach 0.4 COMPACT On $F^+=0.1$
31	R35 Mach 0.4 COMPACT On $F^+=0.2$
32	R35 Mach 0.4 COMPACT On $F^+=0.3$
33	R36 Mach 0.3 COMPACT Off w/Tufts, No ESP
34	R36 Mach 0.3 COMPACT Off After
35	R36 Mach 0.3 COMPACT Blowing
36	R36 Mach 0.3 COMPACT On $F^+=0.1$
37	R36 Mach 0.3 COMPACT On $F^+=0.2$
38	R36 Mach 0.3 COMPACT On $F^+=0.3$
39	R38 Mach 0.3 COMPACT Off w/Tufts
40	R38 Mach 0.3 COMPACT Blowing
41	R38 Mach 0.3 COMPACT On $F^+=0.1$
42	R38 Mach 0.3 COMPACT On $F^+=0.2$ Tuning
43	R38 Mach 0.3 COMPACT On $F^+=0.2$
44	R38 Mach 0.3 COMPACT On $F^+=0.3$
48	R47 Mach 0.1 COMPACT Off

#### *Effect of Open Slot and Bleed Air*

Figure 150 shows the effect at Mach 0.3 of a sequential conversion from the baseline smooth leading edge, to the COMPACT leading edge with the blowing slot taped, to the slot open, and to

the slot open with the bleed air activated. As discussed in the baseline section, installing the segmented COMPACT leading edge with the slot taped (the red symbols) has little effect prior to stall, but reduces  $C_{l,max}$  and causes the post-stall lift coefficient to be significantly lower. Opening the slot (the blue symbols) has little additional impact. Introducing bleed air without combustion (the green symbols) reduces the stall angle from  $\alpha=16^\circ$  to  $\alpha=14.5^\circ$ , lowers  $C_{l,max}$ , but does not further change the post-stall lift. The pitching moment coefficient effects are consistent: the post-stall  $C_m$  becomes more negative with the COMPACT leading edge installed, and again with the slot. Turning on the bleed air reduces the initial drop in  $C_m$ .

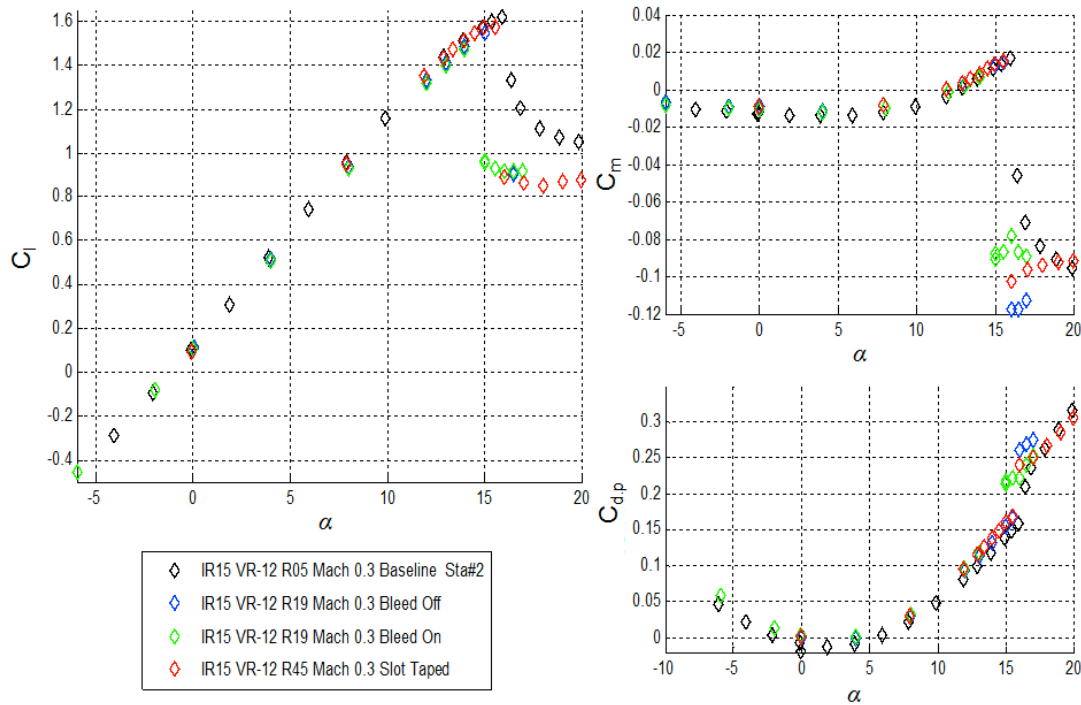


**Figure 150. Lift, drag, and moment coefficients for steady unactuated airfoil, Mach 0.3, Station 2 comparison of baseline, taped slot, open slot, and open slot with bleed air.**

Figure 151 compares the pressure distributions for these unactuated configurations. There is very little effect though  $\alpha=14^\circ$ , but the bleed-on configuration is separated at the leading edge at  $\alpha=15^\circ$ , and the open and taped slots are separated at  $\alpha=16^\circ$ . The baseline maintains a stronger suction peak through  $\alpha=20^\circ$ . Appendix 2 shows load and pressure coefficients at the other Mach numbers.

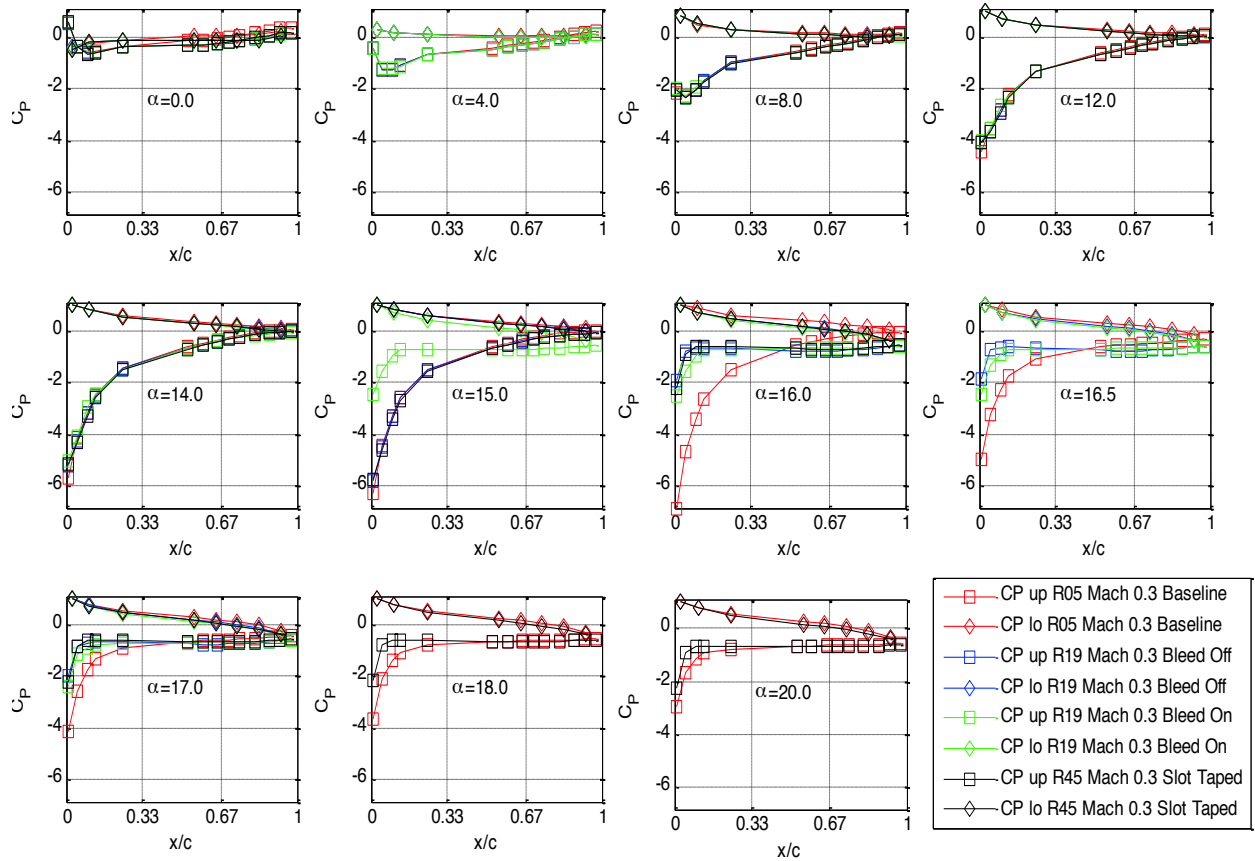
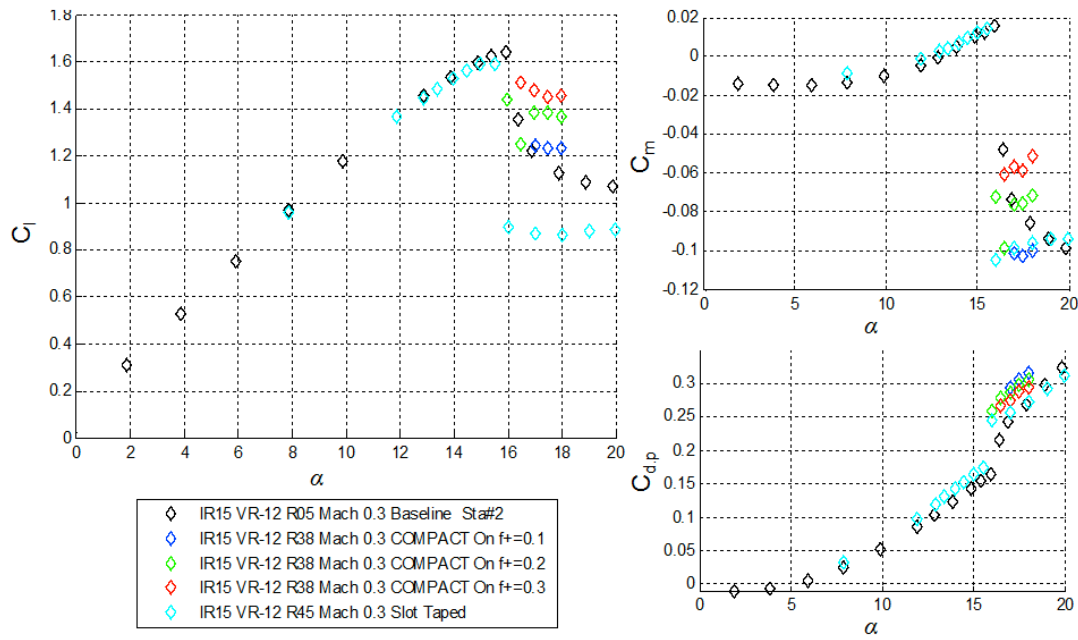


**Figure 151. Pressure coefficients at Station 2 for steady unactuated airfoil, Mach 0.3; comparison of baseline, taped slot, open slot, and open slot with bleed air.**

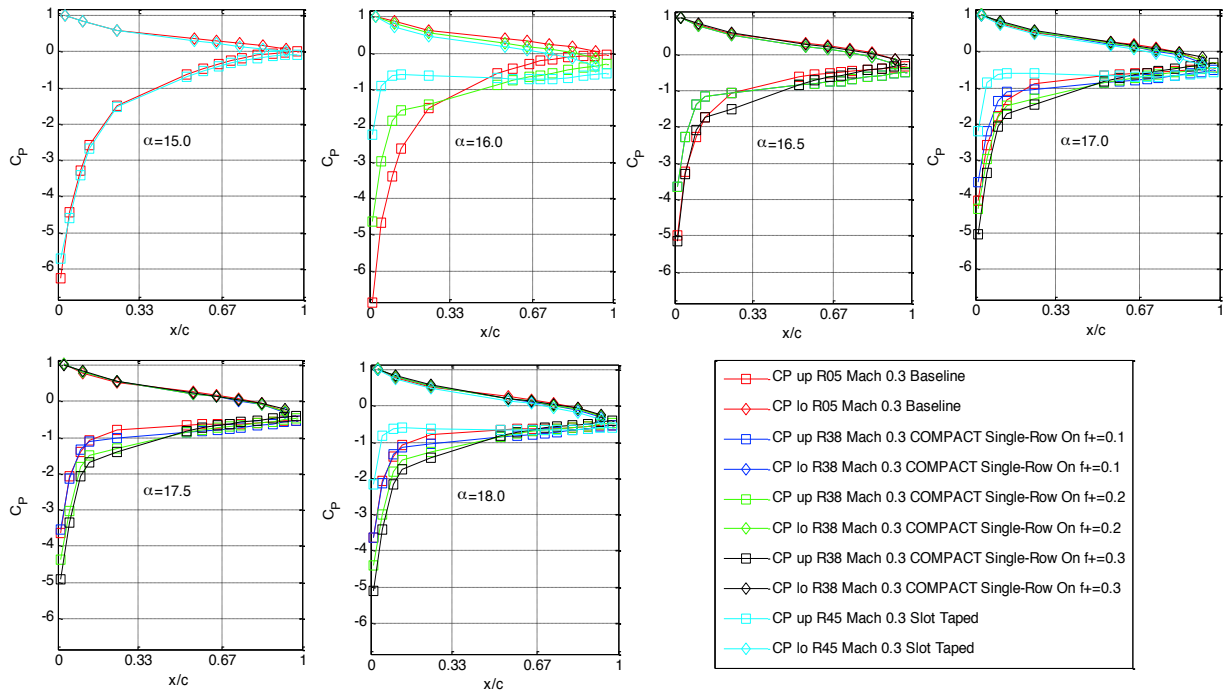
### **COMPACT at Mach 0.3**

Figure 152 shows the effect of actuation on the aerodynamic coefficients at Mach 0.3. Results are provided for the baseline leading edge, the taped slot, and for continuous COMPACT actuation at  $F^+ = 0.1, 0.2$ , and  $0.3$ . At  $F^+ = 0.1$ , the post-stall  $C_l$  has almost recovered to the baseline leading edge values. Increasing actuation frequency improves the stall angle,  $C_{l,max}$ , and the post-stall  $C_l$  and  $C_m$  beyond the baseline. Pressure coefficients for these cases are compared in Figure 153. Above  $\alpha=16^\circ$ , all of the COMPACT-on cases have higher leading edge suction than the baseline, with  $F^+=0.3$  providing the highest benefit. With COMPACT operating continuously at  $F^+=0.3$ , Figure 154 compares Mach 0.3 pressure distributions for the two ESP stations at  $\alpha=16.5^\circ, 17^\circ, 17.5^\circ$ , and  $18^\circ$ , all above the baseline stall angle. For this run, the two leading edge taps at Station 4 were accidentally disconnected. The upper station trailing edge pressures are higher at  $\alpha=16.5^\circ$  and  $17^\circ$ , perhaps indicating lower lift, and lower at  $\alpha=18.5^\circ$  and  $18^\circ$ , indicating stronger flow separation away from the actuated portion of the model.





**Figure 152. Lift, drag, and moment coefficients for steady actuated airfoil, Mach 0.3, Station 2; comparison of baseline, taped slot, and COMPACT at  $F^+ = 0.1, 0.2$ , and  $0.3$ .**



**Figure 153. Pressure coefficients for steady actuated airfoil, Mach 0.3, Station 2; comparison of baseline, taped slot, and COMPACT at  $F^+ = 0.1, 0.2$ , and  $0.3$ .**

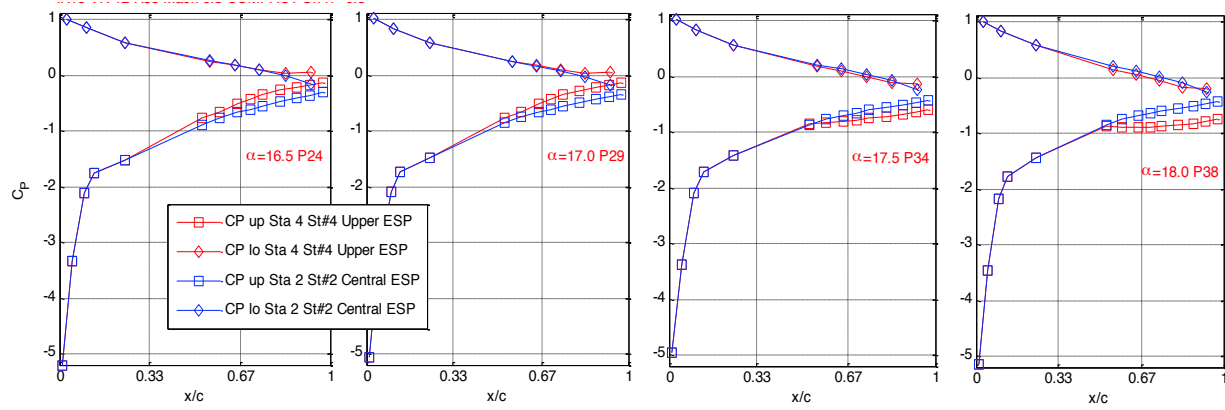


**Figure 154. Surface pressure distributions at central and upper stations for COMPACT at  $F^+=0.3$  and Mach 0.3 at multiple steady angles.**

### **COMPACT at Mach 0.2**

The qualitative load and pressure coefficient results are similar at Mach 0.2, shown in Figure 155, and Figure 156 respectively, are quite similar to those described above for Mach 0.3. The baseline stall characteristics are recovered at low actuation frequency, and the stall and post-stall characteristics are improved at higher frequencies.

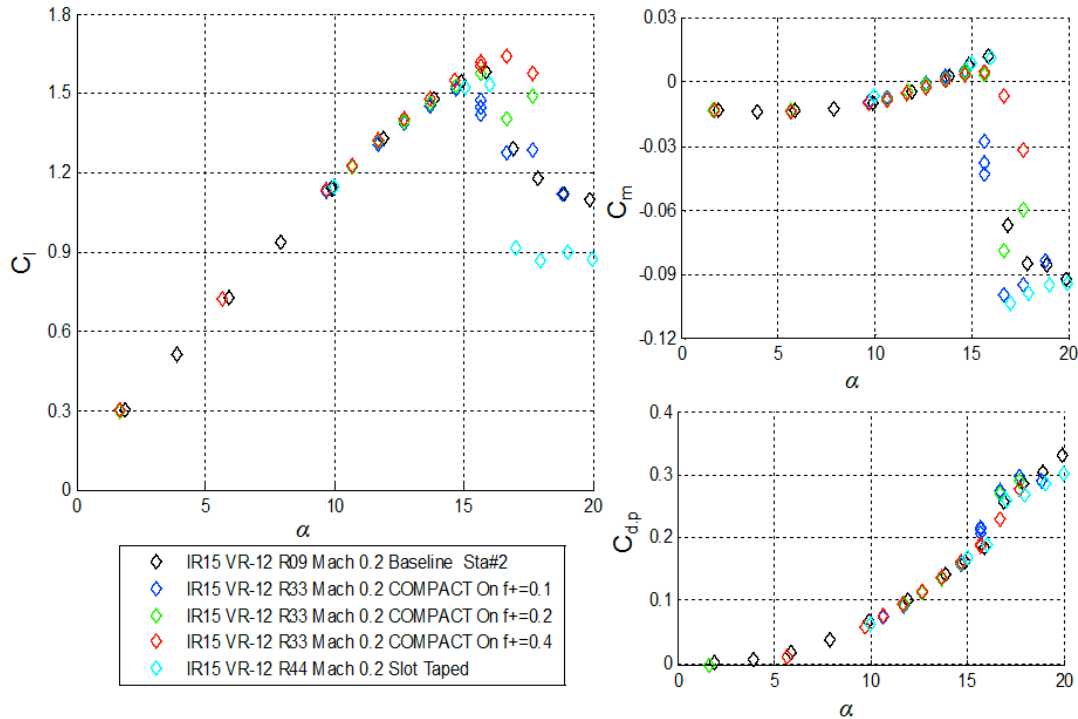


**Figure 155. Lift, drag, and moment coefficients for steady actuated airfoil, Mach 0.2, Station 2; comparison of baseline, taped slot, and COMPACT at  $F^+ = 0.1, 0.2$ , and 04.**

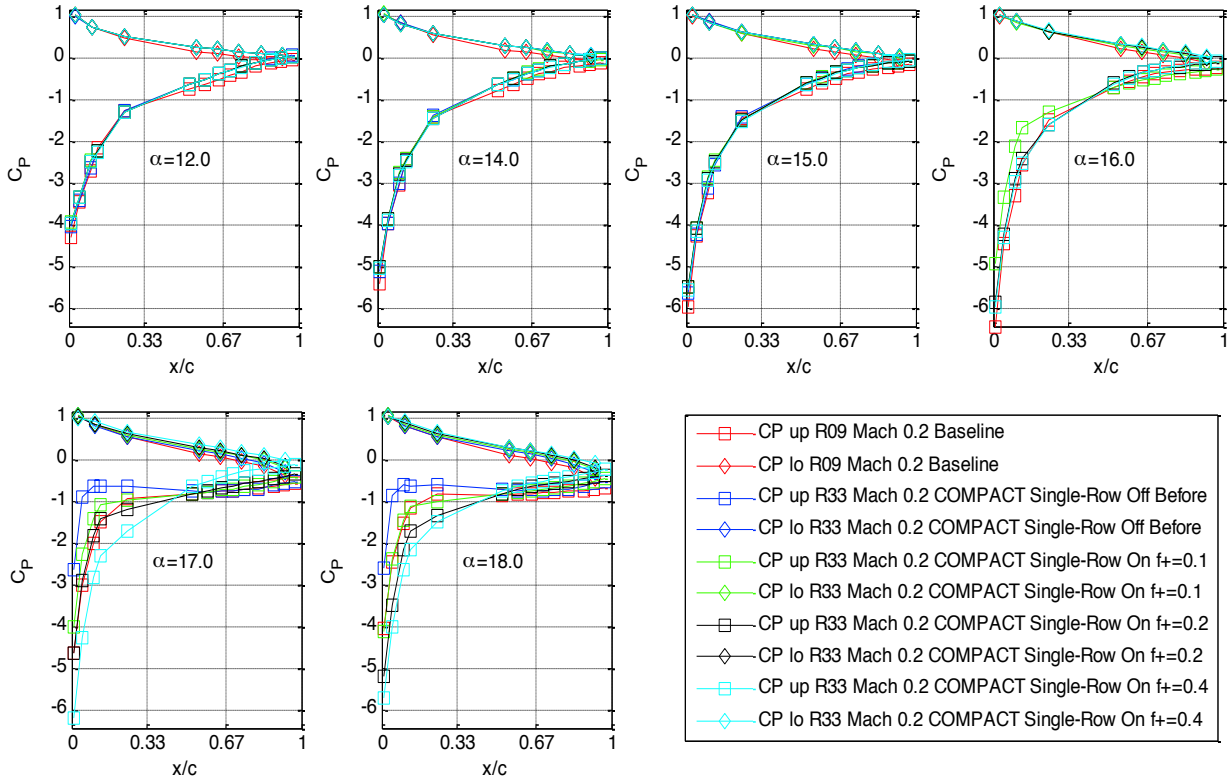


**Figure 156. Pressure coefficients for steady actuated airfoil, Mach 0.2, Station 2; comparison of baseline, taped slot, and COMPACT at  $F^+ = 0.1$ , 0.2, and 0.4.**

### **COMPACT at Mach 0.4 and 0.5**

At Mach 0.4, as shown in Figure 157 and Figure 158, the stall angle and  $C_{l,max}$  are unaffected by actuation, and there are no substantial changes in the post-stall characteristics from the taped slot values. Table 23 shows baseline, open slot, and bleed-on steady results at Mach 0.5. No steady COMPACT or taped slot data were acquired for Mach 0.5. For both of the higher Mach number cases, installing the segmented leading edge, opening the slot, and introducing bleed air all adversely impacted the post stall lift and moment coefficients. The nondimensional actuation flow rates and frequencies available in this first entry were unable to restore the steady baseline characteristics.

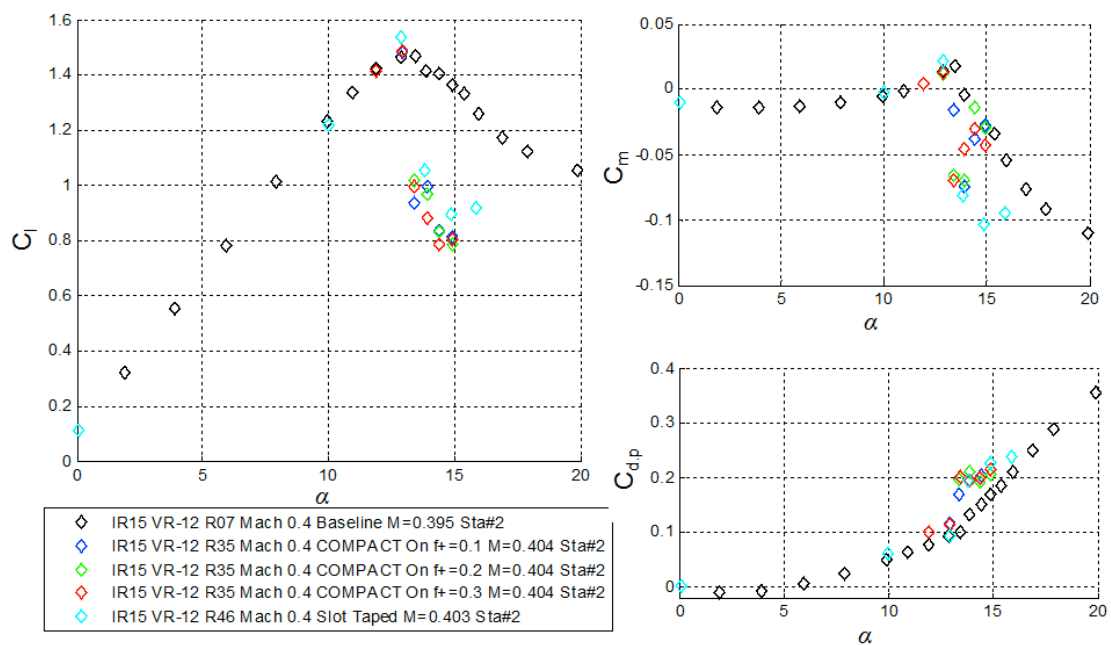


**Figure 157. Lift, drag, and moment coefficients for steady actuated airfoil, Mach 0.4, Station 2; comparison of baseline, taped slot, and COMPACT at  $F^+ = 0.1, 0.2$ , and  $0.3$ .**

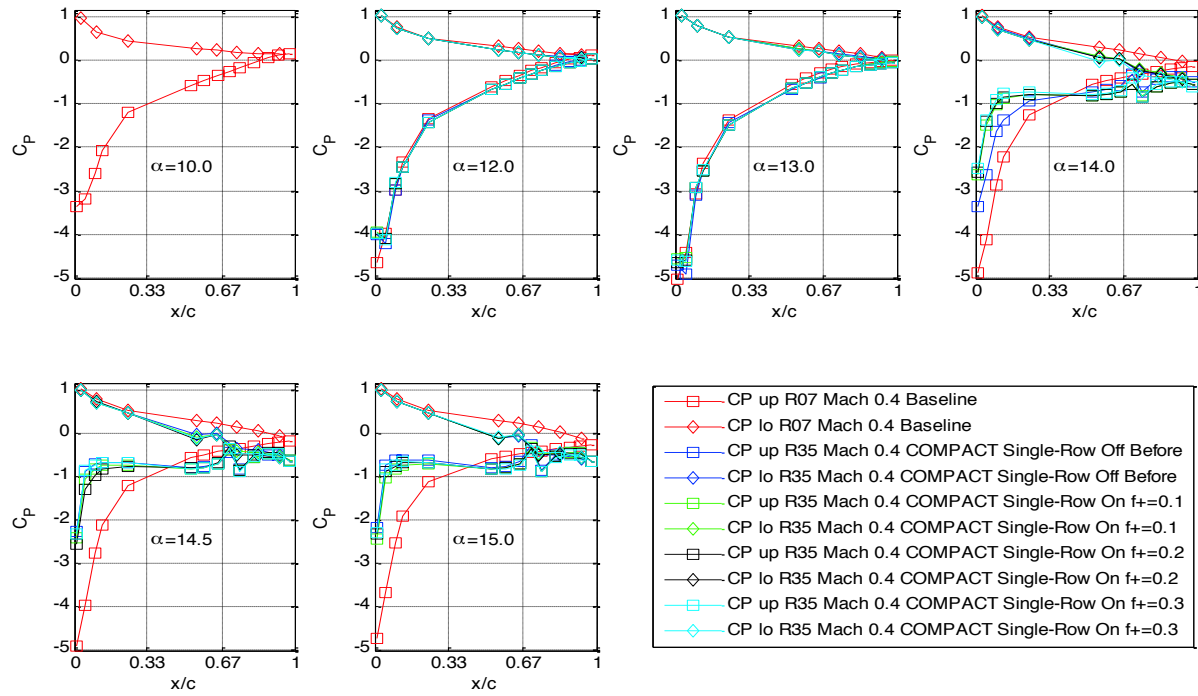


**Figure 158. Pressure coefficients for steady actuated airfoil, Mach 0.4, Station 2; comparison of baseline, taped slot, and COMPACT at  $F^+ = 0.1, 0.2$ , and  $0.3$ .**

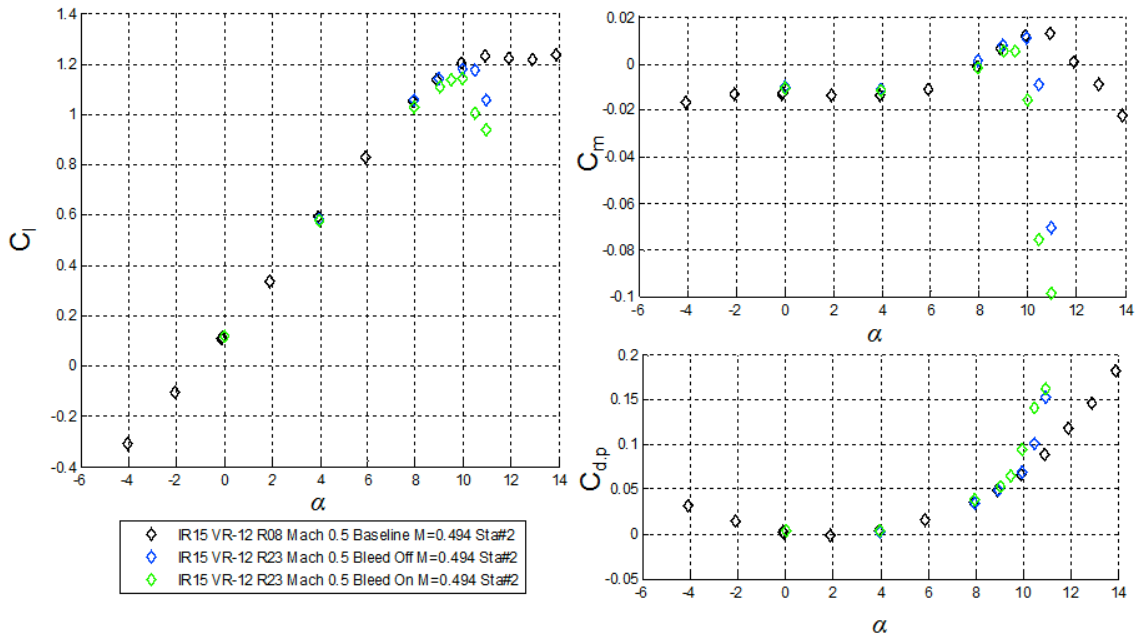


**Figure 159. Lift, drag, and moment coefficients for steady airfoil, Mach 0.5, Station 2; comparison of baseline, open slot, and bleed-on cases.**

## **B. Entry 2**

After the clean baseline leading edge was replaced with the COMPACT single-row actuated leading edge, several sets of runs were performed during the second and third days of Entry 2 to adjust and optimize the flow control system. Following this checkout period, final COMPACT single-row steady runs were performed at Mach 0.2, 0.3, 0.4, and 0.5.

The COMPACT dual-row actuated leading edge was then installed, and operated in several modes, such as front row only, rear row only, dual-row simultaneous, and dual-row alternating. Steady runs were performed at Mach 0.3 and 0.4. On the final test day the firing approach referred to as “alternating sweep” was implemented. Here, the rear actuator was triggered based on assumed fluid convective time scales related to the freestream conditions and distance between the forward and rear slots.

Table 23 identifies the data sets. Section load coefficients at Station 2 for all Entry 2 steady runs will be presented below. A summary of the results is:

- a) Single-row actuation in Entry 2 provided substantial post stall improvements in lift and pitching moment compared to the baseline, and especially compared to the open slot – unactuated leading edge
- b) Dual-row actuation provided much smaller benefits as directly measured. (This observation is likely affected by the dual row configuration having a much smaller spanwise extent)
- c) For the same actuated span, firing both rows typically produced larger aerodynamic gains than the single-row alone.

**Table 23. Entry 2 Steady Data Sets**

<b>Data Set</b>	<b>Name</b>
<b>50</b>	R58 Mach 0.2 Open Slot Bleed-off
<b>51</b>	R67 Mach 0.2 Open Slot Bleed-off
<b>52</b>	R67 Mach 0.2 Open Slot Bleed-on
<b>53</b>	R67 Mach 0.2 COMPACT Single-Row $F^+=0.2,0.4,0.6,0.8$
<b>57</b>	R52 Mach 0.3 Baseline Entry 2
<b>58</b>	R59 Mach 0.3 Open Slot Bleed-off
<b>59</b>	R61 Mach 0.3 Open Slot Bleed-off & On
<b>61</b>	R61 Mach 0.3 COMPACT Single-Row On $F^+=0.2,0.4,0.6,0.8$
<b>65</b>	R62 Mach 0.3 Open Slot Bleed-off & On
<b>67</b>	R62 Mach 0.3 COMPACT Single-Row On $F^+=0.2,0.4,0.6,0.8$
<b>71</b>	R65 Mach 0.3 Open Slot Bleed-off (steady check pts)
<b>72</b>	R78 Mach 0.3 Open Slot Bleed-off & On (extension to 30°)
<b>74</b>	R78 Mach 0.3 COMPACT Single-Row $F^+=0.2-0.8$ (extension to 30°)
<b>80</b>	R60 Mach 0.4 Open Slot Bleed-off & On
<b>82</b>	R60 Mach 0.4 COMPACT Single-Row On $F^+=0.2,0.4,0.6$
<b>85</b>	R63 Mach 0.4 Open Slot Bleed-off (steady check pts)
<b>86</b>	R68 Mach 0.4 Open slot bleed-off (steady check pts)
<b>87</b>	R76 Mach 0.5 Open Slot Bleed-off & On
<b>89</b>	R76 Mach 0.5 COMPACT Single-Row On $F^+=0.2, 0.4$
<b>91</b>	R84 Mach 0.3 COMPACT Dual-Row Open Slot Bleed-off & On
<b>93</b>	R85 Mach 0.3 COMPACT Dual-Row Front $F^+=0.2,0.4,0.6,0.8$
<b>97</b>	R85 Mach 0.3 COMPACT Dual-Row Back $F^+=0.2,0.4,0.6,0.8$
<b>101</b>	R85 Mach 0.3 COMPACT Dual-Row Both Sim $F^+=0.2,0.4,0.6,0.8$
<b>105</b>	R85 Mach 0.3 COMPACT Dual-Row Alt 50 $F^+=0.2,0.4,0.6,0.8$
<b>109</b>	R89 Mach 0.4 COMPACT Dual-Row Open Slot Bleed-off & On
<b>111</b>	R89 Mach 0.4 COMPACT Dual-Row Front $F^+=0.2,0.4,0.6$
<b>114</b>	R89 Mach 0.4 COMPACT Dual-Row Back $F^+=0.2,0.4,0.6$
<b>117</b>	R89 Mach 0.4 COMPACT Dual-Row Both Sim $F^+=0.2,0.4,0.6$
<b>120</b>	R89 Mach 0.4 COMPACT Dual-Row Alt 50 $F^+=0.2,0.4,0.6$
<b>123</b>	R89 Mach 0.4 COMPACT Dual-Row $F^+=0.2,0.4,0.6$ AoA=18 Alt Sweep
<b>126</b>	R90 Mach 0.3 COMPACT Dual-Row Open Slot Bleed-off & On
<b>128</b>	R90 Mach 0.3 COMPACT Dual-Row Front $F^+=0.2,0.4,0.6,0.8$
<b>132</b>	R90 Mach 0.3 COMPACT Dual-Row Back $F^+=0.2,0.4,0.6,0.8$
<b>136</b>	R90 Mach 0.3 COMPACT Dual-Row Both Sim $F^+=0.2,0.4,0.6$
<b>139</b>	R90 Mach 0.3 COMPACT Dual-Row Alt 50 $F^+=0.2,0.4,0.6,0.8$
<b>143</b>	R90 Mach 0.3 COMPACT Dual-Row $F^+=0.2,0.4,0.6,0.8$ AoA=18 Alt Sweep



## COMPACT Single-Row

### Mach 0.3 Load and Pressure Coefficients

Figure 161 to Figure 163 illustrates the initial two steady actuated runs at Mach 0.3. Figure 161 shows the Day 3, Run 61 steady actuated results for four values of  $F^+$ , as well as for the open slot and bleed-on configurations. As in Entry 1, the open slot reduced the post stall lift below the baseline. The lowest frequency actuation at  $F^+ = 0.2$  provided a modest improvement in  $C_L$ , while the higher frequency actuation at  $F^+ = 0.4, 0.6$ , and  $0.8$  provided substantial peak post-stall increases of  $\Delta C_L = 0.5$  and  $\Delta C_m = 0.05$ , with smaller improvements persisting out to  $\alpha = 20^\circ$ .

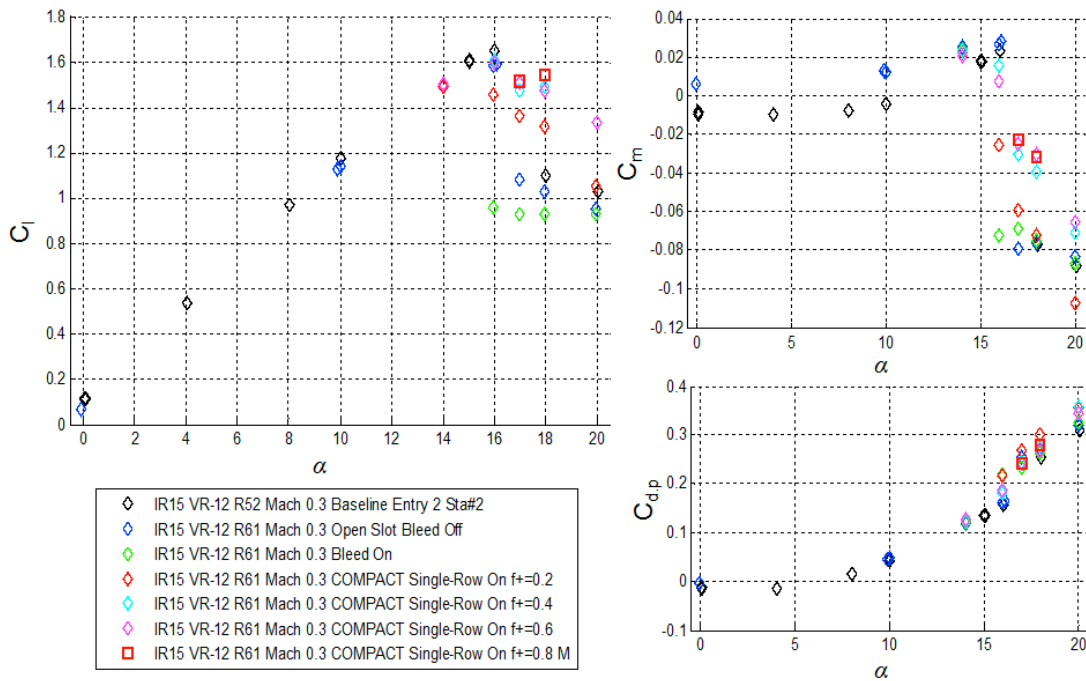


**Figure 160. Lift, drag, and moment coefficients at Mach 0.3 for baseline, open slot, and single-row COMPACT at  $F^+ = 0.2$  to  $0.8$ . Entry 2, Day 3, Run 61.**

Figure 161 shows the corresponding Run 61 pressure coefficients at Station 2 at  $\alpha = 16^\circ, 17^\circ, 18^\circ$ , and  $20^\circ$ . The upper surface pressures for  $F^+ = 0.6$  and  $0.8$  show a particularly large movement away from a flat distribution characteristic of separated flow towards a more gradual gradient typical of attached flow.

The equivalent load and pressure coefficient results for Day 4, Run 62 are shown in Figure 162 and Figure 163, respectively. The post-stall  $\Delta C_L$  and  $\Delta C_m$  at  $F^+ = 0.6$  and  $0.8$  are slightly higher for Run 62, reflected successful adjustments in the COMPACT system.

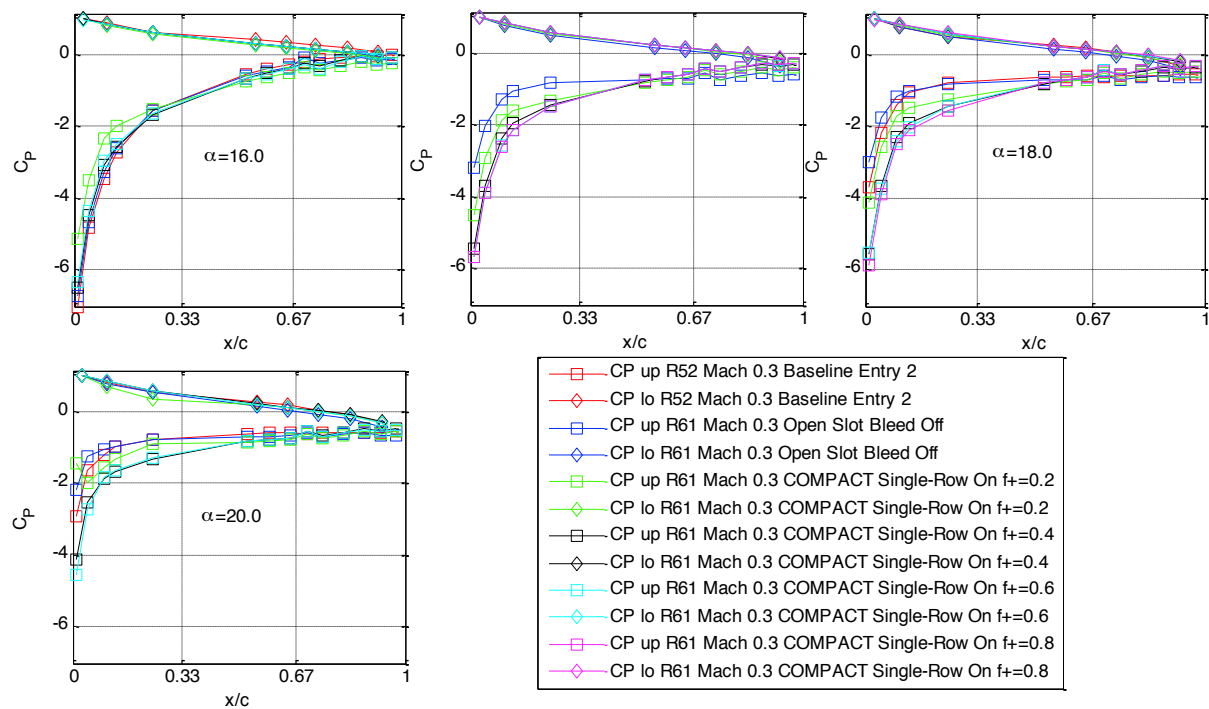


Figure 161. Pressure coefficients at Mach 0.3 for baseline, and single-row COMPACT at  $F^+ = 0.2$  to 0.8. Entry 2, Day 3, Run 61.

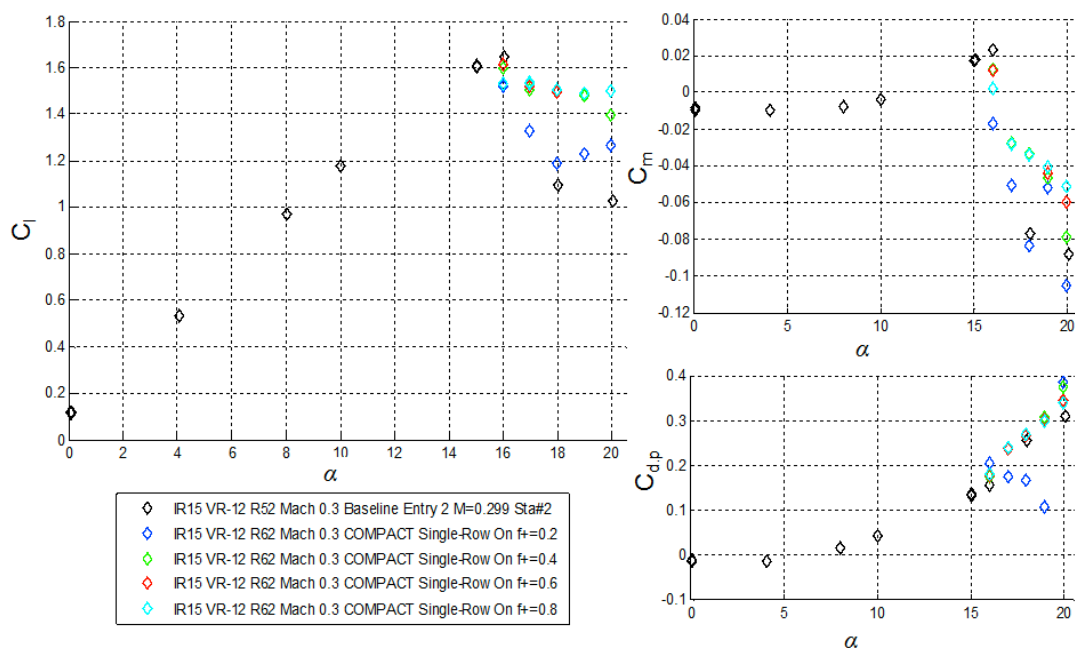
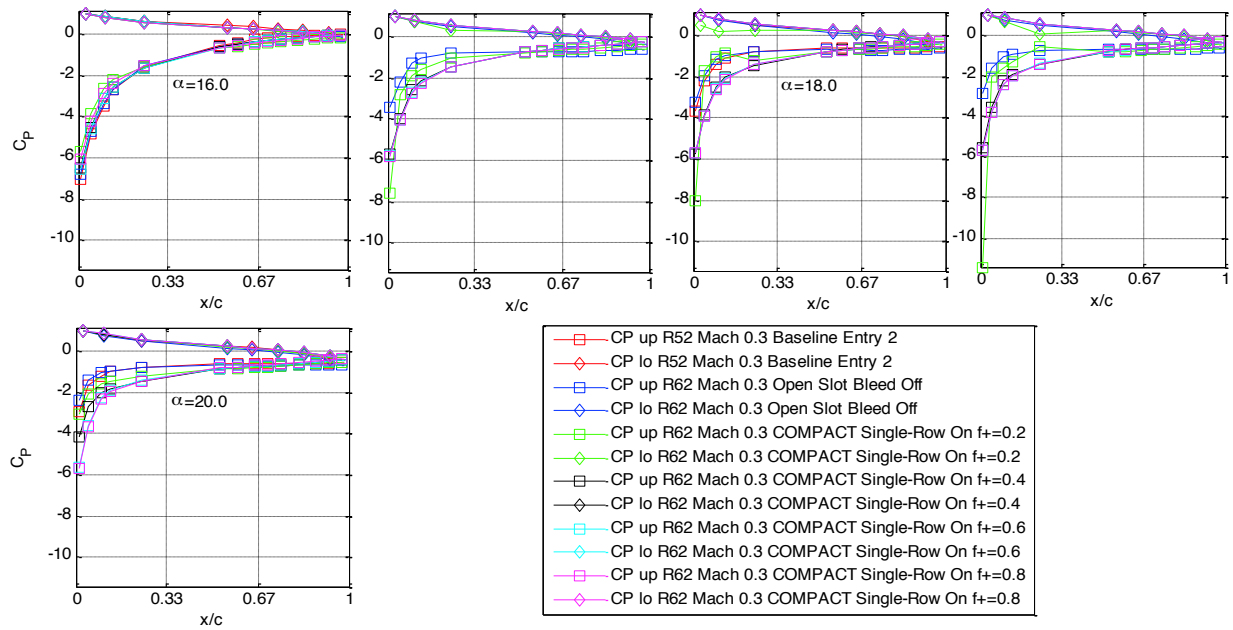
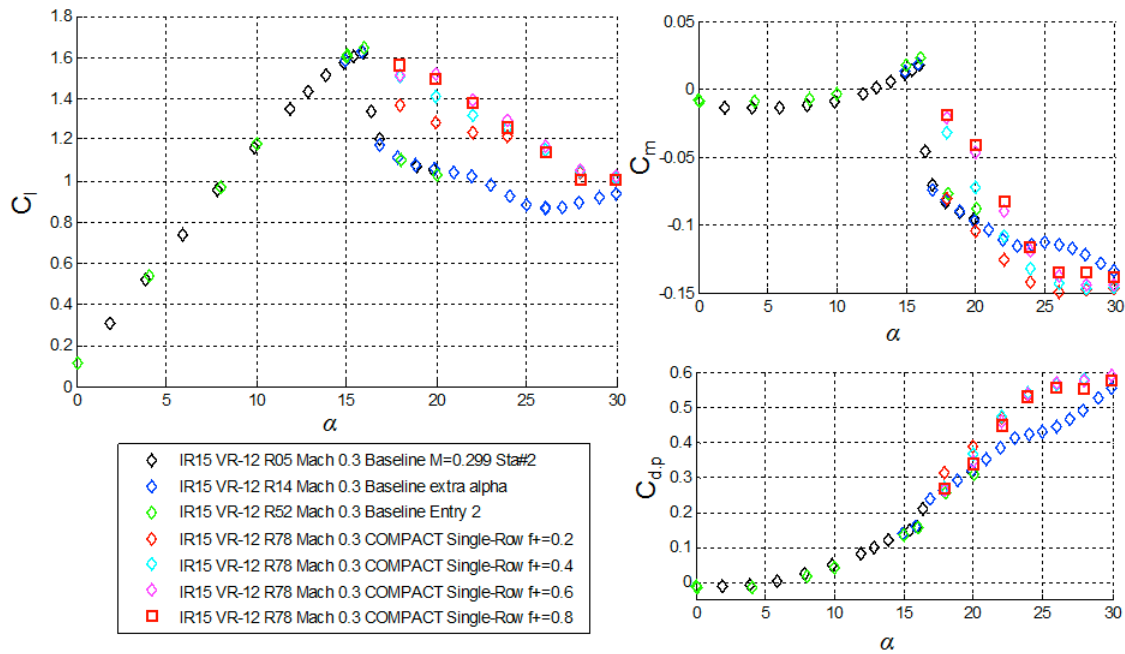


Figure 162. Lift, drag, and moment coefficients at Mach 0.3 for baseline, and single-row COMPACT at  $F^+ = 0.2$  to 0.8. Entry 2, Day 4, Run 62.



**Figure 163. Pressure coefficients at Mach 0.3 for baseline, and single-row COMPACT at  $F^+ = 0.2$  to 0.8. Entry 2, Day 4 Run 62.**

Figure 164 and Figure 165 show the final set of Mach 0.3 single-row results, for Day 4, Run 78, with the angle-of-attack range extended to  $\alpha = 30^\circ$ . The trends with frequency are similar to those shown for  $16^\circ < \alpha \leq 20^\circ$ , but the benefit compared to the baseline is reduced above  $\alpha = 25^\circ$ .



**Figure 164. Extended angle lift, drag, and moment coefficients at Mach 0.3 for baseline, and single-row COMPACT at  $F^+=0.2$  to 0.8. Entry 2, Day 4 Run 78.**

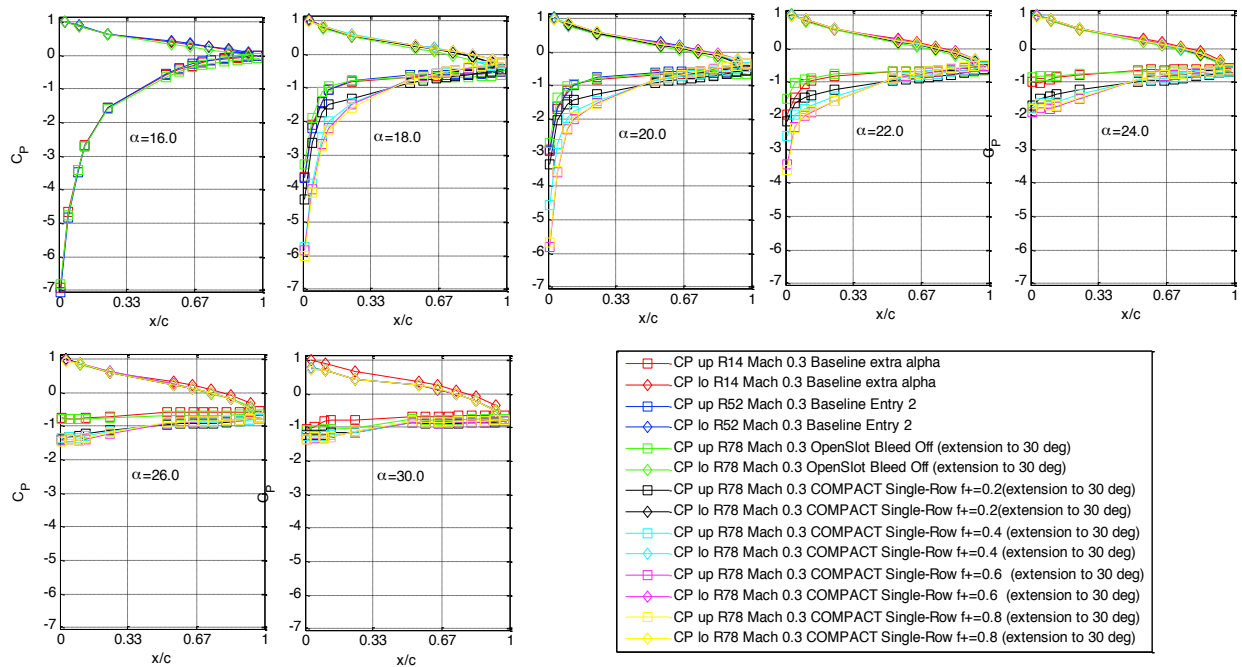


**Figure 165. Extended angle pressure coefficients at Mach 0.3 for baseline, and single-row COMPACT at  $F^+=0.2$  to 0.8. Entry 2, Day 4 Run 78.**

### Spanwise Pressure Variations

Figure 166 and Figure 167 show the spanwise variation in  $C_p$  for actuated cases at Mach 0.2 and 0.3, respectively. The two central locations, Stations #1 and #2, exhibit characteristics of attached flow over the aft region for  $\alpha \geq 18^\circ$ , while the mid and upper stations show flatter profiles, indicating separated flow. Only one of the two leading edge taps at Station #4 was functional, but it also indicated the flow away from the actuated region was more separated.

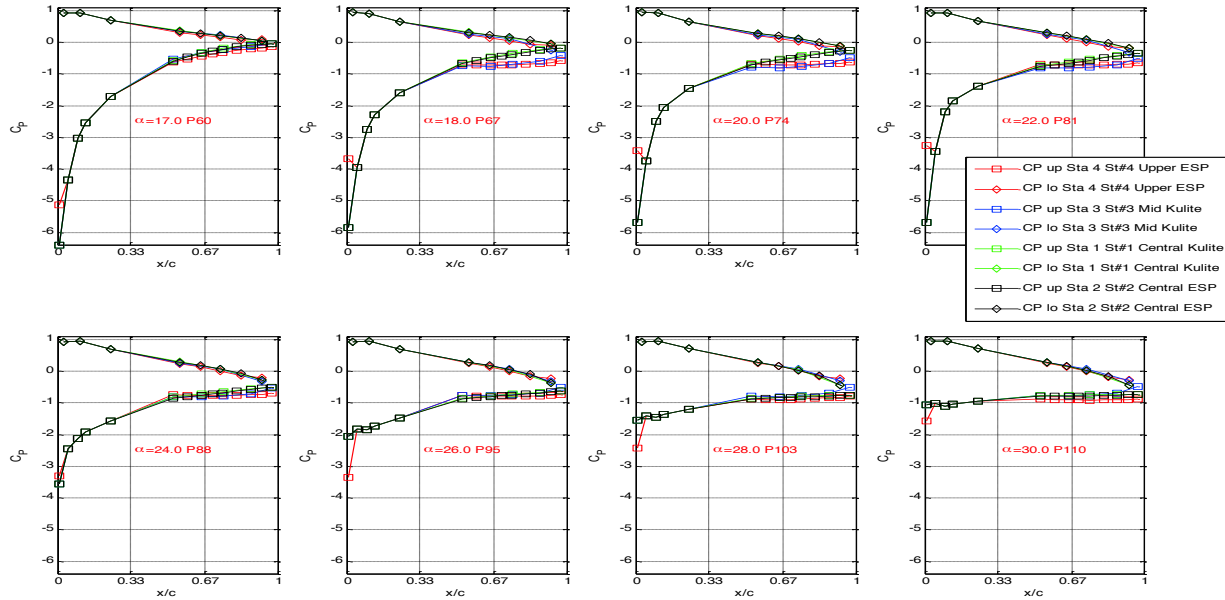


**Figure 166. Pressure coefficient spanwise variation at Mach 0.2 for single-row COMPACT at  $F^+ = 0.4$ . Entry 2, Day 4 Run 67.**

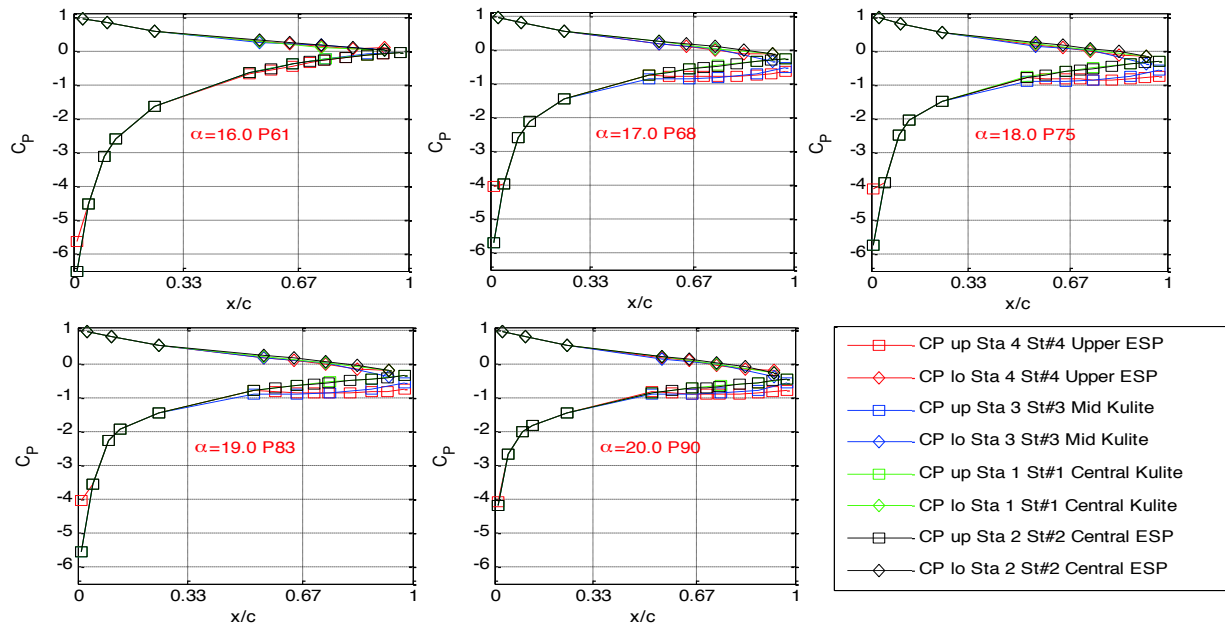


**Figure 167. Pressure coefficient spanwise variation at Mach 0.3 for single-row COMPACT at  $F^+ = 0.4$ . Entry 2, Day 4 Run 62.**

### ***Mach 0.4 Load and Pressure Coefficients***

Single-row COMPACT actuation continues to perform well at Mach 0.4, as shown in Figure 168. Again the higher frequencies of  $F^+=0.4$  and  $0.6$  provided the strongest benefits, up to a post-stall  $\Delta C_l = 0.3$  and  $\Delta C_m = 0.02$ , persisting out to  $\alpha=20^\circ$ .

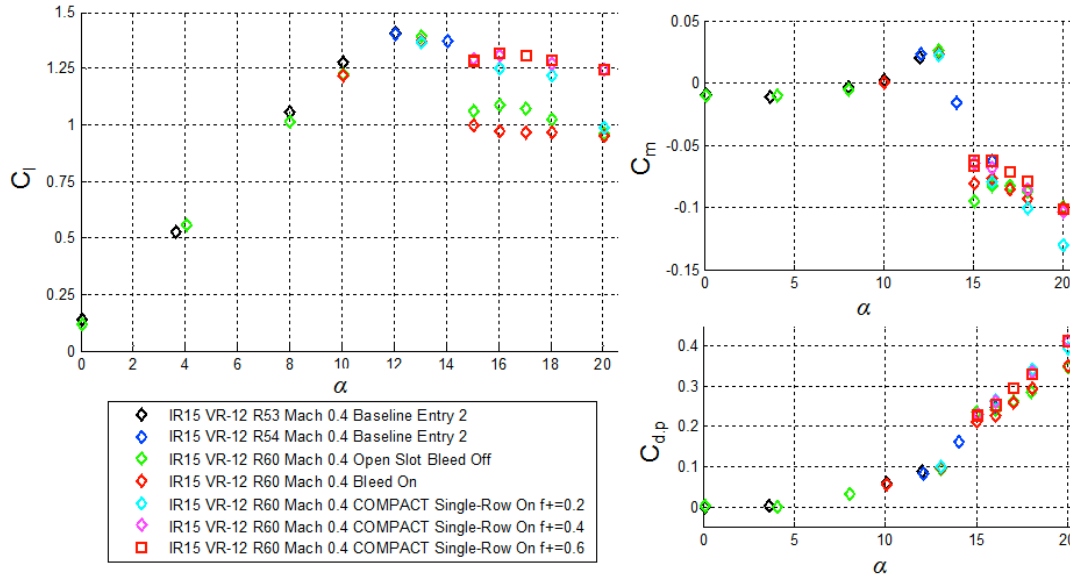


**Figure 168. Lift, drag, and moment coefficients at Mach 0.4 for baseline, open slot, and single-row COMPACT at  $F^+=0.2$  to  $0.68$ . Entry 2, Day 3 Run 60.**

Figure 169 compares pressure distributions at Mach 0.4 for the baseline, open slot, and actuated conditions. They all match below stall at  $\alpha=10^\circ$ , while the open slot separates early at  $\alpha=15^\circ$ . For  $\alpha \geq 16^\circ$  the actuated pressure distributions are fuller at the leading edge and maintain a pressure gradient near the trailing edge, corresponded to a more attached flow.

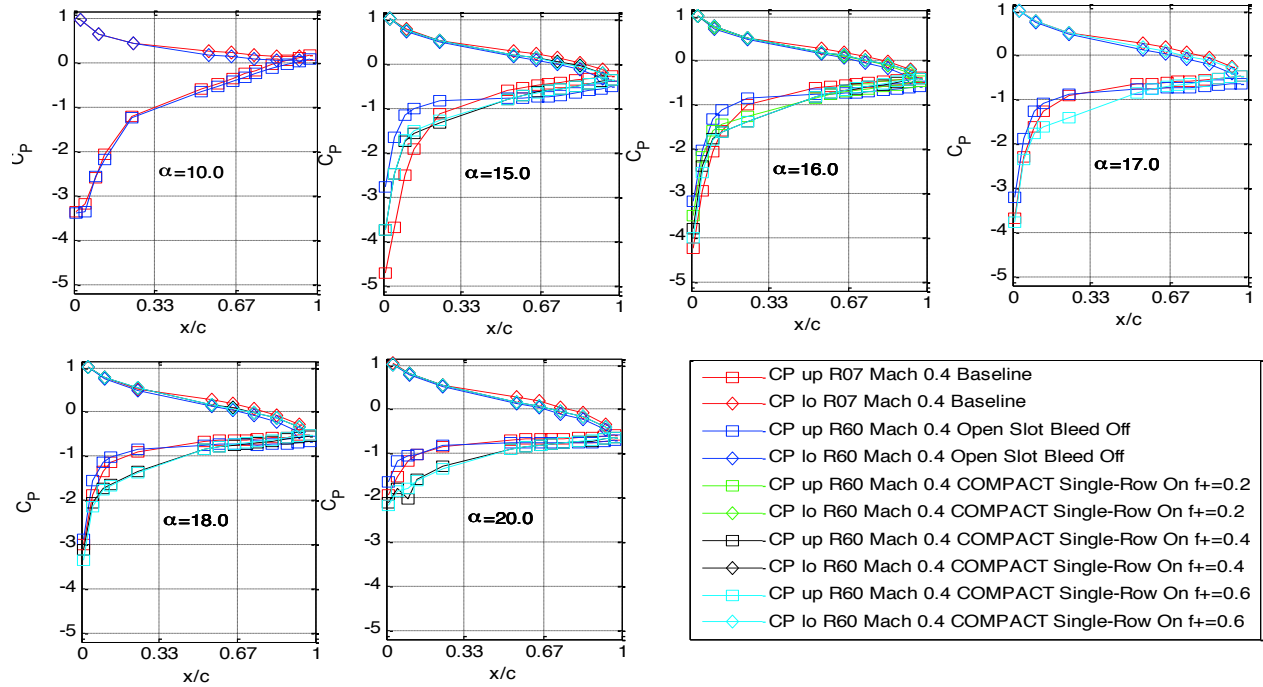


**Figure 169. Pressure coefficients at Mach 0.4 for baseline, open slot, and single-row COMPACT at  $F^+ = 0.2$  to 0.6. Entry 2, Day 3 Run 60.**

#### ***Mach 0.5 Load and Pressure Coefficients***

Little effect was produced by COMPACT at Mach 0.5, as shown in Figure 170. At  $\alpha = 14^\circ$ , the actuated lift is less than the baseline, and the pitching moment is more negative. The only change seen in the Figure 171 pressure distributions is that all the open slot and attempted actuation conditions show more leading edge separation at  $\alpha = 14^\circ$ . As discussed in the actuation and dynamic stall sections, it was likely that COMPACT was not firing properly if at all at the low static pressures produced by the combination of low test section static pressures at Mach 0.5 and leading edge suction.



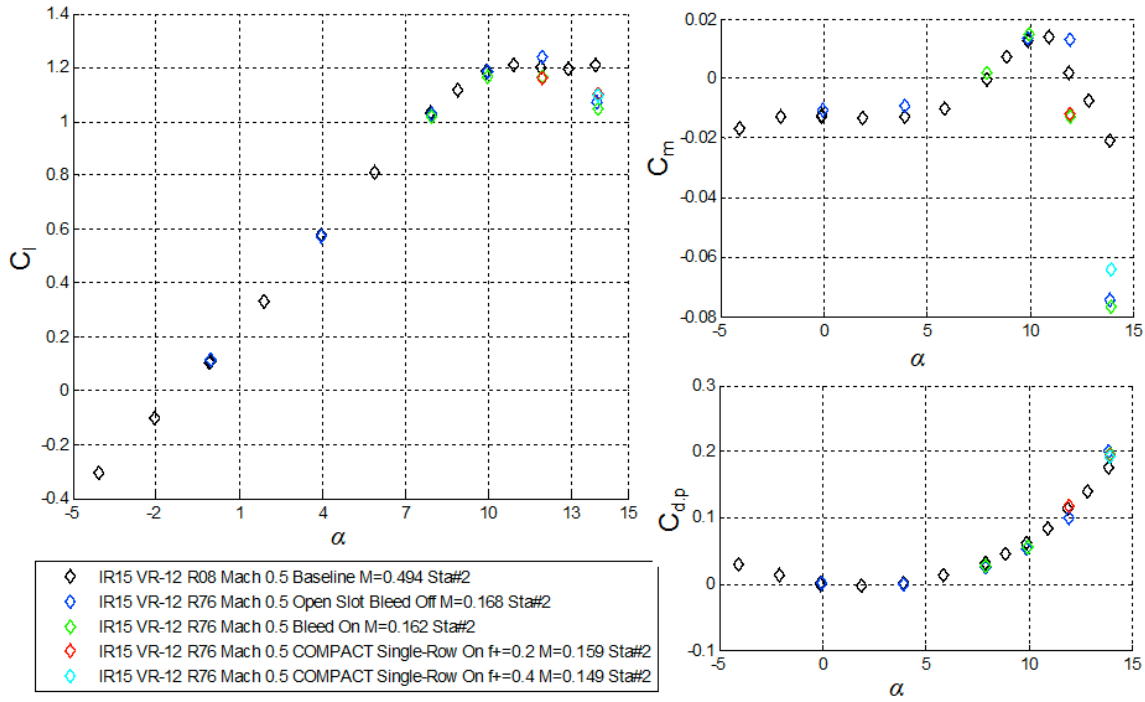


**Figure 170. Lift, drag, and moment coefficients at Mach 0.5 for baseline, open slot, and single-row COMPACT at  $F^+=0.2$  to 0.4. Entry 2, Run 76.**

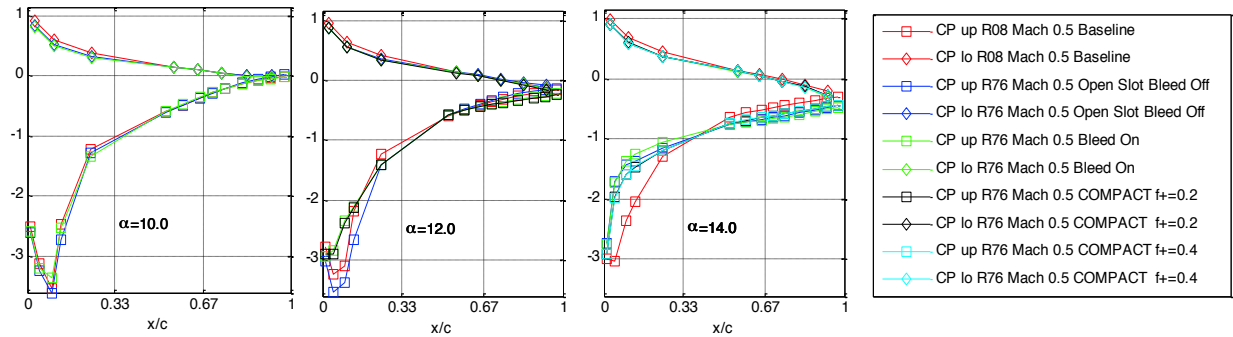


**Figure 171. Pressure coefficients at Mach 0.5 for baseline, open slot, and single-row COMPACT at  $F^+=0.2$  to 0.4. Entry 2, Run 76.**

### ***Mach 0.2 Load and Pressure Coefficients***

The Mach 0.2 results shown in Figure 172 are generally quite similar to those at Mach 0.3, with a peak post-stall  $\Delta C_l=0.6$  and  $\Delta C_m=0.07$ , which persisting out to  $\alpha=25^\circ$ . The benefits taper off by  $\alpha=30^\circ$ . The pressure distributions in Figure 173 show the substantial reduction in leading edge separation for the actuated conditions.

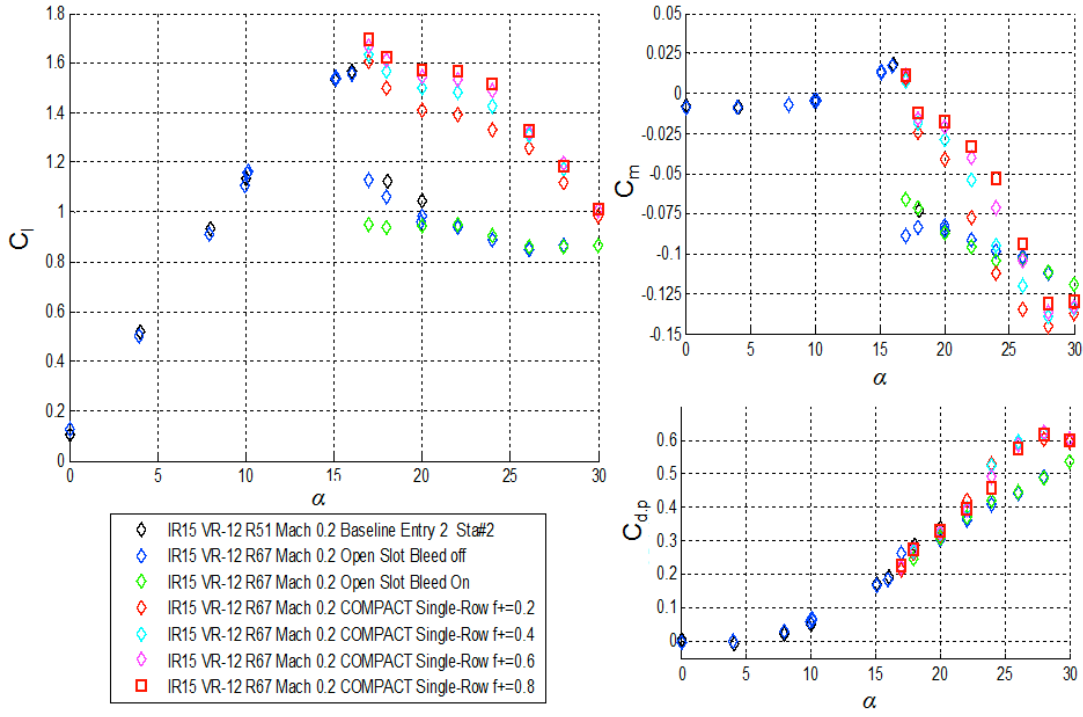


**Figure 172. Lift, drag, and moment coefficients at Mach 0.2 for baseline, open slot, and single-row COMPACT at  $F^+=0.2$  to 0.8. Entry 2, Day 4 Run 67.**

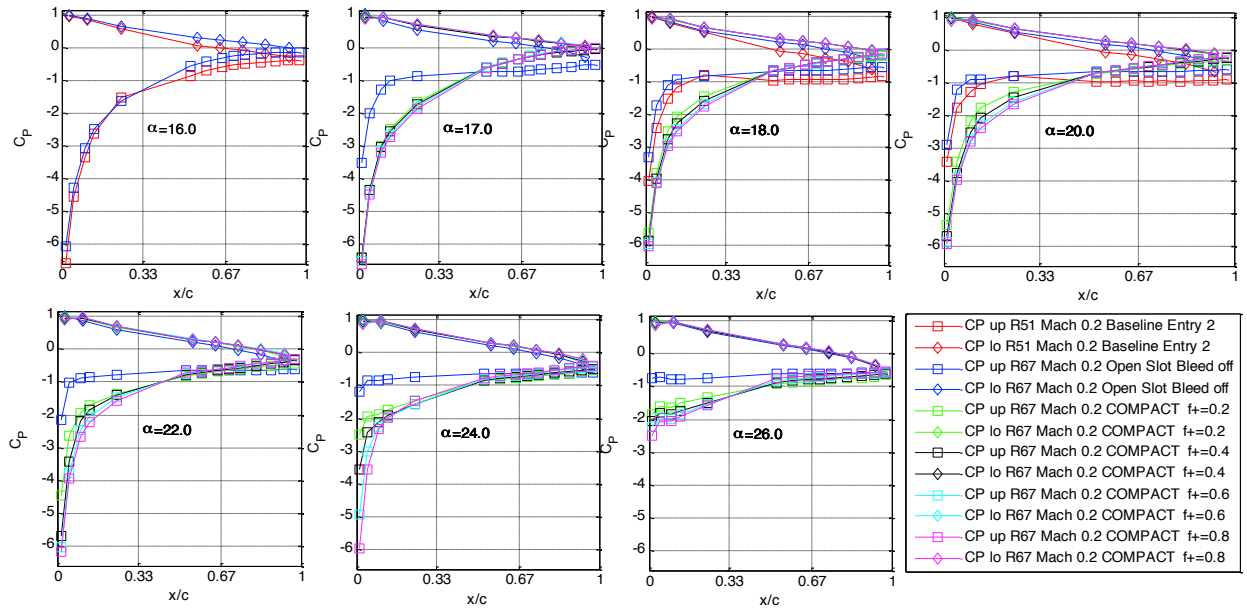
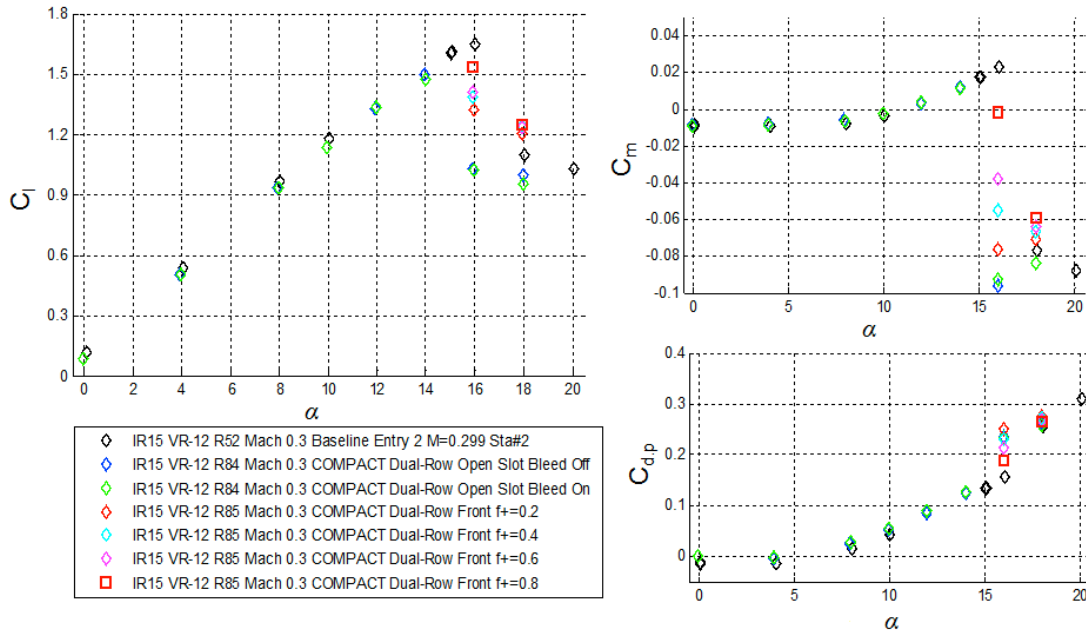


**Figure 173. Pressure coefficients at Mach 0.2 for baseline, open slot, and single-row COMPACT at  $F^+=0.2$  to 0.8. Entry 2, Day 4 Run 67.**

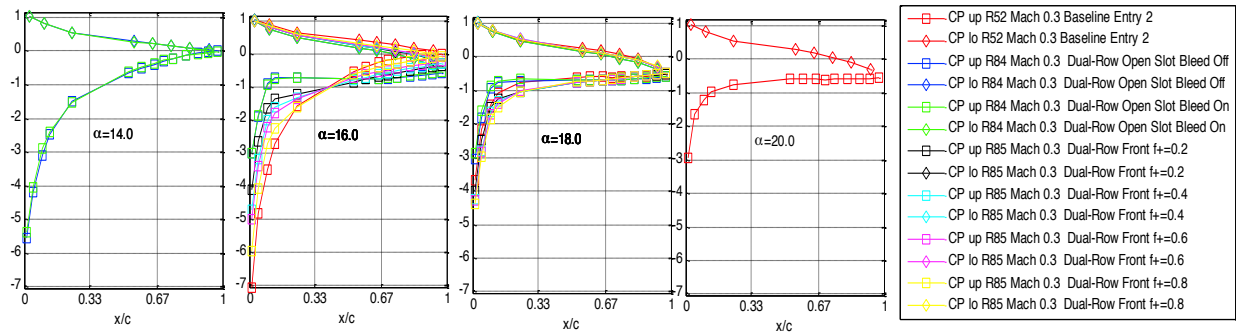
## COMPACT Dual-Row

### Mach 0.3 Load and Pressure Coefficients

The dual-row actuation results at Mach 0.3 are shown in Figure 174 for the dual slot COMPACT, with only the front row actuating. The higher frequency,  $F^+=0.8$  performs best, but in general  $C_{l,max}$  at  $\alpha=16^\circ$  is lower than for the baseline, by  $\Delta C_l=0.1$  to  $0.3$ . There is some improvement at  $\alpha=18^\circ$ , providing a benefit of  $\Delta C_l=0.1$  and  $\Delta C_m=0.02$ . This benefit is lower than that produced by the single-row COMPACT. As will be discussed in the later section on dynamic stall, the smaller spanwise extent of actuators for the dual-row configuration, as shown in Figure 103, is likely to be a significant factor in their low effectiveness compared to single row actuation. The pressure distributions in Figure 175 are consistent with the load coefficients.



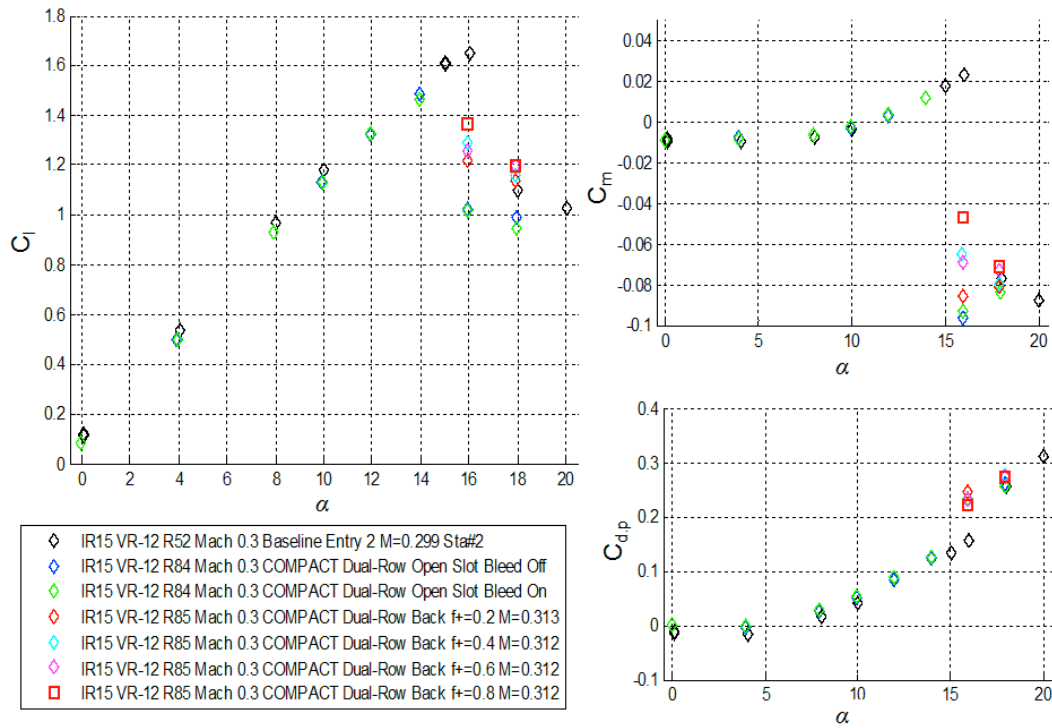
**Figure 174.** Lift, drag, and moment coefficients at Mach 0.3 for baseline, open slot, and dual-row front slot COMPACT at  $F^+=0.2$  to  $0.8$ . Entry 2, Run 85, Station 2.



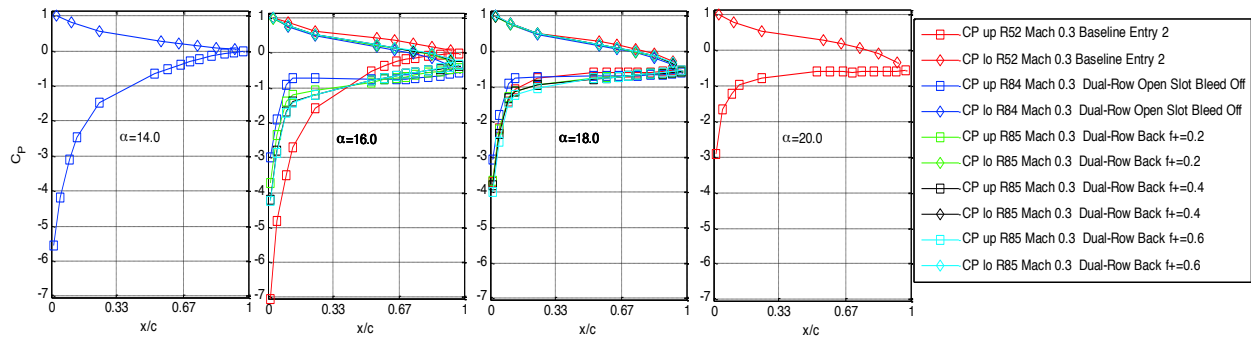
**Figure 175.** Pressure coefficients at Mach 0.3 for baseline, open slot, and dual-row front slot COMPACT at  $F^+=0.2$  to  $0.8$ . Entry 2, Run 85.

Figure 176 through Figure 181 show the load coefficients and pressure distributions for the back row only, dual-row simultaneous, and dual-row alternating configurations, respectively. The

trends are very similar to those for the front row only; no dual row configuration matches single row COMPACT.



**Figure 176. Lift, drag, and moment coefficients at Mach 0.3 for baseline, open slot, and dual-row back slot COMPACT at  $F^+=0.2$  to 0.8. Data from Entry 2.**



**Figure 177. Pressure coefficients at Mach 0.3 for baseline, open slot, and dual-row back slot COMPACT at  $F^+=0.2$  to 0.8. Data from Entry 2.**

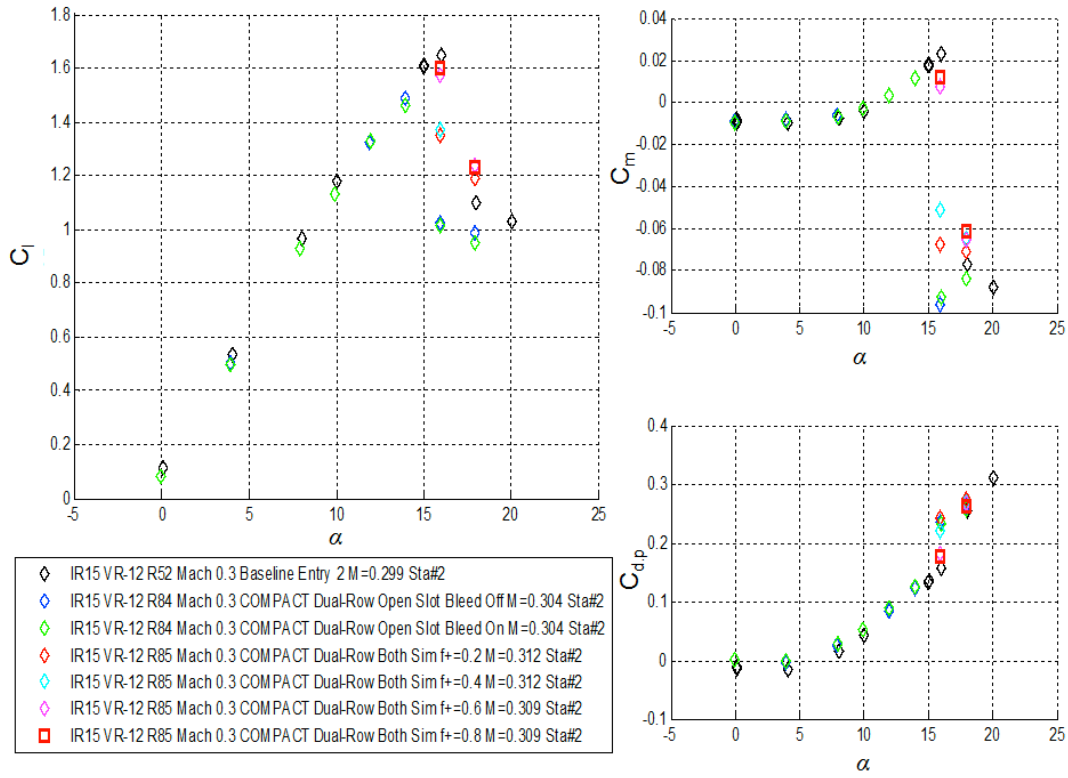


**Figure 178. Lift, drag, and moment coefficients at Mach 0.3 for baseline, open slot, and dual-row simultaneously firing slots COMPACT at  $F^+ = 0.2$  to 0.8. Entry 2, Run 85.**

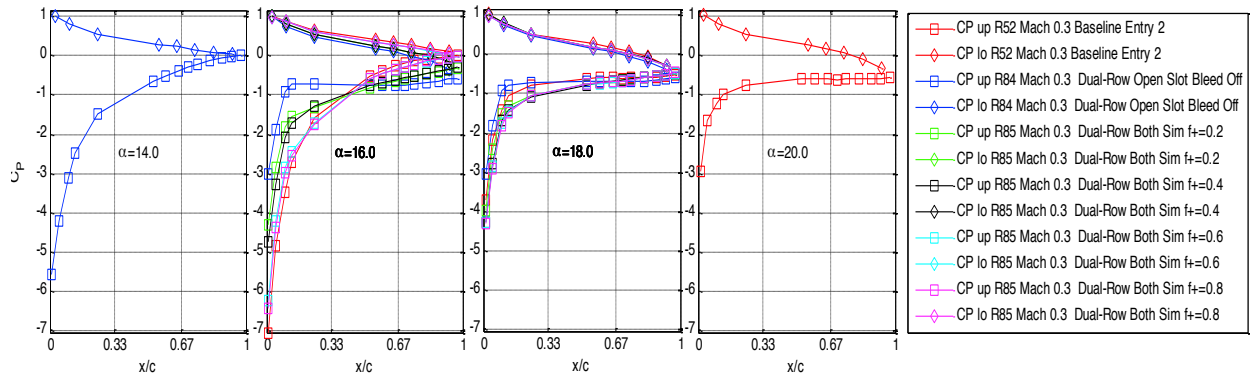


**Figure 179. Pressure coefficients at Mach 0.3 for baseline, open slot, and dual-row simultaneously firing slots COMPACT at  $F^+ = 0.2$  to 0.8. Entry 2, Run 85.**

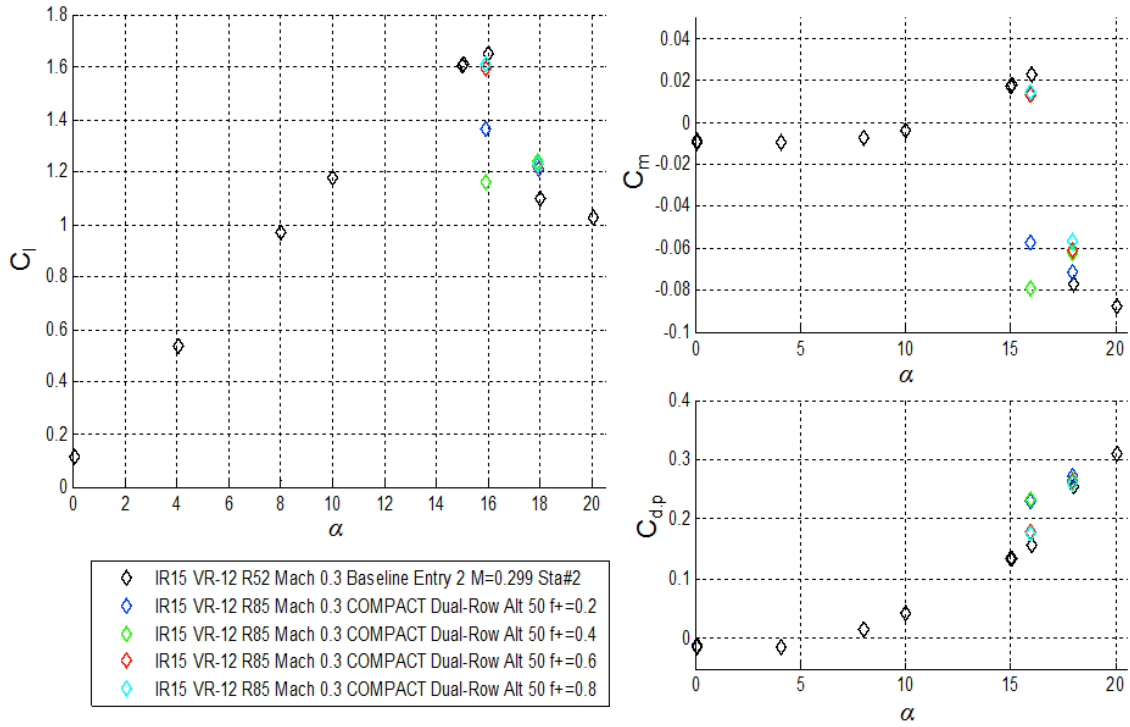


**Figure 180. Lift, drag, and moment coefficients at Mach 0.3 for baseline, open slot, and dual-row alternately firing slots COMPACT at  $F^+=0.2$  to 0.8. Entry 2, Run 85.**

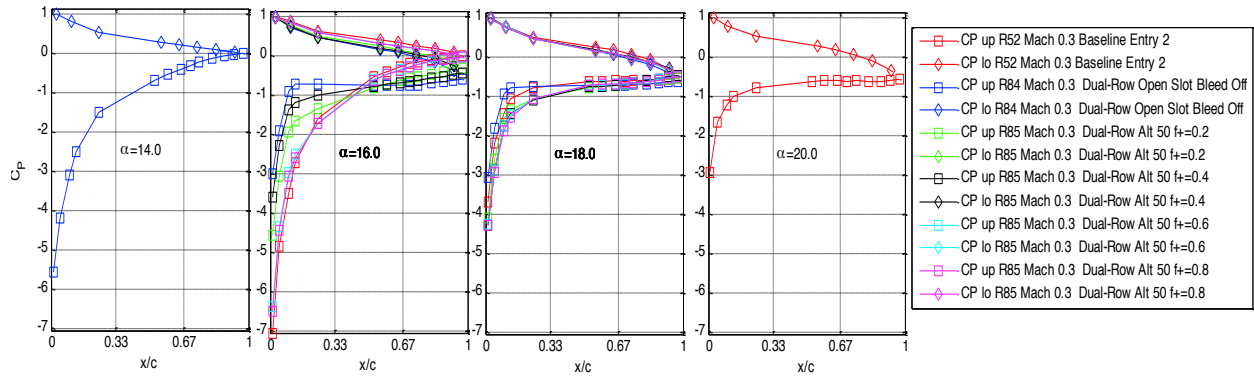


**Figure 181. Pressure coefficients at Mach 0.3 for baseline, open slot, and dual-row alternately firing slots COMPACT at  $F^+=0.2$  to 0.8. Entry 2, Run 85.**

Figure 182 and Figure 183 compare the four dual-row configuration with the baseline and single-row results at Mach 0.3. The dual-row actuation seemed to do slightly better than the front row only or rear row only, but none of them did as well as the single-row actuation.

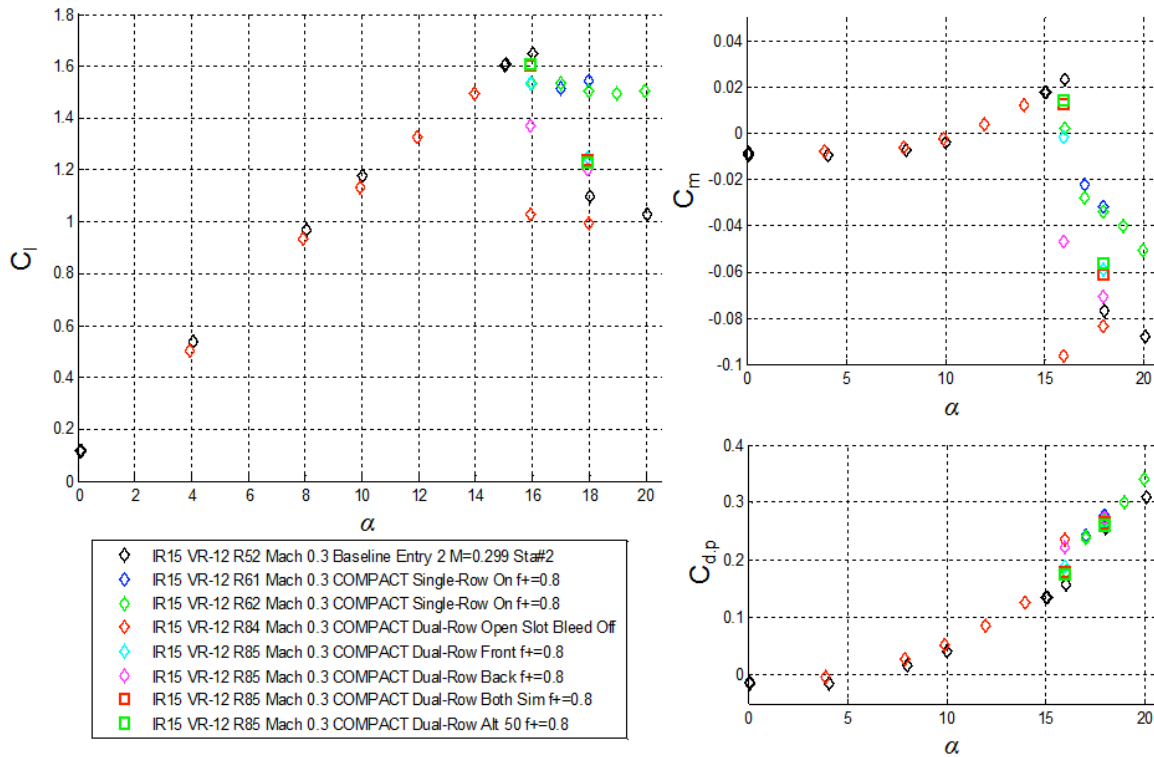


**Figure 182. Lift, drag, and moment coefficients at Mach 0.3 for baseline, open slot, and four dual-row COMPACT configurations at  $F^+=0.8$ . Entry 2, Run 85.**

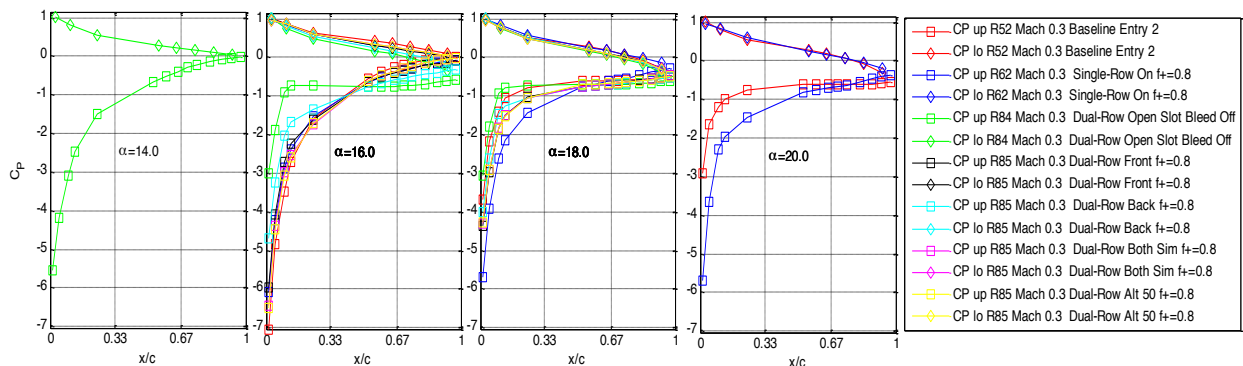


**Figure 183. Pressure coefficients at Mach 0.3 for baseline, single-row, dual open slot, and four dual-row COMPACT configurations at  $F^+=0.8$ . Entry 2, Run 85.**



#### ***Mach 0.4 Load and Pressure Coefficients***

Figure 184 shows a combined plot of the four dual-row actuation configurations at Mach 0.4 and  $F^+=0.6$ . While  $C_{l,max}$  is not reduced, there is also little visible post-stall benefit. The higher frequency,  $F^+=0.6$ , dual-row simultaneous mode does the best, but only recovers the baseline lift and moment levels. The previous single-row COMPACT still performs the best. Figure 185 compares pressure distributions for the four dual-row actuations with the baseline and single-row results at  $F^+=0.6$ . The single-row  $F^+=0.6$  actuation shows the least amount of leading-edge separation, the dual-row open slot shows the greatest amount, and the dual-row  $F^+=0.6$  front row and dual-row provide intermediate benefits. Figure 186 shows the Mach 0.4 alternating sweep results at  $\alpha=18^\circ$ . Some of the points show a slight improvement in  $C_L$ , but one of the  $F^+=0.6$  points is noticeably lower than the baseline.

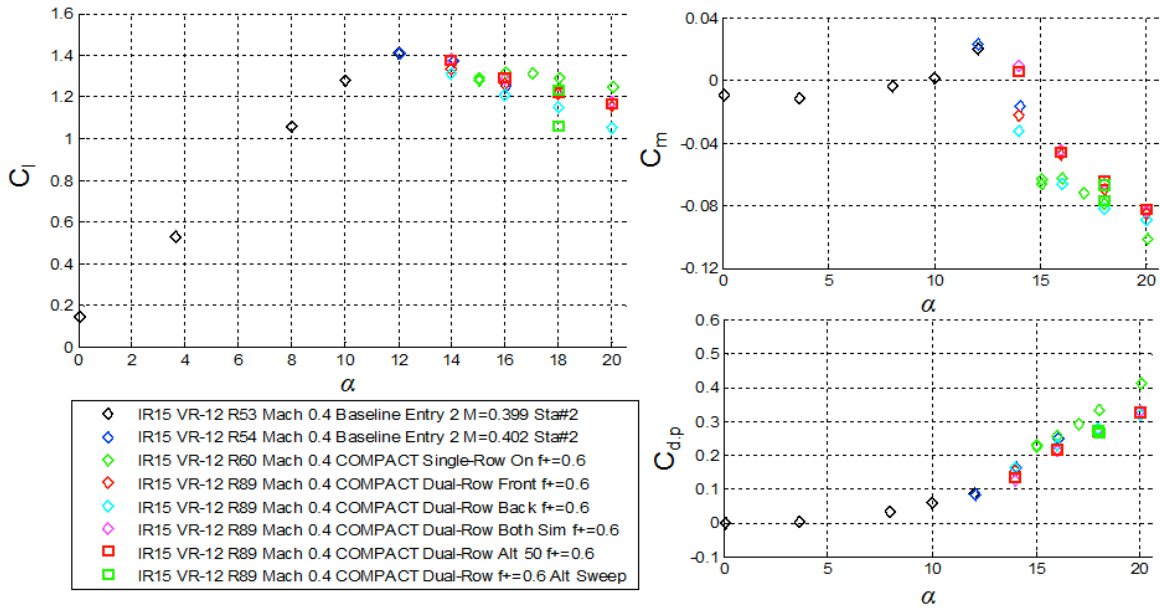


**Figure 184. Lift, drag, and moment coefficients at Mach 0.4 for baseline, and various dual-row COMPACT at  $F^+ = 0.6$ . Entry 2, Run 53-54, 60, and 89.**

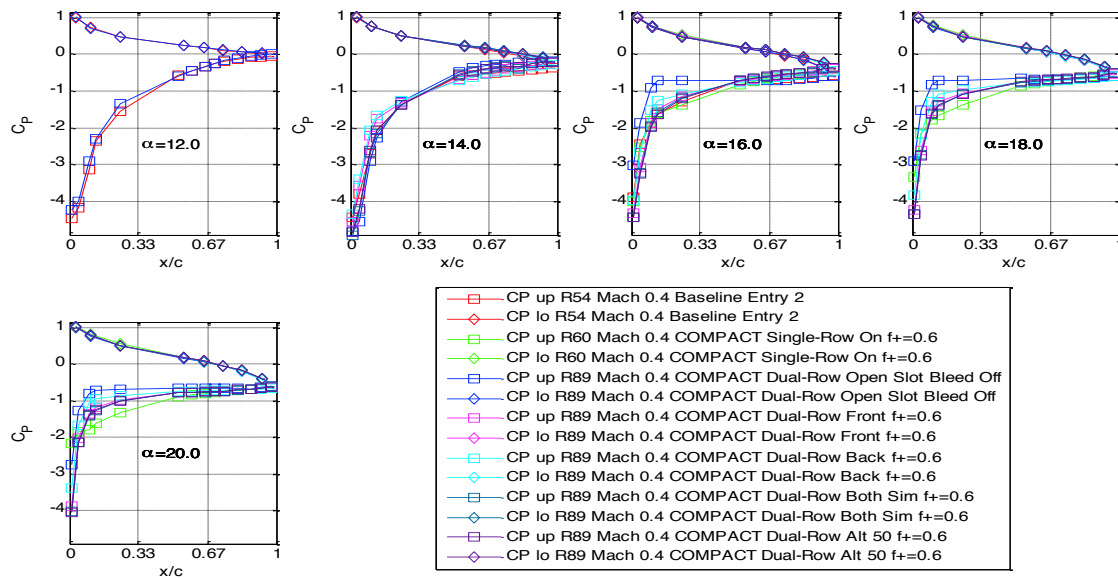


**Figure 185. Pressure coefficients at Mach 0.4 for baseline, single-row, and various dual-row COMPACT at  $F^+ = 0.6$ . Entry 2, Run 54, 60, and 89.**

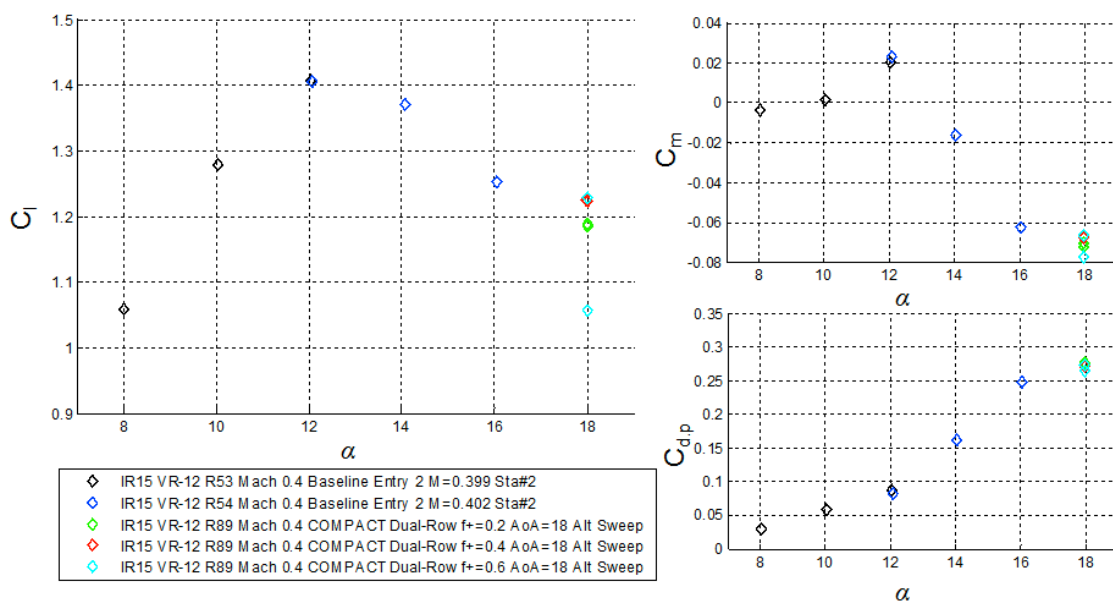


**Figure 186. Lift, drag, and moment coefficients at Mach 0.4 for baseline and dual-row alternating sweep at COMPACT at  $\alpha=18^\circ$   $F^+=0.2$  to 0.6. Entry 2, Day 4 Run 89.**

### ***Mach 0.3 Final Runs***

Figure 187 and Figure 188 show the final day runs with dual-row actuation at Mach 0.3. At the two angles studied,  $\alpha=18^\circ$  and  $\alpha=20^\circ$ , there was again a benefit of  $\Delta C_l \sim 0.2$  with the higher frequency,  $F^+=0.6$  to 0.8 actuation. This run did not repeat the  $\alpha=16^\circ$  condition, so any change in  $C_{l,max}$  was not identified.

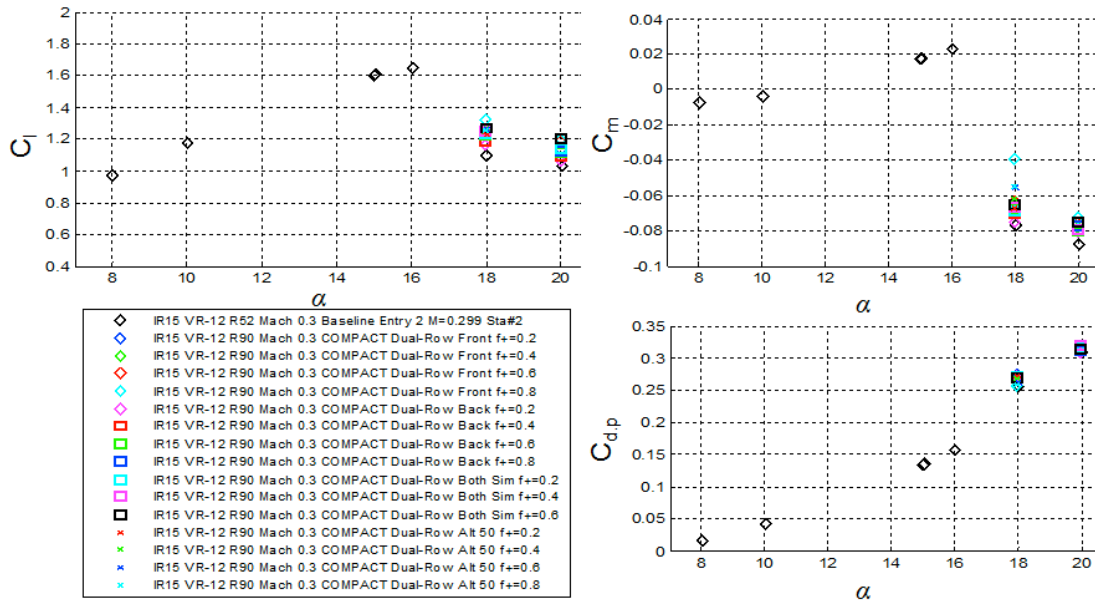


Figure 187. Lift, drag, and moment coefficients at Mach 0.3 for baseline, dual-row front, back, simultaneous and alternating 50 COMPACT;  $F^+=0.2$  to 0.8. Entry 2, Run 90.

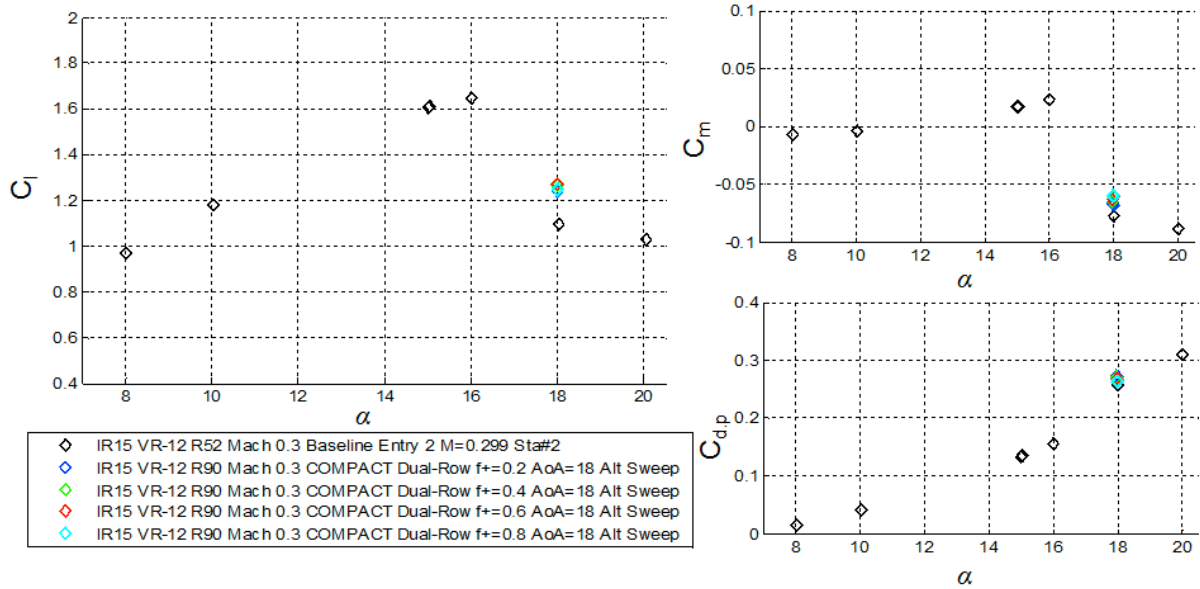


Figure 188. Lift, drag, and moment coefficients at Mach 0.3 for baseline and dual-row alternating sweep COMPACT at  $\alpha=18^\circ$ ;  $F^+=0.2$  to 0.8. Entry 2, Run 90.

#### 4. High-Speed Wind Tunnel Unsteady COMPACT Results

This section compares baseline and COMPACT chord pressures, resultant integrated forces as a function of prescribed incidence, and further extracted key dynamic stall metrics. A large number of pitch trajectories were studied throughout the experimental phase of the program. Representative cases at each Mach number are used to describe the salient effects of COMPACT on suppressing dynamic stall. Datasets, unless otherwise noted, are taken Entry 2. The complete set of actuated case results can be found in Appendix 4.

Table 24 lists the dates, run numbers, configurations, and Mach conditions associated with the data discussed herein. Baseline VR-12 comparisons are made to both Entry 1 and Entry 2 measurements. PIV datasets for the single-row configuration were acquired over the Runs 69-75.

**Table 24. Single- and dual-row COMPACT Control Runs from Test Entry 1.**

Date	Runs	Configuration	Conditions
5-5-15	55	COMPACT Single-Row	Mach 0.3 (limited)
5-6-15	58-61	COMPACT Single-Row	Mach 0.2, 0.3, 0.4
5-7-15	62-63	COMPACT Single-Row	Mach 0.3, 0.4
5-8-15	65-68	COMPACT Single-Row	Mach 0.2, 0.3, 0.4
5-13-15	76-79	COMPACT Single-Row	Mach 0.3, 0.4, 0.5
5-14-15	84-85	COMPACT Dual-Row	Mach 0.3
5-15-15	89-92	COMPACT Dual-Row	Mach 0.2, 0.3, 0.4, 0.5

##### A. Single-Row COMPACT Results

Table 25 provides a list of the run, point numbers, and conditions wherein single-row COMPACT unsteady tests were performed. It was found early in the test that the actuators caused no deleterious effects to the upstroke lift, drag, or moment traits. Therefore, pitch trajectories that did not encompass the stall angle – the so called ‘No stall’ regime – were not investigated. Focus was on light and deep dynamic stall control. For COMPACT, the thrust of the investigation concentrated on varying  $F^+$  to its highest obtainable value, a function of the physical frequency of the actuators and Mach number.

**Table 25. COMPACT Single-Row Unsteady Data Points Acquired**

Run	Mach	k	$\alpha_0$	$\alpha_1$	$F^+$	Pulse Start $\alpha$	$N_{pulses}$	Points
58	0.2	0.07	10	8	0.2-1.0	10	8,17,26,35,42	15-19
59	0.3	0.025	10	8	0.2-0.8	10	24,49,74,100	9-12
		0.025	10	10	0.2-0.8	10	25,49,74,100	15-17,20
		0.025	10	10	0.6	15	37	18
60	0.4	0.025	10	8	0.2-0.6	10	24,49,74	9-11
		0.025	10	8	0.6,0.4,0.2	10	24,49,74	15,14,13

Run	Mach	k	$\alpha_0$	$\alpha_1$	$F^*$	Pulse Start $\alpha$	$N_{\text{pulses}}$	Points
62	0.3	0.05	10	8	0.2-0.8	10	12,24,36,49	13,14,17,18
	0.3	0.05	10	10	0.2-0.8	10	12,24,36,49	24-27
	0.3	0.07	10	8	0.2-0.8	10	8,17,26,35	31-33,35
	0.3	0.07	10	9.5	0.2-0.8	10	8,17,26,35	38-41
	0.3	0.1	10	8	0.2-0.8	10	6,12,18,25	45-48
	0.3	0.1	10	9.5	0.2-0.8	10	6,12,18,25	51-54
63	0.4	0.05	10	8	0.2-0.6	10	12,25,37	9,11,12
	0.4	0.05	10	9.5	0.2-0.6	10	12,25,37	15-17
	0.4	0.07	10	8	0.2-0.6	10	12,25,37	21,22,24
	0.4	0.07	10	9.5	0.2-0.6	10	12,25,37	27-29
	0.4	0.07	12	8	0.2-0.6	12	12,25,37	35-37
	0.4	0.07	12	9.5	0.2-0.6	12	12,25,37	40-42
	0.4	0.07	12	9.5	0.6	13-18	37	44-49
	0.4	0.07	12	9.5	0.6	18	2,4-20,25	50-56
65	0.3	0.025	15	8	0.2-0.8	15	25,50,75,100	9-12
	0.3	0.05	15	8	0.2-0.8	15	12,25,37,50	16-19
66	0.3	0.07	15	8	0.2-0.8	15	8,17,26,35	4-7
	0.3	0.07	10	9.5	0.4	10	1,2-16	12-20
	0.3	0.07	10	9.5	0.6	10	2,4-24	21-27
	0.3	0.07	10	9.5	0.8	10	2,4-32	28-36
	0.3	0.07	10	9.5	0.4	15-19,19D-15D	4,8	40-59
	0.3	0.07	10	9.5	0.6	15-19,19D-15D	6,13	60-71
	0.3	0.07	10	9.5	0.8	15-19,19D-15D	8,17	72-78,80-84
	0.2	0.07	10	10	0.2-1.0	10	8,17,26,35,44	8-12
67	0.2	0.1	10	10	0.2-1.0	10	6,12,18,25,31	17-20,22
	0.2	0.07	15	8	0.2-1.0	15	8,17,26,35,44	27-31
	0.2	0.07	15	10	0.2-1.0	15	8,17,26,35,44	34-38
	0.2	0.1	15	8	0.2-1.0	15	6,12,18,25,31	42-46
	0.2	0.1	15	10	0.2-1.0	15	6,12,18,25,31	49-53
	0.2	0.1	15	10	0.2-1.0	15	6,12,18,25,31	49-53
68	0.4	0.05	10	9.5	0.2-0.6	10	12,25,37	11-13 or 16-18
76	0.5	0.025	8	8	0.2,0.4	8	25,50	20,21
	0.5	0.025	8	5	0.2,0.4	8	25,50	24,25
	0.5	0.05	8	5	0.2,0.4	8	12,25	28,29
	0.5	0.05	8	8	0.2,0.4	8	12,25	32,33
77	0.4	0.05	10	9.5	0.2	10	12	5
	0.4	0.05	10	9.5	0.2	15-19,19D-15D	3,6	6-17
	0.4	0.05	10	9.5	0.4	10	25	18
	0.4	0.05	10	9.5	0.4	15-19,19D-15D	6,12	19-30
	0.4	0.05	10	9.5	0.6	10	37	31
	0.4	0.05	10	9.5	0.6	15-19,19D-15D	9,18	32-43
	0.4	0.05	10	9.5	0.4	16	2-12,16,20	44-51
	0.4	0.05	10	9.5	0.4	18	2-12,16,20	52-59
	0.4	0.05	10	9.5	-	15-18,18.5,19,19.4,19.5D,19D,18.5D,18D-14D,12D,10D,8D	1	60-77
78	0.3	0.07	10	9.5	0.4	17,18,18.6,19,19.5,19D,18.5D,18D-14D,12D,10D,8D	1	50-64
	0.3	0.07	10	9.5	0.4	10	17 odd only	74
	0.3	0.07	10	9.5	0.4	10	17 even only	75
	0.3	0.07	10	9.5	0.4	10	17 H2=70	76
	0.3	0.07	10	9.5	0.4	10	17 H2=80	77



Run	Mach	k	$\alpha_0$	$\alpha_1$	$F^+$	Pulse Start $\alpha$	$N_{pulses}$	Points
	0.3	0.07	10	9.5	0.4	10	17 H2=90	78
79	0.4	0.05	10	9.5	0.4	10	25	4
	0.4	0.05	10	9.5	0.4	15-19,19D-15D	6,12	5-16

The actuator design improvements prior to Entry 2 increased the pulse frequency envelope to 212 Hz. The test allowable or maximum  $F^+$  is shown in Figure 189 based on this frequency and IRT test section conditions for the Mach range of interest. The required physical frequency for each Mach number to achieve a desired  $F^+$  is also shown, demarked by the upper line of each patterned area.  $F^+=1$  was out of reach at Mach 0.3 while  $F^+=0.8$  could not be attained at Mach 0.4.

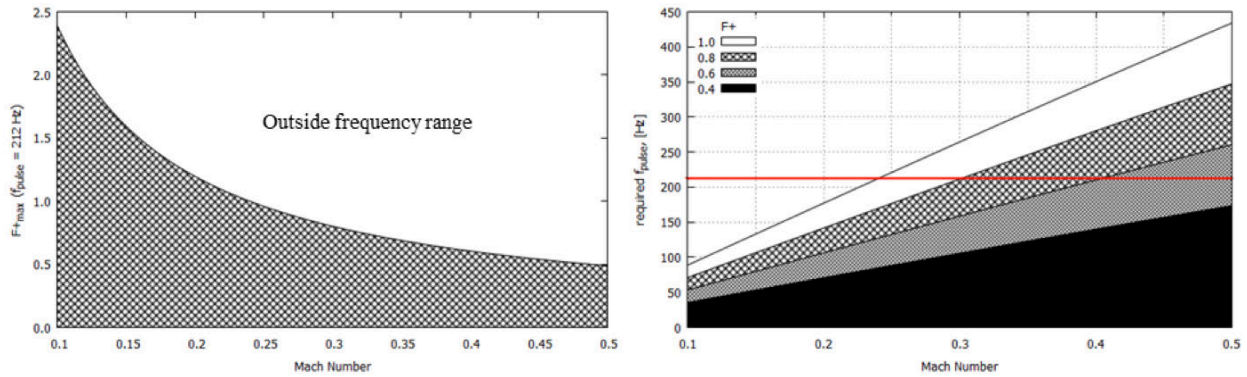


**Figure 189. Maximum COMPACT  $F^+$  (left). Required  $f_{pulse}$  for each Mach number (right). The red line denotes the physical frequency limit of the actuators tested in the current study.**

$F^+$  sweeps relied on continuous pulsing; the number of pulses,  $N_{pulse}$ , is then the lower integer value of the ratio of pulsing frequency to pitch frequency,  $f_{act}/f_{pitch}$ . Pulsing was nominally triggered at the upstroke mean angle each pitch cycle, denoted as ‘Pulse Start  $\alpha$ ’ in Table 25. This firing approach guaranteed incidence phased locked pulsing, and provided small cycle-to-cycle angle differences. Additional sweeps of the pulse start  $\alpha$  and  $N_{pulse}$  were incorporated into the test matrix, focusing on Mach 0.3 and 0.4 deep stall test cases.

For discussion purposes, only a single case from each test Mach number was selected in this section to show the COMPACT impact on the ensemble integrated loads. The unsteady stall parameters are shown in Table 26. The selected dynamic stall cases embody critical retreating-blade stall sectional conditions and, additionally, are commonplace pitch motions found throughout the dynamic stall literature.

**Table 26. Dynamic stall conditions for representative cases.**

Mach	k	$\alpha_0$	$\alpha_1$
0.2	0.10	10°	10°
0.3	0.07	10°	9.5°
0.4	0.05	10°	8°
0.5	0.05	8°	8°

### ***Steady Bleed Effects on Baseline Unsteady Characteristics***

Despite the diminutive mass flow to the actuators, bleed produced an undesirable effect on the unsteady loads compared to the baseline VR-12 and the actuator installation/slot effects previously discussed – similar to the results found for static conditions. A steady bleed detriment occurred without preference to prescribed pitch forcing. Figure 190 shows an example of the transition from the clean, baseline VR-12 load coefficients to those measured with open slot, no bleed, and open slot steady bleed for the Mach 0.3 case considered in Table 26. Figure 191 shows the corresponding Mach 0.4 measured load coefficients. For Mach 0.3, steady bleed decreased moment stall angle by less than  $1^\circ$ . More significantly, it delayed reattachment on the downstroke by roughly  $2.5^\circ$ , simultaneously decreasing downstroke  $C_L$  by as much as -0.17. Similarly to Mach 0.3, the Mach 0.4 case showed little effect of steady bleed on peak lift (although the COMPACT hardware installation/slot caused a large reduction). Overall, the many acquired datasets revealed one reoccurring feature associated with this phenomenon: bleed induced downstroke lift was always a -0.15 to -0.20 reduction and roughly  $2^\circ$  delay in reattachment.

The above item is important to note, as the actuators have a constant gas flow to the combustion chambers and, when operating, the actuator generated disturbances must overcome this deficit. For high enough  $F^+$  (typically 0.4 or 0.6), downstroke increases in lift exceeded  $\Delta C_L = +0.4$ . If considered relative to the steady bleed case, this increment was  $\Delta C_L = +0.6$ .

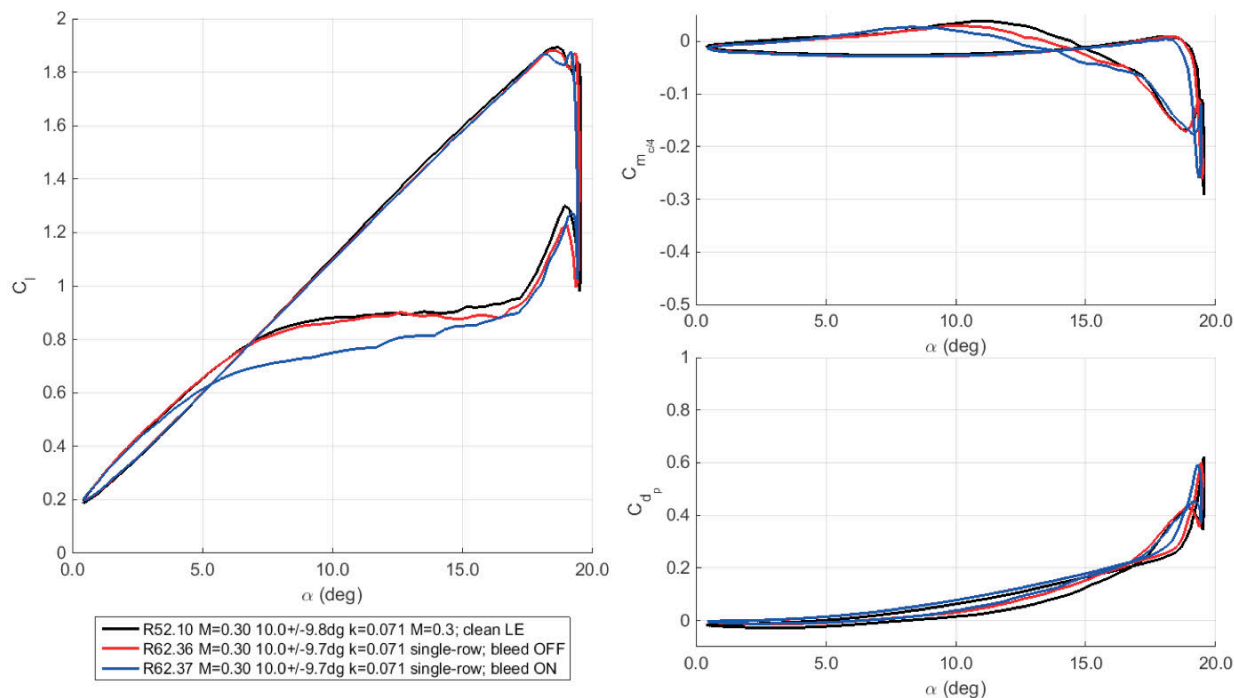


**Figure 190. Unsteady aerodynamic loads with respect to angle-of-attack.  $M = 0.3$ ,  $\alpha = 10^\circ \pm 9.5^\circ$ ,  $k = 0.07$ . Baseline, single-row COMPACT with and without steady bleed.**

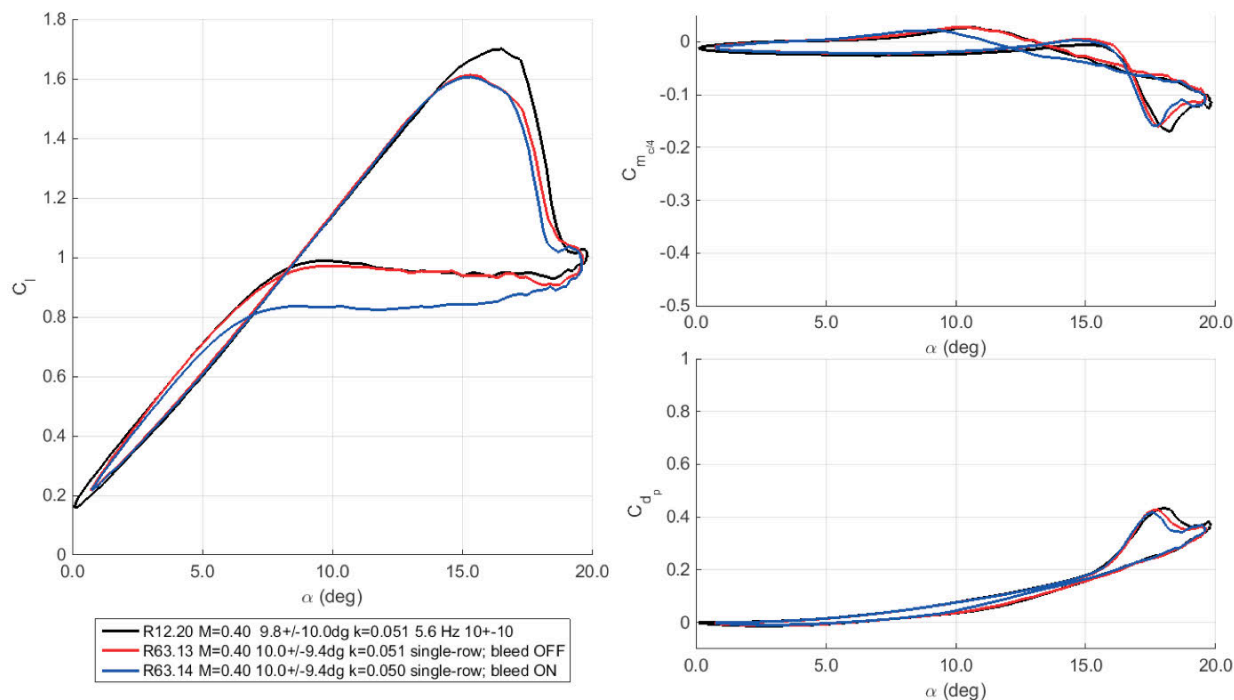


**Figure 191. Unsteady aerodynamic loads with respect to angle-of-attack.  $M = 0.4$ ,  $\alpha = 10^\circ \pm 9.5^\circ$ ,  $k = 0.05$ . Baseline, single-row COMPACT with and without steady bleed.**

### ***Actuation Results***

For a given Mach number, COMPACT actuation produced similar results throughout the classic dynamic stall regimes. Actuation efficacy, particularly in terms of lift recovery, was most prevalent on the airfoil downstroke, producing large gains in both light and deep dynamic stall cases. The limited aspect ratio of the actuated VR-12 span produced detrimental 3D loads, evidenced by the spanwise instrumentation discussed in the following section. It is surmised that, in some cases, these 3D effects reduced or eliminated potential benefits in adverse drag and moment that would otherwise accompany the COMPACT produced flow disturbances.

#### ***M=0.2***

Unsteady pitching results at Mach 0.2 with the single-row COMPACT configuration are provided in Figure 193 - Figure 194 for  $\alpha = 10^\circ - 10^\circ \cos \omega t$ . The cases are plotted uniquely as well as overlaid with respect to incidence and phase. The baseline case should be categorized as light dynamic stall as the stall vortex does not begin its convection aft until the airfoil begins the downstroke, resulting in near simultaneous lift and moment stall. Still, a drop in lift of  $\Delta C_l = -0.94$  occurs from  $20^\circ$  to  $16^\circ$  on the downstroke. The stall vortex reaches the VR-12 trailing edge at  $18.4^\circ$  coinciding with the peak nose-down pitching moment,  $C_m = -0.20$ . At this Mach number, actuation across an  $F^+$  range up to 1.0 was possible with strong actuator performance – uniformity and combustion success – across that range. The internal combustion was aided by low freestream Mach number and a modest absolute level of suction on the upper surface at high angles of attack. As a result, problems related to the actuation spark and combustion at low static pressure were minimized, if not removed. For  $F^+ = 0.2$ , six actuator pulses occur each cycle. Several of the pulses are distinguishable through examination of the integrated loads. A modest  $C_l$  improvement is immediately achieved through actuation at  $F^+ = 0.2$  (note, this overcomes both the installation and steady bleed-on losses previously discussed).

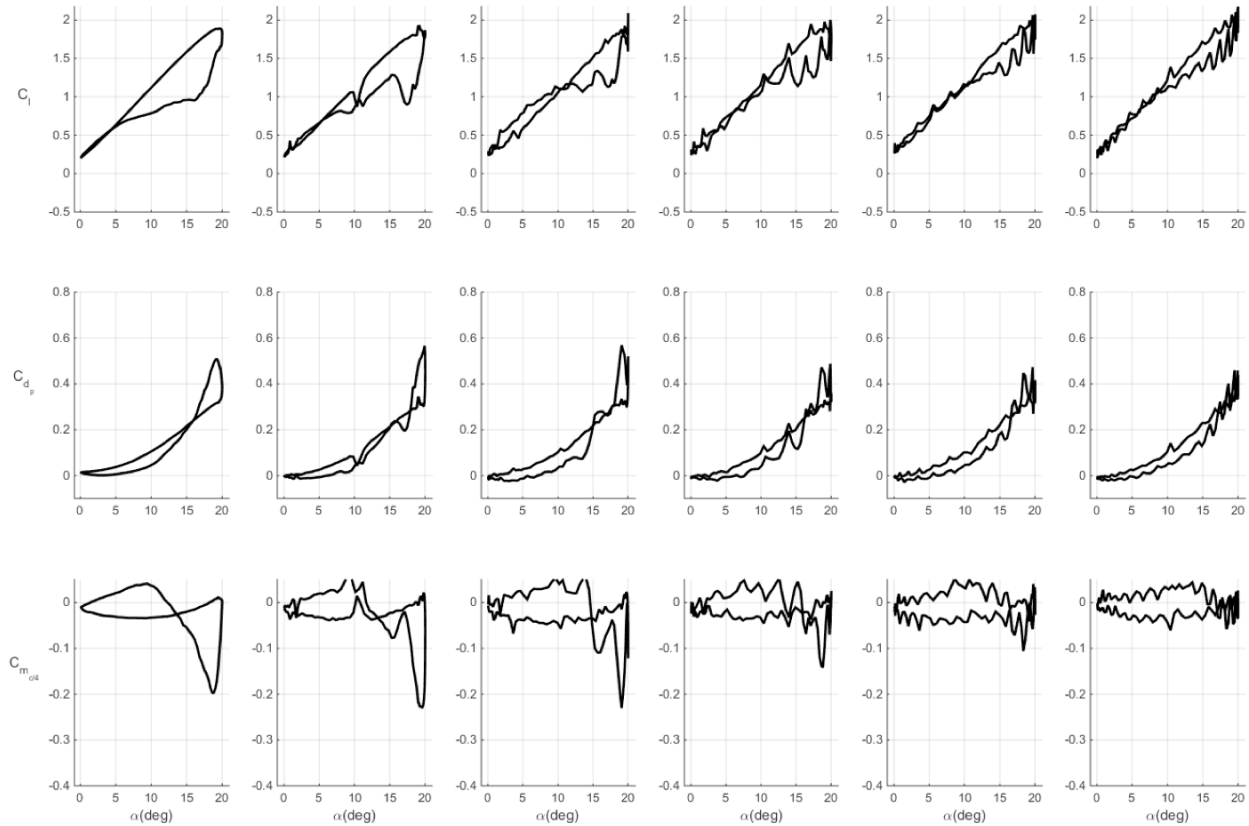
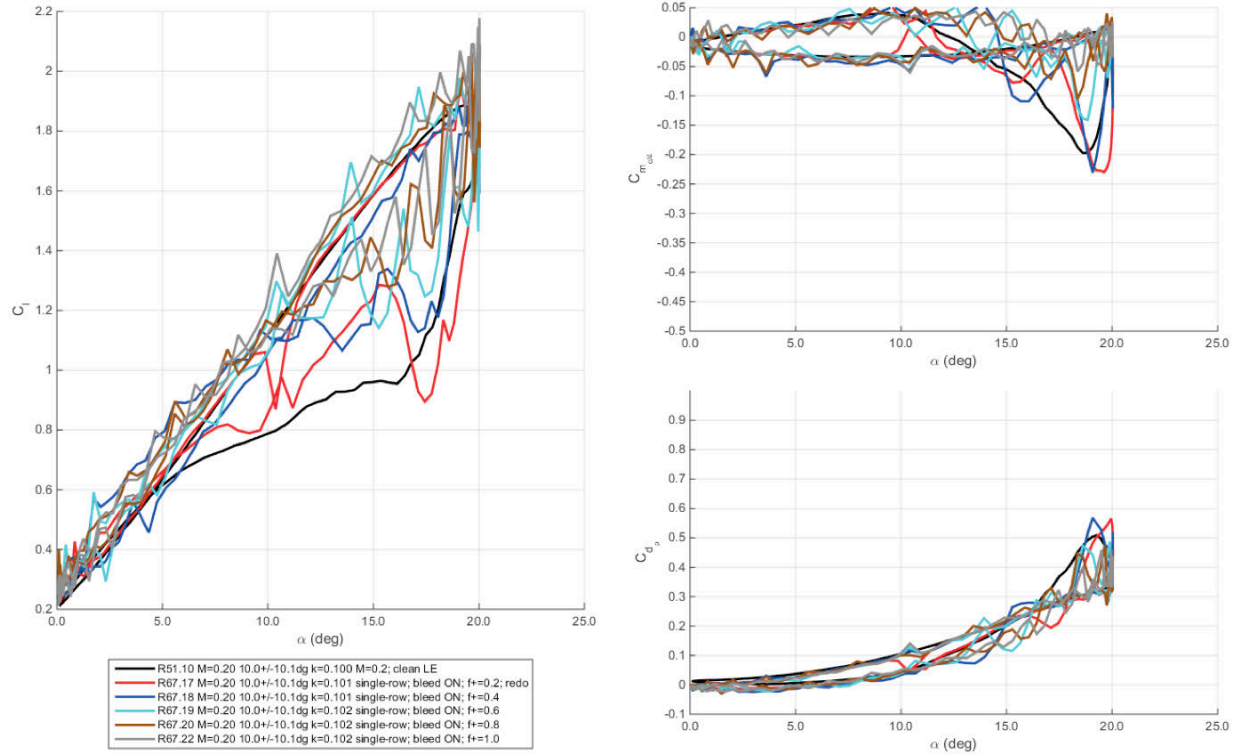


**Figure 192. Unsteady aerodynamic loads with respect to angle-of-attack.  $M = 0.2$ ,  $\alpha = 10^\circ \pm 10^\circ$ ,  $k = 0.10$ . Baseline and single-row COMPACT  $F^+ = 0.2-1.0$  shown in order from left to right. Run 67, Pts 17-22.**

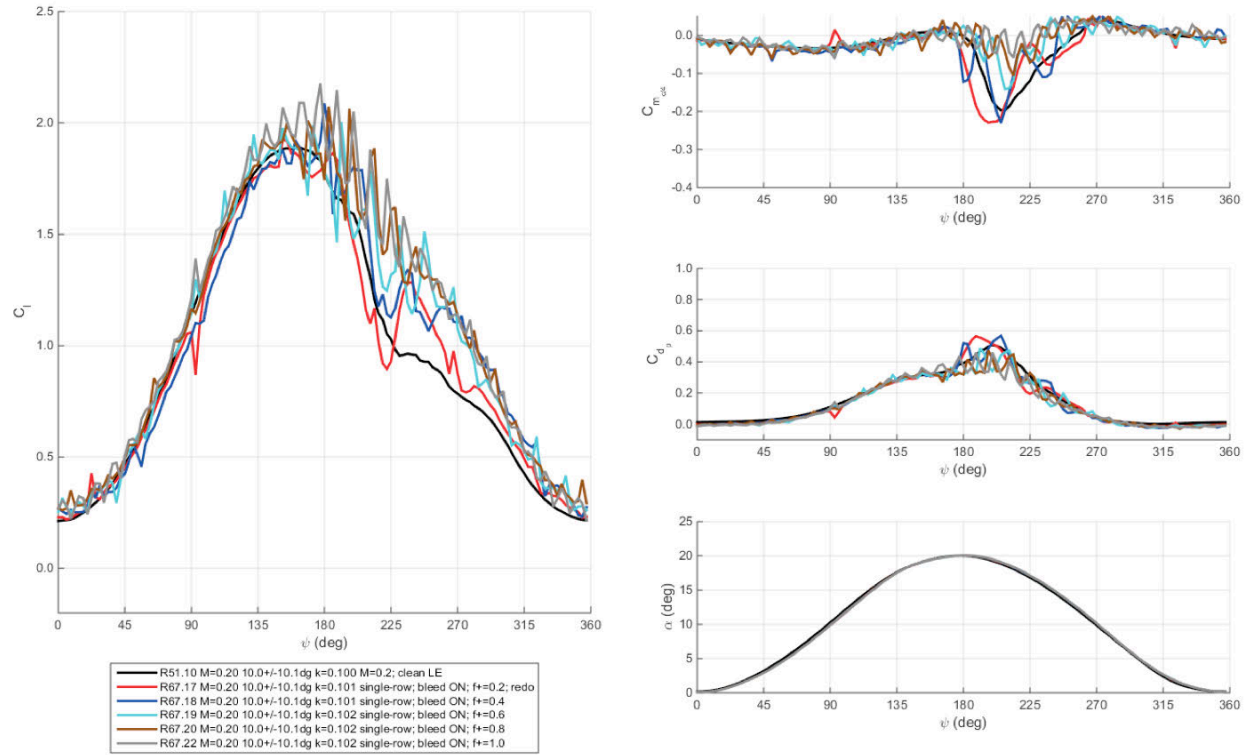
However, the pulse and pitch phase relationship cause an increase in both peak drag and adverse pitching moment. Increasing  $F^+$  to 0.4 doubles the number of pulses producing the ‘noisier’ integrated loads observed. Actuation at this rate significantly decreases the lift deficit but still fails to alleviate the large adverse drag and moment loads. Further increases in actuation frequency cause dramatic improvements in lift, drag, and moment. The nose-down pitching moment is reduced by -28%, -46%, and -69% for  $F^+ = 0.6, 0.8$ , and  $1.0$ , respectively. Drag is reduced by 10% while peak lift is augmented by 17% for  $F^+ = 1.0$ .

Figure 195 compares the ensemble average pressure distribution for selected angles of attack for the six cases considered. The angles represent the upstroke mean angle through the peak angle, and well into the downstroke portion of the pitch motion, stopping at  $13.7^\circ$ . For each case, the error in phase-averaged  $\alpha$  was less than  $0.2^\circ$ . For the first three angles shown, only subtle differences were measured; of interest is a decrease in suction pressure on the upper surface for all actuation cases through the peak angle. This is an effect of the geometric differences between the baseline and clean geometries. At  $x/c = 0.01$  and  $\alpha = 17.6^\circ$ , a peak pressure of  $C_p = -7.0$  was measured for the baseline VR-12.  $C_p = -6.0, -6.5, -6.6, -6.7$ , and  $-6.8$  were measured for the control cases in increasing  $F^+$  order. This trend reverses aft of the slot for  $F^+ > 0.4$ . As the integrated loads suggest, much larger alterations relative to the baseline are found for the downstroke angles. For  $\alpha = 19.1^\circ$ , a clear trend appears for increasing  $F^+$  near the leading edge. The tell-tale signs of separation are removed for both  $F^+ = 0.8$  and  $1.0$ ;  $F^+ = 0.6$  creates

slightly less leading edge loading, but shows strong pressure recovery over the last half chord. The  $F^+ = 0.4$  results indicate improved leading-edge suction compared to the baseline but a large, low-pressure region over the aft chord suggests intermittent separation, behaving similar to the baseline through the average.  $F^+ = 0.2$  provides much less control authority than the other frequencies.



**Figure 193. Unsteady aerodynamic loads with respect to angle-of-attack,  $M = 0.2$ ,  $\alpha = 10^\circ \pm 10^\circ$ ,  $k = 0.10$ . Baseline and single-row COMPACT  $F^+ = 0.2-1.0$ . Run 67, Pts 17-22.**



**Figure 194. Unsteady aerodynamic loads and angle-of-attack with respect to phase,  $M=0.2$ ,  $\alpha=10^\circ \pm 10^\circ$ ,  $k=0.10$ . Baseline and single-row COMPACT  $F^+=0.2-1.0$ . Run 67, Pts 17-22.**



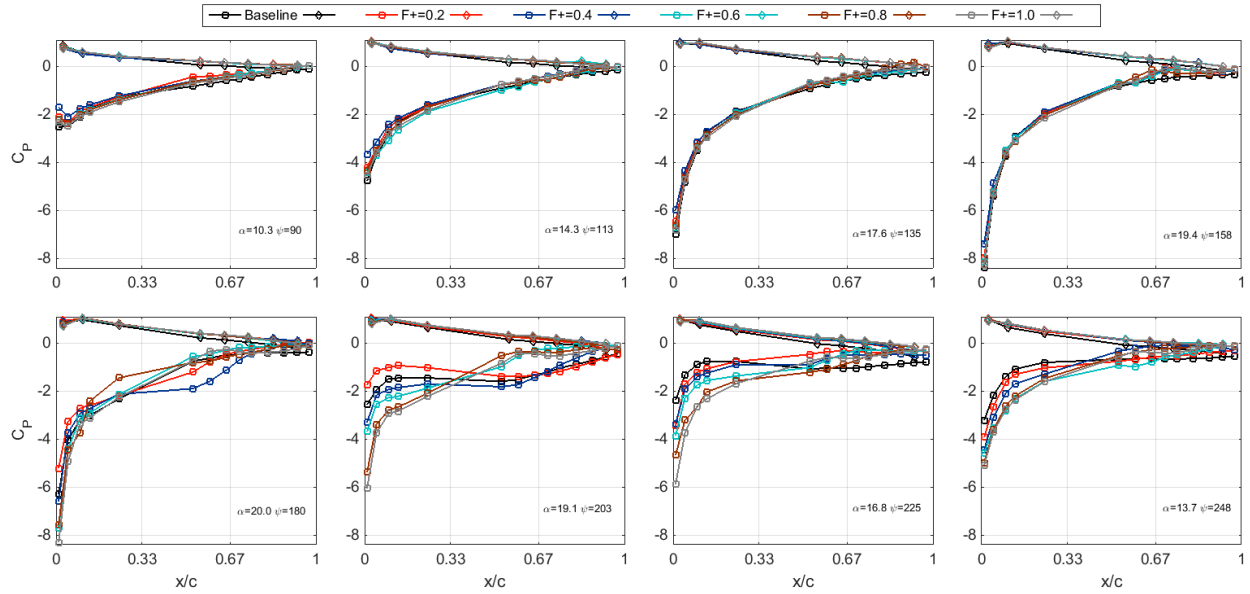


**Figure 195.  $C_p$  comparison of selected  $\alpha$  for  $M = 0.2$ ,  $\alpha = 10^\circ \pm 10^\circ$ ,  $k = 0.10$ . Baseline and  $F^+ = 0.2-1.0$ . Square symbols indicate upper surface, triangles indicate lower surface measurements. Run 67, Pts 17-22.**

Varying degrees of dynamic stall were tested at Mach 0.2 at reduced frequencies of 0.07 and 0.10 and peak angles up to  $25^\circ$ . Of particular interest to rotorcraft performance is the behavior of  $C_{L,max}$ ,  $C_{D,max}$ , and  $C_{M,min}$ . These respective quantities were extracted from the integrated loads for each of the Mach 0.2 baseline and COMPACT dynamic stall cases acquired. Peak lift versus peak nose-down pitching moment is shown in Figure 196 and peak lift versus maximum drag is shown in Figure 196. A solid line is fit through the baseline data for each figure; a dash-dot line demarks a conservative approximation of the load coefficients' behavior as less severe forced pitch motions are applied. Increased aerodynamic performance occurs for increases in lift relative to the baseline without subsequent adverse moment or drag consequences. The datasets are segregated through the COMPACT nondimensional control frequency,  $F^+$ . Inspection of Figure 196 and Figure 197 show that large benefits were realized for  $F^+ = 0.8$  and 1.0. However, these actuation cases fell into two distinct groups. The encircled group in each figure highlights the datasets associated with light stall prescribed motion. In such cases, the actuators strongly modified the DSV, eliminating the large excursions in drag and moment associated with its presence (as shown for  $\alpha = 10^\circ - 10^\circ \cos \omega t$ ,  $k = 0.10$  previously). Conversely, for deep stall, high  $F^+$  produced increased peak lift but adverse moment and drag still followed. Still, performance benefits relative to the baseline trends exceeded +20% lift for equal moment and drag. Through the collective dataset,  $F^+ < 0.8$  did not yield continuous or substantial shifts from the baseline VR-12 traits in terms of the metrics considered here. Low  $F^+$  did have a significant impact on cycle-averaged lift.

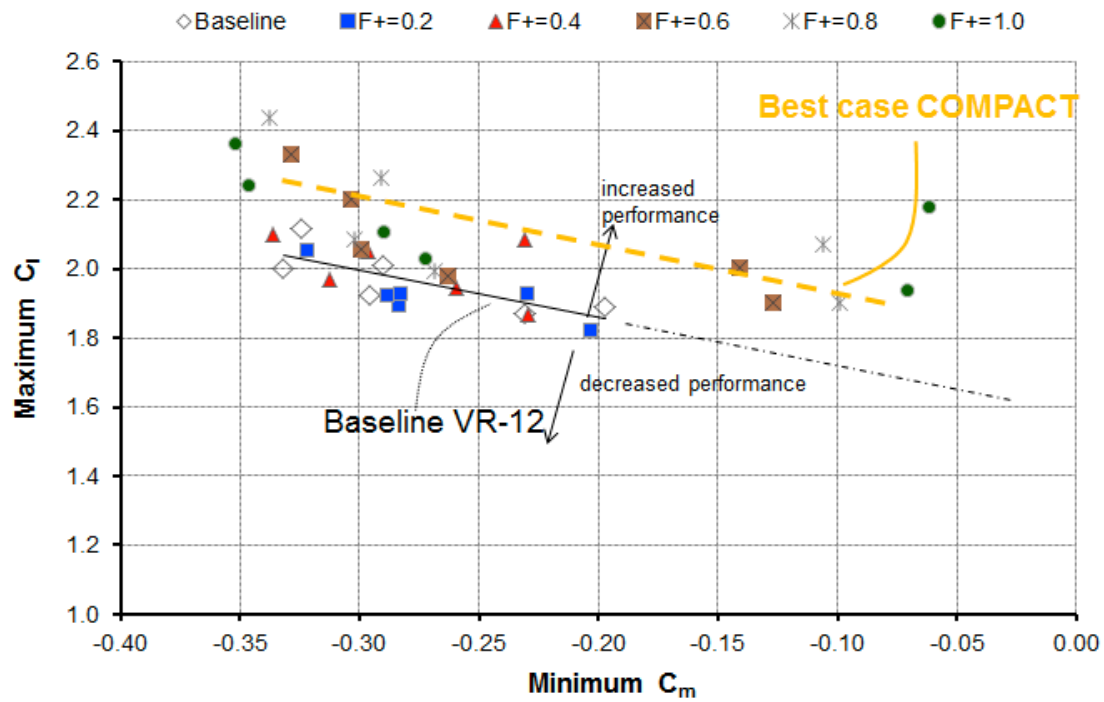
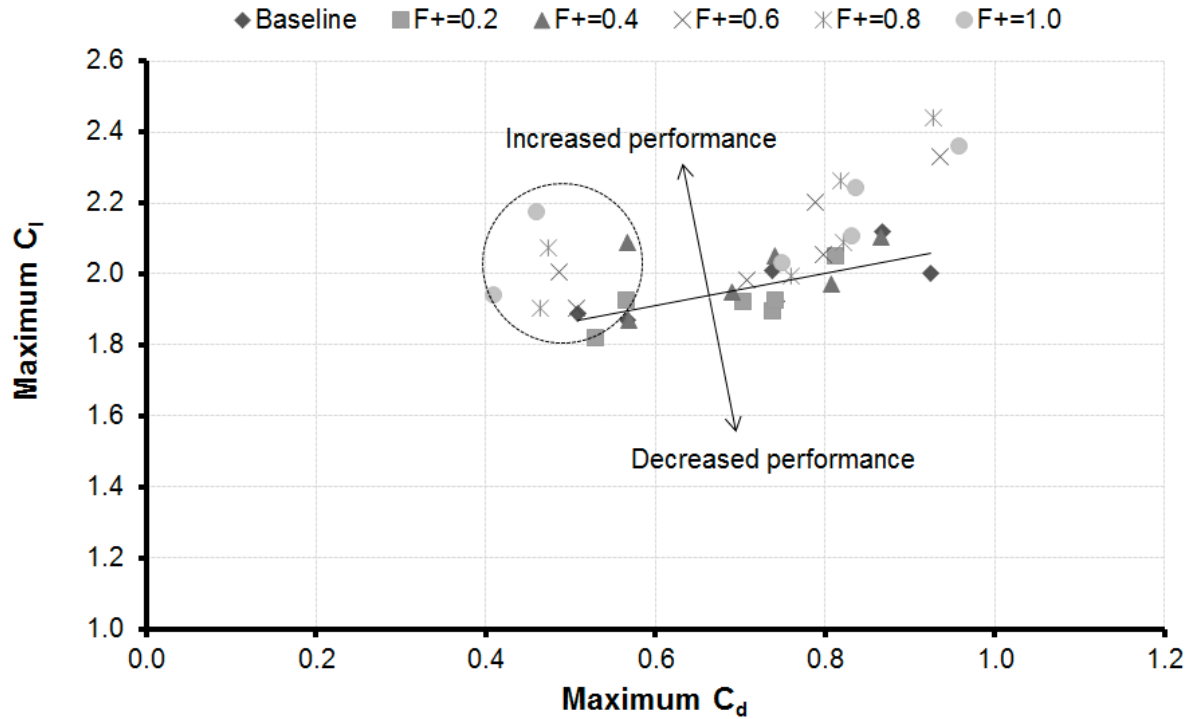


Figure 196. COMPACT effect on Mach 0.2 VR-12 lift and moment traits.



**Figure 197. Mach 0.2 COMPACT effect on VR-12 lift and drag traits. The cases within the circle are light-stall cases.**

The Mach 0.2 datasets were further examined for stall attribute relationships with respect to actuation frequency.  $C_{L,avg}$ ,  $C_{L,max}$ ,  $C_{D,max}$ , and  $C_{M,min}$  are plotted for each tested pitch trajectory in Figure 198 through Figure 201.  $C_{L,avg}$  is used to represent lift hysteresis reduction and is shown in Figure 198. Increasing  $F^+$  had a beneficial impact for both light and deep stall trajectories. This is a testament of COMPACT's ability to improve the downstroke separated flow performance.  $C_{L,max}$  in Figure 199 indicates a weaker correlation with actuation frequency.  $F^+$  of 0.4 was required to regain losses associated with the hardware installation and steady bleed-on performance. Further frequency increases had a positive impact on peak lift. When viewed simultaneously with  $C_{D,max}$  in Figure 200, high peak lift increases for  $\alpha = 15^\circ - 8^\circ \cos \omega t$ ,  $k = 0.10$  and  $\alpha = 15^\circ - 10^\circ \cos \omega t$ ,  $k = 0.10$  were paralleled by high drag. Light stall cases, as previously discussed, realized smaller peak lift increases (a strong function of the pitch motion itself), but large drag reductions. Similarly, COMPACT had little effect on the pitching moment in Mach 0.2 deep stall, but eliminated the moment-break altogether for  $F^+ \geq 0.6$  for the light stall cases.

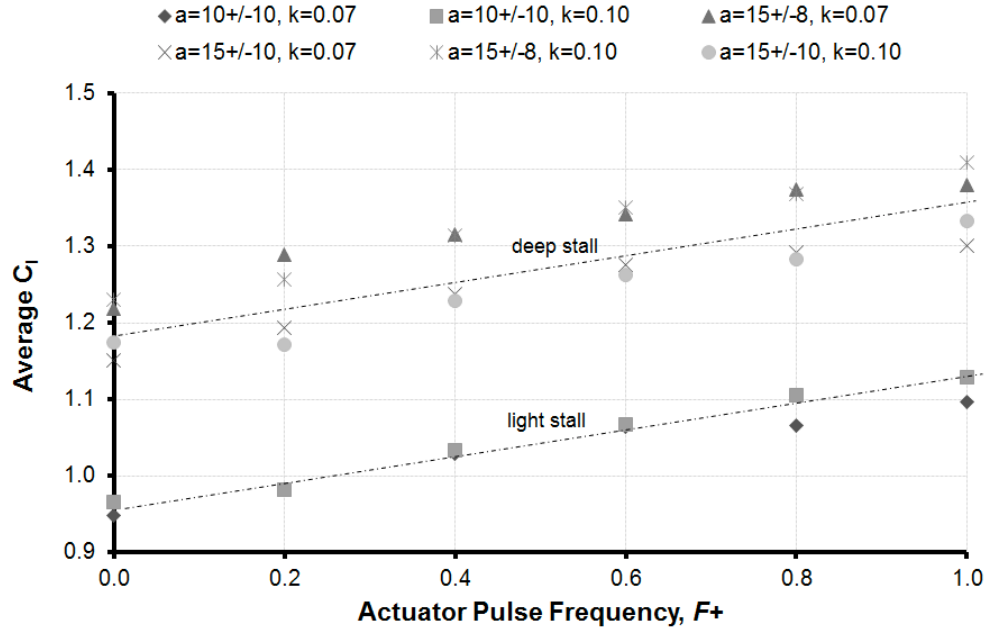


Figure 198. COMPACT actuation frequency effect on Mach 0.2 average lift.

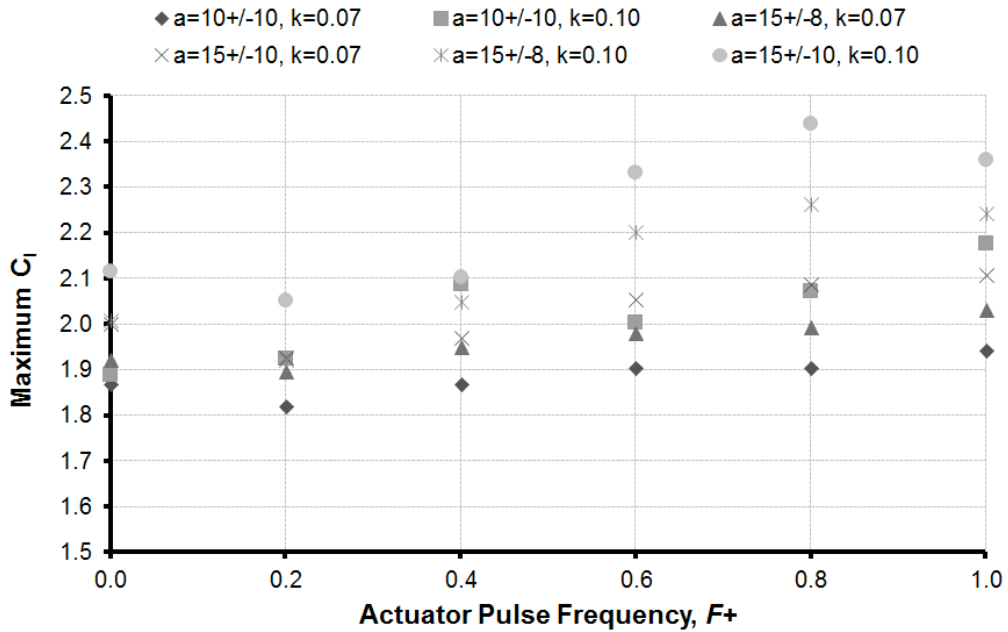


Figure 199. COMPACT actuation frequency effect on Mach 0.2 maximum lift.

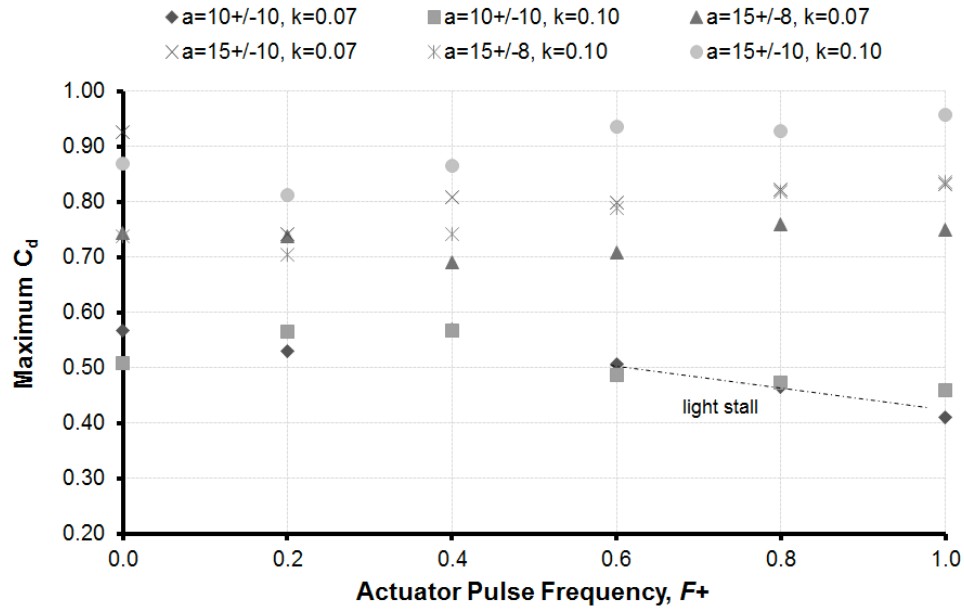


Figure 200. COMPACT actuation frequency effect on Mach 0.2 maximum drag.

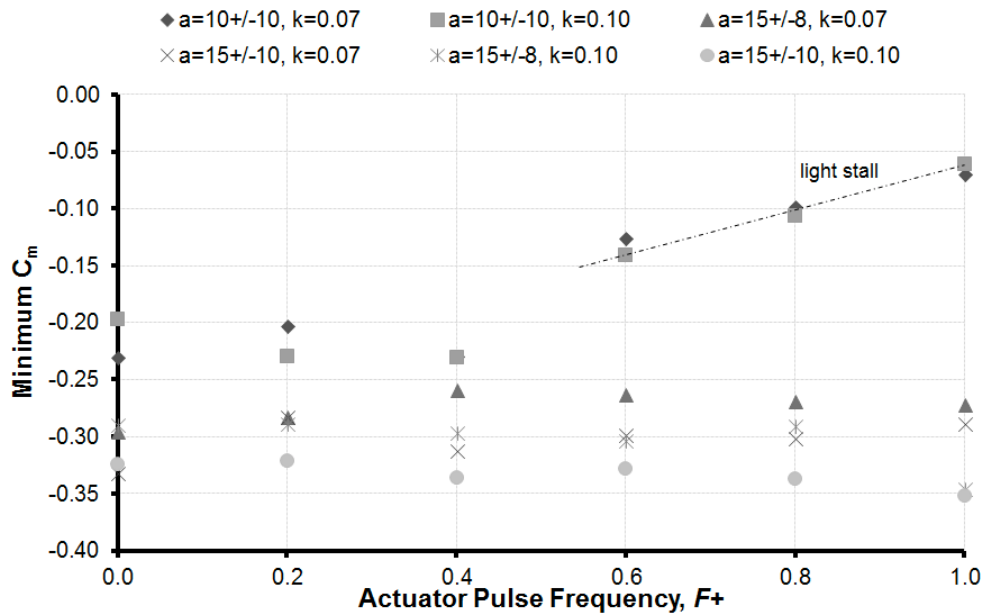


Figure 201. COMPACT actuation frequency effect on Mach 0.2 adverse pitching moment.

### 3D Effects

It is important to note that any streamwise vorticity developed due to the actuated/unactuated wingspan are affected by two items: freestream velocity and stall penetration. Assuming some

margin of stall suppression over the actuated span, augmented center-span lift gains will generate larger, more concentrated longitudinal vortices. The low pressure, stalled flow on the outboard wing sections will encourage a spanwise stretching of the inboard, COMPACT produced disturbances. This behavior weakens their ability to entrain/mix high momentum and near wall flow regimes.

Light stall COMPACT drag benefits were not overwhelmed by induced drag losses as stall occurred across the span in a similar fashion, dictated by the airfoil pitch motion. This was also true for Mach 0.3 light stall cases, as shown in Appendix 4. This is illustrated in Figure 202 by examining the loads integrated at each of the four instrumented stations. Recall, each station's forward airfoil characteristics are represented by the center span leading edge Kulites at Station 1; strictly speaking, the loads shown for Station 3-4 are not well resolved. However, it would be expected that if 3D flow attributes exist, the aft 50% chord would register significant differences between each station. For the integrated loads, this will cause large pitching moment differences. For the case  $\alpha = 10^\circ - 10^\circ \cos \omega t$ ,  $k = 0.10$  discussed previously, lift, drag, and pitching moment all agree in Figure 202, suggesting a uniform load distribution across the wing 4. Inspection of the pressure distribution at  $\alpha = 17.1^\circ$  supports this conclusion.

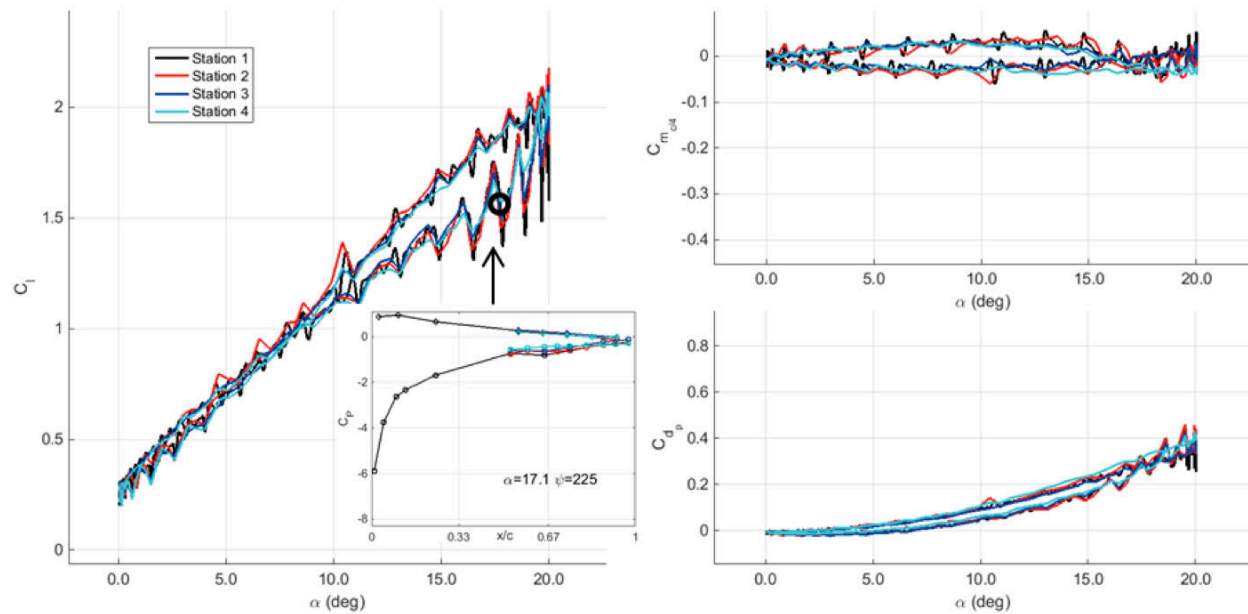


**Figure 202. Comparison of integrated loads at each VR-12 measurement station.  $M=0.2$ ,  $\alpha = 10^\circ \pm 10^\circ$ ,  $k = 0.10$ ,  $F^+ = 1.0$ . Run 67, Pt 22.**

For deep stall, differences between actuated span and unactuated span could be dramatic, particularly near  $\alpha_{max}$ . Several pressure distributions from  $\alpha = 15^\circ - 10^\circ \cos \omega t$ ,  $k = 0.10$ ,  $F^+ = 1.0$  case (Run 67 Pt. 53) are shown in Figure 203. The baseline VR-12 lift-stall occurs at roughly  $23^\circ$  on the upstroke. For the actuated case shown, fairly uniform flow is measured across the span at  $22.7^\circ$  prior to the nominal stall angle. Shortly thereafter however, the DSV forms and large spanwise flow differences abruptly arise. Station 3, which is aligned downstream of the last COMPACT module on the upper actuator bank, witnesses significantly lower pressure than the inboard (Stations 1 and 2) or outboard (Station 4) instrumentation arrays.

It is suspected that this low-pressure region is the signature of a stronger dynamic stall vortex produced over the unactuated spans of the wing. The low pressure invades Station 1 and Station 2, decreasing the pressure that would be measured in a more 2D setting. Consequently, the pitching moment and drag peaks fail to show signs of significant adverse force reduction in the presence of COMPACT. Station 4 has additional 3D effects associated with the open wing tips of the model wing. Station 3 agreement improves at  $24.3^\circ$ , and  $21.9^\circ$  on the downstroke, but diverges again at  $18.7^\circ$  and  $14.8^\circ$ . These measurements suggest a very complicated time-dependent and 3D flow-field for deep stall excursions.

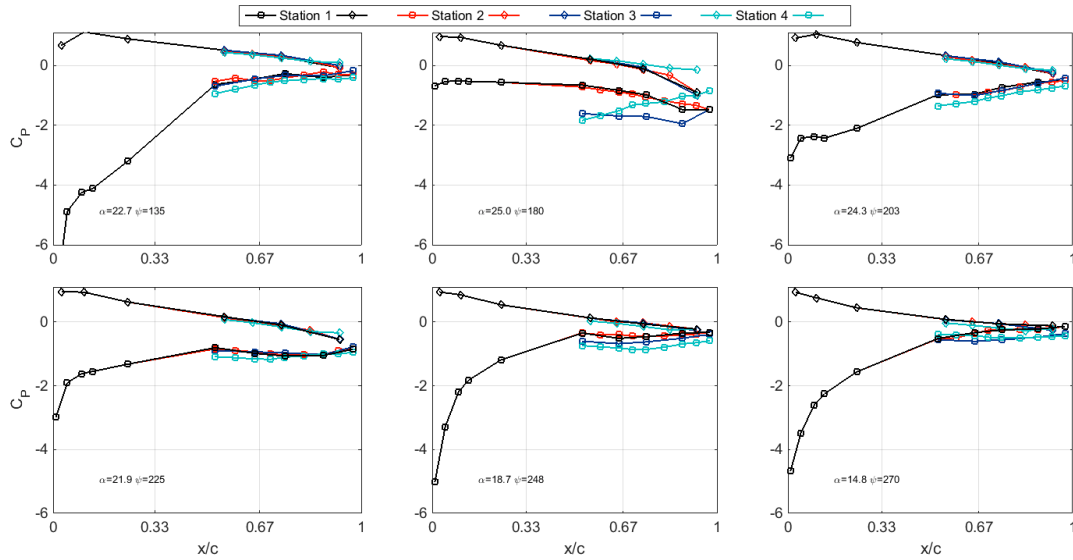


**Figure 203. Chord pressures for  $M = 0.2$ ,  $\alpha = 15^\circ \pm 10^\circ$ ,  $k = 0.10$ ,  $F^+ = 1.0$  for each instrumented station.**

### **$M=0.3$**

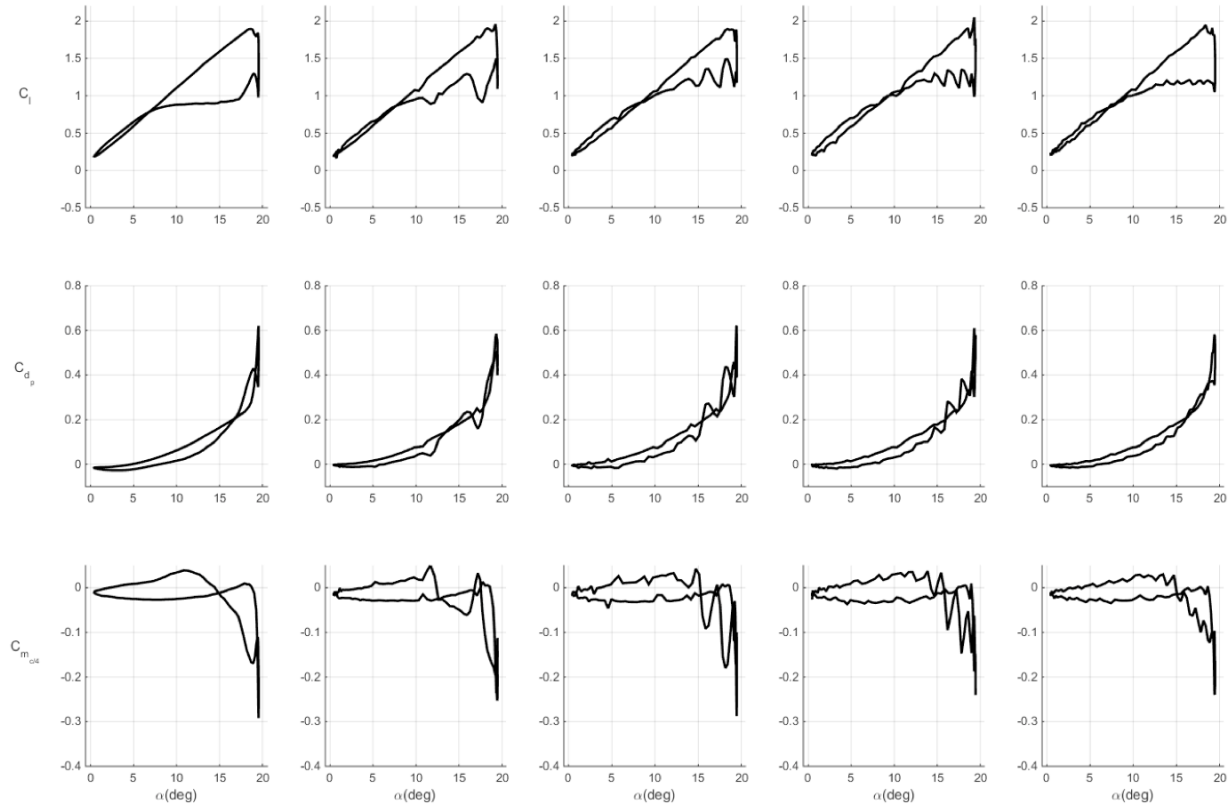
A wide range of conditions were tested at this Mach number — eleven unique combinations of reduced frequency, mean angle, and pitch amplitude were studied. Reduced frequency ranged from 0.025 to 0.10 and peak airfoil angles to  $23^\circ$ . The complete set of  $F^+$  sweeps compared to the VR-12 baseline can be found in the Appendix 4.

Unsteady pitching results at Mach 0.3 are summarized in Figure 204 through Figure 206 for the baseline VR-12 and single-row COMPACT configuration undergoing  $\alpha = 10^\circ \pm 9.5^\circ$ ,  $k = 0.07$  prescribed pitching. At this Mach number, actuation across an  $F^+$  range from 0.2 to 0.8 was conducted; however, firing the actuators at  $F^+ = 0.8$  required actuation at over 200 Hz, as previously noted. Although the actuator banks were proven to fire uniformly in benchtop tests at this frequency, achieving uniform actuation in the wind tunnel proved to be challenging. As will be discussed later with regard to Figure 311, increasing  $F^+$  caused a reduction in combustion chamber pressure. Based on IR images collected during the test, strong actuator performance at this Mach number was likely limited to  $F^+ = 0.6$  or less. Also, absolute suction levels on the upper surface of the airfoil at this Mach number increased, which resulted in added difficulty in executing strong pulses prior to flow separation. The combination of these two limitations reduced the observed trends associated with  $F^+$ .



Unlike the case considered at Mach 0.2, the Mach 0.3 trial discussed herein is best described as deep dynamic stall. The pitching moment breaks at  $18.4^\circ$  and lift stall occurs  $0.5^\circ$  later prior to the airfoil reaching  $\alpha_{max}$ . The stall vortex reaches the trailing edge just as the airfoil reaches its peak angle, causing abrupt lift, drag, and moment responses. In accordance with the Mach 0.2 discussion, this deep stall case likely suffers from larger 3D effects than its light stall counterpart  $\alpha = 10^\circ \pm 8^\circ, k = 0.07$  shown in Appendix 4.

The highest actuation frequencies tested do not result in the greatest lift hysteresis reduction, unlike the outcomes at Mach 0.2. COMPACT performance becomes a trade between the benefit associated with additional pulsing and the degradation in actuator ignition and combustion at the higher frequencies. Best results in terms of lift hysteresis reductions were achieved at  $F^+$  of 0.4 and 0.6. For  $F^+$  of 0.4, a  $\Delta C_L = +0.44$  is promoted at  $16^\circ$  on the downstroke without additional drag production.



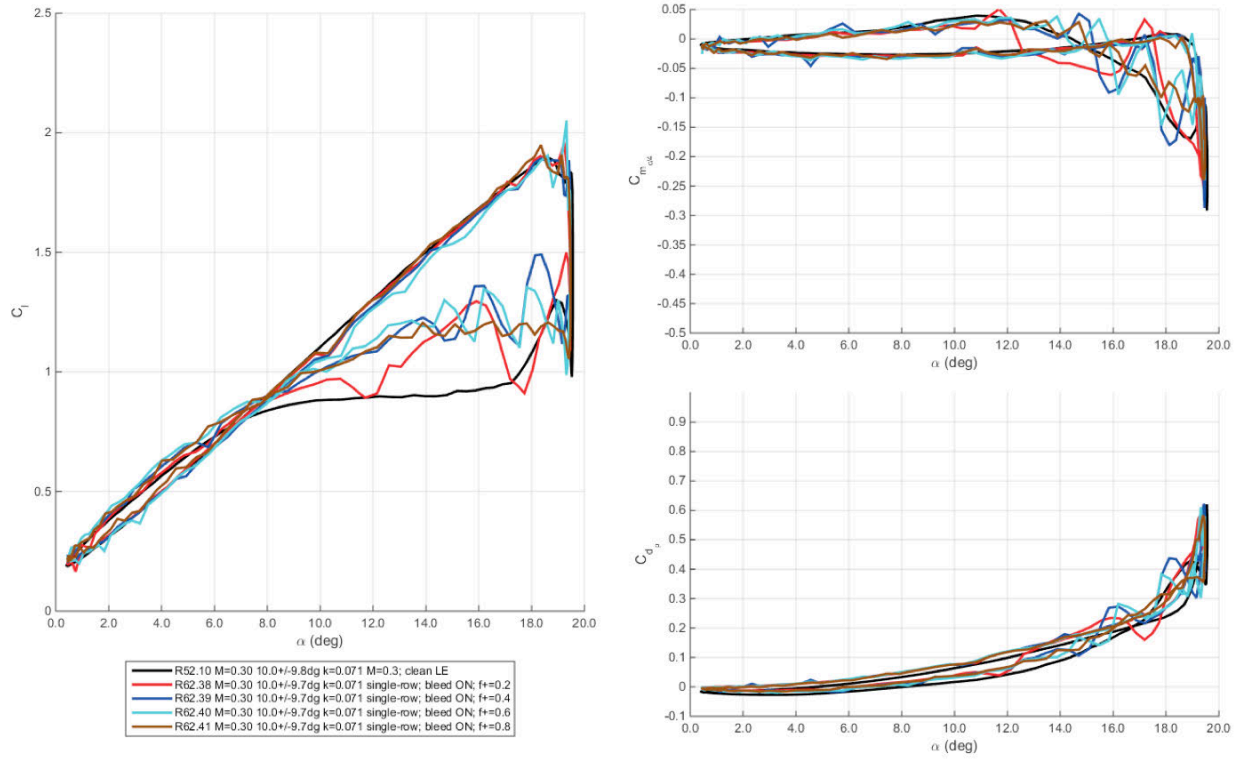
**Figure 204. Unsteady aerodynamic loads with respect to angle-of-attack.  $M = 0.3$ ,  $\alpha = 10^\circ \pm 9.5^\circ$ ,  $k = 0.07$ . Baseline and single-row COMPACT  $F^+ = 0.2-0.8$  shown in order from left to right.**

Figure 207 compares the near peak angle and downstroke ensemble averaged chord pressures for the baseline and COMPACT cases. For  $\alpha = 17.6^\circ$  on the upstroke, little difference is measured between the actuated and baseline pressure distributions. Past stall, the actuator induced

differences are apparent in the pressure distributions. For each angle past  $\alpha = 18.9^\circ$ , and all  $F^+$ , a strong improvement in the leading edge suction peak is measured.

More benefit in terms of lift hysteresis closure is apparent at higher degrees of stall, as shown in Appendix 4. This was expected based on the steady results wherein lift benefits were shown to be strong post-static-stall but relatively small prior to static stall.

Some reductions in peak negative moment are shown for some of the Mach 0.3 prescribed pitch motions, but these effects are small compared to near 70% reduction measured at Mach 0.2. Similarly, small changes in the drag behavior are noted, particularly in terms of large fluctuations, however peak drag remained largely unmodified. Summary figures for  $C_{L,max}$  as a function of  $C_{M,min}$  and  $C_{D,max}$  are shown in Figure 208 and Figure 209. Unlike Mach 0.2, the COMPACT did not result in large peak load differences compared to the baseline. Average lift, however, was significantly modified without increases to drag or moment penalties. Figure 210 shows this as function of minimum pitching moment. From this perspective, each  $F^+$  was found to be effective in producing increased airfoil aerodynamic performance, particularly for deep stall cases.



**Figure 205.** Unsteady aerodynamic loads with respect to angle-of-attack,  $M = 0.3$ ,  $\alpha = 10^\circ \pm 9.5^\circ$ ,  $k = 0.07$ . Baseline and single-row COMPACT  $F^+ = 0.2 - 0.8$ .

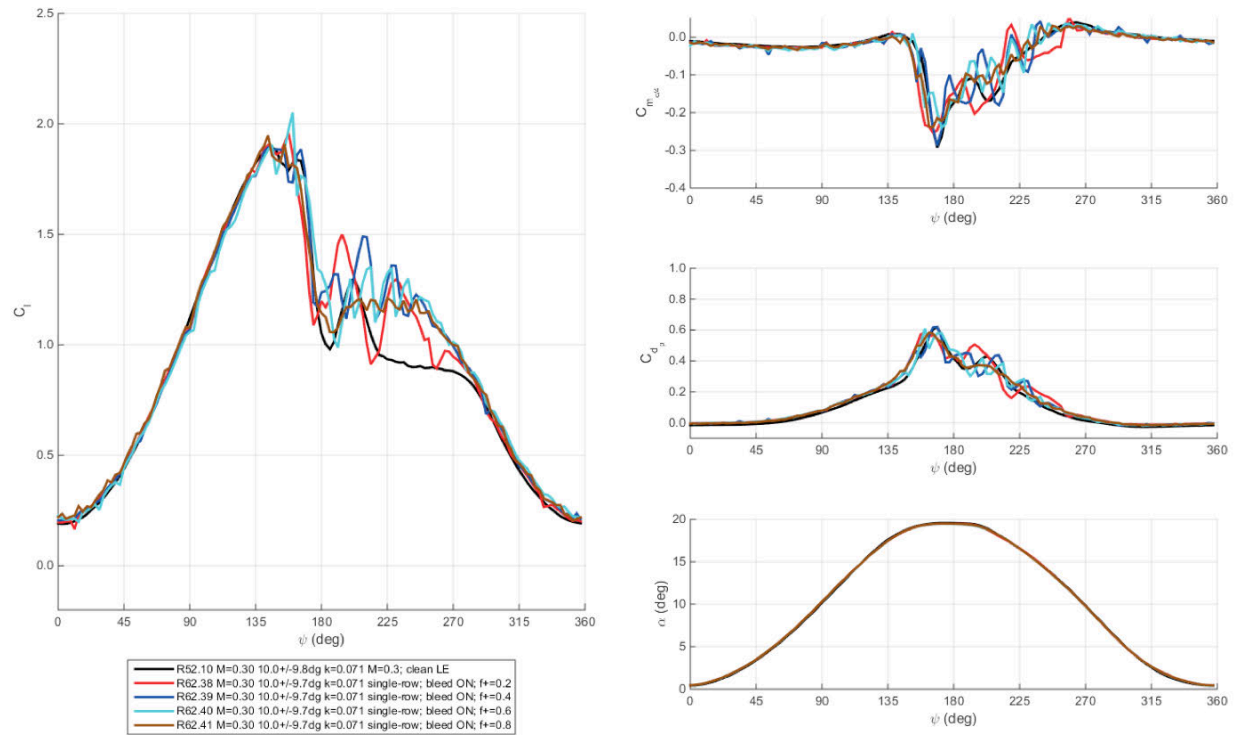


**Figure 206.** Unsteady aerodynamic loads and angle-of-attack with respect to phase,  $M = 0.3$ ,  $\alpha = 10^\circ \pm 9.5^\circ$ ,  $k = 0.07$ . Baseline and single-row COMPACT  $F^+ = 0.2 - 0.8$ .

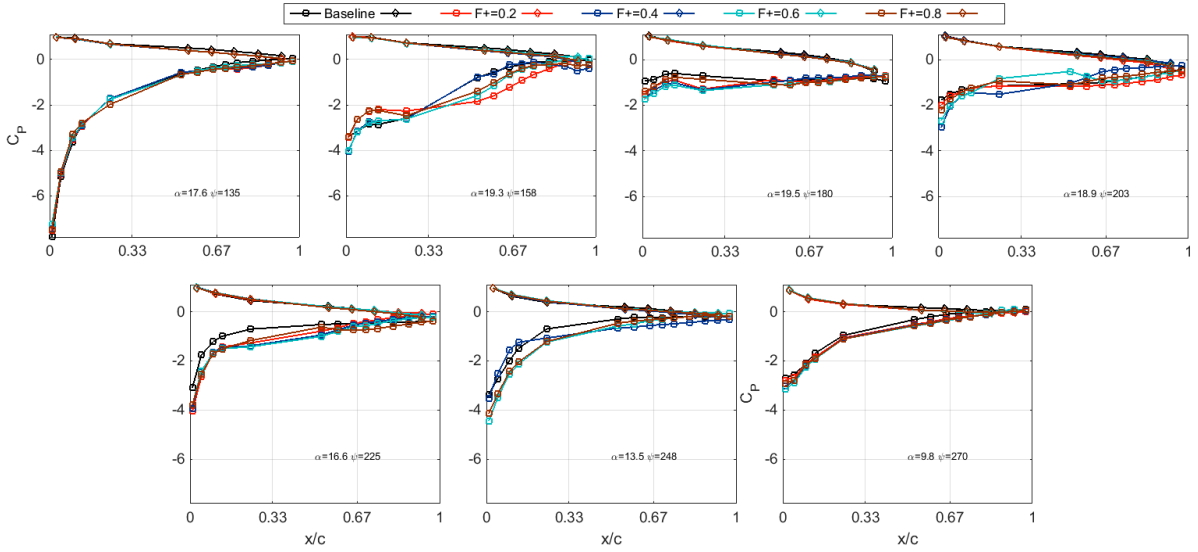


Figure 207. Comparison of selected  $C_p$  for  $M=0.3$ ,  $\alpha = 10^\circ \pm 9.5^\circ$ ,  $k = 0.07$ . Baseline and  $F^+ = 0.2-0.8$ . Square symbols indicate upper surface, triangles indicate lower surface measurements.

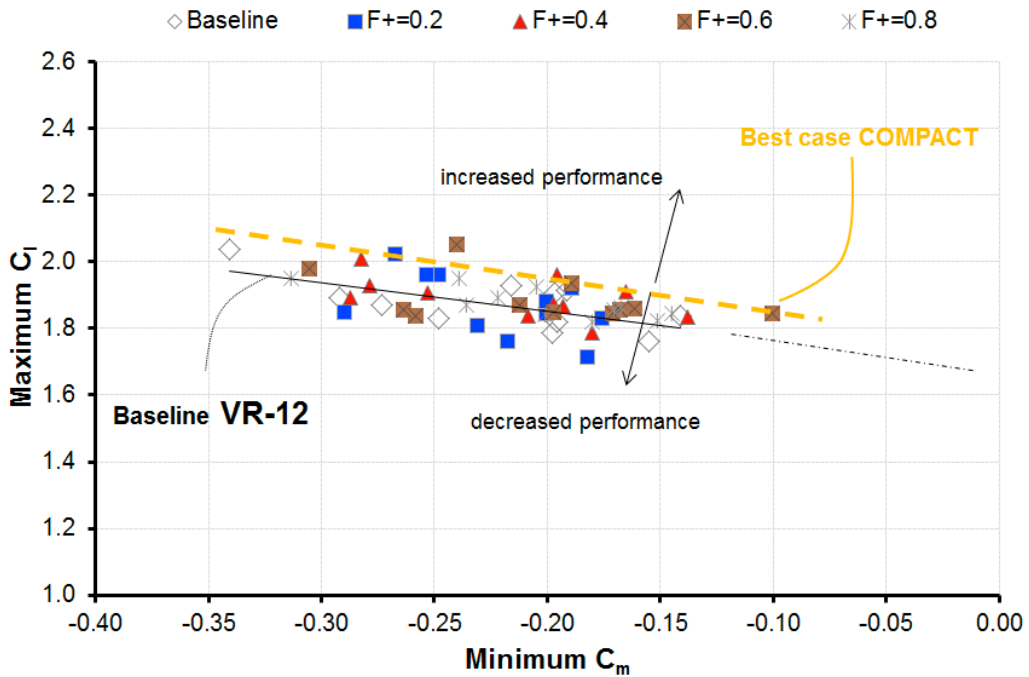


Figure 208. Mach 0.3 COMPACT effect on VR-12 lift and moment traits for full-cycle actuation.

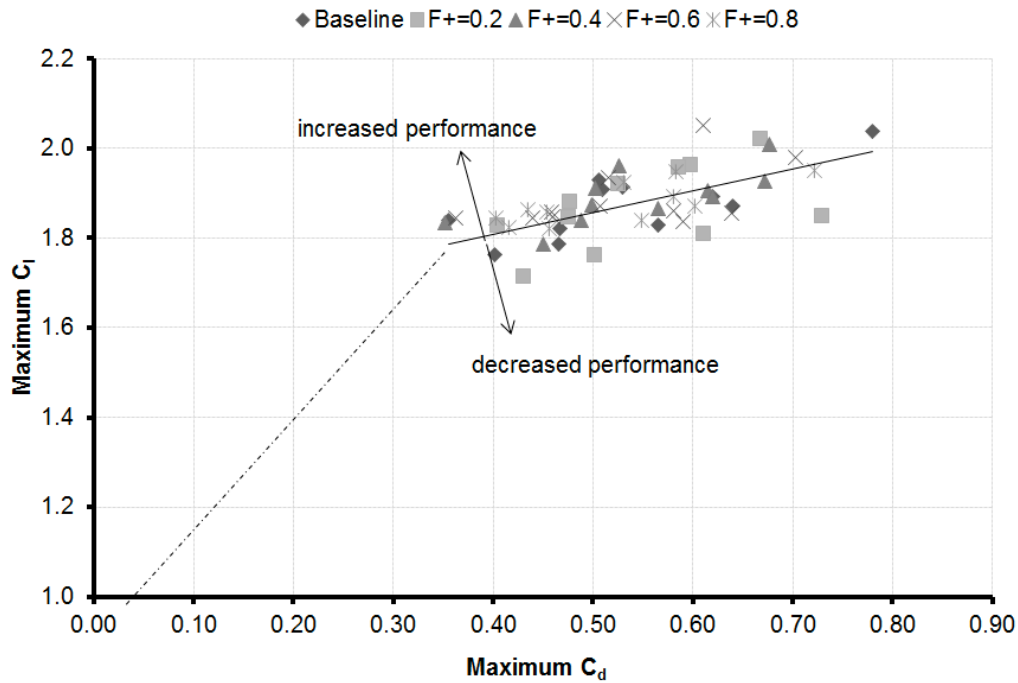


Figure 209. Mach 0.3 COMPACT effect on VR-12 lift and drag traits for full-cycle actuation.

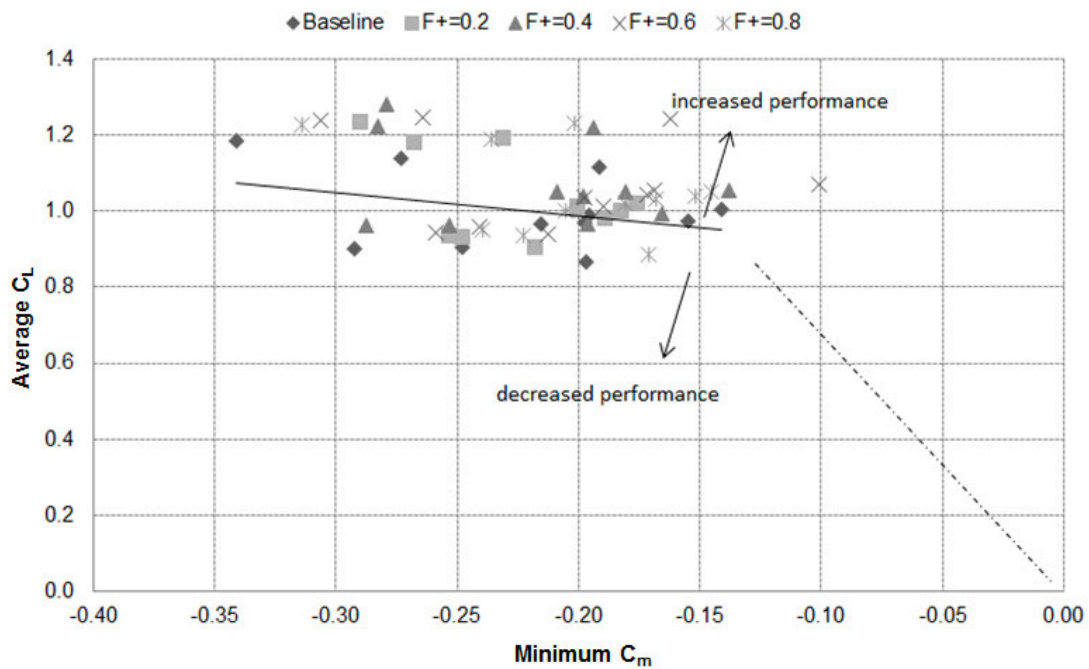


Figure 210. Mach 0.3 COMPACT effect on VR-12 average lift and moment traits for full-cycle actuation.

### Increases to Hydrogen/Air Mixture Ratio

A brief inquiry into the effect of increasing hydrogen in the hydrogen-to-air fuel mixture was also conducted at Mach 0.3. The internal chamber pressure was not measured for these cases; however, previous benchtop tests [28] have shown that a richer mixture yields a larger peak pressure and subsequent pressure ratio. The respective data points for this inquiry are shown in Table 27. The baseline VR-12 integrated loads are compared to the actuated cases in Figure 211. Each COMPACT case is called-out based on the hydrogen rotometer settings. The nominal setting for the actuators at Mach 0.3 varied between 80 and 90. A Flow setting of ‘H2=70’ caused strong downstroke lift increases. Further increasing hydrogen mass flow had additional favorable impact on the downstroke lift as well as a small yet beneficial reduction in peak adverse drag and pitching moment. The H2=90 lift trace is highlighted by symbols in Figure 211 for emphasis. For the highest rotometer setting tested at Mach 0.3, H2=100, shows an overall lift increment similar to that found for H2=80 and H2=90 flow settings. Load fluctuations though undergo a large increase. The observation that a richer gas mixture promotes further dynamic stall alleviation suggests that peak  $C_{\mu}$  and/or impulse are important actuation parameters in controlling dynamic stall, corroborating results from the post-test CFD analysis. However, this only appears true to a certain extent, as larger COMPACT forced disruptions to the flow field result in increased fluctuations without overall separation control benefits.

**Table 27. Data Points Acquired For Mixture Ratio Sweep.**

Run	Mach	$k$	$\alpha_0[^\circ]$	$\alpha_1[^\circ]$	$F^+$	Pulse Start $\alpha[^\circ]$	H2	Points
52	0.3	0.07	10	9.5	NA	NA	NA	10
78	0.3	0.07	10	9.5	0.4	10	70, 80, 90	9-12
62	0.3	0.07	10	9.5	0.4	10	100	39

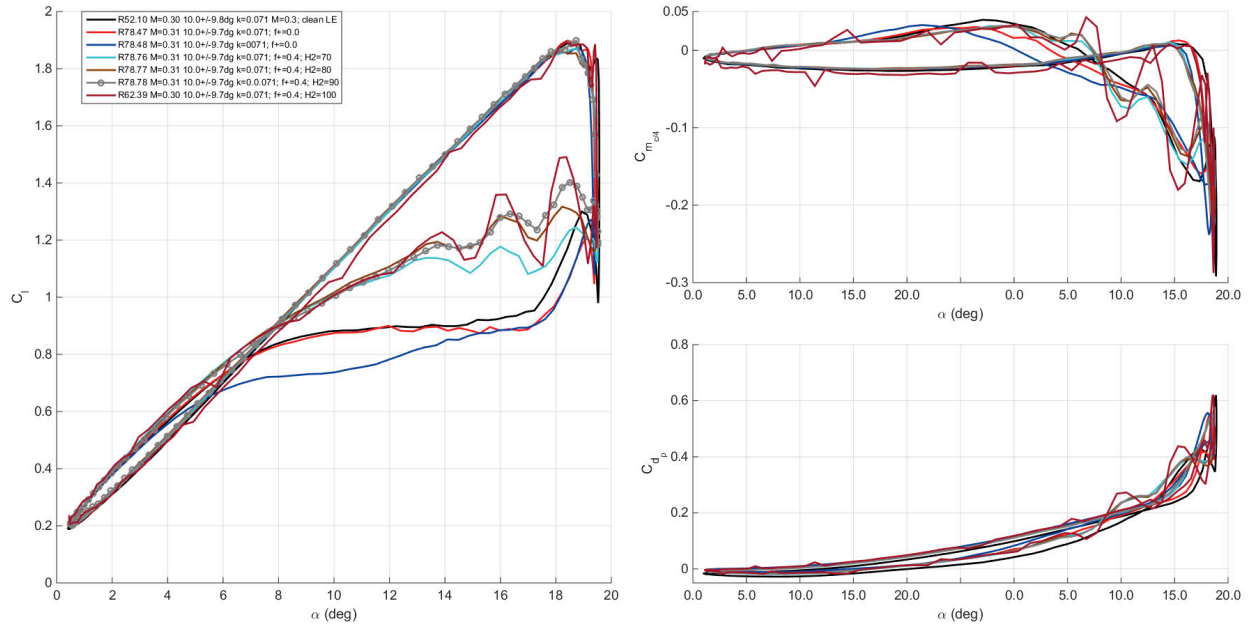


**Figure 211. Effect of increasing hydrogen to COMPACT on unsteady lift, drag, and moment.  $M = 0.3$ ,  $\alpha = 10^\circ \pm 9.5^\circ$ ,  $k = 0.07$ ,  $F^+ = 0.4$ .**

### Number of Pulses

The predominant mode of operation during the wind tunnel test focused on continuous pulsing throughout the pitch cycle. However, a small investigation of the number of pulses required to inhibit dynamic stall was also tested. A reduced number of pulses-per-cycle corresponds to significant COMPACT fuel savings, amongst other fatigue reduction benefits applicable to any periodic system. A pulse start angle of  $17^\circ$  on the upstroke was used for  $F^+ = 0.4, 0.6, 0.8$  actuation. The start angle corresponds to roughly one degree prior to the clean VR-12 moment stall, and about two degrees prior to lift stall. Pulses were varied from a single pulse (for  $F^+ = 0.4$  only) to one pulse shy of continuous. Figure 212 through Figure 214 summarize the  $N_{pulse}$  study. For  $F^+ = 0.4$ , two cases are highlighted with symbols. For  $N_{pulse} = 1$ , little alteration of the steady bleed lift behavior is measured. On closer inspection,  $C_L$  decreases immediately following the actuator pulse at  $17^\circ$ . This drop results in a beneficial decrease in peak moment and drag. It suggests that a single pulse was more disruptive to the formation of the dynamic stall vortex, weakening its strength and impact on all airloads. Without further pulses, separation supervenes and lift on the downstroke suffers. Incrementing the number of pulses, it is observed that the moment and drag benefits disappear. 4 pulses are required to see lift variation on the downstroke. The last pulse for  $N_{pulse} = 4$  occurs at roughly  $19^\circ$  on the downstroke.  $C_L$  climbs from 1.0 to 1.45 at  $18.2^\circ$  and then quickly degrades back to the steady bleed lift levels. The addition of 2 pulses,  $N_{pulse} = 6$ , exceeds the pulse threshold to achieve strong control of the separated downstroke behavior. Additional pulses cause only minor differences throughout the rest of the pitch cycle.  $N_{pulse} = 6$  constitutes a 35% duty-cycle for COMPACT at  $F^+ = 0.4$ . The integrated load coefficient for  $F^+ = 0.6$  and  $0.8$  are also shown below – for  $F^+ = 0.6$ , 8 pulses (31% duty-cycle) is just shy of producing the benefit seen for 12 pulses (46% duty-cycle). For  $F^+ = 0.8$ , 12 pulses (34% duty-cycle) generates the same lift hysteresis closure as that found for continuous pulsing.



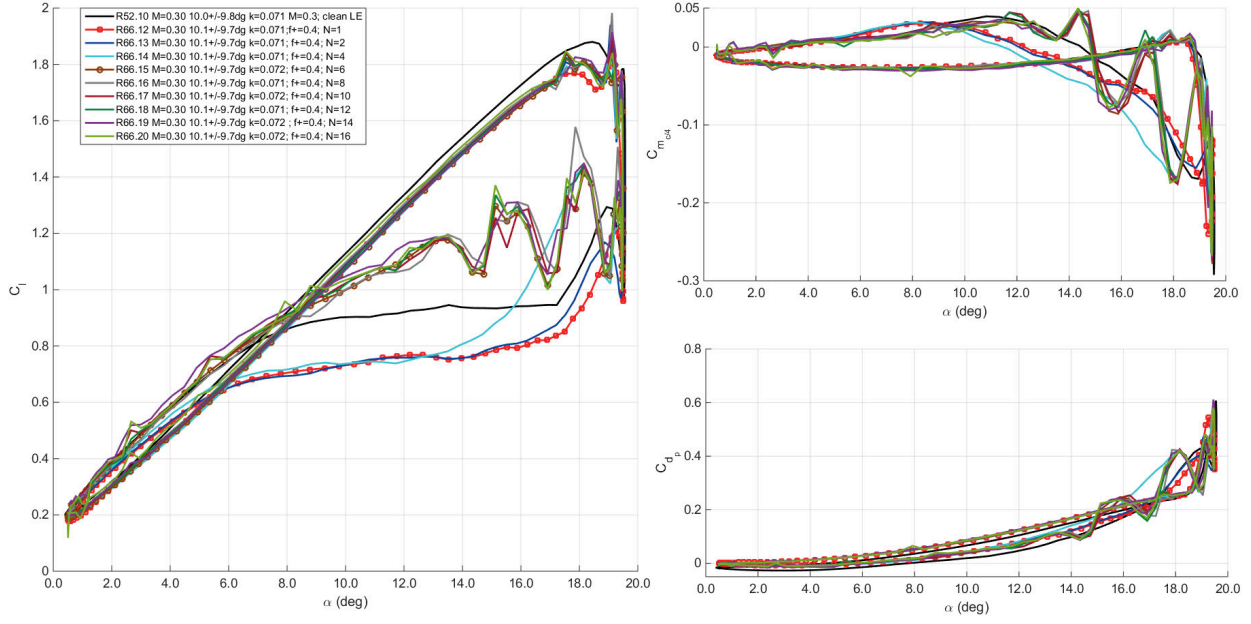


Figure 212. Effect of  $N_{pulse}$  on unsteady lift, drag, and moment.  $M = 0.3$ ,  $\alpha = 10^\circ \pm 9.5^\circ$ ,  $k = 0.07$ ,  $F^+ = 0.4$ ,  $\alpha_{start} = 17^\circ$ .

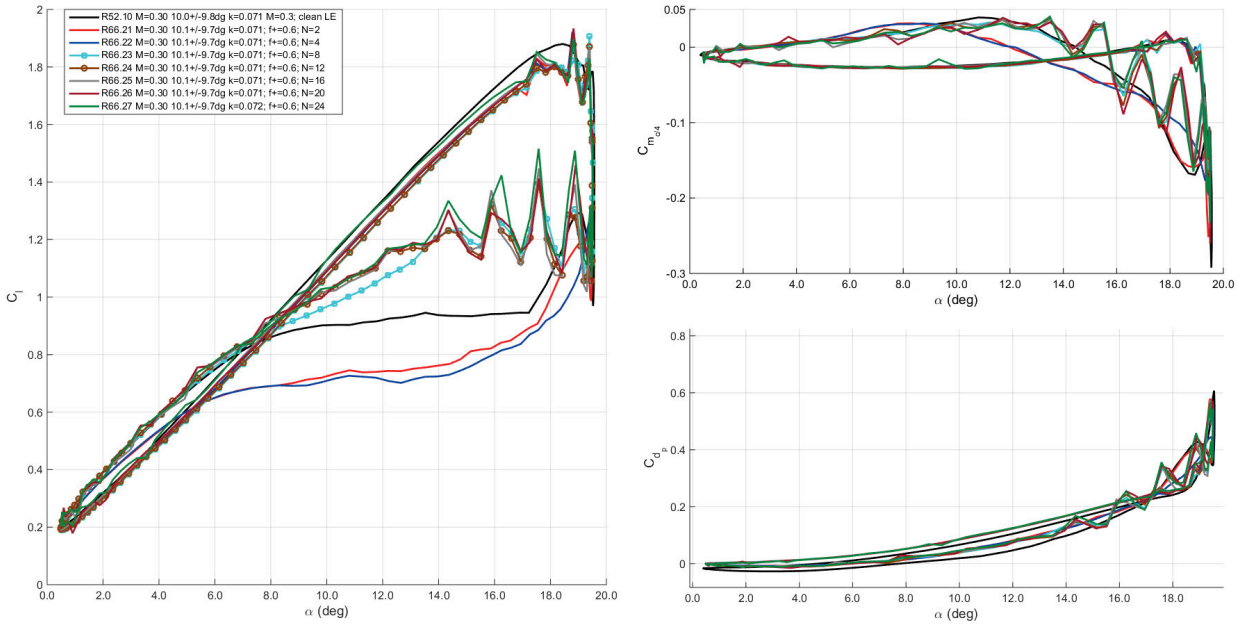
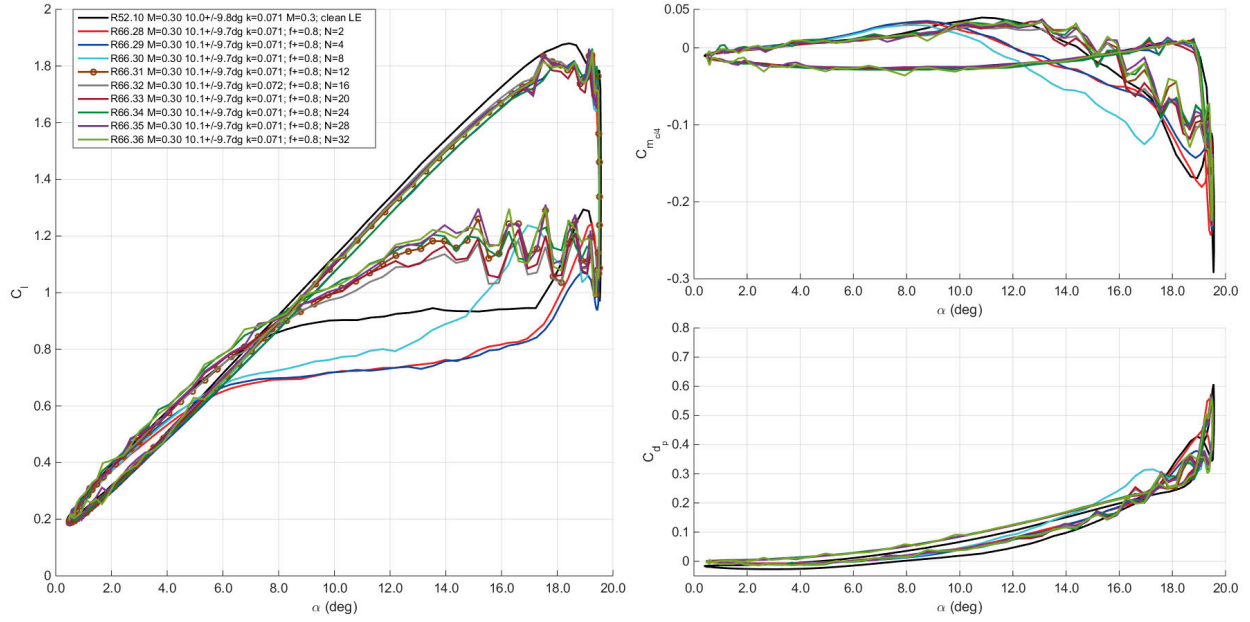
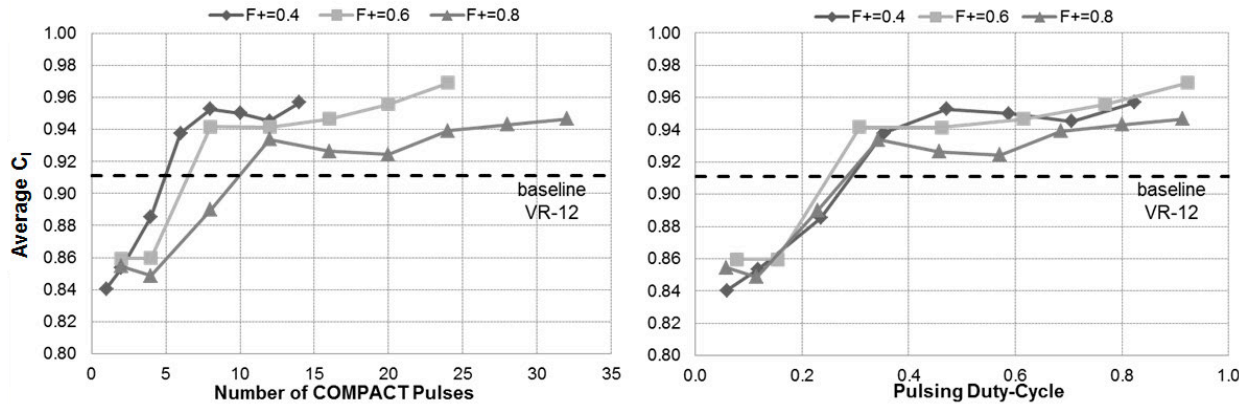


Figure 213. Effect of  $N_{pulse}$  on unsteady lift, drag, and moment.  $M = 0.3$ ,  $\alpha = 10^\circ \pm 9.5^\circ$ ,  $k = 0.07$ ,  $F^+ = 0.6$ ,  $\alpha_{start} = 17^\circ$ .



**Figure 214. Effect of  $N_{pulse}$  on unsteady lift, drag, and moment.  $M = 0.3$ ,  $\alpha = 10^\circ \pm 9.5^\circ$ ,  $k = 0.07$ ,  $F^+ = 0.8$ ,  $N_{pulses} = 4$ ,  $\alpha_{start} = 17^\circ$ .**

Figure 215 summarizes the results of the  $N_{pulse}$  datasets. Each frequency had a threshold number of pulses required to develop a strong lift hysteresis reduction. However, the actual dependency is more aligned with the duration of pulsing relative to the pitch cycle period. For all  $F^+$ , approximately 35% of the pitch-cycle required pulsing. For the forced motion considered here, and given  $\alpha_{start} = 17^\circ$  on the upstroke, actuation was required to  $15.6^\circ$  on the downstroke,  $5^\circ$  higher than the mean pitch angle.



**Figure 215. Average lift from unsteady integrated loads as a function of COMPACT pulse number and actuation duty-cycle.**

#### Pulse Start Angle

An important consideration for unsteady control schemes directed at periodic separation control is the impact of the pulse timing relative to the physical stall event, particularly for non-

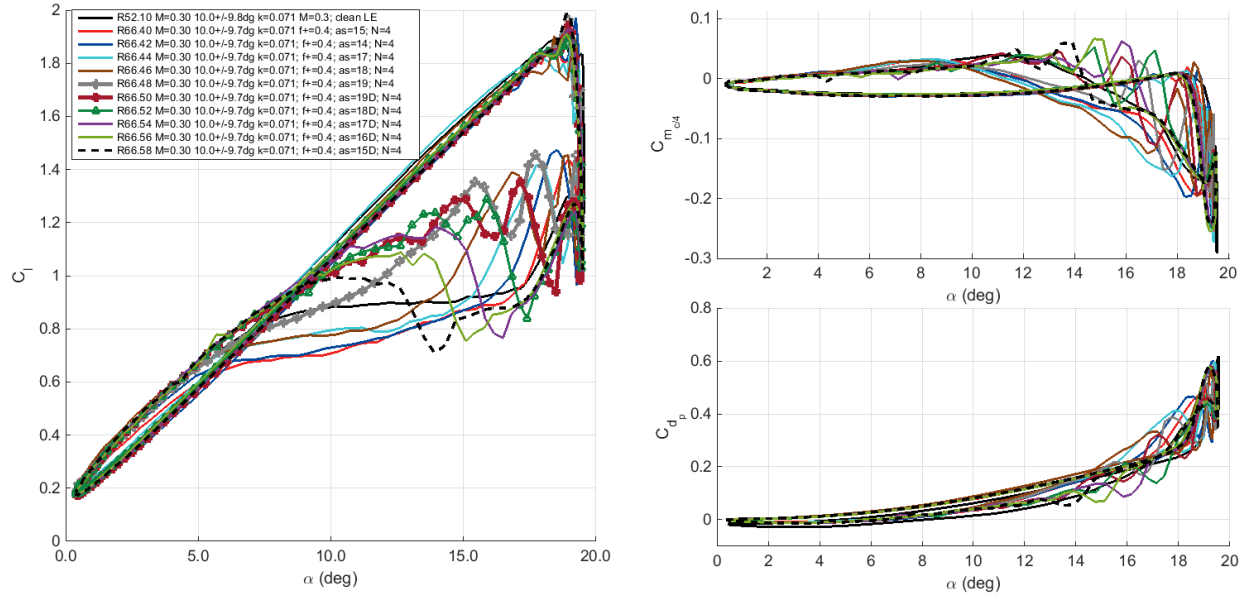
continuous pulsing. A survey of pulse start angles was conducted for quarter-cycle and half-cycle COMPACT at  $F^+ = 0.4, 0.6$ , and  $0.8$ . The associated conditions and data points are shown in Table 28. Figure 216 summarizes the loads as a function of angle-of-attack for  $F^+ = 0.4$ . As expected, several cases show poor downstroke lift enhancement. These correspond to pulse start angles of  $14^\circ, 15^\circ, 17^\circ$  and  $18^\circ$  on the upstroke. Each shows initial modulation of the baseline behavior following the transition from up- to downstroke. The lack of COMPACT thereafter allows the airfoil to return to its steady bleed-on performance level. Similarly, ‘late’ actuation fails to disrupt the transitional aerodynamic behavior, see the load traces for pulse start angles of  $17^\circ, 16^\circ$ , and  $15^\circ$  on the downstroke. That said, a very encouraging result from this study was found for pulse start angles closely matched to the native VR-12 stall behavior. ‘Manual locking’ of the actuation pulses near moment and lift stall yield similar benefits compared to continuous pulsing, as shown in Figure 205. Symbols are added to the three most beneficial lift traces in Figure 216 to distinguish them from the other pulse start angle cases. Pulse start angles of  $19^\circ$  on both the upstroke and downstroke created large improvements in lift hysteresis compared to the clean baseline. A start angle of  $18^\circ$  on the downstroke also resulted in large gains, but was not early enough to reduce the initial drop in  $C_L$ . For each case, drag and pitch moment, aside from the unsteady fluctuations introduced by the actuators, were unaffected. This is likely a repercussion of the deep stall behavior of this case and the 3D nature of the wing flowfield.

Figure 217 shows a similar dataset for  $F^+ = 0.4, N_{pulse} = 8$  corresponding to half-cycle pulsing. The additional pulses reduce the precise timing required as found for  $N_{pulse} = 4$ . For all cases with upstroke pulse start angles, similar lift-hysteresis reduction is obtained. As expected, no merit exists for additional pulses if actuation is delayed to angles following dynamic stall. Comparison of quarter- and half-cycle pulses confirms that, from a system benefit standpoint, half-cycle pulsing is only marginally better than quarter-cycle if scheduled accordingly. Conversely, half-cycle pulsing can be viewed as a more robust scheduling scheme. Although not calculated, it is likely true that from an energy balance, the quarter-cycle scheme is the most cost effective control solution. Active, on-wing ‘stall-monitoring’ to trigger COMPACT simultaneously minimizing pulse count is a possible path to overall maximum system performance.

Increasing  $F^+$  to  $0.6$  and  $0.8$  produced similar differences between quarter- and half-cycle pulse start angle sweeps;  $F^+ = 0.8$ , in accordance with the continuous pulsing cases, performed worse than  $F^+ = 0.4$  or  $0.6$ . This is summarized as a function of start angle for each  $F^+$  in Figure 218. Continuous cycle pulsing produced the strongest lift benefits, although both quarter- and half-cycle pulsing produced very similar gains for appropriate start angle. For quarter cycle-pulsing, the start angle must be near the first signs of dynamic stall,  $\alpha \approx 19^\circ$  ( $\psi \approx 160$ ). For half-cycle pulsing, initial pulses are required between  $\psi = 90^\circ$  and  $160^\circ$ . Actuation near the peak angle,  $\psi = 180^\circ$  was not investigated as several problems arose in the software generated trigger’s selection between upstroke and downstroke. As the stall vortex was already present on the airfoil surface at peak angle, it is believed that further benefits would not be achieved. A similar analysis is made with a focus on peak nose-down pitching moment in Figure 219.

**Table 28. Data Points Acquired for Pulse Start Angle Survey.**

Run	Mach	k	$\alpha_0[^\circ]$	$\alpha_1[^\circ]$	$F^+$	Pulse Start $\alpha[^\circ]$	$N_{pulses}$	Points
52	0.3	0.07	10	9.5	NA	NA	NA	10
66	0.3	0.07	10	9.5	0.4	15 Up to 15 Down	4 (qtr)	40,42,44,46,48,50,52,54,56, 58
66	0.3	0.07	10	9.5	0.4	15 Up to 15 Down	8 (half)	41,43,45,47,49,51,53,55,57, 59
66	0.3	0.07	10	9.5	0.6	15 Up to 15 Down	6 (qtr)	60,62,64,66,68,70
66	0.3	0.07	10	9.5	0.6	15 Up to 15 Down	13 (half)	61,63,65,67,69,71
66	0.3	0.07	10	9.5	0.8	15 Up to 15 Down	8 (qtr)	72,74,76,78,81,83
66	0.3	0.07	10	9.5	0.8	15 Up to 15 Down	17 (half)	73,75,77,80,82,84
66	0.3	0.07	10	9.5	0.4	17	16 (Full)	20
66	0.3	0.07	10	9.5	0.6	17	24 (Full)	27
66	0.3	0.07	10	9.5	0.8	17	32 (Full)	36



**Figure 216. Effect of pulse start angle on COMPACT on unsteady lift, drag, and moment.**  
 $M = 0.3$ ,  $\alpha = 10^\circ \pm 9.5^\circ$ ,  $k = 0.07$ ,  $F^+ = 0.4$ ,  $N_{pulses} = 4$ .

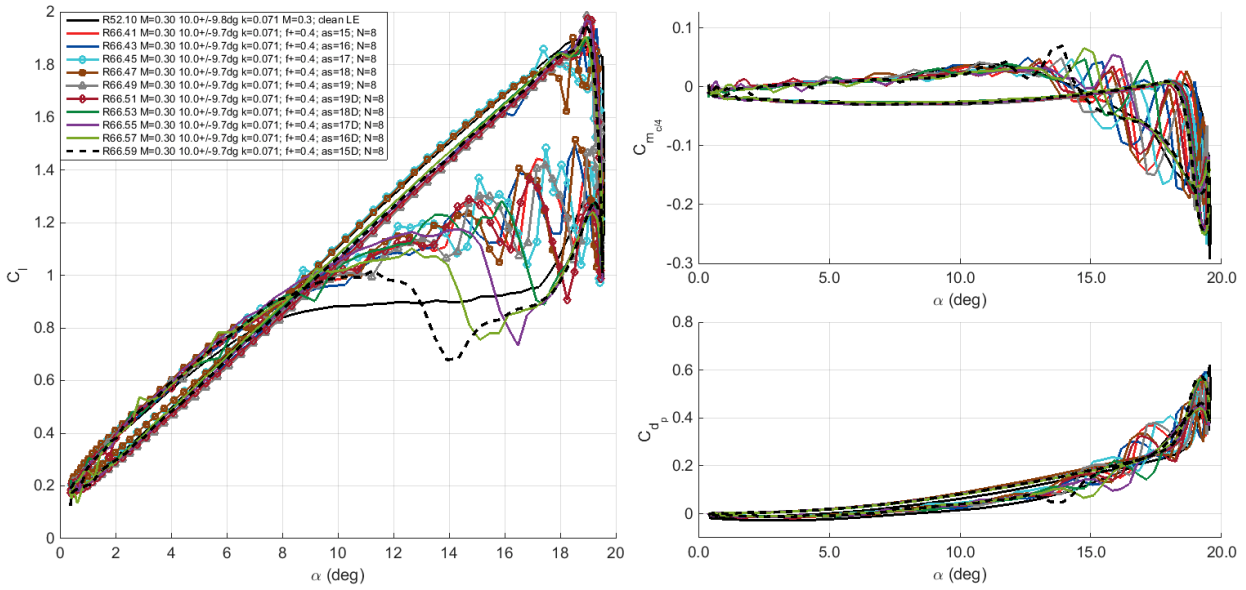


**Figure 217. Effect of pulse start angle on COMPACT on unsteady lift, drag, and moment.**  
 $M = 0.3$ ,  $\alpha = 10^\circ \pm 9.5^\circ$ ,  $k = 0.07$ ,  $F^+ = 0.4$ ,  $N_{pulses} = 8$ .

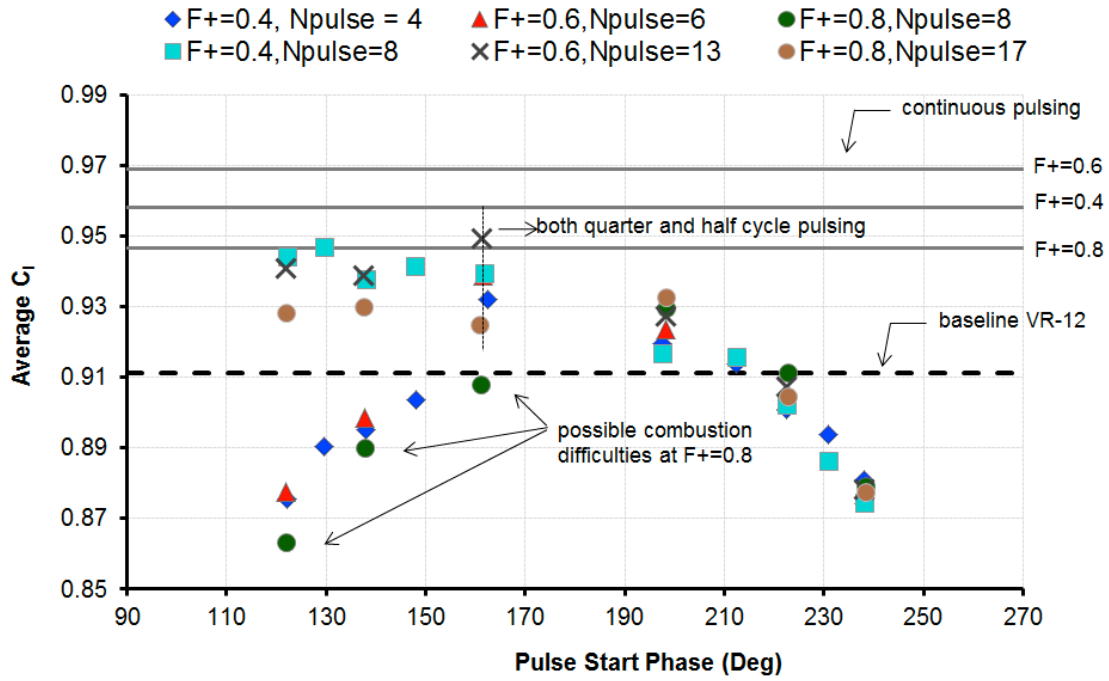


Figure 218. Average lift for varying pulse start angle.  $M=0.3$ ,  $\alpha=10^\circ \pm 9.5^\circ$ ,  $k=0.07$ ,  $F^+ = 0.4-0.8$ . Results for quarter-, half-, and full-cycle COMPACT shown.

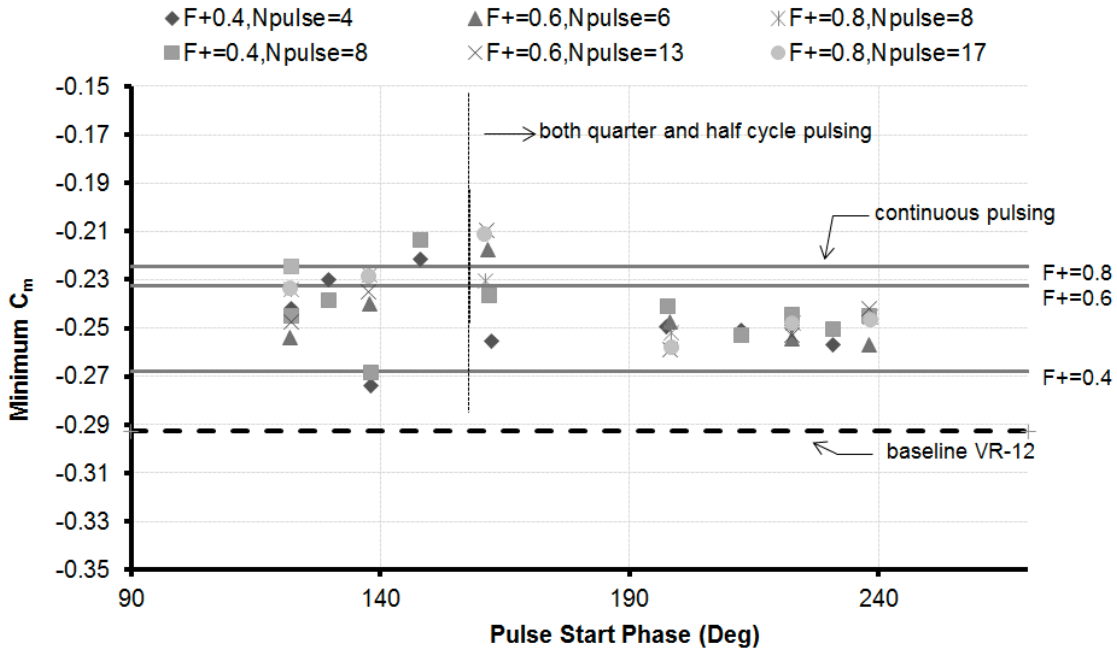
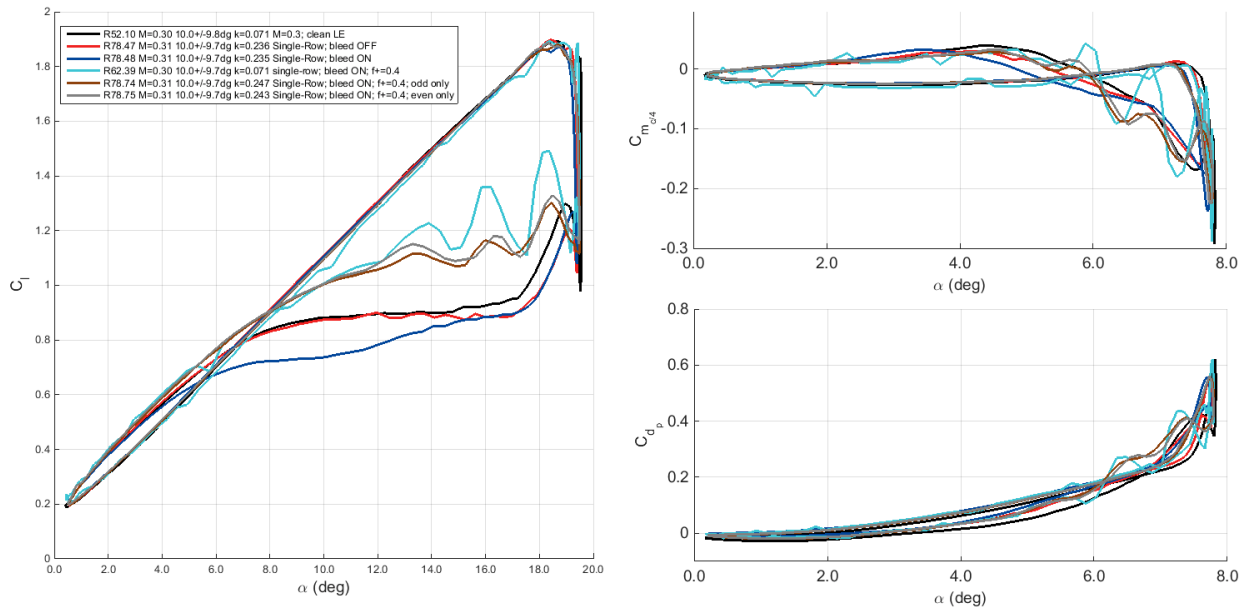


Figure 219. Minimum pitching moment for varying pulse start angle.  $M=0.3$ ,  $\alpha=10^\circ \pm 9.5^\circ$ ,  $k=0.07$ ,  $F^+ = 0.4-0.8$ . Results for both quarter-, half-, and full-cycle COMPACT shown.

### Discontinuous COMPACT Operation

Mach 0.3 was also used to determine the effectiveness of operating the actuators in a more discrete fashion. The CFD cases showed increased stall alleviation for the vanishing gap design. This benefit is predicated on achieving a more 2D COMPACT slot velocity output. To experiment with the necessity of a continuous actuated span both even and odd actuators (every other actuator along the span) were fired independently. The study maintained the same actuated span (33% for even actuators, 31% for odd), but reduced the number of actuators by one-half by turning every other actuator spark ignition off. Figure 220 displays the results for the test. Firing each of the 36 COMPACT modules produced the greatest downstroke lift increases. However, both the odd and even arrays still produced substantial lift improvements without the larger lift fluctuations formed from the full array. This result suggests that fewer COMPACT elements onboard a rotor-blade may be required to achieve strong performance gains, thereby reducing storage requirements and weight penalties.



**Figure 220. Effect of segmented COMPACT arrays on unsteady lift, drag, and moment.  $M=0.3$ ,  $\alpha=10^\circ \pm 9.5^\circ$ ,  $k=0.07$ ,  $F^+ = 0.4$ .**

### $M=0.4$

At this Mach number, actuation across an  $F^+$  range from 0.2 to 0.6 was conducted; however, similar to Mach 0.3,  $F^+ = 0.6$  required actuation at over 200 Hz. Based on IR images collected during the test entry, strong actuator performance was likely limited to  $F^+ = 0.4$  or less. Higher actuation resulted in a tendency toward steady flame in the COMPACT internal chambers as well as a reduction in internal chamber pressure. The latter pressure measurements were not acquired at Mach 0.4 – it is expected that a similar frequency and internal pressure relationships exist as that found for Mach 0.3 (Figure 311).

Several pitch trajectories were tested at this Mach number, including reduced frequencies of 0.025-0.07 and peak angles of  $22^\circ$ . Unsteady pitching results at Mach 0.4 with the single-row COMPACT configuration are provided in Figure 221 through Figure 223 for



$\alpha = 10^\circ \pm 8^\circ, k = 0.05$ . This is the same condition used for the Mach 0.4 PIV measurements and post-test CFD cases. The clean VR-12 stalls at  $15^\circ$  and  $16.2^\circ$  for moment and lift, respectively. A decrease in  $C_L$  of more than 0.6 occurs due to dynamic stall. Peak nose-down pitching moment, owing mostly to a compressibility weakened dynamic stall vortex and smaller reduced frequency, peaks at  $C_M = -0.14$ . For the COMPACT cases,  $F^+ = 0.4$  and  $0.6$  produce similar lift improvement. Little change was measured for drag or moment. Both actuation cases increase the moment stall angle, although only by a fraction of a degree. The  $F^+ = 0.6$  results provide smaller oscillations in lift and drag due to the increased number of COMPACT disturbances above the upper surface. These smaller, more abundant structures reside closer to the airfoil surface, increasing aerodynamic performance more so than structures produced at a less frequent rate. The latter tend to persist for a longer period, but their lack of multiple structures for the convective time-scales of the near-wall flow allow for separation prior to the production of additional structures. If this occurs, load fluctuations increase as the upper surface intermittently separates and attaches. This phenomenon is true for each Mach number and is well resolved by the PIV data. The COMPACT falloff in internal pressure, however, negates some of the trends normally associated with  $F^+$ ; the structures are less energetic as the actuators' physical frequency is increased and the peak internal pressures drop. Similar to the Mach 0.3 results, more benefit in terms of lift-loop closure is apparent at higher degrees of stall, as shown in the  $12^\circ$  mean angle conditions provided in Table 31. No significant changes in peak negative moment are shown through the Mach 0.4 dataset. Increases in peak and mean drag are noted at many of the conditions tested. Both of these results are likely owed to the increased downwash and induced drag created by the low-aspect ratio actuated span.

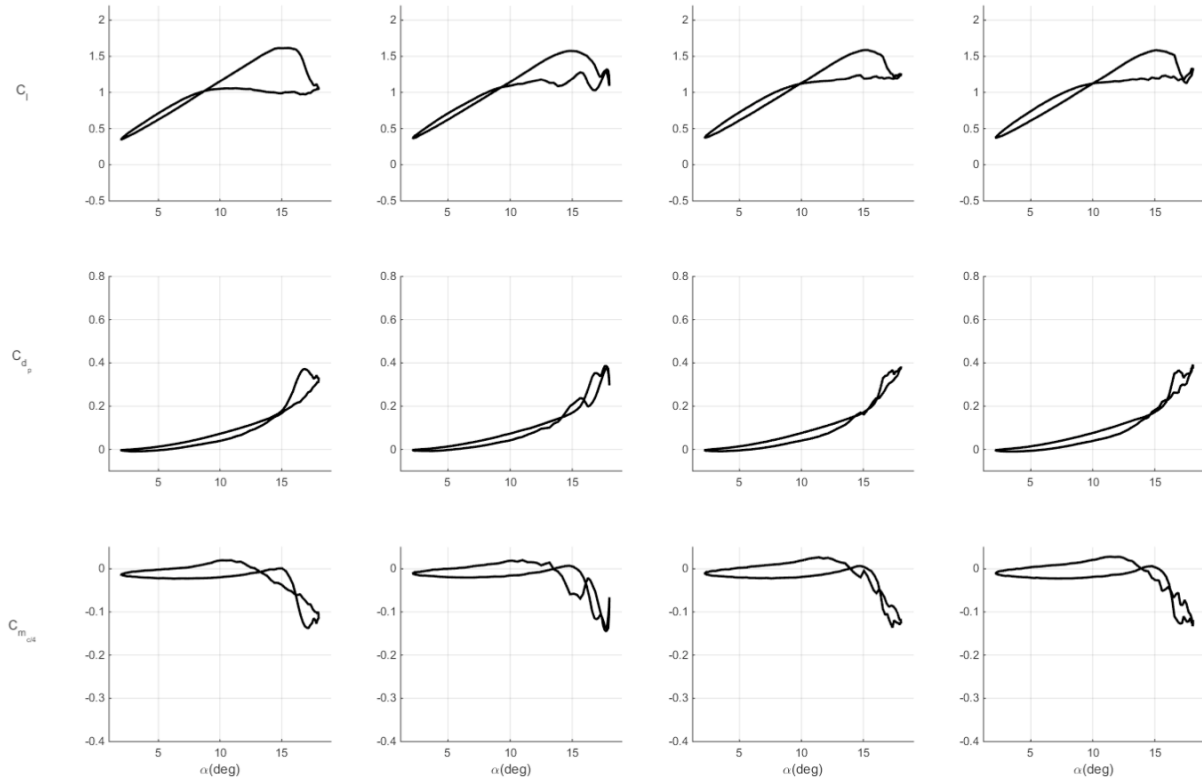


**Figure 221. Unsteady aerodynamic loads with respect to angle-of-attack.  $M=0.4$ ,  $\alpha=10^\circ \pm 8^\circ$ ,  $k=0.05$ . Baseline and single-row COMPACT  $F^+=0.2-0.6$  shown in order from left to right.**

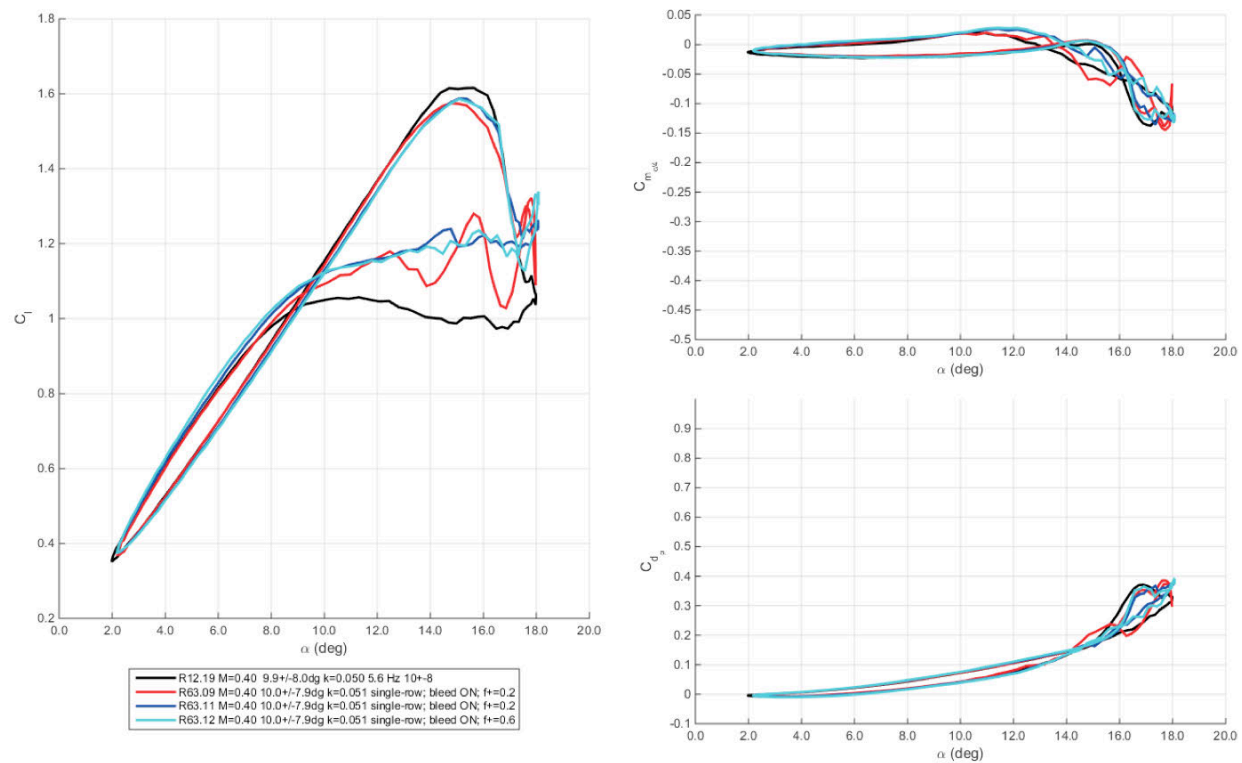


**Figure 222. Unsteady aerodynamic loads with respect to angle-of-attack. Baseline and single-row COMPACT  $F^+ = 0.2-0.6$ .  $M = 0.4$ ,  $\alpha = 10^\circ \pm 8^\circ$ ,  $k = 0.05$ .**

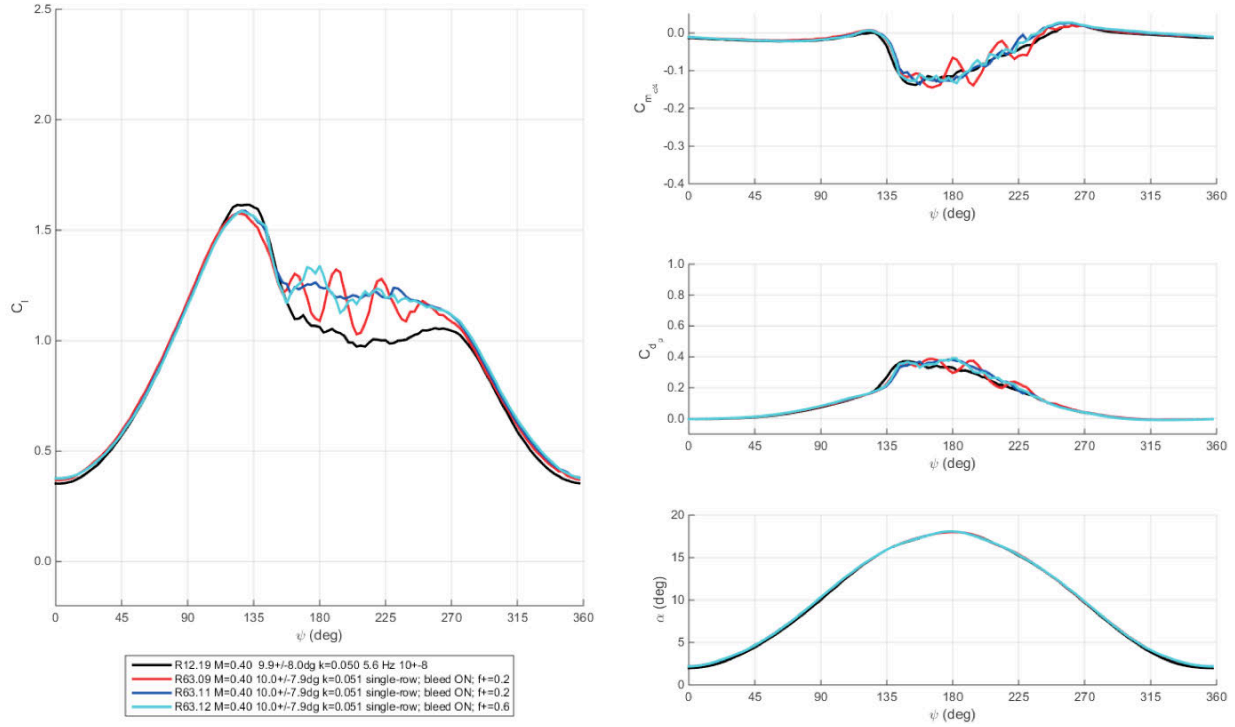


**Figure 223. Unsteady aerodynamic loads and angle-of-attack with respect to phase. Baseline and single-row COMPACT  $F^+=0.2-0.6$ .  $M=0.4$ ,  $\alpha=10^\circ \pm 8^\circ$ ,  $k=0.05$ .**

A more severe stall case,  $\alpha = 10^\circ \pm 9.5^\circ$ ,  $k = 0.05$  was selected at Mach 0.4 for further COMPACT parameter investigations. Baseline lift and moment stall are nearly identical to the  $\alpha_1 = 8^\circ$  unsteady motion discussed. The airfoil remains stalled for a longer duration due to the increased peak incidence. Additional COMPACT parameter studies included a  $N_{pulse}$  sweep, quarter- and half-cycle actuation pulse start angle sweeps at  $F^+$  of 0.2, 0.4, and 0.6, and a check of the effect of a single pulse located at different angles through the pitch motion. Each of these sweeps revealed similar behavior as that found at Mach 0.3. The single pulse sweep provided local and favorable lift load increments when fired on the downstroke.

### Pulse Start Angle

Quarter-cycle pulsing was applied with 6 pulses-per-cycle at  $F^+ = 0.4$ . Due to the moment stall behavior, it might be expected that actuation is required starting near  $\alpha = 15^\circ$  on the upstroke. Conceptually, this offers the potential to disrupt the DSV and prevent dynamic stall altogether, as demonstrated at Mach 0.2. The data, on the other hand, indicates that  $\alpha_{start}$  near moment or lift stall ( $15^\circ$  and  $17^\circ$ , respectively) only modestly alters the subsequent loads. The small number of pulses for the quarter-cycle scheduling does not persist long enough into the downstroke to be effective. Instead, starting actuation following stall, as shown for  $\alpha_{start} = 19^\circ$  on the upstroke, can have as much impact on the lift behavior as continuous pulsing throughout the cycle (red line). Beginning actuation at  $19^\circ$  following the airfoil's change of direction also proved to have a strong impact on lift hysteresis reduction. Actuation later in the cycle produced the largest downstroke lift recovery at  $14.5^\circ$  for  $\alpha_{start} = 17^\circ$  on the downstroke, but the lack of lift preceding the first pulse outweighs these increases through the average.

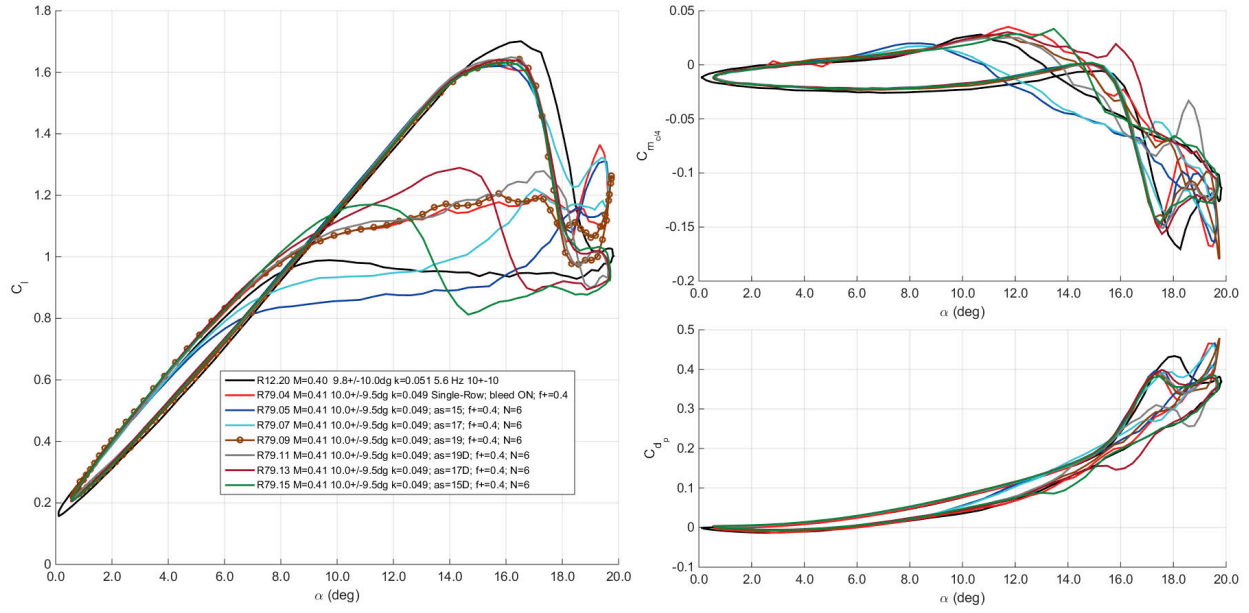


**Figure 224. Effect of pulse start angle on COMPACT on unsteady lift, drag, and moment.  $M=0.3$ ,  $\alpha=10^\circ \pm 9.5^\circ$ ,  $k=0.05$ ,  $F^+ = 0.4$ ,  $N_{pulses} = 6$ .**

Half-cycle pulsing with 12 pulses-per-cycle showed more robustness to start angle, all cases with  $\alpha_{start} \leq 19^\circ$  on the upstroke are well-matched in terms of lift recovery. Figure 225 shows these results. Symbols emphasize the  $\alpha_{start} = 15^\circ$  as it is the first case to match the continuous pulsing loop.

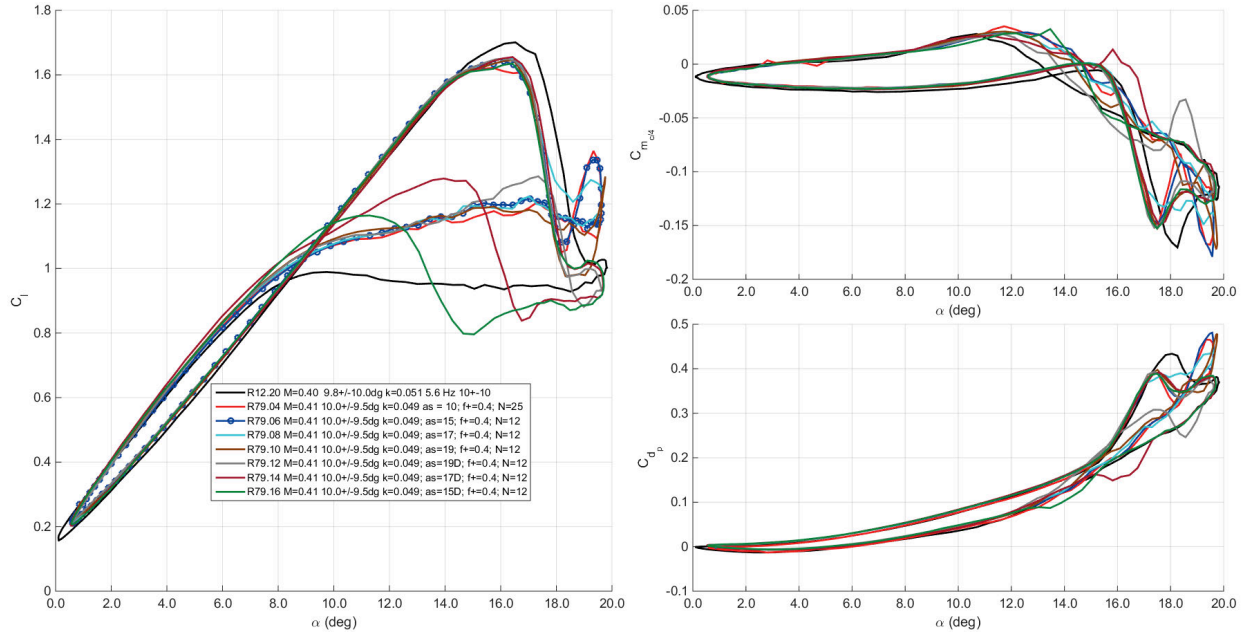


**Figure 225. Effect of pulse start angle on COMPACT on unsteady lift, drag, and moment.  $M=0.3$ ,  $\alpha=10^\circ \pm 9.5^\circ$ ,  $k=0.05$ ,  $F^+ = 0.4$ ,  $N_{pulses} = 12$ .**

#### Number of Pulses

Despite the Mach number differences and deeper stall penetration for  $M=0.4$ ,  $\alpha=10^\circ \pm 9.5^\circ$ ,  $k=0.05$ ,  $N_{pulse}$  required was very similar as that found for Mach 0.3. For  $N_{pulse} \geq 8$ , the continuous pulsing lift benefits are substantially recuperated. In terms of duty-cycle, 8 pulses corresponds to actuation over 32% of the pitch cycle; this requires COMPACT firing to  $\alpha \approx 15^\circ$  on the downstroke,  $5^\circ$  prior to the  $\alpha_0$ . This survey was also attained for  $\alpha_{start} = 18^\circ$ , as shown in Figure 229. 8 pulses remains as the least pulse count to match the continuous pulse lift attributes; that said, the 6 pulse case fairs markedly better than 6 pulses and  $\alpha_{start} = 16^\circ$ . This comparison suggests that onboard logic to determine the flow field's separation state could be used to actively reduce the aggregate actuator workload.

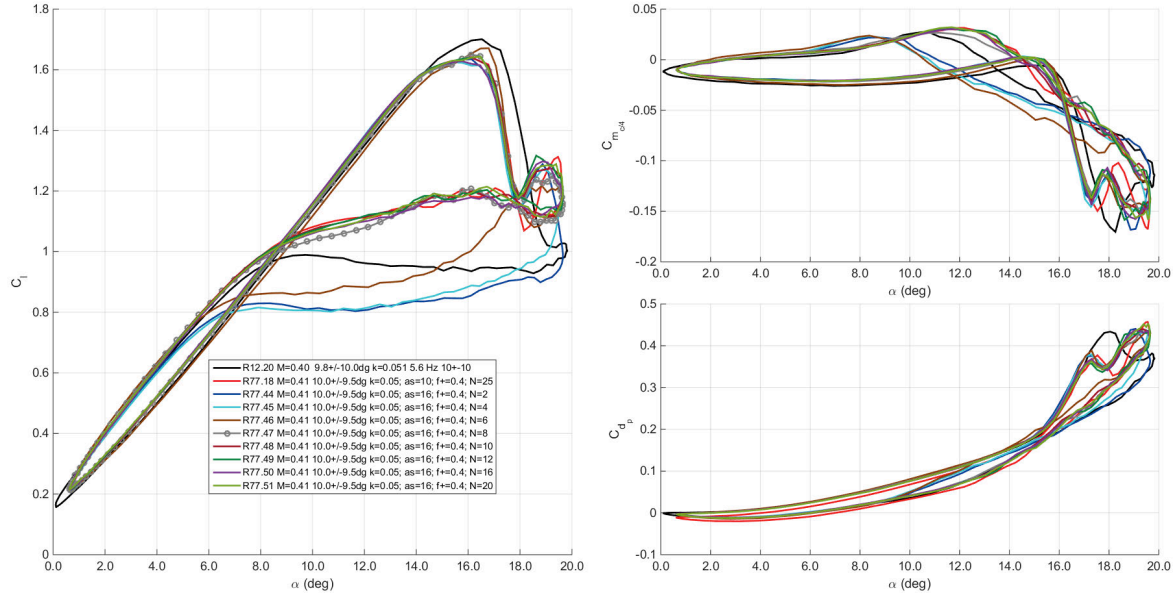


**Figure 226.** Effect of  $N_{pulse}$  on unsteady lift, drag, and moment.  $M = 0.4$ ,  $\alpha = 10^\circ \pm 9.5^\circ$ ,  $k = 0.05$ ,  $F^+ = 0.4$ ,  $\alpha_{start} = 16^\circ$ .

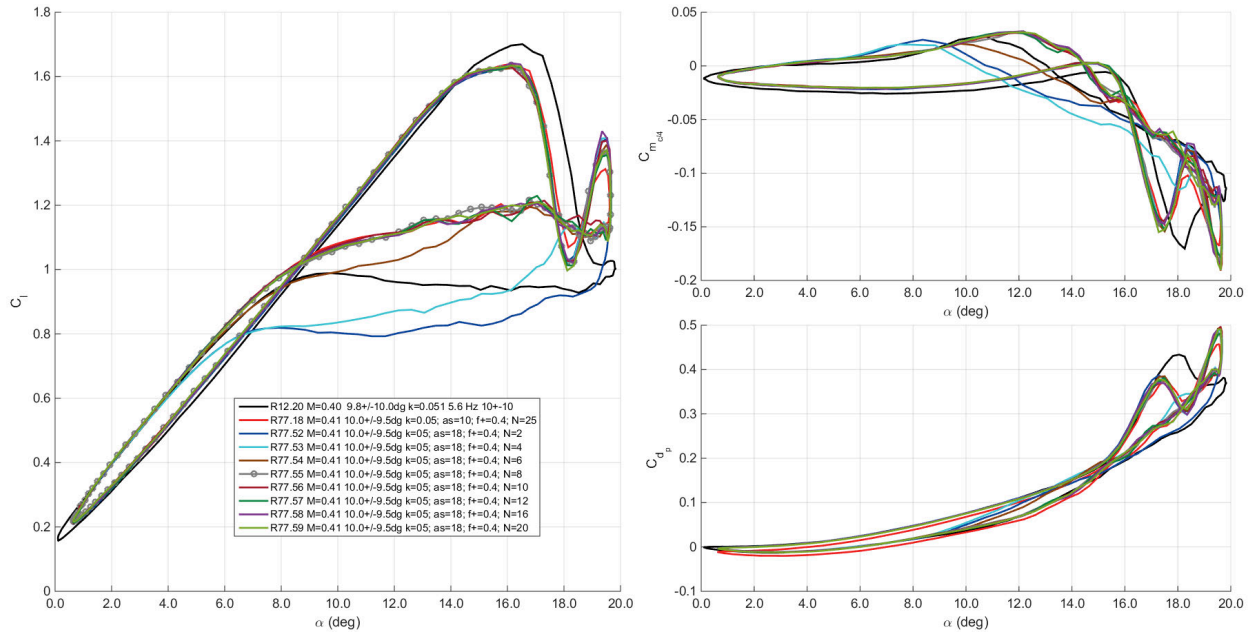


**Figure 227.** Effect of  $N_{pulse}$  on unsteady lift, drag, and moment.  $M = 0.4$ ,  $\alpha = 10^\circ \pm 9.5^\circ$ ,  $k = 0.05$ ,  $F^+ = 0.4$ ,  $\alpha_{start} = 18^\circ$ .

### Single Pulse Effects

A single COMPACT pulse was fired at different angles throughout the stall trajectory. This had dramatic effects on the lift, drag, and moment hysteresis behavior on the downstroke, as shown in Figure 228. On a single pulse cause and effect basis, the response loads were larger than any quarter-, half- or continuous pulse schedule previously discussed. This indicates that the long



delays between pulses,  $1/f_{pitch}$ , significantly aided COMPACT combustion properties. Pulses starting as early as  $18^\circ$  on the upstroke drastically altered the behavior from the slotted VR-12 and steady bleed-on unsteady aerodynamics. For a single pulse fired at  $18^\circ$  on the downstroke (red dashed line), a change in lift of  $\Delta C_L = 0.35$  was measured for this Mach 0.4 condition. Large jumps in moment and drag are also noted. For cases in which the pulse fired between  $17^\circ$  and  $14^\circ$  on the downstroke, the flow reattachment angle improved compared to the baseline VR-12. Both  $17^\circ$  and  $16^\circ$  downstroke pulses hastened reattachment by  $2^\circ$ .

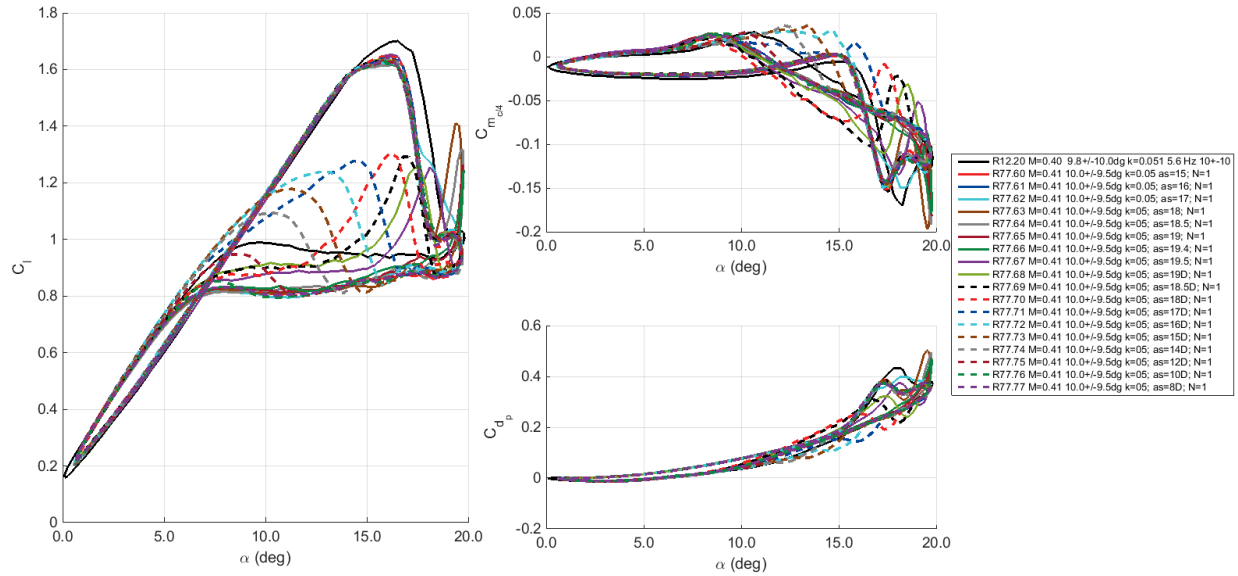


**Figure 228. Effect of single COMPACT pulses on unsteady lift, drag, and moment.  $M=0.4$ ,  $\alpha=10^\circ \pm 9.5^\circ$ ,  $k=0.05$ .**

#### **$M=0.5$**

Unsteady pitching results at Mach 0.5 with the single-row COMPACT configuration are provided in Figure 229 to Figure 231. At this Mach number, actuation was possible only at  $F^+$  of 0.2 and 0.4. Operation at any reduced frequency at this Mach number was a challenge due to the low static pressure. It is viewed as unlikely that the actuators were able to fire reliably at any of the conditions tested, with the exception of instants in the pitch cycle when the pressure on the upper surface is highest. Thus, the results collected in Entry 2 at Mach 0.5 are very similar to the results collected in Entry 1. Although improvements over the baseline aerodynamic loads were not measured, COMPACT did not present any major detriments to the clean VR-12 either.

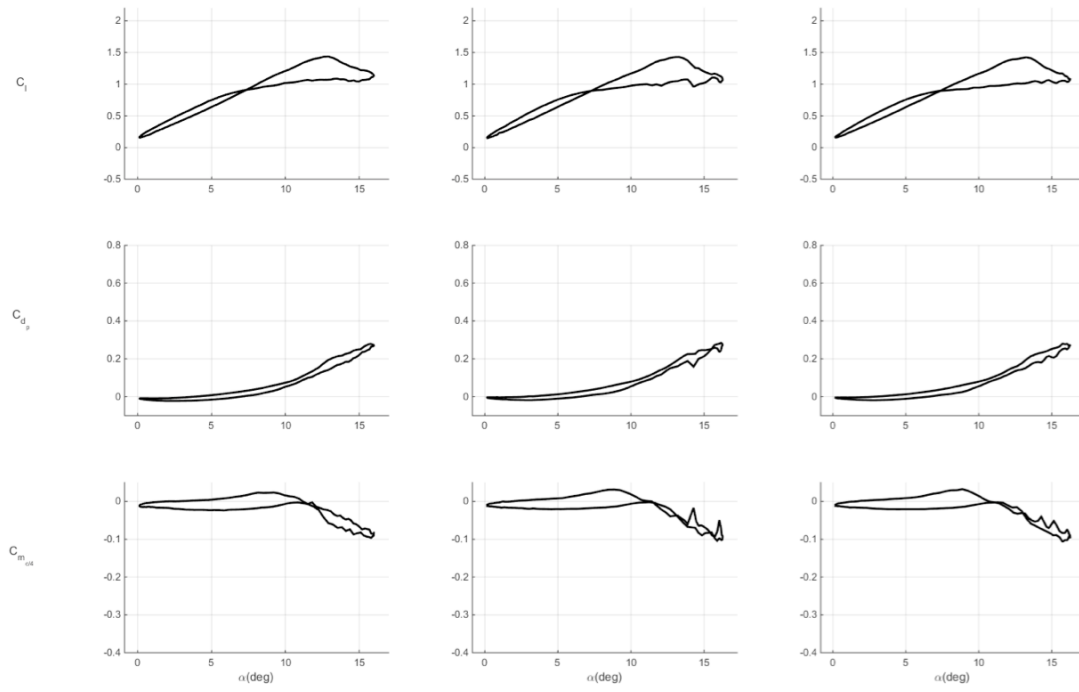


**Figure 229.** Unsteady aerodynamic loads with respect to angle-of-attack.  $M=0.5$ ,  $\alpha=8^\circ \pm 8^\circ$ ,  $k=0.05$ . Baseline and single-row COMPACT  $F^+=0.2-0.4$  shown in order from left to right.

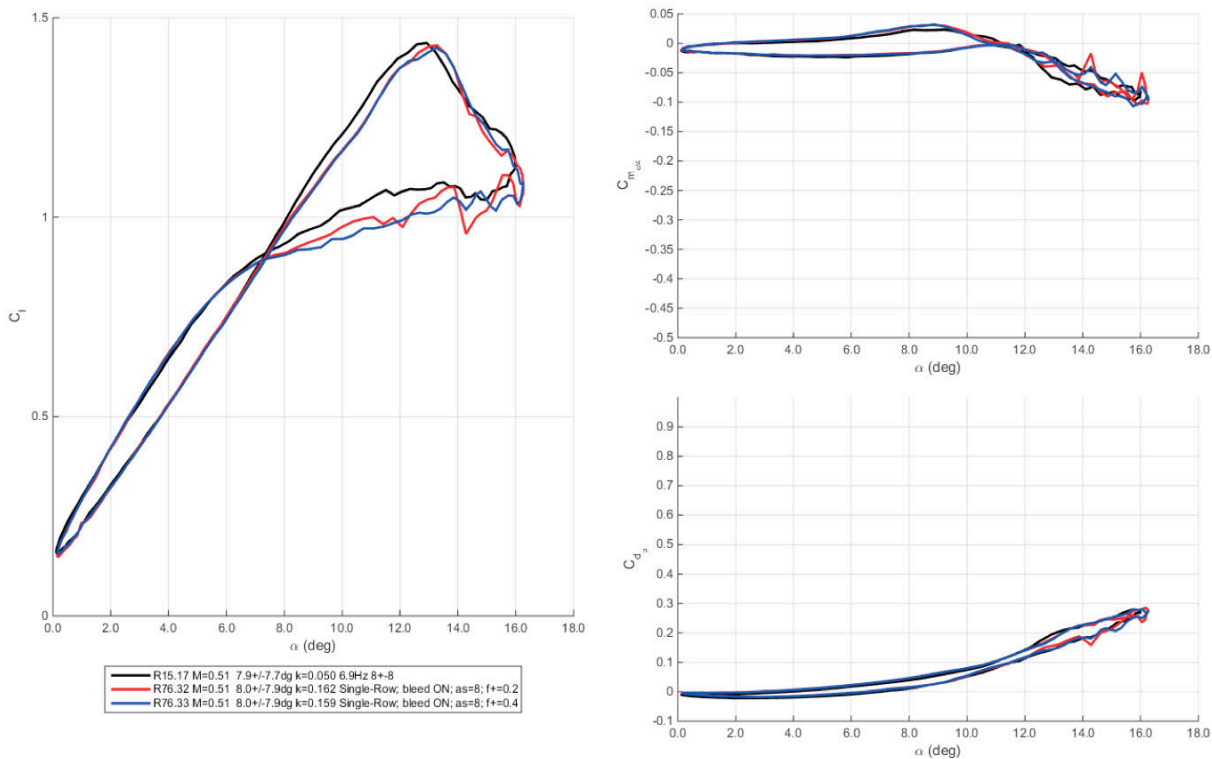


**Figure 230. Unsteady aerodynamic loads with respect to angle-of-attack. Baseline and single-row COMPACT  $F+=0.2-0.4$ .  $M=0.5$ ,  $\alpha=8^\circ \pm 8^\circ$ ,  $k=0.05$ .**

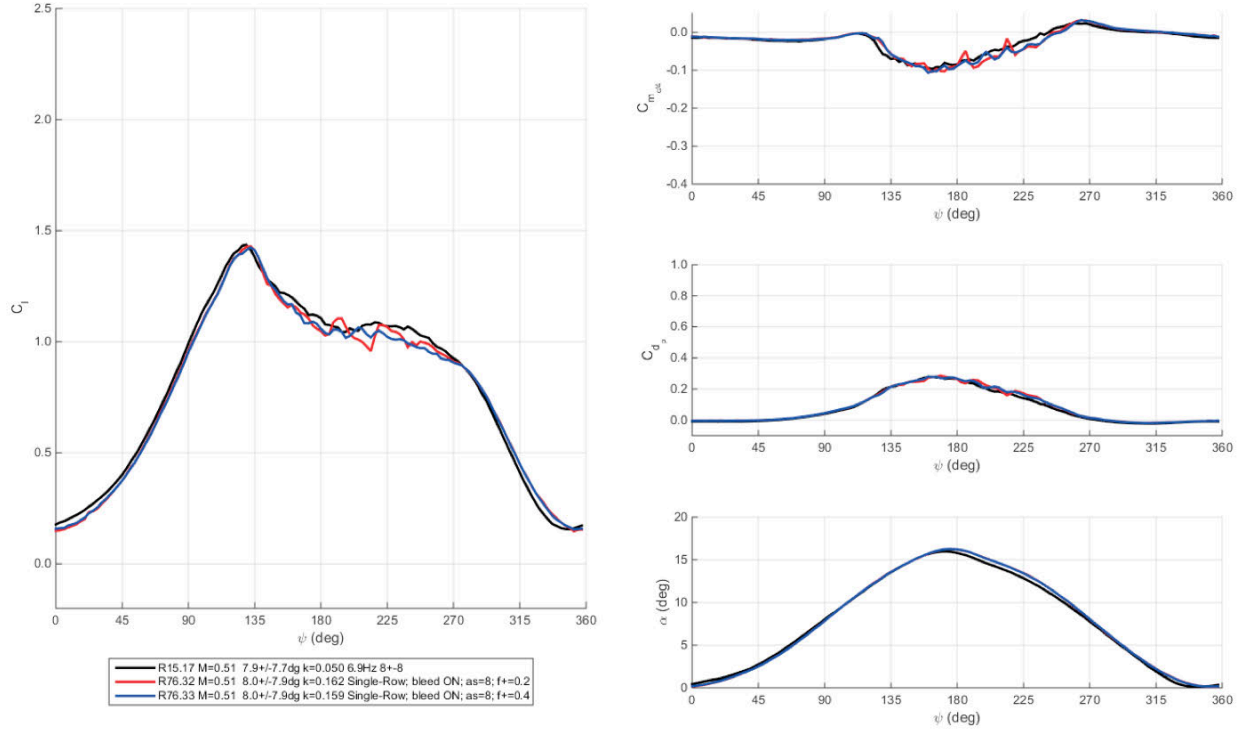


**Figure 231. Unsteady aerodynamic loads and angle-of-attack with respect to phase. Baseline and single-row COMPACT  $F^+=0.2-0.4$ .  $M = 0.5$ ,  $\alpha = 8^\circ \pm 8^\circ$ ,  $k = 0.05$ .**

### Single-Row COMPACT Summary of Results

A summary of key metrics for the single-row COMPACT conditions tested is provided in Table 29 to Table 32. A description of the unsteady conditions tested is provided in the first 9 columns, and the key dynamic stall control metrics are provided in the remaining columns. The first row in each block of data is for the clean leading edge, baseline VR-12, these values are used as the baseline for the percentages provided in the subsequent rows. All metrics are based on the Station 2 sensors. Note that positive percentages in the  $C_m = C_{m, \frac{c}{4}, min}$  parameter indicate a more negative pitch moment peak. In some cases, a clean leading edge baseline was not available, and an open-slot baseline was used instead. It is cautioned that the deltas provided here must not be regarded as true deltas from a clean configuration. In other cases, particularly at Mach 0.3 and 0.4, the clean leading edge baseline mean and amplitude in angle-of-attack did not match the mean and amplitude of the COMPACT test points. In order to minimize bias in the reported percentages due to this, sensitivity factors from numerous baseline runs conducted in Entry 1 were calculated and used to adjust the baseline mean lift and drag, which are provided in separate columns in the tables.

The following observations are made with regard to these metrics (data extracted from  $F^+$  sweeps and does not include Run and Point combinations focused on other COMPACT parameters, e.g.,  $N_{pulse}$ ):

1. At Mach 0.2, single-row COMPACT at  $F^+=0.8$  was shown to increase average lift by +13% to +17%, change peak drag by -28% to 11%, and modify peak moment by -70% to 9%. The highest drag and moment reductions occurred for light dynamic stall. For deep stall, large average lift increases of +15% were measured.

2. At Mach 0.3, single-row COMPACT at  $F^+=0.4$  was shown to increase average lift by +5% to +13%, change peak drag by -11% to +14%, and alter peak moment by -23% to 17%.  $F^+=0.8$  had greater impact on moment and less impact on lift. The highest drag and moment reductions occurred for light dynamic stall. For deep stall, large average lift increases of +13% were measured.
3. At Mach 0.4, single-row COMPACT at  $F^+=0.4$  was shown to increase average lift by 3% to 11%, modify peak drag by -1% to +21%, and vary peak moment by -10% to 16%.
4. At Mach 0.5, single-row COMPACT was ineffective but did not significantly alter the clean VR-12 aerodynamic traits.

The single-row COMPACT results reported here for Entry 2 are significantly improved from the results collected in Entry 1. It is clear that the design enhancements and alterations toward achieving uniform actuator performance and actuating at high frequency greatly increased the performance of COMPACT across all Mach numbers tested.

**Table 29. Summary of key metrics for Mach 0.2 Single-Row COMPACT data sets.**

$M$	$k$	$\alpha_0(^{\circ})$	$\alpha_1(^{\circ})$	Geom	$F^+$	$N_{pulses}$	$\alpha_{start}$	$C_{l,avg}$	$C_{l,max}$	$C_{d,p,avg}$	$C_{d,p,max}$	$C_{m,c/4}$	$C_{m,c/4,min}$
0.20	0.070	10.00	9.99	Clean	NA	NA	NA	0.95	1.87	0.14	0.57	-0.02	-0.23
0.20	0.071	10.00	9.98	Single-Row	0.2	8	10	4%	-3%	-1%	-7%	12%	-12%
0.20	0.071	10.01	9.99	Single-Row	0.4	17	10	9%	0%	-1%	0%	-10%	0%
0.20	0.071	10.02	9.99	Single-Row	0.6	25	10	12%	2%	-4%	-11%	-41%	-45%
0.20	0.071	10.01	9.99	Single-Row	0.8	35	10	12%	2%	-6%	-18%	-58%	-57%
0.20	0.071	10.02	9.99	Single-Row	1.0	44	10	16%	4%	-7%	-28%	-73%	-70%
0.20	0.100	10.08	9.93	Clean	NA	NA	NA	0.97	1.89	0.15	0.51	-0.03	-0.20
0.20	0.101	10.05	9.99	Single-Row	0.2	6	0	2%	2%	-6%	11%	19%	16%
0.20	0.101	10.05	9.99	Single-Row	0.4	12	0	7%	11%	-7%	12%	-5%	17%
0.20	0.102	10.05	9.98	Single-Row	0.6	18	0	10%	6%	-13%	-4%	-48%	-28%
0.20	0.102	10.05	9.98	Single-Row	0.8	25	0	14%	10%	-13%	-7%	-57%	-46%
0.20	0.102	10.05	9.98	Single-Row	1.0	31	0	17%	15%	-14%	-10%	-79%	-69%
0.20	0.069	15.07	8.02	Clean	NA	NA	NA	1.22	1.92	0.25	0.74	-0.04	-0.30
0.20	0.071	15.05	8.03	Single-Row	0.2	8	15	6%	-1%	-1%	-1%	13%	-4%
0.20	0.071	15.05	8.03	Single-Row	0.4	17	15	8%	1%	-3%	-7%	-5%	-12%
0.20	0.071	15.05	8.02	Single-Row	0.6	26	15	10%	3%	-4%	-5%	-23%	-11%
0.20	0.071	15.05	8.03	Single-Row	0.8	35	15	13%	4%	-5%	2%	-33%	-9%
0.20	0.071	15.05	8.03	Single-Row	1.0	44	15	13%	6%	-5%	1%	-37%	-8%
0.20	0.071	15.08	9.93	Clean	NA	NA	NA	1.15	2.00	0.26	0.92	-0.05	-0.33
0.20	0.071	15.05	9.93	Single-Row	0.2	8	15	4%	-4%	-4%	-20%	1%	-15%
0.20	0.071	15.05	9.93	Single-Row	0.4	17	15	8%	-2%	-3%	-13%	-5%	-6%
0.20	0.071	15.06	9.94	Single-Row	0.6	26	15	11%	3%	-3%	-14%	-15%	-10%
0.20	0.071	15.07	9.94	Single-Row	0.8	35	15	12%	4%	-3%	-11%	-23%	-9%
0.20	0.071	15.08	9.96	Single-Row	1.0	44	15	13%	5%	-4%	-10%	-27%	-13%
0.20	0.099	15.04	8.02	Clean	NA	NA	NA	1.23	2.01	0.26	0.74	-0.05	-0.29
0.20	0.101	15.03	7.97	Single-Row	0.2	6	0	2%	-4%	-5%	-5%	7%	-1%
0.20	0.102	15.02	7.96	Single-Row	0.4	12	0	7%	2%	-4%	0%	-5%	2%
0.20	0.102	15.02	7.95	Single-Row	0.6	18	0	10%	10%	-6%	7%	-20%	5%
0.20	0.102	15.01	7.95	Single-Row	0.8	25	0	11%	13%	-6%	11%	-29%	0%
0.20	0.103	15.01	7.96	Single-Row	1.0	31	0	15%	12%	-4%	13%	-33%	19%
0.20	0.100	15.05	9.92	Clean	NA	NA	NA	1.17	2.12	0.28	0.87	-0.06	-0.32
0.20	0.101	15.05	9.99	Single-Row	0.2	6	0	0%	-3%	-5%	-6%	6%	-1%
0.20	0.101	15.03	9.98	Single-Row	0.4	12	0	5%	-1%	-5%	0%	-4%	4%
0.20	0.102	15.01	9.97	Single-Row	0.6	18	0	8%	10%	-5%	8%	-16%	1%
0.20	0.102	15.01	9.97	Single-Row	0.8	25	0	9%	15%	-6%	7%	-20%	4%
0.19	0.103	15.01	9.96	Single-Row	1.0	31	0	14%	12%	-1%	10%	-14%	9%

**Table 30. Summary of key metrics for Mach 0.3 Single-Row COMPACT data sets.**

$M$	$k$	$\alpha_0(^{\circ})$	$\alpha_1(^{\circ})$	Geom	$F^+$	$N_{pulses}$	$\alpha_{start}$	$C_{l,avg}$	$C_{l,avg,corr}$	$C_{l,max}$	$C_{d,p,avg}$	$C_{d,p,avg,corr}$	$C_{d,p,max}$	$C_{m,c/4}$	$C_{m,\xi,min}$
0.30	0.025	10.01	7.98	Clean	NA	NA	NA	0.97	0.97	1.76	0.08	0.08	0.40	-0.02	-0.15
0.30	0.025	10.00	7.96	Single-Row	0.2	24	10	3%	3%	-3%	29%	29%	7%	20%	18%
0.29	0.025	10.01	7.97	Single-Row	0.4	49	10	8%	8%	1%	28%	28%	12%	-6%	17%
0.29	0.025	10.01	7.98	Single-Row	0.6	74	10	8%	8%	5%	28%	28%	14%	-12%	9%
0.30	0.025	10.03	7.98	Single-Row	0.8	100	10	7%	7%	3%	25%	25%	4%	-11%	-2%
0.30	0.025	9.98	9.94	Clean	NA	NA	NA	0.87	0.87	1.91	0.10	0.10	0.51	-0.03	-0.20
0.30	0.025	9.97	9.94	Single-Row	0.2	24	10	5%	5%	-8%	24%	25%	-1%	17%	11%
0.29	0.025	9.96	9.94	Single-Row	0.4	49	10	12%	12%	3%	24%	25%	3%	-5%	0%
0.30	0.025	9.97	9.94	Single-Row	0.6	74	10	9%	9%	-2%	23%	23%	0%	-3%	8%
0.30	0.025	9.97	9.94	Single-Row	0.8	100	10	2%	2%	-3%	19%	19%	-11%	6%	-13%
0.30	0.050	10.01	7.98	Clean	NA	NA	NA	0.97	0.97	1.79	0.09	0.09	0.47	-0.02	-0.20
0.30	0.051	9.98	7.97	Single-Row	0.2	12	10	4%	4%	3%	21%	21%	2%	22%	1%
0.30	0.051	10.01	7.99	Single-Row	0.4	24	10	7%	7%	5%	20%	20%	7%	0%	0%
0.30	0.051	10.00	7.99	Single-Row	0.6	36	10	7%	7%	3%	18%	18%	-1%	-9%	0%
0.30	0.051	10.01	7.99	Single-Row	0.8	49	10	5%	5%	2%	21%	21%	-2%	7%	-9%
0.30	0.050	10.04	9.42	Clean	NA	NA	NA	0.90	0.88	1.83	0.11	0.11	0.57	-0.03	-0.25
0.30	0.051	10.10	10.01	Single-Row	0.2	12	10	3%	6%	7%	29%	21%	6%	33%	0%
0.29	0.051	10.04	9.95	Single-Row	0.4	24	10	6%	10%	4%	29%	21%	9%	17%	2%
0.30	0.050	10.04	9.96	Single-Row	0.6	36	10	4%	8%	0%	22%	15%	4%	3%	4%
0.30	0.051	10.06	9.97	Single-Row	0.8	49	10	4%	7%	3%	23%	15%	3%	9%	-10%
0.30	0.071	10.05	7.97	Clean	NA	NA	NA	0.99	0.98	1.82	0.10	0.10	0.47	-0.02	-0.20
0.30	0.071	9.93	7.98	Single-Row	0.2	8	10	1%	2%	3%	19%	21%	2%	26%	2%
0.29	0.072	9.95	7.99	Single-Row	0.4	17	10	6%	7%	1%	14%	16%	5%	-9%	7%
0.29	0.072	9.93	7.99	Single-Row	0.6	26	10	5%	6%	1%	13%	15%	-6%	-13%	-12%
0.30	0.071	9.93	7.99	Single-Row	0.8	35	10	4%	5%	2%	16%	18%	-7%	6%	-14%
0.30	0.071	9.99	9.58	Clean	NA	NA	NA	0.90	0.90	1.89	0.12	0.12	0.62	-0.03	-0.29
0.30	0.071	9.95	9.51	Single-Row	0.2	8	10	4%	4%	3%	17%	18%	-6%	19%	-13%
0.30	0.071	9.96	9.51	Single-Row	0.4	17	10	7%	7%	0%	14%	15%	0%	2%	-2%
0.30	0.071	9.95	9.51	Single-Row	0.6	26	10	6%	6%	8%	11%	12%	-2%	-7%	-18%
0.30	0.071	9.96	9.51	Single-Row	0.8	35	10	6%	5%	3%	12%	13%	-6%	2%	-18%
0.30	0.101	10.02	7.94	Clean	NA	NA	NA	1.01	1.01	1.84	0.09	0.09	0.36	-0.02	-0.14
0.30	0.102	9.99	7.83	Single-Row	0.2	6	10	1%	1%	-1%	20%	22%	14%	30%	24%
0.30	0.102	9.99	7.84	Single-Row	0.4	12	10	5%	5%	0%	14%	16%	-1%	-7%	-2%
0.30	0.102	9.98	7.83	Single-Row	0.6	18	10	6%	6%	0%	13%	15%	2%	-12%	-28%
0.29	0.102	9.97	7.83	Single-Row	0.8	25	10	5%	4%	0%	20%	22%	13%	15%	3%
0.30	0.101	10.14	9.31	Clean	NA	NA	NA	0.97	0.96	1.93	0.11	0.10	0.51	-0.03	-0.22
0.30	0.101	9.97	9.35	Single-Row	0.2	6	10	2%	3%	0%	17%	20%	4%	19%	-12%
0.30	0.101	9.96	9.36	Single-Row	0.4	12	10	3%	4%	-1%	15%	18%	-1%	9%	-23%
0.30	0.101	9.96	9.35	Single-Row	0.6	18	10	5%	6%	0%	15%	18%	2%	3%	-12%
0.30	0.101	9.95	9.36	Single-Row	0.8	25	10	4%	5%	0%	15%	18%	5%	8%	-5%
0.30	0.025	15.00	7.98	Clean	NA	NA	NA	1.12	1.12	1.91	0.19	0.19	0.53	-0.04	-0.19
0.30	0.025	15.02	8.00	Single-Row	0.2	25	15	7%	7%	-5%	20%	20%	15%	19%	21%
0.30	0.025	15.00	7.98	Single-Row	0.4	50	15	9%	9%	-2%	19%	19%	7%	2%	1%
0.30	0.025	15.00	7.99	Single-Row	0.6	75	15	11%	11%	-3%	17%	17%	10%	-15%	-16%
0.30	0.025	15.00	7.99	Single-Row	0.8	100	15	10%	10%	-4%	18%	18%	4%	-8%	5%
0.30	0.050	15.10	8.00	Clean	NA	NA	NA	1.14	1.14	1.87	0.20	0.20	0.64	-0.05	-0.27
0.30	0.051	14.99	7.90	Single-Row	0.2	12	15	9%	9%	-1%	19%	21%	14%	15%	6%
0.29	0.051	15.03	7.95	Single-Row	0.4	25	15	13%	13%	3%	20%	22%	5%	3%	2%
0.30	0.050	15.01	7.94	Single-Row	0.6	37	15	9%	9%	-1%	15%	16%	0%	-4%	-3%
0.30	0.050	15.04	7.96	Single-Row	0.8	50	15	5%	5%	0%	10%	12%	-6%	-3%	-14%
0.30	0.071	15.15	7.95	Clean	NA	NA	NA	1.19	1.18	2.04	0.22	0.21	0.78	-0.05	-0.34
0.30	0.071	15.04	7.94	Single-Row	0.2	8	15	0%	0%	-1%	6%	7%	-15%	2%	-21%
0.29	0.071	15.05	7.95	Single-Row	0.4	17	15	3%	4%	-1%	8%	9%	-13%	-4%	-17%
0.29	0.071	15.06	7.97	Single-Row	0.6	26	15	4%	5%	-3%	9%	10%	-10%	-4%	-10%
0.29	0.072	15.06	7.97	Single-Row	0.8	35	15	3%	4%	-4%	8%	9%	-7%	-5%	-8%



**Table 31. Summary of key metrics for Mach 0.4 Single-Row COMPACT data sets.**

$M$	$k$	$\alpha_0(^{\circ})$	$\alpha_1(^{\circ})$	Geom	$F^+$	$N_{pulses}$	$\alpha_{start}$	$C_{l,avg}$	$C_{l,avg,corr}$	$C_{l,max}$	$C_{d,p,avg}$	$C_{d,p,avg,corr}$	$C_{d,p,max}$	$C_{m,c/4}$	$C_{m,c,min}$
0.40	0.025	9.84	8.09	Clean	NA	NA	NA	0.93	0.94	1.55	0.11	0.11	0.33	-0.03	-0.12
0.40	0.025	10.02	8.00	Single-Row	0.2	24	10	3%	2%	-3%	8%	6%	21%	4%	24%
0.39	0.025	10.01	7.99	Single-Row	0.4	49	10	5%	4%	-2%	5%	4%	12%	-10%	6%
0.39	0.025	10.01	7.99	Single-Row	0.6	74	10	4%	3%	-3%	5%	3%	10%	-8%	16%
0.40	0.050	9.99	8.00	Clean	NA	NA	NA	0.91	0.92	1.62	0.11	0.11	0.37	-0.03	-0.14
0.40	0.051	10.09	7.89	Single-Row	0.2	12	10	5%	4%	-3%	5%	4%	4%	-11%	5%
0.39	0.051	10.14	7.93	Single-Row	0.4	25	10	7%	6%	-2%	5%	4%	3%	-15%	-1%
0.40	0.051	10.14	7.95	Single-Row	0.6	37	10	7%	6%	-2%	5%	4%	5%	-15%	-3%
0.40	0.051	9.96	9.86	Clean	NA	NA	NA	0.82	0.85	1.70	0.13	0.12	0.43	-0.04	-0.17
0.39	0.051	10.12	9.41	Single-Row	0.2	12	10	10%	6%	-5%	7%	8%	11%	-2%	12%
0.39	0.051	10.14	9.41	Single-Row	0.4	25	10	11%	7%	-5%	6%	7%	4%	-7%	-6%
0.39	0.051	10.15	9.42	Single-Row	0.6	37	10	11%	7%	-5%	5%	6%	1%	-10%	-7%
0.40	0.051	9.96	9.86	Clean	NA	NA	NA	0.82	0.85	1.70	0.13	0.12	0.43	-0.04	-0.17
0.39	0.051	10.14	9.41	Single-Row	0.2	12	10	14%	10%	-3%	10%	11%	15%	2%	18%
0.39	0.051	10.16	9.42	Single-Row	0.4	25	10	15%	10%	-2%	9%	10%	5%	-3%	-3%
0.39	0.051	10.17	9.43	Single-Row	0.6	37	10	15%	11%	-2%	9%	10%	9%	-5%	1%
0.40	0.070	10.03	7.97	Single-Row	NA	NA	NA	0.92	0.93	1.76	0.10	0.10	0.48	-0.03	-0.19
0.40	0.071	10.06	7.89	Single-Row	0.2	8	10	2%	2%	-6%	11%	12%	2%	7%	15%
0.40	0.071	10.05	7.89	Single-Row	0.4	17	10	4%	4%	-6%	10%	10%	1%	-2%	10%
0.39	0.071	10.05	7.89	Single-Row	0.6	26	10	4%	4%	-6%	9%	9%	1%	-6%	11%
0.40	0.071	10.17	9.49	Single-Row	NA	NA	NA	0.84	0.84	1.72	0.12	0.12	0.57	-0.03	-0.23
0.40	0.071	10.16	9.44	Single-Row	0.2	8	10	6%	6%	-1%	8%	8%	2%	14%	7%
0.40	0.071	10.16	9.43	Single-Row	0.4	17	10	7%	7%	-1%	5%	6%	1%	2%	8%
0.40	0.071	10.15	9.43	Single-Row	0.6	26	10	8%	7%	0%	5%	6%	0%	3%	7%
0.40	0.050	12.15	7.92	Single-Row	NA	NA	NA	0.98	0.98	1.60	0.14	0.14	0.43	-0.04	-0.16
0.40	0.051	12.11	7.89	Single-Row	0.2	12	0	7%	7%	0%	8%	9%	14%	9%	14%
0.40	0.051	12.13	7.91	Single-Row	0.4	25	0	8%	8%	0%	9%	9%	2%	6%	-5%
0.40	0.051	12.13	7.91	Single-Row	0.6	37	0	8%	8%	0%	7%	8%	-1%	3%	-10%
0.40	0.050	12.19	9.50	Single-Row	NA	NA	NA	0.91	0.91	1.63	0.16	0.16	0.46	-0.04	-0.18
0.40	0.051	12.13	9.47	Single-Row	0.2	12	12	6%	6%	1%	9%	10%	13%	15%	6%
0.39	0.051	12.16	9.49	Single-Row	0.4	25	12	9%	9%	3%	9%	10%	5%	7%	-4%
0.39	0.051	12.17	9.50	Single-Row	0.6	37	12	7%	8%	1%	8%	8%	-1%	7%	-4%

**Table 32. Summary of key metrics for Mach 0.5 Single-Row COMPACT data sets.**

$M$	$k$	$\alpha_0(^{\circ})$	$\alpha_1(^{\circ})$	Geom	$F^+$	$N_{pulses}$	$\alpha_{start}$	$C_{l,avg}$	$C_{l,max}$	$C_{d,p,avg}$	$C_{d,p,max}$	$C_{m,c/4}$	$C_{m,c,min}$
0.50	0.026	7.86	8.01	Clean	NA	NA	NA	0.80	1.36	0.08	0.27	-0.02	-0.08
0.50	0.080	8.00	7.99	Single-Row	0.2	25	8	-2%	-4%	6%	3%	10%	14%
0.50	0.082	8.00	7.99	Single-Row	0.4	50	8	-2%	-2%	5%	-2%	12%	13%
0.50	0.025	7.85	4.95	Clean	NA	NA	NA	0.92	1.28	0.05	0.16	-0.01	-0.05
0.50	0.080	7.98	5.04	Single-Row	0.2	25	8	-1%	-3%	24%	6%	-8%	13%
0.50	0.080	7.98	5.04	Single-Row	0.4	50	8	-1%	-2%	23%	5%	-8%	14%
0.50	0.050	8.06	7.94	Clean	NA	NA	NA	0.80	1.44	0.08	0.28	-0.02	-0.10
0.50	0.162	8.21	8.06	Single-Row	0.2	12	8	-2%	0%	8%	2%	1%	8%
0.50	0.159	8.22	8.05	Single-Row	0.4	25	8	-2%	-1%	8%	0%	2%	10%
0.50	0.050	7.98	5.06	Clean	NA	NA	NA	0.91	1.35	0.05	0.17	-0.01	-0.05
0.50	0.159	8.14	5.02	Single-Row	0.2	12	8	0%	-3%	17%	3%	-29%	0%
0.50	0.162	8.14	5.02	Single-Row	0.4	25	8	0%	-3%	17%	5%	-25%	5%

### B. Dual-Row COMPACT Results

Due to the limited test entry time dedicated to the dual-row installation, and the much larger operational parameter envelope introduced by the multiple slots, only a limited number of dynamic stall excursions and actuator parameters were investigated over the final three days of the second IRT test entry. The COMPACT parameters included operating the actuators in isolation, firing either the front or back rows independently, as well as the configuration ‘Both’ in Table 33 which indicates that both combustion chambers were triggered simultaneously. Lastly, the actuators could be phased as a percentage of the actuator period,  $1/f_{act}$ . These cases are labeled ‘AltX’ in Table 33, where  $X = t_{delay,R2} \times f_{act}$ . Frequency input to the surface flow was effectively doubled for ‘Alt 50,’ in which the front and rear actuator pulses were time-shifted by one-half the actuator firing period. A schematic representation of the trigger signals sent to the COMPACT spark electronics is shown in Figure 232. Several of the test data points also targeted phase delays based on assumed COMPACT produced disturbance convective speeds, e.g., Run 89 Pts 23, 25, 26 set the phase delay with the assumption that the COMPACT generated fluid structures traveled at speed near  $U_\infty$ . Run 89 Pts 27-29 halve this transit velocity.

**Table 33. COMPACT Dual-Row Unsteady Data Points Acquired**

Run	Mach	k	$\alpha_0$	$\alpha_1$	F+	Pulse Start $\alpha$	Config	Points
80	0.3	0.07	10	9.5	0.2-0.8	10	Front	8-11
	0.3	0.07	10	9.5	0.2-0.8	10	Back	12,14-16
	0.3	0.07	10	9.5	0.2-0.8	10	Both	17-20
	0.3	0.07	10	9.5	0.2-0.8	10	Alt 50	21-24
89	0.4	0.05	10	9.5	0.2-0.6	10	Front	10-12
	0.4	0.05	10	9.5	0.2-0.6	10	Back	13-15
	0.4	0.05	10	9.5	0.2-0.6	10	Both	16,18,19
	0.4	0.05	10	9.5	0.2-0.6	10	Alt 50	20-22
	0.4	0.05	10	9.5	0.2	10	Alt 2	23
	0.4	0.05	10	9.5	0.4	10	Alt 4	25
	0.4	0.05	10	9.5	0.6	10	Alt 6	26
	0.4	0.05	10	9.5	0.2	10	Alt 4	27
	0.4	0.05	10	9.5	0.4	10	Alt 8	28
	0.4	0.05	10	9.5	0.6	10	Alt 12	29
91	0.2	0.07	10	10	0.2-1.0	10	Front	8-12
	0.2	0.07	10	10	0.2-1.0	10	Back	13-17
	0.2	0.07	10	10	0.2-1.0	10	Both	20-24
	0.2	0.07	10	10	0.2-1.0	10	Alt 50	25-29
92	0.5	0.025	8	8	0.2,0.4	8	Front	5-6
	0.5	0.025	8	8	0.2,0.4	8	Back	7-8
	0.5	0.025	8	8	0.2,0.4	8	Both	9-10
	0.5	0.025	8	8	0.2,0.4	8	Alt 50	11-12

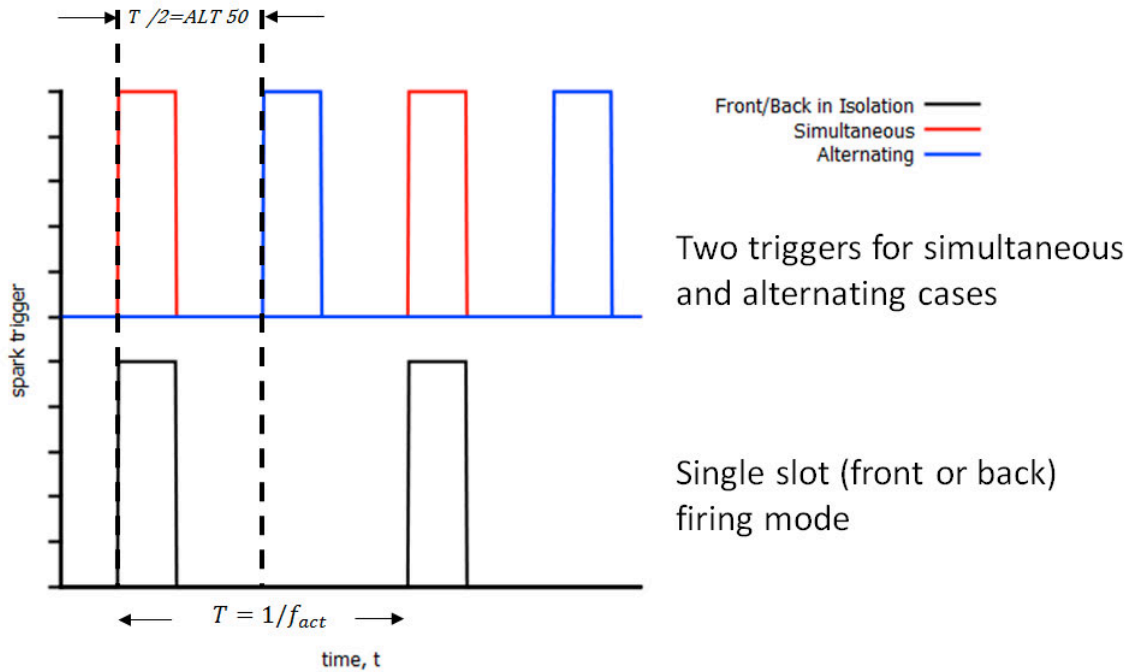


**Figure 232. Schematic of spark triggers for operation of the dual-row COMPACT installation.**

This section of the report presents the primary results associated with the dual-row COMPACT datasets. Figures showcase the individual aerodynamic loads for each test point and comparison cases are overlaid with respect to angle-of-attack and phase.

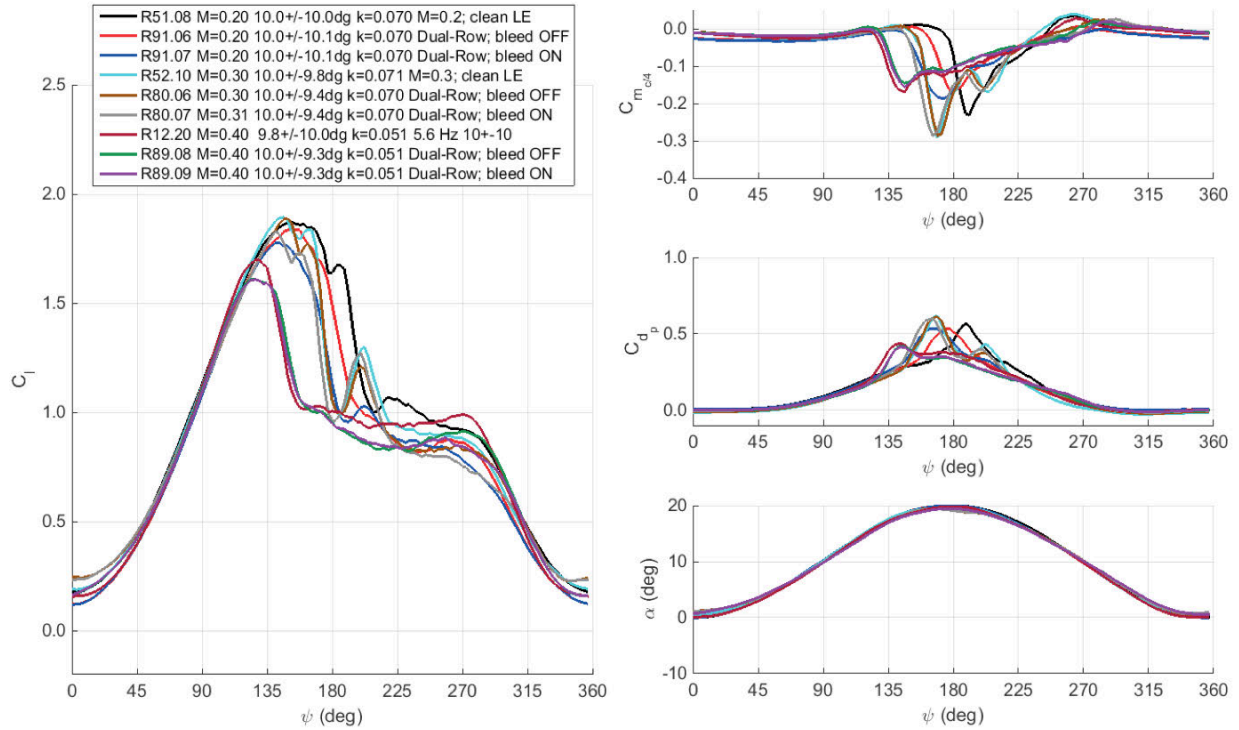


**Figure 233.**  $C_L$ ,  $C_D$ ,  $C_M$  and  $\alpha$  for  $\alpha = 10^\circ \pm 9.5^\circ$  for Mach 0.2, 0.3, and 0.4. Results for the clean VR-12 and dual-row no-bleed and bleed-on cases are shown.

### *Open Slot and Bleed Effects for Dual-Row Configuration*

Open slots with and without steady bleed show similar differences with respect to the clean leading edge VR-12. A comparison of the load traces for Mach numbers of 0.2, 0.3, and 0.4 with respect to pitching motion phase angle show that the effect of the open slot/actuator installation degrades the VR-12 performance. This is believed to be a result of geometric differences and general installation variances between the two tested articles. A single trajectory is shown to highlight this trend, but the trait proved to be ubiquitous for all airfoil pitching motion parameters and freestream conditions. For brevity, these comparisons are neglected in the COMPACT cases subsequently discussed.

### *M=0.2*

This section discusses the results of the different COMPACT configurations and triggering methods investigated for the dual-row actuator installation at Mach 0.2. Many of the trends recorded at Mach 0.2 hold at higher Mach number but begin to degrade as compressibility effects increase and the actuators' struggles with low back pressure increased.

### **Front Row**

A single prescribed motion was studied with the dual-row actuators at Mach 0.2:  $\alpha = 10^\circ - 10^\circ \cos \omega t$ ,  $k = 0.07$ . The actuators were first operated with the front-row only configuration. The individual and overlaid load coefficients from the test points are shown in Figure 234 through. The baseline case exhibits a larger peak lift than any of the actuated cases. This is a

of the effects of the COMAPCT installation and steady gas flow to the actuators on the unsteady loads. Increasing  $F^+$  beyond 0.4 forces a recovery of the peak lift, matching the baseline  $C_L=1.87$  at  $F^+=1.0$ . The actuated cases show an immediate impact on the downstroke lift deficit at  $F^+=0.2$ . Additional actuator pulses improve the flow up to 0.6. Differences between the downstroke lift behavior for  $F^+=0.6$  through 1.0 are small. The actuators had little impact on drag compared to the baseline, although increasing  $F^+$  causes a steady decrease in the peak drag compared to the clean VR-12. More importantly, a large drop in nose-down pitching moment is observed for these conditions. Pitching moment decreases from -0.25 to -0.09 at  $F^+=1.0$ .

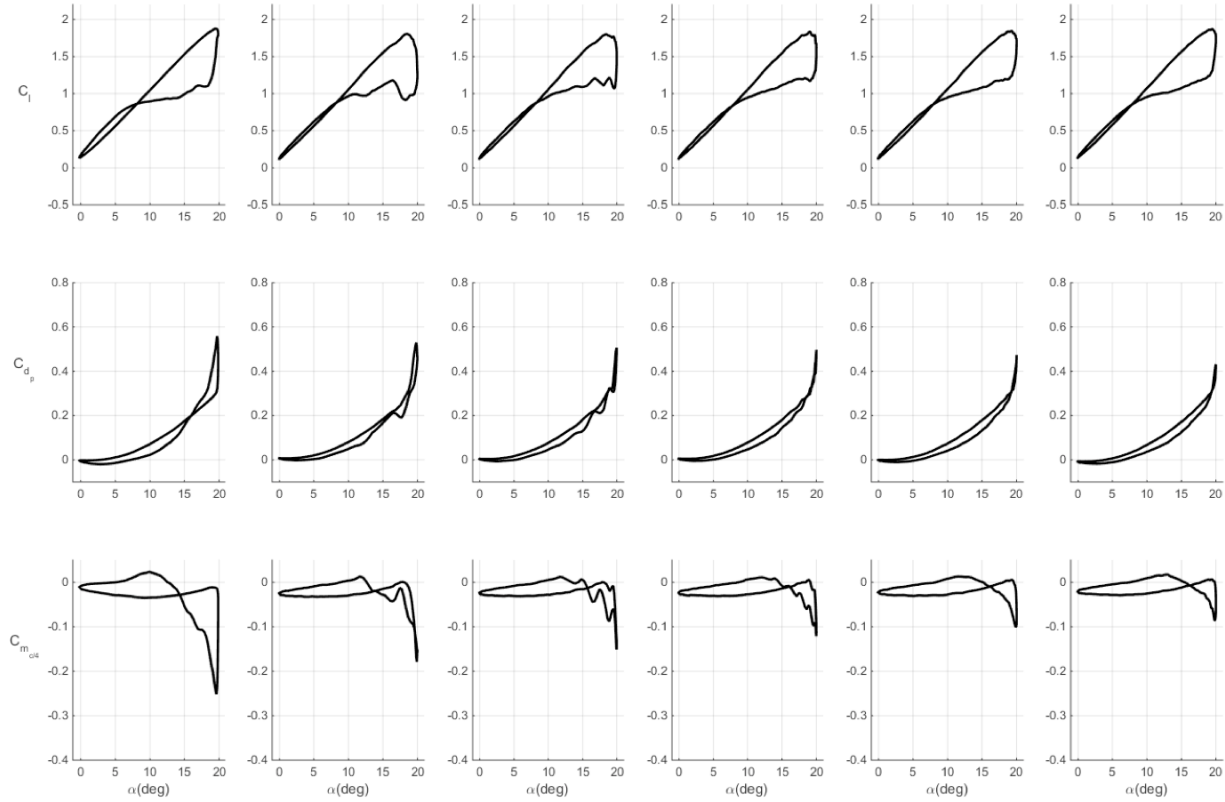


**Figure 234. Lift, drag, and moment coefficients at Mach 0.2,  $\alpha = 10 \pm 10$ ,  $k = 0.07$  for baseline and dual-row COMPACT,  $F^+$  of 0.2 to 1.0. Front actuator only.**

#### Back Row

The back row actuators firing in isolation are shown in Figure 237 through Figure 239. Similar  $F^+$  trends are observed compared to the front-row actuator cases, but the overall impact on the key aerodynamic metrics are considerably reduced. These results suggest, for the same actuated span, a slot location of  $x/c=0.10$  is substantially more effective in controlling dynamic stall than a further rearward positioned slot. As will be shown, increasing freestream Mach number does not alter this key finding. The CFD studies that led to the slot design similarly indicated that a slot at  $x/c=0.15$  was less beneficial than  $x/c=0.10$ .

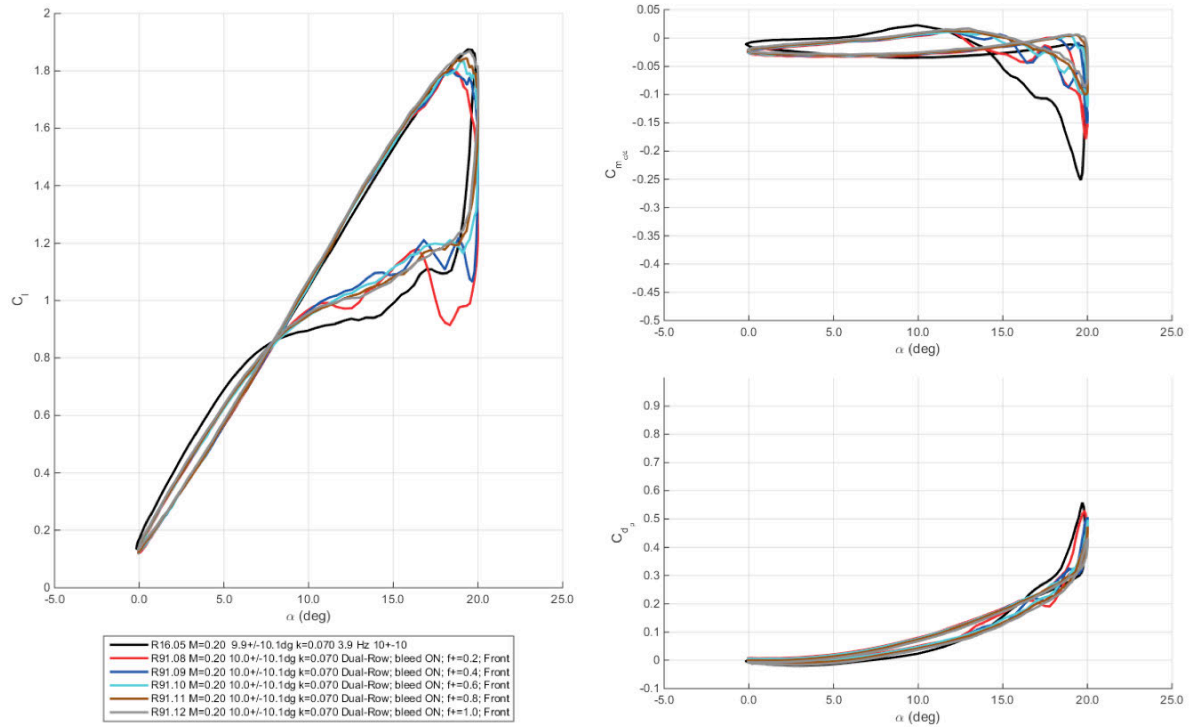


Figure 235. Lift, drag, and moment coefficients at Mach 0.2,  $\alpha = 10^\circ \pm 10^\circ$ ,  $k = 0.07$  for baseline and dual-row COMPACT,  $F^+$  of 0.2 to 1.0. Loads plotted vs. angle-of-attack. Front actuator only.

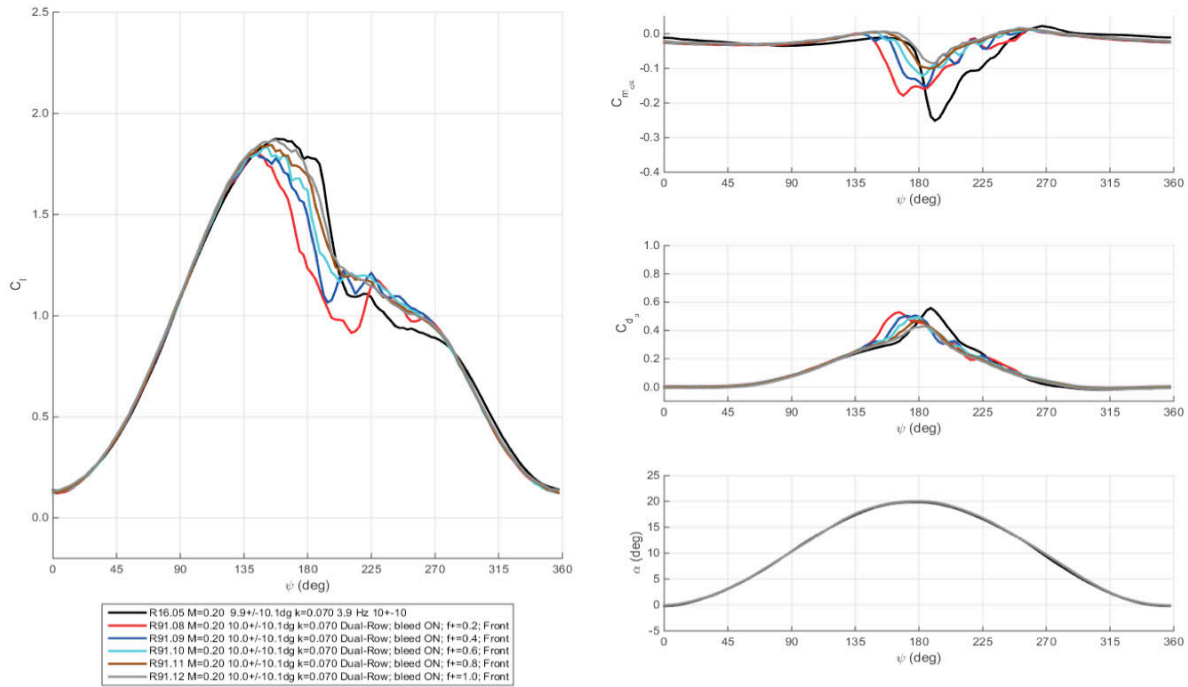
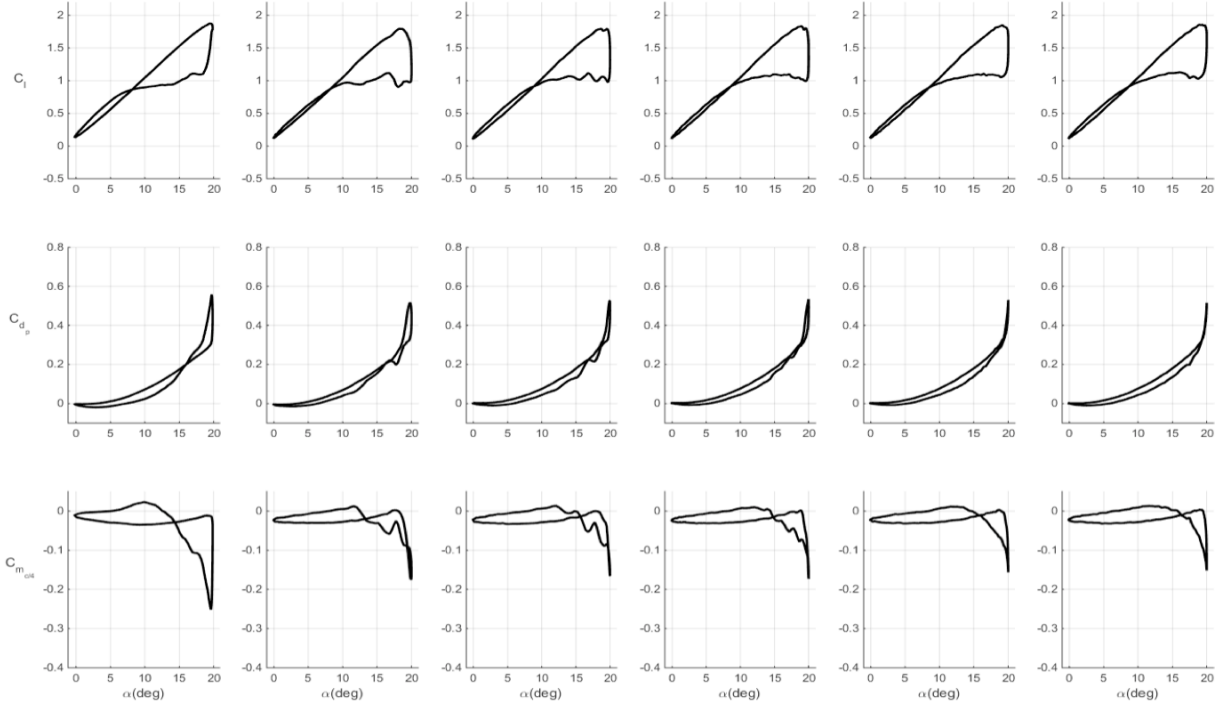
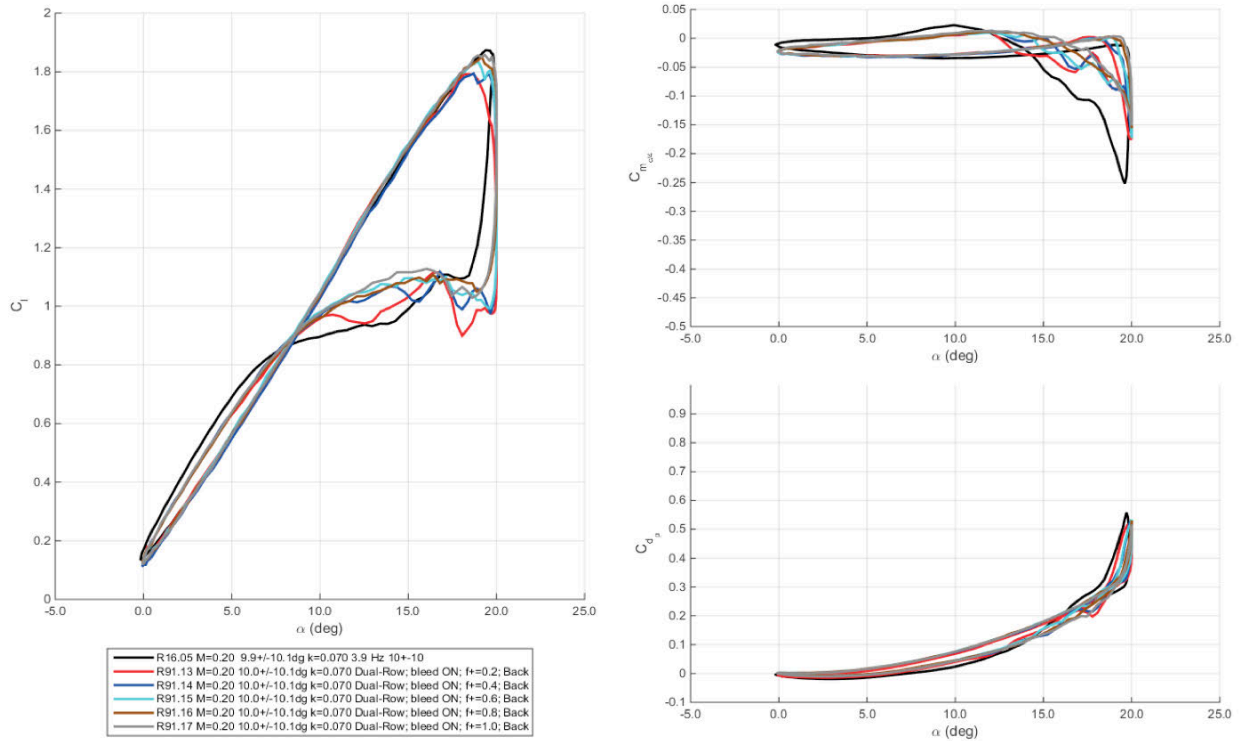


Figure 236. Lift, drag, and moment coefficients at Mach 0.2,  $\alpha = 10^\circ \pm 10^\circ$ ,  $k = 0.07$  for baseline and dual-row COMPACT,  $F^+$  of 0.2 to 1.0. Loads plotted vs. phase angle. Front actuator only.



**Figure 237. Lift, drag, and moment coefficients at Mach 0.2,  $\alpha = 10^\circ \pm 10^\circ$ ,  $k = 0.07$  for baseline and dual-row COMPACT,  $F^+$  of 0.2 to 1.0. Back actuator only.**



**Figure 238. Lift, drag, and moment coefficients at Mach 0.2,  $\alpha = 10^\circ \pm 10^\circ$ ,  $k = 0.07$  for baseline and dual-row COMPACT,  $F^+$  of 0.2 to 1.0. Loads plotted vs. angle-of-attack. Back actuator only.**



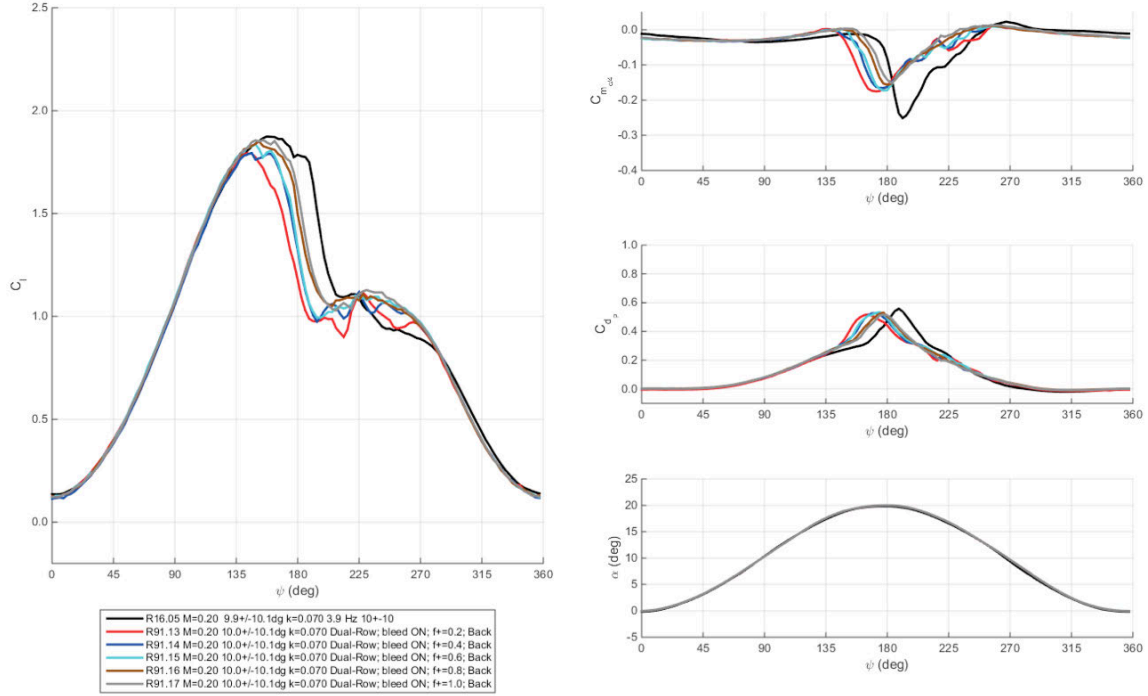


**Figure 239. Lift, drag, and moment coefficients at Mach 0.2,  $\alpha = 10^\circ \pm 10^\circ$ ,  $k = 0.07$  for baseline and dual-row COMPACT,  $F^+$  of 0.2 to 1.0. Loads plotted vs. phase angle. Back actuator only.**

### Simultaneous Slots

Firing both combustion chambers locked in phase produced further aerodynamic impact compared to the baseline case and isolated slot results. Using both spanwise actuators produced a small enhancement in lift and moment compared to operating either slot independently. The load traces for the Mach 0.2  $F^+$  Sweep are shown in Figure 240 through Figure 242. Compared to the baseline, firing both actuators produced increased upstroke lift for all  $F^+$  and increased peak lift for  $F^+ \geq 0.4$ . The downstroke load fluctuations were noticeably increased for this configuration. Pitching moment reduction reached +71% for  $F^+=1.0$ , compared to 66% for the front row, and 40% for the back row.

### Alternating Slots

At Mach 0.2, frequency doubling (actuator pulses separated by  $T/2$ ) was the only out-of-phase slot operation investigated. Additional phase shifted input was tested at Mach 0.4. Usage of the actuators in this mode seeks to lower the individual pulsation requirements for each chamber while achieving the increased performance characteristics often associated higher  $F^+$ . This also alleviates the heat-up of the actuators at high repetition rate and reduces steady flame tendency. Both effects promote actuator endurance. Due to the spatial differences of the two upper surface slots, the interaction of the slot produced disturbances and the local flow topology at the time corresponding to each COMPACT chamber's pulse, these cases cannot be viewed as purely a frequency effect, as in the case of single slot operations (the same is true for the simultaneous slot).

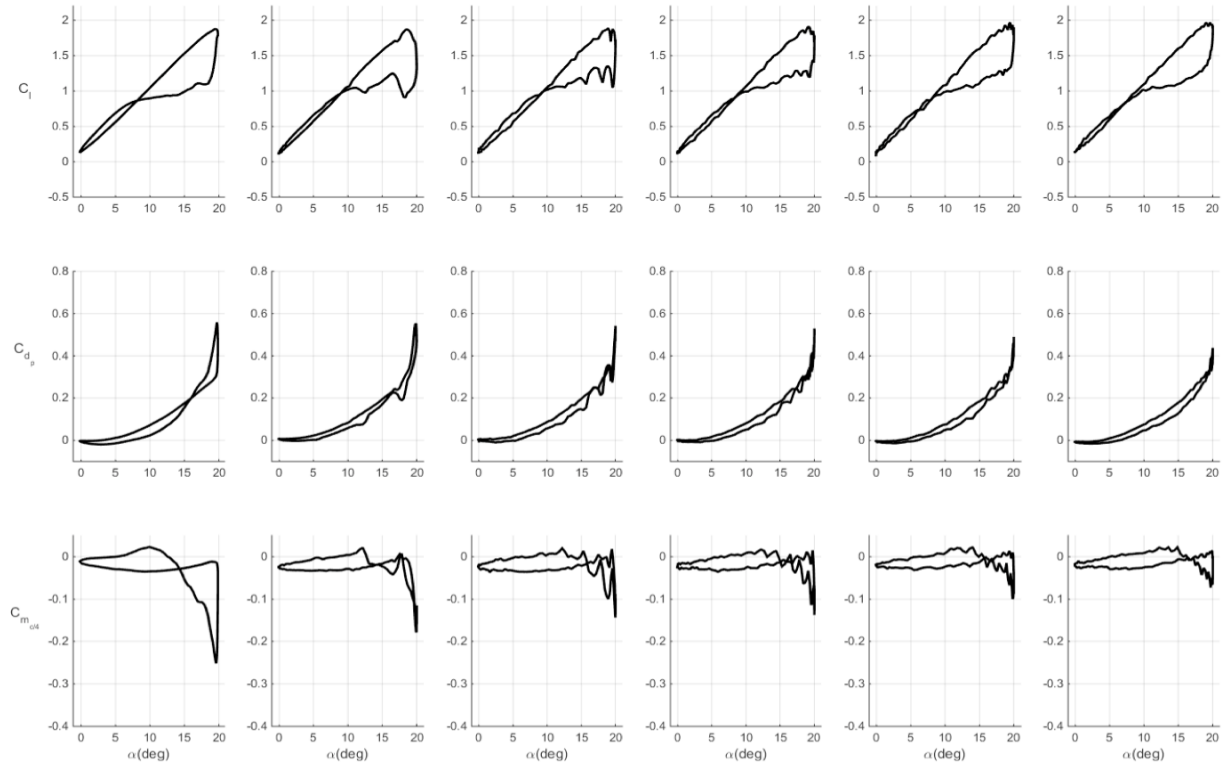


**Figure 240. Lift, drag, and moment coefficients at Mach 0.2,  $\alpha = 10^\circ \pm 10^\circ$ ,  $k = 0.07$  for baseline and dual-row COMPACT,  $F^+$  of 0.2 to 1.0. Front and back actuators firing simultaneously.**

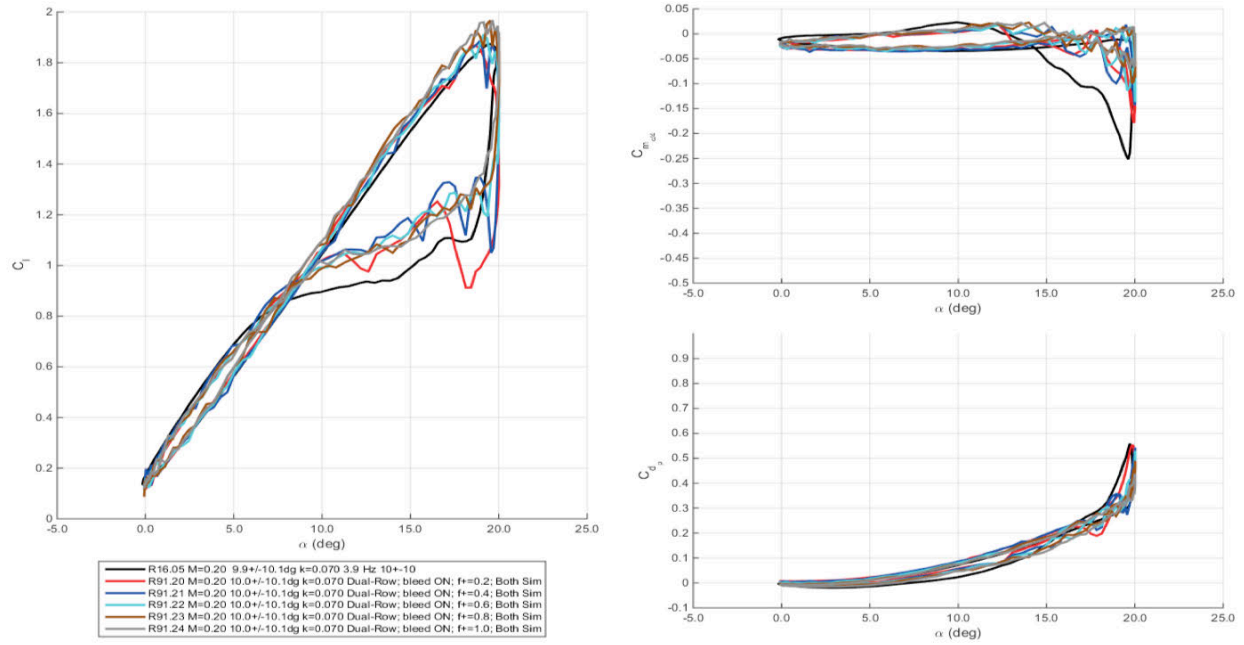


Figure 241. Lift, drag, and moment coefficients at Mach 0.2,  $\alpha = 10^\circ \pm 10^\circ$ ,  $k = 0.07$  for baseline and dual-row COMPACT,  $F^+$  of 0.2 to 1.0. Loads plotted vs. angle-of-attack. Front and back actuators firing simultaneously.

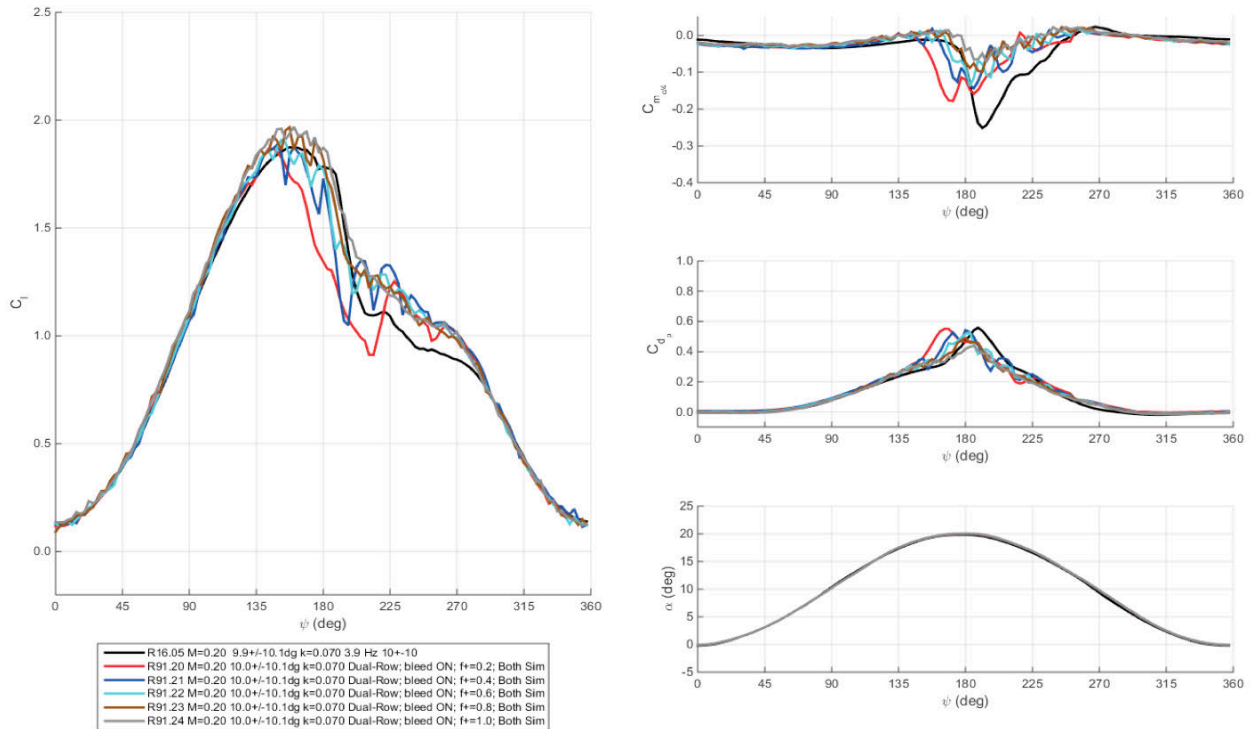
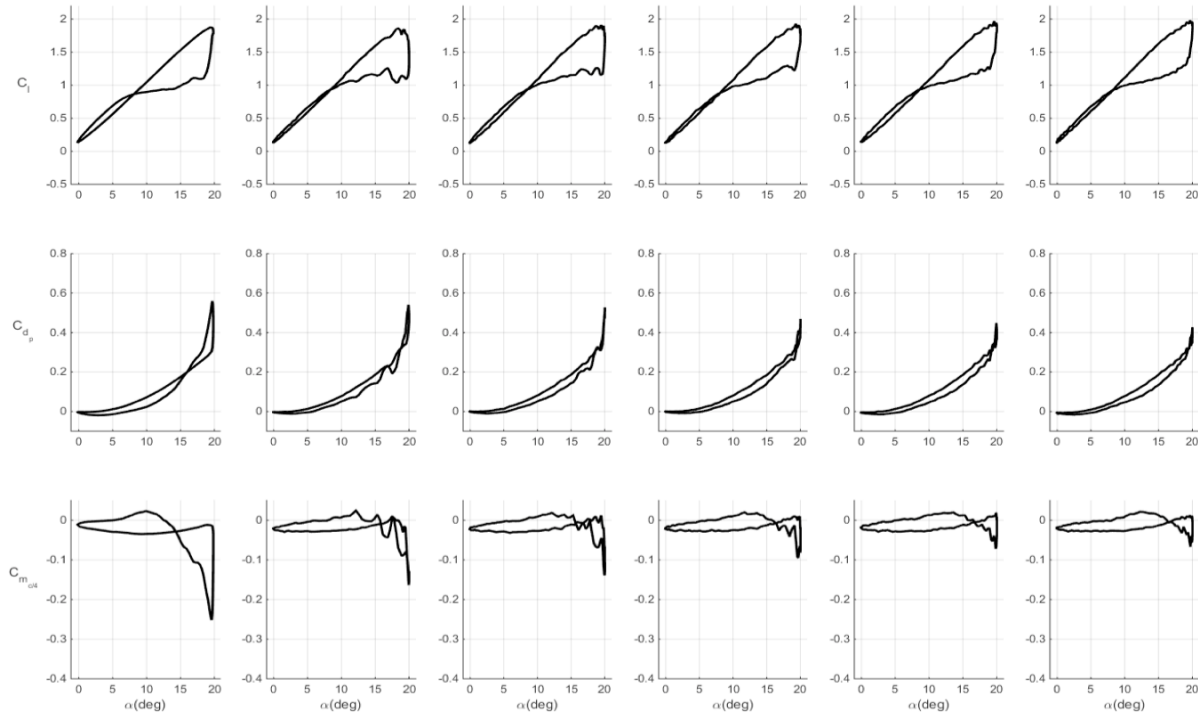


Figure 242. Lift, drag, and moment coefficients at Mach 0.2,  $\alpha = 10^\circ \pm 10^\circ$ ,  $k = 0.07$  for baseline and dual-row COMPACT,  $F^+$  of 0.2 to 1.0. Loads plotted vs. phase angle. Front and back actuators firing simultaneously.

The results from the  $F^+$  sweep of the ‘Alt 50’ configuration are shown in Figure 243 through Figure 245. Figure 244 and Figure 245 call out the individual runs by the  $F^+$  associated with each actuator ( $F^+=0.2$  is therefore  $F^+=0.4$  from the “flow’s perspective,” as provided by the comments above). Trends with respect to increasing  $F^+$  are most similar to the simultaneous actuator for upstroke and peak lift promotion, peak drag reduction, and adverse pitching moment improvement. Out-of-phase operation produced the strongest performance increases from the four configurations tested for equal  $F^+$ .

### Comparison of Configurations

Figure 246 through Figure 250 compare each of the load coefficient ensemble behaviors vs. angle-of-attack at constant  $F^+$ .  $F^+=0.4$  and  $0.8$  contain two cases of the Alternating COMPACT mode (‘Alt 50’). These plots directly compare the effect of the different COMPACT modes of operation. Maximum average lift improvements were 5.6% and 6.3% for  $F^+=1.0$  simultaneous and alternating firing configurations, respectively. The single-row results are also included. It should be noted however that due to trouble with Kulite 5 during Run 67, the single-row results possess slight shifts, particularly in lift, compared to the baseline and dual-row configurations. Kulite 5 was operational for Run 67 but drifted slowly in time. Corrections could be made on a run-by-run basis, and further tweaks are still required for best alignment with other datasets. This problematic sensor was replaced prior to the dual-row datasets.



**Figure 243. Lift, drag, and moment coefficients at Mach 0.2,  $\alpha = 10^\circ \pm 10^\circ$ ,  $k = 0.07$  for baseline and dual-row COMPACT,  $F^+$  of 0.2 to 1.0. Front and back actuator firing out-of-phase to double actuator pulse frequency.**

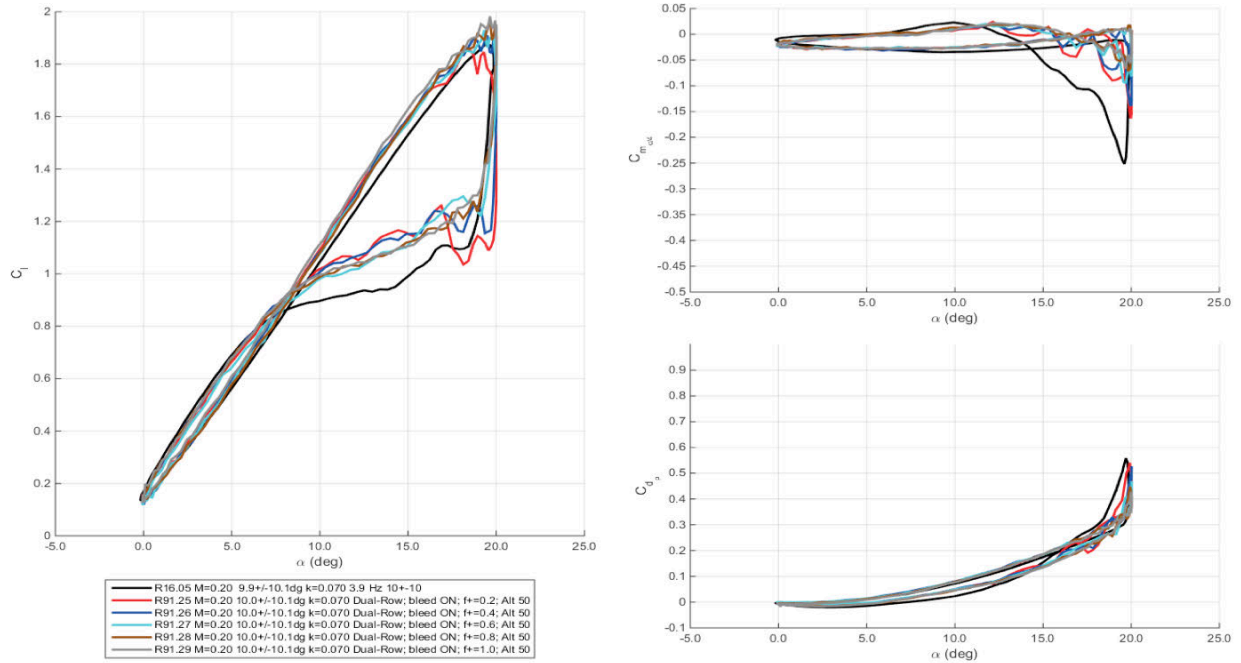


Figure 244. Lift, drag, and moment coefficients at Mach 0.2,  $\alpha = 10^\circ \pm 10^\circ$ ,  $k = 0.07$  for baseline and dual-row COMPACT,  $F^+$  of 0.2 to 1.0. Loads plotted vs. angle-of-attack. Front and back actuator firing out-of-phase to double actuator pulse frequency.

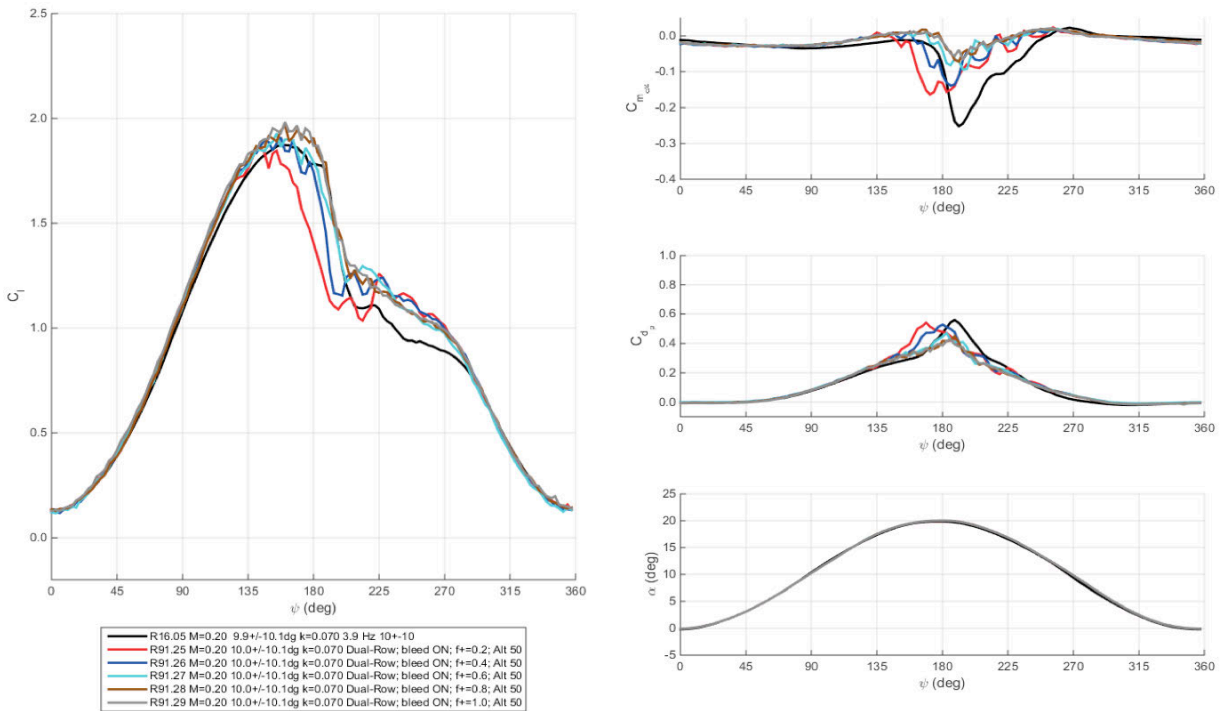
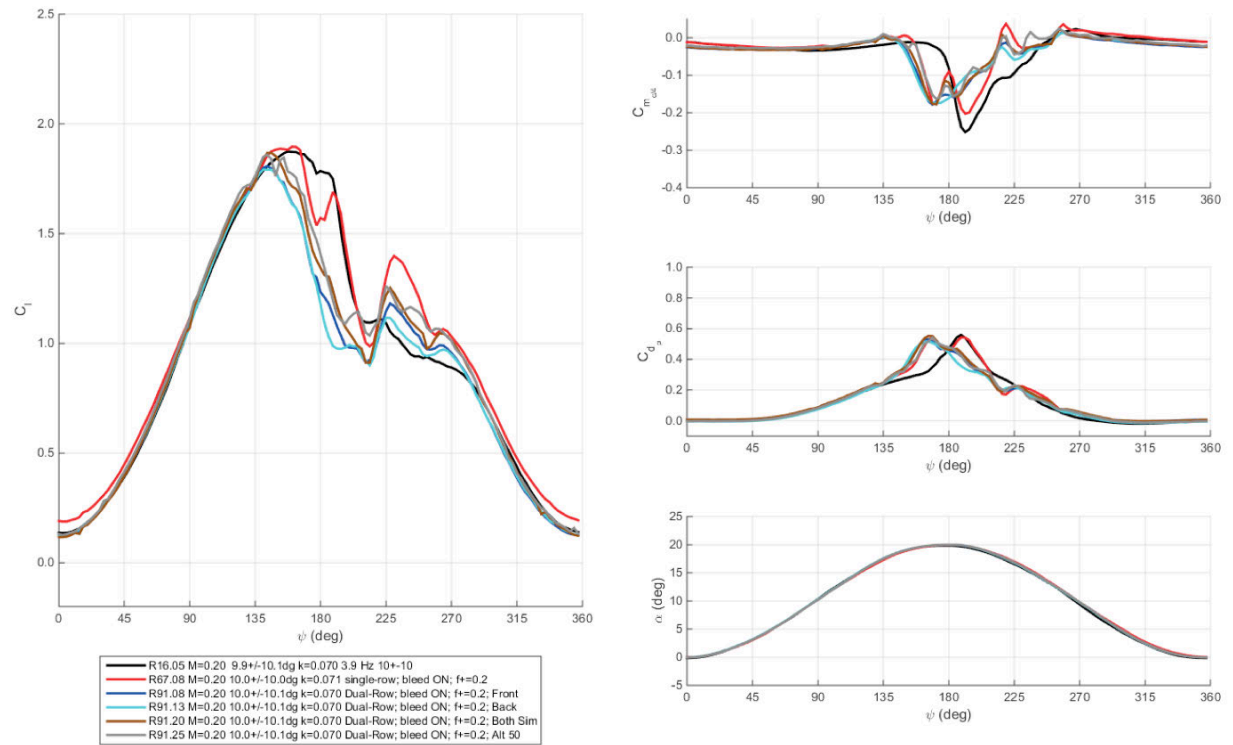


Figure 245. Lift, drag, and moment coefficients at Mach 0.2,  $\alpha = 10^\circ \pm 10^\circ$ ,  $k = 0.07$  for baseline and dual-row COMPACT,  $F^+$  of 0.2 to 1.0. Loads plotted vs. phase angle. Front and back actuator firing out-of-phase to double actuator pulse frequency.

For all  $F^+$ , the single-row COMPACT configuration outperforms the dual-row configurations. This is an effect of the large decrease in the VR-12 wing's COMPACT outfitted span for the dual-row configurations. Comparisons between the single-row and front-row COMPACT modes offer some insight into the performance decrement associated with the decreased span. Installation variances are also embedded in this evaluation. Extension of this limited span argument suggests that increased two-dimensionality, i.e., a larger COMPACT span, would improve the results achieved with the single-row configuration. Aerodynamic effectiveness of the actuators proceeds in the following order: back-row, front-row, simultaneous, alternating, single-row. For the alternating dual-row actuators, pulsing at half the  $F^+$  compared to the other cases, these typically outperformed the isolated front and back row. In Figure 255, the  $F^+=0.4$  case appears to have the best downstroke lift enhancement. This is outweighed, however, by the additional lift near the maximum angle-of-attack found for the simultaneous and alternating,  $F^+=0.8$  cases. This is best illustrated through the average lift and maximum nose-down moment trends with  $F^+$ . Results were extracted from the load coefficient loops for the dual-row cases and plotted against the nondimensional COMPACT pulse frequency in Figure 251 and Figure 252. Baseline values are shown for  $F^+=0$  and indicated by the dash-dot line. Both metrics behave fairly linearly with increasing  $F^+$  across the four dual-row COMPACT configurations. As noted, the alternating case performs best for fixed  $F^+$ . The isolated front fails to enhance the average lift until  $F^+=1$ . The back row never recovers from the installation and bleed. Both the simultaneous and alternating configurations outperform the baseline starting at  $F^+=0.2$ . Moment benefit for the back-row only fails to climb past  $F^+=0.2$ , suggesting the slot's location is too far rearward to impact the formation and strength of the dynamic stall vortex. A comparison of the  $C_p$  on the airfoil's downstroke and the different COMPACT configurations is shown in Figure 253.



**Figure 246. Lift, drag, and moment coefficients at Mach 0.2,  $\alpha = 10^\circ \pm 10^\circ$ ,  $k = 0.07$ ,  $F^+ = 0.2$  for baseline and multiple COMPACT modes.**



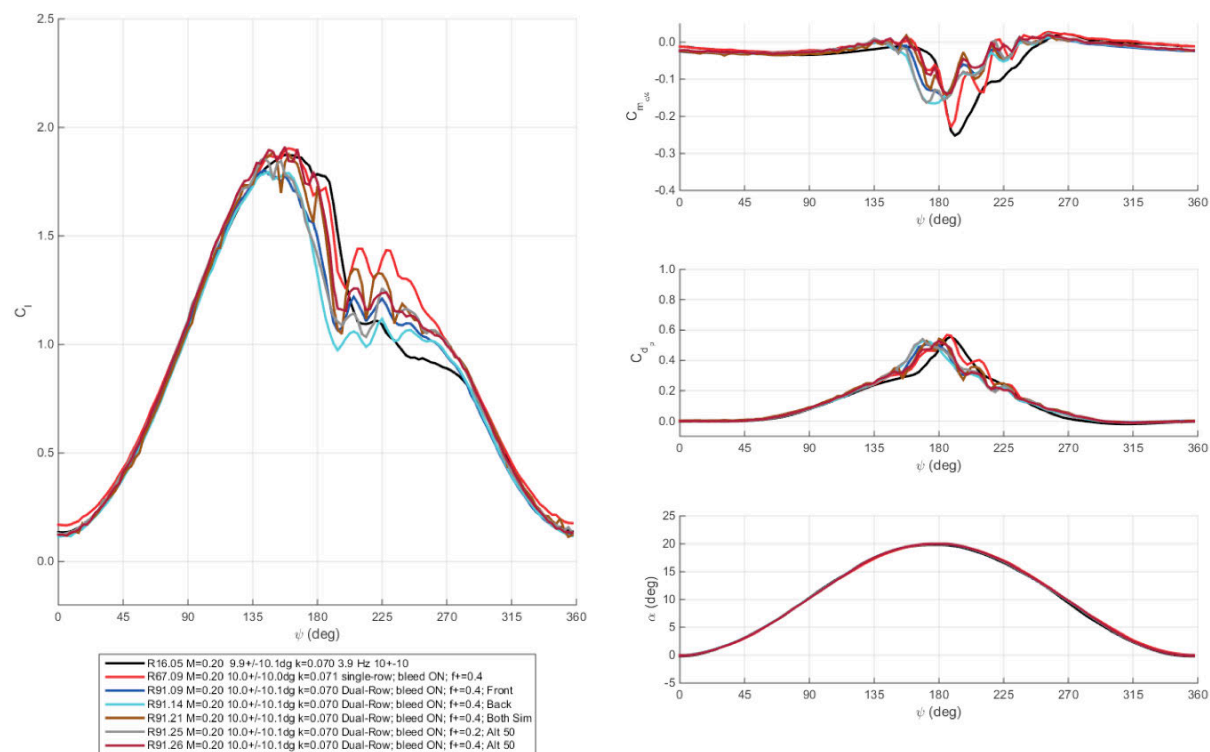


**Figure 247. Lift, drag, and moment coefficients at Mach 0.2,  $\alpha = 10^\circ \pm 10^\circ$ ,  $k = 0.07$ ,  $F^+ = 0.4$  for baseline and multiple COMPACT modes.**

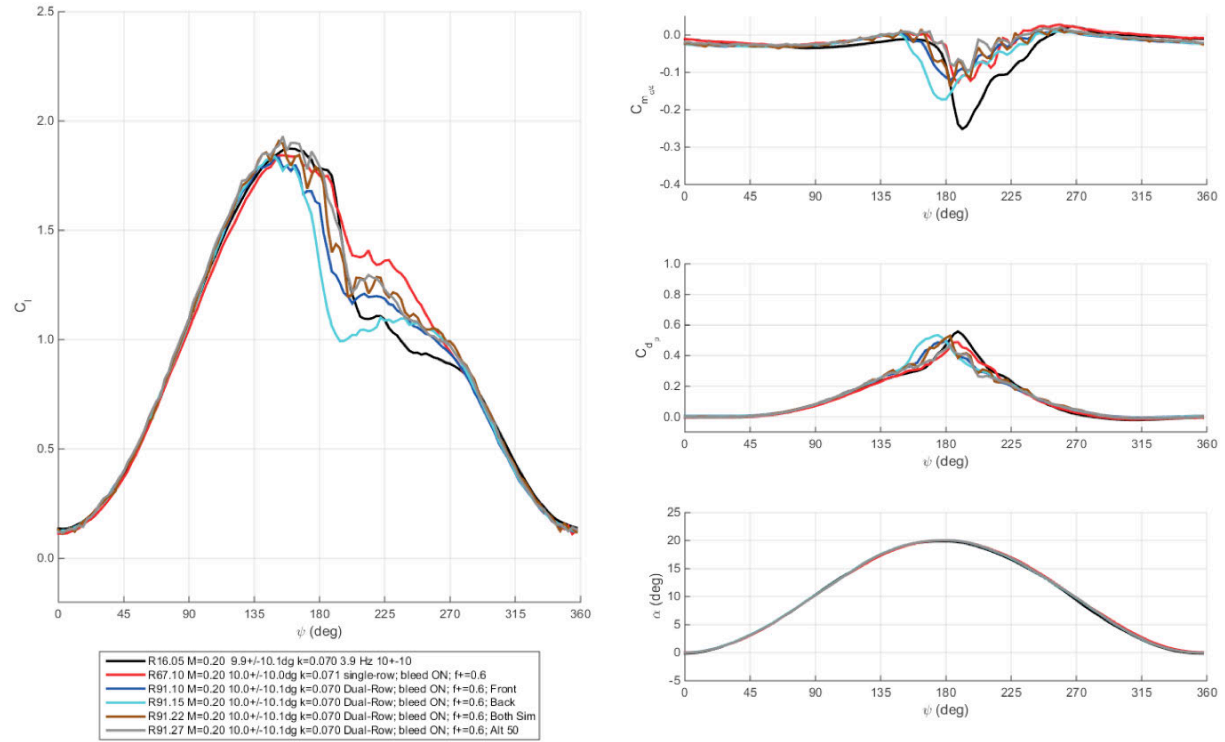


**Figure 248. Lift, drag, and moment coefficients at Mach 0.2,  $\alpha = 10^\circ \pm 10^\circ$ ,  $k = 0.07$ ,  $F^+ = 0.6$  for baseline and multiple COMPACT modes.**

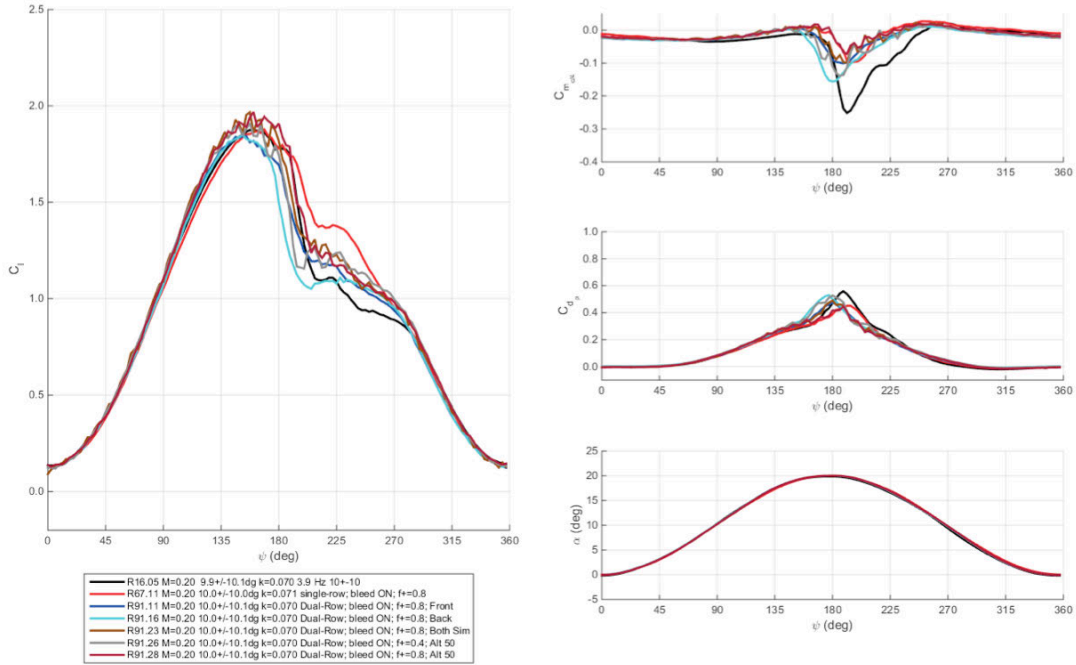


**Figure 249. Lift, drag, and moment coefficients at Mach 0.2,  $\alpha = 10^\circ \pm 10^\circ$ ,  $k = 0.07$ ,  $F^+ = 0.8$  for baseline and multiple COMPACT modes.**

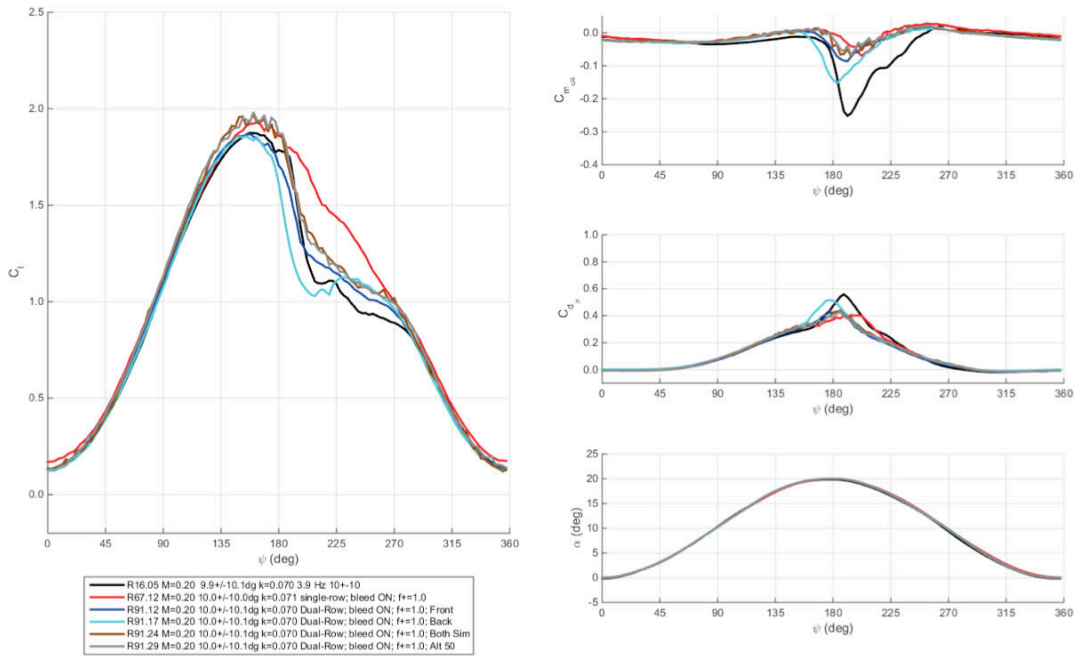


**Figure 250. Lift, drag, and moment coefficients at Mach 0.2,  $\alpha = 10^\circ \pm 10^\circ$ ,  $k = 0.07$ ,  $F^+ = 1.0$  for baseline and multiple COMPACT modes. Loads plotted vs. angle-of-attack.**

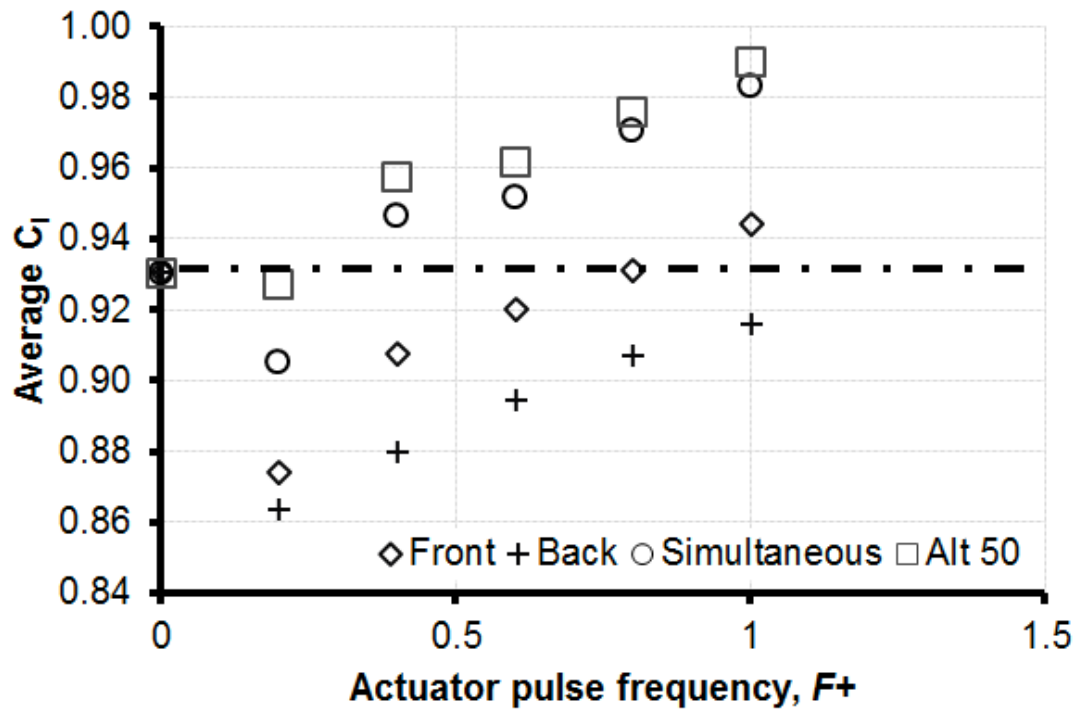


Figure 251. Average lift variation with  $F^+$  for dual-row COMPACT, Mach 0.2,  $\alpha = 10^\circ$ - $10^\circ \cos \omega t$ ,  $k = 0.07$ .

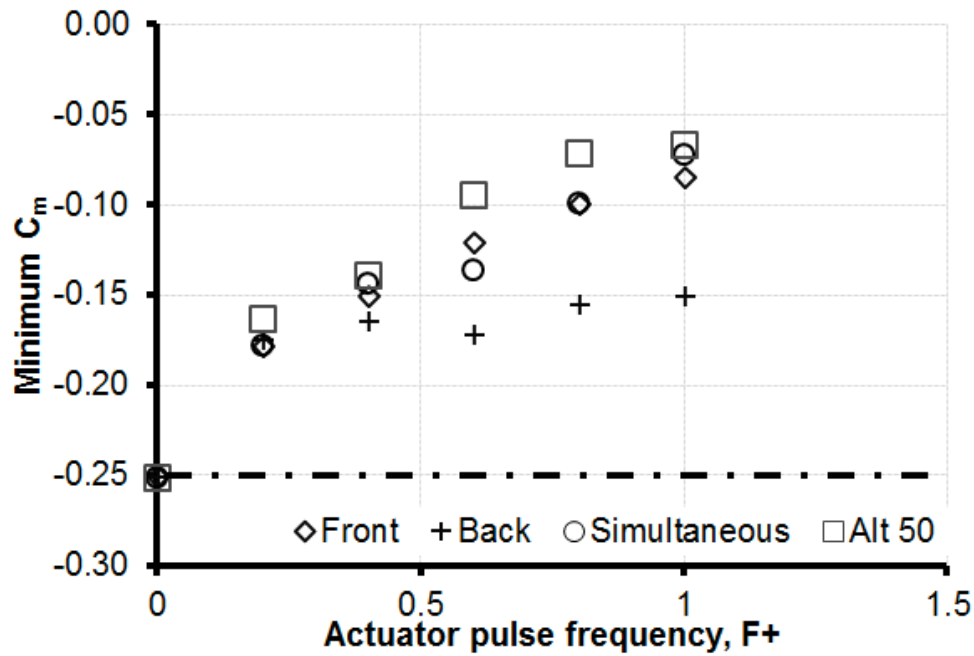


Figure 252. Minimum pitching moment variation with  $F^+$  for dual-row COMPACT, Mach 0.2,  $\alpha = 10^\circ - 10^\circ \cos \omega t$ ,  $k = 0.07$ .

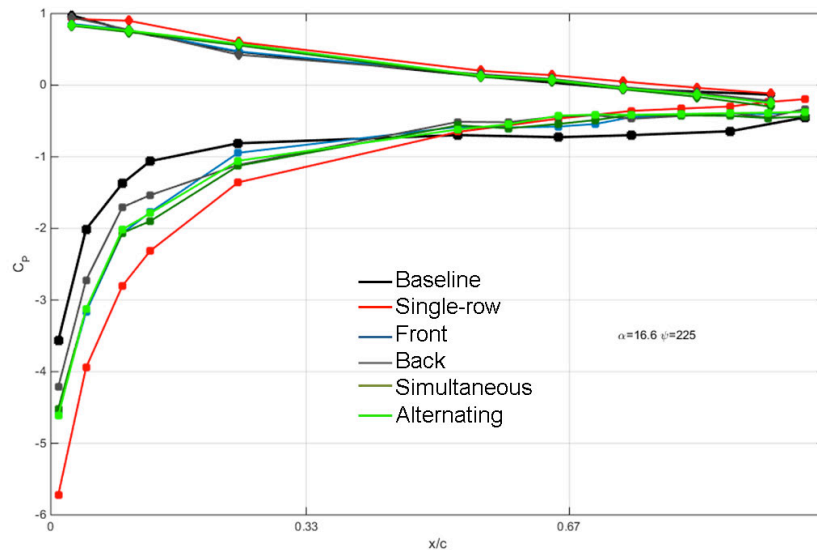
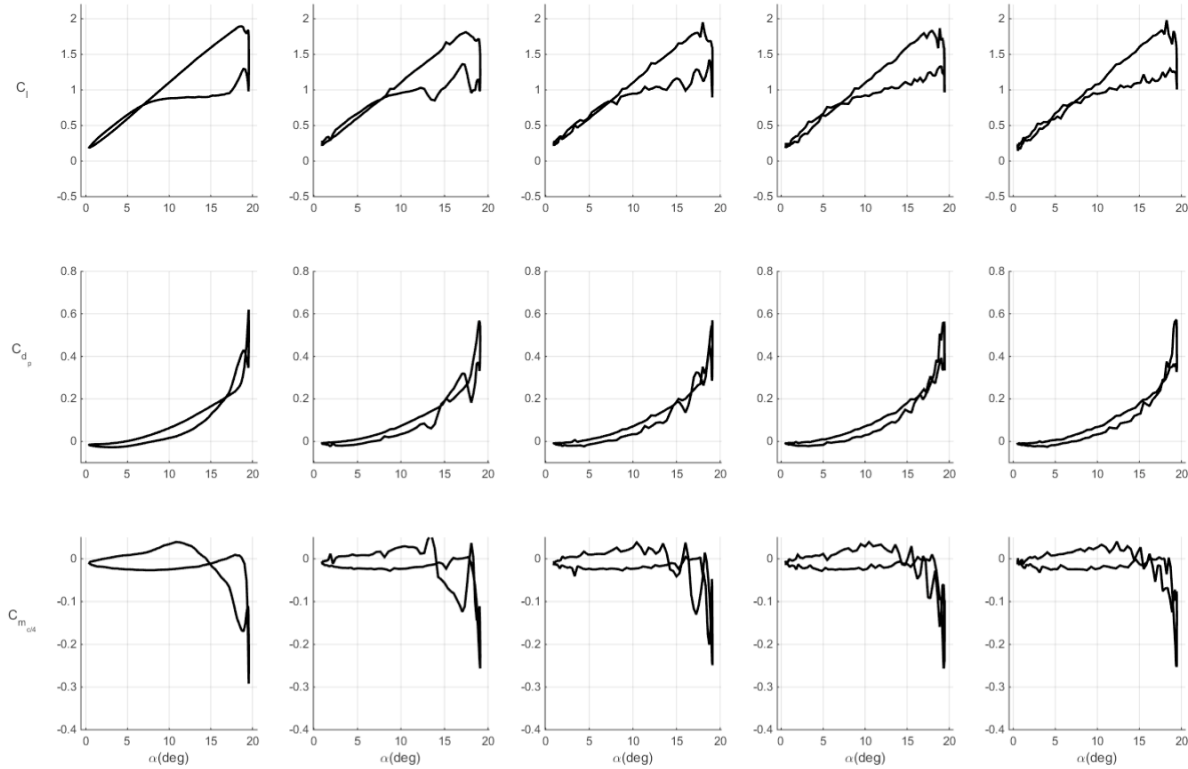


Figure 253. Downstroke,  $\alpha = 16.6^\circ$ , ensemble averaged  $C_p$  for  $F^+=1.0$  and multiple COMPACT configurations.

$M=0.3$

As with the Mach 0.2 dual-row COMPACT investigation, only a single pitching motion was tested at Mach 0.3 freestream conditions:  $\alpha = 10^\circ - 9.5^\circ \cos \omega t$ ,  $k = 0.07$ .  $F^+$  sweeps for the isolated front- or back-row indicate substantial impact for  $F^+=0.4$  with little additional benefit

gained at higher  $F^+$  control inputs. A noticeable drop-off in reattachment capability is seen for the simultaneous firing mode for  $F^+=0.8$  and  $1.0$  in Figure 261. Several possible reasons may exist for the departure in  $F^+$  trends from that observed at Mach 0.2. 160 Hz and 213 Hz physical frequencies were required for  $F^+=0.6$  and  $0.8$ , respectively, at Mach 0.3. These high pulse frequencies led to rapid heating of the COMPACT modules and possibly steady flames during test points as well as the degraded chamber pressures, as discussed in Section 1. Figure 254 through Figure 265 show the individual configuration  $F^+$  sweeps. In contrast to the Mach 0.2 results, the simultaneous and alternating firing modes fail to show upstroke and peak lift enhancement. Adverse pitching moment reduction dropped from more than 70% at Mach 0.2 to 25% for simultaneous firing at  $F^+=0.6$ . The best average lift increment was 2.8% for the front-row only case with  $F^+=0.4$ . Figure 266 through Figure 269 compare the different COMPACT configuration for fixed  $F^+$ . The  $F^+$  impact on the mean cycle lift and peak nose-down pitching moment are summarized in Figure 270 and Figure 271. The front-row only actuator tended to outperform the other configurations in average lift. Each COMPACT mode reached a peak mean  $C_L$  at  $F^+=0.4$ .



**Figure 254. Lift, drag, and moment coefficients at Mach 0.3,  $\alpha = 10^\circ \pm 9.5^\circ$  for baseline and dual-row COMPACT,  $F^+$  of 0.2 to 0.8. Front actuator only.**

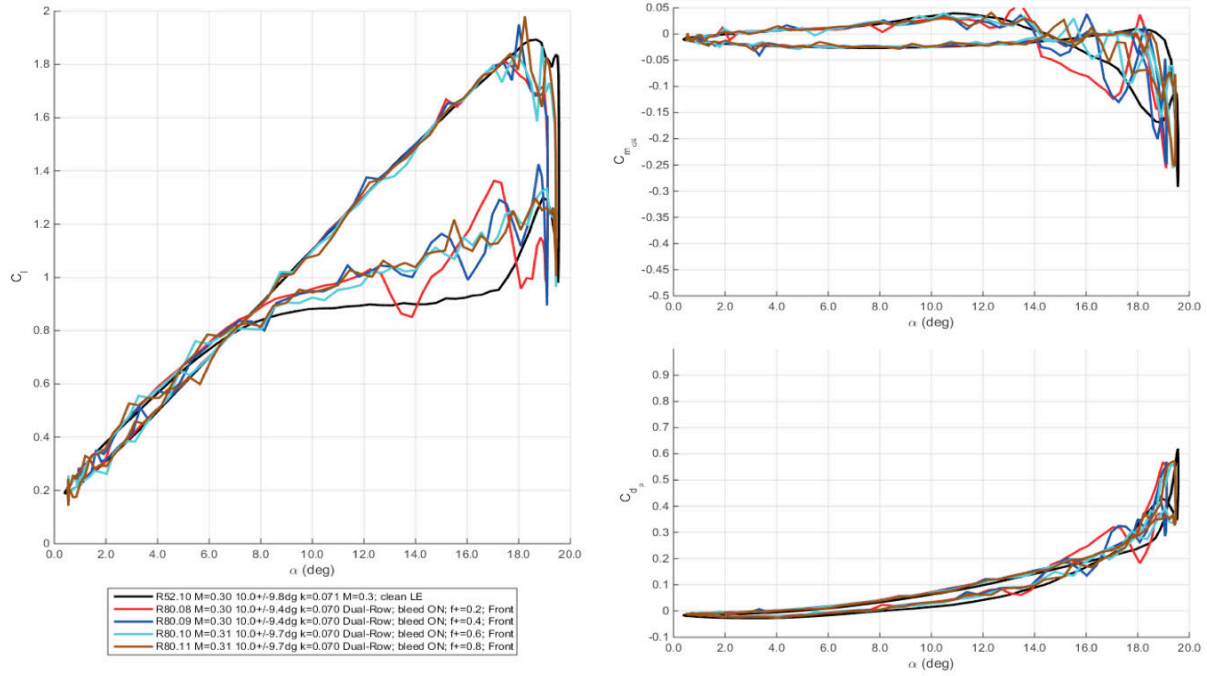


**Figure 255. Lift, drag, and moment coefficients at Mach 0.3,  $\alpha = 10^\circ \pm 9.5^\circ$ ,  $k = 0.07$  for baseline and dual-row COMPACT,  $F^+$  of 0.2 to 0.8. Loads plotted vs. angle-of-attack. Front actuator only.**

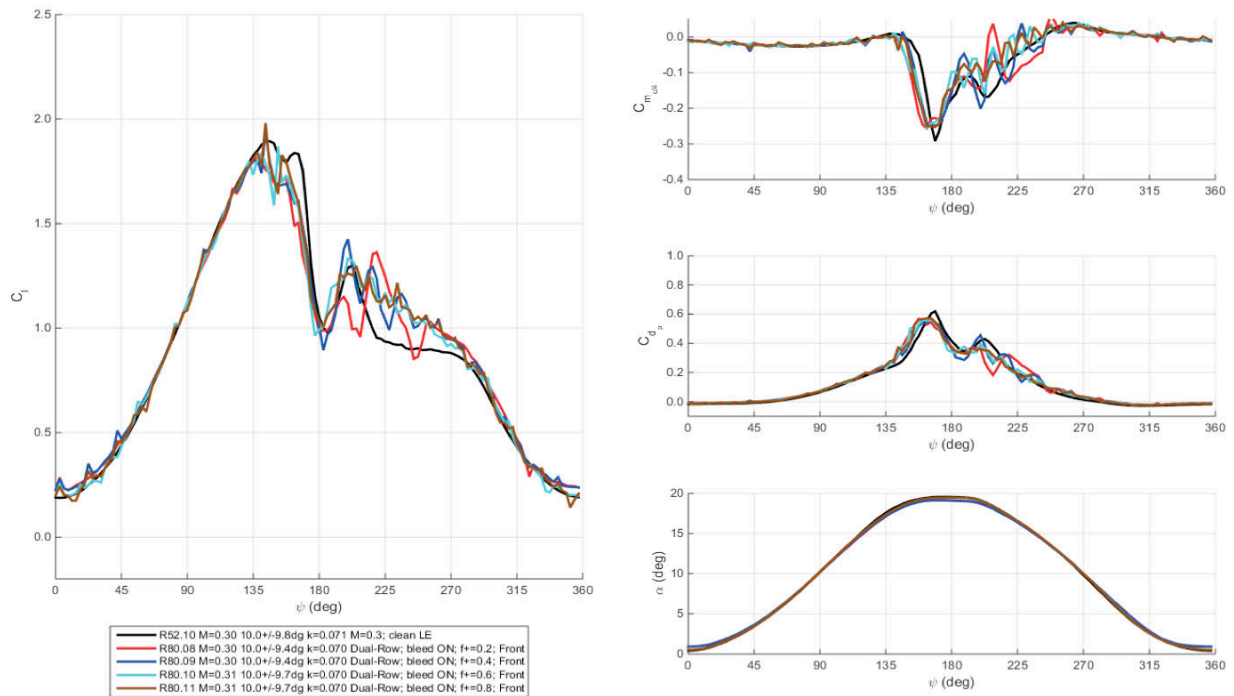


**Figure 256. Lift, drag, and moment coefficients at Mach 0.3,  $\alpha = 10^\circ \pm 9.5^\circ$ ,  $k = 0.07$  for baseline and dual-row COMPACT,  $F^+$  of 0.2 to 0.8. Loads plotted vs. phase angle. Front actuator only.**



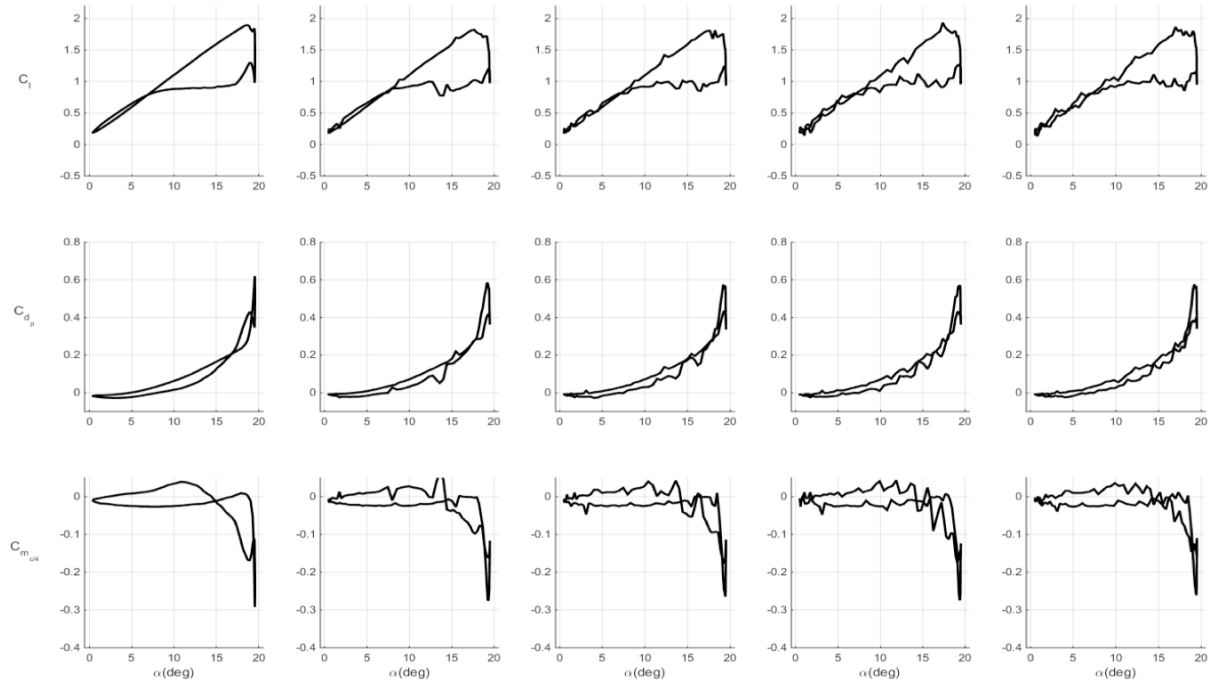


**Figure 257. Lift, drag, and moment coefficients at Mach 0.3,  $\alpha = 10^\circ \pm 9.5^\circ$ ,  $k = 0.07$  for baseline and dual-row COMPACT,  $F^+$  of 0.2 to 0.8. Front actuator only.**

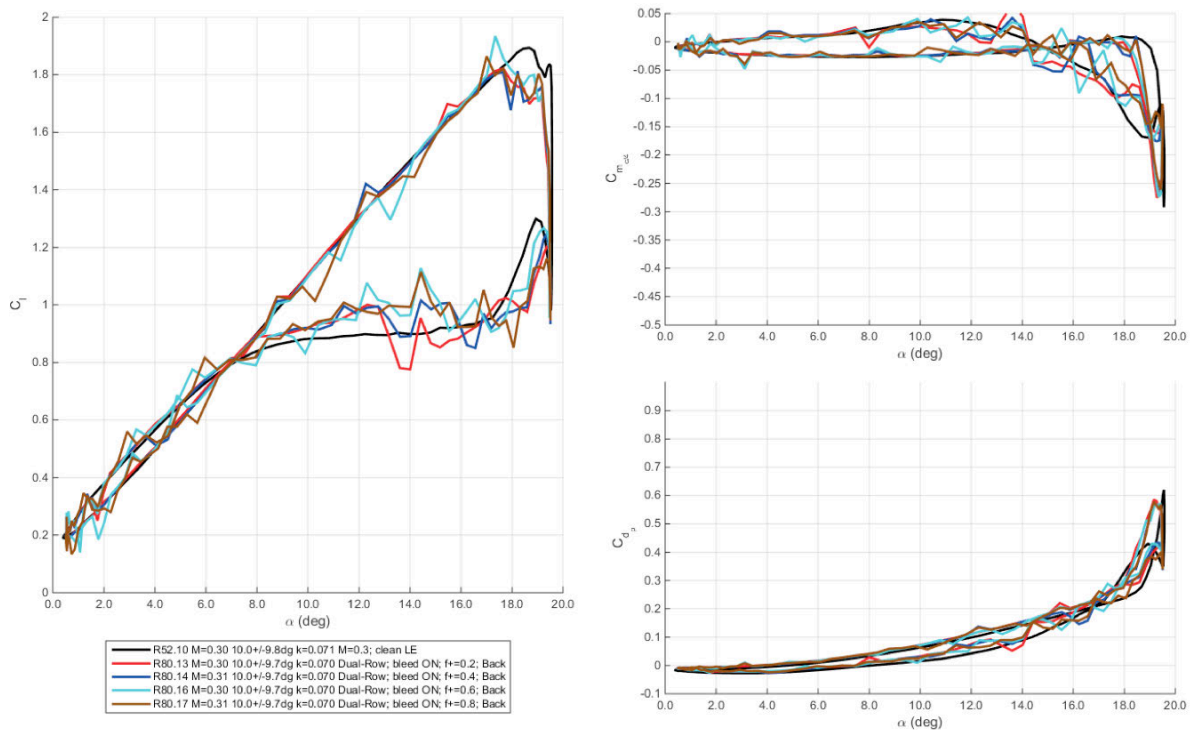


**Figure 258. Lift, drag, and moment coefficients at Mach 0.3,  $\alpha = 10^\circ \pm 9.5^\circ$ ,  $k = 0.07$  for baseline and dual-row COMPACT,  $F^+$  of 0.2 to 0.8. Loads plotted vs. angle-of-attack. Back actuator only.**

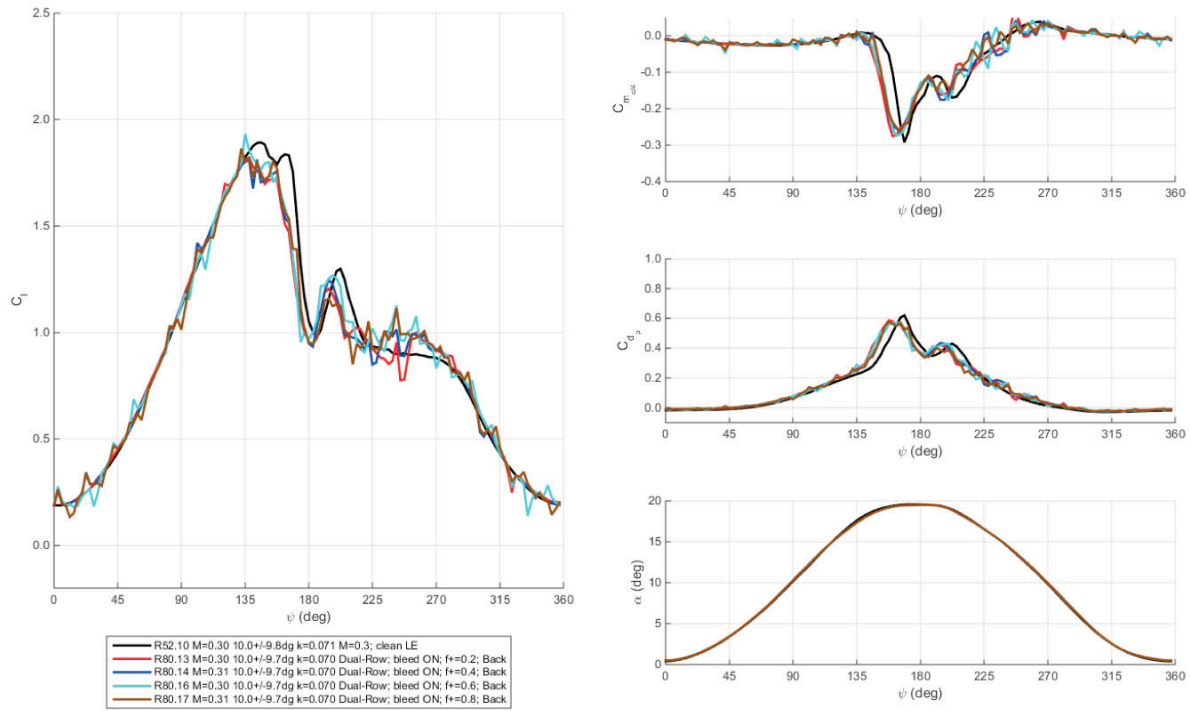


**Figure 259. Lift, drag, and moment coefficients at Mach 0.3,  $\alpha = 10^\circ \pm 9.5^\circ$ ,  $k = 0.07$  for baseline and dual-row COMPACT,  $F^+$  of 0.2 to 0.8. Loads plotted vs. phase angle. Back actuator only.**

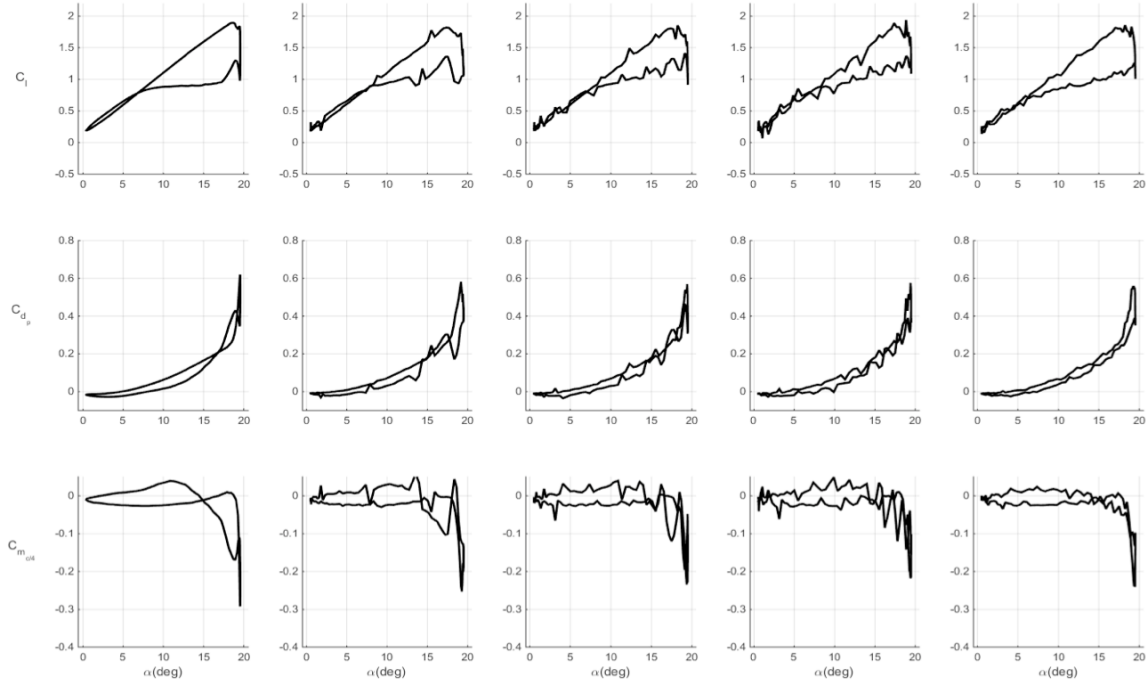


**Figure 260. Lift, drag, and moment coefficients at Mach 0.3,  $\alpha = 10^\circ \pm 9.5^\circ$ ,  $k = 0.07$  for baseline and dual-row COMPACT,  $F^+$  of 0.2 to 0.8. Simultaneous operation.**

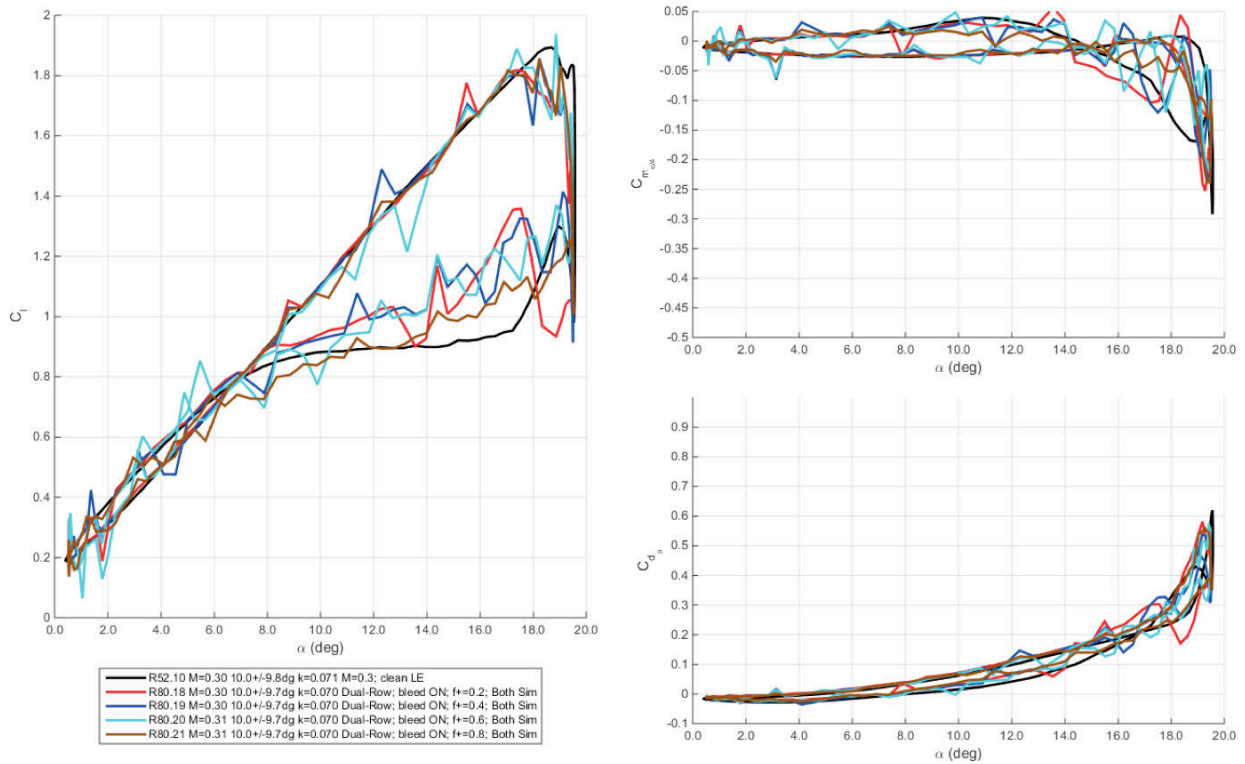


**Figure 261. Lift, drag, and moment coefficients at Mach 0.3,  $\alpha = 10^\circ \pm 9.5^\circ$ ,  $k = 0.07$  for baseline and dual-row COMPACT,  $F^+$  of 0.2 to 0.8. Loads plotted vs. angle-of-attack. Simultaneous operation.**

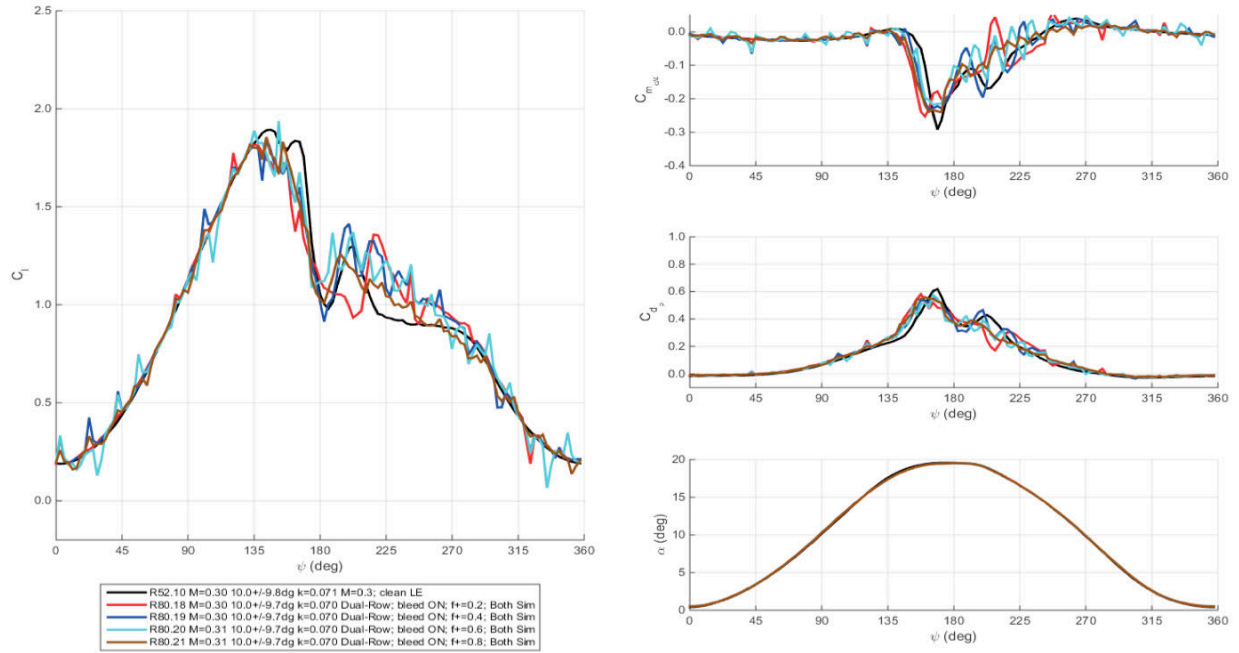


**Figure 262. Lift, drag, and moment coefficients at Mach 0.3,  $\alpha = 10^\circ \pm 9.5^\circ$ ,  $k = 0.07$  for baseline and dual-row COMPACT,  $F^+$  of 0.2 to 0.8. Loads plotted vs. phase angle. Simultaneous operation.**

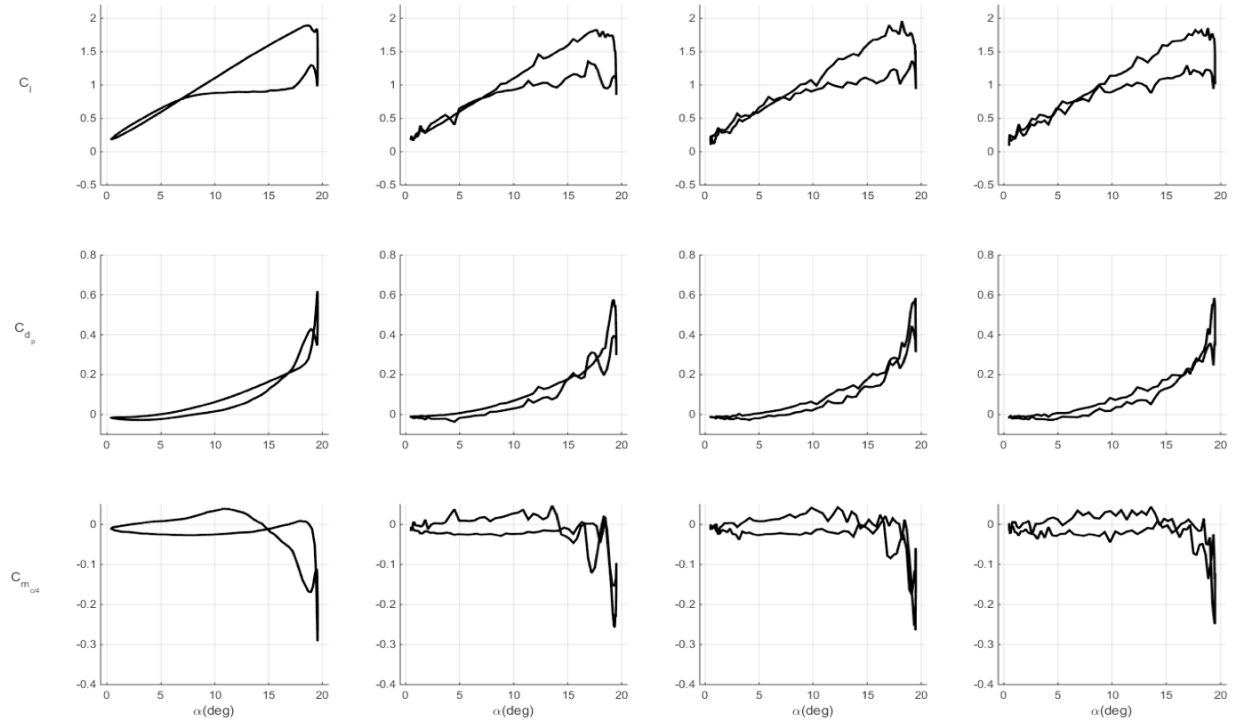


**Figure 263. Lift, drag, and moment coefficients at Mach 0.3,  $\alpha = 10^\circ \pm 9.5^\circ$ ,  $k = 0.07$  for baseline and dual-row COMPACT,  $F^+$  of 0.2 to 0.8. Alternating operation.**

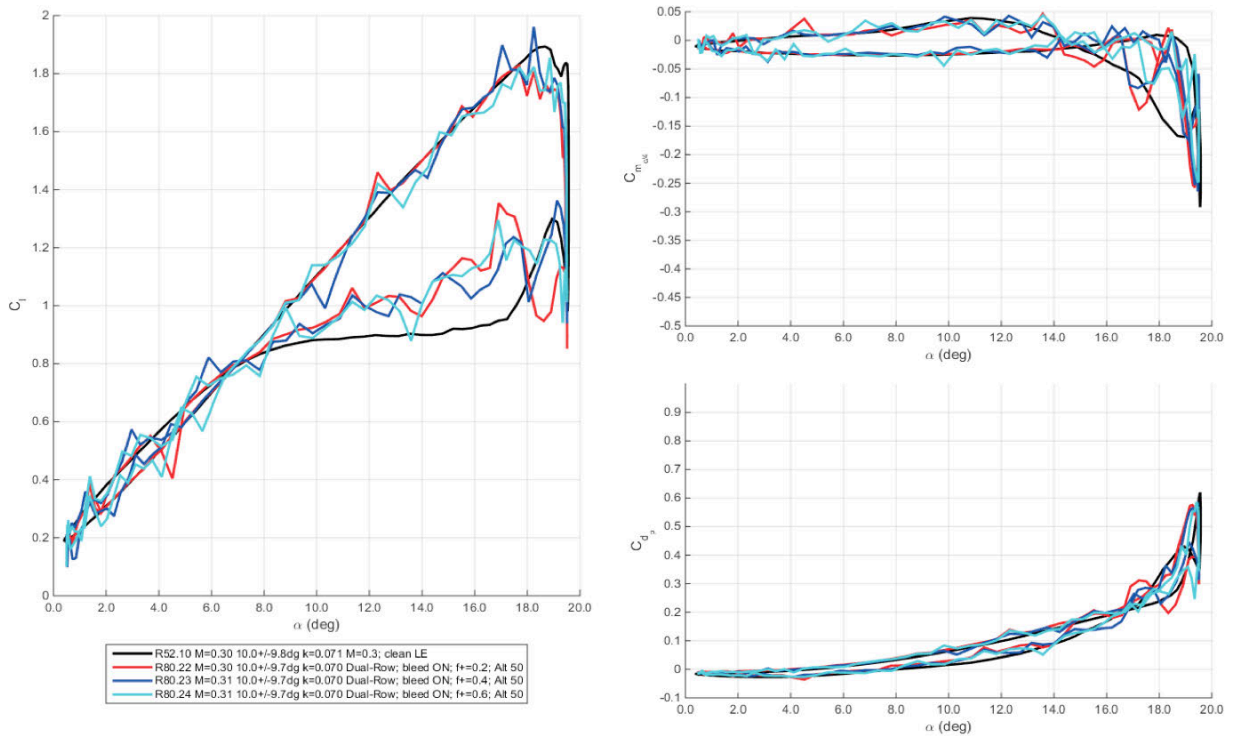


**Figure 264. Lift, drag, and moment coefficients at Mach 0.3,  $\alpha = 10^\circ \pm 9.5^\circ$ ,  $k = 0.07$  for baseline and dual-row COMPACT,  $F^+$  of 0.2 to 0.8. Loads plotted vs. angle-of-attack. Alternating operation.**

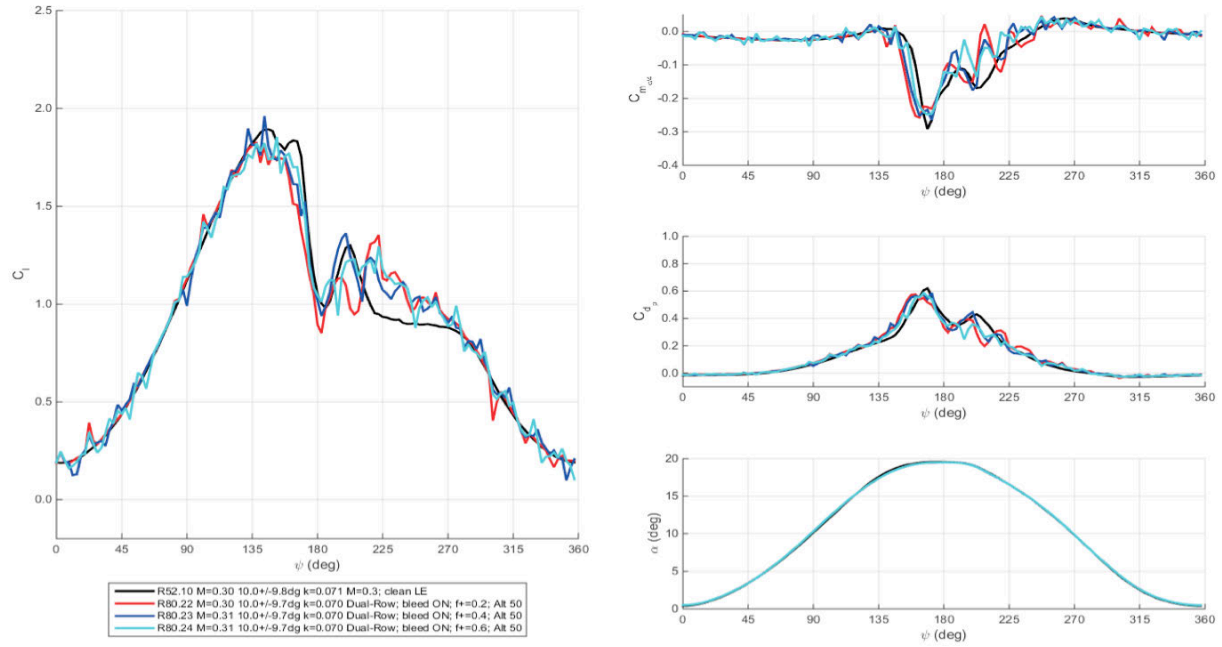


**Figure 265. Lift, drag, and moment coefficients at Mach 0.3,  $\alpha = 10^\circ \pm 9.5^\circ$ ,  $k = 0.07$  for baseline and dual-row COMPACT,  $F^+$  of 0.2 to 0.8. Loads plotted vs. phase angle. Alternating operation.**

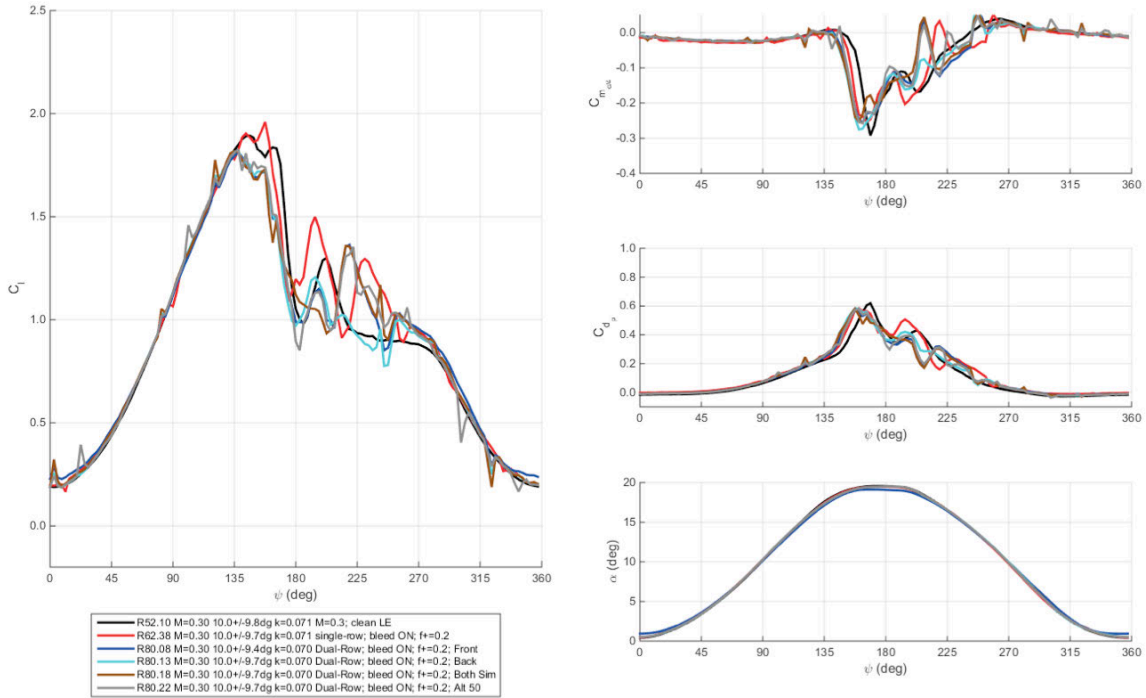


**Figure 266. Lift, drag, and moment coefficients at Mach 0.3,  $\alpha = 10^\circ \pm 9.5^\circ$ ,  $k = 0.07$ ,  $F^+ = 0.2$  for baseline and multiple COMPACT modes.**

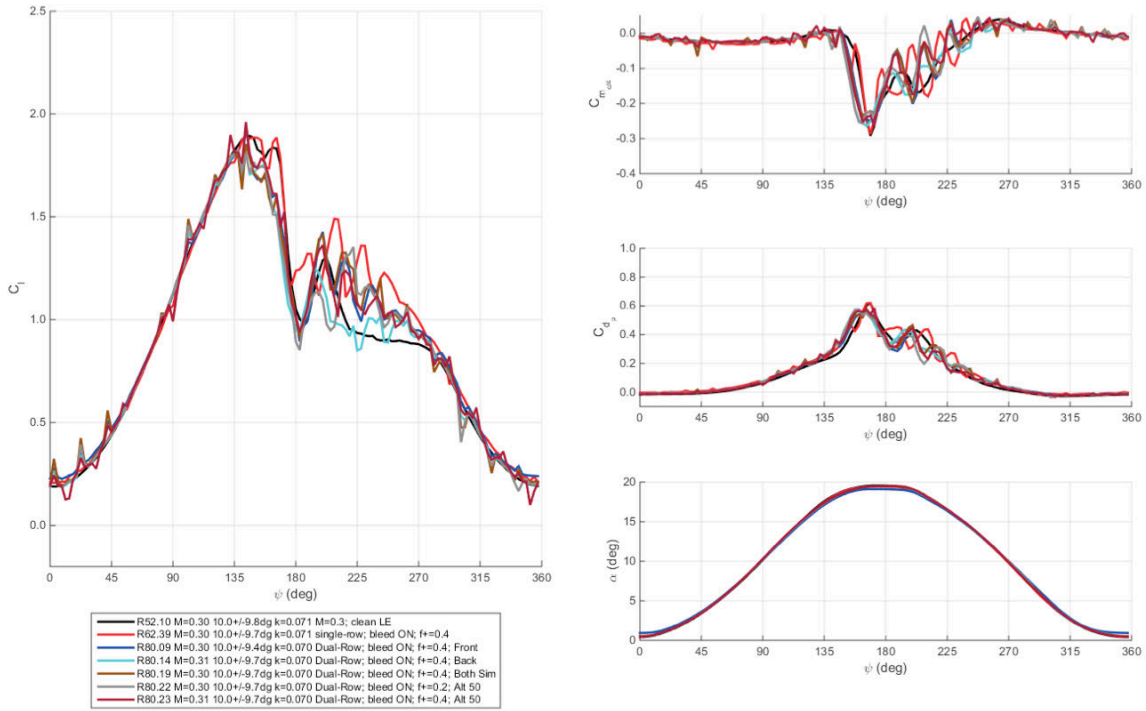


**Figure 267. Lift, drag, and moment coefficients at Mach 0.3,  $\alpha = 10^\circ \pm 9.5^\circ$ ,  $k = 0.07$ ,  $F^+ = 0.4$  for baseline and multiple COMPACT modes.**

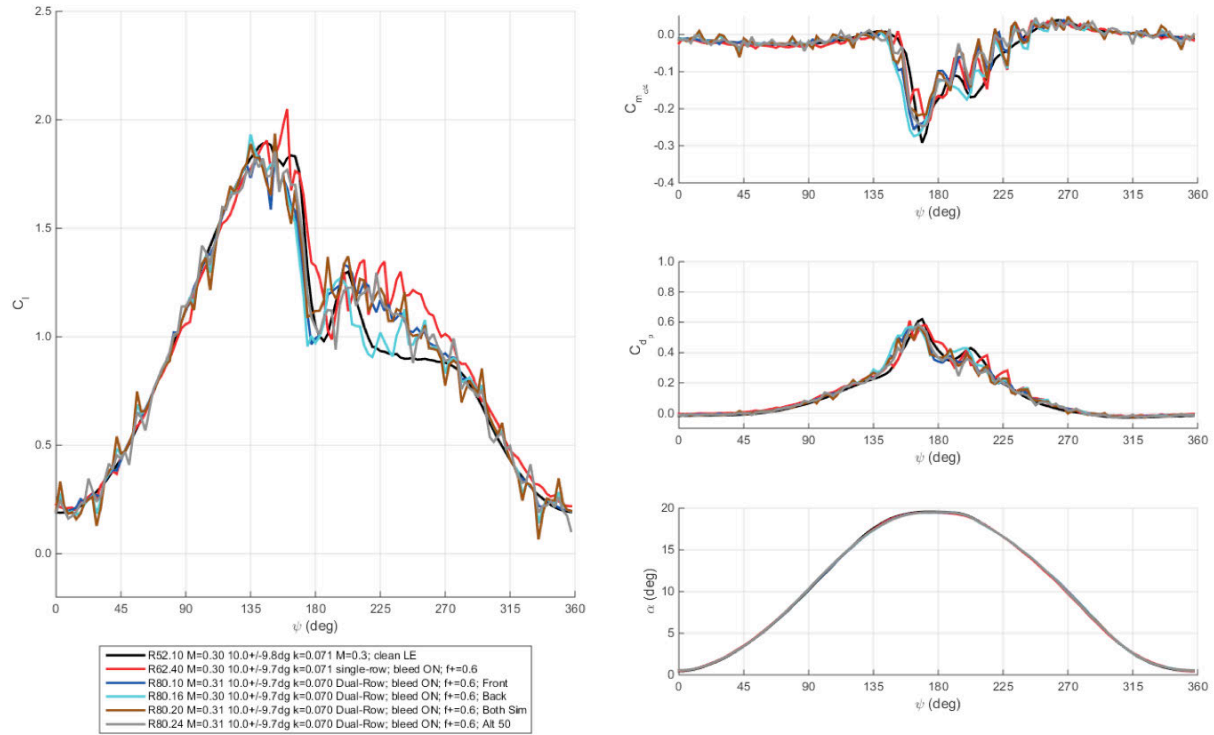


**Figure 268. Lift, drag, and moment coefficients at Mach 0.3,  $\alpha = 10^\circ \pm 9.5^\circ$ ,  $k = 0.07$ ,  $F^+ = 0.6$  for baseline and multiple COMPACT modes.**



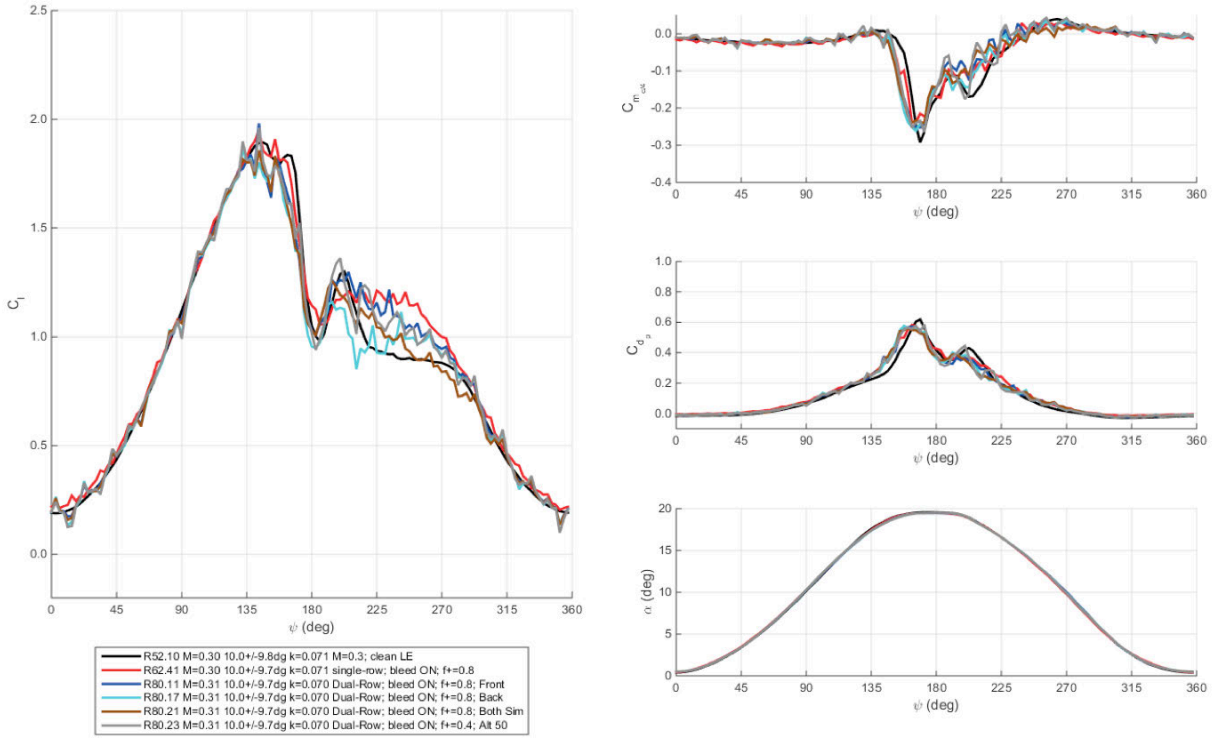


**Figure 269. Lift, drag, and moment coefficients at Mach 0.3,  $\alpha = 10^\circ \pm 9.5^\circ$ ,  $k = 0.07$ ,  $F^+ = 0.8$  for baseline and multiple COMPACT modes.**

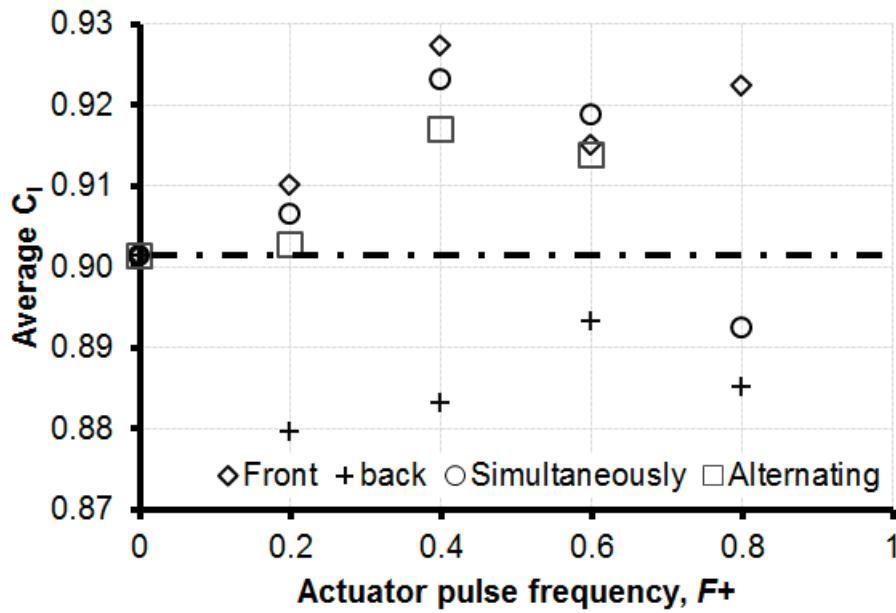


Figure 270. Average lift variation with  $F^+$  for dual-row COMPACT, Mach 0.3,  $\alpha = 10^\circ - 9.5^\circ \cos \omega t$ ,  $k = 0.07$ .

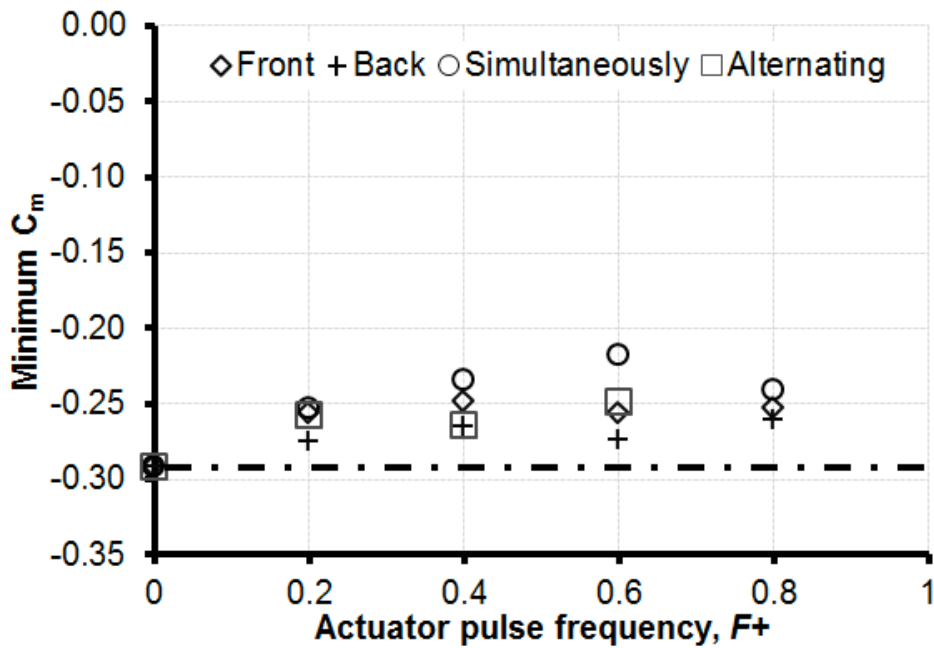


Figure 271. Minimum pitching moment variation with  $F^+$  for dual-row COMPACT, Mach 0.3,  $\alpha = 10^\circ - 9.5^\circ \cos \omega t$ ,  $k = 0.07$ .

#### *M=0.4*

The pitch trajectory  $\alpha = 10^\circ - 9.5^\circ \cos \omega t$ ,  $k = 0.05$  was tested at Mach 0.4. The best comparable baseline case differed slightly in mean angle ( $9.8^\circ$ ) and amplitude ( $10.0^\circ$ ). There were also differences in ambient conditions between the first tunnel entry clean VR-12 case and dual-row case, dominated by higher relative humidity in the latter. The high-humidity produced large amounts of condensation in the flow field. Post-run inspection of the VR-12 wing showed water deposit on the wing surface following the Mach 0.4 data collection with the dual-row actuators. As seen in the subsequent figures, a shift in load exists between the baseline and COMPACT controlled cases. It appears to be a slight variation in  $C_{l_\alpha}$  driving the observed differences; further investigation is warranted to determine the wet-tunnel condition's impact on the integrated loads.

$F^+$  was limited to 0.6 at Mach 0.4. Two additional permutations of the out-of-phase triggering were investigated, targeting COMPACT produced disturbance convection speeds equal to  $U_\infty$  and  $U_\infty/2$ . Here the back-row's pulse coincided with the assumed arrival of the forward slot produced disturbance. Results for each configuration's  $F^+$  sweep are shown individually and overlaid with respect to angle and phase in Figure 272 through Figure 274.

Despite the increase in compressibility in moving to Mach 0.4, lack of span in the dual-row configuration, and the COMPACT struggles with low-back pressure, the actuators were still capable of causing cycle performance increases from the baseline. The control input impact is clearly witnessed during the wing's downstroke when the actuators are operating in a locally higher pressure. Installation and steady bleed effects yield a peak lift decrement, which counterbalances the downstroke lift deficit reduction.

As before, the front row actuators outpace the back in isolation despite the aft travel of the minimum pressure peak on the VR-12's upper surface due to the increase in Mach number. Both simultaneous and the alternating front/back row pulse input test cases show similar effect on dynamic stall. Simultaneous operation fell off at  $F^+=0.4$ , but produced higher average lift than the alternating case for both  $F^+=0.2$  and 0.6. The most intriguing test points however were those associated with the reduced phase delay alternating pulses. Triggering the actuators with a delay equal to the transit time of a freestream particle moving from  $x/c=0.10$  (the location of the first COMPACT slot) to  $x/c=0.175$  (the location of the second COMPACT slot) caused average lift improvement over the entire cycle in excess 5% for each  $F^+$  tested. Changing the transit velocity to  $U/2$  reduced these by approximately 1% at  $F^+=0.2$  and 0.4% at  $F^+=0.4$  and 0.6. This subset of data indicates the potential for further dynamic stall alleviation with dual-row configurations and intelligent phasing between multiple slots. Pitching moment behaved similarly across the different modes of operation as in the Mach 0.3 data.

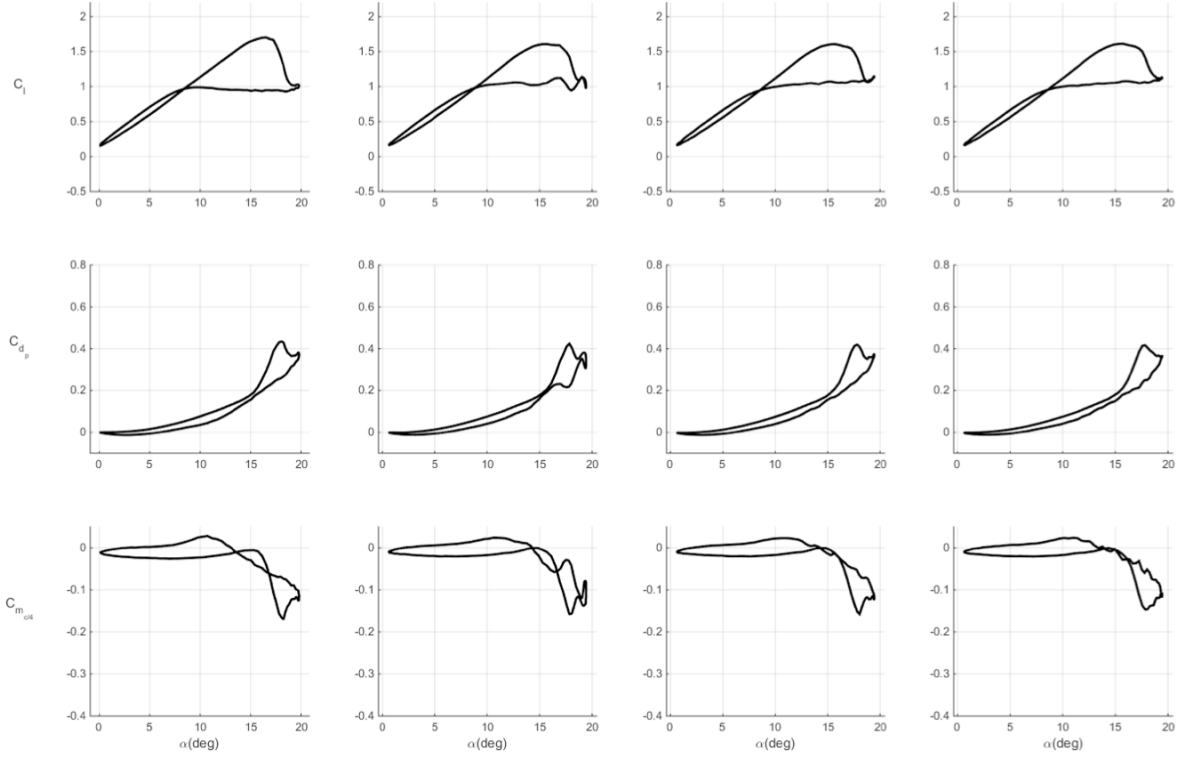


**Figure 272. Lift, drag, and moment coefficients at Mach 0.4,  $\alpha = 10^\circ \pm 9.3^\circ$ ,  $k = 0.05$  for baseline and dual-row COMPACT,  $F^+$  of 0.2 to 0.6. Front actuator only.**

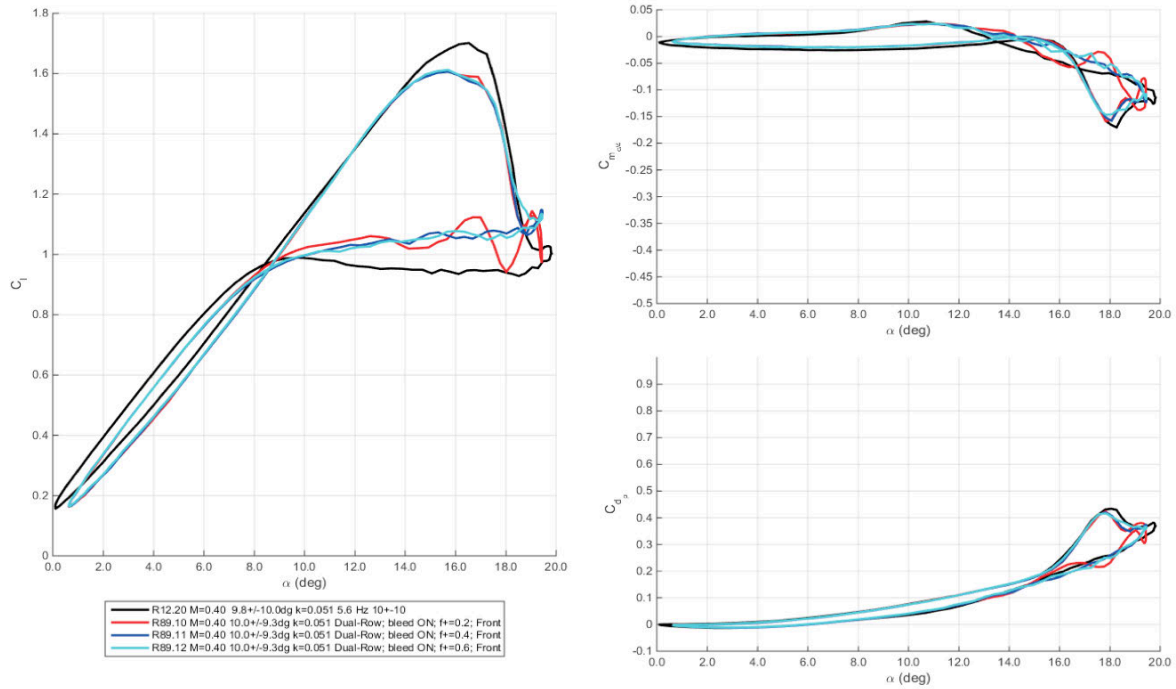


**Figure 273. Lift, drag, and moment coefficients at Mach 0.4,  $\alpha = 10^\circ \pm 9.3^\circ$ ,  $k = 0.05$  for baseline and dual-row COMPACT,  $F^+$  of 0.2 to 0.6. Loads plotted vs. angle-of-attack. Front actuator only.**

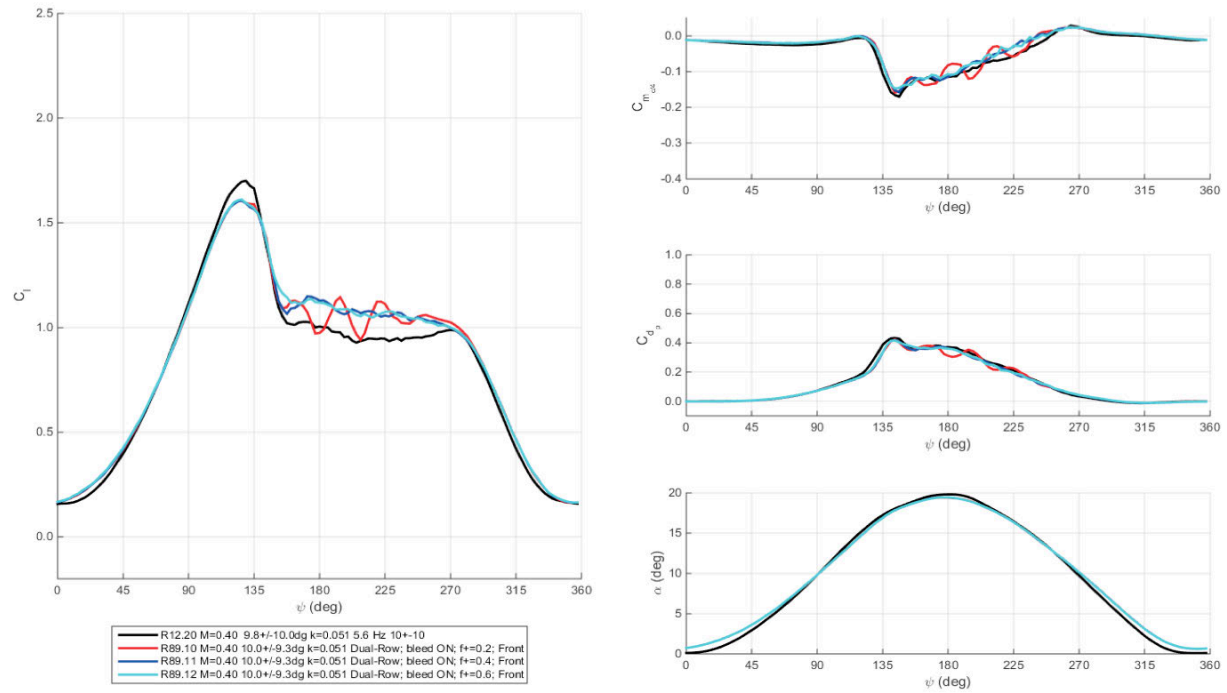


**Figure 274. Lift, drag, and moment coefficients at Mach 0.4,  $\alpha = 10^\circ \pm 9.3^\circ$ ,  $k = 0.05$  for baseline and dual-row COMPACT,  $F^+$  of 0.2 to 0.6. Loads plotted vs. phase angle. Front actuator only.**

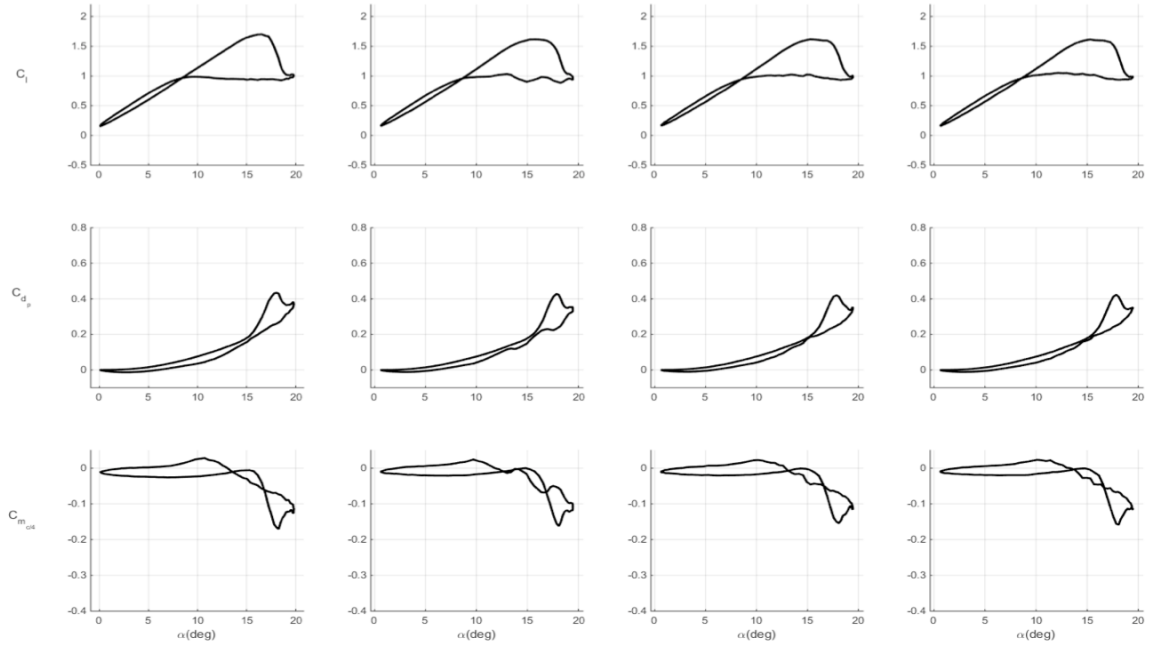


**Figure 275. Lift, drag, and moment coefficients at Mach 0.4,  $\alpha = 10^\circ \pm 9.3^\circ$ ,  $k = 0.05$  for baseline and dual-row COMPACT,  $F^+$  of 0.2 to 0.6. Back actuator only.**

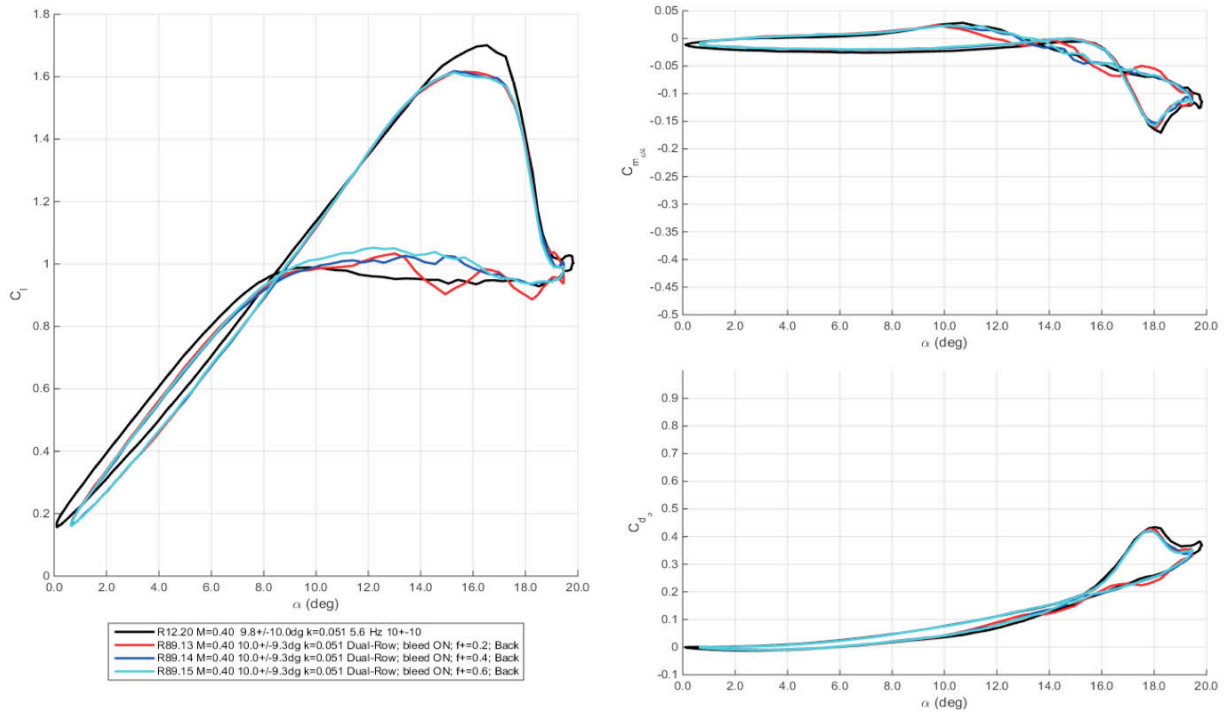


**Figure 276. Lift, drag, and moment coefficients at Mach 0.4,  $\alpha = 10^\circ \pm 9.3^\circ$ ,  $k = 0.05$  for baseline and dual-row COMPACT,  $F^+$  of 0.2 to 0.6. Loads plotted vs. angle-of-attack. Back actuator only.**

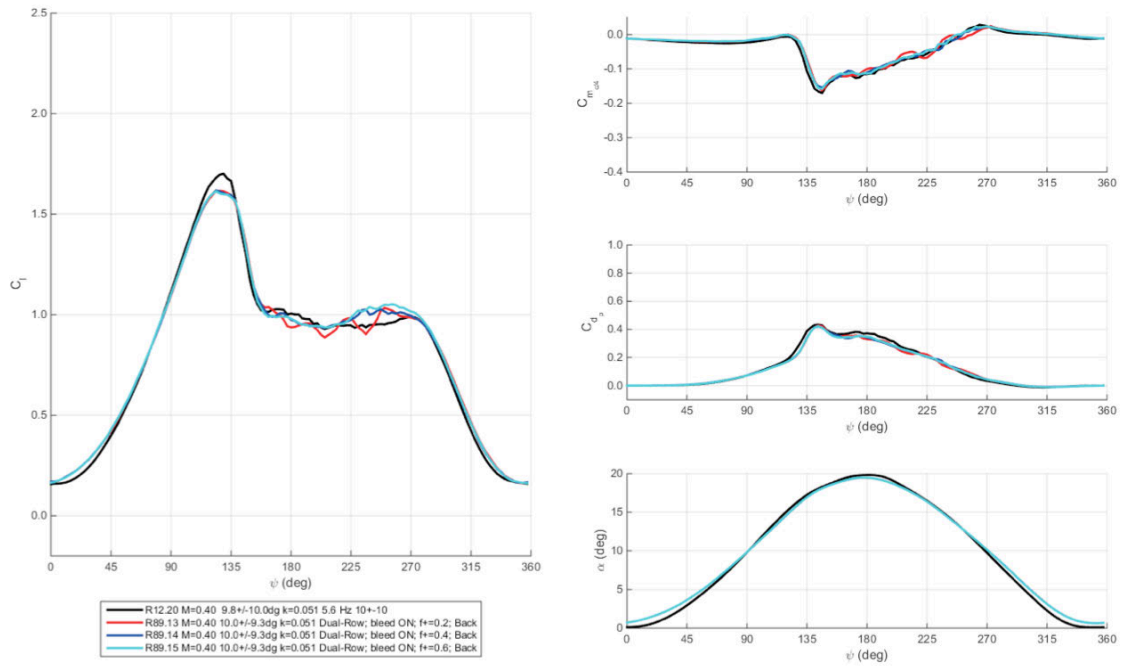


**Figure 277. Lift, drag, and moment coefficients at Mach 0.4,  $\alpha = 10^\circ \pm 9.3^\circ$ ,  $k = 0.05$  for baseline and dual-row COMPACT,  $F^+$  of 0.2 to 0.6. Loads plotted vs. phase angle. Back actuator only.**

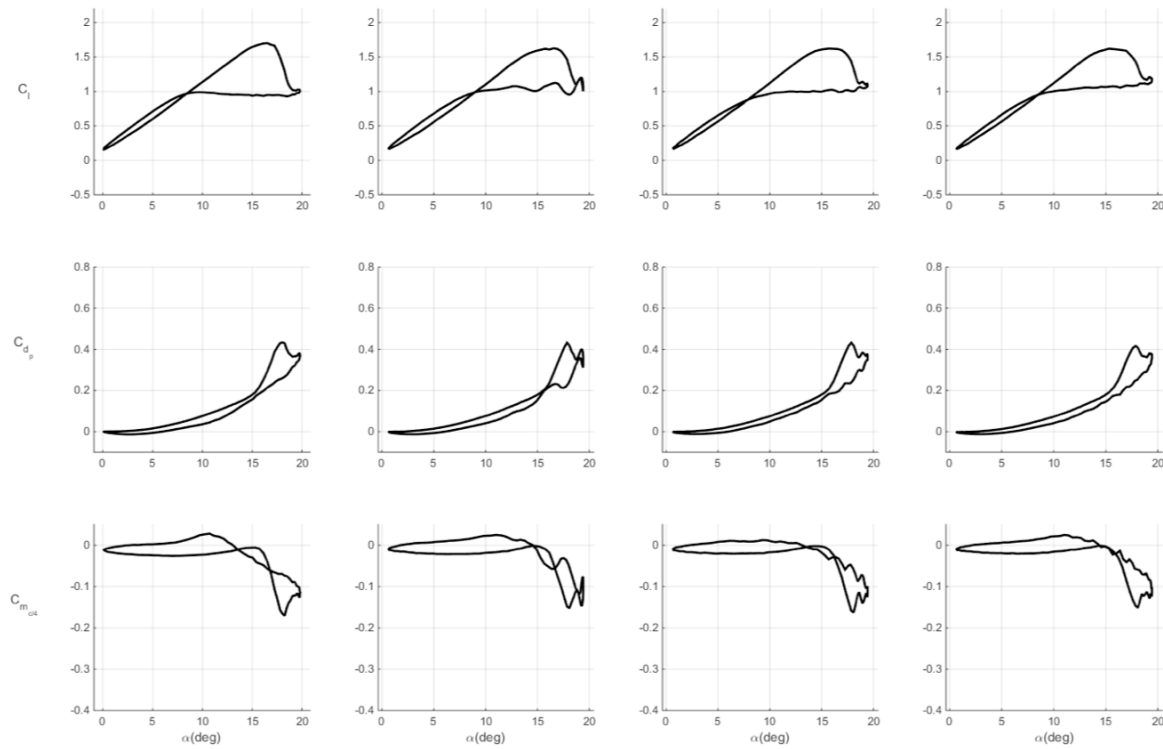


**Figure 278. Lift, drag, and moment coefficients at Mach 0.4,  $\alpha = 10^\circ \pm 9.3^\circ$ ,  $k = 0.05$  for baseline and dual-row COMPACT,  $F^+$  of 0.2 to 0.6. Simultaneous operation.**



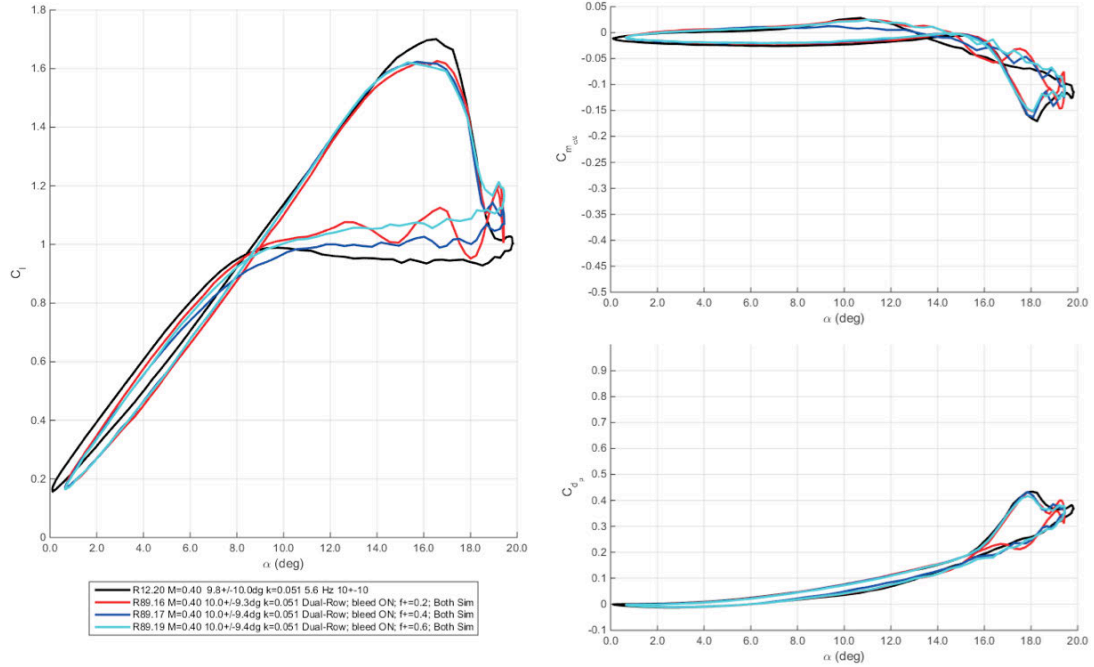


**Figure 279.** Lift, drag, and moment coefficients at Mach 0.4,  $\alpha = 10^\circ \pm 9.3^\circ$ ,  $k = 0.05$  for baseline and dual-row COMPACT,  $F^+$  of 0.2 to 0.6. Loads plotted vs. angle-of-attack. Simultaneous operation.

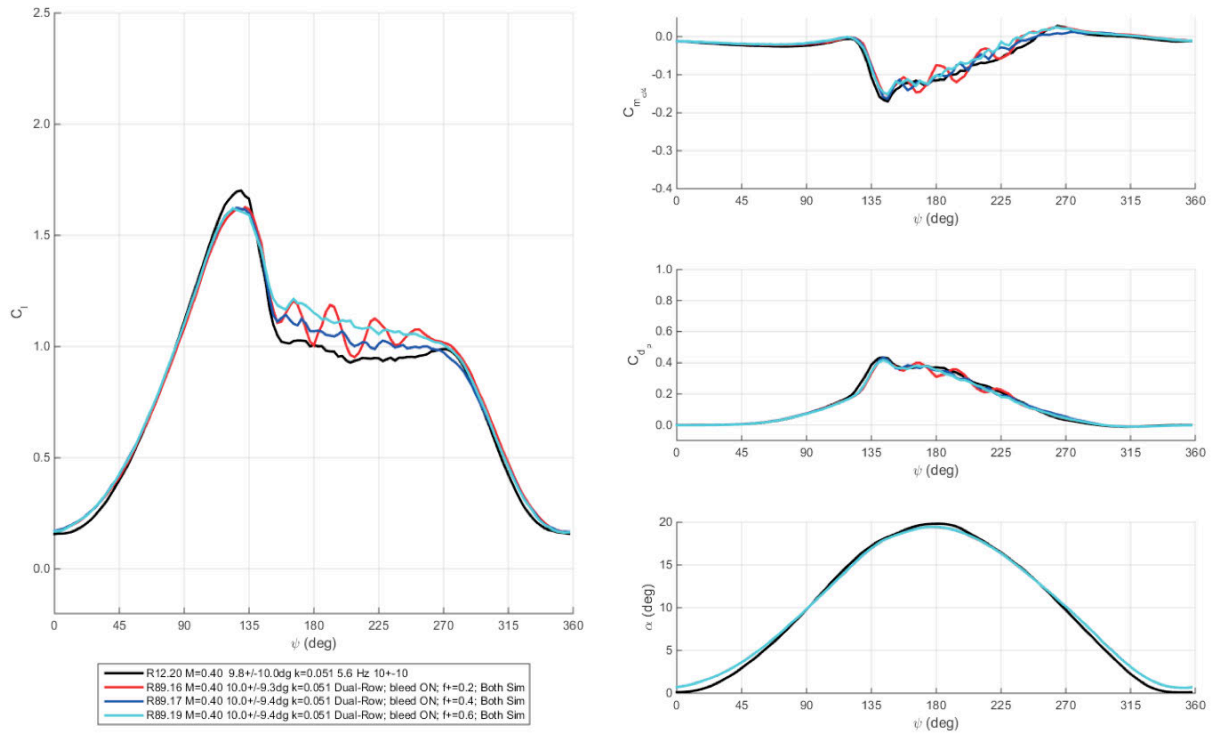


**Figure 280.** Lift, drag, and moment coefficients at Mach 0.4,  $\alpha = 10^\circ \pm 9.3^\circ$ ,  $k = 0.05$  for baseline and dual-row COMPACT,  $F^+$  of 0.2 to 0.6. Loads plotted vs. phase angle. Simultaneous operation.

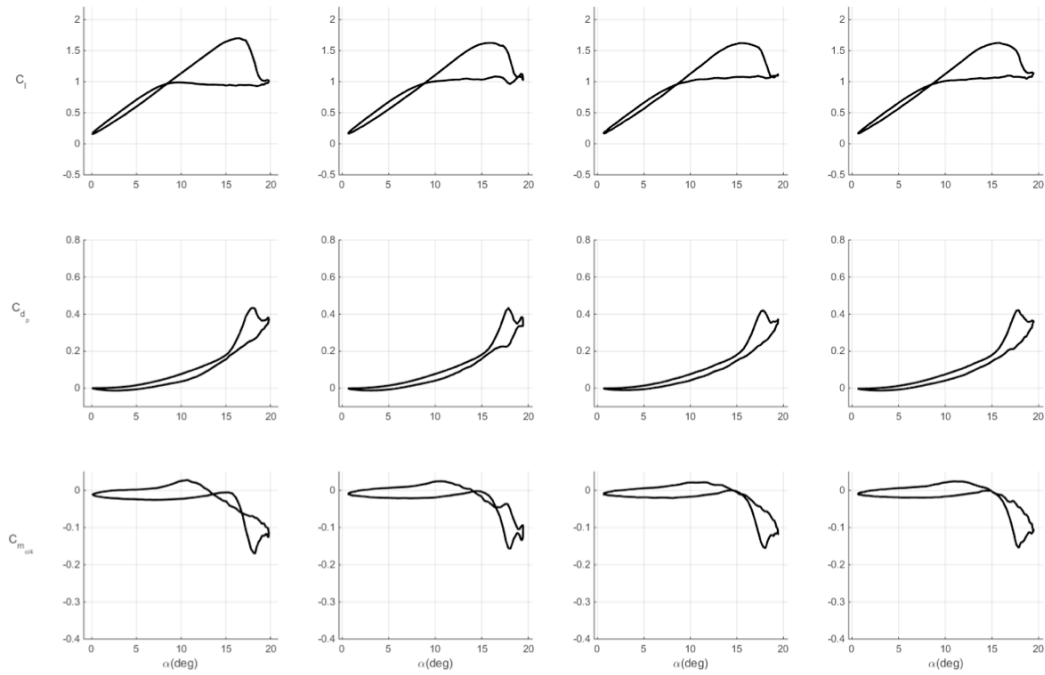


**Figure 281. Lift, drag, and moment coefficients at Mach 0.4,  $\alpha = 10^\circ \pm 9.3^\circ$ ,  $k = 0.05$  for baseline and dual-row COMPACT,  $F^+$  of 0.2 to 0.6. Alternating operation.**

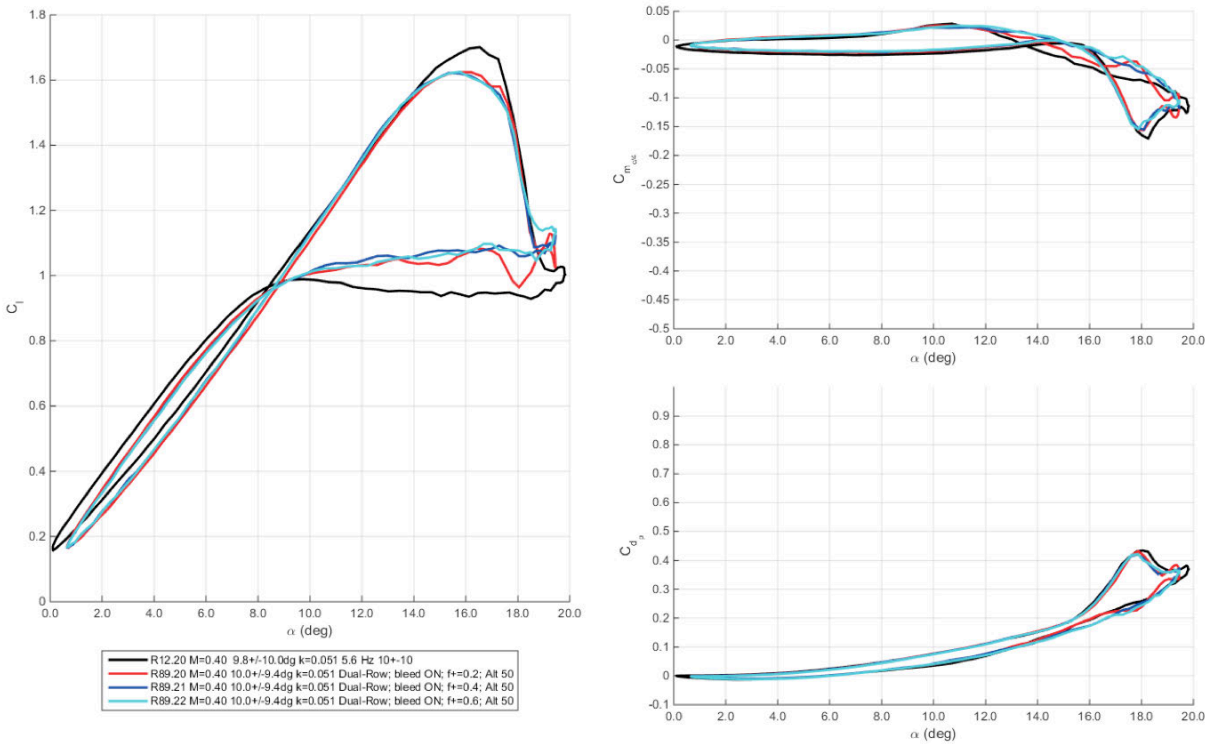


**Figure 282. Lift, drag, and moment coefficients at Mach 0.4,  $\alpha = 10^\circ \pm 9.3^\circ$ ,  $k = 0.05$  for baseline and dual-row COMPACT,  $F^+$  of 0.2 to 0.6. Loads plotted vs. angle-of-attack. Alternating operation.**

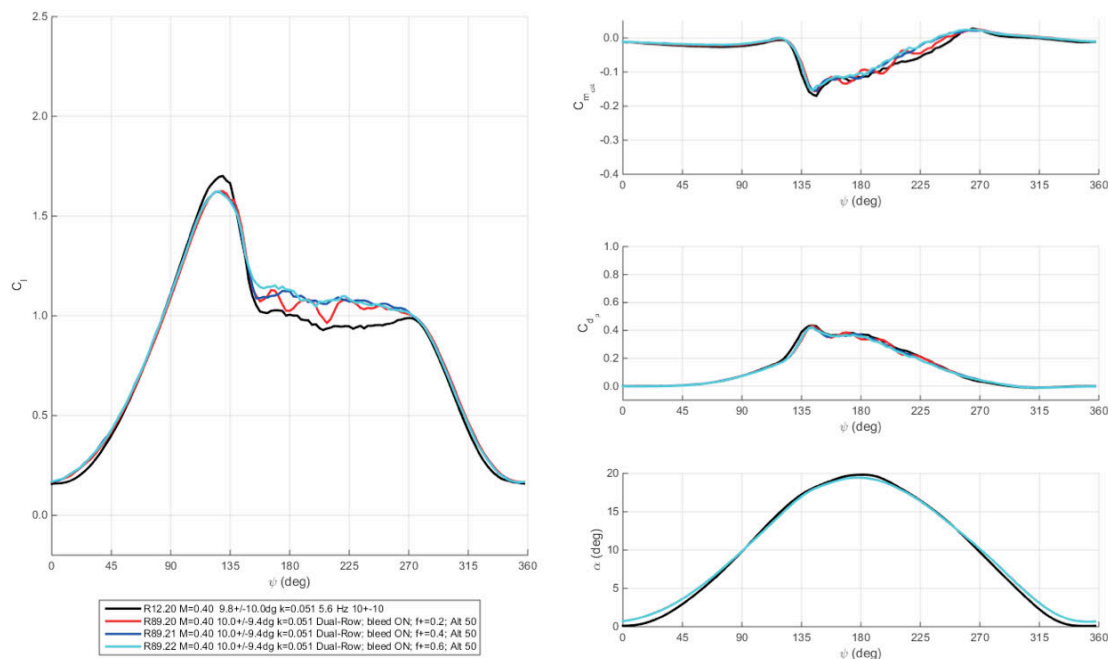


**Figure 283. Lift, drag, and moment coefficients at Mach 0.4,  $\alpha = 10^\circ \pm 9.3^\circ$ ,  $k = 0.05$  for baseline and dual-row COMPACT,  $F^+$  of 0.2 to 0.6. Loads plotted vs. phase angle. Alternating operation.**

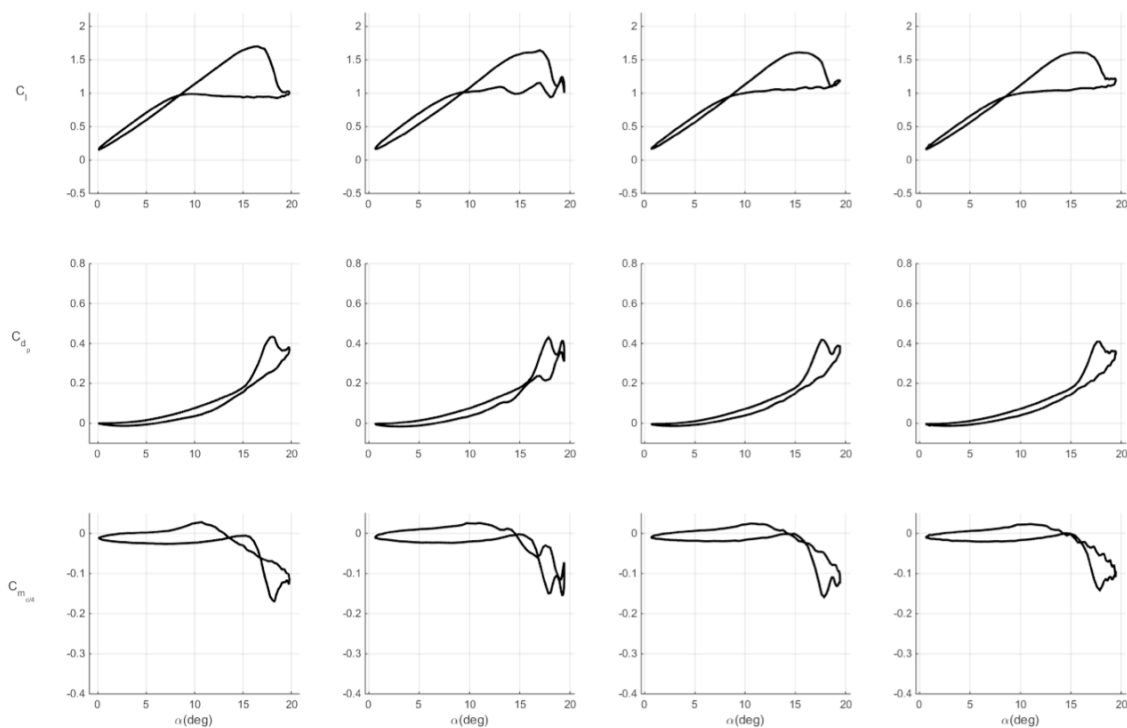


**Figure 284. Lift, drag, and moment coefficients at Mach 0.4,  $\alpha = 10^\circ \pm 9.3^\circ$ ,  $k = 0.05$  for baseline and dual-row COMPACT,  $F^+$  of 0.2 to 0.6. Phase delay 0.075c/U.**

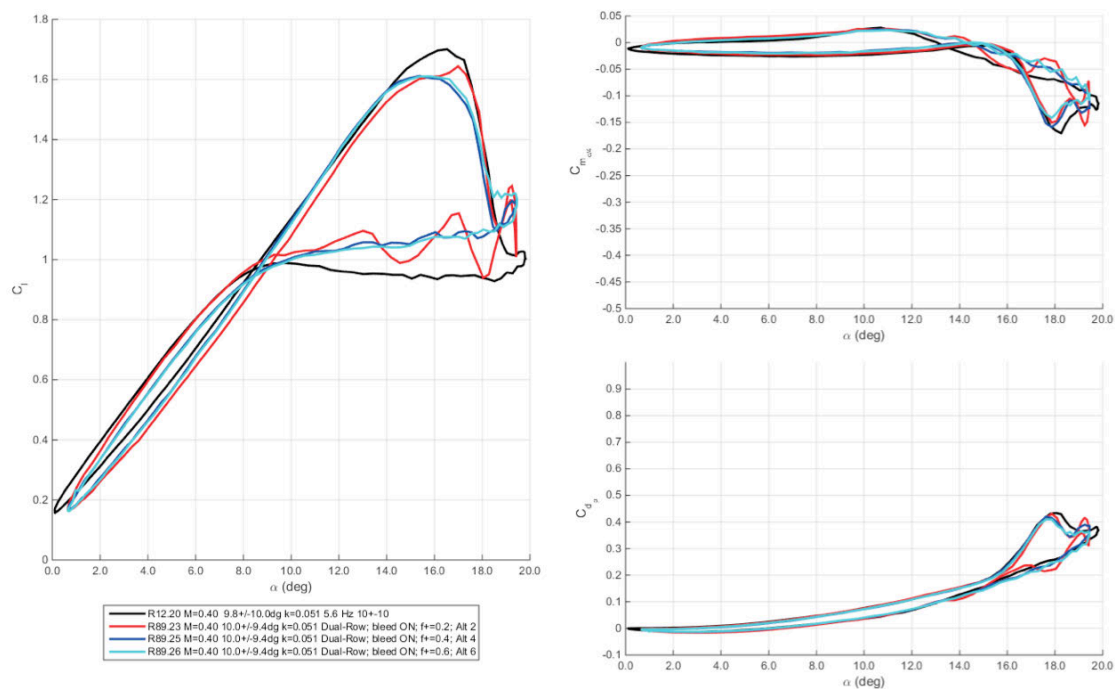


**Figure 285. Lift, drag, and moment coefficients at Mach 0.4,  $\alpha = 10^\circ \pm 9.3^\circ$ ,  $k = 0.05$  for baseline and dual-row COMPACT,  $F^+$  of 0.2 to 0.6. Loads plotted vs. angle-of-attack. Phase delay  $0.075c/U$ .**

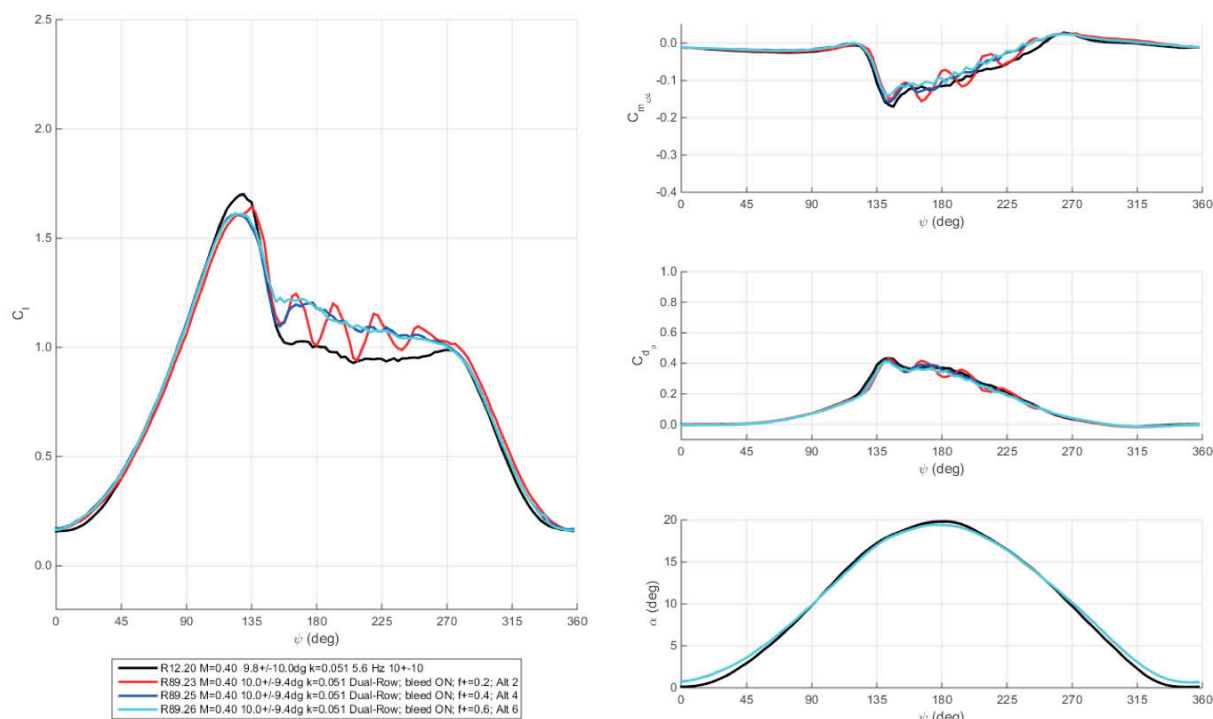


**Figure 286. Lift, drag, and moment coefficients at Mach 0.4,  $\alpha = 10^\circ \pm 9.3^\circ$ ,  $k = 0.05$  for baseline and dual-row COMPACT,  $F^+$  of 0.2 to 0.6. Loads plotted vs. phase angle. Phase delay  $0.075c/U$ .**

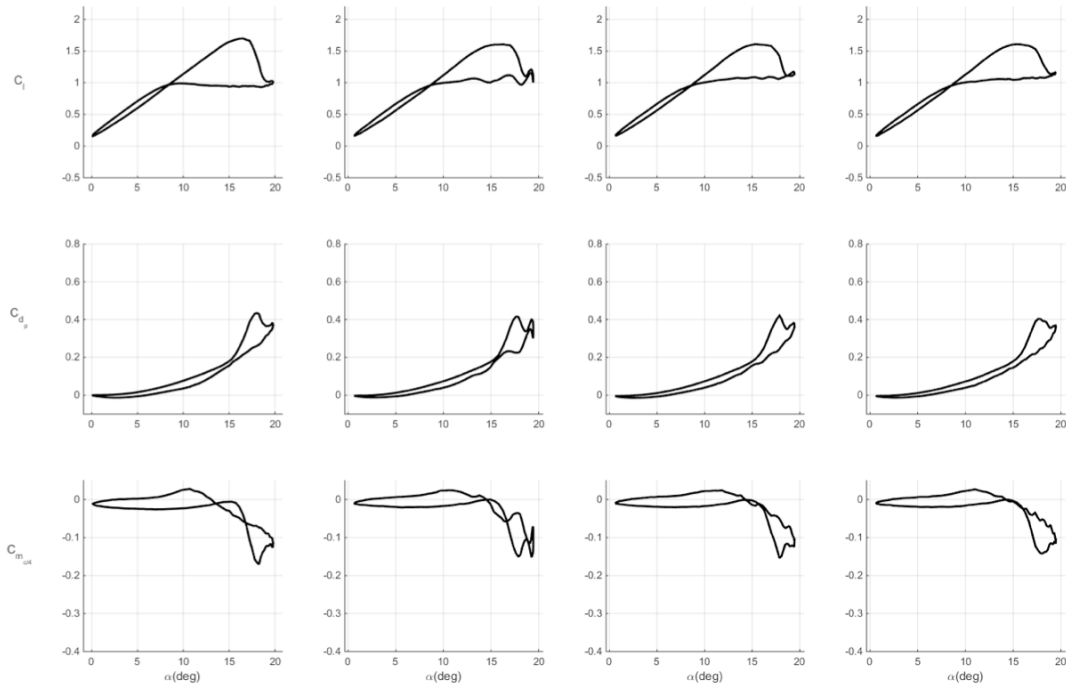


**Figure 287. Lift, drag, and moment coefficients at Mach 0.4,  $\alpha = 10^\circ \pm 9.3^\circ$ ,  $k = 0.05$  for baseline and dual-row COMPACT,  $F^+$  of 0.2 to 0.6. Phase delay  $0.075c/(U/2)$ .**

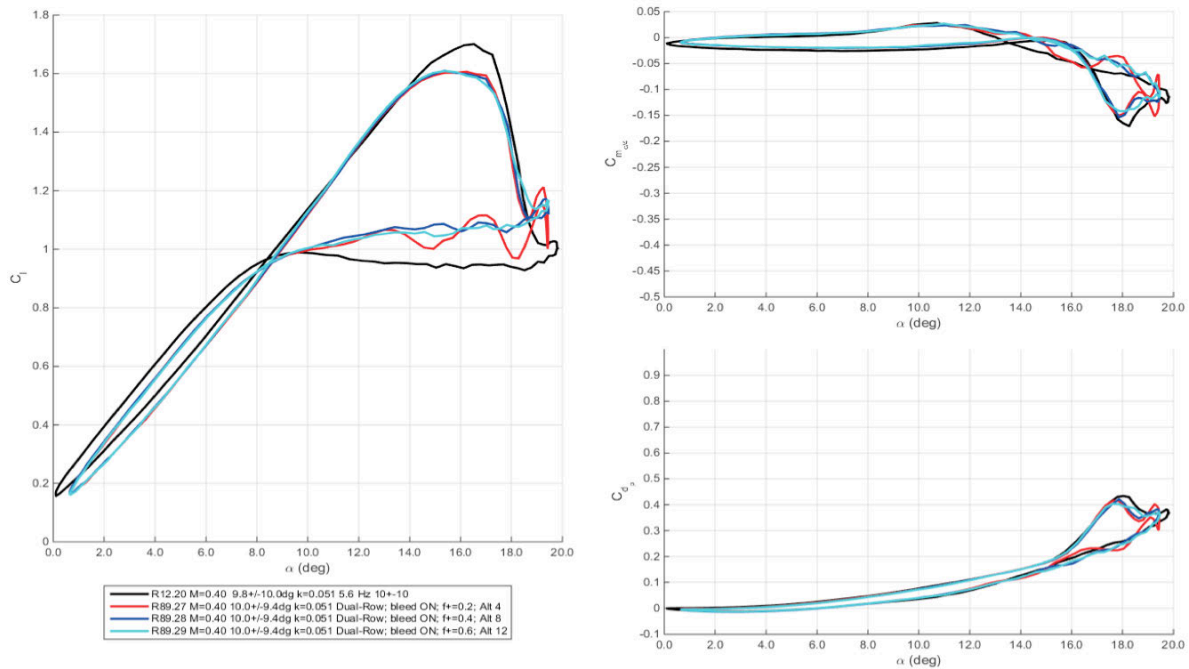


**Figure 288. Lift, drag, and moment coefficients at Mach 0.4,  $\alpha = 10^\circ \pm 9.3^\circ$ ,  $k = 0.05$  for baseline and dual-row COMPACT,  $F^+$  of 0.2 to 0.6. Loads plotted vs. angle-of-attack. Phase delay  $0.075c/(U/2)$ .**

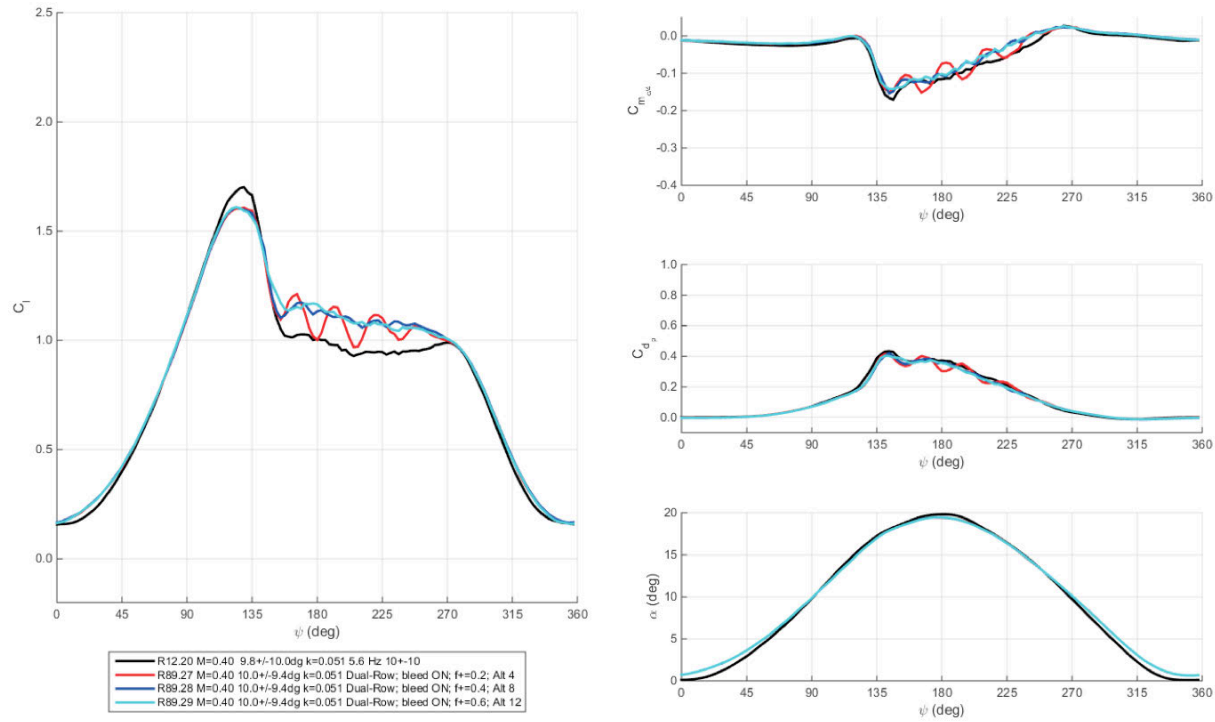


**Figure 289. Lift, drag, and moment coefficients at Mach 0.4,  $\alpha = 10 \pm 9.3$ ,  $k = 0.05$  for baseline and dual-row COMPACT,  $F^+$  of 0.2 to 0.6. Loads plotted vs. phase angle. Phase delay  $0.075c/(U/2)$ .**

Figure 290 through Figure 292 compare each of the different configurations and triggering modes at fixed  $F^+$ . The single-row performance at  $F^+=0.2$  is better than the other actuator configurations; however, relative to the Mach 0.2 and 0.3 results, the dual-row cases are markedly closer. The ‘Alt 2’ case indicates the higher lift performance and is significantly better than the results obtained for simply alternating the front and back actuators. Similar observations are noted for  $F^+=0.4$  and  $F^+=0.6$ . For  $F^+=0.6$ , the change from baseline to controlled lift from  $18^\circ$  on the downstroke ( $\psi = 200^\circ$ ) through pitch-up is nearly indistinguishable for the different control schemes, excluding the back-row case. The varied performance attributes resulted from the actuators ability to alter the flow just past stall,  $\psi = 140^\circ$  to  $190^\circ$ . This is also true for the  $F^+=0.4$  cases, although the simultaneous and alternating triggering cases are noticeably reduced compared to the small phase delay test points. The average lift and pitching moment behavior for the  $F^+$  sweeps are shown in Figure 293 and Figure 294, respectively. Best lift enhancement was achieved for  $F^+=0.6$ . Simultaneous triggering of the actuators slightly performed better than the ‘Alt U’ cases. The largest adverse moment reduction stemmed from  $F^+=0.6$  for both the ‘Alt U’ and ‘Alt U/2’ control inputs (-17%).

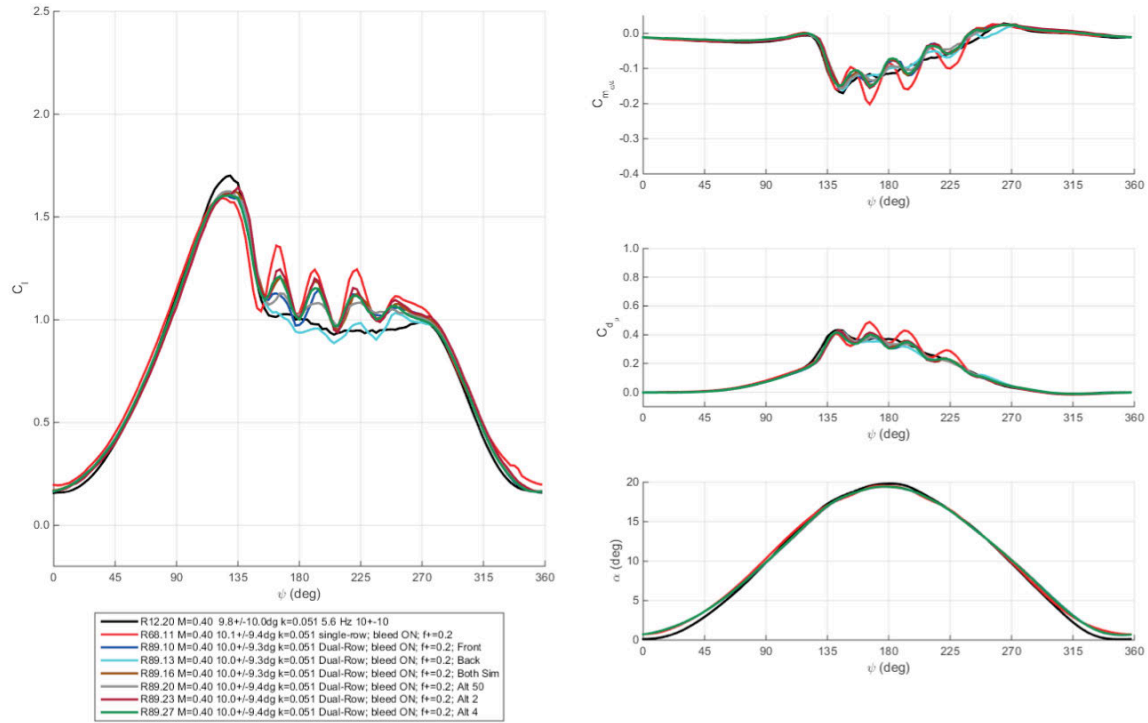


**Figure 290. Lift, drag, and moment coefficients at Mach 0.4,  $\alpha = 10^\circ \pm 9.3^\circ$ ,  $k = 0.07$ ,  $F^+ = 0.2$  for baseline and multiple COMPACT modes.**

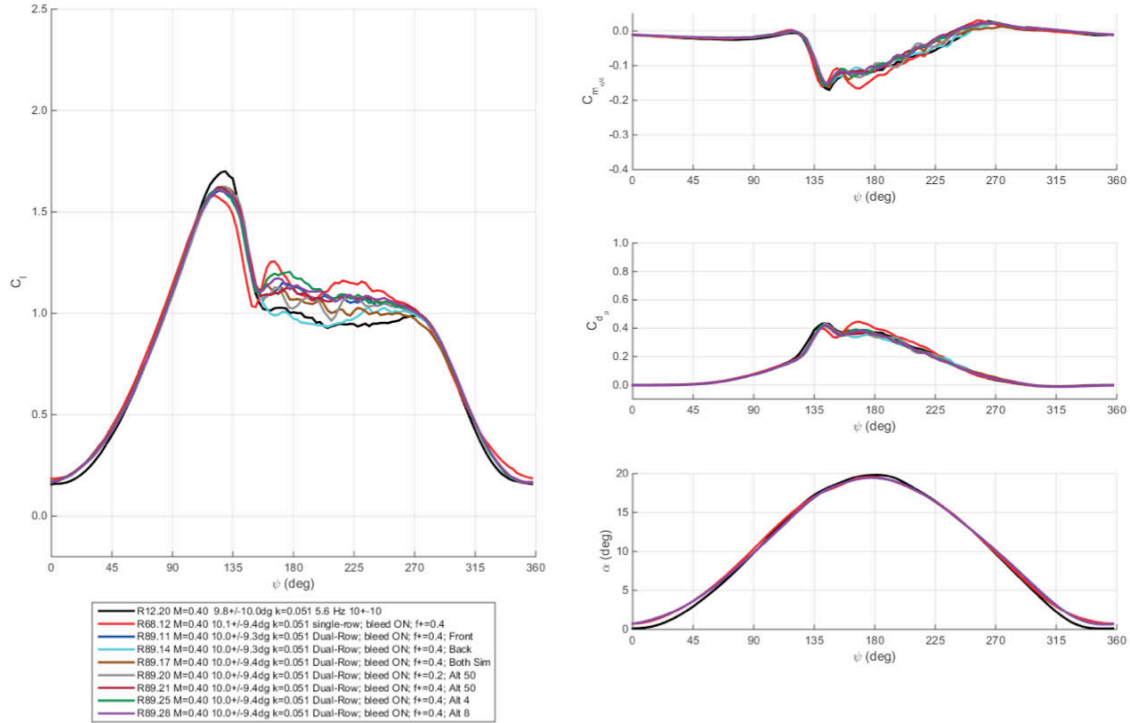


**Figure 291. Lift, drag, and moment coefficients at Mach 0.4,  $\alpha = 10^\circ \pm 9.3^\circ$ ,  $k = 0.05$ ,  $F^+ = 0.4$  for baseline and multiple COMPACT modes.**



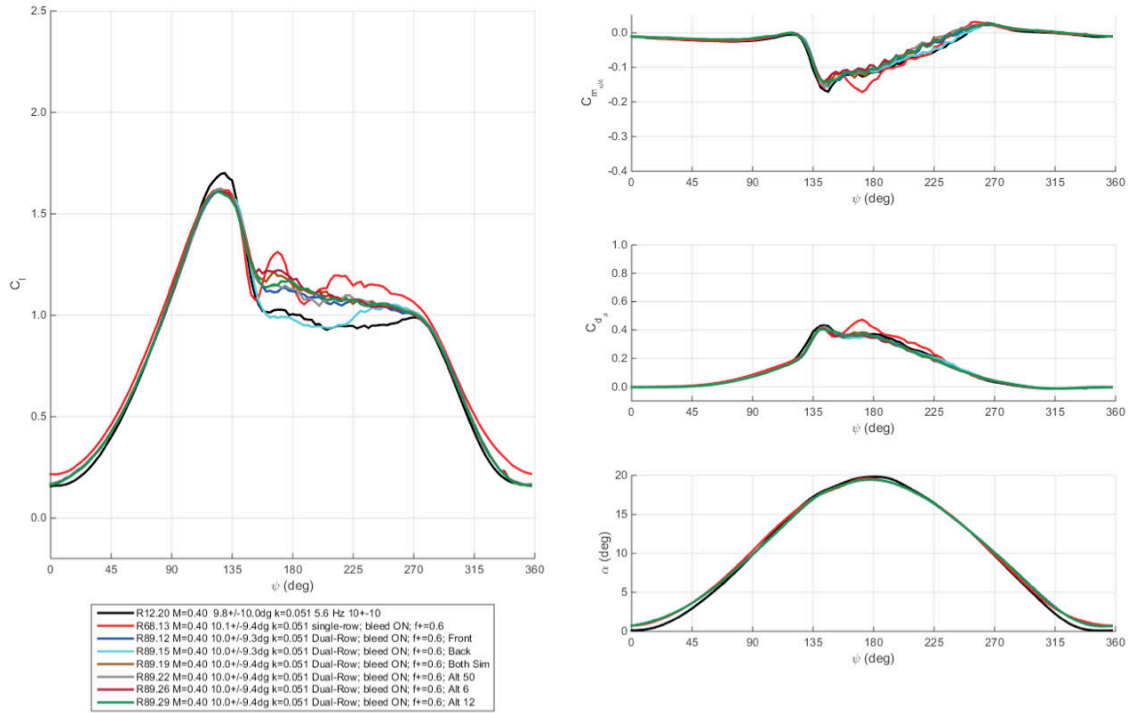


Figure 292. Lift, drag, and moment coefficients at Mach 0.4,  $\alpha = 10^\circ \pm 9.3^\circ$ ,  $k = 0.05$ ,  $F^+ = 0.6$  for baseline and multiple COMPACT modes.

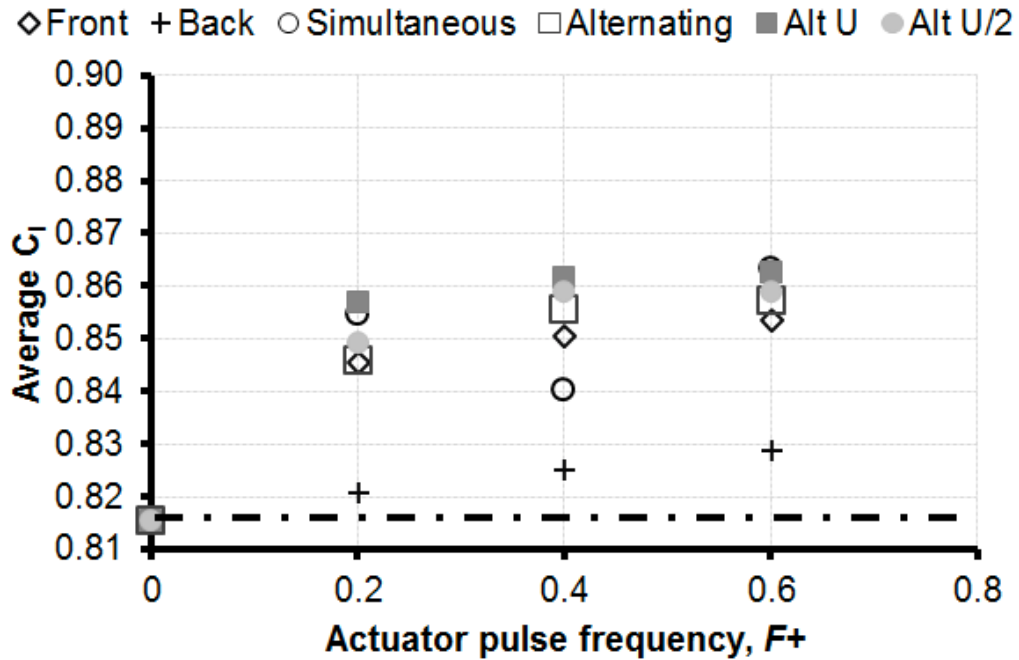
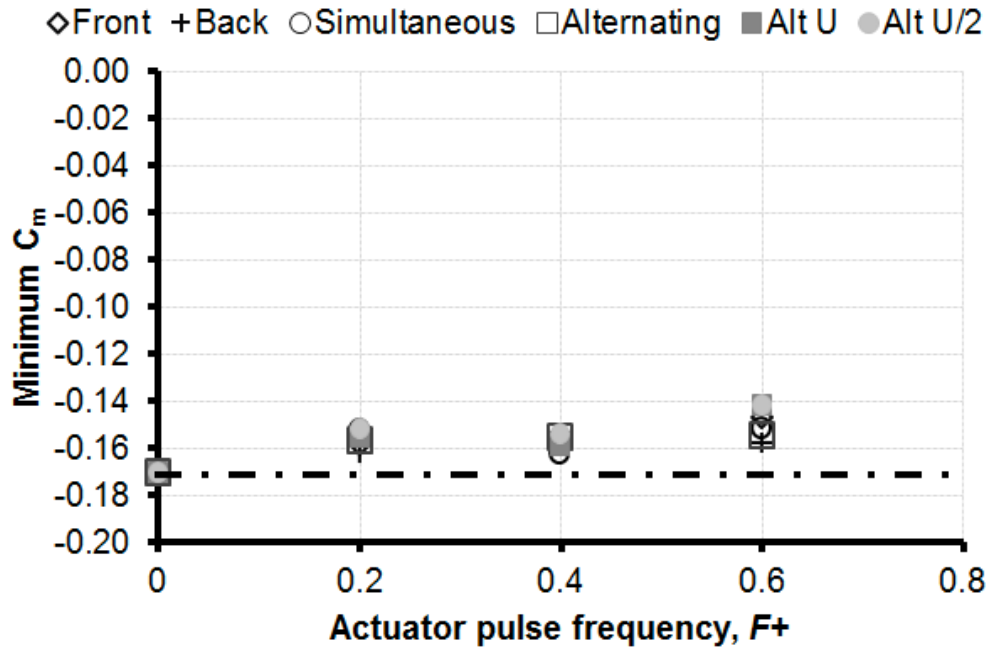


Figure 293. Average lift variation with  $F^+$  for dual-row COMPACT, Mach 0.4,  $\alpha = 10^\circ - 9.3^\circ \cos \omega t$ ,  $k = 0.05$ .



**Figure 294. Minimum pitching moment variation with  $F^+$  for dual-row COMPACT, Mach 0.3,  $\alpha = 10^\circ - 9.3^\circ \cos \omega t$ ,  $k = 0.05$ .**

#### *M=0.5*

The dual-row actuators were briefly tested at Mach 0.5. This was the last acquired data set of the second wind tunnel entry. The pitch trajectory was set for  $\alpha = 8^\circ - 8^\circ \cos \omega t$ ,  $k = 0.025$ . As with the single-row actuators, no positive impact from the actuators was recorded for any of the operating modes. It was believed that, due to the rearward shift of the center of pressure at higher Mach number, the rear-row of actuators might provide additional benefits compared to their near leading edge counterparts. This proved *not* to be the case, although the falloff was much reduced compared to the previous freestream Mach number discussed.

The actuators continued to show the characteristic unsteady load perturbations on the integral loads once the VR-12 stalled, proving that despite the high Mach number conditions, the stall alters the native flow behavior. It is possible that given higher  $F^+$ , the actuators could improve the baseline stall traits. For the limited  $F^+$  available, the control inputs could not recover from the degradation in performance associated with the installation and steady bleed effects. The baseline and controlled test cases for each configuration are shown in Appendix 4. Summary data plots for the cycle averaged lift and minimum pitching moment are shown in Figure 295 and Figure 296.

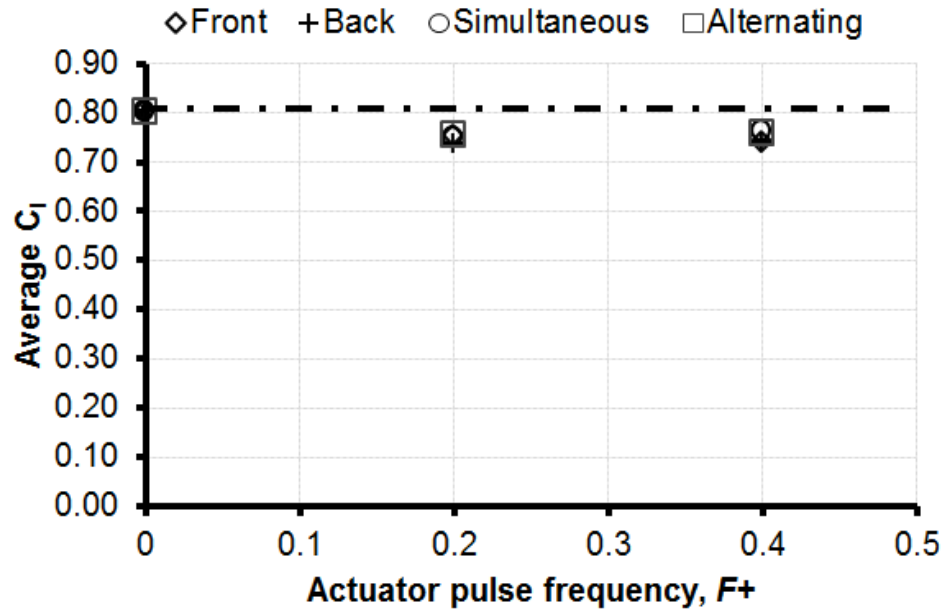


Figure 295. Average lift variation with  $F^+$  for dual-row COMPACT, Mach 0.5,  $\alpha = 8-8 \cos \omega t$ ,  $k = 0.025$ .

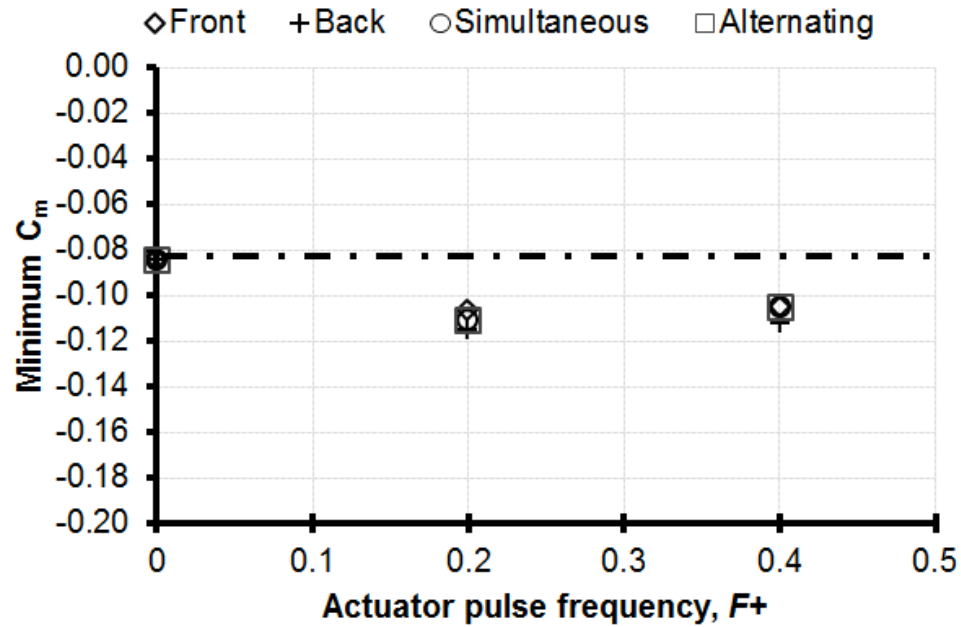


Figure 296. Minimum pitching moment variation with  $F^+$  for dual-row COMPACT, Mach 0.5,  $\alpha = 8-8 \cos \omega t$ ,  $k = 0.025$ .

## Summary Tables

The COMPACT parameters and resultant dynamic stall summary metrics for the dual-row configurations are shown for Mach 0.2 – 0.4 in Table 34 through Table 36. Mach 0.5 results are neglected due to the lack of performance benefits previously discussed. COMPACT effect at Mach 0.4 appears larger than that measured at Mach 0.3. However, the Mach 0.4 dynamic stall cycle spends a longer period of time in separated flow, allowing the actuators an additional period to provide aerodynamic gains compared to the pitching motion prescribed at Mach 0.3. A similar dynamic stall case at Mach 0.3 would likely witness similar, if not larger, performance growths. Lift and drag percentages take into consideration differences between the baseline and controlled prescribed motions to offset the effect of variations in mean angle-of-attack.

### Dual-row COMPACT

1. Similar to the single-row COMPACT results, the dual-row actuator impact on the aerodynamic loads decreased with increasing Mach number. Appreciable, positive differences with respect to an unmodified VR-12 in key dynamic stall metrics were measured up to Mach 0.4.
2. Single-row slots at  $x/c=0.10$  and spanning 33% of the VR-12 wing provided larger dynamic stall alleviation than the 10.4% span dual-row actuators for all test conditions.
3. Comparisons of front and back row actuators operating in isolation indicate that  $x/c=0.10$  is preferable to  $x/c=0.175$  for all Mach and dynamic stall motions studied.
4. Firing multiple actuators simultaneously or with alternating pulses provides additional performance increases compared to single-slot operation at  $x/c=0.10$  for the same span. An optimum phase delay for alternating triggering was not determined, but the limited data acquired here suggests that it is closely associated with the freestream velocity.

**Table 34. Dual-row COMPACT results on key dynamic stall metrics, Mach 0.2.**

$M$	$k$	$\alpha_0(^{\circ})$	$\alpha_1(^{\circ})$	Geom	$F^+$	Bleed	$N_{pulses}$	$\alpha_{start}$	$C_{l,avg}$	$C_{l,max}$	$C_{d,p,avg}$	$C_{d,p,max}$	$C_{m,c/4}$	$C_{m,c/4,min}$
0.40	0.05	9.96	9.86	Clean	0	0	0	NA	0.84	1.70	0.12	0.43	-0.04	-0.17
0.39	0.05	10.03	9.40	Front	0.2	1	12	10	0%	-6%	-3%	-2%	-17%	-7%
0.39	0.05	10.04	9.41	Front	0.4	1	25	10	1%	-6%	-3%	-3%	-20%	-7%
0.39	0.05	10.04	9.41	Front	0.6	1	37	10	1%	-5%	-2%	-4%	-20%	-14%
0.39	0.05	10.05	9.41	Back	0.2	1	12	10	-3%	-5%	-2%	-1%	-12%	-5%
0.39	0.05	10.05	9.42	Back	0.4	1	25	10	-2%	-5%	-2%	-3%	-12%	-10%
0.39	0.05	10.05	9.42	Back	0.6	1	37	10	-2%	-5%	-2%	-3%	-14%	-7%
0.39	0.05	10.03	9.39	Sim	0.2	1	12	10	1%	-4%	-1%	0%	-18%	-11%
0.39	0.05	10.05	9.40	Sim	0.4	1	25	10	0%	-5%	-1%	0%	-14%	-5%
0.39	0.05	10.04	9.40	Sim	0.6	1	37	10	2%	-5%	-3%	-4%	-23%	-11%
0.39	0.05	10.04	9.40	Alt50	0.2	1	12	10	0%	-4%	-1%	-1%	-16%	-8%
0.39	0.05	10.05	9.41	Alt50	0.4	1	25	10	2%	-5%	-2%	-3%	-21%	-9%
0.39	0.05	10.05	9.41	Alt 50	0.6	1	37	10	2%	-4%	-4%	-3%	-25%	-9%
0.39	0.05	10.04	9.39	Alt U	0.2	1	12	10	2%	-3%	-2%	-1%	-19%	-9%
0.39	0.05	10.06	9.40	Alt U	0.4	1	25	10	2%	-5%	-2%	-3%	-20%	-7%
0.39	0.05	10.05	9.40	Alt U	0.6	1	37	10	2%	-5%	-5%	-6%	-27%	-17%
0.40	0.05	10.04	9.40	Alt U/2	0.2	1	12	10	1%	-6%	-2%	-4%	-18%	-11%
0.39	0.05	10.05	9.41	Alt U/2	0.4	1	25	10	2%	-5%	-3%	-3%	-23%	-10%
0.39	0.05	10.06	9.41	Alt U/2	0.6	1	37	10	2%	-5%	-3%	-7%	-23%	-17%

**Table 35. Dual-row COMPACT results on key dynamic stall metrics, Mach 0.3.**

$M$	$k$	$\alpha_0(^{\circ})$	$\alpha_1(^{\circ})$	Geom	$F^+$	Bleed	$N_{pulses}$	$\alpha_{start}$	$C_{l,avg}$	$C_{l,max}$	$C_{d,p,avg}$	$C_{d,p,max}$	$C_{m,c/4}$	$C_{m,\xi_{A'}^{c,min}}$
0.30	0.07	9.99	9.58	Clean	0	0	0	NA	0.91	1.89	0.12	0.62	-0.03	-0.29
0.30	0.07	10.02	9.10	Front	0.2	1	8	10	0%	-4%	10%	-8%	9%	-12%
0.30	0.07	10.03	9.10	Front	0.4	1	17	10	1%	3%	9%	-8%	0%	-15%
0.30	0.07	9.99	9.47	Front	0.6	1	26	10	0%	-1%	7%	-9%	-10%	-12%
0.30	0.07	9.99	9.47	Back	0.8	1	35	10	1%	5%	7%	-8%	-13%	-13%
0.30	0.07	10.01	9.50	Back	0.2	1	8	10	-4%	-4%	12%	-6%	16%	-6%
0.30	0.07	10.00	9.50	Back	0.4	1	17	10	-3%	-4%	11%	-7%	11%	-9%
0.30	0.07	10.00	9.50	Back	0.6	1	26	10	-2%	2%	11%	-8%	10%	-6%
0.30	0.07	10.01	9.50	Sim	0.8	1	35	10	-3%	-2%	9%	-7%	3%	-11%
0.30	0.07	10.00	9.50	Sim	0.2	1	8	10	-1%	-4%	10%	-6%	4%	-13%
0.30	0.07	10.01	9.49	Sim	0.4	1	17	10	1%	-2%	10%	-8%	-3%	-20%
0.30	0.07	10.01	9.49	Sim	0.6	1	26	10	0%	2%	5%	-7%	-18%	-25%
0.30	0.07	10.01	9.50	Alt 50	0.8	1	37	10	-2%	-2%	8%	-10%	-3%	-18%
0.30	0.07	10.00	9.51	Alt 50	0.2	1	8	10	-1%	-3%	8%	-7%	0%	-12%
0.30	0.07	10.00	9.51	Alt 50	0.4	1	17	10	0%	4%	7%	-5%	-9%	-9%
0.30	0.07	10.00	9.51	Alt 50	0.6	1	26	10	0%	-2%	2%	-5%	-18%	-15%

**Table 36. Dual-row COMPACT results on key dynamic stall metrics, Mach 0.4.**

$M$	$k$	$\alpha_0(^{\circ})$	$\alpha_1(^{\circ})$	Geom	$F^+$	Bleed	$N_{pulses}$	$\alpha_{start}$	$C_{l,avg}$	$C_{l,max}$	$C_{d,p,avg}$	$C_{d,p,max}$	$C_{m,c/4}$	$C_{m,\xi_{A'}^{c,min}}$
0.40	0.05	9.96	9.86	Clean	0	0	0	NA	0.84	1.70	0.12	0.43	-0.04	-0.17
0.39	0.05	10.03	9.40	Front	0.2	1	12	10	0%	-6%	-3%	-2%	-17%	-7%
0.39	0.05	10.04	9.41	Front	0.4	1	25	10	1%	-6%	-3%	-3%	-20%	-7%
0.39	0.05	10.04	9.41	Front	0.6	1	37	10	1%	-5%	-2%	-4%	-20%	-14%
0.39	0.05	10.05	9.41	Back	0.2	1	12	10	-3%	-5%	-2%	-1%	-12%	-5%
0.39	0.05	10.05	9.42	Back	0.4	1	25	10	-2%	-5%	-2%	-3%	-12%	-10%
0.39	0.05	10.05	9.42	Back	0.6	1	37	10	-2%	-5%	-2%	-3%	-14%	-7%
0.39	0.05	10.03	9.39	Sim	0.2	1	12	10	1%	-4%	-1%	0%	-18%	-11%
0.39	0.05	10.05	9.40	Sim	0.4	1	25	10	0%	-5%	-1%	0%	-14%	-5%
0.39	0.05	10.04	9.40	Sim	0.6	1	37	10	2%	-5%	-3%	-4%	-23%	-11%
0.39	0.05	10.04	9.40	Alt50	0.2	1	12	10	0%	-4%	-1%	-1%	-16%	-8%
0.39	0.05	10.05	9.41	Alt50	0.4	1	25	10	2%	-5%	-2%	-3%	-21%	-9%
0.39	0.05	10.05	9.41	Alt 50	0.6	1	37	10	2%	-4%	-4%	-3%	-25%	-9%
0.39	0.05	10.04	9.39	Alt U	0.2	1	12	10	2%	-3%	-2%	-1%	-19%	-9%
0.39	0.05	10.06	9.40	Alt U	0.4	1	25	10	2%	-5%	-2%	-3%	-20%	-7%
0.39	0.05	10.05	9.40	Alt U	0.6	1	37	10	2%	-5%	-5%	-6%	-27%	-17%
0.40	0.05	10.04	9.40	Alt U/2	0.2	1	12	10	1%	-6%	-2%	-4%	-18%	-11%
0.39	0.05	10.05	9.41	Alt U/2	0.4	1	25	10	2%	-5%	-3%	-3%	-23%	-10%
0.39	0.05	10.06	9.41	Alt U/2	0.6	1	37	10	2%	-5%	-3%	-7%	-23%	-17%

## 5. Particle-Image Velocimetry Measurements

Particle-image velocimetry (PIV) measurements were performed for both static and pitching airfoil tests. Table 37 - Table 39 provide summaries of the data points and conditions acquired. All measurements were carried out at a plane centered on the midspan of an actuator relatively close to the overall airfoil midspan. At the outset of PIV tests, the laser sheet was placed at the actuator second closest to the midspan on the lower bank. At Run 72 Point 16, the laser sheet was moved to the actuator closest to the midspan on the lower bank. Finally, at the beginning of Run 74, the laser sheet was moved again to the actuator closest to the midspan on the upper bank.

**Table 37. Bleed-off/On Single-Row PIV Steady Data Points**

Run	Mach	$\alpha_0$	Points (Bleed-off, Bleed-on)
72	0.2	15	5,6
	0.2	18	13,14
	0.2	20	34,35
	0.2	25	55,56
	0.3	20	84,85
73	0.3	20	2,3
	0.3	25	26,27
	0.3	18	62,63
	0.4	16	92,94
74	0.4	16	3,4
	0.4	18	26,27
	0.4	20	47,48

**Table 38. COMPACT Single-Row PIV Steady Data Points**

Run	Mach	$\alpha_0$		F+	PIV trigger delay (ms)	Points
72	0.2	15	0.2		0,1,2,3	7-10
	0.2	18	0.2		0,1,2,3,4,5,6,7,14,21	15-24
	0.2	18	0.4		0,1,2,3,4,5,6,7,10.5	25-33
	0.2	25	0.2		0,1,2,3,4,5,6,7,14,21	36-45
	0.2	25	0.4		0,1,2,3,4,5,6,7,10.5	46-54
	0.2	25	0.2		0,1,2,3,4,5,6,7,14,21	57-66
	0.2	25	0.4		0,1,2,3,4,5,6,7,10.5	67-75
	0.2	25	0.6		0,1,2,3,4,5,6,7	76-83
	0.3	20	0.2		0,0.7,1.4,2.1,2.8,3.5,4.2,4.9,9.3,14.1	86-95
	0.3	20	0.4		0,0.7,1.4,2.1,2.8,3.5,4.2,4.9,7	4-11,13
73	0.3	20	0.6		0,0.7,1.4,2.1,2.8,3.5,4.2,4.9	16-20,23-25
	0.3	25	0.4		0,0.7,1.4,2.1,2.8,3.5,4.2,4.9,7	29-37
	0.3	25	0.2		0,1.4,2.1,2.8,3.5,4.2,4.9,9.3,14.1	39,42,44,45,47-51
	0.3	25	0.6		0,0.7,1.4,2.1,2.8,3.5,4.2,4.9	52,54-57,59-61
	0.3	18	0.4		0,0.7,1.4,2.1,2.8,3.5,4.2,4.9,7	67,68,70-74,79,80
	0.3	18	0.6		0,0.7,1.4,2.1,2.8,3.5,4.2,4.9	81-83,85-88,91
	0.4	16	0.2		0,0.5,1,1.5,2,2.5,3,3.5,7,10.6	97,98,100,104,107,108,109,111,112,113
	0.4	16	0.4		0,0.5,1,1.5,2,2.5,3,3.5,5.3	6-15
74	0.4	16	0.2		0,0.5,1,1.5,2,2.5,3,3.5,7,10.6	17-25
	0.4	18	0.2		0,0.5,1,1.5,2,2.5,3,3.5,7,10.6	28-37

Run	Mach	$\alpha_0$	F+	PIV trigger delay (ms)	Points
	0.4	18	0.4	0,0.5,1,1.5,2,2.5,3,3.5,5.3	38-46
	0.4	20	0.2	0,0.5,1,1.5,2,2.5,3,3.5,7,10.6	49-58
	0.4	20	0.4	0,0.5,1,1.5,2,2.5,3,3.5,5.3	59-67

**Table 39. COMPACT Single-Row PIV Unsteady Data Points**

Run	Mach	k	$\alpha_0$	$\alpha_1$	F+	Pulse Start $\alpha$	PIV trigger	Points
73	0.4	0.05	10	8	0.4	10	$\alpha=10-16,17, 17D,15D,14D, 13D,12D,11D, 10D-4D,3D,3, 4,6,8$	115-118, 120-135
74	0.3	0.07	10	9.5	0	10	$\omega t = 40^\circ:8^\circ:224^\circ$	71-94
75	0.3	0.07	10	9.5	0.4	10	$\omega t = 40^\circ:8^\circ:224^\circ$	4,6-9,11-15,18-26, 28,29,31-33
	0.4	0.05	10	8	0	10	$\omega t = 40^\circ:8^\circ:224^\circ$	34-57
	0.4	0.05	10	8	0.4	10	$\omega t = 40^\circ:8^\circ:224^\circ$	58,60-79,81,83,85
	0.2	0.07	10	10	0	10	$\omega t = 40^\circ:8^\circ:224^\circ$	86-105,108, 107,109,110
	0.2	0.07	10	10	0.4	10	$\omega t = 40^\circ:8^\circ:224^\circ$	111-134
	0.5	0.025	8	8	0	8	$\omega t = 40^\circ:8^\circ:224^\circ$	136-148, 150-151, 153-161
	0.5	0.025	8	8	0.2	8	$\omega t = 40^\circ:8^\circ:224^\circ$	163-166,168-171,173,174,176-186,188-190

A comprehensive set of figures documenting all the PIV results collected is provided in Appendix 5. Select figures from this set are used in the following discussions. Please note that X and Z are provided in inches for all plots. The coordinate system used has its origin at the airfoil leading edge when the airfoil is at zero angle-of-attack.

#### **A. Images and Seed Particles**

As discussed previously, water droplets were used to seed the flow in the IRT. Sample images for select points are shown in Figure 297 - Figure 302. Here, several of the phenomena are present, which were shown previously in risk-reduction tests performed well-ahead of the these tests. Separated flow causes conglomeration of particles, which increases the visible intensity, as shown in Figure 297. However, excellent cross-correlation was still possible in these bright regions. Figure 298 shows the bright region of the same image-pair but with the intensity adjusted to reveal a reasonable cloud of seed particles.

Bright streaks separating good particle images from dark regions had been shown in previous tests, a phenomena, which appears clearly in Figure 299. Although it appears that good cross-correlation may not be possible in the dark region (close to airfoil surface), adjusting the intensity once again, as shown in Figure 300 reveals that good seed particles do exist in the dark regions, although they are more sparse.



Finally, one of the most egregious examples of the bright streak with dark region phenomenon is shown in Figure 301 and Figure 302. Here, particles in the dark region become very blurry, and this does result in some invalid vectors in these regions. Overall, good cross-correlation was achieved across the entire range of conditions (steady and unsteady) with generally >95% of vectors being valid.

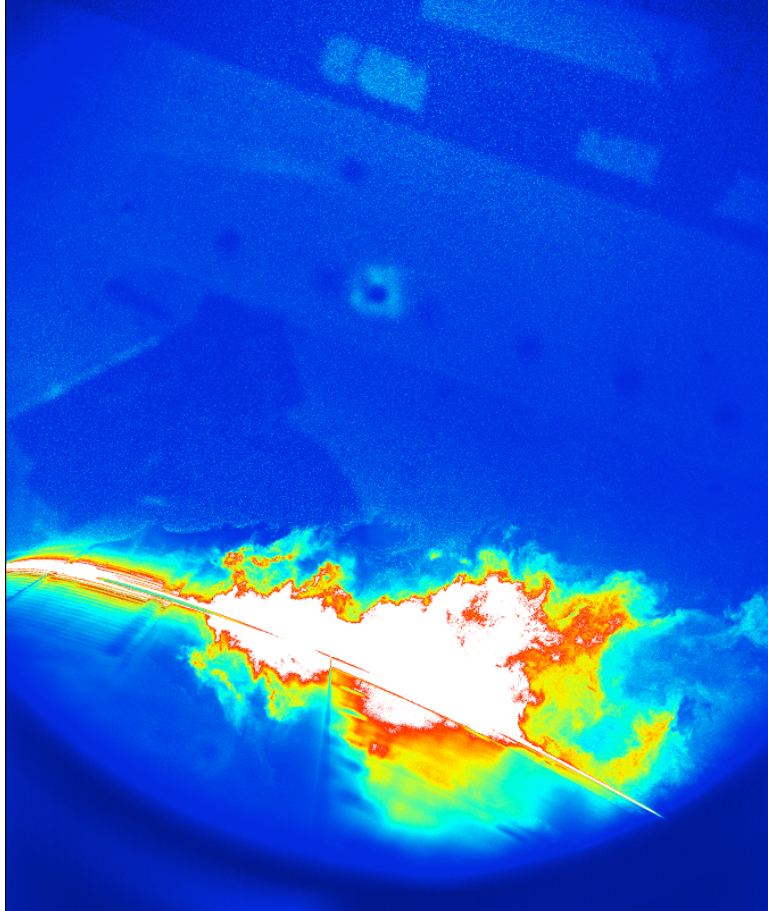


**Figure 297.** Sample PIV image from Run 73, Point 4. Conditions are steady, Mach 0.3,  $\alpha = 20^\circ$ ,  $F^+ = 0.4$ .

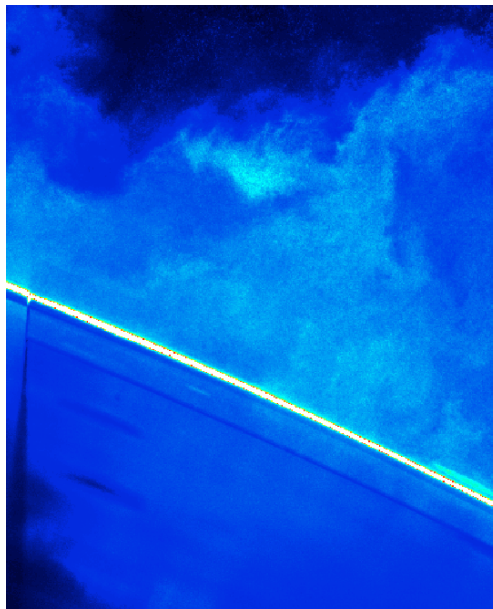


**Figure 298.** Sample PIV image from Run 73, Point 4, zoomed in at separated region. Conditions are steady, Mach 0.3,  $\alpha = 20^\circ$ ,  $F^+ = 0.4$ .

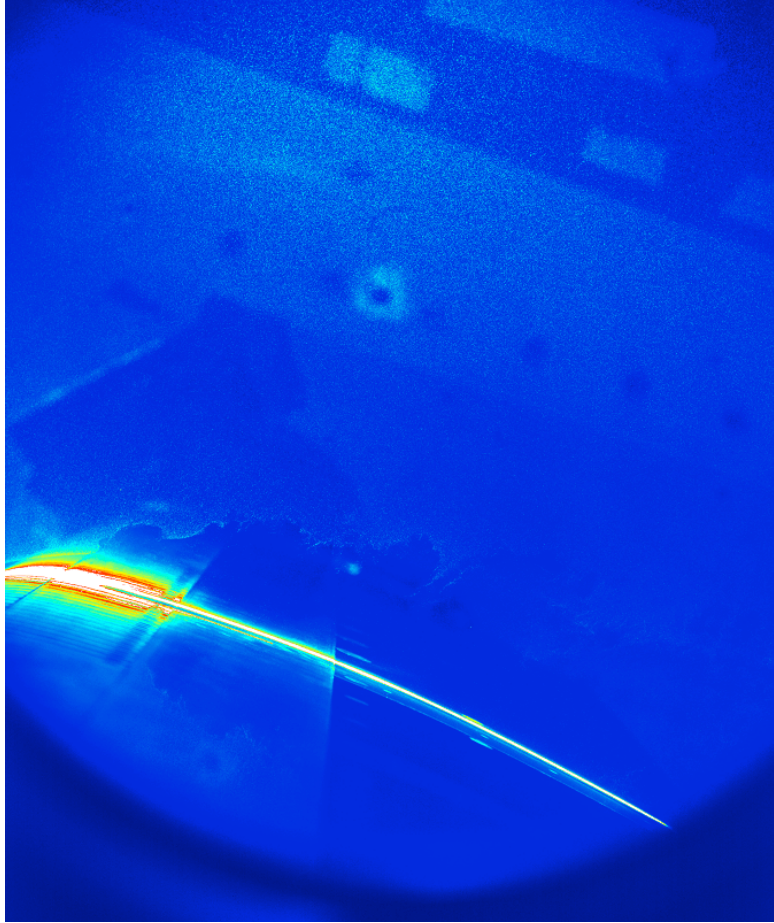


**Figure 299.** Sample PIV image from Run 73, Point 5. Conditions are steady, Mach 0.3,  $\alpha = 20^\circ$ ,  $F^+ = 0.4$ .

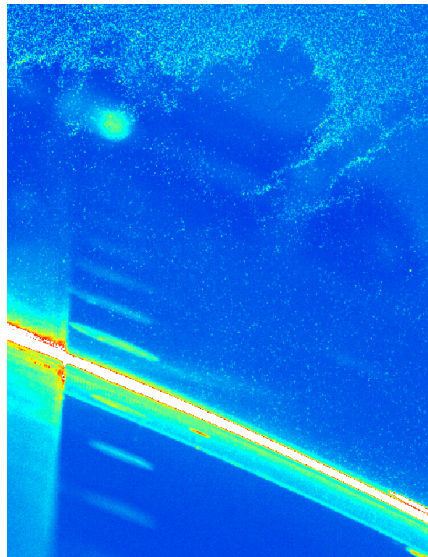


**Figure 300.** Sample PIV image from Run 73, Point 5, zoomed in at separated region. Conditions are steady, Mach 0.3,  $\alpha = 20^\circ$ ,  $F^+ = 0.4$ .

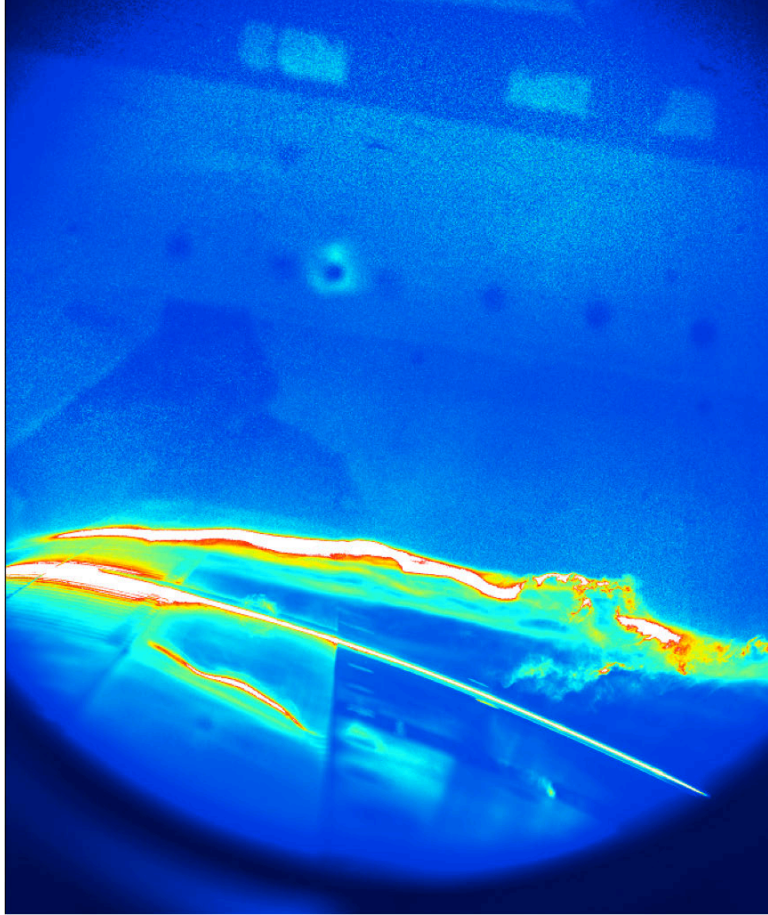


**Figure 301.** Sample PIV image from Run 75, Point 36. Conditions are unsteady, Mach 0.4,  $\omega t = 56^\circ$ , no actuation.

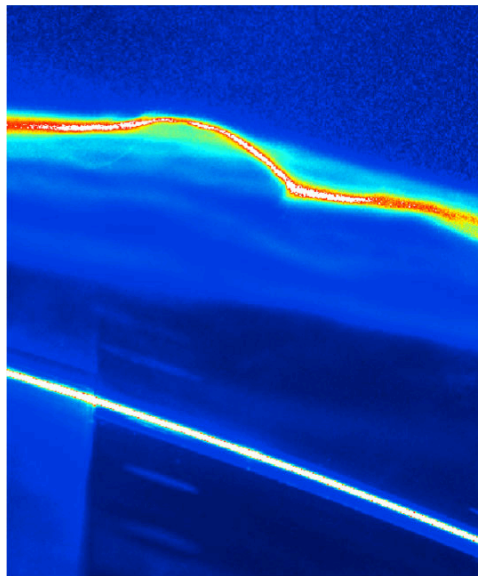


**Figure 302.** Sample PIV image from Run 75, Point 36, zoomed in at separated region. Conditions are unsteady, Mach 0.4,  $\omega t = 56^\circ$ , no actuation.



## B. Steady Results

Figure 303 shows baseline (single-row COMPACT) post-stall flow-field measurements at Mach numbers from 0.2-0.4. For the left column in the figure the bleed air is off, while in the right column the bleed air is on. In each case, the airfoil is at approximately four degrees past the baseline static stall angle. Focusing on the bleed-off cases, it appears that at Mach 0.2 and 0.3, the separation starts immediately aft of the slot. The region immediately upstream of the slot still sees high-speed attached flow. At Mach 0.4, it is not as clear whether the flow has begun to separate upstream of the slot. Further past stall, it was shown that the separated region starts well forward of the slot, likely extending to the leading edge in many cases. With bleed air on, only very small differences are apparent with respect to the bleed air off results, most of which can likely be attributed to the statistical uncertainty in these measurements.

In studying the results for actuation-on cases, it was found that examining  $M'$ , the Mach number in a reference frame moving with the freestream, was very effective in revealing and illustrating flow structures due to the actuation pulse. For clarity,  $M'$  is defined as follows:

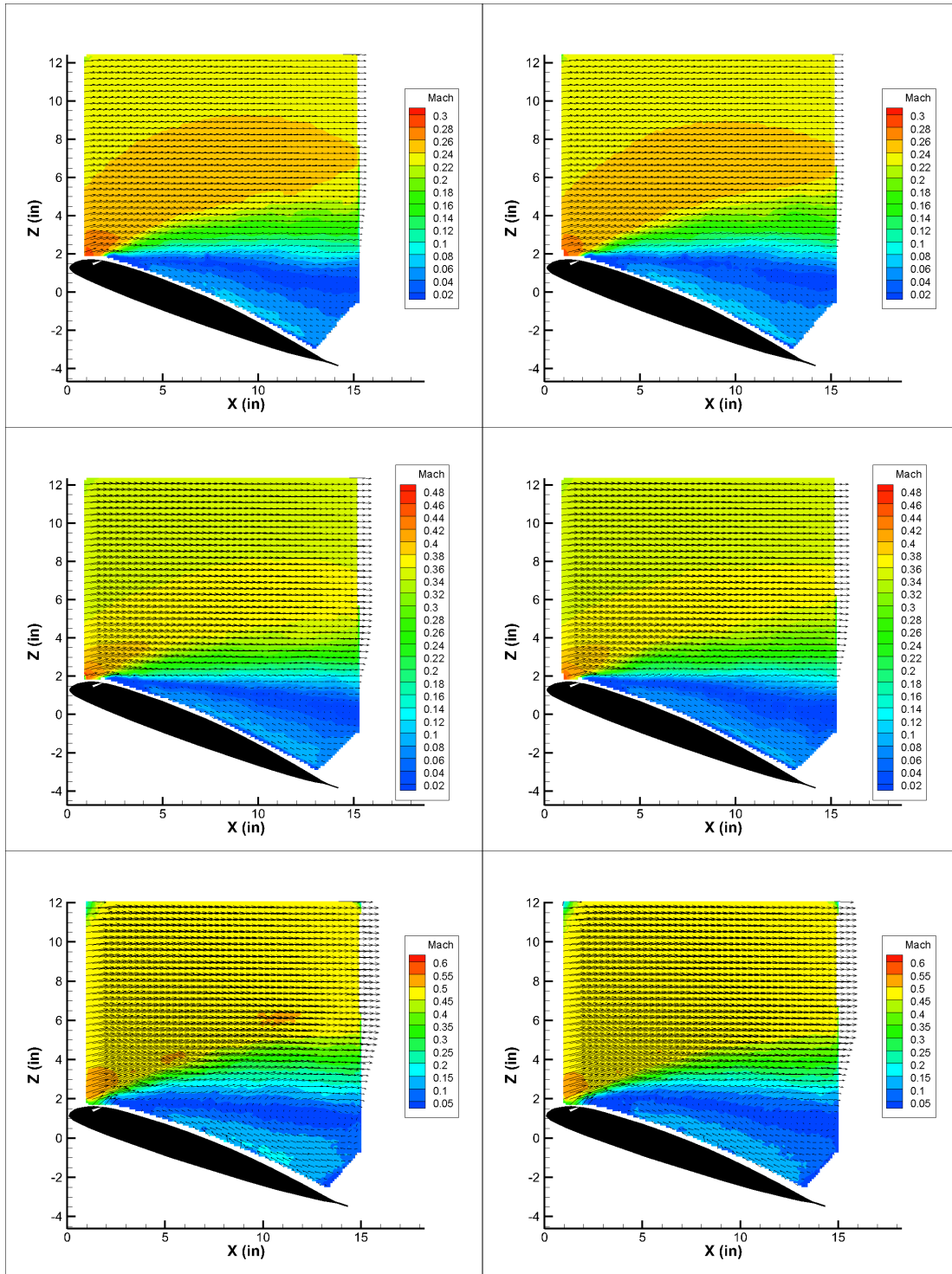
$$M' = \frac{\sqrt{(u-U_\infty)^2 + (v)^2}}{a_\infty}.$$

Figure 304 and Figure 305 show the detailed evolution of a single pulse through phase-average vector fields at various delay times,  $\Delta t$ , where a pulse is initiated at  $\Delta t = 0$ . Figure 304 shows contours of Mach number whereas Figure 305 shows contours of  $M'$ . In this case, the freestream Mach number is 0.3, and  $\alpha = 20^\circ$ , approximately  $4^\circ$  past baseline static stall for this Mach number. Here, actuation occurs at  $F^+ = 0.4$ , therefore; from previously shown pressure measurements, it is known that the lift is significantly increased due to actuation. Comparison against the no-actuation case, shown also in Figure 304, illustrates that even as the pulse is first generated, the flow is more attached. Proceeding in time, the effect of the pulse is seen to sweep across the upper surface of the airfoil creating a higher-speed flow region upstream of itself. Qualitatively, the results appear very similar to what has been shown previously at significantly lower Mach numbers. Focusing on the  $M'$  contours of Figure 305 we see in more detail the flow structure responsible for the reattachment. Again, similar to what has been shown at lower Mach numbers in previous studies, immediately after the pulse it appears that the large and growing boundary layer present on the upper surface of the airfoil is penetrated by the pulse, resulting in the creation of a small vortex with the same directionality that a dynamic stall vortex would have for a pitching airfoil. The strength is significantly lower than a dynamic stall vortex; however, the size of this “compact vortex” is shown to extend more than half of the airfoil chord length above the upper surface by the time it has approached the airfoil trailing edge.

The path that the compact vortex takes as it proceeds downstream appears to vary strongly with  $F^+$ , as shown in Figure 306. Here the airfoil is at the same conditions, Mach number of 0.3 and  $\alpha = 20^\circ$ , while  $F^+$  is varied from 0.2 to 0.6 going from top to bottom. First, it is clear that the compact vortex tends to stay closer to the airfoil as  $F^+$  is increased. It appears that at low  $F^+$ , a large amount of time between pulses allows the boundary layer to grow, causing flow above the airfoil surface to be directed in more of an upward direction, away from the airfoil surface. This observation is supported by the smaller lift increments observed at lower  $F^+$ . As  $F^+$  is increased, the additional COMPACT generated disturbances present on the airfoil upper surface maintain a smaller boundary layer keeping the flow directed more along the airfoil surface.

Second, it is clear that at higher  $F^+$ , the compact vortex tends to move more rapidly along the airfoil surface. This is very much a corollary to the previous observation. Not only does higher  $F^+$  direct the flow more along the airfoil surface, it reduces the native adverse pressure gradient and helps the flow to maintain a higher speed. This is, again, supported by the lift increment measurements and enhanced aft pressure distribution recovery.

Finally, we compare the flow structure evolution seen across Mach numbers from 0.2 to 0.4, as shown in Figure 307. For each row, the airfoil is  $4^\circ$  past the baseline static stall angle for that Mach number. For Mach 0.2 and 0.3, it appears that both the size and path of the compact vortex are very similar. At Mach 0.4, although the structure of the compact vortex is not as well-defined, there remain strong similarities. Although the compact vortex is less circular, flatter from top to bottom, the directionality is as expected, and the center of rotation appears to track closely with the lower Mach cases.



**Figure 303. Mach contours and vector fields for bleed-off (left) and bleed-on (right) at Mach 0.2,  $\alpha = 20^\circ$  (top), Mach 0.3,  $\alpha = 20^\circ$  (middle), and Mach 0.4,  $\alpha = 18^\circ$ .**



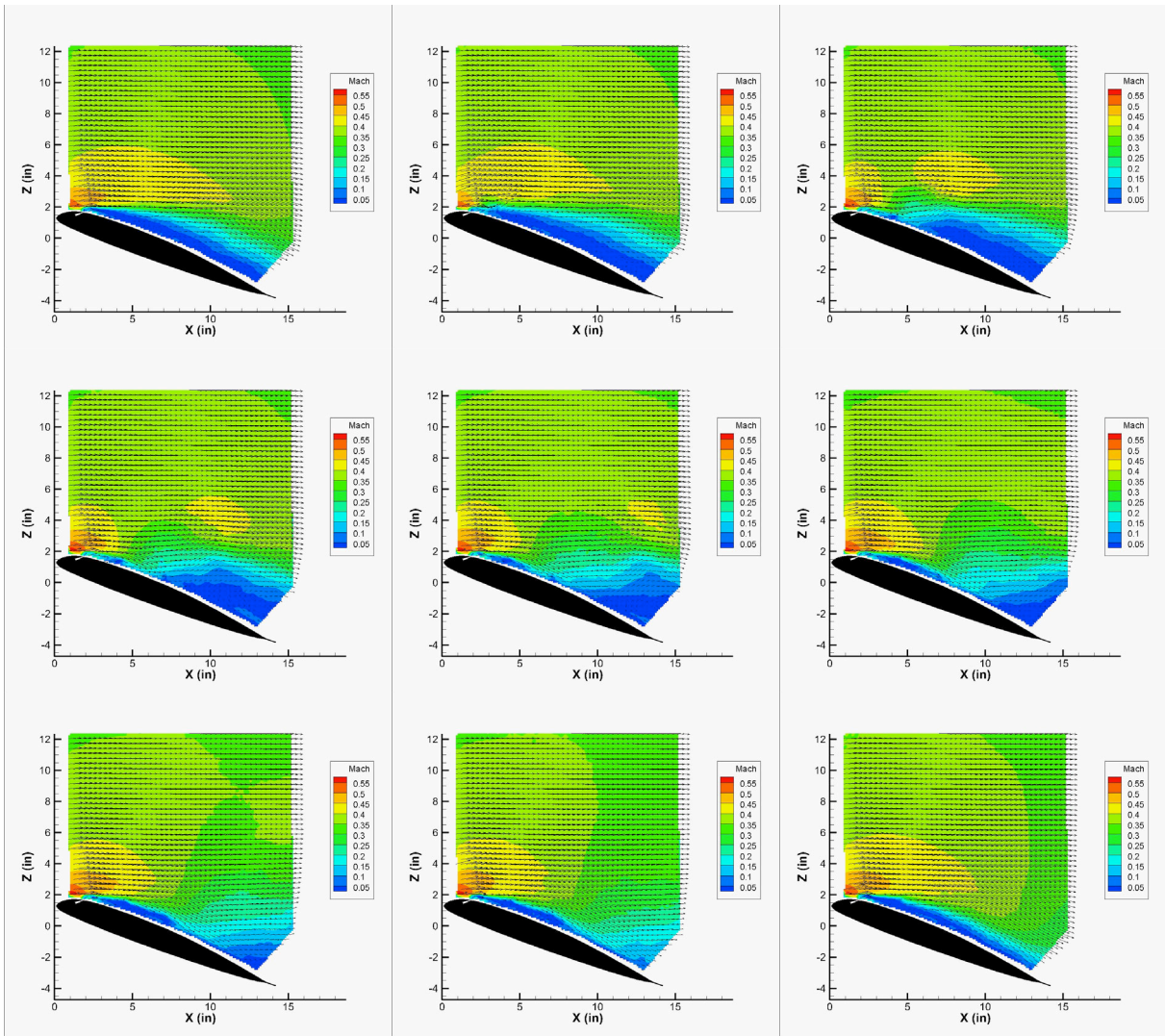
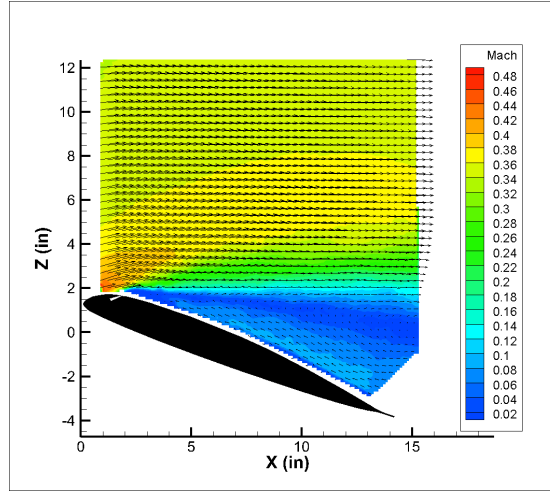
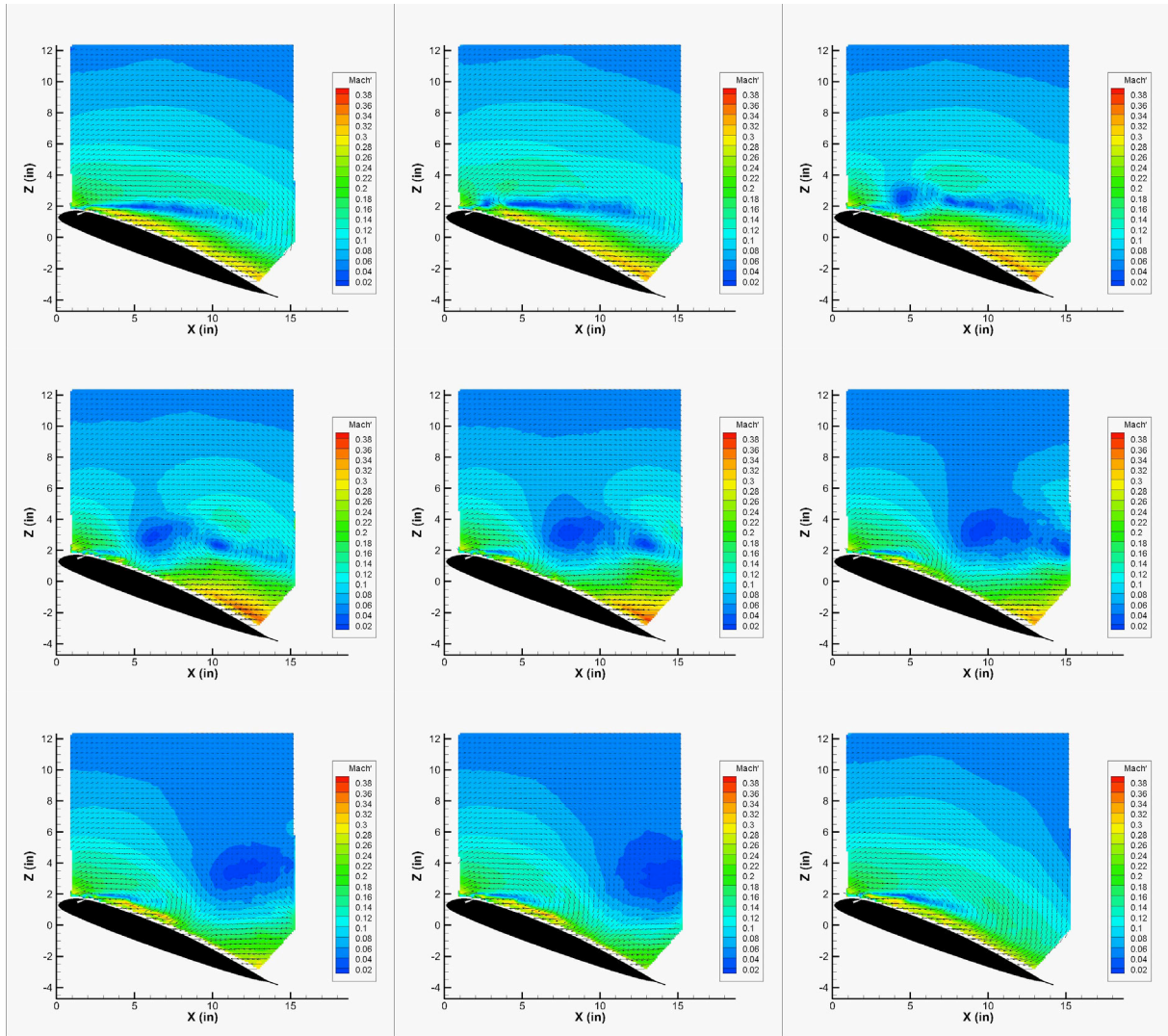


Figure 304. Mach contours, Mach 0.3,  $\alpha = 20^\circ$ ,  $F^+ = 0.4$ ,  $\Delta t = 0, 0.7, 1.4, 2.1, 2.8, 3.5, 4.2, 4.9, 7$  ms. No actuation case shown at top-center.



**Figure 305. Mach' contours, Mach 0.3,  $\alpha = 20^\circ$ ,  $F^+ = 0.4$ ,  $\Delta t = 0, 0.7, 1.4, 2.1, 2.8, 3.5, 4.2, 4.9, 7$  ms in order from top-left to bottom-right.**

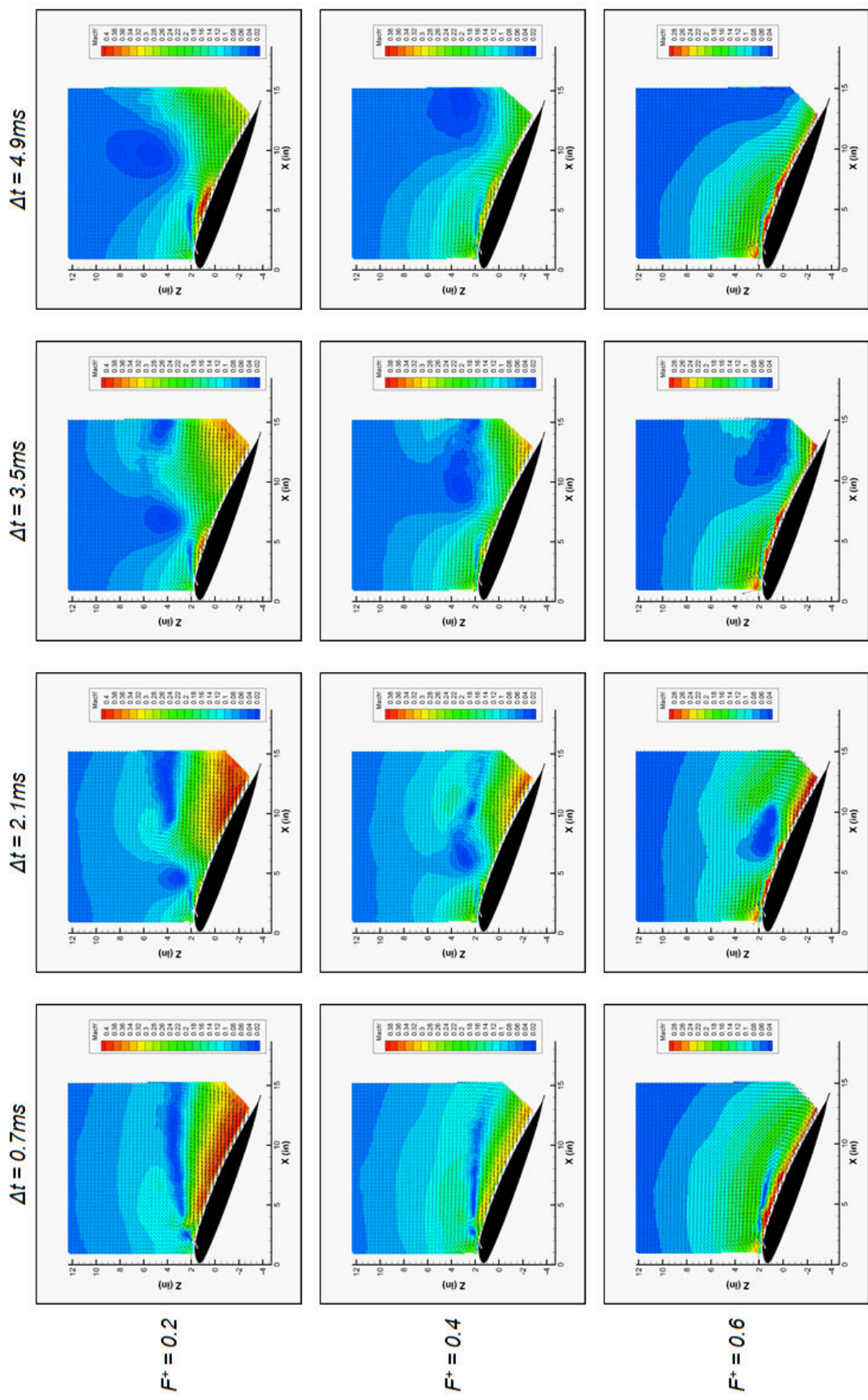


Figure 306. Comparison of COMPACT flow structure development for different  $F^+$  with Mach number of 0.3,  $\alpha = 20^\circ$ . Contours are of  $M'$ .



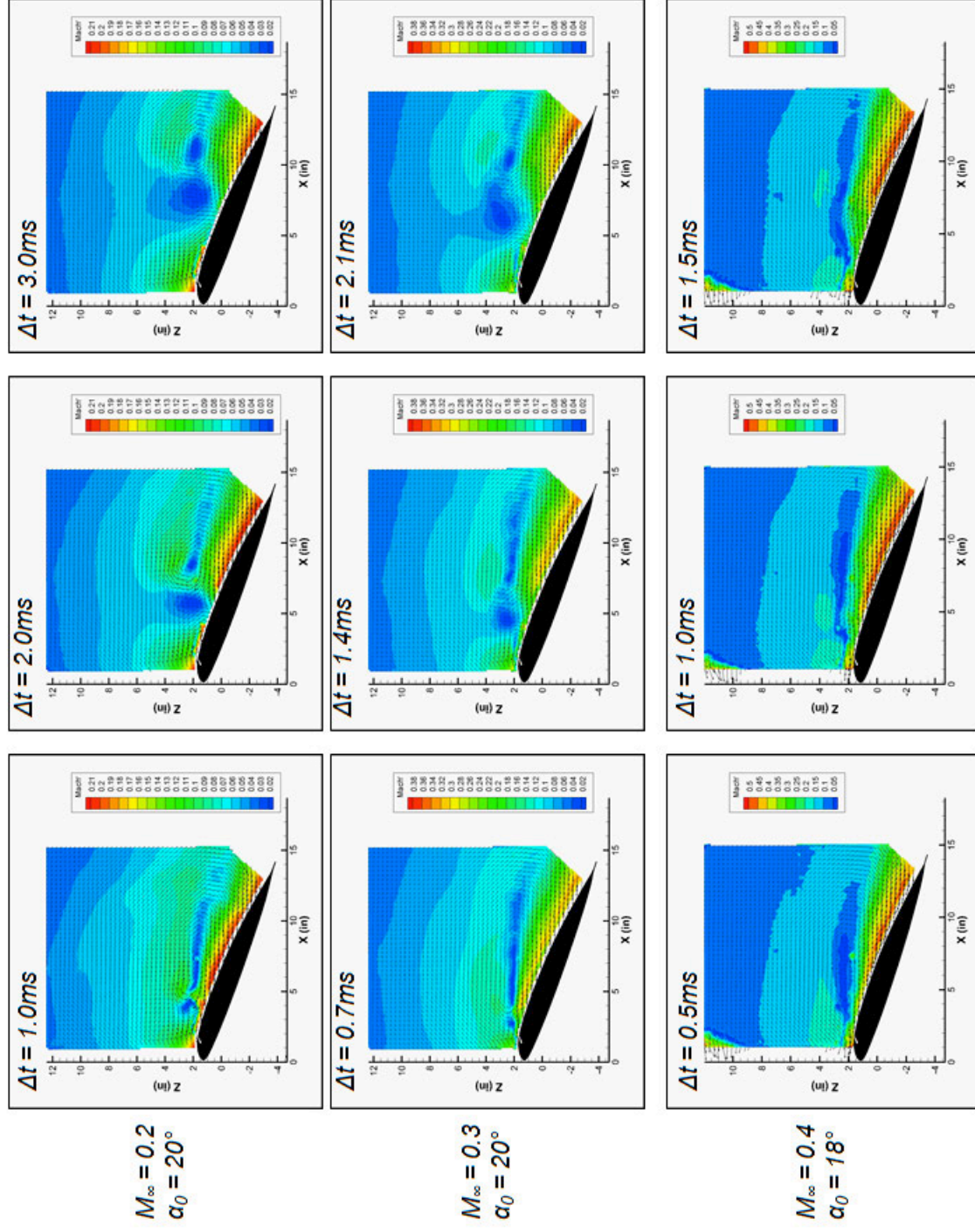


Figure 307. Comparison of early COMPACT flow structure development across Mach number range at  $F^+ = 0.4$ . Contours are of  $M'$ .

### **C. Unsteady Results**

Given the large acquisition time associated with collecting PIV data for pitching airfoil conditions measurements were only obtained at select conditions. Figure 308 and Figure show baseline and  $F^+ = 0.4$  actuation results at Mach 0.3 and Mach 0.4 conditions. Both Mach and  $M'$  contours are shown. Note that for brevity in the figures, only a select number of phase points are provided, which span across the peak angle-of-attack and thereafter for some time. In these cases, acquisition of the PIV images were phase locked with the airfoil motion rather than the pulse train. Synchronization between all three systems was strong such that flow structures similar to what were shown in the steady results do appear in these acquisitions. Focusing first on Mach 0.3, as shown in Figure 308, the effect of the actuation pulse becomes present just as the flow begins to stall. This is consistent with the lift measurements, which showed increases in lift after the flow has significantly separated on the downstroke, the effectiveness of the actuation pulses in reducing the size of the separated region are apparent in the last few phase angles shown in the figures. Interestingly, the results at Mach 0.4 in Figure appear very similar to the results at Mach 0.3. Again, the effectiveness of the actuation pulse in suppressing stall is seen most after the flow has separated significantly as shown in the last three rows of Figure , and the same flow structures shown in the steady results appear in the  $M'$  contours.

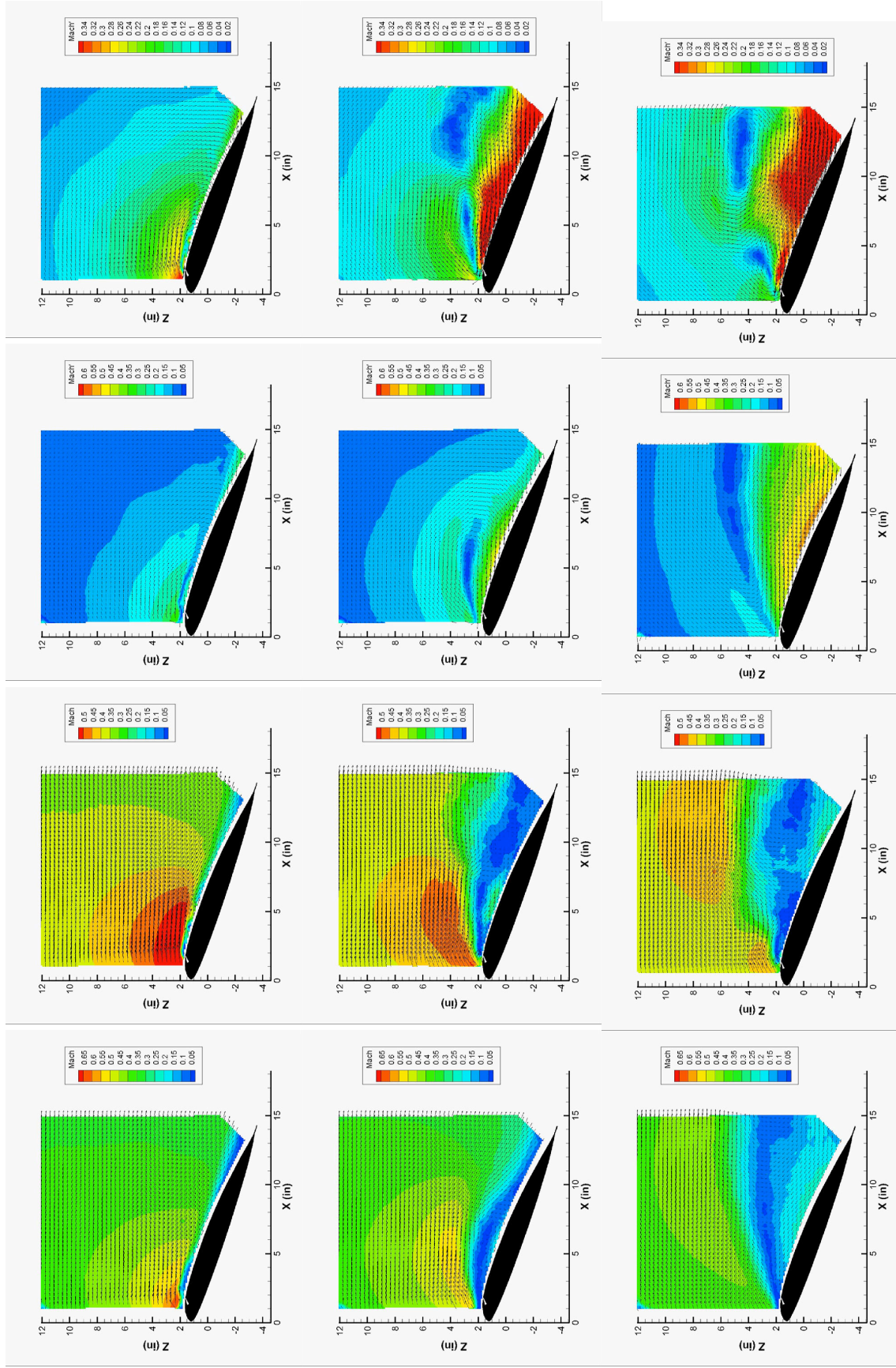


Figure 308. Mach and Mach' contours, Mach 0.3,  $\alpha_0 = 10^\circ$ ,  $\alpha_1 = 9.5^\circ$ , baseline slotted (left), COMPACT  $F^+ = 0.4$  (right),  $\omega t = 64^\circ$ ,  $80^\circ$ ,  $96^\circ$ ,  $112^\circ$ ,  $128^\circ$ ,  $144^\circ$  (from top to bottom, split across two pages).



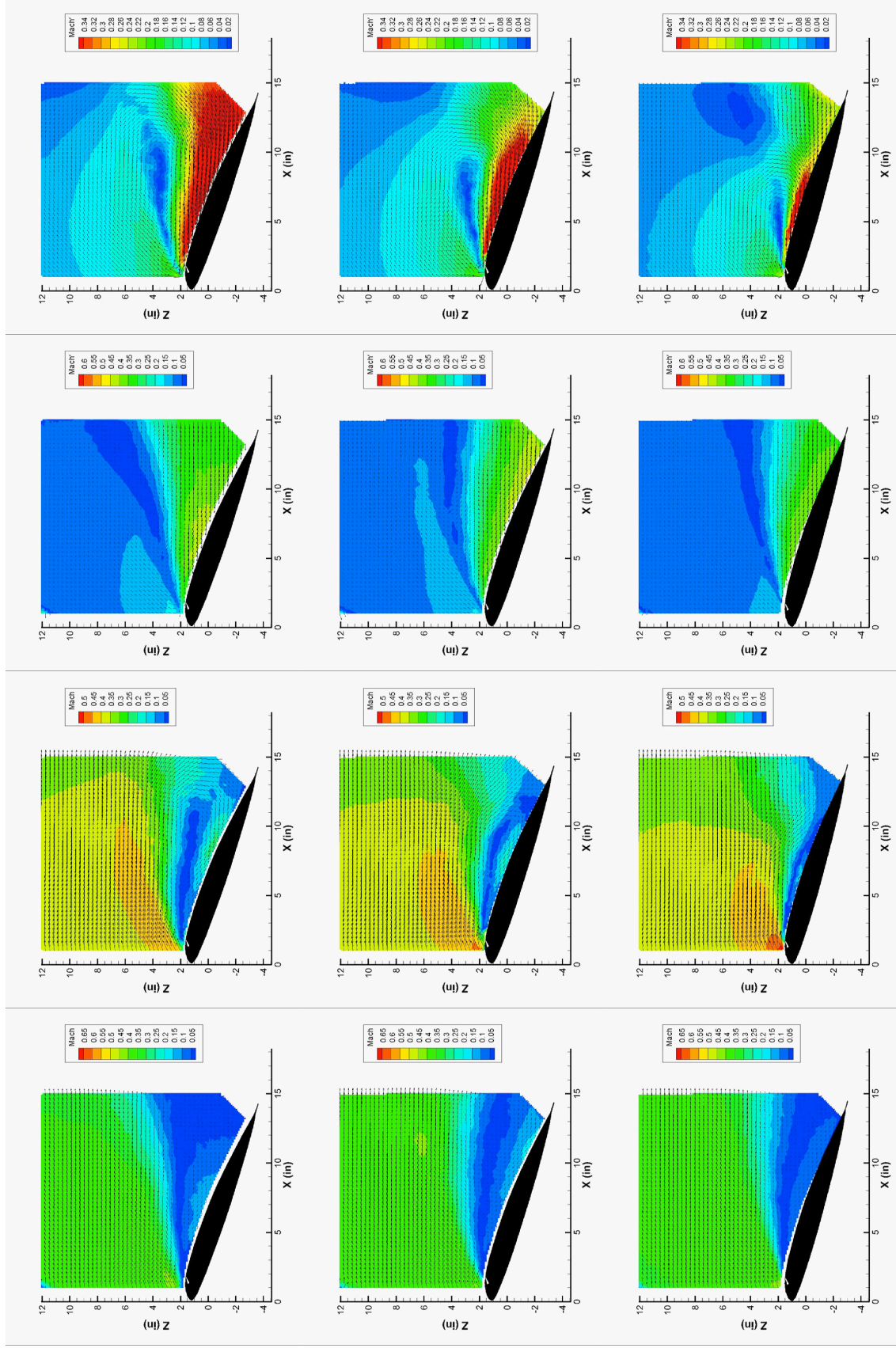


Figure 308 (Continued).



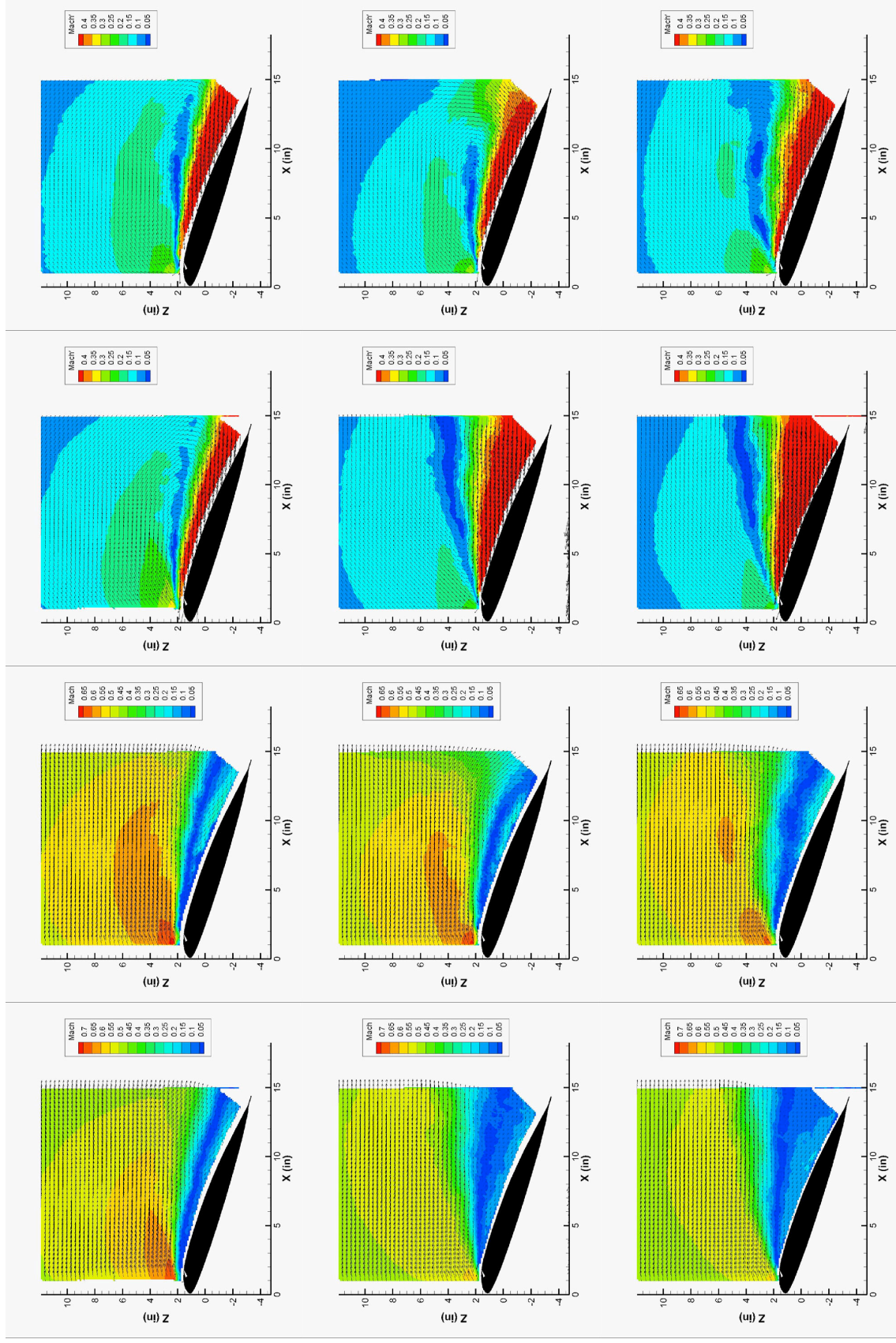


Figure 309. Mach and Mach' contours, Mach 0.4,  $\alpha_I = 10^\circ$ ,  $\alpha_\theta = 8^\circ$ , baseline slotted (left), COMPACT  $F^+ = 0.4$  (right),  $\omega t = 64^\circ, 80^\circ, 96^\circ, 112^\circ, 128^\circ, 144^\circ$  (from top to bottom, split across two pages).

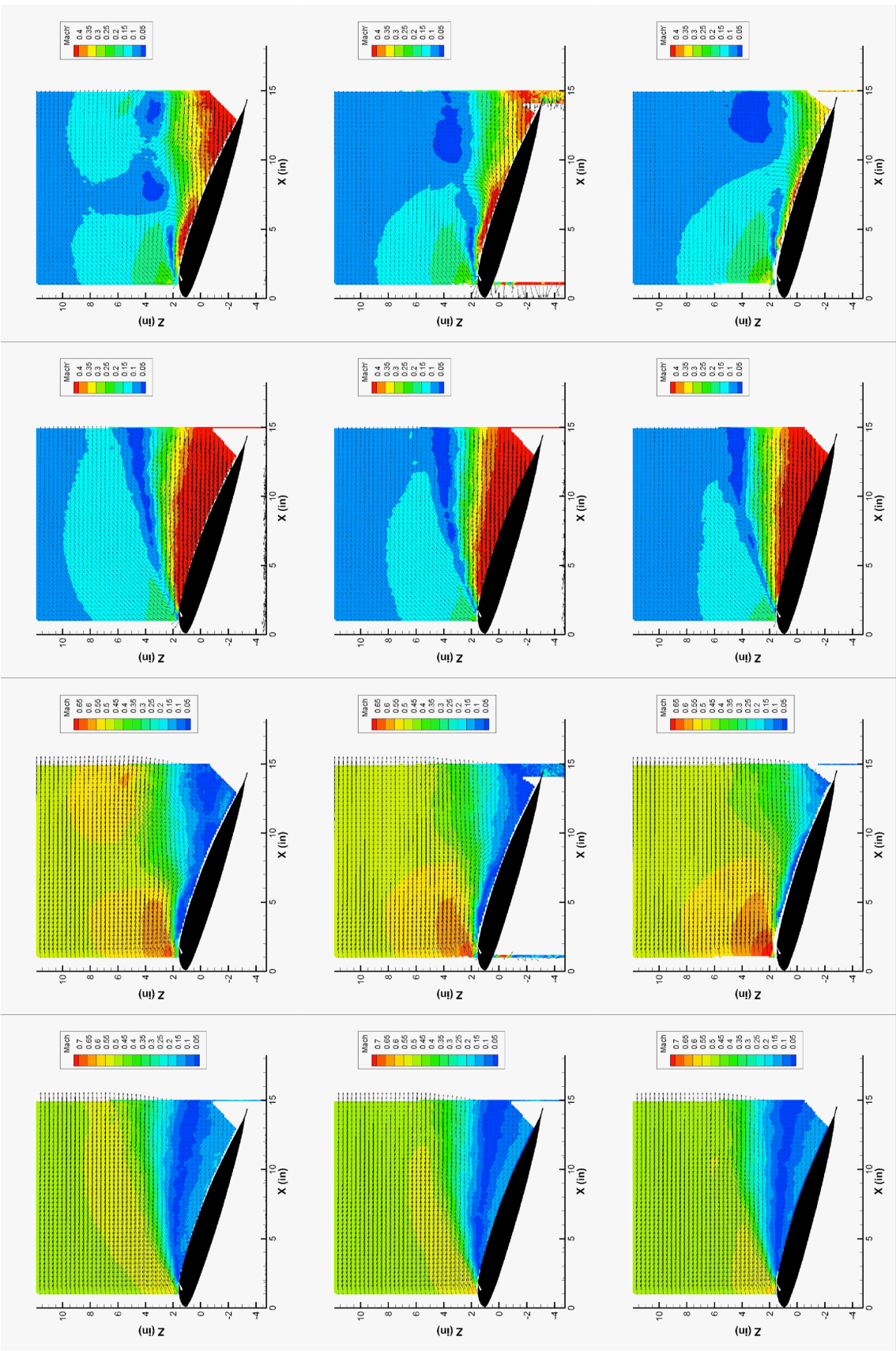


Figure 309 (Continued)

## 6. COMPACT Chamber Pressure Measurements

A limited effort was put forth to measure the pressure inside the chambers furthest from the airfoil midspan. A commercially available Endevco pressure sensor was connected via steel tube to the actuator chamber to collect high-bandwidth measurements in a variety of configurations. A photograph of the tube (without sensor) is provided in Figure 310. Unfortunately, due to difficulties in correcting the data given the presence of the tubing as shown in benchtop tests performed after the second wind tunnel test entry, very little usable data was collected. Data collected was highly uncertain; however, a best attempt was made to estimate the realistic peak pressures attained in order to improve the CFD model of the actuator boundary condition. Those results are summarized in Figure 311. These measurements also provided an indication of the approximate actuation pulse-width or duration, another important parameter for the CFD model. A single pulse-width was measured to be approximately 0.7ms for all frequencies plotted in Figure 311.

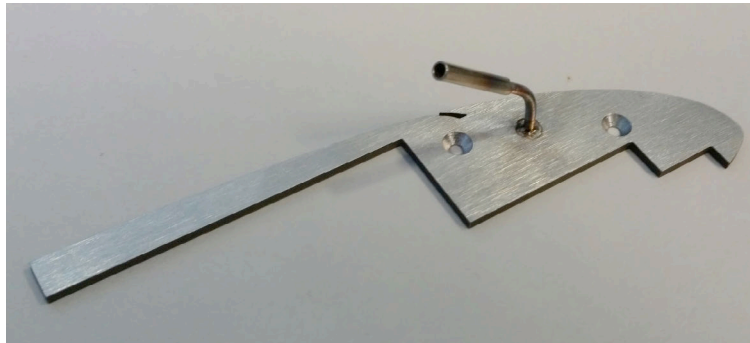


Figure 310. Tube for measuring chamber pressure.

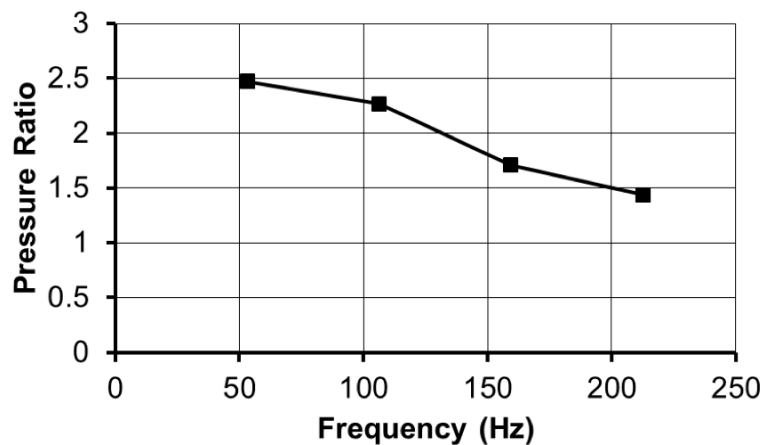


Figure 311. Pressure ratio as a function of frequency as measured from chamber pressure sensors at Mach 0.3,  $\alpha = 18^\circ$  conditions.

## 7. Comments on Three-Dimensional Effects

The limited span of the actuated region had important effects on the coefficients measured at the midspan for actuation-on cases. Although no attempt was made to correct the coefficients for



these effects, the following analysis provides estimates on how the coefficients measured, particularly drag, may be affected by the limited actuated span.

Only 33.1% of the span of the airfoil was actuated in the single-row configuration. As such, when actuation is working effectively and reattaching flow in this region, raising the local lift coefficient at the midspan, a loading distribution wherein high-lift occurs at the midspan while nominal lift occurs elsewhere is created, as shown in the schematic of Figure 312. When the local lift coefficient varies about the span in this manner, the local circulation varies as well, and this suggests that spanwise vorticity will occur about this, region resulting in counter-rotating vortices oriented as in Figure 312. These vortices create a downwash over the wing, which can be calculated using Biot-Savart law for an array of semi-infinite vortices governed by

$$dw = \frac{\frac{d\Gamma}{dx}dy}{4\pi(y_0-y)}.$$

For the purposes of this analysis,  $y$  is defined as shown in Figure 312. Since the loading distribution is not known, two loading distributions were assumed and used to band the range of induced drag at the midspan. Results for elliptic and rectangular loading distributions are shown in Figure 313. To construct these distributions, experimental results from Mach 0.3,  $\alpha = 20^\circ$  cases for the clean leading edge and  $F^+ = 0.4$  are used. The lift coefficient measured for  $F^+ = 0.4$  was used to set the peak value in the distribution (at  $y = 0$ ). The lift coefficient measured for the clean leading edge was used to set the minimum value. The rectangular loading distribution keeps the vortices at a significant distance from the midspan; thus the resultant downwash and induced drag at the midspan are reduced. On the other hand, the elliptic distribution allows some vorticity to occur nearer to the midspan, resulting in higher induced drag (note that the total induced drag is still minimized by the elliptic distribution, as expected).

These results suggest that induced drag for the conditions below may result in 0.086-0.13 increases in drag coefficient at the midspan for actuation-on cases. The magnitude of the induced drag is thus very significant in comparison with the amounts measured and would tend to increase the measured drag for actuation-on cases compared to what might be expected from a truly two-dimensional test.

Finally, the effects of three-dimensionality are not limited to drag only. It is expected that this three-dimensionality has a strong effect on the moment by modifying the pressure along the aft portion of the airfoil, which can highly impact moment coefficient. This was evidenced by inspection of the deep dynamic stall case at Mach 0.2, see Figure 202. Also, depending on the slope of the lift-curve, which tends to be negative in the post-stall regions where COMPACT is particularly effective, the downwash, which creates induced drag, may also change the measured lift.

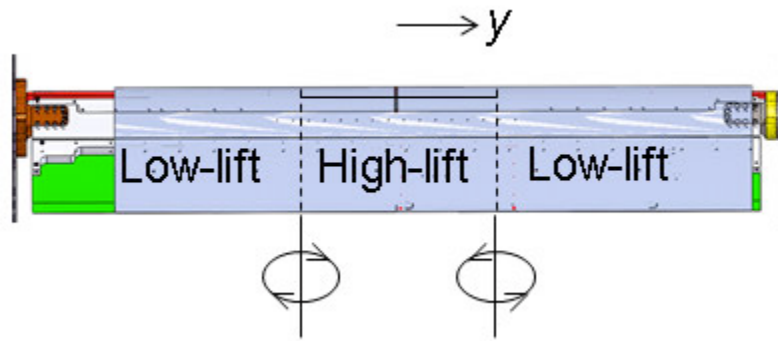


Figure 312. Schematic representation of the spanwise vortices created due to high-lift created in the actuated region.

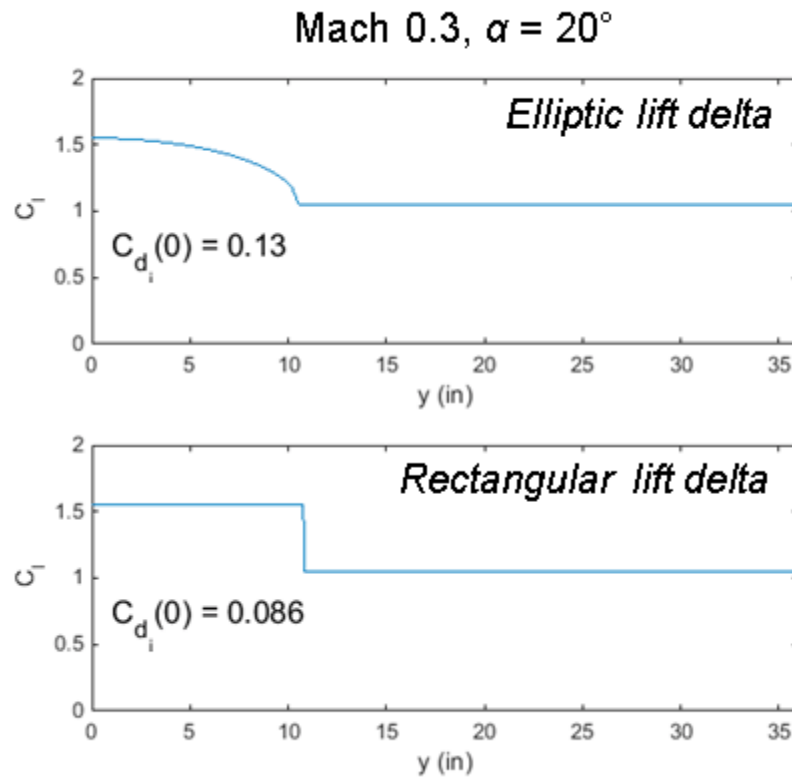
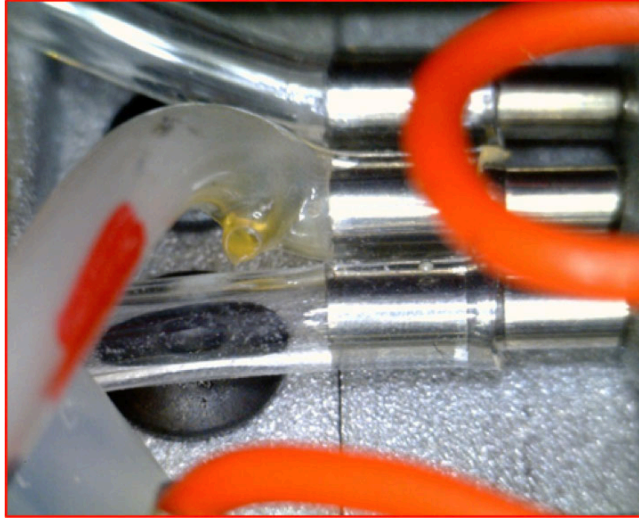


Figure 313. Induced drag results based on two assumed lift distributions.

## **8. Post-Test Actuator Examination**

Following the test entry, several noteworthy things were observed regarding the condition of the actuators as the model was disassembled. For both the single and dual-row actuator arrays, the urethane tubing of the hydrogen lines experienced an appreciable discoloration and clouding over roughly the first inch immediately upstream of the actuators. No similar discoloration was observed on any of the air lines for any of the actuators. This is likely due to the higher flow rates in the air lines, which provide both increased cooling and reduced backflow into the lines during the high pressure burst of the combustor. Both of these impacts expose the tubing to less heat, either from conduction through the metal tubulation or hot combustion products momentarily flowing back into the tubing.

For the single-row actuator arrays, this heating seems to have had no detrimental impact on the gas lines or actuator operation. However, the dual-row actuator arrays experienced a number of failures in the gas lines that were only observed at the end of the test entry. A typical failure is seen in Figure 314, where a rupture to the hydrogen line may be seen in close proximity to the metal tubulation (the previously described discoloration of the line is also visible). Of the 32 total actuators in the dual-row configuration, 8 experienced ruptures in their hydrogen lines: actuators 1, 4, 7, 9, 11, and 16 on the lower array; i.e., the array closer on the tunnel floor side of the model centerline, and actuators 7 and 13 on the upper array (for reference, the actuator numbers may be seen in the picture in Figure 315). The line ruptures in the dual-row arrays are likely the result of higher overall temperatures compared to the single-row arrays (with some indications of this observed during testing with the IR camera imaging) due to denser packing of the actuators. In addition, the tight packing of the actuator rows necessitated shorter bulged tubulations to be used for the tubing connections (with roughly 0.25" length protruding from the actuators versus 0.45" for the single-row). To the extent the tubulations act as cooling fins, the longer ones may be expected to transfer less heat to the attached urethane tubing. Increased use of metal tubing (or increased lengths of metal tubing prior to a transition to plastic tubing) can be expected to mitigate this problem in future designs.



**Figure 314. Magnified view of ruptured hydrogen line from dual-row actuator array.**



**Figure 315. Assembled dual-row actuator array with actuator numbering shown.**

The increased heat exposure is also seen in thermal wear on the spark electrodes for some of the dual-row actuators. Figure 316 shows the spark electrodes for actuators 16 and 11 of the lower array. Actuator 16 (at left) shows appreciable pitting in the surface of the electrode wire (made from a silver-plated copper wire), while actuator 11 (right) has experienced actual melting of the closest electrode. Electrode degradation of this type is seen primarily on those actuators, which also experienced hydrogen line failures, suggesting that they may have experienced a steady flame condition for extended periods. It is not believed that this type of wear to the spark gap would have precluded spark firing or ignition; however more robust materials may be advisable for future implementations.





**Figure 316. Spark electrodes for actuators 16 (left) and 11 (right) of lower array of dual-row actuators.**

Any actuator with a ruptured hydrogen line was definitely no longer functional by the end of the two days of testing with the dual-row arrays. Detailed review of the data collected from the IR camera for Run 92 (Mach 0.5) reveals that actuator 13 from the upper bank, and actuators 11, 9, and 1 from the lower bank had exhibited significant standing flames for large portions of time, which likely rendered them inoperable. Ultimately, it may be said that the results from the dual-row tests represent a floor for the actuator performance and one that is likely to be improved upon in any future testing.

## **9. High-Speed Test Concluding Remarks**

The results collected through Entry 1 and Entry 2 at the NASA Glenn IRT wind tunnel indicate that COMPACT actuation is capable of increasing post-stall steady lift and suppressing deep dynamic stall on a VR-12 airfoil at Mach 0.2, Mach 0.3, and Mach 0.4. No significant benefits were shown at Mach 0.5.

Throughout Entry 1, COMPACT was limited to relatively low frequencies,  $F^+ = 0.2$  to  $0.4$ . The improved single-row actuation in the second entry substantially improved actuator capability and spanwise uniformity at higher frequencies,  $F^+ = 0.4$  to  $1.0$  at Mach 0.2, greatly increasing the performance of COMPACT for Mach numbers up to 0.4.

These benefits were determined relative to the baseline VR-12 airfoil, and occurred even though replacing the smooth, baseline leading edge with the COMPACT leading edge lowered the static stall angle and reduced post stall lift for conditions when the actuation slots were sealed, when they were open without actuation, and when they were open with steady bleed air present.

Partial cycle COMPACT operation proved as advantageous in increasing cycle-averaged lift coefficient as full-cycle operation. For all actuation frequencies at Mach 0.3 and 0.4, actuation was only required over  $1/3^{\text{rd}}$  of the pitch cycle. The optimum actuation incidence range corresponded to starting COMPACT prior to moment stall and continuing through the start of the downstroke. Actuation through the mean angle on the downstroke was not shown to be necessary.

Although not as impactful as uninterrupted spanwise actuation, non-continuous span operation of the single-row COMPACT configuration showed a strong ability to improve post-stall lift behavior. This offers potential for hydrogen storage reduction.

The single-row slots at  $x/c=0.10$  spanning 33.1% of the VR-12 wing provided larger dynamic stall alleviation at the centerline than the dual-row actuators spanning 14.9%, for all test conditions. Comparisons of front and back row actuators operating in isolation indicate that  $x/c=0.10$  is preferable to  $x/c=0.175$  for all Mach and dynamic stall motions studied.

Firing multiple actuators simultaneously or with alternating pulses provides additional performance increases compared to single-slot operation at  $x/c=0.10$  for the same span. An optimum phase delay for alternating triggering was not determined but the limited data acquired here suggests that it is closely associated with the freestream velocity.

The marginal aerodynamic increases found through dual-row operation, relative to single-row, coupled with the added complexity introduced and problems observed post-test suggest that multiple slots are not the best path forward at this time.

## XII. Post-Test CFD and Comparisons with Experiments

After completion of the high-speed wind tunnel tests, modifications were made to the CFD methodology and additional cases were executed. Since two-dimensional CFD was heavily used for the aerodynamic design before the IRT test (see Section 5), the post-test CFD effort only includes 2D simulations. CFD results were compared with relevant experimental data. Differences between CFD and the experiments were discussed. Effects of the actuator frequency on the COMPACT performance were investigated for potential improvements to the actuator.

### 1. Modified computational methods

Four major features are different from the pre-test CFD.

- The actual COMPACT slot geometry is used in the post-test CFD.
- The actuator boundary condition (Eq. 1) was replaced with Eqs. 3 and 4 below.
- The pulse duration  $T_{pulse}$  is reduced to 0.7 msec from 1 msec.
- Actuator frequencies in the IRT test are used in the post-test CFD, whereas  $F^+ = 0.74$  ( $M=0.3$ ) and  $F^+ = 0.56$  ( $M=0.4$ ) were used for pre-test CFD.

The exact COMPACT geometry was introduced in the CFD, as shown in Figure 317. Similar to the previous approach, the slot geometry is included in the CFD grid, but the chamber is not. Boundary conditions relevant to COMPACT are applied to the bottom of the CFD actuator.

To incorporate a more realistic pressure ratio, the actuator boundary condition was modified. Experimental data of the pressure ratio  $P_r(t)$  are based on the variation in the measured chamber pressure. CFD without actuation indicates that the chamber pressure is similar to the pressure outside of the actuator  $P_{act,out}$ , particularly the pressure on the upstream surface (see Figure 318). It is expected that the chamber pressure just before the next pulse  $P_{act,b,0}$  is close to the pressure at the actuator outlet  $P_{act,out}$ . Consequently, the following pressure boundary condition Eq. 2 is obtained.

$$P_{act,b} = P_r(t)P_{act,b,0} \quad (2)$$

The new reference pressure  $P_{act,b,0}$  holds its value only during the pulsation. It is updated with the extrapolated pressure on the boundary just before the next pulse starts. Note that the previous boundary condition in Section 5 used the free-stream pressure as the reference pressure, which does not well represent the test condition. This is because the free-stream pressure is often larger than the actuator outlet pressure on the suction surface  $P_\infty > P_{act,out}$  for conditions considered here. In post-test CFD, when the pressure is set to  $P_{act,b}(t)$ , the density  $\rho_{act,b}$  and the velocity  $\vec{u}_{act,b}$  are extrapolated. This approach is similar to the original CFL3D boundary type 2002; a notable difference is the time-dependent pressure. Note that the stagnation relationship in pre-test CFD (see Eq. 1) for the velocity boundary condition is not used in post-test CFD anymore.

It was observed that the flow can leave the CFD domain through the actuator boundary due to the pressure fluctuation on the suction-side surface. The pressure oscillation is generated by the nominal shedding, which leads to outflow via the actuator boundary when  $P_{act,b,0} < P_{act,out}$ . It was observed that such outflow can cause CFD instability. To remedy this numerical issue,

throttling the flow between pulses was pursued. For simplicity, the jet velocity is set to zero between pulses. The pressure is extrapolated, and the density is set so that the temperature at the actuator boundary is equal to the free-stream value. The complete boundary condition is written as Eqs. 3 and 4. Eq. 3 is used for the pulse duration, and Eq. 4 is used between pulses. The wall velocity  $\vec{u}_{wall}$  is set by the airfoil motion.

$$\begin{aligned}\rho_{act,b} &: \text{extrapolated} \\ \vec{u}_{act,b} &: \text{extrapolated} \\ P_{act,b} &= P_r(t)P_{act,b,0}\end{aligned}\tag{3}$$

$$\begin{aligned}\rho_{act,b} &= \rho_{\infty}(P_{act,b}/P_{\infty}) \\ \vec{u}_{act,b} &= \vec{u}_{jet} + \vec{u}_{wall}, \vec{u}_{jet}=0 \\ P_{act,b} &: \text{extrapolated}\end{aligned}\tag{4}$$

Based on measurements, it was confirmed that a sinusoidal profile in time represents the measured  $P_r(t)$  well during the actuation duration  $T_{pulse} = 0.7msec$ . Peak values of the pressure ratio were obtained from the measurements at  $\alpha = 18^\circ$  and  $M=0.3$  for selected frequencies  $f_{act} = 53.1, 106, 159$ , and  $212$  Hz. In post-test CFD, it is assumed that the peak pressure ratio  $P_{r,peak}$  only depends on the dimensional frequency  $f_{act}$  due to the limited measurement. For other frequencies considered in the post-test CFD,  $P_{r,peak}$  is linearly interpolated. The dimensional frequency  $f$  and its nondimensional value for the current CFD are summarized in Table 40.

Other aspects of the computational method including unsteady RANS with the SA model remain same. Only 2D CFD computations were conducted.

## 2. Post-test CFD results

### A. Steady airfoils

Steady airfoils were simulated for three Mach numbers  $M = 0.3, 0.4$ , and  $0.5$ , as shown in Figure 319. The aerodynamic lift and moment agree well with the experimental data for the clean airfoil. Slight differences between computational and experimental data for the clean airfoil are probably related to any 3D features in test conditions, which are not captured in the 2D CFD. No tunnel walls were included in the CFD. Any effects associated with the finite wing span cannot be captured in the 2D CFD. It should be noted that the CFD drag is the total drag, whereas the experimental drag is the pressure drag only. Also note that the experimental measurement of the pressure drag was limited by the small number of pressure taps at a single station. Consequently, quantitative comparison between the CFD and the experimental drag is not pursued here.

CFD results indicate negligible differences in the aerodynamic forces between the clean and the modified VR-12 airfoils across the Mach numbers and the angles of attack. The experimental data however indicates that the nominal steady stall behavior could be significantly altered by the modified airfoil. The difference is clear for  $M = 0.4$ , and it is noticeable for  $M = 0.2$  in the lift and moment profiles (Figure 319). Based on the experiments, the modified airfoil tends to yield a sharper stall behavior compared to the clean airfoil. Such differences could be related to slight modifications in the airfoil leading edge (LE) due to the assembly of actuator modules. Any LE

modifications potentially related to the hardware fabrication are not modeled in the current computations.

The current CFD predicts that COMPACT does not change the aerodynamic lift before the nominal stall angle, as observed in the experimental data (Figure 319). A noticeable reduction in the drag was obtained in computations before the nominal stall. Benefits from COMPACT were reasonably predicted for angles a few degrees higher than the nominal stall angle. The lift enhancement is predicted well up to  $\alpha = 18^\circ - 19^\circ$  for  $M = 0.2$  and  $0.3$ . However, for higher angles, CFD over-predicts the lift enhancement across the Mach numbers. Pressure profiles were compared for three selected angles at  $M = 0.3$ , as shown in Figure 320. At  $\alpha = 16^\circ$  and  $18^\circ$ , CFD pressure profiles agree well with the experimental profiles with and without the actuation. At the higher angle  $\alpha = 20^\circ$ , CFD predicts significant lift enhancement on the aft suction side, which leads to the large nose-down moment. The experimental pressure profile at  $\alpha = 20^\circ$  is similar to that of  $\alpha = 18^\circ$ , which yields no significant differences in the aerodynamic forces between these two angles. There is a notch in the CFD lift profile around  $\alpha = 18^\circ$ , which was not observed in the experiments. This notch could be related to a strong dependency of the external flow on the actuator frequency for particular flow conditions. For example, at  $\alpha = 20^\circ$  and  $M = 0.3$ , CFD predicts a sharp rise in both  $C_L$  and  $C_D$  with a sharp drop in  $C_M$  as the frequency increases to  $F^+ = 0.4$  (see Figure 321). The trend in the aerodynamic forces is opposite as the frequency continuously increases to  $F^+ = 1$ . CFD results for  $\alpha = 18^\circ$  in Figure 321 indicate that the frequency dependency could be sensitive to flow conditions.

Several factors could lead to the difference between the current CFD and the experiments. The assumption of  $P_{r,peak} = P_{r,peak}(f_{act} \text{ only})$  could be limited.  $P_{r,peak}$ , which was measured at  $\alpha = 18^\circ$  and  $M = 0.3$ , could depend on external flow conditions such as  $\alpha$  and  $M$ . More measurements would help to better construct  $P_{r,peak}$  for various flow conditions. The discrepancy between CFD and experiment, particularly at high angles of attack, could be related to the limits of the current 2D CFD approach. Analysis described in Section 10 indicated that the low actuated aspect ratio can generate 3D flow, which could significantly impact sectional aerodynamic forces. The capability of the one-equation SA RANS model for modeling multi-scale flow features associated with COMPACT and the stall phenomena is also open to question.

Effects of the actuator frequency  $F^+$  on the COMPACT performance were numerically investigated as shown in Figure 321. CFD results indicate that at least  $F^+ \sim 1$  is preferable for steady airfoil  $\alpha = 20^\circ$ . For example, the lift-to-drag ratio  $L/D$  is almost unchanged for the range of  $F^+ = 0 - 0.6$ , but it dramatically increases around  $F^+ = 0.8$  for  $\alpha = 20^\circ$ . The system-level analysis (see Section 12) indicates that the lift-to-drag ratio significantly impacts the rotor performance prediction. Future aerodynamic design of flow control devices would need to consider the impact of the control devices on  $L/D$  for overall benefit prediction.

### **B. Pitching airfoils**

CFD simulations were conducted for selected experimental conditions for pitching airfoils. The actuator frequency  $F^+ = 0.4$  was used for three Mach numbers  $M = 0.3, 0.4$ , and  $0.5$ . One more frequency  $F^+ = 0.8$  was added for  $M = 0.3$ . Phase-averaged aerodynamic forces were obtained using ten pitch cycles. It was observed that more than six cycles are enough for the statistics. Computational aerodynamic forces were compared with relevant experimental data. Effects of the actuator frequency on the COMPACT performance were numerically investigated with additional frequencies and the same peak pressure ratio.

### ***M=0.2***

Current computational results were compared with experimental data for two pitching frequencies  $k = 0.07$  (Figure 322) and  $0.1$  (Figure 323). Based on the hysteresis loop comparison, the gross feature of the baseline dynamic stall is reasonably well predicted in the current computations. The lift hysteresis loop of the clean airfoil at  $k = 0.07$  (Figure 322) agrees well with the experimental loop. The location of the negative moment peak and the peak magnitude help to determine how well the CFD is able to capture the dynamic stall. The moment stall at  $k = 0.07$  is predicted slightly earlier in the upstroke compared to the experimental measurement for the clean airfoil. The large negative moment peak in CFD is probably related to the stall vortex confined in the 2D domain. The confinement could lead to a stable stall vortex and help the vortex grow even further, resulting in the large negative peak. Although detailed features associated to the baseline dynamic stall were not exactly captured in the current computations, the overall agreement is acceptable for the following actuator performance investigation.

The benefit of COMPACT for the dynamic stall was simulated with the actuator frequency  $F^+ = 0.4$  (see Figure 322) for the pitching frequency  $k = 0.07$ . The current CFD predicts a large lift enhancement in the first half of the downstroke, as observed in the experiments. The moment negative peak shifts to about one degree earlier in the upstroke, which is also noticed in the experimental data, the drag peak was reduced in CFD. As stated previously, experimental drag was modified significantly by 3D effects, and therefore, quantitative drag comparison is not pursued here.

Two actuator frequencies  $F^+ = 0.4$  and  $0.8$ , were simulated with the pitching frequency  $k = 0.1$  (see Figure 323). Similar to the  $k = 0.07$  case, the overall COMPACT benefit to the lift was well-predicted in the current simulations. The two actuator frequencies show significant lift enhancement in the overall downstroke region. The lift enhancement is larger for the higher actuator frequency, as observed in the experiments. CFD provides large reduction in the negative peak moment for both the actuator frequencies, whereas the experimental data show noticeable reduction only for the higher frequency  $F^+ = 0.8$ . Similar to the  $k = 0.07$  case, the current computations predict a large reduction in the drag peak with COMPACT.

### ***M=0.3***

Current computational results were compared with experimental data for two pitching frequencies  $k = 0.07$  (Figure 324) and  $0.1$  (Figure 325). Similar to the  $M = 0.2$  cases, the gross feature of the baseline dynamic stall is reasonably well predicted in the current computations. The lift hysteresis loop of the clean airfoil agrees well with the experimental loop for each frequency. Although the current CFD provides a good prediction of lift, it is likely that the general 2D CFD approach is limited to an accurate prediction for drag and moment hysteresis loops. The phase of the negative peak agrees well with the experimental data. However, CFD is limited in providing accurate values for the negative peak.

The performance of COMPACT with  $F^+ = 0.4$  was also well captured in the lift enhancement during the downstroke (Figure 324 and Figure 325). Since the current 2D CFD was not able to capture the baseline moment peak, predicting the moment modulation due to COMPACT is also challenging. In both the pitching frequencies, CFD provides reductions in the moment peak amplitude, whereas the experimental data shows a noticeable reduction for the higher frequency  $k = 0.1$ .

### ***M=0.4***

The baseline and COMPACT results for the  $M = 0.4$  case provide the similar observation made for other Mach numbers. The baseline lift hysteresis loop was reasonably captured in the current CFD. Regardless of the good prediction in the lift hysteresis loop, the 2D CFD approach is limited to an accurate prediction for the drag and moment even for the baseline. The peak moment prediction, including its shape, location, and the peak value, is overall the most challenging for 2D CFD.

The COMPACT performance in the lift was reasonably captured with the enhanced lift in the downstroke. Both CFD and experiments show no significant change in the upstroke. The moment stall was not significantly altered by COMPACT in both CFD and experiments. Based on the CFD and experimental studies for  $k = 0.07$  across the Mach number range, it is expected that COMPACT is more effective in lower Mach dynamic stall, e.g., the  $M = 0.2$  case.

### ***Actuator frequency effects***

Effects of the actuator frequency  $F^+$  on the COMPACT performance for the pitching airfoil were numerically investigated, as shown in Figure 327. Two additional frequencies  $f = 140$  and  $280$  Hz were simulated. The corresponding nondimensional  $F^+$  is listed in Table 40. Similar to the steady airfoil (Figure 321), a higher frequency provides more control benefits. The  $M = 0.2$  case shows a continuous step change in the downstroke lift, as the frequency  $F^+$  is continuously doubled. The current CFD predicts that the additional benefit from high  $F^+$  persists for higher Mach numbers. To achieve this potential benefit from high  $F^+$ , the actuator needs to maintain a sufficient fuel/air refill rate, which could require further improvement in COMPACT. The current actuator would struggle to deliver strong pulses at  $M = 0.3$  with  $F^+ \approx 1$  because the peak pressure ratio is approximated to about 1.1 (Table 40).

### ***Overall COMPACT benefits***

In the aerodynamic design before high-speed tests (Section 5), three parameters were used for the analysis on the overall COMPACT benefit. The same parameters,  $C_{L,avg}$ ,  $C_{D,avg}$ , and  $C_{M,peak}$ , were computed for the new cases conducted in the post-test simulations. Their values were compared with the relevant experimental data and pre-test CFD results. The key performance metrics for COMPACT are summarized in Table 41. As expected from the lift hysteresis modification, the enhancement in the mean lift per the pitch cycle was reasonably predicted in the post-test CFD. The change in the mean lift due to COMPACT  $\Delta C_{L,avg} = (C_{L,avg} - C_{L,avg,COMPACT})/C_{L,avg}$  (%) is plotted in Figure 328. The post-test CFD provided the lift enhancement  $\Delta C_{L,avg}$  within 3%. The pre-test CFD provided much larger lift enhancement probably because of (1) the 30% larger pulse duration  $T_{pulse} = 1 \text{ msec}$ , (2) higher  $F^+$ , and (3) the free-stream pressure  $P_\infty$ , which is  $P_\infty > P_{act,out}$ , used for the reference of  $P_r$  in the pre-test CFD. As seen in drag and moment hysteresis loops, the post-test CFD over-predicted the COMPACT performance in the mean drag and moment peak reduction (Table 41) partly because of 3D and installation effects.

### ***C. Summary***

The post-test CFD activity involved modifications in the computational method for the actual slot geometry and the COMPACT parameters used in high-speed tests. The actuator boundary condition was modified to better represent the pressure rise in the actuator. Because 2D CFD



was heavily used for the COMPACT design in the pre-test computations, post-test CFD involves only 2D computations. A reasonably good agreement to experimental data was achieved for the aerodynamic lift in both the steady and pitching conditions. The lift enhancement from COMPACT was also well captured. The mean lift improvement per the pitch cycle, one of the key metrics, agrees well with the experimental values.

Although the lift enhancement was predicted well, impacts of COMPACT on the drag and moment show noticeable differences to the experiments. This is primarily because of 3D and installation effects, but could also be related to detail flow features not captured well in the current 2D CFD. Higher-fidelity 3D CFD such as large-eddy simulation or detached-eddy simulation would help to capture detail COMPACT performance and 3D features observed in experiments. Furthermore, better definition of actuator parameters, particularly in terms of how the actuators will perform when subjected to full Mach number and pitching conditions (which is difficult at this time to determine prior to tests) could improve the fidelity of simulations.

**Table 40. The peak pressure ratio  $P_{r,peak}$  for selected flow conditions. The bold font indicates the measured values at  $\alpha = 18^\circ$  and  $M=0.3$ .**

$f_{act}$ (Hz)	$F^+$ , M=0.2	$F^+$ , M=0.3	$F^+$ , M=0.4	$P_{r,peak}$
<b>53.1</b>	0.30	<b>0.20</b>	0.15	<b>2.47</b>
71.7	0.40	0.27	0.20	2.40
<b>106</b>	0.59	<b>0.40</b>	0.30	<b>2.27</b>
140	0.78	0.52	0.39	1.91
<b>159</b>	0.89	<b>0.59</b>	0.45	<b>1.71</b>
<b>212</b>	1.19	<b>0.79</b>	0.59	<b>1.44</b>
280	1.57	1.05	0.78	1.10

**Table 41. Summary of key performance metrics for COMPACT compared with experimental data**

Ma	k	$F^+$	Geom	$C_{L,avg}$ post-test CFD	$C_{D,avg}$ post-test CFD	$C_{M,min}$ post-test CFD	$C_{L,avg}$ EXP	$C_{D,avg}$ EXP	$C_{M,min}$ EXP	$C_{L,avg}$ pre-test CFD*	$C_{D,avg}$ pre-test CFD*	$C_{M,min}$ pre-test CFD*
0.2	0.07	-	clean	1.03	0.07	-0.34	0.95	0.14	-0.23	-	-	-
0.2	0.07	0	modified	1.02	0.07	-0.37	-	-	-	-	-	-
0.2	0.07	0.4	modified	7%	-28%	-17%	9%	-1%	0%	-	-	-
0.2	0.1	-	clean	1.03	0.06	-0.18	0.97	0.15	-0.20	-	-	-
0.2	0.1	0	modified	1.03	0.07	-0.24	-	-	-	-	-	-
0.2	0.1	0.4	modified	10%	-44%	-74%	7%	-7%	17%	-	-	-
0.2	0.1	0.8	modified	12%	-49%	-77%	14%	-13%	-46%	-	-	-
0.3	0.07	-	clean	-	-	-	0.90	0.12	-0.29	-	-	-
0.3	0.07	0	modified	1.03	0.10	-0.51	-	-	-	-	-	-
0.3	0.07	0.4	modified	7%	-18%	-14%	7%	14%	-2%	-	-	-
0.3	0.1	-	clean	1.09	0.10	-0.54	0.97	0.11	-0.22	1.09	0.10	-0.54
0.3	0.1	0	modified	1.08	0.10	-0.52	-	-	-	1.08	0.10	-0.53
0.3	0.1	0.4	modified	2%	-16%	-16%	3%	15%	-23%	9%	-53%	-78%
0.4	0.07	-	clean	0.96	0.11	-0.46	-	-	-	0.96	0.11	-0.46
0.4	0.07	0	modified	0.95	0.11	-0.46	0.84	0.12	-0.23	0.95	0.11	-0.45
0.4	0.07	0.4	modified	4%	-3%	-3%	7%	5%	8%	13%	-8%	-15%

\*Four major features are different to the post-test CFD: (1) COMPACT slot geometry, (2)  $F^+ = 0.74$  ( $M=0.3$ ) and  $F^+ = 0.56$  ( $M=0.4$ ) for pre-test CFD, (3)  $T_{pulse} = 1msec$  for pre-test CFD, and (4) the previous actuator boundary condition (Eq. 1 of Section 5)

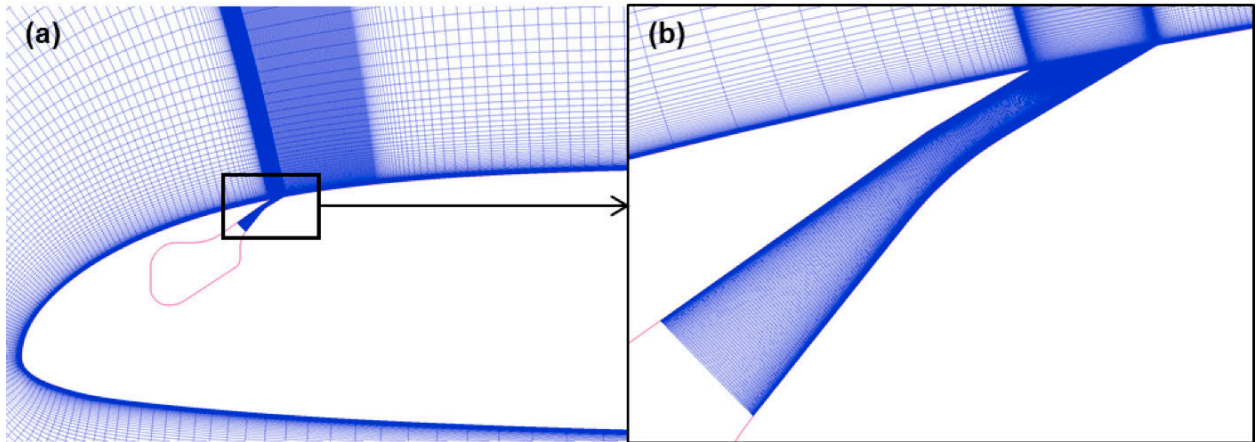


Figure 317. Grid used in the post-test CFD with the exact slot geometry used in the IRT test

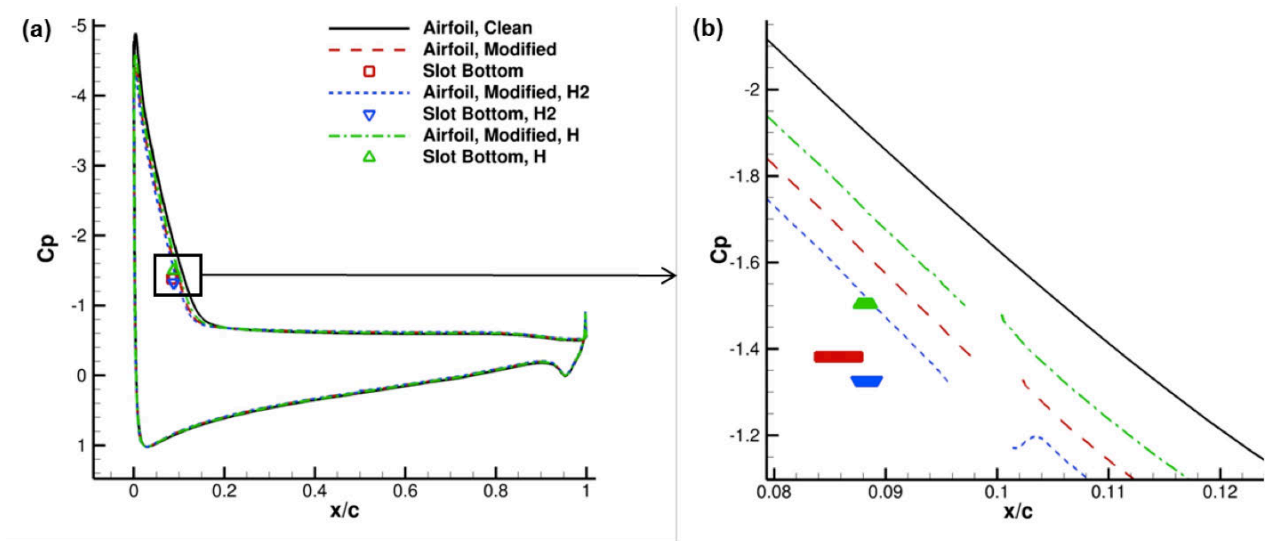


Figure 318. Pressure profiles obtained from CFD simulations at Mach=0.3 and  $\alpha = 18^\circ$ . Four airfoils were simulated: clean, the modified with the actual slot geometry, and two modified airfoils (H and H2) in the pre-test CFD.

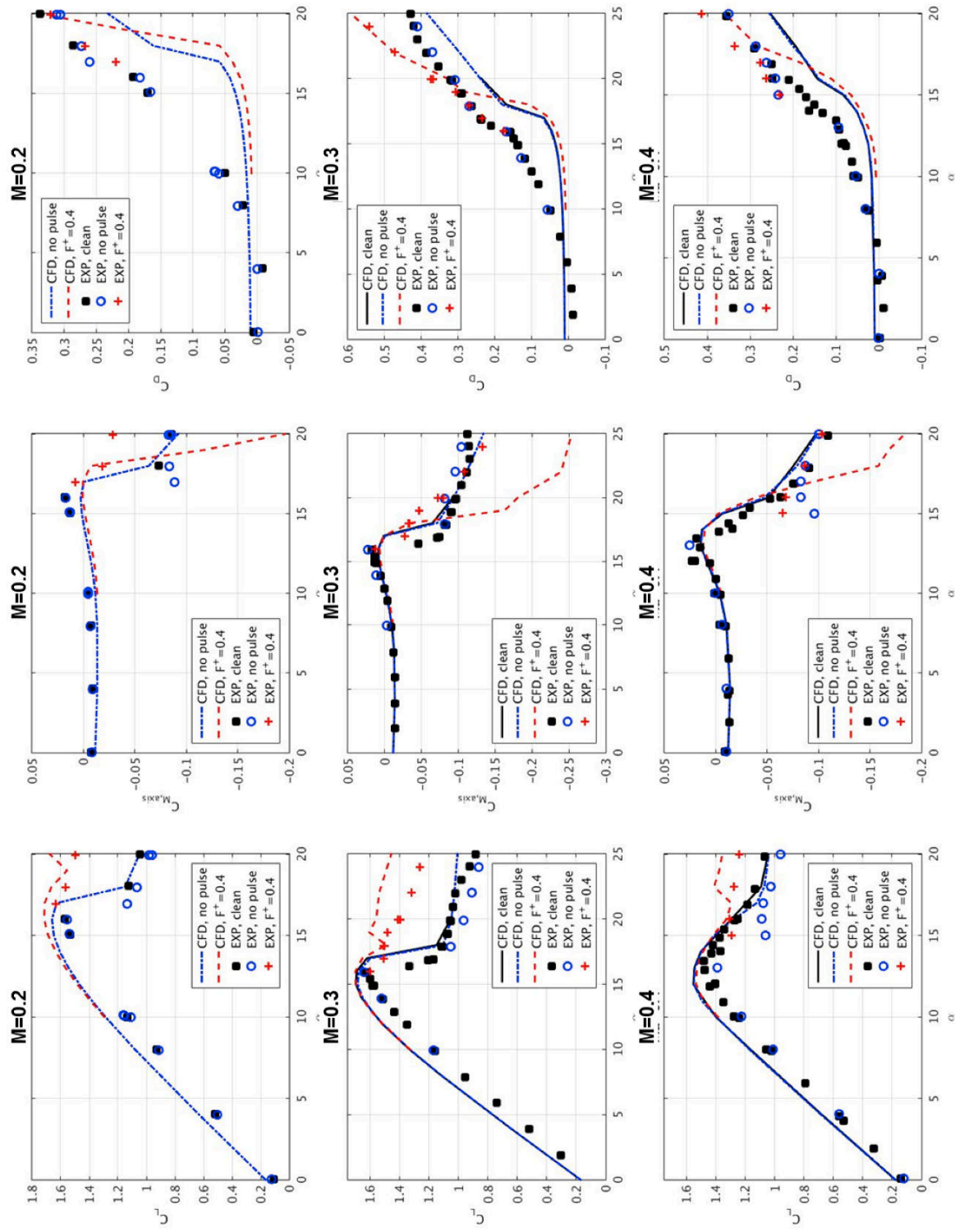


Figure 319. Aerodynamic forces on steady airfoils at  $M=0.2$ ,  $0.3$  and  $0.4$  compared with experimental data

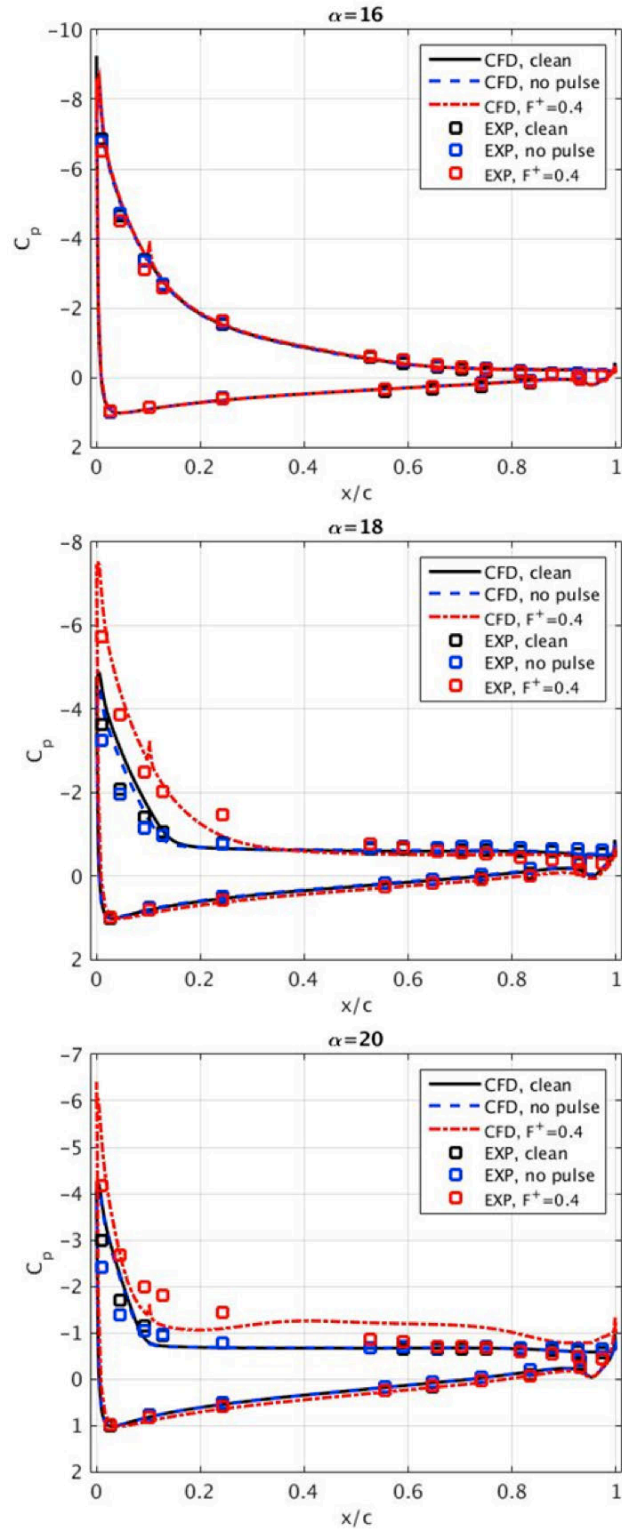
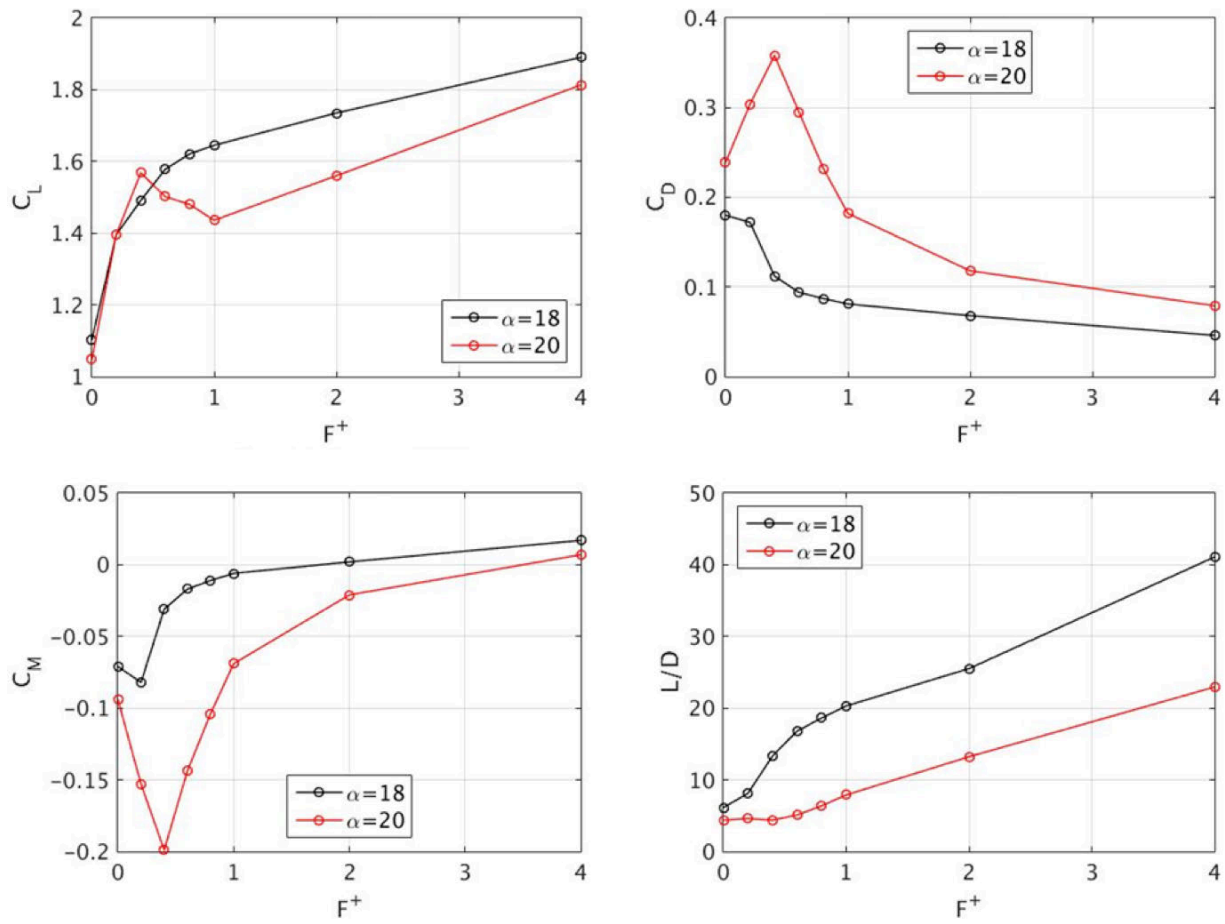


Figure 320. Pressure profiles with and without COMPACT at  $M=0.3$  compared with experiments



**Figure 321. Effects of the actuator frequency  $F^+$  with the fixed peak pressure ratio  $P_{r,peak} = 2.27$  at  $M=0.3$**

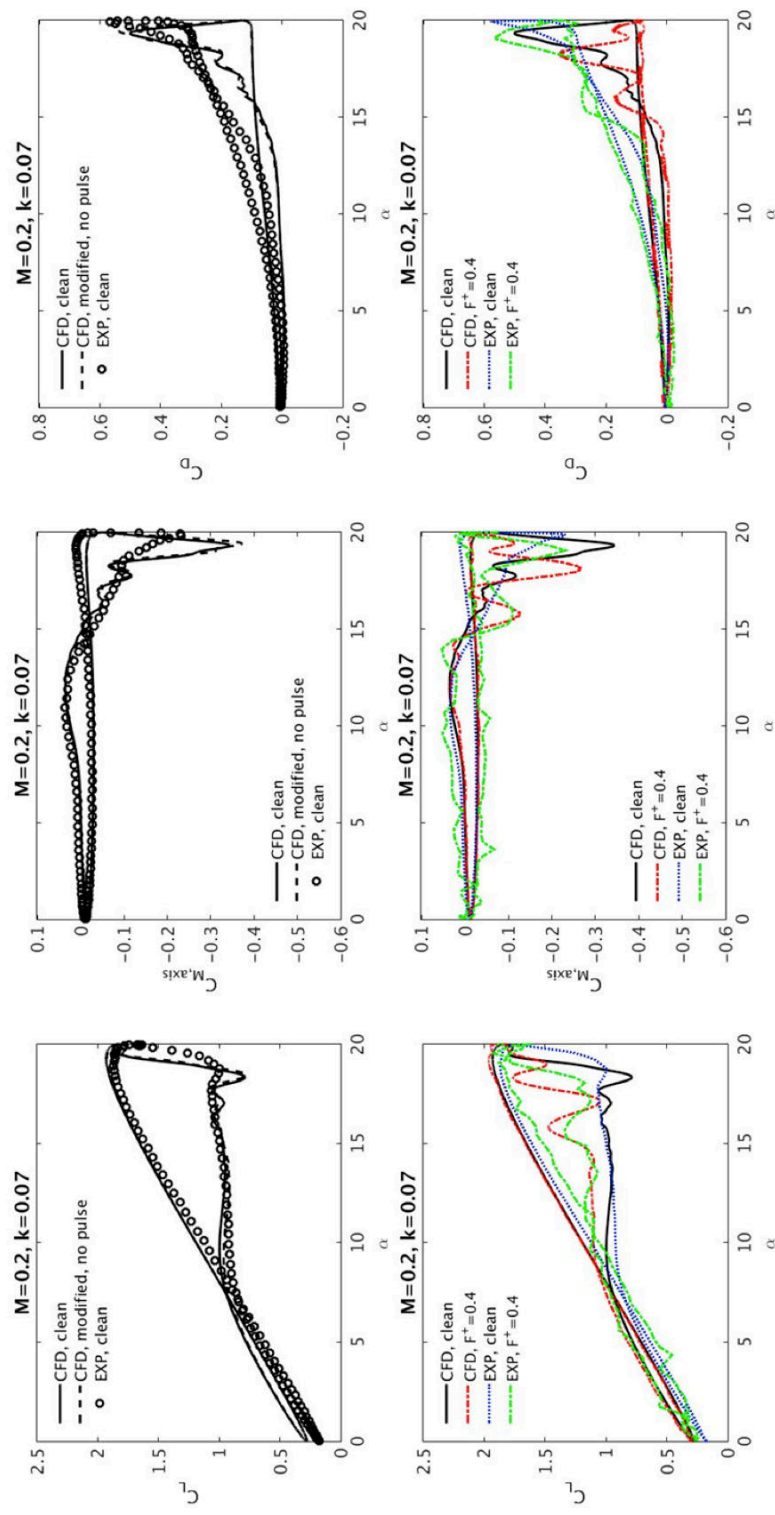


Figure 322. Aerodynamic forces on pitching airfoils at  $M=0.2$  and  $k=0.07$  compared with experimental data



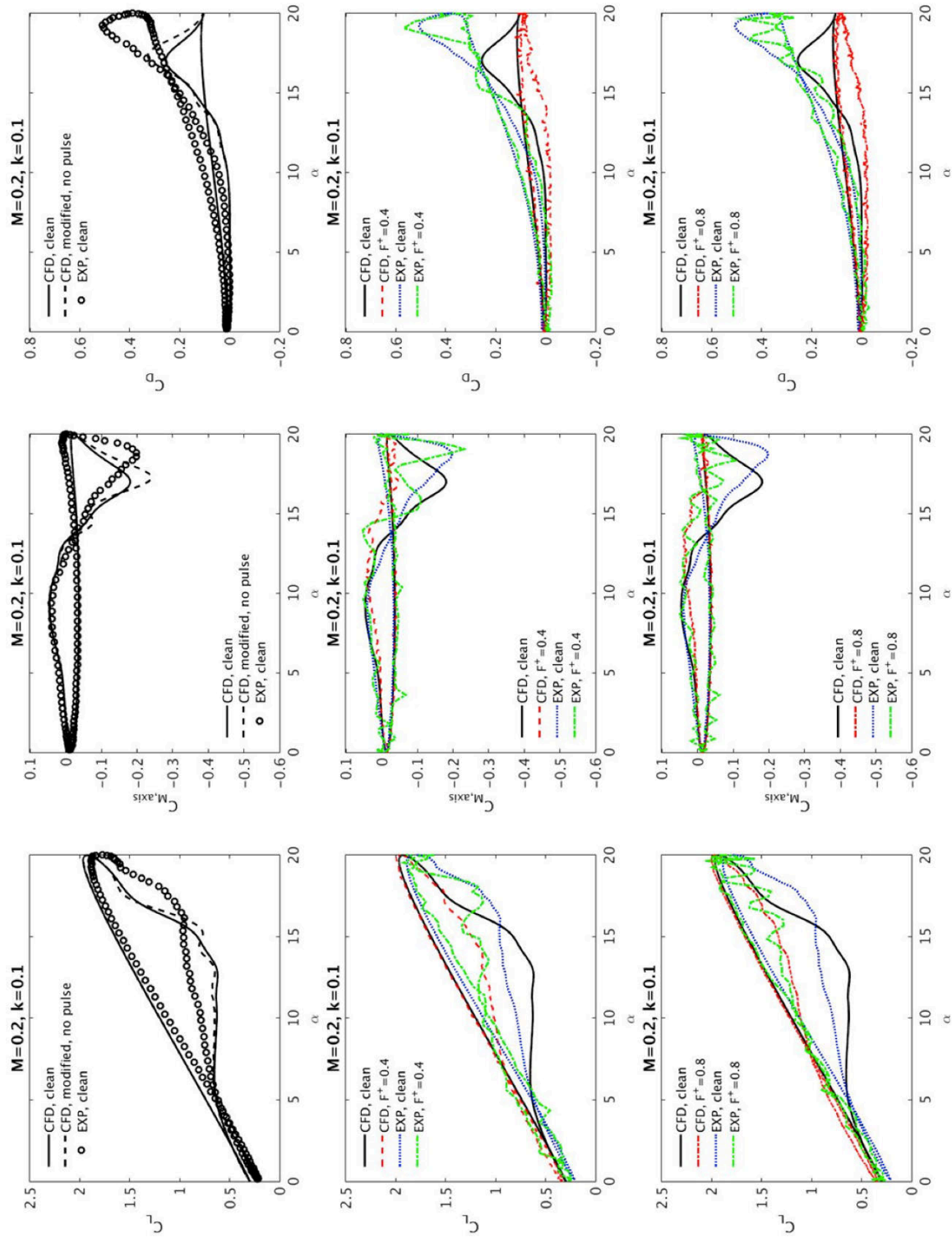


Figure 323. Aerodynamic forces on pitching airfoils at  $M=0.2$  and  $k=0.1$  compared with experimental data

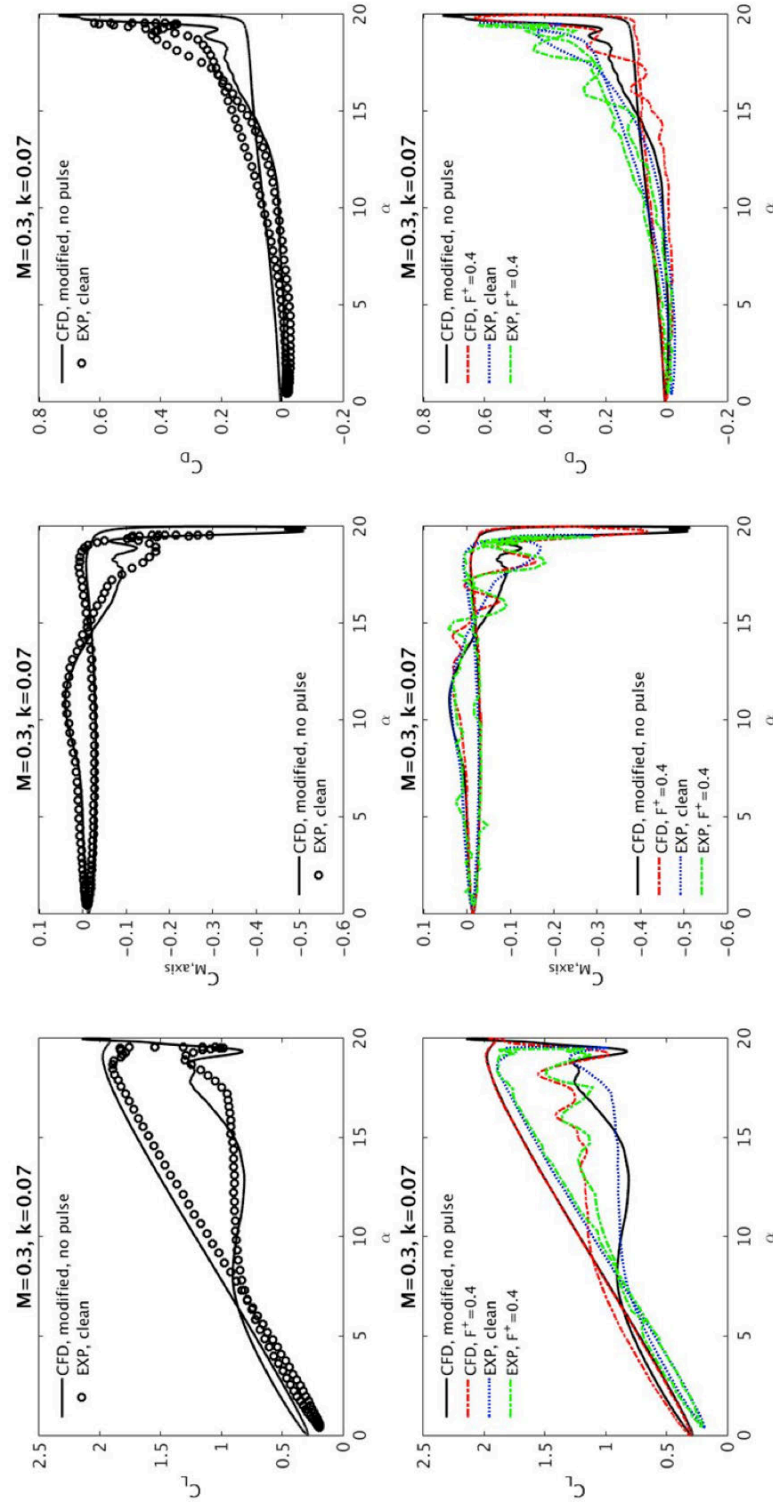


Figure 324. Aerodynamic forces on pitching airfoils at  $M=0.3$  and  $k=0.07$  compared with experimental data

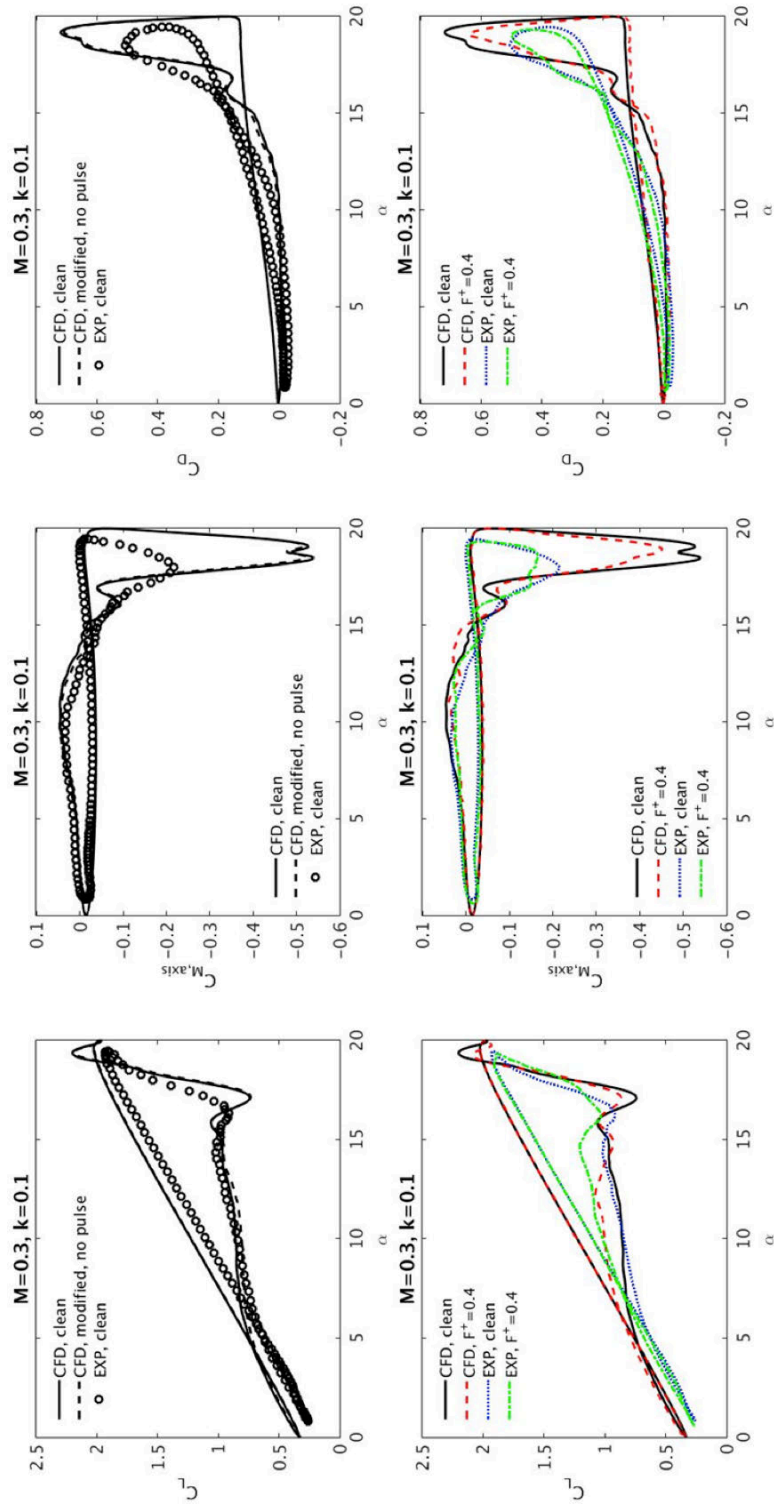


Figure 325. Aerodynamic forces on pitching airfoils at  $M=0.3$  and  $k=0.1$  compared with experimental data

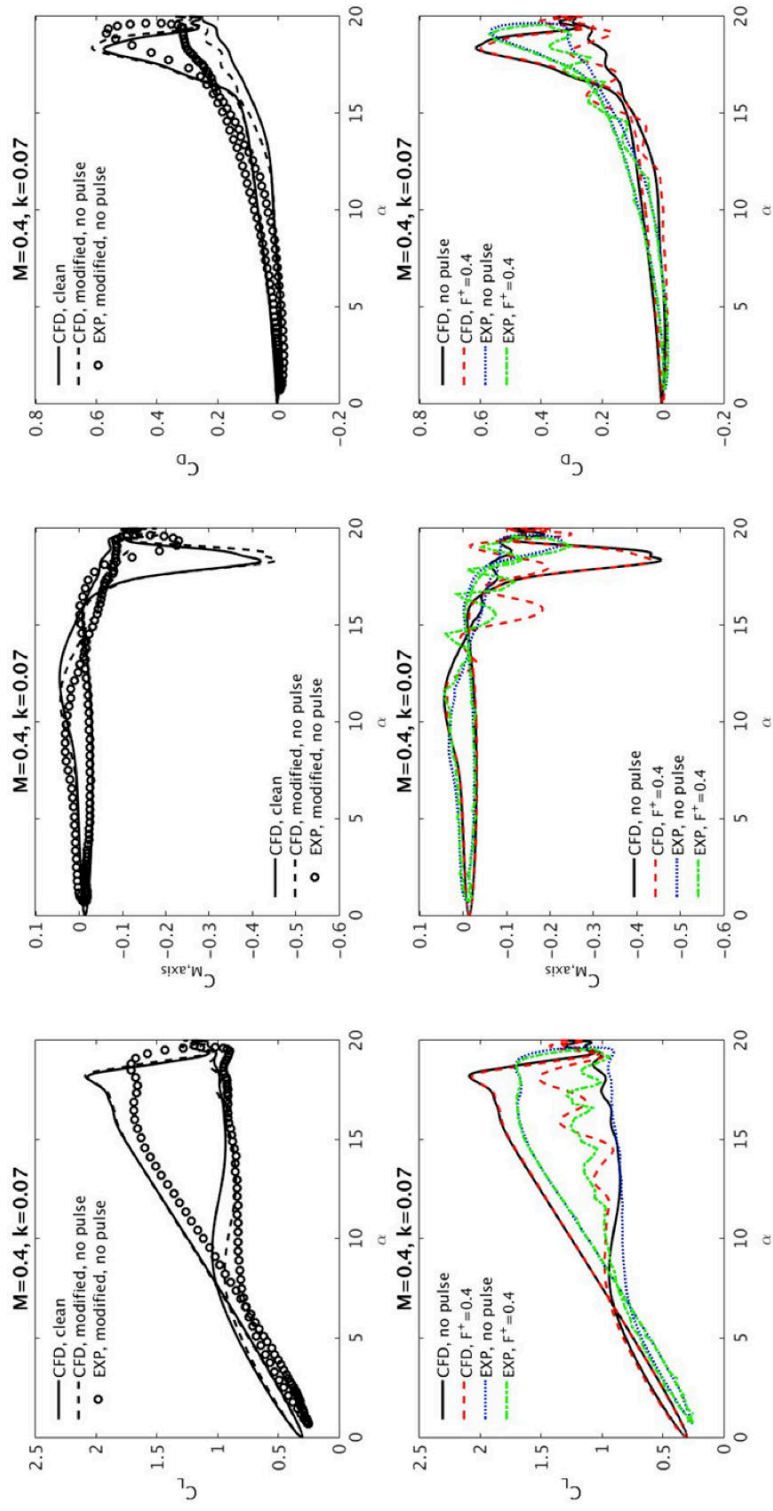


Figure 326. Aerodynamic forces on pitching airfoils at  $M=0.4$  and  $k=0.07$  compared with experimental data

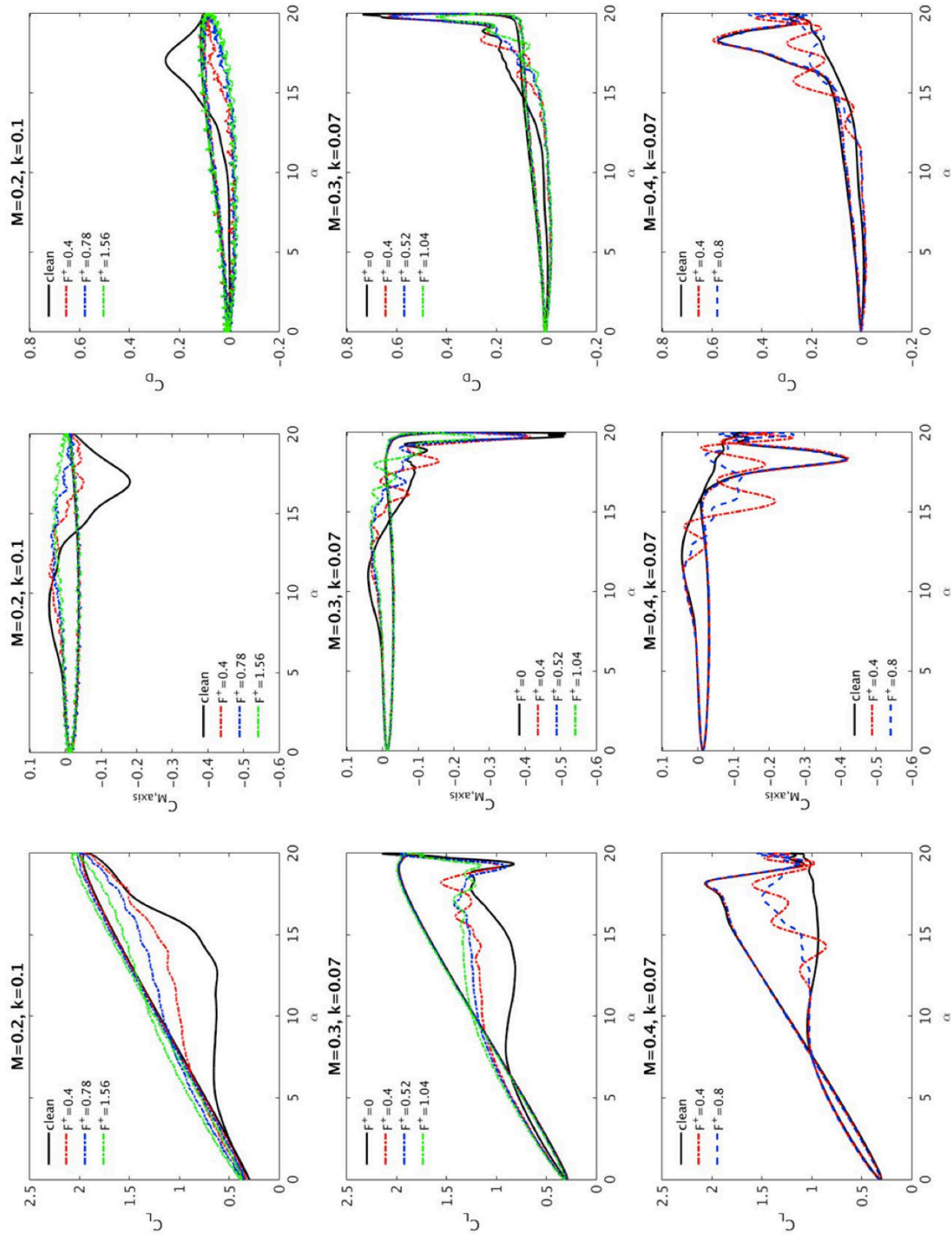
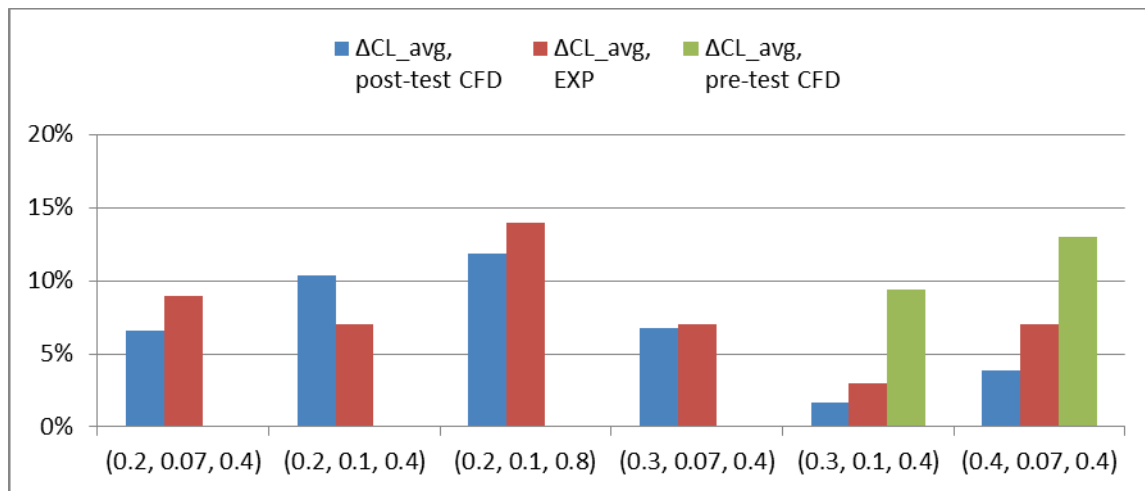


Figure 327. Effects of the actuator frequency  $F^+$  with the fixed peak pressure ratio  $P_{rpeak} = 2.27$



**Figure 328.** The enhancement in the aerodynamic lift predicted in CFD and measured in the IRT test for flow conditions denoted by  $(M, k, F^+)$ .

### **XIII. System-Level Modeling**

The results obtained from the CFD studies and high-speed wind tunnel experiments were reduced and used to estimate the system-level benefits of COMPACT applied to a full-scale rotor. A simple modeling approach has been developed to represent the difference between baseline and COMPACT blade. The study was focused on identifying potential performance benefits that can be realized by COMPACT, especially at high speed and high thrust conditions. The emphasis is also towards maneuver (maximum thrust) and speed improvements, since the technology would likely be used in this manner more than for rotor efficiency.

#### **1. System-Level Modeling Approach**

##### ***A. Trim Solver***

An in-house rotor-trim blade-element analysis (GENTRIM) was used for COMPACT evaluation. The solver was developed at Georgia Tech for rigid blade trim calculations, and further modified at UTRC. The primary reason for selecting this solver is its ease of manipulation for first order estimations of rotor blade designs and control concepts, such as COMPACT. It assumes rigid blades with uniform inflow and harmonic flapping. Its airloads are based on a linear model or airfoil table look-up. To evaluate rotor performance benefits resulting from modified dynamic-stall hysteresis loops, an unsteady hysteresis-loop table was added to the analysis. However, other unsteady corrections or dynamic stall models were not employed. It is also noted that using uniform inflow at high speed conditions typically produces optimistic performance values. The current study evaluates rotor performance in terms of differences from the baseline rotor, and the model is considered appropriate for this purpose. Future analyses would need a more sophisticated wake model.

For the current study, the rotor was trimmed for a specified thrust and zero hub moments. Shaft angle was fixed at 3 degree forward tilt for all flight conditions. For simple and robust simulation, flapping was not allowed. Steady airfoil tables were used for radial sections lower than 0.5R. Both steady and dynamic hysteresis loops were used for outboard sections based on prescribed conditions. The primary focus of the current study was toward high speed and high thrust conditions. Evaluations were performed at  $\mu = 0.3, 0.4, \text{ and } 0.5$  with extended speed sweeps at high-thrust conditions.

##### ***B. Rotor Model***

As a representative rotor, a UH-60A-sized rotor with 4 blades was used. It has a 26.83 ft radius and hover tip speed of 725 ft/s. A straight tip is assumed without 3D tip effects. The VR-12 airfoil is used for inboard sections, while the SSC-A09 airfoil is used for outboard stations beyond 90%R, which differs from a standard UH-60A. The blade has non-linear twist and chord distribution similar to the UH-60A. Several parameters are similar to the UH-60A for the purposes of this analysis, but these calculations do not represent UH-60A performance evaluations.



### C. Dynamic Stall Table

In order to select a proper dynamic stall table, the rotor-blade sectional Mach number ranges were examined at three advance ratios, as shown in Figure 53. On the retreating side ( $\psi = 270^\circ$ ), local Mach number for 0.5R - 0.9R varies between 0.15 – 0.40 at  $\mu = 0.3$ , 0.1-0.35 at  $\mu = 0.4$ , and 0.0-0.25 at  $\mu = 0.5$ . Higher Mach number is also experienced over the aft rotor disk section up to  $M = 0.6$ . Dynamic stall may occur at this location depending on the blade's aeroelastic recoil effect or trim state. However, the current study assumed retreating side stall without elastic motion, and the airfoil table was selected based on the retreating side local Mach range. Table 1 summarizes selected airfoil tables. All dynamic stall loops were generated from 2D CFD simulations. CFD calculations were used in lieu of the high-speed test COMPACT results due to the 3D effects that marginalized COMPACT drag benefits at Mach 0.3 and 0.4. Evidence of these effects are presented and discussed in Chapter 10. For COMPACT rotor cases, the actuation frequency was  $F^+ = 0.78$  for the  $M = 0.2$  case and 0.75 for  $M = 0.3$  case. All hysteresis loops have a mean angle at  $10^\circ$  with  $10^\circ$  amplitude. Reduced frequency for  $M = 0.2$  and  $M = 0.3$  loops was 0.1, and 0.07 for the  $M = 0.4$  loop. The dynamic stall loop was activated only if local Mach remained below 0.5, sectional reduced frequency was greater than 0.01, and if local angle-of-attack remained within the table angle-of-attack range. Otherwise, steady airfoil table data was used. Outboard sections beyond 0.9R used baseline unsteady data only. Typically, blades may have thin airfoils with sweep/taper or anhedral tip shapes, which introduce practical difficulty for COMPACT installation.

Figure 330 compares the dynamic stall hysteresis loops used in this study. In determining the pitch-up/downstroke, blade pitch motion was used instead of angle-of-attack. During the blade upstroke, lift and drag from the upstroke portion is used. Likewise, the downstroke portion is used for blade pitch down motion. For simplicity, the radial distribution of the tables was fixed for all flight conditions. However, the angle-of-attack range and aerodynamic loads were re-scaled based on the rotor-blade local angle-of-attack range as described in the next section.

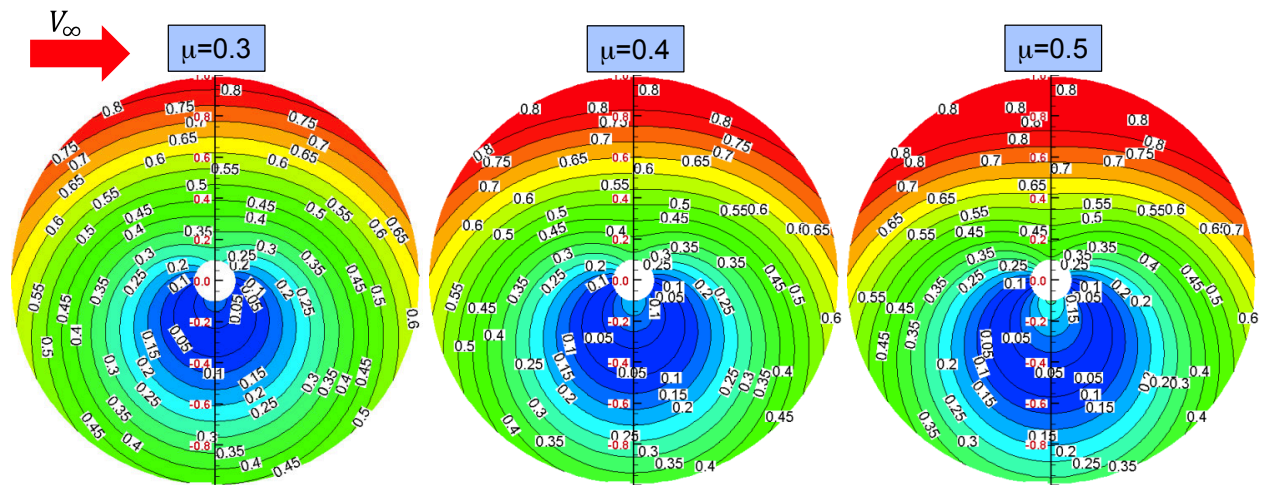
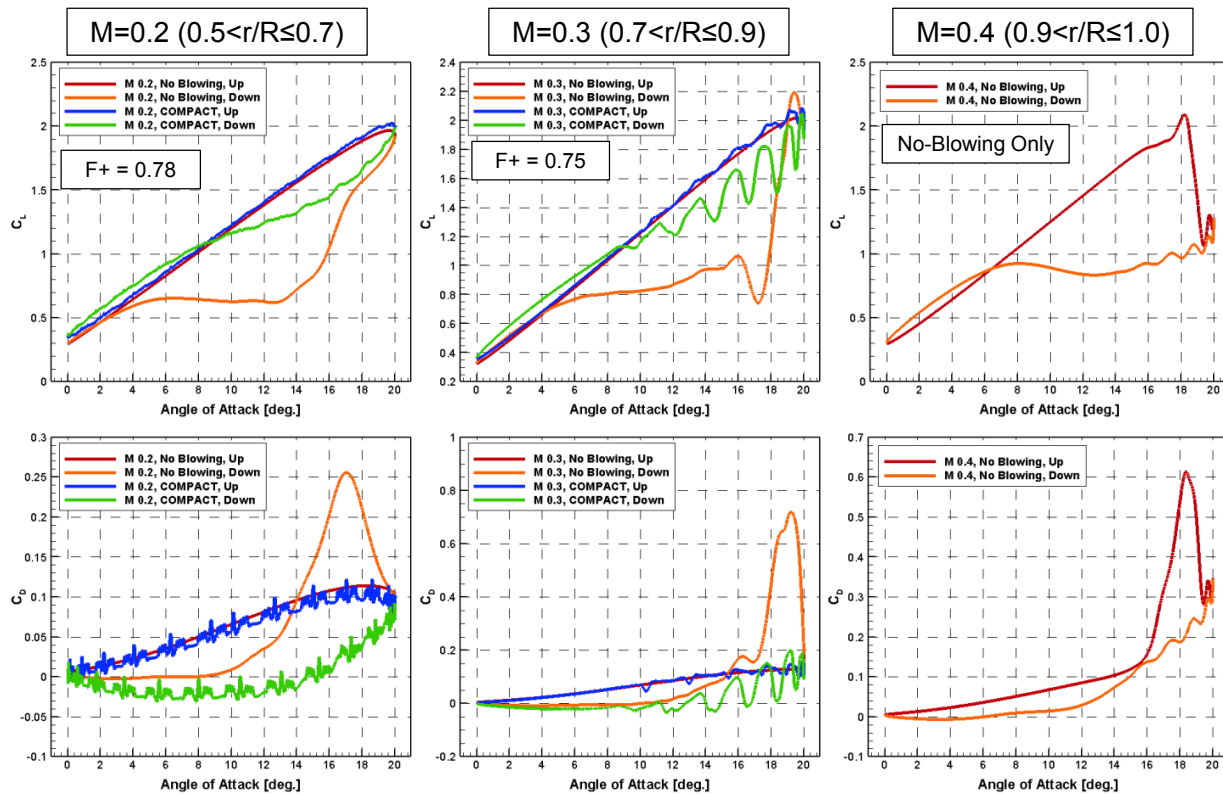


Figure 329. Angle-of-attack distribution at high speed condition.

**Table 42. Dynamic stall hysteresis loop selection.**

Radial section	Table Type	Table Mach	Steady Table (if dynamic stall not activated)
$0.0 < r/R \leq 0.5$	Steady	0.0 - 1.0	VR-12
$0.5 < r/R \leq 0.7$	Dynamic stall (No-blowing & Blowing)	0.2	VR-12
$0.7 < r/R \leq 0.9$	Dynamic stall (No-blowing & Blowing)	0.3	VR-12
$0.9 < r/R \leq 1.0$	Dynamic stall (No-blowing)	0.4	SSC-A09



**Figure 330. Utilized Dynamic Stall Hysteresis Loop.**

#### **D. Dynamic Stall Hysteresis Loop Scaling**

As the trim solver converges to a trimmed pitch condition, each blade section experiences a different angle-of-attack range of over one revolution. The blade's sectional minimum and maximum angle-of-attack may be considerably different from the angle range provided in the unsteady dynamic stall tables. Using unmodified tables may result in abrupt changes in lift and

drag. For example, if the rotor section's upstroke ends in the middle of the table's angle-of-attack range, a non-realistic stall behavior is artificially introduced. Also, the size of the hysteresis loops will vary based on mean angle and amplitude as the airfoil transitions through the different dynamic stall regimes. In order to account for this behavior, the loads and angle-of-attack ranges were re-scaled at each rotor-blade radial section based on the rotor angle-of-attack range over one revolution. Figure 331 illustrates the scaling used in the current study. The loop is shifted based on mean angle, and the shifting follows the original lift slope connecting minimum and maximum angles of attack. Once lift is scaled, drag is determined based on the original L/D. Other modifications are also applied in the scaling process. If scaling is applied to the entire angle-of-attack range, stall occurs only at maximum angle-of-attack, which is too optimistic. Thus, the scaling is applied only if the local angle-of-attack range is within the original unsteady stall table angle range, and local Mach is lower than 0.5. The original loop is used if minimum and maximum angles of attack are outside the original angle range.

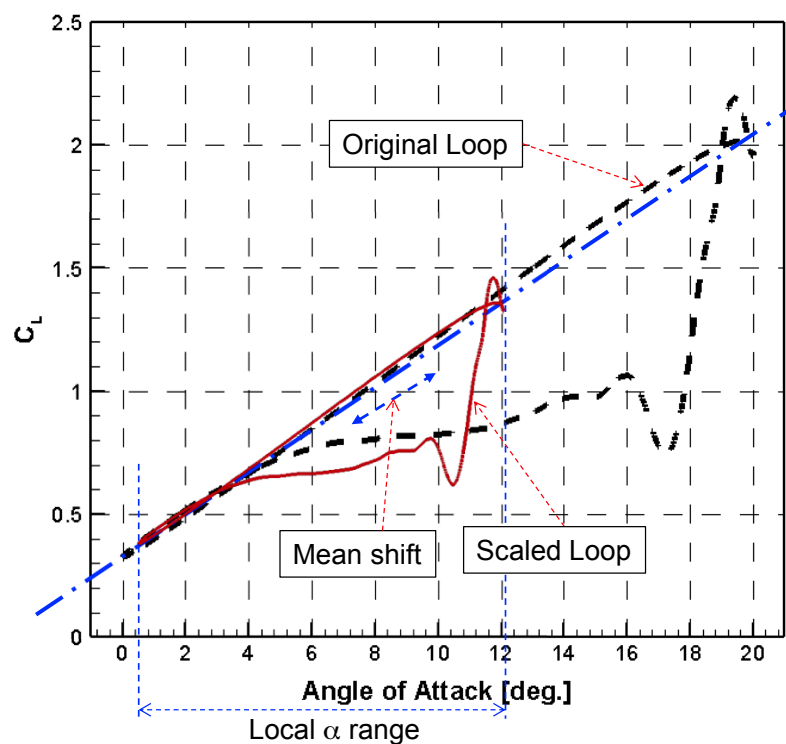


**Figure 331. Dynamic Stall Hysteresis Loop Scaling.**

## 2. Performance Analysis Results

### A. Thrust Sweep

A thrust sweep was performed at three speed conditions ( $\mu=0.3, 0.4, 0.5$ ) and the resultant  $L/De$  and torque is plotted in Figure 332 and Figure 333, respectively. It is clear that the actuation from COMPACT provides substantial performance benefits at all speed regimes simulated here; the benefit increases with increasing thrust and speed. At  $\mu=0.4$ , thrust was increased 12% for

the same  $L/De$  compared to operation without COMPACT at  $C_T/\sigma=0.12$ . At  $\mu=0.5$ , a 20% thrust increase was achieved compared to the no-blowing case at  $C_T/\sigma$  near 0.1. The performance benefit is realized through substantial torque reduction. The blowing and no-blowing cases are compared at a representative high thrust condition ( $C_T/\sigma=0.127$ ) at  $\mu=0.4$ . Figure 334 shows the activated airfoil tables and trimmed pilot control input. As expected, dynamic stall loops were required over most of the retreating side region, but deactivated on the advancing side due to high local Mach greater than 0.5. The pilot control input shows less collective and cyclic control with COMPACT, resulting from the COMPACT augmented lift capability on the retreating side. Figure 335 compares the angle-of-attack distribution, showing a reduction in angle-of-attack on the retreating side by more than 2 degrees from the baseline rotor. Figure 336 compares the thrust and in-plane drag distribution. It is noticed that COMPACT produces higher thrust in the 4<sup>th</sup> quadrant between 70-90% radius and lower thrust through the fore/aft disk section. This results in a more favorable uniform loading distribution compared to the baseline case. The difference in drag is also notable. The benefits are a combination of the local dynamic stall benefits, and the complementary adjustments made throughout the rotor disc. The no-blowing case shows high peak drag near  $\psi = 270^\circ$  due to high  $C_D$  around peak angle-of-attack (Figure 330). It also shows higher drag near  $\psi = 0^\circ$  because of its high angle-of-attack. Notice that this region uses steady airfoil table because local Mach is greater than 0.5. Reduced pitch from the COMPACT case reduced drag in this region. Figure 337 compares section loading at  $r/R=0.8$ . The  $C_L$  and  $C_D$  curves are plotted as function of local angle-of-attack to show the employed hysteresis loop. It can be seen that the unsteady data was activated at an angle-of-attack range greater than  $\sim 9^\circ$ . Because of the high lift capability introduced through COMPACT, the angle-of-attack range is reduced and the hysteresis loop is reduced. The no-blowing case has large drag peak at  $\psi = 270^\circ$ - $320^\circ$ , around its peak angle-of-attack. The COMPACT case produces more thrust for  $\psi = 300^\circ$ - $360^\circ$  during the downstroke, and lower negative peak on the advancing side.

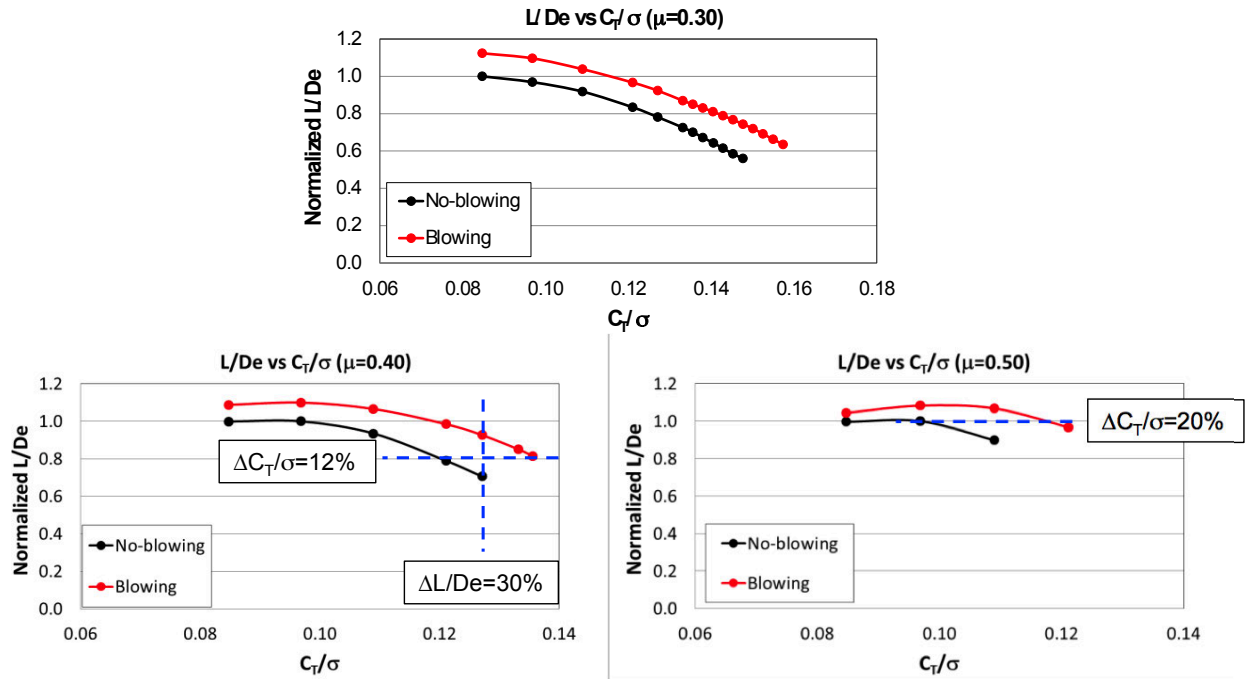


Figure 332. Thrust sweep at  $\mu=0.3, 0.4, 0.5$ : L/De

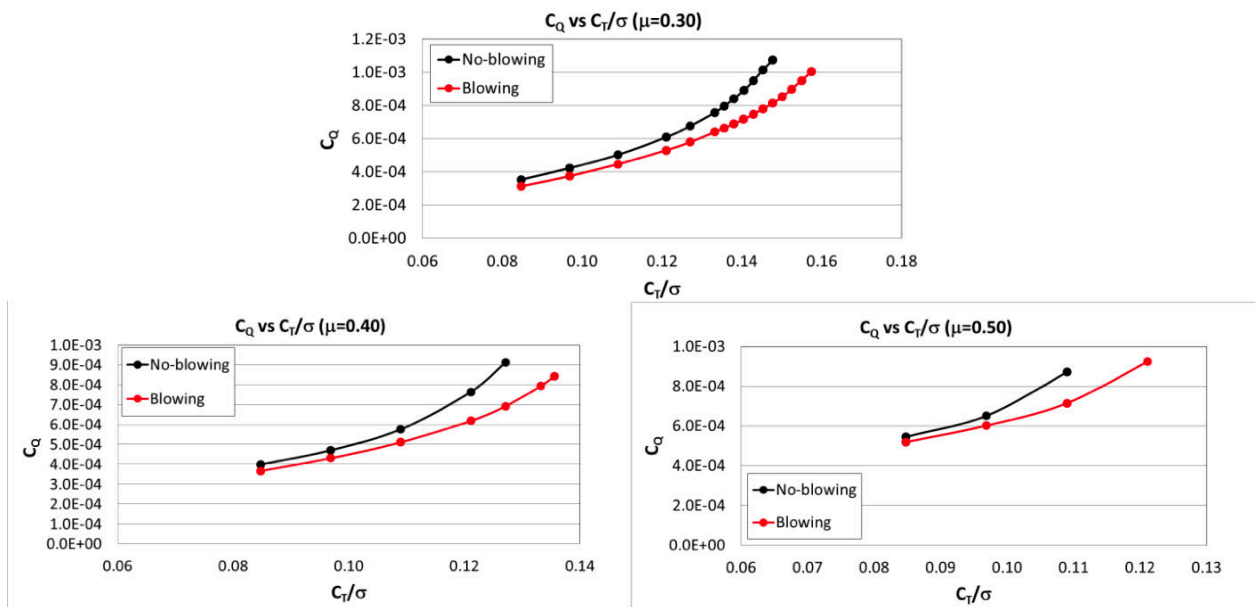


Figure 333. Thrust sweep at  $\mu=0.3, 0.4, 0.5$ : Torque

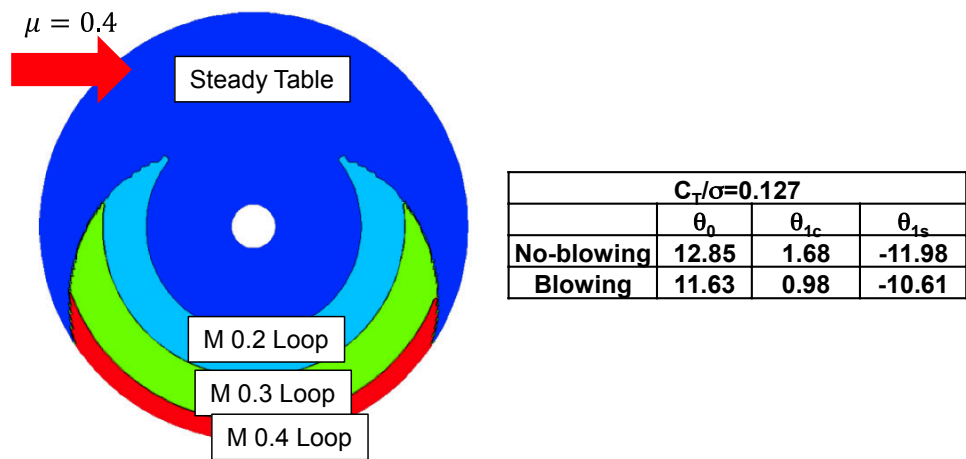


Figure 334. Activated dynamic stall loop and trimmed control input ( $\mu=0.4$ ,  $C_T/\sigma=0.127$ )

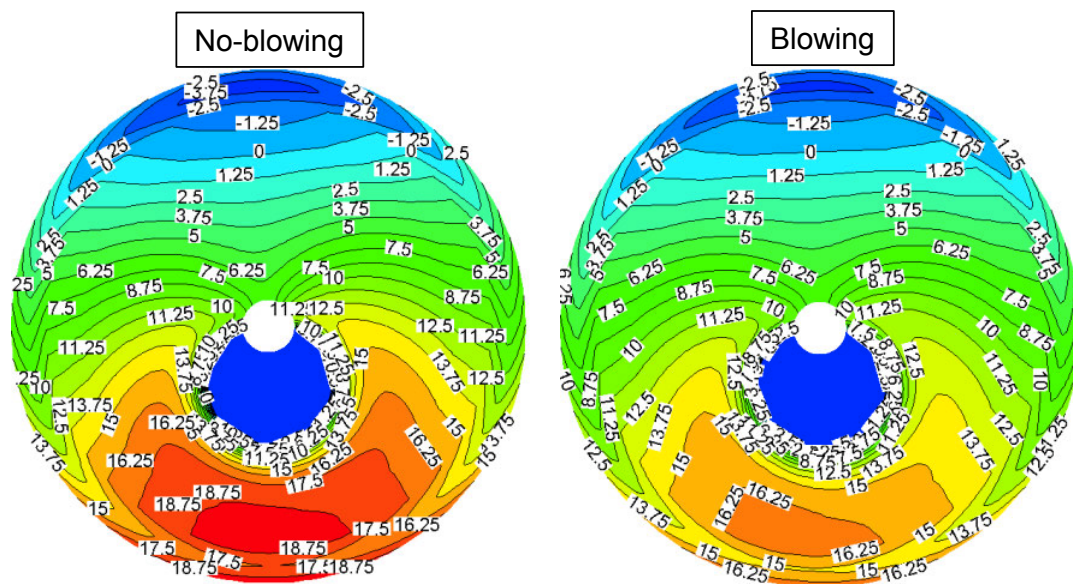


Figure 335. Trimmed angle-of-attack distribution ( $\mu=0.4$ ,  $C_T/\sigma=0.127$ )



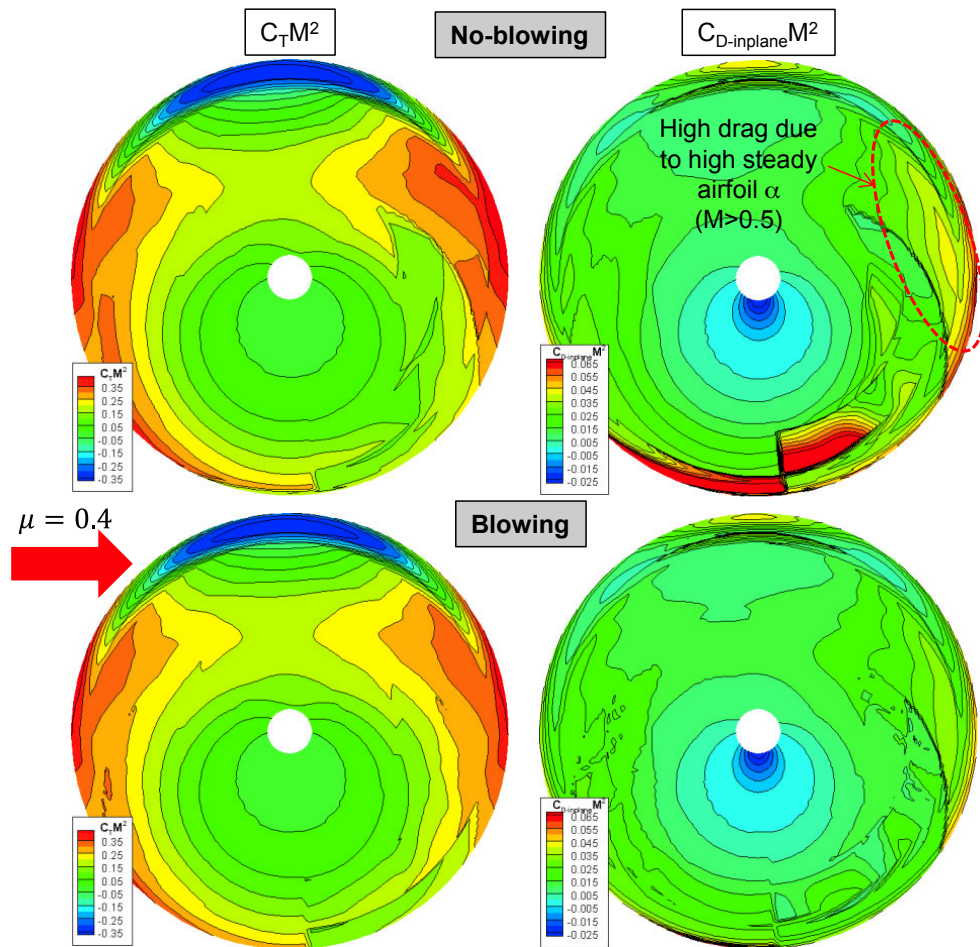


Figure 336. Trimmed loading distribution ( $\mu=0.4$ ,  $C_T/\sigma=0.127$ )



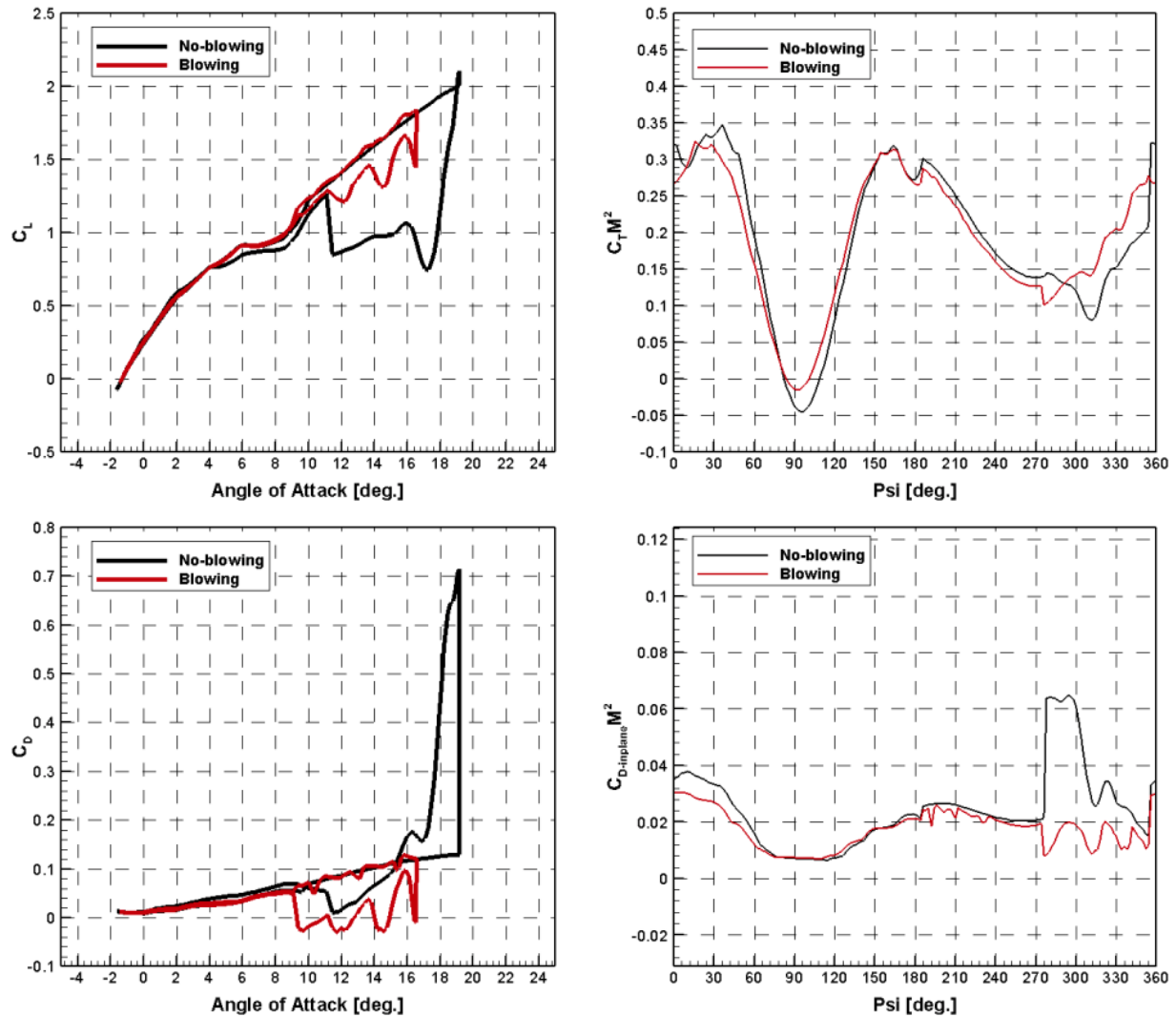


Figure 337. Section  $C_L$ ,  $C_D$  and loading comparison ( $\mu=0.4$ ,  $C_T/\sigma=0.127$ ,  $r/R=0.8$ )

### B. Power and Thrust Benefit

Extending the flight envelope can be realized by useable power and thrust capability at maximum power condition. Assuming nominal available power of 2500 HP at a standard sea-level condition and 1600 HP at a “high-hot” condition (6 K ft, 95 F), available thrust and power were evaluated at  $\mu=0.4$ . Figure 338 shows power vs. thrust at standard sea-level conditions and Figure 339 compares operation at the high-hot condition. With a nominal power limit of 2500 HP, blowing achieved 2200 lbf additional thrust at sea-level condition. Assuming all other parameters are the same, this is equivalent to an 8% blade chord reduction. This can also be viewed as a substantial increase in maneuver margin (thrust beyond gross weight). A similar thrust increase was also obtained at the high-hot condition, which produced 1400 lbf additional thrust (7% increment). For these conditions, the thrust increase represents a substantial increase in payload, since these thrust values are less than nominal gross weight. The additional thrust of 1400 lbf can be viewed as an increment of 4.5 fully armed soldiers (300 lb per each) on board the vehicle. On the other hand, if thrust is fixed at its maximum without blowing, blowing at sea-

level provides an additional 400 HP power margin (16% of total available power), which can be used for maneuvering in the same condition. The power margin was 11% (180 HP) at the high-hot condition.

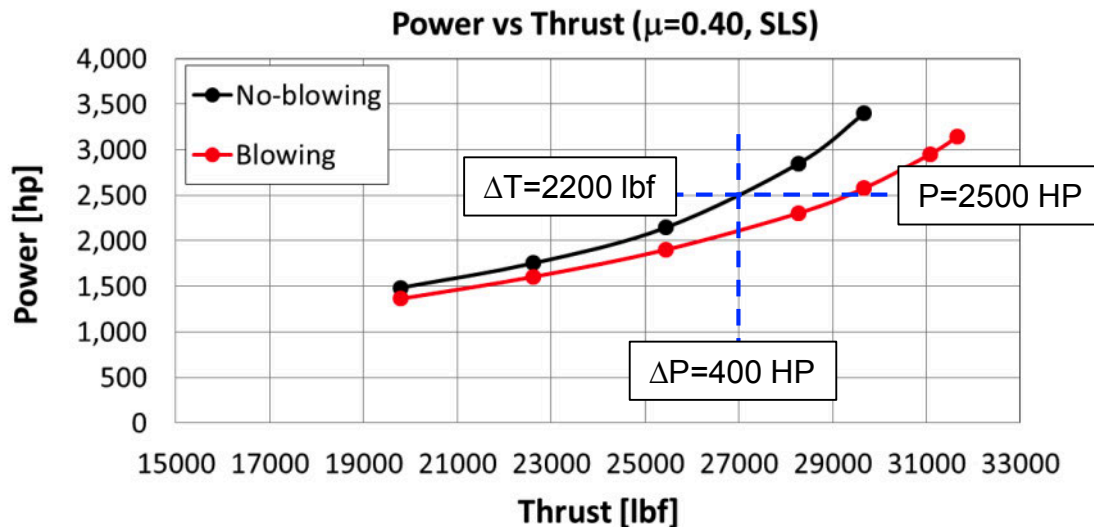


Figure 338. Power vs. Thrust ( $\mu=0.4$ , Sea-Level Standard)

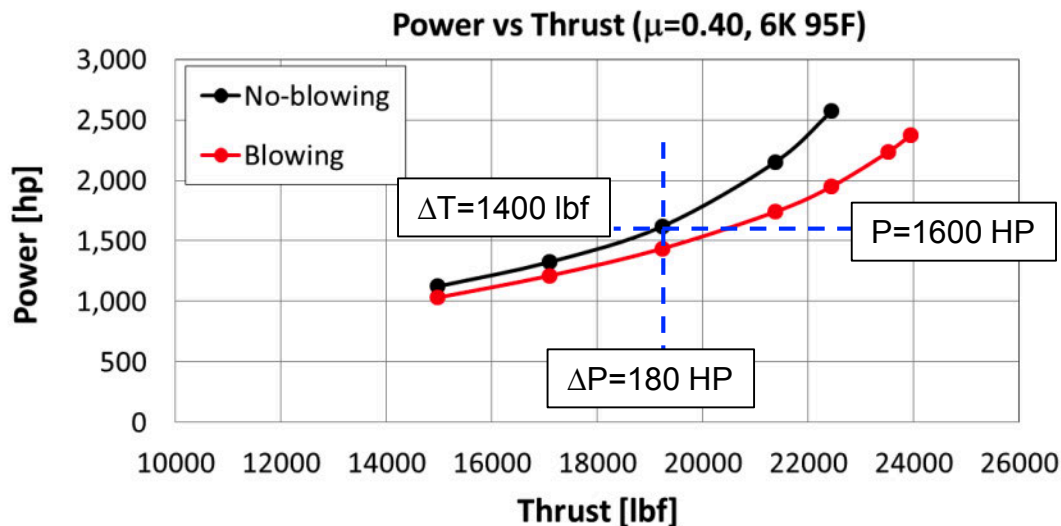


Figure 339. Power vs. Thrust ( $\mu=0.4$ , 6 K ft, 95 F)

### C. Speed Envelope Benefit

In order to examine its speed envelope benefit, rotor speed sweeps at two high thrust conditions were performed. Figure 340 shows these results for  $C_T/\sigma=0.11$  and Figure 341 shows the speed sweep at  $C_T/\sigma=0.12$ . Assuming nominal available power of 2500 HP at sea-level, blowing achieved 10% and 16% increases in speed for  $C_T/\sigma=0.11$  and 0.12, respectively.

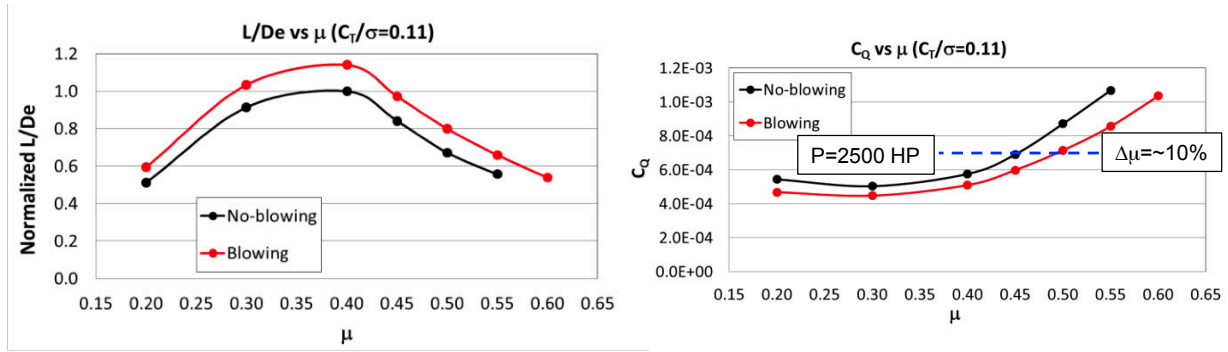


Figure 340. Speed sweep at  $C_T/\sigma=0.11$ (left:  $L/D_e$ , right: Torque)

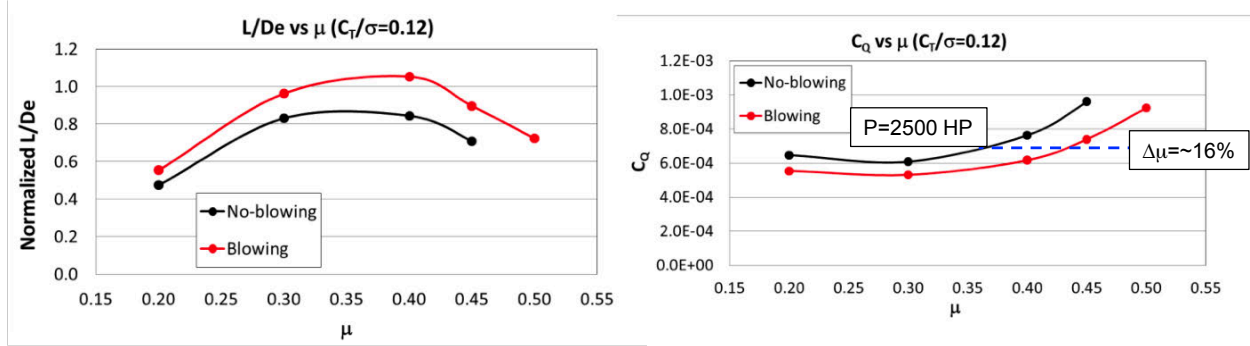


Figure 341. Speed sweep at  $C_T/\sigma=0.12$  (left:  $L/D_e$ , right: Torque)

#### D. Summary

A simplified rotor system analysis was performed to evaluate performance benefits from COMPACT. For this simplified modeling approach, rigid blades with uniform inflow were assumed. For evaluation of performance improvements provided by modified dynamic stall hysteresis loop from COMPACT, a new approach has been developed to efficiently reflect hysteresis loop modification. Including modified hysteresis loops in the analysis is a challenge, but viewed as an improvement over using steady airfoil tables. A UH-60A sized rotor model was used with combination of steady and unsteady airfoil tables. Analysis showed substantially increased rotor performance through COMPACT. For three high speed conditions ( $\mu=0.3, 0.4, 0.5$ ), COMPACT showed improved  $L/D_e$  at all conditions. At a nominal maximum power at  $\mu=0.4$ , thrust was increased by 7-8% at high-hot and sea-level conditions, which is equivalent to a 7-8% chord reduction. At the maximum thrust conditions of the baseline rotor, available power was increased to 16% at sea-level, and 11% at the high-hot condition. This available power can be used for additional maneuvering flight at the given thrust condition. At high thrust conditions, the speed envelope was extended by 10% ( $C_T/\sigma=0.11$ ) and 16% ( $C_T/\sigma=0.12$ ). Examination of blade loading and angle-of-attack distribution showed the benefit of COMPACT comes not only from its high lift capability and lower drag, but also from its resultant low control pitch angle, reduced dynamic stall hysteresis loop, low drag due to low pitch, and more uniform loading distributions throughout the rotor disc. Thus, in order to maximize system benefits, lift hysteresis reduction with high frequency blowing is recommended. Although current system analysis was successfully executed, employing the COMPACT dynamic stall benefits into the system analysis is quite limited. It uses 2D airfoil tables with fixed aerodynamic functional shapes at a given radial section without accounting for local flow variations and the resultant and very different

aerodynamic behaviors found through the different dynamic stall regimes. It is recommended to extend this system analysis to a higher-fidelity simulation. One such approach is a development of more rigorous methodology that accounts for local variation of reduced frequency, angle-of-attack range (mean and amplitude), local Mach number, and actuation frequency ( $F^+$ ) using a significantly larger airfoil table database or advanced dynamic stall model. Another recommended approach is full 3D CFD simulations coupled with a CSD solver to account for all 3D effects and local flow variations based on first principles. The fully-coupled CFD/CSD simulations are recommended for follow-on efforts prior to large scale wind tunnel rotor testing.

## XIV. Comparisons with Other Flow Control Techniques

The results gathered in this investigation are compared with results from several other experiments evaluating control of static and dynamic stall at helicopter retreating blade conditions. The set of concepts reviewed is not comprehensive; the focus here is on published, experimental results that reached Reynolds numbers greater than  $10^6$  and Mach numbers of at least 0.3. Table 43 identifies a spectrum of prior work.

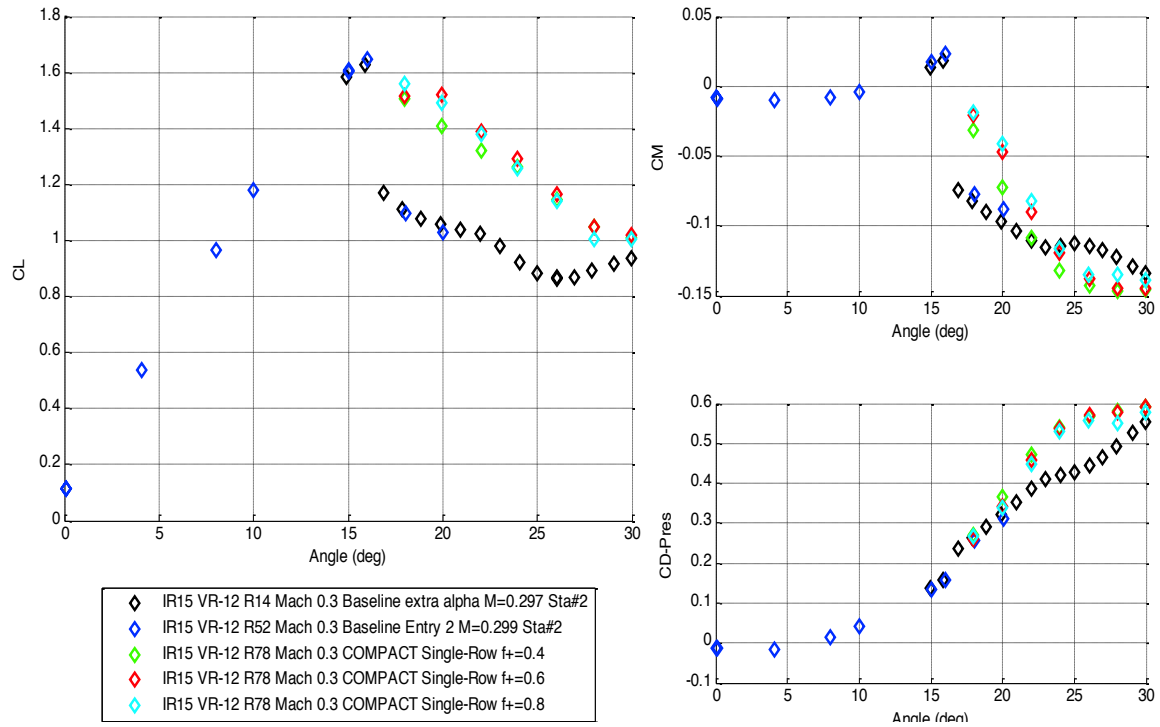
**Table 43 Flow Control Approaches**

Control Concept	Reference	Experimental Approach
<b>COMPACT</b>	[47], current	Combustion powered pulsed blowing
<b>Synthetic Jets</b>	[48], [49], [50], [51]	Suction and blowing
<b>Directed Synthetic Jets</b>	[52], [53]	Directed suction and blowing
<b>Steady Blowing</b>	[54], [55]*, [56]	Steady blowing
<b>Leading-edge Slats</b>	[57], [58], [59], [60]	Variable Multi-element airfoil
<b>Deformable geometry</b>	[61], [62], [38], [63]	Variable camber, leading edge droop, airfoil shape modification
<b>Vortex generators</b>	[64], [65]*, [66], [67]	Vortex generation by solid objects
<b>Vortex generator jets</b>	[68], [69], [70]	Vortex generation by air jets
<b>Discrete Jet Blowing</b>	[71], [72], [73], [74], [75], [76]	Trailing-edge flaps
<b>Trailing-edge plain flaps</b>	[77], [78], [79]	Gurney flaps
<b>Trailing-edge Gurney / MiTES</b>	[80], [81], [82], [83], [84], [85]	Higher harmonic angle control
<b>Active blade pitch and twist</b>	[86]*, [87], [88]	Various Plasma Discharge Techniques

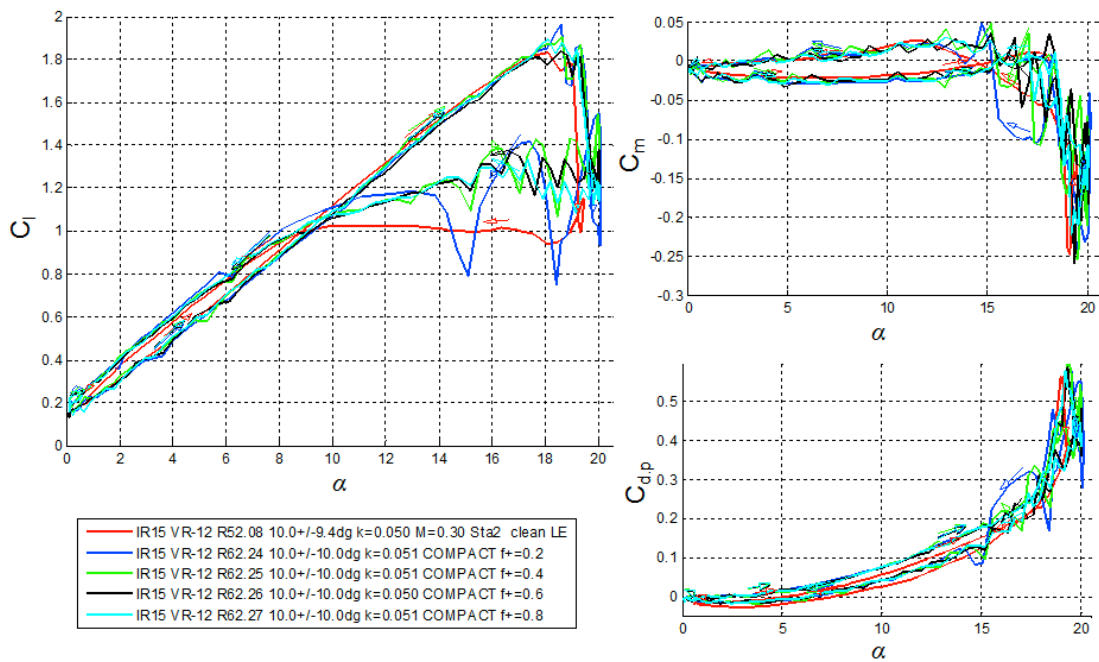
\*Note that Refs. [55], [64], [86] refer to incompressible conditions. Figure 342 and Figure 343 repeat the respective steady and unsteady performance of the current COMPACT actuation at Mach 0.3, and provide the reference for comparison to the other approaches. Only one example of each of the selected concepts will be discussed here.

Figure 344 summarizes Mach 0.3 results from the leading-edge slat test reported in [58]. This used a 24" chord airfoil between sidewalls, with a slat located at several positions relative to the leading edge. Since the baseline was a similar generation helicopter blade high lift airfoil, it performed comparably to the current baseline. In the highest lift location (Slat 6), there was a large increase in steady stall angle and  $C_{L,max}$ . There was also a substantial closure of the dynamic stall lift and moment loops, and a reduction in the peak negative pitching moment.

Figure 345 shows a higher amplitude condition, which shows a similar benefit. The slat was therefore aerodynamically quite effective, as would be expected from its widespread application to fixed wing aircraft. The primary drawback for helicopter blade application is that in order to avoid advancing side drag penalties, the slat should be retracted or relocated once per revolution. Practical implementation of such an active slat has proven to be quite challenging.



**Figure 342. Lift, drag, and moment coefficients for steady COMPACT,  $M = 0.3$ .**



**Figure 343. Lift, drag, and moment for unsteady COMPACT,  $M = 0.3$ ,  $k=0.05$ ,**



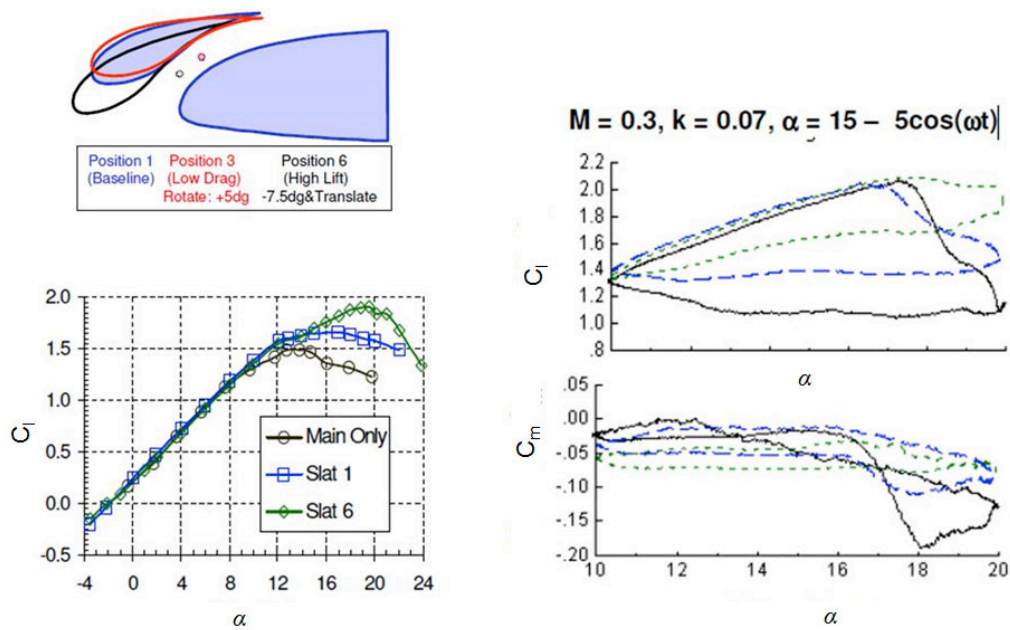


Figure 344. Steady and unsteady results for leading-edge slats, Ref. [58].

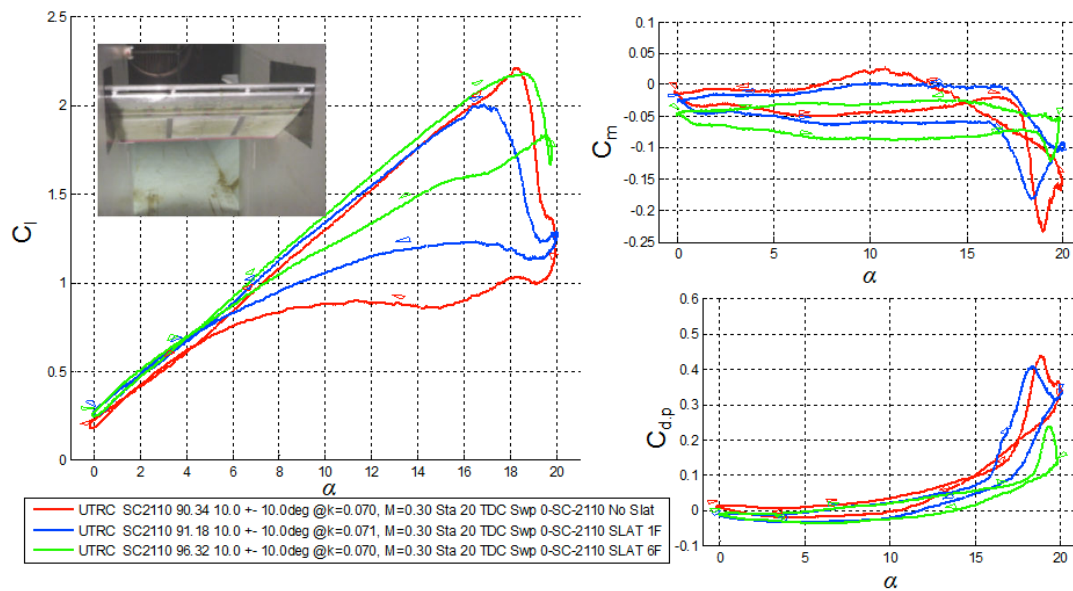


Figure 345. Lift, drag, and moment coefficients for leading-edge slats, Ref. [58],  $M = 0.3$ ,  $k=0.07$

Figure 346 summarizes for a zero net mass flux directed synthetic jet (DSJ) using the same baseline model as was used for the slat, as presented in Refs. [52] and [53]. A resonant electromechanical actuator was located in the model leading edge, with the flow coming in and out of a slot located at a similar chordwise location and exit angle, as with the COMPACT slot. The excitation frequency was in the  $F^+ = 0.5$  to  $0.8$  range. The primary limitation of the DSJ was the control authority. They were designed for  $C_u$  of 0.004 at Mach 0.2 and 0.001 at Mach 0.4, based on the peak positive outflow and inflow velocity. This was sufficient at Mach 0.2 to extend the steady stall as shown in the upper right charts and increase the unsteady post stall lift as shown in the lower middle chart. The lower nondimensional authority available at Mach 0.3 and Mach 0.4 proved insufficient to extend the steady lift curve or provide significant benefit for unsteady lift and moment. This observation was a strong motivation for pursuing the higher authority COMPACT concept. Another relevant observation from the DSJ test was that the open unactuated slot caused a noticeable degradation in the stall characteristics. The COMPACT slot was quite a bit narrower, so it had less impact; but as described previously, the spanwise variations in the tested COMPACT leading edge also degraded the stall characteristics with the actuation off. Ref. [51] also showed DSJ actuators could be effective in controlling compressible dynamic stall. For smaller pitch oscillation amplitudes,  $\alpha_1 = 5$  deg, and reduced frequency,  $k = 0.05$ , the DSJs achieved lift hysteresis closure and increased  $C_{l,max}$ .

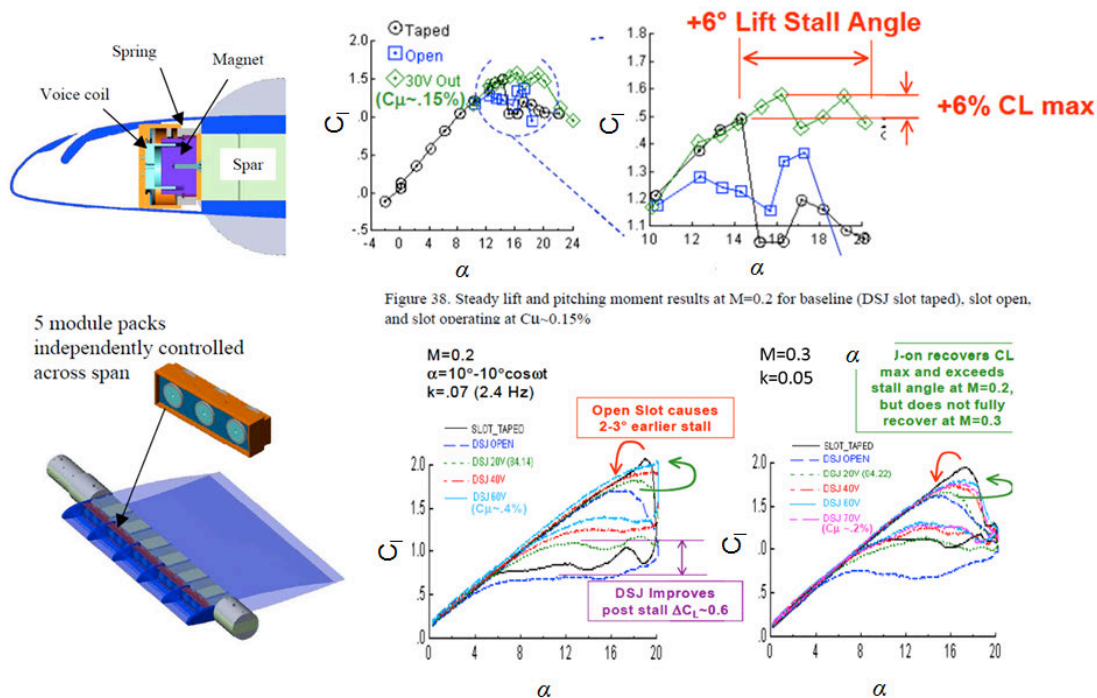


Figure 346. Lift, drag, and moment coefficients for directed synthetic jets Refs. [53] & [52].

Figure 347 summarizes some of the results from Ref. [63], which evaluated application of fixed and variable leading-edge droop. This experiment was performed for a VR-12 airfoil, at similar Mach numbers and reduced frequencies as those previously described, but the Reynolds number was lower ( $1.2 \times 10^6$ ). The Mach 0.3,  $k=0.10$  lift loops pictured show a modest level of hysteresis closure during the start of the downstroke for the fixed and variable droop configurations. Droop negatively impacted lift throughout the cycle but favorably decreased the drag and peak nose down pitching-moment on the VR-12.

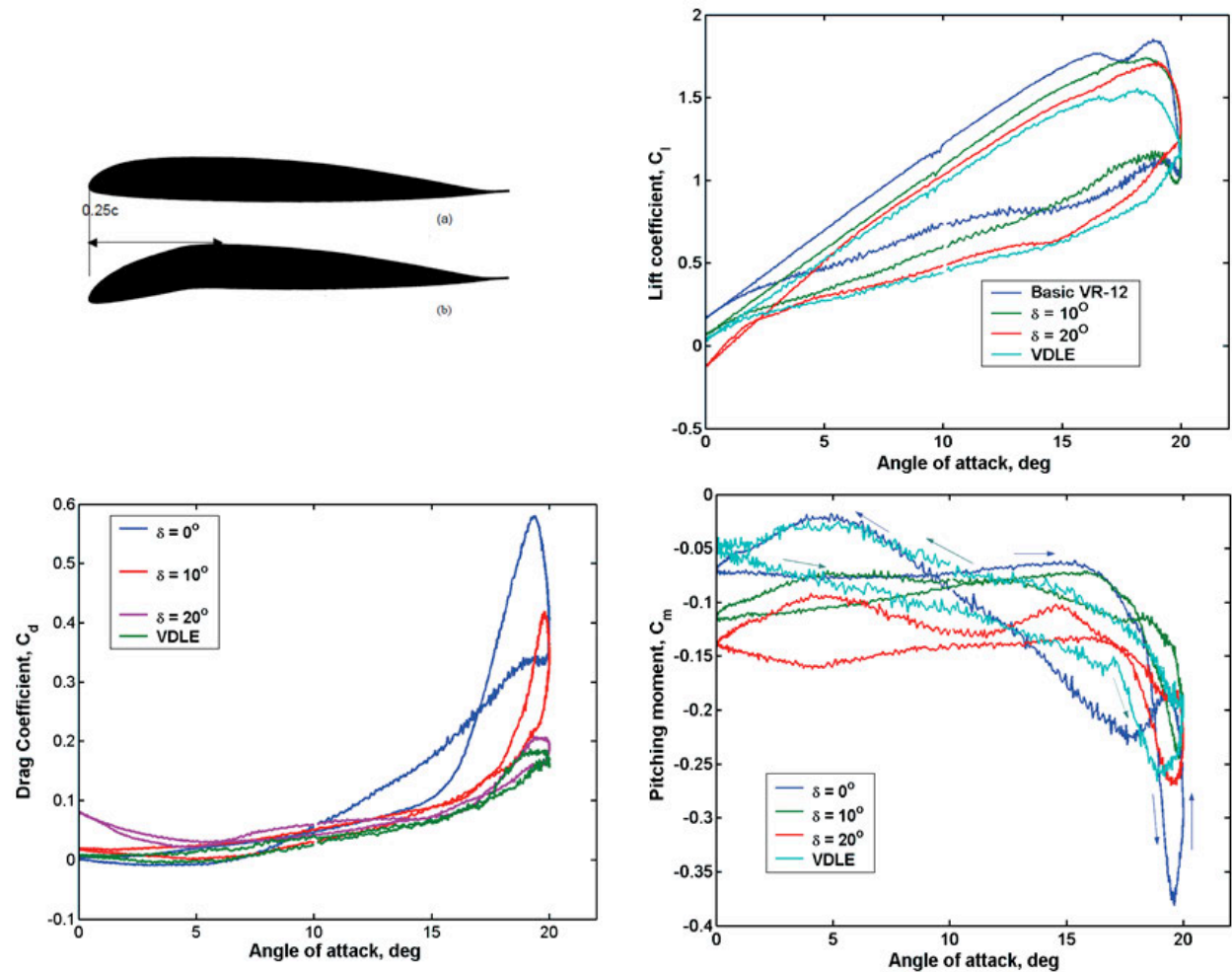
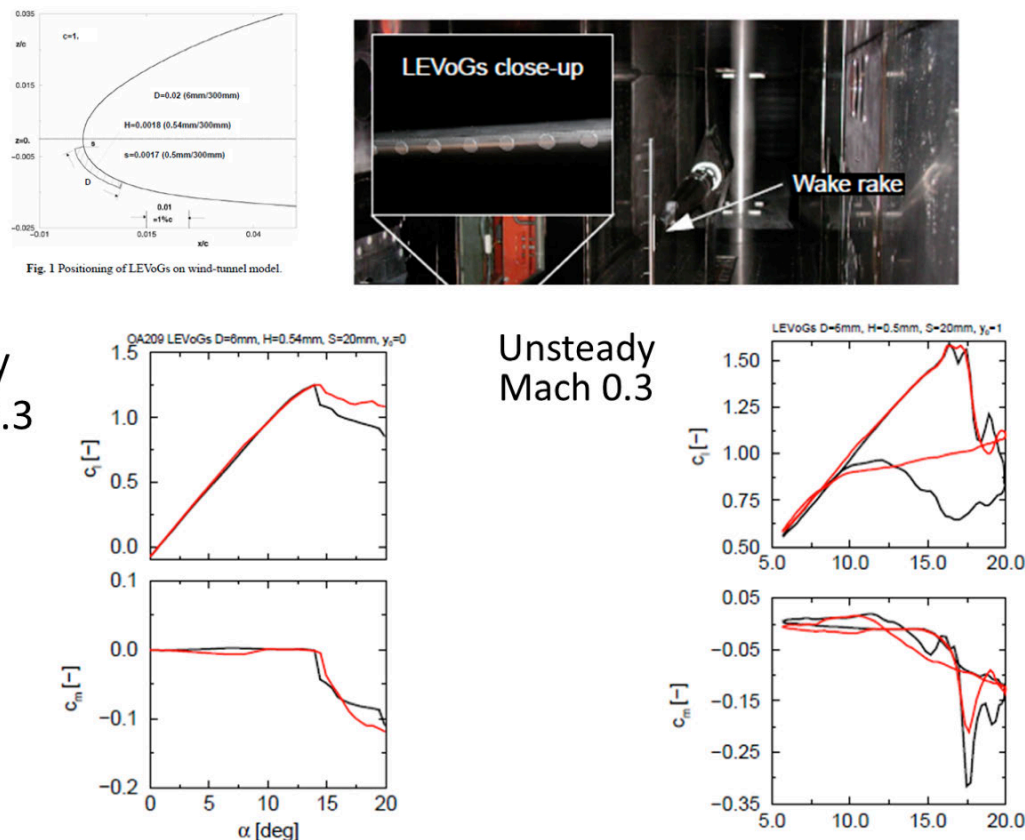


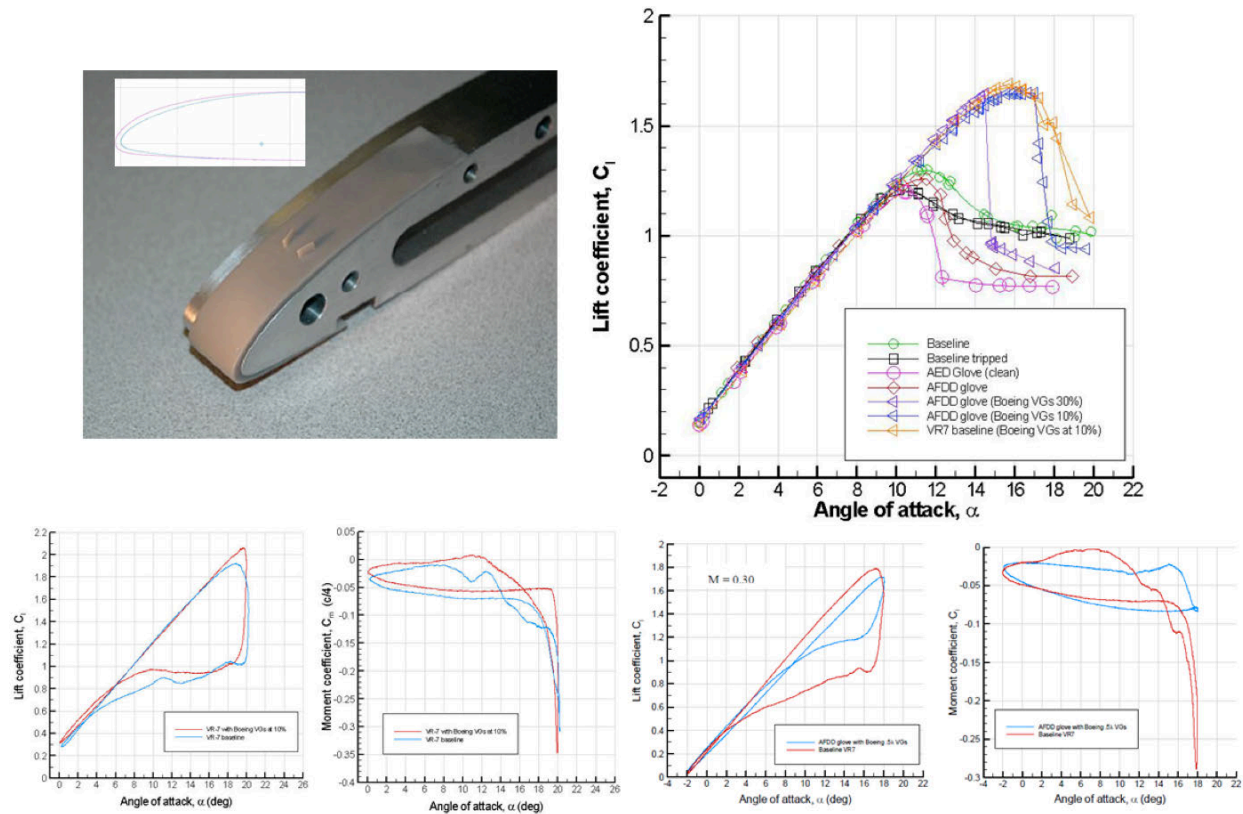
Figure 347. Lift, moment, and drag coefficients for leading-edge droop Ref. [38]

Figure 348 shows result from a recent experiment using solid leading-edge vortex generators, from Ref. [64]. The baseline airfoil appears to be more optimized for low drag rather than high lift, based on the steady  $C_{L,max}$  and the installation was a channel-spanning model at high Reynolds number. Like the COMPACT results, the steady VG results show a relatively small increase in peak lift, but a more significant increase in post-stall lift. The unsteady results show significant post-stall lift loop closure and reduction of the peak negative pitching moment. Peak drag, although not shown, was also reduced. Ref. [65] considers a similar control approach, but compares both ‘ramp’ and ‘plow’ VG designs to the circular cylinder tested in Ref. [64]. Conditions for the experiment were limited to Mach 0.16. Both the circular cylinder and backward-edge or ‘plow’ produced considerable lift hysteresis closure but failed to cause substantial drag or nose-down pitching moment improvement under deep stall conditions.



**Figure 348. Lift, drag, and moment coefficients for leading-edge vortex generators Ref. [64].**

The combination of leading-edge droop and passive, vane-type vortex generators was investigated in Ref. [66]. Figure 349 highlights the most relevant cases from the study for the discussion here. Static lift is shown for Mach 0.27; it can be seen that droop caused a negative impact on lift compared to the Baseline VR-7. In contrast, the VGs applied to 10% chord produced a dramatic extension of the baseline lift stall angle. Combination of the two passive controls, particularly with the VGs at 10% chord, resulted in peak lift increases (1.25 to 1.65) and stall delay (12° to 17°). Unsteady results with the VGs indicate some gains in maximum lift as well as lift hysteresis closure but without moment alleviation. Less severe stall cases (lower reduced frequency) were greatly improved with the addition of the VGs. The addition of droop significantly improved the hysteresis closure, although both upstroke and peak lift were reduced. Peak moment was all but eliminated in the presence of both controls approaches. It should be noted however, that the favorable control results found at Mach 0.3, particularly in pitching-moment, disappeared as Mach number neared 0.4.



**Figure 349. Droop and passive, vane-type vortex generators applied to the VR-7 airfoil. Steady lift and unsteady lift and moment coefficients for leading-edge droop, VGs, and their combination Ref [66].**



Ref. [88] investigates two methods for controlling static airfoil stall with plasma discharge control systems. Unlike the other steady and unsteady summaries provided in this section, this investigation was conducted on airfoil geometry intended for fixed wing cruise conditions (NASA Energy Efficient Transport (EET) airfoil). As such, the baseline stall angle is less at  $10^\circ$ , although the airfoil produced a respective lift coefficient of roughly 1.4 at this condition despite noted 3D effects. For Mach 0.3 near stall angle, the actuators compared favorably despite the different physics behind the control schemes. AC DBD increased peak lift and delayed stall with quasi-steady (5kHz carrier frequency) and unsteady ( $F^+=1$ ) actuation. NSP actuation produced slightly less peak lift benefit but shows good post-stall lift enhancement. Drag and pitching-moment were similarly improved for each control case.

Refs [77], [78], and [43] investigate deployable Gurney flaps, also known as Miniature Trailing-Edge Effectors (MiTEs) for a variety of aerodynamic benefits. Though much of the work available in the literature is at fairly low Mach numbers, some simulations have been carried out at higher Mach numbers. Figure 350 shows results from [79], which were collected at a relatively low Mach number for a NACA 4412 airfoil. The results shown are considered optimistic, more recent results produced at UTRC using Fluent are shown in Figure 351 for a  $0.02c$  Gurney flap. These simulations were carried out at Mach 0.3 on a VR-12 airfoil.

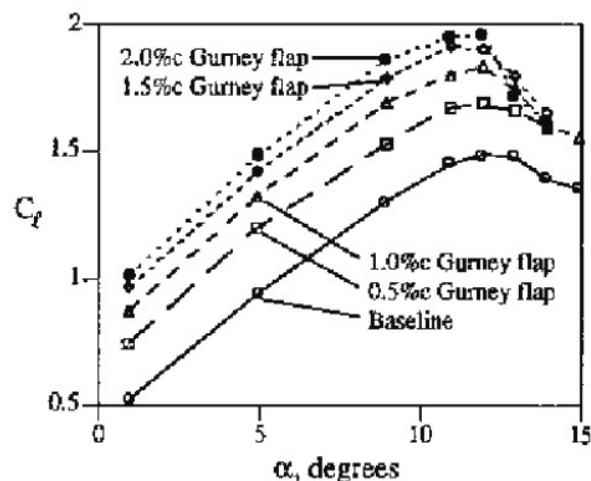
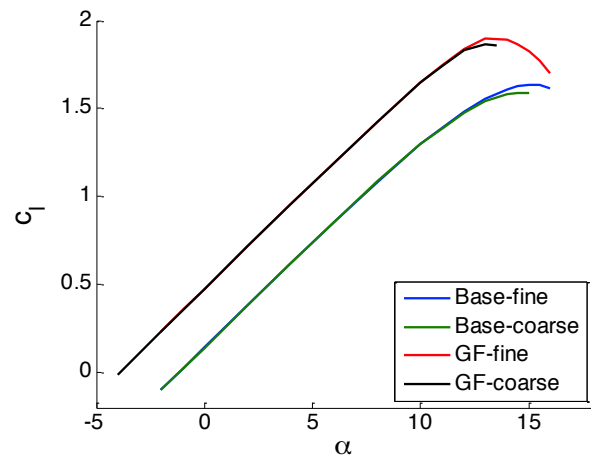


Figure 350. Results from [79] on a NACA 4412 airfoil at low Mach number.



**Figure 351. Results from recent simulations performed at UTRC using Fluent on a VR-12 airfoil at Mach 0.3 with a  $0.02c$  Gurney flap.**



Table 44 summarizes the specific concepts discussed in this section with respect to several simple performance metrics that could be estimated from the published figures. Based solely on this table, COMPACT does quite well comparatively increasing post stall lift for both unsteady and steady conditions, but has much less effect on stall delay than several of the other concepts.

**Table 44. Selected Flow Control Approaches (at Mach 0.3)**

Control	$\Delta$ Steady $C_L$ max	$\Delta$ Steady $\alpha$ stall	$\Delta$ Steady Post-Stall $C_L$ & $C_M$	$\Delta$ Unsteady $C_L$ max & $\alpha$	$\Delta$ Unsteady Post-Stall $C_L$ & $C_M$
COMPACT Peak $C_{\mu} \sim = \dots$	No	No	+0.5 $C_L$	No	+0.4 $C_L$
Steady Blowing $C_{\mu} \sim 0.03$	+0.3 $C_L$	Small	+0.6 $C_L$	Small	+0.6 $C_L$
DSJ Blowing/Suction Unsteady $C_{\mu} \sim 0.0015$	+0.1 $C_L$	+5°	+0.3 $C_L$	No	+0.6 $C_L$ @M=0.2 +0.2 $C_L$ @M=0.3
LE Slat	+0.4 $C_L$	+5°	+0.3 $C_L$	Small	+0.6 $C_L$
LE Droop (lower Reyn)	??	??	??	Small	Small
LE Physical VGs	Small	Small	+0.3 $C_L$	No	+0.4 $C_L$ +0.1 $C_M$
Droop + Vane VGs	+0.4 $C_L$	+5°	+0.6 $C_L$	-0.1 $C_L$ None	+0.3 $C_L$ +0.2 $C_M$
Plasma Actuation (AC/DBD)	+0.2 $C_L$	+2°	+0.4 $C_L$	NA	NA
Plasma Actuation (NSP)	+0 $C_L$	+2°	+0.4 $C_L$	NA	NA
TE Flaps or MiTES	+0.3 $C_L$	+2°	+0.2 $C_L$	??	??

## **XV. Conclusions**

Each phase of this long-term project resulted in conclusions that had impact on subsequent portions of the project. Detailed descriptions of specific conclusions relevant to each task have been left to the preceding sections of this report. Overall conclusions, as well as some recommendations going forward are provided below. All statements made are with regard to a VR-12 airfoil with a tab of 5% chord in length.

1. The baseline airfoil quantitative results and trends with Mach number, angle-of-attack, and reduced frequency were consistent internally and with previous results for similar airfoils and Reynolds numbers. The baseline results were also consistent between the two test entries.
2. The baseline flow appeared highly two-dimensional more than 0.5 chord from the walls, based on pressure distributions measured.
3. COMPACT has been shown effective in increasing maximum static lift coefficient at Mach numbers up to 0.2.
4. COMPACT has been shown effective in increasing static post-stall lift at Mach numbers up to 0.4.
5. These benefits were determined relative to the baseline, and occurred even though replacing the smooth baseline leading edge with the COMPACT leading edge lowered the static stall angle and reduced post stall lift for conditions when the actuation slots were sealed, when they were open without actuation, and when they were open with steady bleed air present.
6. COMPACT has been shown effective in increasing cycle-averaged lift coefficient at Mach numbers up to 0.4 and a variety of reduced frequencies, amplitudes, and mean angles, which range from light to deep stall.
7. COMPACT has been shown effective in alleviating drag and moment penalties for light dynamic stall cases at Mach numbers up to 0.2.
8. Partial cycle COMPACT operation proved as advantageous in increasing cycle-averaged lift coefficient as full-cycle operation. For all actuation frequencies at Mach 0.3 and Mach 0.4, actuation was only required over 1/3<sup>rd</sup> of the pitch cycle. The optimum actuation incidence range corresponded to starting COMPACT prior to moment stall and continuing through the start of the downstroke. Actuation through the mean angle on the downstroke was not shown to be necessary.
9. Although not as impactful as uninterrupted spanwise actuation, non-continuous span operation of the single-row COMPACT configuration showed a strong ability to improve post-stall lift behavior. This offers potential for hydrogen storage reduction.
10. Simultaneous or alternating operation of the dual-row COMPACT configuration outperformed single-row post-stall lift benefits for the same actuated wing span.
11. Changes in equivalent 2D drag coefficient due to COMPACT were not quantified from experiments because the relatively low actuated span caused significant induced drag.

12. Compared to several other rotor blade stall control concepts, COMPACT was one of the most beneficial in terms of increasing post-stall or cycle-averaged lift. Compared to leading-edge slats or periodic suction and blowing, COMPACT provided less of an increase in steady stall angle and maximum lift, and did not reduce the peak dynamic stall pitching moment as much.
13. Flowfield measurements at Mach numbers up to 0.4 showed that the physical mechanisms responsible for enhancements shown previously at very low Mach numbers operate in very much the same way at Mach numbers up to 0.4.
14. A strong dependency in effectiveness upon actuation frequency was shown in both the simulations and experiments, suggesting a continued need to push the boundary on maximum possible frequency. However, nondimensional actuation frequencies ( $F^+$ ) as low as 0.4 were shown effective in producing strong lift benefits at Mach 0.4.
15. The ability for COMPACT to operate at higher Mach numbers was limited primarily by the low static pressures present at such conditions, particularly at high-lift conditions. This had an impact on both the ability to generate adequate and consistent sparks as well as the ignition of hydrogen. Improving low-pressure operability is a key requirement toward realizing further aerodynamic gains through COMPACT.
16. Applying the aerodynamic benefits shown in 2D simulations to a reduced-order rotorcraft trim model of a UH-60A-size rotor showed that the system-level benefits are substantial, however, this analysis is viewed as optimistic and must be followed-up with CFD/CSD analysis to better quantify expected benefits.
17. The system-level benefits viewed with the understanding that COMPACT will require a healthy supply of hydrogen fuel suggest that the greatest overall benefit will be in providing the ability to enhance maneuverability or provide short-term speed and efficiency benefits. While further design and analysis will be required to assess benefits in cruise speed or cruise efficiency, it is expected that the weight required to carry significant amounts of additional fuel will likely degrade the benefits substantially.

## **XVI. New Technology**

### **1. Discoveries**

The work done under this contract contributes to the large bodies of knowledge that already exist in the areas of dynamic stall and active flow control. However, notable discoveries made in this work can be summarized as follows:

1. COMPACT technology, previously shown to be effective for stall suppression at low Mach, is indeed effective at up to Mach 0.4 based on the data collected.
2. Stall suppression can be achieved with pulses that begin as stall occurs; there is no need to begin pulsing earlier.

### **2. Software**

Through the course of this work, modifications have been made to various subroutines of the NASA code CFL3D in order to enable modeling of COMPACT. These changes are documented in detail in sections 5 and 11.

## **XVII. References**

- [1] P. Lorber, A. Bagai and B. Wake, "Design and Evaluation of Slatted Airfoils for Improved Rotor Performance," AHS International 62nd Annual Forum, 2006.
- [2] A. Mishra, S. Ananthan, J. D. Baeder, D. G. Opoku, B. E. Wake and L. R-S, "Coupled CFD/CSD Prediction of the Effects of Leading Edge Slat on Rotor Performance," AHS International 65th Annual Forum, 2009.
- [3] M. P. Kinzel, M. D. Maughmer and G. A. Lesieutre, "Miniature Trailing-Edge Effectors for Rotorcraft Performance Enhancement," Journal of the American Helicopter Society, Vol. 52, No. 2, 2005.
- [4] P. Martin, J. Wilson, T. C. Wong, M. Moulton and M. McVeigh, "Passive Control of Compressible Dynamic Stall," 26th AIAA Applied Aerodynamics Conference, 2008.
- [5] A. Le Pape, M. Costes, F. Richez, G. Joubert, F. David and J.-M. Deluc, "Dynamic Stall Control Using Deployable Leading edge Vortex Generators," AIAA Journal, Vol. 50 No. 10, 2012.
- [6] A. J. Lombardi, P. O. Bowles and T. C. Corke, "Closed Loop Dynamic Stall Using a Plasma Actuator," AIAA Paper, 2012.
- [7] C. L. Kelley, P. Bowles, J. Cooney, C. He, T. C. Corke, B. Osborne, J. Silkey and J. Zehnle, "High Mach Number Leading edge Flow Separation Using AC DBD Plasma Actuators," AIAA Paper, 2012.
- [8] Y. H. Yu, S. Lee, K. W. McAlister, C. Tung and C. M. Wang, "Dynamic Stall Control for Advanced Rotorcraft Application," AIAA Journal, Vol. 33, No. 2, 1995.
- [9] D. Weaver, K. W. McAlister and J. Tso, "Control of VR-7 Dynamic Stall by Strong Steady Blowing," Journal of Aircraft, Vol. 41, No. 6, 2004.
- [10] C. Singh, D. J. Peake, A. Kokkalis, V. Khodagolian, F. N. Coton and R. A. Galbraith, "Control of Rotorcraft Retreating Blade Stall Using Air-Jet Vortex Generators," Journal of Aircraft, Vol. 43, No. 4, 2006.
- [11] H. F. Muller-Vahl, C. N. Nayeri, C. O. Paschereit and D. Greenblatt, "Control of Unsteady Aerodynamic Loads Using Adaptive Blowing," 32nd AIAA Applied Aerodynamics Conference, 2014.
- [12] D. Greenblatt and I. Wygnanski, "Dynamic Stall Control by Periodic Excitation, Part I: NACA 0015 Parametric Study," Journal of Aircraft, Vol. 38, No. 3, 2001.
- [13] L. W. Traub, A. Miller and O. Rediniotis, "Effects of Synthetic Jet Actuation on a Ramping NACA 0015 Airfoil," Journal of Aircraft, Vol. 41, No. 5, 2004.
- [14] L. W. Traub, A. Miller, O. Rediniotis, K. Kim, S. Jayasuriya and G. Jung, "Effects of

- Synthetic Jets on Large-Amplitude Sinusoidal Pitch Motions," *Journal of Aircraft*, Vol. 42, No. 1, 2005.
- [15] R. Raju, R. Mittal and L. Cattafesta, "Dynamics of Airfoil Separation Control Using Zero-Net Mass-Flux Forcing," *AIAA Journal*, Vol. 46, No. 12, 2008.
  - [16] M. Visbal, "Numerical Exploration of Flow Control for Delay of Dynamic Stall on a Pitching Airfoil," 32nd AIAA Applied Aerodynamics Conference, 2014.
  - [17] H. Nagib, J. Kiedaisch, D. Greenblatt, I. Wygnanski and A. Hassan, "Effective Flow Control for Rotorcraft Applications at Flight Mach Numbers," 31st AIAA Fluid Dynamics Conference and Exhibit, 2001.
  - [18] B. E. Wake and E. A. Lurie, "Computational Evaluation of Directed Synthetic Jets for Dynamic Stall Control," AHS International 57th Annual Forum, 2001.
  - [19] P. F. Lorber, D. McCormick, T. Anderson, B. E. Wake, D. MacMartin, M. Pollack and T. B. K. Corke, "Rotorcraft Retreating Blade Stall Control," Fluids 2000 Conference and Exhibit, AIAA Paper, 2000.
  - [20] R. Florea and B. E. Wake, "Parametric Analysis of Directed-Synthetic Jets for Improved Dynamic-Stall Performance," 41st Aerospace Sciences Meeting and Exhibit, 2003.
  - [21] A. Lefebvre and G.-C. Zha, "Numerical Simulation of Pitching Airfoil Performance Using Co-Flow Jet Flow Control," 31st AIAA Applied Aerodynamics Conference, 2013.
  - [22] A. Lefebvre and G. Zha, "Pitching Airfoil Performance Enhancement Using Co-Flow Jet Control at High Mach Number," 52nd Aerospace Sciences Meeting, AIAA Paper, 2014.
  - [23] A. D. Gardner, T. Knopp, K. Richter and H. Rosemann, "Numerical Investigation of Pulsed Air Jets for Dynamic Stall Control on the OA-209 Airfoil, New Results in Numerical and Experimental Fluid Mechanics," Notes on Numerical Fluid Mechanics and Multidisciplinary Design, Springer-Verlag, Berlin, 2013.
  - [24] A. D. Gardner, K. Richter, H. Mai and D. Neuhaus, "Experimental Investigation of Air Jets for the Control of Compressible Dynamic Stall," *Journal of the American Helicopter Society*, Vol. 58, No. 4, 2013.
  - [25] A. D. Gardner, K. Richter, H. Mai and D. Neuhaus, "Experimental Investigation of High-Pressure Pulsed Blowing for Dynamic Stall Control," *CEAS Aeronautical Journal*, Vol. 5, No. 2, 2014.
  - [26] A. D. R. Gardner, K. H. Mai and D. Neuhaus, "Experimental Investigation of Air Jets to Control Shock-Induced Dynamic Stall," *Journal of the American Helicopter Society*, Vol. 59, No. 2, 2014.
  - [27] T. Crittenden, A. Glezer, R. Funk and D. Parekh, "Combustion-Driven Jet Actuators for Flow Control," 31st AIAA Fluid Dynamics Conference and Exhibit, AIAA Paper, 2001.
  - [28] T. Crittenden, B. Warta and A. Glezer, "Characterization of Combustion Powered Actuators for Flow Control," 3rd AIAA Flow Control Conference, AIAA Paper, 2006.

- [29] T. Crittenden, G. Woo and A. Glezer, "Combustion Powered Actuators for Separation Control," AIAA Paper, 2012.
- [30] R. Funk, T. Crittenden, D. Parekh and A. Glezer, "Transient Separation Control Using Pulse Combustion Actuation," AIAA Paper, 2002.
- [31] D. Brzozowski and A. Glezer, "Transient Separation Control Using Pulse-Combustion Actuation," AIAA Paper, 2006.
- [32] G. Woo, T. Crittenden and A. Glezer, "Transitory Control of a Pitching Airfoil Using Pulse Combustion Actuation," AIAA Paper, 2008.
- [33] G. Woo, T. Crittenden and A. Glezer, "Transitory Separation Control over a Stalled Airfoil," AIAA Paper, 2009.
- [34] D. Brzozowski, G. Woo, J. Culp and A. Glezer, "Transient Separation Control Using Pulse-Combustion Actuation," AIAA Journal, Vol. 48, No. 11, 2010.
- [35] S. Jee, C. Matalanis, B.-Y. Min, P. Bowles, B. Wake, T. Crittenden and A. Glezer, "Computations of Dynamic Stall Control with Combustion-Powered Actuation," AHS 71st Annual Forum, Virginia Beach, VA, 2015.
- [36] C. Matalanis, B.-Y. Min, P. Bowles, S. Jee, B. Wake, T. Crittenden, G. Woo and A. Glezer, "Combustion-Powered Actuation for Dynamic Stall Suppression - Simulations and Low-Mach Experiments," AHS 70th Annual Forum, Montreal, QC, Canada, 2014.
- [37] P. Spalart and S. Allmaras, "A One-Equation Turbulence Model for Aerodynamic Flows," Recherche Aerospatiale, 1994.
- [38] P. Martin, K. McAlister, M. Chandrasekhara and W. Geissler, "Dynamic Stall Measurements and Computations for a VR-12 Airfoil with a Variable Droop Leading Edge," American Helicopter Society 59th Annual Forum, Phoenix AZ, 2003.
- [39] J. Kearney and A. Glezer, "Aerodynamic Control using Distributed Bleed," 6th AIAA Flow Control Conference, New Orleans, LA, 2012.
- [40] P. Lorber, R. Flemming, J. O'Neill, R. Narducci, T. Reinert, L. Sankar and J. Kim, "Oscillating Iced Airfoil Pressure Measurement and Computation," American Helicopter Society 69th Annual Forum, Fort Worth Texas, May 21-23, 2013.
- [41] M. Marcolini, P. Lorber, W. Miller and A. Covino, "Frequency Response Calibration of Recess-Mounted Pressure Transducers," NASA Technical Memorandum 104031, March, 1991.
- [42] A. Stroud and D. Secrest, "Gaussian Quadrature Formulas," Prentice Hall, Englewood Cliffs, NJ, 1966.
- [43] R. Soeder, D. Sheldon, R. Ide, D. Spera and C. Andracchio, "NASA Glenn Icing Research Tunnel User Manual," NASA/TM-2003-212004, 2003.
- [44] P. Lorber and F. Carta, "Unsteady Stall Penetration Experiments at High Reynolds



- Number," United Technologies Research Center, 1987.
- [45] P. Lorber and F. Carta, "Airfoil Dynamic Stall at Constant Pitch Rate and High Reynolds Number," *Journal of Aircraft*, 1988.
  - [46] W. McCroskey, K. McAlister and L. Carr, "Dynamic Stall Experiments on Oscillating Airfoils," *AIAA Journal*, Jan. 1976.
  - [47] T. Crittenden, A. Glezer, R. Funk and D. Parekh, "Combustion-Driven Jet Actuators for Flow Control," 31st AIAA Fluid Dynamics Conference and Exhibit, Anaheim, CA, 2001.
  - [48] D. Greenblatt and I. Wygnanski, "Parameters Affecting Dynamic Stall Control by Oscillatory Excitation," AIAA 17th Applied Aerodynamics Conference, Norfolk, VA, 1999.
  - [49] M. Amitay, B. Smith and A. Glezer, "Aerodynamic Flow Control Using Synthetic Jet Technology," AIAA 37th Aerospace Sciences Meeting, 1999.
  - [50] I. Wygnanski and A. Seifert, "The Control of Separation by Periodic Oscillations," AIAA 18th Aerospace Ground Testing Conference, Colorado Springs CO, 1994.
  - [51] H. Nagib, J. Kiedaisch, D. Greenblatt, I. Wygnanski and A. Hassan, "Effective Flow Control for Rotorcraft Applications at Flight Mach Numbers," AIAA 31st Fluid Dynamics Conference, 11-14 June, Anaheim, CA, 2001.
  - [52] P. Lorber, D. McCormick, T. Anderson, B. Wake, D. MacMartin, M. Pollack, T. Corke and K. Breuer, "Rotorcraft Retreating Blade Stall Control," AIAA FLUIDS 2000 Conference and Exhibit, Denver, Colorado, 2000.
  - [53] P. Lorber, D. McCormick, B. Wake and R. Florea, "Separation Control for Rotorcraft: Final Progress Report," UTRC Report 2002-5.200.0015-5, 2002.
  - [54] P. Lorber and W. Lord, "Centrifugal Air Flow Control". US Patent US 6,203,269 B1, 20 March 2001.
  - [55] D. Weaver, K. McAlister and J. Tso, "Control of VR-7 Dynamic Stall by Strong Steady Blowing," *Journal of Aircraft*, 2004.
  - [56] D. Weaver, K. McAlister and J. Tso, "Suppression of Dynamic Stall by Steady and Pulsed Upper Surface Blowing," 16th AIAA Applied Aerodynamics Conference, 1998.
  - [57] L. Carr and K. McAlister, "The Effect of a Leading Edge Slat on the Dynamic Stall of an Oscillating Airfoil," AIAA/AHS Aircraft Design Systems and Operations Meeting, 1983.
  - [58] P. Lorber, A. Bagai and B. Wake, "Design and Evaluation of Slatted Airfoils for Improved Rotor Performance," American Helicopter Society 62d Annual Forum, Phoenix, AZ, May 9-11, 2006.
  - [59] K. Noonan, D. Allison and S. Stanaway, "Investigation of a Slotted Rotorcraft Airfoil at Mach Numbers from 0.2 to 0.88," AHS Aeromechanics Specialists Conference, San Francisco, CA, 1994.

- [60] J. Narramore, "High-Lift Multielement Airfoils for Tiltrotor Vehicles," American Helicopter Society Aerodynamics, Acoustics, and Test and Evaluation Technical Specialists' Meeting, San Francisco CA, January 23–25, 2002.
- [61] W. Geissler and H. Sobieczky, "Dynamic Stall Control by Variable Airfoil Camber," AGARD Aerodynamics and Aeroacoustics of Rotorcraft Symposium, Berlin, 1994.
- [62] W. Geissler, G. Dietz, H. Mai, B. Junker and T. Lorkowski, "Dynamic Stall Control Investigations on a Full Size Chord Blade Section," European Rotorcraft Forum, 2004.
- [63] M. Chandrasekhara, P. B. Martin and C. Tung, "Compressible Dynamic Stall Control Using a Variable Droop Leading Edge Airfoil," vol. 41, no. 4, 2004.
- [64] H. Mai, G. Deitz, W. Geissler, K. Richter, J. Bosbach and H. Richard, "Dynamic Stall Control by Leading Edge Vortex Generators," American Helicopter Society 62nd Annual Forum, Phoenix, AZ, May 9–11, 2006.
- [65] B. Heine, K. Mulleners, G. Joubert and M. Raffel, "Dynamic Stall Control by Passive Disturbance Generators," AIAA Journal, Vol. 51, No. 9, 2013.
- [66] P. B. Martin, J. S. Wilson, J. D. Berry, T.-C. Wong, M. Moulton and M. A. McVeigh, "Passive Control of Compressible Dynamic Stall," 26th AIAA Applied Aerodynamic Conference, Honolulu, 2008.
- [67] M. A. McVeigh and R. F. Maciolek, "Vortex Generators on Rotor Blades to Delay an Onset of Large Oscillatory". USA Patent 2008/0145219, 19 June 2008.
- [68] A. Gardner, K. Richter, H. Mai and D. Neuhaus, "Experimental Investigation of Air Jets for the Control of Compressible Dynamic Stall," AHS Journal, 2013.
- [69] A. Gardner, K. Richter and H. Rosemann, "Numerical Investigation of Air Jets for Dynamic Stall Control on the OA209 Airfoil," 36th European Rotorcraft Forum, Paris, France, 2010.
- [70] J. Magill and K. McManus, "Control of Dynamic Stall Using Pulsed Vortex Generator Jets," AIAA Aerospace Sciences Meeting, Jan 12-15, Reno NV, 1998.
- [71] B. Grohmann, F. Müller, E. Ahci, R. Pfaller, M. Bauer, C. Maucher, O. Dieterich, S. Storm and P. Jänker, "Design, Evaluation and Test of Active Trailing Edge," American Helicopter Society 67th Annual Forum, Virginia Beach VA, May 3-5, 2011.
- [72] A. Hassan, F. Straub and K. Noonan, "Experimental/Numerical Evaluation of Integral Trailing-Edge Flaps for Helicopter Rotor Applications," American Helicopter Society 56th Annual Forum, Virginia Beach, VA, May 2-4, 2000.
- [73] R. Jain, H. Yeo and I. Chopra, "An Examination of Rotor Loads due to On-Blade Active Controls for Performance Enhancement using CFD/CSD Analysis," American Helicopter Society Specialists' Conference on Aeromechanics, San Francisco, CA, January 20-22, 2010.
- [74] P. F. Lorber, "Active Flap Full-Scale Oscillating Blade Section Experiment," AHS NE Region Technical Specialists' Meeting, Bridgeport, CT, 2000.

- [75] K. Ravichandran, I. Chopra, B. Wake and B. Hein, "Active Flaps and Slats for Rotor Performance Enhancement," American Helicopter Society 67th Annual Forum, Virginia Beach VA, May 3-5, 2011.
- [76] F. Straub and V. Anand, "Aeromechanics of the SMART Active Flap Rotor," American Helicopter Society 63rd Annual Forum, Virginia Beach VA, May 1-3, 2007.
- [77] C. G. Matalanis, B. E. Wake, D. Opoku, B.-Y. Min, N. Yeshala and L. Sankar, "Aerodynamic Evaluation of Miniature Trailing-Edge Effectors for Active Rotor Control," J. Aircraft, 2011.
- [78] P. Giguere, J. Lemay and G. Dumas, "Gurney Flap Effects and Scaling for Low Speed Airfoils," 1995.
- [79] B. L. Storms and C. S. Jang, "Lift Enhancement of an Airfoil Using a Gurney Flap and Vortex Generators," Journal of Aircraft, Vol. 31, No. 3, 1994.
- [80] T. R. Norman, C. Theodore, P. Shinoda, D. Fuerst, Arnold, U.T.P., S. Makinen, P. Lorber and J. O'Neill, "Full-Scale Wind Tunnel Test Of A UH-60 Individual Blade Control System For Performance Improvement And Vibration, Loads, And Noise Control," American Helicopter Society 65th Annual Forum, Grapevine TX, May 27-29, 2009.
- [81] H. Yeo, "Assessment of Active Controls for Rotor Performance Enhancement," American Helicopter Society 62nd Annual Forum, Phoenix, AZ, May 9–11, 2006.
- [82] U. Arnold, "Recent IBC Flight Test Results from the CH-53G Helicopter," 29th European Rotorcraft Forum, Friedrichshafen, Germany, September 16-18, 2003.
- [83] M. L. Wilbur, W. T. J. Yeager and M. K. Sekula, "Further Examination of the Vibratory Loads Reduction Results from the NASA/Army/MIT Active Twist Rotor Test," American Helicopter Society 58th Annual Forum, Montreal, Canada, June 11-13, 2002.
- [84] P. Lorber, C. Park, D. Polak, J. O'Neill and W. Welsh, "Active Rotor Experiments at Mach Scale Using Root Pitch IBC," American Helicopter Society 57th Annual Forum, Washington DC, May 9-11, 2001.
- [85] H. Yeo, I. Chopra and R. Jain, "CFD-CSD Analysis of Active Control of Helicopter Rotor for Performance Improvement," American Helicopter Society 65th Annual Forum, Grapevine TX, May 27-29, 2009.
- [86] M. Post and T. Corke, "Separation Control Using Plasma Actuators: Dynamic Stall Vortex Control on Oscillating Airfoil," AIAA Journal, Vol. 4, No. 12, 2006.
- [87] M. Frankhouser, K. Hird, S. Naigle, J. Gregory and J. Bons, "Nanosecond Dielectric Barrier Discharge Plasma Actuator Flow Control of Compressible Dynamic Stall," AIAA Aviation Conference, June 22-26, Dallas, TX, 2015.
- [88] C. Kelley, P. Bowles, J. Cooney, C. He, T. Corke, B. Osborne, J. Silkey and J. Zehnle, "Leading edge Separation Control Using Alternating-Current and Nanosecond-Pulse Plasma Actuators," AIAA Journal, Vol. 52, No. 9, 2014.

- [89] J. Tomblin, J. McKenna, Y. Ng and K. Raju, "B-Basis Design Allowables for Epoxy-Based Prepreg Newport E-Glass Fabric 7781/NB321," Report no. AGATE-WP3.3-033051-097, 2001.
- [90] P. Martin and M. Chandrasehkara, "Dynamic Stall Measurements and Computations for a VR-12 Airfoil with a Variable Droop Leading Edge," American Helicopter Society 59th Annual Forum, Phoenix, AZ, 2003.
- [91] P. Lorber, "Dynamic Stall of Sinusoidally Oscillating 3D Swept and Unswept Wings in Compressible Flow," 48th Annual Forum of the American Helicopter Society, June 3-5, Washington DC, 1992.

## Appendix 1. Structural Analysis

### 1. Main Airfoil and Supporting Hardware

#### A. Overview

The spar described previously is the main structural element of the pitching airfoil apparatus. The two main load paths, as shown in Figure 352, originate at the spar. Aerodynamic loads are transferred by the trailing edge skin and leading edge elements to the spar of the airfoil. Loads are carried through a lower load path and an upper load path. On the upper load path, forces (no pitch moment) are transferred to an upper pivot post, through the upper spherical roller bearing, and then terminate at a ceiling plate, which integrates with the structure of the wind tunnel. On the lower load path, forces (no pitch moment) are transferred to a lower pivot post, through the lower spherical roller bearing, and then terminate at a base plate, which integrates to the structure of the wind tunnel. The pitch moment is transferred to a turntable and this moment is reacted by forces from the hydraulic cylinders.

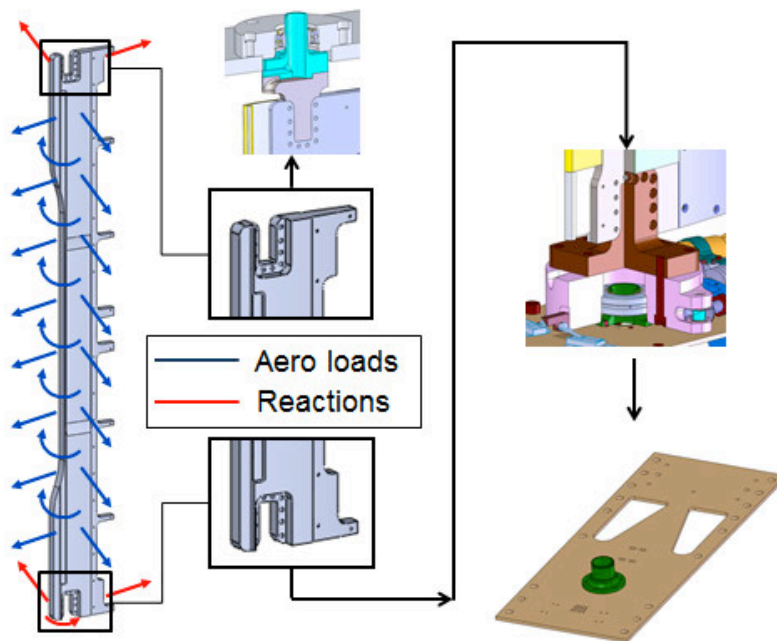
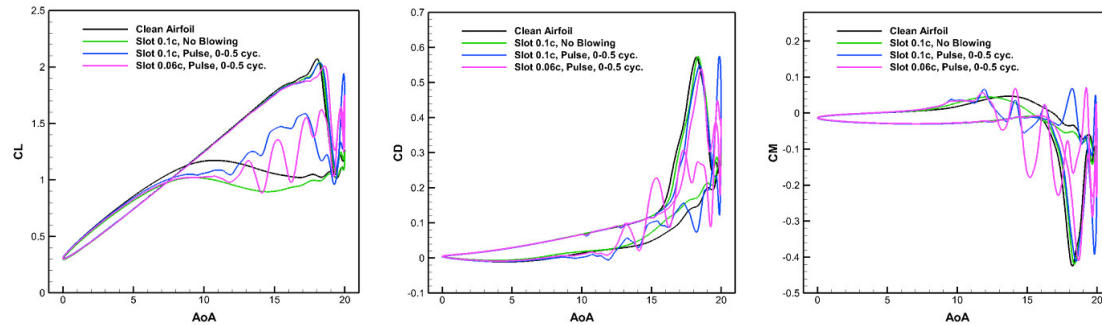


Figure 352. Main loads applied to spar and main load paths.

Worst-case load conditions are derived from the CFD results shown in Figure 353. Peak lift, peak drag, and peak negative moment values were used to apply a steady load condition on the structure. Given the finite dynamic response time of the spar to brief spikes in load, this is a conservative assumption. These loads were distributed evenly across the span of the airfoil. Inertial forces that occur because the center of gravity is aft of the pitch axis are neglected. Inertial moments are small, would reduce the moment load, and are thus, neglected.



**Figure 353. Lift, drag, and moment results for Mach 0.4,  $k=0.07$ ,  $10^\circ \pm 10^\circ$  condition.**

An overview of the different analyses performed for each component of the design is provided in Table 45. The material used for each component is provided in Table 46.

**Table 45. Overview of structural analysis.**

Component	Analyses Performed
Spar	Finite element model (ANSYS Workbench)
Lower Pivot Post	Variable geometry beam analysis, bolt analysis at base plate attachment points
Upper Pivot Post	Finite element model (Solidworks)
Base Plate	Compressive and shear stress analyses at pivot post and cylinder pivot bracket attachment points
Cylinder Pivot Bracket	Bolt analysis at base plate attachment points
Manifold Bracket	Natural frequency and vibration analysis
Cylinder Pins	Shear stress analysis of pins at static and moving attachment points
Upper mount plate	Finite element model (Solidworks)
Upper bearing housing	Finite element model (Solidworks)
TE skins	Finite volume model (Star-CCM+)

**Table 46. Overview of component materials and properties.**

<b>Component</b>	<b>Material</b>	<b>Source</b>
Spar	17-4PH Steel hardened to 155 ksi UTS	New design
Spar Adaptors	4340 Steel	RS630-15000RevC sheet 08
Lower Pivot Post	AMS 5659, TYPE1 15-5PH H1025	RS630-15000RevC sheet 05
Upper Pivot Post	17-4 H1150	New design
Base Plate	4340 Steel	RS630-15000RevC sheet 07
Cylinder Pivot Bracket	AMS 5659, TYPE1 15-5PH H1025	RS630-15000RevC sheet 06
Manifold Bracket	A36 Steel	RS630-15000RevC sheet 04
Cylinder Pins	Alloy Steel ASME B18.8.2	MathCAD file, McMaster PN 97352A430
Upper mount plate	Aluminum 6061-T6	New design
Upper bearing housing	Aluminum 6061-T6	New design
TE skins	Newport NB321 7781 fiberglass	New design

**Spar**

A CAD rendering of the spar is shown in Figure 354 along with the worst-case load conditions used for this analysis. The spar was meshed and analyzed using ANSYS Workbench to perform finite element analysis (FEA). Renderings of the computational mesh are provided in Figure 355. Results from the FEA are shown in Figure 356 - Figure 358.

Nominal stresses along the surface of the spar were generally low, as shown in Figure 356. Max principal and von Mises stresses were very similar and had a maximum of approximately 30 ksi. A significant stress concentration, however, occurs at a hole near the midspan trailing edge of the spar. Here, the maximum principal stress was approximately 62 ksi. Based on the ultimate tensile strength of the material, this provides a safety factor of approximately 2.5.

Data for the same material hardened to 202 ksi UTS are shown in Figure 359. For the purpose of fatigue analysis, the load conditions described above are treated as the cycle maximum while the minimum condition is approximately no load. This is a conservative assumption as the true minimum will be a small load oriented in the same direction. The stress ratio is thus approximately zero. The data in Figure 359 shows that the endurance limit in terms of maximum stress is 140 ksi for a stress ratio of 0.1. To account for the difference of UTS between the material for which data is shown and the material to be used, the endurance limit is decremented by 47 ksi to 93 ksi. In accordance with standard practice, the working limit is decremented by 30% to give a working limit of 65.1 ksi, which is higher than the maximum expected load of 62 ksi. Thus, for the worst-case loading conditions, the spar is designed for infinite life.



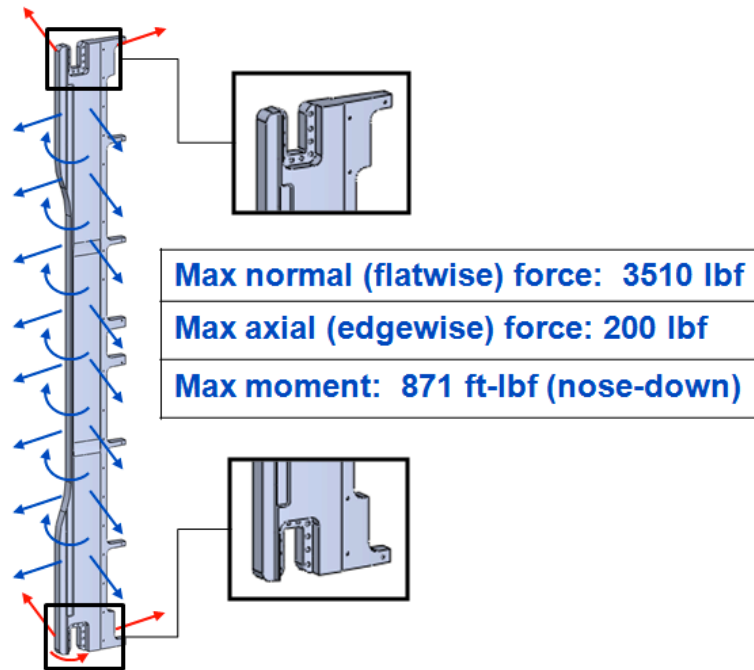


**Figure 354. Spar loading.** Aerodynamic load shown in blue, reaction loads shown in red, directions shown would result in positive values. Visible surface of the spar is upper surface.

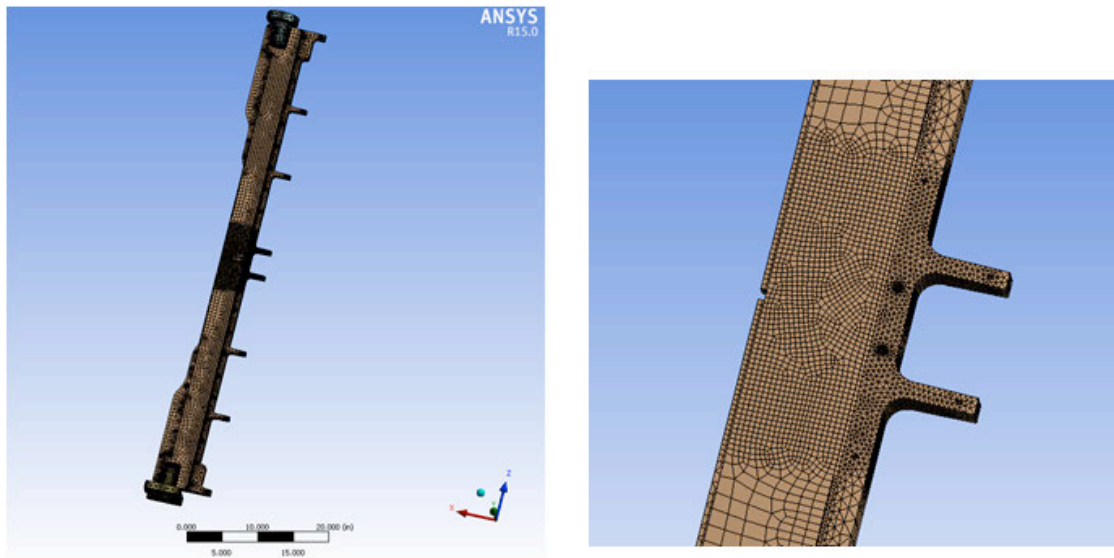


**Figure 355. Computational mesh used for the spar finite element model.**

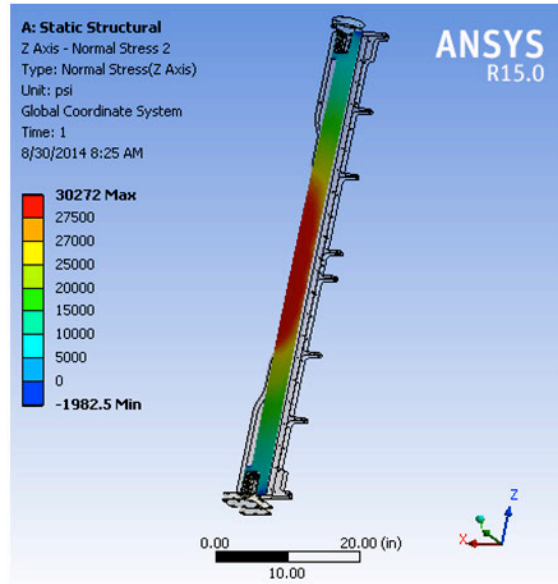
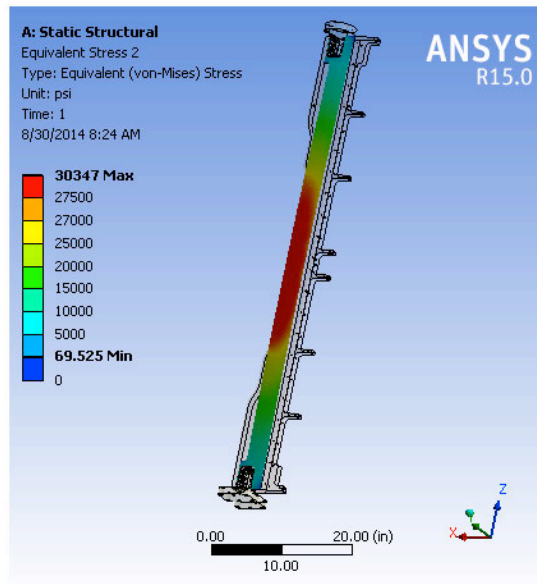


**Figure 356. Spar FEA results: normal and von Mises stresses at the load conditions shown in Figure 354.**

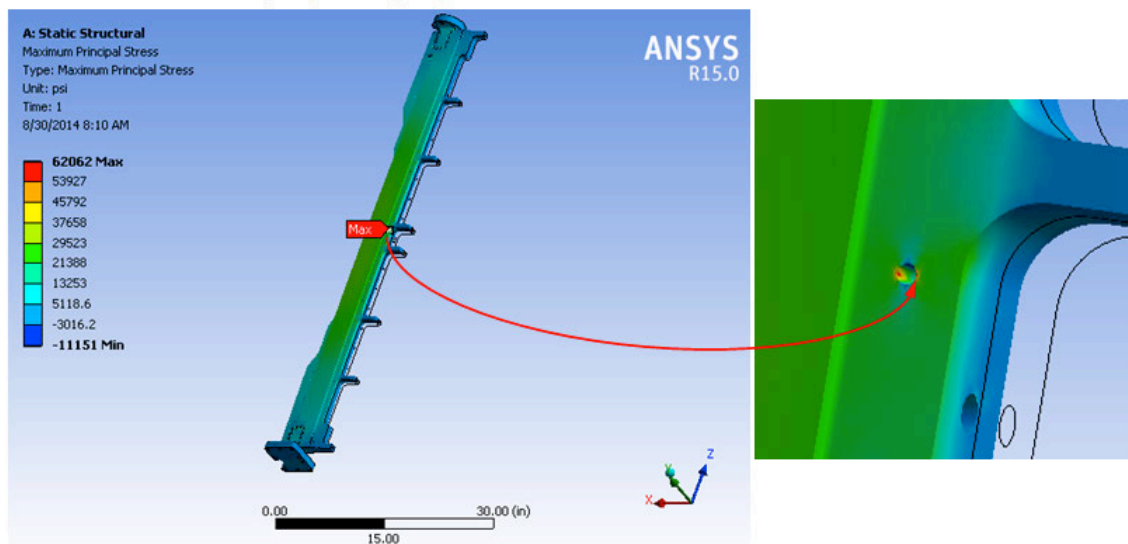


**Figure 357. Spar FEA results: max principal stress at the highest stress point.**

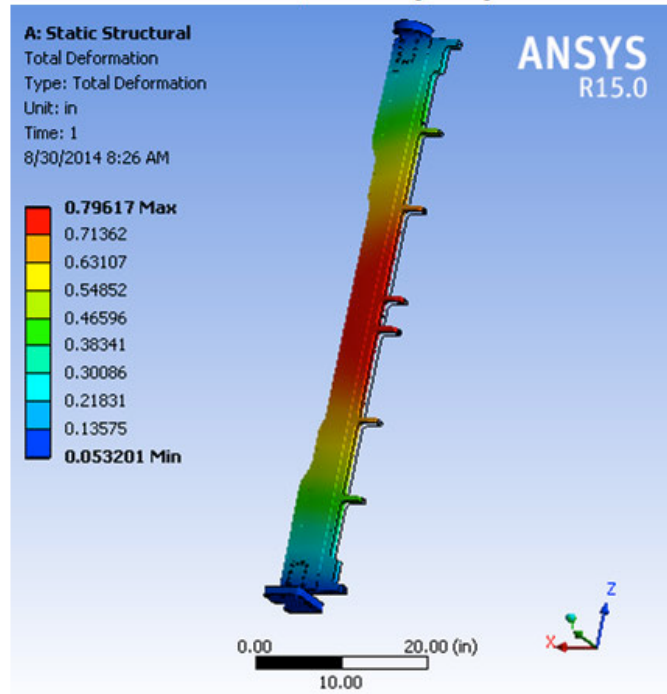


Figure 358. Spar FEA results: total deformation, mostly in the normal (y) direction.

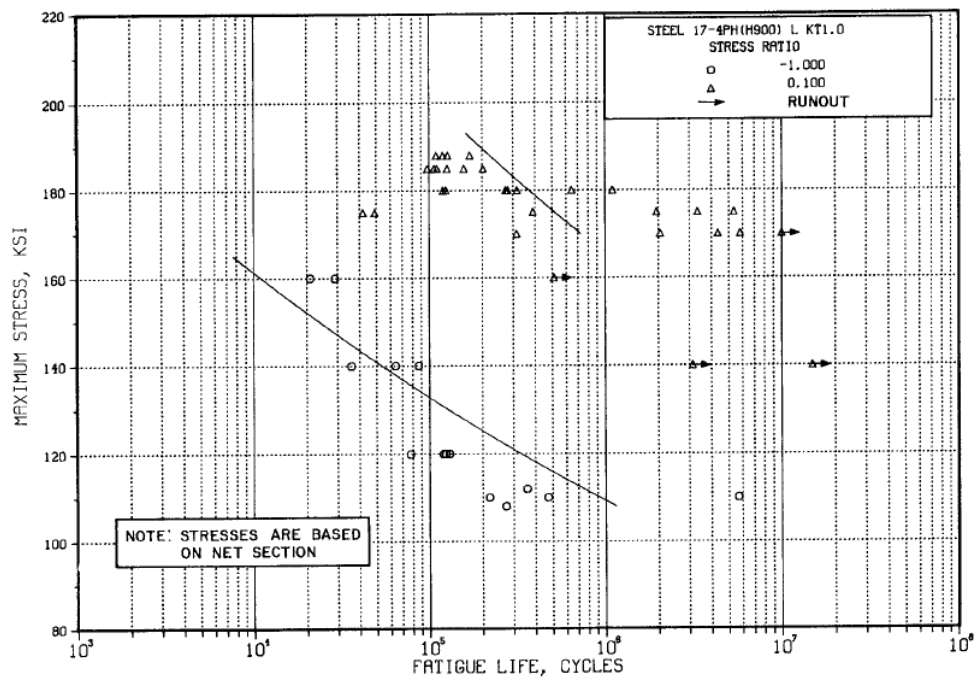


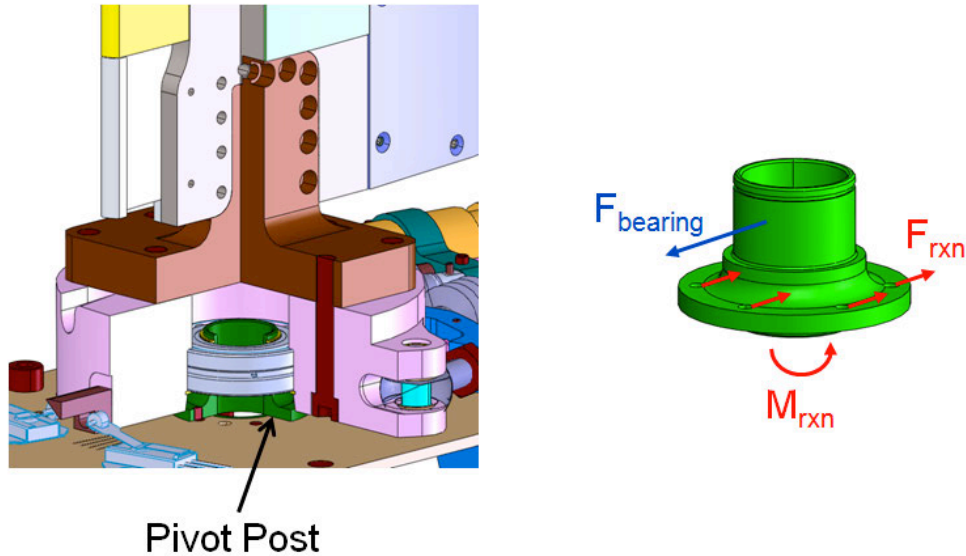
Figure 359. Fatigue data and curve fits from MIL-HDBK-5 for 17-4PH steel hardened to 202 ksi ultimate tensile stress.

### Lower Pivot Post

The pivot post shown in Figure 360 was analyzed as a cylindrical beam of variable cross-section with stress concentration factors shown in Table 47. The material is 15-5PH steel with 155 ksi UTS. The OD of this component is in contact with the ID of the spherical roller bearing; thus, the pivot post is not subjected to significant moments. The maximum load applied to the pivot post,  $React_6$  is given by equation 1. The lift and drag force were evaluated at the maximum conditions described above.  $F_{ext1}$  and  $F_{ret2}$  are the forces output by the hydraulic cylinders 1 and 2 as they extend and retract, respectively. These forces depend on the hydraulic pressure,  $P$ , and the angle-of-attack,  $\alpha$ . A dynamic analysis was performed to determine the maximum pressure that will be required to achieve the desired waveforms under all loads, and it was found that the maximum operating pressure of the system of 3000 psi would be substantially more than the maximum required. However, to be conservative, the pressure used to determine  $React_6$  was 3000 psi. The maximum value of  $React_6$  is 2965 lbf.

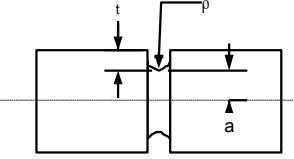
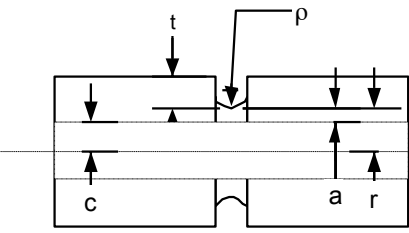
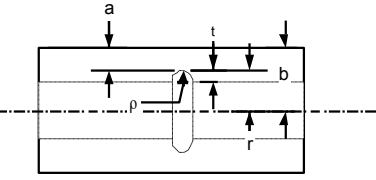
$$React_6(\alpha, t, P) := \left| \frac{Lift(V_{tun}, \theta(t)) + Drag(V_{tun}, \theta(t))}{2} + F_{ext1}(P, \alpha) + F_{ret2}(P, \alpha) \right| \quad (1)$$

Under these load conditions, the maximum stress in the pivot post is 30.7 ksi, which results in a safety factor of 5.1.



**Figure 360. Pivot post loading with key dimensions and applied load from bearing**

**Table 47. Stress concentration factors from Roarke used for pivot post analysis.**

Type of Shaft and Notch	Type of load	Formulae for nominal stress	$\sqrt{\frac{t}{\rho}}$ Series	$\sqrt{\frac{a}{\rho}}$ Curve	$\sqrt{\frac{r}{\rho}}$ Curve
solid shaft 	Tension	$\frac{P}{\pi \cdot a^2}$	b	1	-
	Bending	$\frac{4 \cdot M}{\pi \cdot a^3}$	b	2	-
	Shear	$\frac{1.23 \cdot V}{\pi \cdot a^2}$	a	3	-
	torsion	$\frac{2 \cdot T}{\pi \cdot a^3}$	a	4	-
hollow shaft 	Tension	$\frac{P}{\pi \cdot (r^2 - c^2)}$	b	5	1
	Bending	$\frac{4 \cdot M \cdot r}{\pi \cdot (r^4 - c^4)}$	b	5	2
	Shear	$\frac{(1.23 \cdot r^2 + 2.77 \cdot c^2) \cdot V}{\pi \cdot (r^4 - c^4)}$	a	6	3
	torsion	$\frac{2 \cdot T \cdot r}{\pi \cdot (r^4 - c^4)}$	a	6	4
hollow shaft 	Tension	$\frac{P}{\pi \cdot (b^2 - r^2)}$	b	5	5
	Bending	$\frac{4 \cdot M \cdot r}{\pi \cdot (b^4 - r^4)}$	b	5	6
	Shear	$\frac{(1.23 \cdot r^2 + 2.77 \cdot b^2) \cdot V}{\pi \cdot (b^4 - r^4)}$	a	6	7
	torsion	$\frac{2 \cdot T \cdot r}{\pi \cdot (b^4 - r^4)}$	a	6	8

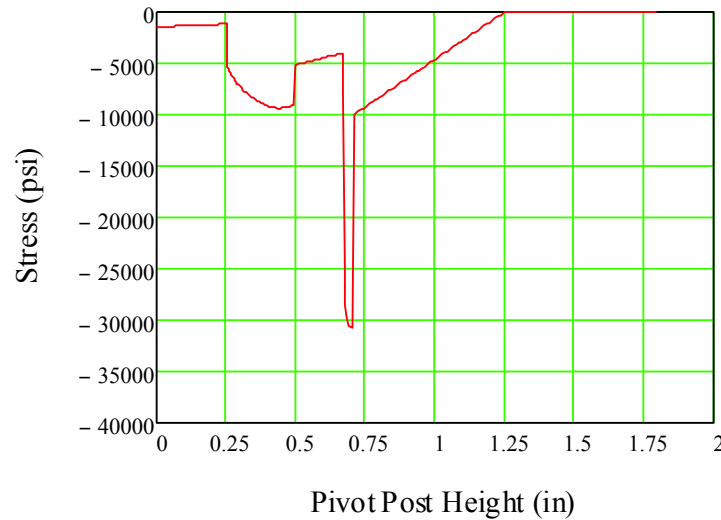


**Figure 361. Stress along the height of the pivot post.**

Bolt pattern analysis was also conducted on the pivot post. Loads were shared based on distance from the hinge line. The bolts used for the pivot post are  $\frac{1}{4}$ -28 UNF fasteners with 5730 lbf ultimate strength. The same load as shown above was applied for this analysis. Based on this, the bolt pattern is shown to be robust with a safety factor of 10.2.

#### **Cylinder Pivot Bracket**

This component was analyzed based on two hinge-lines, as shown in Figure 362. The material is 15-5PH steel with 155 ksi UTS. The same loads used for the pivot post analysis, based on maximum cylinder pressure, were used here. It was assumed that fasteners bear all moments and that loads are shared based on distance from the hinge line. The minimum safety factor found occurs when the vertical hinge line is considered and the fasteners are subjected the shear. The minimum shear safety factor is 9.0.

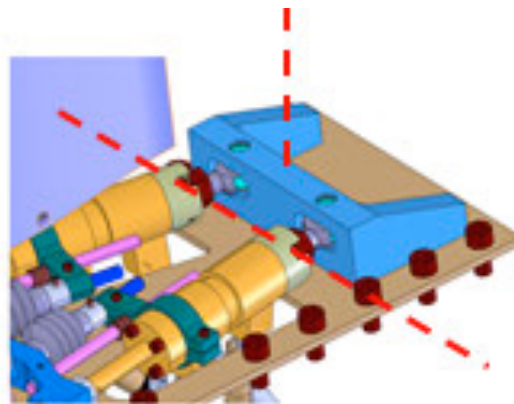


**Figure 362. Cylinder pivot bracket, hinge lines considered shown in red.**

### Base Plate

The base plate, as shown in Figure 363, was analyzed at the locations where the pivot post and cylinder pivot bracket are mounted. The material of the base plate is 4340 steel with 125 ksi UTS. For the pivot post location, the worst-case reaction load from the pivot post analysis was applied at the piloted hole. Shear and compressive stresses were evaluated, and the minimum safety factor was found to be 21.1 for compressive load. At the cylinder pivot bracket location, the maximum load from that analysis was applied to the plate via two shear pins. Again, both shear and compressive stresses were evaluated, and the minimum safety factor was found to be 7.3 for compressive stress.

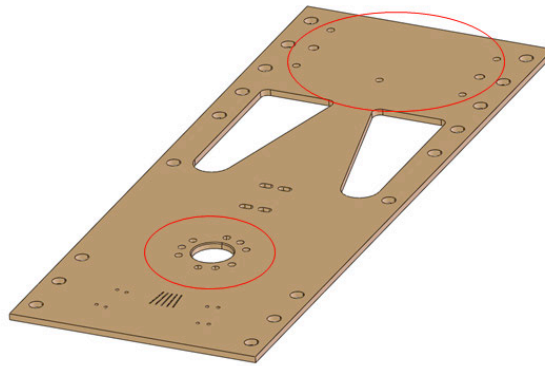


**Figure 363. Base plate analysis, two areas considered.**

### Spherical Roller Bearings

The bearings to be used at the top and bottom of the airfoil are SKF spherical roller bearings (P/N: BS2-2208-2CS-VT143\*), shown schematically in Figure 364. Given that the bearings will be subjected to small oscillations rather than full rotation, an equivalent static load was calculated based on the analytical guidelines and equations provided by SKF. These calculations are shown in Figure 365. The maximum radial load,  $F_r$ , is taken to be the same as the maximum load applied to the pivot post,  $React_6$ . The axial load,  $F_a$ , is based on the total weight supported by the bearing. Using the values and equations provided by SKF, the bearing safety factor is acceptable at 5.4.



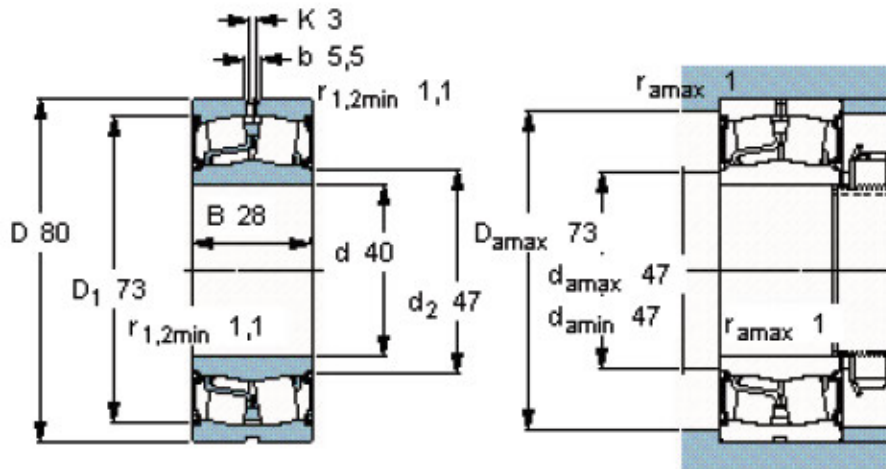


Figure 364. Schematic diagram of spherical roller bearing SKF BS2-2208-2CS-VT143\*, from SKF catalog.

	Static	Dynamic
$e := .28$		
$Y_1 := 2.4$	$C_0 := 90\text{kN}$	$C := 96.5\text{kN}$
$Y_2 := 3.6$	$X_0 := 1$	$X := .67$
$Y_0 := 2.5$	$C_0 = 2.023 \times 10^4 \cdot \text{lbf}$	$Y := 3.6$
	$F_r := 2956\text{lbf}$	
	$F_a := 330\text{lbf}$	

#### Bearing Dynamic Load Check

if  $F_a/F_r < e$

$$P_1 := F_r + Y_1 \cdot F_a \quad P_1 = 3.748 \times 10^3 \cdot \text{lbf}$$

if  $F_a/F_r > e$

$$P_2 := .67 \cdot F_r + Y_2 \cdot F_a \quad P_2 = 1.188 \times 10^3 \cdot \text{lbf}$$

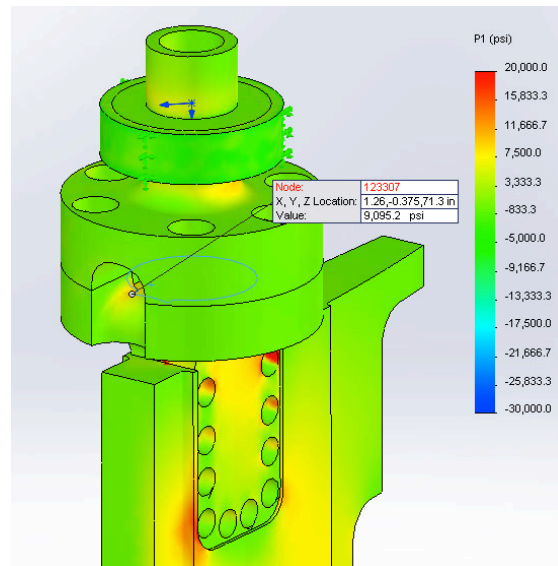
$$s_0 := \frac{C_0}{P_1} \quad s_0 = 5.398$$

Figure 365. Bearing calculations.

#### Upper Pivot Post

A finite element model of the upper pivot post was created using Solidworks. Components to either side of the upper pivot post along the load path were included in the model to provide good boundary conditions. The material used was 17-4 H1150 steel with an UTS of 155 ksi. As

shown in Figure 366, the maximum first principal stress was approximately 9 ksi, which results in a safety factor of 17.



**Figure 366. Upper pivot post FEA results: first principal stress.**

### Upper Plate and Bearing Housing

A finite element model of the upper plate and bearing housing was created using Solidworks. Stress levels in these components were shown to be below 3 ksi, as shown in Figure 367. Based on an ultimate tensile strength of 45 ksi for Aluminum 6061-T6, a safety factor of 15 is achieved.

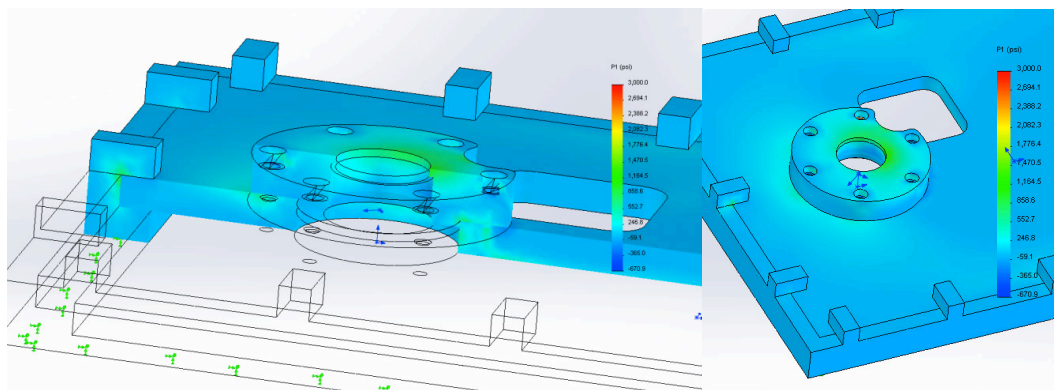


**Figure 367. Upper plate and bearing housing.**

### Trailing edge Skins

The load condition at which to analyze the TE skins was determined as follows. Unsteady pressure distributions from the CFD analysis were post-processed to evaluate two parameters as a function of time: the lift force, and the moment about a hinge-line that runs in the spanwise direction along the leading edge of the TE skins. All Mach numbers of interest were considered

and it was shown that Mach 0.3 provides the worst case loadings for these parameters. The values of these parameters through one pitch cycle are shown in Figure 368. The maximum values are noted in the figure. Next, the pressure distribution at the peaks was examined as shown in Figure 369. Through this, it was shown that the peak liftwise force found in Figure 368 is distributed fairly evenly across the TE skin.

Thus, the load condition shown in Figure 370 was established with a liftwise load of 60 lbf acting on one repeating section of the TE skins. The model was supported via fixed-geometry boundary conditions applied to the flat-head fastener locations. A computational mesh was created using Star-CCM+, as shown also in Figure 370. Given the presence of the fixed geometry, a singularity was expected at this point; thus, the model was run with three levels of mesh refinement to help evaluate this singularity. The results are shown in Figure 371. The stresses from all three meshes agree quite well until we approach the hole, which is further indication of singularity. The peak stress at the hole is determined using standard stress normalization, extrapolating from the point nearest to the hole where all three meshes agree (approximately  $x = -0.3175''$ ) thus giving a peak stress of approximately 10 ksi. The Newport NB321 7781 fiberglass pre-preg planned to be used for the TE skins has an ultimate tensile strength of greater than 50 ksi using B-basis results from Ref. 1. Thus, the minimum safety factor on the composite panels is approximately 5.

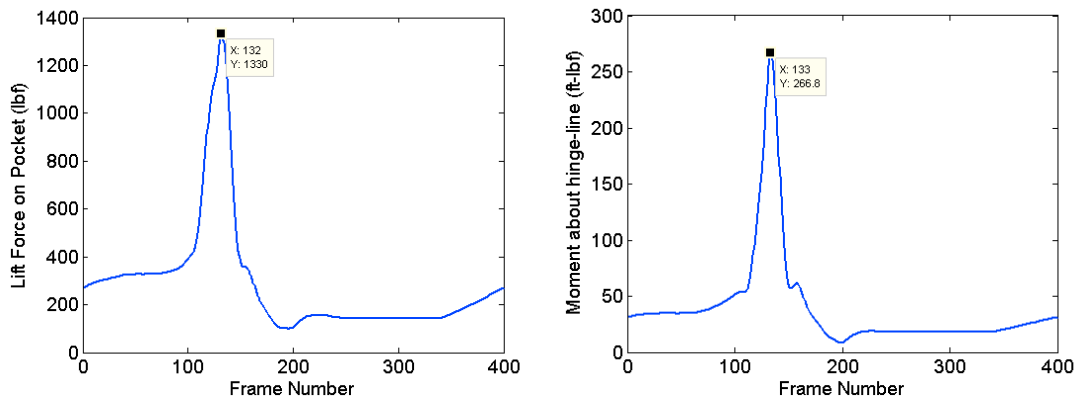


**Figure 368. Lift force and moment about hinge-line acting on the trailing edge skins (pocket) of the airfoil. Results based on CFD analysis at Mach 0.3,  $10^\circ \pm 10^\circ$  at  $k=0.1$ .**

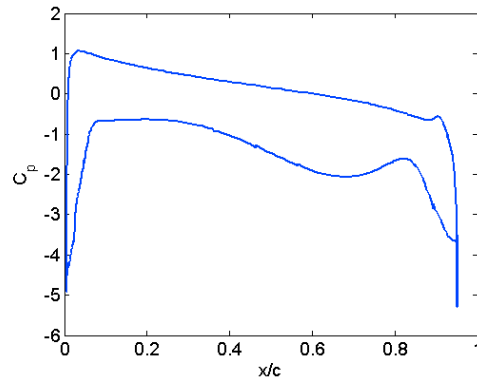


**Figure 369. Worst-case pressure distribution based on the peaks from Figure 368.**

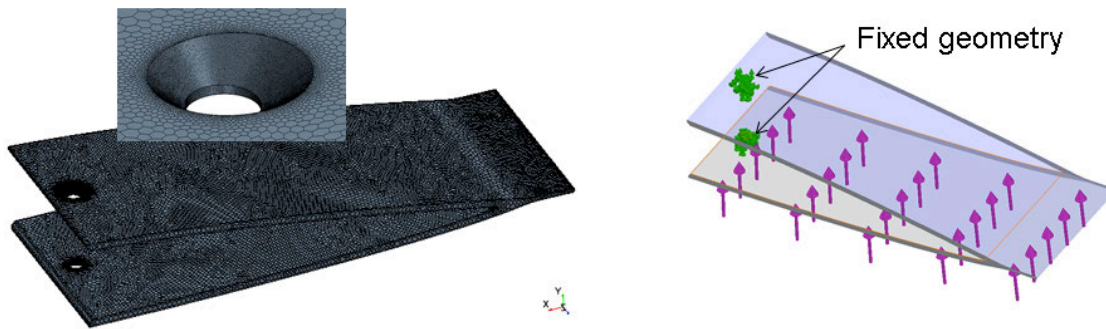


**Figure 370. Computational mesh and load distribution of the trailing edge skins.**

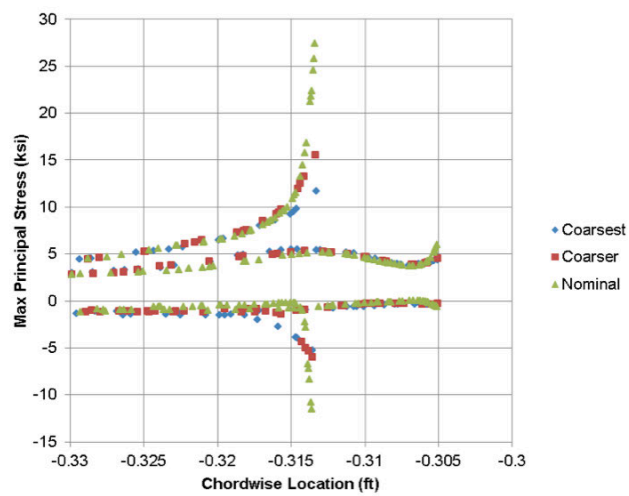


**Figure 371. Max principal stress at 3 different levels of mesh refinement.**

**Table 48. Summary of all pitching airfoil components analyzed and their associated safety factors.**

<b>Component</b>	<b>Safety Factor</b>
Spar	2.5 / Infinite Life
Lower Pivot Post	5.1
Lower Pivot Post to Baseplate Fasteners	10.2
Cylinder Pivot Bracket to Base Plate Fasteners	9.0
Base Plate	21.1
Cylinder Pivot Bracket to Base Plate Shear Pins	7.3
Spherical Roller Bearings	5.4
Upper Pivot Post	17
Upper Plate and Bearing Housing	15
Trailing edge Skins	5

### ***B. Actuators and Leading edge Components***

Structural analysis was performed on the actuators, gas plenum, and outboard covers for the leading of the model. Solidworks finite element analysis (FEA) was used in all cases with the materials treated as 6061 aluminum allow (18 ksi UTS). Bolt analysis was also conducted on the spar/gas plenum fasteners treating them as alloy steel (150 ksi UTS). For these calculations, an extremely rigorous condition was used with the entire maximum expected lift force on the model (3510 lbf) applied at the leading edge of the model normal to the chord line (distributed evenly over the span). This represents an extreme worst case both in terms of the load (which will actually be significantly less for most test cases and even over the pitching cycle for the highest test case), and the distribution of that load (which will be distributed over the model rather than acting with the longest possible moment arm as is the case with it fully applied at the LE). The analysis also considers each part individually and does not include the strength that is added by mechanical connections. For example, Figure 372 shows the displacement of a single actuator unit under this loading while fixing its attachment to the gas plenum, but does not include strength, which may be expected to be gained from the addition of the lower cover plate. Nonetheless, a displacement of less than 1 mm at the airfoil leading edge is calculated (and although not shown here, von Mises values are well below the yield strength).

Displacement and stress results for the gas plenum base are shown in Figure 373. Very minimal displacement is shown here (less than 0.015 mm) with stress levels a factor of 5 below the yield strength. Beyond the forces on the body itself, the screw attachment of the gas plenum to the spar is critical. The screws attach the gas plenum base to the spar in the streamwise direction and the force exerted on the screws is calculated treating the forces as simple moment arms as shown in Figure 374 (with any strength added by the interface with the key on the spar ignored). With 8 4-40 alloy steel screws holding the base to the spar, the force on each screw comes out to 281 lbf. This maintains a factor of safety of approximately 3.5 for the screw attachment.

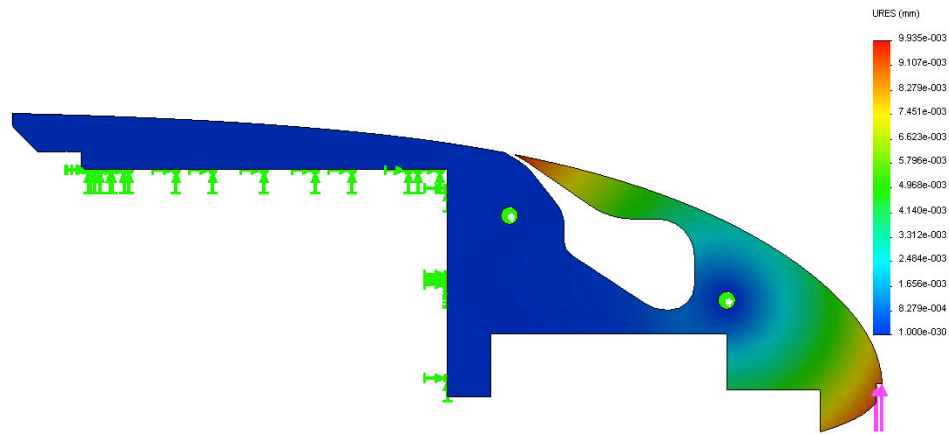


**Figure 372. FEA displacement on an individual actuator unit.**

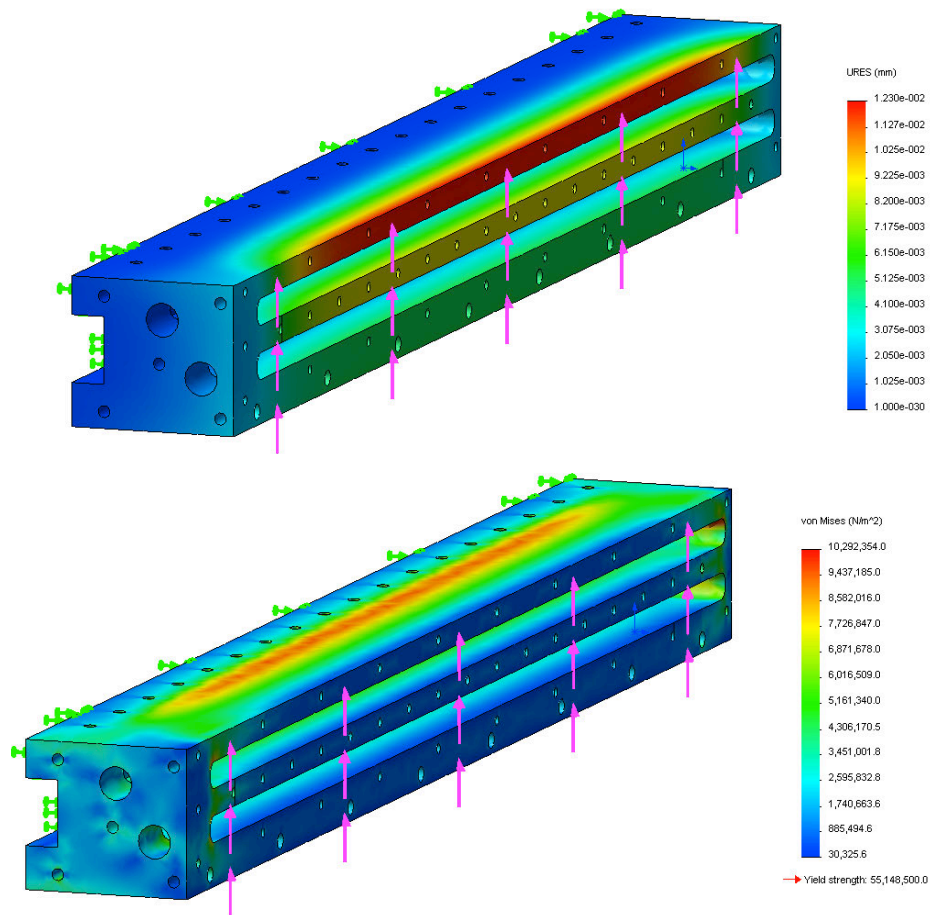


**Figure 373. FEA on gas plenum base showing displacement (above) and stress (below)**

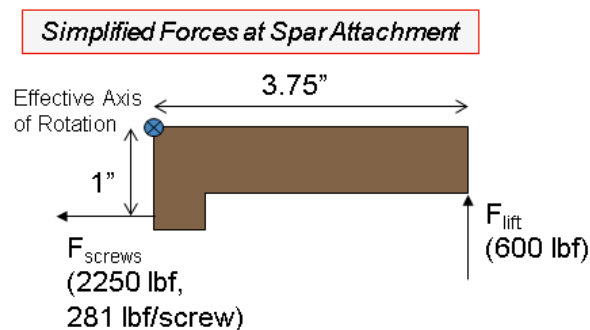


**Figure 374. Bolt analysis treating forces as simple moment arm**

Finally, Figure 375 and Figure 376 show the FEA results for the outboard covers for displacement and stress, respectively. Displacement values are again very reasonable ( $< 0.25\text{mm}$ ) and not expected to be problematic. There are some high stress concentrations indicated near the countersinks for the attachment screws on the upper surface of the model, similar to those indicated for the mounting screws for the trailing edge. A similar mesh refinement approach was used to handle these singularities, extrapolating from the point where



the meshes are in agreement, and indicating a real expected peak of 35 MPa (5 ksi), and leaving a factor of safety of roughly 3.5.

A summary table of all analyzed components and associated safety factors is provided in Table 49.

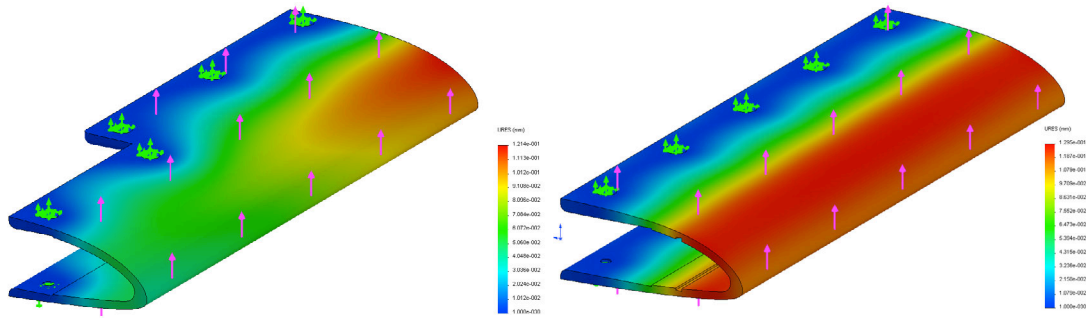


**Figure 375. FEA displacement results on LE outboard covers.**

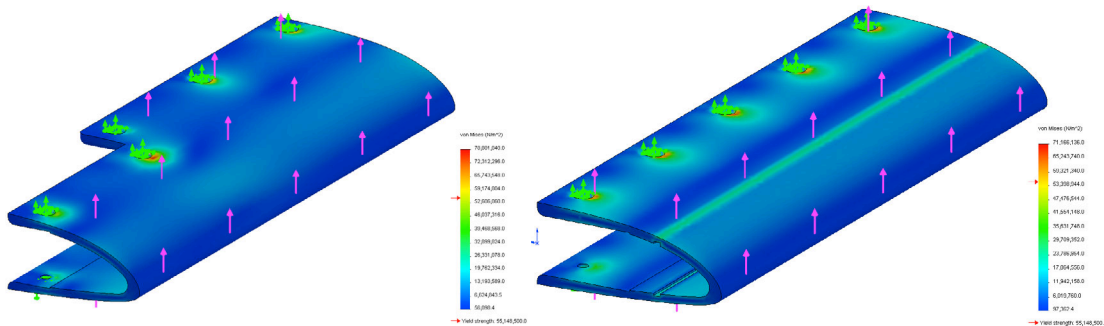


**Figure 376. FEA stress results on LE outboard covers.**

**Table 49. Summary of all actuator and LE components analyzed and their associated safety factors.**

Component	Safety factor
Gas plenum	5
Gas plenum to spar fasteners	3.5
LE outboard covers	3.5

## 2. References

1. Tomblin, J., J. McKenna, Y. Ng, and K.S. Raju, "B – Basis Design Allowables for Epoxy – Based Prepreg Newport E-Glass Fabric 7781 / NB321," Report no. AGATE-WP3.3-033051-097, July 2001.

2. Soeder, R.H., D.W. Sheldon, R.F. Ide, D.A. Spera, and C.R. Andracchio, "NASA Glenn Icing Research Tunnel User Manual," NASA/TM—2003-212004.

## Appendix 2. Low-Speed Wind Tunnel Test – Load Measurements

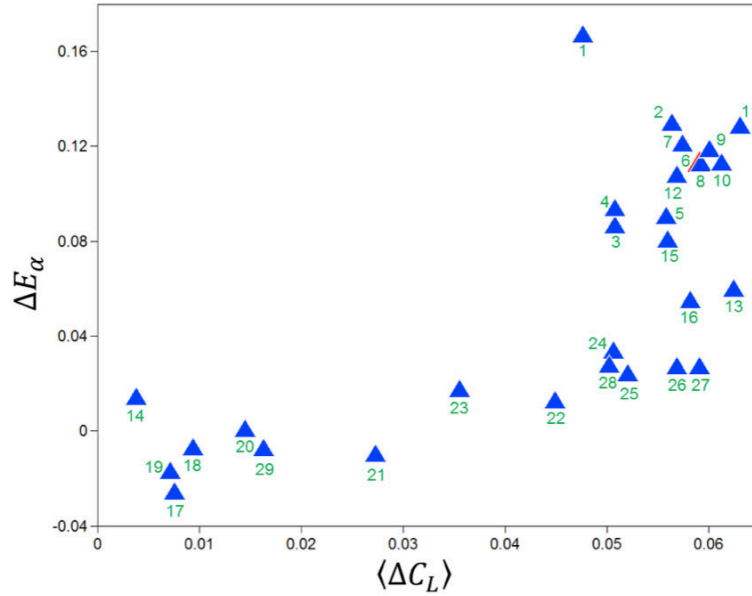


Figure 377. Change in cycle averaged lift coefficient versus damping coefficient with actuation patterns 1 through 29 labeled for  $10^\circ \leq \alpha \leq 20^\circ$  at  $M = 0.06$  and  $k = 0.06$ .

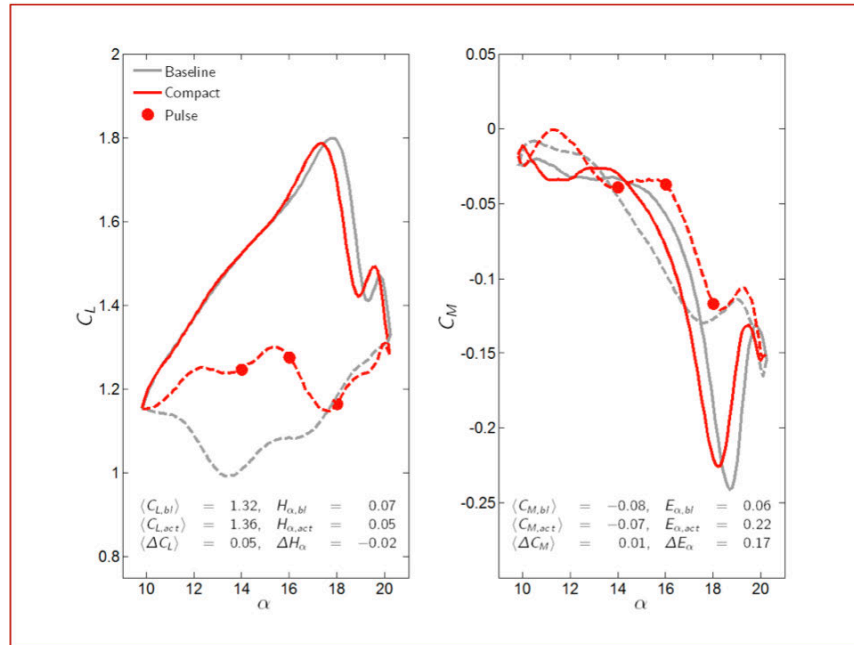


Figure 378. Lift and moment profiles for actuation pattern 1 (downstroke firing at  $\alpha = 18^\circ$ ,  $16^\circ$ , and  $14^\circ$ ) for  $10^\circ \leq \alpha \leq 20^\circ$  at  $M = 0.06$  and  $k = 0.06$ .

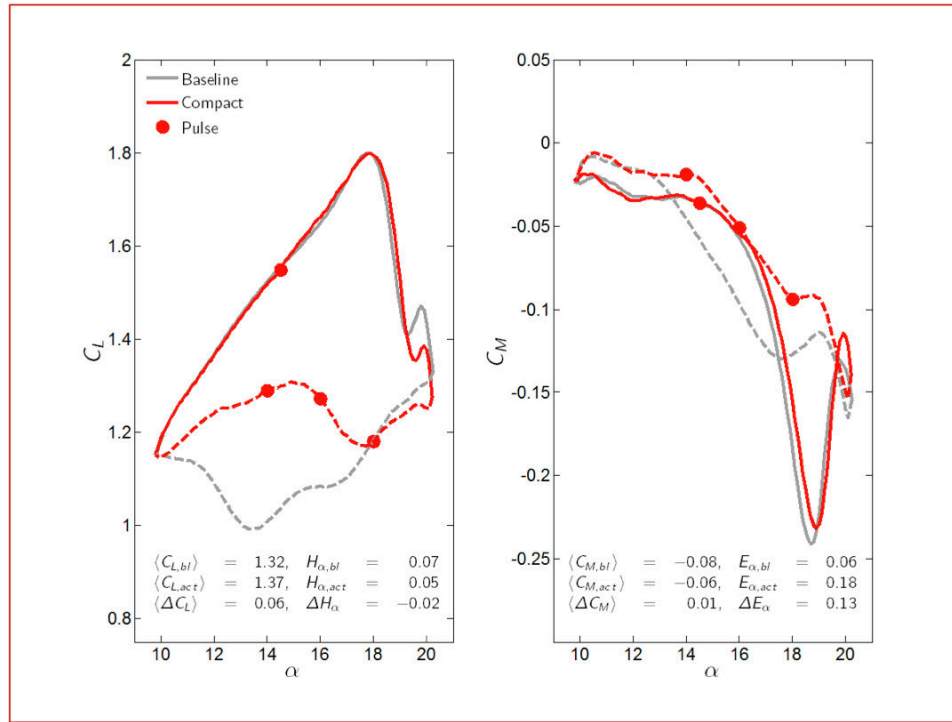


Figure 379. Lift and moment profiles for actuation pattern 2 (upstroke firing at  $\alpha = 14.5^\circ$ ; downstroke firing at  $\alpha = 18^\circ, 16^\circ$ , and  $14^\circ$ ) for  $10^\circ \leq \alpha \leq 20^\circ$  at  $M = 0.06$  and  $k = 0.06$ .

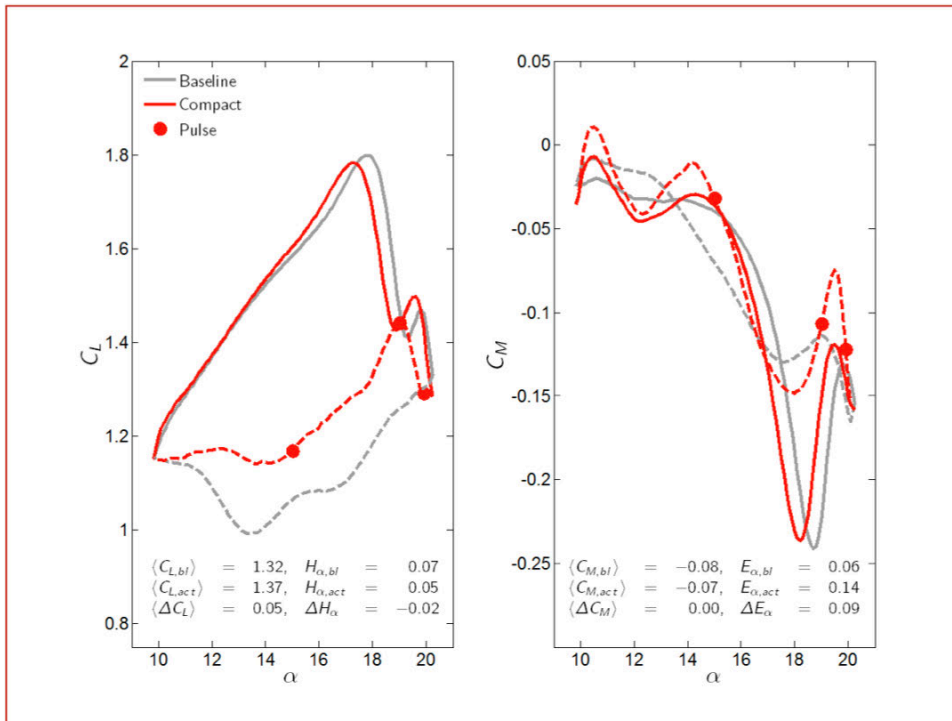
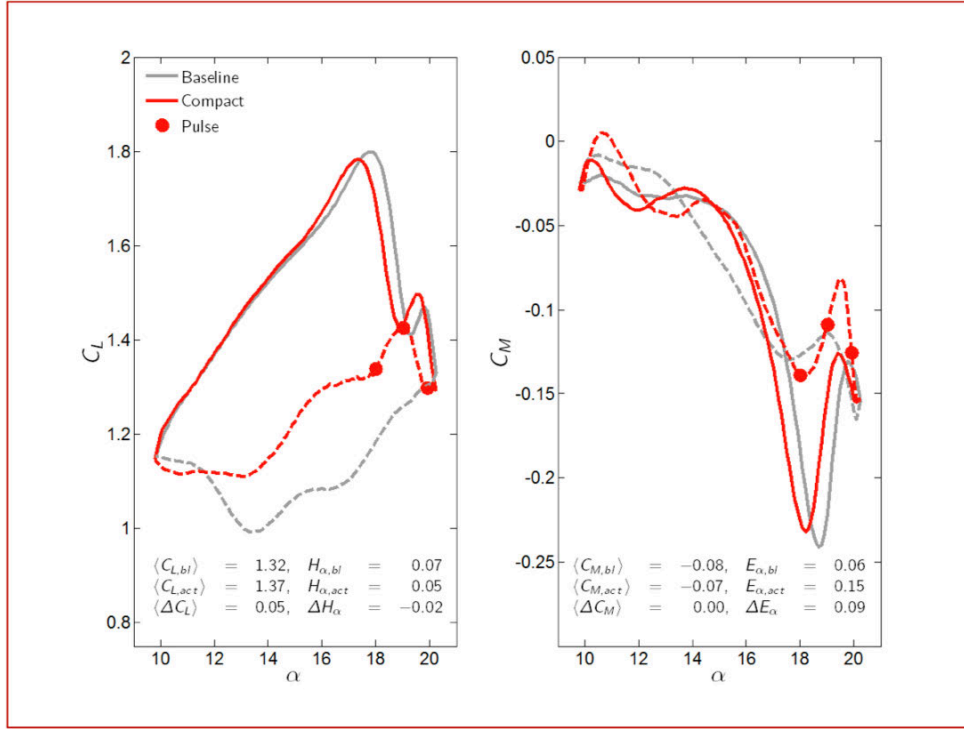
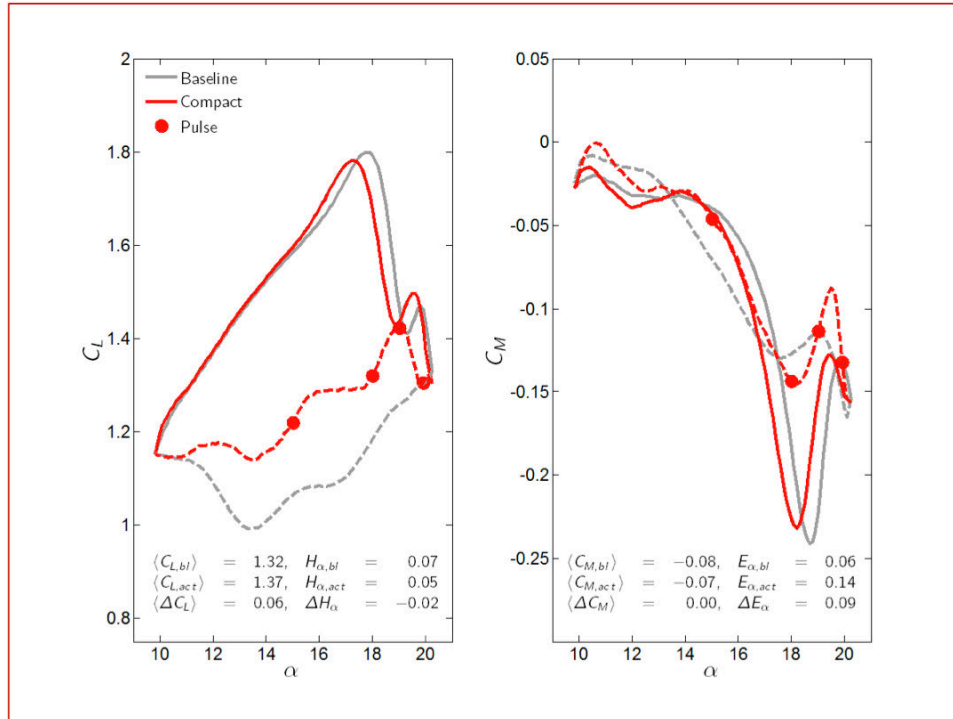


Figure 380. Lift and moment profiles for actuation pattern 3 (downstroke firing at  $\alpha = 19.9^\circ, 19^\circ$ , and  $15^\circ$ ) for  $10^\circ \leq \alpha \leq 20^\circ$  at  $M = 0.06$  and  $k = 0.06$ .



**Figure 381. Lift and moment profiles for actuation pattern 4 (downstroke firing at  $\alpha = 19.9^\circ, 19^\circ, \text{ and } 18^\circ$ ) for  $10^\circ \leq \alpha \leq 20^\circ$  at  $M = 0.06$  and  $k = 0.06$ .**



**Figure 382. Lift and moment profiles for actuation pattern 5 (downstroke firing at  $\alpha = 19.9^\circ, 19^\circ, 18^\circ, \text{ and } 15^\circ$ ) for  $10^\circ \leq \alpha \leq 20^\circ$  at  $M = 0.06$  and  $k = 0.06$ .**

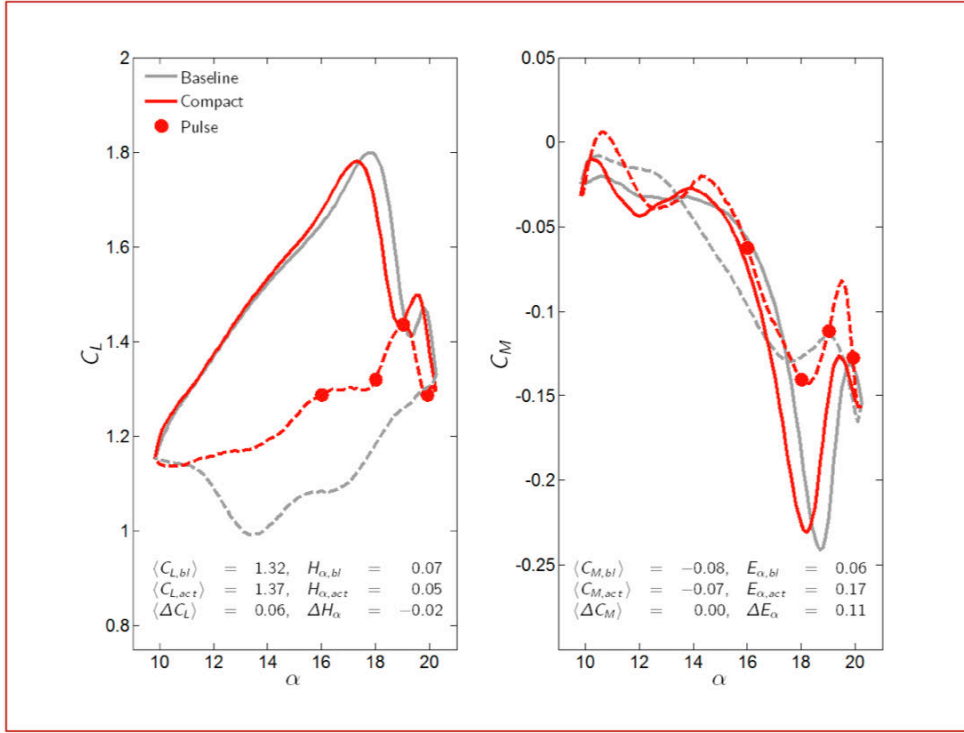


**Figure 383.** Lift and moment profiles for actuation pattern 6 (downstroke firing at  $\alpha = 19.9^\circ, 19^\circ, 18^\circ$ , and  $16^\circ$ ) for  $10^\circ \leq \alpha \leq 20^\circ$  at  $M = 0.06$  and  $k = 0.06$ .

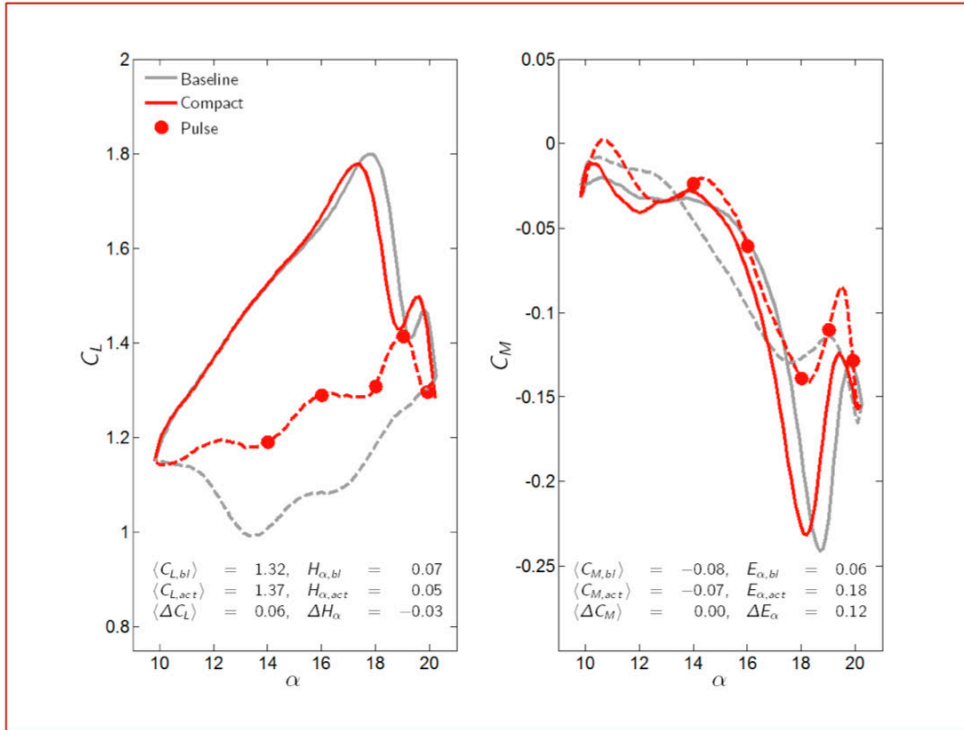


**Figure 384.** Lift and moment profiles for actuation pattern 7 (downstroke firing at  $\alpha = 19.9^\circ, 19^\circ, 18^\circ, 16^\circ$ , and  $14^\circ$ ) for  $10^\circ \leq \alpha \leq 20^\circ$  at  $M = 0.06$  and  $k = 0.06$ .

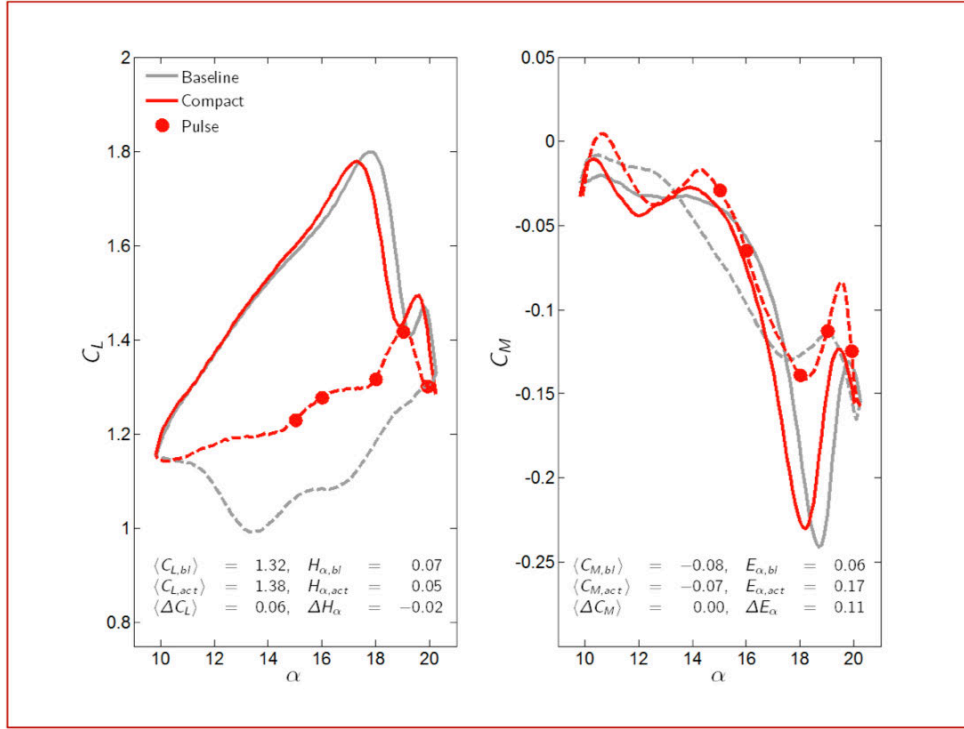


**Figure 385. Lift and moment profiles for actuation pattern 8 (downstroke firing at  $\alpha = 19.9^\circ, 19^\circ, 18^\circ, 16^\circ, \text{ and } 15^\circ$ ) for  $10^\circ \leq \alpha \leq 20^\circ$  at  $M = 0.06$  and  $k = 0.06$ .**

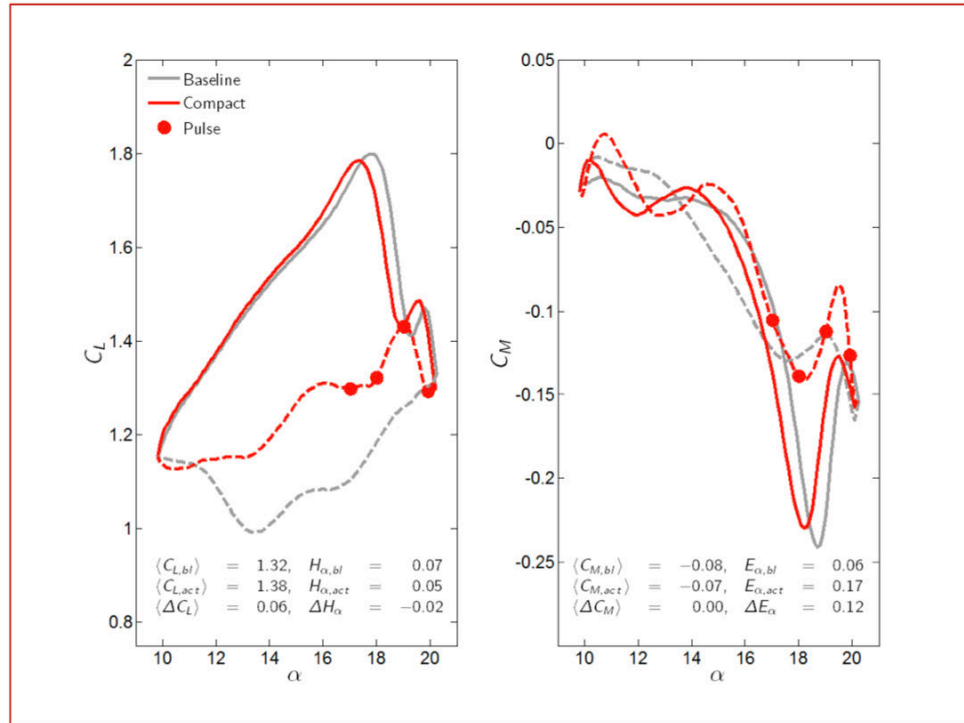


**Figure 386. Lift and moment profiles for actuation pattern 9 (downstroke firing at  $\alpha = 19.9^\circ, 19^\circ, 18^\circ, \text{ and } 17^\circ$ ) for  $10^\circ \leq \alpha \leq 20^\circ$  at  $M = 0.06$  and  $k = 0.06$ .**



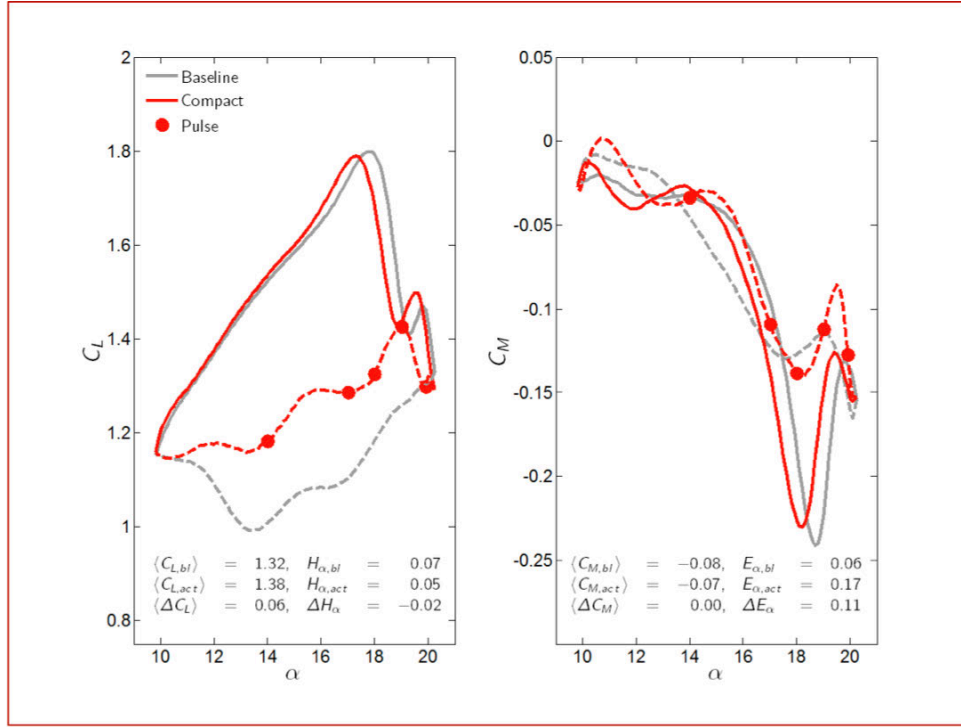


**Figure 387. Lift and moment profiles for actuation pattern 10 (downstroke firing at  $\alpha = 19.9^\circ, 19^\circ, 18^\circ, 17^\circ$ , and  $14^\circ$ ) for  $10^\circ \leq \alpha \leq 20^\circ$  at  $M = 0.06$  and  $k = 0.06$ .**

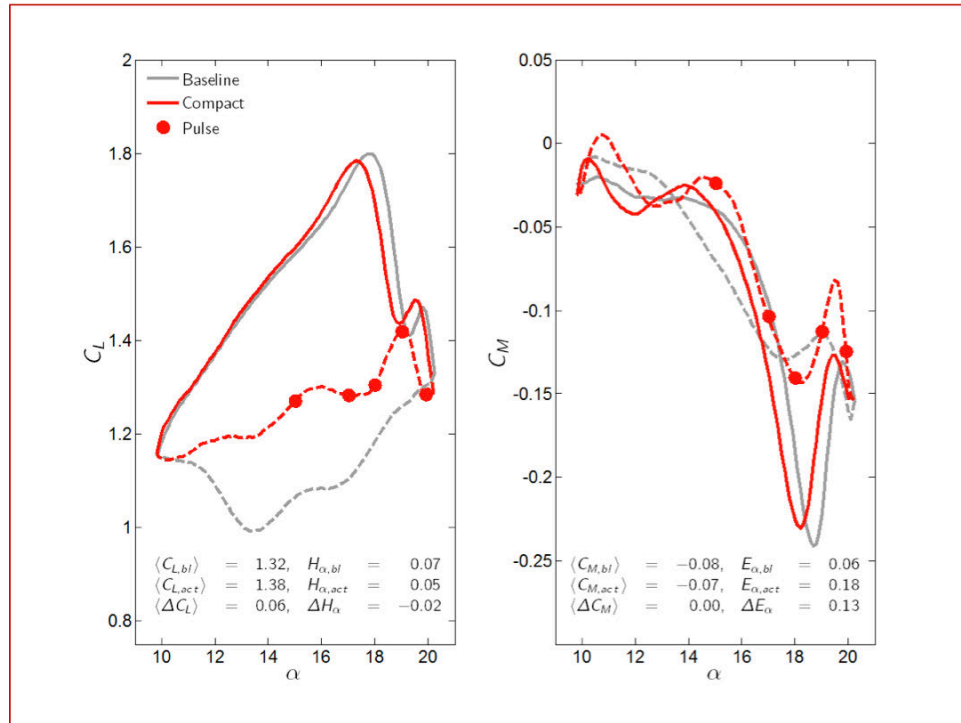


**Figure 388. Lift and moment profiles for actuation pattern 11 (downstroke firing at  $\alpha = 19.9^\circ, 19^\circ, 18^\circ, 17^\circ$ , and  $15^\circ$ ) for  $10^\circ \leq \alpha \leq 20^\circ$  at  $M = 0.06$  and  $k = 0.06$ .**

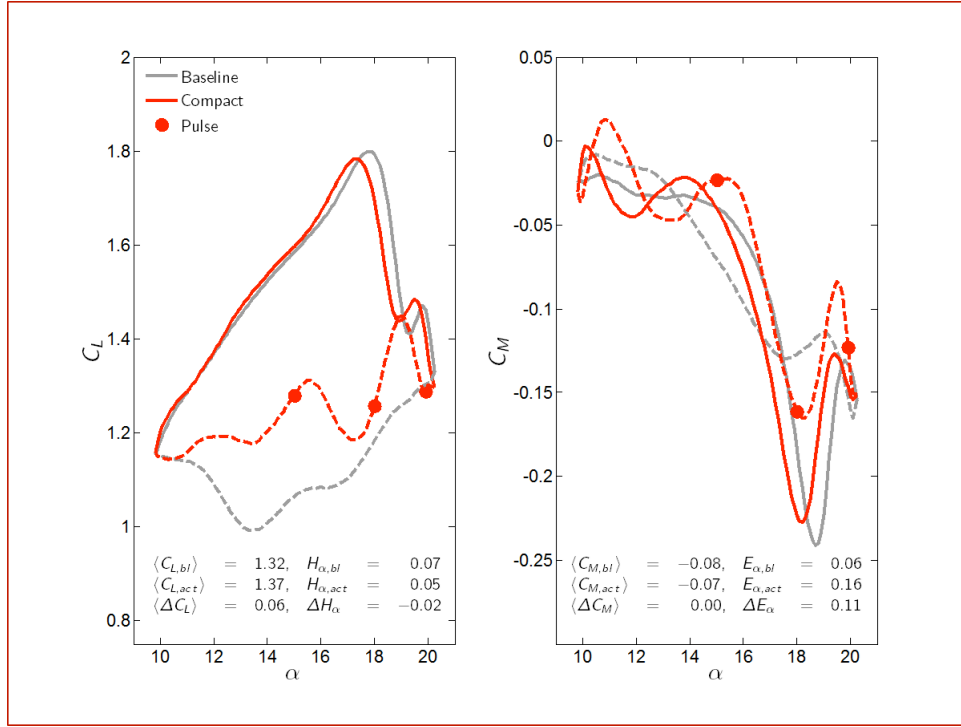


**Figure 389. Lift and moment profiles for actuation pattern 12 (downstroke firing at  $\alpha = 19.9^\circ, 18^\circ, \text{ and } 15^\circ$ ) for  $10^\circ \leq \alpha \leq 20^\circ$  at  $M = 0.06$  and  $k = 0.06$ .**

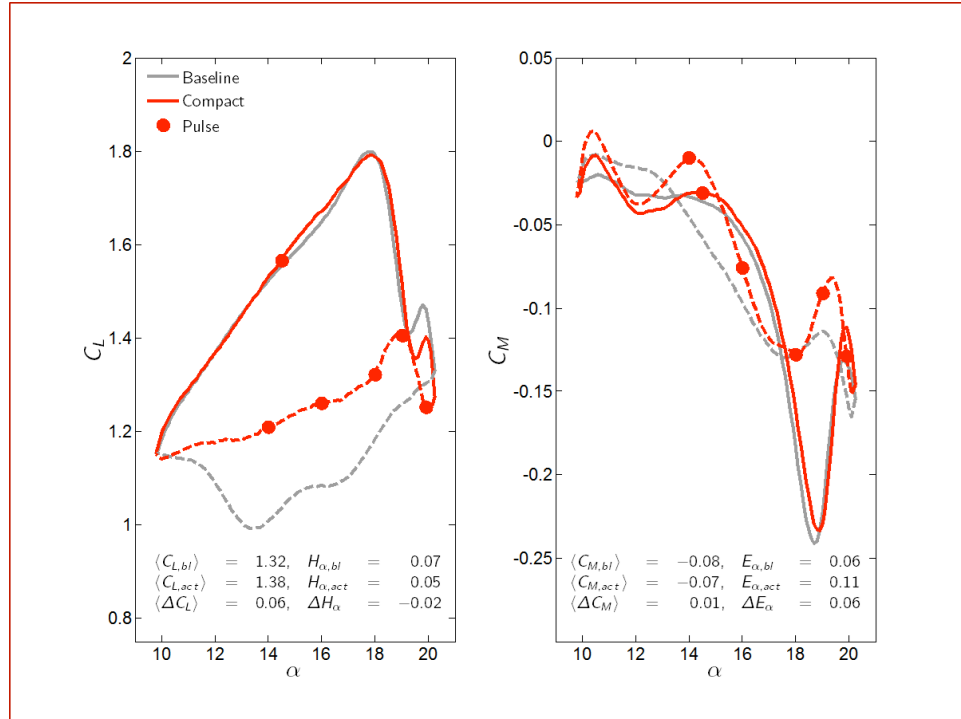


**Figure 390. Lift and moment profiles for actuation pattern 13 (upstroke firing at  $\alpha = 14.5^\circ$ ; downstroke firing at  $\alpha = 19.9^\circ, 19^\circ, 18^\circ, 16^\circ, \text{ and } 14^\circ$ ) for  $10^\circ \leq \alpha \leq 20^\circ$  at  $M = 0.06$  and  $k = 0.06$ .**

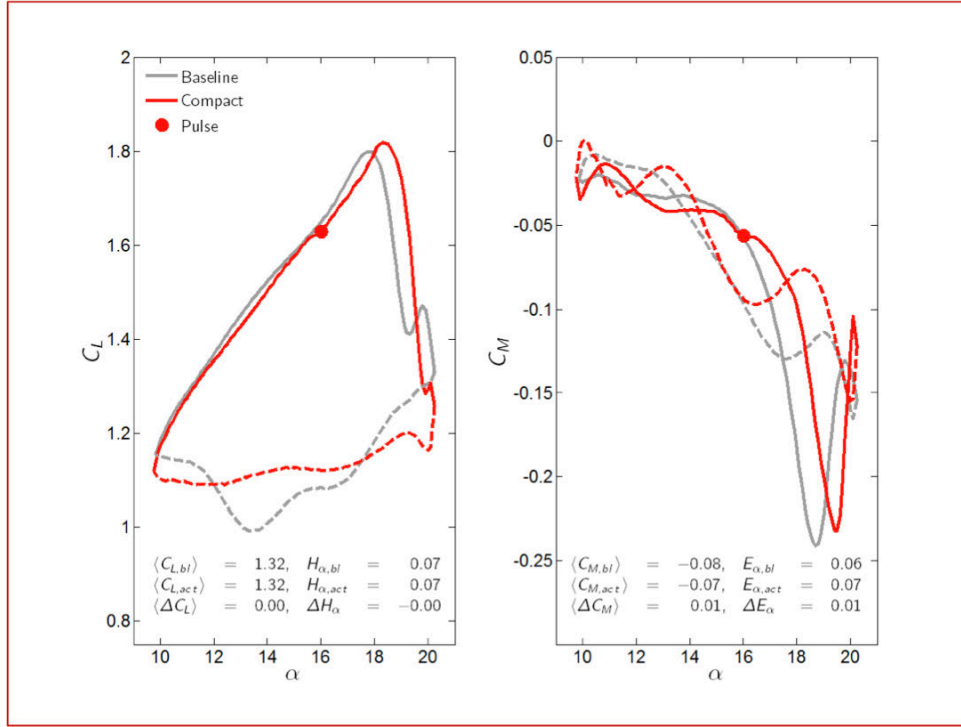


**Figure 391. Lift and moment profiles for actuation pattern 14 (upstroke firing at  $\alpha = 16^\circ$ ) for  $10^\circ \leq \alpha \leq 20^\circ$  at  $M = 0.06$  and  $k = 0.06$ .**

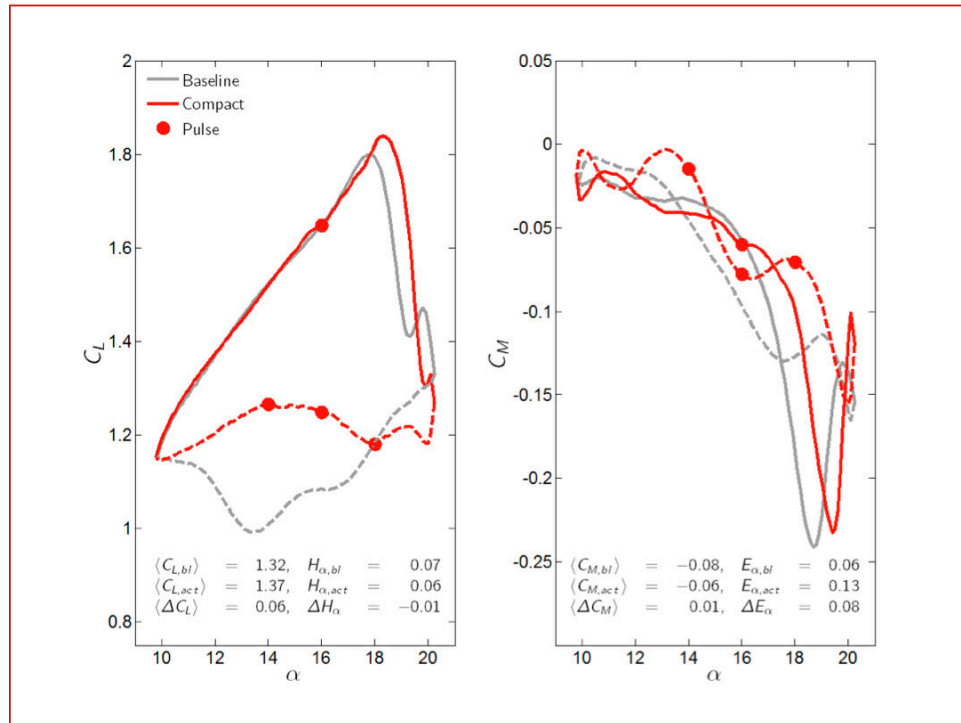


**Figure 392. Lift and moment profiles for actuation pattern 15 (upstroke firing at  $\alpha = 16^\circ$ ; downstroke firing at  $\alpha = 18^\circ, 16^\circ$ , and  $14^\circ$ ) for  $10^\circ \leq \alpha \leq 20^\circ$  at  $M = 0.06$  and  $k = 0.06$ .**

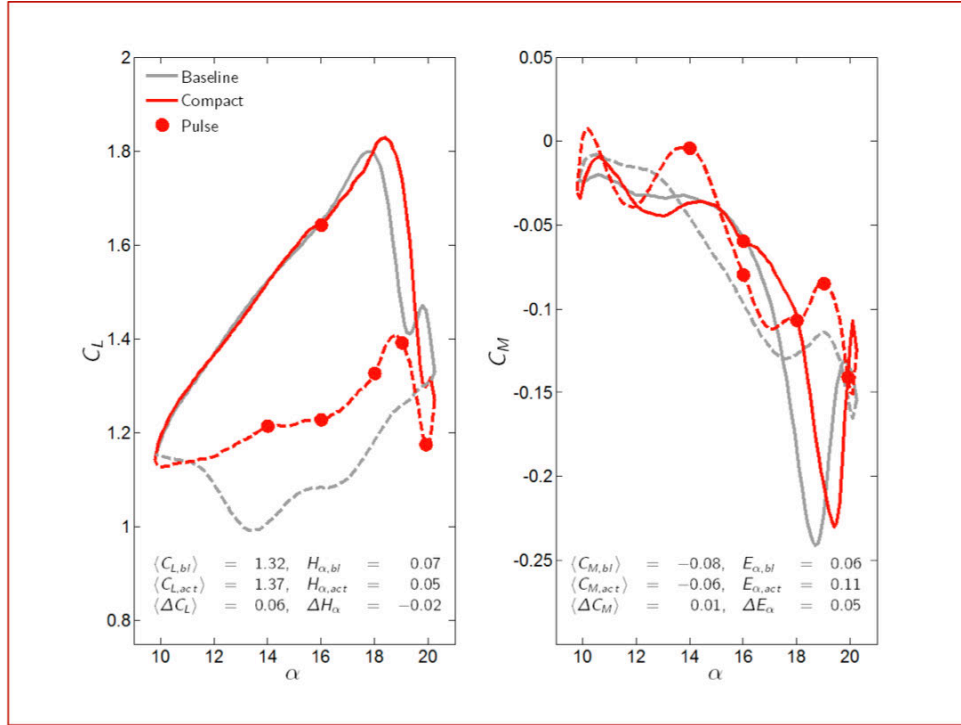


Figure 393. Lift and moment profiles for actuation pattern 16 (upstroke firing at  $\alpha = 16^\circ$ ; downstroke firing at  $\alpha = 19.9^\circ, 19^\circ, 18^\circ, 16^\circ$ , and  $14^\circ$ ) for  $10^\circ \leq \alpha \leq 20^\circ$  at  $M = 0.06$  and  $k = 0.06$ .

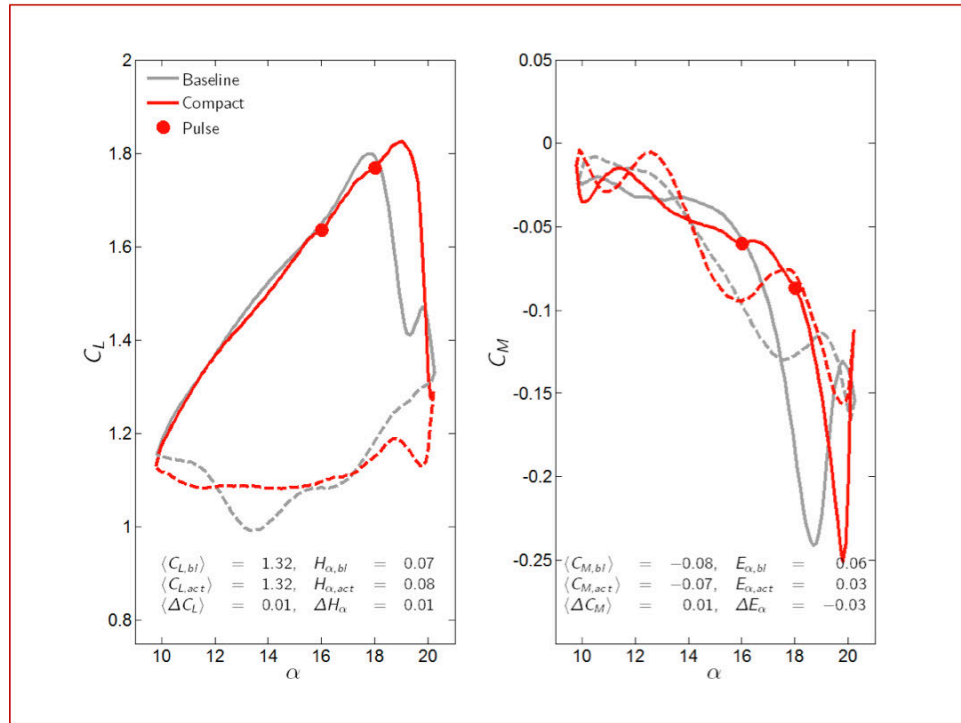


Figure 394. Lift and moment profiles for actuation pattern 17 (upstroke firing at  $\alpha = 16^\circ$  and  $18^\circ$ ) for  $10^\circ \leq \alpha \leq 20^\circ$  at  $M = 0.06$  and  $k = 0.06$ .

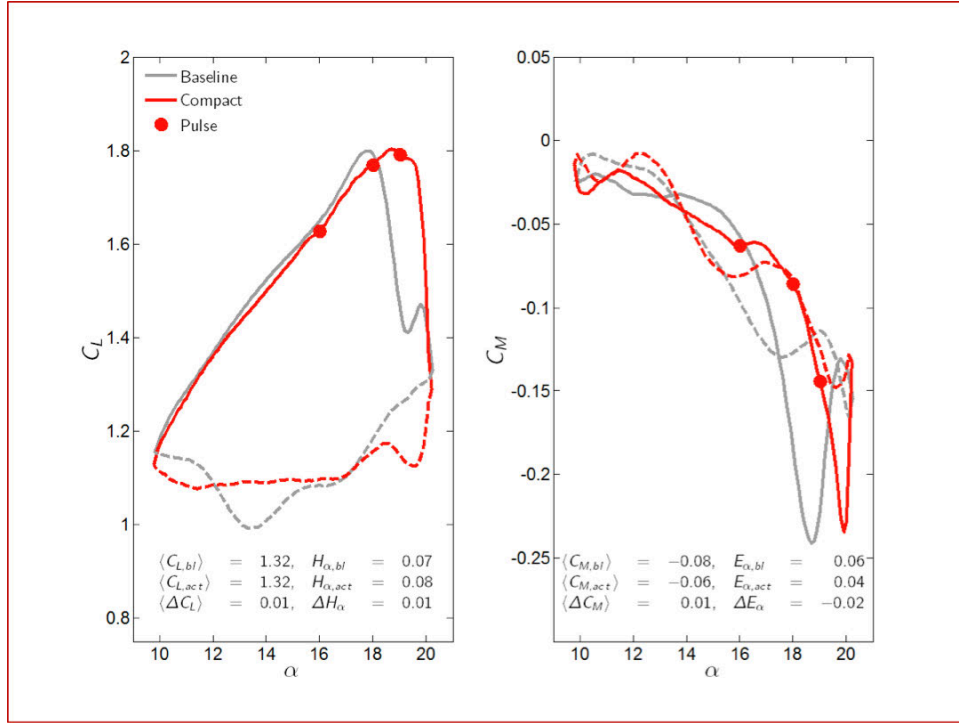


Figure 395. Lift and moment profiles for actuation pattern 18 (upstroke firing at  $\alpha = 16^\circ$ ,  $18^\circ$ , and  $19^\circ$ ) for  $10^\circ \leq \alpha \leq 20^\circ$  at  $M = 0.06$  and  $k = 0.06$ .

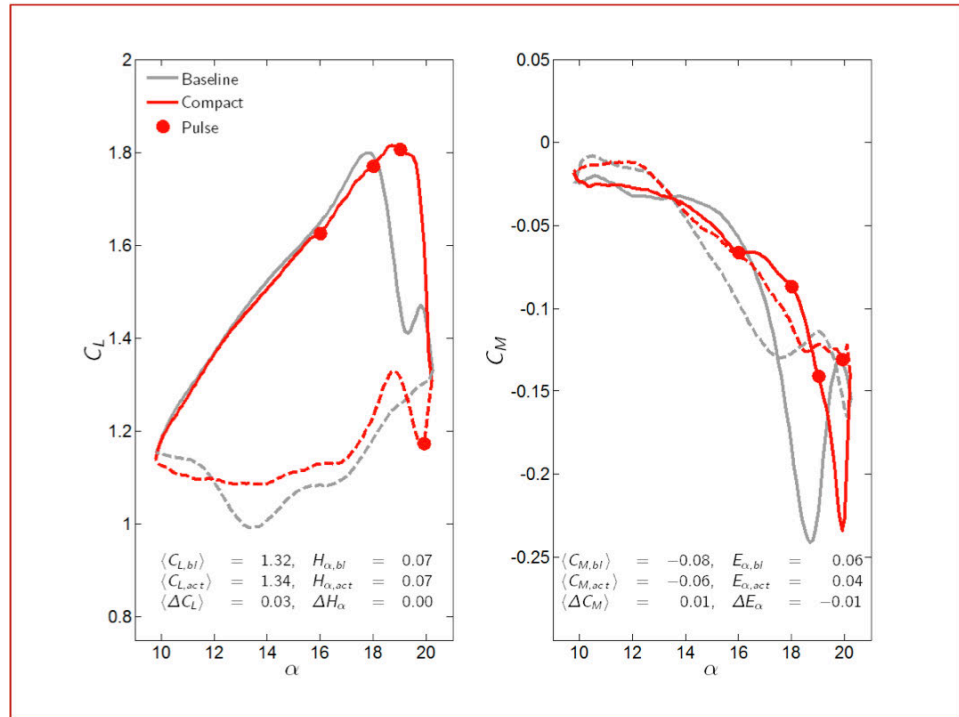


Figure 396. Lift and moment profiles for actuation pattern 19 (upstroke firing at  $\alpha = 16^\circ$ ,  $18^\circ$ , and  $19^\circ$ ; downstroke firing at  $\alpha = 19.9^\circ$ ) for  $10^\circ \leq \alpha \leq 20^\circ$  at  $M = 0.06$  and  $k = 0.06$ .

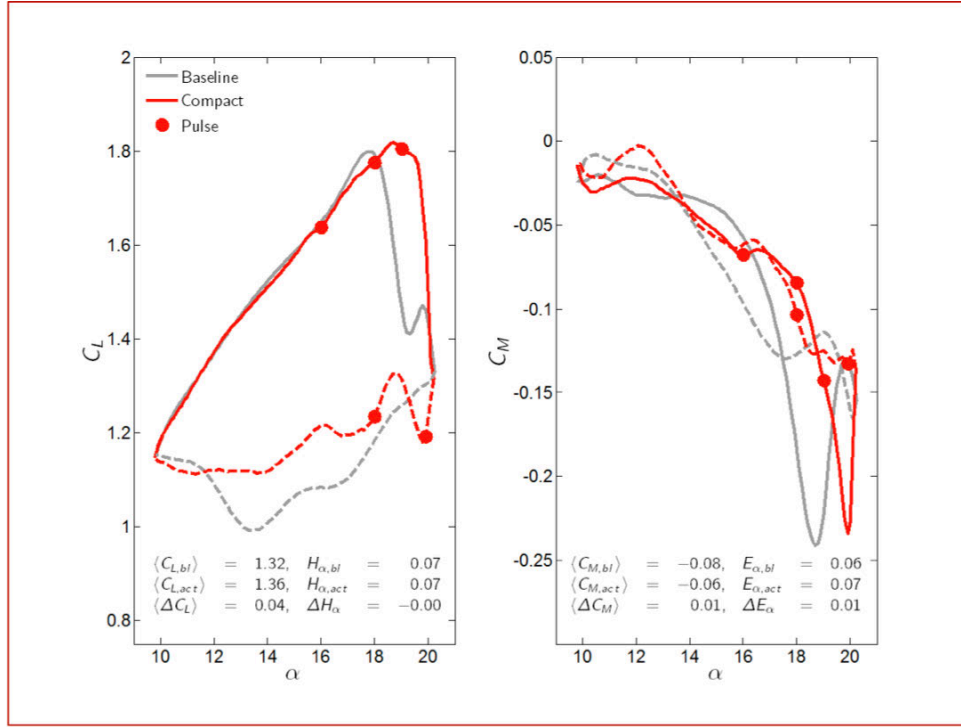


Figure 397. Lift and moment profiles for actuation pattern 20 (upstroke firing at  $\alpha = 16^\circ$ ,  $18^\circ$ , and  $19^\circ$ ; downstroke firing at  $\alpha = 19.9^\circ$  and  $18^\circ$ ) for  $10^\circ \leq \alpha \leq 20^\circ$  at  $M = 0.06$  and  $k = 0.06$ .

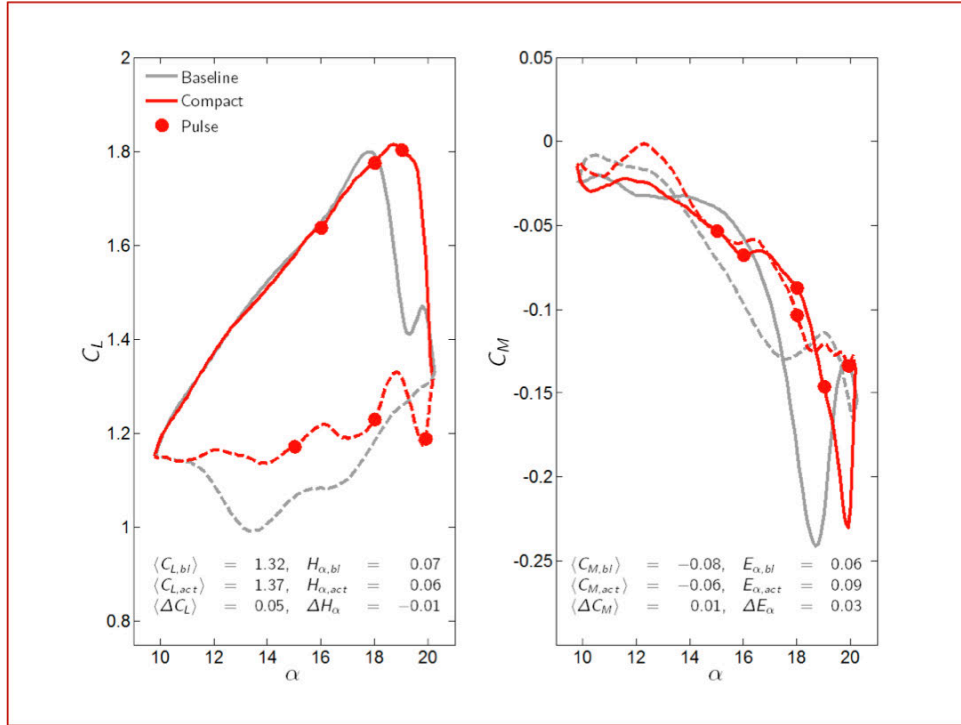


Figure 398. Lift and moment profiles for actuation pattern 21 (upstroke firing at  $\alpha = 16^\circ$ ,  $18^\circ$ , and  $19^\circ$ ; downstroke firing at  $\alpha = 19.9^\circ$ ,  $18^\circ$ , and  $15^\circ$ ) for  $10^\circ \leq \alpha \leq 20^\circ$  at  $M = 0.06$  and  $k = 0.06$ .

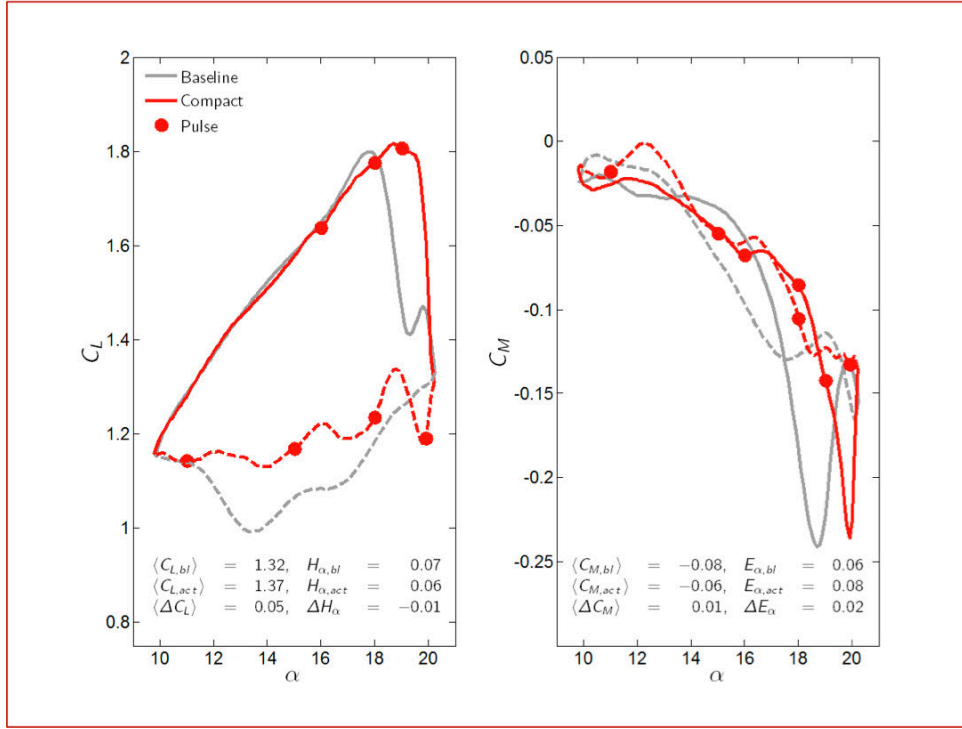


Figure 399. Lift and moment profiles for actuation pattern 22 (upstroke firing at  $\alpha = 16^\circ$ ,  $18^\circ$ , and  $19^\circ$ ; downstroke firing at  $\alpha = 19.9^\circ$ ,  $18^\circ$ ,  $15^\circ$ , and  $11^\circ$ ) for  $10^\circ \leq \alpha \leq 20^\circ$  at  $M = 0.06$  and  $k = 0.06$ .

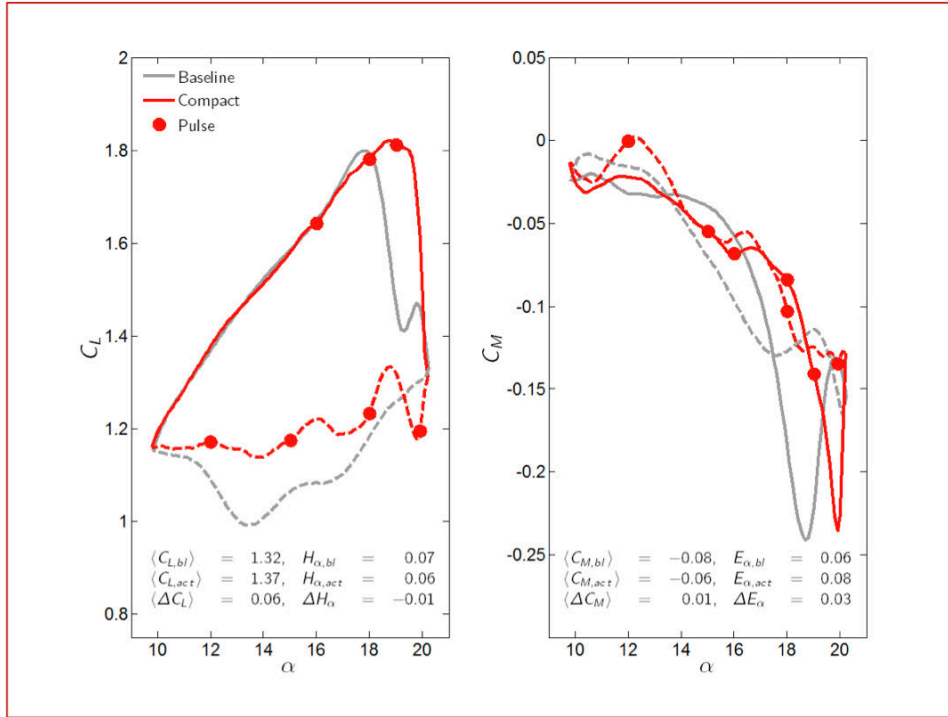


Figure 400. Lift and moment profiles for actuation pattern 23 (upstroke firing at  $\alpha = 16^\circ$ ,  $18^\circ$ , and  $19^\circ$ ; downstroke firing at  $\alpha = 19.9^\circ$ ,  $18^\circ$ ,  $15^\circ$ , and  $12^\circ$ ) for  $10^\circ \leq \alpha \leq 20^\circ$  at  $M = 0.06$  and  $k = 0.06$ .



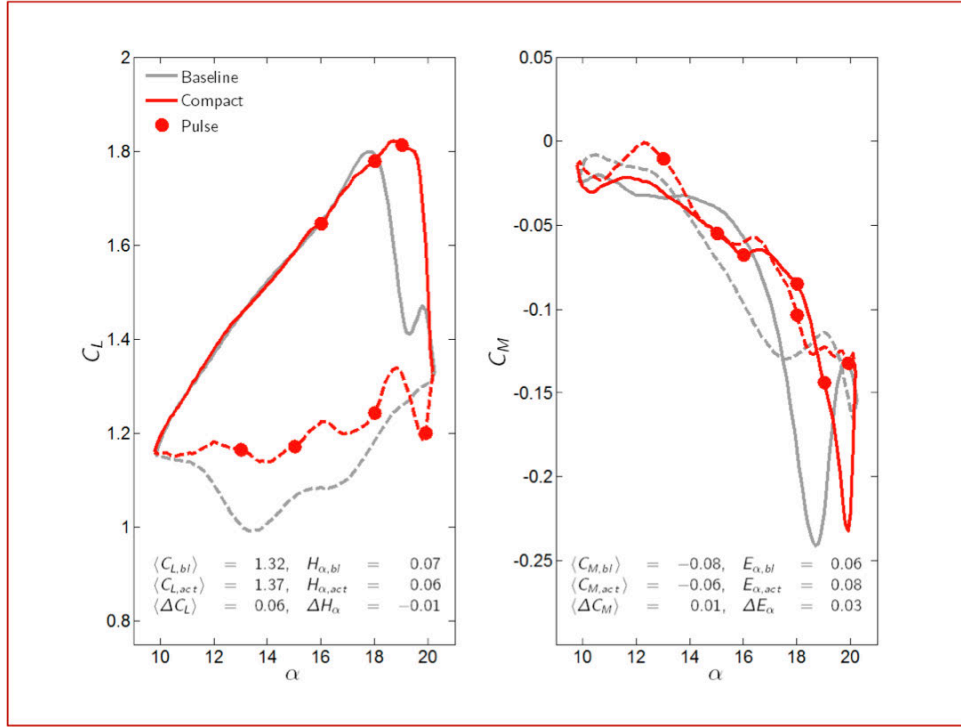


Figure 401. Lift and moment profiles for actuation pattern 24 (upstroke firing at  $\alpha = 16^\circ$ ,  $18^\circ$ , and  $19^\circ$ ; downstroke firing at  $\alpha = 19.9^\circ$ ,  $18^\circ$ ,  $15^\circ$ , and  $13^\circ$ ) for  $10^\circ \leq \alpha \leq 20^\circ$  at  $M = 0.06$  and  $k = 0.06$ .

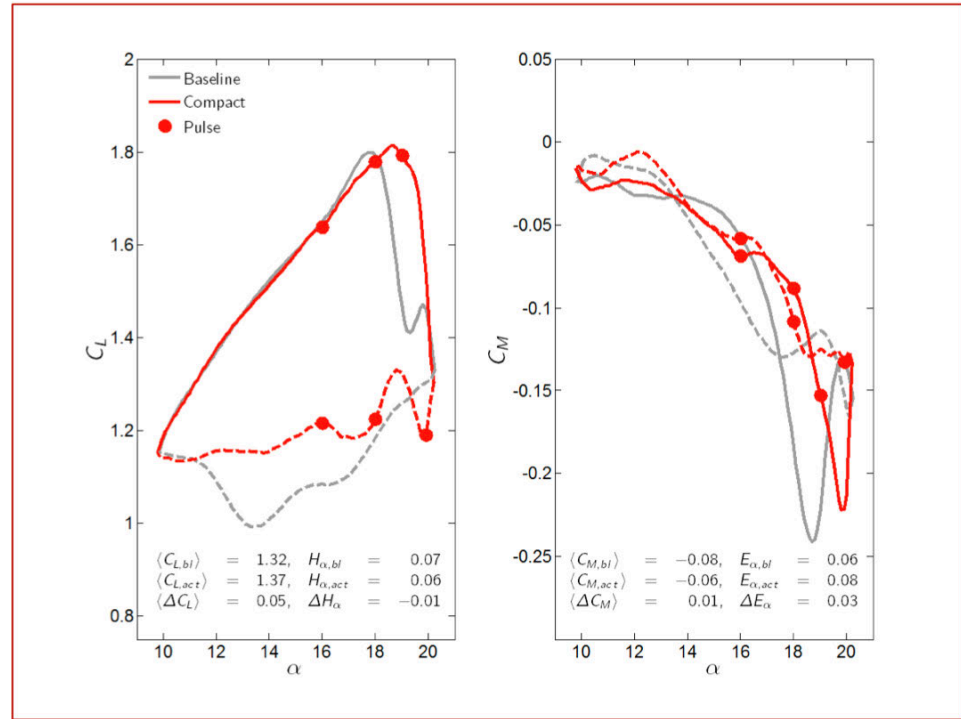


Figure 402. Lift and moment profiles for actuation pattern 25 (upstroke firing at  $\alpha = 16^\circ$ ,  $18^\circ$ , and  $19^\circ$ ; downstroke firing at  $\alpha = 19.9^\circ$ ,  $18^\circ$ , and  $16^\circ$ ) for  $10^\circ \leq \alpha \leq 20^\circ$  at  $M = 0.06$  and  $k = 0.06$ .

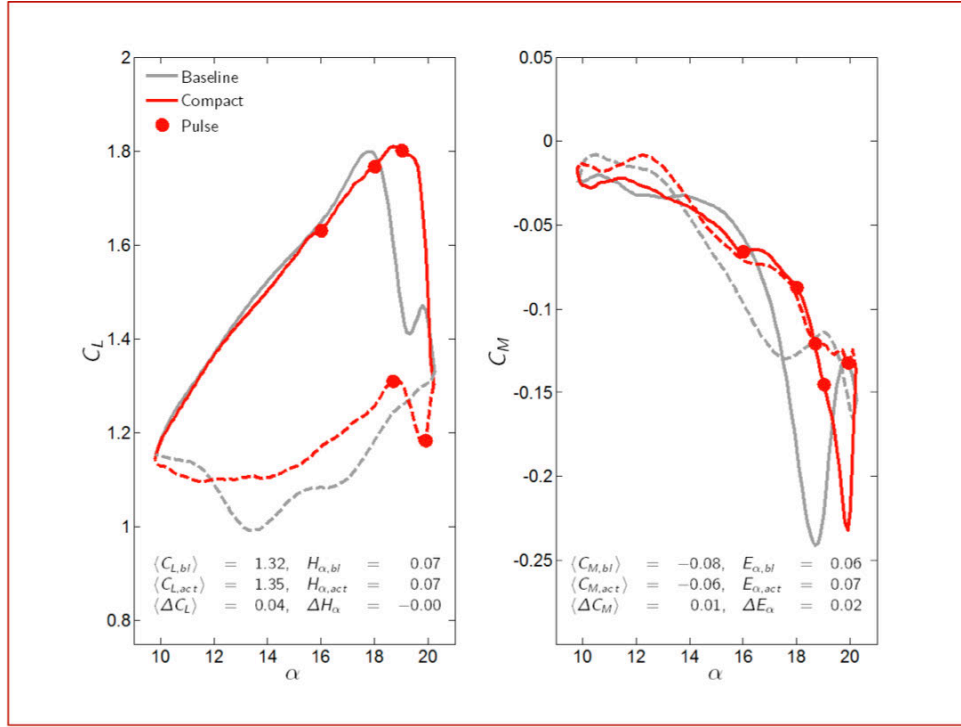


Figure 403. Lift and moment profiles for actuation pattern 26 (upstroke firing at  $\alpha = 16^\circ$ ,  $18^\circ$ , and  $19^\circ$ ; downstroke firing at  $\alpha = 19.9^\circ$  and  $18.75^\circ$ ) for  $10^\circ \leq \alpha \leq 20^\circ$  at  $M = 0.06$  and  $k = 0.06$ .

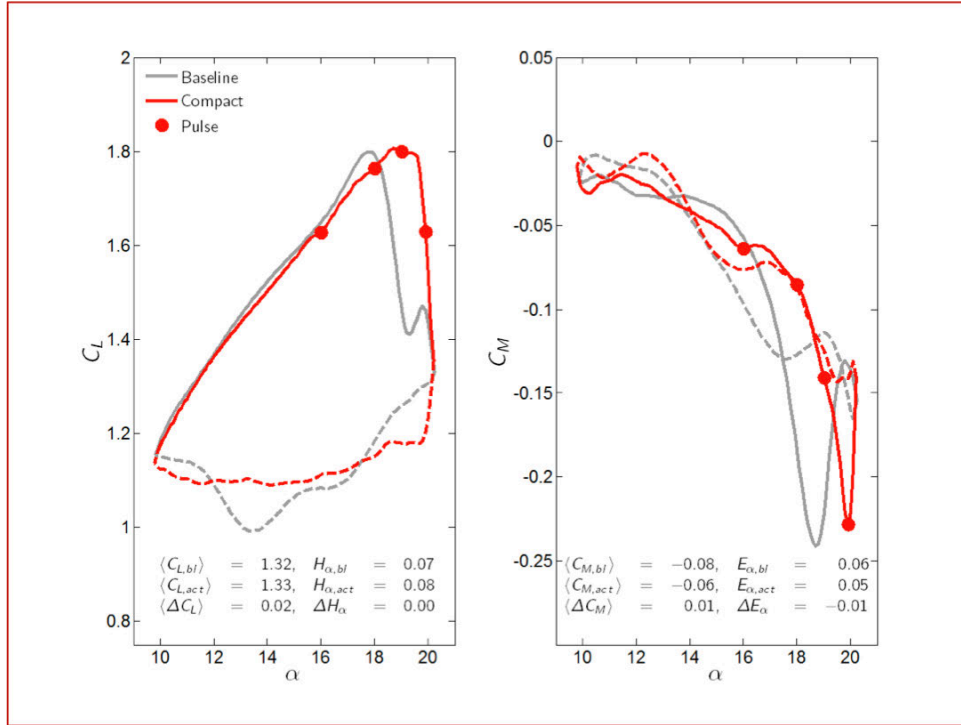
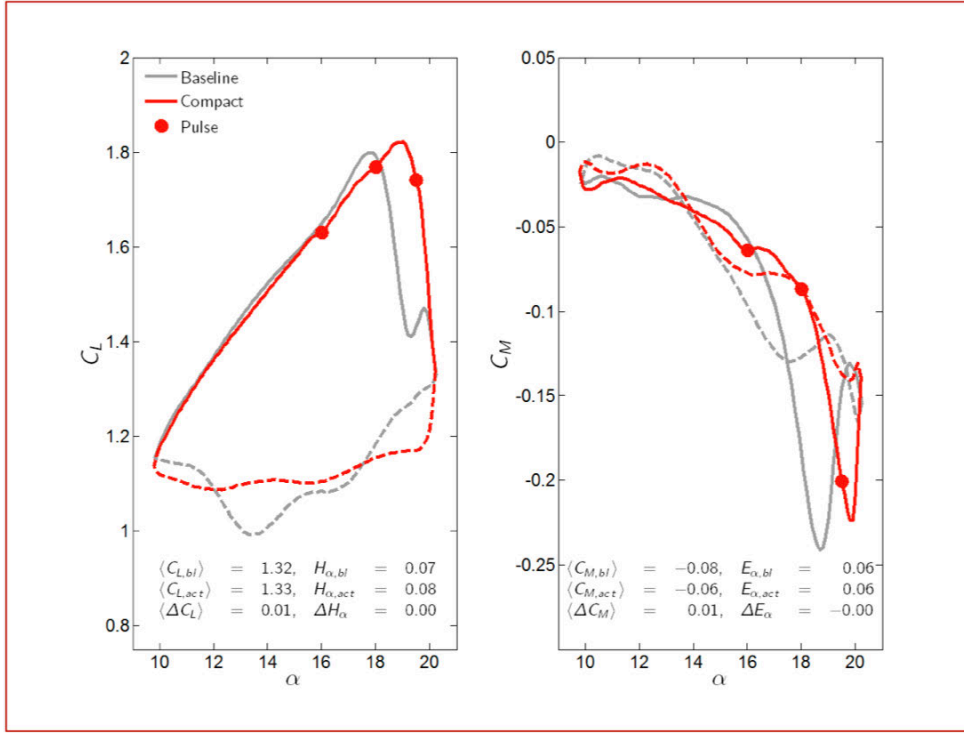
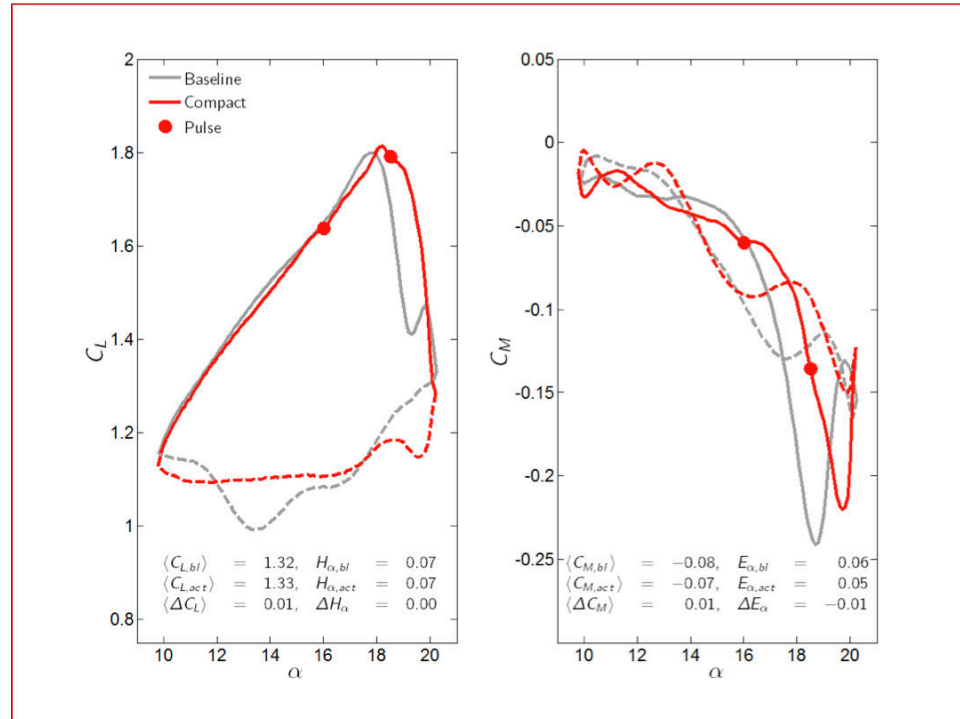


Figure 404. Lift and moment profiles for actuation pattern 27 (upstroke firing at  $\alpha = 16^\circ$ ,  $18^\circ$ ,  $19^\circ$ , and  $19.9^\circ$ ) for  $10^\circ \leq \alpha \leq 20^\circ$  at  $M = 0.06$  and  $k = 0.06$ .



**Figure 405.** Lift and moment profiles for actuation pattern 28 (upstroke firing at  $\alpha = 16^\circ$ ,  $18^\circ$ , and  $19.5^\circ$ ) for  $10^\circ \leq \alpha \leq 20^\circ$  at  $M = 0.06$  and  $k = 0.06$ .



**Figure 406.** Lift and moment profiles for actuation pattern 29 (upstroke firing at  $\alpha = 16^\circ$  and  $18.5^\circ$ ) for  $10^\circ \leq \alpha \leq 20^\circ$  at  $M = 0.06$  and  $k = 0.06$ .

### Appendix 3. High Speed Test Baseline Data

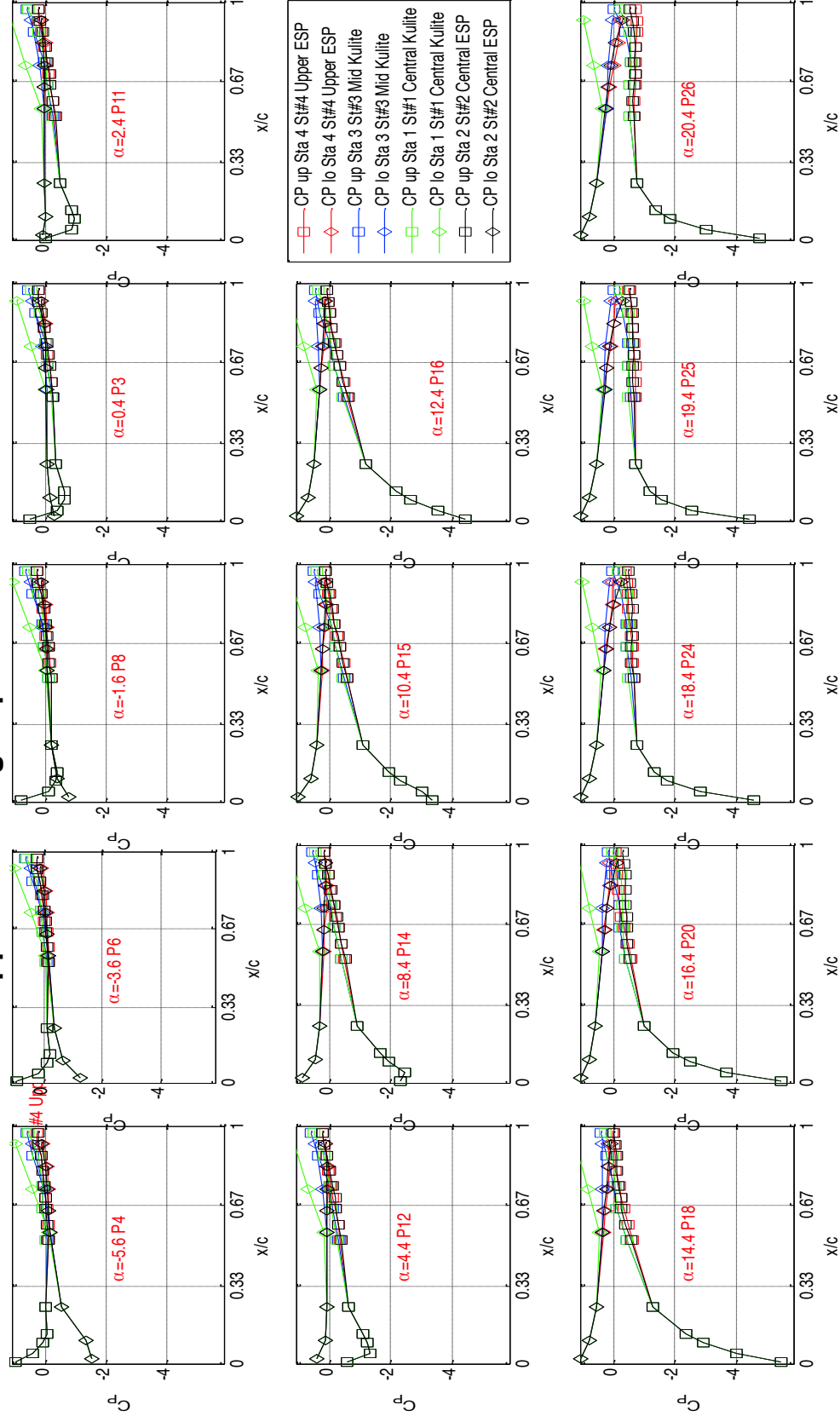


Figure 407. Pressure distributions for steady baseline at  $M=0.1$ , Run 02.

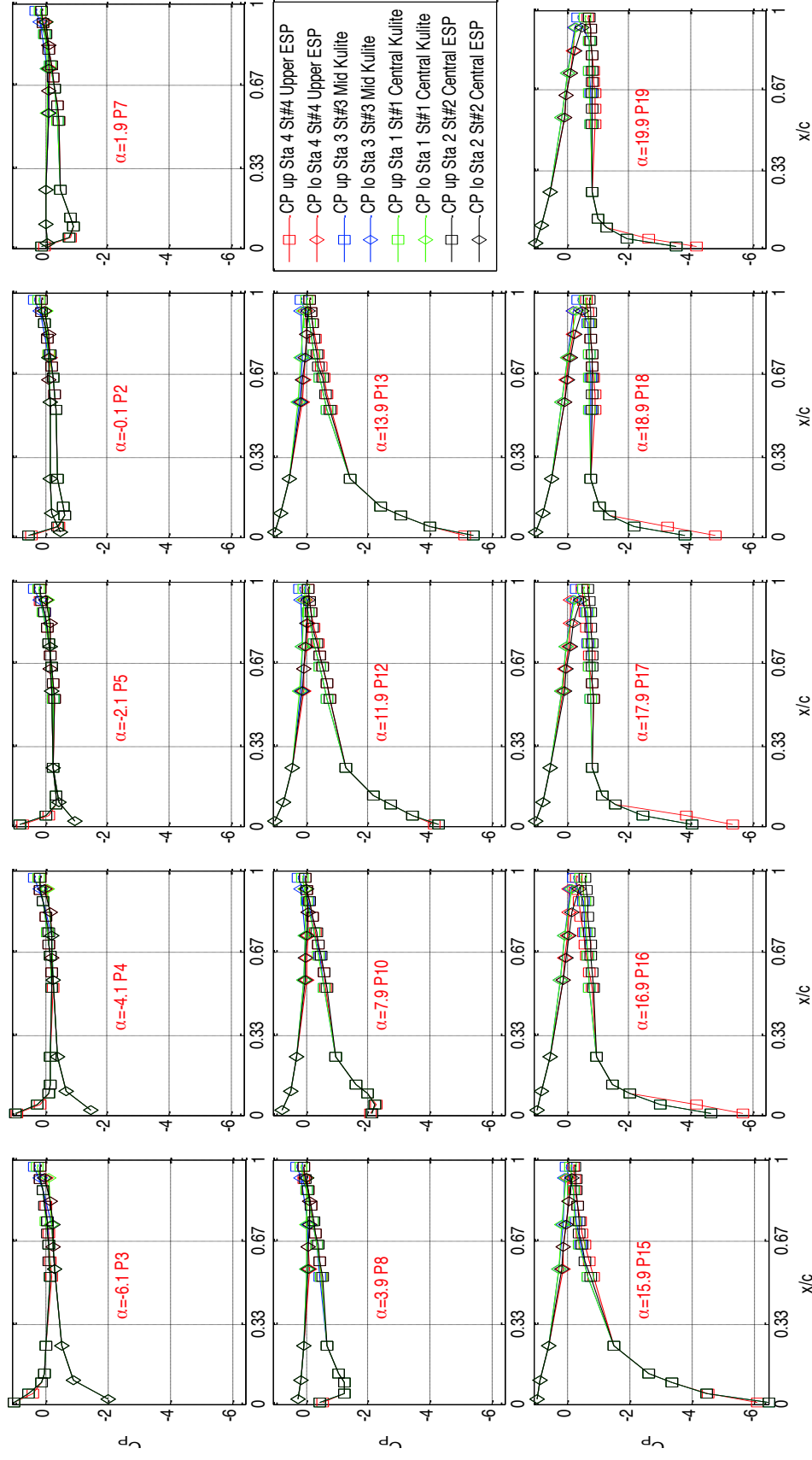


Figure 408. Pressure distributions for steady baseline at  $M=0.2$ , Run 09.

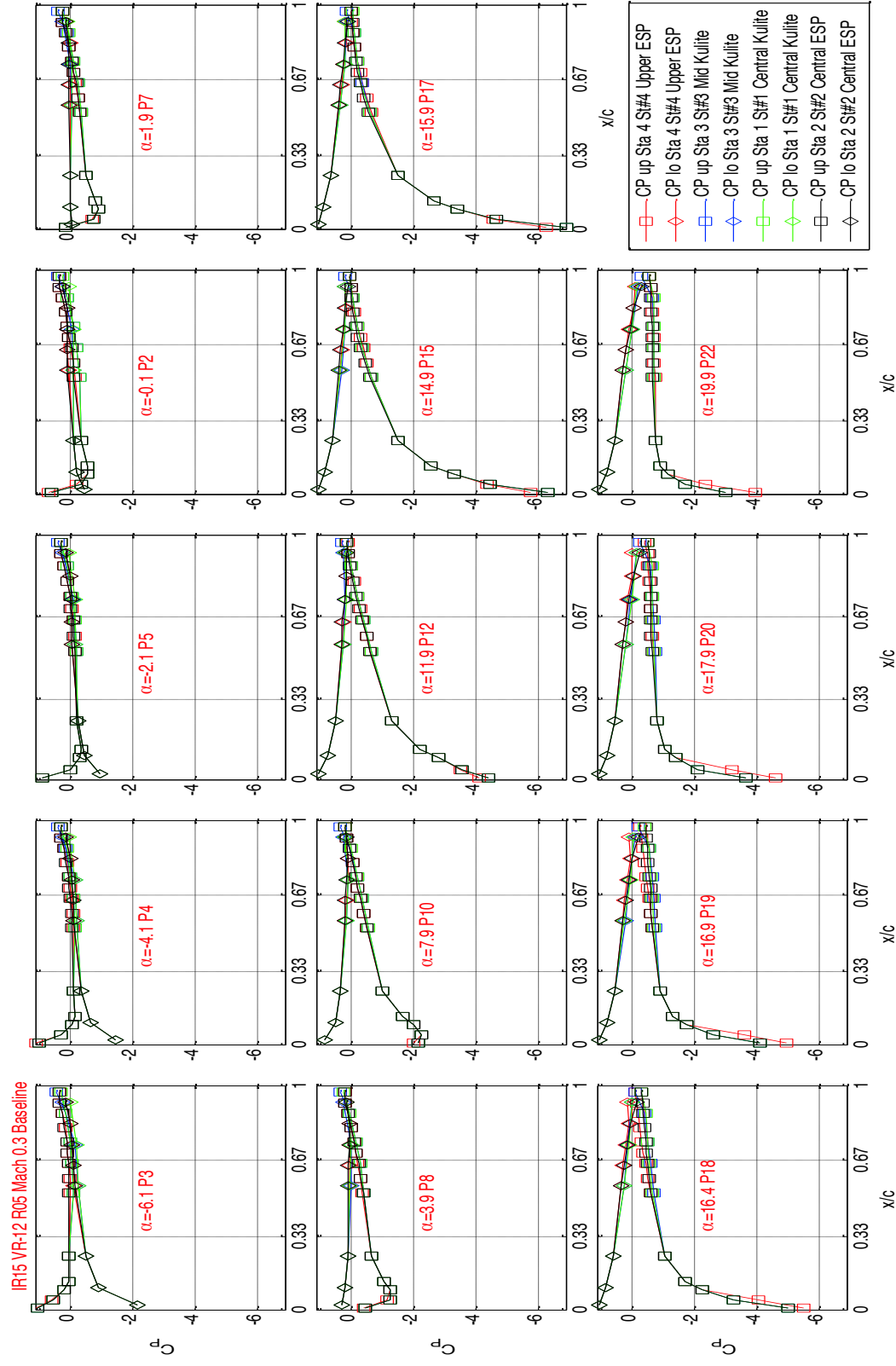


Figure 409. Pressure distributions for steady baseline at  $M=0.3$ , Run 05

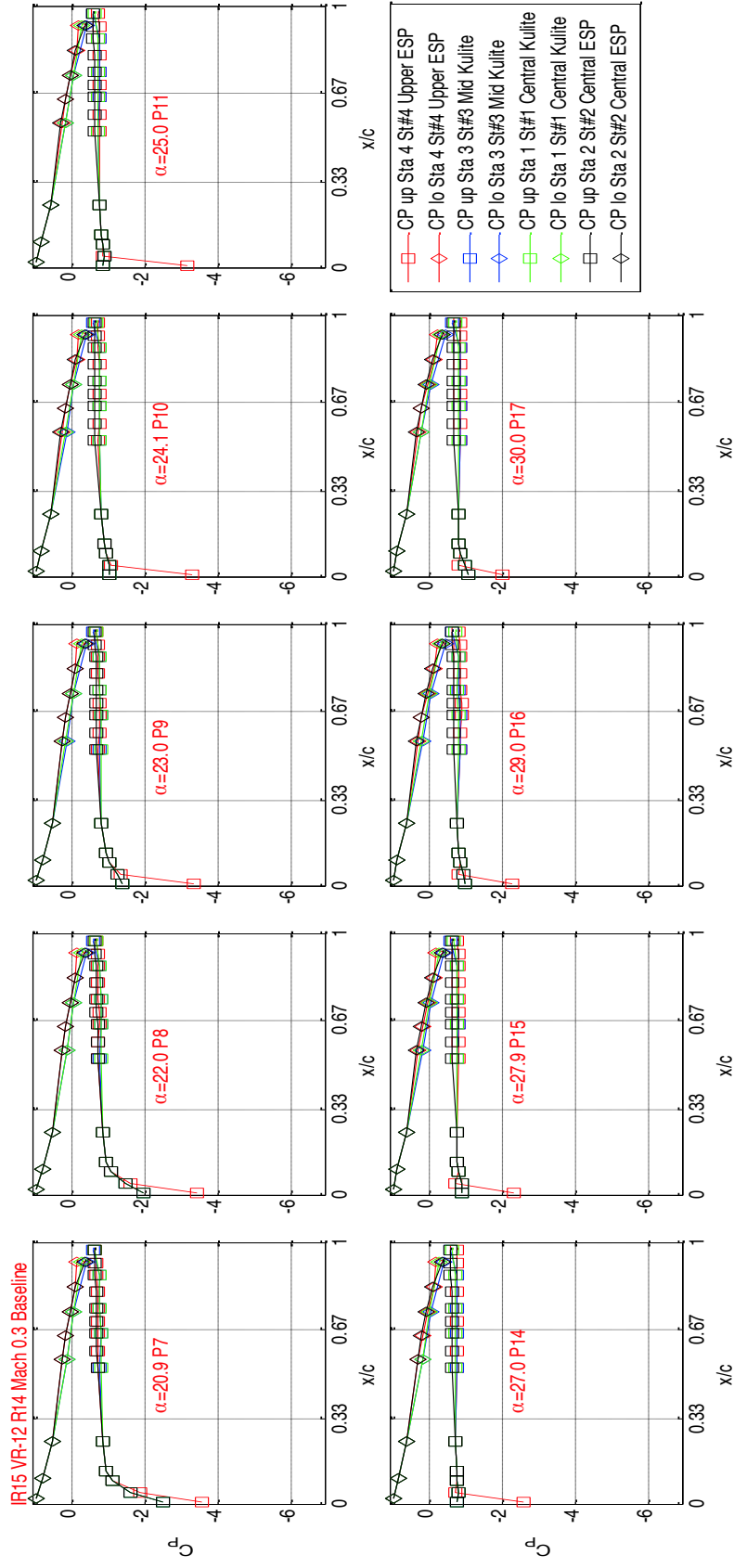
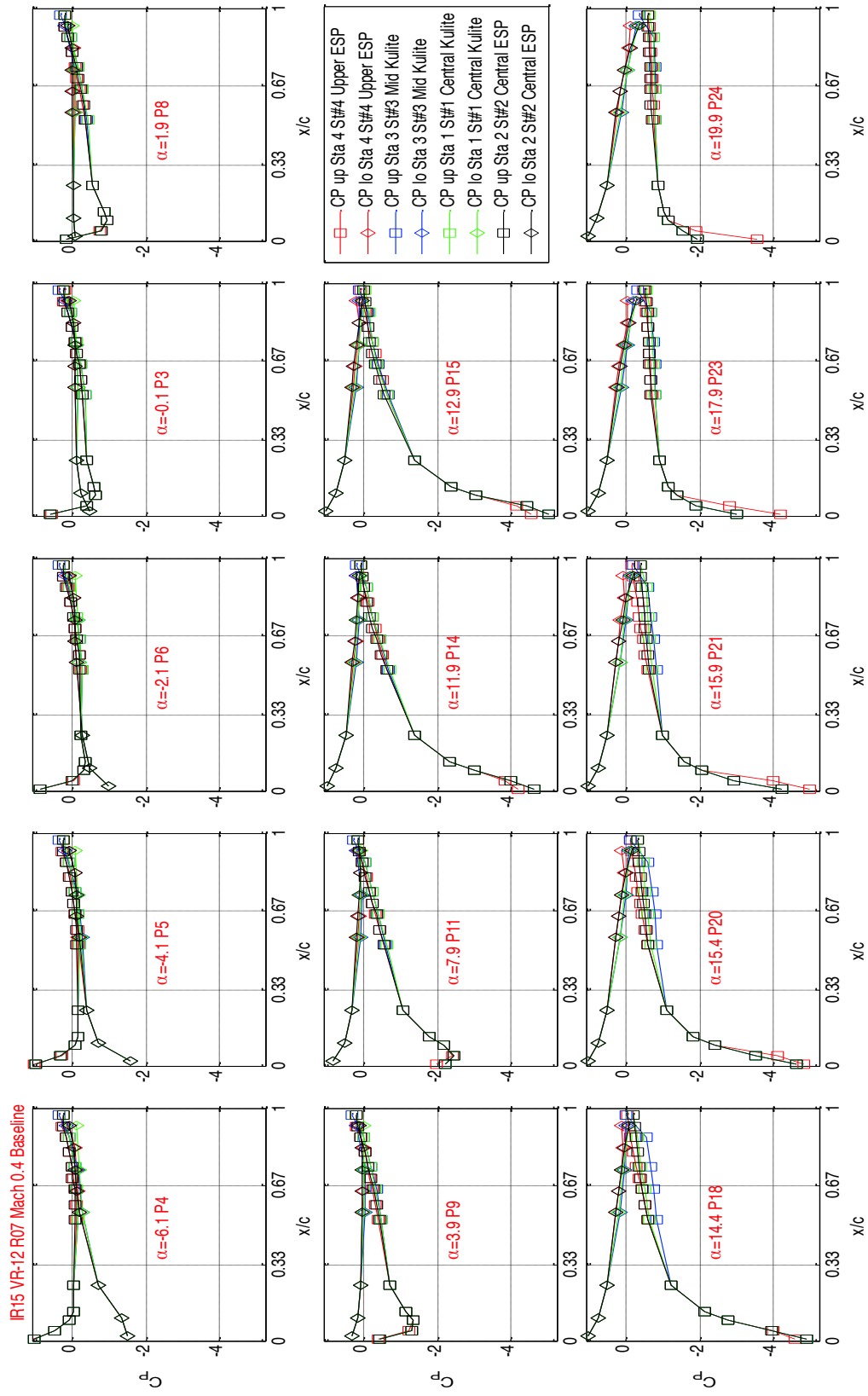


Figure 410. Pressure distributions for steady baseline at  $M=0.3$ , Run 14.





**Figure 411. Pressure distributions for steady baseline at M=0.4, Run 04.**

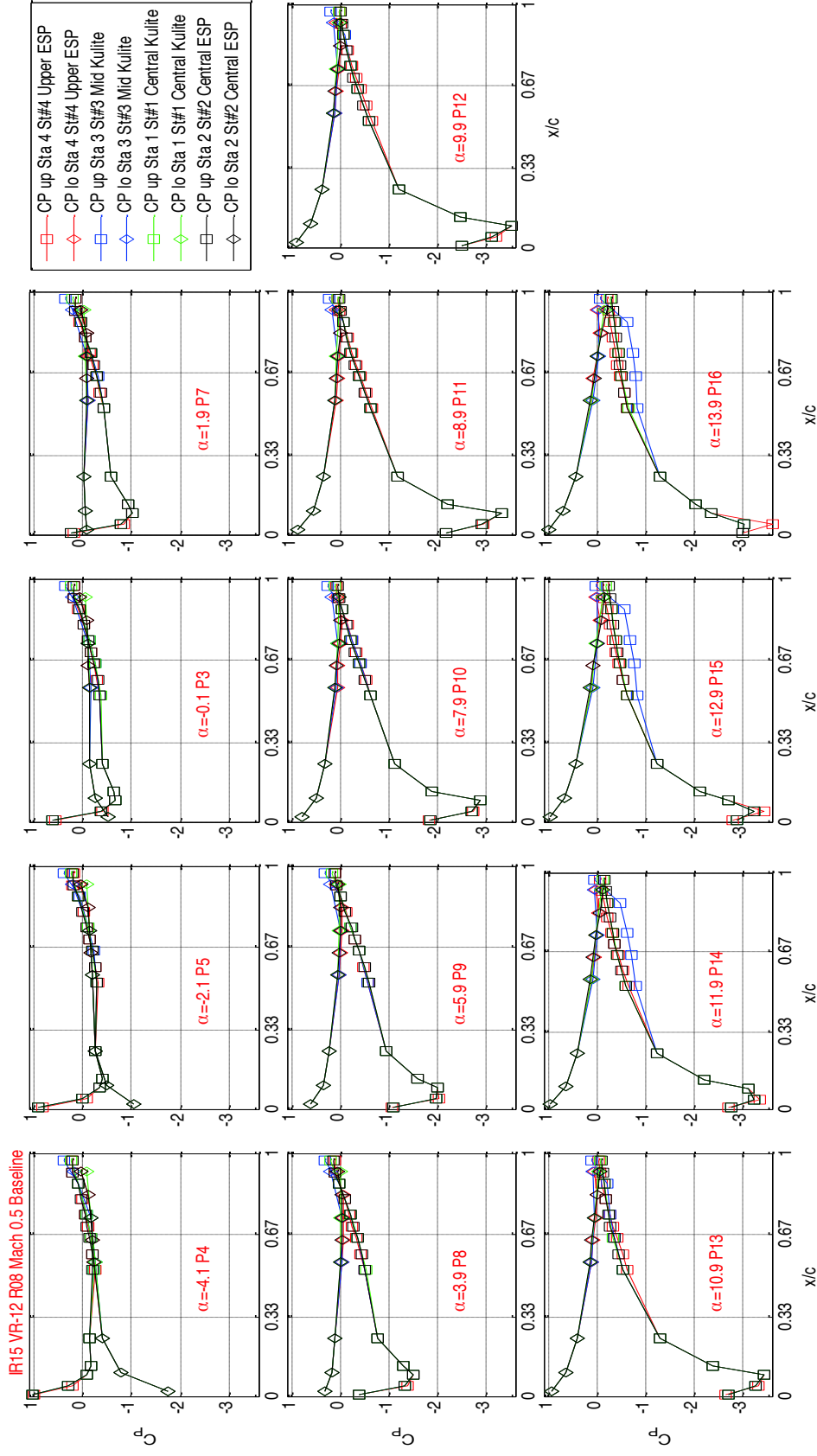


Figure 412. Pressure distributions for steady baseline at M=0.5, Run 08

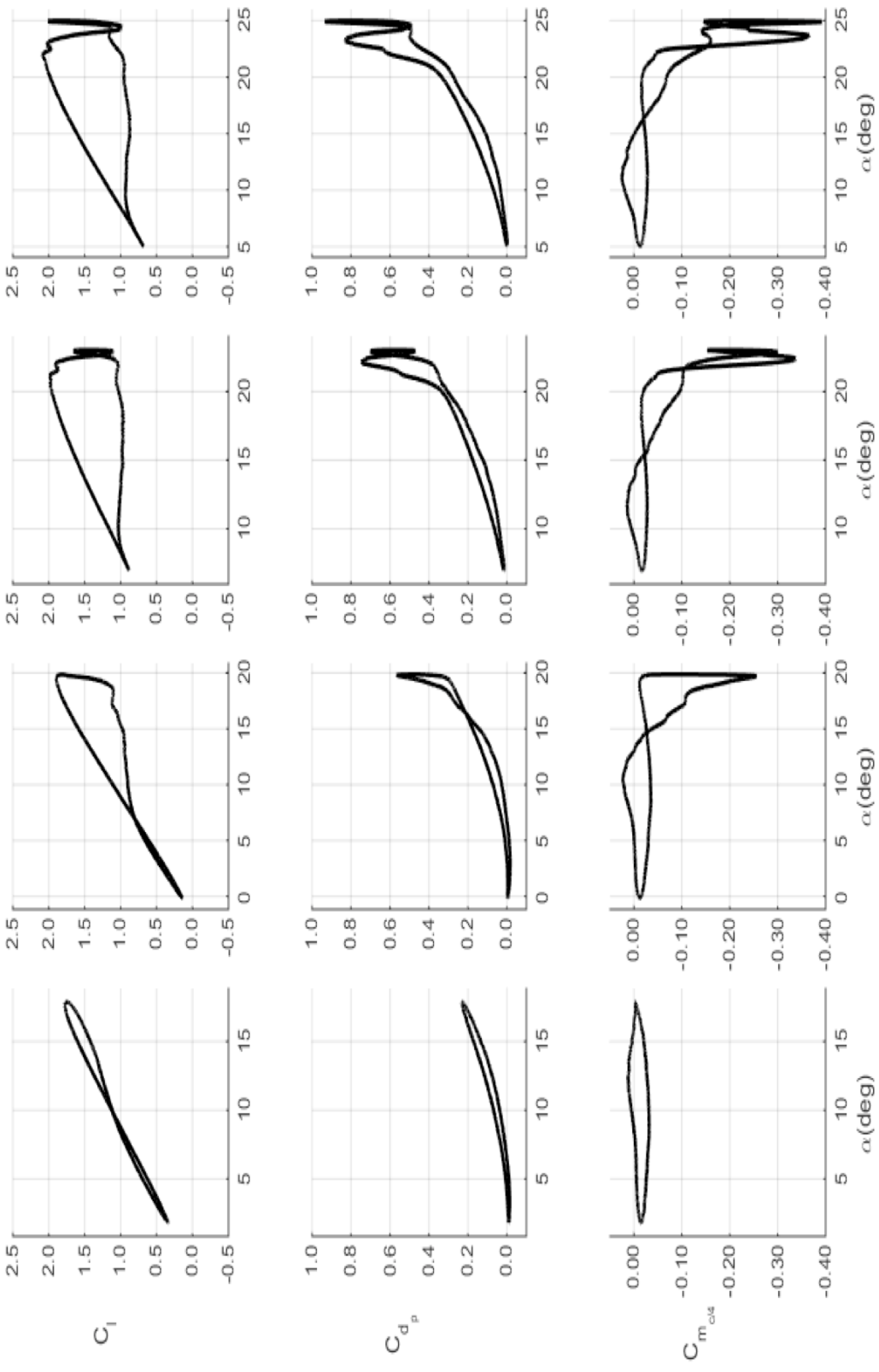


Figure 413. Mach 0.2 baseline unsteady loads for  $k=0.07$ .  $\alpha = 10 \pm 8, \alpha = 10 \pm 10, \alpha = 15 \pm 8, \alpha = 15 \pm 10$ . From left to right:

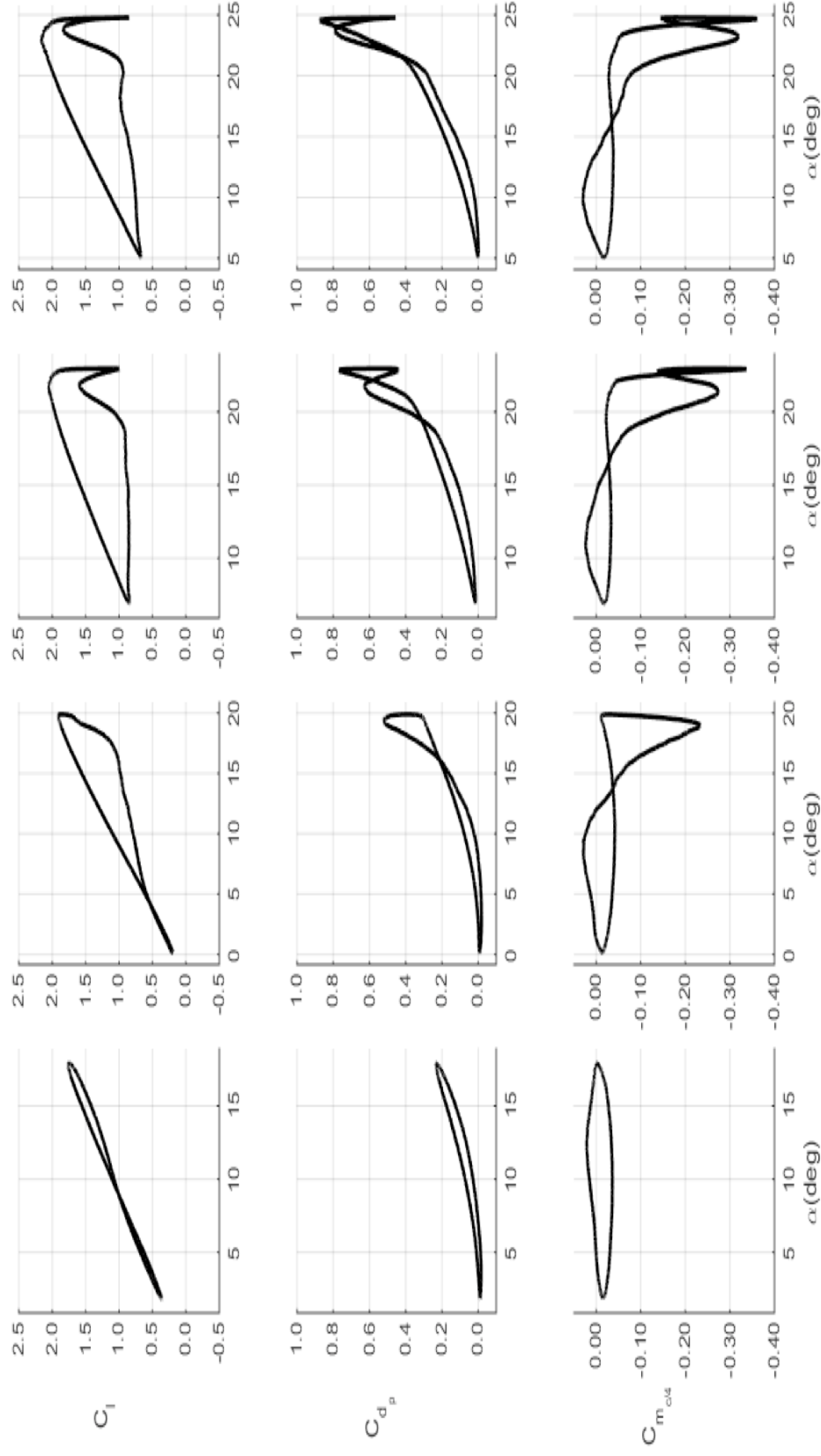


Figure 414. Mach 0.2 baseline unsteady loads for  $k=0.10$ . From left to right:  $\alpha = 10 \pm 8$ ,  $\alpha = 10 \pm 10$ ,  $\alpha = 15 \pm 8$ ,  $\alpha = 15 \pm 10$ .

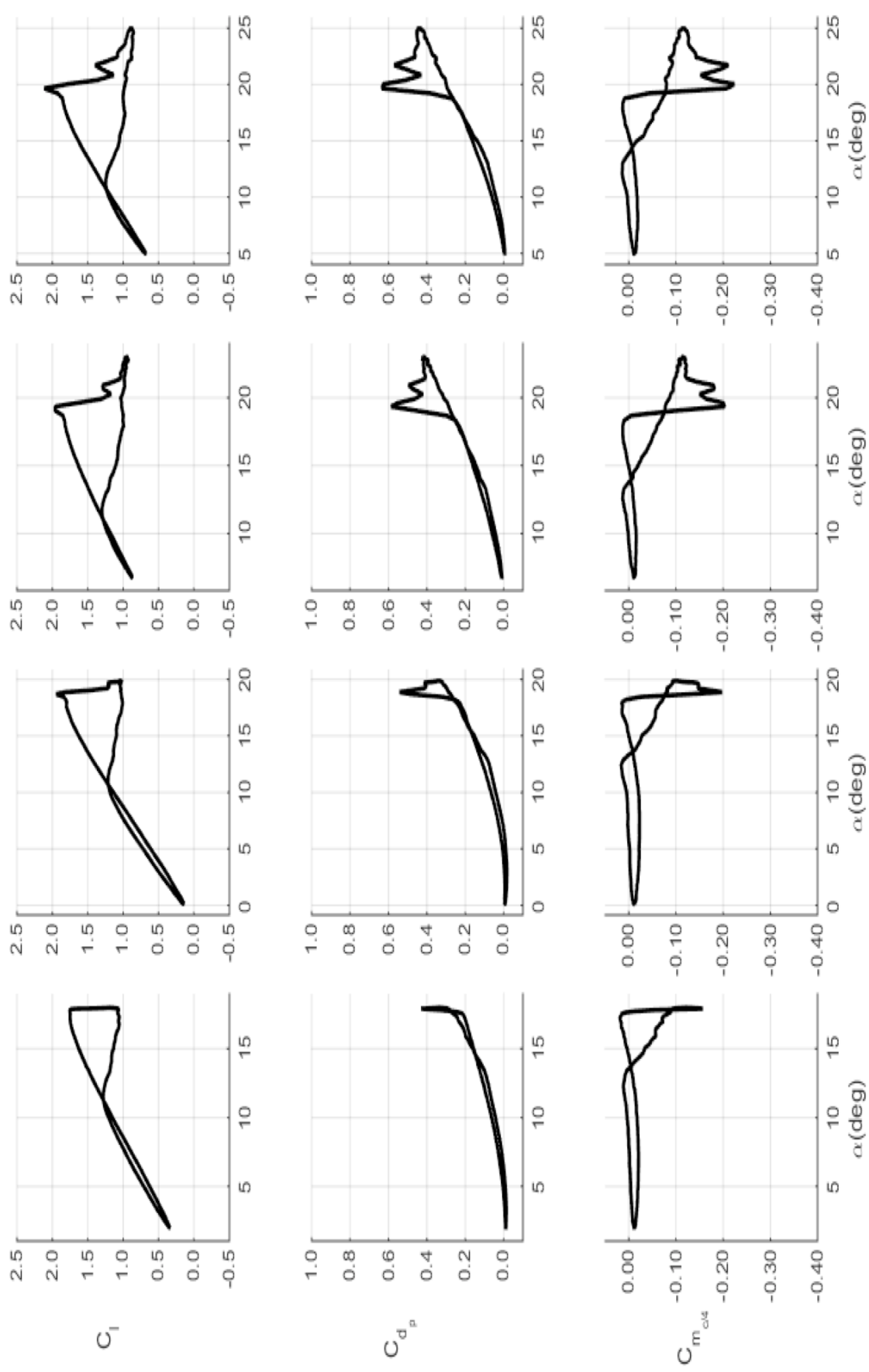
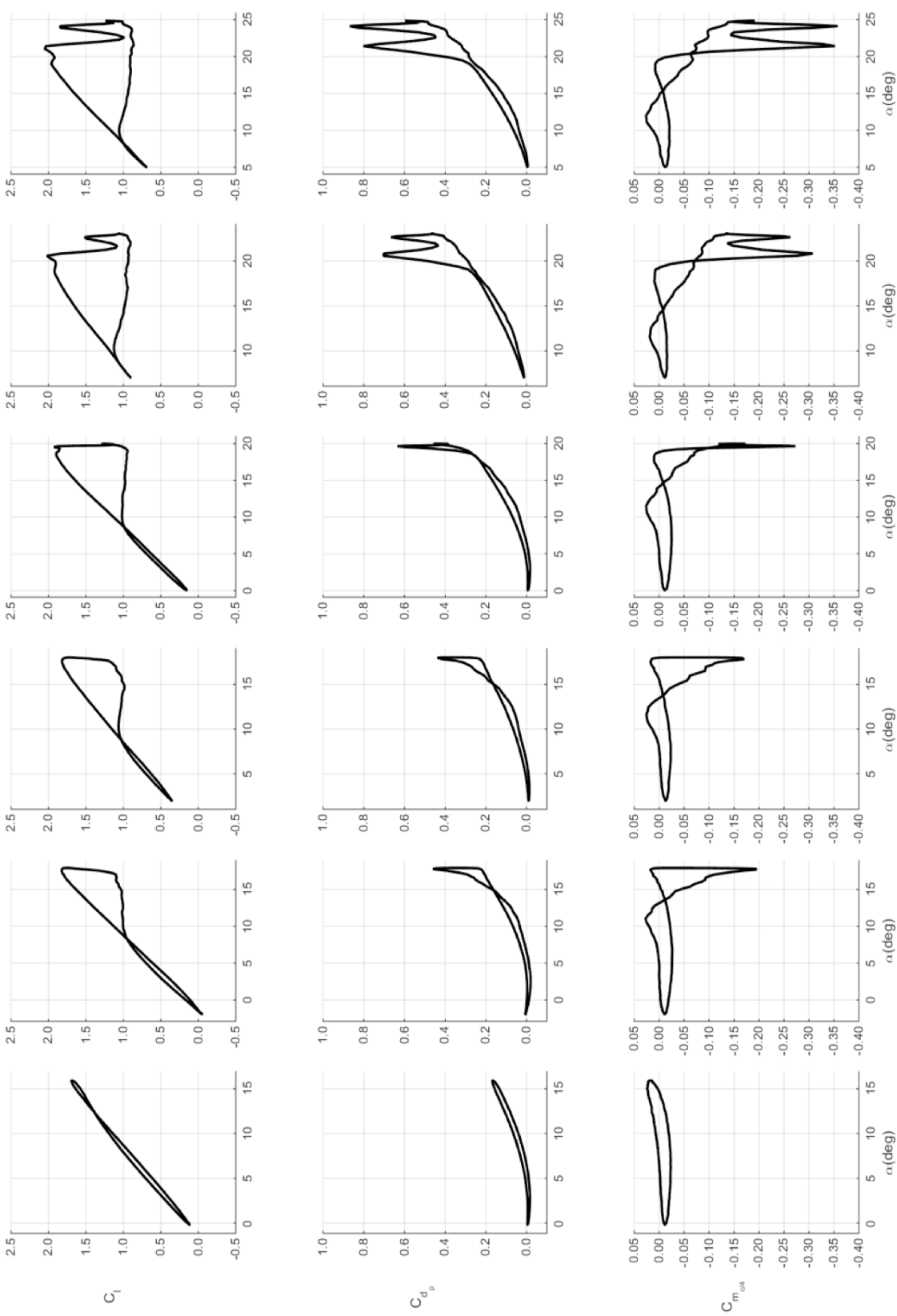
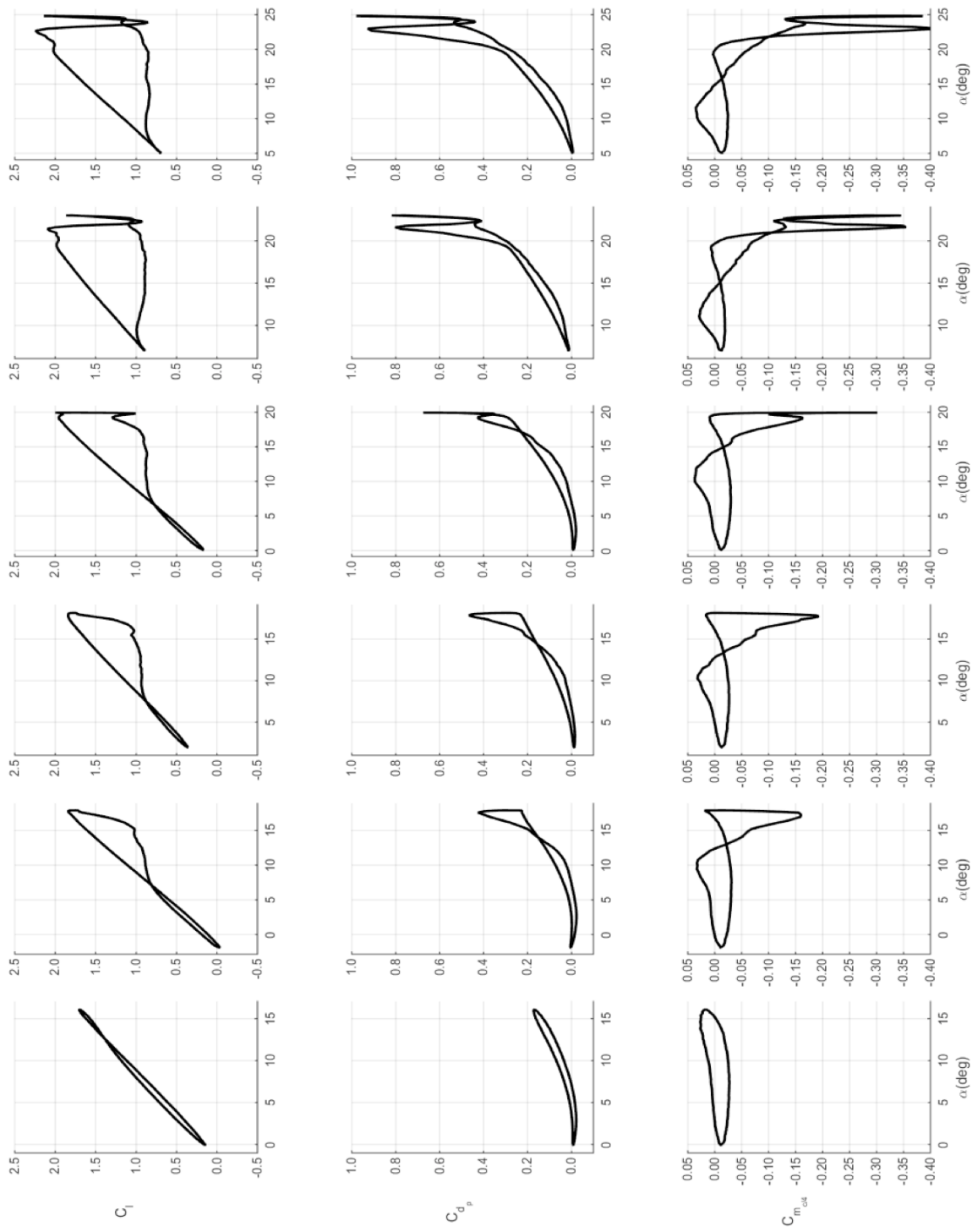


Figure 415. Mach 0.3 baseline unsteady loads for  $k=0.025$ . From left to right:  $\alpha = 10 \pm 8, \alpha = 10 \pm 10, \alpha = 15 \pm 8, \alpha = 15 \pm 10$ .



**Figure 416. Mach 0.3 baseline unsteady loads for  $k=0.05$ .  $\alpha = 8 \pm 8$ ,  $\alpha = 10 \pm 10$ ,  $\alpha = 15 \pm 8$ ,  $\alpha = 15 \pm 10$ . From left to right:**



**Figure 417. Mach 0.3 baseline unsteady loads for  $k=0.07$ . From left to right:  $\alpha = 8 \pm 8, \alpha = 10 \pm 8, \alpha = 10 \pm 10, \alpha = 15 \pm 8, \alpha = 15 \pm 10$ .**



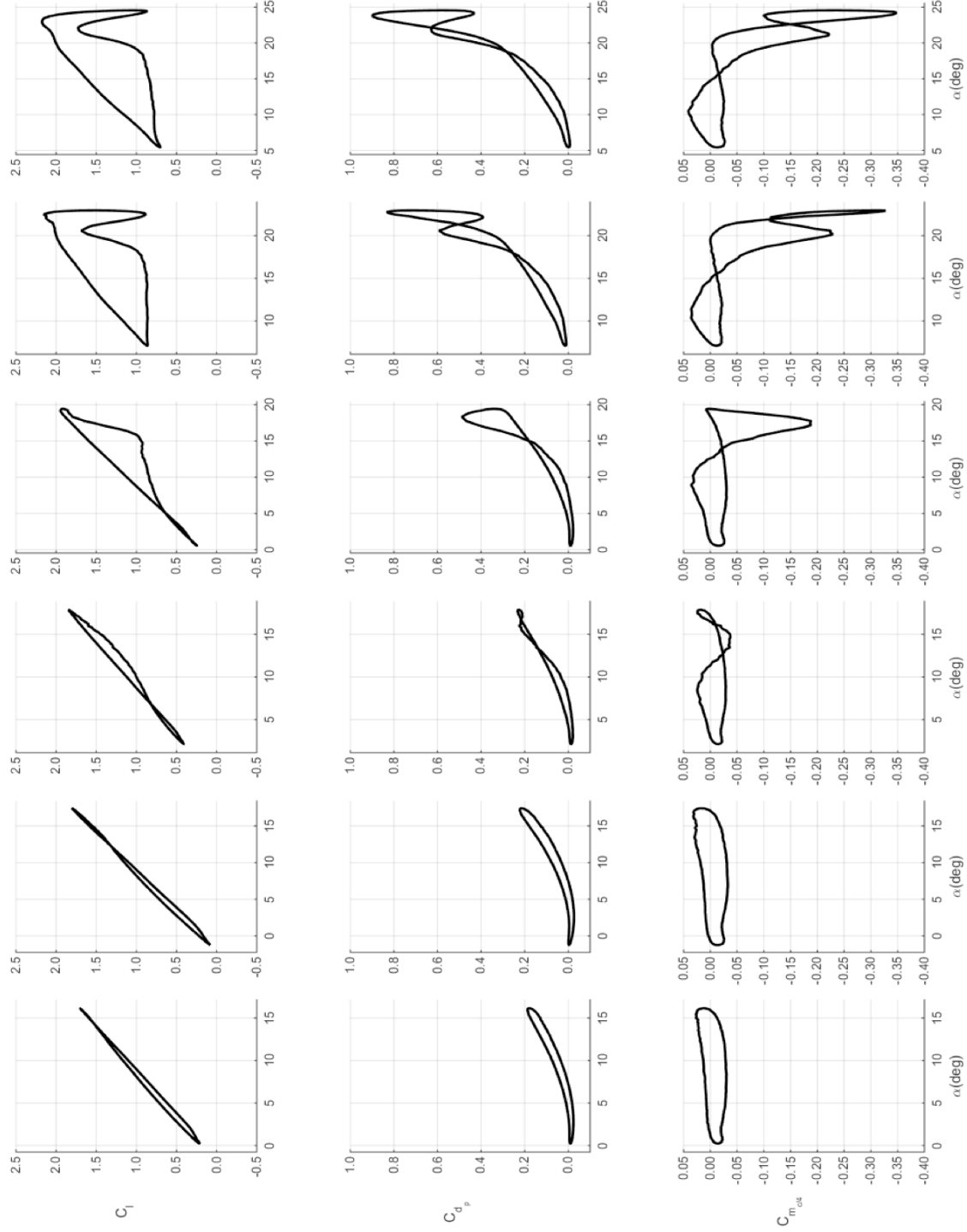


**Figure 418. Mach 0.3 baseline unsteady loads for  $k=0.10$ . From left to right:  $\alpha=8\pm8$ ,  $\alpha=8\pm10$ ,  $\alpha=10\pm10$ ,  $\alpha=15\pm8$ ,  $\alpha=15\pm10$ .**

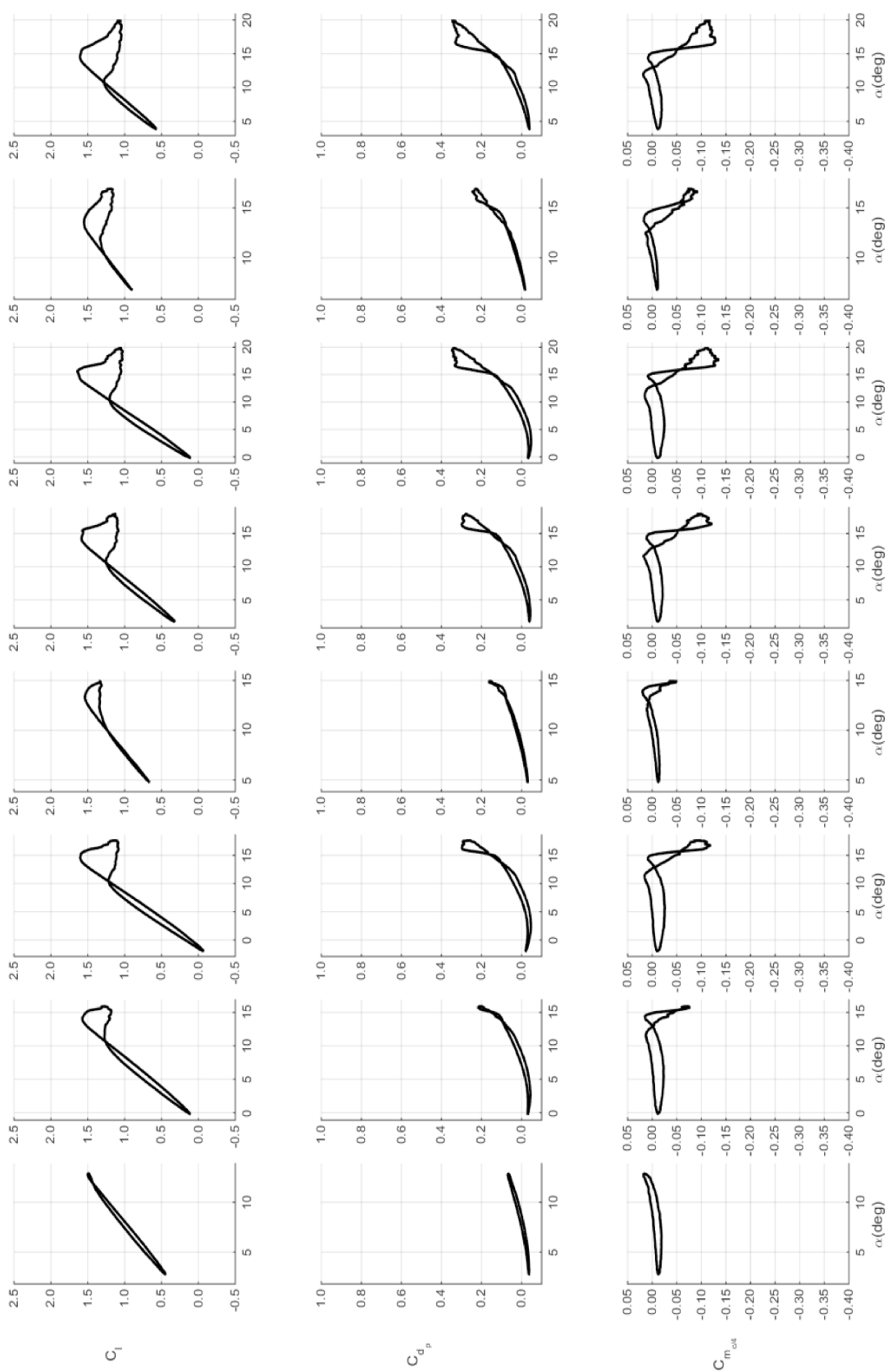


**Figure 419. Mach 0.4 baseline unsteady loads for  $k=0.025$ . From left to right:  $\alpha=8\pm5$ ,  $\alpha=8\pm8$ ,  $\alpha=10\pm10$ ,  $\alpha=10\pm5$ ,  $\alpha=10\pm8$ ,  $\alpha=10\pm10$ ,  $\alpha=12\pm5$ ,  $\alpha=12\pm8$ .**

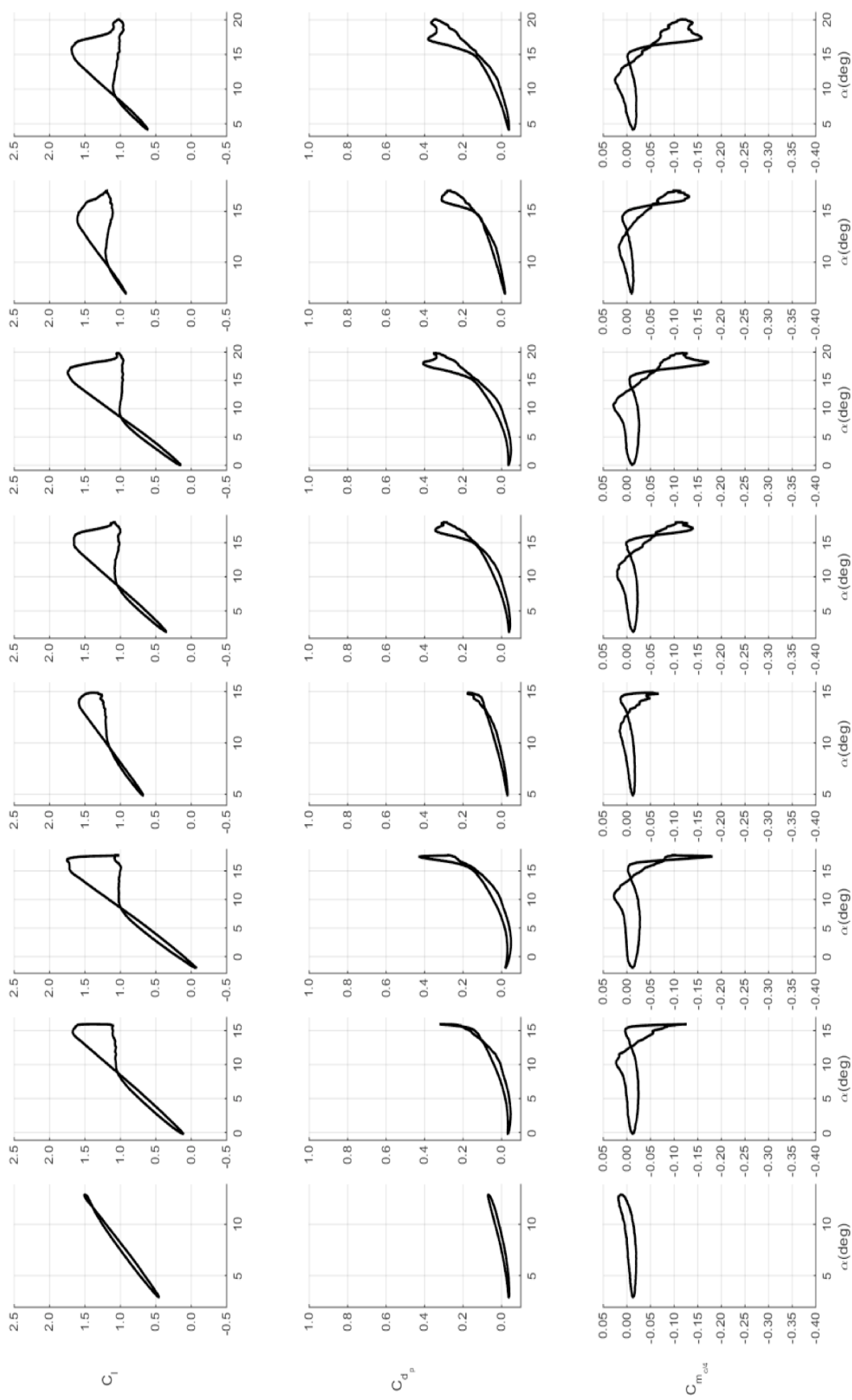


**Figure 420. Mach 0.4 baseline unsteady loads for  $k=0.05$ . From left to right:  $\alpha=8\pm5$ ,  $\alpha=8\pm8$ ,  $\alpha=10\pm5$ ,  $\alpha=10\pm8$ ,  $\alpha=10\pm10$ ,  $\alpha=10\pm5$ ,  $\alpha=10\pm10$ ,  $\alpha=10\pm5$ .**

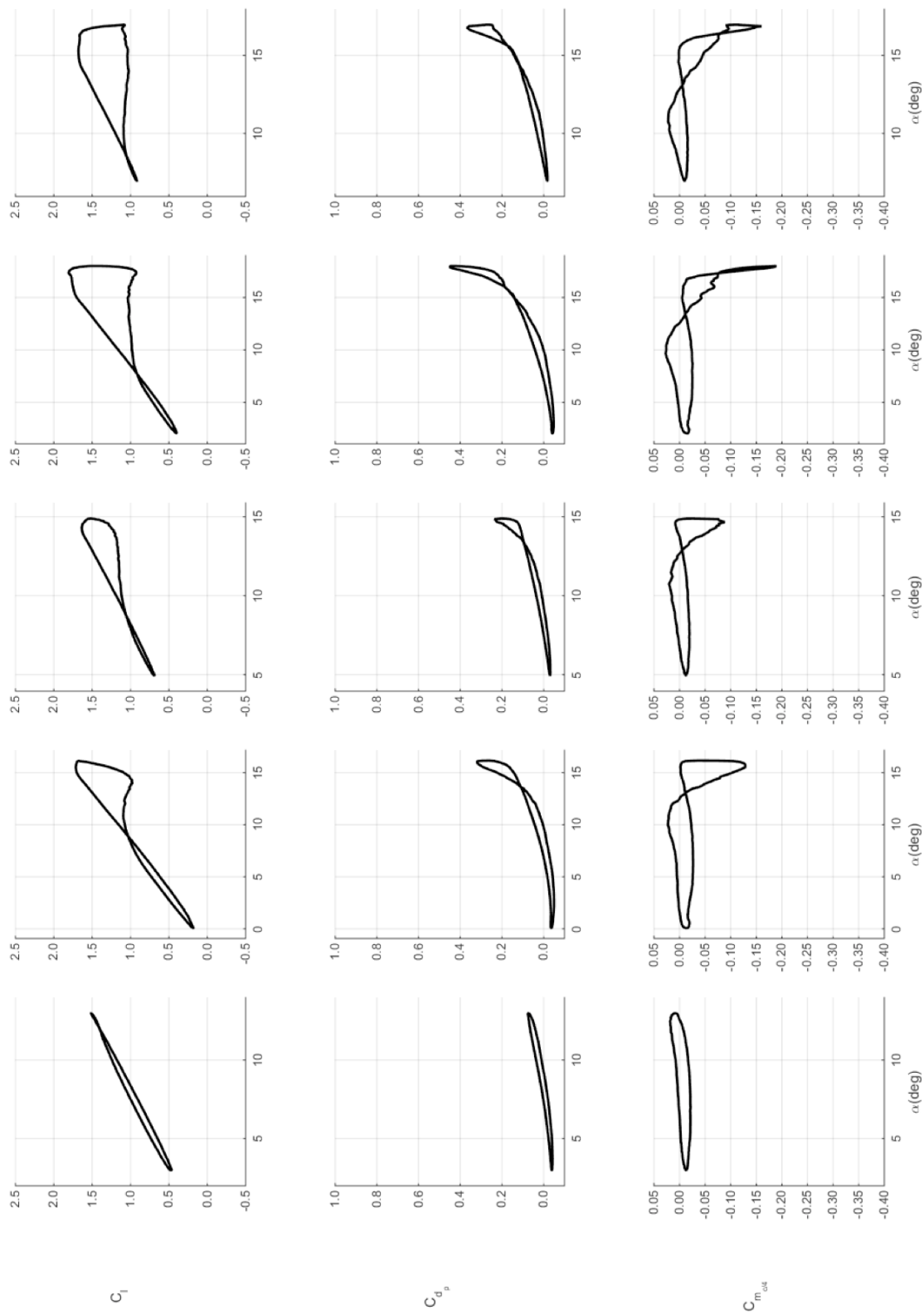


**Figure 421. Mach 0.4 baseline unsteady loads for  $k=0.07$ . From left to right:  $\alpha=8^\circ$ ,  $\alpha=10^\circ$ ,  $\alpha=12^\circ$ .**

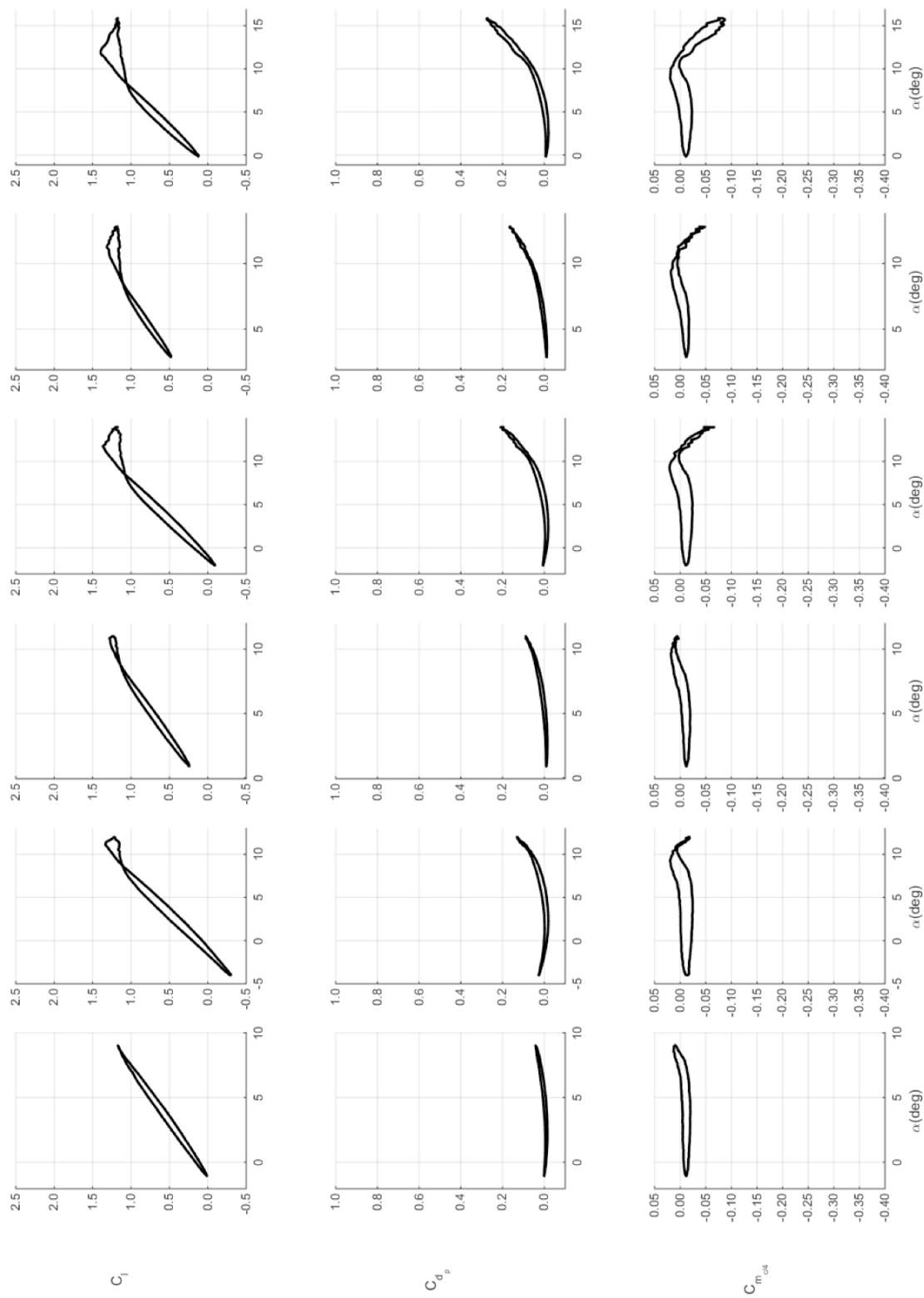


**Figure 422. Mach 0.5 baseline unsteady loads for  $k=0.025$ . From left to right:  $\alpha=4\pm5$ ,  $\alpha=6\pm5$ ,  $\alpha=8\pm5$ ,  $\alpha=8\pm8$ ,  $\alpha=8\pm8$ .**

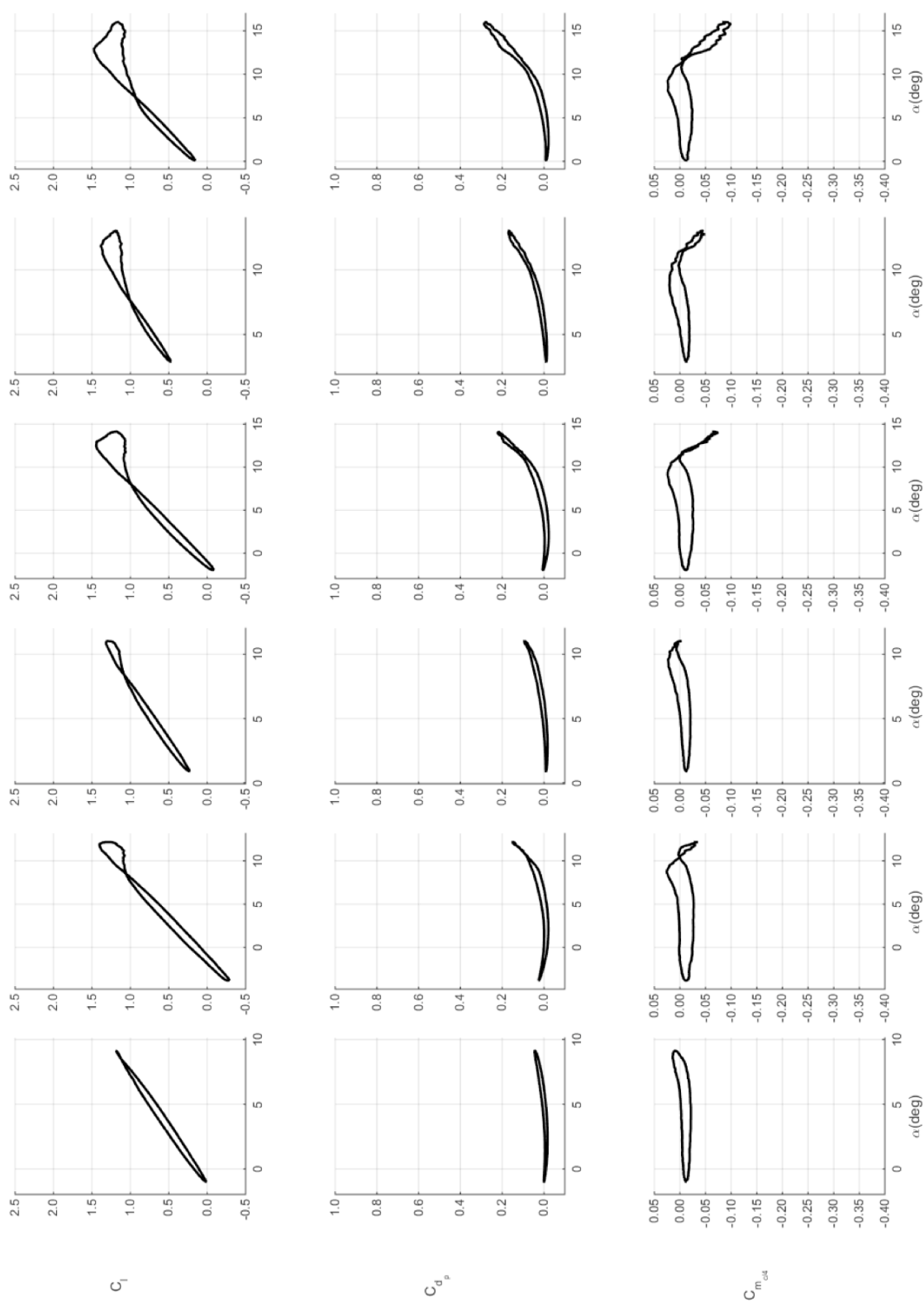


**Figure 423. Mach 0.5 baseline unsteady loads for  $k=0.05$ . From left to right:  $\alpha=4\pm 8$ ,  $\alpha=6\pm 5$ ,  $\alpha=8\pm 8$ .**

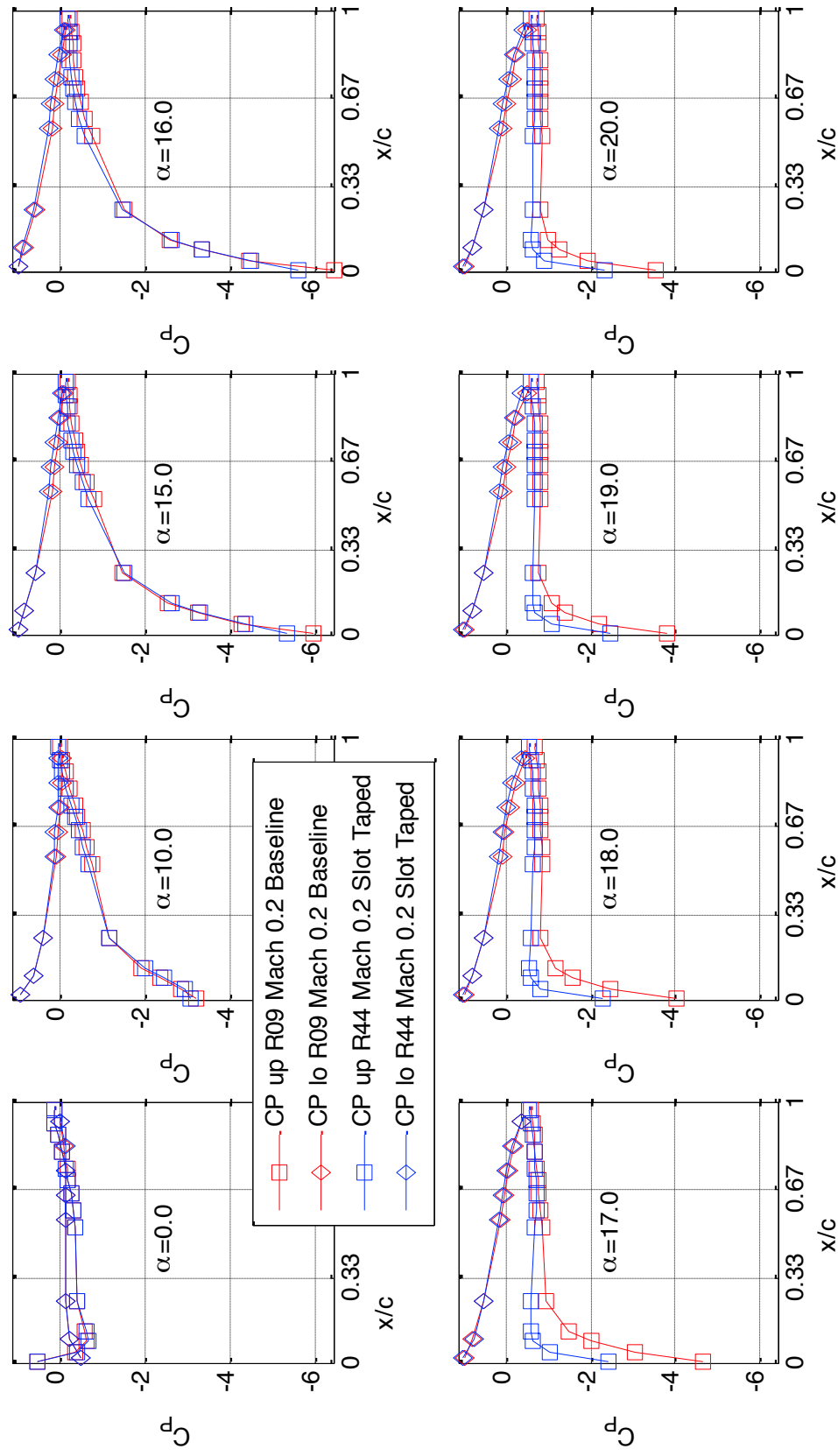


Figure 424. Mach 0.2 baseline and taped slot steady pressures.



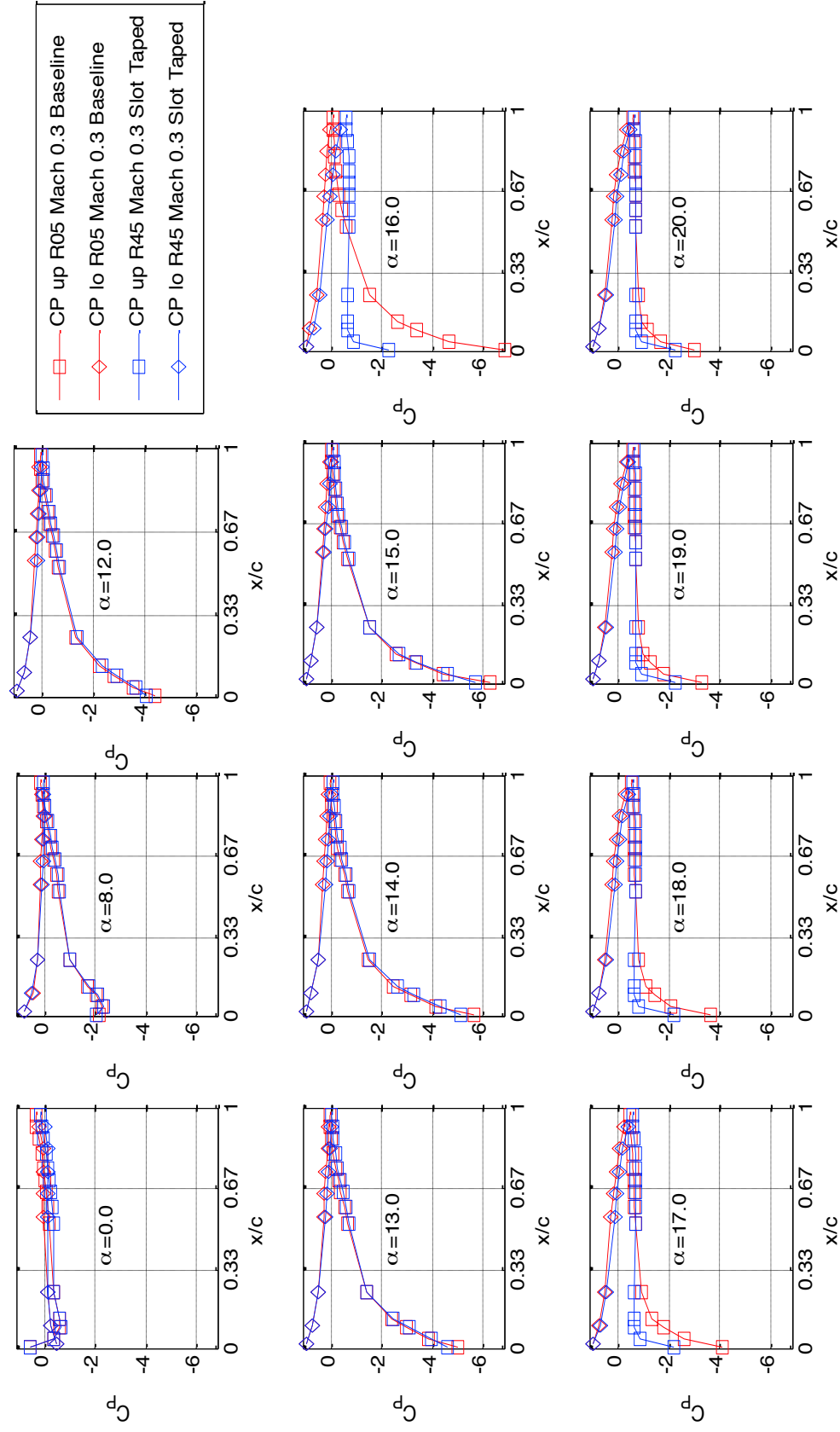


Figure 425. Mach 0.3 baseline and taped slot steady pressures.

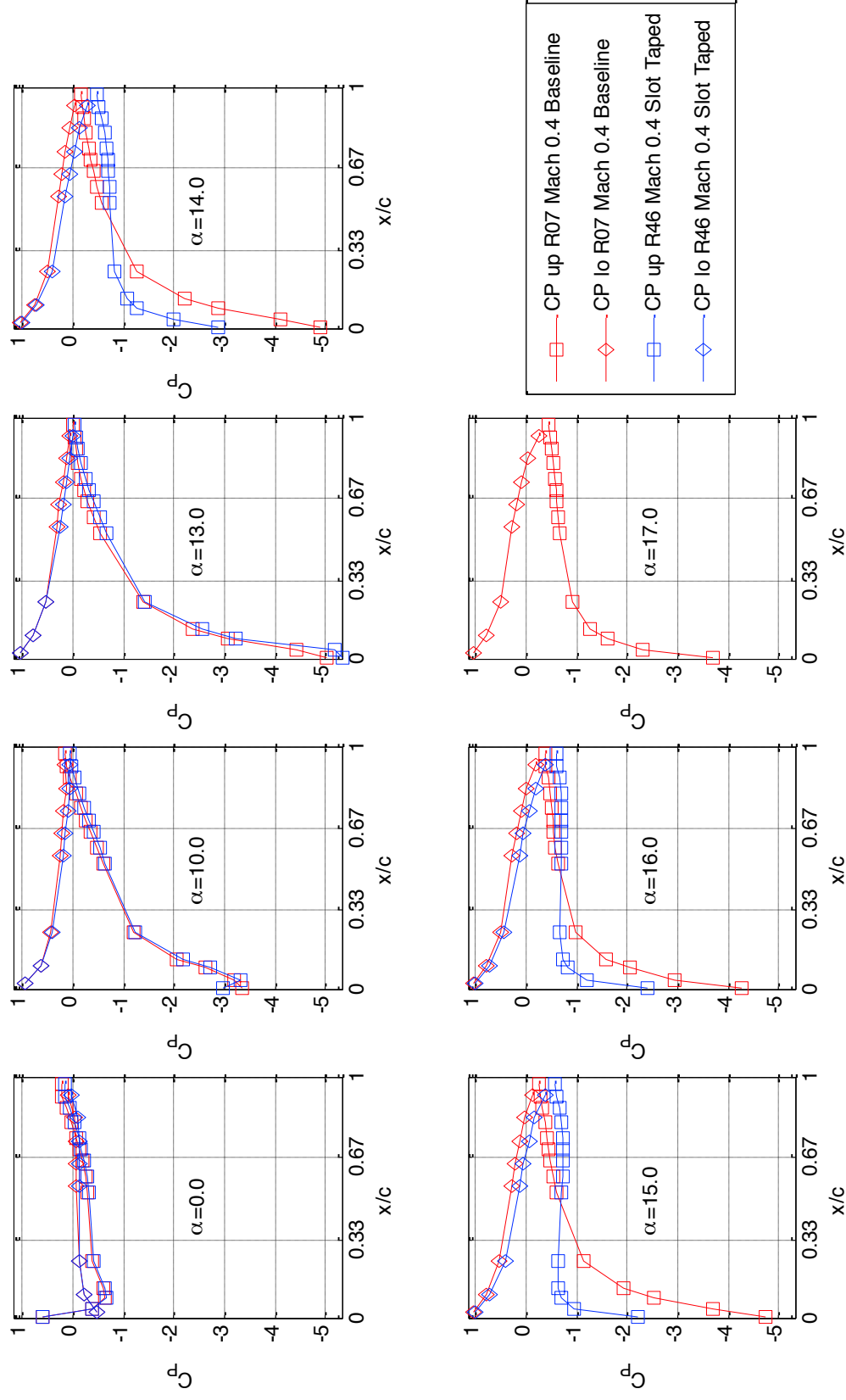
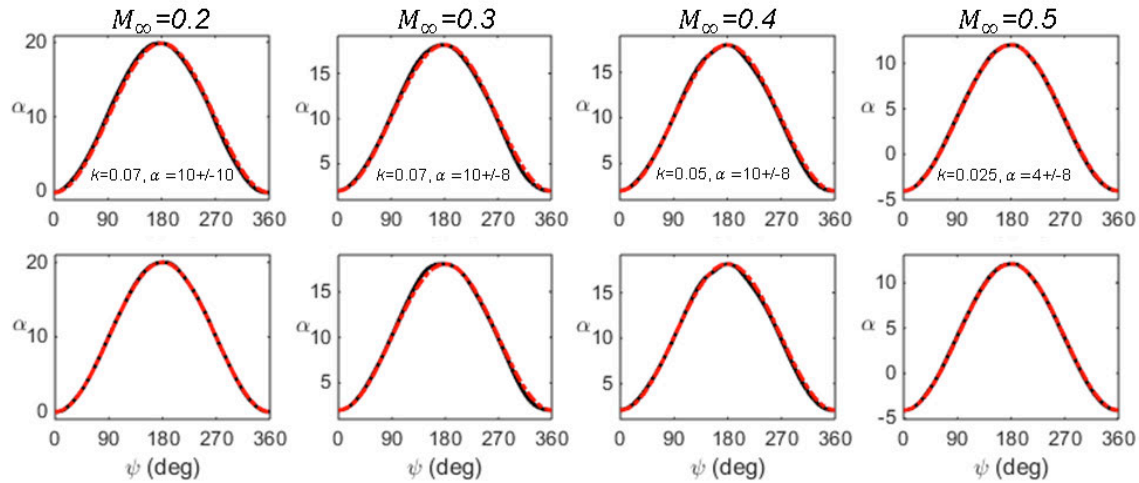


Figure 426. Mach 0.4 baseline and taped slot steady pressures.

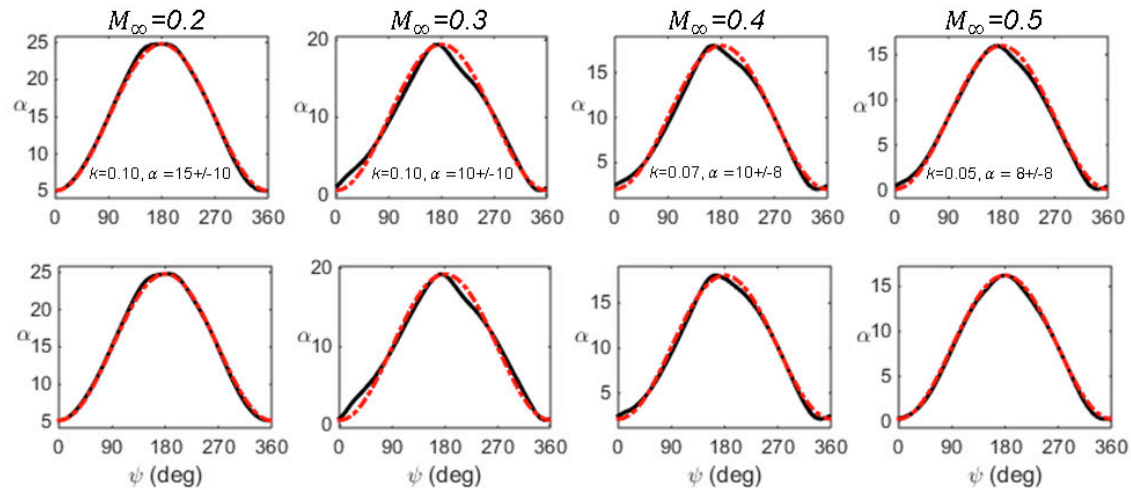
## Appendix 4. High-Speed Wind Tunnel Tests – Unsteady Results

### 1. Test Entry I – Test Results

#### A. Unsteady Results

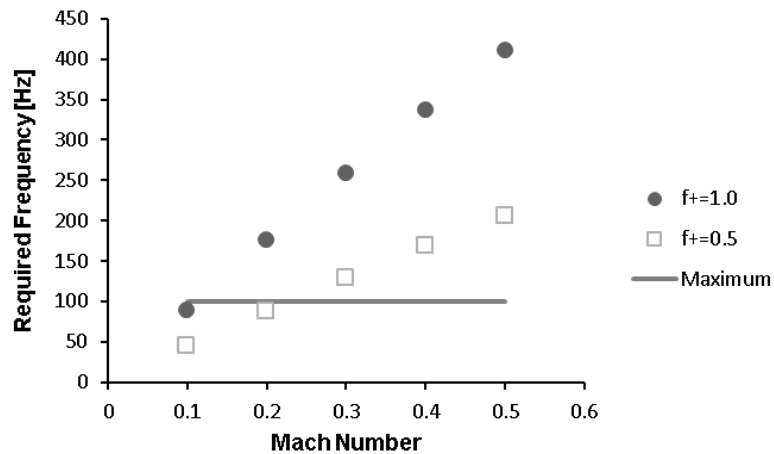


**Figure 427. Ensemble averaged angle-of-attack vs phase for Mach 0.2 through 0.5 for light dynamic stall air loads. The clean VR-12 is shown in the top row; the COMPACT wing is shown on the bottom row. The dashed red line indicates the desired trajectory.**



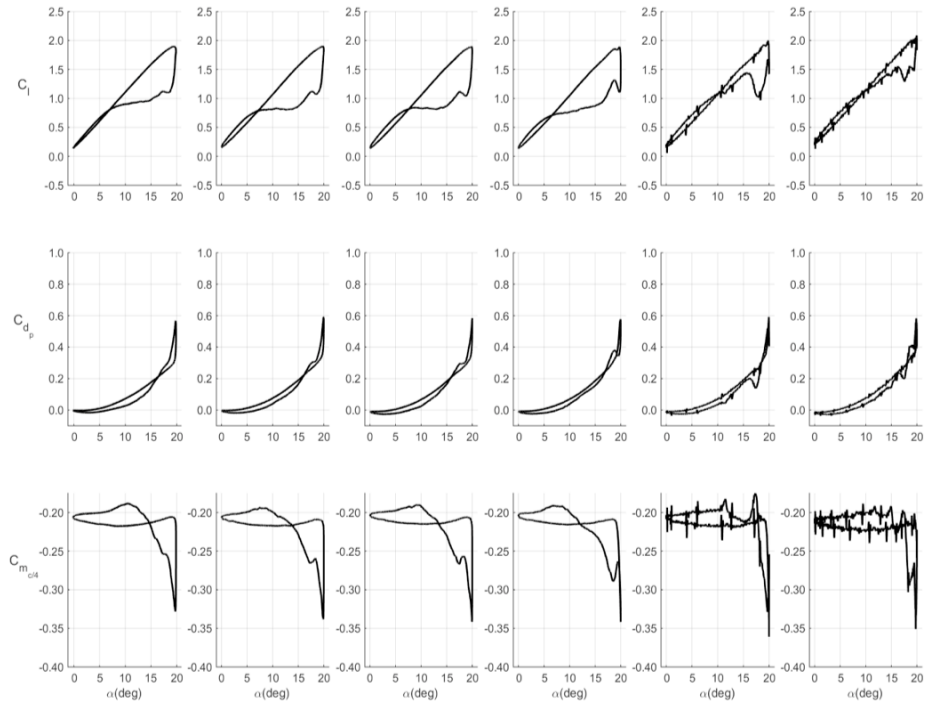
**Figure 428.** Ensemble averaged angle-of-attack vs phase for Mach 0.2 through 0.5 for deep dynamic stall air loads. The clean VR-12 is shown in the top row; the COMPACT wing is shown on the bottom row. The dashed red line indicates the desired trajectory.

#### *COMPACT Unsteady Loads*

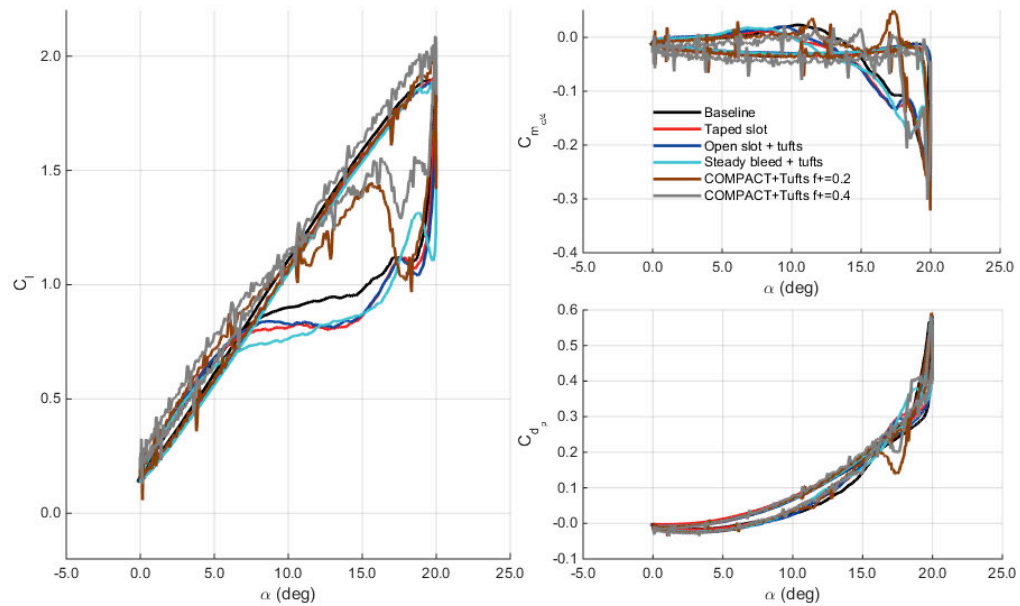


**Figure 429.** Required physical actuator pulsing frequency to achieve targeted  $F^+$  values over the IRT Mach range.

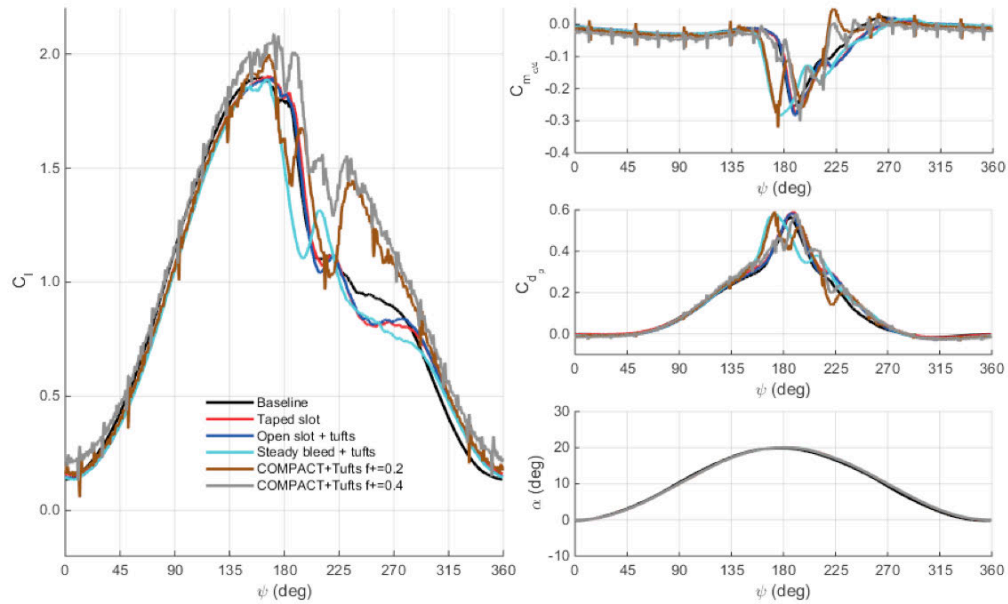
**Mach 0.2**



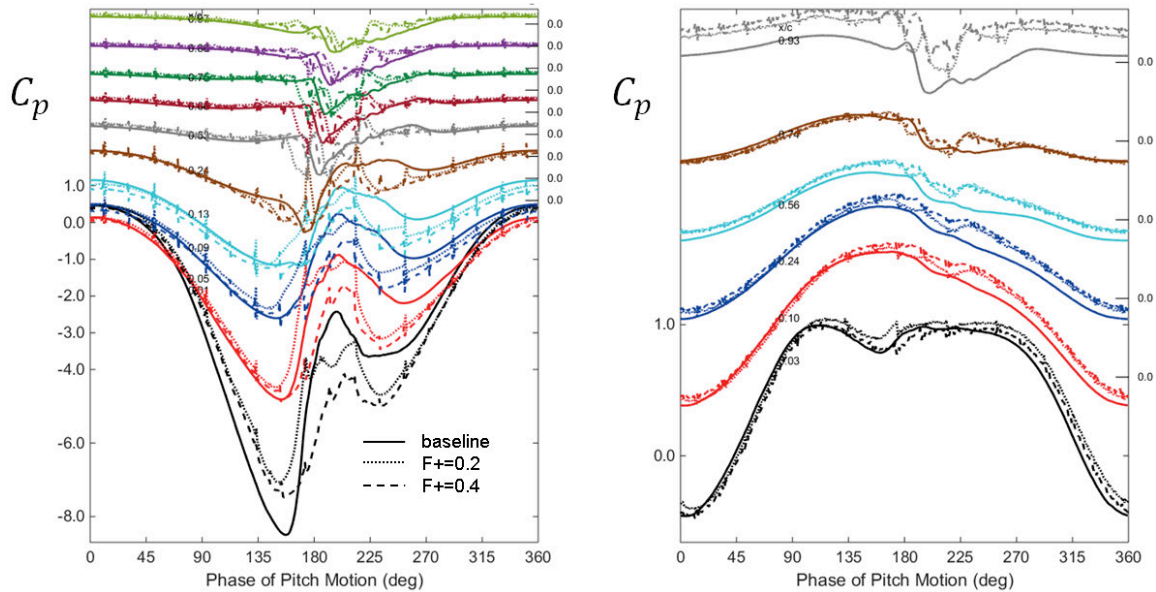
**Figure 430. Unsteady aerodynamic loads with respect to angle-of-attack.  $M=0.2$ ,  $\alpha = 10^\circ \pm 10^\circ$ ,  $k=0.07$ . Baseline, taped, open slot, steady bleed, COMPACT  $F^+ = 0.2$  and  $0.4$  shown in order from left to right.**



**Figure 431. Unsteady aerodynamic loads with respect to angle-of-attack.  $M=0.2$ ,  $\alpha = 10^\circ \pm 10^\circ$ ,  $k=0.07$ .**



**Figure 432. Unsteady aerodynamic loads with respect to pitch phase angle.  $M=0.2$ ,  $\alpha = 10^\circ \pm 10^\circ$ ,  $k=0.07$ .**



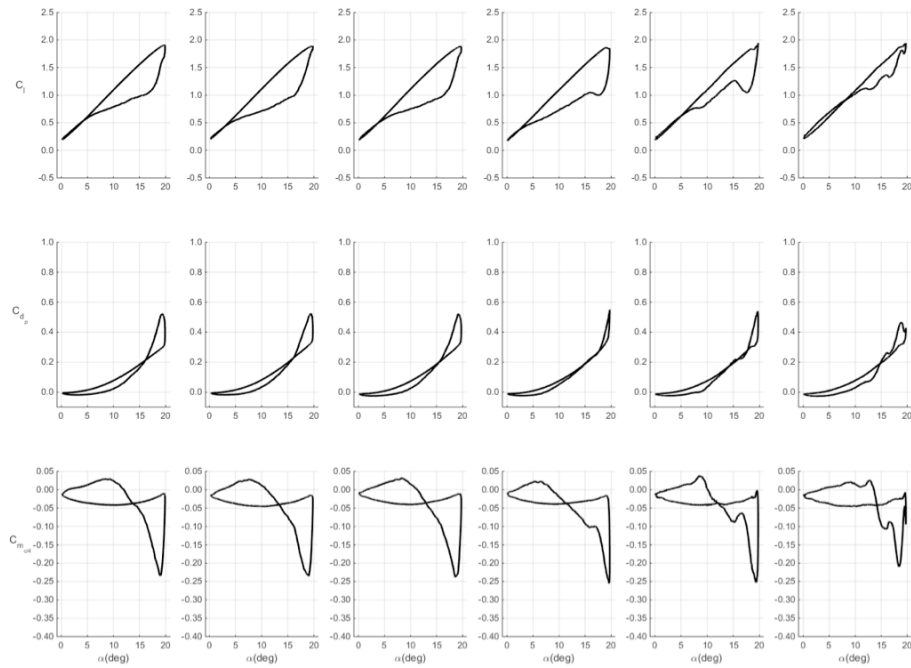


**Figure 434. Unsteady aerodynamic loads with respect to angle-of-attack.  $M=0.2$ ,  $\alpha = 10^\circ \pm 10^\circ$ ,  $k=0.10$ . Baseline, taped, open slot, steady bleed, COMPACT  $F^+ = 0.2$  and  $0.4$  shown in order from left to right.**

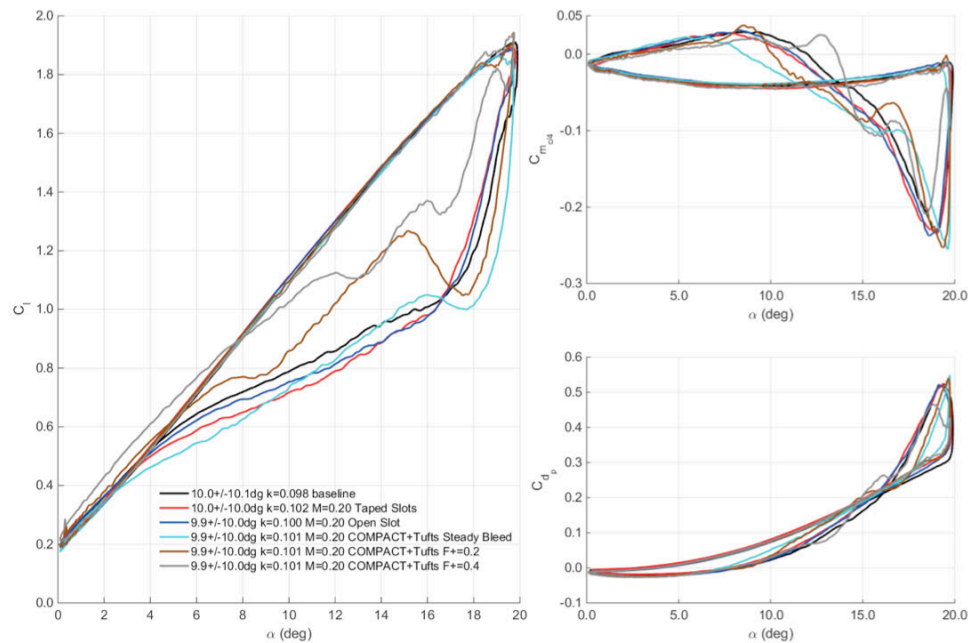


**Figure 435. Unsteady aerodynamic loads with respect to angle-of-attack.  $M=0.2$ ,  $\alpha = 10^\circ \pm 10^\circ$ ,  $k=0.10$ .**



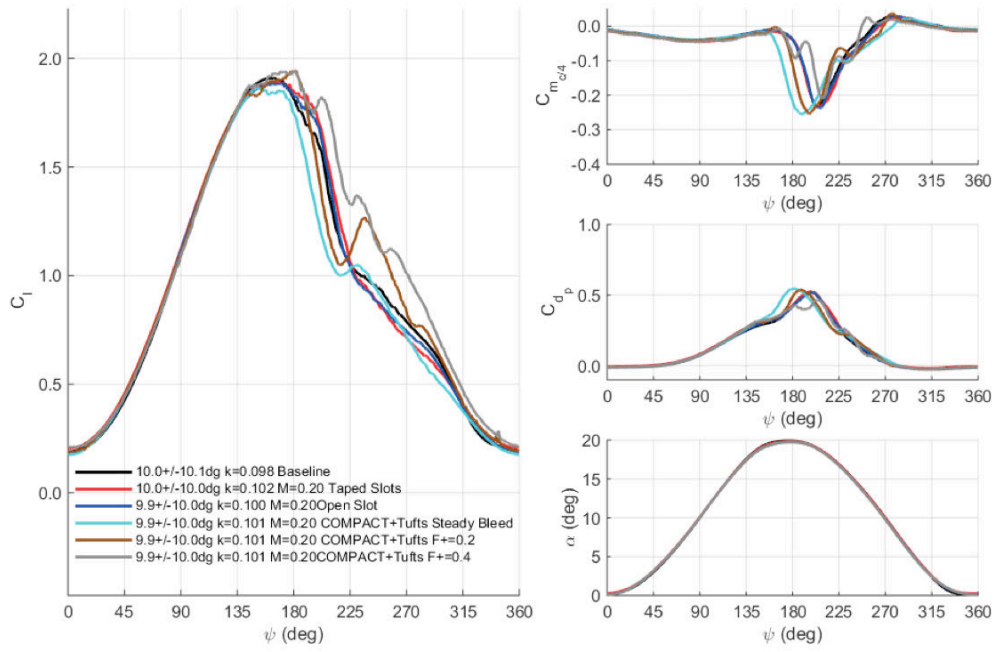


**Figure 436. Unsteady aerodynamic loads with respect to phase.  $M=0.2$ ,  $\alpha = 10^\circ \pm 10^\circ$ ,  $k=0.10$ .**

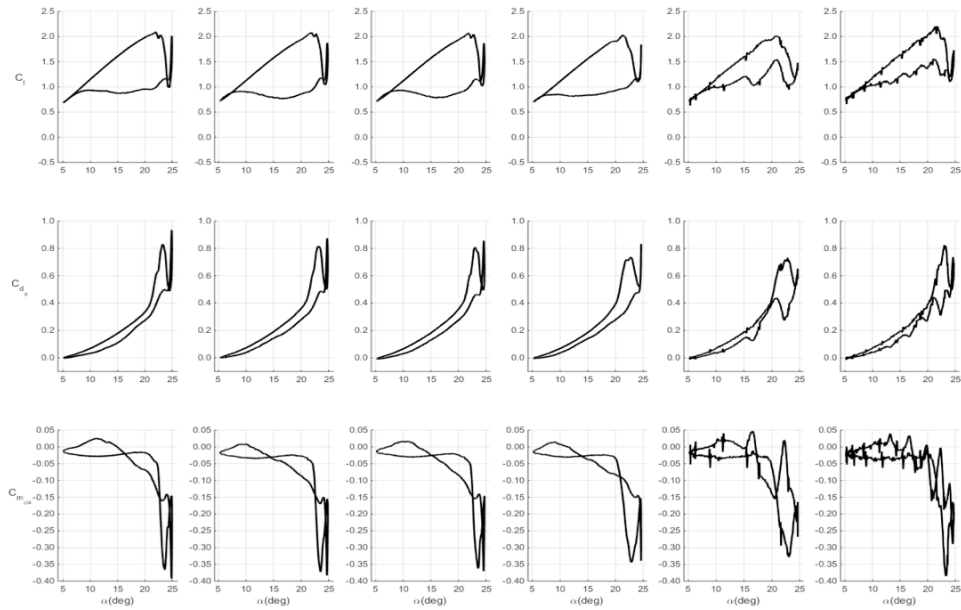


**Figure 437 Unsteady aerodynamic loads with respect to angle-of-attack.  $M=0.2$ ,  $\alpha=15^\circ \pm 10^\circ$ ,  $k=0.10$ . Baseline, taped, open slot, steady bleed, COMPACT  $F^+=0.2$  and  $0.4$  shown in order from left to right.**

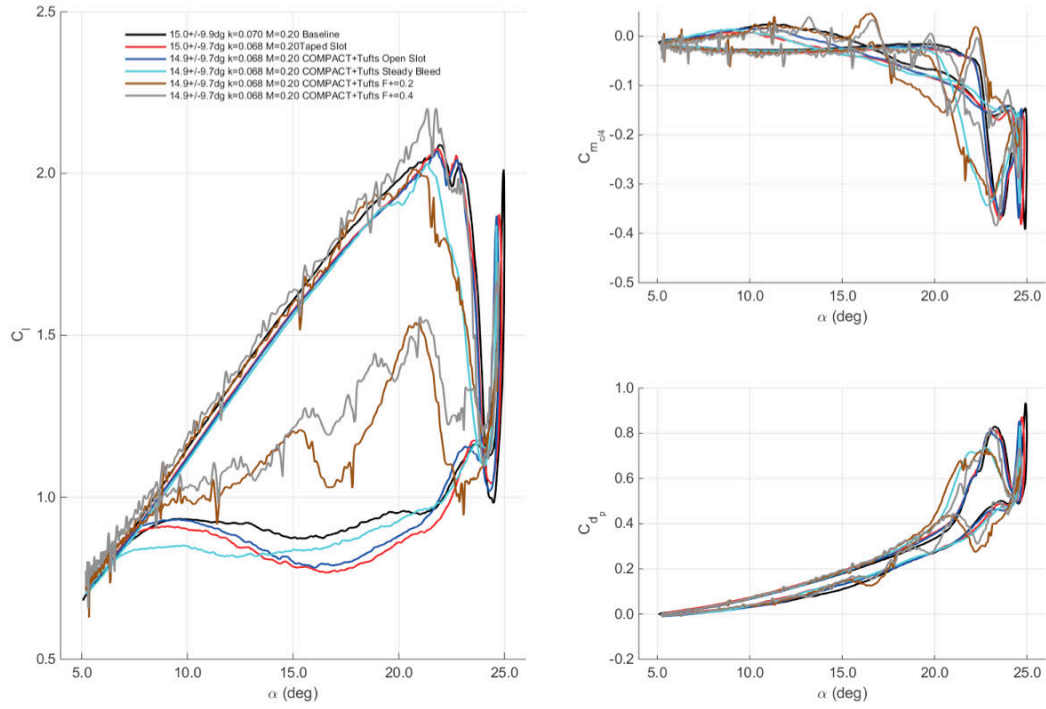


**Figure 438 Unsteady aerodynamic loads with respect to angle-of-attack.  $M=0.2$ ,  $\alpha=15^\circ \pm 10^\circ$ ,  $k=0.07$ .**

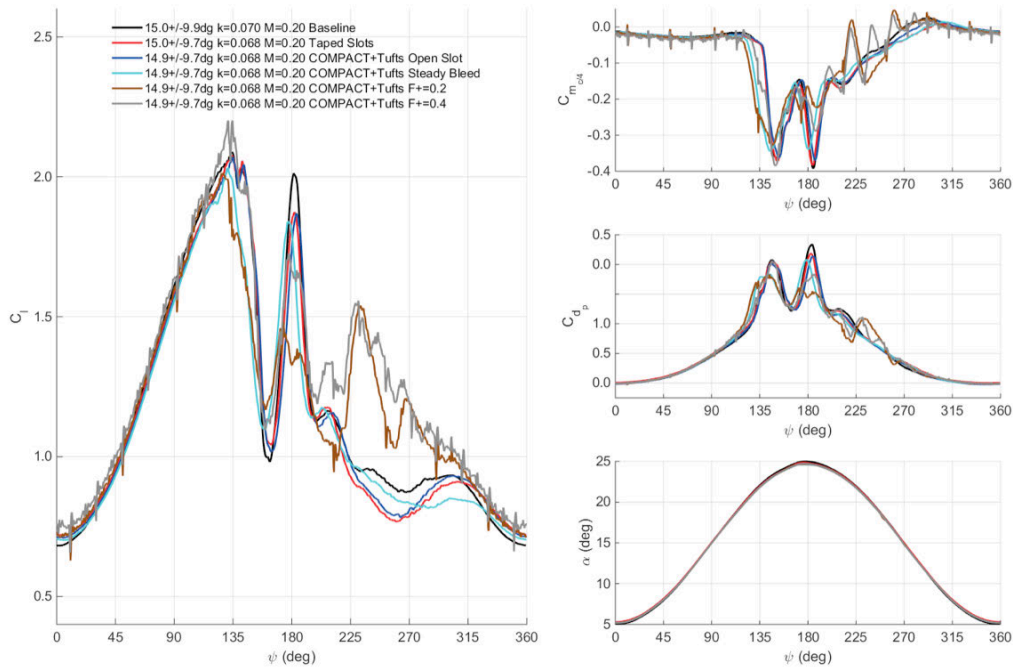


**Figure 439. Unsteady aerodynamic loads with respect to phase.  $M=0.2$ ,  $\alpha=15^\circ \pm 10^\circ$ ,  $k=0.07$ .**

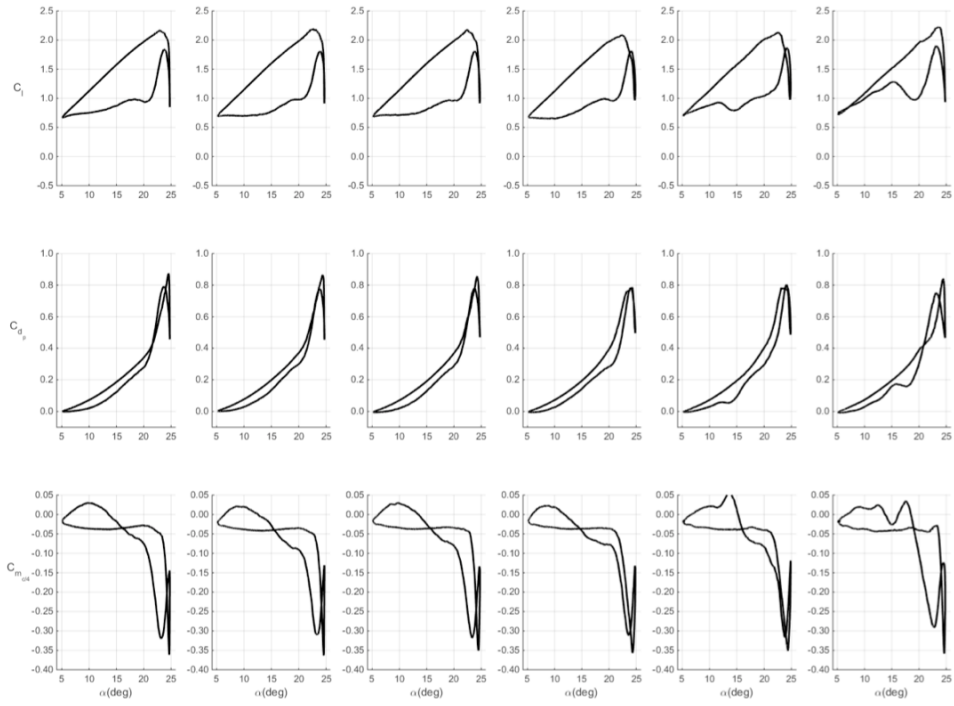


**Figure 440 Unsteady aerodynamic loads with respect to angle-of-attack.  $M=0.2$ ,  $\alpha=15^\circ \pm 10^\circ$ ,  $k=0.10$ . Baseline, taped, open slot, steady bleed, COMPACT  $F^+=0.2$  and  $0.4$  shown in order from left to right.**

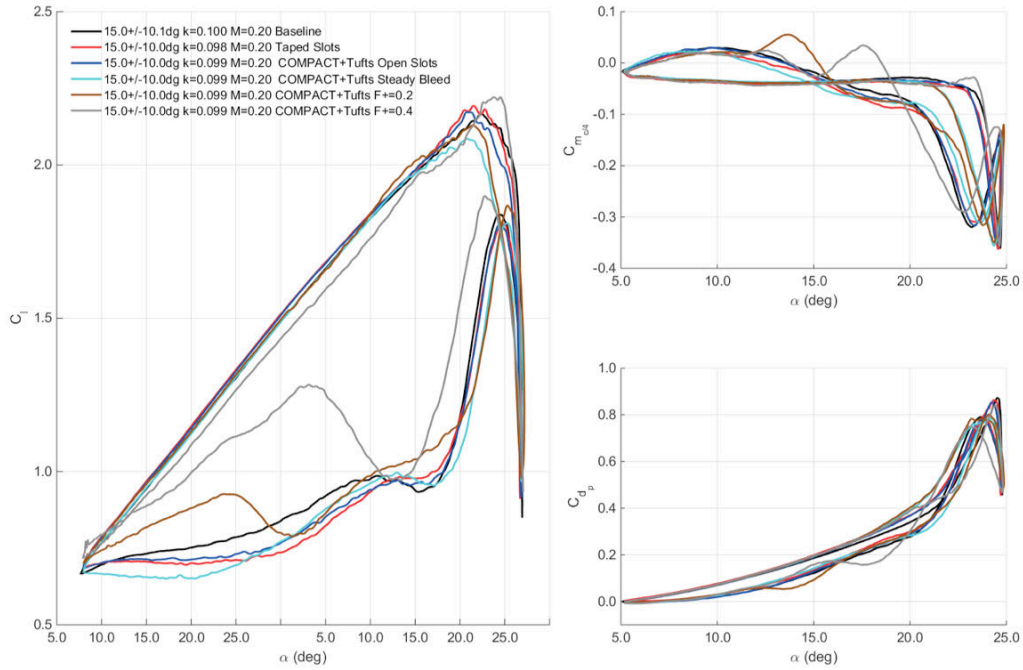


**Figure 441. Unsteady aerodynamic loads with respect to angle-of-attack.  $M=0.2$ ,  $\alpha=15^\circ \pm 10^\circ$ ,  $k=0.10$ .**

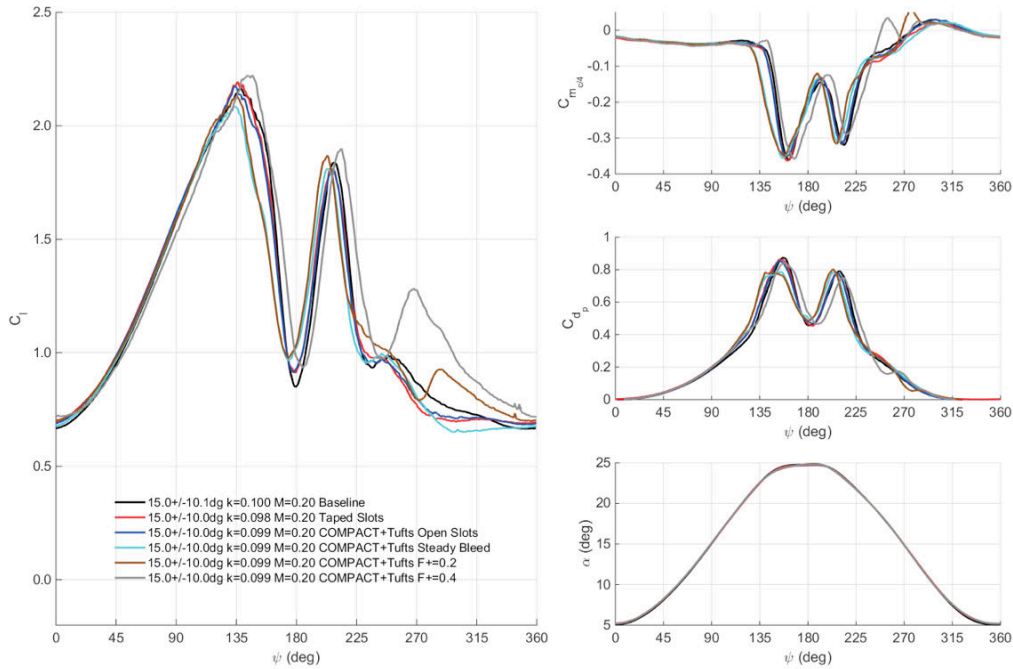


**Figure 442. Unsteady aerodynamic loads with respect to phase.  $M=0.2$ ,  $\alpha=15^\circ \pm 10^\circ$ ,  $k=0.10$ .**

**Mach 0.3**

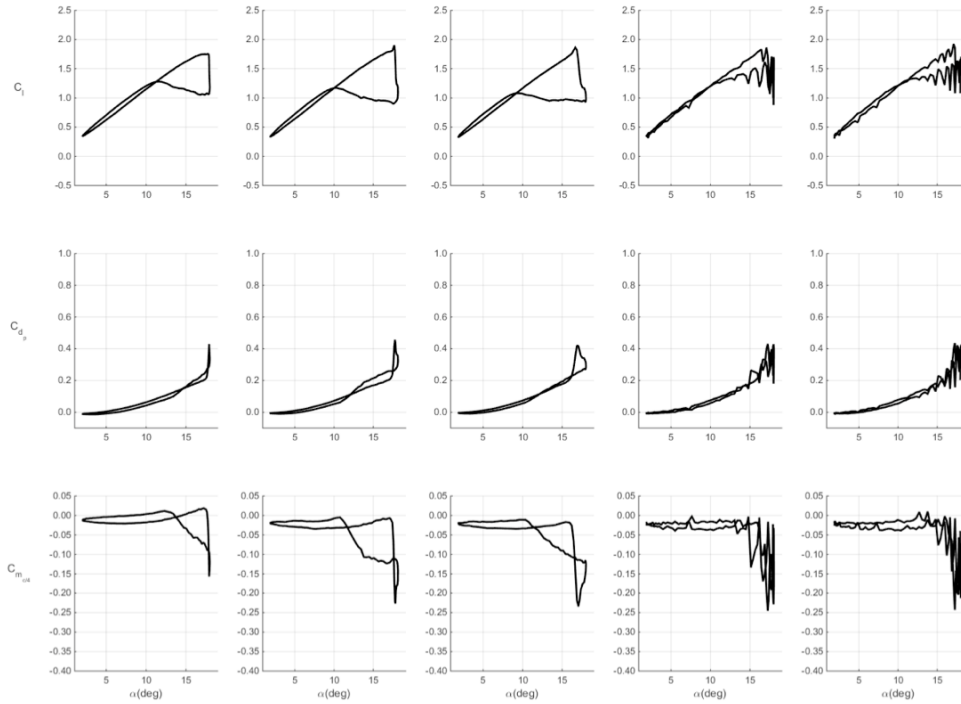


**Figure 443. Effect of COMPACT on aerodynamic loads.  $M=0.3$ ,  $\alpha=10^\circ \pm 8^\circ$ ,  $k=0.025$ . Baseline, open slot, steady bleed, COMPACT  $F^+ = 0.2$  and  $0.3$  shown in order from left to right.**

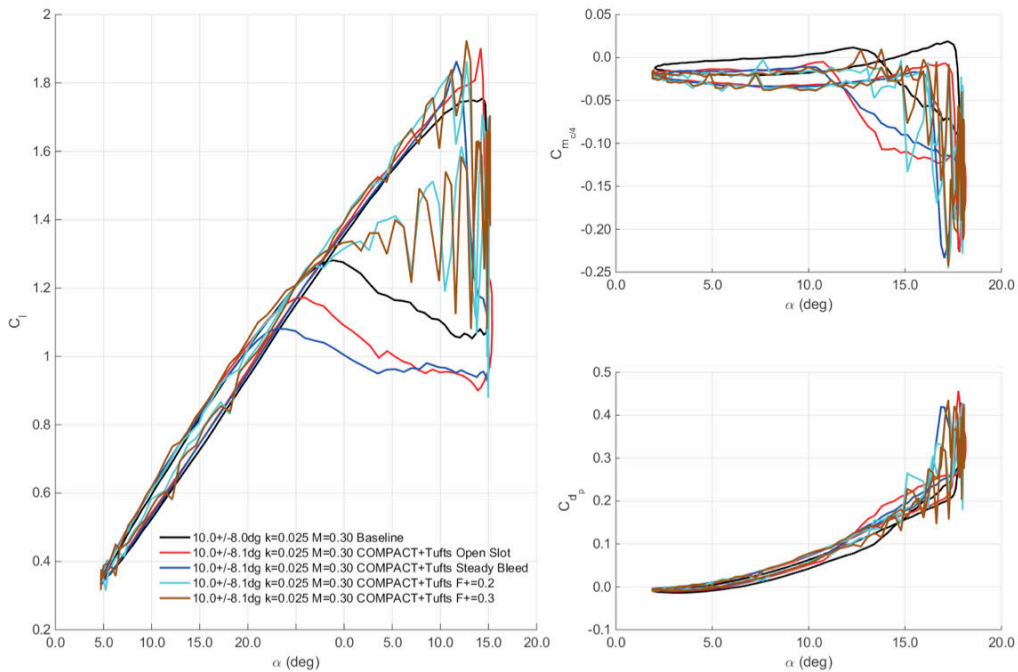


**Figure 444. Effect of COMPACT on VR-12 unsteady airloads,  $M=0.3$ ,  $\alpha=10^\circ \pm 8^\circ$ ,  $k=0.025$ .**

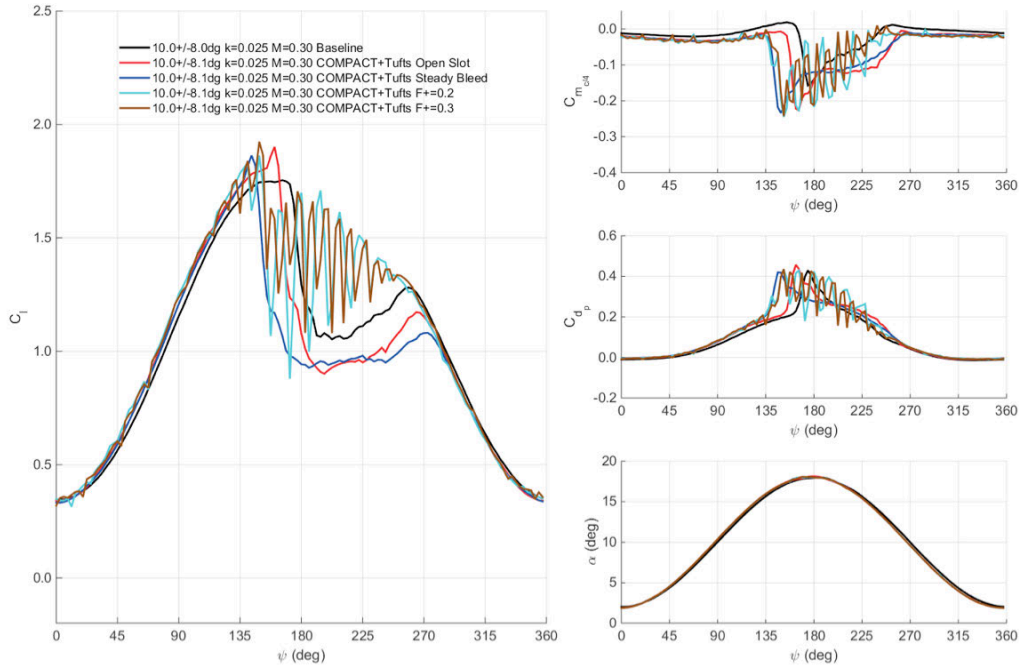


**Figure 445. Effect of COMPACT on VR-12 unsteady airloads,  $M=0.3$ ,  $\alpha=10^\circ \pm 8^\circ$ ,  $k=0.025$ .**

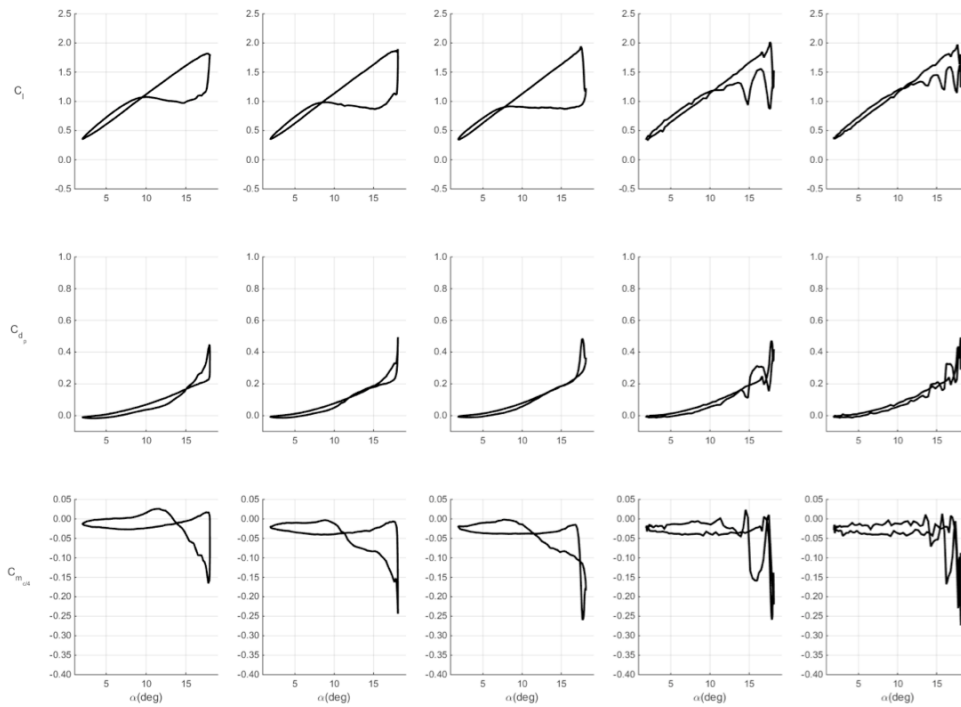


**Figure 446. Effect of COMPACT on aerodynamic loads.  $M=0.3$ ,  $\alpha=10^\circ \pm 8^\circ$ ,  $k=0.05$ . Baseline, open slot, steady bleed, COMPACT  $F^+ = 0.2$  and  $0.3$  shown in order from left to right.**

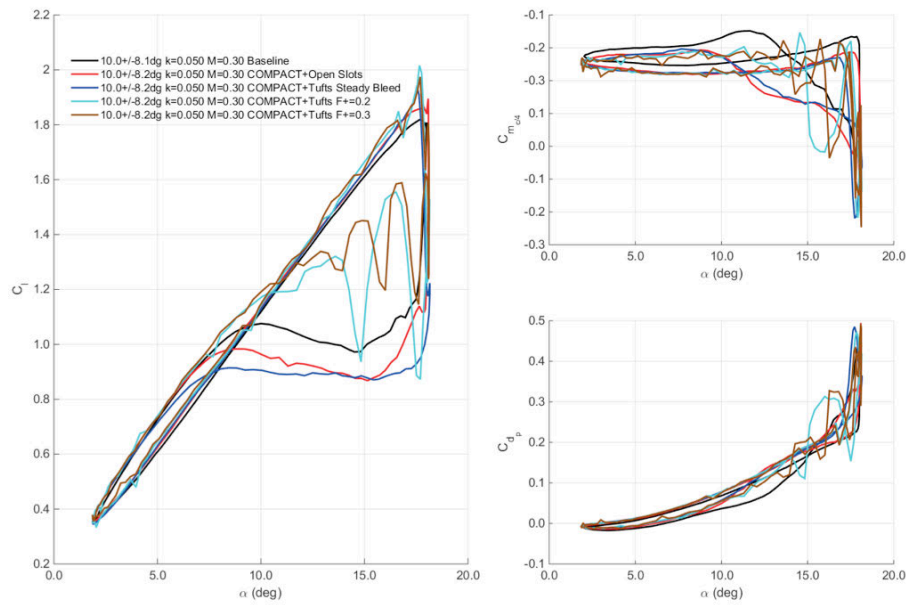


Figure 447. Effect of COMPACT on VR-12 unsteady airloads,  $M=0.3$ ,  $\alpha=10^\circ \pm 8^\circ$ ,  $k=0.05$ .

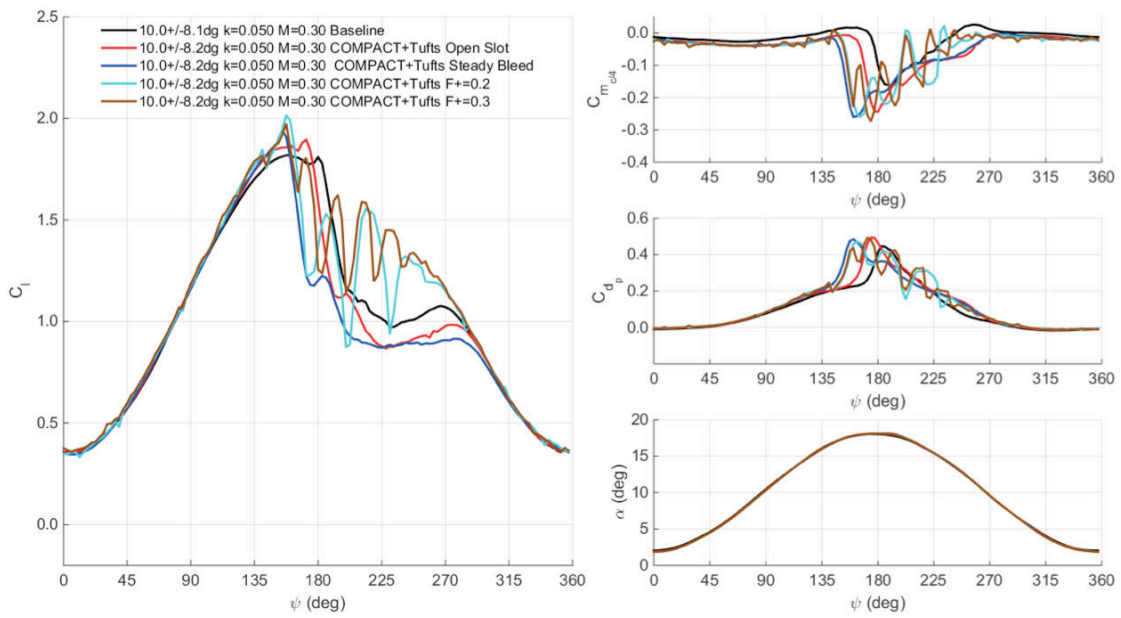
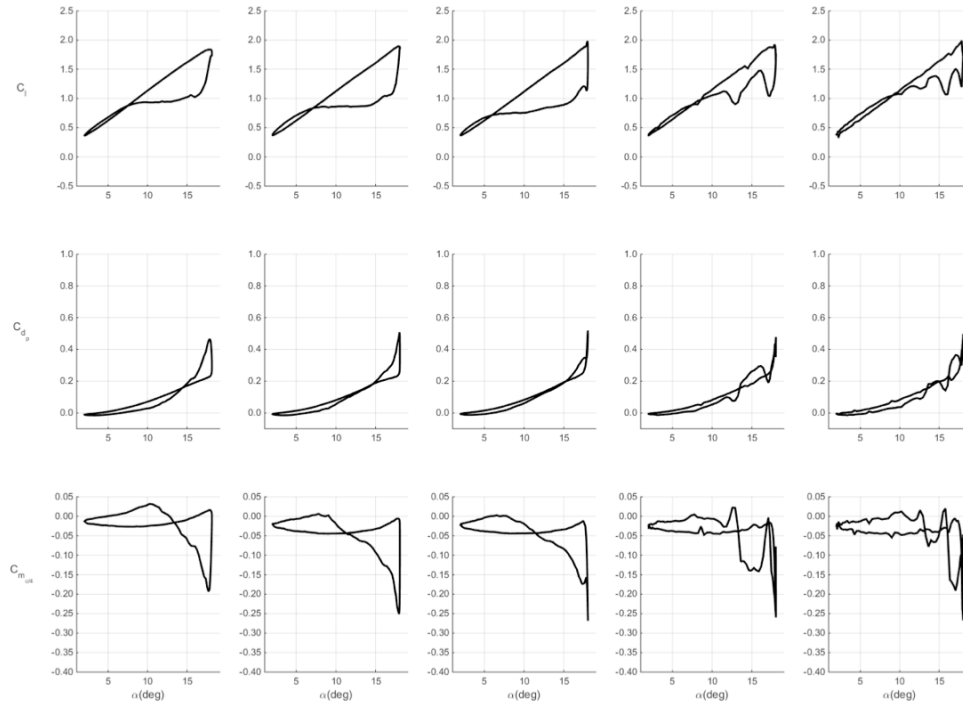
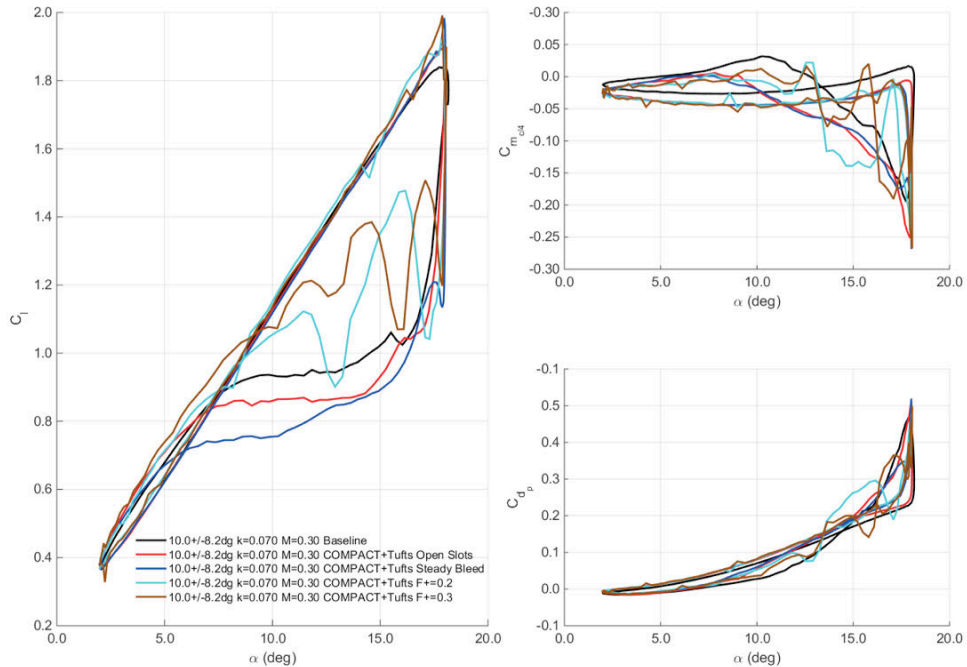


Figure 448. Effect of COMPACT on VR-12 unsteady airloads,  $M=0.3$ ,  $\alpha=10^\circ \pm 8^\circ$ ,  $k=0.05$ .





**Figure 449 Effect of COMPACT on VR-12 unsteady airloads,  $M=0.3$ ,  $\alpha=10^\circ\pm 8^\circ$ ,  $k=0.07$ . Baseline, open slot, steady bleed, COMPACT  $F^+=0.2$  and  $0.3$  shown in order from left to right.**



**Figure 450. Effect of COMPACT on VR-12 unsteady airloads,  $M=0.3$ ,  $\alpha=10^\circ\pm 8^\circ$ ,  $k=0.07$ .**

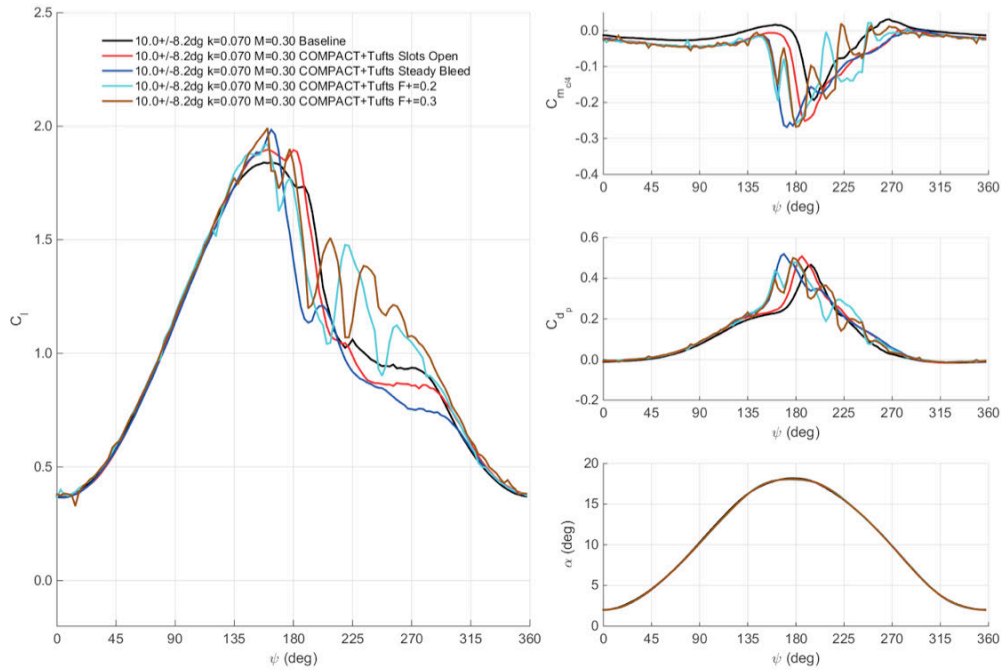


**Figure 451. Effect of COMPACT on VR-12 unsteady airloads,  $M=0.3$ ,  $\alpha=10^\circ\pm 8^\circ$ ,  $k=0.07$ .**

*Mach 0.4 and 0.5*

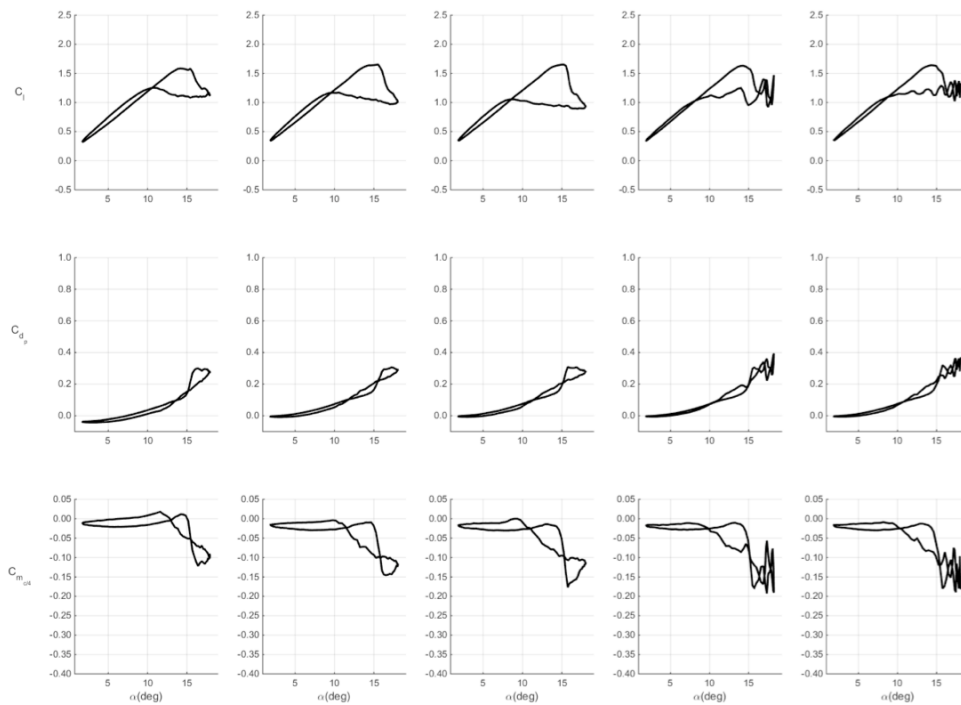


**Figure 452. Effect of COMPACT on VR-12 unsteady airloads,  $M=0.4$ ,  $\alpha=10^\circ\pm 8^\circ$ ,  $k=0.025$ . Baseline, open slot, steady bleed, COMPACT  $F^+=0.1$  and  $0.2$  shown in order from left to right.**

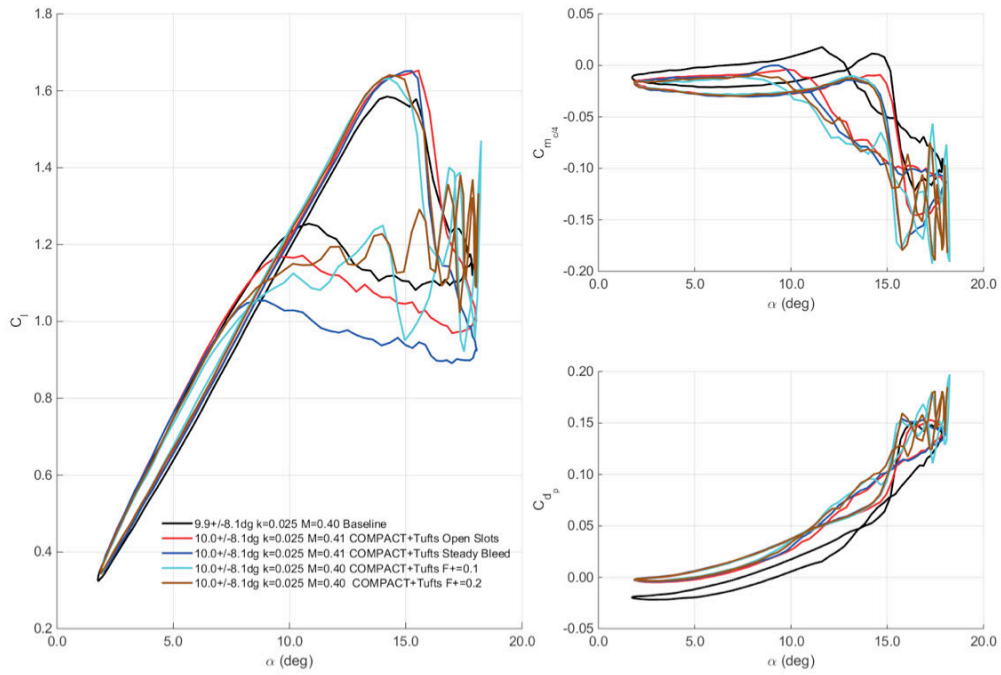


**Figure 453. Effect of COMPACT on VR-12 unsteady airloads,  $M=0.4$ ,  $\alpha=10^\circ\pm8^\circ$ ,  $k=0.025$ .**

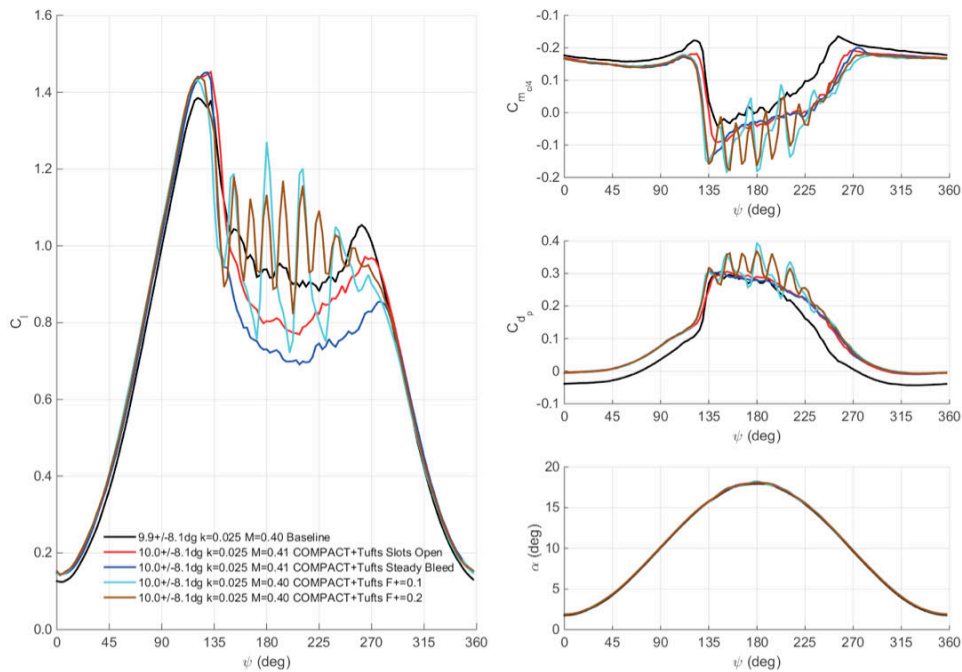


**Figure 454. Effect of COMPACT on VR-12 unsteady airloads,  $M=0.4$ ,  $\alpha=10^\circ\pm8^\circ$ ,  $k=0.025$ .**

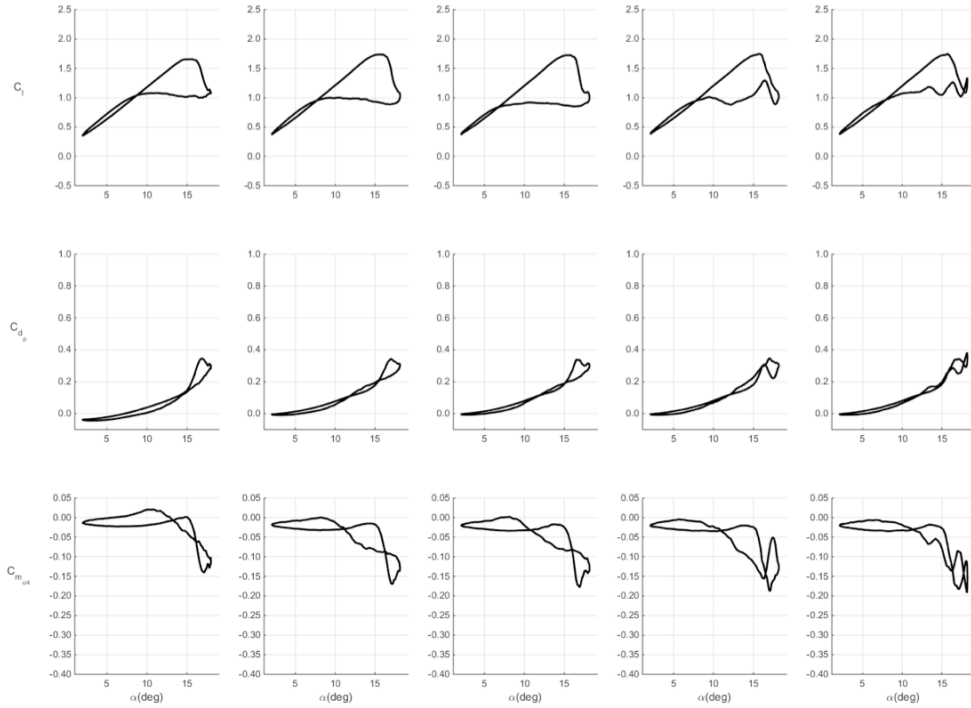


**Figure 455. Effect of COMPACT on VR-12 unsteady airloads,  $M=0.4$ ,  $\alpha=10^\circ\pm8^\circ$ ,  $k=0.05$ . Baseline, open slot, steady bleed, COMPACT  $F^+=0.1$  and  $0.2$  shown in order from left to right.**

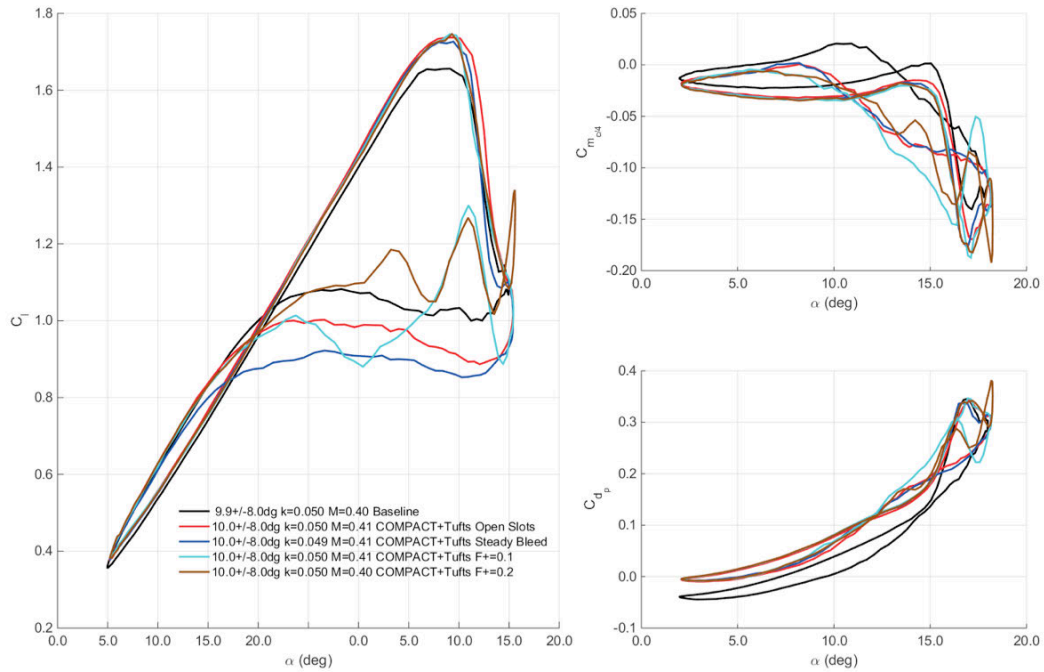


**Figure 456. Effect of COMPACT on VR-12 unsteady airloads,  $M=0.4$ ,  $\alpha=10^\circ\pm8^\circ$ ,  $k=0.05$ .**

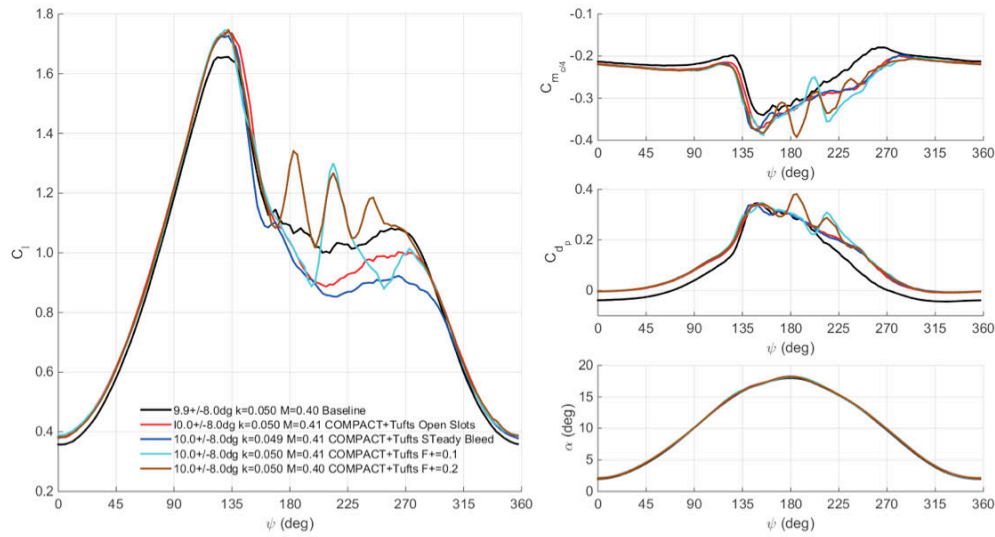


**Figure 457. Effect of COMPACT on VR-12 unsteady airloads,  $M=0.4$ ,  $\alpha=10^\circ\pm 8^\circ$ ,  $k=0.05$ .**

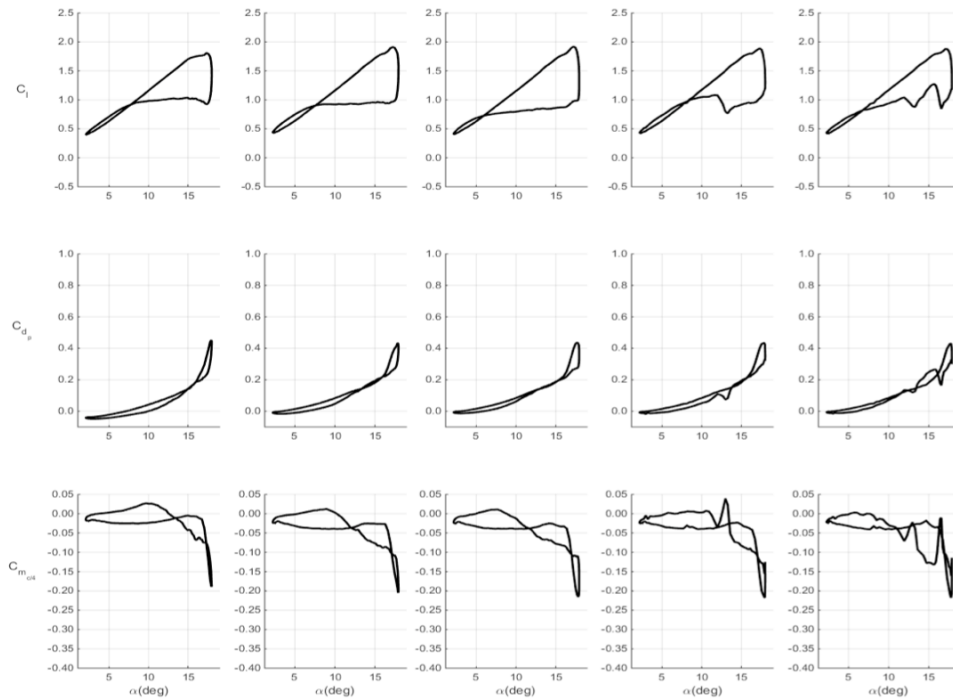


**Figure 458. Effect of COMPACT on VR-12 unsteady airloads,  $M=0.4$ ,  $\alpha=10^\circ\pm 8^\circ$ ,  $k=0.07$ . Baseline, open slot, steady bleed, COMPACT  $F^+=0.1$  and  $0.2$  shown in order from left to right.**

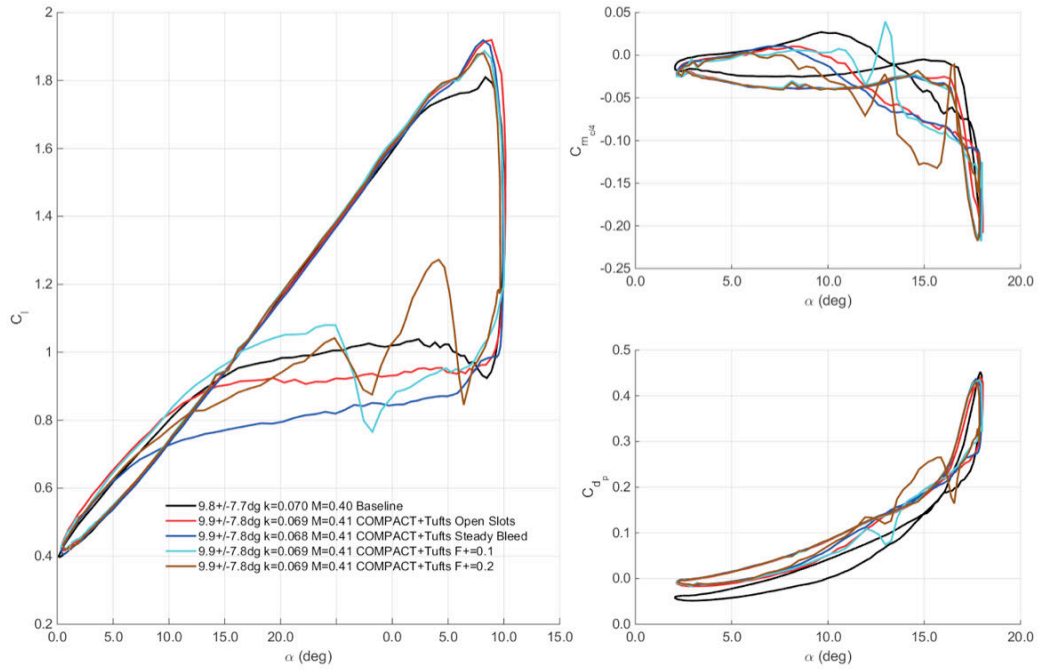


**Figure 459. Effect of COMPACT on VR-12 unsteady airloads,  $M=0.4$ ,  $\alpha=10^\circ\pm 8^\circ$ ,  $k=0.07$ .**

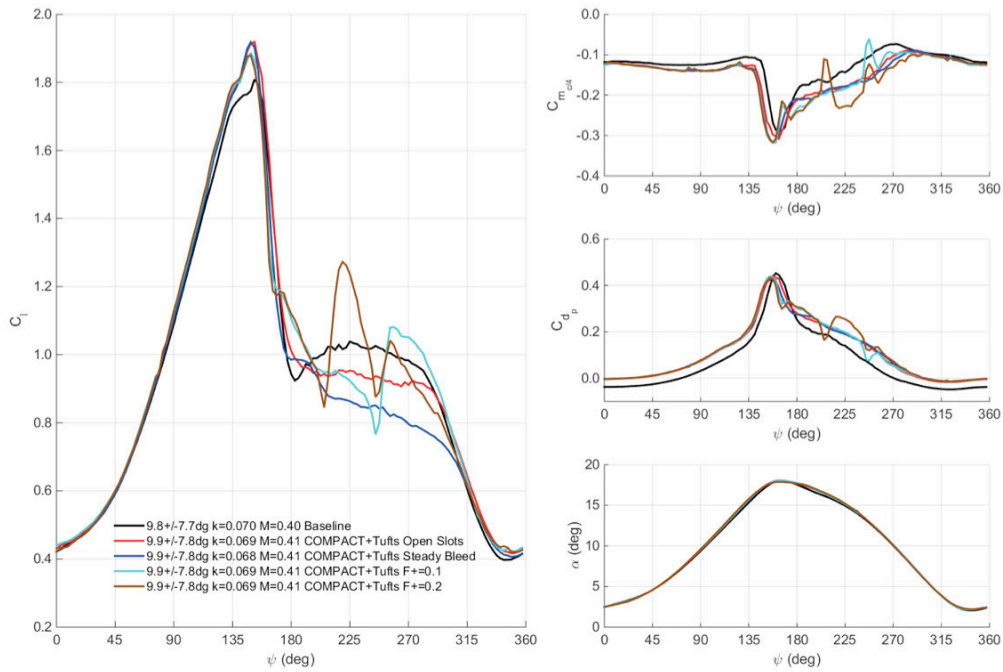


**Figure 460. Effect of COMPACT on VR-12 unsteady airloads,  $M=0.4$ ,  $\alpha=10^\circ\pm 8^\circ$ ,  $k=0.07$ .**

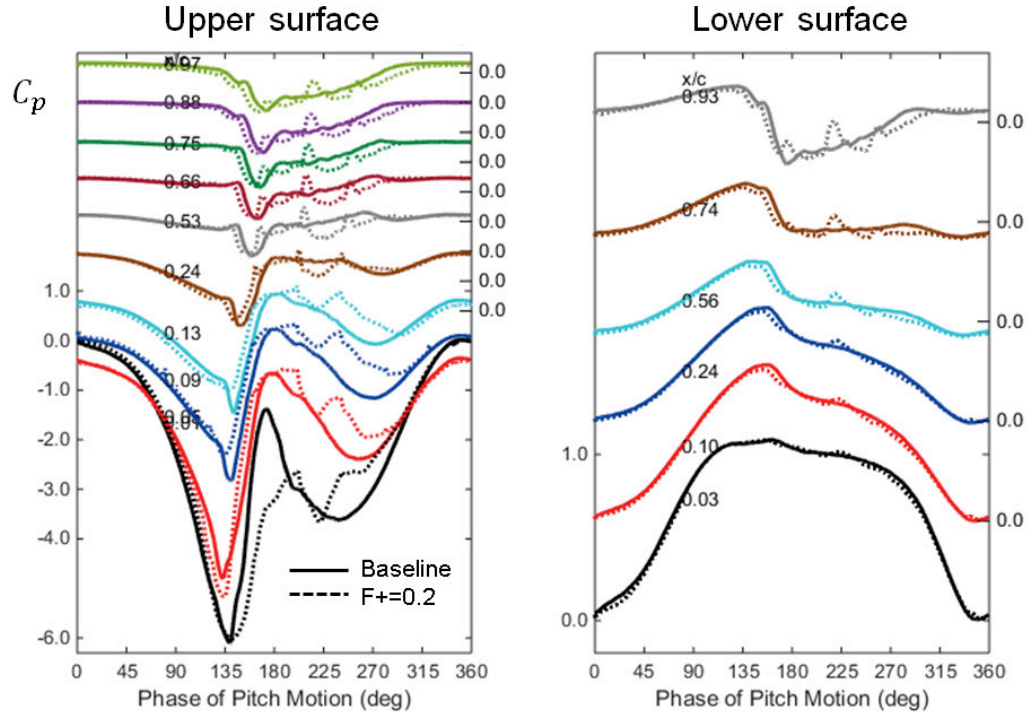


Figure 461. Comparison of baseline and COMPACT  $F^+ = 0.2$  operation. Upper (left) and lower surface (right) pressure coefficients throughout the prescribed pitch motion.

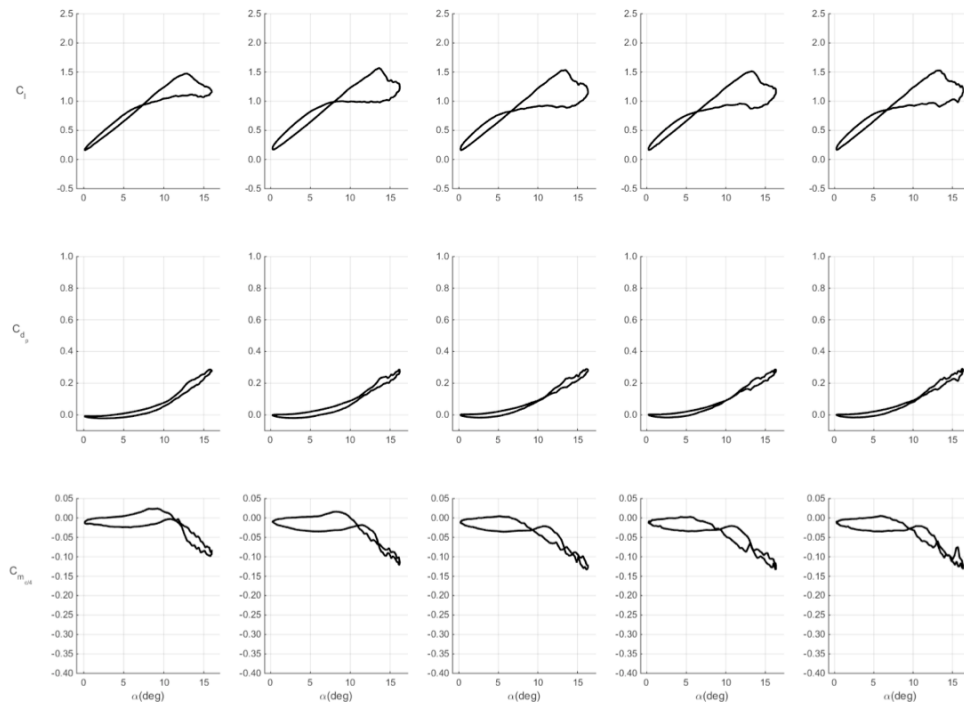
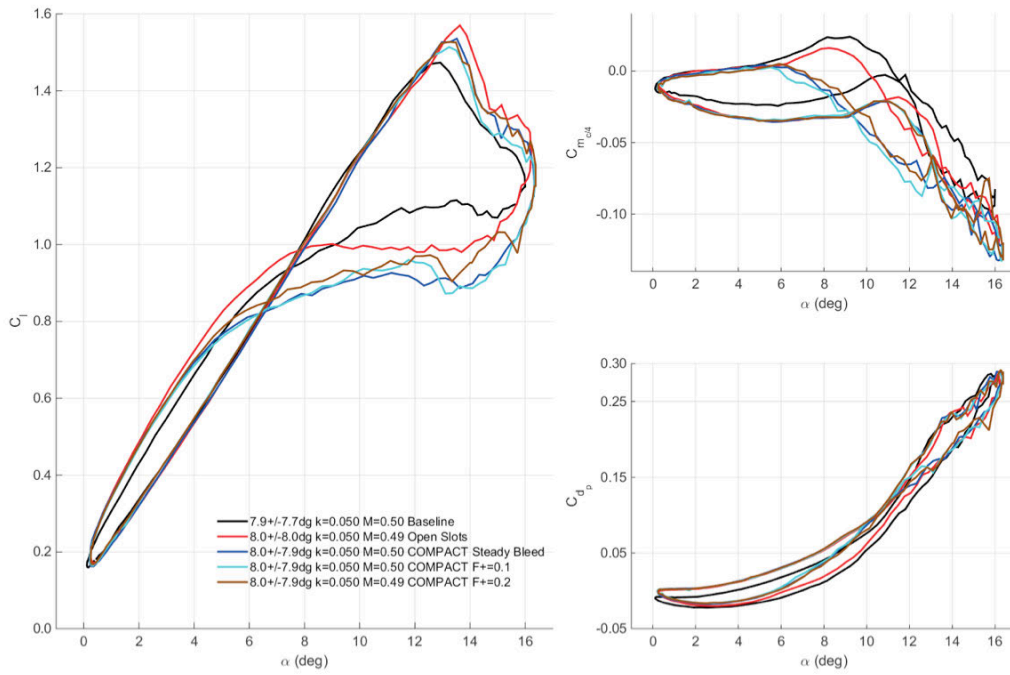
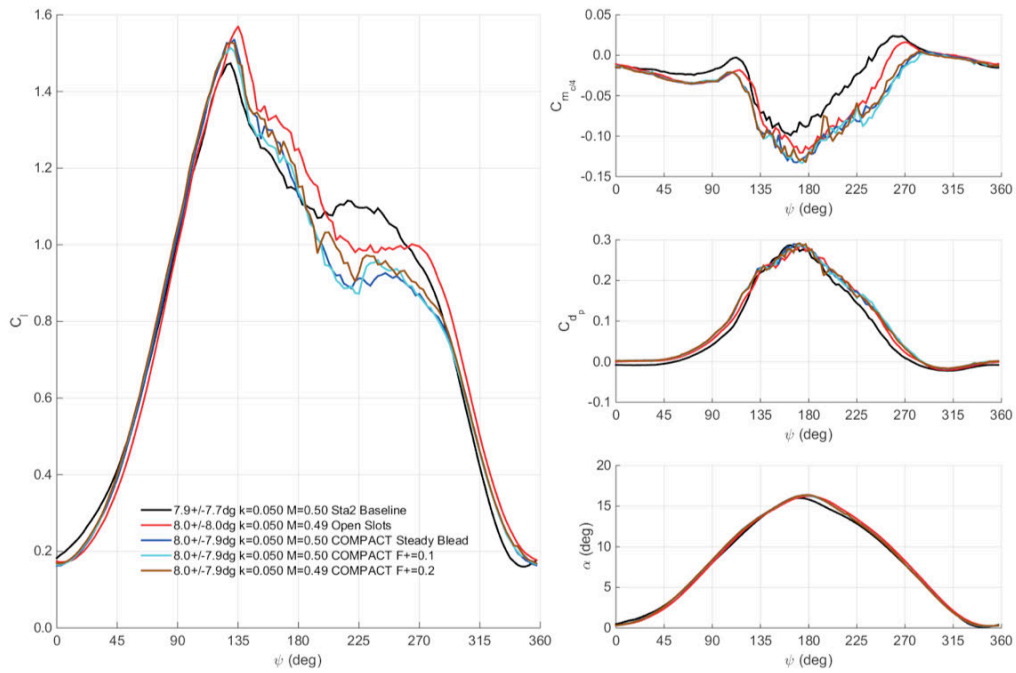


Figure 462. Effect of COMPACT on VR-12 unsteady airloads,  $M=0.5$ ,  $\alpha=8^\circ \pm 8^\circ$ ,  $k=0.05$ . Baseline, open slot, steady bleed, COMPACT  $F^+ = 0.1$  and  $0.2$  shown in order from left to right.





**Figure 463. Effect of COMPACT on VR-12 unsteady airloads,  $M=0.5$ ,  $\alpha=8^\circ \pm 8^\circ$ ,  $k=0.05$ .**



**Figure 464. Effect of COMPACT on VR-12 unsteady airloads,  $M=0.5$ ,  $\alpha=8^\circ \pm 8^\circ$ ,  $k=0.05$ .**

### Phase-Sweep and Summary of Results

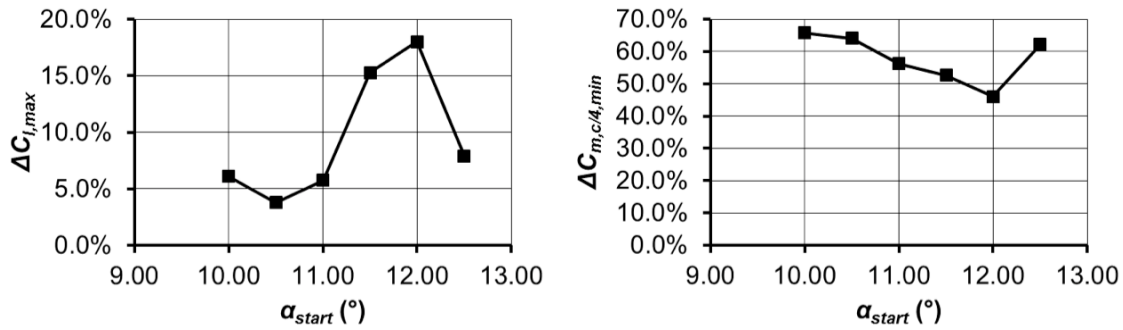


Figure 465. Dependency of peak quantities on start angle of pulsing for Mach 0.3,  $k=0.05$ ,  $\alpha=10^\circ \pm 8^\circ$ , 12 pulses.

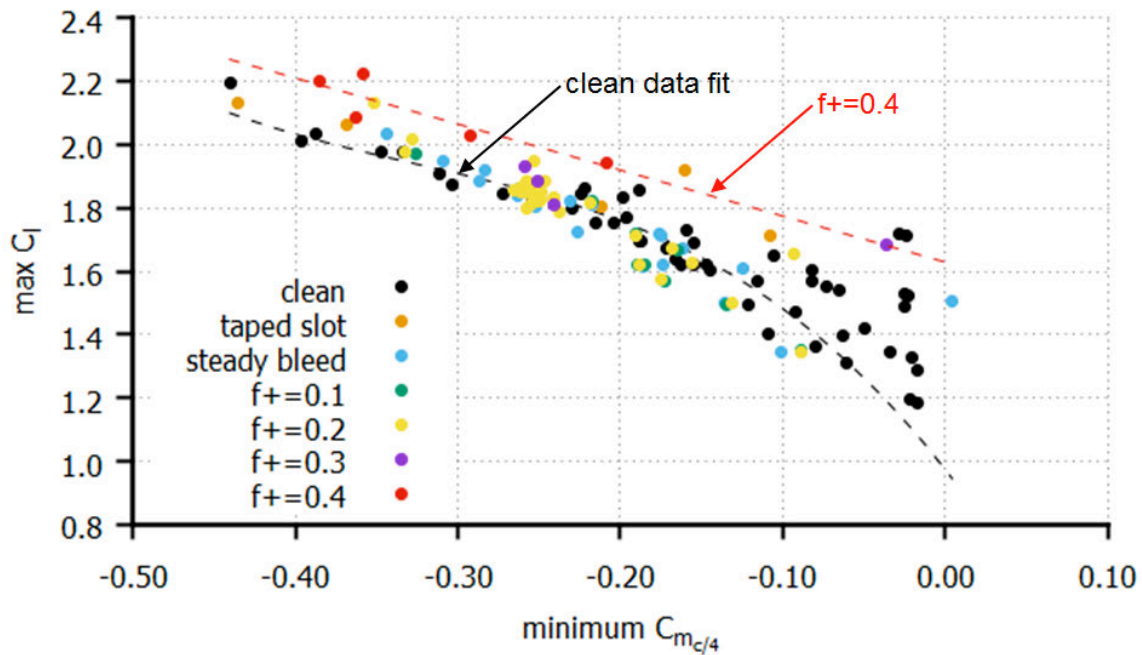


Figure 466. Max lift coefficient and minimum pitching moment for all unsteady data points  $M>0.1$ .

**Table 50. Summary of key metrics for Mach 0.2 cases.**

$M$	$k$	$\alpha_0(^{\circ})$	$\alpha_1(^{\circ})$	Geom	$F^+$	Bleed	$N_{pulses}$	$\alpha_{start}$	$C_{l,avg}$	$C_{l,max}$	$C_{d,p,avg}$	$C_{d,p,max}$	$C_{m,c/4}$	$C_{m,\xi_{min}}$
0.20	0.070	9.85	10.01	Clean	0.00	0	0.00	0.00	0.94	1.90	0.12	0.57	-0.04	-0.26
0.19	0.071	10.00	10.00	Taped	0.00	0	0.00	0.00	-1.2%	0.3%	12.7%	5.5%	31.7%	12.8%
0.20	0.070	10.00	10.01	Slot	0.00	0	0.00	0.00	-2.1%	-0.2%	3.9%	3.9%	12.2%	17.2%
0.20	0.071	9.99	10.01	Slot	0.00	1	0.00	0.00	-5.0%	-0.5%	10.8%	2.4%	62.7%	17.4%
0.20	0.071	9.99	10.01	Slot	0.20	0	9.00	10.00	5.4%	5.7%	5.0%	5.5%	20.4%	41.6%
0.20	0.071	10.00	10.01	Slot	0.40	0	18.00	10.00	15.2%	10.8%	7.3%	3.6%	29.2%	29.1%
0.20	0.098	10.03	9.87	Clean	0.00	0	0.00	0.00	0.95	1.91	0.13	0.52	-0.04	-0.23
0.20	0.102	10.02	9.78	Taped	0.00	0	0.00	0.00	0.8%	-1.1%	7.7%	0.5%	20.7%	0.3%
0.20	0.100	9.93	9.81	Slot	0.00	0	0.00	0.00	-0.2%	-1.2%	-2.1%	-0.2%	1.2%	2.2%
0.20	0.101	9.91	9.82	Slot	0.00	1	0.00	0.00	-4.3%	-2.6%	5.4%	6.2%	62.2%	13.6%
0.20	0.101	9.91	9.83	Slot	0.20	0	6.00	10.00	2.5%	1.9%	0.7%	4.1%	29.9%	12.1%
0.20	0.101	9.93	9.83	Slot	0.40	0	12.00	10.00	8.7%	1.8%	-3.6%	-13.3%	-11.2%	-16.1%
0.20	0.070	15.03	9.96	Clean	0.00	0	0.00	0.00	1.17	2.09	0.24	0.93	-0.07	-0.39
0.20	0.068	15.08	9.78	Taped	0.00	0	0.00	0.00	-2.0%	-0.7%	2.3%	-14.3%	42.5%	-6.0%
0.20	0.068	14.96	9.76	Slot	0.00	0	0.00	15.00	-2.0%	-1.0%	-7.1%	-18.3%	15.5%	-14.0%
0.20	0.068	14.92	9.71	Slot	0.00	1	0.00	15.00	-4.4%	-3.2%	-4.1%	-23.7%	45.2%	-31.0%
0.20	0.068	14.93	9.73	Slot	0.20	0	6.00	15.00	3.1%	-4.3%	-6.6%	-47.0%	16.2%	-40.9%
0.20	0.068	14.96	9.76	Slot	0.40	0	12.00	15.00	10.5%	6.4%	-1.9%	-25.7%	7.4%	-4.8%
0.20	0.100	14.92	9.86	Clean	0.00	0	0.00	0.00	1.18	2.17	0.26	0.87	-0.07	-0.36
0.20	0.098	14.95	9.76	Taped	0.00	0	0.00	0.00	0.0%	1.6%	8.6%	-2.1%	27.4%	1.1%
0.20	0.099	14.97	9.80	Slot	0.00	0	0.00	15.00	-0.5%	0.4%	1.3%	-4.2%	7.2%	-7.2%
0.20	0.099	15.02	9.84	Slot	0.00	1	0.00	15.00	-3.7%	-4.6%	4.7%	-20.4%	42.8%	-3.3%
0.20	0.099	15.03	9.85	Slot	0.20	0	6.00	15.00	1.1%	-2.1%	4.1%	-16.4%	28.5%	-6.7%
0.20	0.099	15.00	9.82	Slot	0.40	0	12.00	15.00	7.9%	3.2%	3.5%	-7.4%	-6.0%	-2.0%

**Table 51. Summary of key metrics for Mach 0.3 cases.**

$M$	$k$	$\alpha_0(^{\circ})$	$\alpha_1(^{\circ})$	Geom	$F^+$	Bleed	$N_{pulses}$	$\alpha_{start}$	$C_{l,avg}$	$C_{l,max}$	$C_{d,p,avg}$	$C_{d,p,max}$	$C_{m,c/4}$	$C_{m,\xi_{min}}$
0.30	0.025	10.01	7.97	Clean	0.0	0	0	0	1.01	1.75	0.09	0.43	-0.02	-0.16
0.30	0.025	10.02	8.13	Slot	0.0	0	0	0	-3.7%	8.4%	15.8%	6.3%	132.7%	44.5%
0.30	0.025	9.95	8.06	Slot	0.0	1	0	0	-8.5%	6.2%	18.4%	-2.3%	156.2%	48.9%
0.30	0.025	9.96	8.08	Slot	0.2	0	25	10	4.7%	6.2%	25.0%	0.2%	142.9%	56.2%
0.30	0.025	9.98	8.09	Slot	0.3	0	40	10	6.0%	9.7%	20.2%	1.5%	113.2%	54.6%
0.30	0.050	10.02	7.99	Clean	0.0	0	0	0	1.01	1.82	0.10	0.44	-0.02	-0.17
0.30	0.050	10.00	8.10	Slot	0.0	0	0	0	-2.8%	4.2%	14.6%	12.9%	129.6%	42.9%
0.30	0.050	10.01	8.14	Slot	0.0	1	0	0	-7.3%	6.7%	19.0%	10.7%	162.4%	52.3%
0.30	0.050	10.01	8.14	Slot	0.2	0	12	10	3.1%	10.8%	19.7%	7.7%	139.0%	52.0%
0.30	0.050	9.99	8.13	Slot	0.3	0	18	10	6.4%	8.6%	19.7%	12.4%	124.8%	60.4%
0.30	0.070	10.08	8.08	Clean	0.0	0	0	0	1.02	1.84	0.10	0.47	-0.02	-0.19
0.30	0.070	10.03	8.01	Slot	0.0	0	0	0	-1.2%	3.1%	13.0%	9.0%	117.3%	30.2%
0.30	0.070	10.02	8.01	Slot	0.0	1	0	0	-5.7%	7.8%	20.7%	11.5%	160.3%	39.1%
0.30	0.070	10.01	8.02	Slot	0.2	0	8	10	2.4%	4.3%	18.8%	2.6%	137.8%	34.6%
0.30	0.070	10.02	8.04	Slot	0.3	0	13	10	5.5%	14.7%	16.0%	9.3%	115.7%	32.7%

**Table 52. Summary of key metrics for Mach 0.4 cases.**

$M$	$k$	$\alpha_0(^{\circ})$	$\alpha_1(^{\circ})$	Geom	$F^+$	Bleed	$N_{pulses}$	$\alpha_{start}$	$C_{l,avg}$	$C_{l,max}$	$C_{d,p,avg}$	$C_{d,p,max}$	$C_{m,c/4}$	$C_{m,c,min}$
0.40	0.025	9.84	8.09	Clean	0.0	0	0	0	0.95	1.59	0.07	0.30	-0.03	-0.12
0.41	0.025	9.97	8.08	Slot	0.0	0	0	0	-2.1%	2.3%	32.9%	1.9%	60.5%	19.6%
0.41	0.025	9.97	8.08	Slot	0.0	1	0	0	-6.8%	1.6%	35.0%	4.6%	76.6%	40.4%
0.40	0.025	10.06	8.18	Slot	0.1	0	12	10	-0.5%	1.9%	43.9%	20.2%	102.1%	42.8%
0.40	0.025	10.00	8.12	Slot	0.2	0	25	10	2.0%	2.0%	46.0%	15.7%	102.3%	42.0%
0.40	0.050	9.99	8.00	Clean	0.0	0	0	0	0.93	1.66	0.08	0.34	-0.03	-0.14
0.41	0.050	10.12	8.04	Slot	0.0	0	0	0	-1.0%	4.2%	34.1%	-1.0%	61.8%	20.0%
0.41	0.049	10.13	8.03	Slot	0.0	1	0	0	-4.3%	3.3%	35.1%	-2.2%	68.8%	22.2%
0.41	0.050	10.14	8.03	Slot	0.1	0	6	10	0.0%	3.4%	41.7%	1.4%	91.8%	31.9%
0.40	0.050	10.17	8.07	Slot	0.2	0	13	10	3.6%	3.3%	42.7%	8.1%	87.4%	31.6%
0.40	0.070	10.03	7.97	Clean	0.0	0	0	0	0.94	1.81	0.07	0.45	-0.03	-0.19
0.41	0.069	10.10	7.84	Slot	0.0	0	0	0	0.6%	5.8%	41.3%	-4.8%	86.9%	10.2%
0.41	0.069	10.10	7.96	Slot	0.0	0	0	0	0.1%	6.3%	42.7%	-2.7%	90.4%	12.4%
0.41	0.068	10.06	7.91	Slot	0.0	1	0	0	-3.7%	6.2%	44.6%	-3.7%	102.3%	17.0%
0.41	0.069	10.08	7.94	Slot	0.1	0	4	10	0.8%	4.4%	43.5%	-4.2%	94.2%	18.2%
0.41	0.069	10.04	7.83	Slot	0.2	0	8	10	1.6%	4.0%	49.6%	-5.2%	121.5%	18.3%

**Table 53. Summary of key metrics for Mach 0.5 cases.**

$M$	$k$	$\alpha_0(^{\circ})$	$\alpha_1(^{\circ})$	Geom	$F^+$	Bleed	$N_{pulses}$	$\alpha_{start}$	$C_{l,avg}$	$C_{l,max}$	$C_{d,p,avg}$	$C_{d,p,max}$	$C_{m,c/4}$	$C_{m,c,min}$
0.50	0.050	8.06	7.94	Clean	0.0	0	0	0	0.83	1.47	0.08	0.29	-0.02	-0.10
0.49	0.050	8.24	7.98	Slot	0.0	0	0	10	1.5%	5.5%	10.7%	0.4%	59.6%	13.7%
0.50	0.050	8.27	8.06	Slot	0.0	1	0	10	-2.3%	3.6%	15.5%	0.7%	99.2%	21.3%
0.50	0.050	8.28	8.06	Slot	0.1	0	6	10	-2.2%	2.3%	15.5%	0.2%	103.1%	21.7%
0.49	0.050	8.32	8.06	Slot	0.2	0	12	10	-0.7%	3.1%	14.8%	1.2%	95.3%	21.3%

## 2. Test Entry II – Test Results

### A. Unsteady Actuated Results

#### COMPACT Single-Row

Table 54. Clean LE Unsteady Data Points Acquired

Run	Mach	k	$\alpha_0$	$\alpha_1$	F <sup>+</sup>	Pulse Start $\alpha$	N <sub>pulses</sub>	Points
50	0.2	0.07	10	8,10	Clean LE	Clean LE	-	7-8
		0.10	10	8,10	Clean LE	Clean LE	-	9-10
51	0.2	0.07	15	8,10	Clean LE	Clean LE	-	12-13
		0.10	15	8,10	Clean LE	Clean LE	-	14-15
52	0.3	0.025	10	8,10	Clean LE	Clean LE	-	5-6
		0.05	10	8,9.5	Clean LE	Clean LE	-	7-8
		.070	10	8,9.6	Clean LE	Clean LE	-	9-10
		.100	10	9.5	Clean LE	Clean LE	-	11-12
		0.025-0.07	15	8	Clean LE	Clean LE	-	14-16
53	0.4	0.025-0.07	10	8	Clean LE	Clean LE	-	7-9
		.050	10	8	Clean LE	Clean LE	-	10-24
54	0.4	.025-0.05	12	8	Clean LE	Clean LE	-	3-4

Table 55. COMPACT Single-Row Unsteady Data Points Acquired

Run	Mach	k	$\alpha_0$	$\alpha_1$	F <sup>+</sup>	Pulse Start $\alpha$	N <sub>pulses</sub>	Points
58	0.2	0.07	10	8	0.2-1.0	10	8,17,26,35,42	15-19
59	0.3	0.025	10	8	0.2-0.8	10	24,49,74,100	9-12
		0.025	10	10	0.2-0.8	10	25,49,74,100	15-17,20
		0.025	10	10	0.6	15	37	18
60	0.4	0.025	10	8	0.2-0.6	10	24,49,74	9-11
		0.025	10	8	0.6,0.4,0.2	10	24,49,74	15,14,13
62	0.3	0.05	10	8	0.2-0.8	10	12,24,36,49	13,14,17,18
	0.3	0.05	10	10	0.2-0.8	10	12,24,36,49	24-27
	0.3	0.07	10	8	0.2-0.8	10	8,17,26,35	31-33,35
	0.3	0.07	10	9.5	0.2-0.8	10	8,17,26,35	38-41
	0.3	0.1	10	8	0.2-0.8	10	6,12,18,25	45-48
	0.3	0.1	10	9.5	0.2-0.8	10	6,12,18,25	51-54
63	0.4	0.05	10	8	0.2-0.6	10	12,25,37	9,11,12
	0.4	0.05	10	9.5	0.2-0.6	10	12,25,37	15-17
	0.4	0.07	10	8	0.2-0.6	10	12,25,37	21,22,24
	0.4	0.07	10	9.5	0.2-0.6	10	12,25,37	27-29
	0.4	0.07	12	8	0.2-0.6	12	12,25,37	35-37
	0.4	0.07	12	9.5	0.2-0.6	12	12,25,37	40-42
	0.4	0.07	12	9.5	0.6	13-18	37	44-49
	0.4	0.07	12	9.5	0.6	18	2,4-20,25	50-56

Run	Mach	k	$\alpha_0$	$\alpha_1$	$F^+$	Pulse Start $\alpha$	$N_{\text{pulses}}$	Points
65	0.3	0.025	15	8	0.2-0.8	15	25,50,75,100	9-12
	0.3	0.05	15	8	0.2-0.8	15	12,25,37,50	16-19
66	0.3	0.07	15	8	0.2-0.8	15	8,17,26,35	4-7
	0.3	0.07	10	9.5	0.4	10	1,2-16	12-20
	0.3	0.07	10	9.5	0.6	10	2,4-24	21-27
	0.3	0.07	10	9.5	0.8	10	2,4-32	28-36
	0.3	0.07	10	9.5	0.4	15-19,19D-15D	4,8	40-59
	0.3	0.07	10	9.5	0.6	15-19,19D-15D	6,13	60-71
	0.3	0.07	10	9.5	0.8	15-19,19D-15D	8,17	72-78,80-84
67	0.2	0.07	10	10	0.2-1.0	10	8,17,26,35,44	8-12
	0.2	0.1	10	10	0.2-1.0	10	6,12,18,25,31	17-20,22
	0.2	0.07	15	8	0.2-1.0	15	8,17,26,35,44	27-31
	0.2	0.07	15	10	0.2-1.0	15	8,17,26,35,44	34-38
	0.2	0.1	15	8	0.2-1.0	15	6,12,18,25,31	42-46
	0.2	0.1	15	10	0.2-1.0	15	6,12,18,25,31	49-53
68	0.4	0.05	10	9.5	0.2-0.6	10	12,25,37	11-13 or 16-18
76	0.5	0.025	8	8	0.2,0.4	8	25,50	20,21
	0.5	0.025	8	5	0.2,0.4	8	25,50	24,25
	0.5	0.05	8	5	0.2,0.4	8	12,25	28,29
	0.5	0.05	8	8	0.2,0.4	8	12,25	32,33
77	0.4	0.05	10	9.5	0.2	10	12	5
	0.4	0.05	10	9.5	0.2	15-19,19D-15D	3,6	6-17
	0.4	0.05	10	9.5	0.4	10	25	18
	0.4	0.05	10	9.5	0.4	15-19,19D-15D	6,12	19-30
	0.4	0.05	10	9.5	0.6	10	37	31
	0.4	0.05	10	9.5	0.6	15-19,19D-15D	9,18	32-43
	0.4	0.05	10	9.5	0.4	16	2-12,16,20	44-51
	0.4	0.05	10	9.5	0.4	18	2-12,16,20	52-59
	0.4	0.05	10	9.5	-	15-18,18.5,19,19.4,19.5D,19D,18.5D,18D-14D,12D,10D,8D	1	60-77
78	0.3	0.07	10	9.5	0.4	17,18,18.6,19,19.5,19D,18.5D,18D-14D,12D,10D,8D	1	50-64
	0.3	0.07	10	9.5	0.4	10	17 odd only	74
	0.3	0.07	10	9.5	0.4	10	17 even only	75
	0.3	0.07	10	9.5	0.4	10	17 H2=70	76
	0.3	0.07	10	9.5	0.4	10	17 H2=80	77
	0.3	0.07	10	9.5	0.4	10	17 H2=90	78
79	0.4	0.05	10	9.5	0.4	10	25	4
	0.4	0.05	10	9.5	0.4	15-19,19D-15D	6,12	5-16

**Table 56. COMPACT Single-Row PIV Unsteady Data Points**

Run	Mach	k	$\alpha_0$	$\alpha_1$	$F^+$	Pulse Start $\alpha$	PIV trigger	Points
73	0.4	0.05	10	8	0.4	10	$\alpha=10-16,17,17D,15D,14D,13D,12D,11D,10D-4D,3D,3,4,6,8$	115-118, 120-135
74	0.4	0.07	10	9.5	0.4	10	$\Phi=40-224$	71-94
75	0.3	0.07	10	9.5	0.4	10	$\Phi=40-224$	4,6-9,11-15,18-26, 28,29,31-33
	0.4	0.05	10	8	?	10	$\Phi=40-224$	34-57
	0.4	0.05	10	8	0.4	10	$\Phi=40-224$	58,60-79,81,83,85
	0.2	0.07	10	10	0.2	10	$\Phi=40-224$	86-105,108,107,109,110
	0.2	0.07	10	10	0.4	10	$\Phi=40-224$	111-134
	0.5	0.025	8	8	?	8	$\Phi=40-224$	136-148, 150-161
	0.5	0.025	8	8	0.2	8	$\Phi=40-224$	163-166,168-171,173,174,176-186,188-190



$M=0.2$

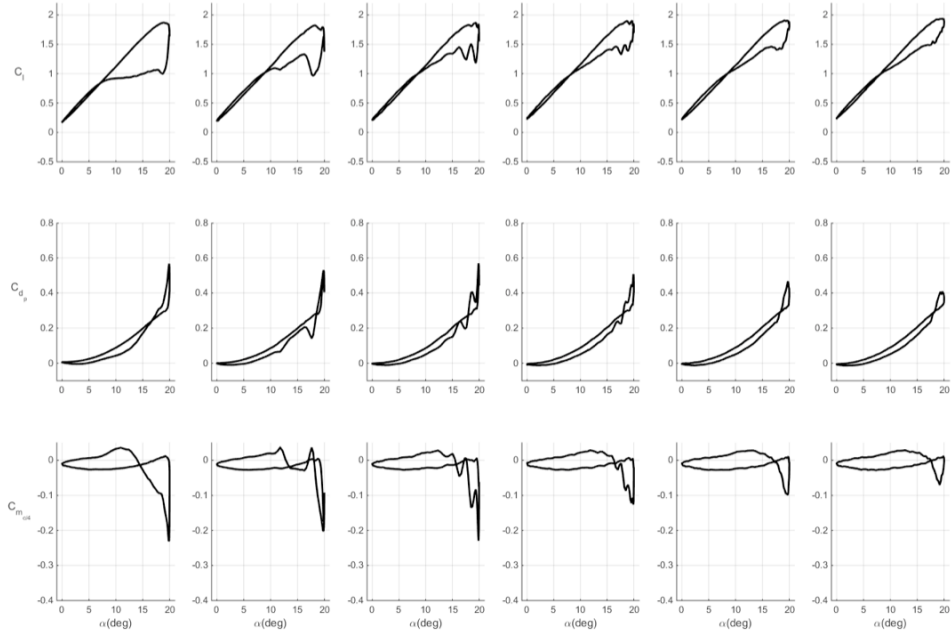


**Figure 467. Unsteady aerodynamic loads with respect to angle-of-attack.  $M=0.2$ ,  $\alpha=10^\circ\pm 10^\circ$ ,  $k=0.07$ . Baseline and single-row COMPACT  $F^+=0.2-1.0$  shown in order from left to right.**

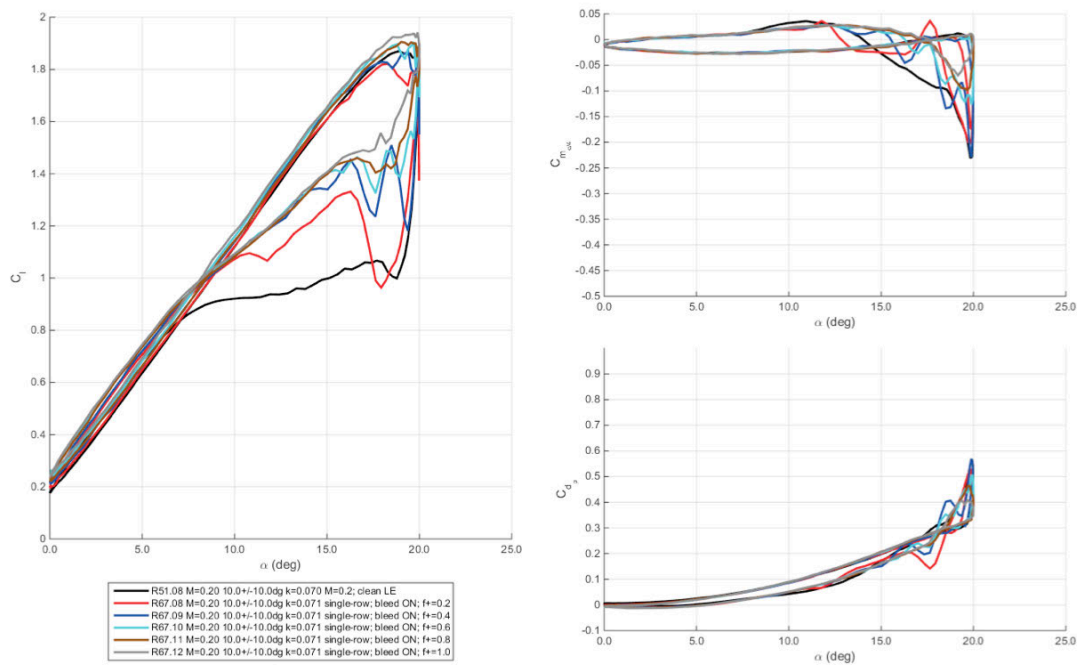


**Figure 468. Unsteady aerodynamic loads with respect to angle-of-attack. Baseline and single-row COMPACT  $F^+=0.2-1.0$ .**

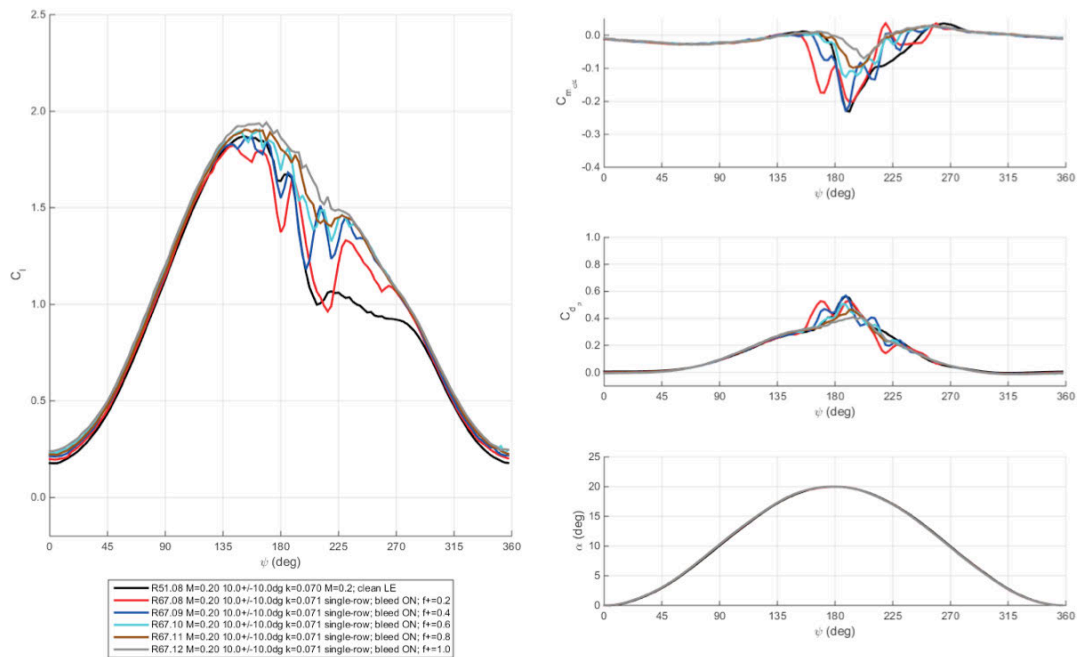


**Figure 469. Unsteady aerodynamic loads and angle-of-attack with respect to phase. Baseline and single-row COMPACT  $F^+=0.2-1.0$ .**

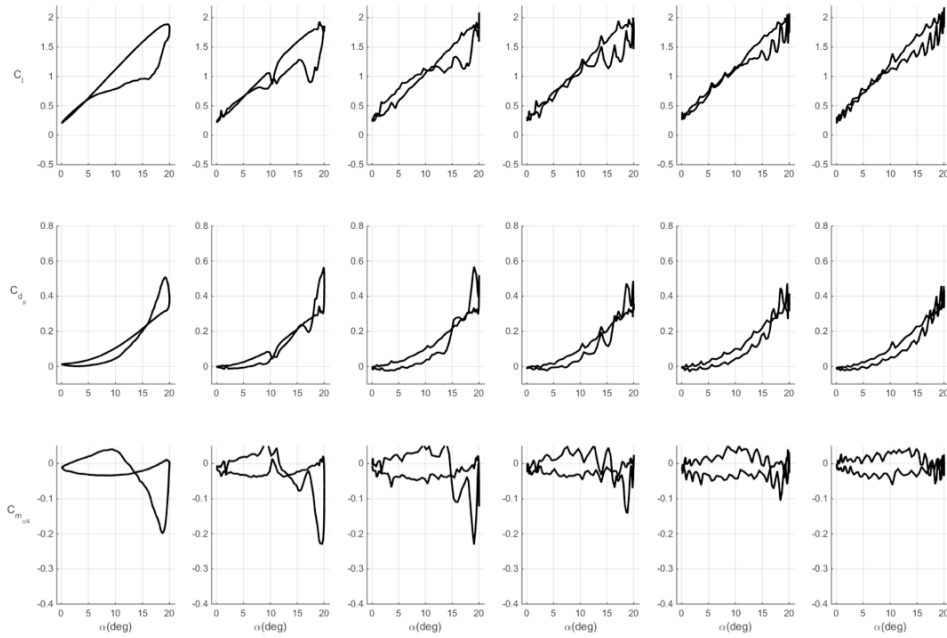


**Figure 470. Unsteady aerodynamic loads with respect to angle-of-attack.  $M=0.2$ ,  $\alpha=10^\circ \pm 10^\circ$ ,  $k=0.1$ . Baseline and single-row COMPACT  $F^+=0.2-1.0$  shown in order from left to right.**

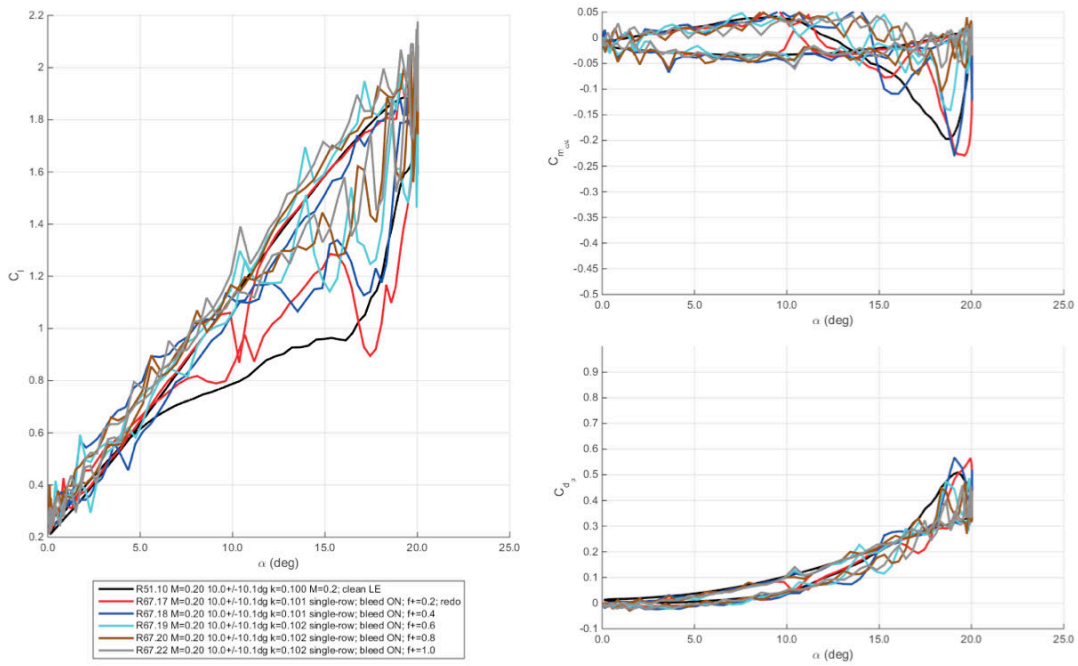


**Figure 471. Unsteady aerodynamic loads with respect to angle-of-attack. Baseline and single-row COMPACT  $F^+=0.2-1.0$ .**

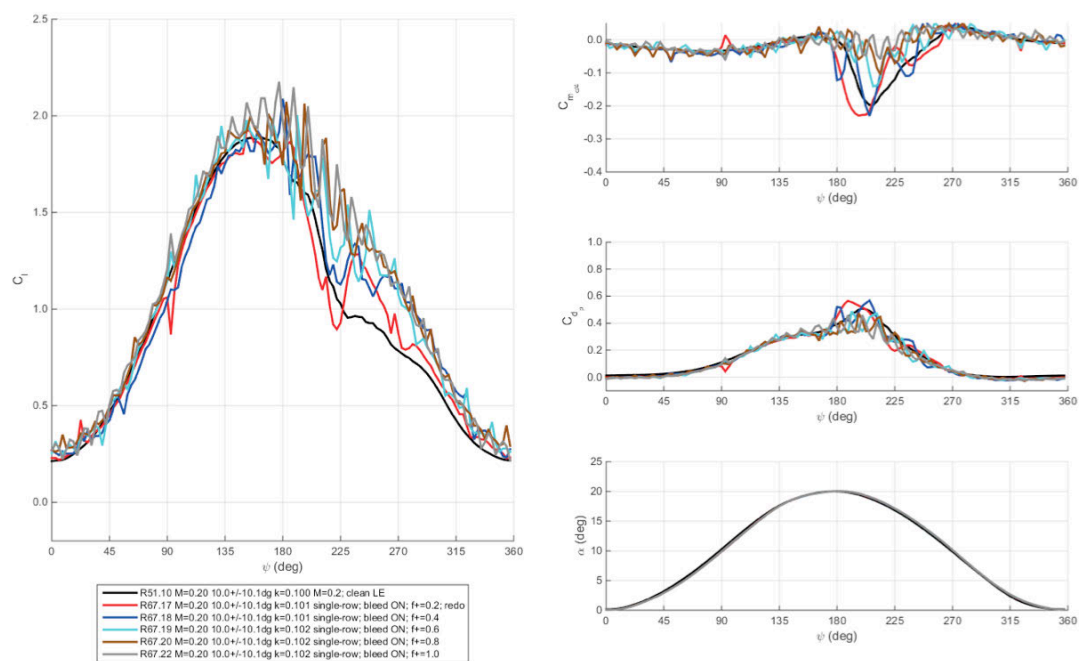


**Figure 472. Unsteady aerodynamic loads and angle-of-attack with respect to phase. Baseline and single-row COMPACT  $F^+ = 0.2-1.0$ .**

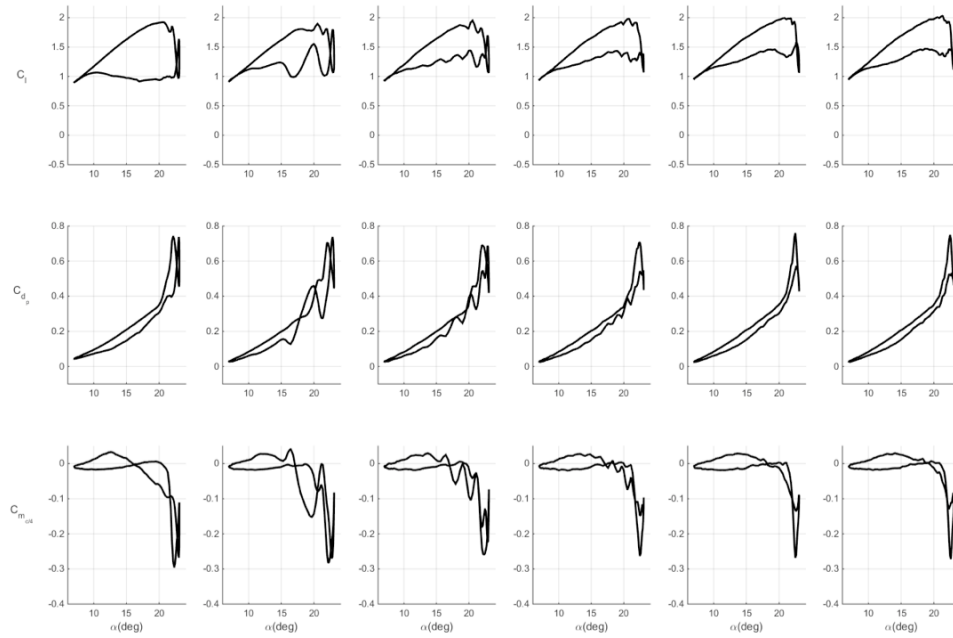


**Figure 473. Unsteady aerodynamic loads with respect to angle-of-attack.  $M=0.2$ ,  $\alpha=15^\circ \pm 8^\circ$ ,  $k=0.07$ . Baseline and single-row COMPACT  $F^+=0.2-1.0$  shown in order from left to right.**

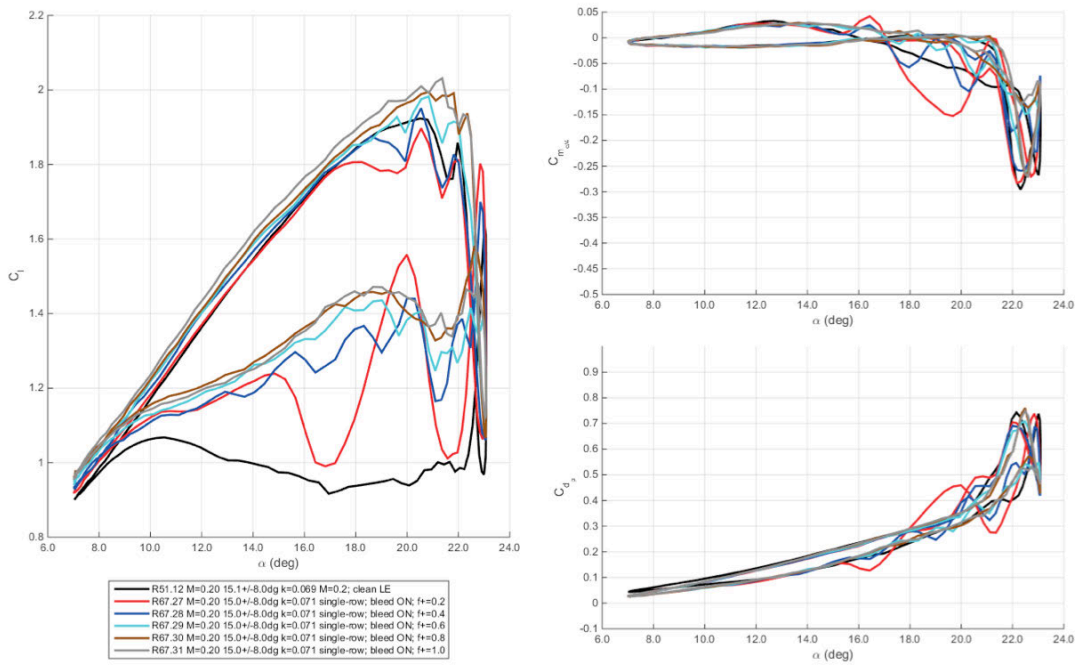


**Figure 474. Unsteady aerodynamic loads with respect to angle-of-attack. Baseline and single-row COMPACT  $F^+=0.2-1.0$ .**

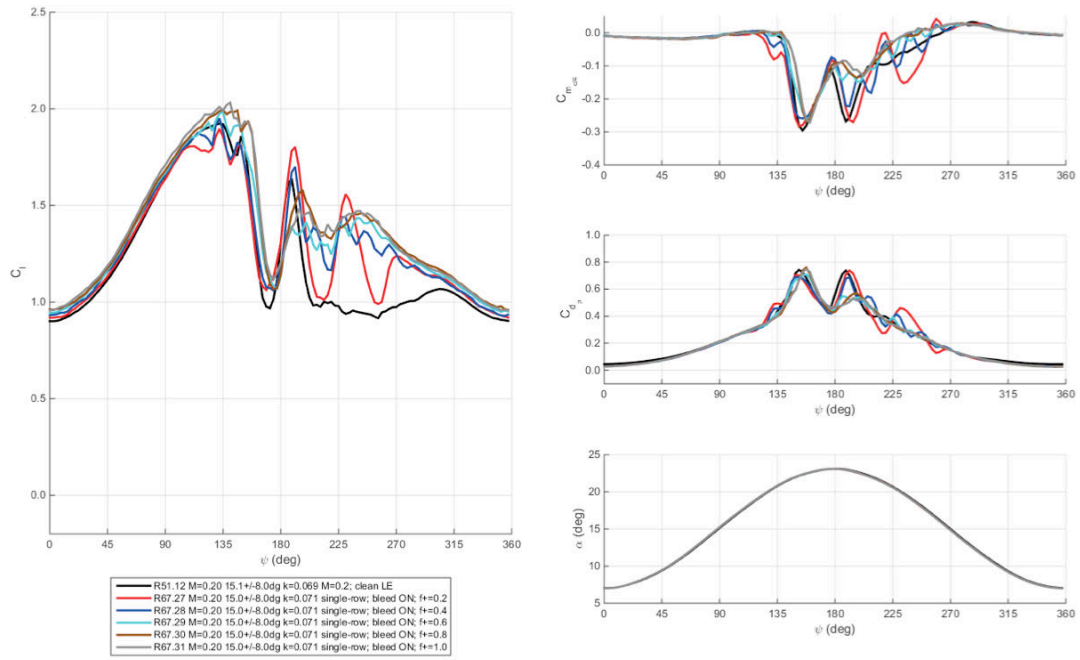


**Figure 475. Unsteady aerodynamic loads and angle-of-attack with respect to phase. Baseline and single-row COMPACT  $F^+ = 0.2-1.0$ .**

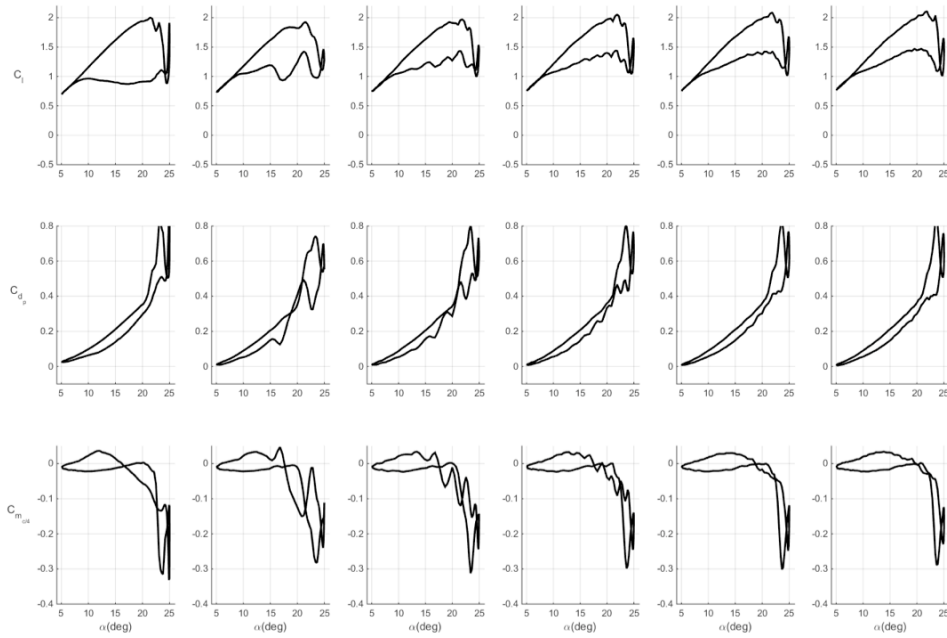


**Figure 476. Unsteady aerodynamic loads with respect to angle-of-attack.  $M=0.2$ ,  $\alpha=15^\circ \pm 10^\circ$ ,  $k=0.07$ . Baseline and single-row COMPACT  $F^+=0.2-1.0$  shown in order from left to right.**

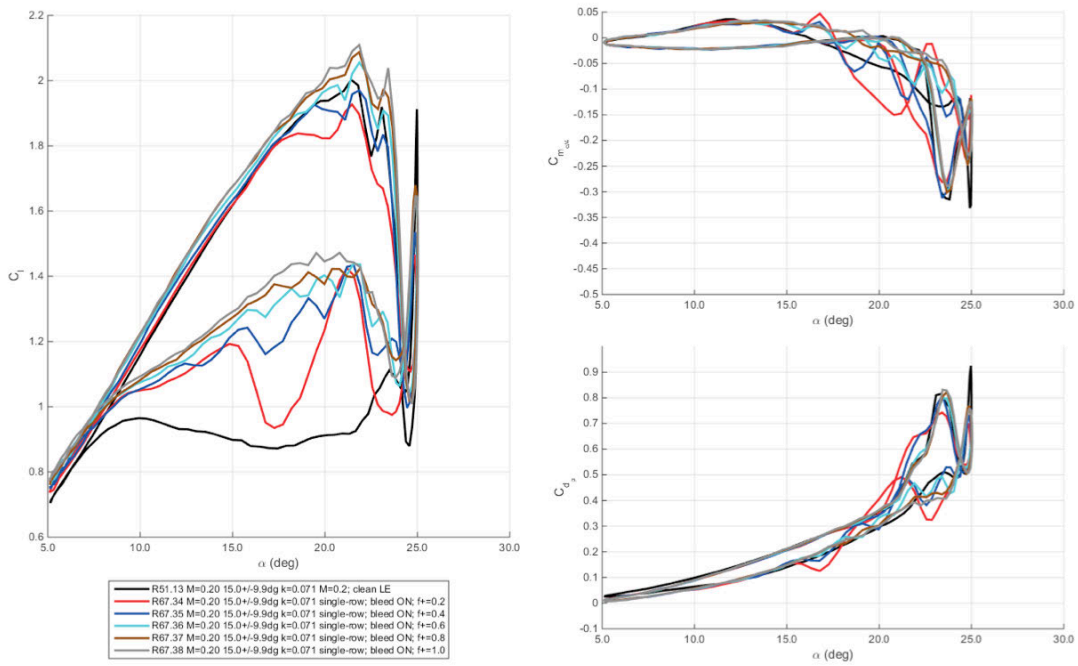


**Figure 477. Unsteady aerodynamic loads with respect to angle-of-attack. Baseline and single-row COMPACT  $F^+=0.2-1.0$ .**



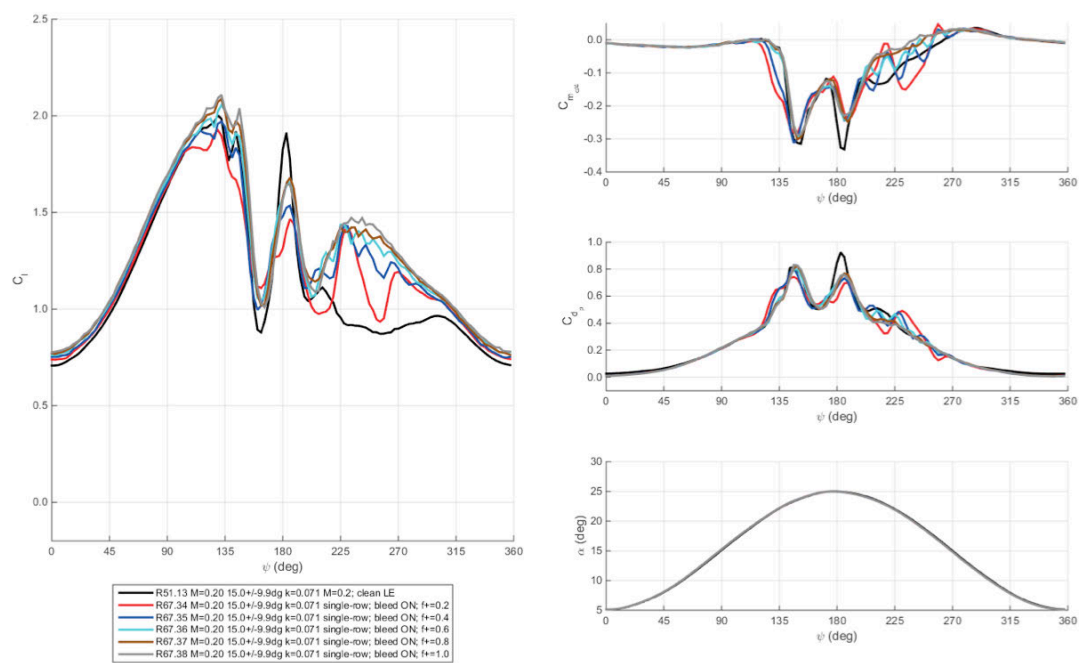


**Figure 478. Unsteady aerodynamic loads and angle-of-attack with respect to phase. Baseline and single-row COMPACT  $F^+ = 0.2-1.0$ .**

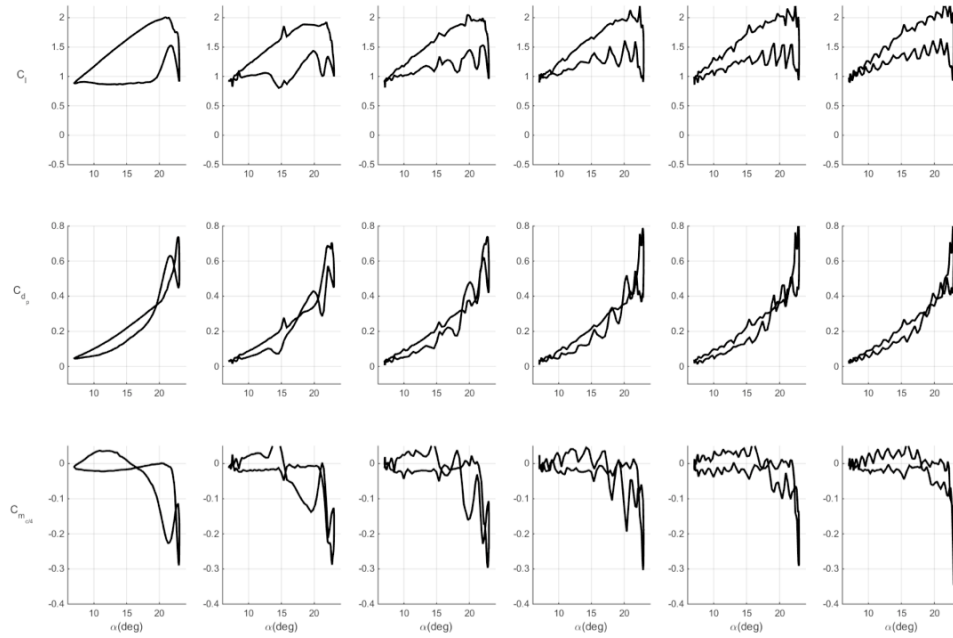


**Figure 479. Unsteady aerodynamic loads with respect to angle-of-attack.  $M=0.2$ ,  $\alpha=15^\circ \pm 8^\circ$ ,  $k=0.1$ . Baseline and single-row COMPACT  $F^+=0.2-1.0$  shown in order from left to right.**

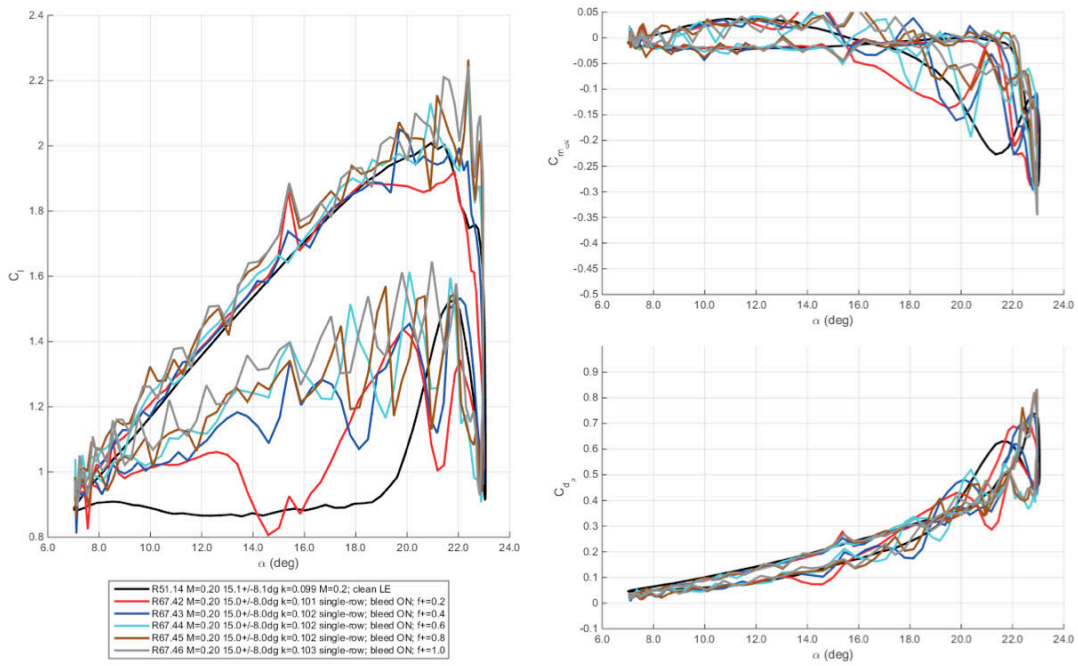


**Figure 480. Unsteady aerodynamic loads with respect to angle-of-attack. Baseline and single-row COMPACT  $F^+=0.2-1.0$ .**

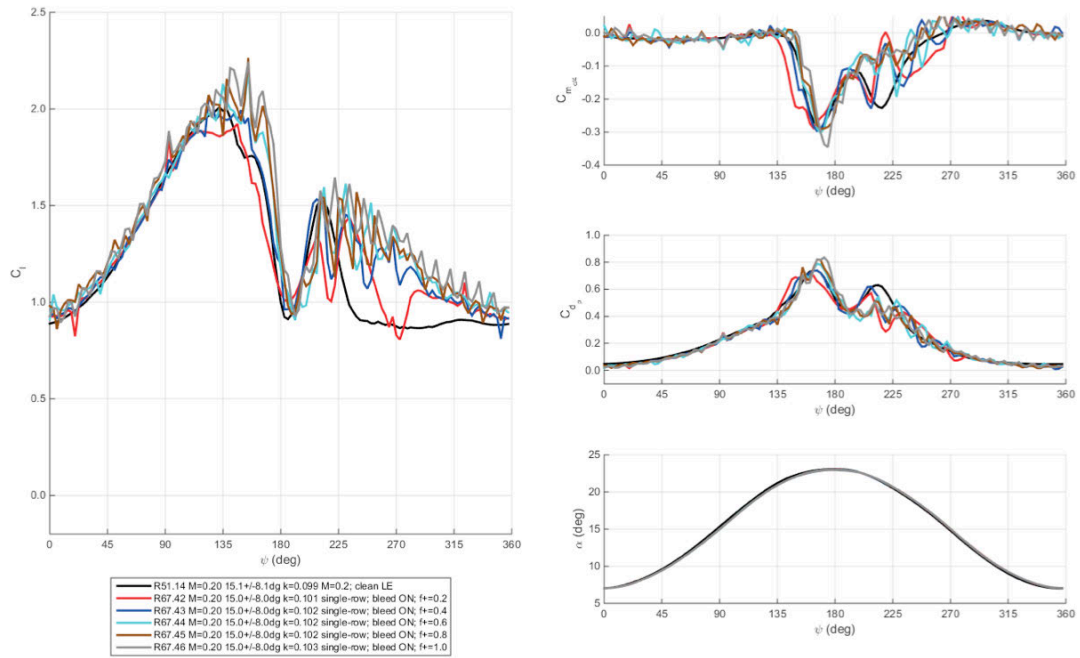


**Figure 481. Unsteady aerodynamic loads and angle-of-attack with respect to phase. Baseline and single-row COMPACT  $F^+ = 0.2-1.0$ .**

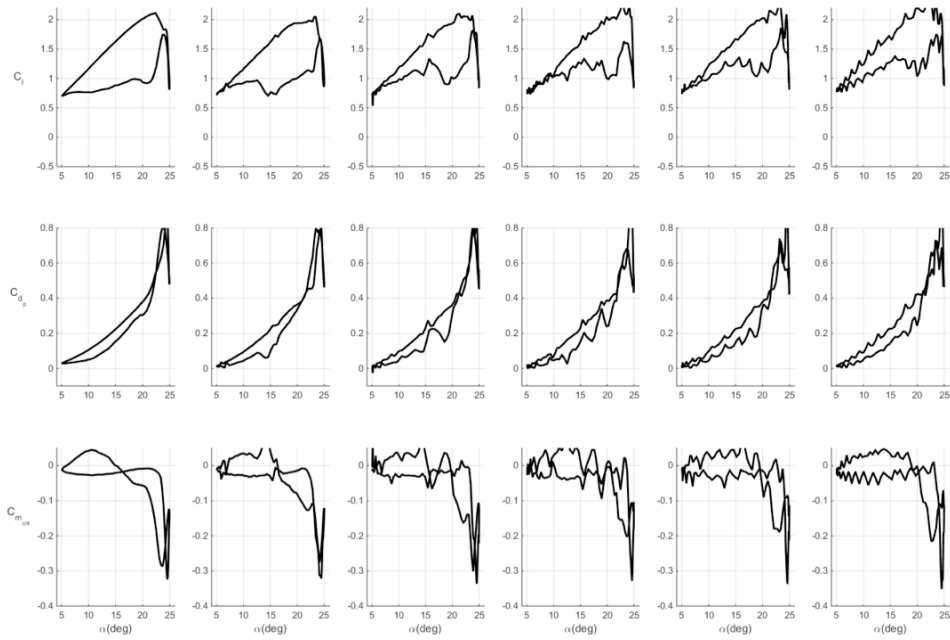


**Figure 482. Unsteady aerodynamic loads with respect to angle-of-attack.  $M=0.2$ ,  $\alpha=15^\circ \pm 10^\circ$ ,  $k=0.1$ . Baseline and single-row COMPACT  $F^+=0.2-1.0$  shown in order from left to right.**

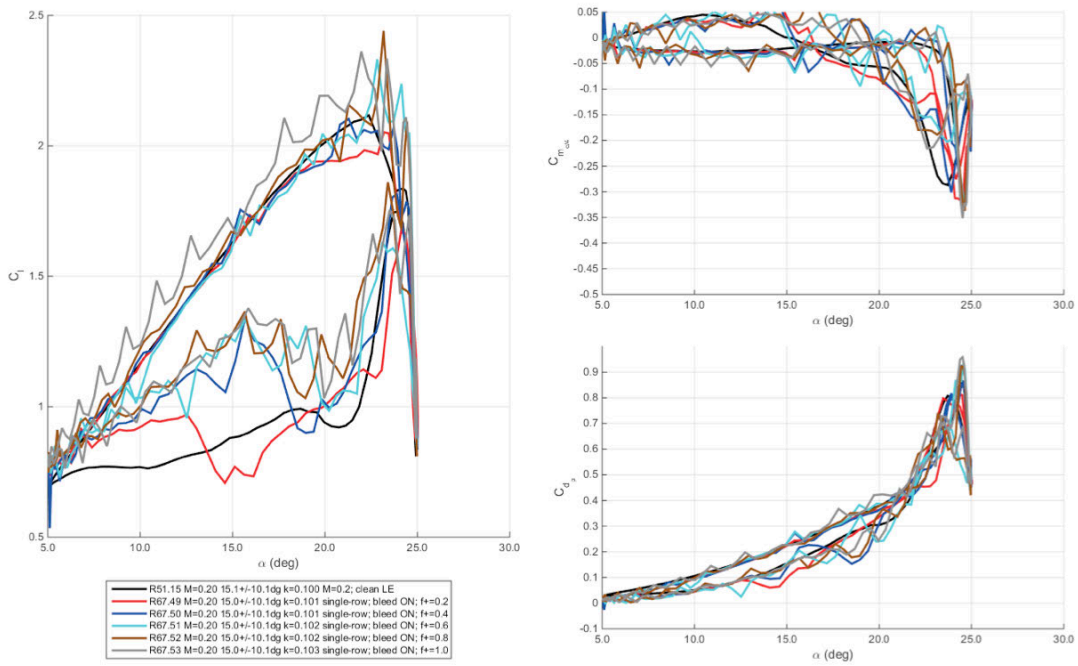


**Figure 483. Unsteady aerodynamic loads with respect to angle-of-attack. Baseline and single-row COMPACT  $F^+=0.2-1.0$ .**

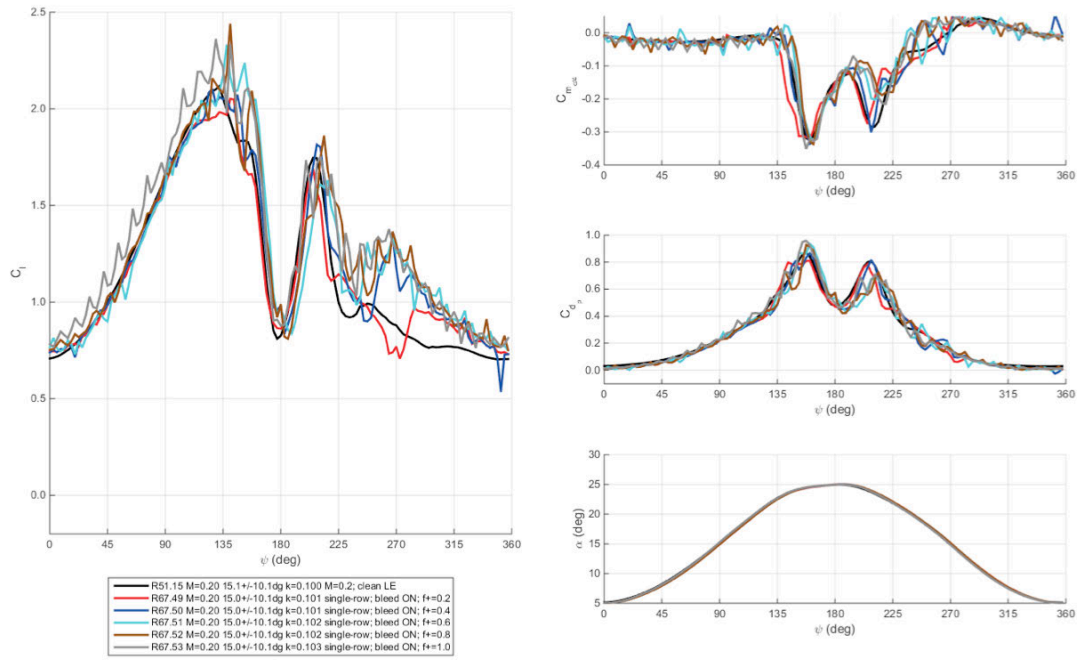


**Figure 484. Unsteady aerodynamic loads and angle-of-attack with respect to phase. Baseline and single-row COMPACT  $F^+ = 0.2-1.0$ .**

$M=0.3$

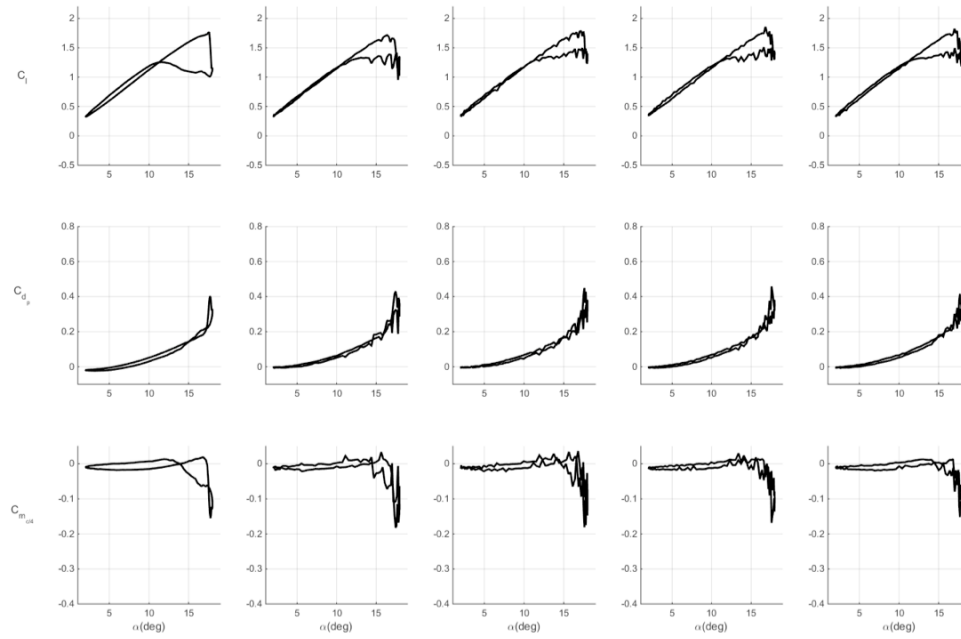


**Figure 485. Unsteady aerodynamic loads with respect to angle-of-attack.  $M=0.3$ ,  $\alpha=10^\circ \pm 8^\circ$ ,  $k=0.025$ . Baseline and single-row COMPACT  $F^+ = 0.2-0.8$  shown in order from left to right.**

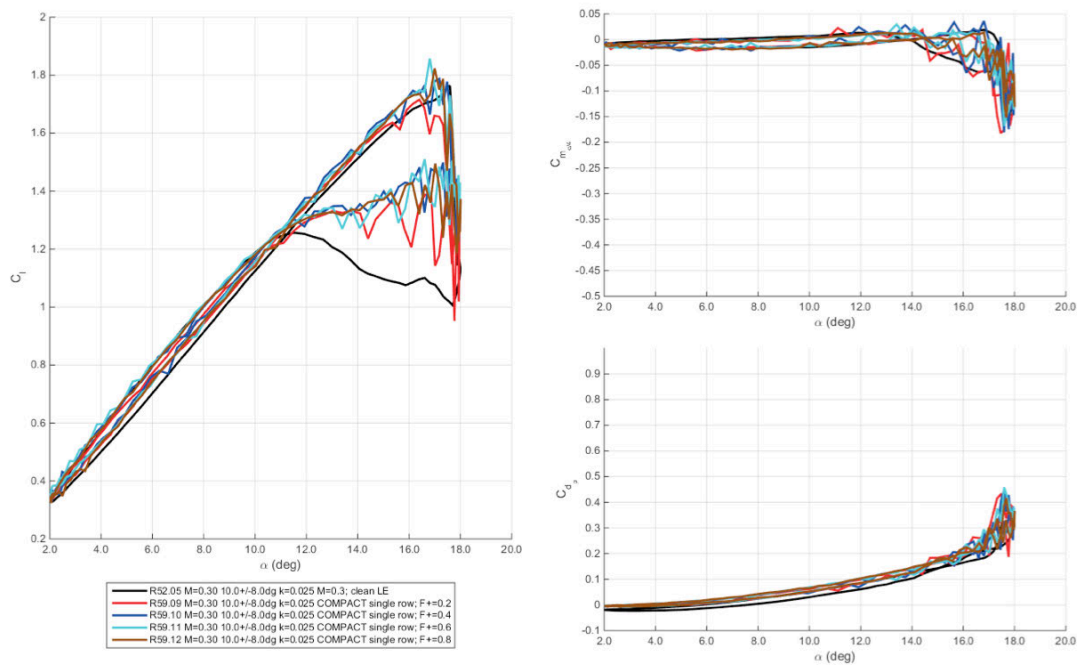


**Figure 486. Unsteady aerodynamic loads with respect to angle-of-attack. Baseline and single-row COMPACT  $F^+ = 0.2-0.8$ .**

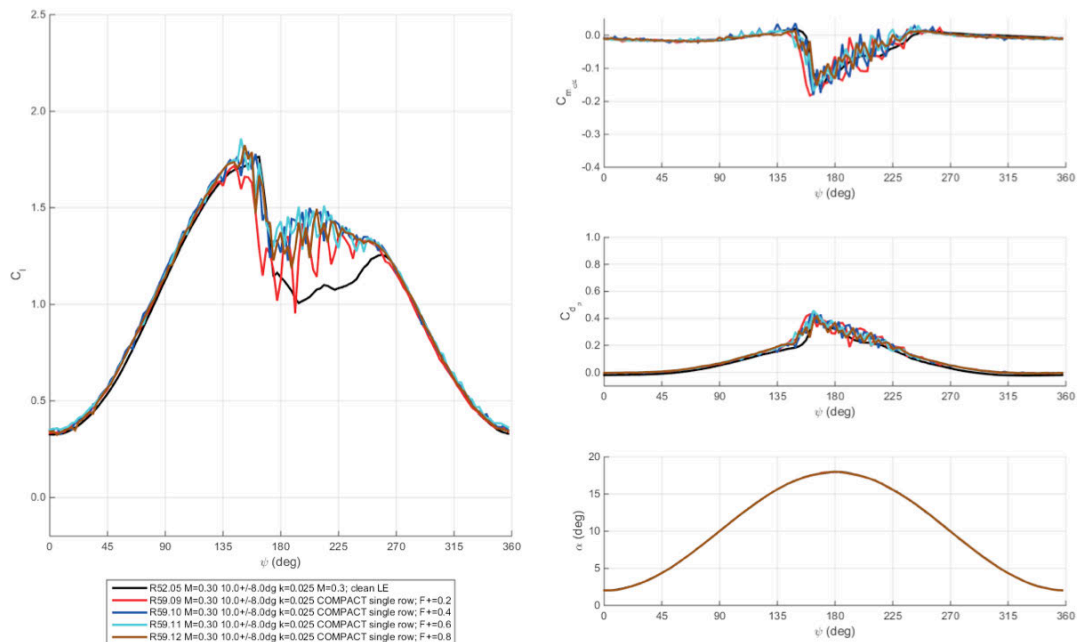


**Figure 487. Unsteady aerodynamic loads and angle-of-attack with respect to phase. Baseline and single-row COMPACT  $F^+ = 0.2-0.8$ .**



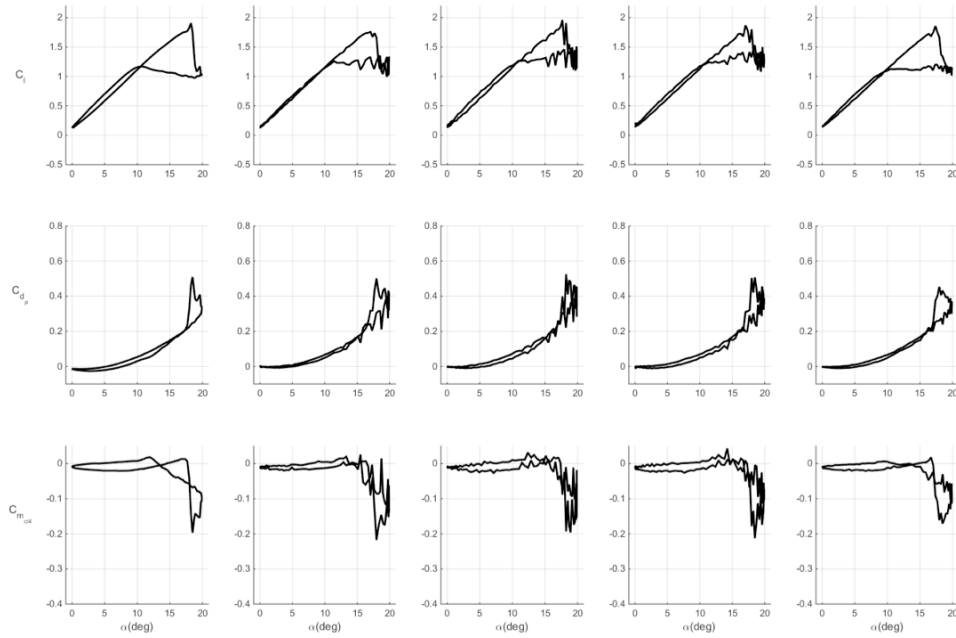


**Figure 488. Unsteady aerodynamic loads with respect to angle-of-attack.  $M=0.3$ ,  $\alpha=10^\circ \pm 10^\circ$ ,  $k=0.025$ . Baseline and single-row COMPACT  $F^+=0.2-0.8$  shown in order from left to right.**

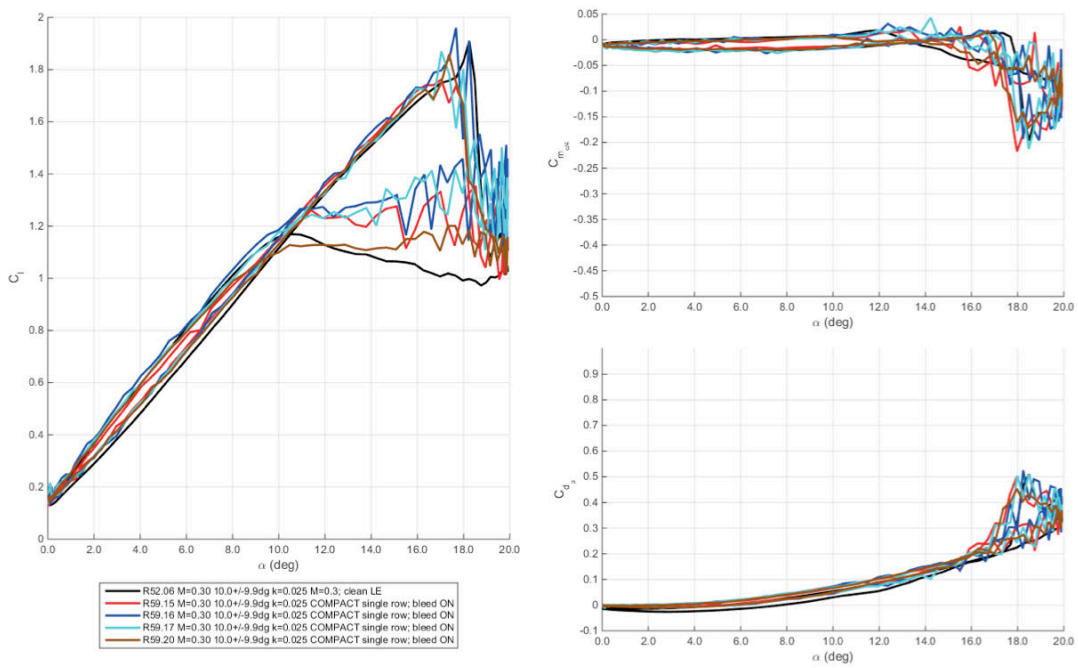


**Figure 489. Unsteady aerodynamic loads with respect to angle-of-attack. Baseline and single-row COMPACT  $F^+=0.2-0.8$ .**

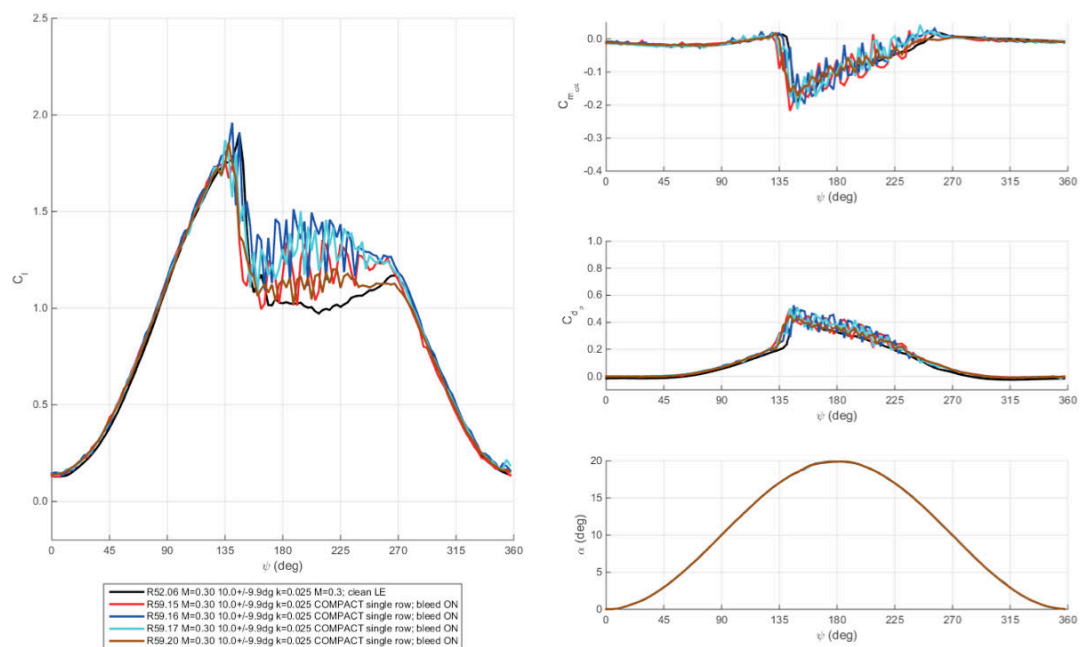


**Figure 490. Unsteady aerodynamic loads and angle-of-attack with respect to phase. Baseline and single-row COMPACT  $F^+ = 0.2-0.8$ .**

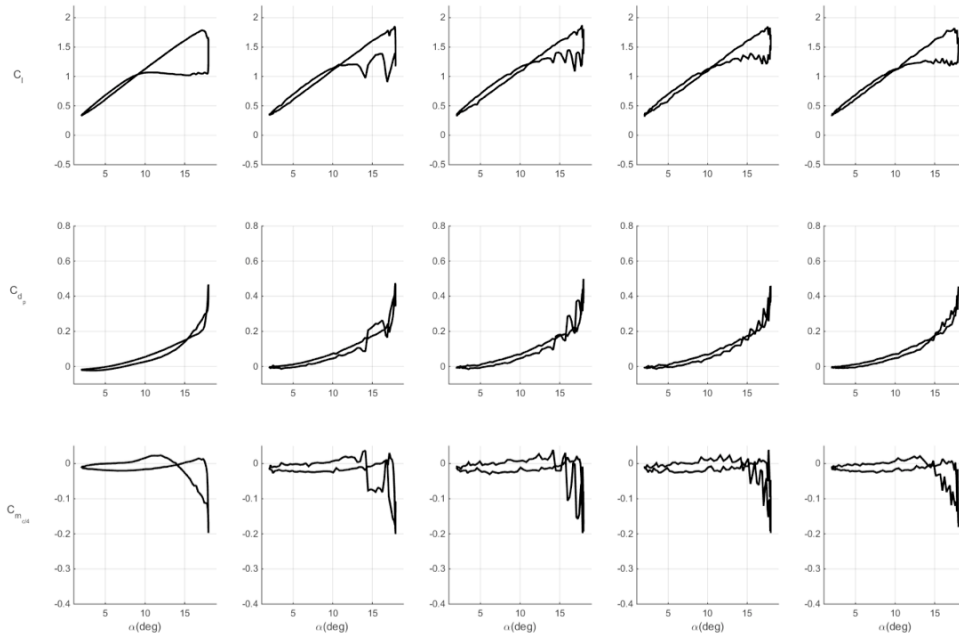


**Figure 491. Unsteady aerodynamic loads with respect to angle-of-attack.  $M=0.3$ ,  $\alpha=10^\circ \pm 8^\circ$ ,  $k=0.05$ . Baseline and single-row COMPACT  $F^+=0.2-0.8$  shown in order from left to right.**

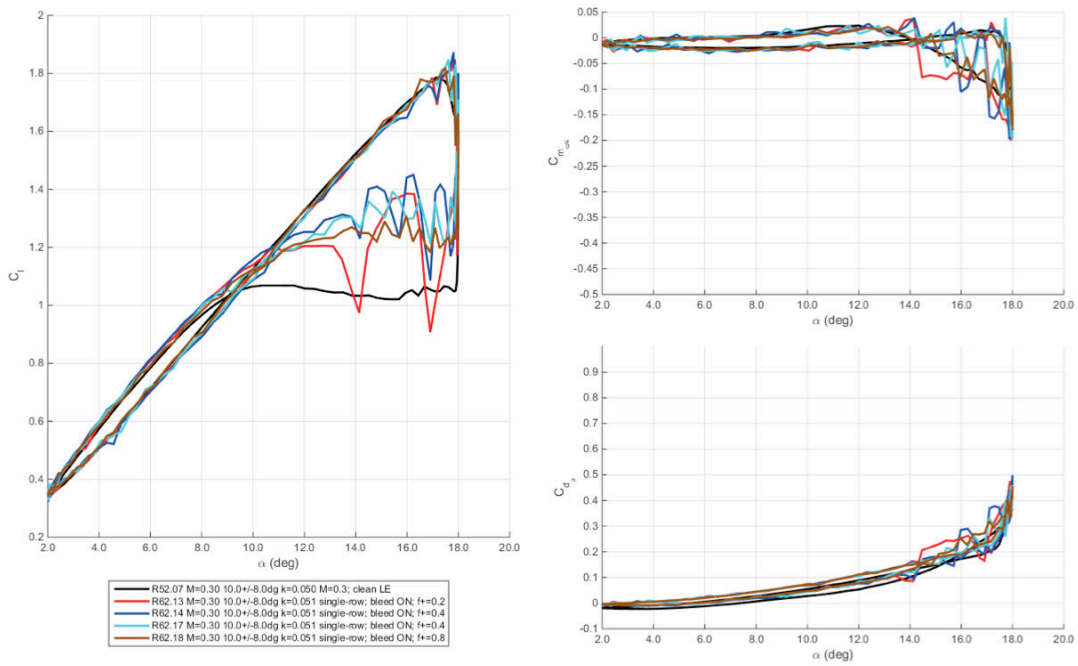


**Figure 492. Unsteady aerodynamic loads with respect to angle-of-attack. Baseline and single-row COMPACT  $F^+=0.2-0.8$ .**

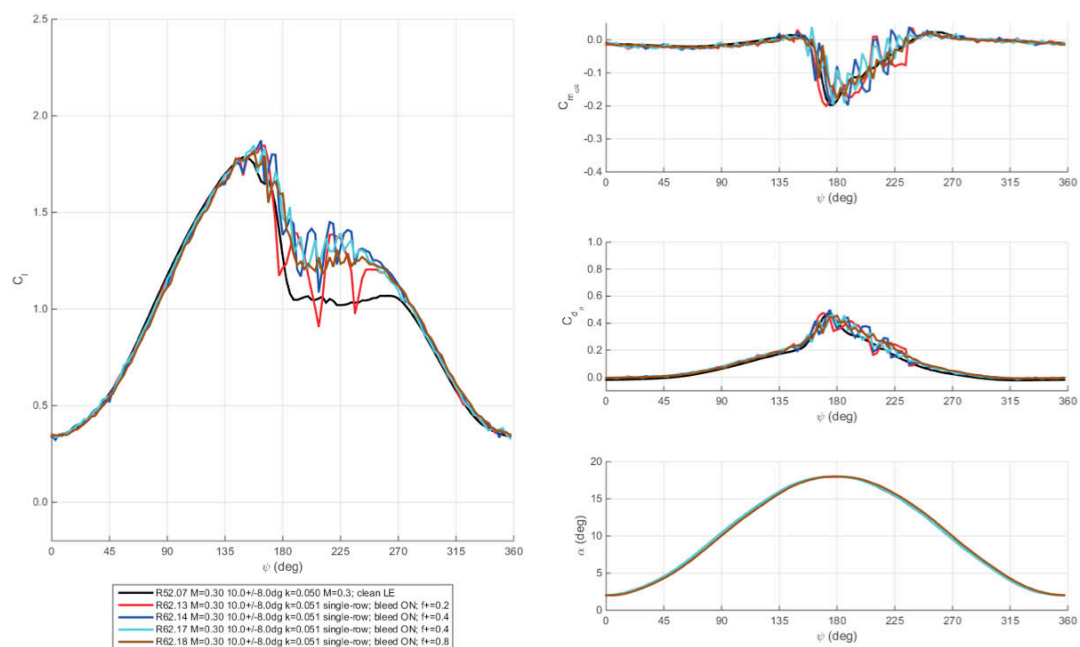


**Figure 493. Unsteady aerodynamic loads and angle-of-attack with respect to phase. Baseline and single-row COMPACT  $F^+ = 0.2-0.8$ .**

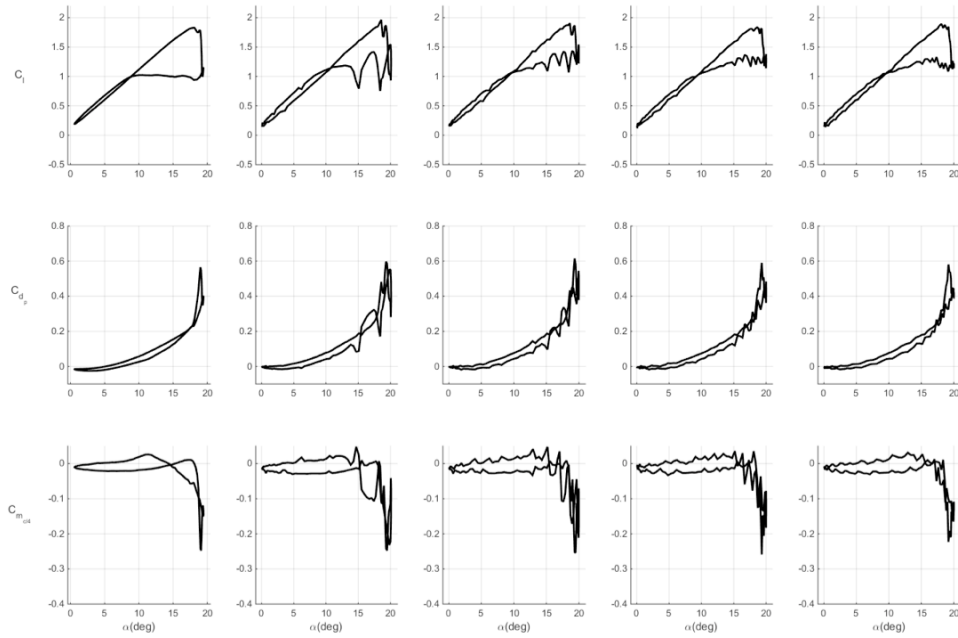


**Figure 494. Unsteady aerodynamic loads with respect to angle-of-attack.  $M=0.3$ ,  $\alpha=10^\circ \pm 10^\circ$ ,  $k=0.05$ . Baseline and single-row COMPACT  $F^+=0.2-0.8$  shown in order from left to right.**

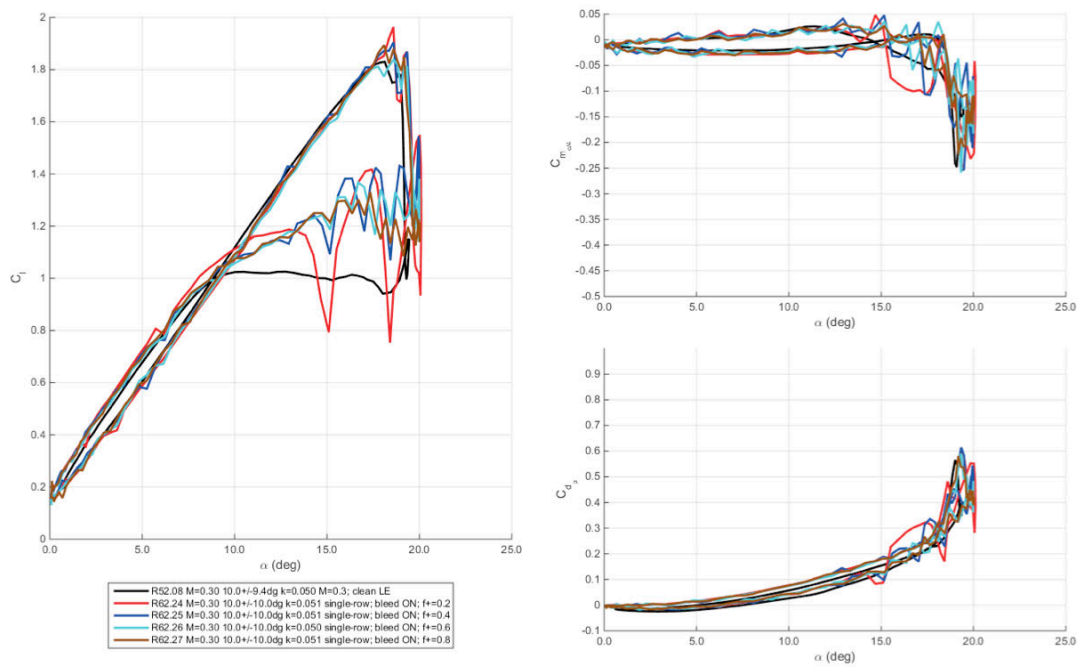


**Figure 495. Unsteady aerodynamic loads with respect to angle-of-attack. Baseline and single-row COMPACT  $F^+=0.2-0.8$ .**

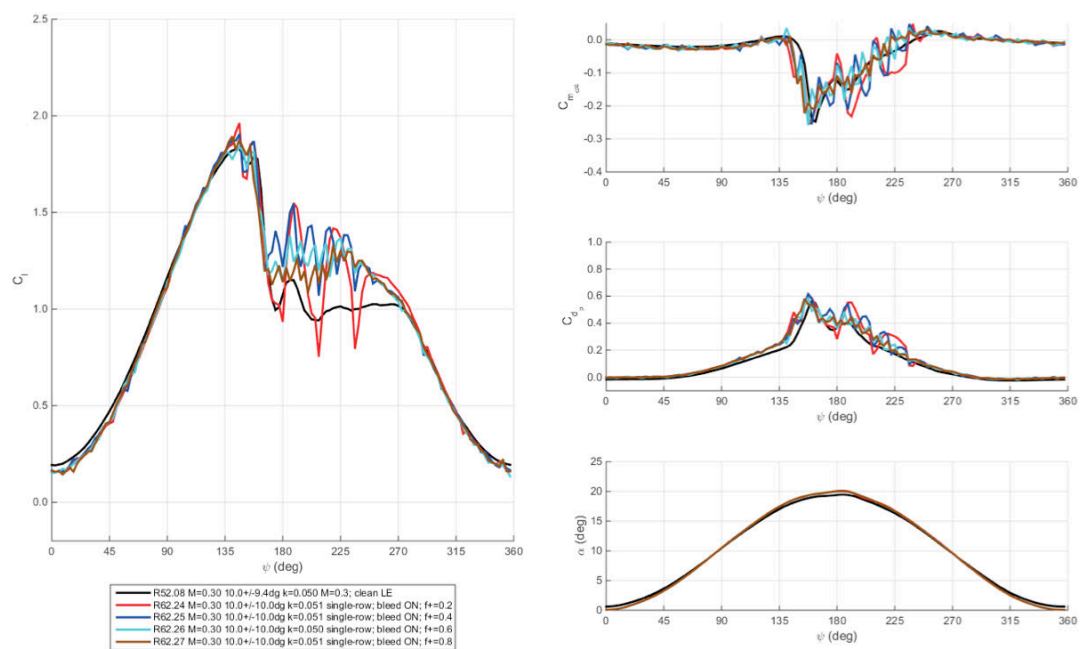


**Figure 496. Unsteady aerodynamic loads and angle-of-attack with respect to phase. Baseline and single-row COMPACT  $F^+ = 0.2-0.8$ .**

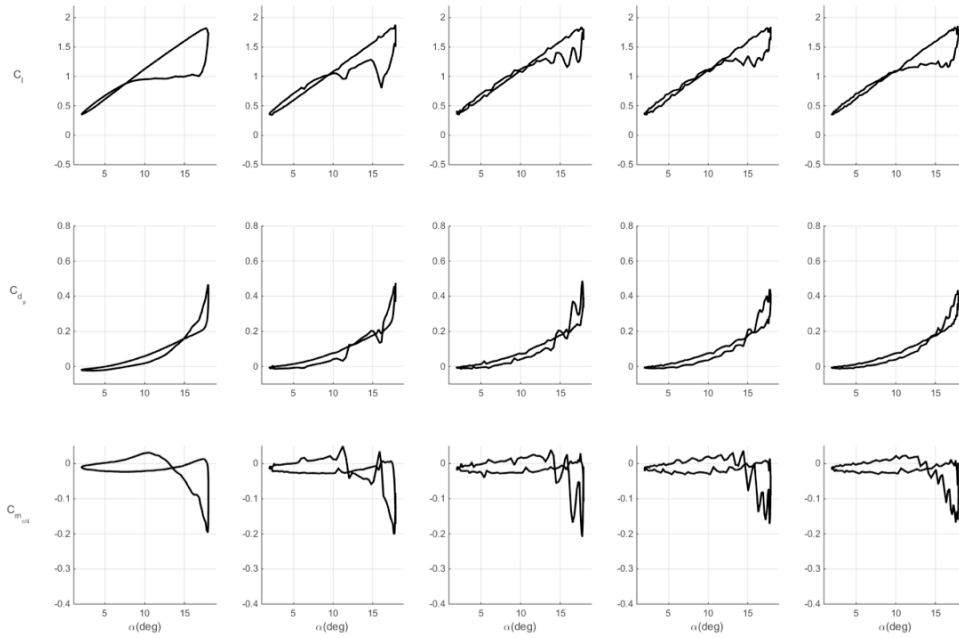


**Figure 497. Unsteady aerodynamic loads with respect to angle-of-attack.  $M=0.3$ ,  $\alpha=10^\circ\pm 8^\circ$ ,  $k=0.07$ . Baseline and single-row COMPACT  $F^+=0.2-0.8$  shown in order from left to right.**

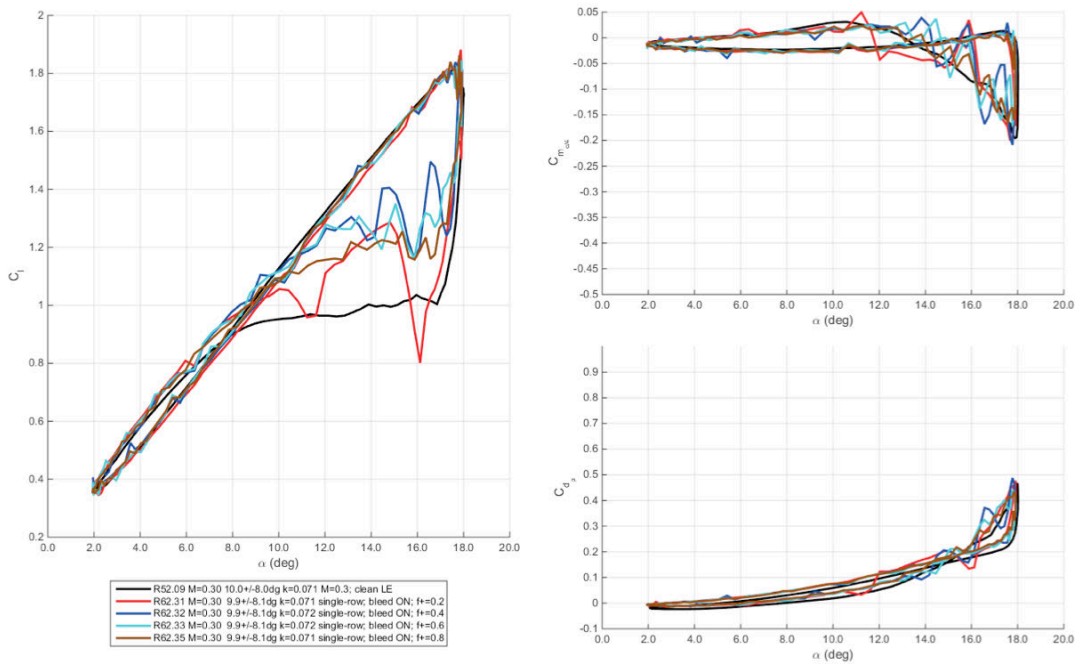


**Figure 498. Unsteady aerodynamic loads with respect to angle-of-attack. Baseline and single-row COMPACT  $F^+=0.2-0.8$ .**



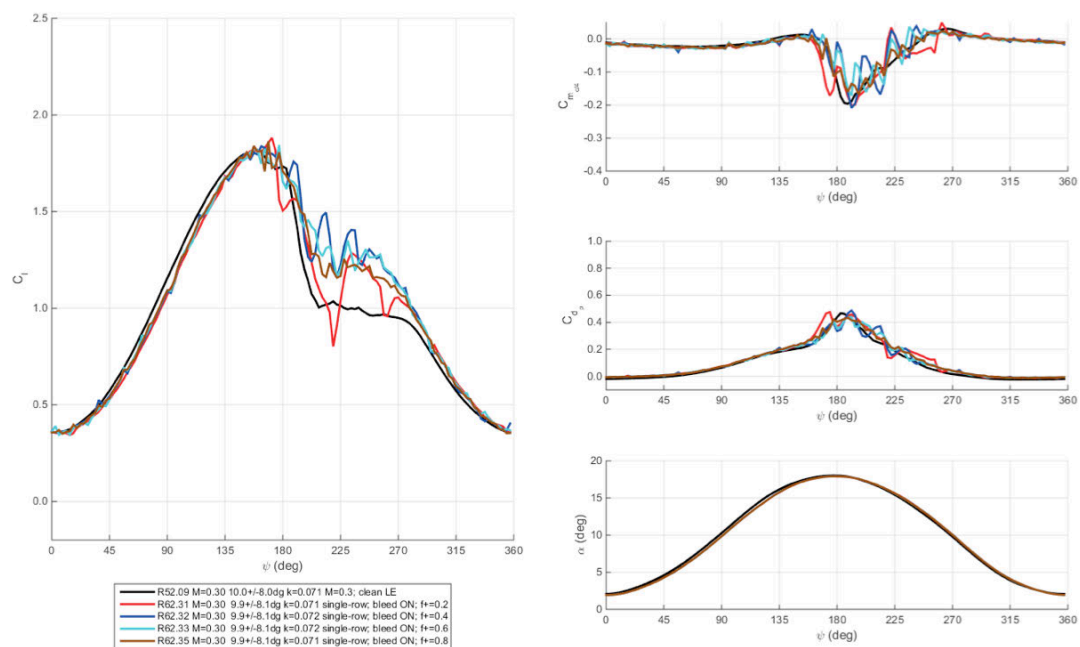


**Figure 499. Unsteady aerodynamic loads and angle-of-attack with respect to phase. Baseline and single-row COMPACT  $F^+ = 0.2-0.8$ .**

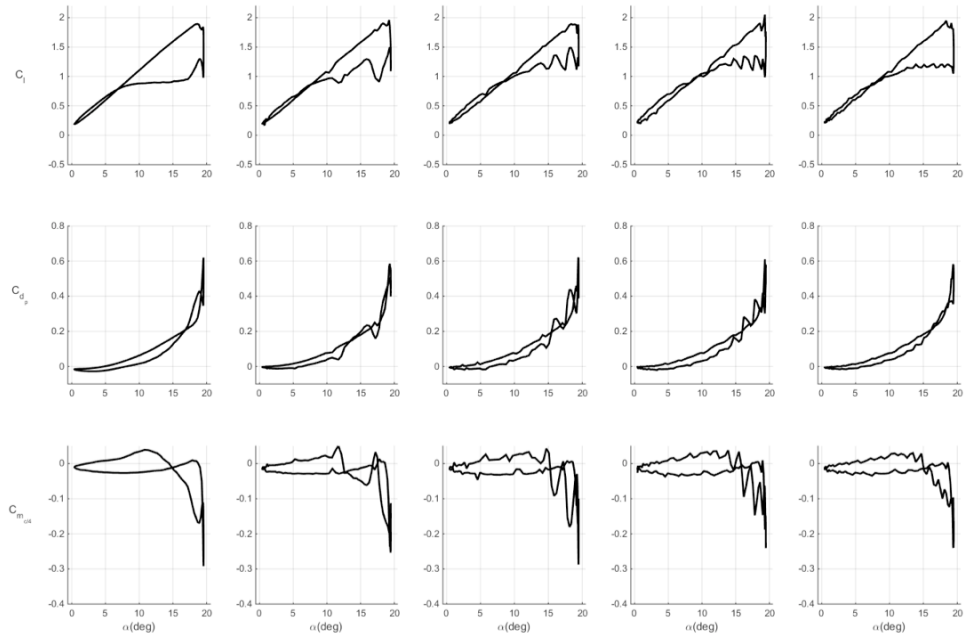


**Figure 500. Unsteady aerodynamic loads with respect to angle-of-attack.  $M=0.3$ ,  $\alpha=10^\circ \pm 10^\circ$ ,  $k=0.07$ . Baseline and single-row COMPACT  $F^+=0.2-0.8$  shown in order from left to right.**

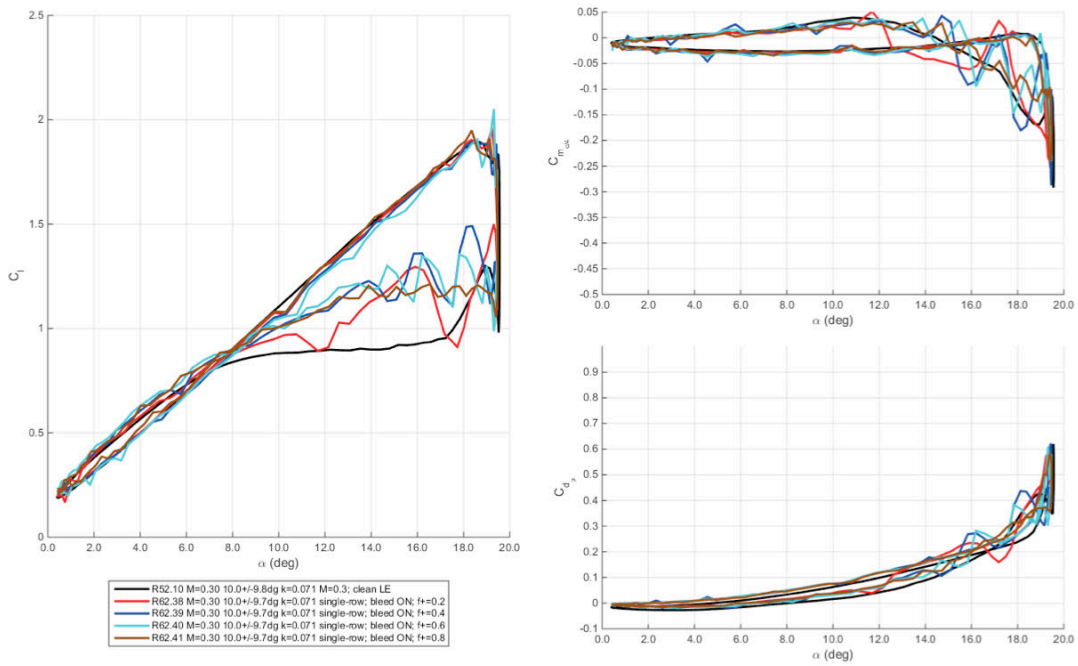


**Figure 501. Unsteady aerodynamic loads with respect to angle-of-attack. Baseline and single-row COMPACT  $F^+=0.2-0.8$ .**

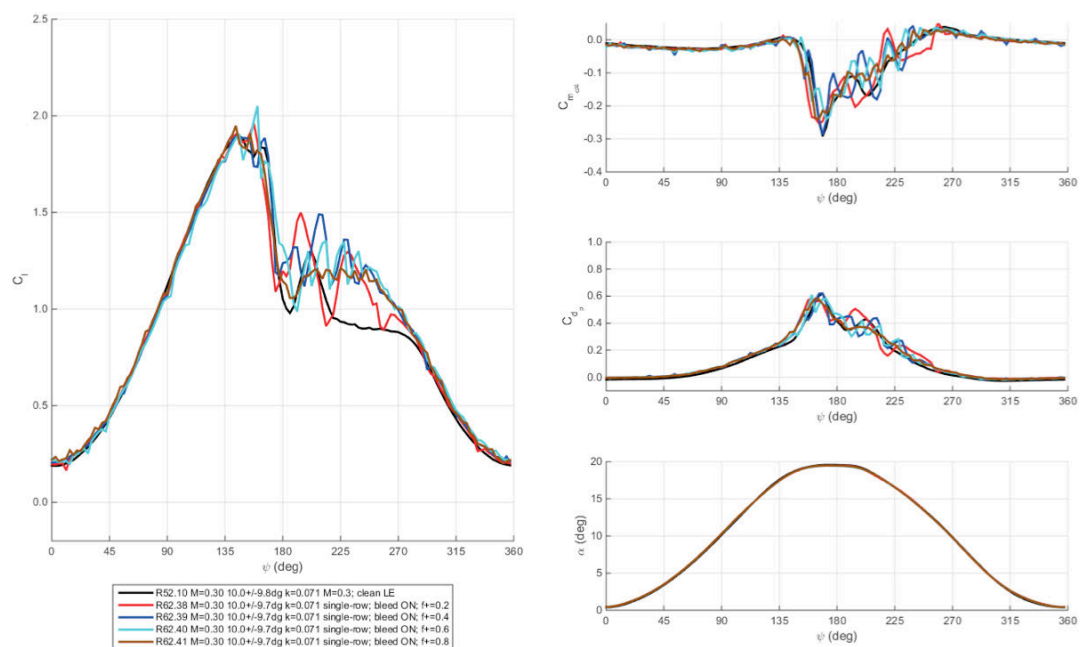


**Figure 502. Unsteady aerodynamic loads and angle-of-attack with respect to phase. Baseline and single-row COMPACT  $F^+ = 0.2-0.8$ .**

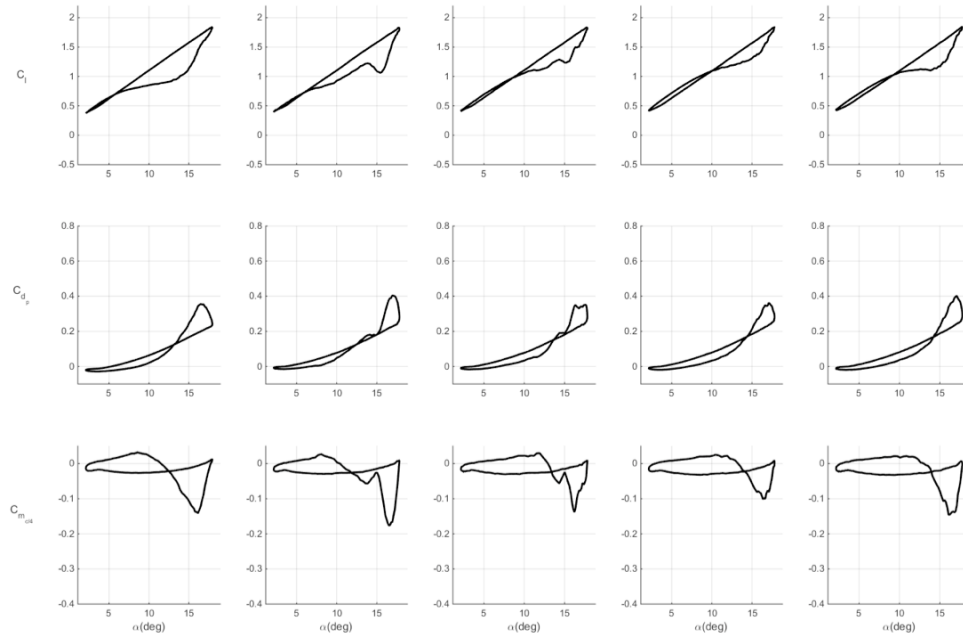


**Figure 503. Unsteady aerodynamic loads with respect to angle-of-attack.  $M=0.3$ ,  $\alpha=10^\circ \pm 8^\circ$ ,  $k=0.1$ . Baseline and single-row COMPACT  $F^+=0.2-0.8$  shown in order from left to right.**

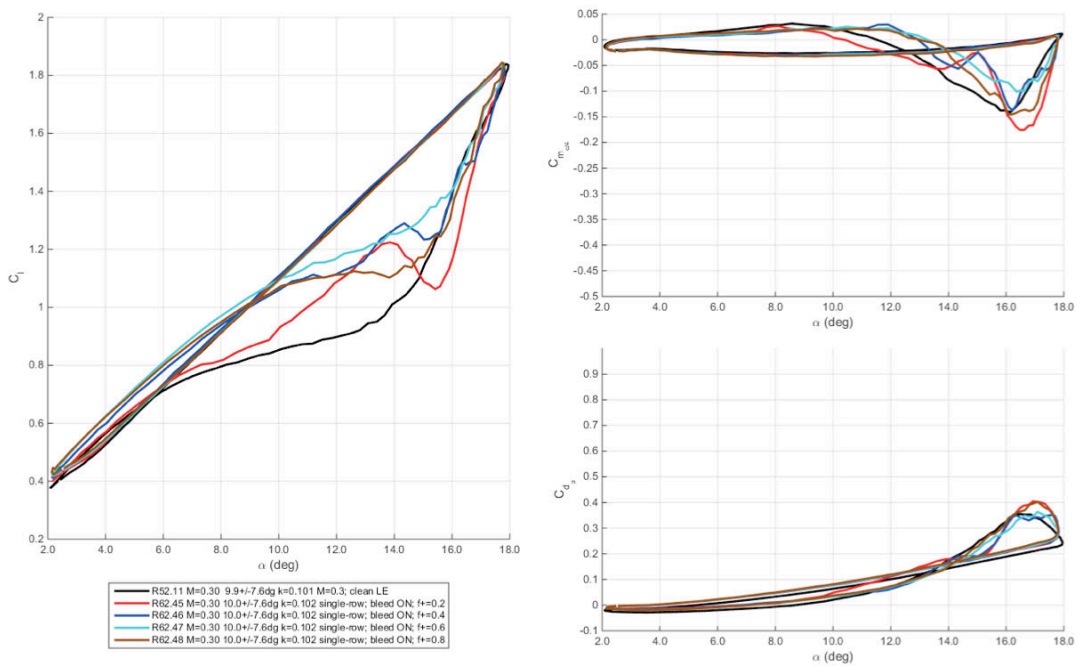


**Figure 504. Unsteady aerodynamic loads with respect to angle-of-attack. Baseline and single-row COMPACT  $F^+=0.2-0.8$ .**

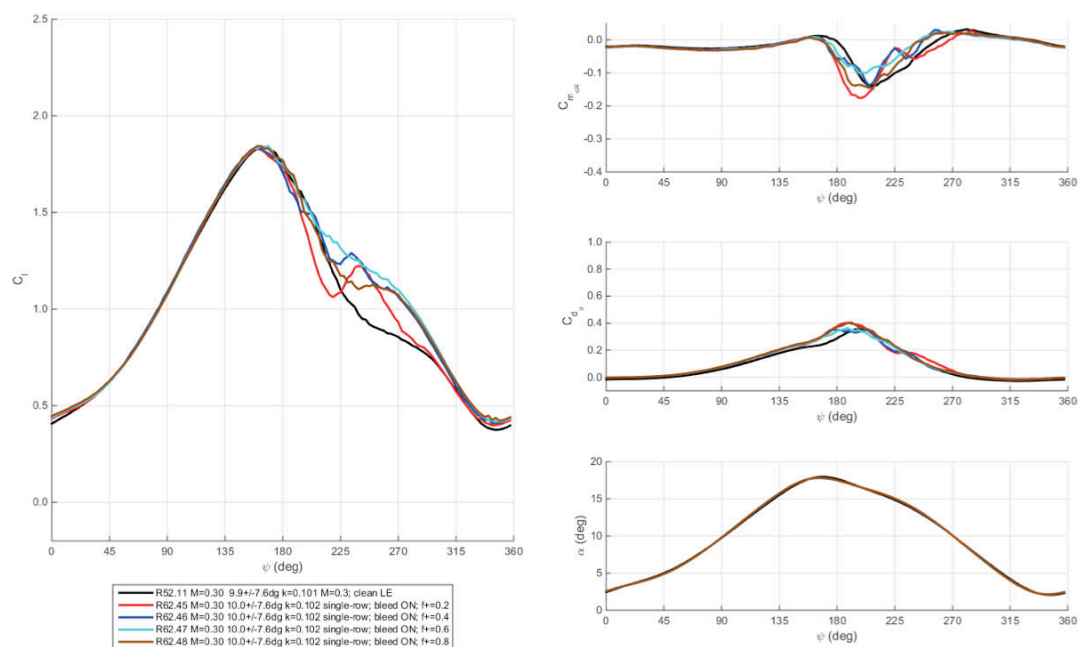


**Figure 505. Unsteady aerodynamic loads and angle-of-attack with respect to phase. Baseline and single-row COMPACT  $F^+ = 0.2-0.8$ .**

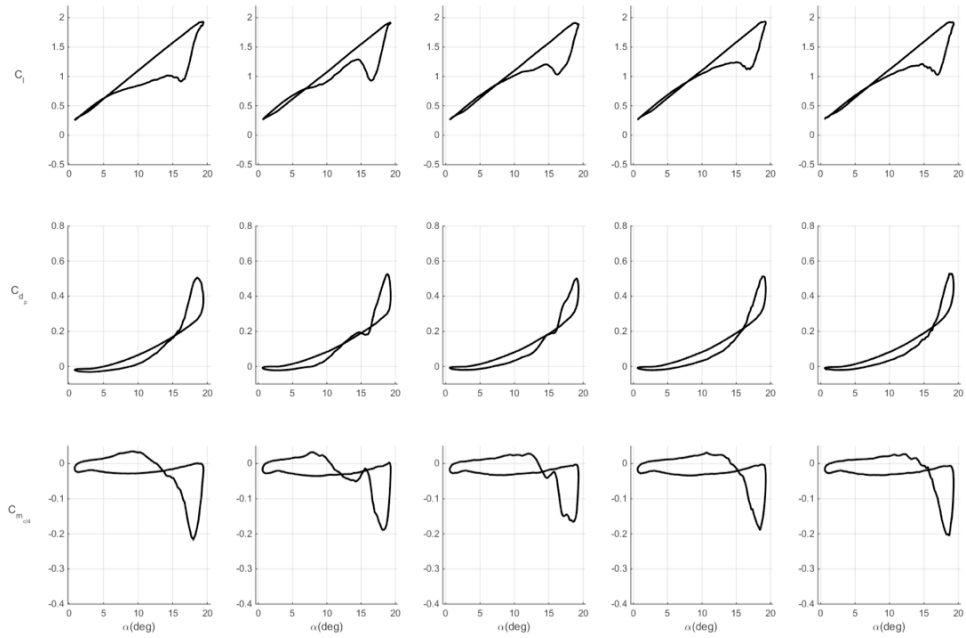


**Figure 506. Unsteady aerodynamic loads with respect to angle-of-attack.  $M=0.3$ ,  $\alpha=10^\circ \pm 9^\circ$ ,  $k=0.1$ . Baseline and single-row COMPACT  $F^+=0.2-0.8$  shown in order from left to right.**

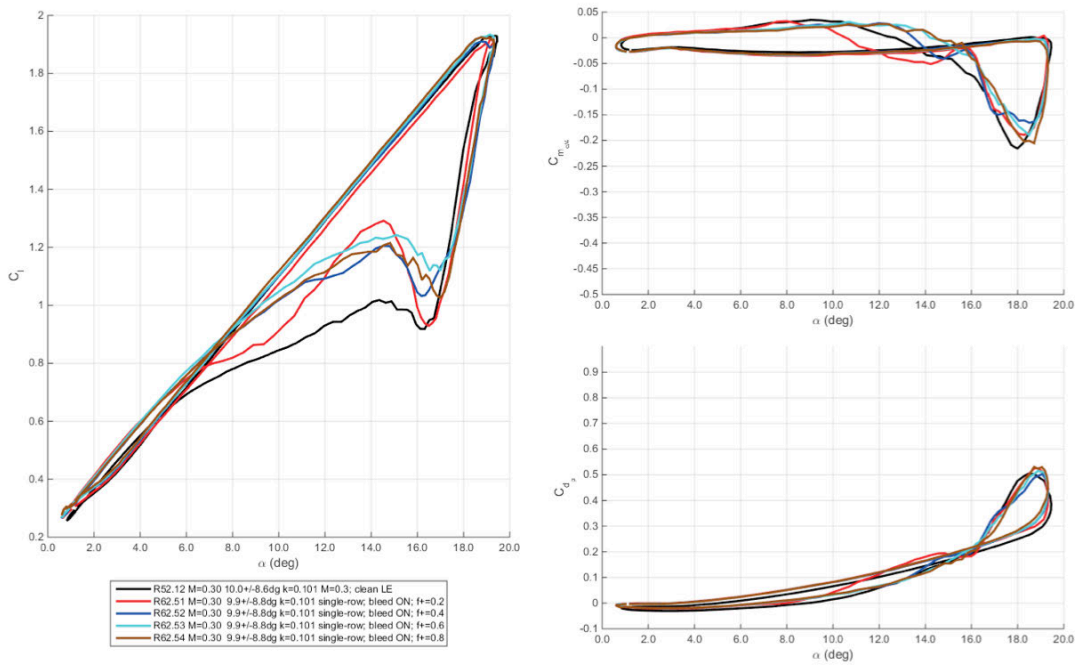


**Figure 507. Unsteady aerodynamic loads with respect to angle-of-attack. Baseline and single-row COMPACT  $F^+=0.2-0.8$ .**

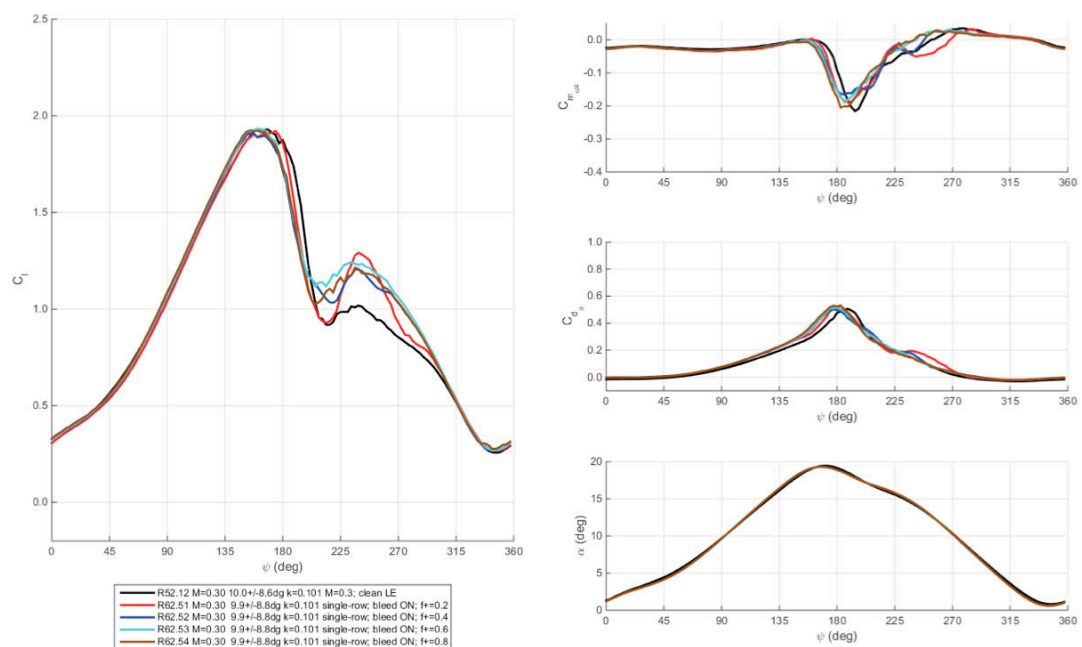


**Figure 508. Unsteady aerodynamic loads and angle-of-attack with respect to phase. Baseline and single-row COMPACT  $F^+=0.2-0.8$ .**



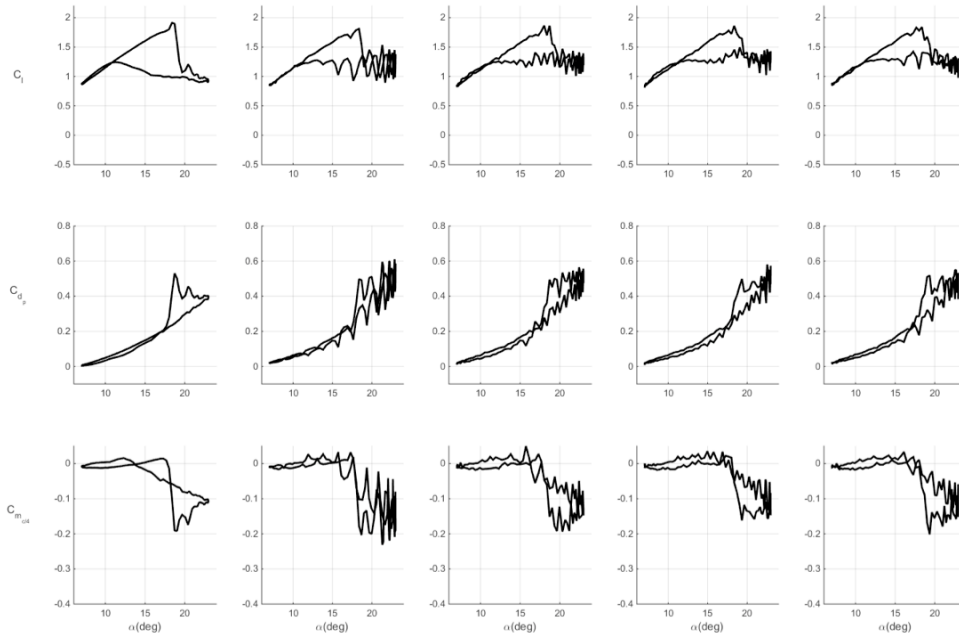


**Figure 509. Unsteady aerodynamic loads with respect to angle-of-attack. M=0.3,  $\alpha=15^\circ\pm8^\circ$ ,  $k=0.025$ . Baseline and single-row COMPACT  $F^+=0.2-1.0$  shown in order from left to right.**

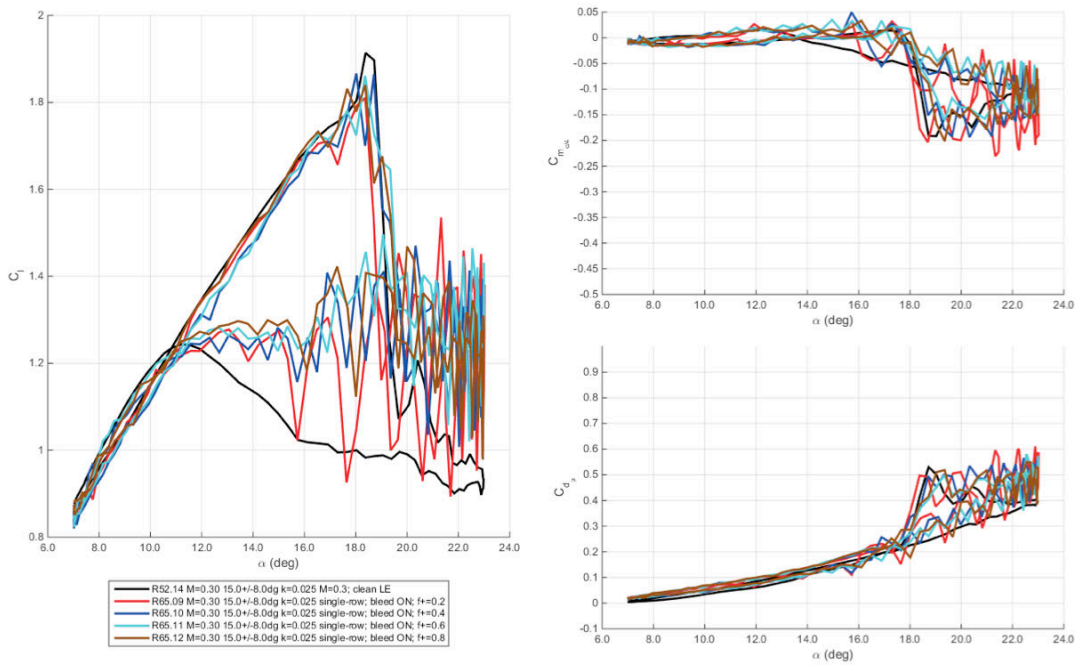


**Figure 510. Unsteady aerodynamic loads with respect to angle-of-attack. Baseline and single-row COMPACT  $F^+=0.2-0.8$ .**

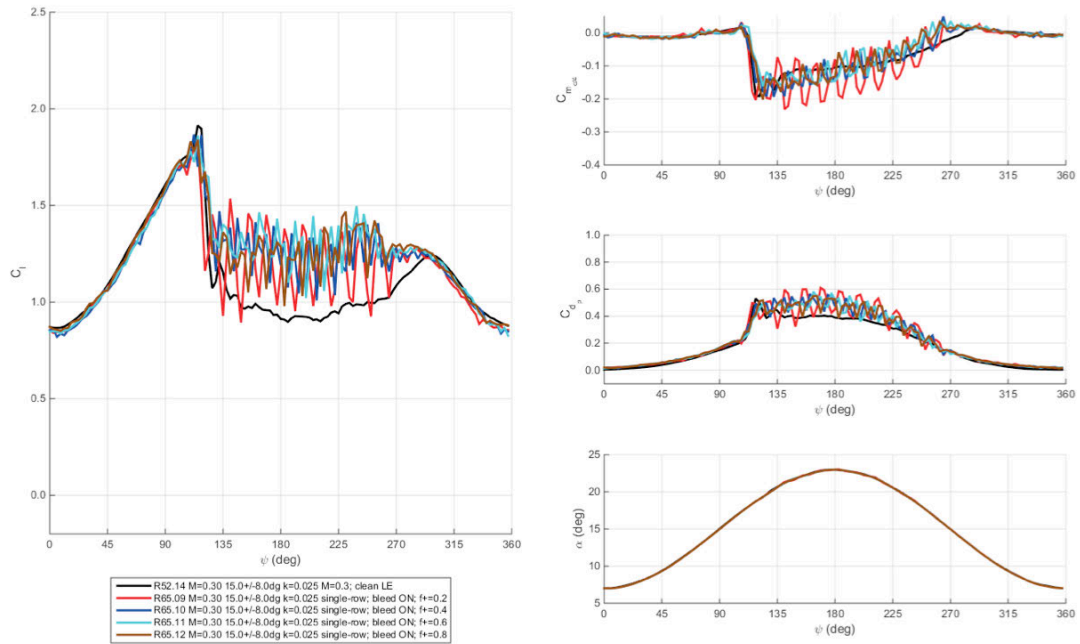


**Figure 511. Unsteady aerodynamic loads and angle-of-attack with respect to phase. Baseline and single-row COMPACT  $F^+ = 0.2-0.8$ .**

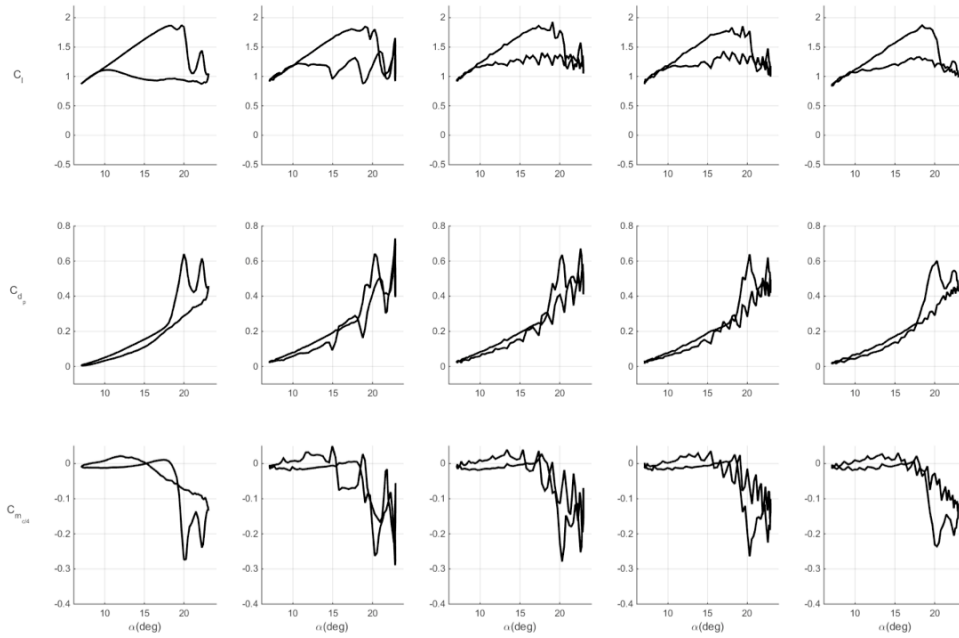


**Figure 512. Unsteady aerodynamic loads with respect to angle-of-attack.  $M=0.3$ ,  $\alpha=15^\circ \pm 8^\circ$ ,  $k=0.05$ . Baseline and single-row COMPACT  $F^+=0.2-0.8$  shown in order from left to right.**

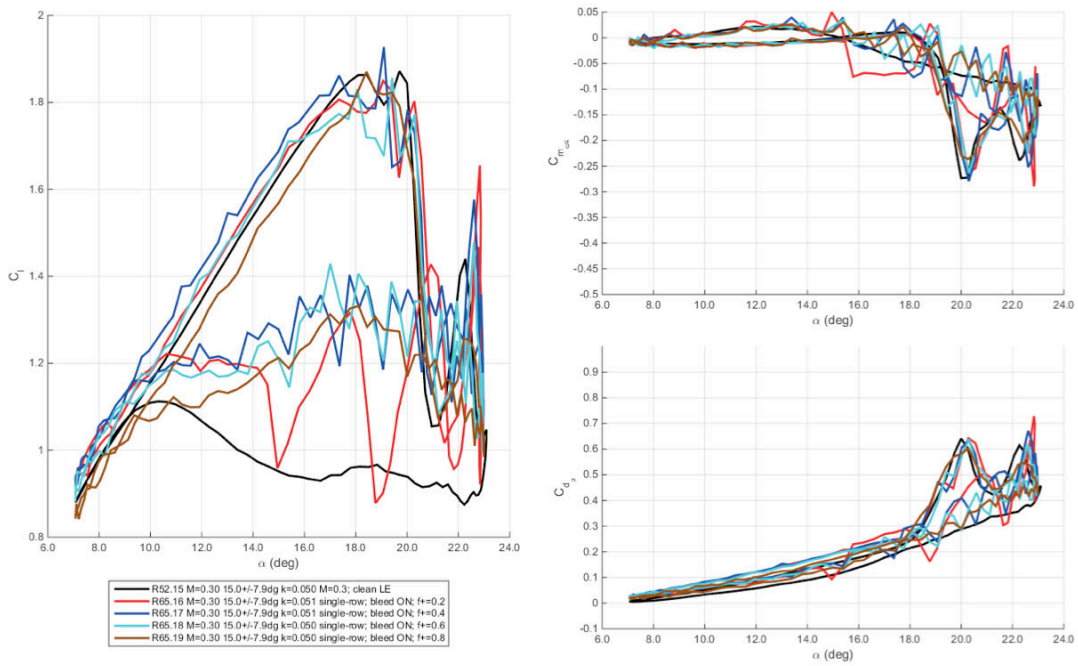


**Figure 513. Unsteady aerodynamic loads with respect to angle-of-attack. Baseline and single-row COMPACT  $F^+=0.2-0.8$ .**

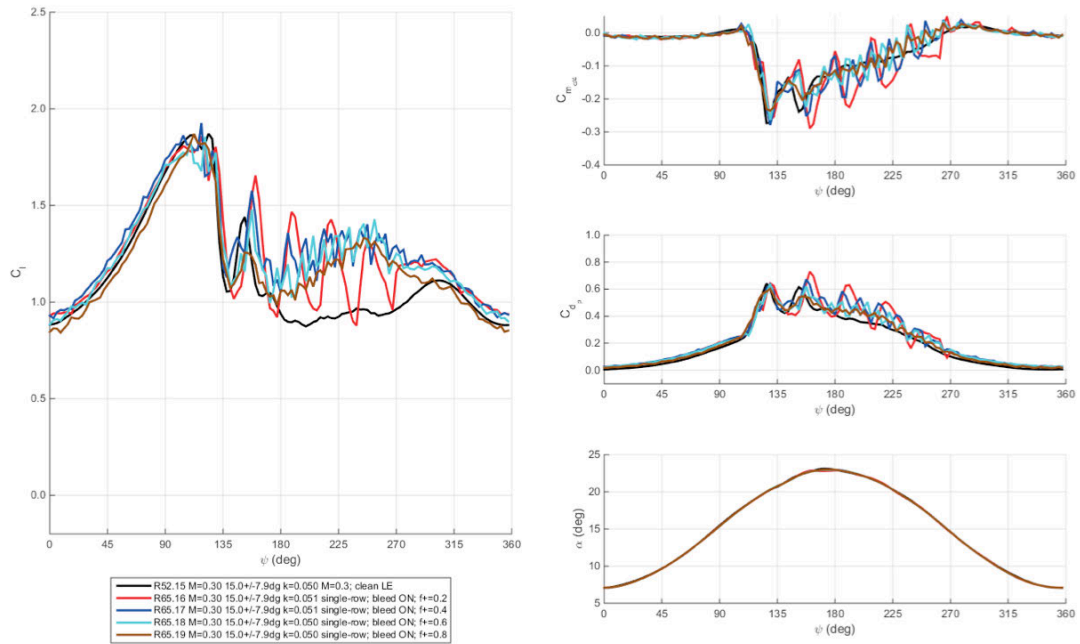


**Figure 514. Unsteady aerodynamic loads and angle-of-attack with respect to phase. Baseline and single-row COMPACT  $F^+=0.2-0.8$ .**

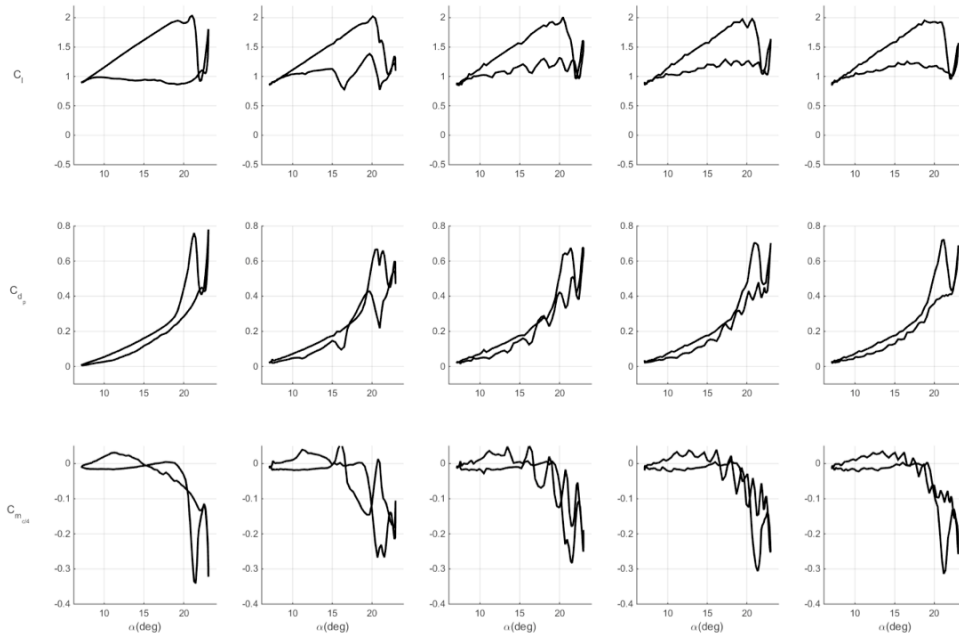


**Figure 515. Unsteady aerodynamic loads with respect to angle-of-attack.  $M=0.3$ ,  $\alpha=15^\circ \pm 8^\circ$ ,  $k=0.07$ . Baseline and single-row COMPACT  $F^+=0.2-0.8$  shown in order from left to right.**

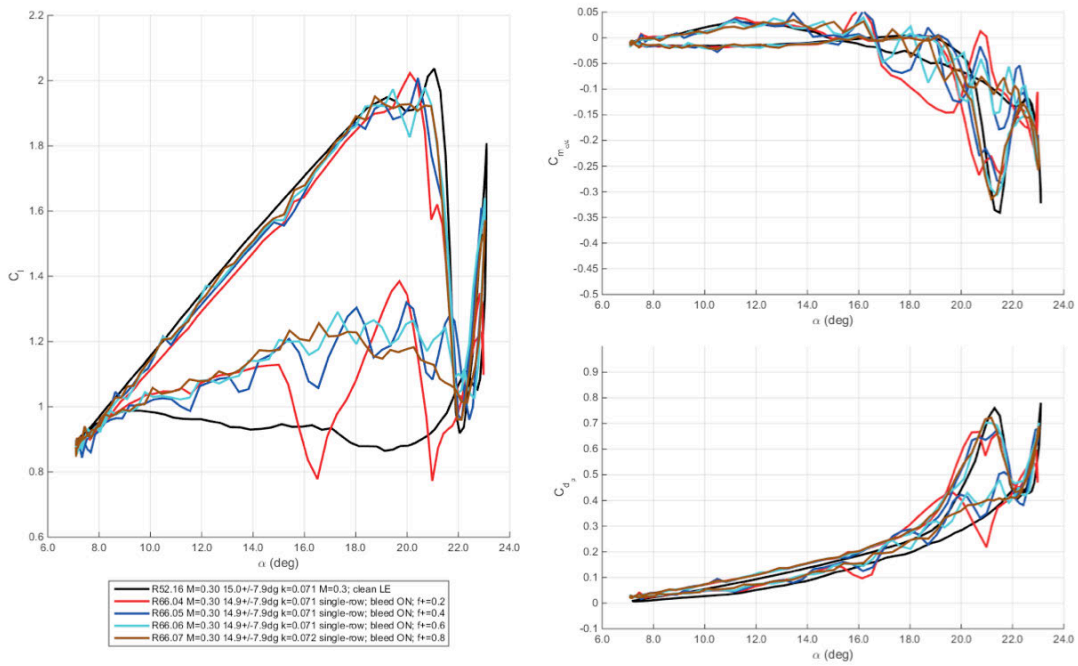


**Figure 516. Unsteady aerodynamic loads with respect to angle-of-attack. Baseline and single-row COMPACT  $F^+=0.2-0.8$ .**

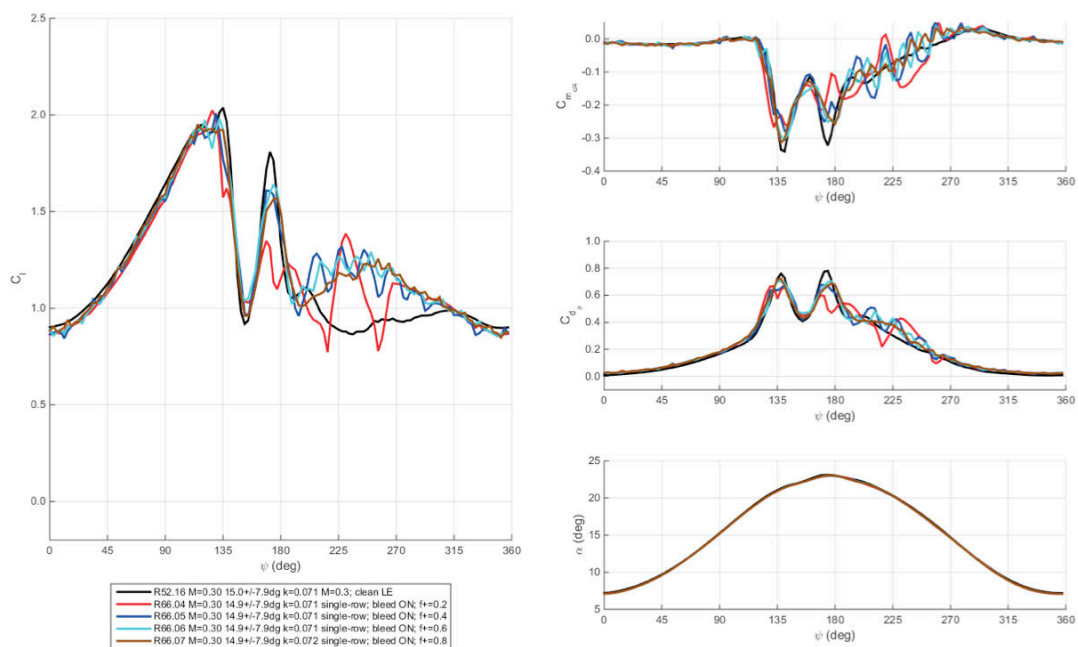


**Figure 517. Unsteady aerodynamic loads and angle-of-attack with respect to phase. Baseline and single-row COMPACT  $F^+ = 0.2-0.8$ .**

$M=0.4$

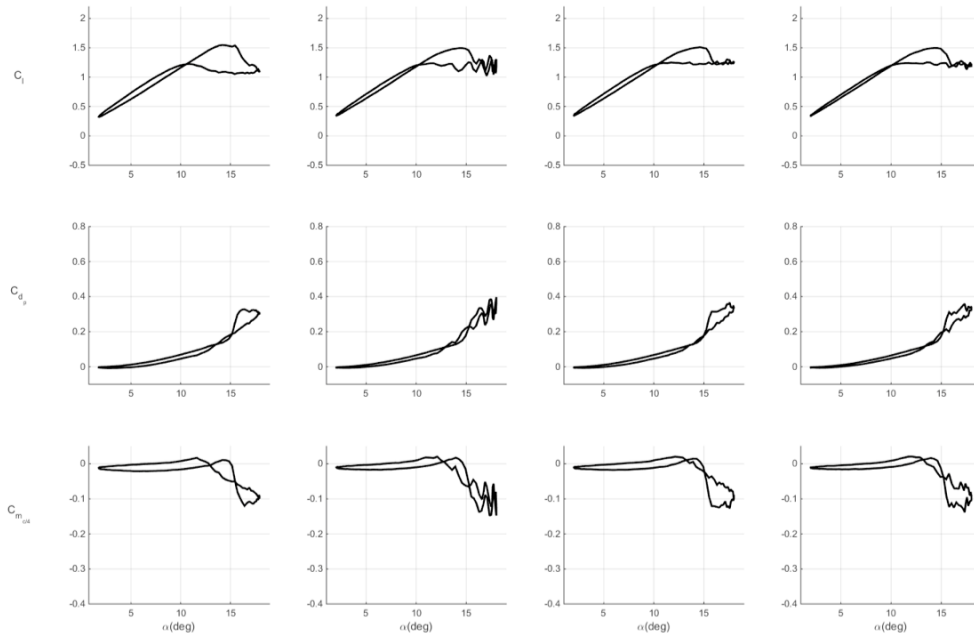


**Figure 518. Unsteady aerodynamic loads with respect to angle-of-attack.  $M=0.4$ ,  $\alpha=10^\circ \pm 8^\circ$ ,  $k=0.025$ . Baseline and single-row COMPACT  $F^+ = 0.2-0.6$  shown in order from left to right.**



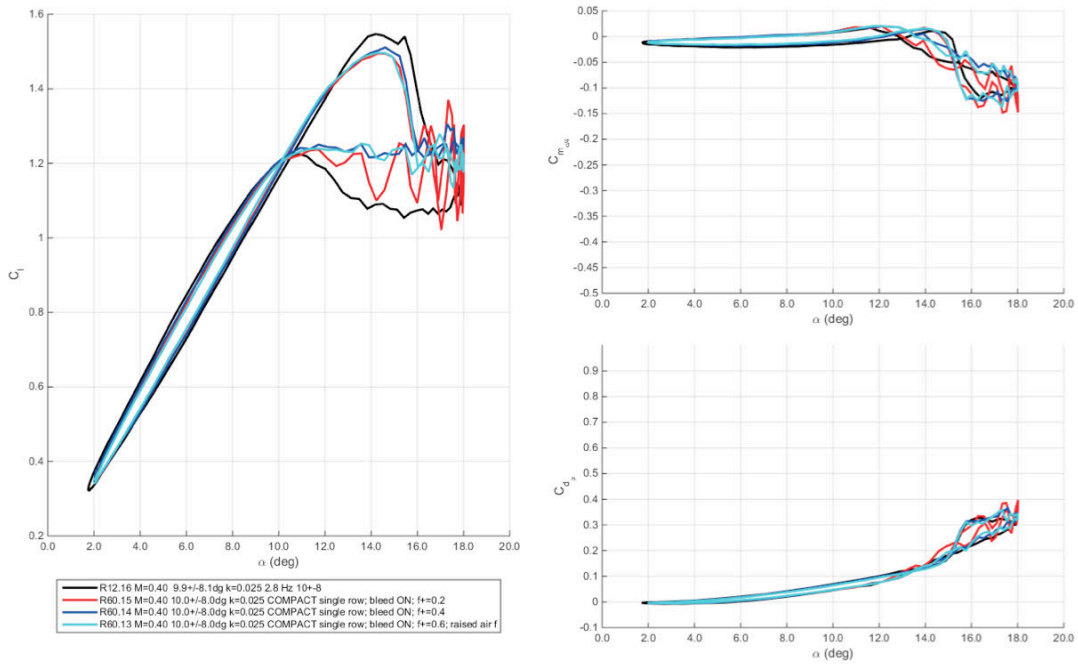


**Figure 519. Unsteady aerodynamic loads with respect to angle-of-attack. Baseline and single-row COMPACT  $F^+ = 0.2-0.6$ .**

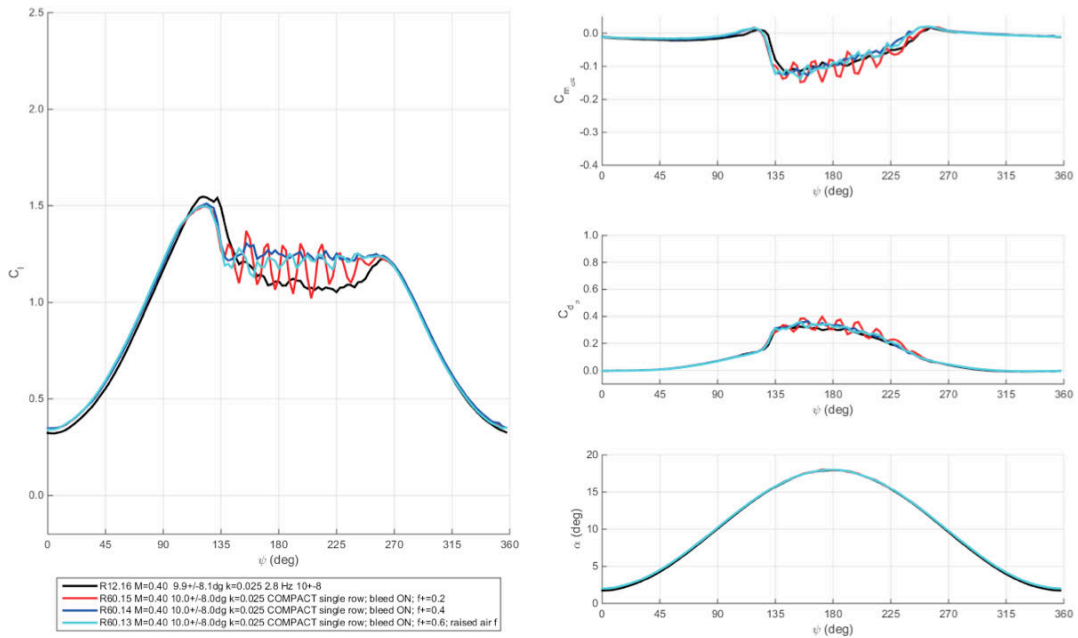


**Figure 520. Unsteady aerodynamic loads and angle-of-attack with respect to phase. Baseline and single-row COMPACT  $F^+ = 0.2-0.6$ .**

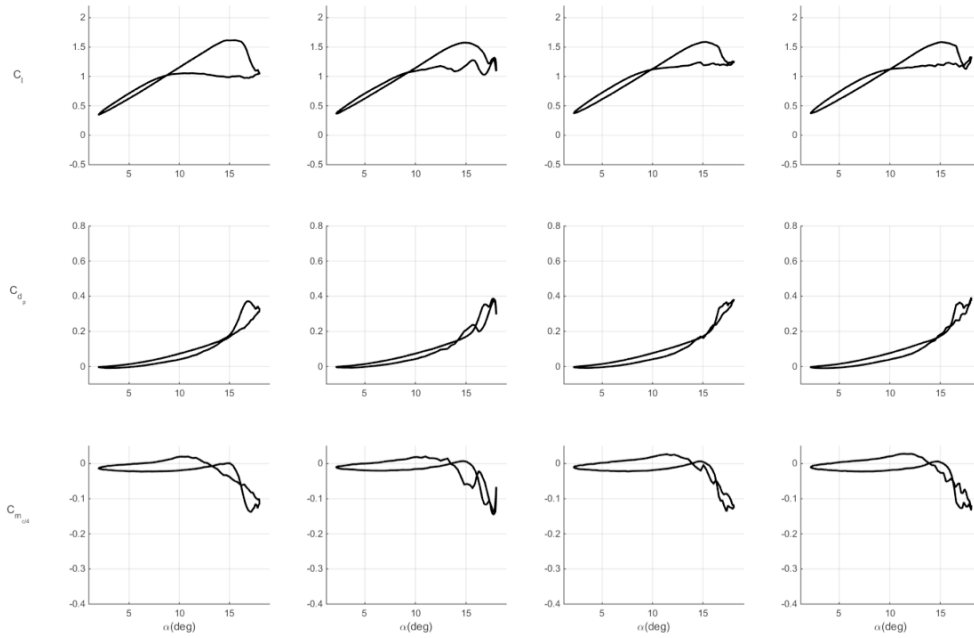


**Figure 521. Unsteady aerodynamic loads with respect to angle-of-attack. M=0.4,  $\alpha=10^\circ \pm 8^\circ$ ,  $k=0.05$ . Baseline and single-row COMPACT  $F^+=0.2-0.6$  shown in order from left to right.**

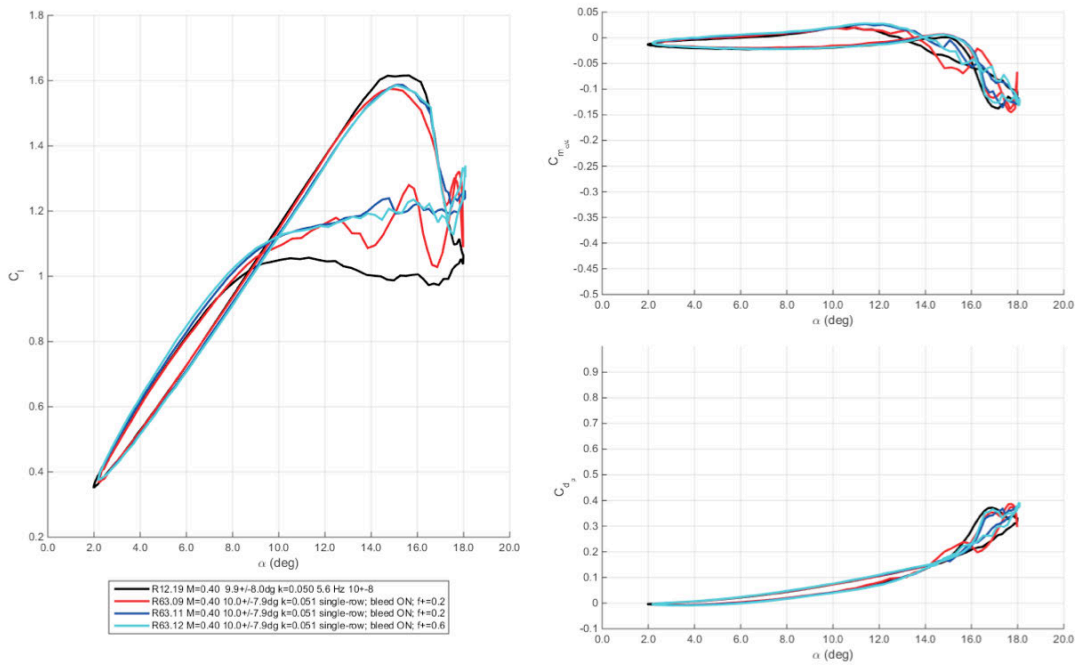


**Figure 522. Unsteady aerodynamic loads with respect to angle-of-attack. Baseline and single-row COMPACT  $F^+=0.2-0.6$ .**

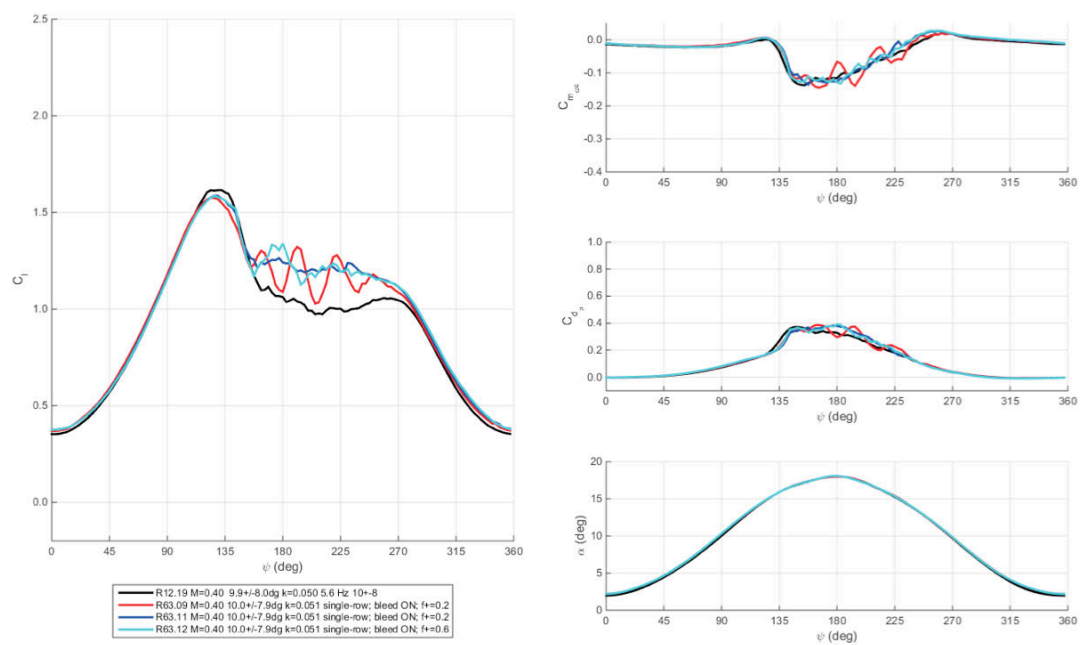


**Figure 523. Unsteady aerodynamic loads and angle-of-attack with respect to phase. Baseline and single-row COMPACT  $F^+ = 0.2-0.6$ .**

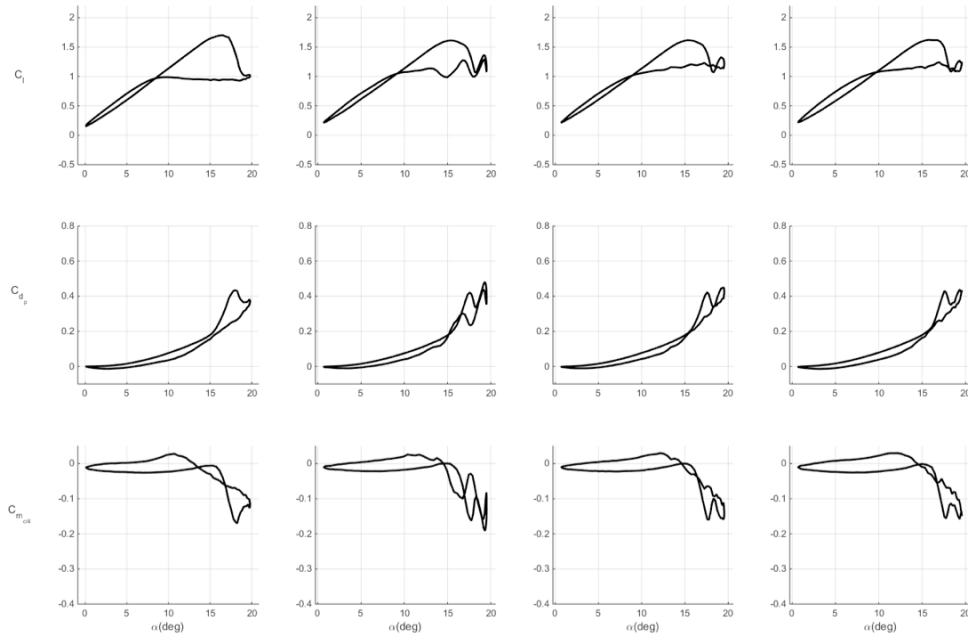


**Figure 524. Unsteady aerodynamic loads with respect to angle-of-attack.  $M=0.4$ ,  $\alpha=10^\circ \pm 10^\circ$ ,  $k=0.05$ . Baseline and single-row COMPACT  $F^+=0.2-0.6$  shown in order from left to right.**

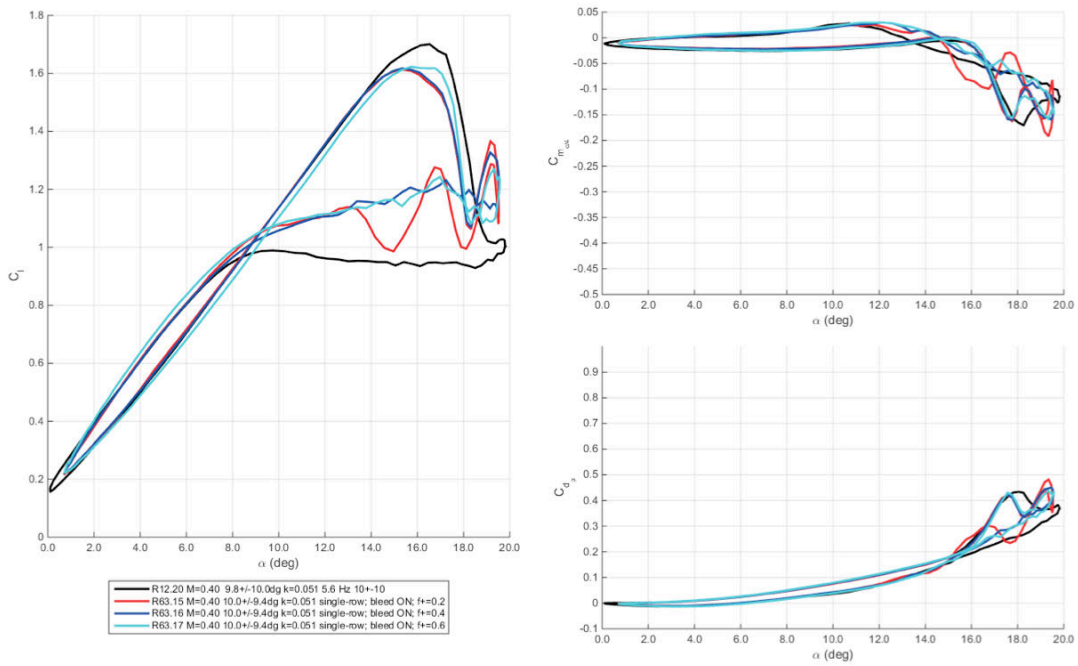


**Figure 525. Unsteady aerodynamic loads with respect to angle-of-attack. Baseline and single-row COMPACT  $F^+=0.2-0.6$ .**

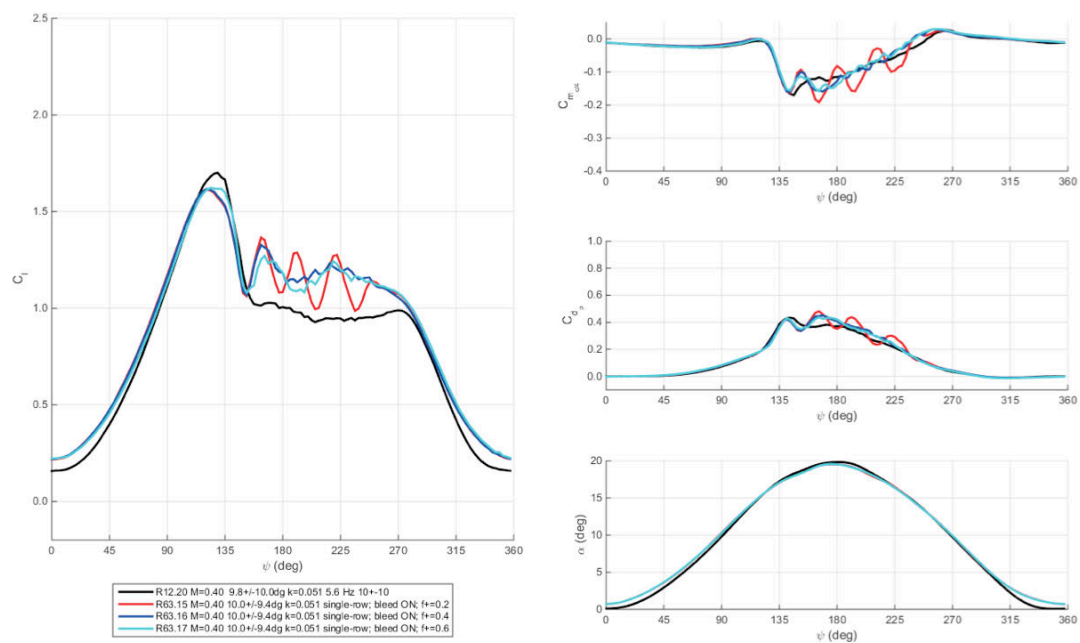


**Figure 526. Unsteady aerodynamic loads and angle-of-attack with respect to phase. Baseline and single-row COMPACT  $F^+ = 0.2-0.6$ .**

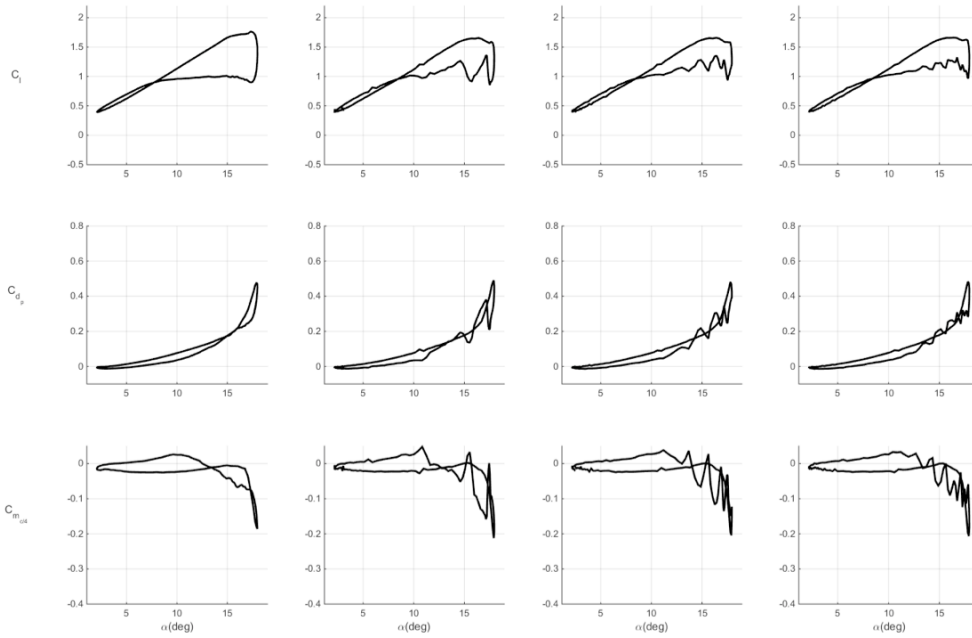


**Figure 527. Unsteady aerodynamic loads with respect to angle-of-attack.  $M=0.4$ ,  $\alpha=10^\circ \pm 8^\circ$ ,  $k=0.07$ . Baseline and single-row COMPACT  $F^+=0.2-0.6$  shown in order from left to right.**

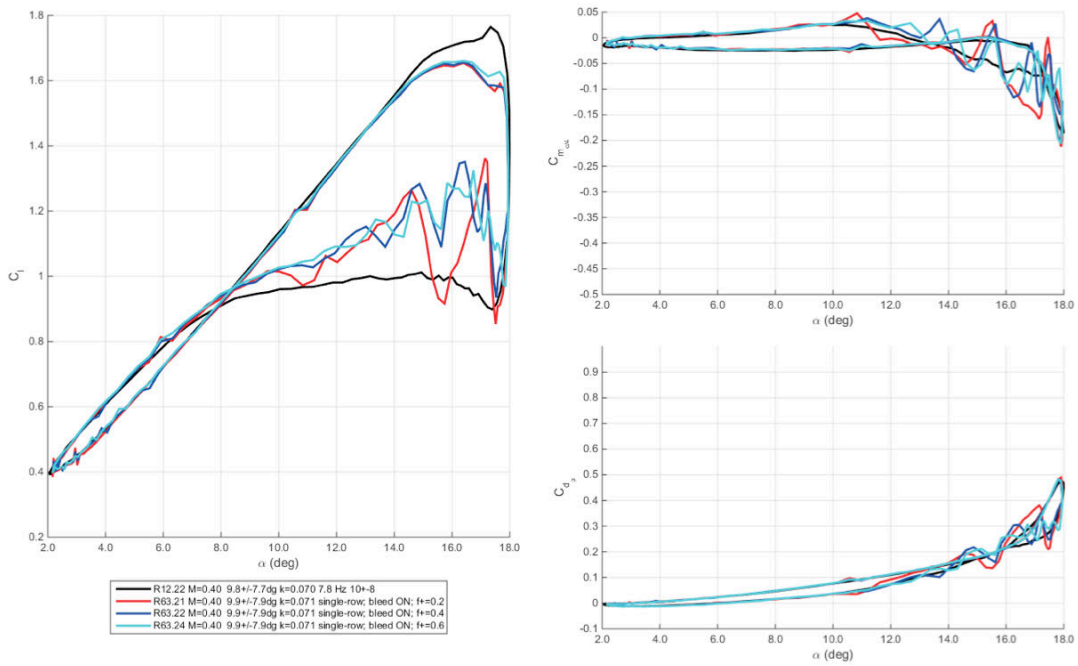


**Figure 528. Unsteady aerodynamic loads with respect to angle-of-attack. Baseline and single-row COMPACT  $F^+=0.2-0.6$ .**

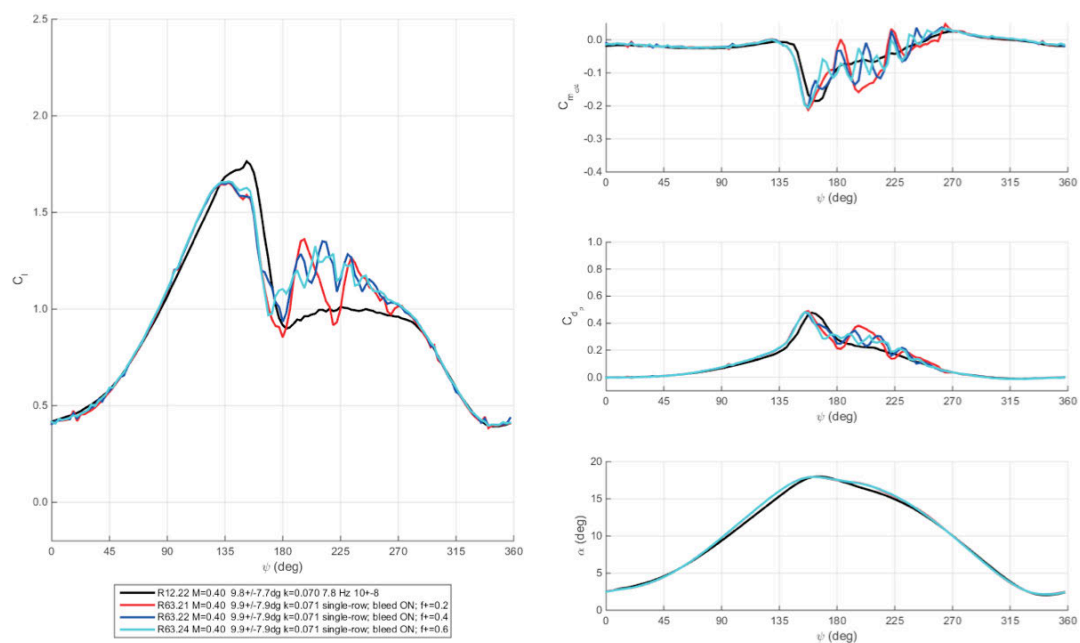


**Figure 529. Unsteady aerodynamic loads and angle-of-attack with respect to phase. Baseline and single-row COMPACT  $F^+ = 0.2-0.6$ .**



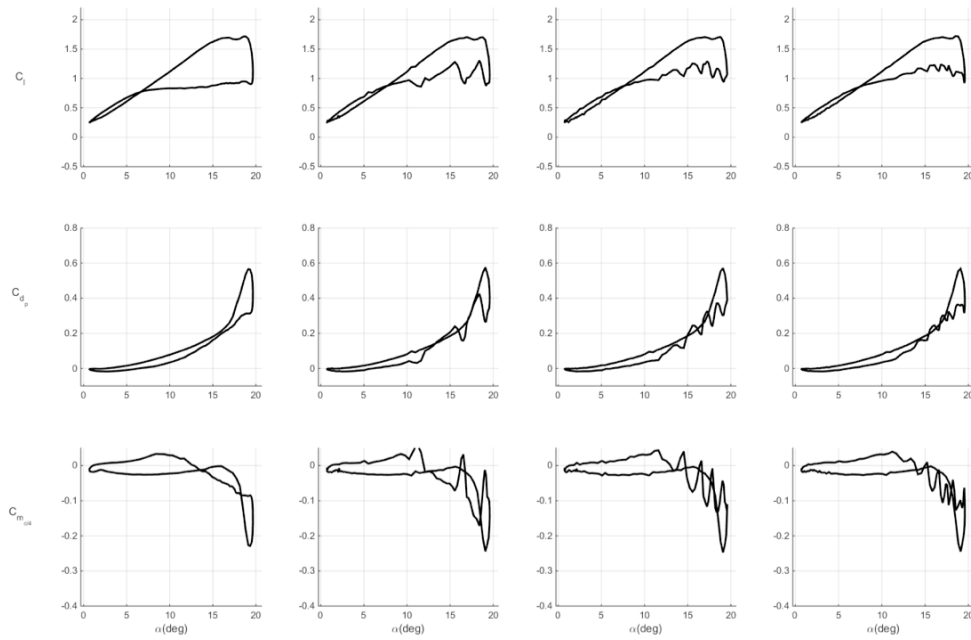


**Figure 530. Unsteady aerodynamic loads with respect to angle-of-attack.  $M=0.4$ ,  $\alpha=10^\circ \pm 9^\circ$ ,  $k=0.07$ . Baseline and single-row COMPACT  $F^+=0.2-0.6$  shown in order from left to right. Note that baseline includes open slot, no clean LE baseline was data available.**

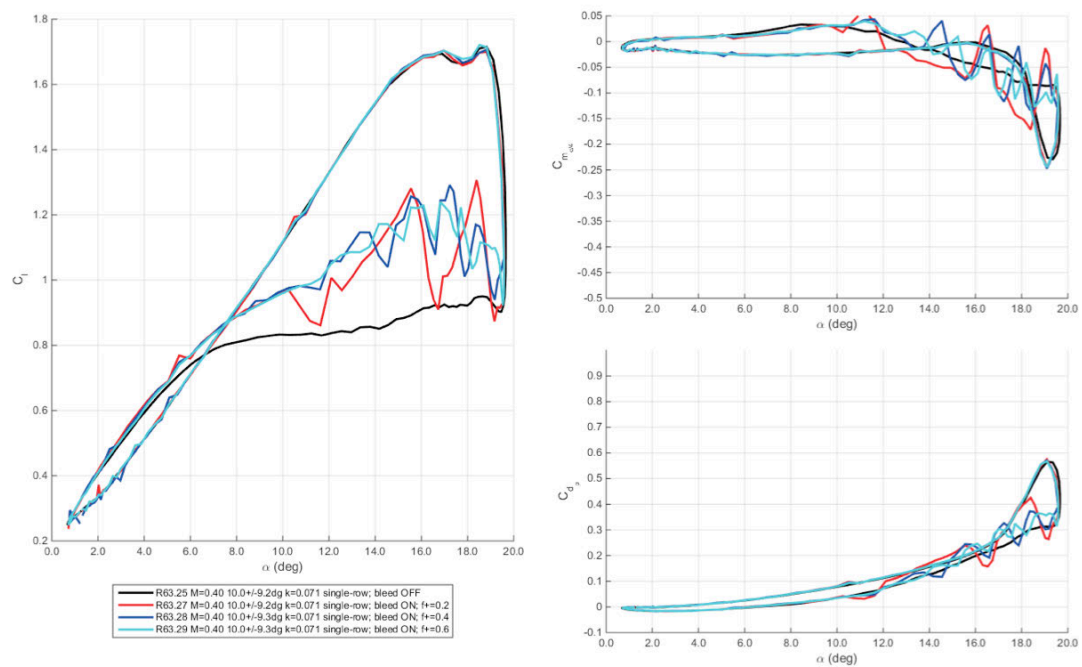


**Figure 531. Unsteady aerodynamic loads with respect to angle-of-attack. Baseline and single-row COMPACT  $F^+ = 0.2-0.6$ . Note that baseline includes open slot, no clean LE baseline was data available.**

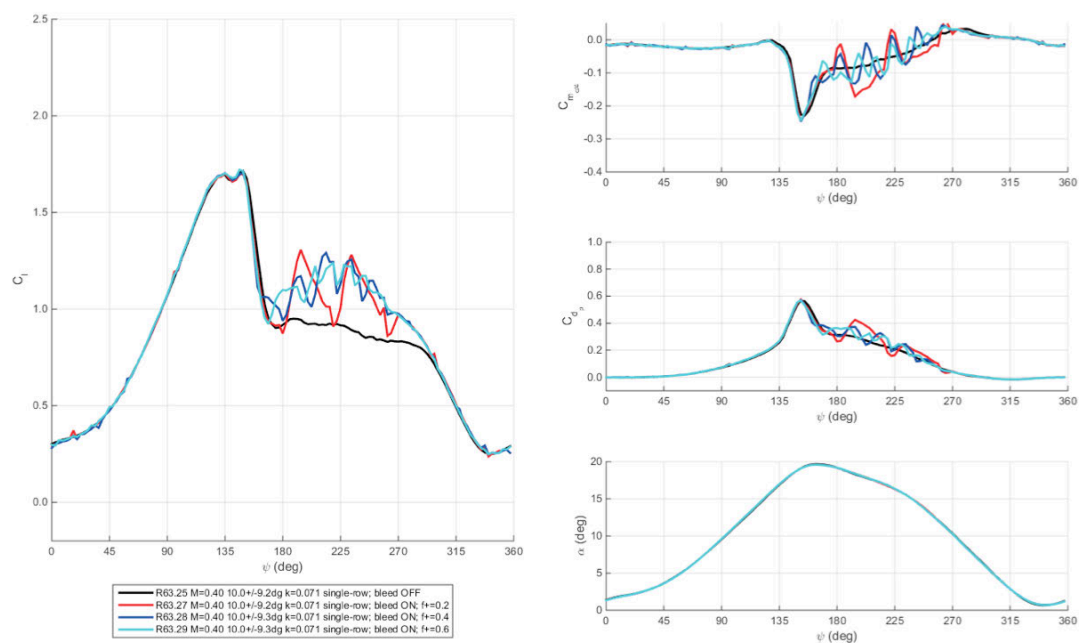


**Figure 532. Unsteady aerodynamic loads and angle-of-attack with respect to phase. Baseline and single-row COMPACT  $F^+ = 0.2-0.6$ . Note that baseline includes open slot, no clean LE baseline was data available.**

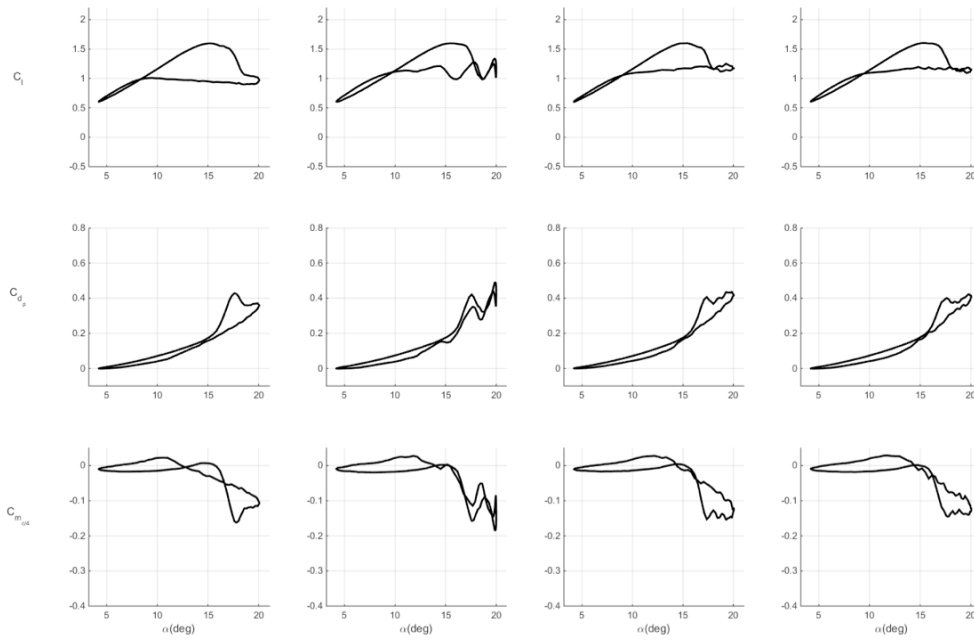


**Figure 533. Unsteady aerodynamic loads with respect to angle-of-attack.  $M=0.4$ ,  $\alpha=12^\circ \pm 8^\circ$ ,  $k=0.05$ . Baseline and single-row COMPACT  $F^+=0.2-0.6$  shown in order from left to right. Note that baseline includes open slot, no clean LE baseline was data available.**

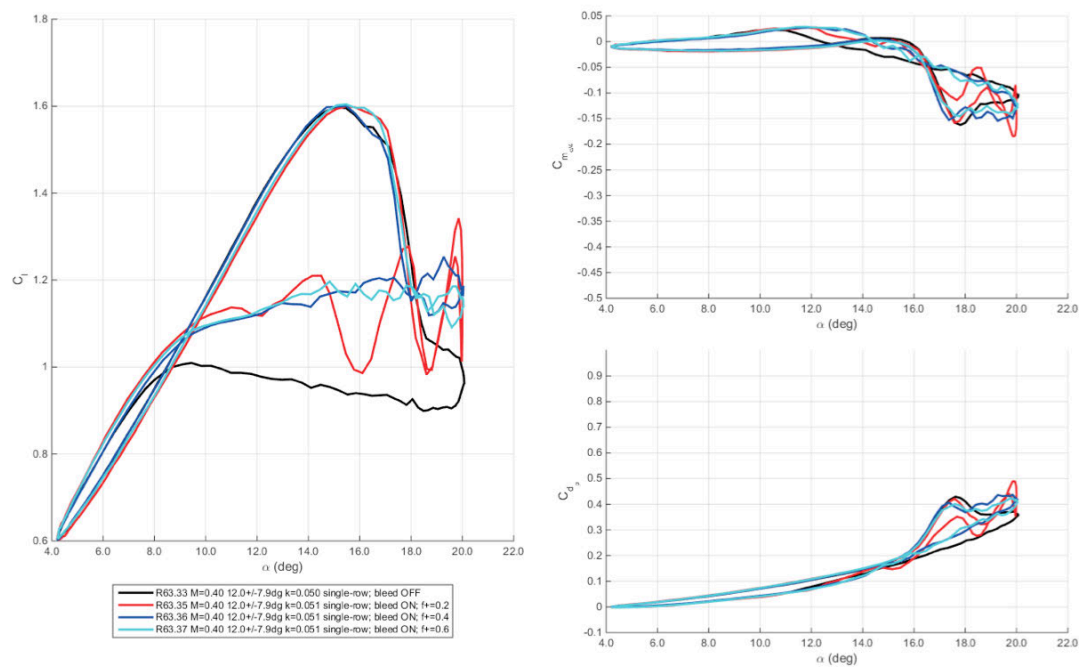


**Figure 534. Unsteady aerodynamic loads with respect to angle-of-attack. Baseline and single-row COMPACT F+=0.2-0.6. Note that baseline includes open slot, no clean LE baseline was data available.**

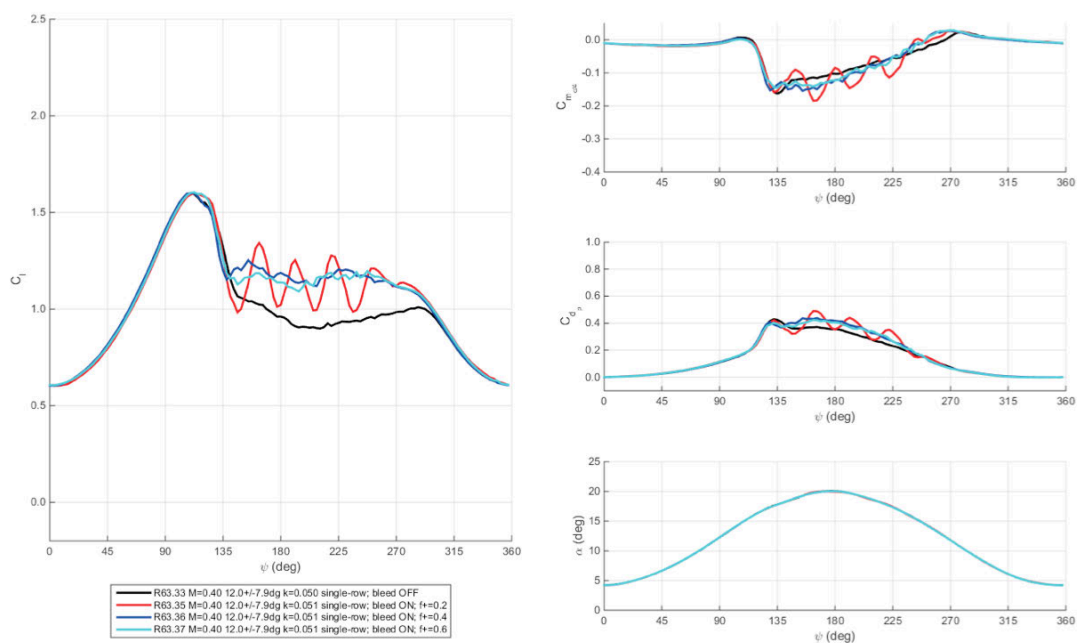


**Figure 535. Unsteady aerodynamic loads and angle-of-attack with respect to phase. Baseline and single-row COMPACT  $F^+ = 0.2-0.6$ . Note that baseline includes open slot, no clean LE baseline was data available.**

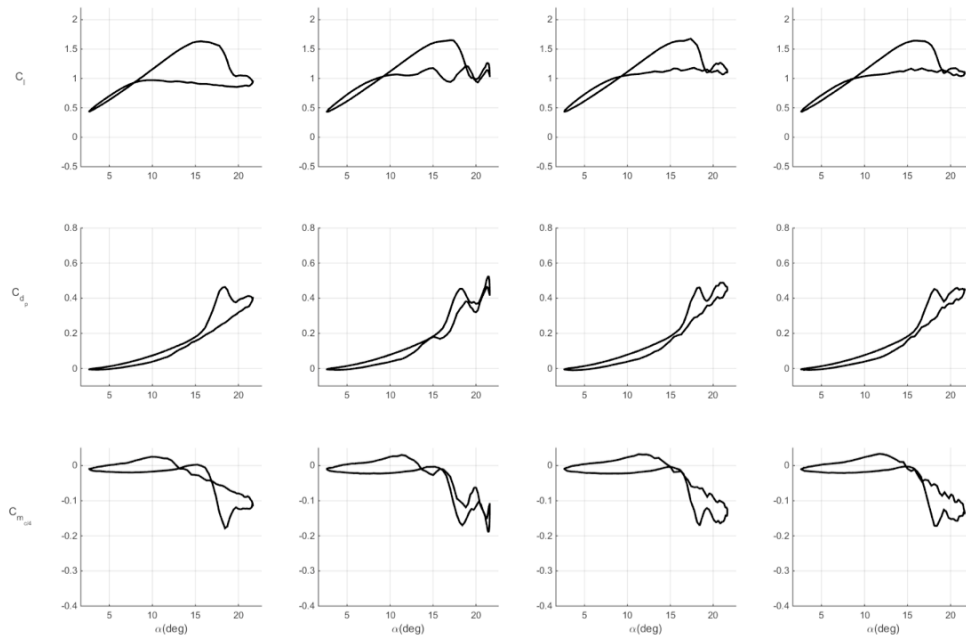


**Figure 536. Unsteady aerodynamic loads with respect to angle-of-attack.  $M=0.4$ ,  $\alpha=12^\circ \pm 9.5^\circ$ ,  $k=0.05$ . Baseline and single-row COMPACT  $F^+=0.2-0.6$  shown in order from left to right. Note that baseline includes open slot, no clean LE baseline was data available.**



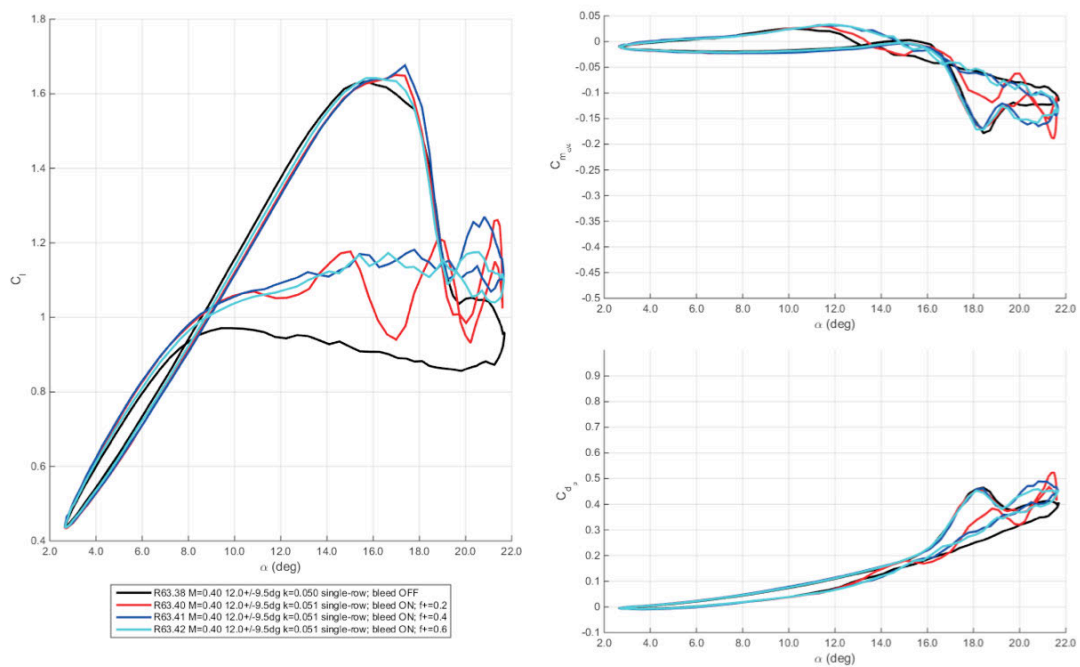


**Figure 537. Unsteady aerodynamic loads with respect to angle-of-attack. Baseline and single-row COMPACT  $F^+ = 0.2-0.6$ . Note that baseline includes open slot, no clean LE baseline was data available.**

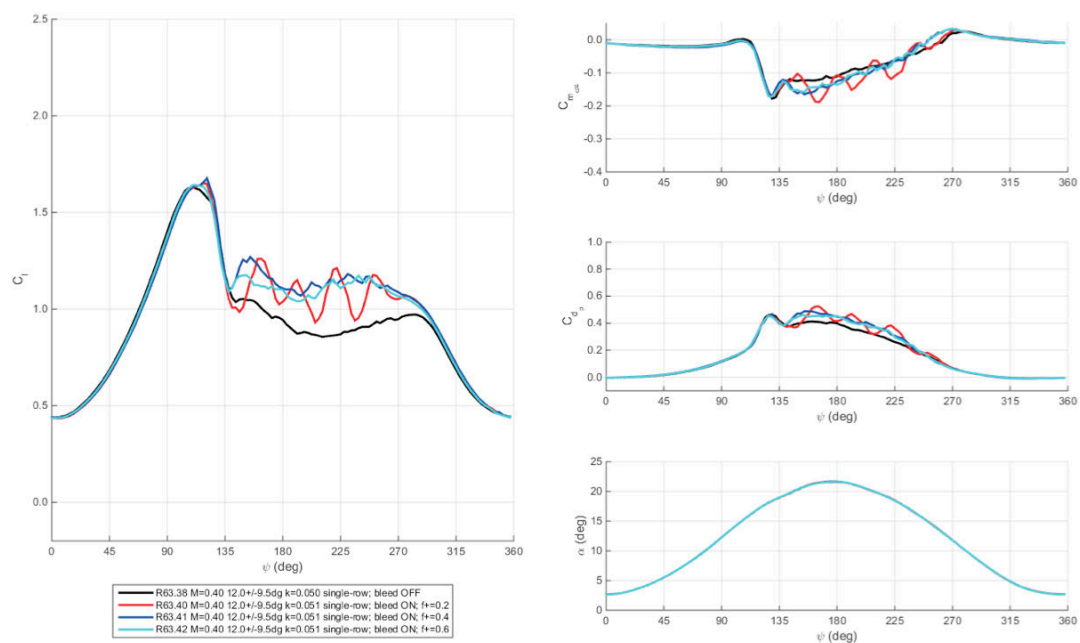


**Figure 538. Unsteady aerodynamic loads and angle-of-attack with respect to phase. Baseline and single-row COMPACT  $F^+ = 0.2-0.6$ . Note that baseline includes open slot, no clean LE baseline was data available.**

$M=0.5$

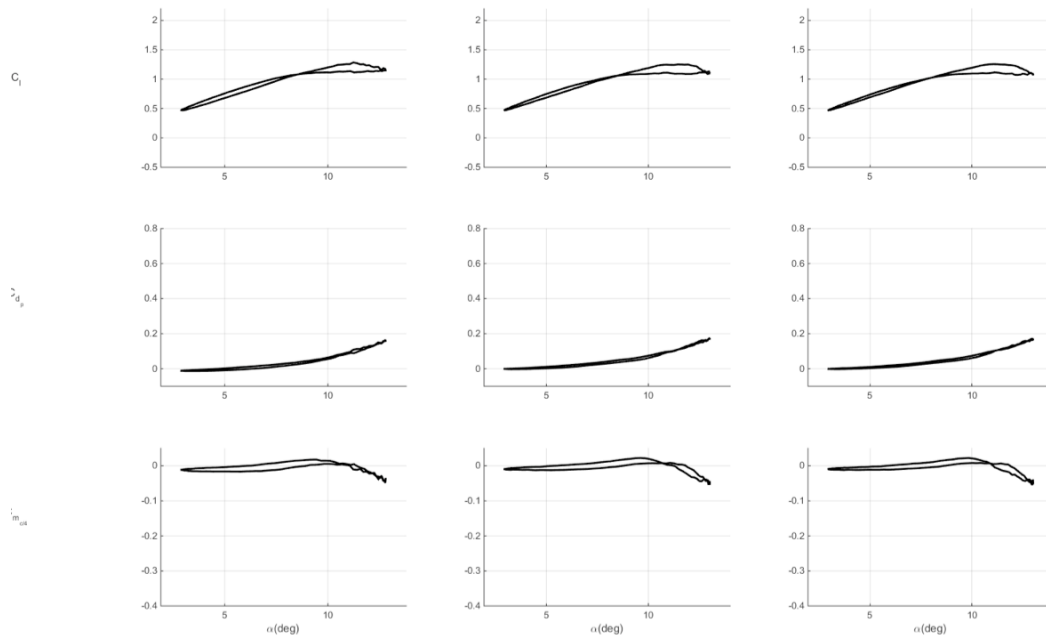


**Figure 539. Unsteady aerodynamic loads with respect to angle-of-attack.  $M=0.5$ ,  $\alpha=8^\circ \pm 5^\circ$ ,  $k=0.025$ . Baseline and single-row COMPACT  $F^+ = 0.2-0.4$  shown in order from left to right.**

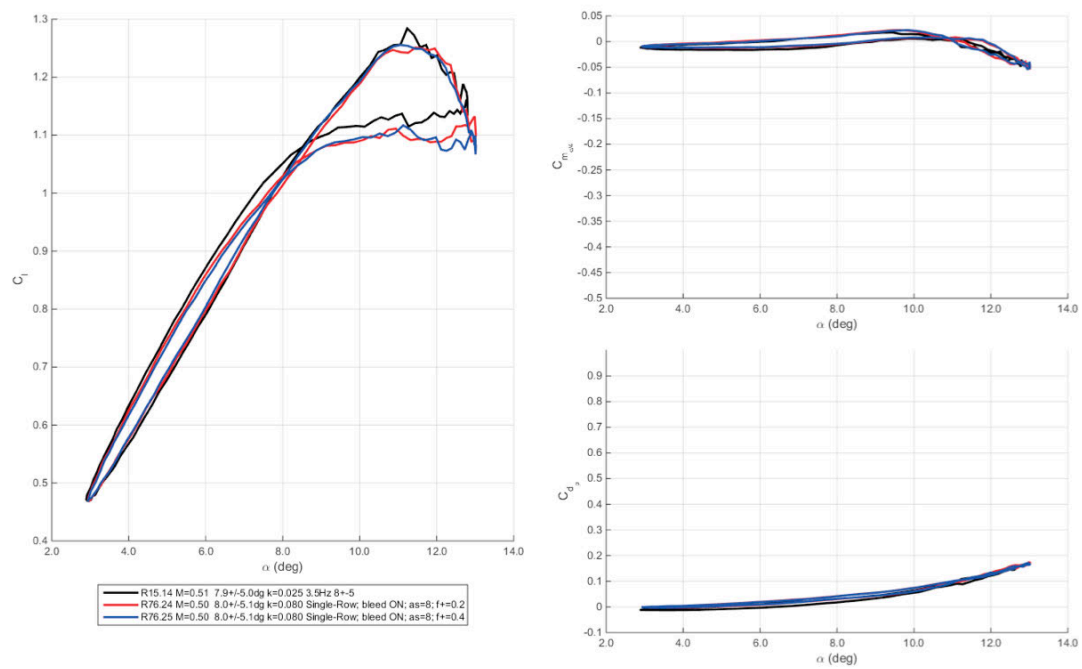


**Figure 540. Unsteady aerodynamic loads with respect to angle-of-attack. Baseline and single-row COMPACT  $F^+ = 0.2-0.4$ .**

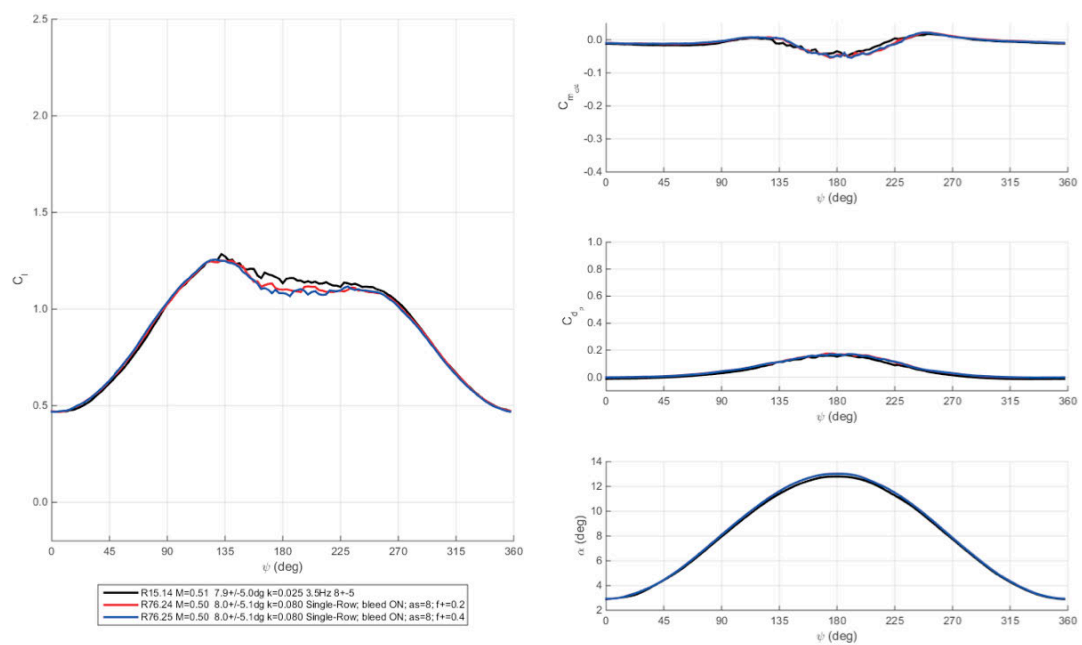


**Figure 541. Unsteady aerodynamic loads and angle-of-attack with respect to phase. Baseline and single-row COMPACT  $F^+ = 0.2-0.4$ .**

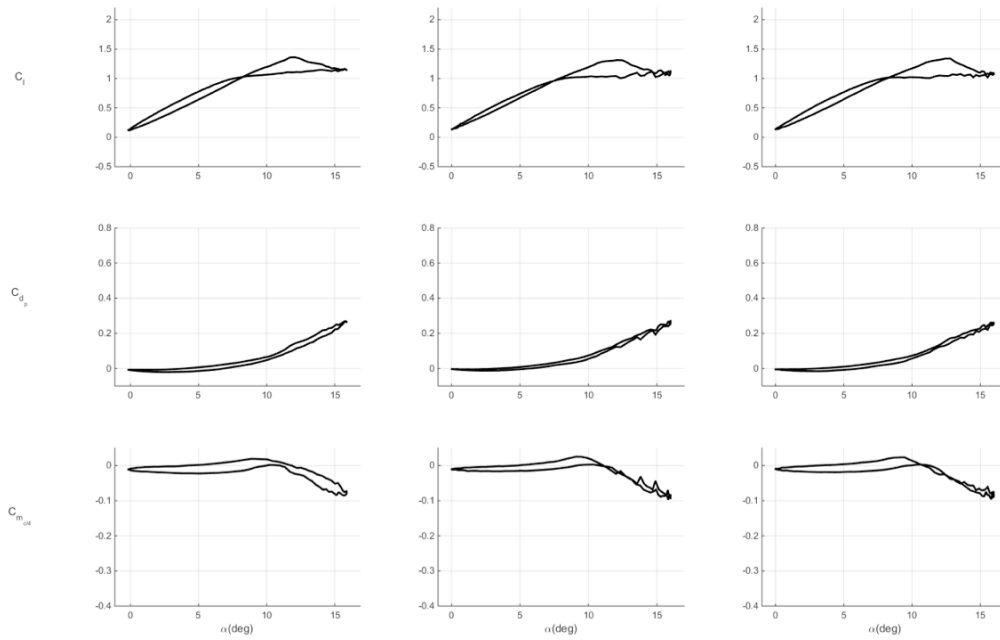


**Figure 542. Unsteady aerodynamic loads with respect to angle-of-attack.  $M=0.5$ ,  $\alpha=8^\circ \pm 8^\circ$ ,  $k=0.025$ . Baseline and single-row COMPACT  $F^+=0.2-0.4$  shown in order from left to right.**

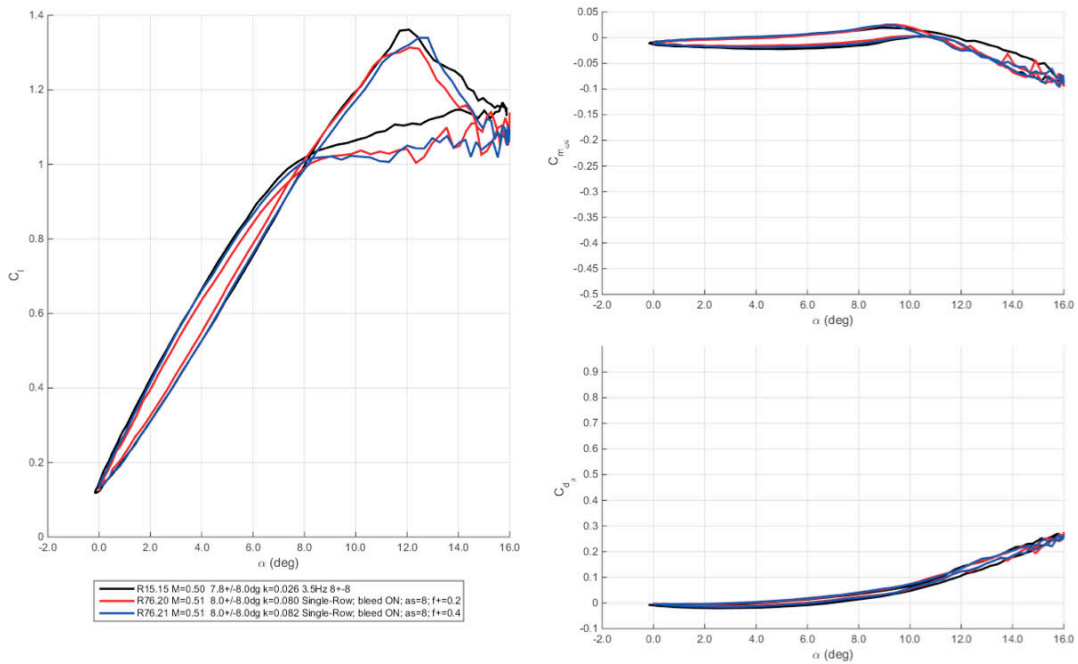


**Figure 543. Unsteady aerodynamic loads with respect to angle-of-attack. Baseline and single-row COMPACT  $F^+=0.2-0.4$ .**

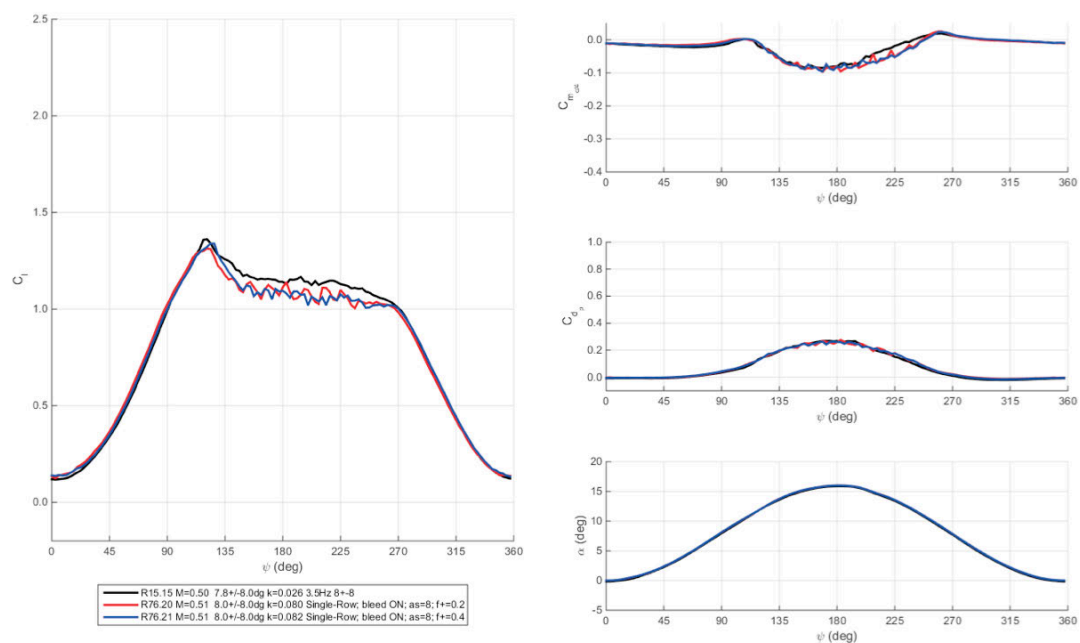


**Figure 544. Unsteady aerodynamic loads and angle-of-attack with respect to phase. Baseline and single-row COMPACT  $F^+ = 0.2-0.4$ .**



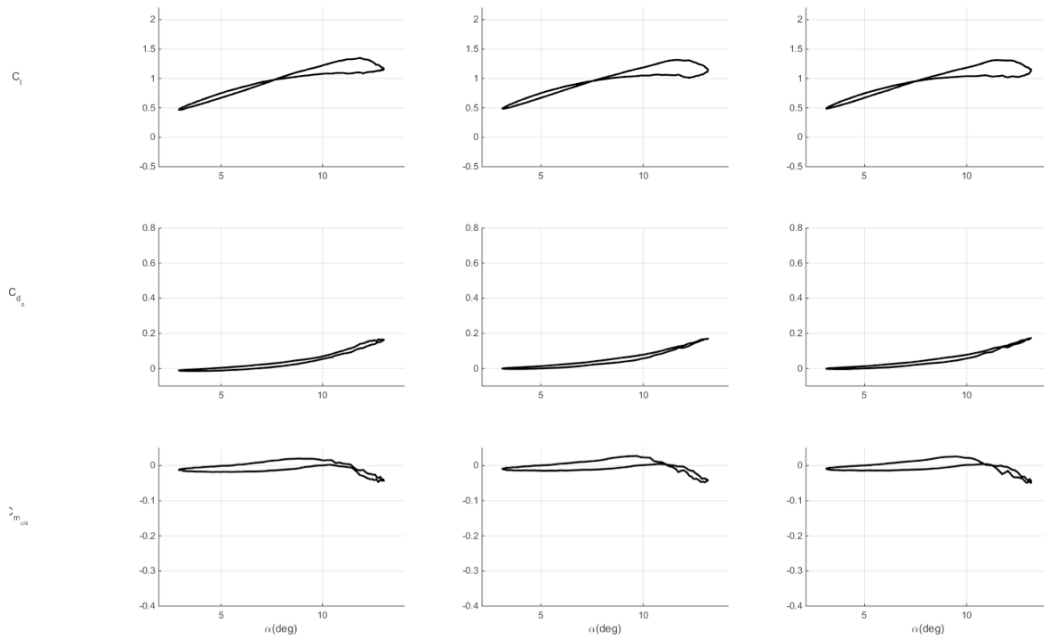


**Figure 545. Unsteady aerodynamic loads with respect to angle-of-attack.  $M=0.5$ ,  $\alpha=8^\circ \pm 5^\circ$ ,  $k=0.05$ . Baseline and single-row COMPACT  $F^+ = 0.2-0.4$  shown in order from left to right.**

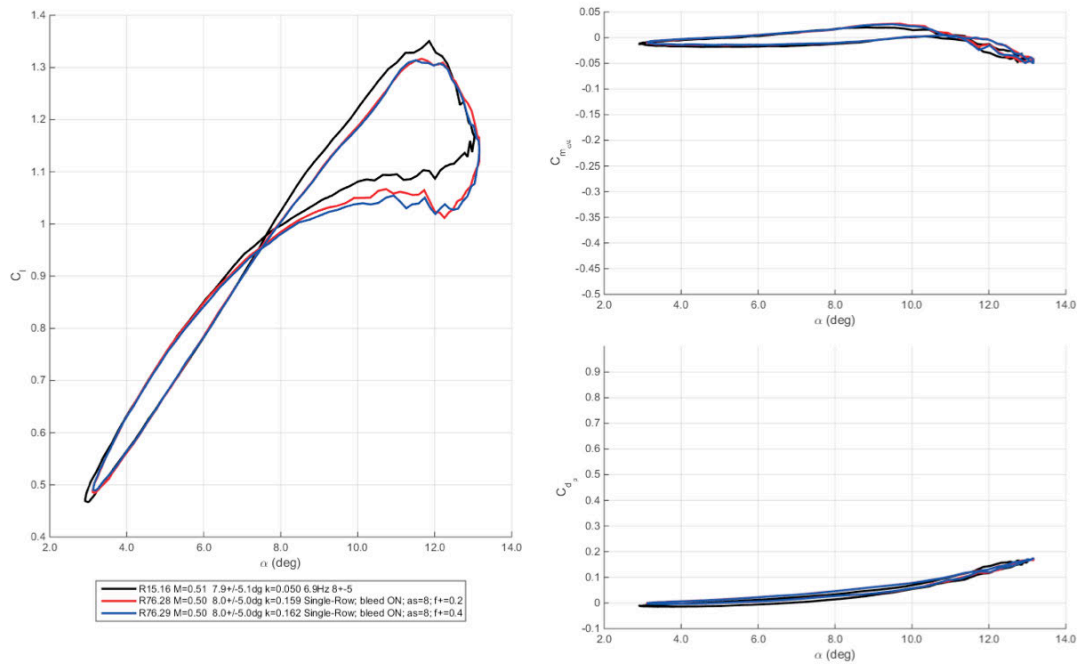


**Figure 546. Unsteady aerodynamic loads with respect to angle-of-attack. Baseline and single-row COMPACT  $F^+ = 0.2-0.4$ .**

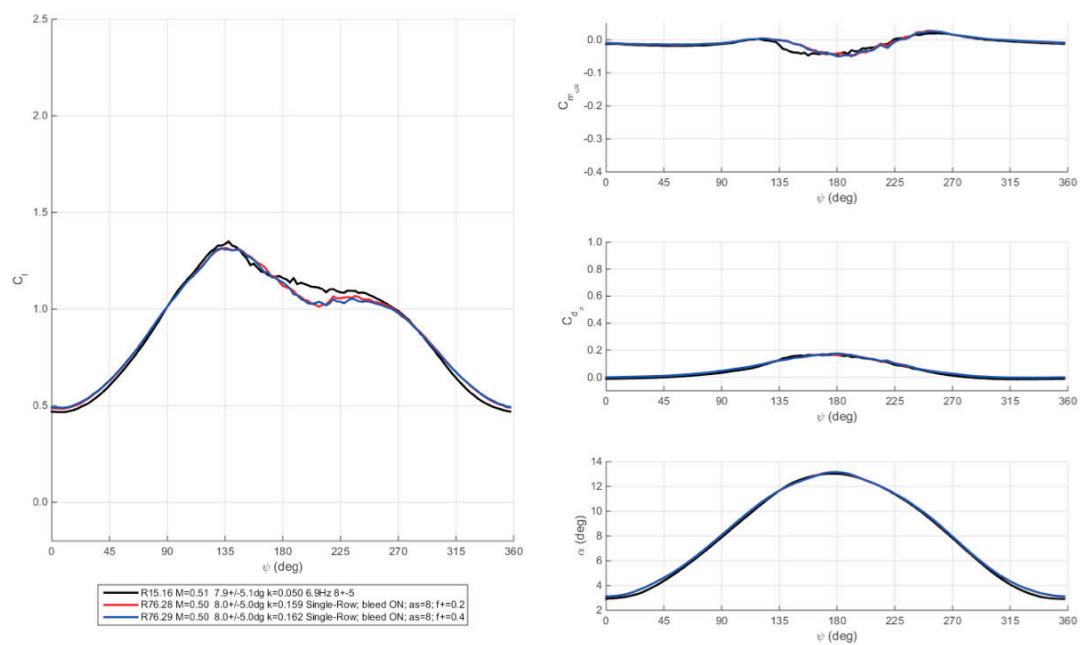


**Figure 547. Unsteady aerodynamic loads and angle-of-attack with respect to phase. Baseline and single-row COMPACT  $F^+ = 0.2-0.4$ .**

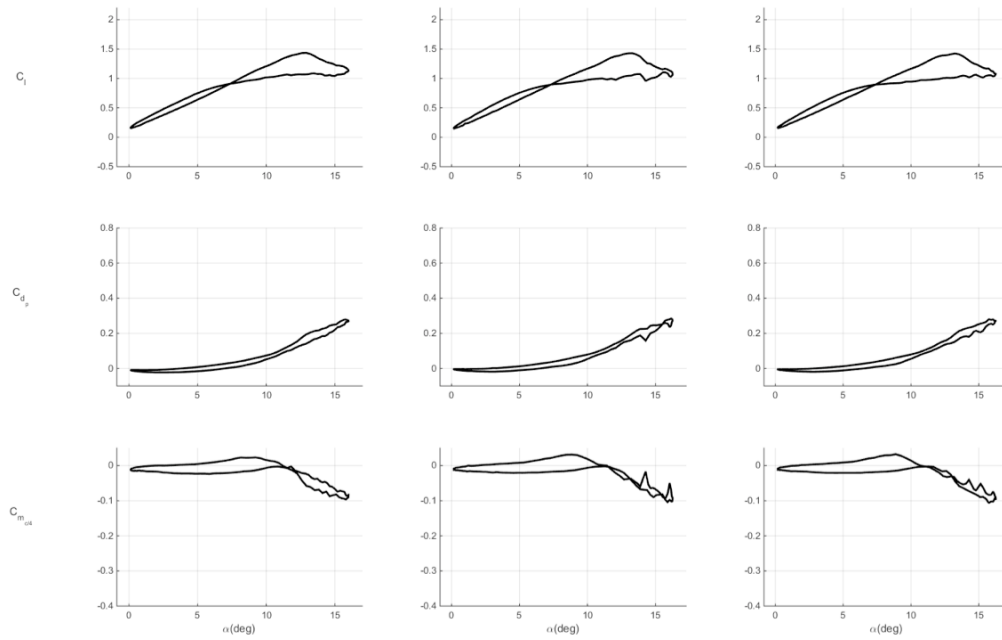


**Figure 548. Unsteady aerodynamic loads with respect to angle-of-attack.  $M=0.5$ ,  $\alpha=8^\circ \pm 8^\circ$ ,  $k=0.05$ . Baseline and single-row COMPACT  $F^+=0.2-0.4$  shown in order from left to right.**

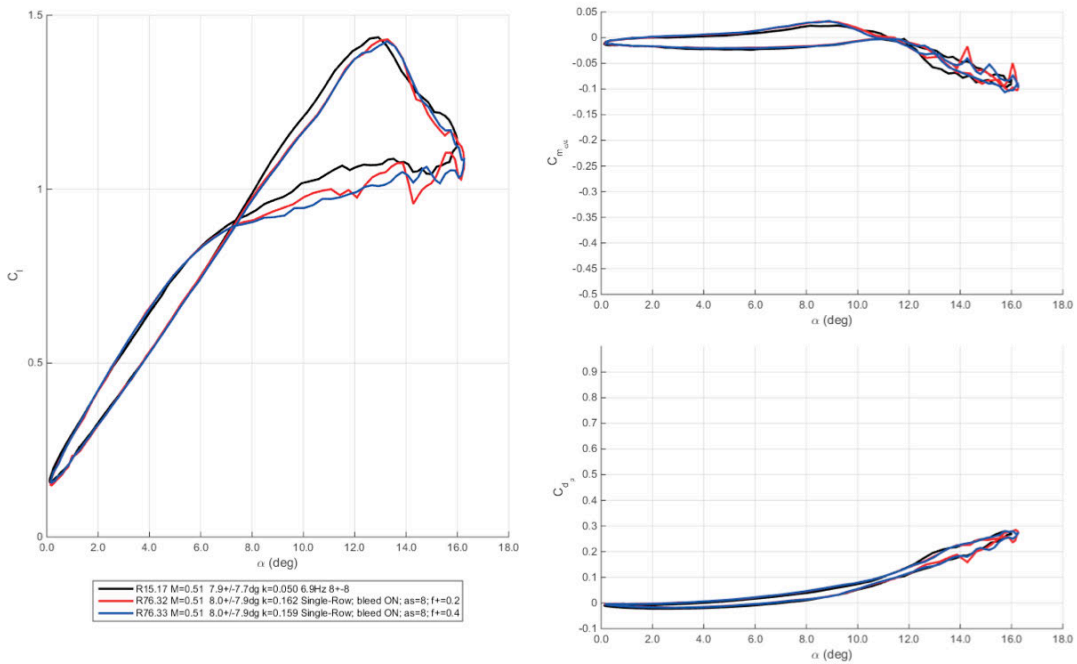


**Figure 549. Unsteady aerodynamic loads with respect to angle-of-attack. Baseline and single-row COMPACT  $F^+=0.2-0.4$ .**

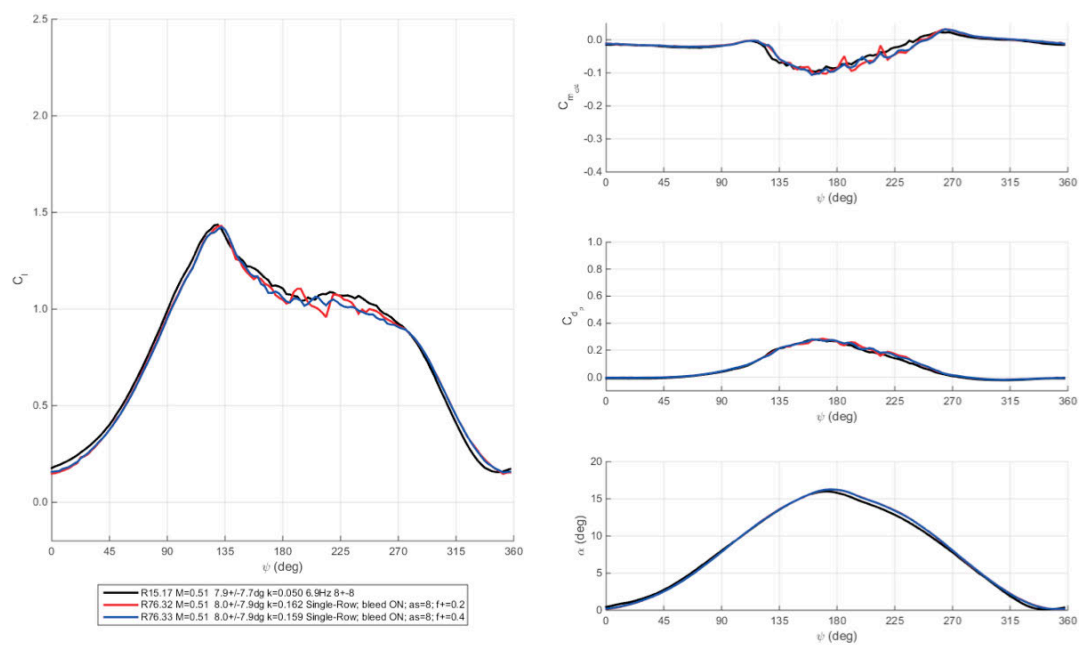


**Figure 550. Unsteady aerodynamic loads and angle-of-attack with respect to phase. Baseline and single-row COMPACT  $F^+ = 0.2-0.4$ .**

## Summary of Results

**Table 57. Summary of key metrics for Mach 0.2 Single-Row COMPACT data sets.**

$M$	$k$	$\alpha_0(^{\circ})$	$\alpha_1(^{\circ})$	Geom	$F^+$	$N_{pulses}$	$\alpha_{start}$	$C_{l,avg}$	$C_{l,max}$	$C_{d,p,avg}$	$C_{d,p,max}$	$C_{m,c/4}$	$C_{m,c/4}^e$	$C_{m,c/4}^{min}$
0.20	0.070	10.00	9.99	Clean	NA	NA	NA	0.95	1.87	0.14	0.57	-0.02	-0.23	
0.20	0.071	10.00	9.98	Single-Row	0.2	8	10	4%	-3%	-1%	-7%	12%	-12%	
0.20	0.071	10.01	9.99	Single-Row	0.4	17	10	9%	0%	-1%	0%	-10%	0%	
0.20	0.071	10.02	9.99	Single-Row	0.6	25	10	12%	2%	-4%	-11%	-41%	-45%	
0.20	0.071	10.01	9.99	Single-Row	0.8	35	10	12%	2%	-6%	-18%	-58%	-57%	
0.20	0.071	10.02	9.99	Single-Row	1.0	44	10	16%	4%	-7%	-28%	-73%	-70%	
0.20	0.100	10.08	9.93	Clean	NA	NA	NA	0.97	1.89	0.15	0.51	-0.03	-0.20	
0.20	0.101	10.05	9.99	Single-Row	0.2	6	0	2%	2%	-6%	11%	19%	16%	
0.20	0.101	10.05	9.99	Single-Row	0.4	12	0	7%	11%	-7%	12%	-5%	17%	
0.20	0.102	10.05	9.98	Single-Row	0.6	18	0	10%	6%	-13%	-4%	-48%	-28%	
0.20	0.102	10.05	9.98	Single-Row	0.8	25	0	14%	10%	-13%	-7%	-57%	-46%	
0.20	0.102	10.05	9.98	Single-Row	1.0	31	0	17%	15%	-14%	-10%	-79%	-69%	
0.20	0.069	15.07	8.02	Clean	NA	NA	NA	1.22	1.92	0.25	0.74	-0.04	-0.30	
0.20	0.071	15.05	8.03	Single-Row	0.2	8	15	6%	-1%	-1%	-1%	13%	-4%	
0.20	0.071	15.05	8.03	Single-Row	0.4	17	15	8%	1%	-3%	-7%	-5%	-12%	
0.20	0.071	15.05	8.02	Single-Row	0.6	26	15	10%	3%	-4%	-5%	-23%	-11%	
0.20	0.071	15.05	8.03	Single-Row	0.8	35	15	13%	4%	-5%	2%	-33%	-9%	
0.20	0.071	15.05	8.03	Single-Row	1.0	44	15	13%	6%	-5%	1%	-37%	-8%	
0.20	0.071	15.08	9.93	Clean	NA	NA	NA	1.15	2.00	0.26	0.92	-0.05	-0.33	
0.20	0.071	15.05	9.93	Single-Row	0.2	8	15	4%	-4%	-4%	-20%	1%	-15%	
0.20	0.071	15.05	9.93	Single-Row	0.4	17	15	8%	-2%	-3%	-13%	-5%	-6%	
0.20	0.071	15.06	9.94	Single-Row	0.6	26	15	11%	3%	-3%	-14%	-15%	-10%	
0.20	0.071	15.07	9.94	Single-Row	0.8	35	15	12%	4%	-3%	-11%	-23%	-9%	
0.20	0.071	15.08	9.96	Single-Row	1.0	44	15	13%	5%	-4%	-10%	-27%	-13%	
0.20	0.099	15.04	8.02	Clean	NA	NA	NA	1.23	2.01	0.26	0.74	-0.05	-0.29	
0.20	0.101	15.03	7.97	Single-Row	0.2	6	0	2%	-4%	-5%	-5%	7%	-1%	
0.20	0.102	15.02	7.96	Single-Row	0.4	12	0	7%	2%	-4%	0%	-5%	2%	
0.20	0.102	15.02	7.95	Single-Row	0.6	18	0	10%	10%	-6%	7%	-20%	5%	
0.20	0.102	15.01	7.95	Single-Row	0.8	25	0	11%	13%	-6%	11%	-29%	0%	
0.20	0.103	15.01	7.96	Single-Row	1.0	31	0	15%	12%	-4%	13%	-33%	19%	
0.20	0.100	15.05	9.92	Clean	NA	NA	NA	1.17	2.12	0.28	0.87	-0.06	-0.32	
0.20	0.101	15.05	9.99	Single-Row	0.2	6	0	0%	-3%	-5%	-6%	6%	-1%	
0.20	0.101	15.03	9.98	Single-Row	0.4	12	0	5%	-1%	-5%	0%	-4%	4%	
0.20	0.102	15.01	9.97	Single-Row	0.6	18	0	8%	10%	-5%	8%	-16%	1%	
0.20	0.102	15.01	9.97	Single-Row	0.8	25	0	9%	15%	-6%	7%	-20%	4%	
0.19	0.103	15.01	9.96	Single-Row	1.0	31	0	14%	12%	-1%	10%	-14%	9%	

**Table 58. Summary of key metrics for Mach 0.3 Single-Row COMPACT data sets.**

$M$	$k$	$\alpha_0(^{\circ})$	$\alpha_1(^{\circ})$	Geom	$F^+$	$N_{pulses}$	$\alpha_{start}$	$C_{l,avg}$	$C_{l,avg,corr}$	$C_{l,max}$	$C_{d,p,avg}$	$C_{d,p,avg,corr}$	$C_{d,p,max}$	$C_{m,c/4}$	$C_{m,\xi,min}$
0.30	0.025	10.01	7.98	Clean	NA	NA	NA	0.97	0.97	1.76	0.08	0.08	0.40	-0.02	-0.15
0.30	0.025	10.00	7.96	Single-Row	0.2	24	10	3%	3%	-3%	29%	29%	7%	20%	18%
0.29	0.025	10.01	7.97	Single-Row	0.4	49	10	8%	8%	1%	28%	28%	12%	-6%	17%
0.29	0.025	10.01	7.98	Single-Row	0.6	74	10	8%	8%	5%	28%	28%	14%	-12%	9%
0.30	0.025	10.03	7.98	Single-Row	0.8	100	10	7%	7%	3%	25%	25%	4%	-11%	-2%
0.30	0.025	9.98	9.94	Clean	NA	NA	NA	0.87	0.87	1.91	0.10	0.10	0.51	-0.03	-0.20
0.30	0.025	9.97	9.94	Single-Row	0.2	24	10	5%	5%	-8%	24%	25%	-1%	17%	11%
0.29	0.025	9.96	9.94	Single-Row	0.4	49	10	12%	12%	3%	24%	25%	3%	-5%	0%
0.30	0.025	9.97	9.94	Single-Row	0.6	74	10	9%	9%	-2%	23%	23%	0%	-3%	8%
0.30	0.025	9.97	9.94	Single-Row	0.8	100	10	2%	2%	-3%	19%	19%	-11%	6%	-13%
0.30	0.050	10.01	7.98	Clean	NA	NA	NA	0.97	0.97	1.79	0.09	0.09	0.47	-0.02	-0.20
0.30	0.051	9.98	7.97	Single-Row	0.2	12	10	4%	4%	3%	21%	21%	2%	22%	1%
0.30	0.051	10.01	7.99	Single-Row	0.4	24	10	7%	7%	5%	20%	20%	7%	0%	0%
0.30	0.051	10.00	7.99	Single-Row	0.6	36	10	7%	7%	3%	18%	18%	-1%	-9%	0%
0.30	0.051	10.01	7.99	Single-Row	0.8	49	10	5%	5%	2%	21%	21%	-2%	7%	-9%
0.30	0.050	10.04	9.42	Clean	NA	NA	NA	0.90	0.88	1.83	0.11	0.11	0.57	-0.03	-0.25
0.30	0.051	10.10	10.01	Single-Row	0.2	12	10	3%	6%	7%	29%	21%	6%	33%	0%
0.29	0.051	10.04	9.95	Single-Row	0.4	24	10	6%	10%	4%	29%	21%	9%	17%	2%
0.30	0.050	10.04	9.96	Single-Row	0.6	36	10	4%	8%	0%	22%	15%	4%	3%	4%
0.30	0.051	10.06	9.97	Single-Row	0.8	49	10	4%	7%	3%	23%	15%	3%	9%	-10%
0.30	0.071	10.05	7.97	Clean	NA	NA	NA	0.99	0.98	1.82	0.10	0.10	0.47	-0.02	-0.20
0.30	0.071	9.93	7.98	Single-Row	0.2	8	10	1%	2%	3%	19%	21%	2%	26%	2%
0.29	0.072	9.95	7.99	Single-Row	0.4	17	10	6%	7%	1%	14%	16%	5%	-9%	7%
0.29	0.072	9.93	7.99	Single-Row	0.6	26	10	5%	6%	1%	13%	15%	-6%	-13%	-12%
0.30	0.071	9.93	7.99	Single-Row	0.8	35	10	4%	5%	2%	16%	18%	-7%	6%	-14%
0.30	0.071	9.99	9.58	Clean	NA	NA	NA	0.90	0.90	1.89	0.12	0.12	0.62	-0.03	-0.29
0.30	0.071	9.95	9.51	Single-Row	0.2	8	10	4%	4%	3%	17%	18%	-6%	19%	-13%
0.30	0.071	9.96	9.51	Single-Row	0.4	17	10	7%	7%	0%	14%	15%	0%	2%	-2%
0.30	0.071	9.95	9.51	Single-Row	0.6	26	10	6%	6%	8%	11%	12%	-2%	-7%	-18%
0.30	0.071	9.96	9.51	Single-Row	0.8	35	10	6%	5%	3%	12%	13%	-6%	2%	-18%
0.30	0.101	10.02	7.94	Clean	NA	NA	NA	1.01	1.01	1.84	0.09	0.09	0.36	-0.02	-0.14
0.30	0.102	9.99	7.83	Single-Row	0.2	6	10	1%	1%	-1%	20%	22%	14%	30%	24%
0.30	0.102	9.99	7.84	Single-Row	0.4	12	10	5%	5%	0%	14%	16%	-1%	-7%	-2%
0.30	0.102	9.98	7.83	Single-Row	0.6	18	10	6%	6%	0%	13%	15%	2%	-12%	-28%
0.29	0.102	9.97	7.83	Single-Row	0.8	25	10	5%	4%	0%	20%	22%	13%	15%	3%
0.30	0.101	10.14	9.31	Clean	NA	NA	NA	0.97	0.96	1.93	0.11	0.10	0.51	-0.03	-0.22
0.30	0.101	9.97	9.35	Single-Row	0.2	6	10	2%	3%	0%	17%	20%	4%	19%	-12%
0.30	0.101	9.96	9.36	Single-Row	0.4	12	10	3%	4%	-1%	15%	18%	-1%	9%	-23%
0.30	0.101	9.96	9.35	Single-Row	0.6	18	10	5%	6%	0%	15%	18%	2%	3%	-12%
0.30	0.101	9.95	9.36	Single-Row	0.8	25	10	4%	5%	0%	15%	18%	5%	8%	-5%
0.30	0.025	15.00	7.98	Clean	NA	NA	NA	1.12	1.12	1.91	0.19	0.19	0.53	-0.04	-0.19
0.30	0.025	15.02	8.00	Single-Row	0.2	25	15	7%	7%	-5%	20%	20%	15%	19%	21%
0.30	0.025	15.00	7.98	Single-Row	0.4	50	15	9%	9%	-2%	19%	19%	7%	2%	1%
0.30	0.025	15.00	7.99	Single-Row	0.6	75	15	11%	11%	-3%	17%	17%	10%	-15%	-16%
0.30	0.025	15.00	7.99	Single-Row	0.8	100	15	10%	10%	-4%	18%	18%	4%	-8%	5%
0.30	0.050	15.10	8.00	Clean	NA	NA	NA	1.14	1.14	1.87	0.20	0.20	0.64	-0.05	-0.27
0.30	0.051	14.99	7.90	Single-Row	0.2	12	15	9%	9%	-1%	19%	21%	14%	15%	6%
0.29	0.051	15.03	7.95	Single-Row	0.4	25	15	13%	13%	3%	20%	22%	5%	3%	2%
0.30	0.050	15.01	7.94	Single-Row	0.6	37	15	9%	9%	-1%	15%	16%	0%	-4%	-3%
0.30	0.050	15.04	7.96	Single-Row	0.8	50	15	5%	5%	0%	10%	12%	-6%	-3%	-14%
0.30	0.071	15.15	7.95	Clean	NA	NA	NA	1.19	1.18	2.04	0.22	0.21	0.78	-0.05	-0.34
0.30	0.071	15.04	7.94	Single-Row	0.2	8	15	0%	0%	-1%	6%	7%	-15%	2%	-21%
0.29	0.071	15.05	7.95	Single-Row	0.4	17	15	3%	4%	-1%	8%	9%	-13%	-4%	-17%
0.29	0.071	15.06	7.97	Single-Row	0.6	26	15	4%	5%	-3%	9%	10%	-10%	-4%	-10%
0.29	0.072	15.06	7.97	Single-Row	0.8	35	15	3%	4%	-4%	8%	9%	-7%	-5%	-8%

**Table 59. Summary of key metrics for Mach 0.4 Single-Row COMPACT data sets.**

$M$	$k$	$\alpha_0(^{\circ})$	$\alpha_1(^{\circ})$	Geom	$F^+$	$N_{pulses}$	$\alpha_{start}$	$C_{l,avg}$	$C_{l,avg,corr}$	$C_{l,max}$	$C_{d,p,avg}$	$C_{d,p,avg,corr}$	$C_{d,p,max}$	$C_{m,c/4}$	$C_{m,c/4,min}$
0.40	0.025	9.84	8.09	Clean	NA	NA	NA	0.93	0.94	1.55	0.11	0.11	0.33	-0.03	-0.12
0.40	0.025	10.02	8.00	Single-Row	0.2	24	10	3%	2%	-3%	8%	6%	21%	4%	24%
0.39	0.025	10.01	7.99	Single-Row	0.4	49	10	5%	4%	-2%	5%	4%	12%	-10%	6%
0.39	0.025	10.01	7.99	Single-Row	0.6	74	10	4%	3%	-3%	5%	3%	10%	-8%	16%
0.40	0.050	9.99	8.00	Clean	NA	NA	NA	0.91	0.92	1.62	0.11	0.11	0.37	-0.03	-0.14
0.40	0.051	10.09	7.89	Single-Row	0.2	12	10	5%	4%	-3%	5%	4%	4%	-11%	5%
0.39	0.051	10.14	7.93	Single-Row	0.4	25	10	7%	6%	-2%	5%	4%	3%	-15%	-1%
0.40	0.051	10.14	7.95	Single-Row	0.6	37	10	7%	6%	-2%	5%	4%	5%	-15%	-3%
0.40	0.051	9.96	9.86	Clean	NA	NA	NA	0.82	0.85	1.70	0.13	0.12	0.43	-0.04	-0.17
0.39	0.051	10.12	9.41	Single-Row	0.2	12	10	10%	6%	-5%	7%	8%	11%	-2%	12%
0.39	0.051	10.14	9.41	Single-Row	0.4	25	10	11%	7%	-5%	6%	7%	4%	-7%	-6%
0.39	0.051	10.15	9.42	Single-Row	0.6	37	10	11%	7%	-5%	5%	6%	1%	-10%	-7%
0.40	0.051	9.96	9.86	Clean	NA	NA	NA	0.82	0.85	1.70	0.13	0.12	0.43	-0.04	-0.17
0.39	0.051	10.14	9.41	Single-Row	0.2	12	10	14%	10%	-3%	10%	11%	15%	2%	18%
0.39	0.051	10.16	9.42	Single-Row	0.4	25	10	15%	10%	-2%	9%	10%	5%	-3%	-3%
0.39	0.051	10.17	9.43	Single-Row	0.6	37	10	15%	11%	-2%	9%	10%	9%	-5%	1%
0.40	0.070	10.03	7.97	Single-Row	NA	NA	NA	0.92	0.93	1.76	0.10	0.10	0.48	-0.03	-0.19
0.40	0.071	10.06	7.89	Single-Row	0.2	8	10	2%	2%	-6%	11%	12%	2%	7%	15%
0.40	0.071	10.05	7.89	Single-Row	0.4	17	10	4%	4%	-6%	10%	10%	1%	-2%	10%
0.39	0.071	10.05	7.89	Single-Row	0.6	26	10	4%	4%	-6%	9%	9%	1%	-6%	11%
0.40	0.071	10.17	9.49	Single-Row	NA	NA	NA	0.84	0.84	1.72	0.12	0.12	0.57	-0.03	-0.23
0.40	0.071	10.16	9.44	Single-Row	0.2	8	10	6%	6%	-1%	8%	8%	2%	14%	7%
0.40	0.071	10.16	9.43	Single-Row	0.4	17	10	7%	7%	-1%	5%	6%	1%	2%	8%
0.40	0.071	10.15	9.43	Single-Row	0.6	26	10	8%	7%	0%	5%	6%	0%	3%	7%
0.40	0.050	12.15	7.92	Single-Row	NA	NA	NA	0.98	0.98	1.60	0.14	0.14	0.43	-0.04	-0.16
0.40	0.051	12.11	7.89	Single-Row	0.2	12	0	7%	7%	0%	8%	9%	14%	9%	14%
0.40	0.051	12.13	7.91	Single-Row	0.4	25	0	8%	8%	0%	9%	9%	2%	6%	-5%
0.40	0.051	12.13	7.91	Single-Row	0.6	37	0	8%	8%	0%	7%	8%	-1%	3%	-10%
0.40	0.050	12.19	9.50	Single-Row	NA	NA	NA	0.91	0.91	1.63	0.16	0.16	0.46	-0.04	-0.18
0.40	0.051	12.13	9.47	Single-Row	0.2	12	12	6%	6%	1%	9%	10%	13%	15%	6%
0.39	0.051	12.16	9.49	Single-Row	0.4	25	12	9%	9%	3%	9%	10%	5%	7%	-4%
0.39	0.051	12.17	9.50	Single-Row	0.6	37	12	7%	8%	1%	8%	8%	-1%	7%	-4%

**Table 60. Summary of key metrics for Mach 0.5 Single-Row COMPACT data sets.**

$M$	$k$	$\alpha_0(^{\circ})$	$\alpha_1(^{\circ})$	Geom	$F^+$	$N_{pulses}$	$\alpha_{start}$	$C_{l,avg}$	$C_{l,max}$	$C_{d,p,avg}$	$C_{d,p,max}$	$C_{m,c/4}$	$C_{m,c/4,min}$
0.50	0.026	7.86	8.01	Clean	NA	NA	NA	0.80	1.36	0.08	0.27	-0.02	-0.08
0.50	0.080	8.00	7.99	Single-Row	0.2	25	8	-2%	-4%	6%	3%	10%	14%
0.50	0.082	8.00	7.99	Single-Row	0.4	50	8	-2%	-2%	5%	-2%	12%	13%
0.50	0.025	7.85	4.95	Clean	NA	NA	NA	0.92	1.28	0.05	0.16	-0.01	-0.05
0.50	0.080	7.98	5.04	Single-Row	0.2	25	8	-1%	-3%	24%	6%	-8%	13%
0.50	0.080	7.98	5.04	Single-Row	0.4	50	8	-1%	-2%	23%	5%	-8%	14%
0.50	0.050	8.06	7.94	Clean	NA	NA	NA	0.80	1.44	0.08	0.28	-0.02	-0.10
0.50	0.162	8.21	8.06	Single-Row	0.2	12	8	-2%	0%	8%	2%	1%	8%
0.50	0.159	8.22	8.05	Single-Row	0.4	25	8	-2%	-1%	8%	0%	2%	10%
0.50	0.050	7.98	5.06	Clean	NA	NA	NA	0.91	1.35	0.05	0.17	-0.01	-0.05
0.50	0.159	8.14	5.02	Single-Row	0.2	12	8	0%	-3%	17%	3%	-29%	0%
0.50	0.162	8.14	5.02	Single-Row	0.4	25	8	0%	-3%	17%	5%	-25%	5%

**COMPACT Dual-Row**

**Table 61. COMPACT Dual-Row Unsteady Data Points Acquired**

Run	Mach	k	$\alpha_0$	$\alpha_1$	$F^+$	Pulse Start	Config	Points
						$\alpha$		
80	0.3	0.07	10	9.5	0.2-0.8	10	Front	8-11
	0.3	0.07	10	9.5	0.2-0.8	10	Back	12,14-16
	0.3	0.07	10	9.5	0.2-0.8	10	Both	17-20
	0.3	0.07	10	9.5	0.2-0.8	10	Alt 50	21-24
89	0.4	0.05	10	9.5	0.2-0.6	10	Front	10-12
	0.4	0.05	10	9.5	0.2-0.6	10	Back	13-15
	0.4	0.05	10	9.5	0.2-0.6	10	Both	16,18,19
	0.4	0.05	10	9.5	0.2-0.6	10	Alt 50	20-22
	0.4	0.05	10	9.5	0.2	10	Alt 2	23
	0.4	0.05	10	9.5	0.4	10	Alt 4	25
	0.4	0.05	10	9.5	0.6	10	Alt 6	26
	0.4	0.05	10	9.5	0.2	10	Alt 4	27
	0.4	0.05	10	9.5	0.4	10	Alt 8	28
	0.4	0.05	10	9.5	0.6	10	Alt 12	29
	0.2	0.07	10	10	0.2-1.0	10	Front	8-12
	0.2	0.07	10	10	0.2-1.0	10	Back	13-17
	0.2	0.07	10	10	0.2-1.0	10	Both	20-24
	0.2	0.07	10	10	0.2-1.0	10	Alt 50	25-29
92	0.5	0.025	8	8	0.2,0.4	8	Front	5-6
	0.5	0.025	8	8	0.2,0.4	8	Back	7-8
	0.5	0.025	8	8	0.2,0.4	8	Both	9-10
	0.5	0.025	8	8	0.2,0.4	8	Alt 50	11-12



## Open Slot and Bleed Effects for Dual-Row Datasets

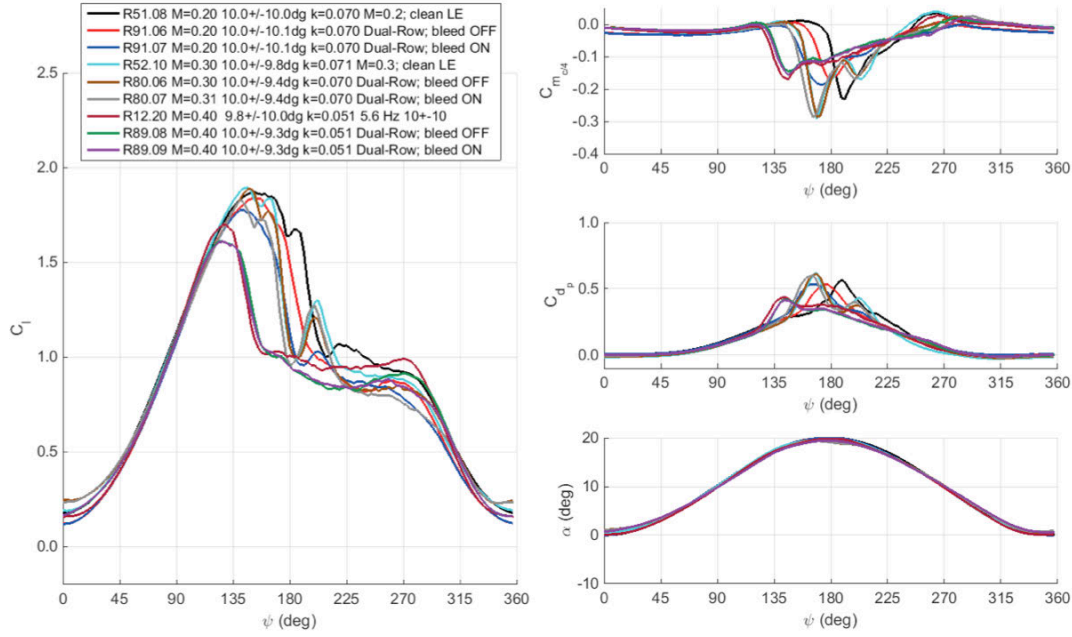


Figure 551.  $C_l$ ,  $C_d$ ,  $C_m$  and  $\alpha$  for  $\alpha = 10^\circ \pm \sim 9.5^\circ$  for Mach 0.2, 0.3, and 0.4. Results for the clean VR-12 and dual-row no-bleed and bleed-on cases are shown.

M=0.2

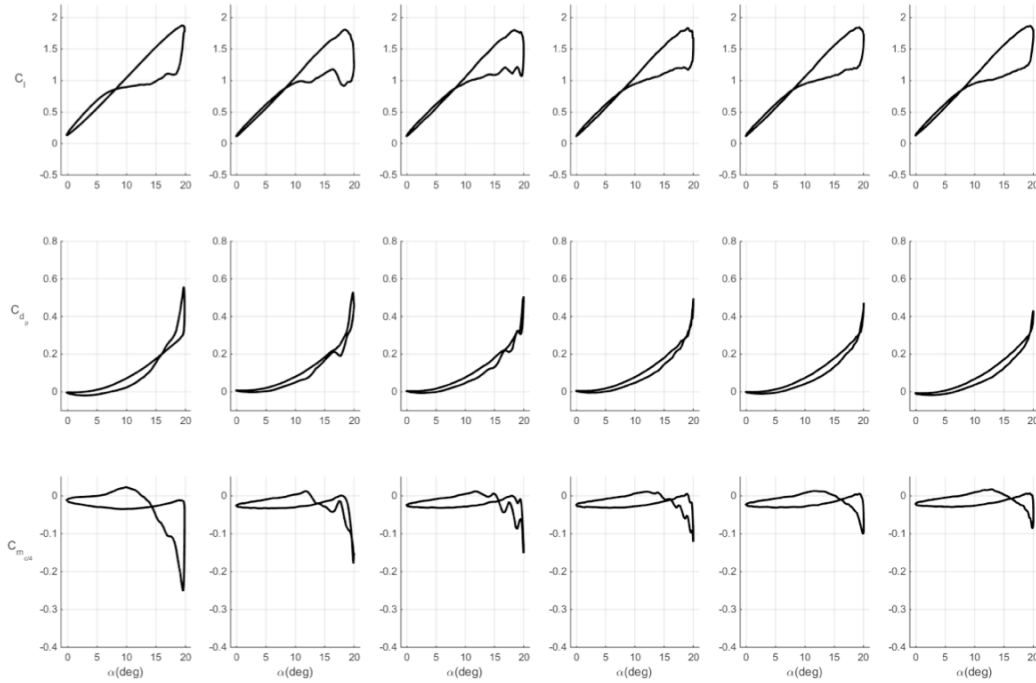
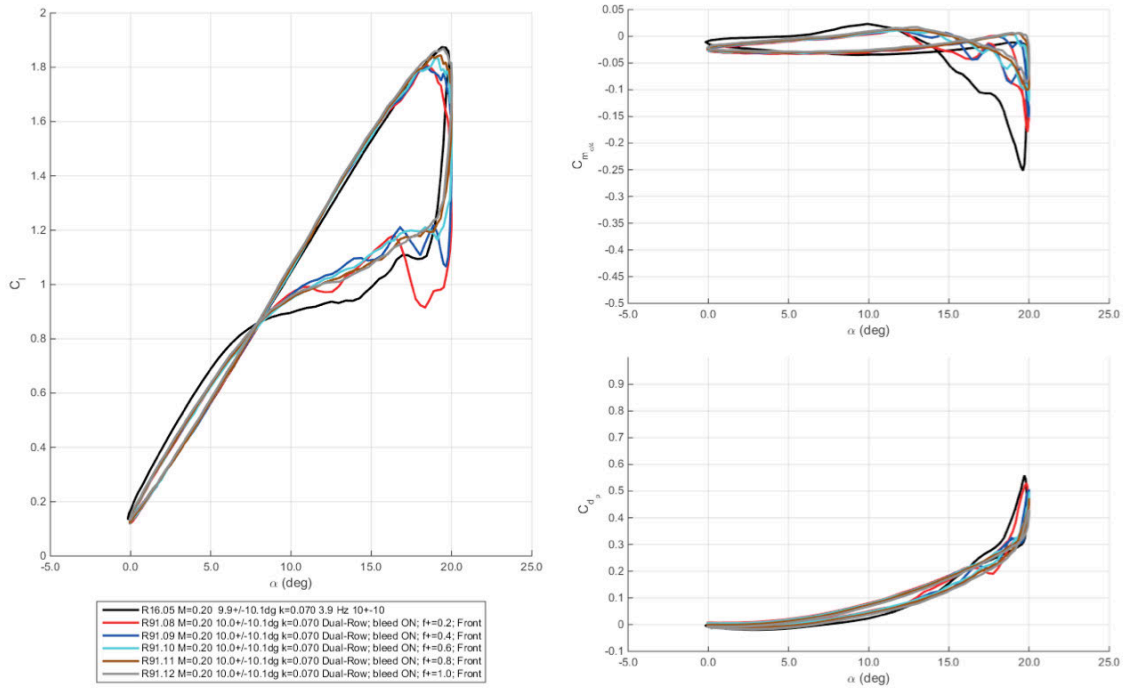
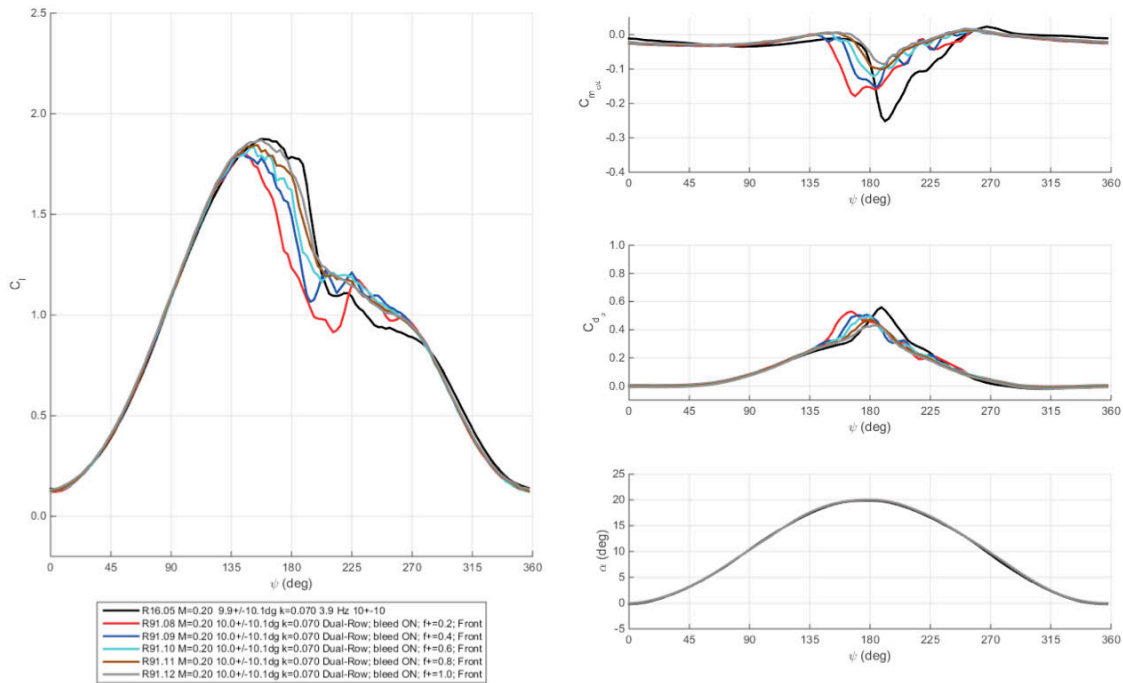


Figure 552. Lift, drag, and moment coefficients at Mach 0.2,  $\alpha = 10^\circ \pm 10^\circ$ ,  $k = 0.07$  for baseline and dual-row COMPACT,  $F^+$  of 0.2 to 1.0. Front actuator only.

## Back Row



**Figure 553. Lift, drag, and moment coefficients at Mach 0.2,  $\alpha = 10^\circ \pm 10^\circ$ ,  $k = 0.07$  for baseline and dual-row COMPACT,  $F^+$  of 0.2 to 1.0. Loads plotted vs. angle-of-attack. Front actuator only.**



**Figure 554. Lift, drag, and moment coefficients at Mach 0.2,  $\alpha = 10^\circ \pm 10^\circ$ ,  $k = 0.07$  for baseline and dual-row COMPACT,  $F^+$  of 0.2 to 1.0. Loads plotted vs. phase angle. Front actuator only.**

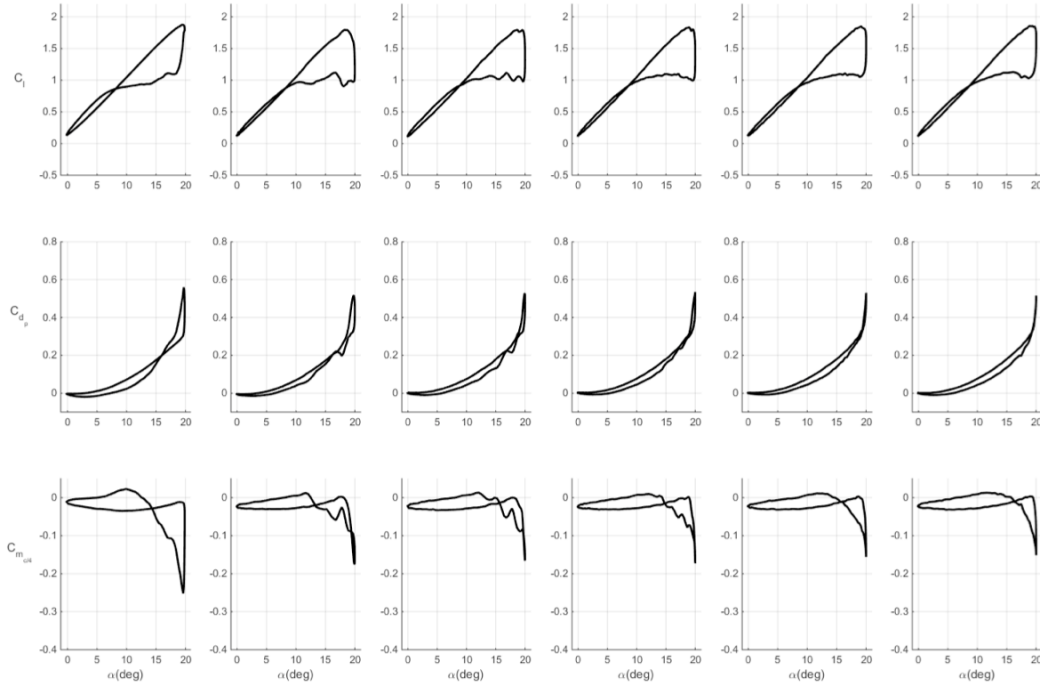


**Figure 555. Lift, drag, and moment coefficients at Mach 0.2,  $\alpha = 10^\circ \pm 10^\circ$ ,  $k = 0.07$  for baseline and dual-row COMPACT,  $F^+$  of 0.2 to 1.0. Back actuator only.**

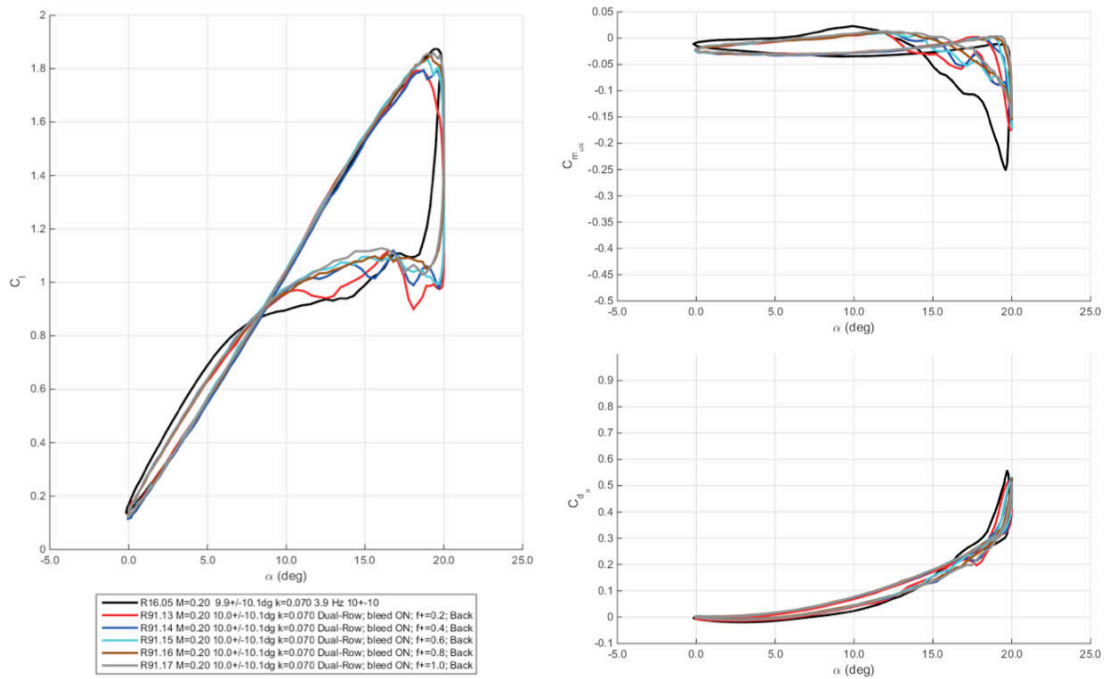


**Figure 556. Lift, drag, and moment coefficients at Mach 0.2,  $\alpha = 10^\circ \pm 10^\circ$ ,  $k = 0.07$  for baseline and dual-row COMPACT,  $F^+$  of 0.2 to 1.0. Loads plotted vs. angle-of-attack. Back actuator only.**

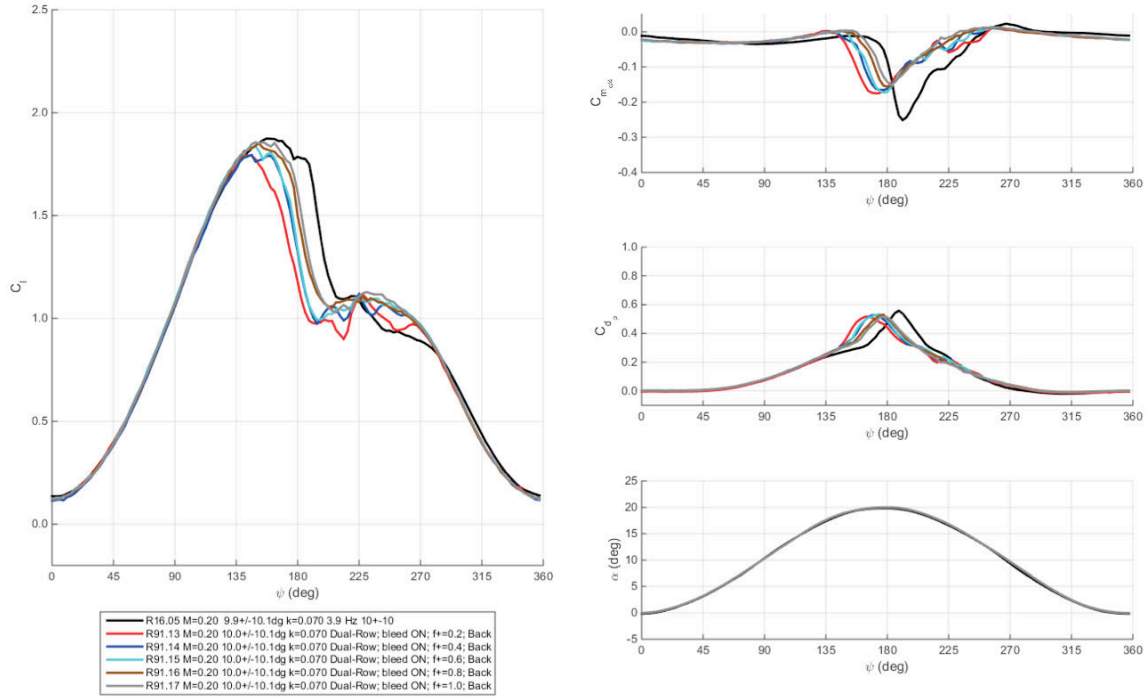


**Figure 557. Lift, drag, and moment coefficients at Mach 0.2,  $\alpha = 10^\circ \pm 10^\circ$ ,  $k = 0.07$  for baseline and dual-row COMPACT,  $F^+$  of 0.2 to 1.0. Loads plotted vs. phase angle. Back actuator only.**

## Simultaneous Slots

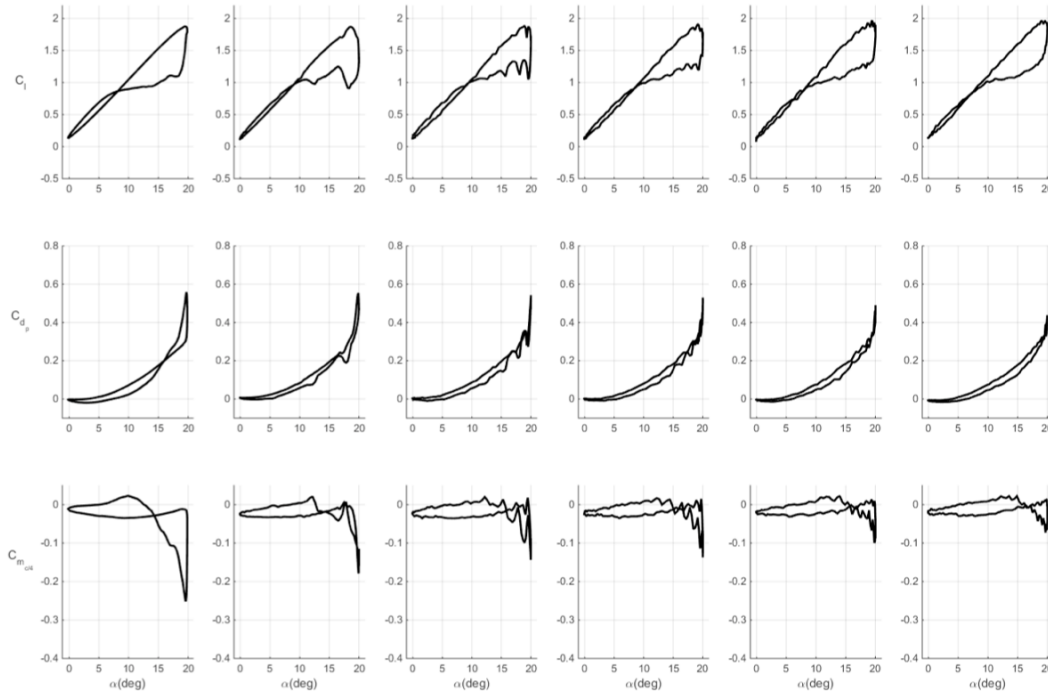


**Figure 558.** Lift, drag, and moment coefficients at Mach 0.2,  $\alpha = 10^\circ \pm 10^\circ$ ,  $k = 0.07$  for baseline and dual-row COMPACT,  $F^+$  of 0.2 to 1.0. Front and back actuators firing simultaneously.

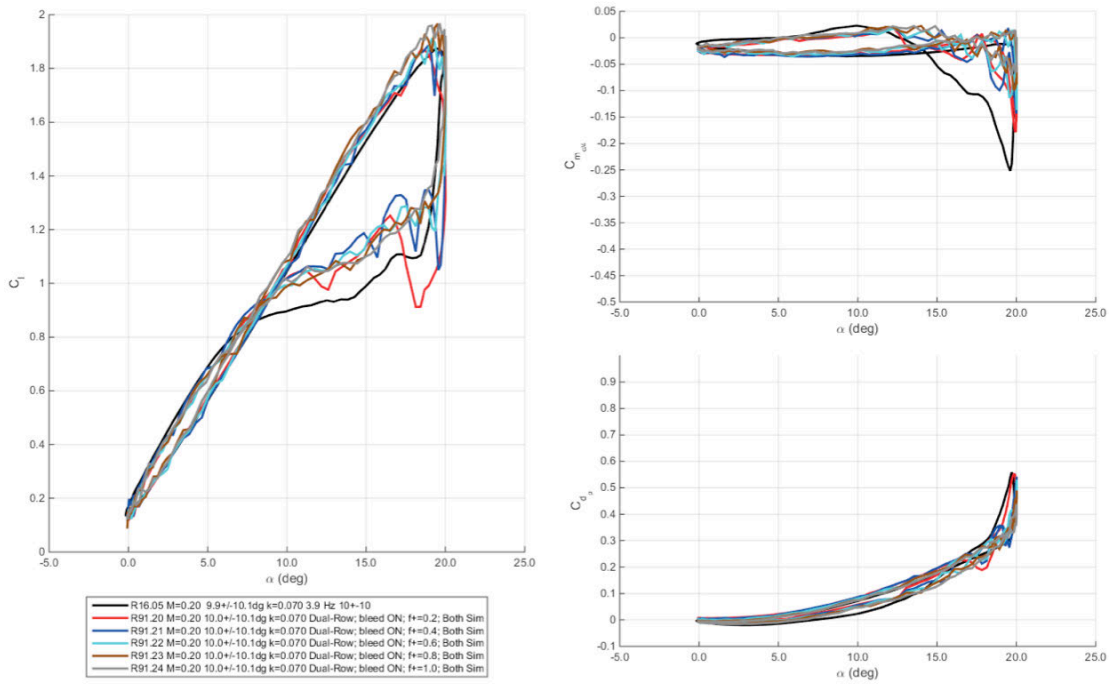


**Figure 559.** Lift, drag, and moment coefficients at Mach 0.2,  $\alpha = 10^\circ \pm 10^\circ$ ,  $k = 0.07$  for baseline and dual-row COMPACT,  $F^+$  of 0.2 to 1.0. Loads plotted vs. angle-of-attack. Front and back actuators firing simultaneously.

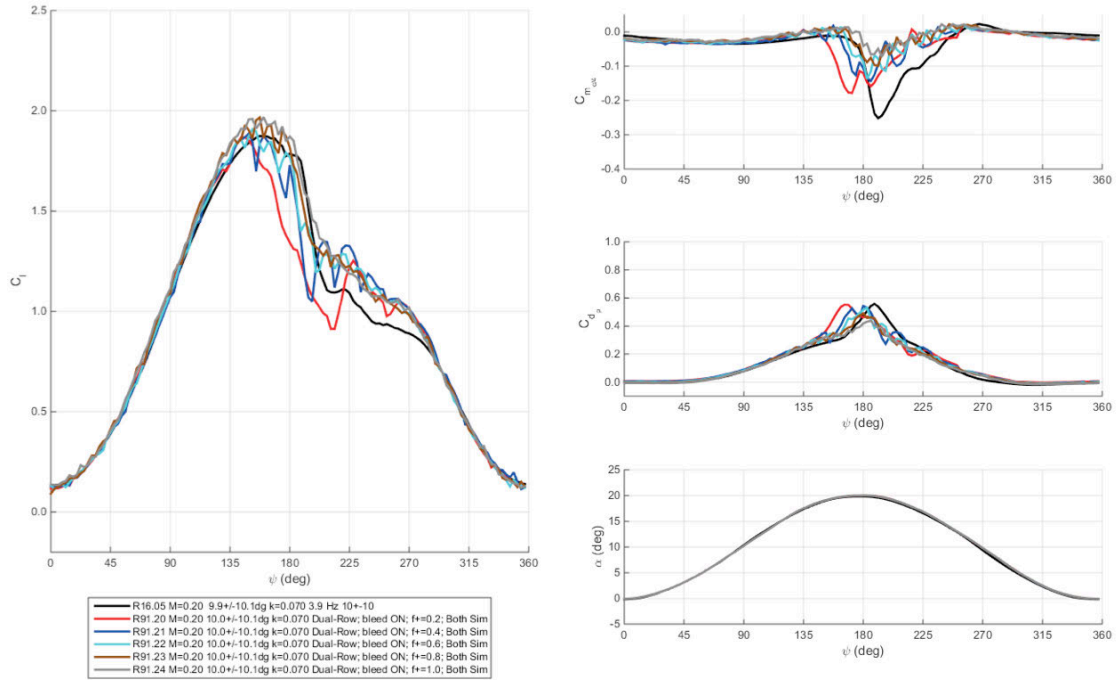


**Figure 560. Lift, drag, and moment coefficients at Mach 0.2,  $\alpha = 10^\circ \pm 10^\circ$ ,  $k = 0.07$  for baseline and dual-row COMPACT,  $F^+$  of 0.2 to 1.0. Loads plotted vs. phase angle. Front and back actuators firing simultaneously.**

## Alternating Slots

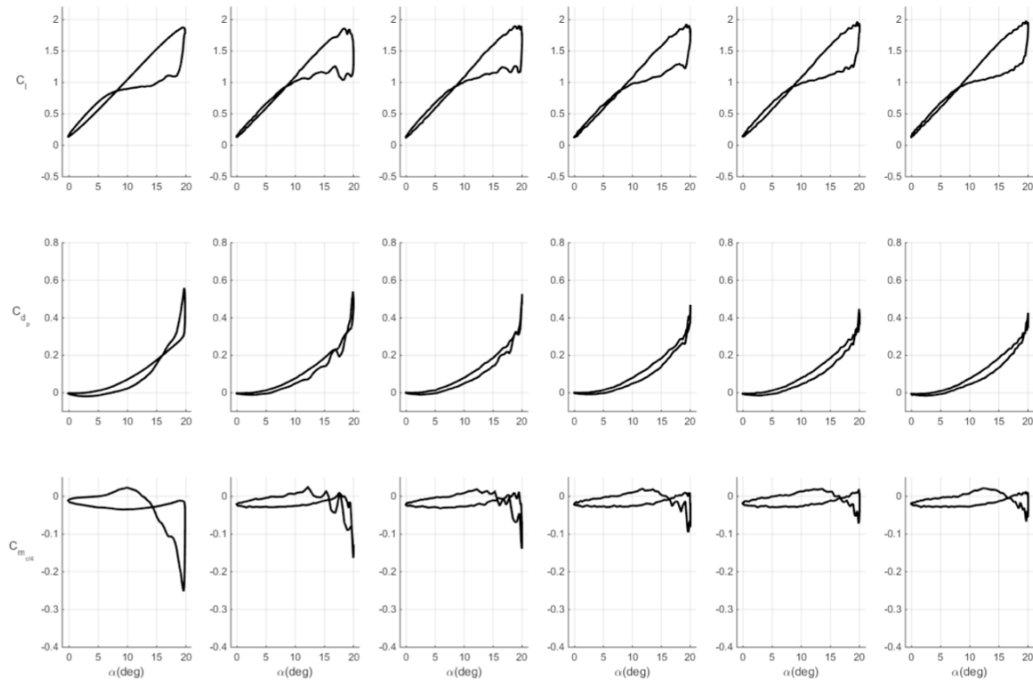


Figure 561. Lift, drag, and moment coefficients at Mach 0.2,  $\alpha = 10^\circ \pm 10^\circ$ ,  $k = 0.07$  for baseline and dual-row COMPACT,  $F^+$  of 0.2 to 1.0. Front and back actuator firing out-of-phase to double actuator pulse frequency.

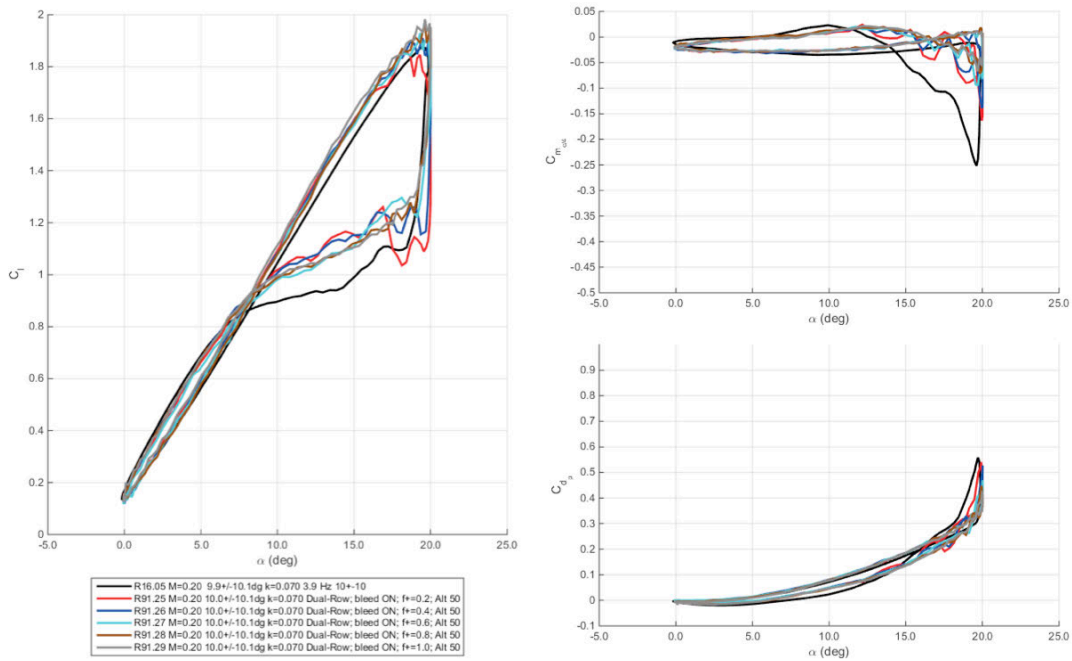
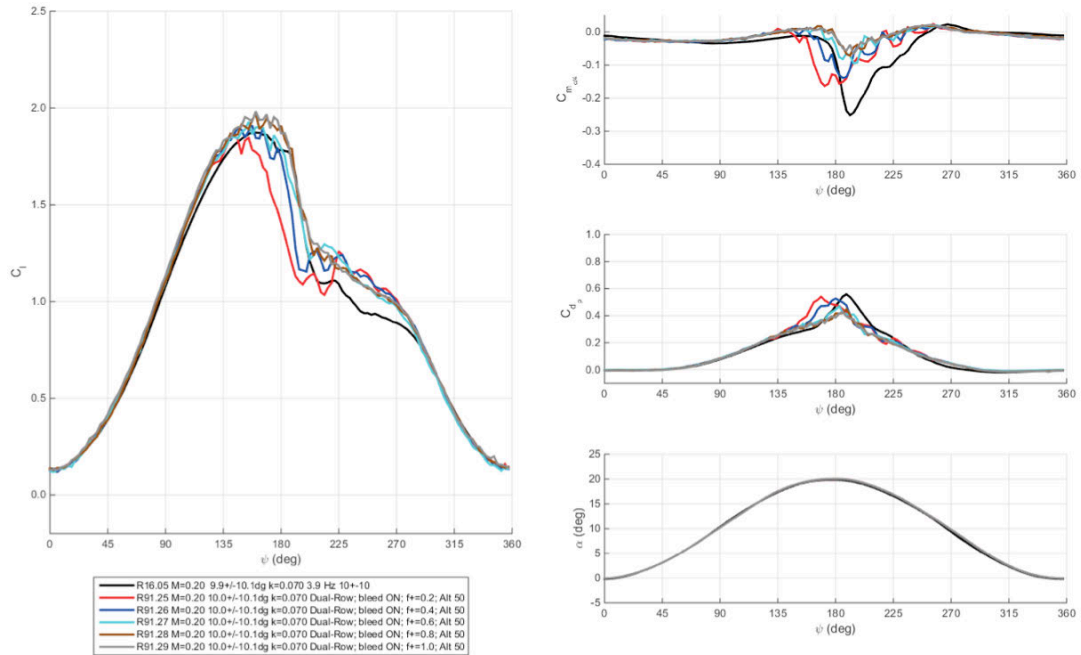


Figure 562. Lift, drag, and moment coefficients at Mach 0.2,  $\alpha = 10^\circ \pm 10^\circ$ ,  $k = 0.07$  for baseline and dual-row COMPACT,  $F^+$  of 0.2 to 1.0. Loads plotted vs. angle-of-attack. Front and back actuator firing out-of-phase to double actuator pulse frequency.



**Figure 563. Lift, drag, and moment coefficients at Mach 0.2,  $\alpha = 10^\circ \pm 10^\circ$ ,  $k = 0.07$  for baseline and dual-row COMPACT,  $F^+$  of 0.2 to 1.0. Loads plotted vs. phase angle. Front and back actuator firing out-of-phase to double actuator pulse frequency.**



## Comparison of Configurations

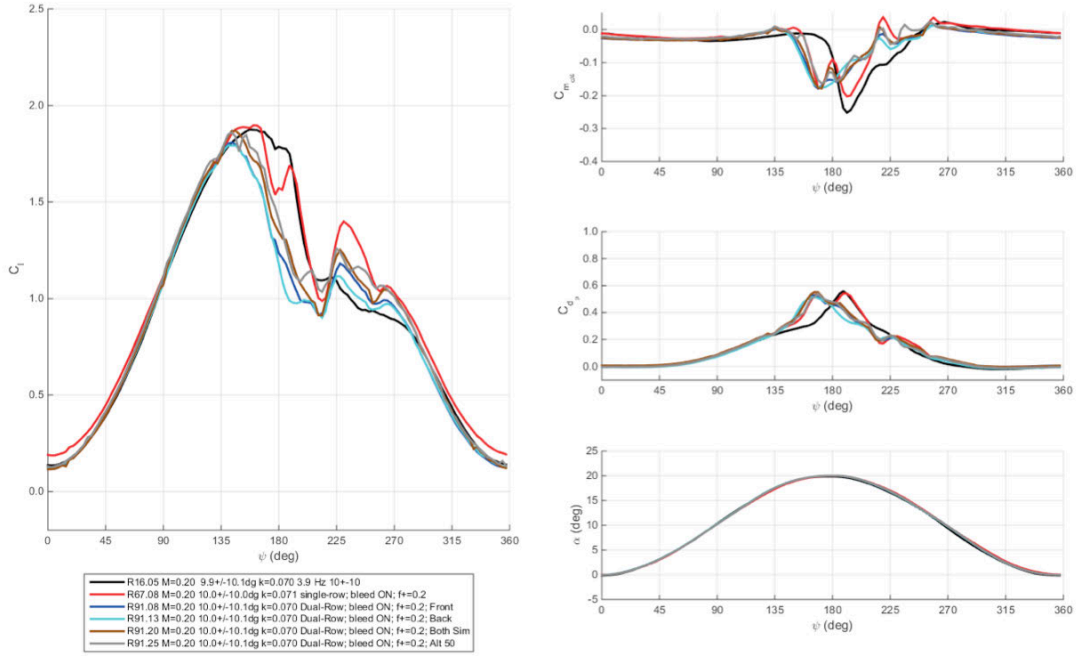


**Figure 564.** Lift, drag, and moment coefficients at Mach 0.2,  $\alpha = 10^\circ \pm 10^\circ$ ,  $k = 0.07$ ,  $F^+ = 0.2$  for baseline and multiple COMPACT modes.

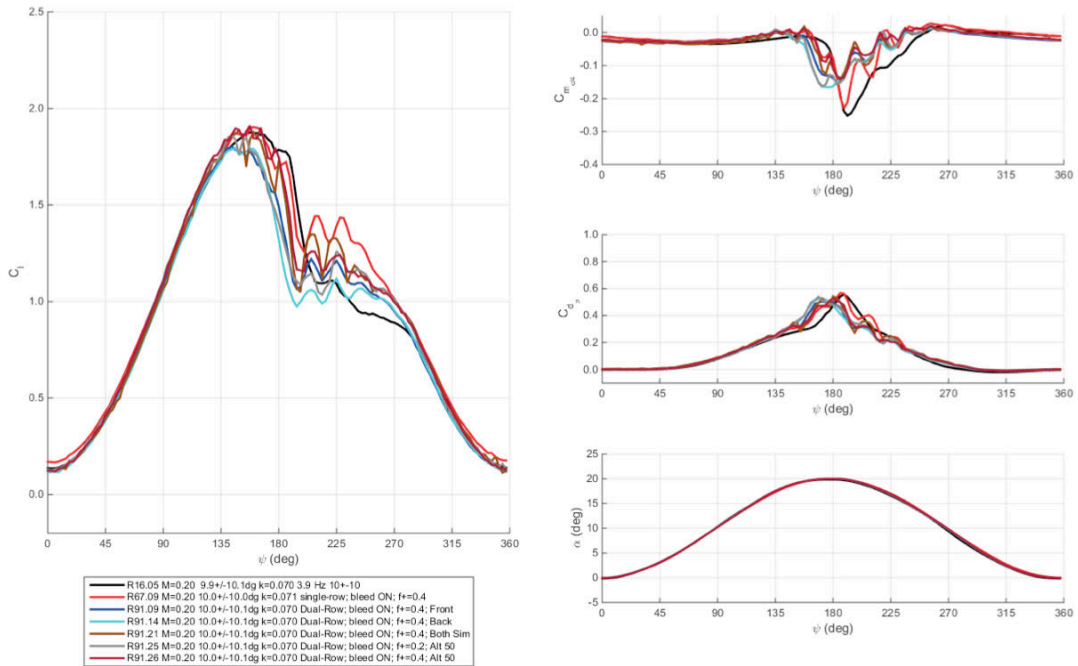


**Figure 565.** Lift, drag, and moment coefficients at Mach 0.2,  $\alpha = 10^\circ \pm 10^\circ$ ,  $k = 0.07$ ,  $F^+ = 0.4$  for baseline and multiple COMPACT modes.

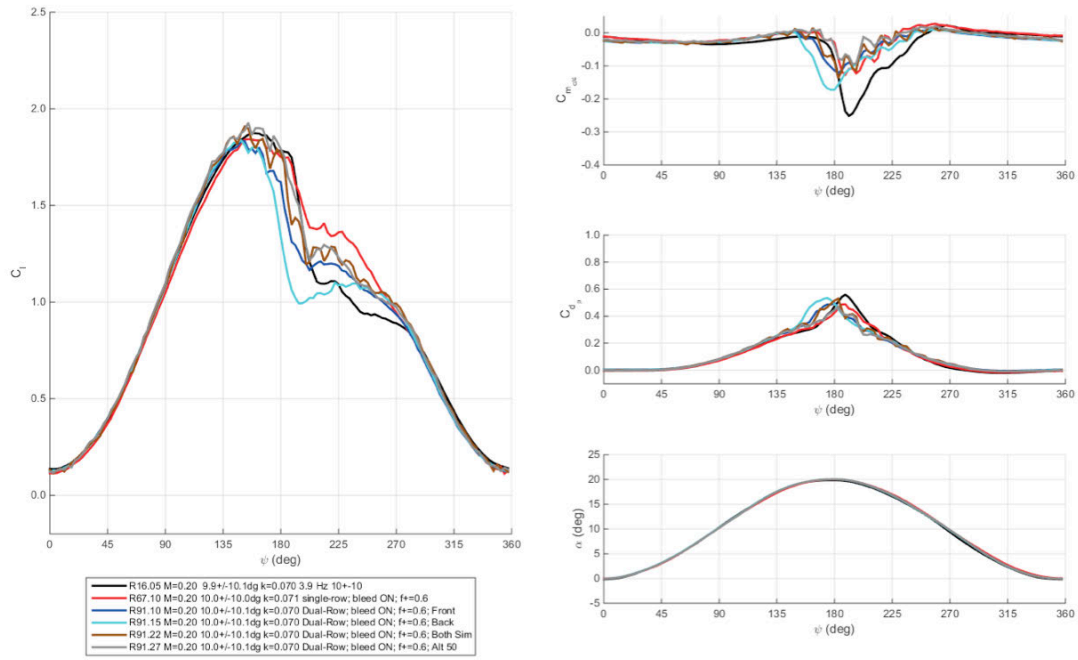


**Figure 566. Lift, drag, and moment coefficients at Mach 0.2,  $\alpha = 10^\circ \pm 10^\circ$ ,  $k = 0.07$ ,  $F^+ = 0.6$  for baseline and multiple COMPACT modes.**

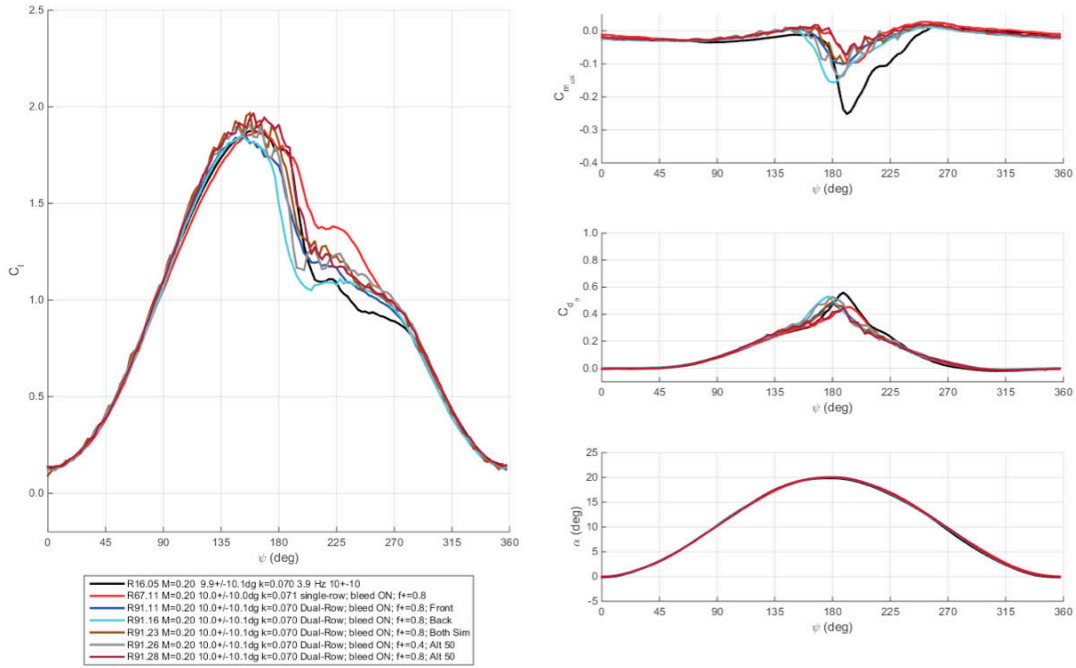


**Figure 567. Lift, drag, and moment coefficients at Mach 0.2,  $\alpha = 10^\circ \pm 10^\circ$ ,  $k = 0.07$ ,  $F^+ = 0.8$  for baseline and multiple COMPACT modes.**

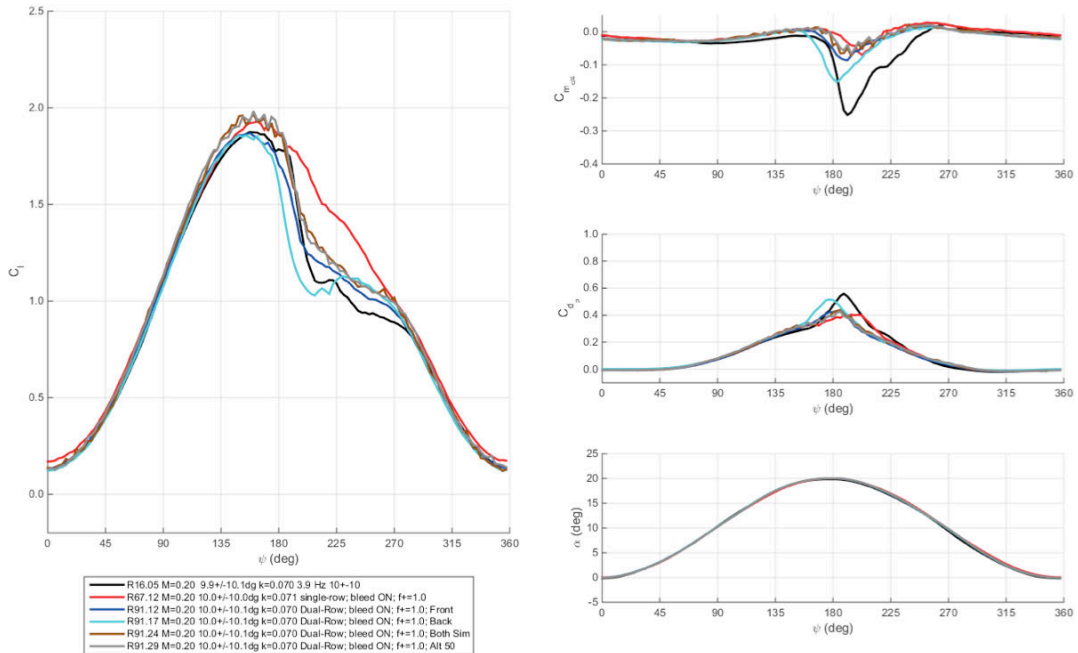


**Figure 568. Lift, drag, and moment coefficients at Mach 0.2,  $\alpha = 10^\circ \pm 10^\circ$ ,  $k = 0.07$ ,  $F^+ = 1.0$  for baseline and multiple COMPACT modes. Loads plotted vs. angle-of-attack.**

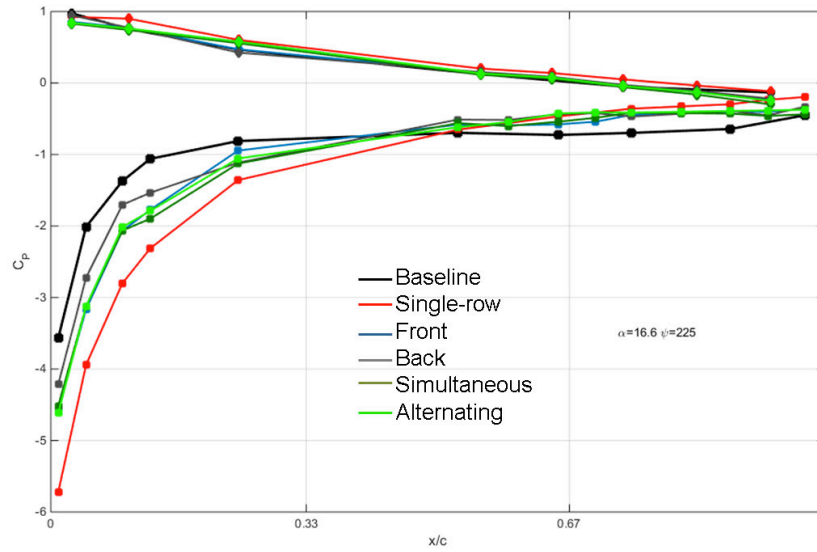


**Figure 569. Downstroke,  $\alpha = 16.6^\circ$ , ensemble averaged  $C_p$  for  $F^+ = 1.0$  and multiple COMPACT configurations.**

**M=0.3**

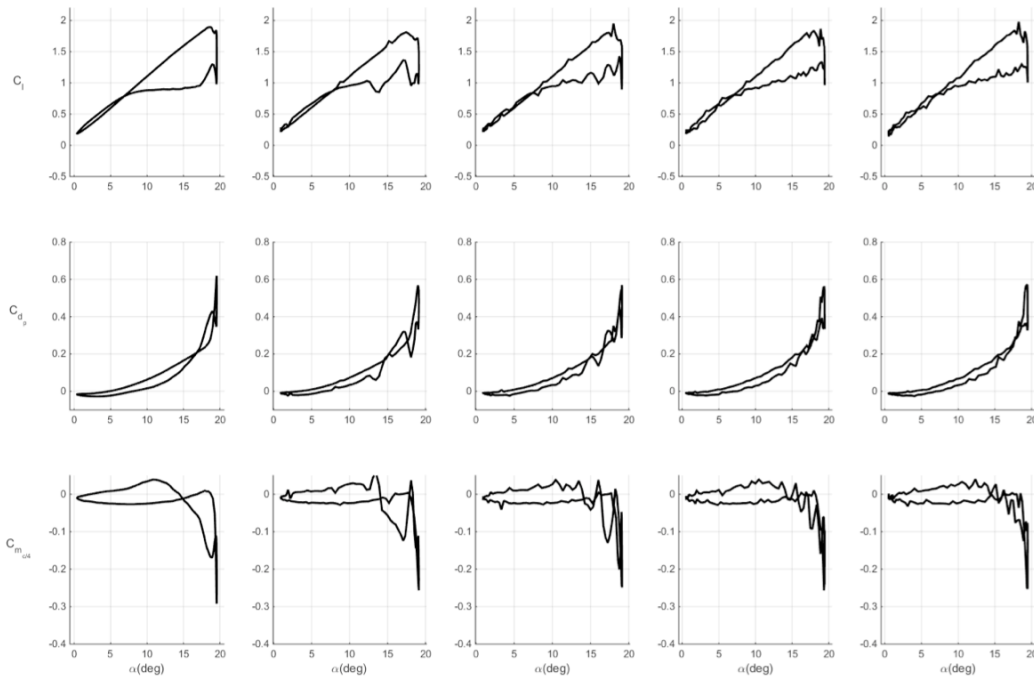


**Figure 570. Lift, drag, and moment coefficients at Mach 0.3,  $\alpha = 10^\circ \pm 9.5^\circ$ ,  $k = 0.07$  for baseline and dual-row COMPACT,  $F^+$  of 0.2 to 0.8. Front actuator only.**

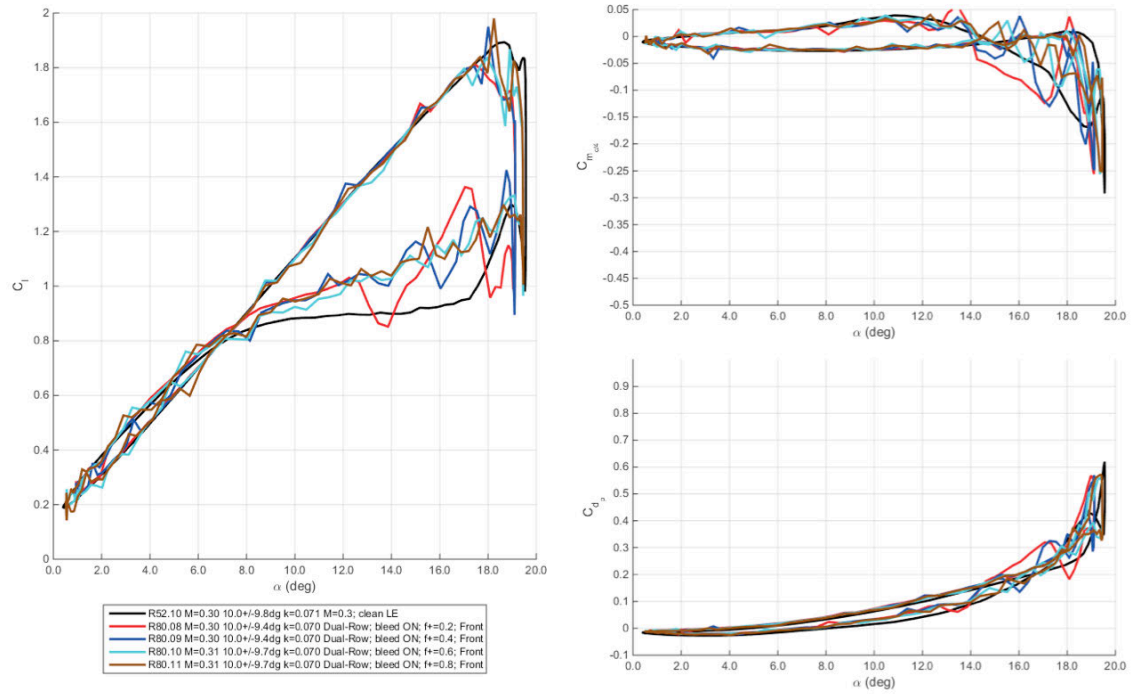


**Figure 571. Lift, drag, and moment coefficients at Mach 0.3,  $\alpha = 10^\circ \pm 9.5^\circ$ ,  $k = 0.07$  for baseline and dual-row COMPACT,  $F^+$  of 0.2 to 0.8. Loads plotted vs. angle-of-attack. Front actuator only.**

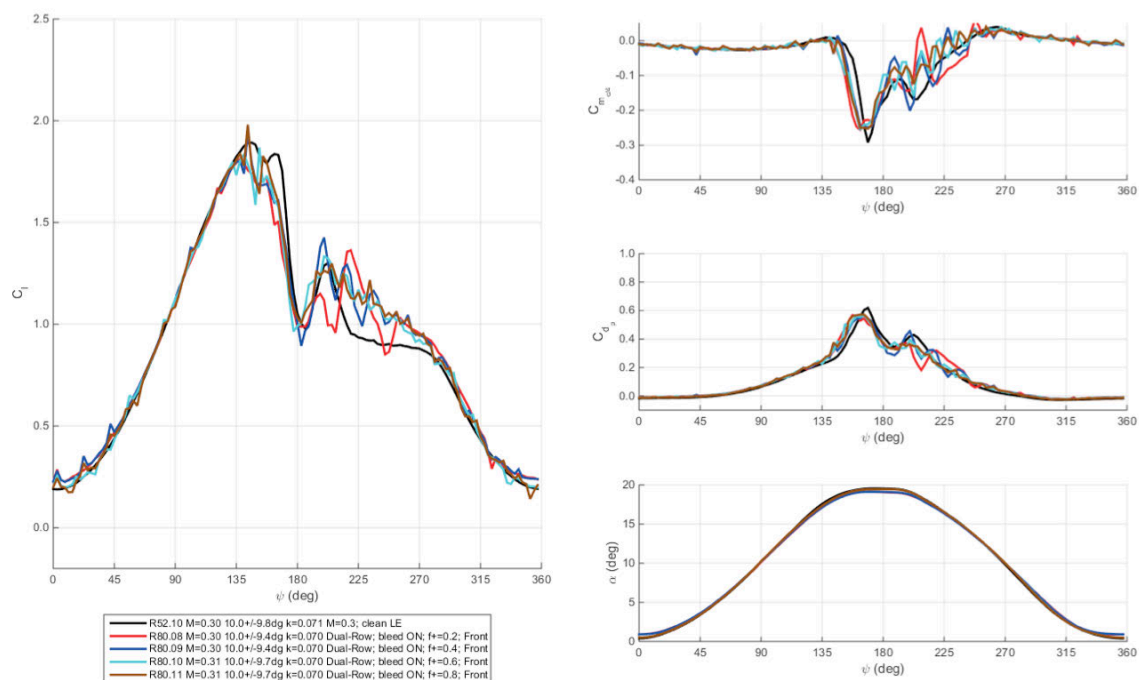


**Figure 572. Lift, drag, and moment coefficients at Mach 0.3,  $\alpha = 10^\circ \pm 9.5^\circ$ ,  $k = 0.07$  for baseline and dual-row COMPACT,  $F^+$  of 0.2 to 0.8. Loads plotted vs. phase angle. Front actuator only.**

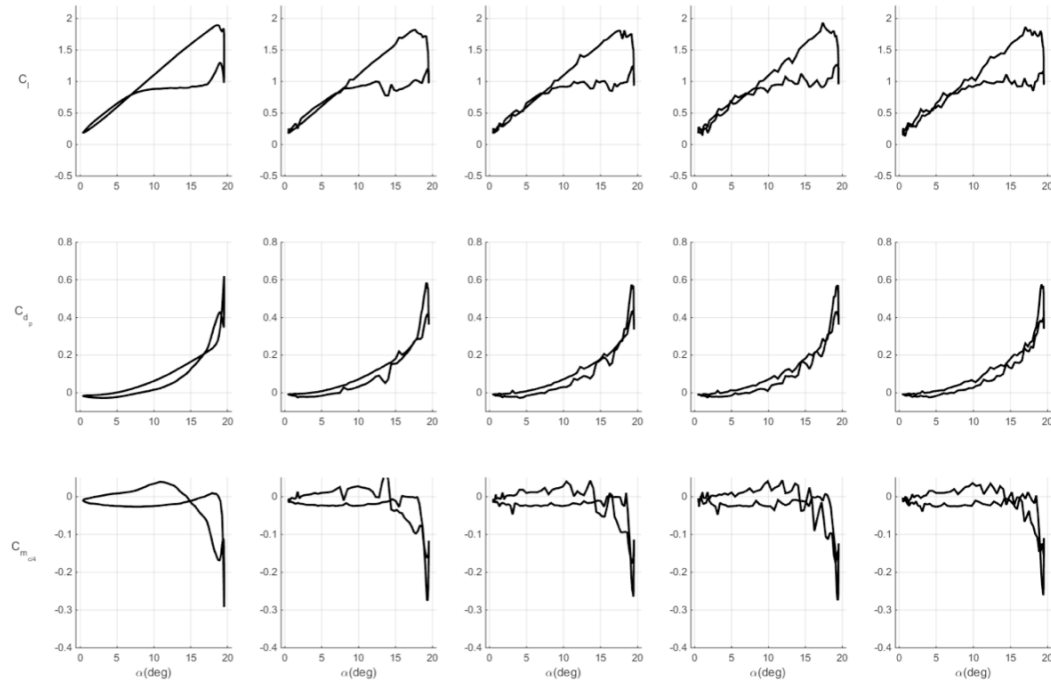


**Figure 573. Lift, drag, and moment coefficients at Mach 0.3,  $\alpha = 10^\circ \pm 9.5^\circ$ ,  $k = 0.07$  for baseline and dual-row COMPACT,  $F^+$  of 0.2 to 0.8. Front actuator only.**

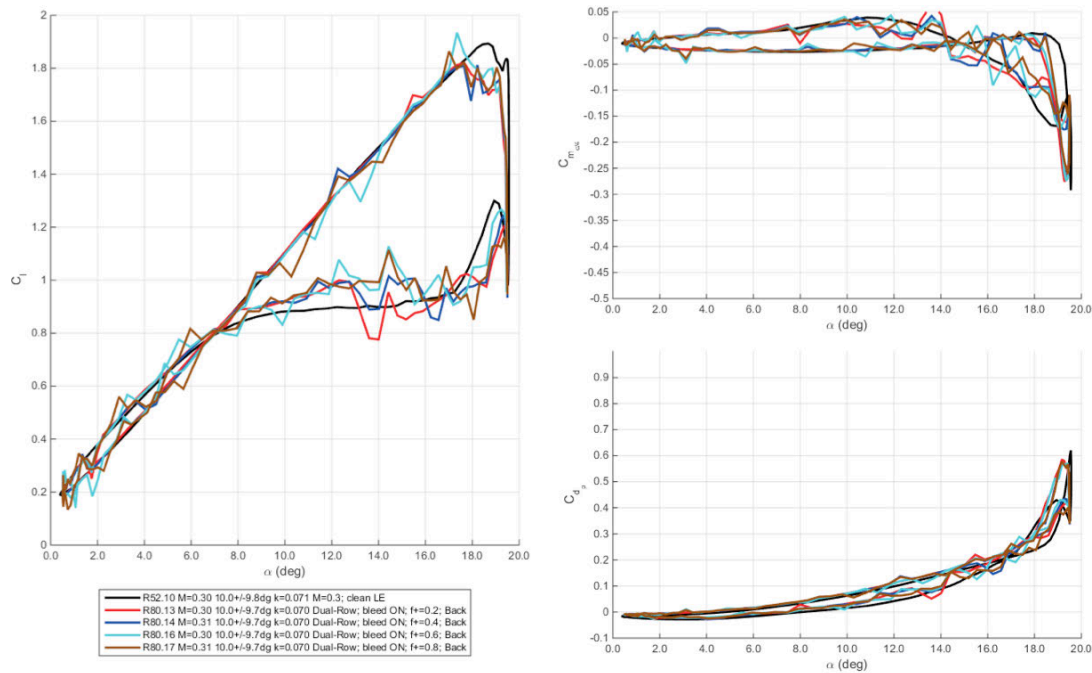


**Figure 574. Lift, drag, and moment coefficients at Mach 0.3,  $\alpha = 10^\circ \pm 9.5^\circ$ ,  $k = 0.07$  for baseline and dual-row COMPACT,  $F^+$  of 0.2 to 0.8. Loads plotted vs. angle-of-attack. Back actuator only.**

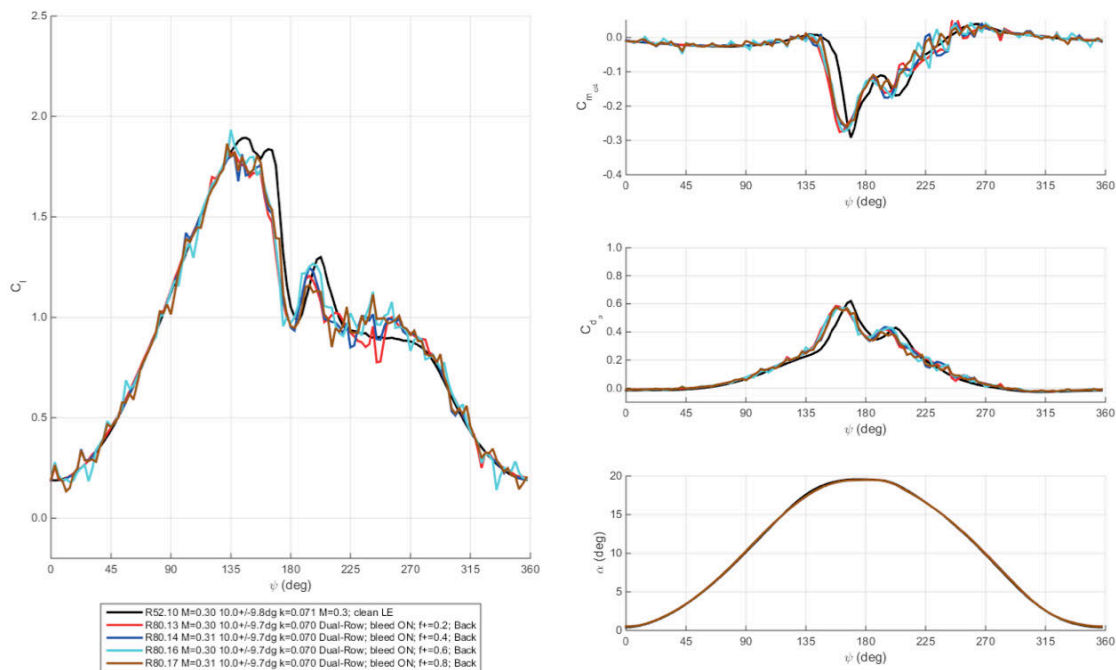


**Figure 575. Lift, drag, and moment coefficients at Mach 0.3,  $\alpha = 10^\circ \pm 9.5^\circ$ ,  $k = 0.07$  for baseline and dual-row COMPACT,  $F^+$  of 0.2 to 0.8. Loads plotted vs. phase angle. Back actuator only.**



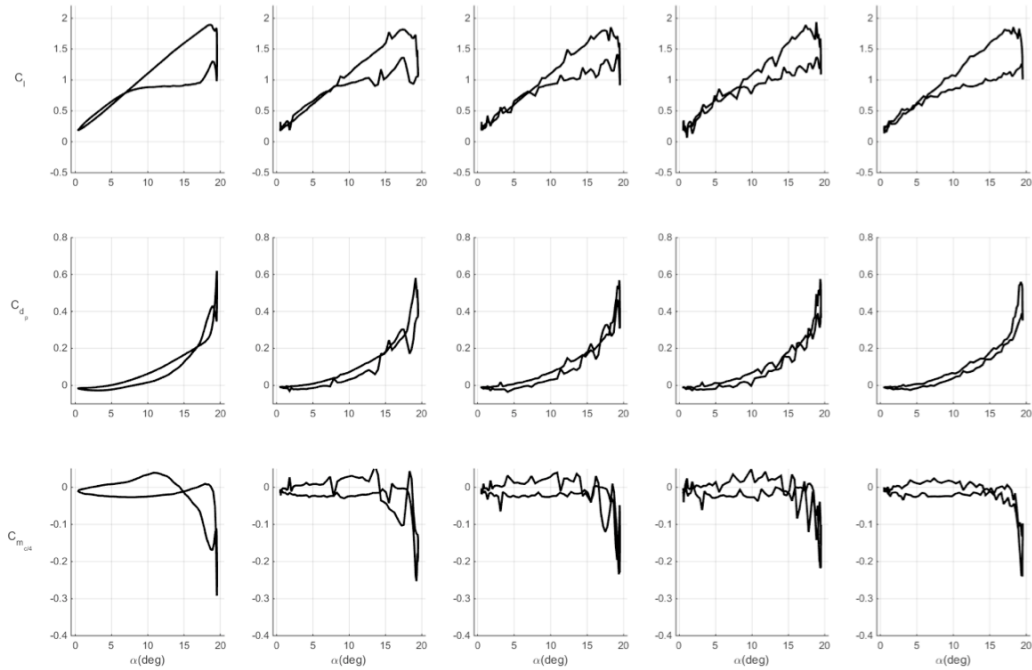


**Figure 576. Lift, drag, and moment coefficients at Mach 0.3,  $\alpha = 10^\circ \pm 9.5^\circ$ ,  $k = 0.07$  for baseline and dual-row COMPACT,  $F^+$  of 0.2 to 0.8. Simultaneous operation.**

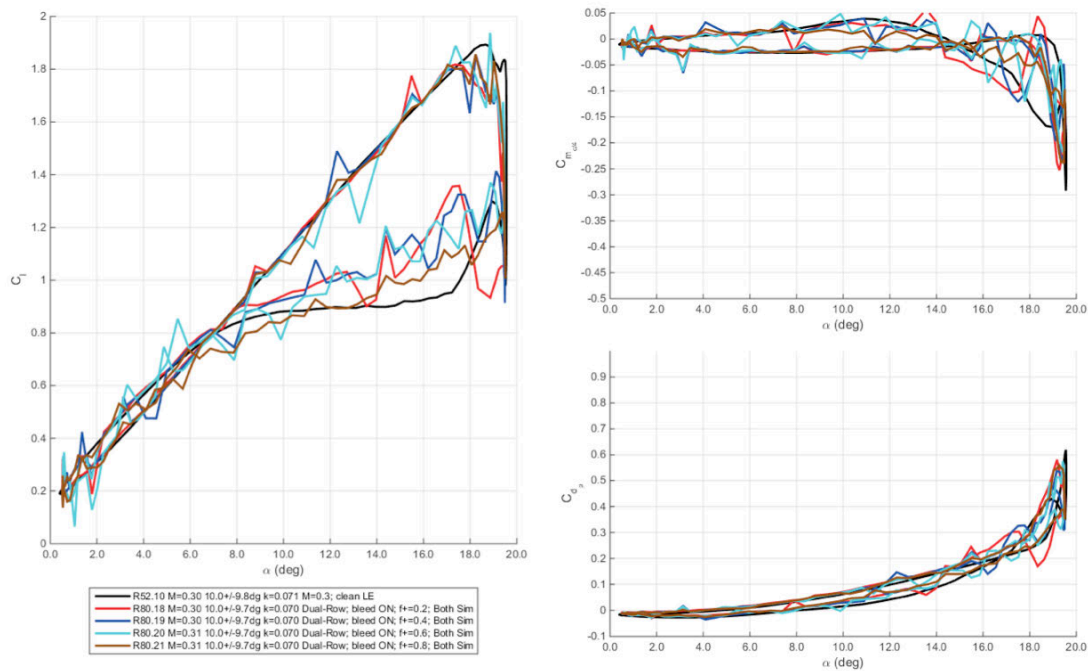


**Figure 577. Lift, drag, and moment coefficients at Mach 0.3,  $\alpha = 10^\circ \pm 9.5^\circ$ ,  $k = 0.07$  for baseline and dual-row COMPACT,  $F^+$  of 0.2 to 0.8. Loads plotted vs. angle-of-attack. Simultaneous operation.**

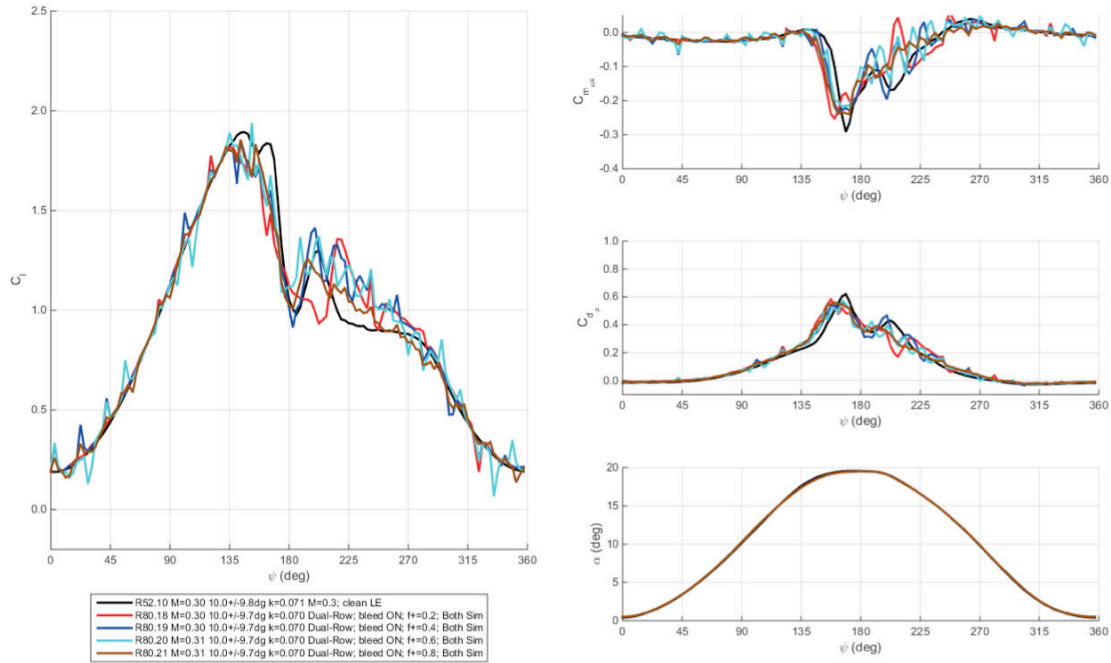


**Figure 578. Lift, drag, and moment coefficients at Mach 0.3,  $\alpha = 10^\circ \pm 9.5^\circ$ ,  $k = 0.07$  for baseline and dual-row COMPACT,  $F^+$  of 0.2 to 0.8. Loads plotted vs. phase angle. Simultaneous operation.**

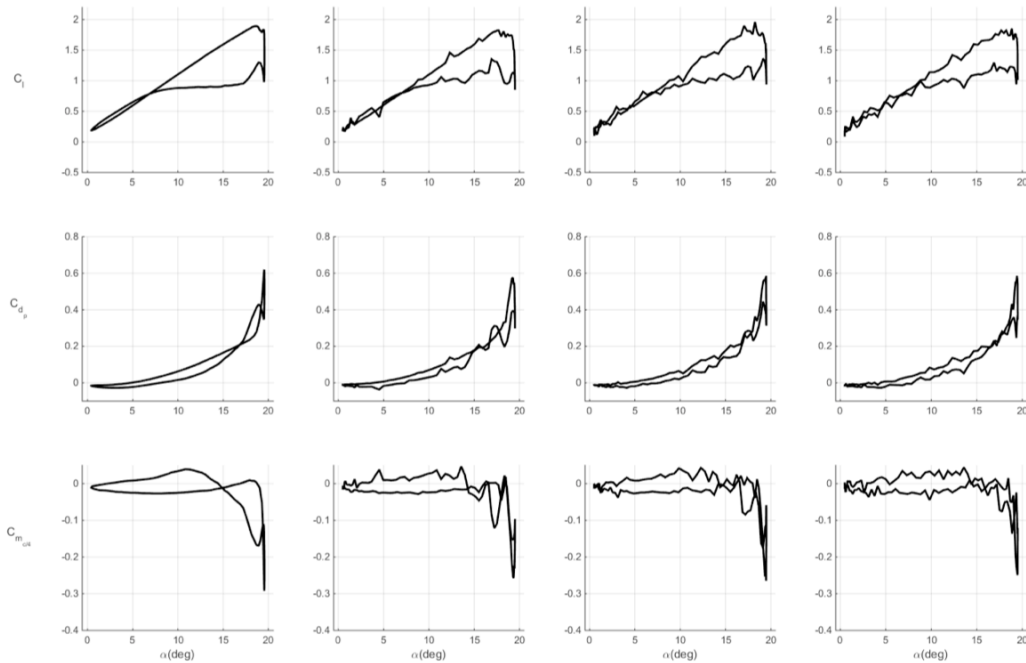


**Figure 579. Lift, drag, and moment coefficients at Mach 0.3,  $\alpha = 10^\circ \pm 9.5^\circ$ ,  $k = 0.07$  for baseline and dual-row COMPACT,  $F^+$  of 0.2 to 0.8. Alternating operation.**

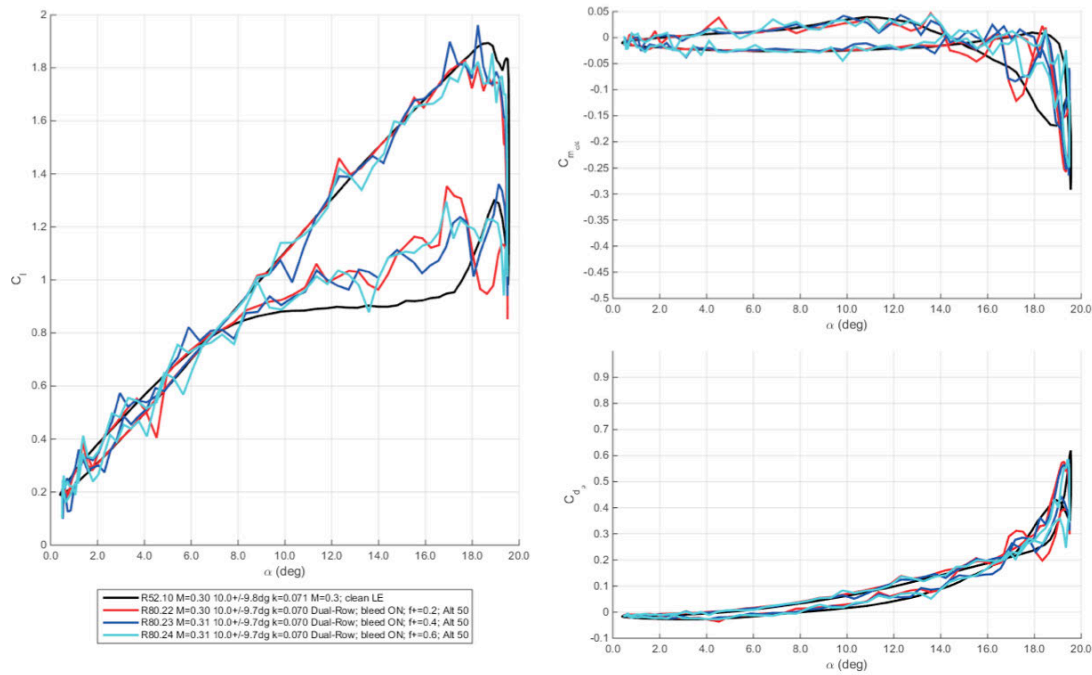


**Figure 580.** Lift, drag, and moment coefficients at Mach 0.3,  $\alpha = 10^\circ \pm 9.5^\circ$ ,  $k = 0.07$  for baseline and dual-row COMPACT,  $F^+$  of 0.2 to 0.8. Loads plotted vs. angle-of-attack. Alternating operation.

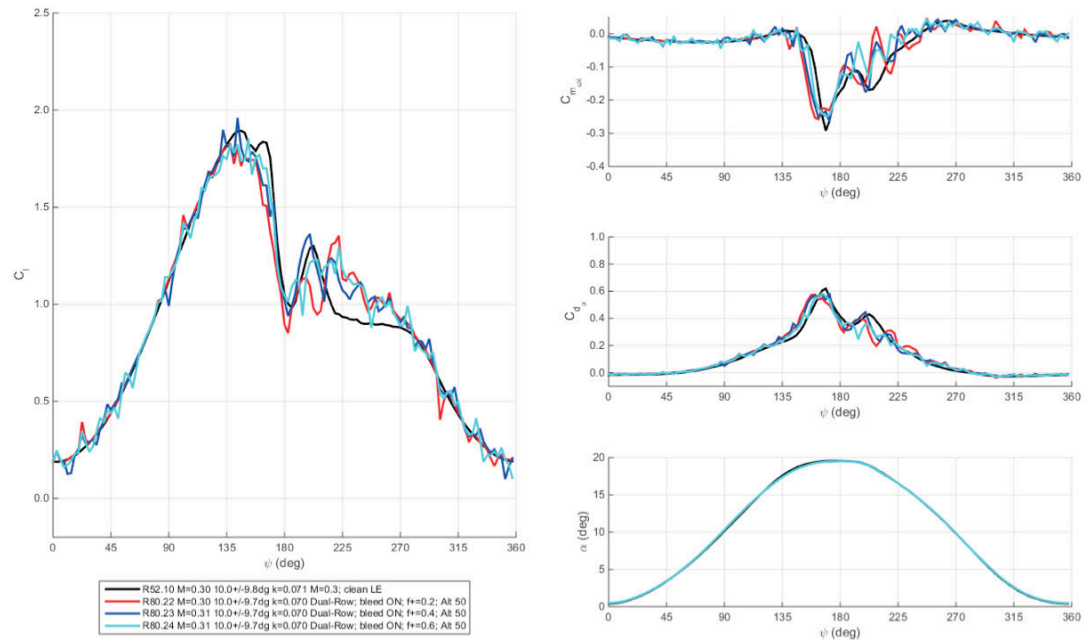


**Figure 581.** Lift, drag, and moment coefficients at Mach 0.3,  $\alpha = 10^\circ \pm 9.5^\circ$ ,  $k = 0.07$  for baseline and dual-row COMPACT,  $F^+$  of 0.2 to 0.8. Loads plotted vs. phase angle. Alternating operation.

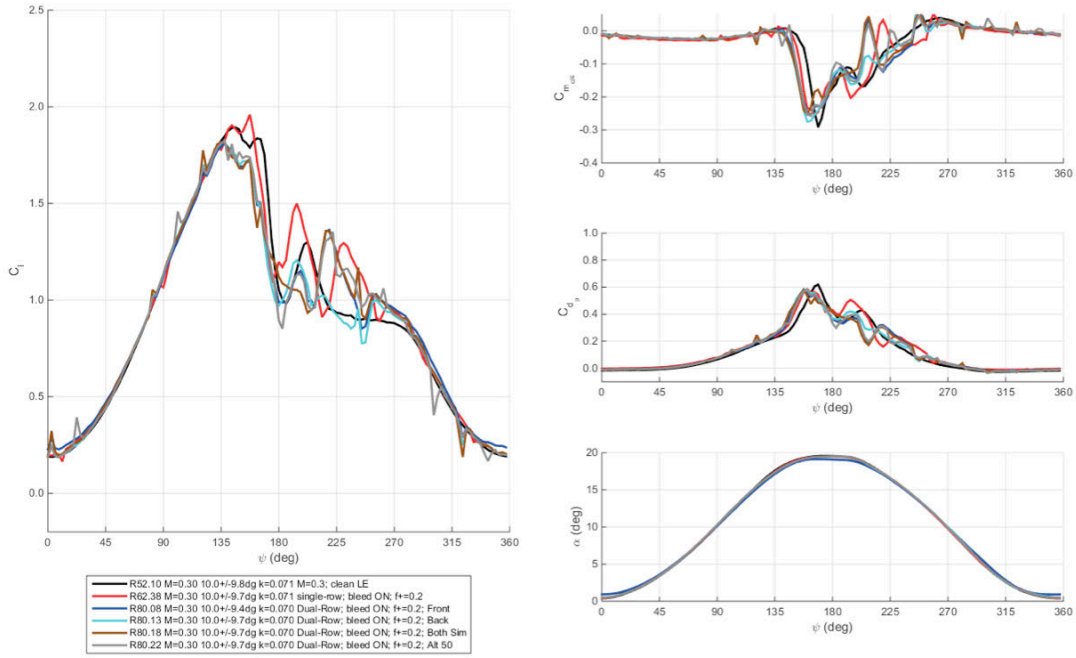


**Figure 582. Lift, drag, and moment coefficients at Mach 0.3,  $\alpha = 10^\circ \pm 9.5^\circ$ ,  $k = 0.07$ ,  $F^+ = 0.2$  for baseline and multiple COMPACT modes.**

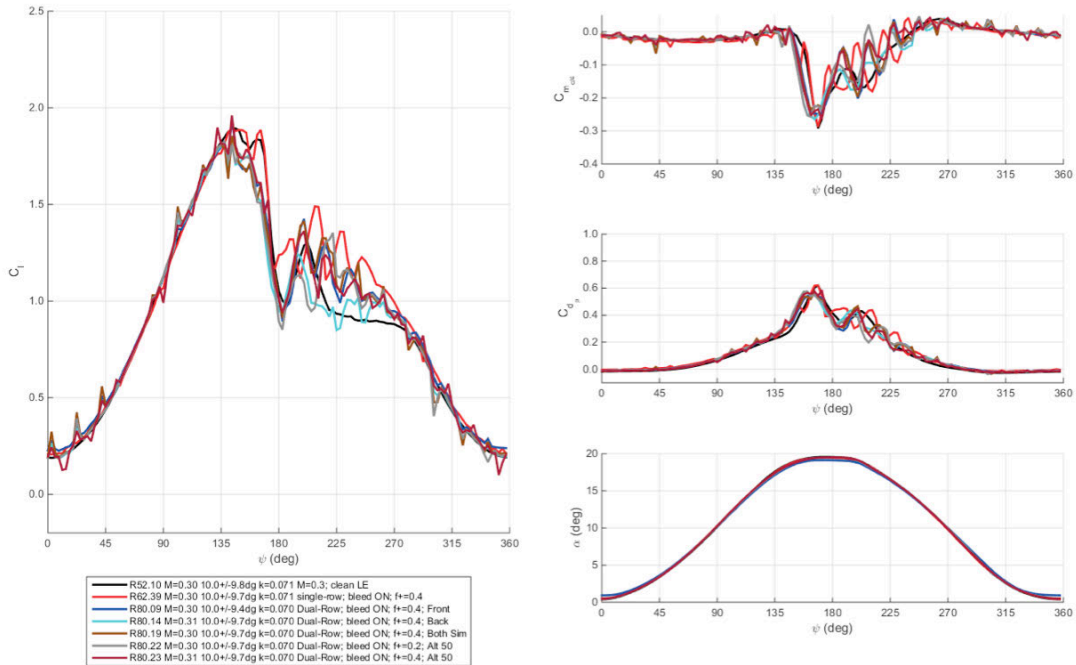


**Figure 583. Lift, drag, and moment coefficients at Mach 0.3,  $\alpha = 10^\circ \pm 9.5^\circ$ ,  $k = 0.07$ ,  $F^+ = 0.4$  for baseline and multiple COMPACT modes.**

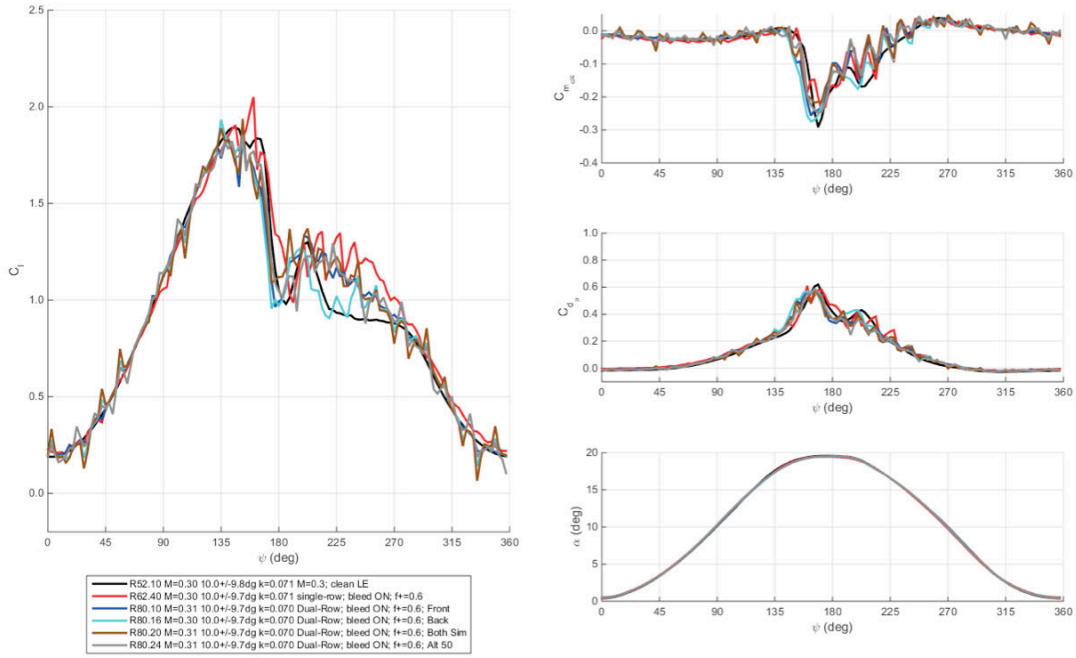


**Figure 584. Lift, drag, and moment coefficients at Mach 0.3,  $\alpha = 10^\circ \pm 9.5^\circ$ ,  $k = 0.07$ ,  $F^+ = 0.6$  for baseline and multiple COMPACT modes.**

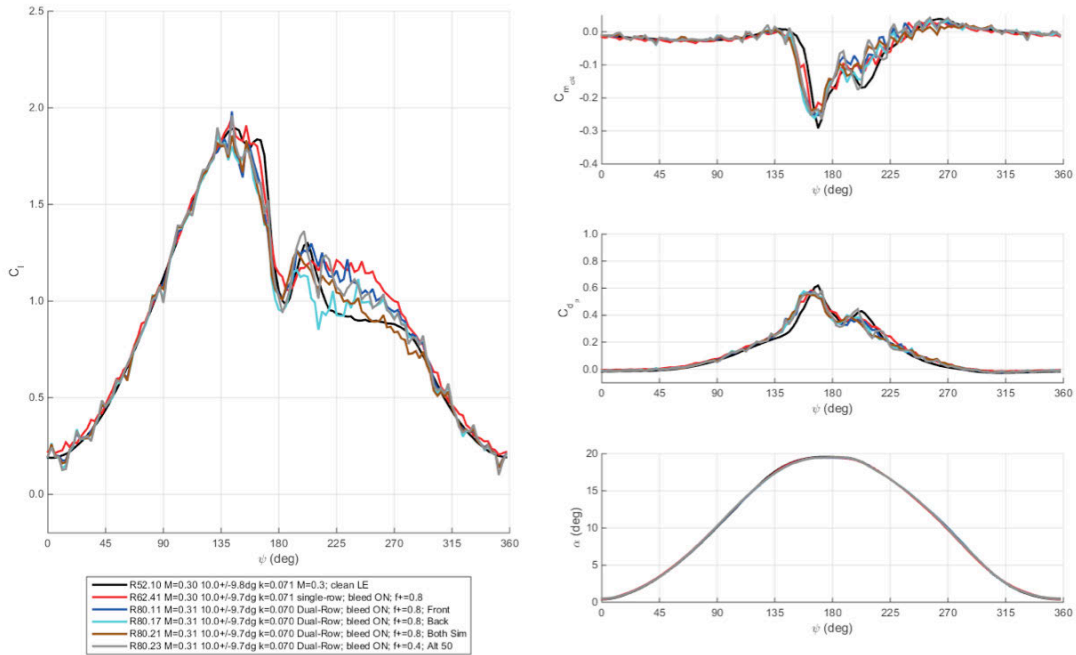


**Figure 585. Lift, drag, and moment coefficients at Mach 0.3,  $\alpha = 10^\circ \pm 9.5^\circ$ ,  $k = 0.07$ ,  $F^+ = 0.8$  for baseline and multiple COMPACT modes.**

**M=0.4**

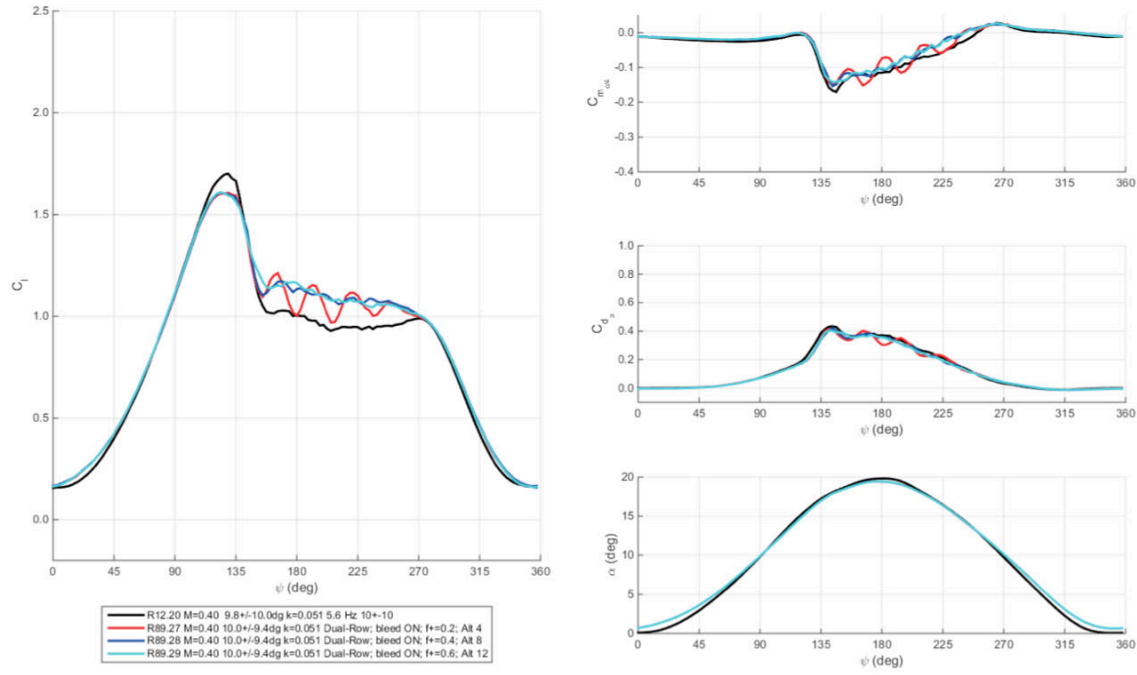


**Figure 184. Lift, drag, and moment coefficients at Mach 0.4,  $\alpha = 10^\circ \pm 9.3^\circ$ ,  $k = 0.05$  for baseline and dual-row COMPACT,  $F^+$  of 0.2 to 0.6. Front actuator only.**

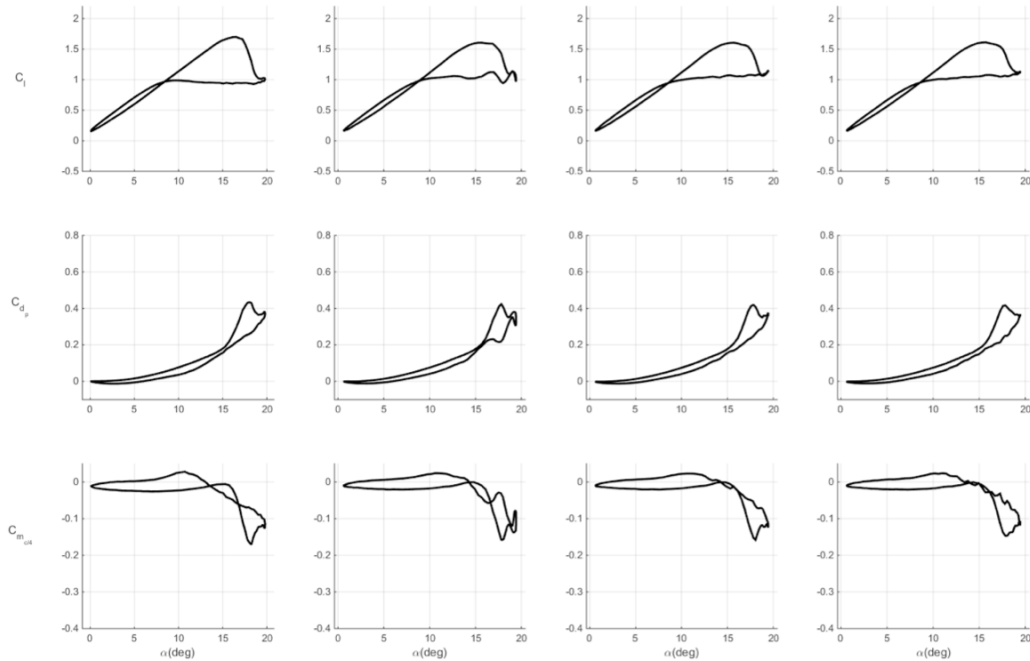


**Figure 586. Lift, drag, and moment coefficients at Mach 0.4,  $\alpha = 10^\circ \pm 9.3^\circ$ ,  $k = 0.05$  for baseline and dual-row COMPACT,  $F^+$  of 0.2 to 0.6. Front actuator only.**

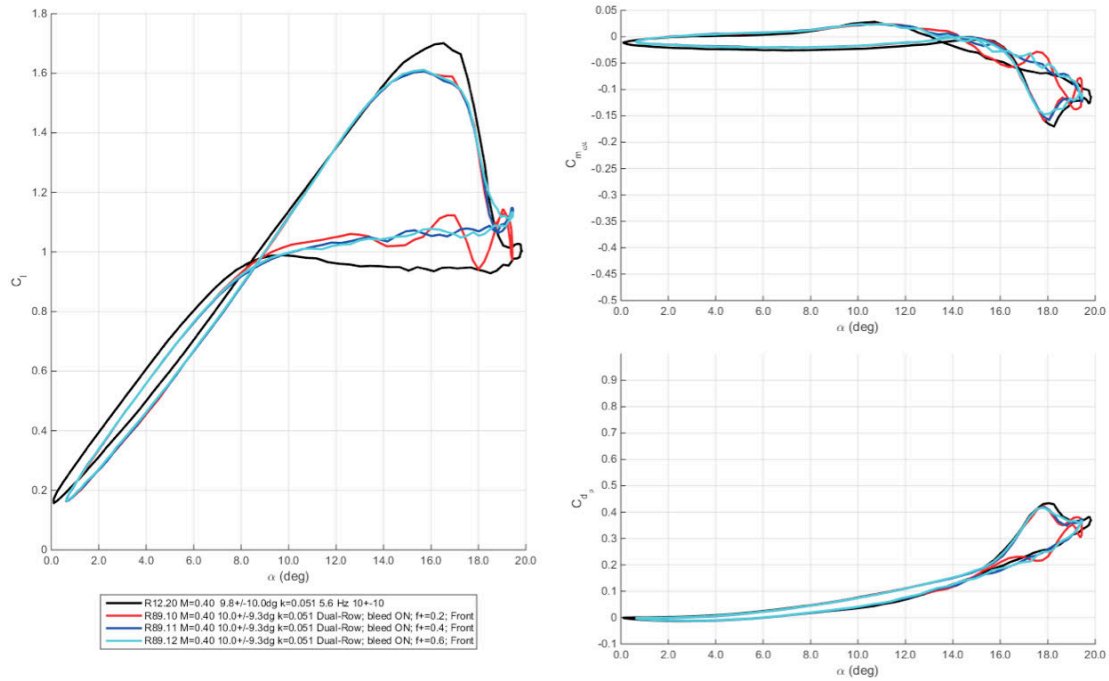


**Figure 587. Lift, drag, and moment coefficients at Mach 0.4,  $\alpha = 10^\circ \pm 9.3^\circ$ ,  $k = 0.05$  for baseline and dual-row COMPACT,  $F^+$  of 0.2 to 0.6. Loads plotted vs. angle-of-attack. Front actuator only.**



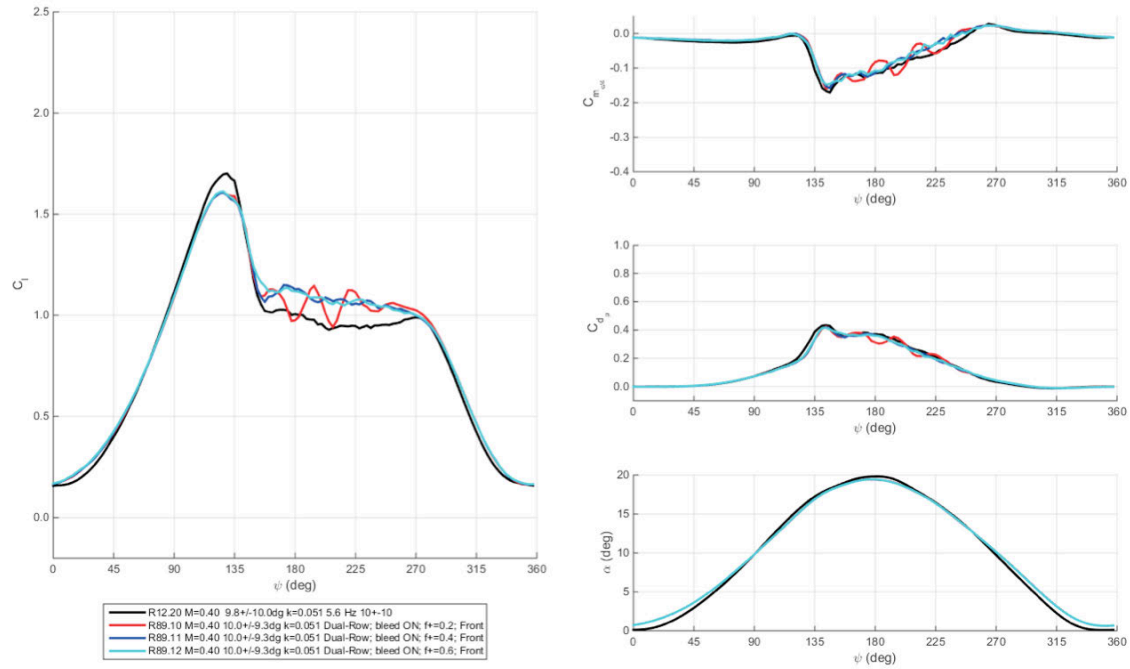


**Figure 588.** Lift, drag, and moment coefficients at Mach 0.4,  $\alpha = 10^\circ \pm 9.3^\circ$ ,  $k = 0.05$  for baseline and dual-row COMPACT,  $F^+$  of 0.2 to 0.6. Loads plotted vs. phase angle. Front actuator only.

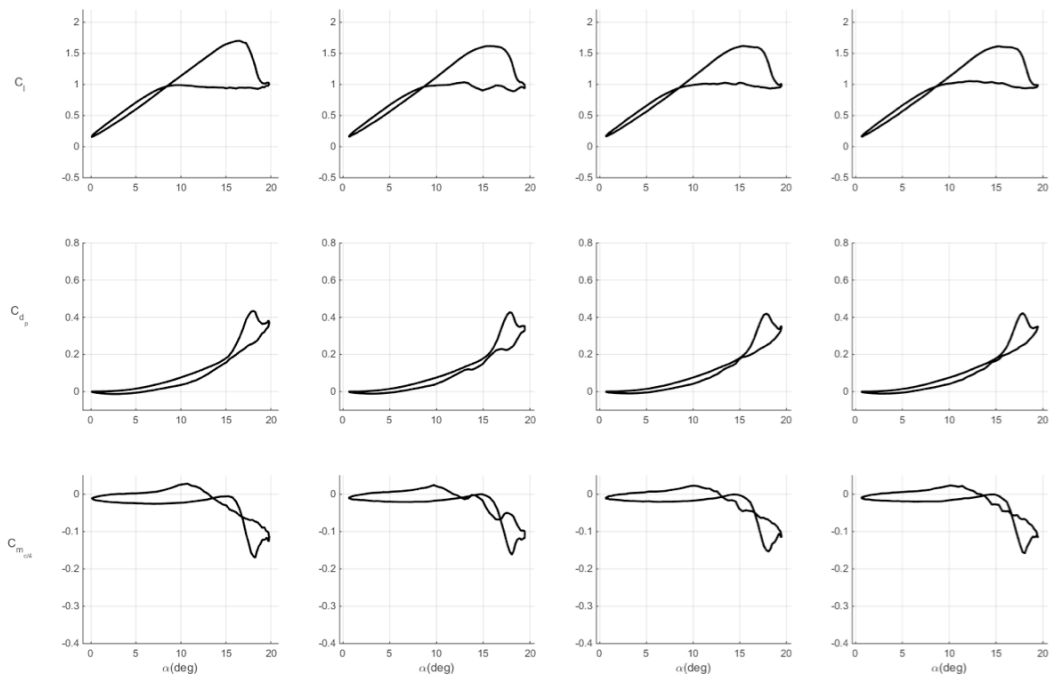


**Figure 589.** Lift, drag, and moment coefficients at Mach 0.4,  $\alpha = 10^\circ \pm 9.3^\circ$ ,  $k = 0.05$  for baseline and dual-row COMPACT,  $F^+$  of 0.2 to 0.6. Back actuator only.



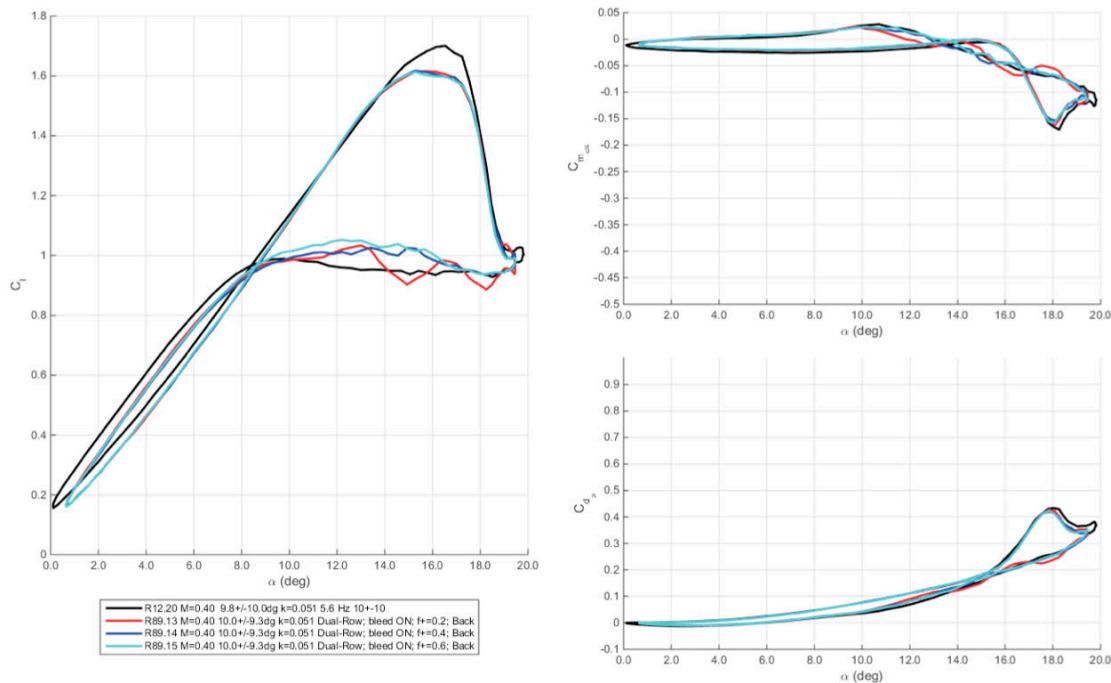


**Figure 590. Lift, drag, and moment coefficients at Mach 0.4,  $\alpha = 10 \pm 9.3$ ,  $k = 0.05$  for baseline and dual-row COMPACT,  $F^+$  of 0.2 to 0.6. Loads plotted vs. angle-of-attack. Back actuator only.**

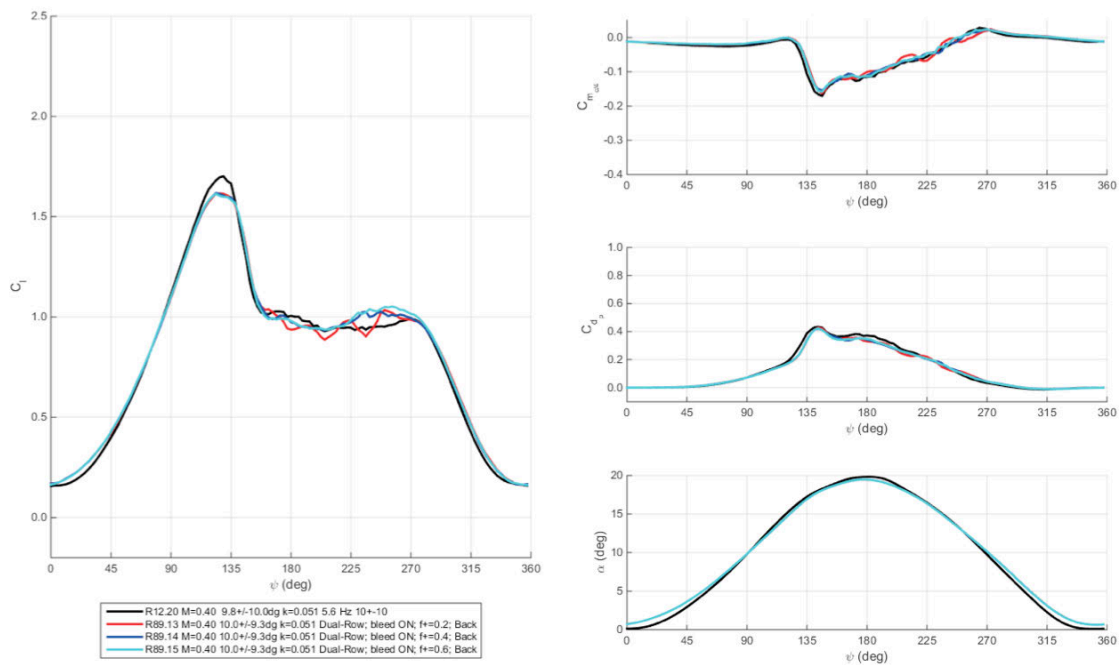


**Figure 591. Lift, drag, and moment coefficients at Mach 0.4,  $\alpha = 10^\circ \pm 9.3^\circ$ ,  $k = 0.05$  for baseline and dual-row COMPACT,  $F^+$  of 0.2 to 0.6. Loads plotted vs. phase angle. Back actuator only.**

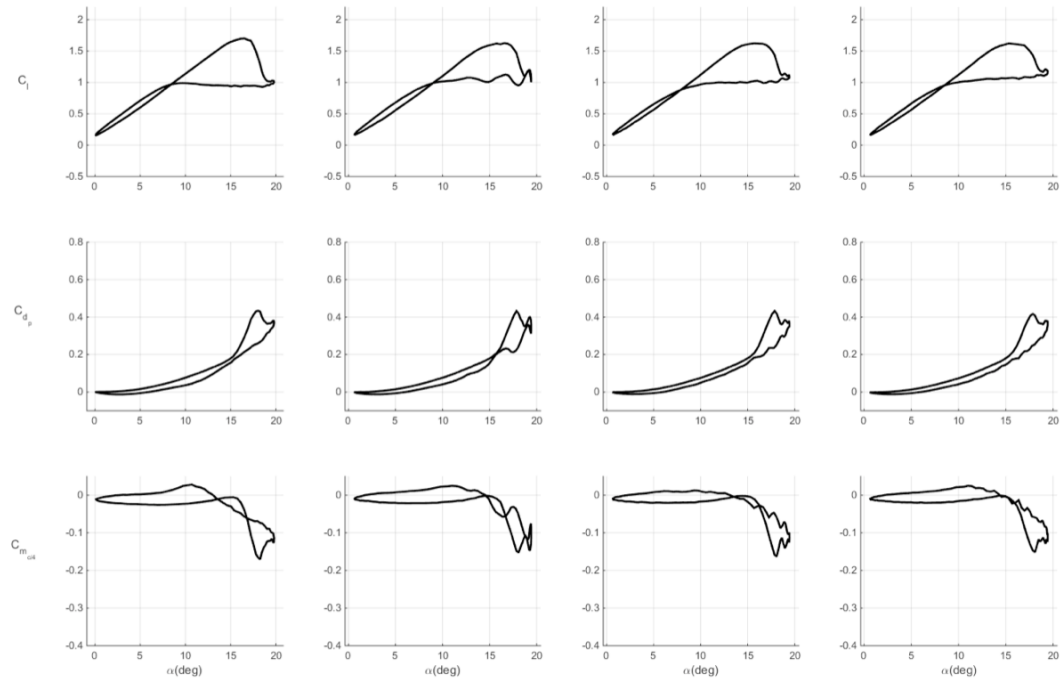


**Figure 592. Lift, drag, and moment coefficients at Mach 0.4,  $\alpha = 10^\circ \pm 9.3^\circ$ ,  $k = 0.05$  for baseline and dual-row COMPACT,  $F^+$  of 0.2 to 0.6. Simultaneous operation.**

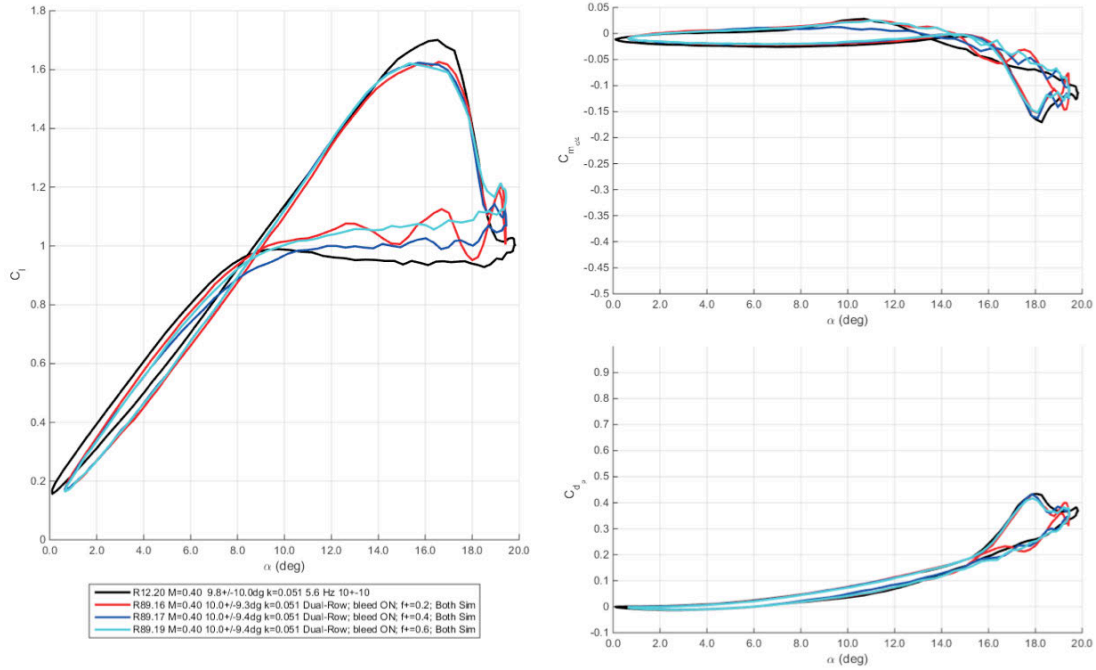


**Figure 593. Lift, drag, and moment coefficients at Mach 0.4,  $\alpha = 10^\circ \pm 9.3^\circ$ ,  $k = 0.05$  for baseline and dual-row COMPACT,  $F^+$  of 0.2 to 0.6. Loads plotted vs. angle-of-attack. Simultaneous operation.**

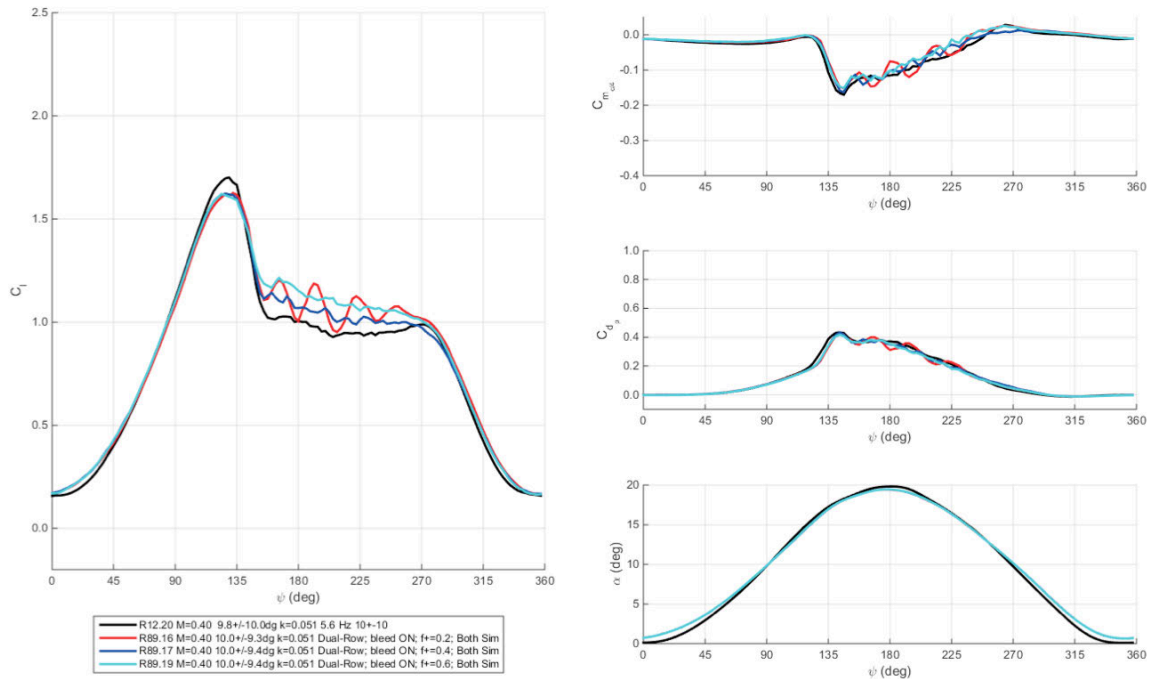


**Figure 594. Lift, drag, and moment coefficients at Mach 0.4,  $\alpha = 10^\circ \pm 9.3^\circ$ ,  $k = 0.05$  for baseline and dual-row COMPACT,  $F^+$  of 0.2 to 0.6. Loads plotted vs. phase angle. Simultaneous operation.**

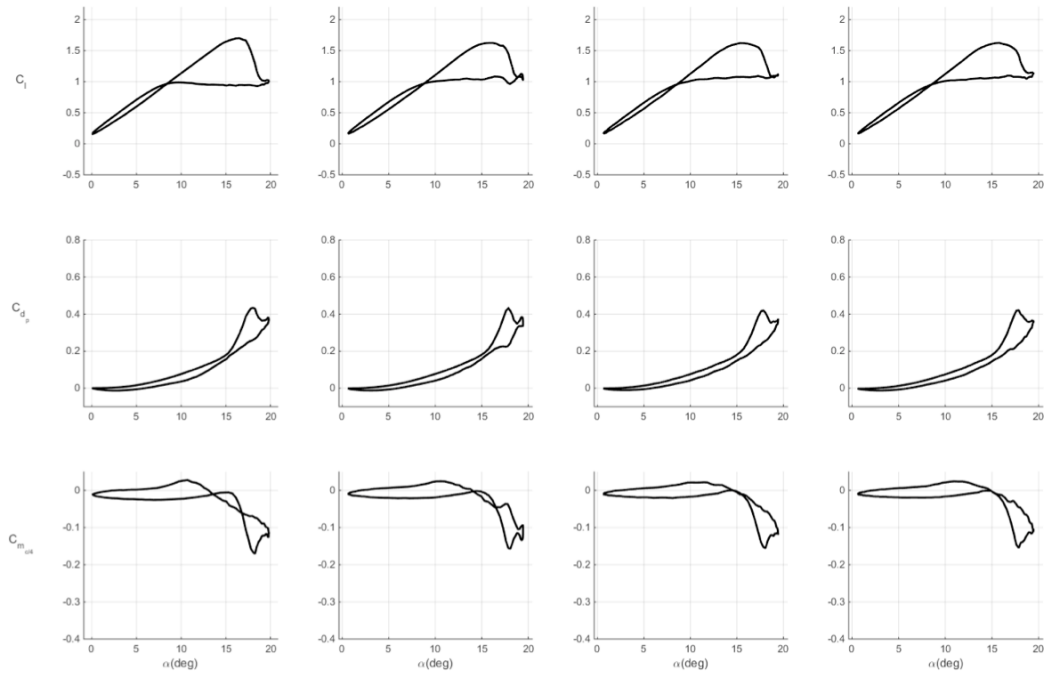


**Figure 595. Lift, drag, and moment coefficients at Mach 0.4,  $\alpha = 10^\circ \pm 9.3^\circ$ ,  $k = 0.05$  for baseline and dual-row COMPACT,  $F^+$  of 0.2 to 0.6. Alternating operation.**

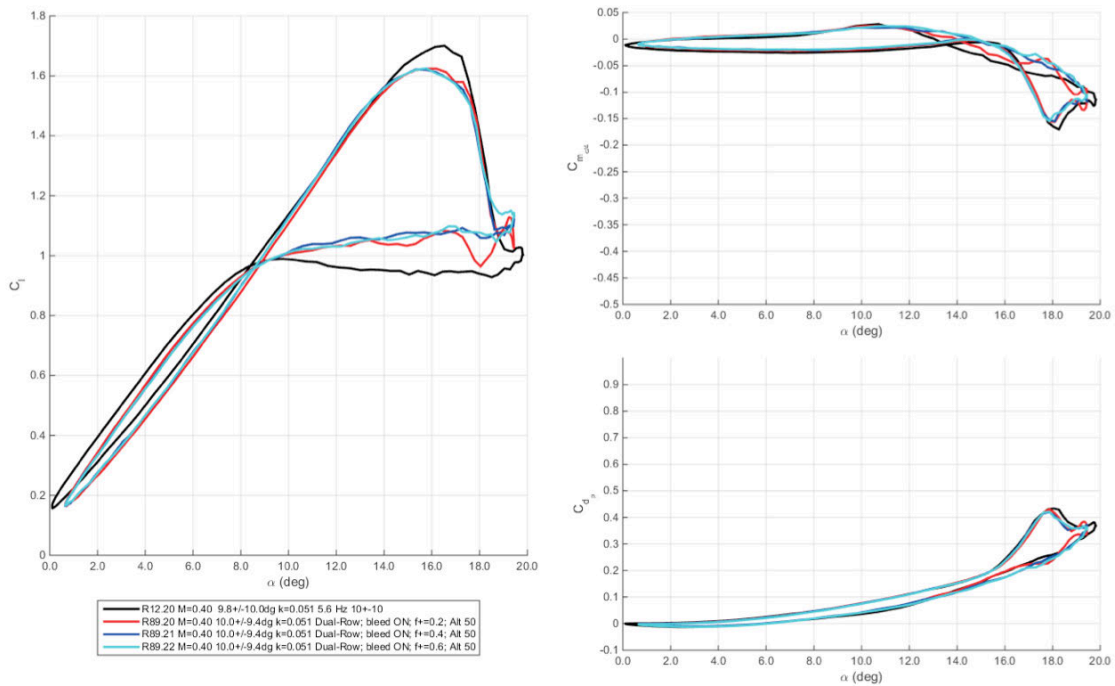


**Figure 596. Lift, drag, and moment coefficients at Mach 0.4,  $\alpha = 10^\circ \pm 9.3^\circ$ ,  $k = 0.05$  for baseline and dual-row COMPACT,  $F^+$  of 0.2 to 0.6. Loads plotted vs. angle-of-attack. Alternating operation.**

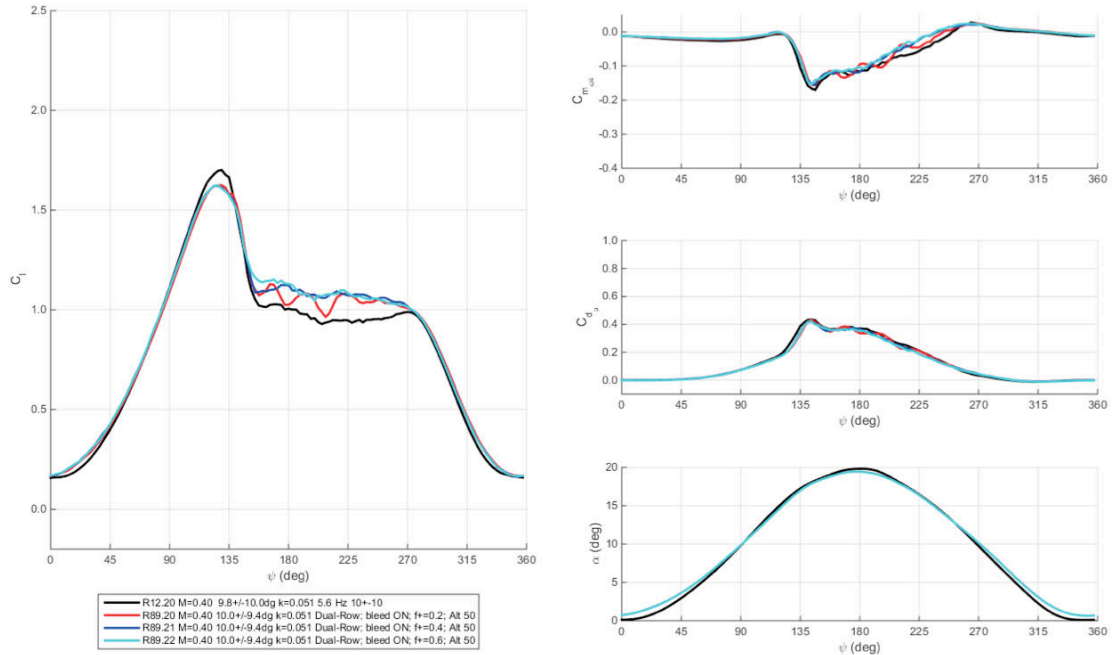


**Figure 597. Lift, drag, and moment coefficients at Mach 0.4,  $\alpha = 10^\circ \pm 9.3^\circ$ ,  $k = 0.05$  for baseline and dual-row COMPACT,  $F^+$  of 0.2 to 0.6. Loads plotted vs. phase angle. Alternating operation.**

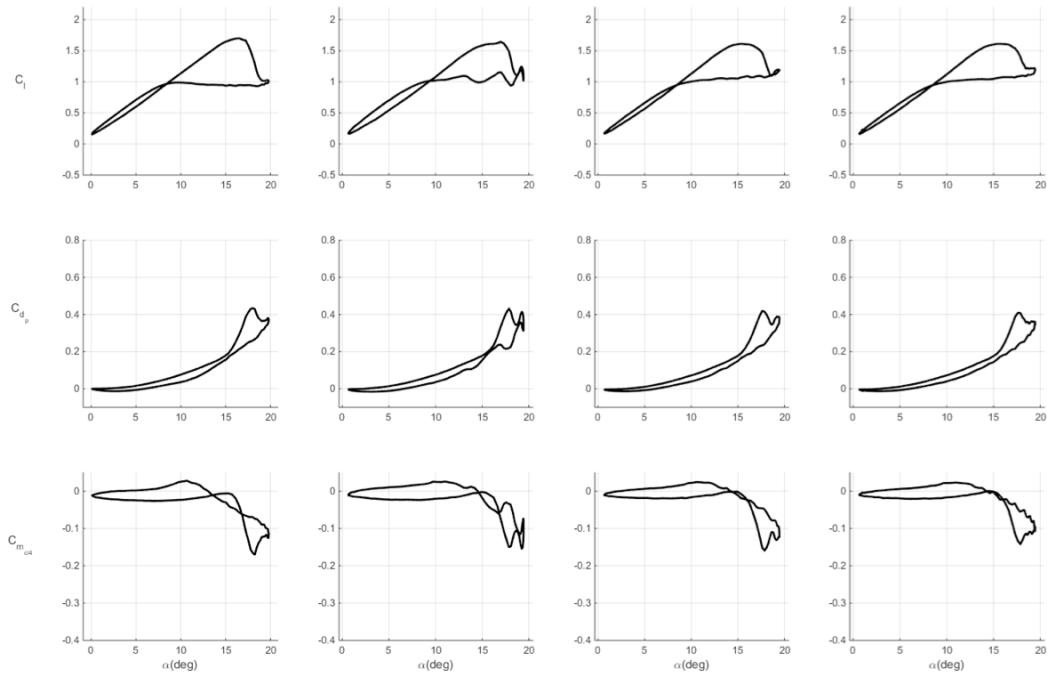


**Figure 598. Lift, drag, and moment coefficients at Mach 0.4,  $\alpha = 10^\circ \pm 9.3^\circ$ ,  $k = 0.05$  for baseline and dual-row COMPACT,  $F^+$  of 0.2 to 0.6. Phase delay 0.075c/U.**

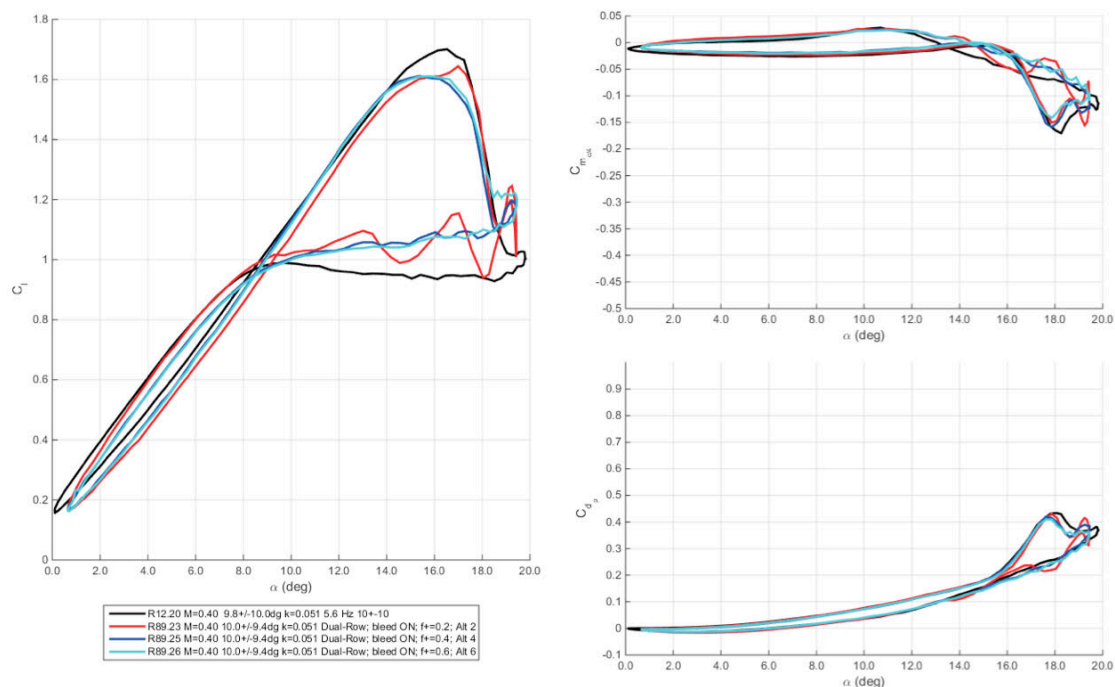


**Figure 599.** Lift, drag, and moment coefficients at Mach 0.4,  $\alpha = 10^\circ \pm 9.3^\circ$ ,  $k = 0.05$  for baseline and dual-row COMPACT,  $F^+$  of 0.2 to 0.6. Loads plotted vs. angle-of-attack. Phase delay  $0.075c/U$ .

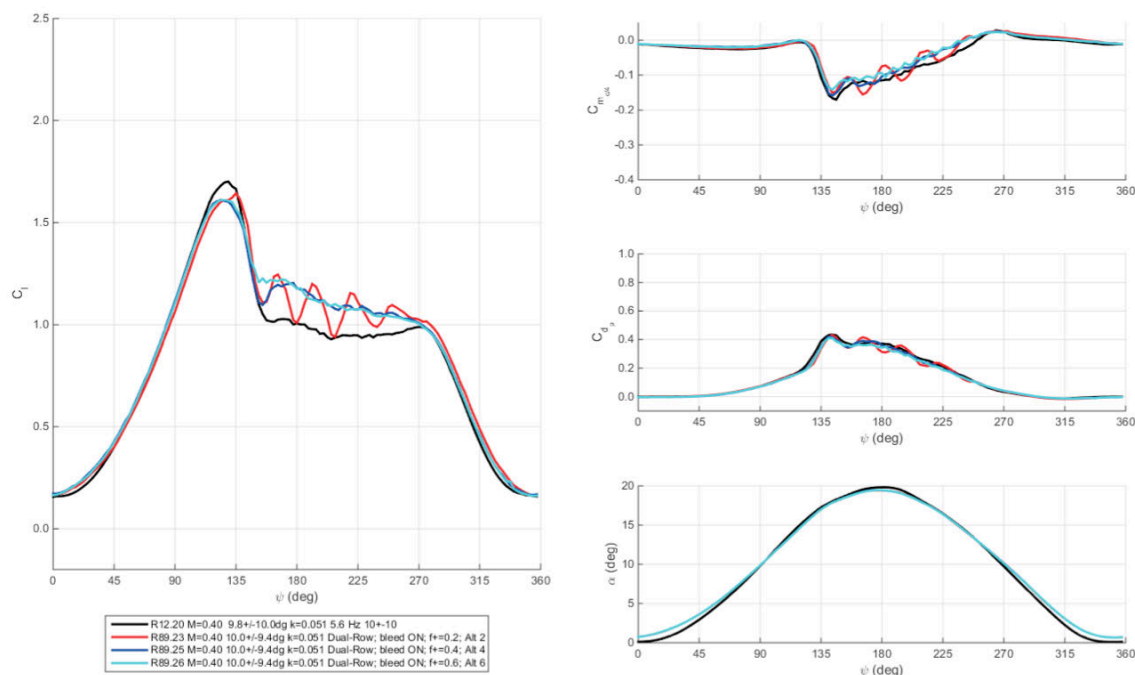


**Figure 600.** Lift, drag, and moment coefficients at Mach 0.4,  $\alpha = 10^\circ \pm 9.3^\circ$ ,  $k = 0.05$  for baseline and dual-row COMPACT,  $F^+$  of 0.2 to 0.6. Loads plotted vs. phase angle. Phase delay  $0.075c/U$ .

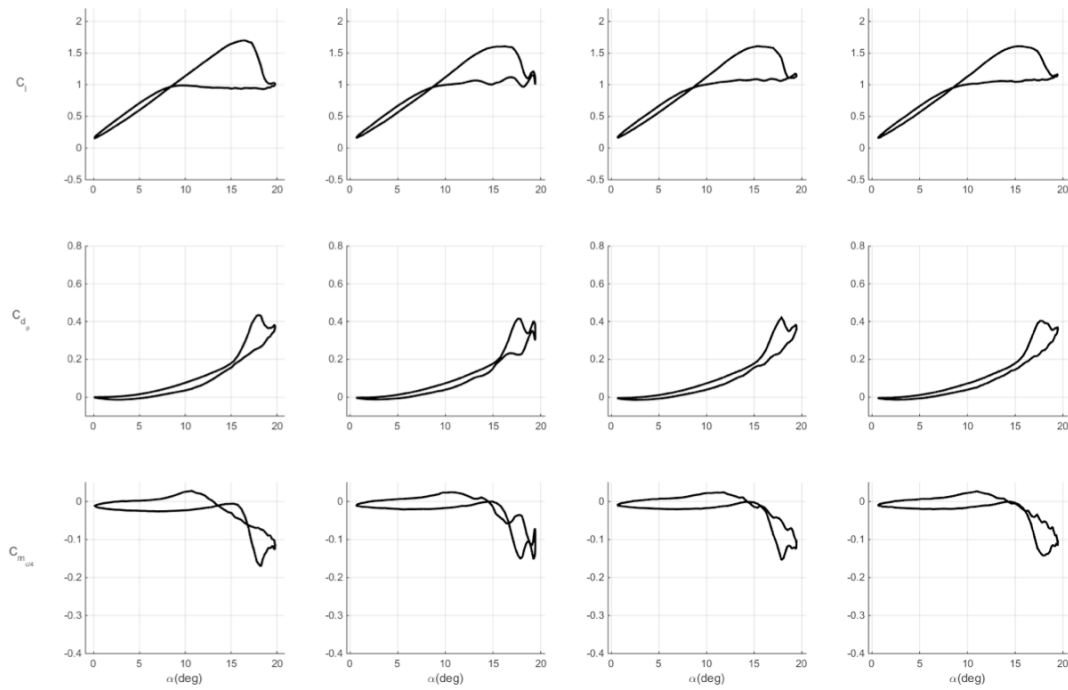


**Figure 601. Lift, drag, and moment coefficients at Mach 0.4,  $\alpha = 10^\circ \pm 9.3^\circ$ ,  $k = 0.05$  for baseline and dual-row COMPACT,  $F^+$  of 0.2 to 0.6. Phase delay  $0.075c/(U/2)$ .**

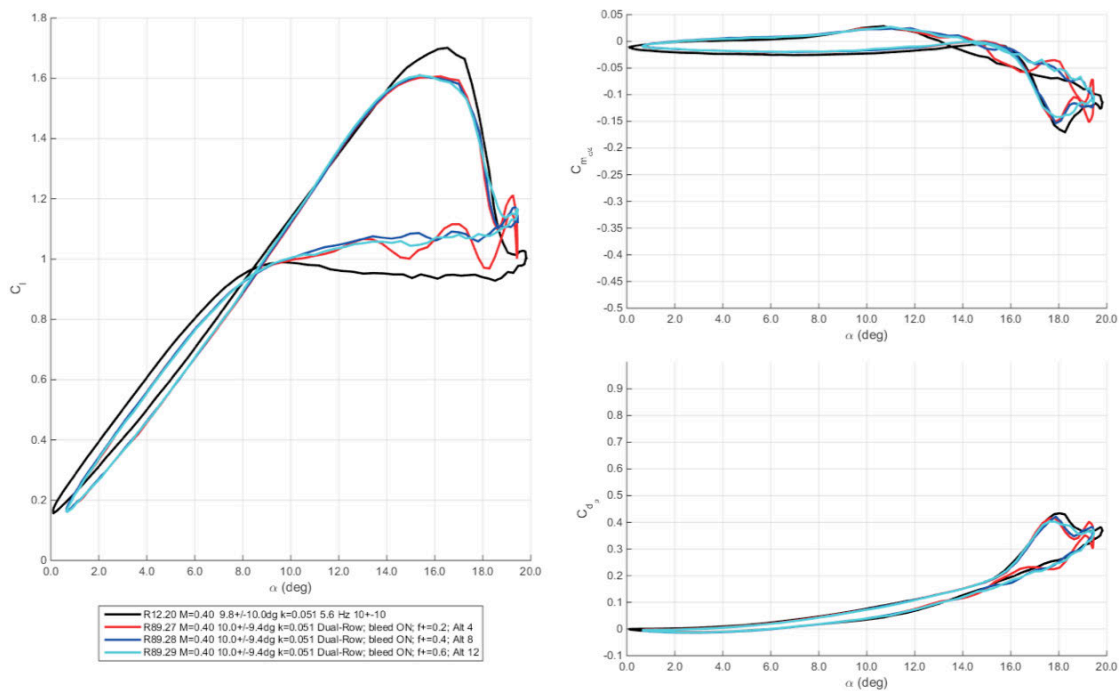


**Figure 602. Lift, drag, and moment coefficients at Mach 0.4,  $\alpha = 10^\circ \pm 9.3^\circ$ ,  $k = 0.05$  for baseline and dual-row COMPACT,  $F^+$  of 0.2 to 0.6. Loads plotted vs. angle-of-attack. Phase delay  $0.075c/(U/2)$ .**

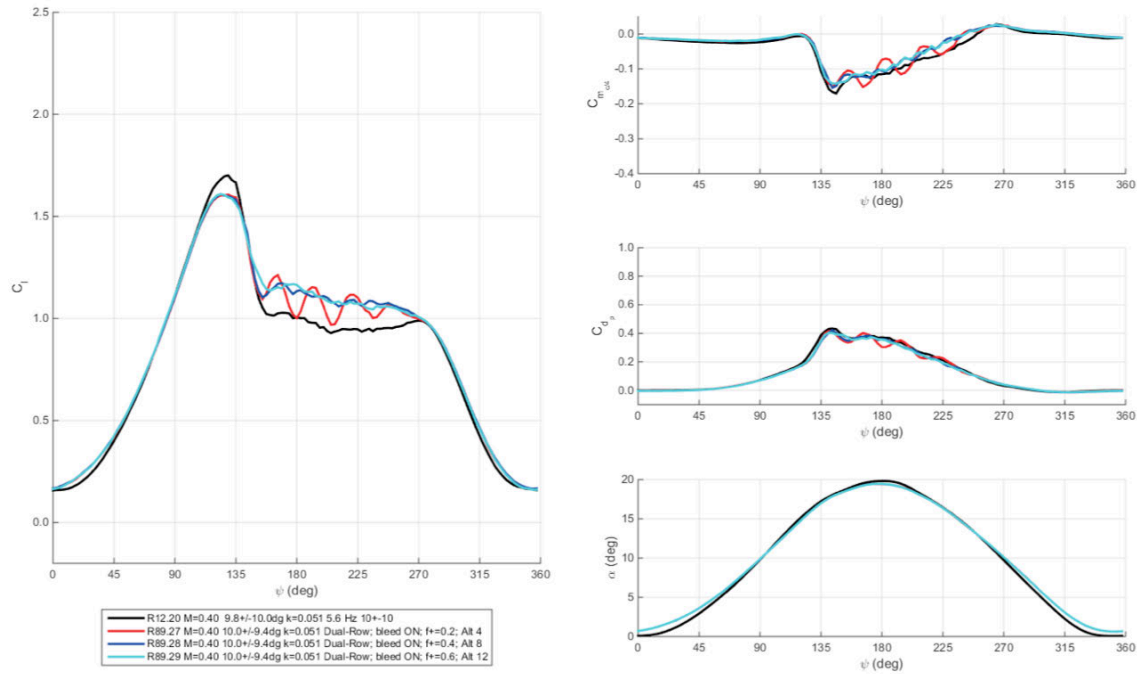


**Figure 603. Lift, drag, and moment coefficients at Mach 0.4,  $\alpha = 10^\circ \pm 9.3^\circ$ ,  $k = 0.05$  for baseline and dual-row COMPACT,  $F^+$  of 0.2 to 0.6. Loads plotted vs. phase angle. Phase delay  $0.075c/(U/2)$ .**



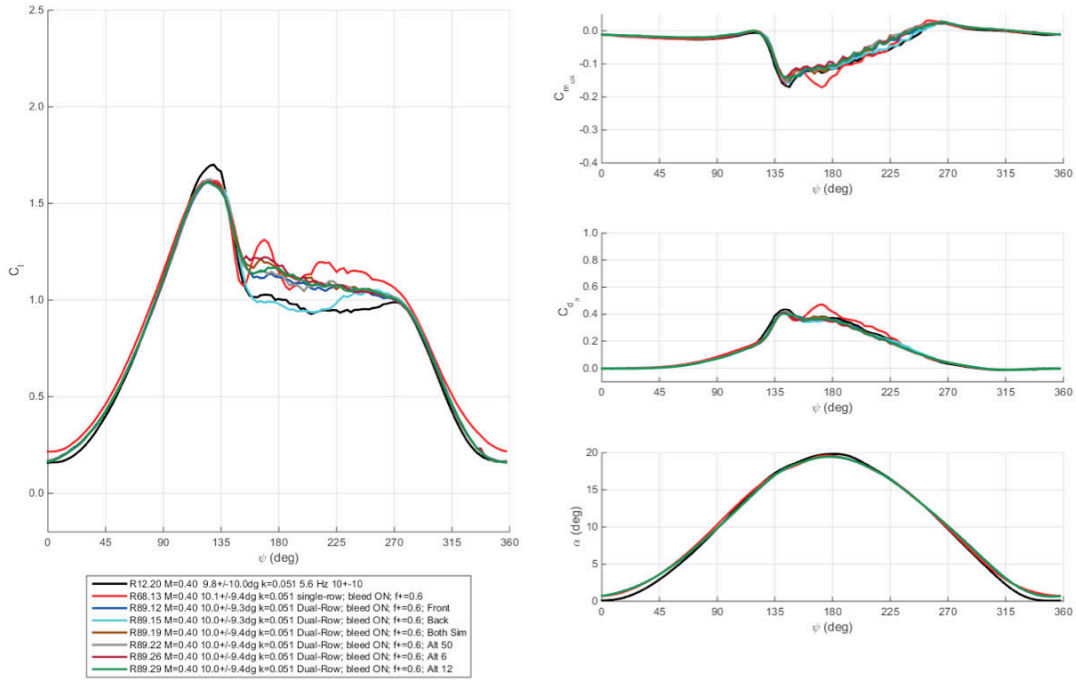


**Figure 604. Lift, drag, and moment coefficients at Mach 0.4,  $\alpha = 10^\circ \pm 9.4^\circ$ ,  $k = 0.05$ ,  $F^+ = 0.6$  for baseline and multiple COMPACT modes.**

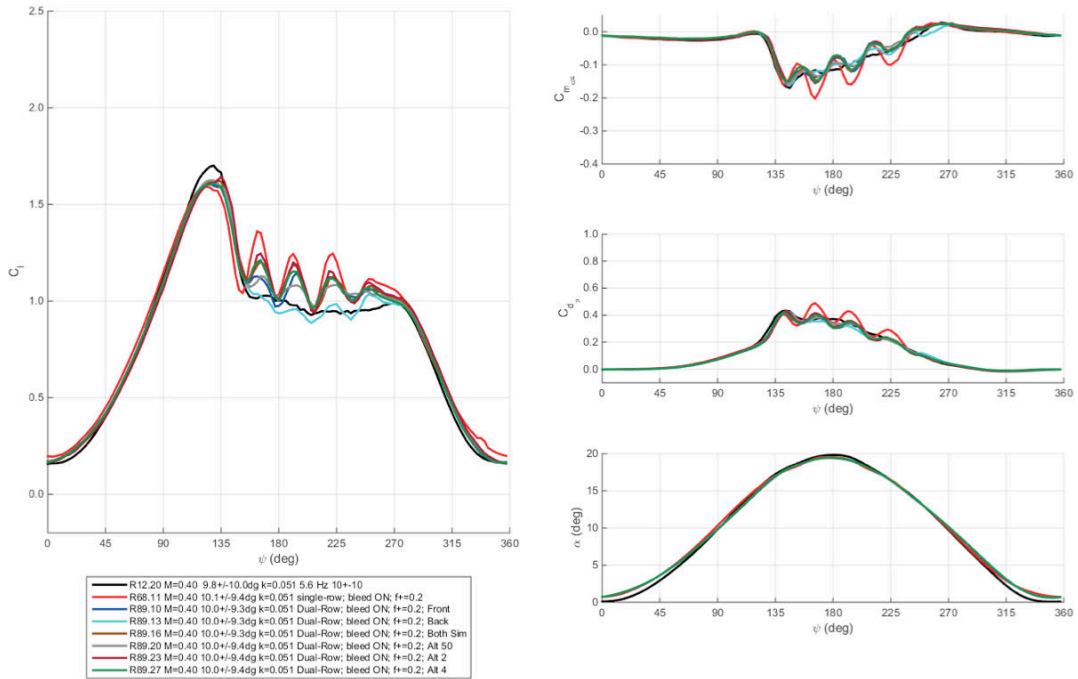


**Figure 605. Lift, drag, and moment coefficients at Mach 0.4,  $\alpha = 10^\circ \pm 9.3^\circ$ ,  $k = 0.07$ ,  $F^+ = 0.2$  for baseline and multiple COMPACT modes.**

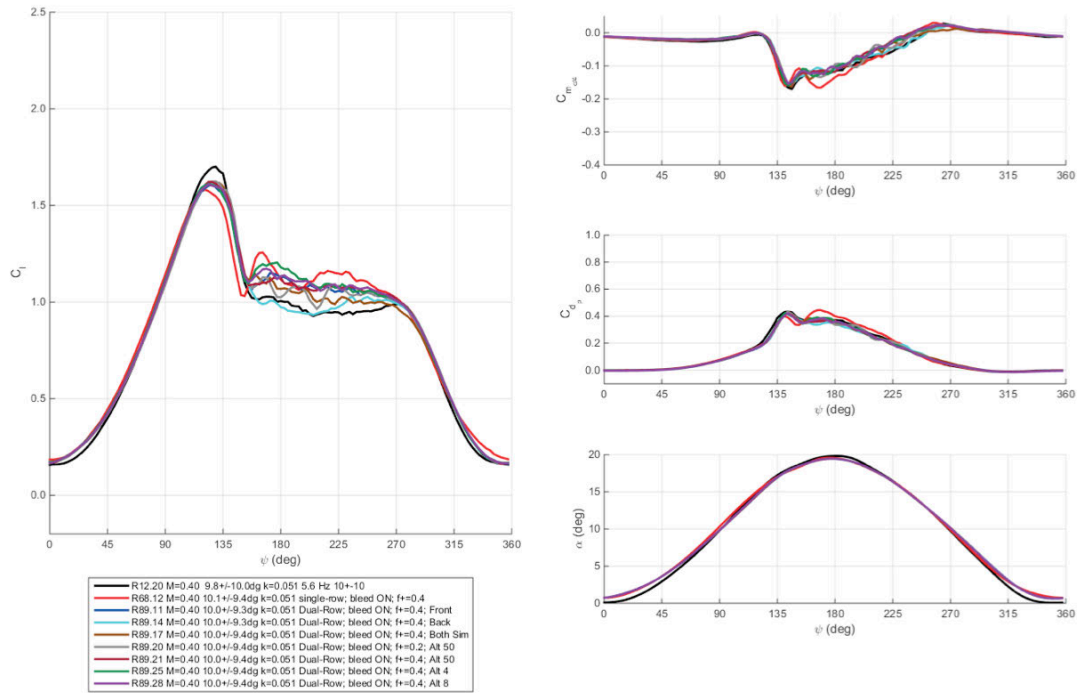


**Figure 606. Lift, drag, and moment coefficients at Mach 0.4,  $\alpha = 10^\circ \pm 9.3^\circ$ ,  $k = 0.05$ ,  $F^+ = 0.4$  for baseline and multiple COMPACT modes.**

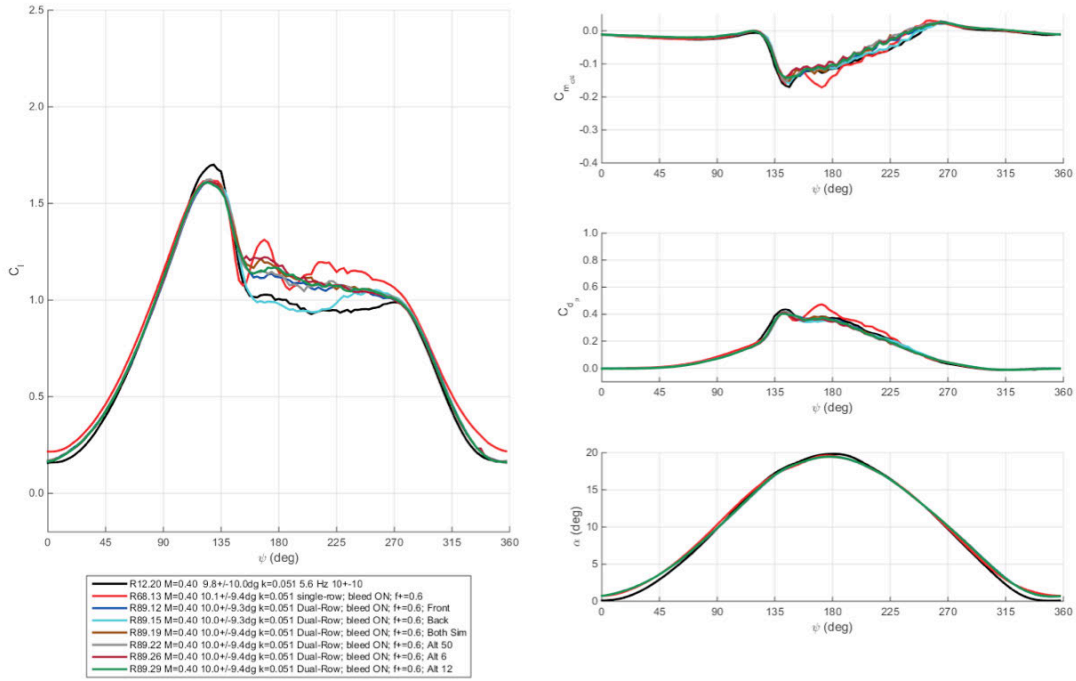


**Figure 607. Lift, drag, and moment coefficients at Mach 0.4,  $\alpha = 10^\circ \pm 9.3^\circ$ ,  $k = 0.05$ ,  $F^+ = 0.6$  for baseline and multiple COMPACT modes.**

**M=0.5**

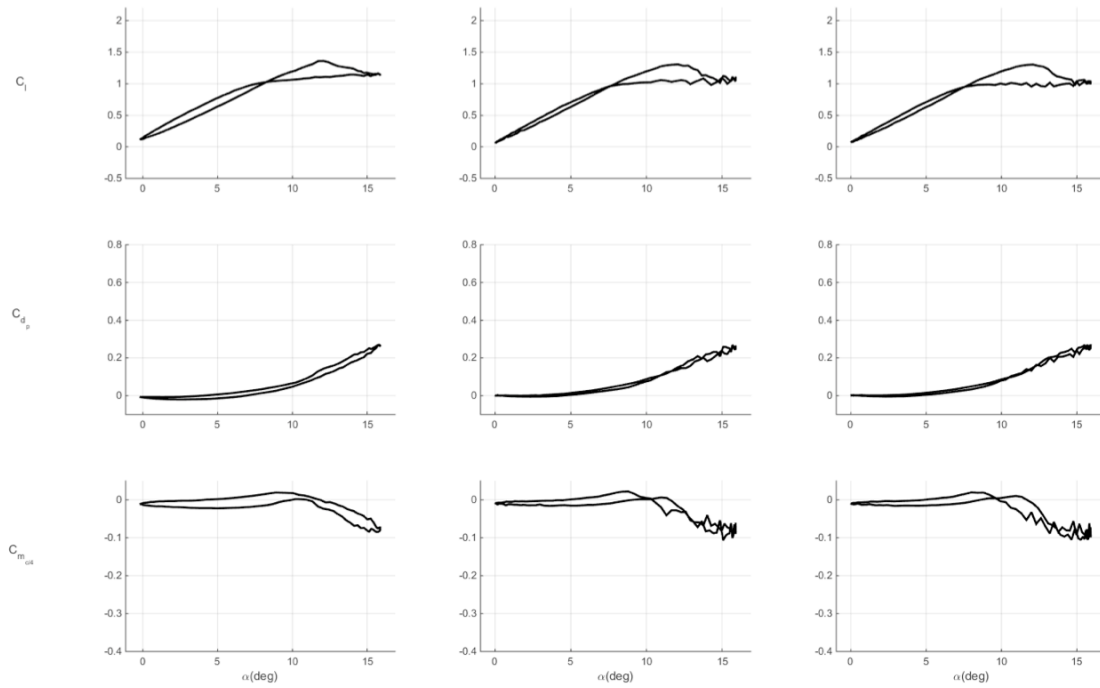


**Figure 608. Lift, drag, and moment coefficients at Mach 0.5,  $\alpha = 8^\circ \pm 8^\circ$ ,  $k = 0.025$  for baseline and dual-row COMPACT,  $F^+$  of 0.2 and 0.4. Front actuator only.**

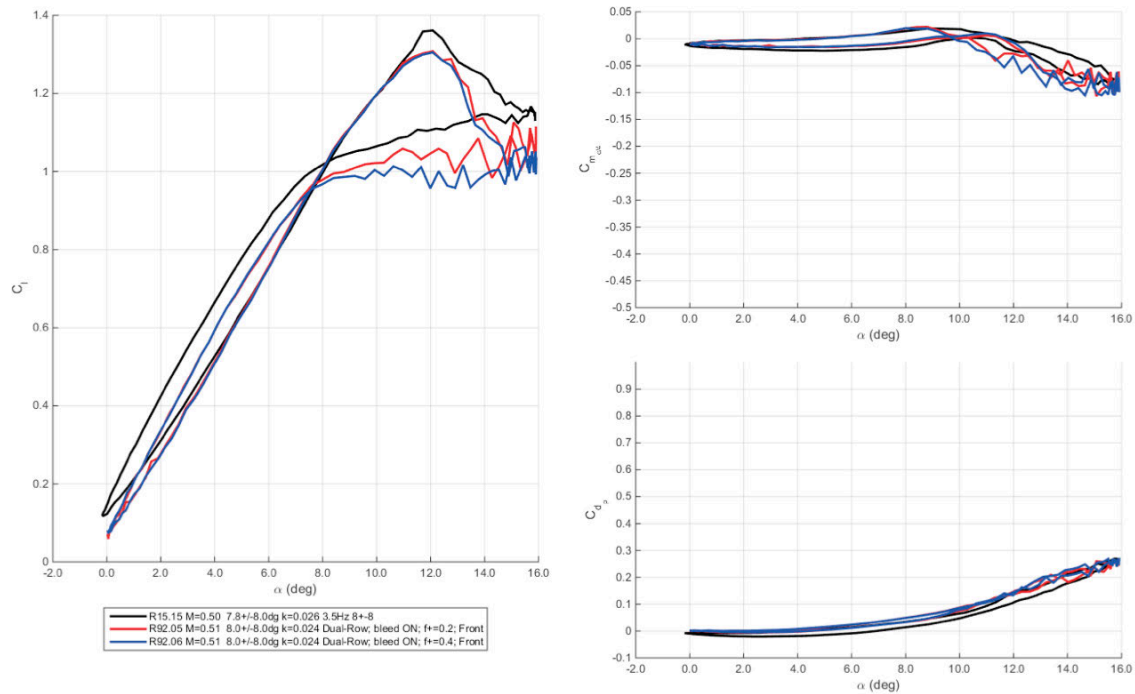


**Figure 609. Lift, drag, and moment coefficients at Mach 0.5,  $\alpha = 8^\circ \pm 8^\circ$ ,  $k = 0.025$  for baseline and dual-row COMPACT,  $F^+$  of 0.2 and 0.4. Loads plotted vs. angle-of-attack. Front actuator only.**

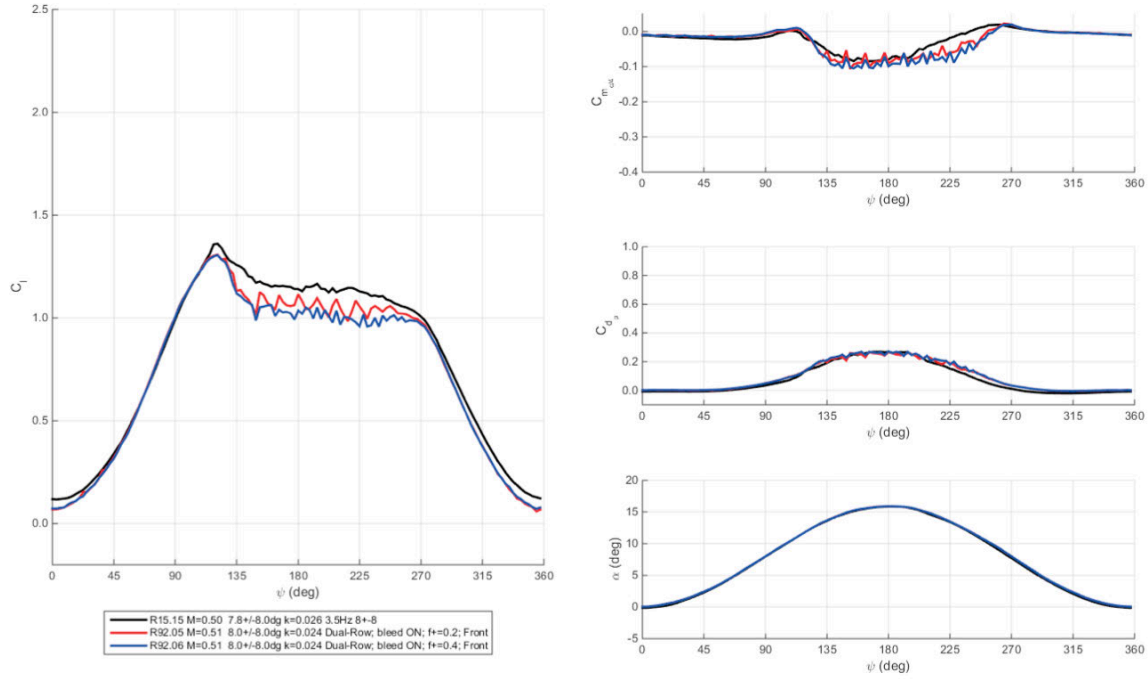


**Figure 610. Lift, drag, and moment coefficients at Mach 0.5,  $\alpha = 8^\circ \pm 8^\circ$ ,  $k = 0.025$  for baseline and dual-row COMPACT,  $F^+$  of 0.2 and 0.4. Loads plotted vs. phase angle. Front actuator only.**

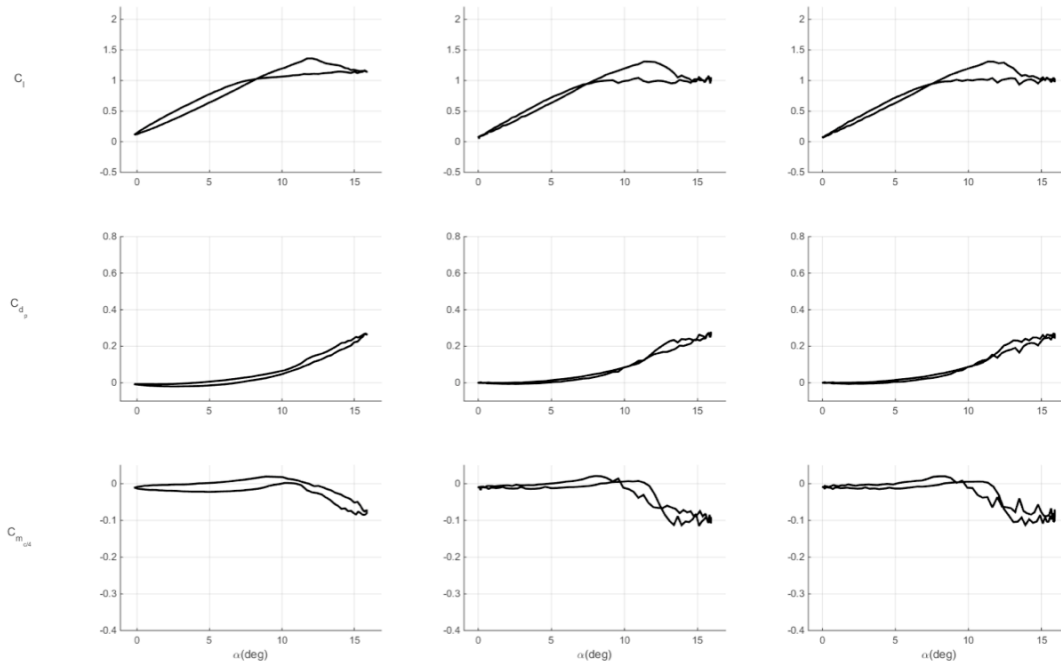


**Figure 611. Lift, drag, and moment coefficients at Mach 0.5,  $\alpha = 8^\circ \pm 8^\circ$ ,  $k = 0.025$  for baseline and dual-row COMPACT,  $F^+$  of 0.2 and 0.4. Back actuator only.**

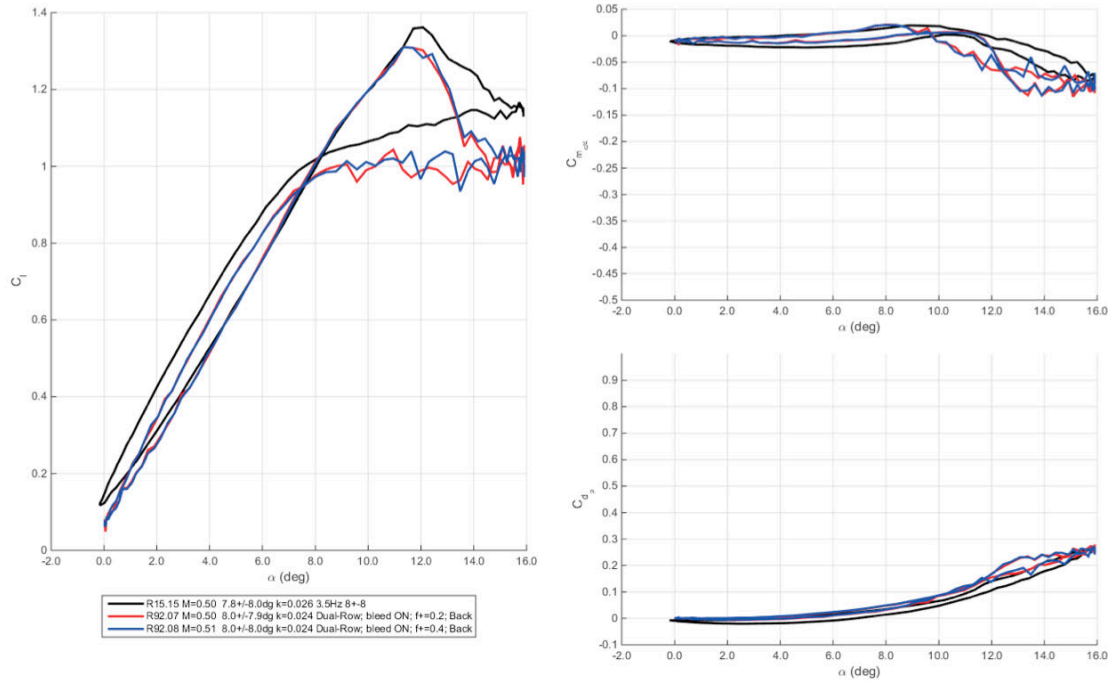


**Figure 612.** Lift, drag, and moment coefficients at Mach 0.5,  $\alpha = 8^\circ \pm 8^\circ$ ,  $k = 0.025$  for baseline and dual-row COMPACT,  $F^+$  of 0.2 and 0.4. Loads plotted vs. angle-of-attack. Back actuator only.

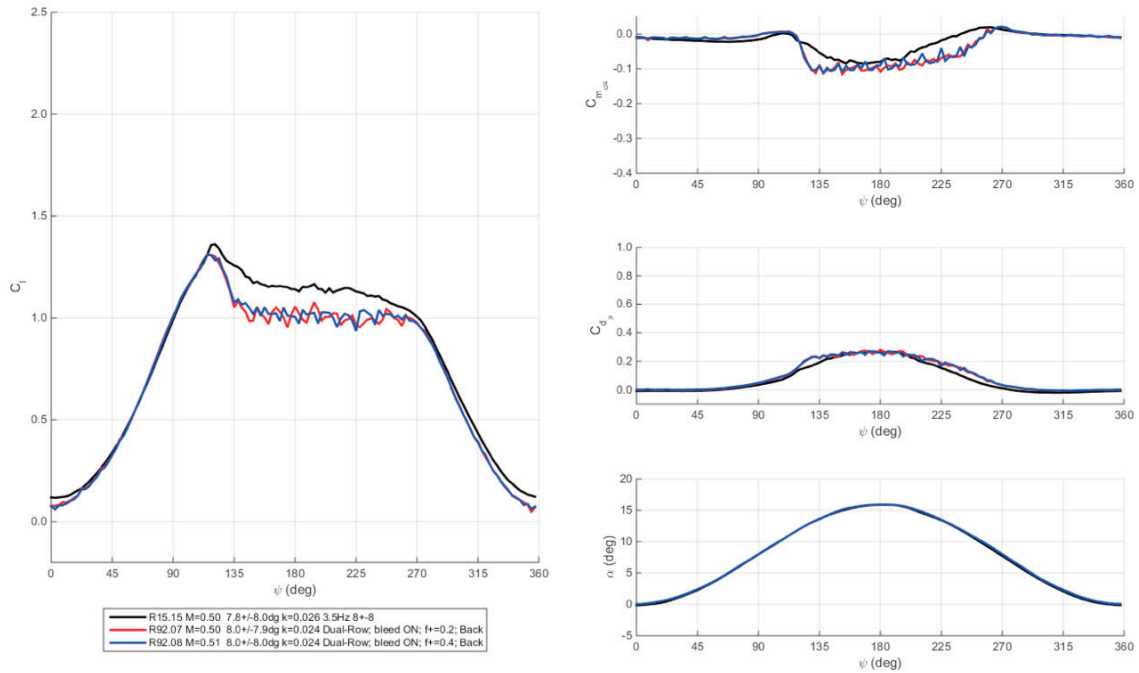


**Figure 613.** Lift, drag, and moment coefficients at Mach 0.5,  $\alpha = 8^\circ \pm 8^\circ$ ,  $k = 0.025$  for baseline and dual-row COMPACT,  $F^+$  of 0.2 and 0.4. Loads plotted vs. phase angle. Back actuator only.

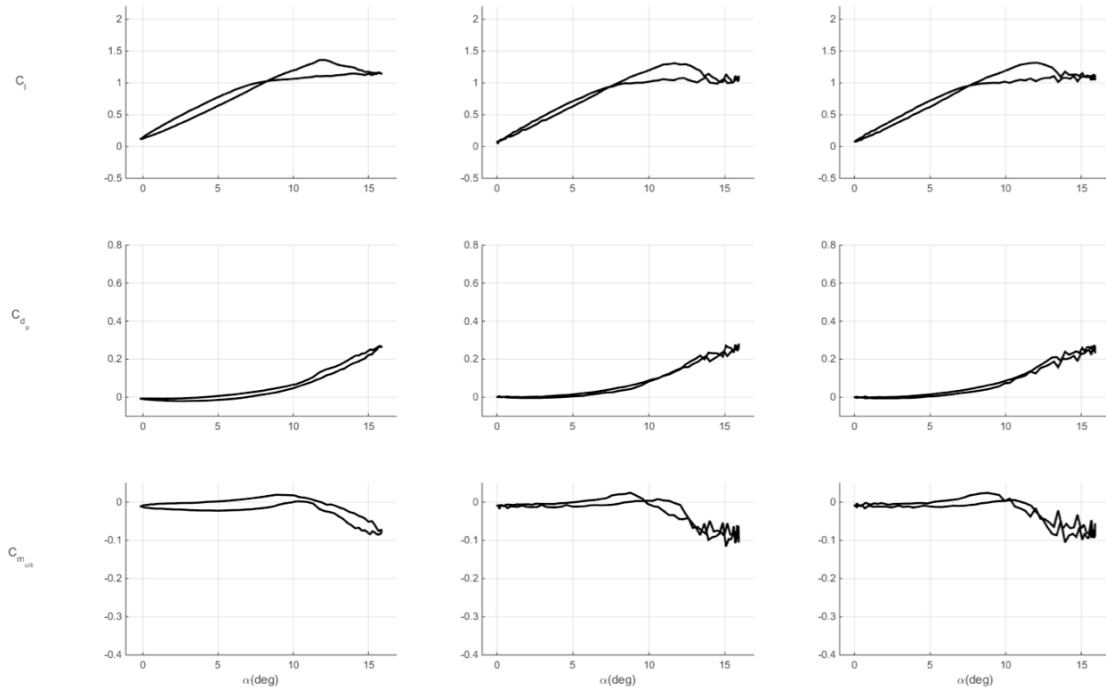


**Figure 614. Lift, drag, and moment coefficients at Mach 0.5,  $\alpha = 8^\circ \pm 8^\circ$ ,  $k = 0.025$  for baseline and dual-row COMPACT,  $F^+$  of 0.2 and 0.4. . Simultaneous operation.**

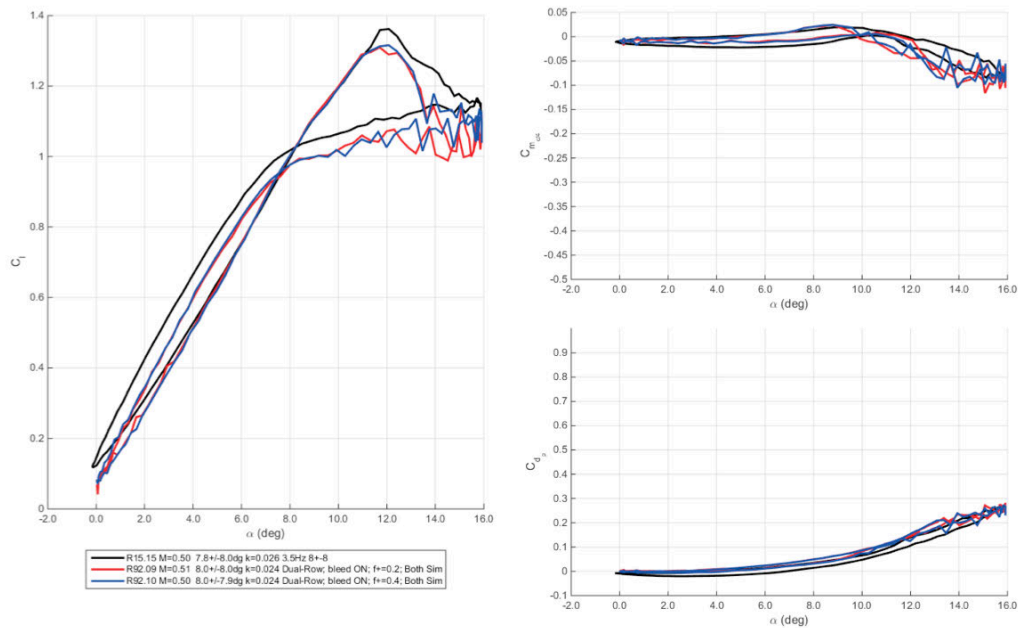


**Figure 615. Lift, drag, and moment coefficients at Mach 0.5,  $\alpha = 8^\circ \pm 8^\circ$ ,  $k = 0.025$  for baseline and dual-row COMPACT,  $F^+$  of 0.2 and 0.4. Loads plotted vs. angle-of-attack. . Simultaneous operation.**

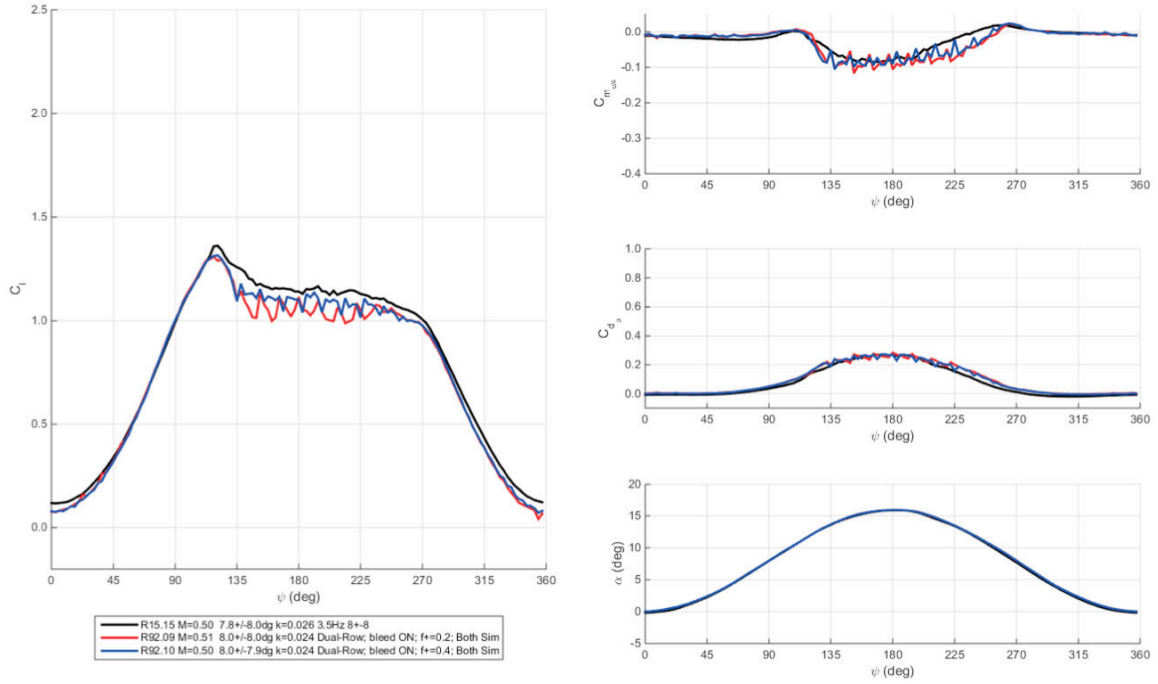


**Figure 616. Lift, drag, and moment coefficients at Mach 0.5,  $\alpha = 8^\circ \pm 8^\circ$ ,  $k = 0.025$  for baseline and dual-row COMPACT,  $F^+$  of 0.2 and 0.4. Loads plotted vs. phase angle. Simultaneous operation.**

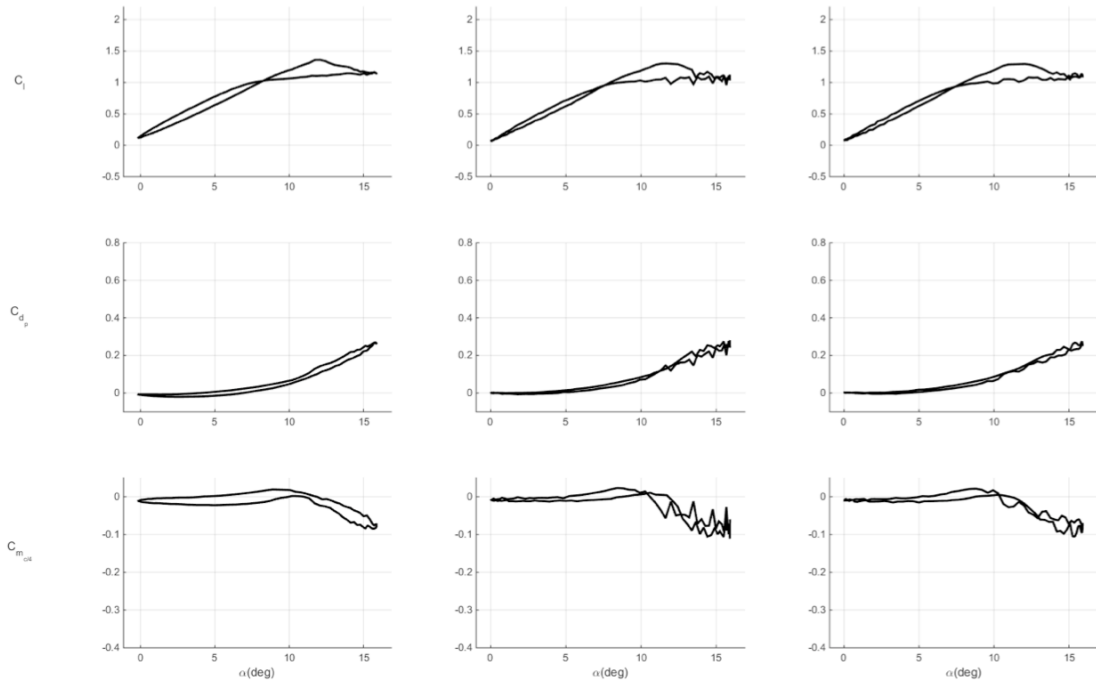


**Figure 617. Lift, drag, and moment coefficients at Mach 0.5,  $\alpha = 8^\circ \pm 8^\circ$ ,  $k = 0.025$  for baseline and dual-row COMPACT,  $F^+$  of 0.2 and 0.4. Alternating operation.**



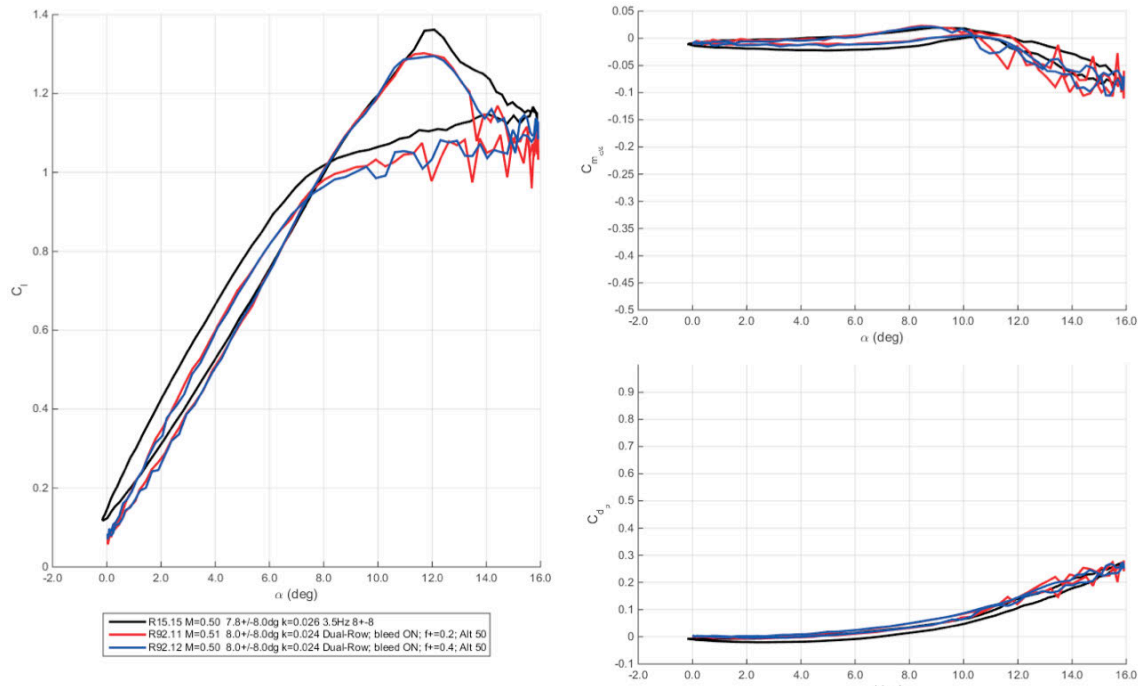


**Figure 618. Lift, drag, and moment coefficients at Mach 0.5,  $\alpha = 8^\circ \pm 8^\circ$ ,  $k = 0.025$  for baseline and dual-row COMPACT,  $F^+$  of 0.2 and 0.4. Loads plotted vs. angle-of-attack. . Alternating operation.**

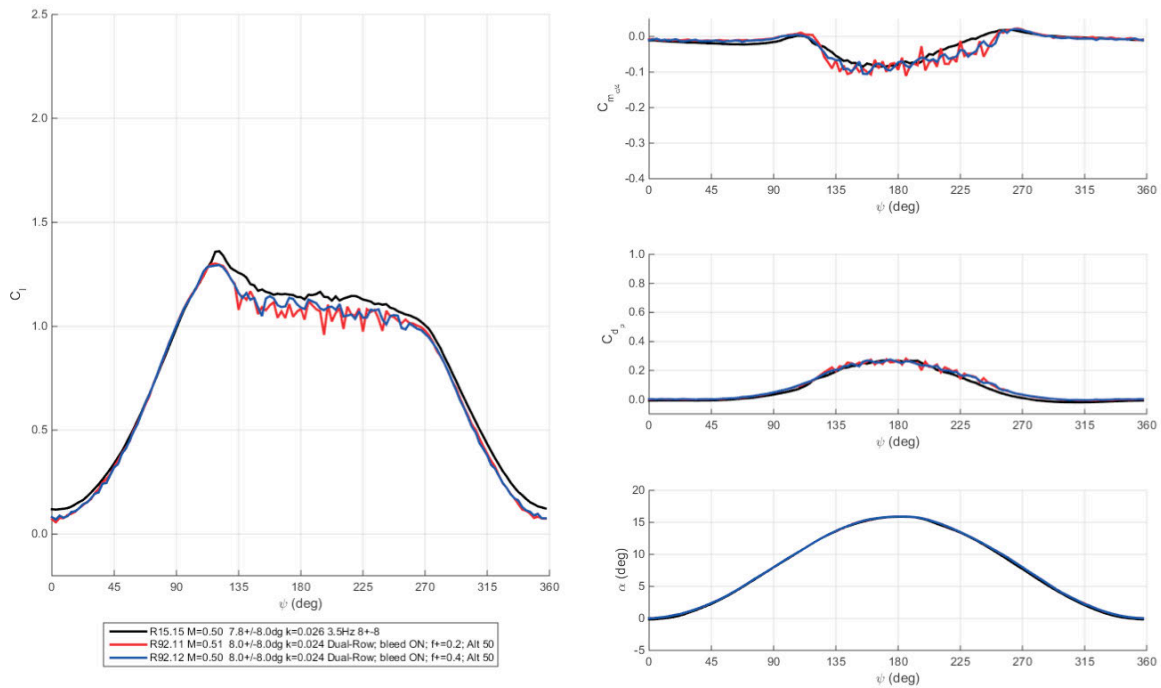


**Figure 619. Lift, drag, and moment coefficients at Mach 0.5,  $\alpha = 8^\circ \pm 8^\circ$ ,  $k = 0.025$  for baseline and dual-row COMPACT,  $F^+$  of 0.2 and 0.4. Loads plotted vs. phase angle. Alternating operation.**

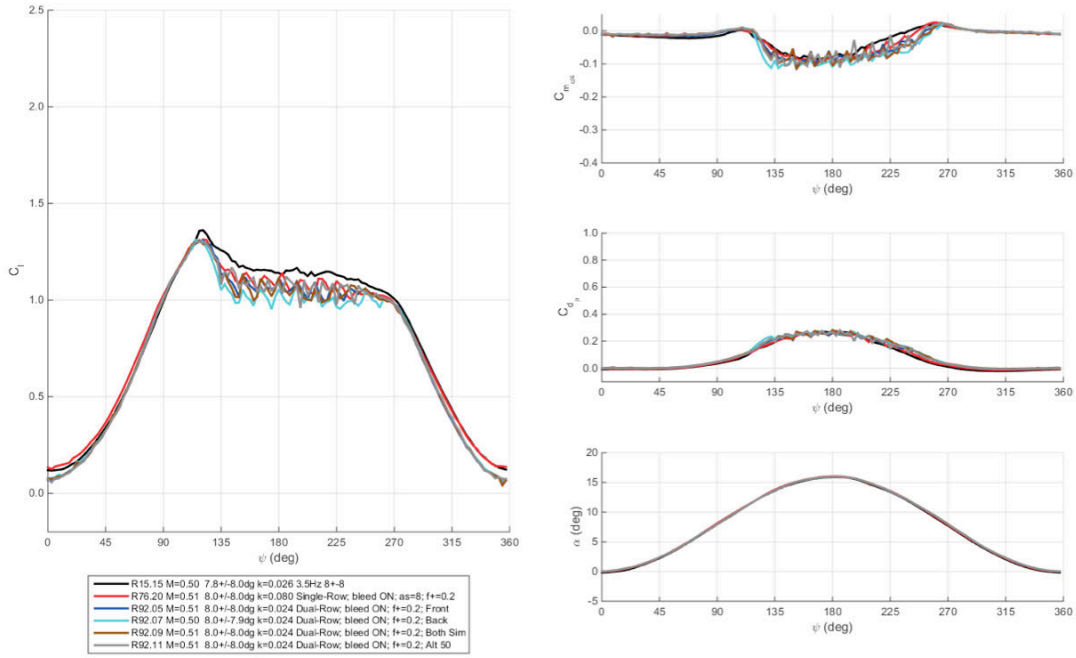


**Figure 620. Lift, drag, and moment coefficients at Mach 0.5,  $\alpha = 8^\circ \pm 8^\circ$ ,  $k = 0.025$ ,  $F^+ = 0.2$  for baseline and multiple COMPACT modes.**

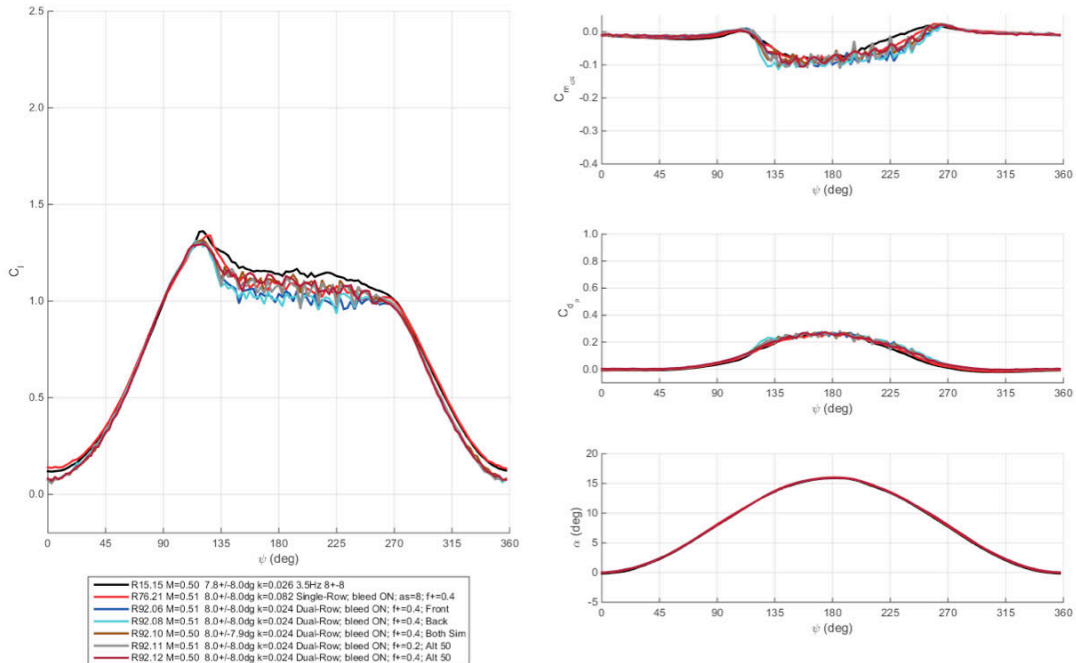


**Figure 621. Lift, drag, and moment coefficients at Mach 0.5,  $\alpha = 8^\circ \pm 8^\circ$ ,  $k = 0.025$ ,  $F^+ = 0.4$  for baseline and multiple COMPACT modes.**

## Summary Tables

**Table 62. Dual-row COMPACT results on key dynamic stall metrics, Mach 0.2.**

$M$	$k$	$\alpha_0(^{\circ})$	$\alpha_1(^{\circ})$	Geom	$F^+$	Bleed	$N_{pulses}$	$\alpha_{start}$	$C_{l,avg}$	$C_{l,max}$	$C_{d,p,avg}$	$C_{d,p,max}$	$C_{m,c/4}$	$C_{m,c/4,min}$
0.40	0.05	9.96	9.86	Clean	0	0	0	NA	0.84	1.70	0.12	0.43	-0.04	-0.17
0.39	0.05	10.03	9.40	Front	0.2	1	12	10	0%	-6%	-3%	-2%	-17%	-7%
0.39	0.05	10.04	9.41	Front	0.4	1	25	10	1%	-6%	-3%	-3%	-20%	-7%
0.39	0.05	10.04	9.41	Front	0.6	1	37	10	1%	-5%	-2%	-4%	-20%	-14%
0.39	0.05	10.05	9.41	Back	0.2	1	12	10	-3%	-5%	-2%	-1%	-12%	-5%
0.39	0.05	10.05	9.42	Back	0.4	1	25	10	-2%	-5%	-2%	-3%	-12%	-10%
0.39	0.05	10.05	9.42	Back	0.6	1	37	10	-2%	-5%	-2%	-3%	-14%	-7%
0.39	0.05	10.03	9.39	Sim	0.2	1	12	10	1%	-4%	-1%	0%	-18%	-11%
0.39	0.05	10.05	9.40	Sim	0.4	1	25	10	0%	-5%	-1%	0%	-14%	-5%
0.39	0.05	10.04	9.40	Sim	0.6	1	37	10	2%	-5%	-3%	-4%	-23%	-11%
0.39	0.05	10.04	9.40	Alt50	0.2	1	12	10	0%	-4%	-1%	-1%	-16%	-8%
0.39	0.05	10.05	9.41	Alt50	0.4	1	25	10	2%	-5%	-2%	-3%	-21%	-9%
0.39	0.05	10.05	9.41	Alt 50	0.6	1	37	10	2%	-4%	-4%	-3%	-25%	-9%
0.39	0.05	10.04	9.39	Alt U	0.2	1	12	10	2%	-3%	-2%	-1%	-19%	-9%
0.39	0.05	10.06	9.40	Alt U	0.4	1	25	10	2%	-5%	-2%	-3%	-20%	-7%
0.39	0.05	10.05	9.40	Alt U	0.6	1	37	10	2%	-5%	-2%	-6%	-27%	-17%
0.40	0.05	10.04	9.40	Alt U/2	0.2	1	12	10	1%	-6%	-2%	-4%	-18%	-11%
0.39	0.05	10.05	9.41	Alt U/2	0.4	1	25	10	2%	-5%	-3%	-3%	-23%	-10%
0.39	0.05	10.06	9.41	Alt U/2	0.6	1	37	10	2%	-5%	-3%	-7%	-23%	-17%

**Table 63. Dual-row COMPACT results on key dynamic stall metrics, Mach 0.3.**

$M$	$k$	$\alpha_0(^{\circ})$	$\alpha_1(^{\circ})$	Geom	$F^+$	Bleed	$N_{pulses}$	$\alpha_{start}$	$C_{l,avg}$	$C_{l,max}$	$C_{d,p,avg}$	$C_{d,p,max}$	$C_{m,c/4}$	$C_{m,c/4,min}$
0.30	0.07	9.99	9.58	Clean	0	0	0	NA	0.91	1.89	0.12	0.62	-0.03	-0.29
0.30	0.07	10.02	9.10	Front	0.2	1	8	10	0%	-4%	10%	-8%	9%	-12%
0.30	0.07	10.03	9.10	Front	0.4	1	17	10	1%	3%	9%	-8%	0%	-15%
0.30	0.07	9.99	9.47	Front	0.6	1	26	10	0%	-1%	7%	-9%	-10%	-12%
0.30	0.07	9.99	9.47	Back	0.8	1	35	10	1%	5%	7%	-8%	-13%	-13%
0.30	0.07	10.01	9.50	Back	0.2	1	8	10	-4%	-4%	12%	-6%	16%	-6%
0.30	0.07	10.00	9.50	Back	0.4	1	17	10	-3%	-4%	11%	-7%	11%	-9%
0.30	0.07	10.00	9.50	Back	0.6	1	26	10	-2%	2%	11%	-8%	10%	-6%
0.30	0.07	10.01	9.50	Sim	0.8	1	35	10	-3%	-2%	9%	-7%	3%	-11%
0.30	0.07	10.00	9.50	Sim	0.2	1	8	10	-1%	-4%	10%	-6%	4%	-13%
0.30	0.07	10.01	9.49	Sim	0.4	1	17	10	1%	-2%	10%	-8%	-3%	-20%
0.30	0.07	10.01	9.49	Sim	0.6	1	26	10	0%	2%	5%	-7%	-18%	-25%
0.30	0.07	10.01	9.50	Alt 50	0.8	1	37	10	-2%	-2%	8%	-10%	-3%	-18%
0.30	0.07	10.00	9.51	Alt 50	0.2	1	8	10	-1%	-3%	8%	-7%	0%	-12%
0.30	0.07	10.00	9.51	Alt 50	0.4	1	17	10	0%	4%	7%	-5%	-9%	-9%
0.30	0.07	10.00	9.51	Alt 50	0.6	1	26	10	0%	-2%	2%	-5%	-18%	-15%

**Table 64. Dual-row COMPACT results on key dynamic stall metrics, Mach 0.4.**

$M$	$k$	$\alpha_0(^{\circ})$	$\alpha_1(^{\circ})$	Geom	$F^+$	Bleed	$N_{pulses}$	$\alpha_{start}$	$C_{l,avg}$	$C_{l,max}$	$C_{d,p,avg}$	$C_{d,p,max}$	$C_{m,c/4}$	$C_{m,c/4,min}$
0.40	0.05	9.96	9.86	Clean	0	0	0	NA	0.84	1.70	0.12	0.43	-0.04	-0.17
0.39	0.05	10.03	9.40	Front	0.2	1	12	10	0%	-6%	-3%	-2%	-17%	-7%
0.39	0.05	10.04	9.41	Front	0.4	1	25	10	1%	-6%	-3%	-3%	-20%	-7%
0.39	0.05	10.04	9.41	Front	0.6	1	37	10	1%	-5%	-2%	-4%	-20%	-14%
0.39	0.05	10.05	9.41	Back	0.2	1	12	10	-3%	-5%	-2%	-1%	-12%	-5%
0.39	0.05	10.05	9.42	Back	0.4	1	25	10	-2%	-5%	-2%	-3%	-12%	-10%
0.39	0.05	10.05	9.42	Back	0.6	1	37	10	-2%	-5%	-2%	-3%	-14%	-7%
0.39	0.05	10.03	9.39	Sim	0.2	1	12	10	1%	-4%	-1%	0%	-18%	-11%
0.39	0.05	10.05	9.40	Sim	0.4	1	25	10	0%	-5%	-1%	0%	-14%	-5%
0.39	0.05	10.04	9.40	Sim	0.6	1	37	10	2%	-5%	-3%	-4%	-23%	-11%
0.39	0.05	10.04	9.40	Alt50	0.2	1	12	10	0%	-4%	-1%	-1%	-16%	-8%
0.39	0.05	10.05	9.41	Alt50	0.4	1	25	10	2%	-5%	-2%	-3%	-21%	-9%
0.39	0.05	10.05	9.41	Alt 50	0.6	1	37	10	2%	-4%	-4%	-3%	-25%	-9%
0.39	0.05	10.04	9.39	Alt U	0.2	1	12	10	2%	-3%	-2%	-1%	-19%	-9%
0.39	0.05	10.06	9.40	Alt U	0.4	1	25	10	2%	-5%	-2%	-3%	-20%	-7%
0.39	0.05	10.05	9.40	Alt U	0.6	1	37	10	2%	-5%	-5%	-6%	-27%	-17%
0.40	0.05	10.04	9.40	Alt U/2	0.2	1	12	10	1%	-6%	-2%	-4%	-18%	-11%
0.39	0.05	10.05	9.41	Alt U/2	0.4	1	25	10	2%	-5%	-3%	-3%	-23%	-10%
0.39	0.05	10.06	9.41	Alt U/2	0.6	1	37	10	2%	-5%	-3%	-7%	-23%	-17%

## Appendix 5. High-Speed Wind Tunnel Test – PIV Results

Please note that X and Z are given in inches for all plots.

### 1. Steady Baseline Results

#### A. Mach 0.2

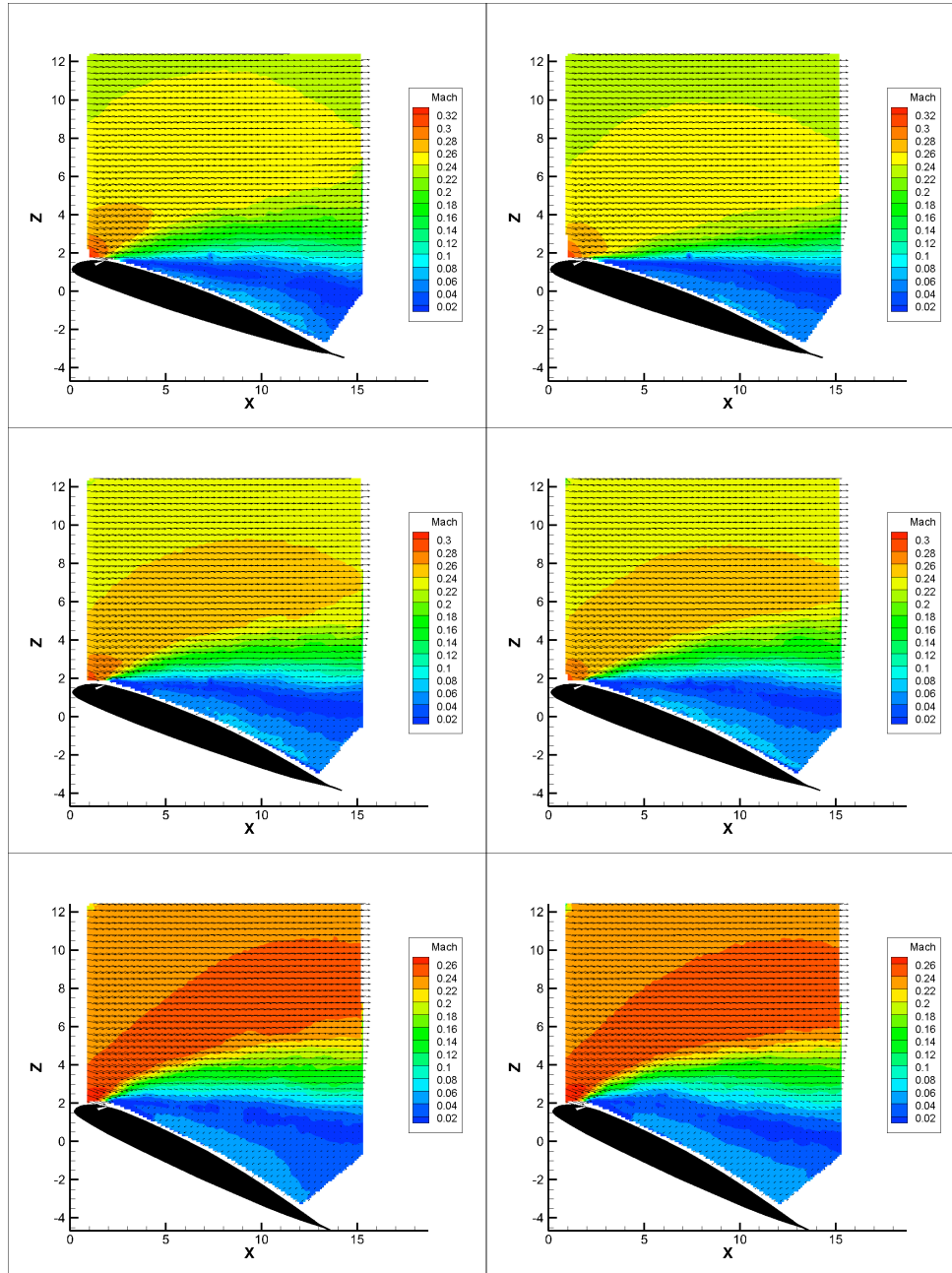


Figure 622. Mach contours for bleed-off (left) and bleed-on (right) results at Mach 0.2,  $\alpha = 18^\circ, 20^\circ, \text{ and } 25^\circ$  (top to bottom)

## B. Mach 0.3

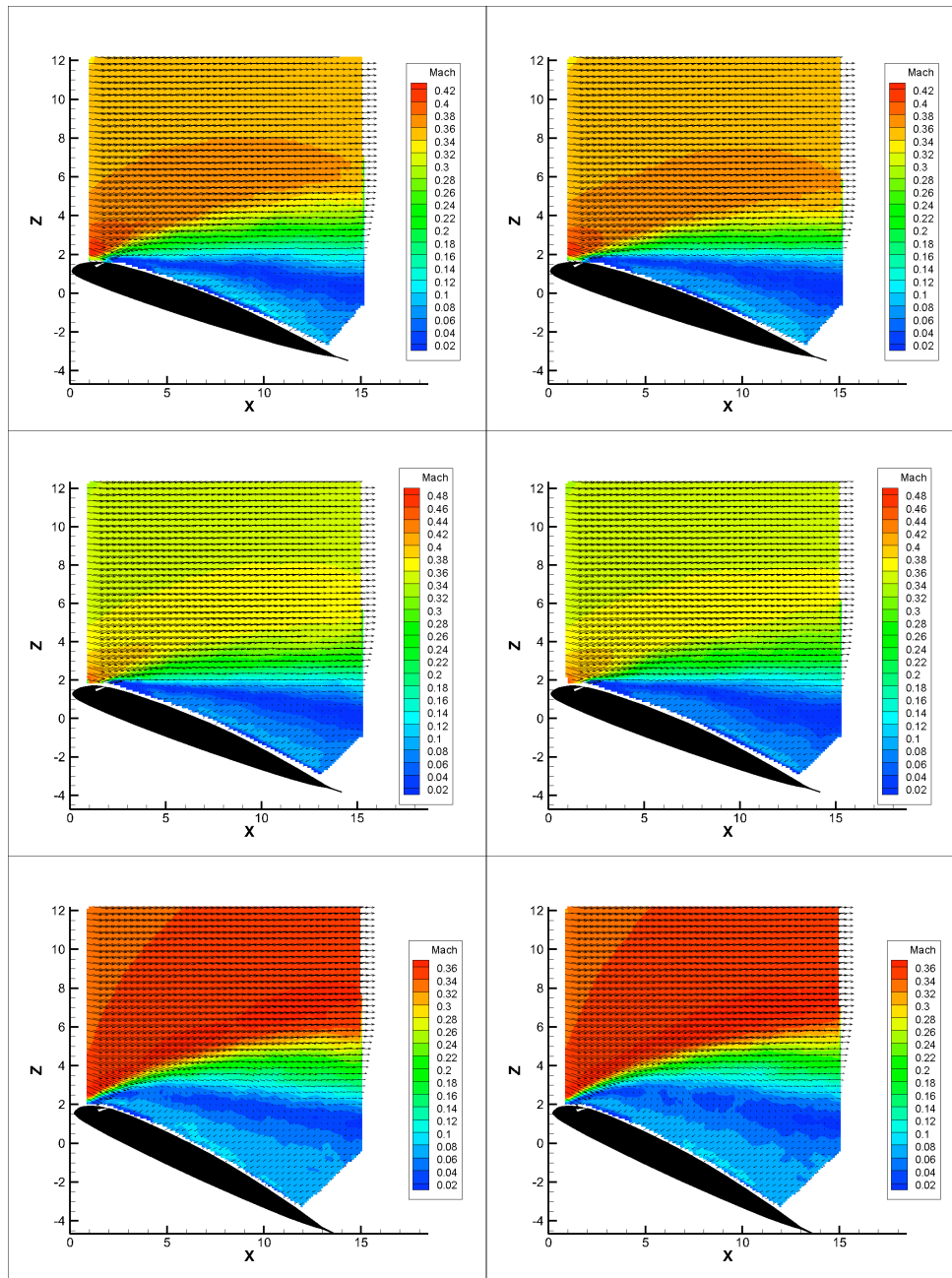
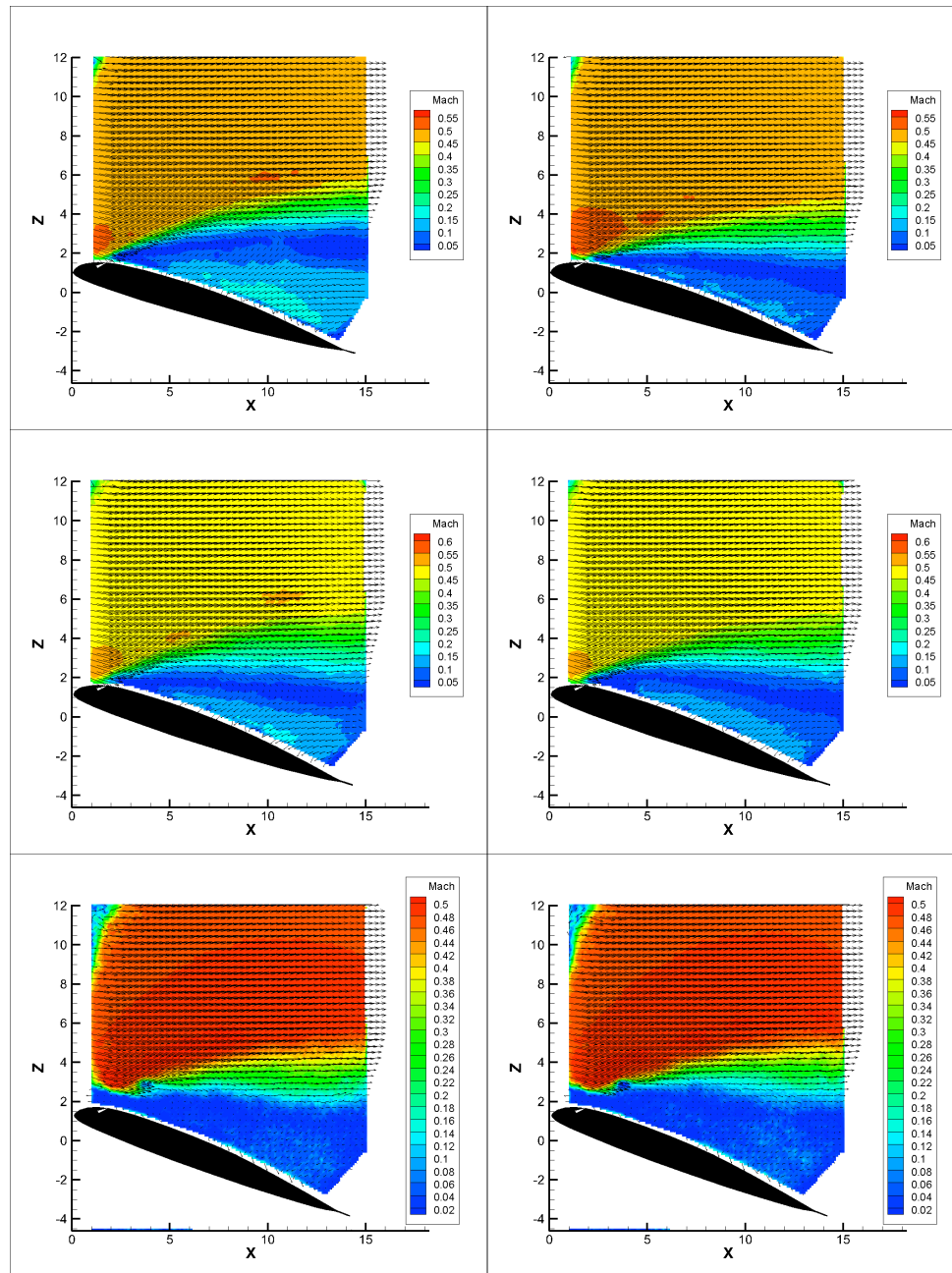


Figure 623. Mach contours for bleed-off (left) and bleed-on (right) results at Mach 0.3,  $\alpha = 18^\circ, 20^\circ$ , and  $25^\circ$  (top to bottom).

### C. Mach 0.4



**Figure 624. Mach contours for bleed-off (left) and bleed-on (right) results at Mach 0.4,  $\alpha = 16^\circ, 18^\circ$ , and  $20^\circ$  (top to bottom).**



## 2. Steady Results

### A. Mach 0.2

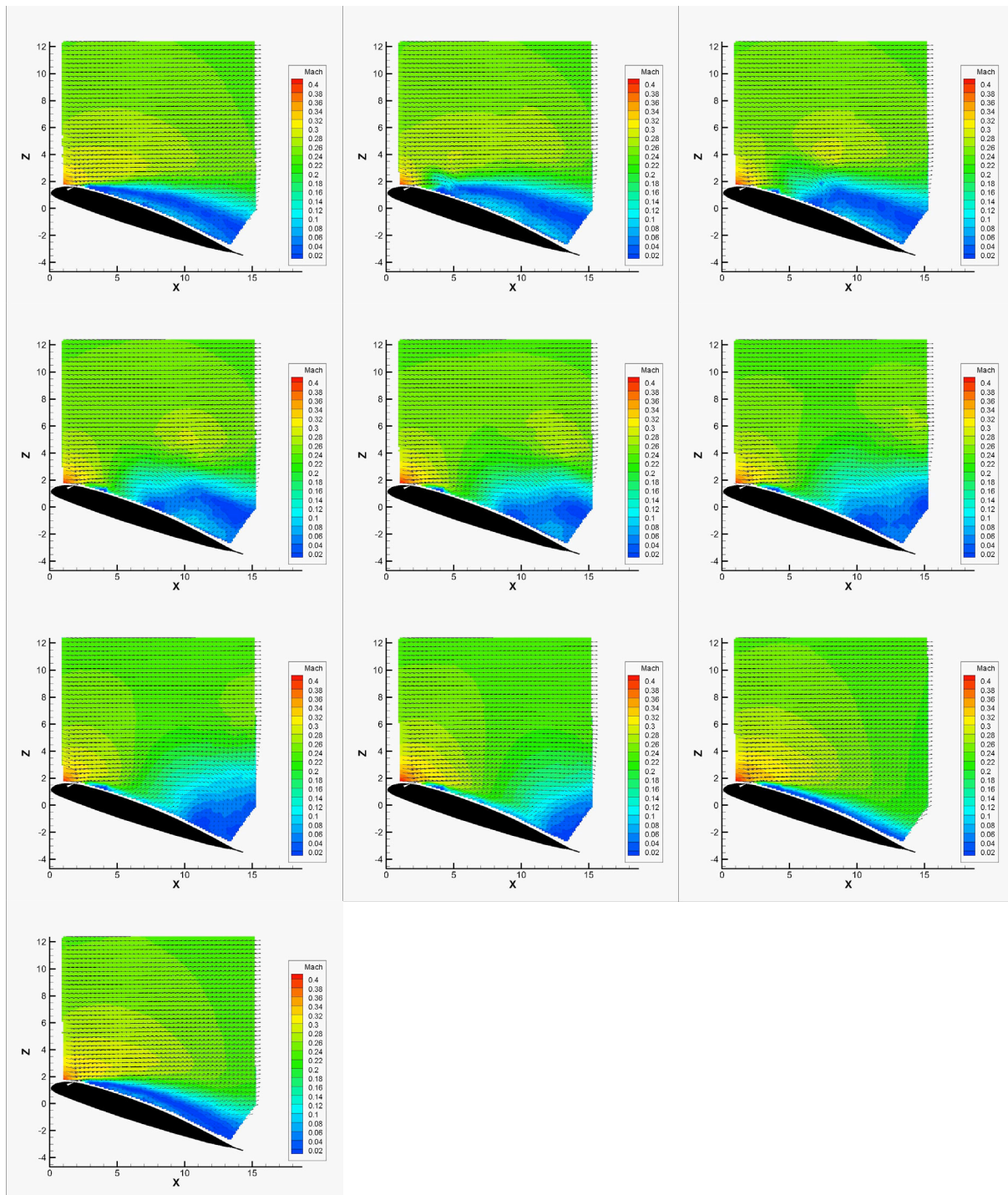
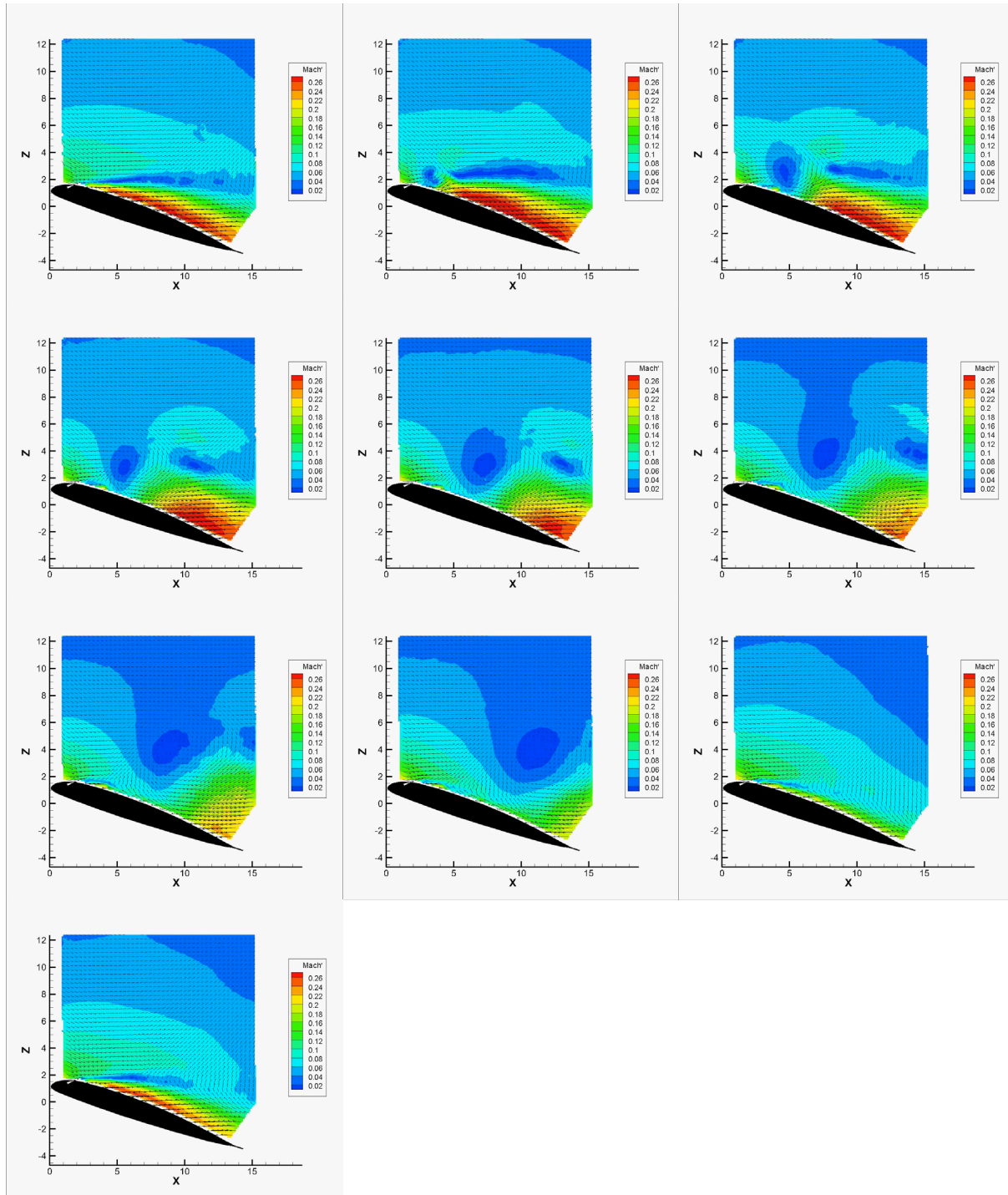
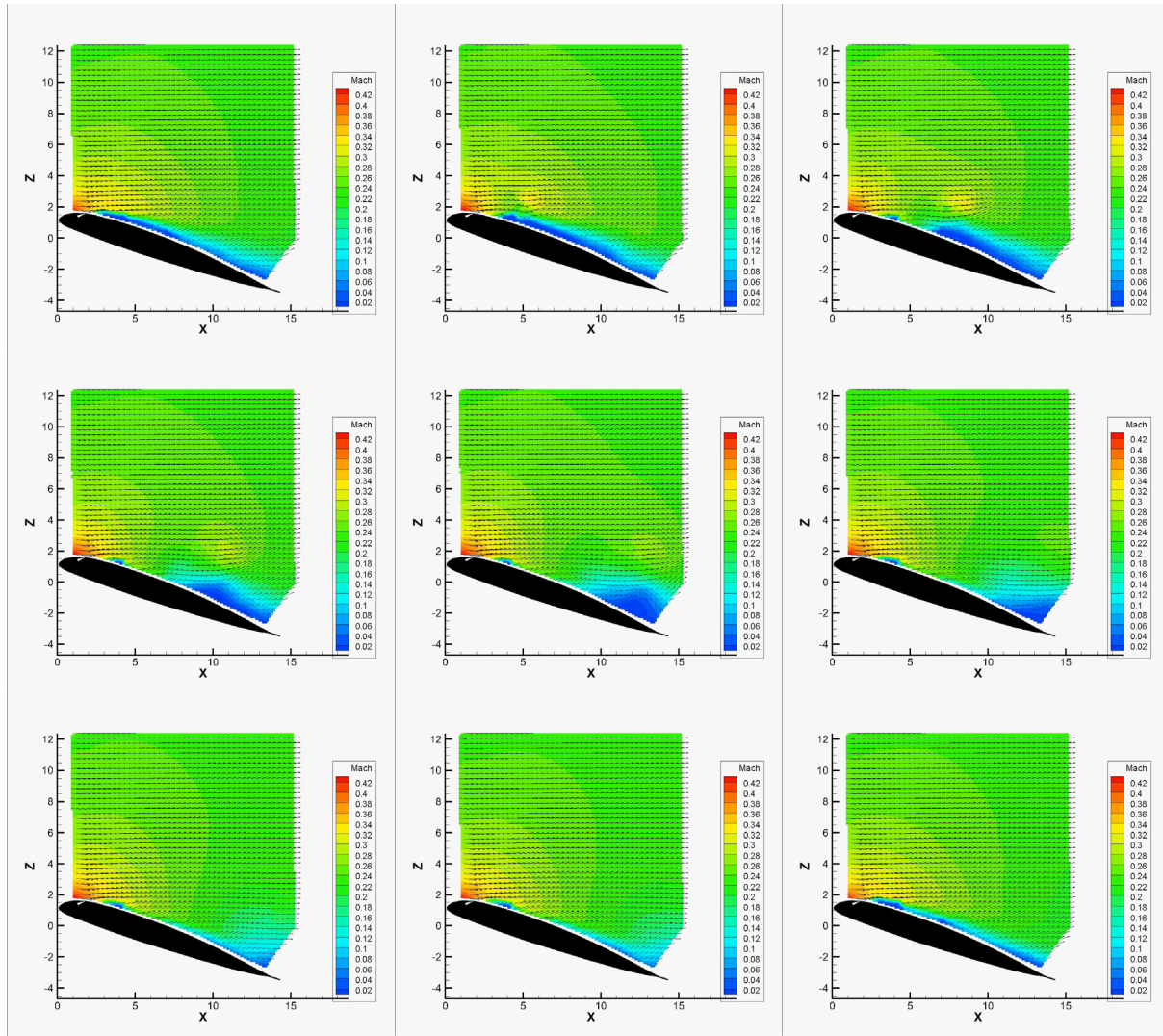


Figure 625. Mach contours, Mach 0.2,  $\alpha = 18^\circ$ ,  $F^+ = 0.2$ ,  $\Delta t = 0, 1, 2, 3, 4, 5, 6, 7, 14, 21$  ms.





**Figure 626.** Mach' contours, Mach 0.2,  $\alpha = 18^\circ$ ,  $F^+ = 0.2$ ,  $\Delta t = 0, 1, 2, 3, 4, 5, 6, 7, 14, 21$  ms.



**Figure 627. Mach contours, Mach 0.2,  $\alpha = 18^\circ$ ,  $F^+ = 0.4$ ,  $\Delta t = 0, 1, 2, 3, 4, 5, 6, 7, 10.5$  ms.**

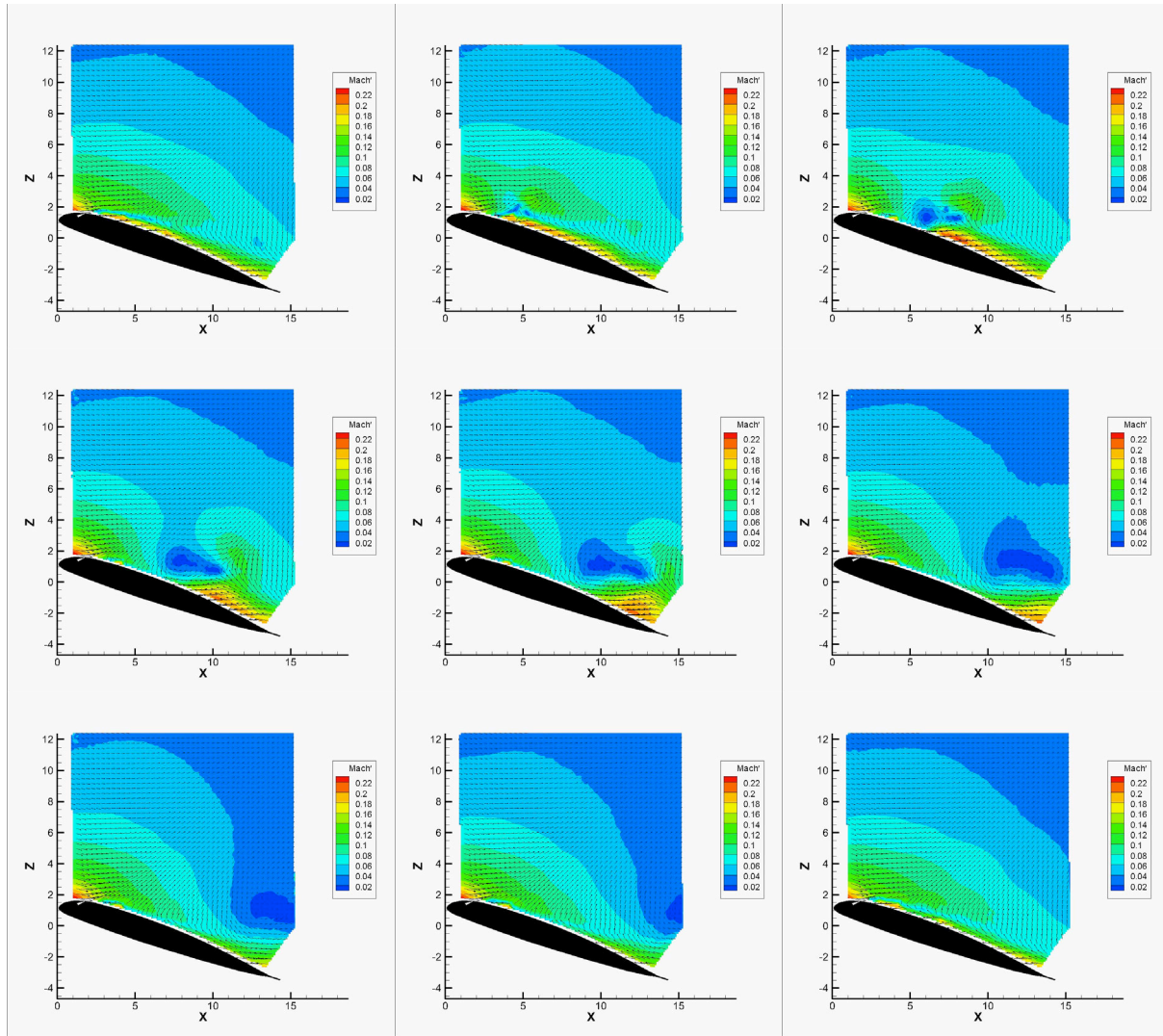


**Figure 628.** Mach' contours, Mach 0.2,  $\alpha = 18^\circ$ ,  $F^+ = 0.4$ ,  $\Delta t = 0, 1, 2, 3, 4, 5, 6, 7, 10.5$  ms.



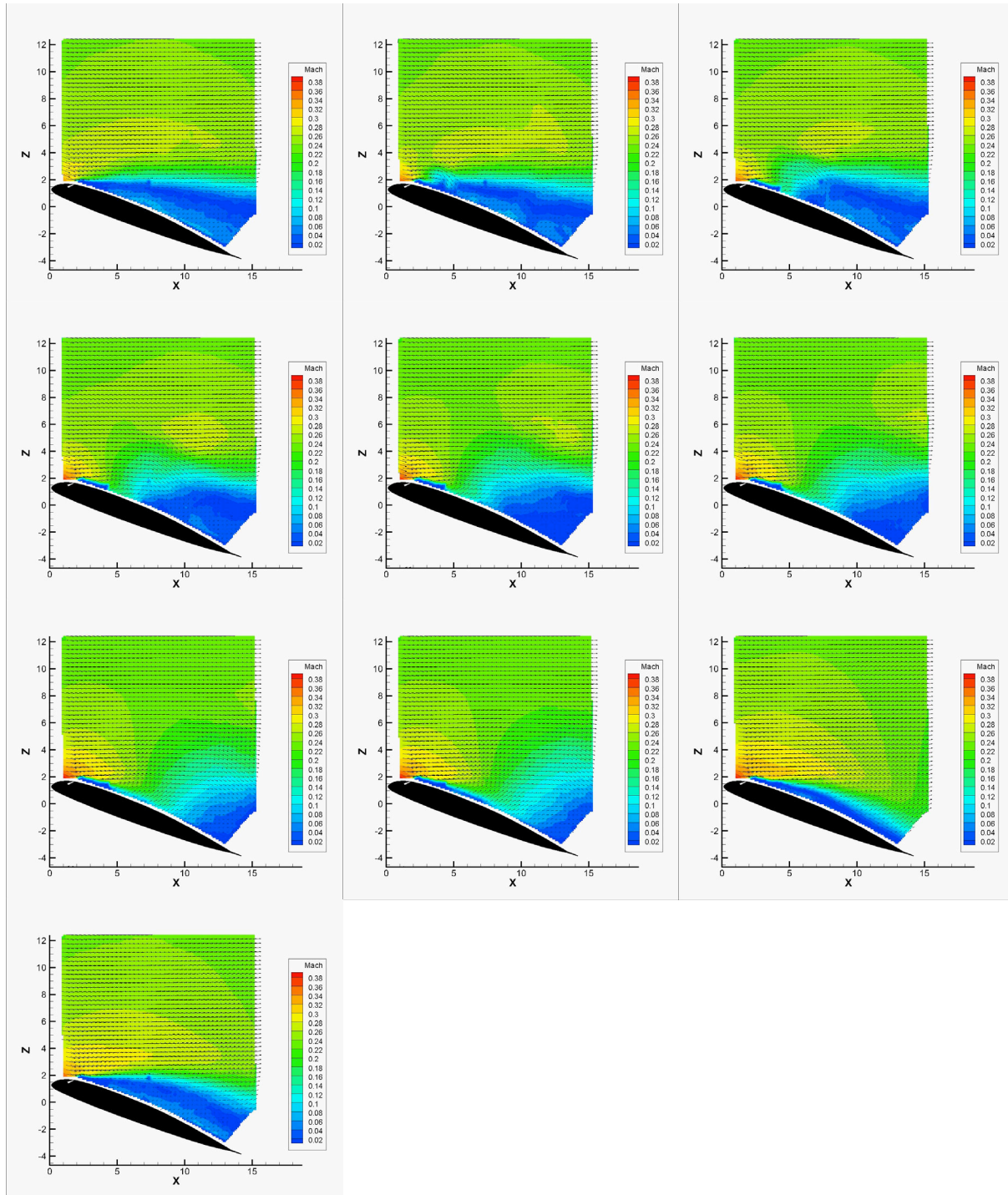


**Figure 629. Mach contours, Mach 0.2,  $\alpha = 20^\circ$ ,  $F^+ = 0.2$ ,  $\Delta t = 0, 1, 2, 3, 4, 5, 6, 7, 14, 21$  ms.**

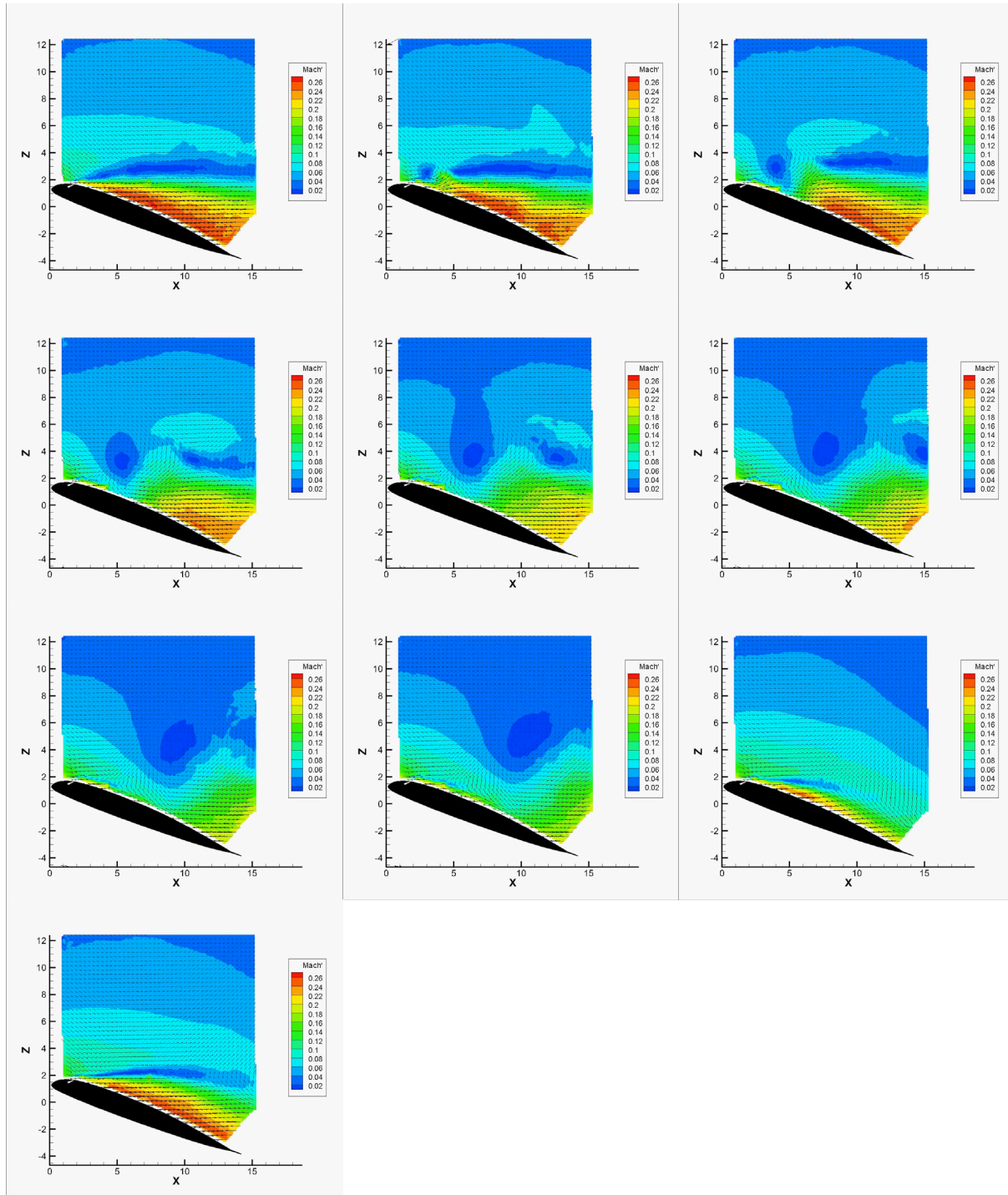


**Figure 630. Mach' contours, Mach 0.2,  $\alpha = 20^\circ$ ,  $F^+ = 0.2$ ,  $\Delta t = 0, 1, 2, 3, 4, 5, 6, 7, 14, 21$  ms.**

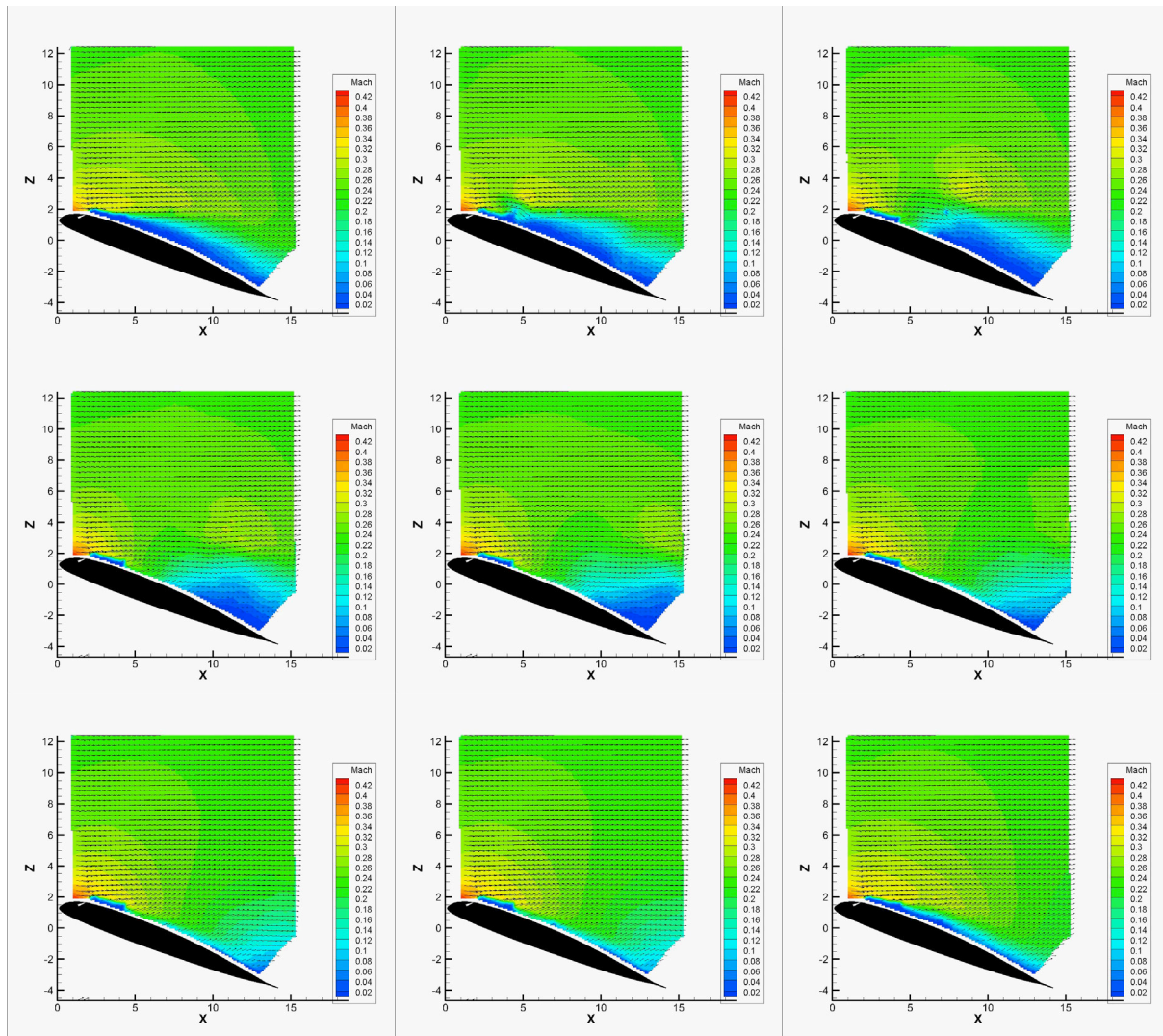
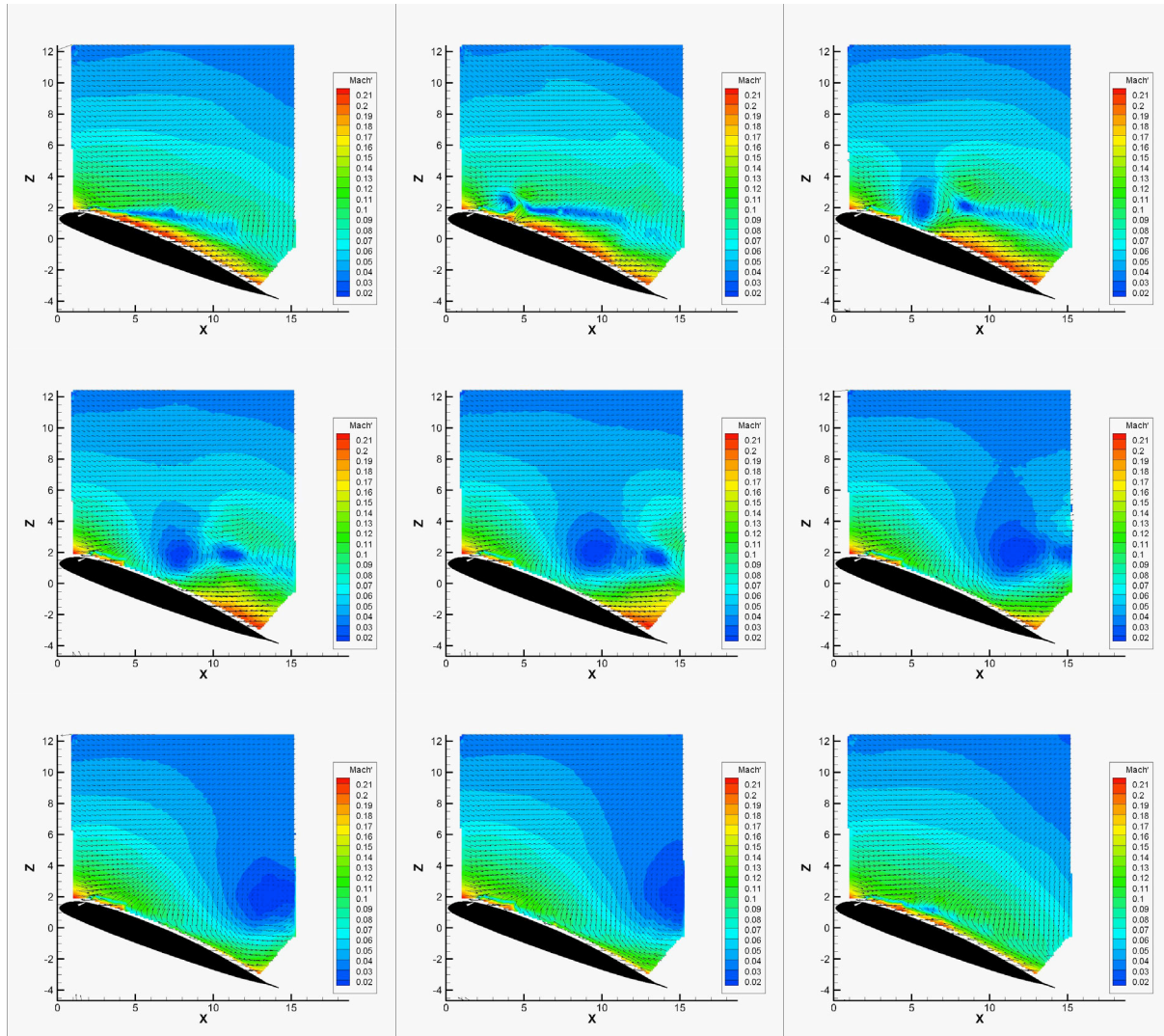
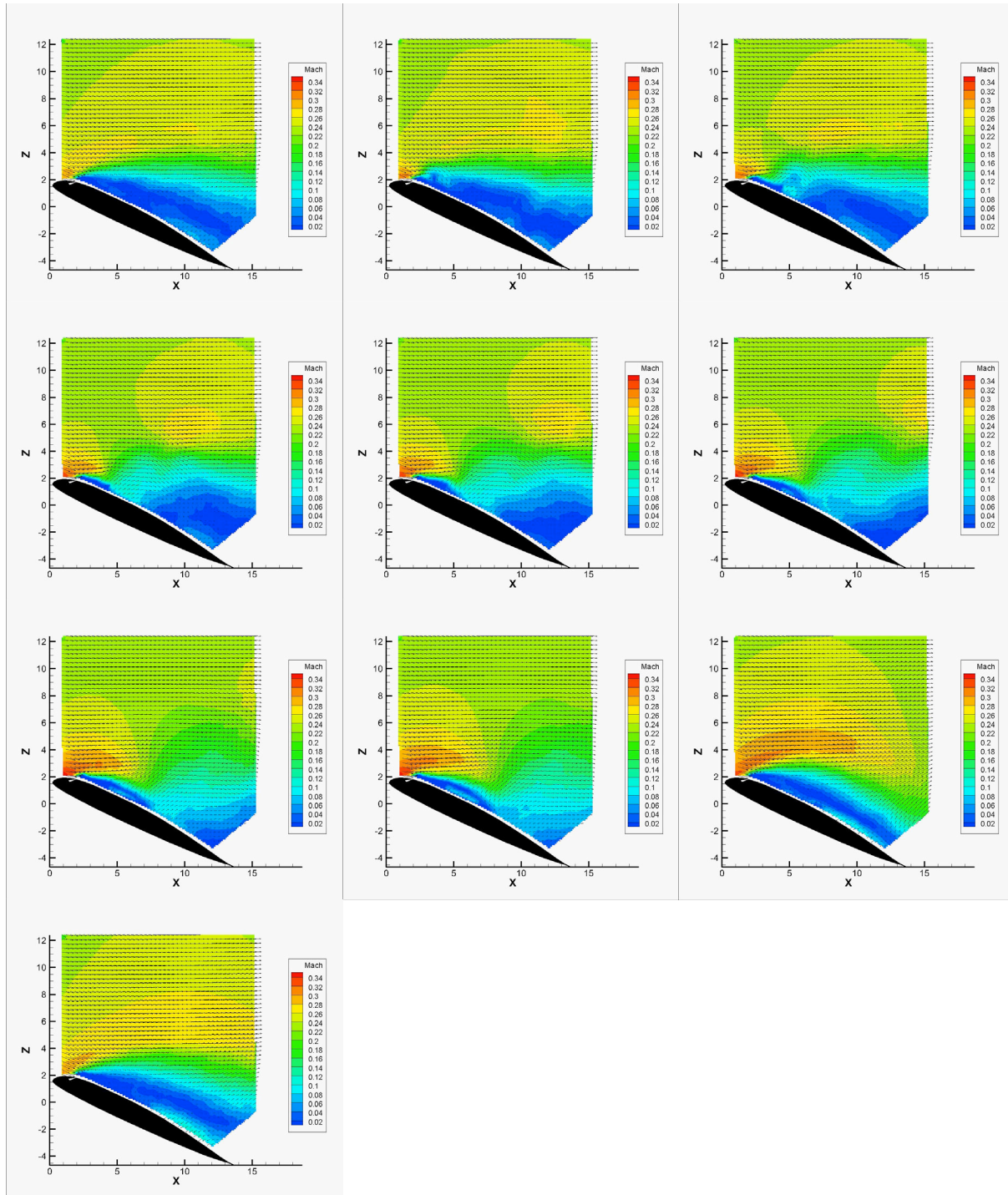


Figure 631. Mach contours, Mach 0.2,  $\alpha = 20^\circ$ ,  $F^+ = 0.4$ ,  $\Delta t = 0, 1, 2, 3, 4, 5, 6, 7, 10.5$  ms.





**Figure 632.** Mach' contours, Mach 0.2,  $\alpha = 20^\circ$ ,  $F^+ = 0.4$ ,  $\Delta t = 0, 1, 2, 3, 4, 5, 6, 7, 10.5$  ms.



**Figure 633. Mach contours, Mach 0.2,  $\alpha = 25^\circ$ ,  $F^+ = 0.2$ ,  $\Delta t = 0, 1, 2, 3, 4, 5, 6, 7, 14, 21$  ms.**



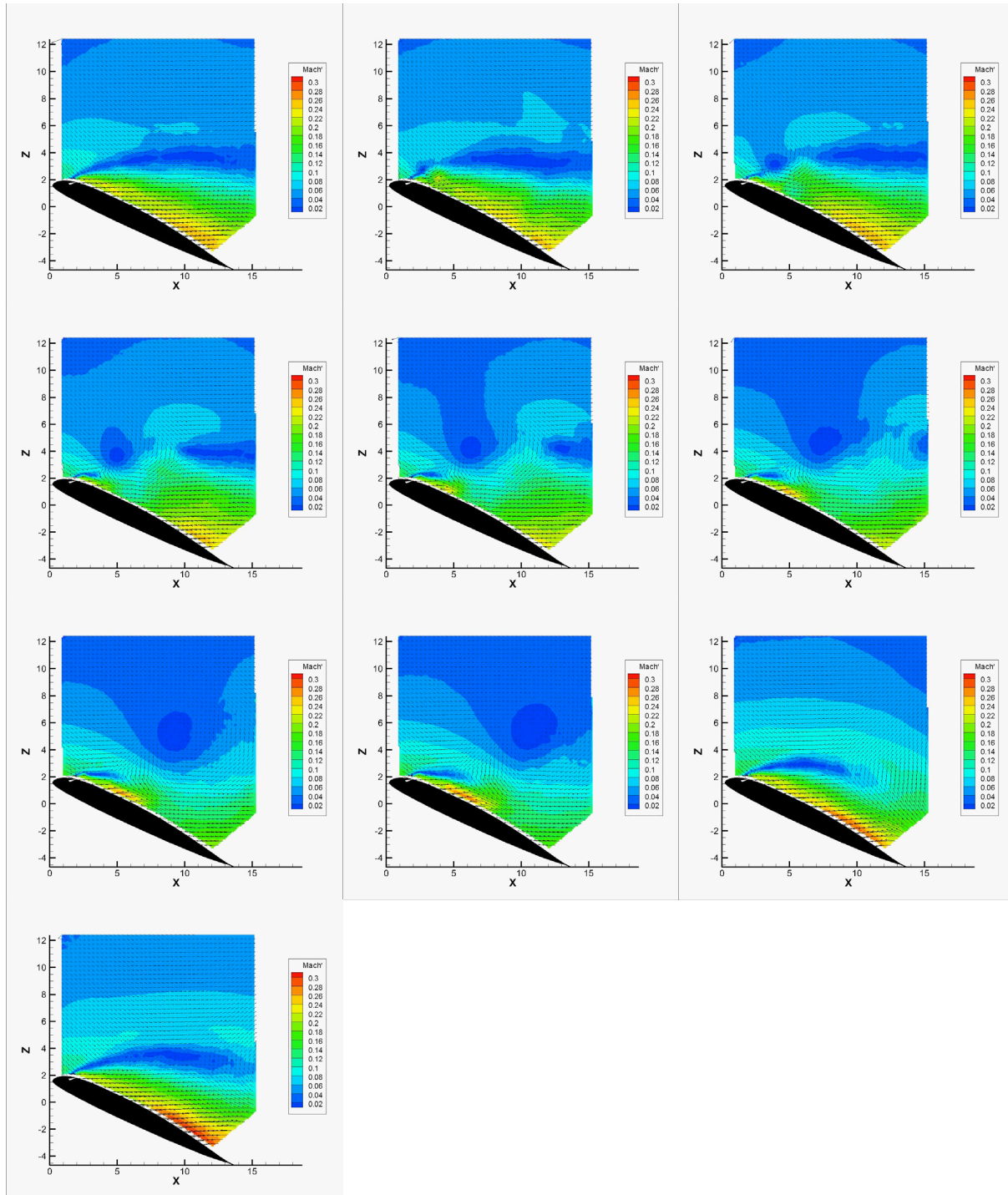


**Figure 634.** Mach' contours, Mach 0.2,  $\alpha = 25^\circ$ ,  $F^+ = 0.2$ ,  $\Delta t = 0, 1, 2, 3, 4, 5, 6, 7, 14, 21$  ms.

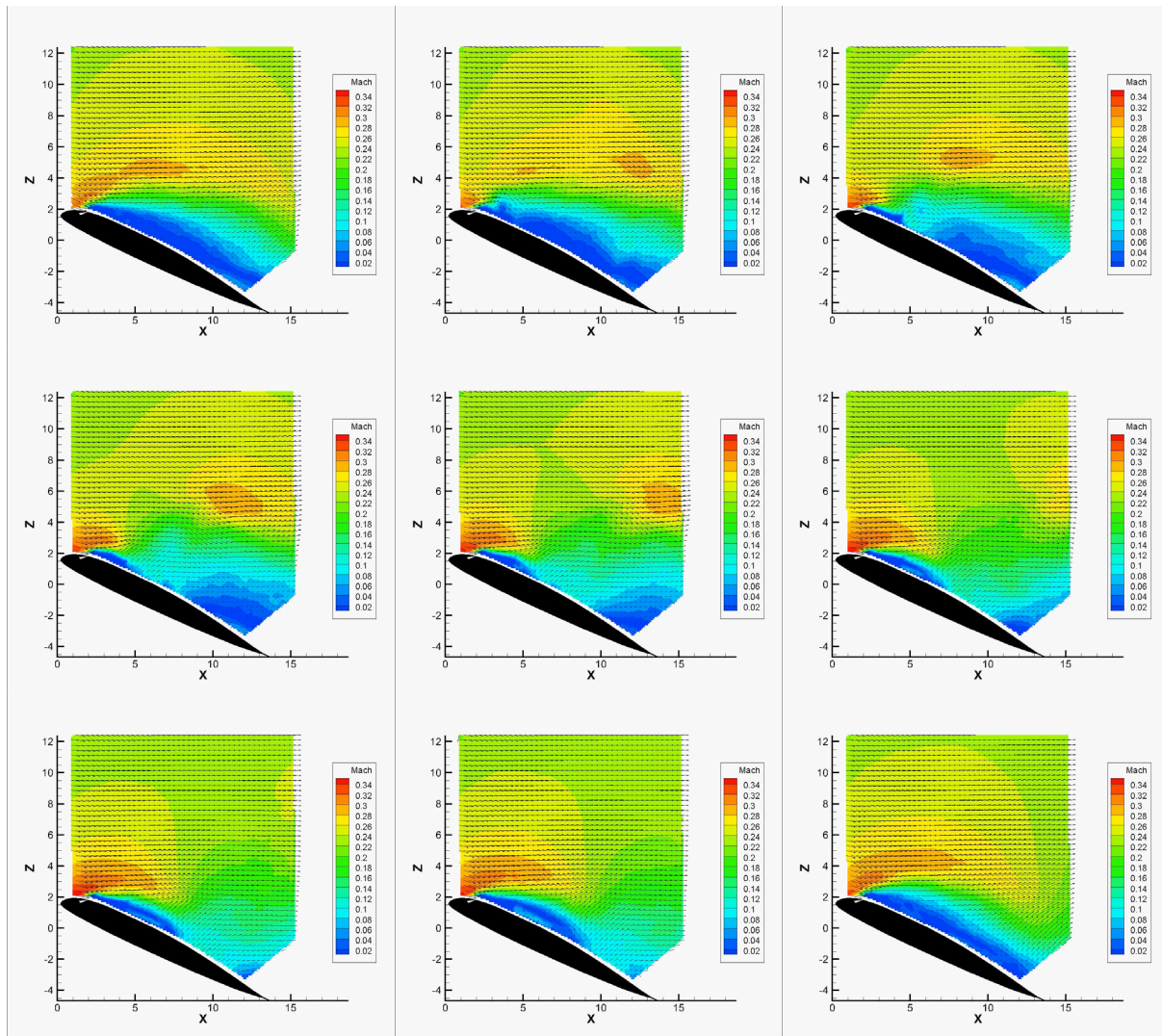
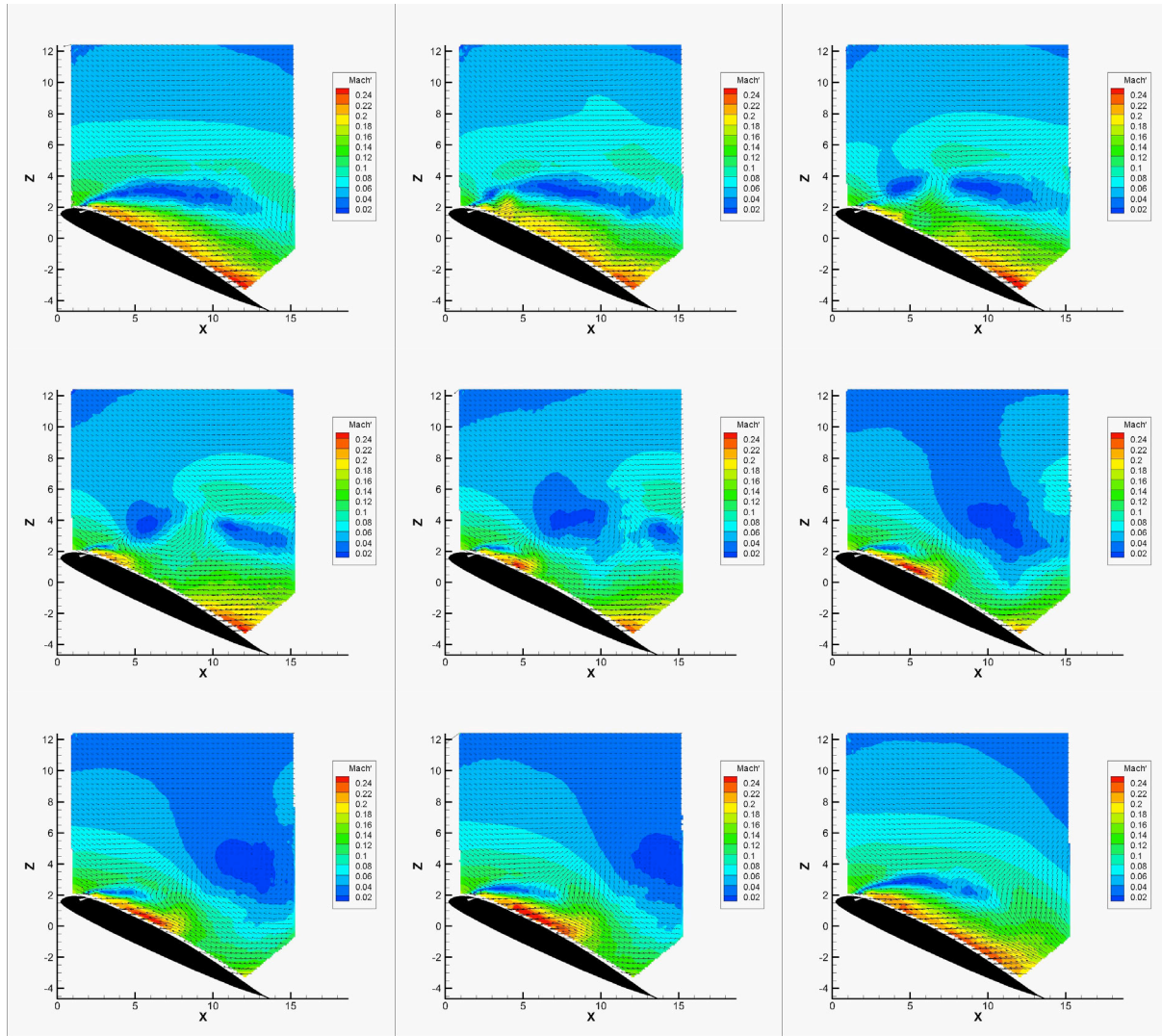


Figure 635. Mach contours, Mach 0.2,  $\alpha = 25^\circ$ ,  $F^+ = 0.4$ ,  $\Delta t = 0, 1, 2, 3, 4, 5, 6, 7, 10.5$  ms.



**Figure 636. Mach' contours, Mach 0.2,  $\alpha = 25^\circ$ ,  $F^+ = 0.4$ ,  $\Delta t = 0, 1, 2, 3, 4, 5, 6, 7, 10.5$  ms.**



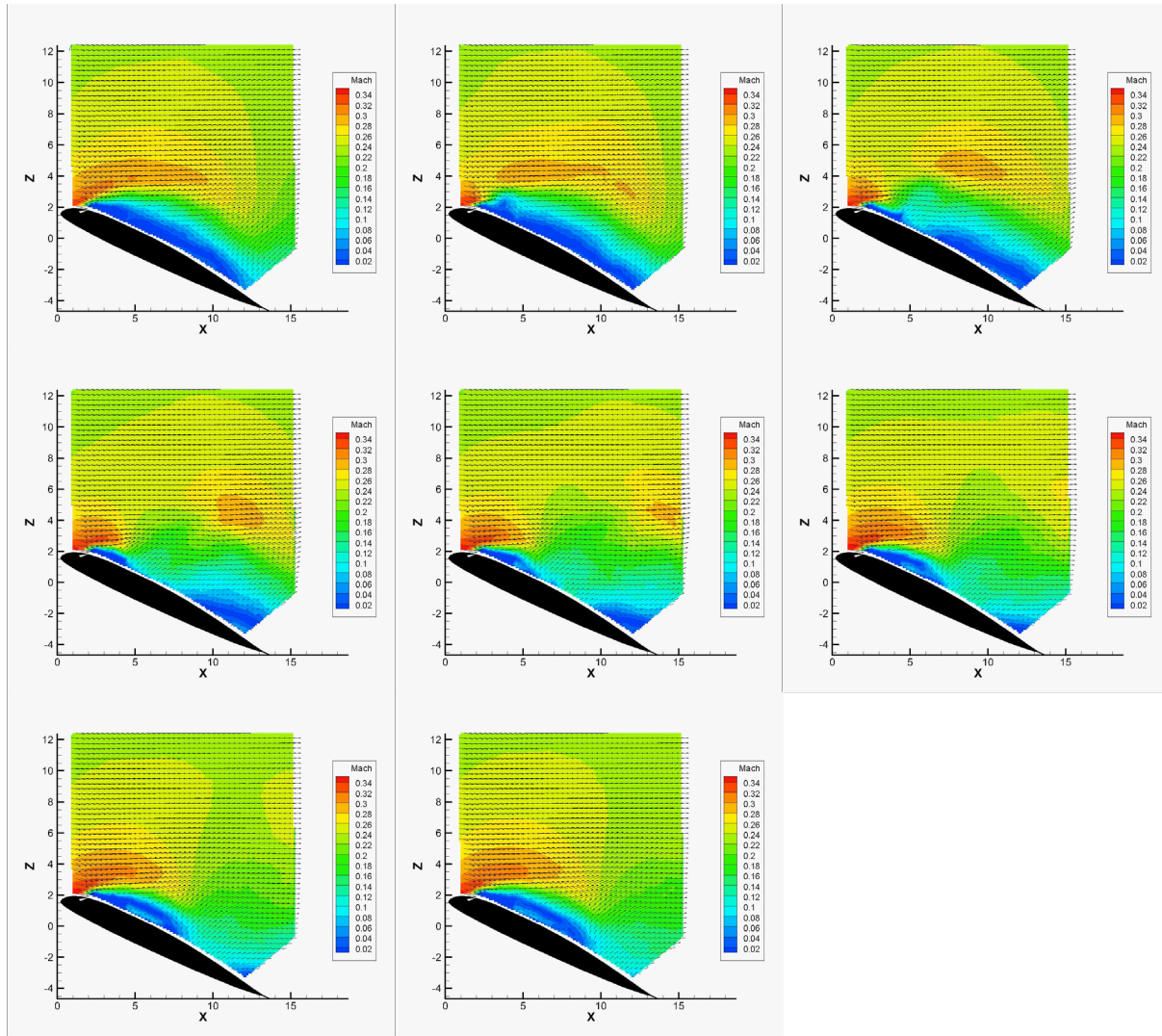
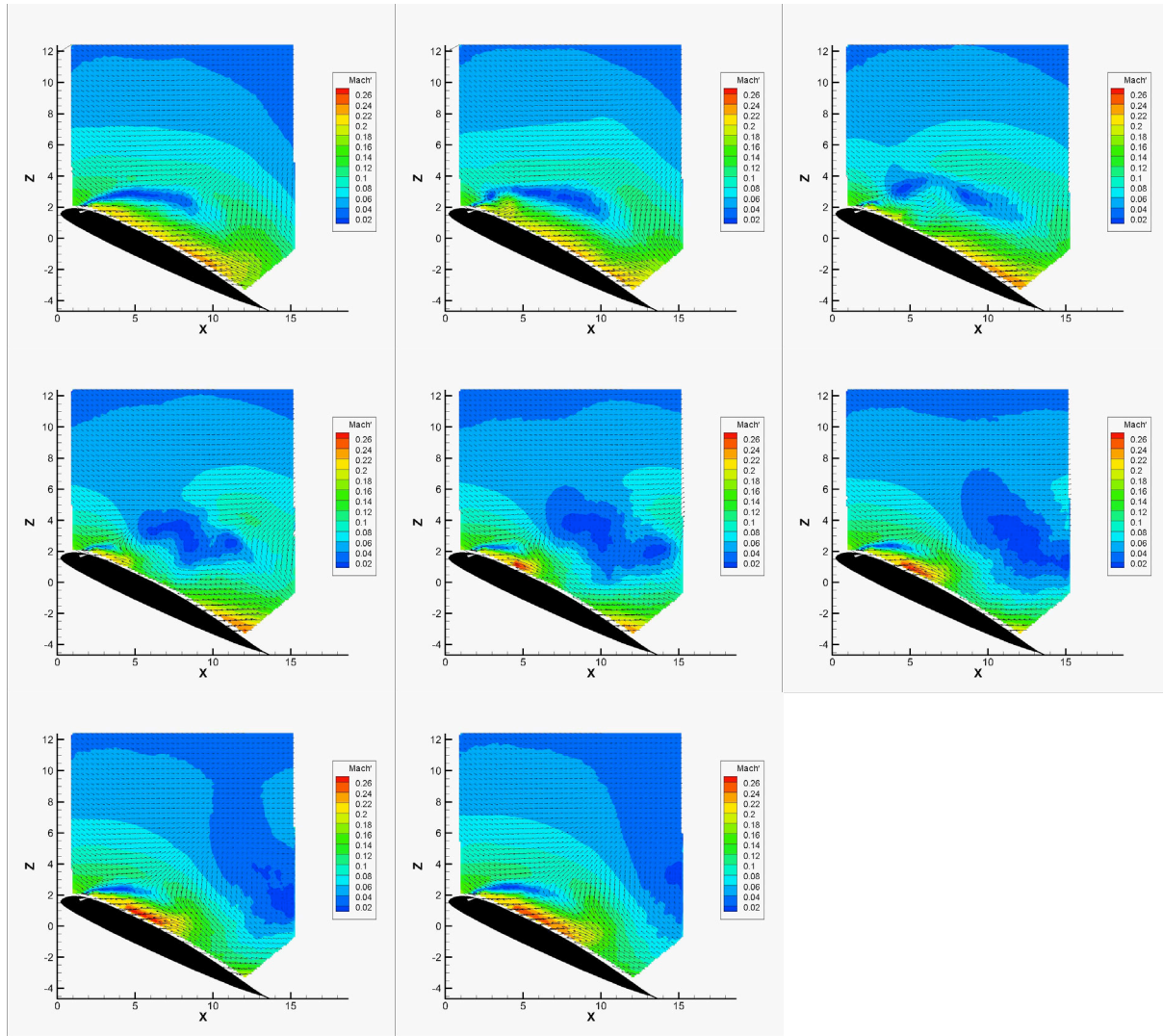


Figure 637. Mach contours, Mach 0.2,  $\alpha = 25^\circ$ ,  $F^+ = 0.6$ ,  $\Delta t = 0, 1, 2, 3, 4, 5, 6, 7$  ms.



**Figure 638.** Mach' contours, Mach 0.2,  $\alpha = 25^\circ$ ,  $F^+ = 0.6$ ,  $\Delta t = 0, 1, 2, 3, 4, 5, 6, 7$  ms.

## B. Mach 0.3

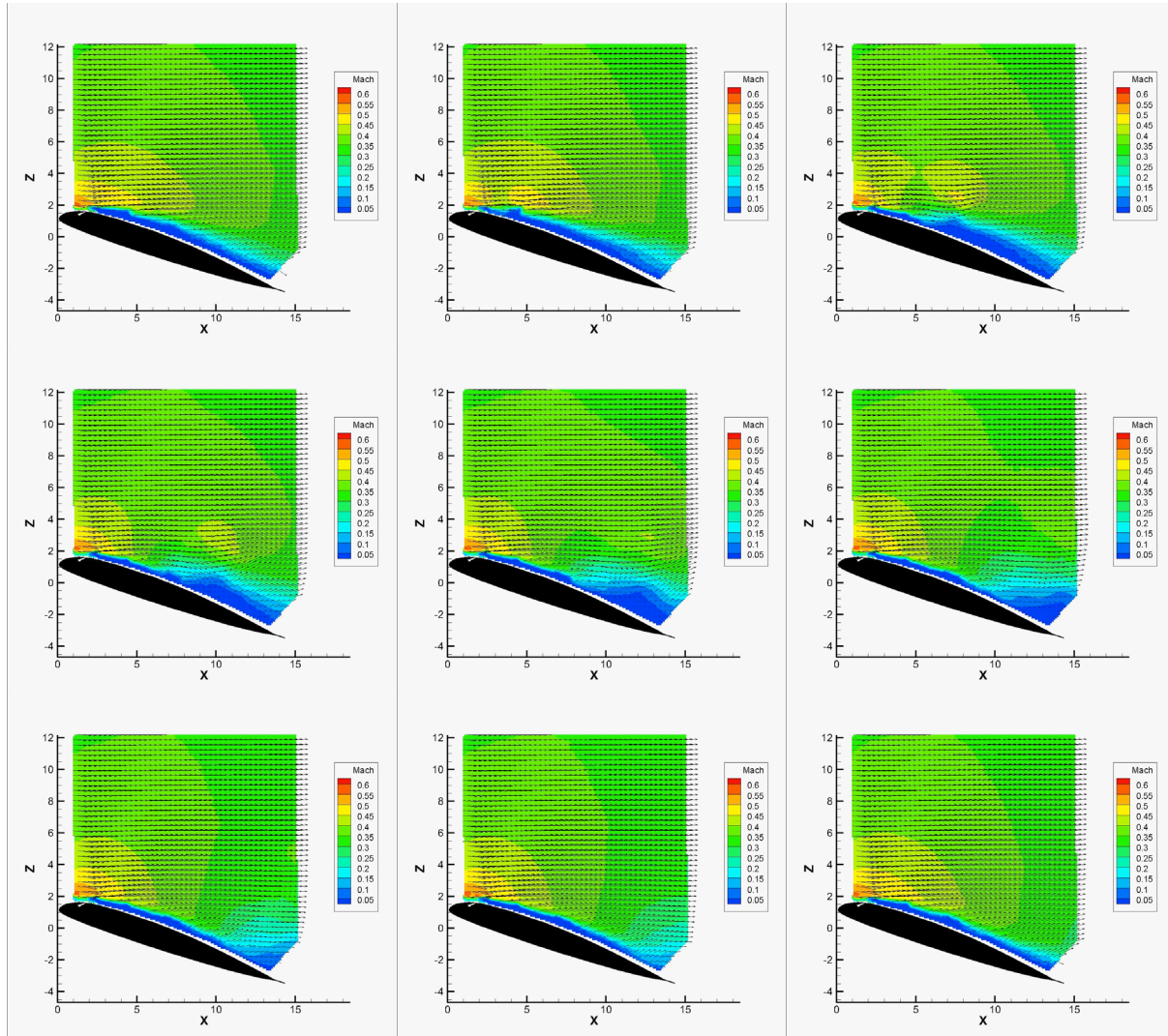
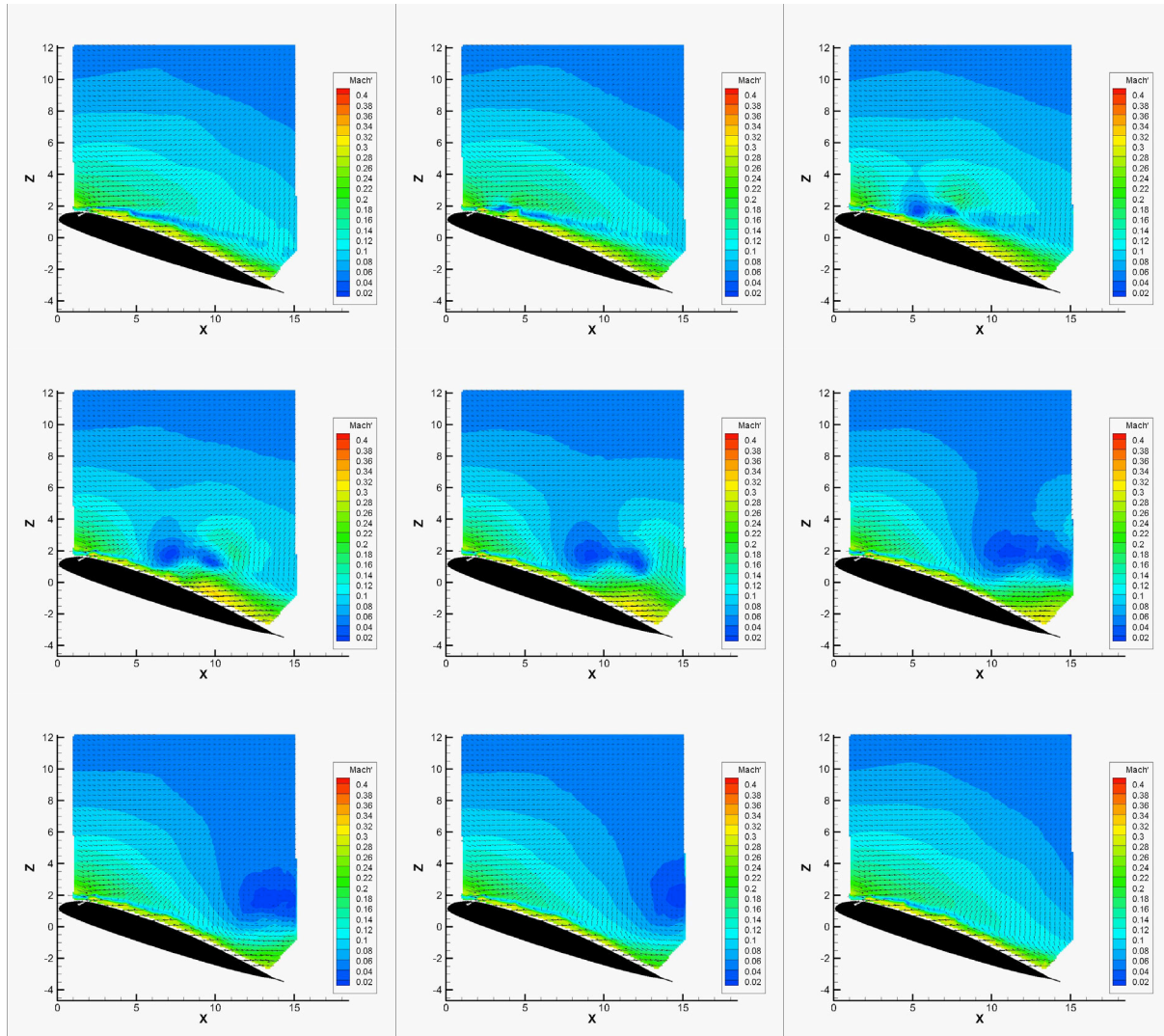


Figure 639. Mach contours, Mach 0.3,  $\alpha = 18^\circ$ ,  $F^+ = 0.4$ ,  $\Delta t = 0, 0.7, 1.4, 2.1, 2.8, 3.5, 4.2, 4.9, 7$  ms.





**Figure 640.** Mach' contours, Mach 0.3,  $\alpha = 18^\circ$ ,  $F^+ = 0.4$ ,  $\Delta t = 0, 0.7, 1.4, 2.1, 2.8, 3.5, 4.2, 4.9, 7$  ms.



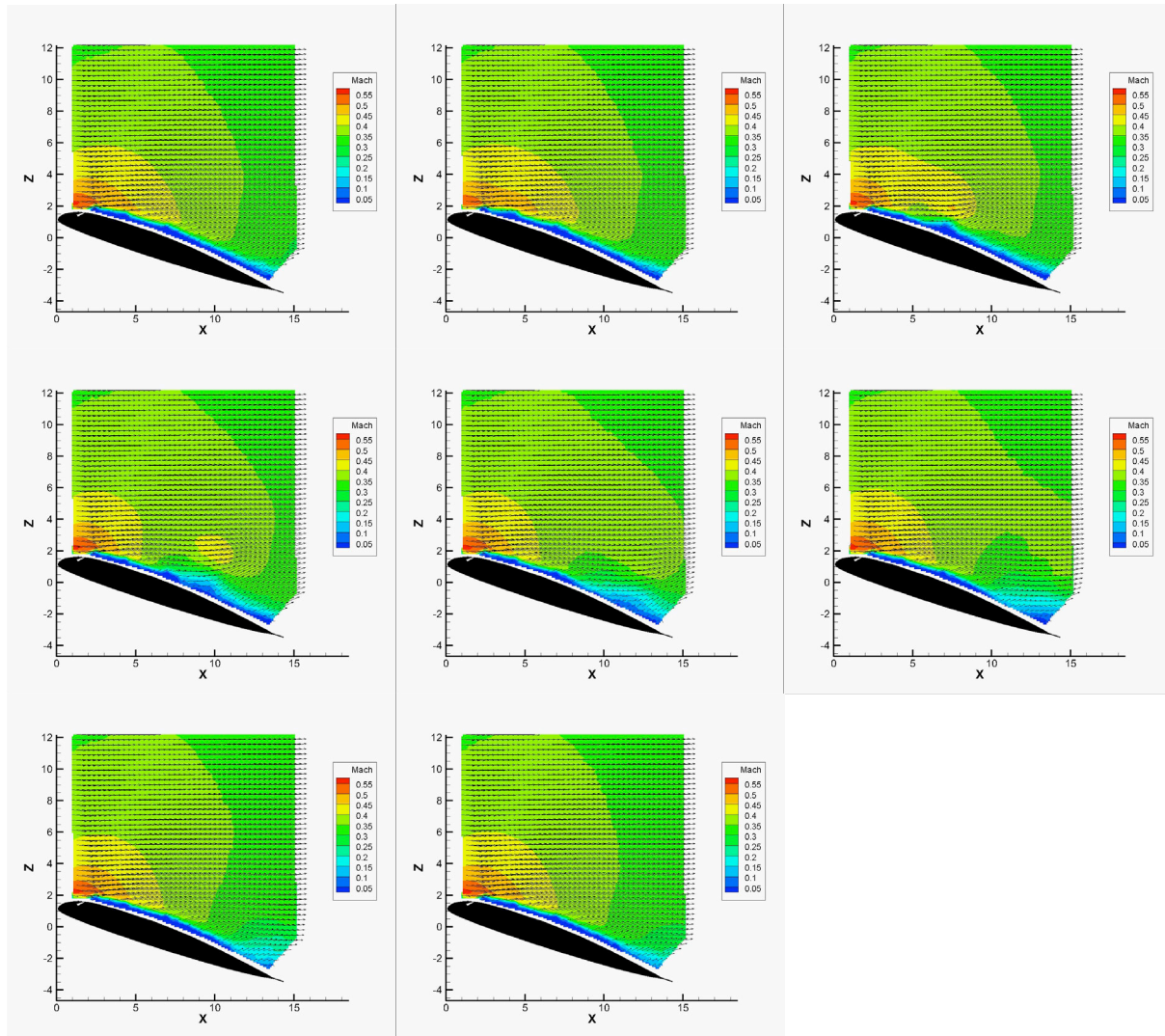


**Figure 641.** Mach contours, Mach 0.3,  $\alpha = 18^\circ$ ,  $F^+ = 0.6$ ,  $\Delta t = 0, 0.7, 1.4, 2.1, 2.8, 3.5, 4.2, 4.9$  ms.

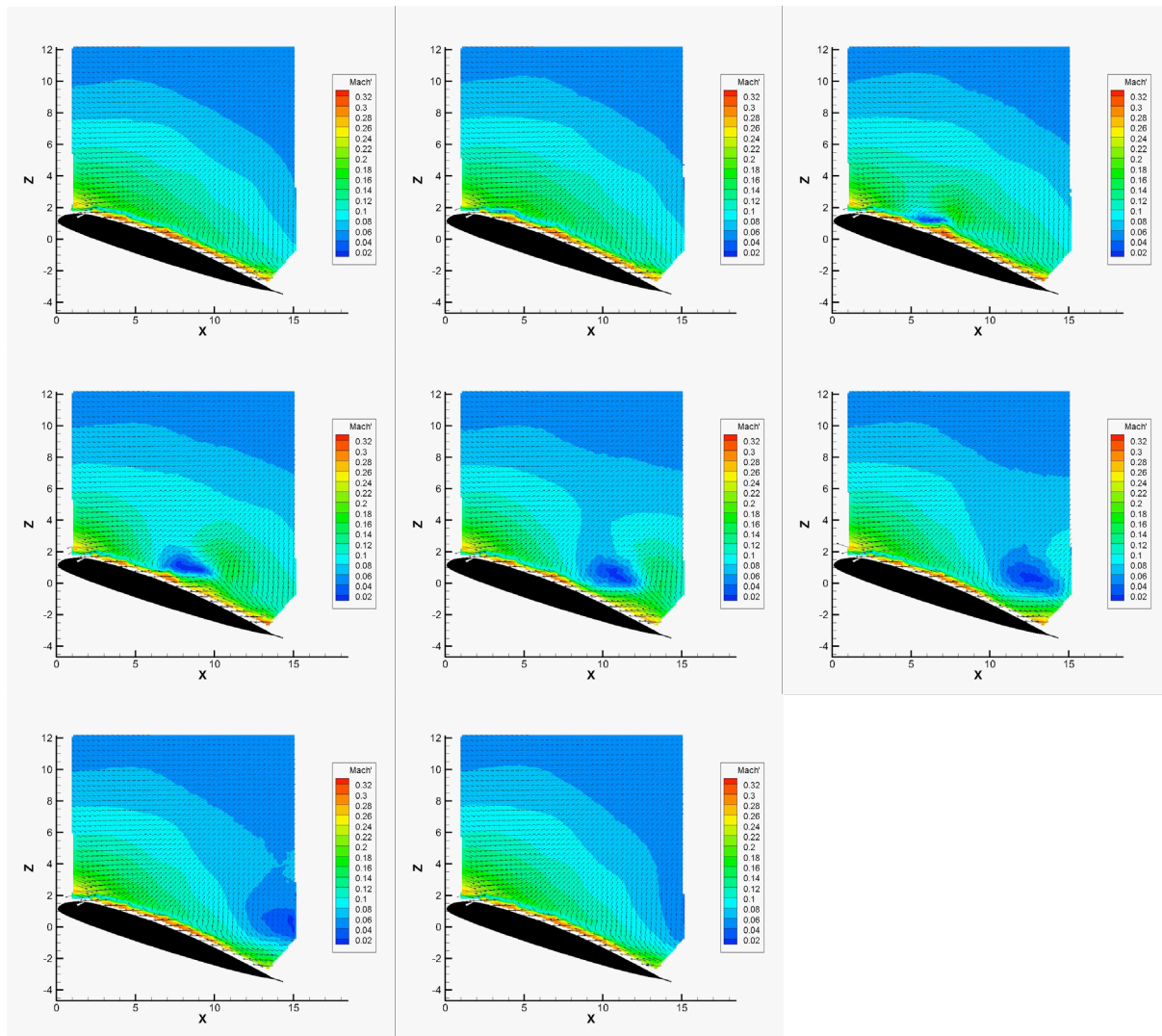
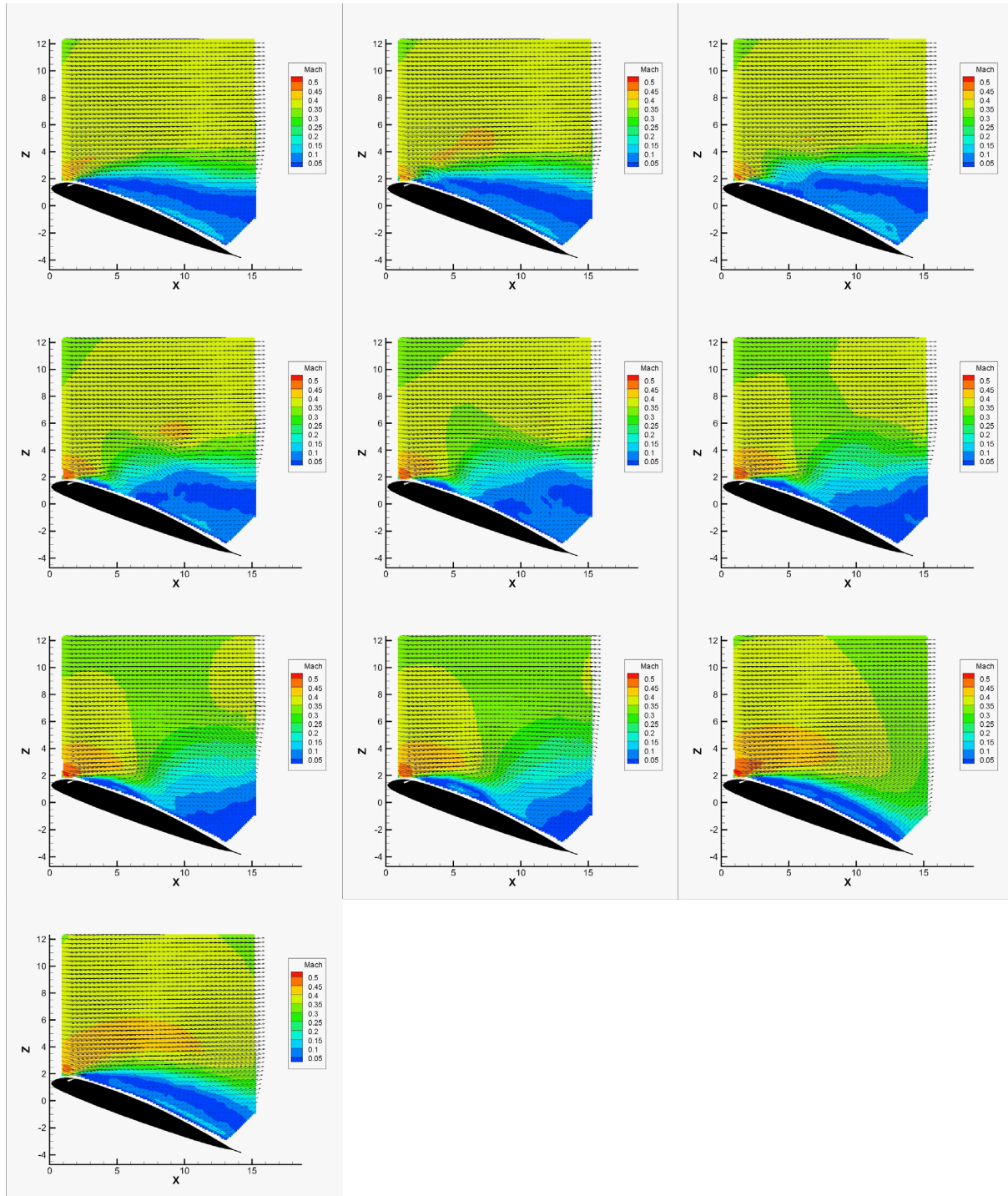
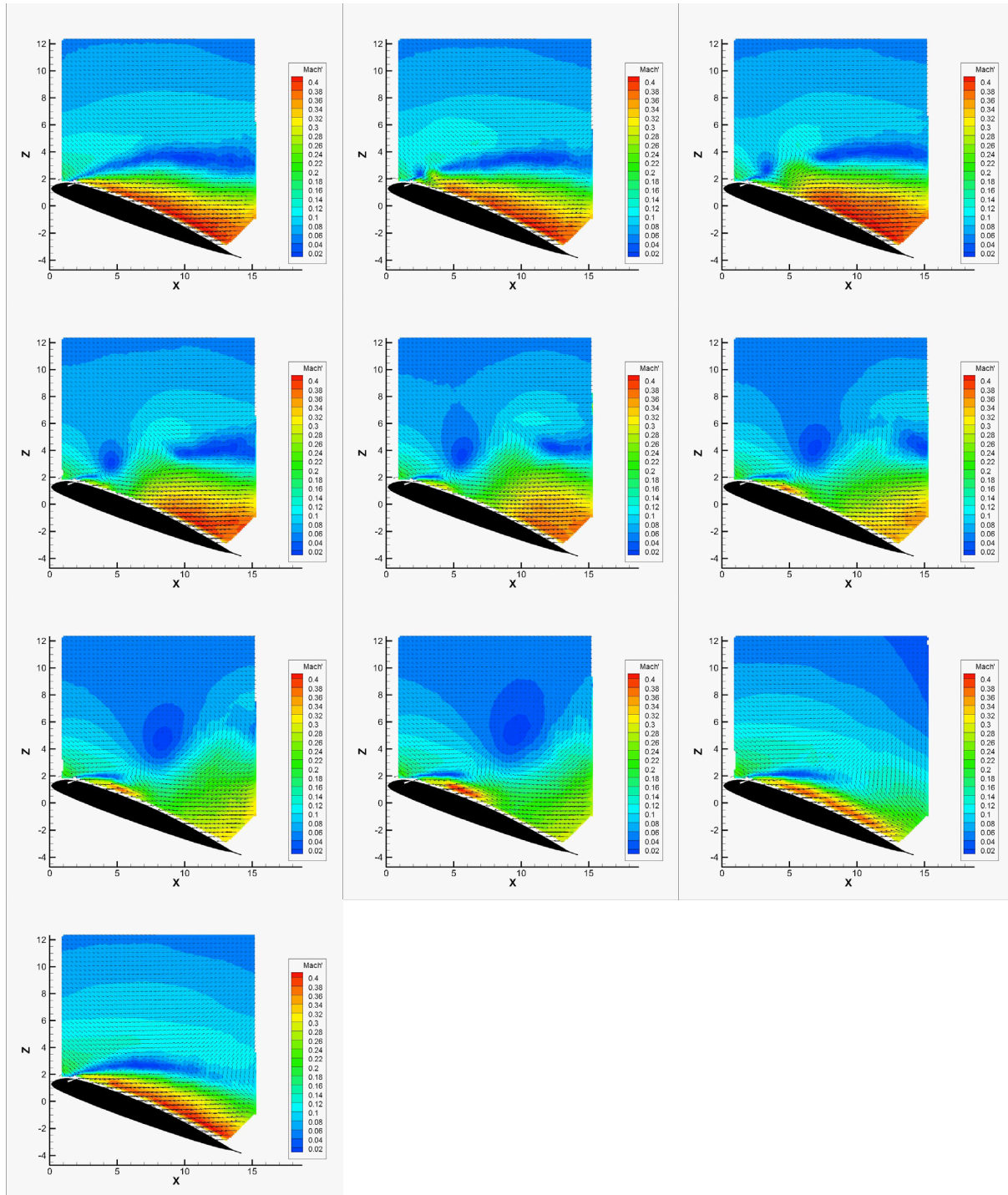


Figure 642. Mach' contours, Mach 0.3,  $\alpha = 18^\circ$ ,  $F^+ = 0.6$ ,  $\Delta t = 0, 0.7, 1.4, 2.1, 2.8, 3.5, 4.2, 4.9$  ms.



**Figure 643. Mach contours, Mach 0.3,  $\alpha = 20^\circ$ ,  $F^+ = 0.2$ ,  $\Delta t = 0, 0.7, 1.4, 2.1, 2.8, 3.5, 4.2, 4.9, 9.3, 14.1$  ms.**





**Figure 644. Mach' contours, Mach 0.3,  $\alpha = 20^\circ$ ,  $F^+ = 0.2$ ,  $\Delta t = 0, 0.7, 1.4, 2.1, 2.8, 3.5, 4.2, 4.9, 9.3, 14.1$  ms.**

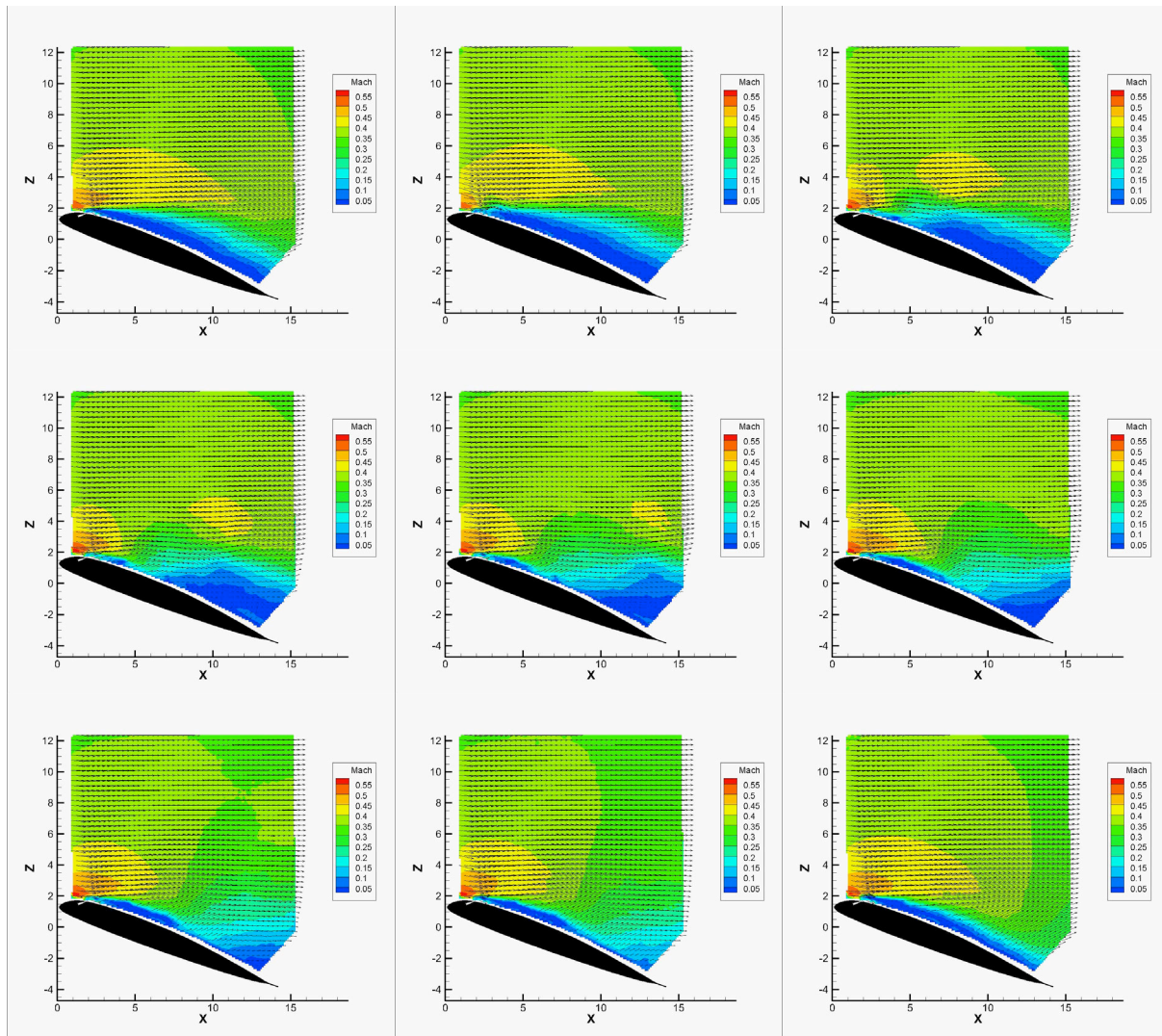


**Figure 645.** Mach contours, Mach 0.3,  $\alpha = 20^\circ$ ,  $F^+ = 0.4$ ,  $\Delta t = 0, 0.7, 1.4, 2.1, 2.8, 3.5, 4.2, 4.9, 7$  ms.

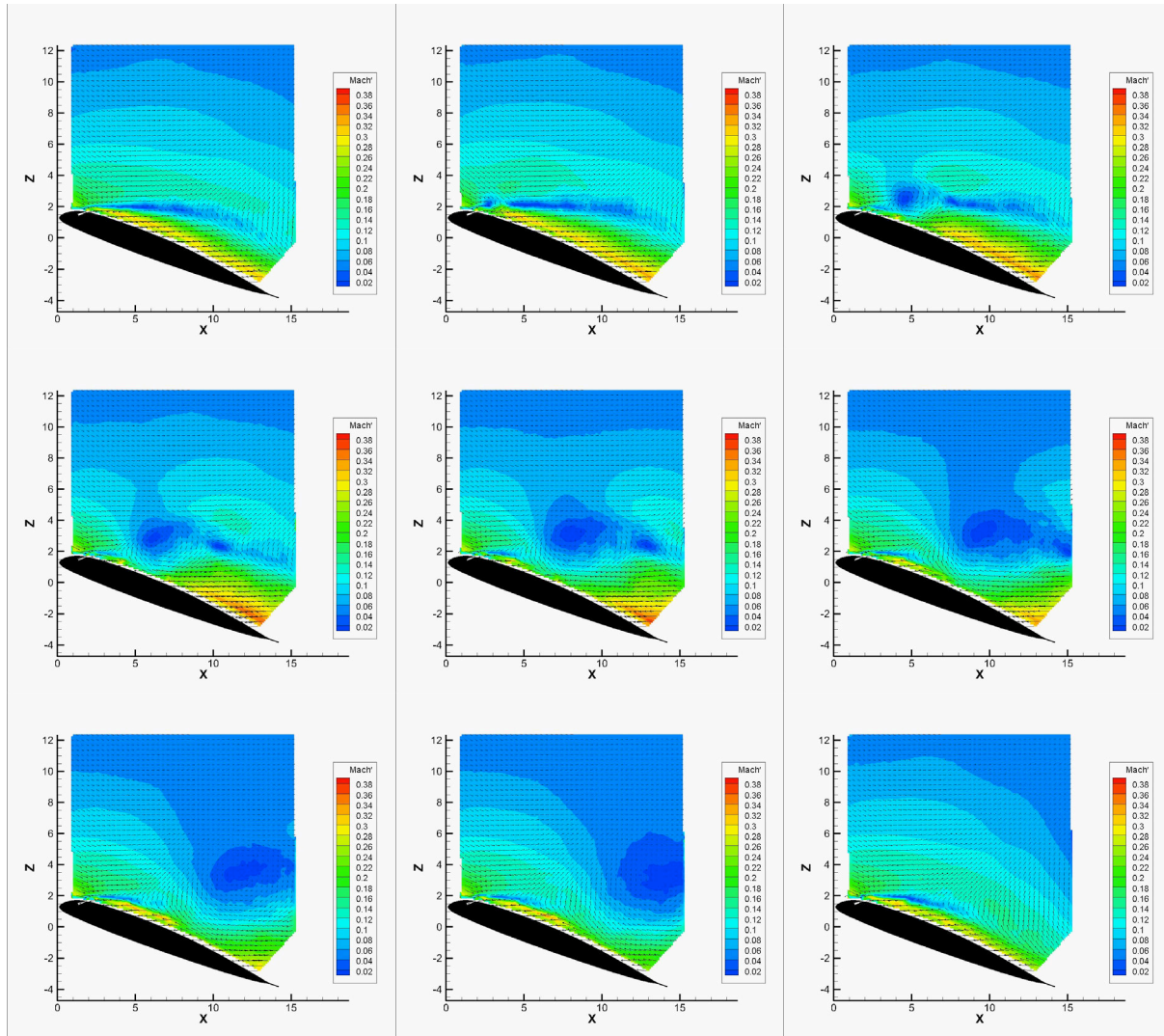


**Figure 646.** Mach' contours, Mach 0.3,  $\alpha = 20^\circ$ ,  $F^+ = 0.4$ ,  $\Delta t = 0, 0.7, 1.4, 2.1, 2.8, 3.5, 4.2, 4.9, 7$  ms.



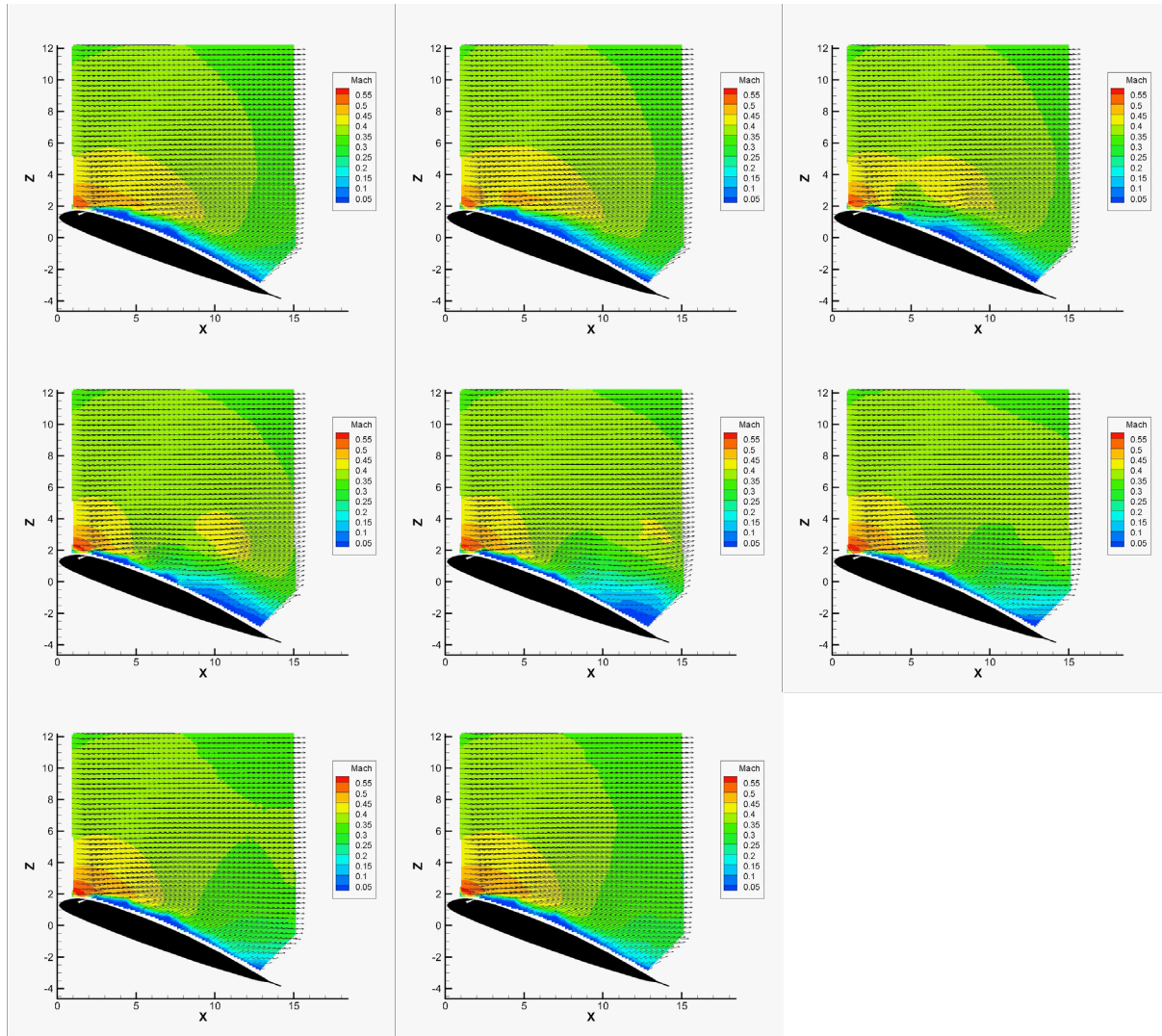


**Figure 647. Mach contours, Mach 0.3,  $\alpha = 20^\circ$ ,  $F^+ = 0.6$ ,  $\Delta t = 0, 0.7, 1.4, 2.1, 2.8, 3.5, 4.2, 4.9$  ms.**



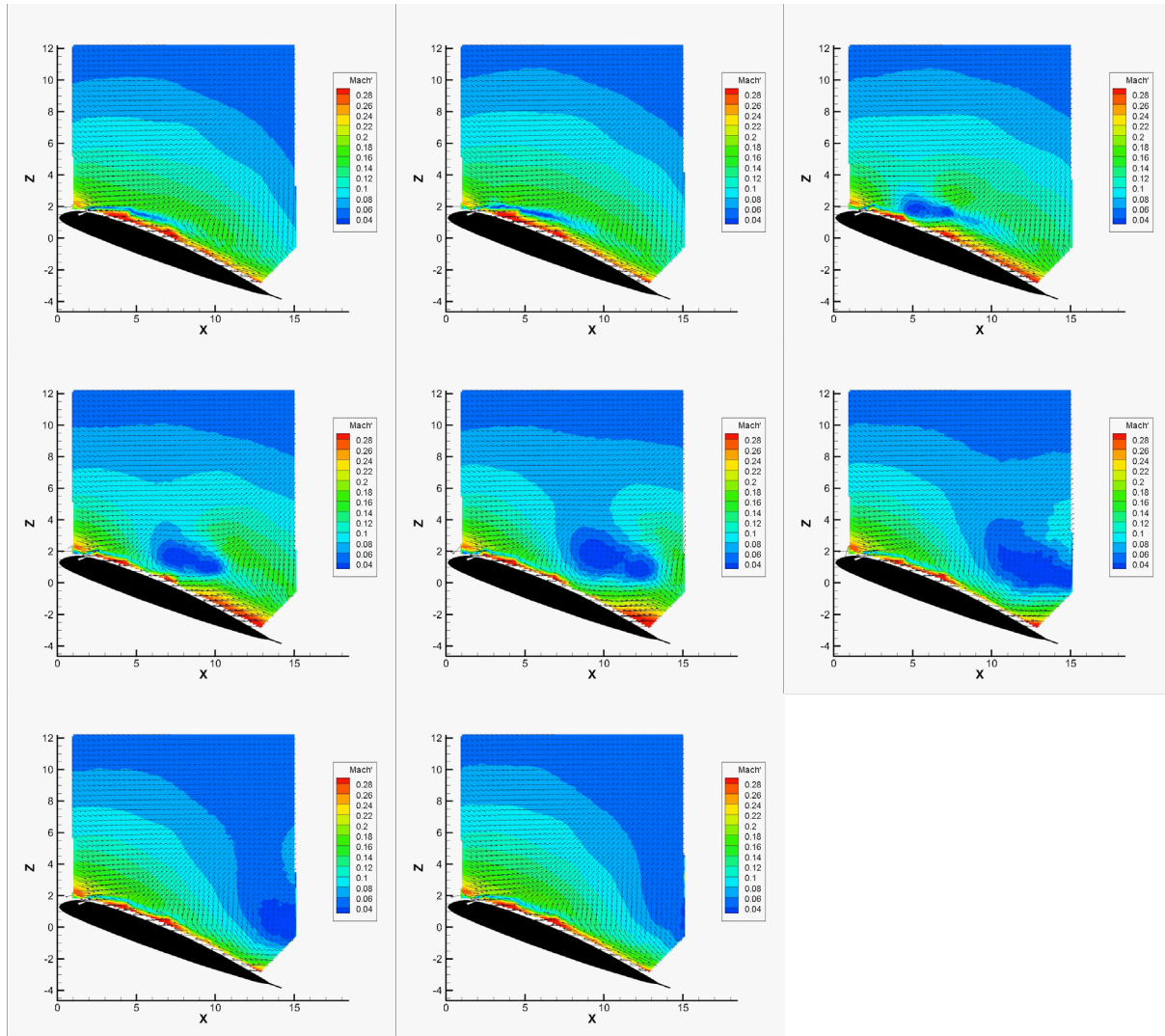


**Figure 648.** Mach' contours, Mach 0.3,  $\alpha = 20^\circ$ ,  $F^+ = 0.6$ ,  $\Delta t = 0, 0.7, 1.4, 2.1, 2.8, 3.5, 4.2, 4.9$  ms.

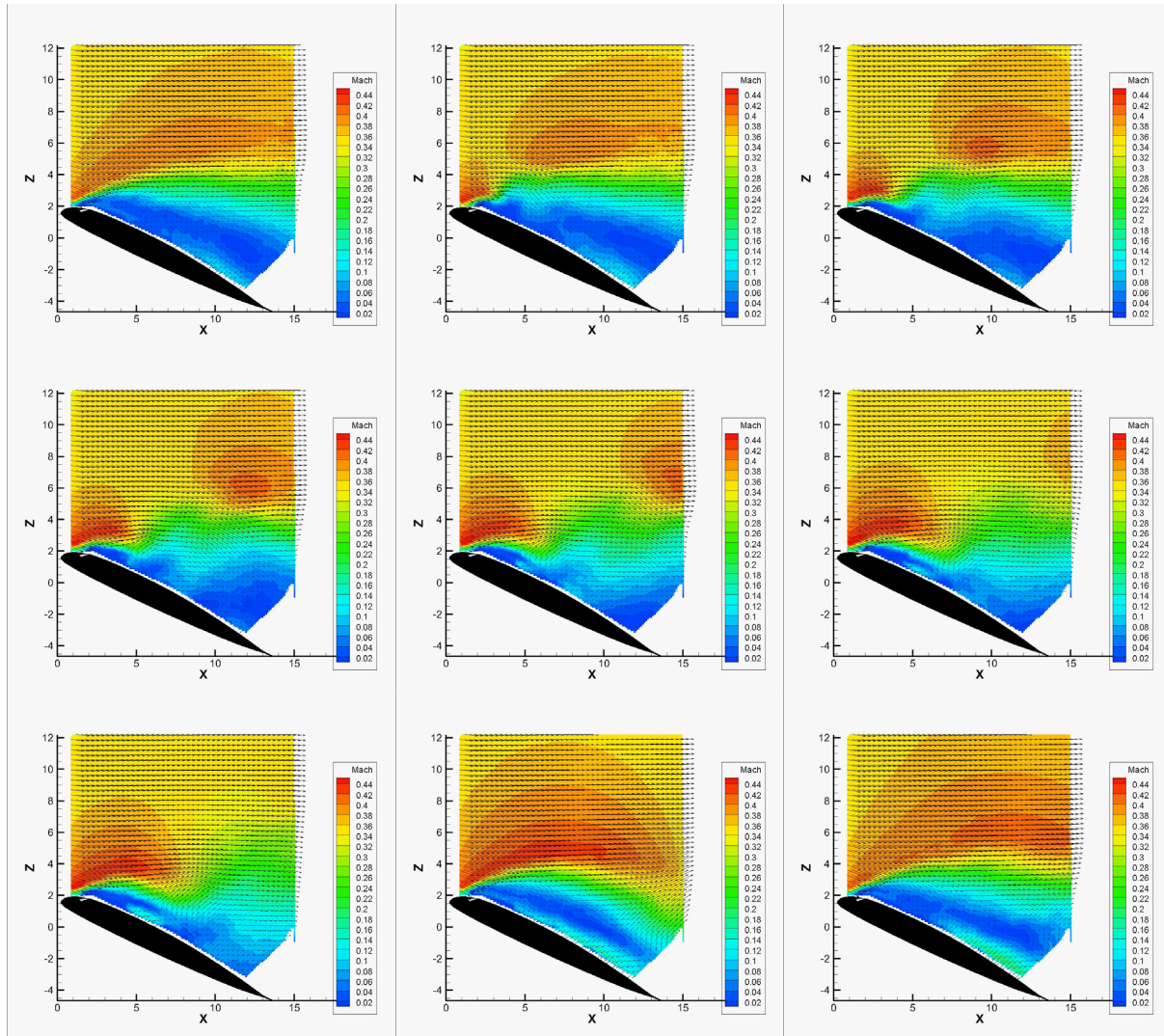


**Figure 649.** Mach contours, Mach 0.3,  $\alpha = 25^\circ$ ,  $F^+ = 0.2$ ,  $\Delta t = 0, 1.4, 2.1, 2.8, 3.5, 4.2, 4.9, 9.3, 14.1$  ms.

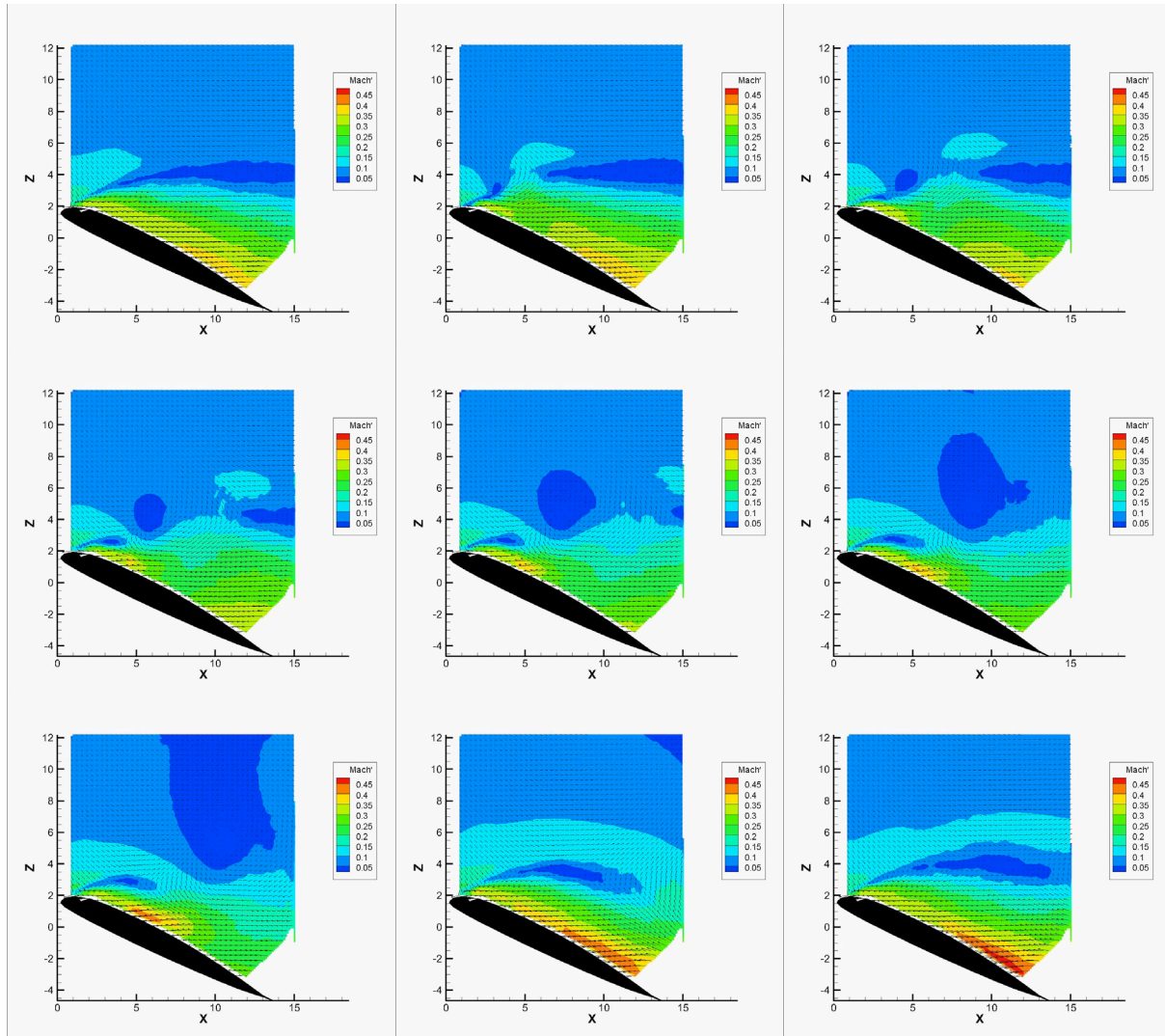


**Figure 650. Mach' contours, Mach 0.3,  $\alpha = 25^\circ$ ,  $F^+ = 0.2$ ,  $\Delta t = 0, 1.4, 2.1, 2.8, 3.5, 4.2, 4.9, 9.3, 14.1$  ms.**



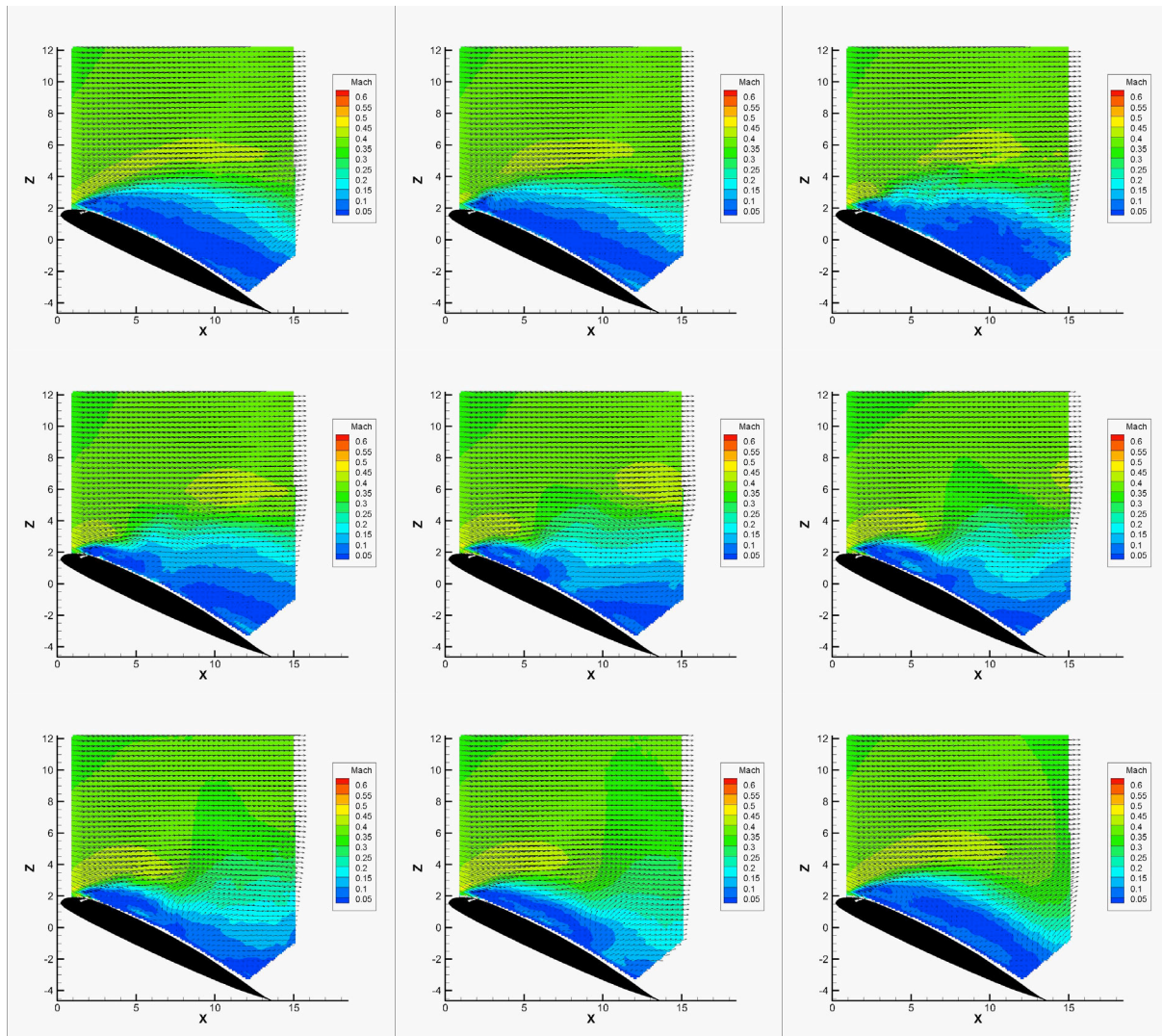


**Figure 651.** Mach contours, Mach 0.3,  $\alpha = 25^\circ$ ,  $F^+ = 0.4$ ,  $\Delta t = 0, 0.7, 1.4, 2.1, 2.8, 3.5, 4.2, 4.9, 7$  ms.

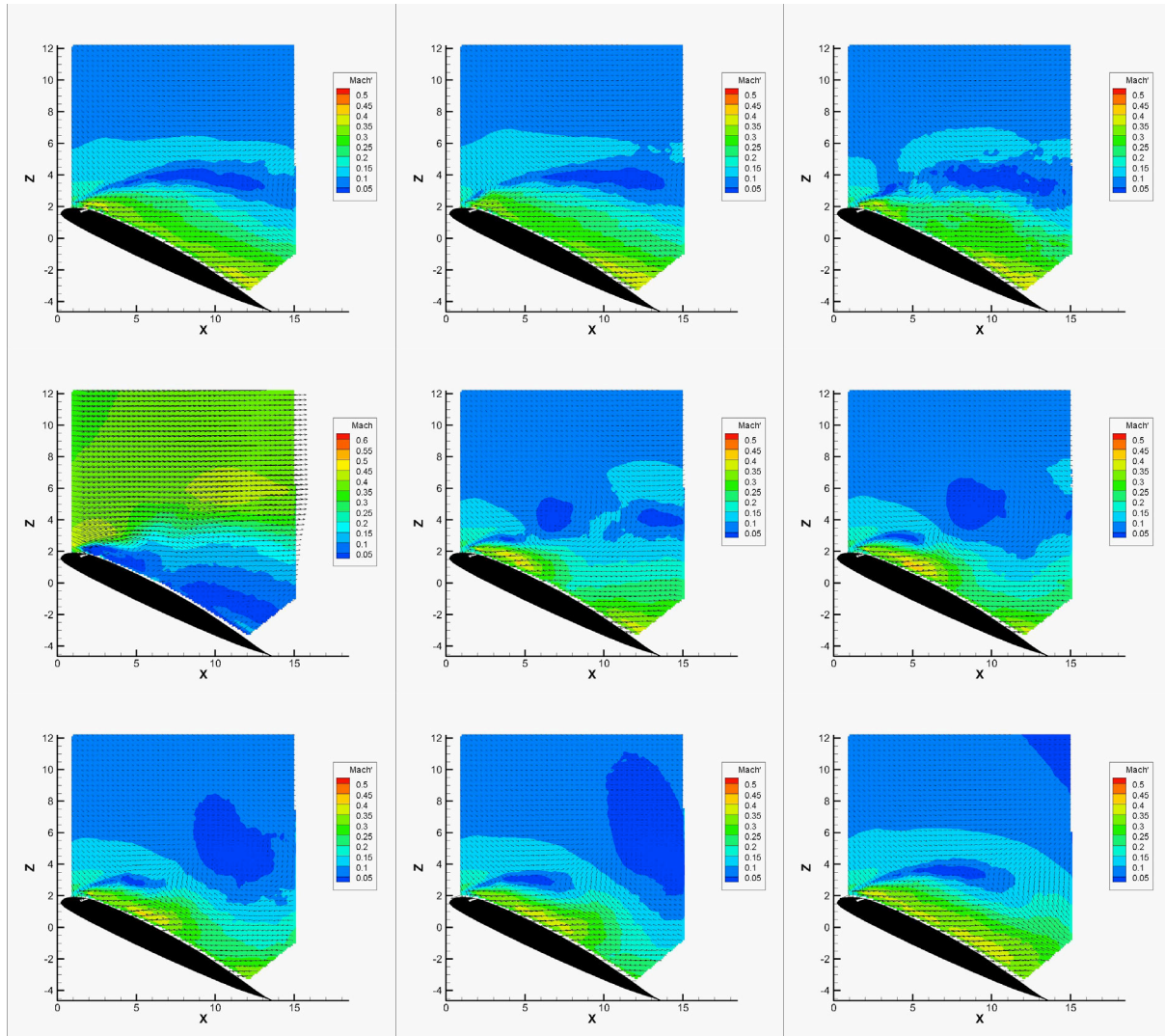


**Figure 652.**  $Mach'$  contours,  $Mach\ 0.3$ ,  $\alpha = 25^\circ$ ,  $F^+ = 0.4$ ,  $\Delta t = 0, 0.7, 1.4, 2.1, 2.8, 3.5, 4.2, 4.9, 7\ ms$ .

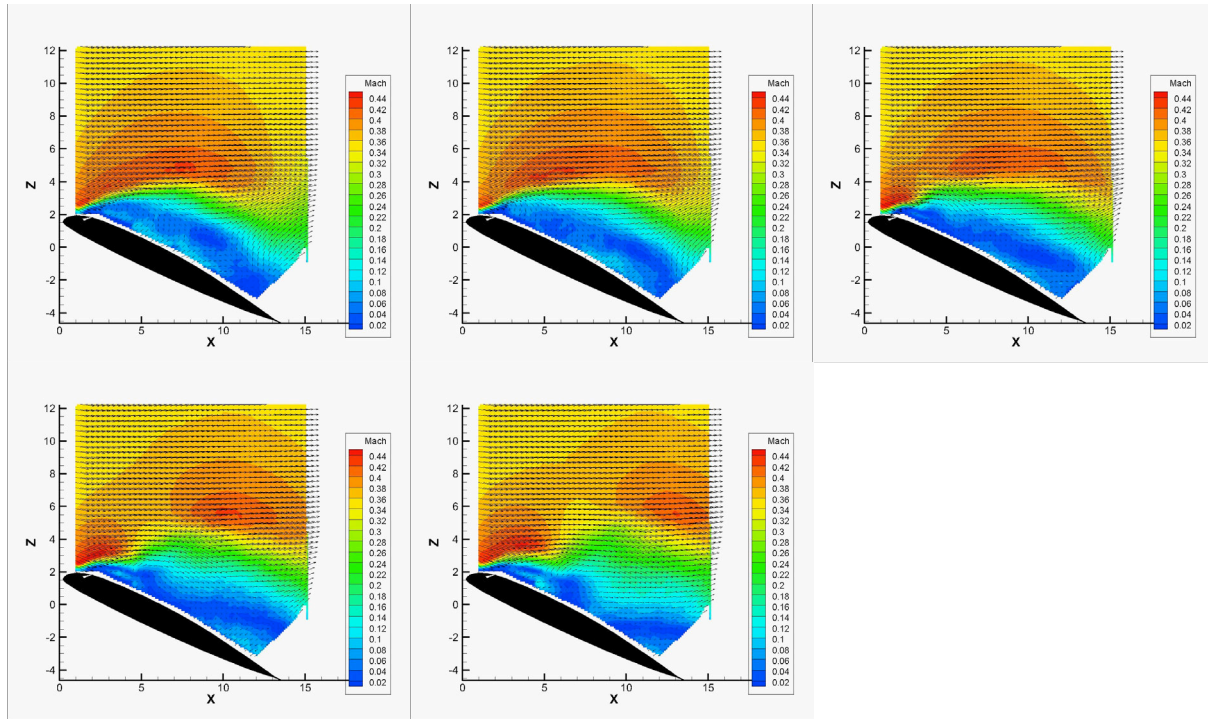


Figure 653. Mach contours, Mach 0.3,  $\alpha = 25^\circ$ ,  $F^+ = 0.6$ ,  $\Delta t = 0, 0.7, 1.4, 2.1, 2.8$  ms.

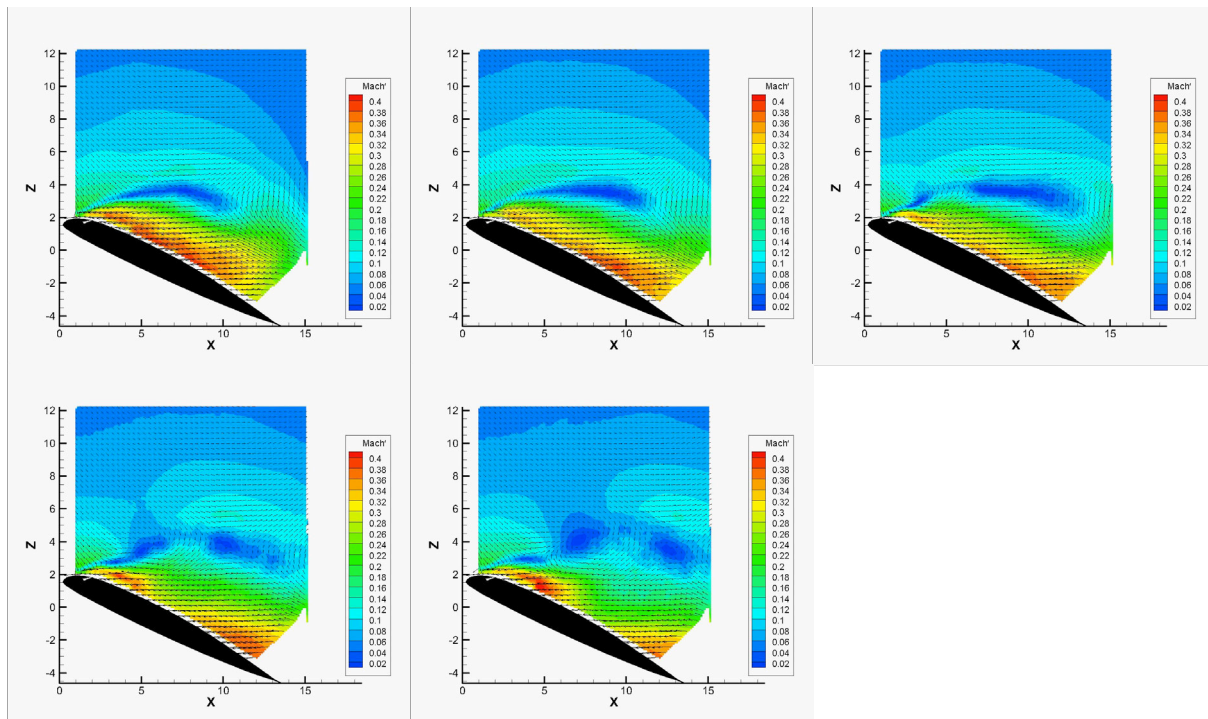


Figure 654. Mach' contours, Mach 0.3,  $\alpha = 25^\circ$ ,  $F^+ = 0.6$ ,  $\Delta t = 0, 0.7, 1.4, 2.1, 2.8$  ms.



### C. Mach 0.4

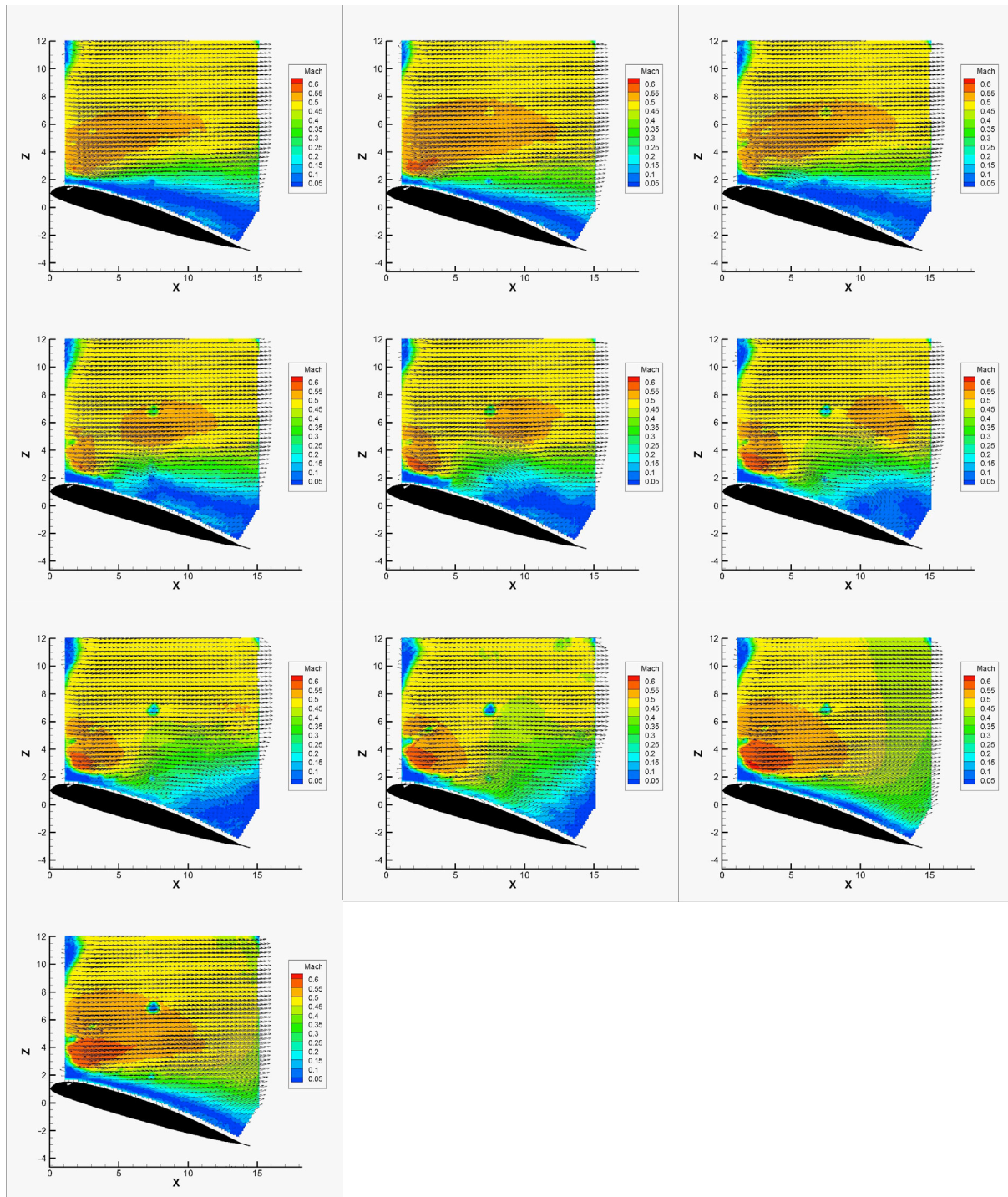
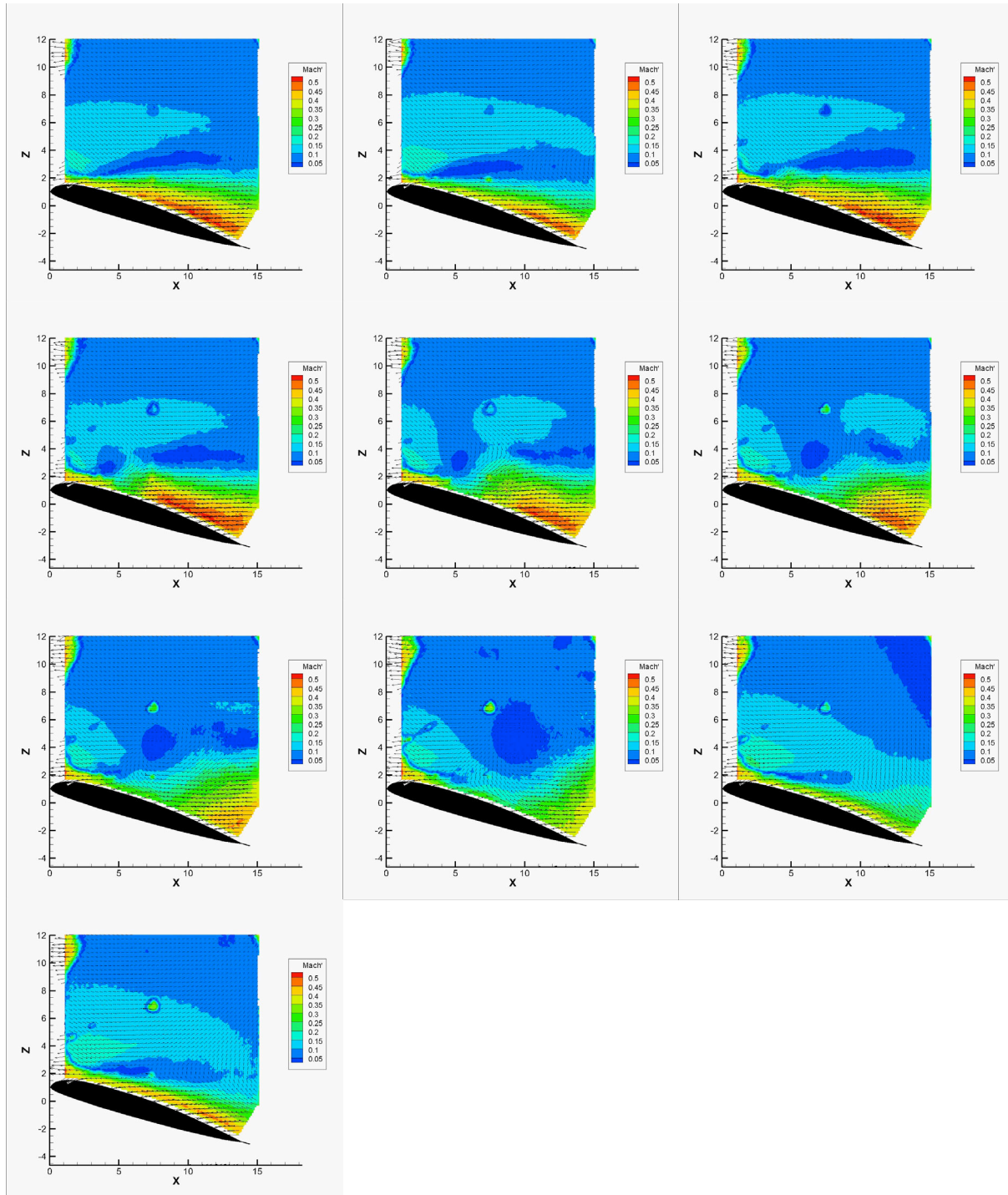
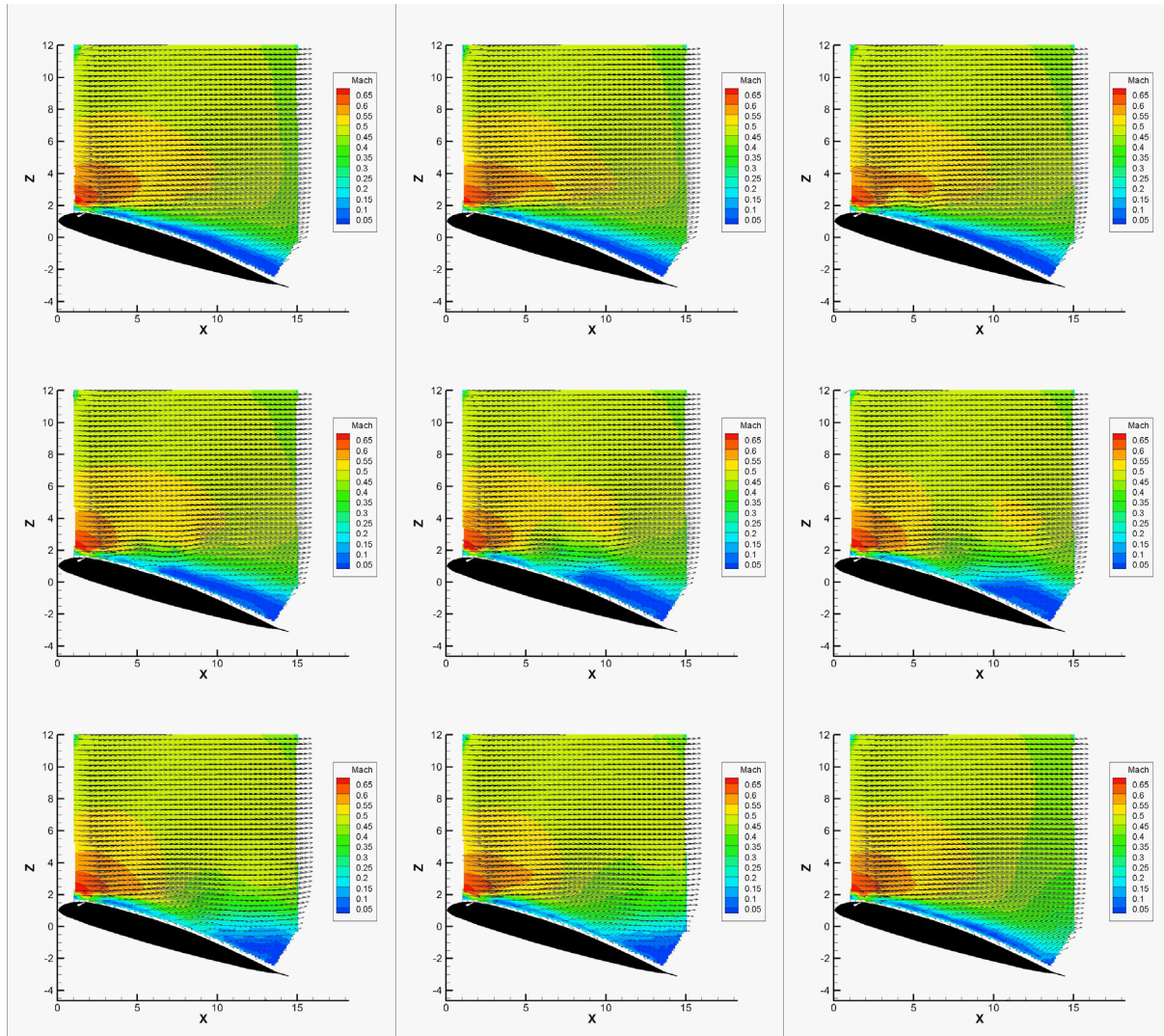


Figure 655. Mach contours, Mach 0.4,  $\alpha = 16^\circ$ ,  $F^+ = 0.2$ ,  $\Delta t = 0, 0.5, 1.0, 1.5, 2.0, 2.5, 3.0, 3.5, 7, 10.6$  ms.





**Figure 656. Mach' contours, Mach 0.4,  $\alpha = 16^\circ$ ,  $F^+ = 0.2$ ,  $\Delta t = 0, 0.5, 1.0, 1.5, 2.0, 2.5, 3.0, 3.5, 7, 10.6$  ms.**



**Figure 657.** Mach contours, Mach 0.4,  $\alpha = 16^\circ$ ,  $F^+ = 0.4$ ,  $\Delta t = 0, 0.5, 1.0, 1.5, 2.0, 2.5, 3.0, 3.5, 5.3$  ms.

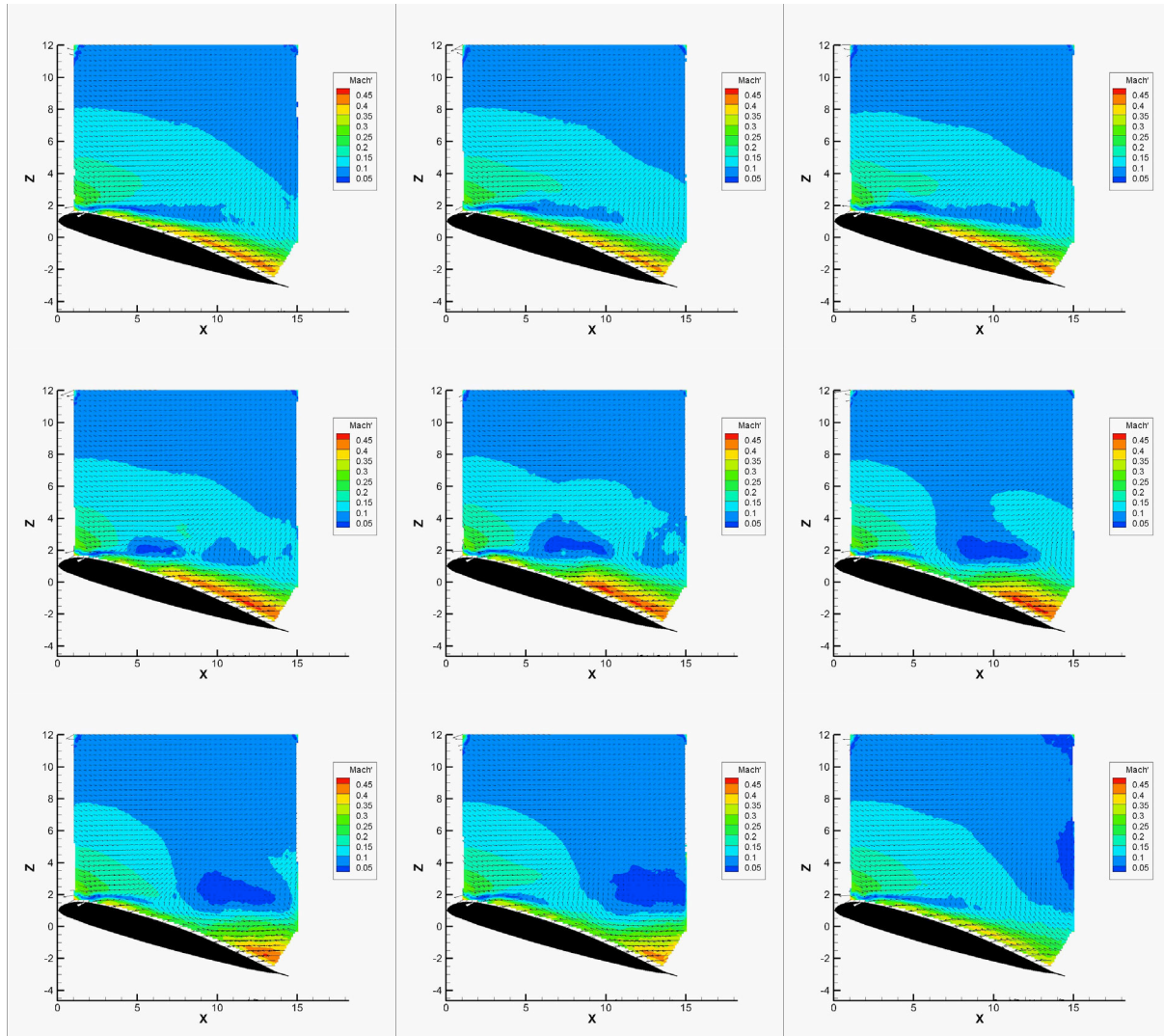


**Figure 658.** Mach' contours, Mach 0.4,  $\alpha = 16^\circ$ ,  $F^+ = 0.4$ ,  $\Delta t = 0, 0.5, 1.0, 1.5, 2.0, 2.5, 3.0, 3.5, 5.3$  ms.



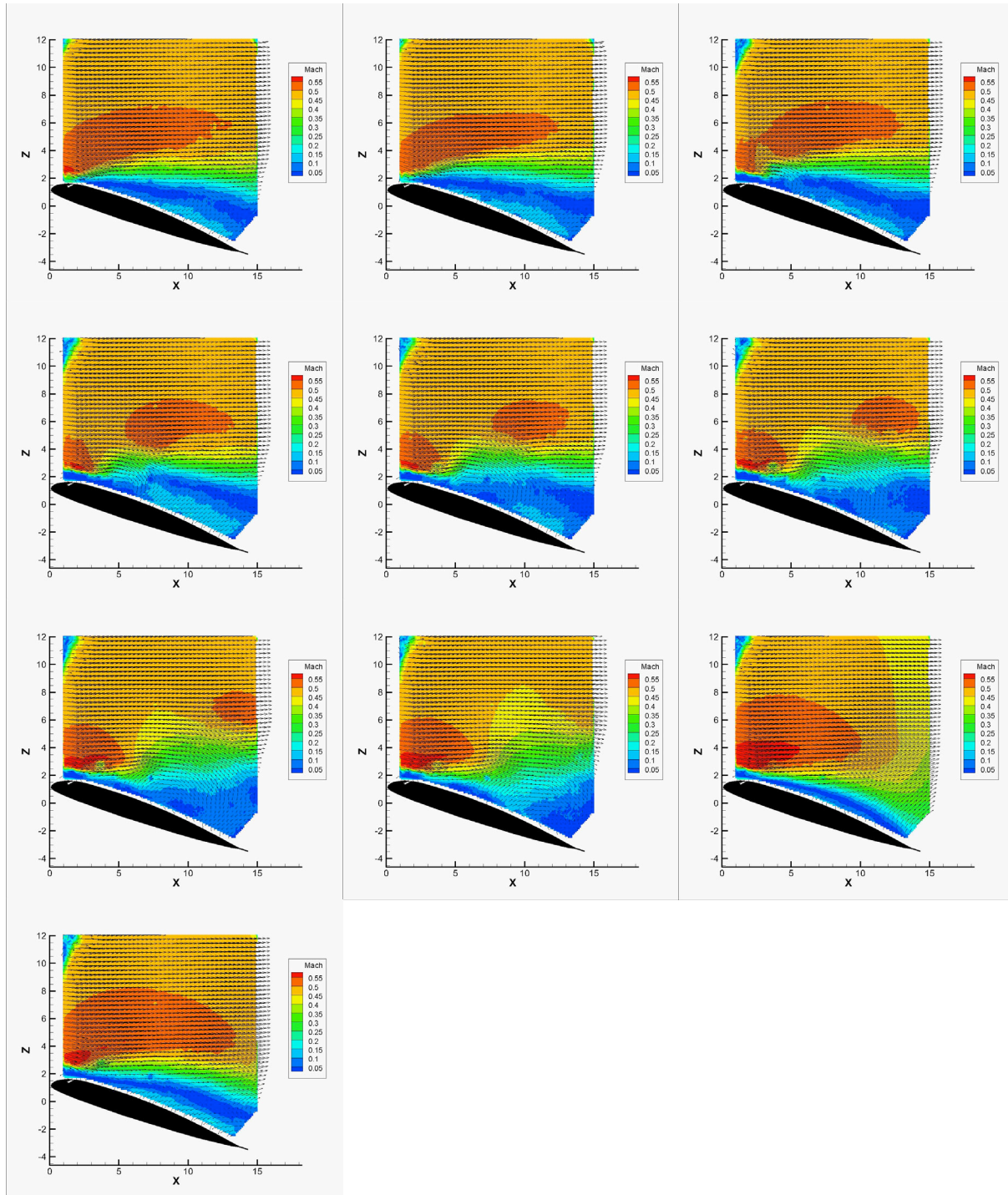


**Figure 659. Mach contours, Mach 0.4,  $\alpha = 18^\circ$ ,  $F^+ = 0.2$ ,  $\Delta t = 0, 0.5, 1.0, 1.5, 2.0, 2.5, 3.0, 3.5, 7, 10.6$  ms.**

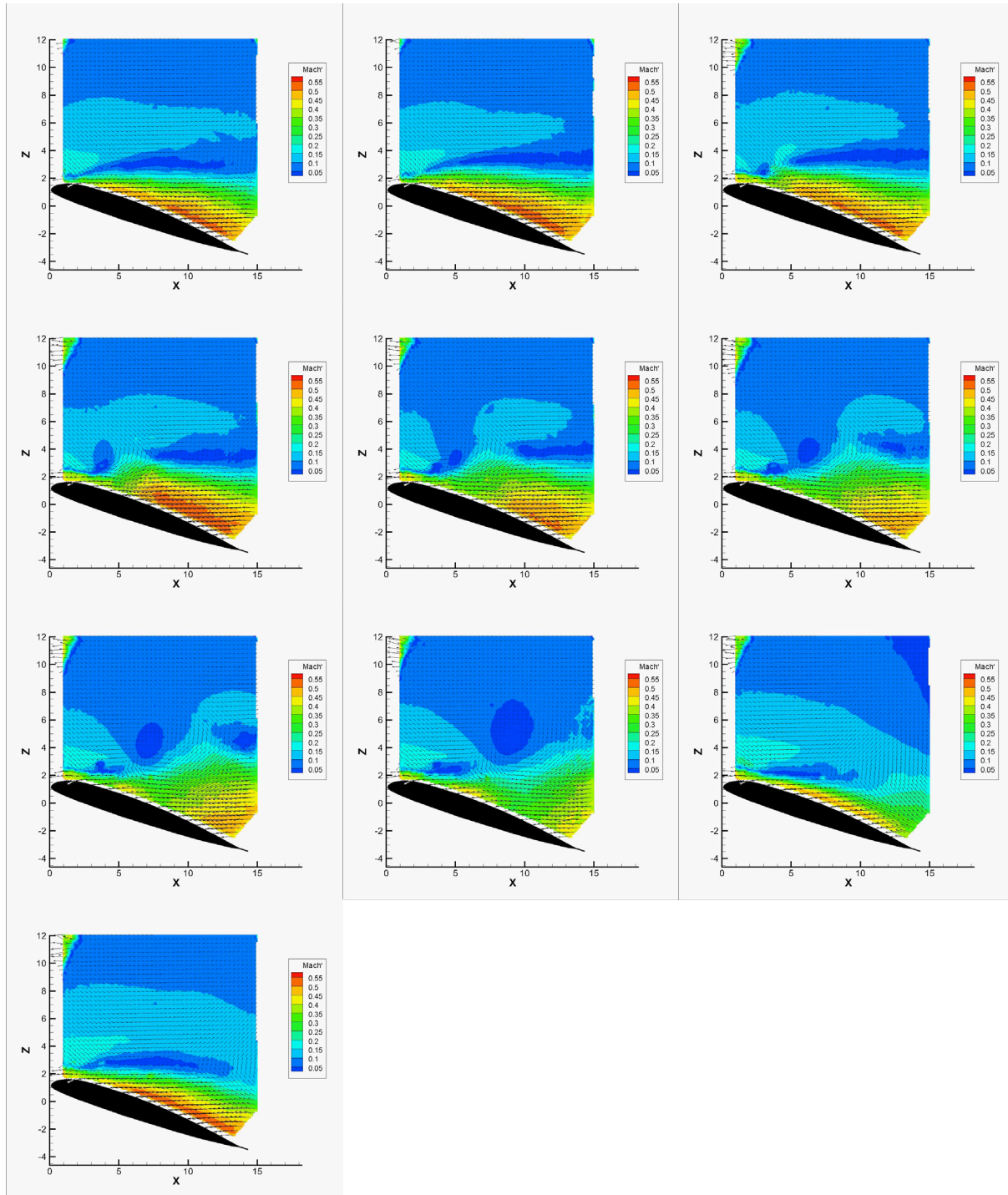


**Figure 660. Mach' contours, Mach 0.4,  $\alpha = 18^\circ$ ,  $F^+ = 0.2$ ,  $\Delta t = 0, 0.5, 1.0, 1.5, 2.0, 2.5, 3.0, 3.5, 7, 10.6$  ms.**

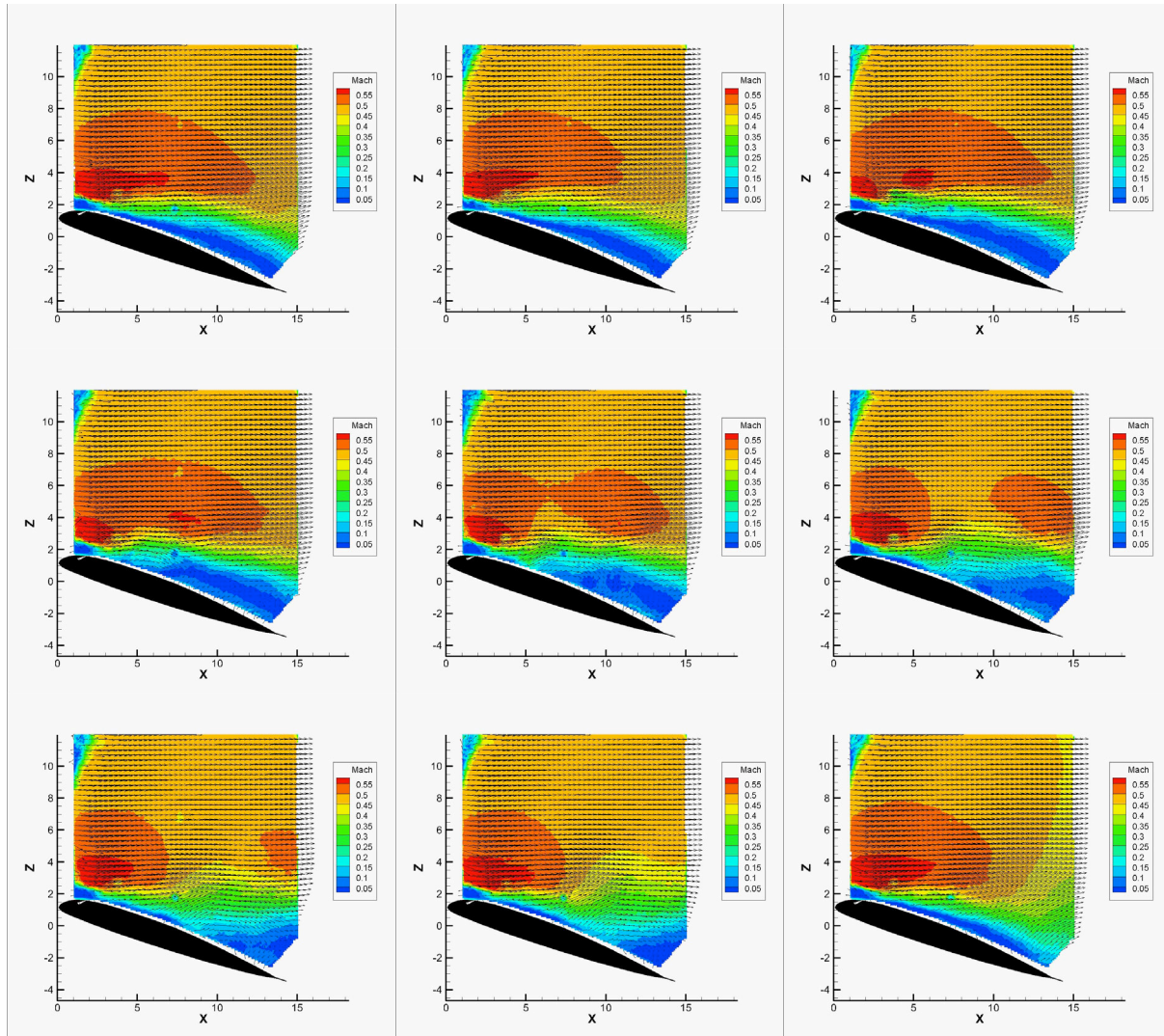


**Figure 661.** Mach contours, Mach 0.4,  $\alpha = 18^\circ$ ,  $F^+ = 0.4$ ,  $\Delta t = 0, 0.5, 1.0, 1.5, 2.0, 2.5, 3.0, 3.5, 5.3$  ms.



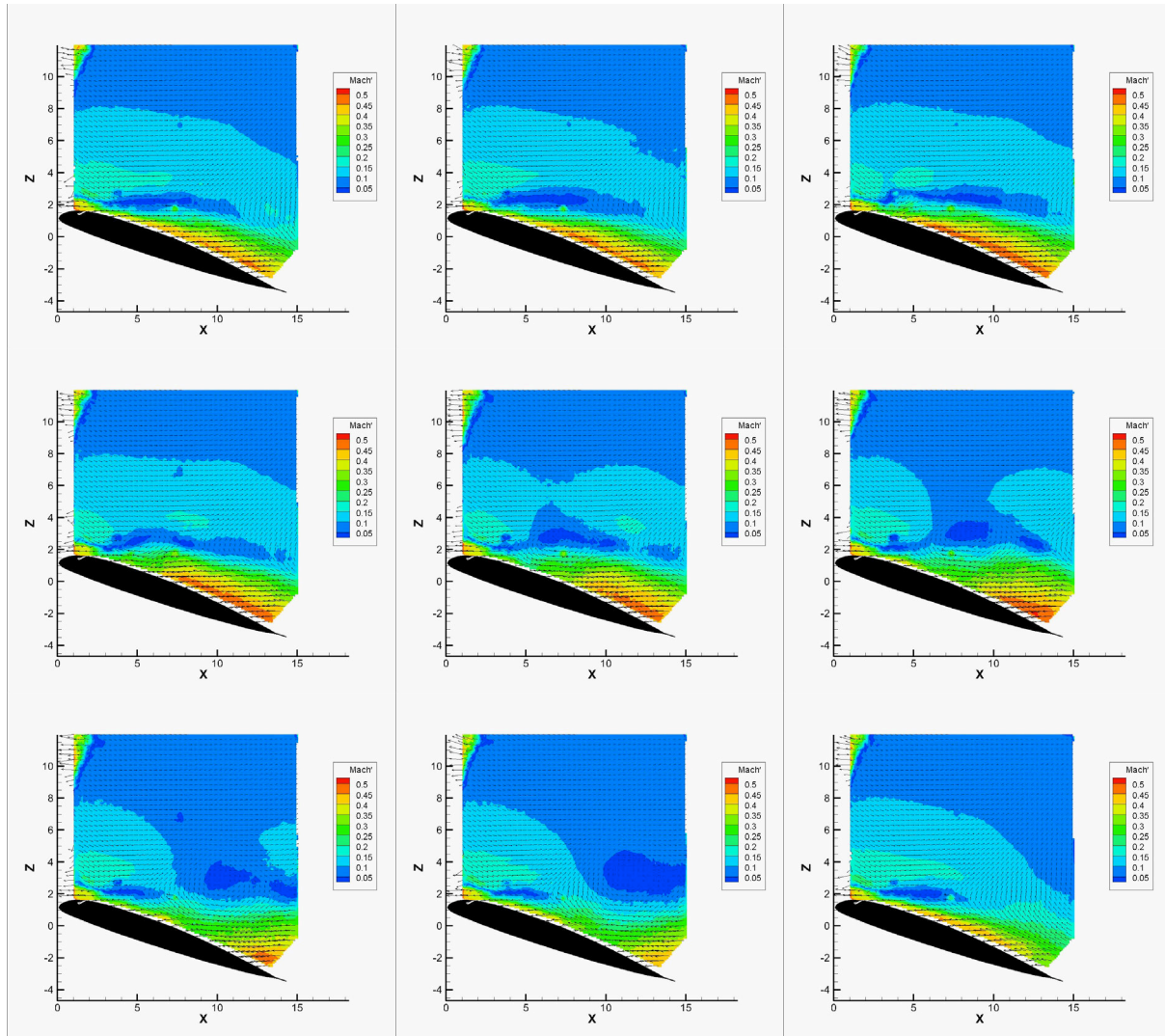


**Figure 662.** Mach' contours, Mach 0.4,  $\alpha = 18^\circ$ ,  $F^+ = 0.4$ ,  $\Delta t = 0, 0.5, 1.0, 1.5, 2.0, 2.5, 3.0, 3.5, 5.3$  ms.



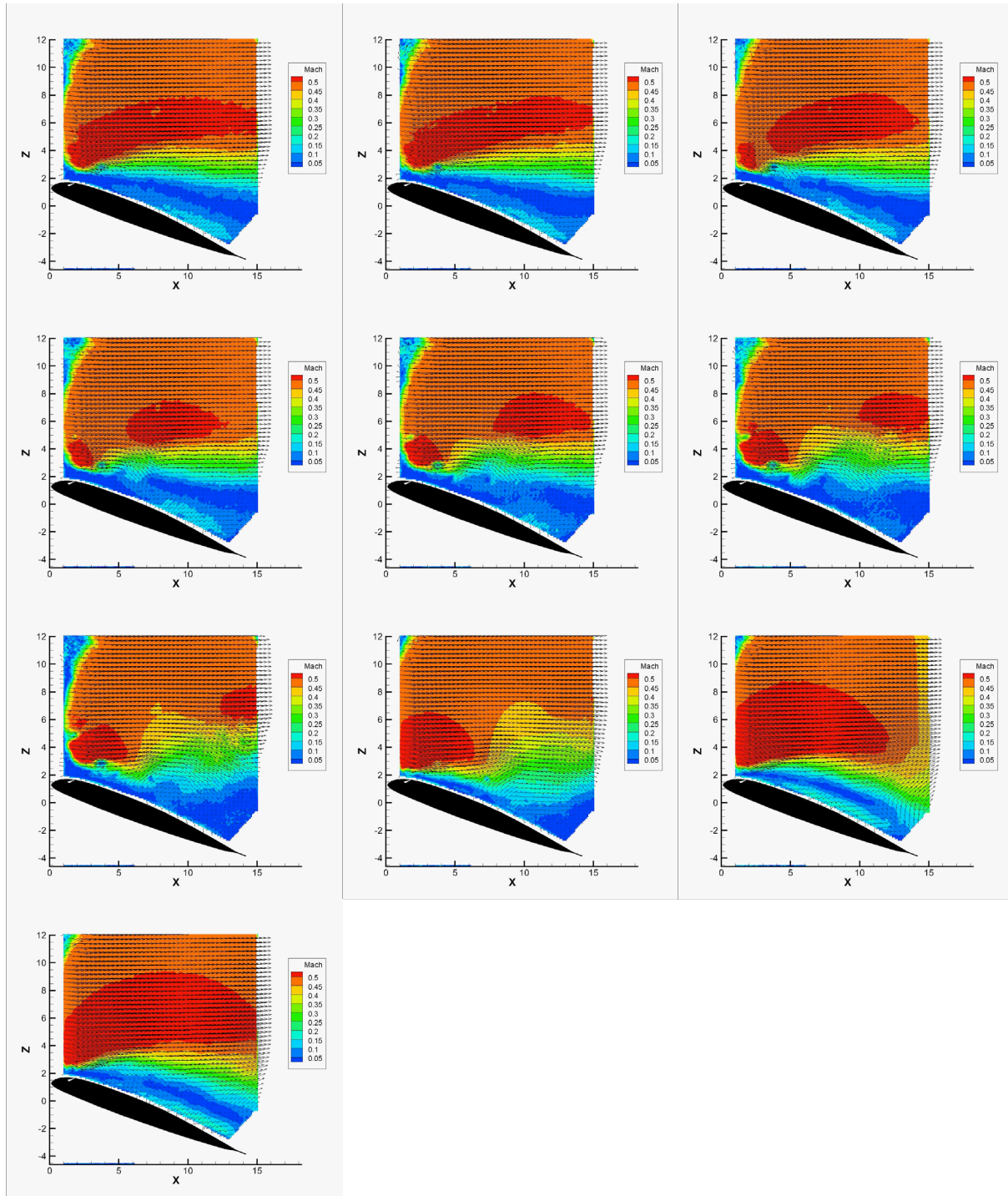


**Figure 663. Mach contours, Mach 0.4,  $\alpha = 20^\circ$ ,  $F^+ = 0.2$ ,  $\Delta t = 0, 0.5, 1.0, 1.5, 2.0, 2.5, 3.0, 3.5, 7, 10.6$  ms.**

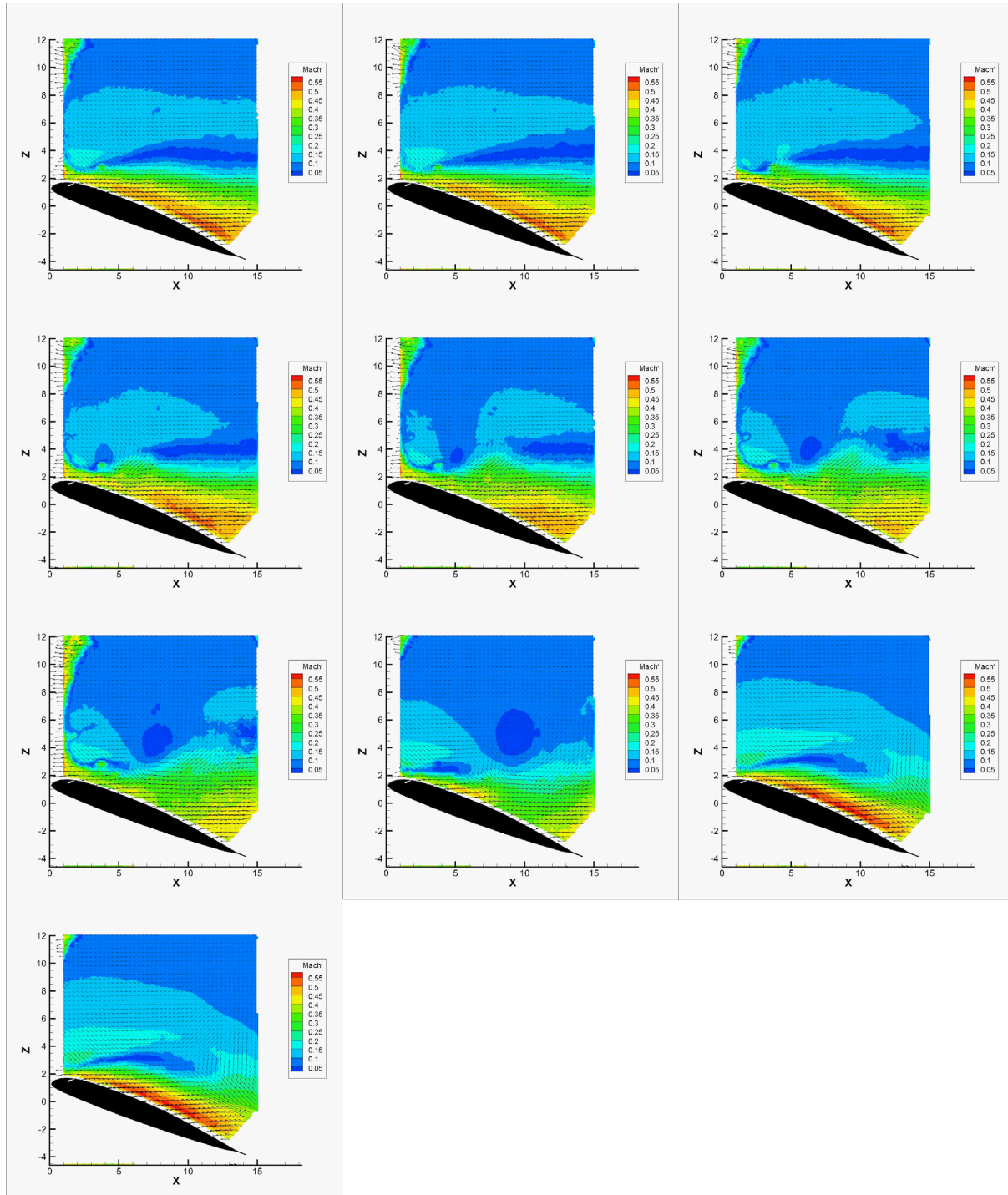


**Figure 664. Mach' contours, Mach 0.4,  $\alpha = 20^\circ$ ,  $F^+ = 0.2$ ,  $\Delta t = 0, 0.5, 1.0, 1.5, 2.0, 2.5, 3.0, 3.5, 7, 10.6$  ms.**

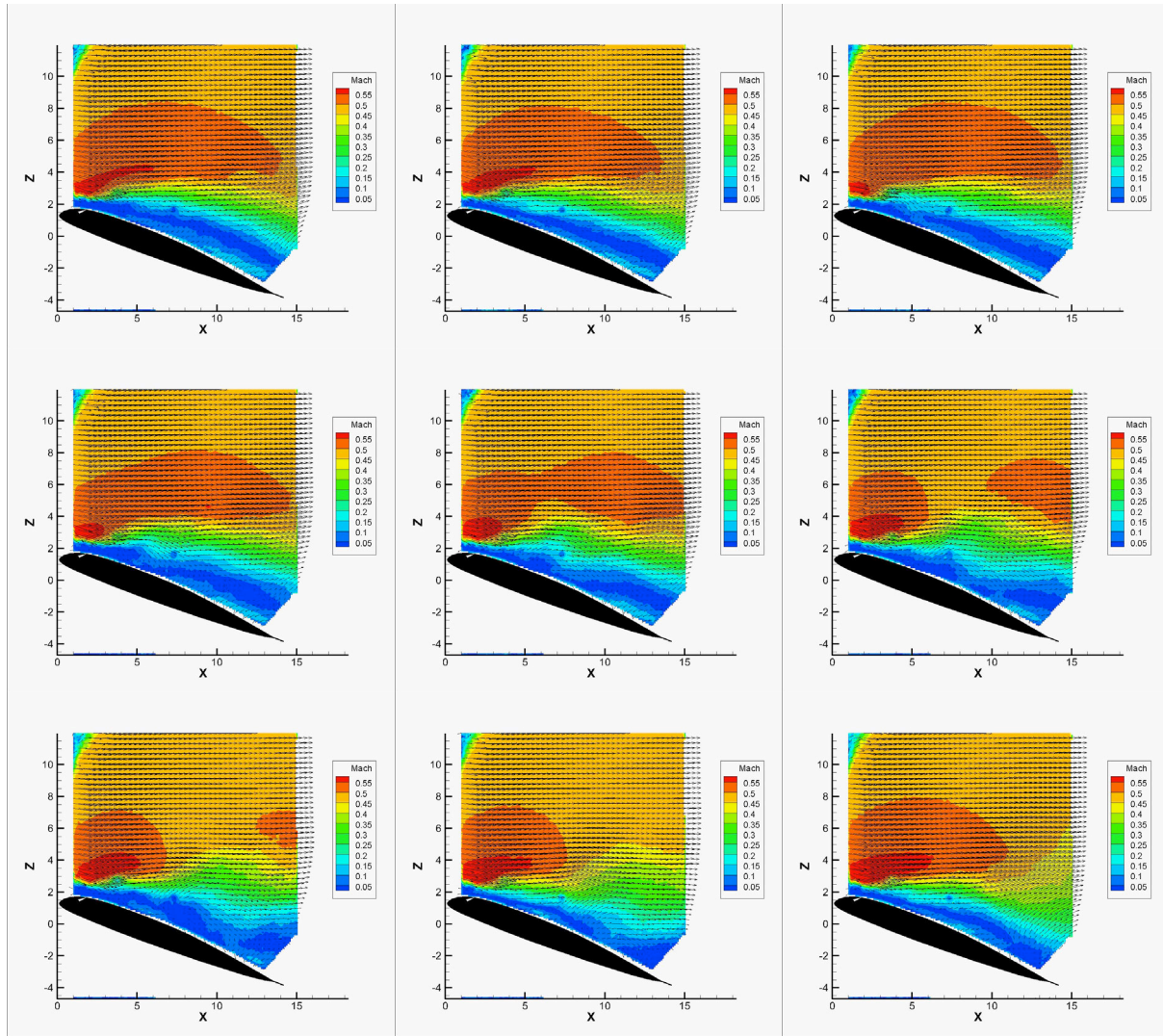


**Figure 665.** Mach contours, Mach 0.4,  $\alpha = 20^\circ$ ,  $F^+ = 0.4$ ,  $\Delta t = 0, 0.5, 1.0, 1.5, 2.0, 2.5, 3.0, 3.5, 5.3$  ms.



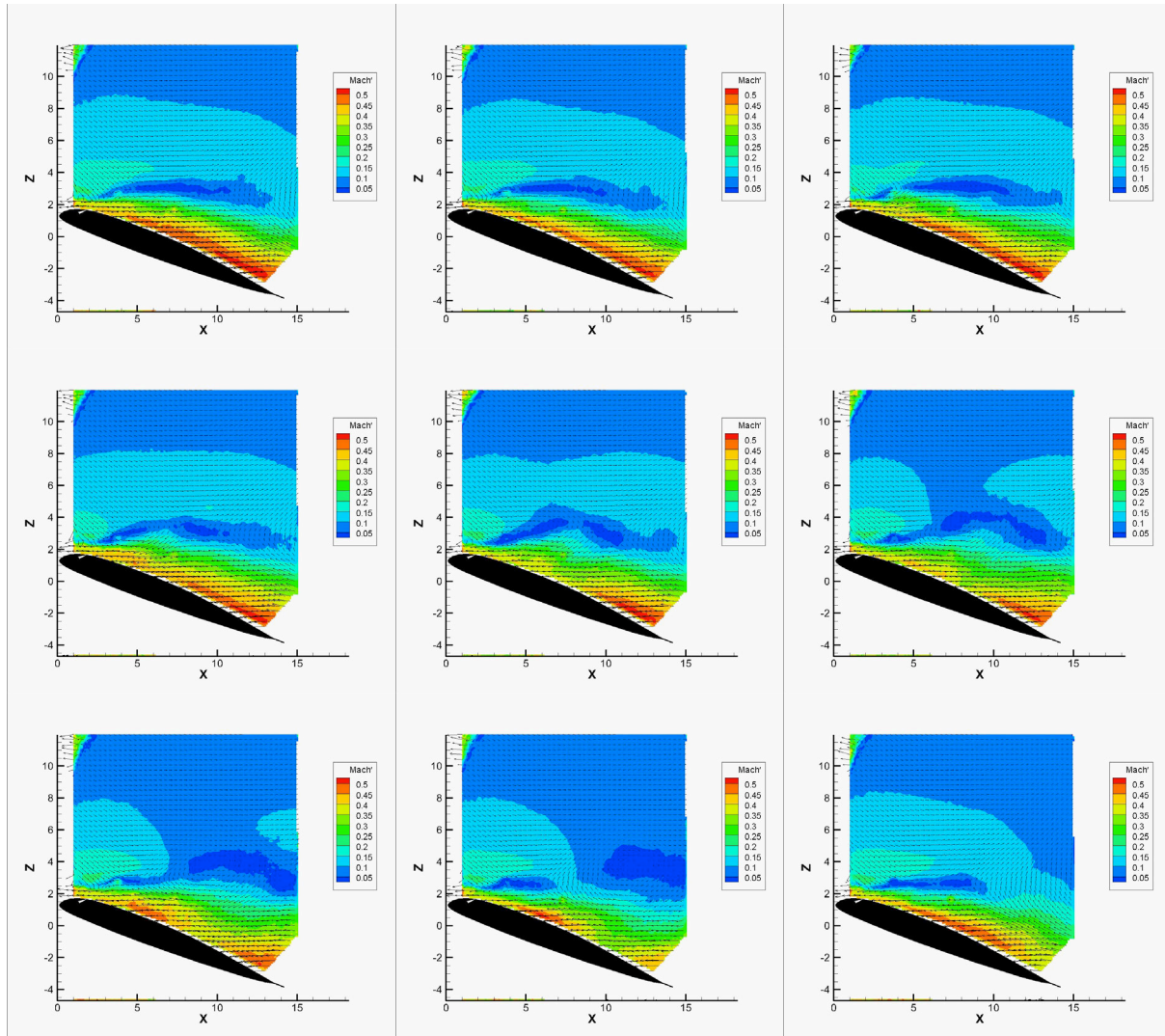


**Figure 666.** Mach' contours, Mach 0.4,  $\alpha = 20^\circ$ ,  $F^+ = 0.4$ ,  $\Delta t = 0, 0.5, 1.0, 1.5, 2.0, 2.5, 3.0, 3.5, 5.3$  ms.

### 3. Unsteady Results

#### A. Mach 0.3

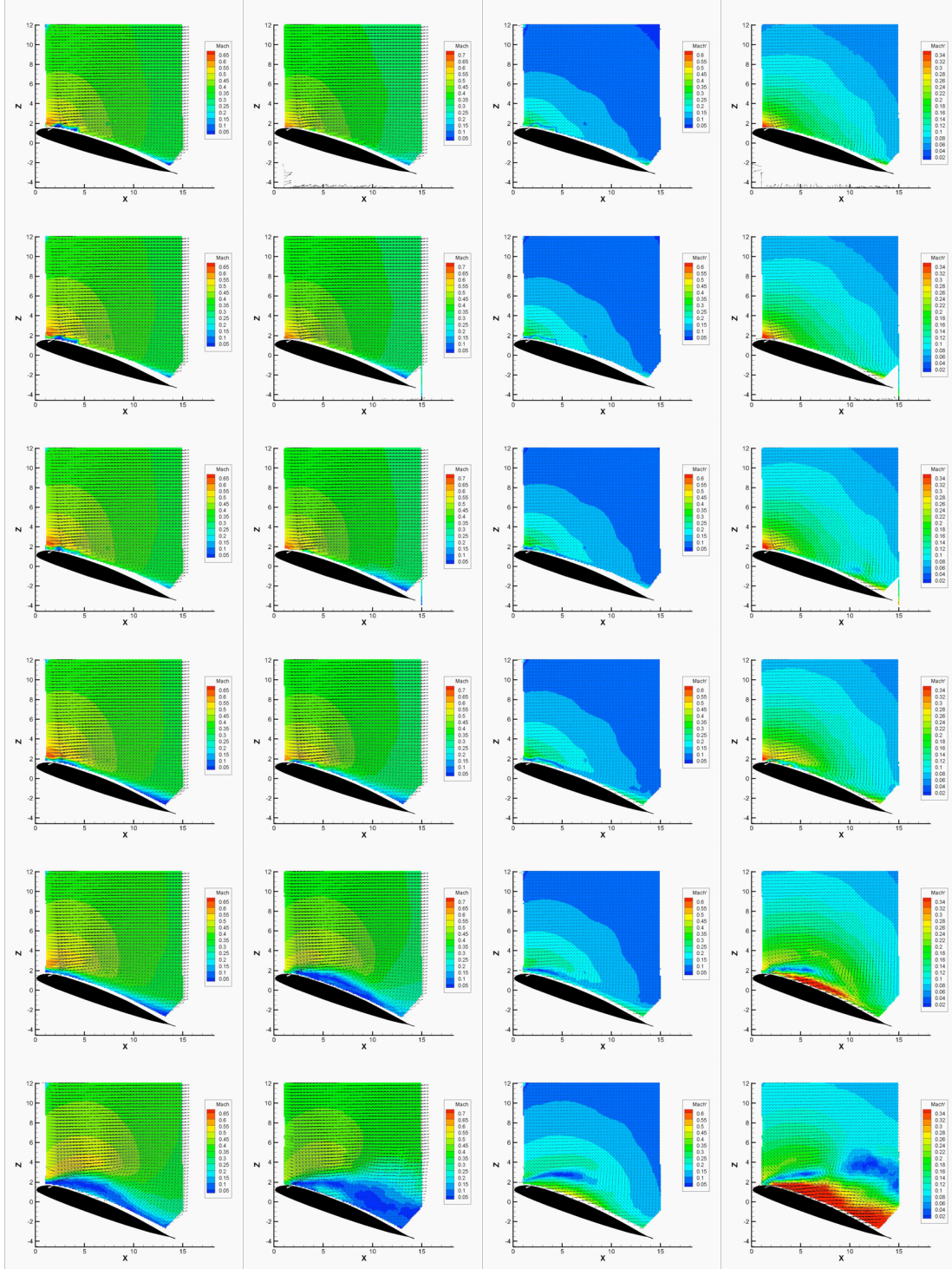


Figure 667. Mach and Mach' contours, Mach 0.3,  $\alpha_0 = 10^\circ$ ,  $\alpha_l = 9.5^\circ$ , baseline slotted (left),  $F^+ = 0.4$  (right),  $\omega t = 40^\circ:8^\circ:80^\circ$  (from top to bottom).



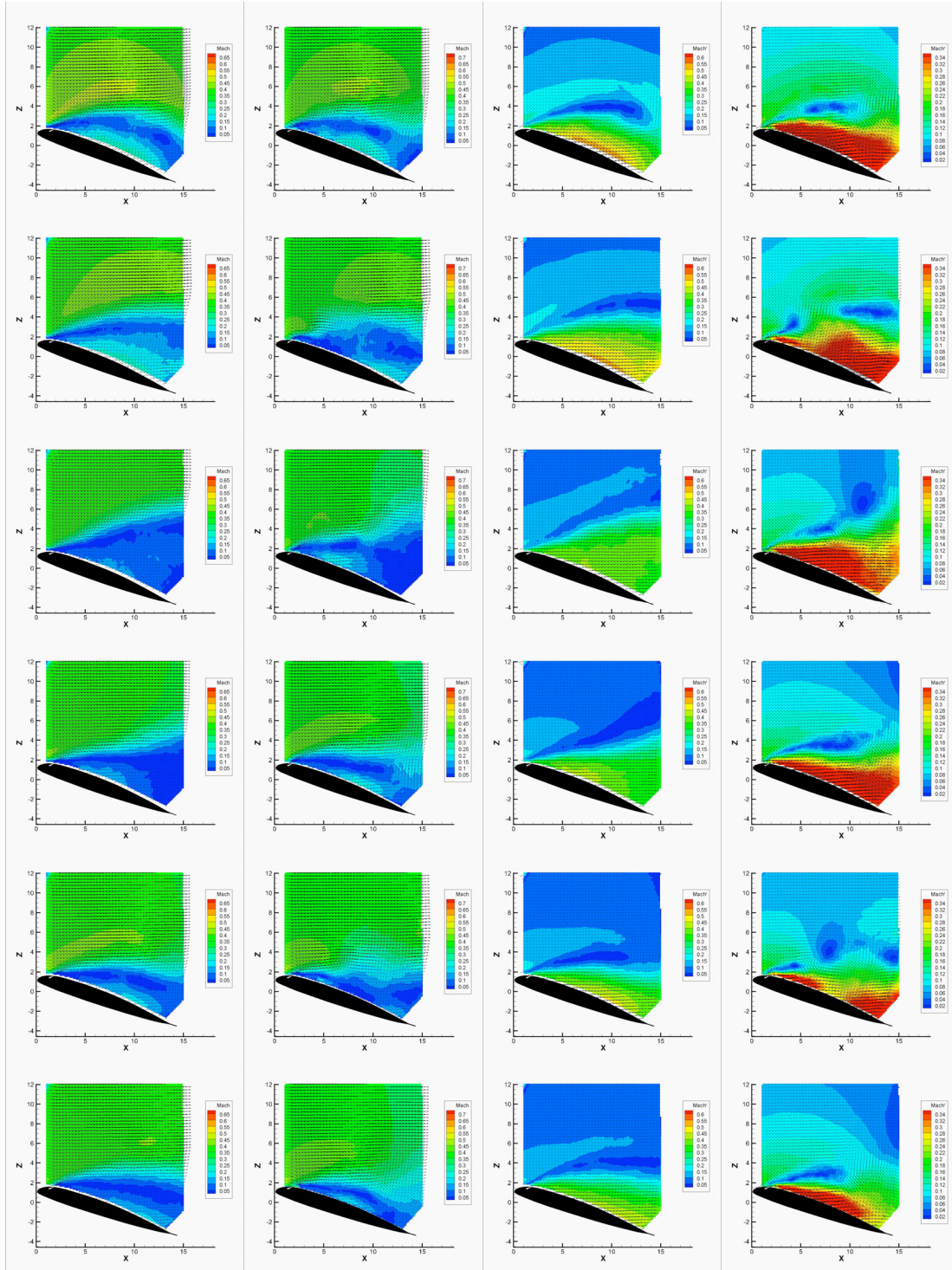
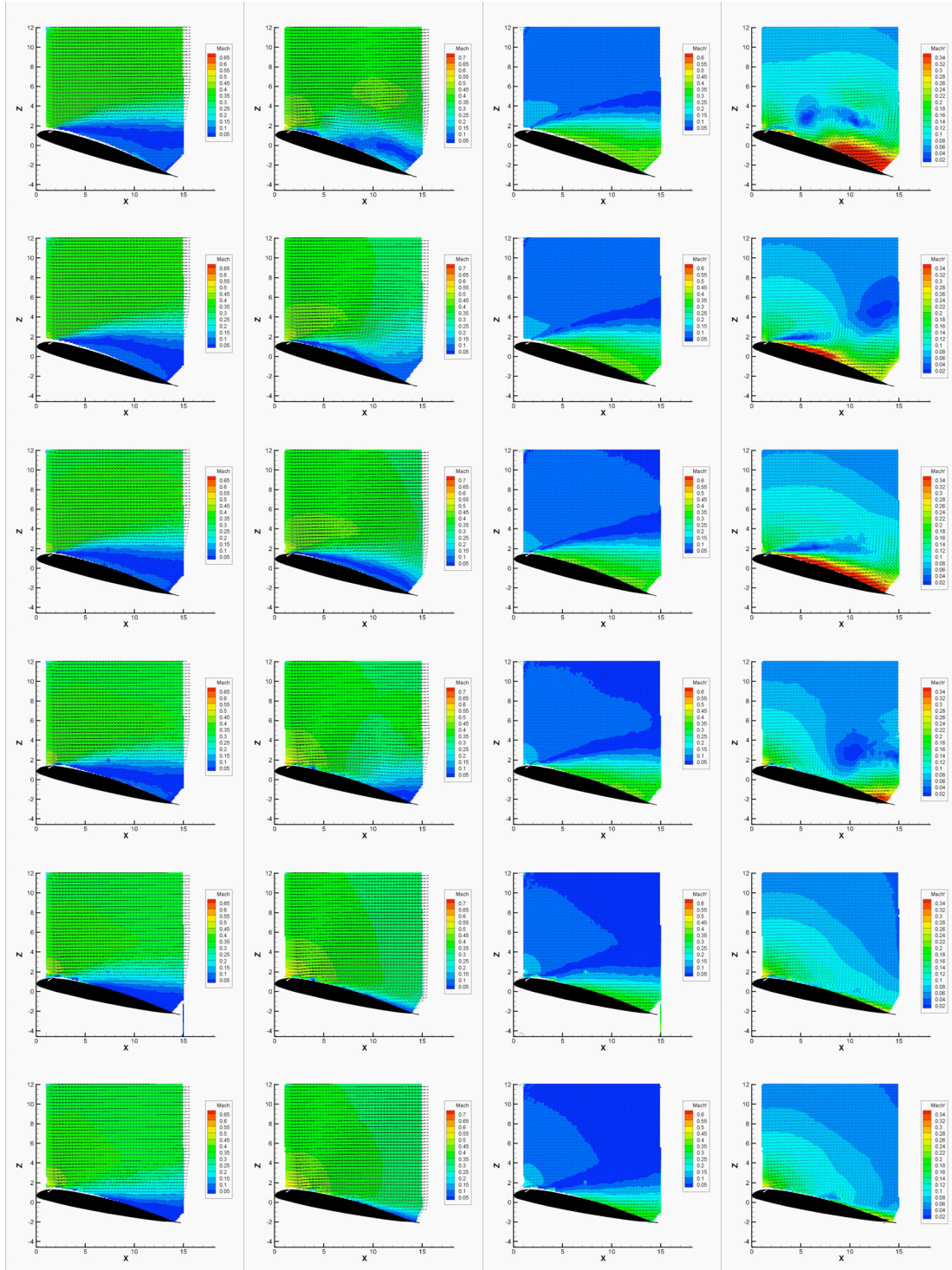
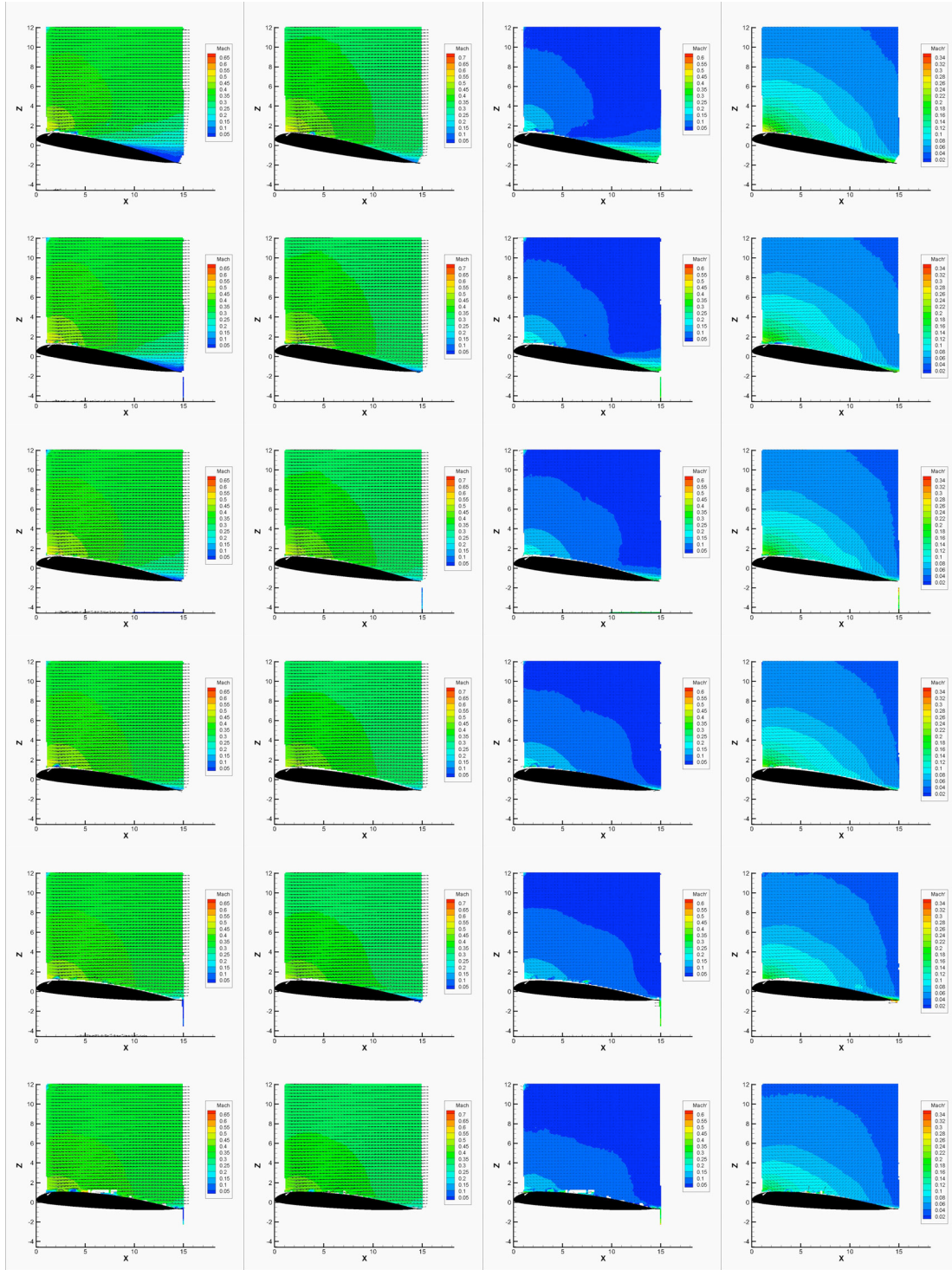


Figure 668. Mach and Mach' contours, Mach 0.3,  $\alpha_0 = 10^\circ$ ,  $\alpha_l = 9.5^\circ$ , baseline slotted (left),  $F^+ = 0.4$  (right),  $\omega t = 88^\circ:8^\circ:128^\circ$  (from top to bottom).



**Figure 669. Mach and Mach' contours, Mach 0.3,  $\alpha_0 = 10^\circ$ ,  $\alpha_l = 9.5^\circ$ , baseline slotted (left),  $F^+ = 0.4$  (right),  $\omega t = 136^\circ:8^\circ:176^\circ$  (from top to bottom).**





**Figure 670. Mach and Mach' contours, Mach 0.3,  $\alpha_0 = 10^\circ$ ,  $\alpha_l = 9.5^\circ$ , baseline slotted (left),  $F^+ = 0.4$  (right),  $\omega t = 184^\circ:8^\circ:224^\circ$  (from top to bottom).**

## B. Mach 0.4

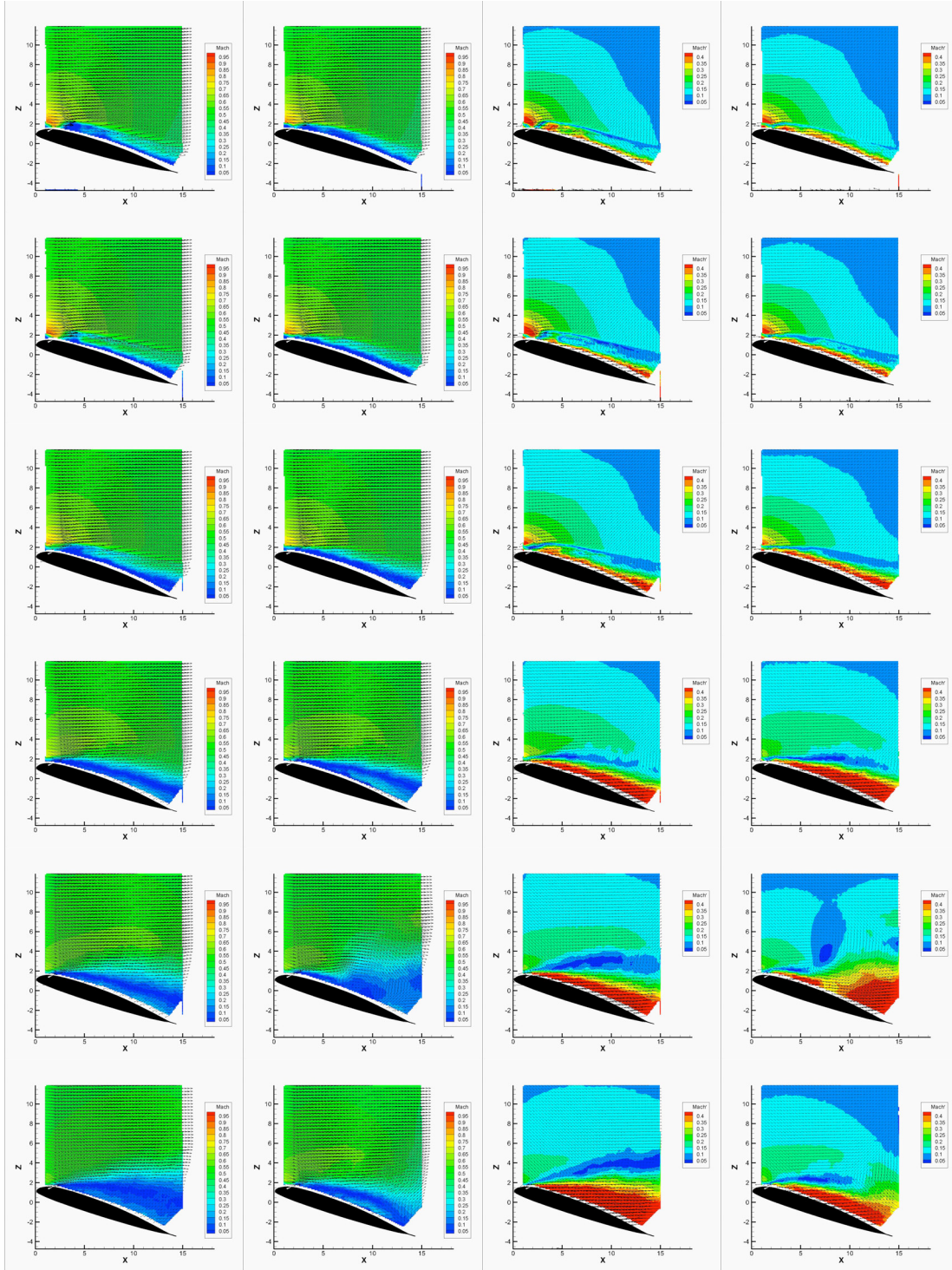


Figure 671. Mach and Mach' contours, Mach 0.4,  $\alpha_0 = 10^\circ$ ,  $\alpha_I = 8^\circ$ , baseline slotted (left),  $F^+ = 0.4$  (right),  $\omega t = 40^\circ:8^\circ:80^\circ$  (from top to bottom).



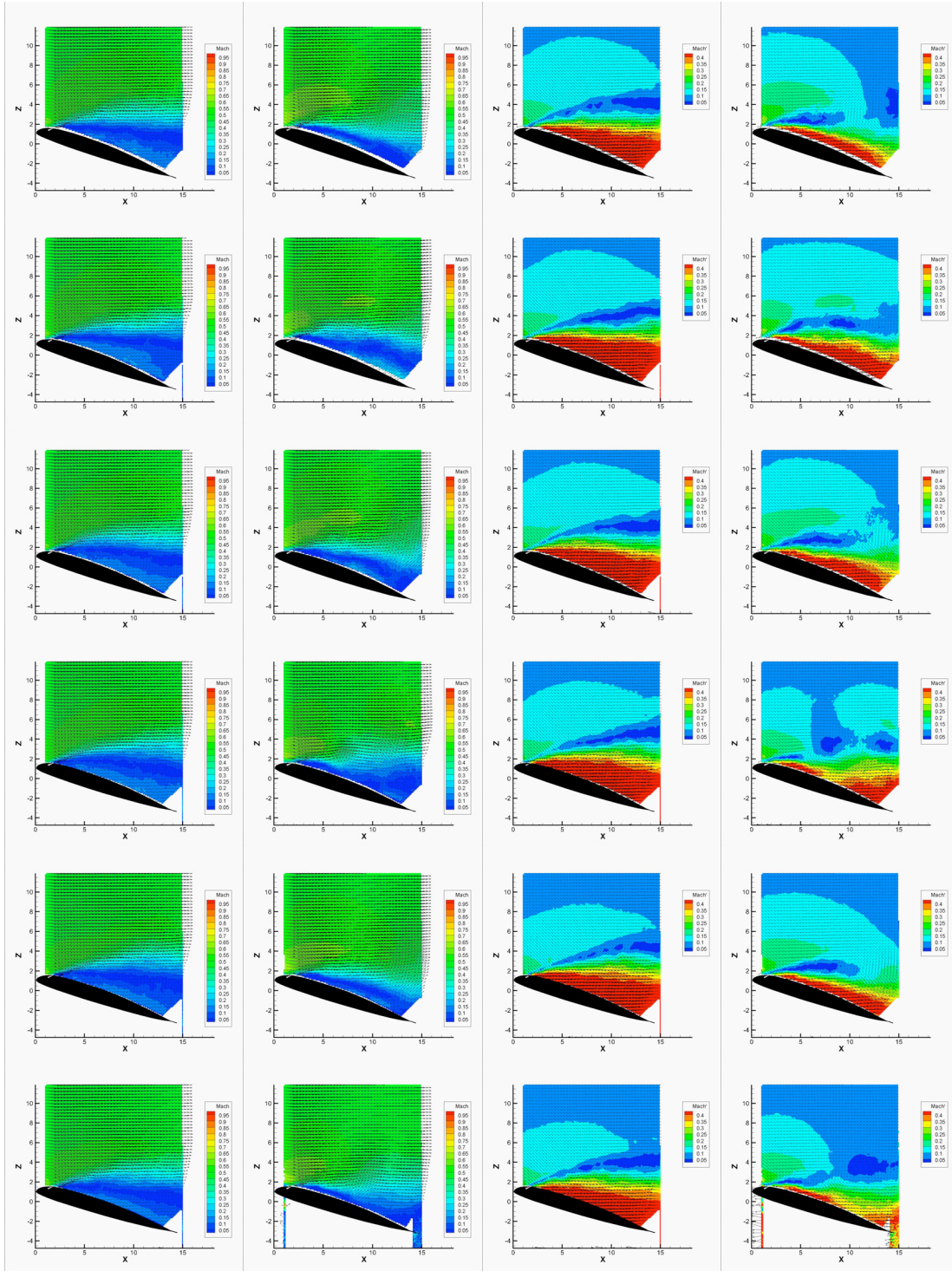
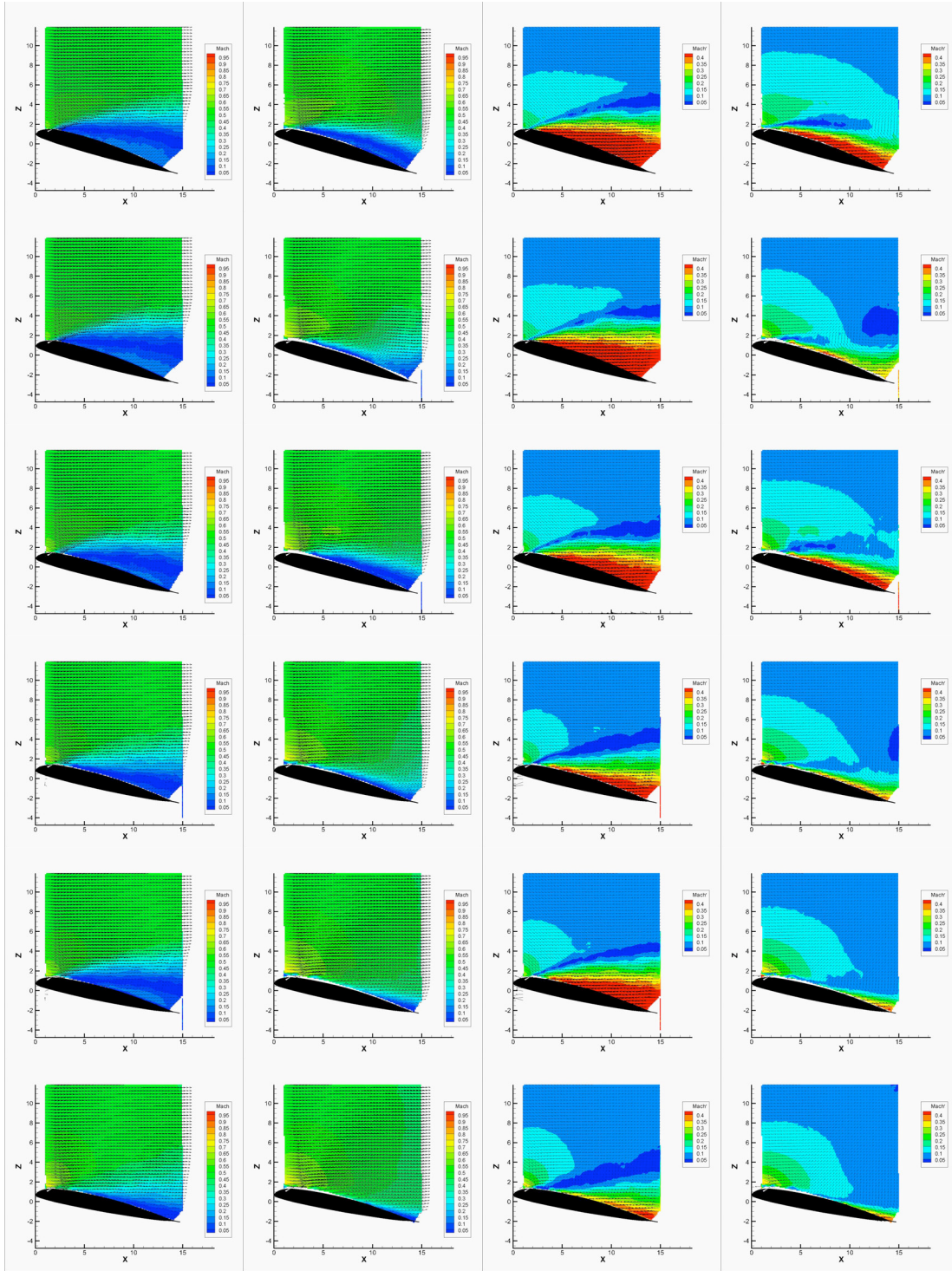


Figure 672. Mach and Mach' contours, Mach 0.4,  $\alpha_0 = 10^\circ$ ,  $\alpha_l = 8^\circ$ , baseline slotted (left),  $F^+ = 0.4$  (right),  $\omega t = 88^\circ:8^\circ:128^\circ$  (from top to bottom).



**Figure 673. Mach and Mach' contours, Mach 0.4,  $\alpha_0 = 10^\circ$ ,  $\alpha_l = 8^\circ$ , baseline slotted (left),  $F^+ = 0.4$  (right),  $\omega t = 136^\circ:8^\circ:176^\circ$  (from top to bottom).**



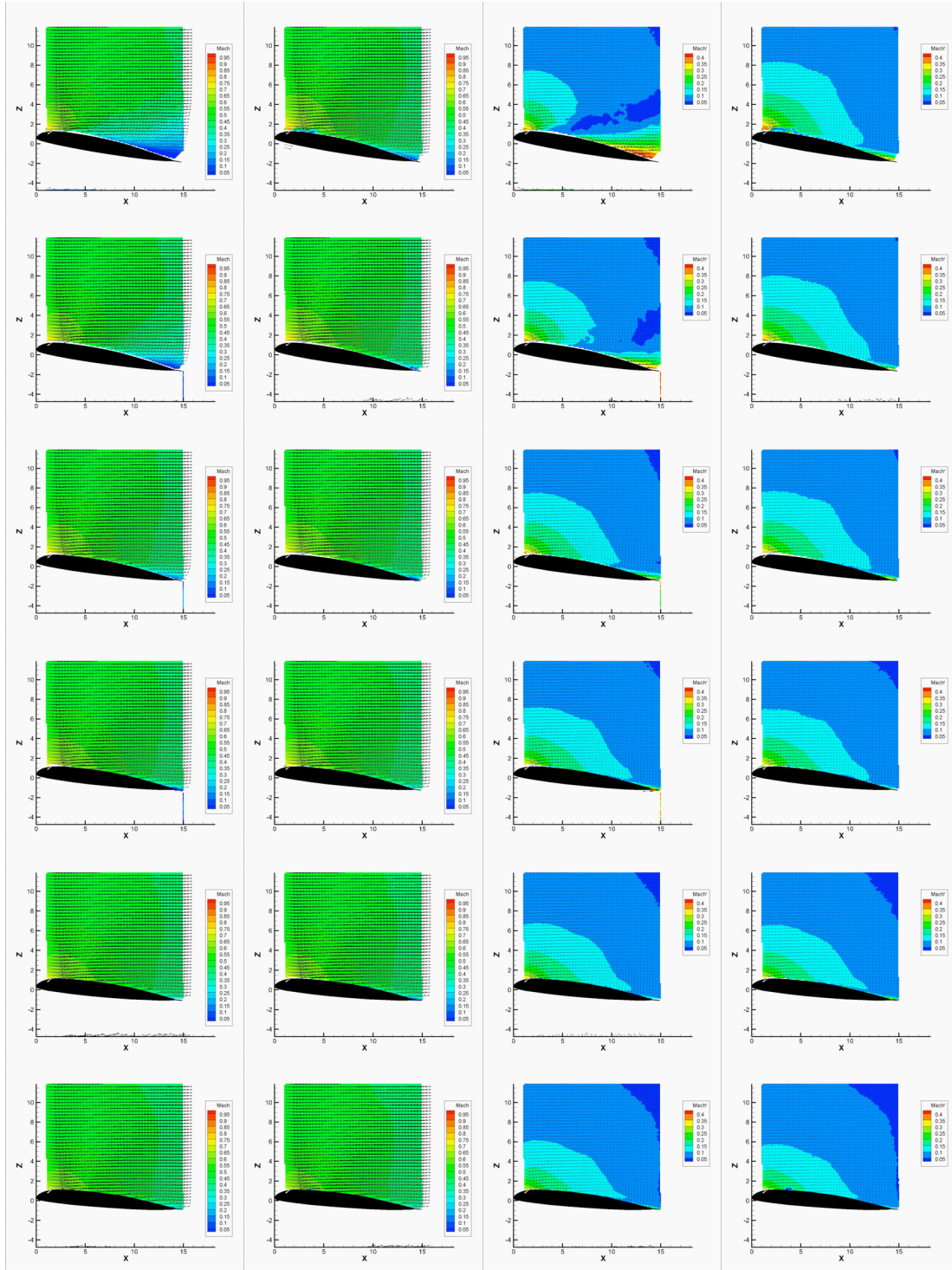


Figure 674. Mach and Mach' contours, Mach 0.4,  $\alpha_0 = 10^\circ$ ,  $\alpha_l = 8^\circ$ , baseline slotted (left),  $F^+ = 0.4$  (right),  $\omega t = 184^\circ:8^\circ:224^\circ$  (from top to bottom).

## Appendix 6. Error in PIV Results due to Particle Size

Due to reasonable constraints imposed by the normal operating conditions of the NASA Glenn Icing Research Tunnel, the only particles, which could be used to seed the flow, were water droplets produced by creating a dry fog in the tunnel. This was performed by lowering the tunnel static temperature in the test section to be near the dew point. This produced excellent images across a range of Mach numbers, examples of which were shown in Figure 297 - Figure 302. The particle size however, ranged from 1 to 5 microns in diameter based on measurements performed in the IRT, which are fairly large compared to typical PIV seed particles. In order to estimate the impact of these large particles on the results collected, the analysis described below was performed.

We consider the following equations:

$$m_p \frac{D\vec{u}_p}{Dt} = m_p \left( \frac{\partial \vec{u}_p}{\partial t} + \vec{u}_p \cdot \nabla \vec{u}_p \right) = \frac{1}{2} \rho_f C_d A_p (\vec{u} - \vec{u}_p) |\vec{u} - \vec{u}_p| \quad (1)$$

$$C_d = \frac{24}{Re_p} (1 + 0.15 Re_p^{0.687}) \quad (2)$$

$$Re_p = \frac{d_p |\vec{u}_p - \vec{u}|}{\nu_f} \quad (3)$$

$$D_{Stokes} = 3\pi\mu_f d_p (\vec{u} - \vec{u}_p) \quad (4)$$

$\vec{u}$ : Fluid velocity field (Eulerian)

$\vec{u}_p$ : Particle velocity field (Eulerian)

$d_p$ : Particle diameter

$\nu_f$ : Fluid kinematic viscosity

$\mu_f$ : Fluid dynamic viscosity

$m_p$ : Mass of single particle

$A_p$ : Projected area of single particle

$\rho_f$ : Fluid density

$Re_p$ : Particle Reynolds number

$D_{Stokes}$ : Stokes' drag

Eqn. (1) is Newton's 2<sup>nd</sup> law written for a single particle subjected only to forces created by the fluid velocity field. This analysis assumes that the presence of particles does not influence the fluid velocity field. This equation can be derived also by beginning with the Basset-Boussinesq-Oseen equation and making the following assumptions:

1. Neglect terms that are small based on very low Reynolds number and a much larger particle density compared to the fluid density
2. Use the empirical equation for  $C_d$  to approximate the Stokes' drag and pressure gradient terms (can also replace this term with Stokes' drag equation as will be shown).
3. Neglect the Basset force

Eqn. (2) is the drag coefficient valid for Reynolds numbers less than 1000. Particle Reynolds number is given by eqn. (3). Eqns. (2) and (3) can be found in *Multiphase Flow and Fluidization: Continuum and Kinetic Theory Descriptions* (D. Gidaspow, 1994). Other references recommend that the Stokes' drag formula (eqn. 4) be used due to the very low expected particle Reynolds number. Both will be used and compared in this analysis.

The error estimation methodology is as follows. We consider steady CFD simulations for high angles of attack at Mach 0.4. We examine the fluid acceleration at key locations to determine the highest levels of acceleration, and tabulate the results as shown in Table 65.

**Table 65. Acceleration levels for a VR-12 airfoil at Mach 0.4 based on CFD analysis.**

Angle-of-attack (Deg)	Fluid acceleration at mid-chord near upper surface (m/s <sup>2</sup> )
12	57312
14	51379
16	8152
18	7278

Assuming that differences between the particle and fluid velocity fields will be the largest in regions of highest acceleration, and to be conservative, we assume a maximum fluid acceleration of 100,000 m/s<sup>2</sup>. Figure 675 shows acceleration magnitude contours near the airfoil for Mach 0.4, 18° angle-of-attack, steady CFD simulations. Based on this, a peak value of 100,000 m/s<sup>2</sup> covers the entire region of interest.



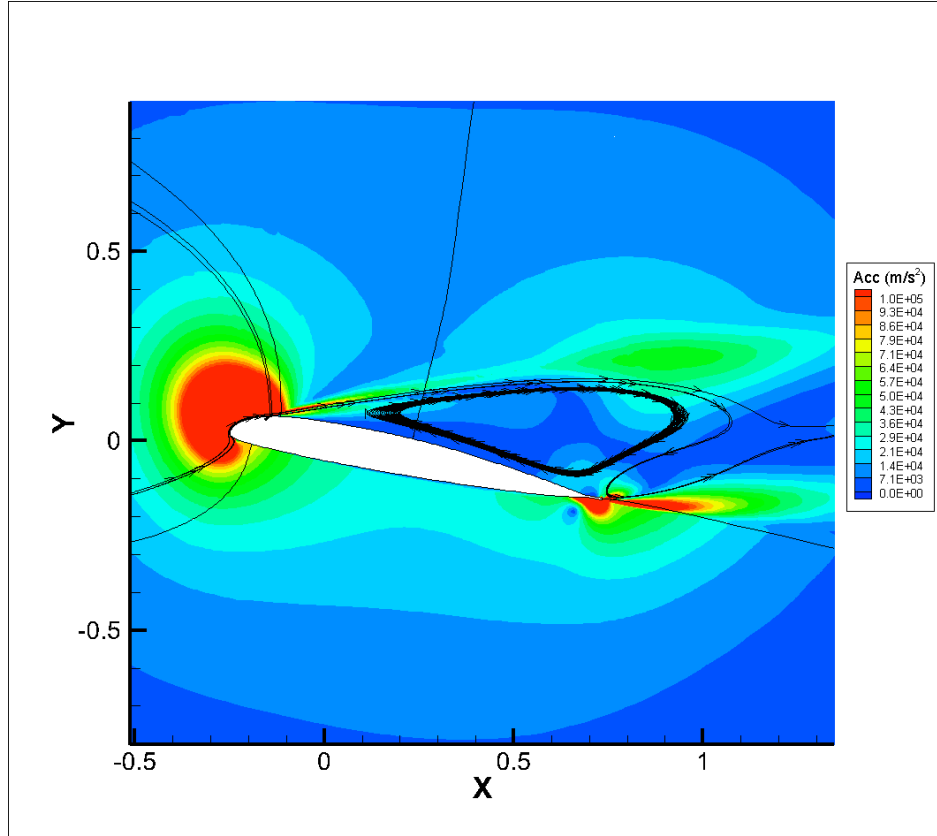


**Figure 675. Steady CFD simulation results showing contours of acceleration magnitude for Mach 0.4, 18° angle-of-attack.**

Next, we construct a simple two-dimensional auxiliary flowfield that achieves this level of maximum acceleration, a simple inviscid vortex. The reason for using this auxiliary flowfield rather than the CFD flowfield is primarily to simplify the discretization of eqn. (1). The objective will be to take this auxiliary flowfield, assume a particle size and mass, then solve for the particle velocity field given a known fluid velocity field. Eqn. (1) derivatives are discretized in time and space, but the time discretization is only to allow us to march towards a steady solution. 1<sup>st</sup> order forward-differencing is used for time, 1<sup>st</sup> order upwind differencing used for space, and  $Re_p$  and  $C_d$  are updated at each time step. The solution for particle velocity field is carried forward until the particle velocity field achieves a steady-state. This scheme is provided in eqns. (5) and (6), where  $i$  denotes x-direction indices,  $j$  denotes y-direction indices, and  $n$  denotes the time index. The velocity vectors,  $\vec{u}$  and  $\vec{u}_p$  are broken into their respective x- and y-components,  $(u, v)$  and  $(u_p, v_p)$ . Finally, the coefficients  $A_x$ ,  $B_x$ ,  $C_x$  are determined based on the sign of  $u$  as shown in Table 66.  $A_y$ ,  $B_y$ , and  $C_y$  are determined in a similar fashion based on  $v$ .

$$u_p^{n+1,i,j} = \frac{\rho_f C_d A_p \Delta t}{2m_p} (u^{i,j} - u_p^{n,i,j}) \sqrt{(u^{i,j} - u_p^{n,i,j})^2 + (v^{i,j} - v_p^{n,i,j})^2} - \frac{u_p^{n,i,j} \Delta t}{\Delta x} (A_x u_p^{n,i+1,j} + B_x u_p^{n,i,j} + C_x u_p^{n,i-1,j}) - \frac{v_p^{n,i,j} \Delta t}{\Delta y} (A_y u_p^{n,i,j+1} + B_y u_p^{n,i,j} + C_y u_p^{n,i,j-1}) \quad (5)$$

$$v_p^{n+1,i,j} = \frac{\rho_f C_d A_p \Delta t}{2m_p} (v^{i,j} - v_p^{n,i,j}) \sqrt{(u^{i,j} - u_p^{n,i,j})^2 + (v^{i,j} - v_p^{n,i,j})^2} - \frac{u_p^{n,i,j} \Delta t}{\Delta x} (A_x u_p^{n,i+1,j} + B_x u_p^{n,i,j} + C_x u_p^{n,i-1,j}) - \frac{v_p^{n,i,j} \Delta t}{\Delta y} (A_y v_p^{n,i,j+1} + B_y v_p^{n,i,j} + C_y v_p^{n,i,j-1}) \quad (6)$$

**Table 66. Upwind differencing scheme.**

Condition	A	B	C
$u > 0$	0	1	-1
$u \leq 0$	1	-1	0

Comparing the converged solution for the particle velocity field to the known fluid velocity field, the maximum difference (or error) can be calculated at any region in the auxiliary flowfield, particularly in the areas of highest acceleration. The results from simulations of five different particle sizes are shown in Figure 676 and Table 67. The vectors in Figure 676 appear as expected wherein the particle velocity field exhibits a radial velocity not present in the fluid field due to the inertia of the particles with respect to the fluid. The location of maximum error occurs at the location of maximum acceleration, and the errors in flow angle and velocity magnitude are shown in Table 67. Based on particle size measurements collected recently by the IRT staff, it is expected that approximately 90% of the condensation cloud particles that occur are 3  $\mu\text{m}$  in diameter. Thus, it can be estimated that the error introduced by the use of these droplets as seed particles is no more than 1.1° in flow angle and 2.5% in velocity magnitude based on the  $C_d$  drag formulation. To confirm the validity of this formulation, the first term on the RHS of eqns. 5 and 6 were rewritten using the Stokes' drag formulation (which significantly simplifies this term), and those results are also provided in Table 67. The results are very similar at up to 3  $\mu\text{m}$  particle diameter.

Thus, it is estimated that the water droplets used for all PIV measurements discussed in this report result in an uncertainty no greater than  $\pm 1.2^\circ$  in flow angle and  $\pm 2.8\%$  in velocity magnitude.

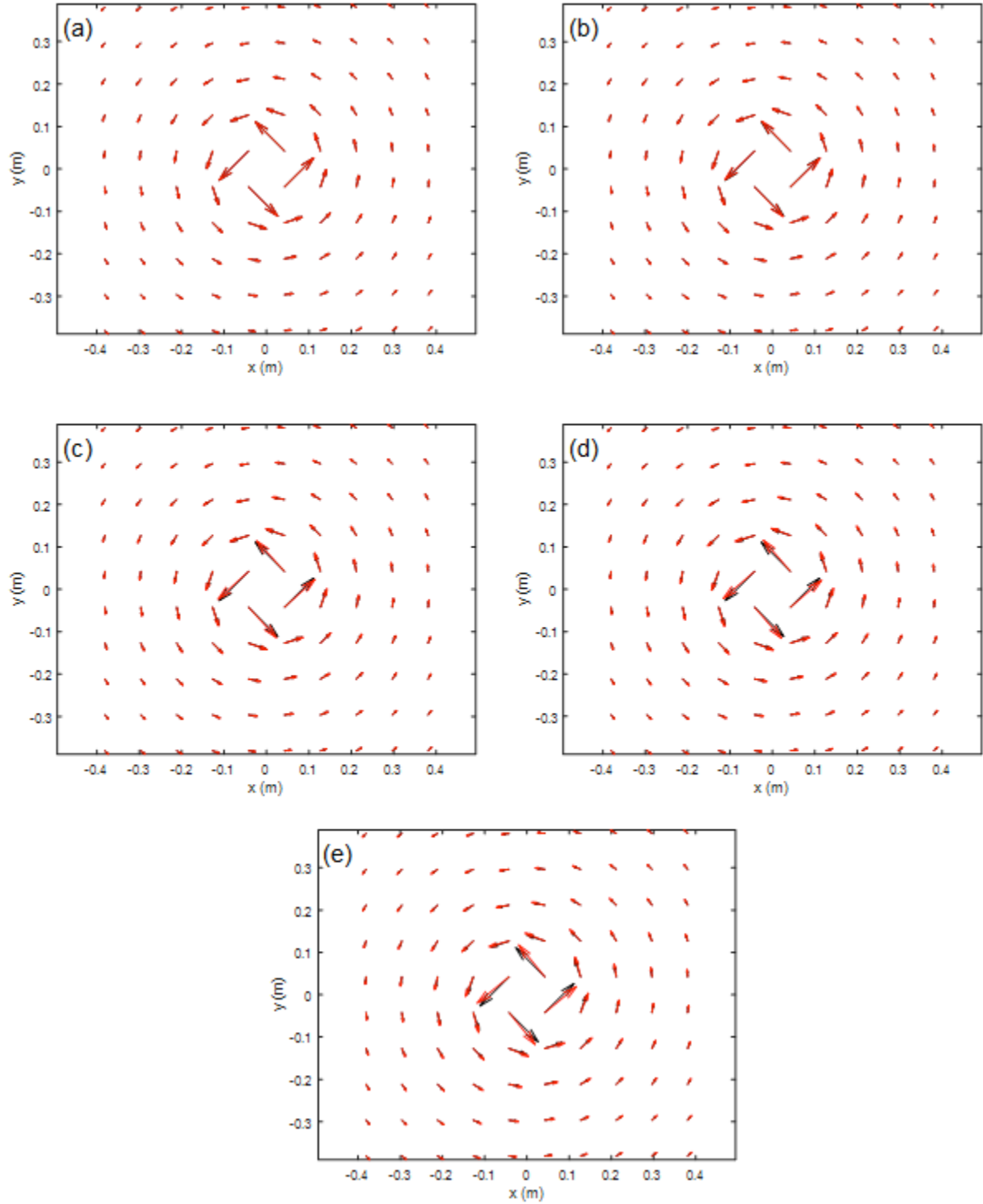


**Figure 676. Fluid (black vectors) and particle (red vectors) velocity fields. Calculations performed using  $C_d$  formulation for particle drag. Particle diameters are as follows: (a) 1  $\mu\text{m}$ , (b) 3  $\mu\text{m}$ , (c) 5  $\mu\text{m}$ , (d) 7  $\mu\text{m}$ , and (e) 9  $\mu\text{m}$ .**

**Table 67. Maximum differences in flow angle and velocity magnitude for water particles of various diameters in the auxiliary simplified flowfield. Results provided for both drag formulations.**

Particle diameter ( $\mu\text{m}$ )	Flow Angle Error ( $^{\circ}$ ) – $C_d$ Formulation	Velocity Magnitude Error (%) - $C_d$ Formulation	Flow Angle Error ( $^{\circ}$ ) – Stokes Formulation	Velocity Magnitude Error (%) - Stokes Formulation
1	0.1	0.3	0.1	0.3
3	1.1	2.5	1.2	2.8
5	2.6	5.9	3.1	7.1
7	4.1	9.4	5.5	12.4
9	5.7	12.8	8.2	18.1

## Appendix 7. Weighting Factor Adjustments for Improved Drag Coefficient Measurements

The strong agreement between the post-test CFD and experimentally integrated VR-12 quantities,  $C_L$  and  $C_M$ , reinforced the desire to diminish the larger discrepancies found in the drag comparisons previously discussed. Recall, the tap layout was constructed to minimize lift and pitching moment quadrature errors. Drag, consequently, was a byproduct of the resultant tap distribution. Figure 677 plots the final tap distribution used for the IRT wind tunnel test. Lift and drag integrals based on this layout are shown for several quadrature methods as well as the high spatially resolved CFD solution. Through the design of the optimization, the segmented Gauss integrated lift and CFD lift are nearly identical for each angle in the trajectory whereas the drag values show large differences for each angle of attack. The latter error is shown explicitly in Figure 678. The maximum deviation occurs on the upstroke, near 19.5 deg. The CFD solution predicts a relatively constant drag from 16 to 20 deg on the upstroke, whereas the segmented Gauss shows increasing drag up to the stall vortex formation as the airfoil changes direction. Note, trapezoidal integration outperforms the segmented Gauss over this region of the pitch trajectory, but similarly under predicts the low-angle of attack drag.

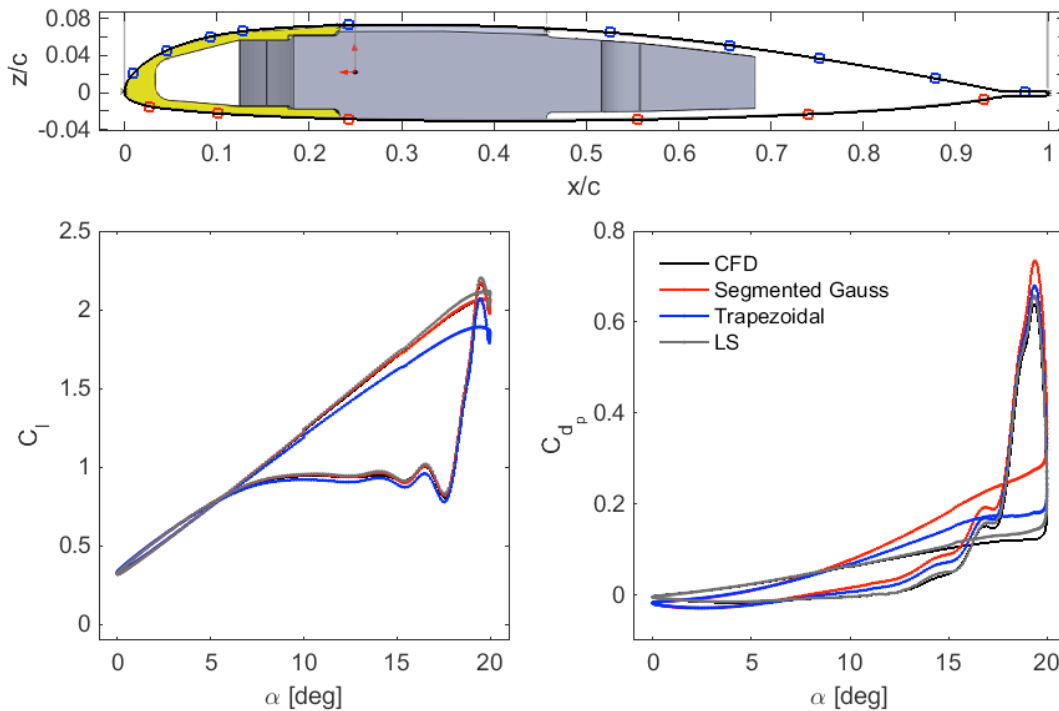


**Figure 677. Schematic of the final VR-12 tap distribution (top). Lift (bottom left) and drag (bottom right) comparison for several integration schemes,  $M=0.3$ ,  $\alpha=10\pm10$  deg.**

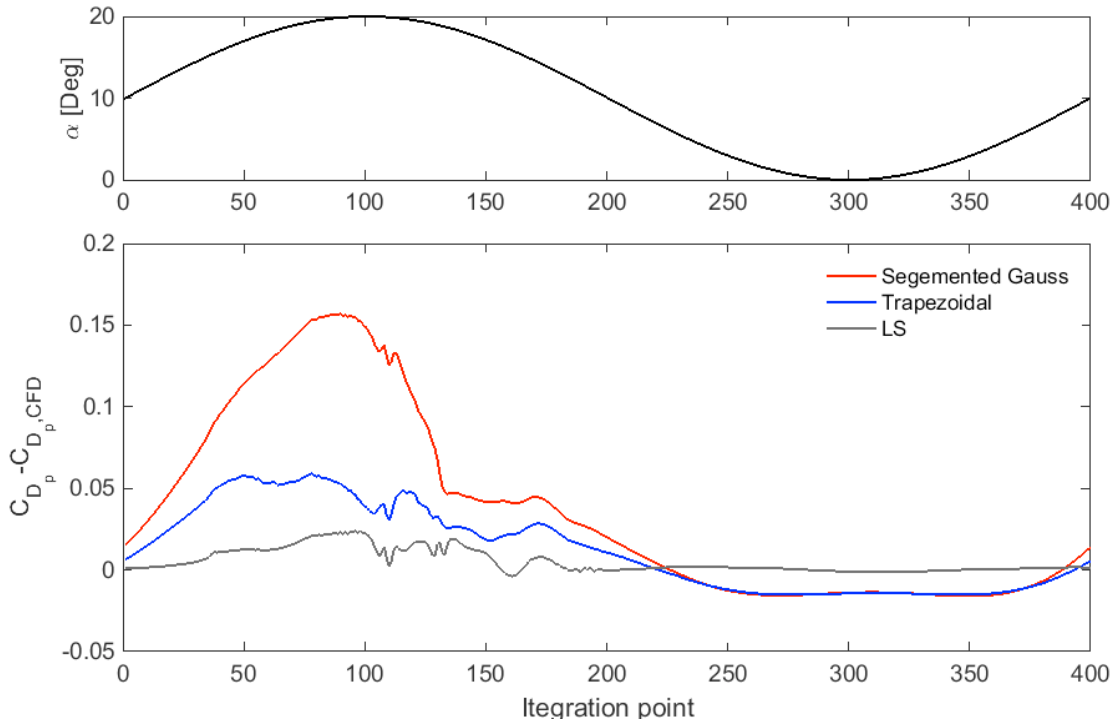


**Figure 678. Drag errors associated with different quadrature methods.**

In order to improve the drag calculations, the quadrature problem was revisited. Any integral through discretization can be represented as a summation of weights and the integrand, e.g., drag can be evaluated as

$$C_{D_p}^i = \sum_{j=1}^N A_j C_{p_{i,j}} \frac{dy_j}{dx_j} dx_j$$

where  $A_j$  is the assigned weight to location  $x_j$  (in this case, a tap position) and  $C_{p_{i,j}}$  is the measured pressure at  $x_j$  at time  $i$ . The segmented Gauss weights are determined through the Legendre polynomial and the optimization problem is then to find the best  $x_j$  to minimize the integration error. However, given that the drag was of less concern in the original tap distribution, the  $x_j$  locations and resultant Gauss weights create a poor approximation of the solution. Discarding the segmented Gauss weights and retaining the now fixed transducer geometry, the above equation can be used to solve for the ‘best-fit’ weights through inversion of the right-hand-side, i.e.

$$A_j = [C_{p_{i,j}} \frac{dy_j}{dx_j}]^{-1} * C_{D_p}^i$$

The weights were found through least squares fit of the pre-test Mach 0.3 and 0.4 VR-12 CFD solutions. These were the same datasets used to determine the original tap distribution layout. As such, lift, pitching moment, and drag integration results are based on the same ‘input’ data. Using the linear least squares solution, the drag error is reduced to less than 0.025 for all angles

of attack, as highlighted for the Mach 0.3 CFD case in Figure 678. These quadrature weights were subsequently applied to the IRT datasets and produced much more satisfactory comparisons between the post-test CFD and test results. The overall drag agreement matches that found for lift and pitching moment. Example results for Mach 0.3 and  $k = 0.07$  are shown in Figure 679. The ensemble average, unique data points,  $\pm 2\sigma$ , and CFD lines are all displayed.

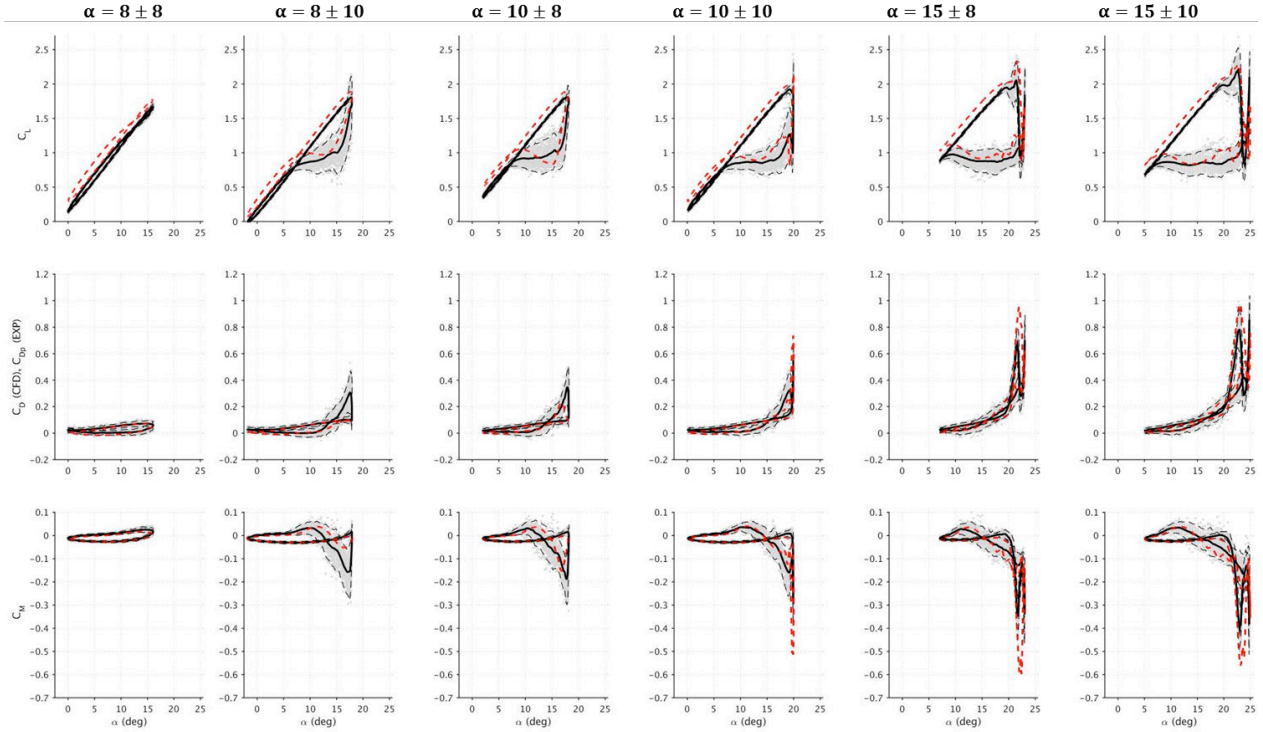


**Figure 679. Mach 0.3  $k=0.07$  baseline VR-12 CFD and experiment comparison. Drag calculated through the method described in this appendix. Gray points display individual points, black solid lines show the ensemble average, dashed black  $\pm 2\sigma$ , and the dashed red indicate the post-test CFD solutions.**



REPORT DOCUMENTATION PAGE				Form Approved OMB No. 0704-0188	
<p>The public reporting burden for this collection of information is estimated to average 1 hour per response, including the time for reviewing instructions, searching existing data sources, gathering and maintaining the data needed, and completing and reviewing the collection of information. Send comments regarding this burden estimate or any other aspect of this collection of information, including suggestions for reducing this burden, to Department of Defense, Washington Headquarters Services, Directorate for Information Operations and Reports (0704-0188), 1215 Jefferson Davis Highway, Suite 1204, Arlington, VA 22202-4302. Respondents should be aware that notwithstanding any other provision of law, no person shall be subject to any penalty for failing to comply with a collection of information if it does not display a currently valid OMB control number.</p> <p><b>PLEASE DO NOT RETURN YOUR FORM TO THE ABOVE ADDRESS.</b></p>					
1. REPORT DATE (DD-MM-YYYY) 01-09-2016		2. REPORT TYPE Contractor Report		3. DATES COVERED (From - To) 10/2012-9/2015	
4. TITLE AND SUBTITLE Dynamic Stall Suppression Using Combustion-Powered Actuation (COMPACT)				5a. CONTRACT NUMBER NNC12CA36C	
				5b. GRANT NUMBER	
				5c. PROGRAM ELEMENT NUMBER	
6. AUTHOR(S) Claude G. Matalanis, Patrick O. Bowles, Solkeun Jee, Byung-Young Min, Andrzej E. Kuczek, Paul F. Croteau, Brian E. Wake, Thomas Crittenden, Ari Glezer, Peter F. Lorber				5d. PROJECT NUMBER	
				5e. TASK NUMBER	
				5f. WORK UNIT NUMBER	
7. PERFORMING ORGANIZATION NAME(S) AND ADDRESS(ES) United Technologies Research Center East Hartford, CT				8. PERFORMING ORGANIZATION REPORT NUMBER Final Report	
9. SPONSORING/MONITORING AGENCY NAME(S) AND ADDRESS(ES) National Aeronautics and Space Administration Washington, DC 20546-0001				10. SPONSOR/MONITOR'S ACRONYM(S) NASA	
				11. SPONSOR/MONITOR'S REPORT NUMBER(S) NASA/CR-2016-219336	
12. DISTRIBUTION/AVAILABILITY STATEMENT Unclassified-Unlimited Subject Category 34 Availability: NASA STI Program (757) 864-9658					
13. SUPPLEMENTARY NOTES An electronic version can be found at <a href="http://ntrs.nasa.gov">http://ntrs.nasa.gov</a> .					
14. ABSTRACT Retreating blade stall is a well-known phenomenon that limits rotorcraft speed, maneuverability, and efficiency. Airfoil dynamic stall is a simpler problem, which demonstrates many of the same flow phenomena. Combustion Powered Actuation (COMPACT) is an active flow control technology, which at the outset of this work, had been shown to mitigate static and dynamic stall at low Mach numbers and showed great promise for success at higher Mach numbers. The work detailed in this report documents a 3-year effort focused on assessing the effectiveness of COMPACT for dynamic stall suppression at freestream conditions up to Mach 0.5. The work done has focused on implementing COMPACT on a high-lift rotorcraft airfoil: the VR-12. This selection was made in order to ensure that any measured benefits are over and above the capabilities of state-of-the-art high-lift rotorcraft airfoils. The detailed Computational Fluid Dynamics (CFD) simulations, wind-tunnel experiments, and system-level modeling conducted have shown the following: (1) COMPACT, in its current state of development, is capable of reducing the adverse effects of deep dynamic stall at Mach numbers up to 0.4; (2) The two-dimensional (2D) CFD results trend well compared to the experiments; (3) Implementation of the CFD results into a system-level model suggest that significant rotor-level benefits are possible.					
15. SUBJECT TERMS Dynamic Stall, Active Flow Control, Rotorcraft, Aerodynamics, Combustion Actuator, COMPACT					
16. SECURITY CLASSIFICATION OF:			17. LIMITATION OF ABSTRACT	18. NUMBER OF PAGES	19a. NAME OF RESPONSIBLE PERSON
a. REPORT	b. ABSTRACT	c. THIS PAGE			STI Information Desk (email: <a href="mailto:help@sti.nasa.gov">help@sti.nasa.gov</a> )
U	U	U	UU	616	19b. TELEPHONE NUMBER (Include area code) (757) 864-9658

---